Diagnostics in Ocular Imaging

Cornea, Retina, Glaucoma and Orbit

Mehrdad Mohammadpour
Editor

Springer

Diagnostics in Ocular Imaging

Mehrdad Mohammadpour
Editor

Diagnostics in Ocular Imaging

Cornea, Retina, Glaucoma and Orbit

Springer

Editor
Mehrdad Mohammadpour
Farabi Eye Hospital
Tehran University of Medical Sciences
Tehran, Iran

ISBN 978-3-030-54862-9 ISBN 978-3-030-54863-6 (eBook)
https://doi.org/10.1007/978-3-030-54863-6

This Springer imprint is published by the registered company Springer Nature Switzerland AG
The registered company address is: Gewerbestrasse 11, 6330 Cham, Switzerland

Thanks to my Compassionate God for all his helps in all aspects of my life from creature to present and for teaching the human being to write their experiences.

To my Parents and Teachers who learned me gratis from the very beginning to the present time.

To my Wife Prof. Maryam Hassanzad for her patients and inexhaustible encourage as a real angel during all this 25 years of common life.

To my Students: Past, Present and future who let me transfer my knowledge to make change in their behavior to help those who need their services.

& finally
To my patients who let me be their physician and to get this expertise.

Foreword

It is my honor to write the foreword for this new book, *Diagnostics in Ocular Imaging: Cornea, Retina, Glaucoma and Orbit*. I congratulate my colleague Dr. Mehrdad Mohammadpour who spearheaded this collaborative endeavor and all contributors, especially Dr. Fedra Hajizadeh, Dr. Sasan Moghimi and Dr. Mohammad Taher Rajabi for providing an outstanding resource for the scientific community.

The rapid technological advances in recent decades have provided us with increasingly more reliable and high-resolution visualization of ocular structures, and ocular imaging has become an integral part of the daily ophthalmic practice for performing screening and diagnostic tests and monitoring responses to treatment. *Diagnostics in Ocular Imaging: Cornea, Retina, Glaucoma and Orbit* is a comprehensive atlas that introduces the reader to the state-of-the-art imaging modalities including computerized corneal topographers, corneal biomechanics analyzers, ultrasound biomicroscopes, aberrometers, optical coherence tomographers and angiographers. Throughout this well-conceived book, which is nicely organized in five main parts and 30 interesting chapters, there are illustrations and fascinating cases that keep the reader engaged regardless of their subspecialty or level of expertise.

Diagnostics in Ocular Imaging: Cornea, Retina, Glaucoma and Orbit is a welcome addition to the libraries of every eye care practitioner and an absolute must-have resource for professionals in the field of ophthalmology. I highly recommend this book as a definitive learning resource to all, especially our residents and fellows in training.

Hassan Hashemi, M.D.
Professor of Ophthalmology, Department of Ophthalmology Farabi Eye Hospital, Tehran University of Medical Sciences Tehran, Iran

Preface

It is a great honor for me to introduce this comprehensive book entitled *Diagnostics in Ocular Imaging; Cornea, Retina, Glaucoma and Orbit* which covers nicely all four major subspecialties of ophthalmology that needs ocular imaging before any major diagnosis or intervention.

Nowadays, computerized imaging has become the cornerstone and sin qua none component for diagnosis and treatment both in medical and surgical fields of ophthalmology.

This book has both benefits of a Textbook and an Atlas with introducing not only the common and routine daily practice but also challenging and rare cases that one would encounter in his or her lifelong carrier in all fields of Ophthalmology.

Another major outstanding feature of this book is its potential for training ophthalmology Residents and Fellows in all ocular fields and its future role to be considered as a Reference for Board Examinations.

Therefore, it can benefit not only the postgraduate ophthalmologists in all ocular fields but also is a great help for all ophthalmic trainees.

I cordially thank all the authors for their fantastic contribution in composing all 30 well-organized chapters covering all fields of ophthalmology and updates on emerging technologies of new devices for ocular imaging in detail.

I eagerly wait for the readers' feedbacks, opinions and their constructive reviews for considering them for next editions of the book and hope my colleagues find it helpful in their daily practice.

Best Wishes

Mehrdad Mohammadpour, M.D.
Professor of Ophthalmology, Farabi Excellence
Center of Ophthalmology and Eye Hospital
Tehran University of Medical
Sciences, Tehran, Iran

Contents

Corneal Imaging: Topography Versus Tomography

Topographic Pattern Recognition: Normal Versus Keratoconus

Sepehr Feizi

Introduction

Two-thirds of the ocular refractive power is contributed by cornea. The majority of refraction takes place at the air-tear film interface due to the maximum difference in the refractive index between air and tear film. Therefore, the shape of the anterior corneal surface plays a major role in the formation of retinal images. The posterior corneal surface has a lower radius of curvature and is steeper as compared to the anterior surface. The refractive power of posterior corneal surface is −6.0 D because the refractive index of the corneal stroma (1.376) is greater than that of the aqueous humor (1.373); therefore, the light diverges as it passes from the corneal stroma to the aqueous humor. The summation of refractive power of the anterior and posterior corneal surfaces provides a total corneal power of approximately 43.5 D at the corneal center.

True refractive power of an optical system is the summation of the refractive power of each elements. The power of each refractive surface is calculated according to the following formula:

$$P = n2 - n1/r$$

where n1 and n2 are refractive indices surrounding the refractive surface and r is the radius of curvature of this surface. The refractive power of the anterior corneal surface can be measured using a Placido disc-based corneal topographer which determines the radius of curvature of this surface. However, this device is unable to measure the refractive power of the posterior corneal surface. To consider the effect of refractive power of the posterior cornea, standard keratometric index (1.3375) rather than true corneal refractive index (1.373) is used by the

S. Feizi (✉)
Shahid Beheshti University of Medical Sciences, Tehran, Iran
e-mail: sepehrfeizi@yahoo.com

M. Mohammadpour (ed.), *Diagnostics in Ocular Imaging*,
https://doi.org/10.1007/978-3-030-54863-6_1

topographers to estimate the total corneal power. For example, a cornea with a radius of curvature of 7.7 mm in the anterior surface has an approximate power of 43.83 D (337.5/7.7).

Corneal Asphericity

Cornea is considered spheric at the central 4-mm area. Beyond this area, it takes an aspheric shape which means the corneal power decreases from the center to the periphery. This feature provide a prolate profile for the cornea. In some conditions, like after refractive surgeries performed for the correction of myopia, the dioptric power of the corneal is lower in the central area than that in the peripheral area, producing an oblate profile. Table 1 provides the asphericity values (Q values) which determine how corneal asphericity changes from the center to the periphery.

Astigmatism

Astigmatism is caused by unequal corneal powers at different meridians resulting in the formation of two or more focal lines from a point object. Astigmatism is divided into regular and irregular. The corneal power changes regularly from flat meridian to steep meridian in regular astigmatism, whereas changes in corneal power between different meridians have no consistent patterns in irregular astigmatism. Based on the orientation of the steep meridian, regular astigmatism is further categorized into with-the-rule, against-the-rule, and oblique astigmatism. The orientation of the steep meridian is between 60 and 120 degrees in with-the-rule astigmatism and between 0 and 30 degrees or 150 and 180 degrees in against-the-rule astigmatism. In oblique astigmatism, the orientation of two principle meridians is neither horizontal nor vertical.

Table 1 Asphericity (Q) values of different corneas

Asphericity	Shape	Description	Example
>0	Oblate	Cornea is flatter in the central area as compared to the peripheral area	After refractive surgeries for the correction of myopia
0	Spherical	Similar curvature at the center and periphery	Ball
$-0.26 \leq Q < 0$	Prolate	Cornea is steeper at the central area as compared to the peripheral area	Normal cornea
<-0.26	Hyperprolate	Cornea is abnormally steep in the central area	Keratoconus and after refractive surgeries performed for the correction of hyperopia

Principles of Placido Disc-Based Topography

In this technique of corneal imaging, the Placido disc is used to project a set of concentric rings on the cornea, and the shape of the corneal surface is characterized by assessing the reflection of rings off the anterior corneal surface. The corneal curvature and power are directly calculated from the data of thousands of points on the rings via sophisticated algorithms. Based on the type of the Placido discs, there are two types of topographers: topographers that use small-cone Placido disc and those that use large-cone Placido disc. Both types of topographers project a series of concentric rings of light on the anterior corneal surface. Small-cone Placido disc topographers have some advantages over large-cone Placido disc topographers including projection of more rings on the cornea and having a shorter working distance. Therefore, small-cone Placido disc systems provide a large number of measurement points and can provide more accurate data of the corneal periphery. However, these systems require a steady hand to ensure that the data acquisition is accurate. The Magellan Mapper (Nidek), Medmont E300 (Medmont), and Scout and Keratron (EyeQuip) are prototypes of small-cone topography systems. Large-cone Placido disc systems project fewer rings onto the cornea and have a longer working distance as compared to small-cone topographers. The longer working distance can mitigate the detrimental effects of eye misalignment on the accuracy of data; however, this longer distance results in the obscuration of the corneal periphery due to the shadow of nose and eyebrows (Fig. 1). Prototypes of large-cone topographers are the ReSeeVit (Veatch Ophthalmic Instruments), ATLAS 995 and 9000 (CarlZeiss Meditec), and Tomey (Computed Anatomy TMS-1).

Color Scale Settings

Different color scales are used in corneal topography maps to exhibit curvature data; areas with greater power are illustrated in warm colors including red and orange, whereas areas with lower power are depicted in cool colors including green and blue. Topographers use two different scales to display color maps including “normalized” and “absolute (or standard)” scales. The normalized scale displays the range of color codes calculated from the specific map(s). In this scale, the software determines the lowest and the highest power of the evaluated cornea and then, uses a determined number of color codes to display the map. These color codes adapt to the range of powers on the corneal surface and vary for each cornea. This scale provides an excellent general view of the entire cornea, as the scale shows the flattest to steepest readings. The same map plotted with a different scale or a different step size looks very different; relative scales or large step sizes mask characteristic patterns of irregular astigmatism (i.e. keratoconus), while small step sizes tend to exaggerate normal patterns to appear like abnormal ones (Fig. 2).

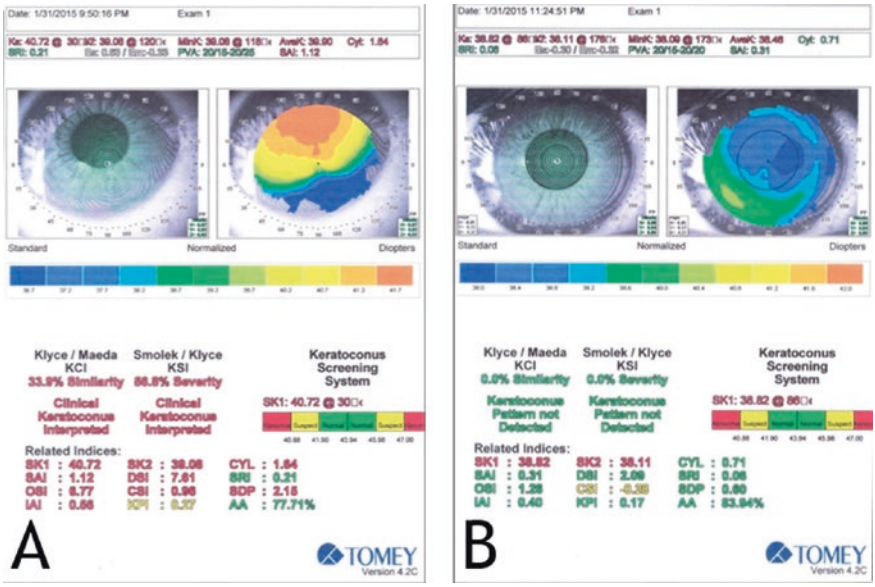

Fig. 1 Effects of the subject's fixation on the results of corneal topography. **a** Upward rotation of the eye. The topographic pattern and indices suggest that the subject has keratoconus. **b** Central fixation. Appropriate fixation of the same subject results in the normalization of all parameters. Note, the subject has undergone corneal refractive surgery and the central cornea is flatter than the peripheral area (oblate profile). The shadow of eyelashes obscures the peripheral zone of the image

The absolute (standard) scale shows a fixed range of color codes selected in the settings of the topographer irrespective of the map selected. The dioptric range, step size and number of colors are constant with this scale which allows for easier comparison to other examinations (Fig. 2).

Axial Map

The axial or sagittal map, the most common map used, displays the curvature of the anterior corneal surface in relation to the visual axis. This map, which gives an average picture (i.e. smoother appearance) of the anterior corneal curvature and is mainly used for screening, allows to correlate the anterior surface shape to the subject's refractive status. In this map, the cornea is considered as a sphere and the distance between a defined point and visual axis determines the radius of curvature of the cornea at that point. The drawback of this map is its inability to evaluate subtle changes in the corneal curvature, especially at the corneal periphery (Figs. 3 and 4).

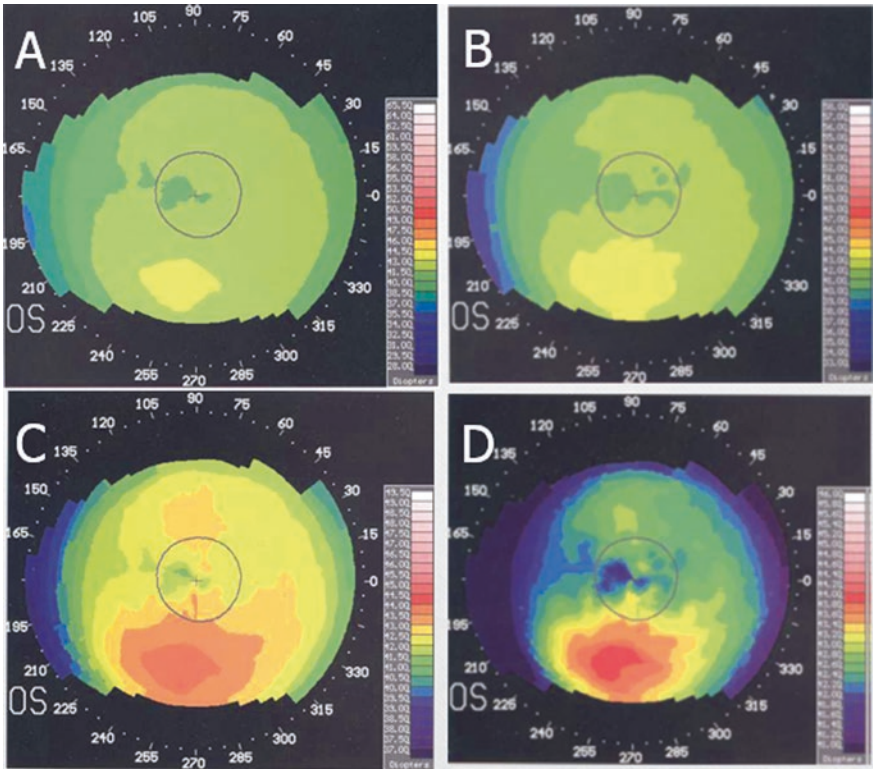

Fig. 2 Effect of different step sizes (**a**: 1.0 D, **b**: 0.75 D, **c**: 0.50 D, and **d**: 0.25 D) on the topographic pattern. An absolute scale is used to depict a cornea with keratoconus. The range of color codes used in the scale is wider than that used in the map. As indicated, large step sizes (**a** and **b**) mask an inferior steepening pattern in a keratoconus-affected cornea, whereas small step sizes (**c** and **d**) exaggerate this pattern

Tangential Map

The tangential or instantaneous map calculates each measured point of data at a 90° "tangent" to its surface and provides a more detailed description of the corneal shape, especially at the corneal periphery. Therefore, this map can define small curvature changes and provide a clearer view of the anterior surface curvatures in corneal pathologies like keratoconus. This feature is very useful to localize the size and location of corneal pathologies which can be used for the diagnosis of corneal diseases and determining an appropriate treatment plan such as the ideal lens design and the position of the intrastromal corneal ring segments for the treatment of keratoconus. Although the tangential or instantaneous map shows true radius of curvature data at each point, it appears more noisy/irregular (Fig. 3).

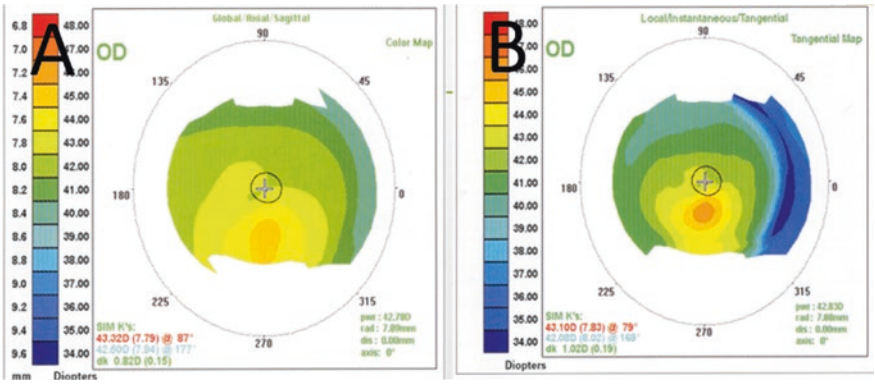

Fig. 3 Comparison of axial (**a**) and tangential (**b**) map of the same cornea. The tangential map provides a more detailed description of the corneal shape (**b**)

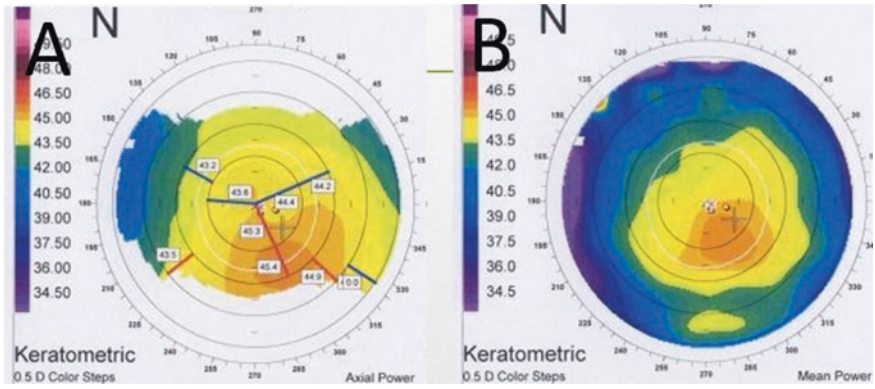

Fig. 4 Comparison of axial (**a**) and refractive power (**b**) map of the same cornea. The refractive power map demonstrates the quality of the retinal image produced by this cornea (**b**)

Refractive Power Map

The refractive power (mean power) map determines the quality of vision a subject may achieve from the corneal surface throughout the pupillary zone (Fig. 4). Refractive power maps are less commonly used but are most helpful for understanding the imaging power of the cornea and analyzing surgical effects; more uniform refractive power within the entrance pupil indicates the better ability of the anterior corneal surface to refract light properly. The drawback of this map is that it does not provide information on the shape of the anterior corneal surface.

However, this map is very effective for the interpretation of the quality of vision attainable from a subject's anterior corneal surface. For example, when comparing preoperative and postoperative corneal reshaping procedures, the refractive map demonstrates the extent that corneal surface alters contribute to the subject's quality of vision.

Elevation Map

The elevation map determines the height of the cornea in relation to the sphere that best matches the average curvature of the cornea (best fit sphere). Placido disc topography systems do not actually measure elevation; instead, they use sophisticated algorithms to extrapolate elevation data by reconstructing actual curvature. The elevation data which are represented in microns indicate the difference between the actual corneal surface and the best-fit reference sphere.

Indications

Advances in digital photography and computer processing have vastly increased the utility of corneal topography. Corneal topography is indicated for the screening of refractive surgery candidates; diagnosis of corneal diseases including keratoconus, pellucid marginal degeneration, terrien marginal degeneration; contact lens fit; evaluation of the effect of surgical interventions including corneal collagen crosslink and intrastromal corneal ring segment implantation; and selective suture removal after corneal transplantation. This diagnosis device is also used for the monitoring of the corneal disease progression.

Nomenclature of Keratoconus

Different terms are used to refer to the different stages of keratoconus. Three terms are widely used in the literature for the earliest stage of the diseases, including forme fruste keratoconus, preclinical or subclinical keratoconus, and keratoconus suspect. One needs to differentiate the early stage of the disease from other conditions that can cause abnormal topographic patterns, including corneal warpage due to contact lens wear, a prominent tear meniscus, dry eye disease with poor precorneal tear film, misalignment of the eye during obtaining the topography, displaced apex syndrome, and unintentional external pressure on the eye. The contact lens-induced cornea warpage can linger for quite a long period.

Forme Fruste Keratoconus

Forme fruste keratoconus which was first introduced by Amsler in 1961 is described as the fellow eyes of unilateral keratoconus with no clinical findings (corneal thinning, Fleischer's ring, or Vogt's striae), scissoring on retinoscopy, or any significant topographic changes such as inferior steepening.

Subclinical Keratoconus

Subclinical keratoconus is defined as the fellow eyes of unilateral keratoconus that have no history of ocular trauma, ocular surgery, contact lens wear, or slit-lamp or clinical findings (retinoscopic, keratometric, or biomicroscopic) of keratoconus but demonstrate inferior steepening or asymmetric bowtie pattern with SRAX in corneal topography.

Keratoconus Suspect

This term should appropriately be reserved for corneas that have no manifestation of clinical keratoconus in either eye but demonstrates subtle changes in corneal topography, including a localized area of inferior steepening, or an asymmetrical, truncated or skewed-axis bowtie.

Computerized Corneal Topography for the Diagnosis of Keratoconus

Corneal topography is an essential tool to perform the evaluation in refractive surgery preoperatively; it presents the curvature properties of the anterior corneal surface and is used to measure and evaluate its pattern and profile. The advances in corneal refractive surgery techniques have made it necessary to precisely analyze the topographic features of the cornea and differentiate normal corneas from the diseased ones to avoid iatrogenic ectasia postoperatively. Subclinical keratoconus, which is the most important risk factor for the development of post-refractive surgery ectasia, is usually asymptomatic and can be undiagnosed in a routine ophthalmic examination. The conventional keratometer only determines an estimation of the anterior corneal power at the paracental area but is inappropriate for the evaluation of candidates for refractive surgery. Recently, rapid advances in corneal imaging techniques have paralleled those of corneal refractive surgery, and evaluation of the cornea by computerized topography has become the standard

preoperative evaluation in clinical practice. The main purpose of this evaluation is to diagnose epithelial irregularities and stromal abnormalities, measure corneal astigmatism, and determine refractive stability or undiagnosed corneal diseases, such as forme fruste keratoconus, and pellucid marginal degeneration. Computerized topography provides three different data sets, including keratometric data, statistical indices, and map patterns.

Keratometric Data

Keratometric measurement provides a good accuracy in diagnosing keratoconus. Central keratometry is the mean value of corneal power for the areas with diameters of 2, 3 and 4 mm. A central keratometry between 47.2 D and 48.7 D is suggestive of keratoconus and a central keratometry larger than 48.7 diopters indicate clinical manifest keratoconus. In addition, a difference in central keratometry >1.0 D between two eyes is considered for differentiating subclinical keratoconus and normal eyes.

Maximum keratometry refers to the power of a point in the cornea that has the greatest power. This point can be inside or outside the central area. Minimum keratometry refers to the power of a point in the cornea that has the lowest power and can be inside or outside the central area.

Simulated keratometry is similar to the measurement achieved by manual keratometry and indicates the corneal power of the flat and steep meridian at the 3-mm paracentral area. If these two meridians are not perpendicular, the machine measures the magnitude of the steep meridian and that of 90 degrees apart from the steep meridian. Mean simulated keratometrty is the average of these two measurements and keratometric astigmatism is the difference between these two measurements. Astigmatism has been shown to be higher in keratoconus. Keratometric astigmatism of >1.5 D has an acceptable ability for the screening of keratoconus.

Statistical Indices

Corneal topography provides several quantitative indices which can be used to screen for keratoconus. These indices are either simple that evaluate one parameter or combined that use multivariate combinations of the topographic indices to provide one index. Simple indices include surface asymmetry index (SAI), surface regularity index (SRI), predicted visual acuity (PVA), Inferior–superior (I–S) value, irregular astigmatism index (IAI), opposite sector index (OSI), differential sector index (DSI), central/surround index (CSI), average central dioptric power (ACP), and analyzed area (AA). Combined indices include keratoconus severity index (KSI), keratoconus prediction index (KPI), and keratoconus percentage index (KPI). The combined indices are calculated using artificial neural networks.

Simple Indices

SAI is an index that shows a mean value of the power differences among the points spatially located at 180° from 128 equidistant meridians. A radially symmetrical optical surface has a SAI value of zero, and this value increases as the amount of asymmetry increases. A SAI value >0.5 is considered abnormal.

SRI is a local descriptor of regularity in a central zone of 4.5 mm of diameter that consists of the central ten rings of Placido disc. This index measures power gradient differences between successive pairs of rings in 256 equidistant semi-meridians and has good correlation with the visual acuity. A SRI value >1 is considered abnormal.

I–S value, which computes the vertical gradient cornea power of 6 mm region (inferior-superior dioptric asymmetry), is the refractive power difference between the 5 inferior points and the 5 superior points of the corneal area located at 3 mm from the corneal apex at 30 degree intervals. A negative value indicates steeper superior curvature while a positive value indicates steeper inferior curvature. An I–S value between 1.4 and 1.8 D suggests a keratoconus suspect, while a greater value suggests clinical keratoconus.

Relative skewing of the steepest radial axes above and below the horizontal meridian (SRAX) is defined as the angle between the orientation of more curved superior hemi-meridian and that of more curved inferior hemi-meridian and is an index that reflects the irregular astigmatism. An asymmetric bowtie pattern with a SRAX >21 degrees on corneal topography has a high accuracy in detecting keratoconus-affected corneas. This value is only important if keratometric astigmatism is >1.5 D. It has been found that a central keratometry >47.20 D, I–S higher than 1.5 D and SRAX index above 21° can identify 98% of the patients with keratoconus.

IAI is a measure of dioptric variables along each hemi-meridian, which is normalized by the number of measured points and the mean corneal power. An IAI value of >0.5 is considered an abnormality thresholds of keratoconus.

AA is the ratio of the area analyzed to the area circumscribed by the outermost peripheral ring.

CSI is an index that quantifies the average power difference between the central area of 3 mm diameter and a half-peripheral ring that is 3 and 6 mm diameters. CSI >1.0 is considered abnormal.

DSI is another index indicating the average power difference between sectors of 45° with the lowest and highest power. A DSI value > 3.50 is considered abnormal.

OSI is an index that quantifies average power difference between opposing sectors of 45°. A value of >2.10 is considered abnormal.

Combined Indices

Keratoconus prediction index (KPI) is a linear discriminate analysis of eight quantitative topographic indices from videokeratography to detect keratoconus. These

indices include simulated K1, simulated K2, SAI, CSI, DSI, OSI, IAI and AA. A KPI score >0.23 is suggestive of keratoconus. However, it is not always useful for the screening of keratoconus suspect because it has a significant overlapping between keratoconus suspect and keratoconus in its scoring system. This index has a sensitivity of 68% and a specificity of 99% for the detection of keratoconus.

KCI, also known as the Klyce-Maeda method, is derived by using a binary decision-making tree and linear discriminant analysis of eight indices obtained by the corneal topogrpahy. This method can discriminate a keratoconic cornea from a normal cornea. A KCI value of >0 is suggestive of keratoconus.

KSI, also known as the Smolek-Klyce method, is an index derived from neural network algorithm using ten topographic indices as inputs. This multivariate system computes the severity of keratoconus, which possibly differentiates among a normal cornea, a suspected keratoconic cornea and a keratoconus-affected cornea. A KSI value of less than 15% is considered normal, values between 15 and 30% as keratoconus suspect, and above this value is considered clinical keratoconus.

The KISA% index provides an algorithm to quantify outputs from corneal topography and is computed from four indices as follows;

$$\text{KISA\%} = \frac{(\text{K}) \times (\text{I} - \text{S}) \times (\text{AST}) \times (\text{SRAX}) \times 100}{300}$$

where, K is central keratometry value, I–S is inferior to superior value, AST is the regular astigmatism (difference between the magnitude of the steepest and flattest simulated keratometry), and SRAX is the skewed radial axis index (an expression of irregular astigmatism). This index is highly sensitive and specific in differentiating a healthy cornea from a keratoconus-affected cornea. A value of between 60 and 100% represents keratoconus suspect and that greater than 100% is highly suggestive of clinical keratoconus with minimal overlapping with normal corneas. This index, however, has a major drawback in its use as a tool for screening keratoconus in refractive surgery candidates because it has a significant number of false negatives. The abovementioned neural network systems are the 3 most widely used diagnostic systems based on corneal topography to differentiate healthy cornea, keratoconus suspect, subclinical keratoconus, and clinical keratoconus.

Topographic Maps

Different colors are used to represent dioptric values in the topographic map: cooler colors illustrate flatter curvatures (lower power), and warmer colors exhibit steeper curvatures (higher power). Ten different topographical patterns are proposed by Rabinowitz et al. in 1996, based on the quantitative indices and database of videokeratography patterns in the 390 corneas of normal subjects. These patterns include round, oval, superior steepening, inferior steepening, irregular, symmetric bowtie, symmetric bowtie with SRAX, asymmetric bowtie with inferior

steepening, asymmetric bowtie with superior steepening, and asymmetric bowtie with SRAX (Fig. 5). These patterns have different distribution in the normal population: round pattern 22.6%, oval pattern 20.8%, symmetric bowtie pattern 17.5%, asymmetric bowtie pattern 32.1%, and irregular pattern 7.0%. Some of these patterns are associated with normal corneas and the others are abnormal and indicate corneal diseases. Recently, 3 additional patterns related to pellucid marginal degeneration were added. These patterns include butterfly, crab claw, and junctional (Fig. 5).

Round pattern indicates a normal cornea with no significant astigmatism. This pattern is located centrally and the amount of displacement from the corneal center is less than 1 mm. However, it should be noticed that central keratoconus may have nipple cones with a diameter of $\leq$5 mm and are located in the center or slightly below the center of the cornea. In this situation, central keratometry is abnormally high.

Oval pattern indicates a normal cornea with an insignificant amount of astigmatism. This pattern is rarely encountered in keratoconus-affected corneas; in this situation, the pattern may displace inferotemporally or inferonasally.

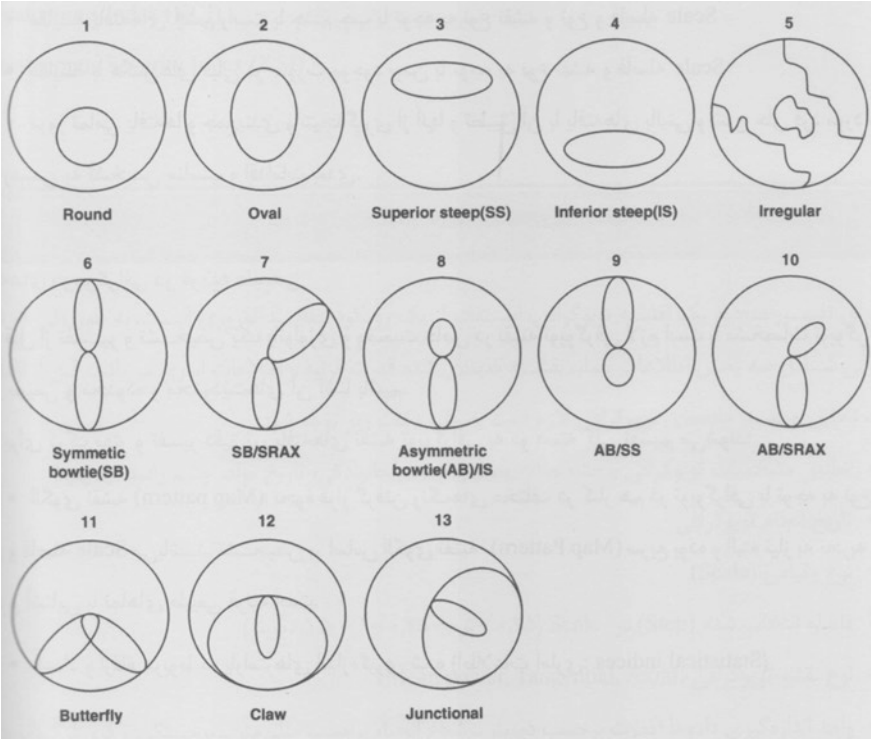

Fig. 5 Different topographical patterns of cornea

In the superior steepening pattern, the steepest area is located superiorly. Inferior corneal steepening is the most common pattern encountered in keratoconus (approximately 80% of keratoconus patients). In this pattern, the steepest area is located inferior or inferotemporal to the corneal center.

Irregular pattern demonstrates steep and flat areas with random distribution. This pattern is encountered in corneal opacities, corneal scars due to trauma, and after corneal transplantation.

Symmetric bowtie pattern which indicates regular astigmatism is located vertically, horizontally, or obliquely, depending on the type of astigmatism. Rarely, this pattern can be encountered in central keratoconus. In this situation, however, the size of the bowtie is small and the power of the cornea is abnormally high.

Symmetric bowtie pattern with SRAX indicates a non-orthogonal (irregular) astigmatism. The two segments are equal but not aligned. SRAX >21 degrees is highly suggestive of keratoconus in a cornea with astigmatism >1.5 D.

Asymmetric bowtie pattern with inferior steepening has two segments that are different in size, shape, and power, and the larger segment is located inferiorly. The vertical asymmetry is defined as the difference between the average inferior and the average superior values at the 5-mm central ring (the second circle of numbers) greater than 1.5 D. In asymmetric bowtie with superior steepening, the superior part of the bowtie is larger or more powerful than the inferior part and the difference between the average superior and the average inferior values at the 5-mm central ring is greater than 2.5 D.

Asymmetric bowtie pattern with SRAX has two different segments which are not aligned. This pattern is considered as abnormal when the angle between the axes of the superior and inferior segments in the innermost circle (3 mm) is more than 21 degrees and simulated keratometric astigmatism is greater than 1.5 D.

The butterfly and crab claw (kissing birds) patterns which are encountered in pellucid marginal degeneration indicate an against-the-rule astigmatism.

Case Presentation

Case 1

A 32 year-old man has a manifest refraction of $-3.5\ -4.25 \times 15^{\circ}$ OD and $-2.75\ -4.50 \times 160^{\circ}$ OS. Best-spectacle corrected visual acuity is 20/20 OU. Corneal topography demonstrates a symmetric bowtie pattern in both eyes. Corneal astigmatism is with-the-rule which means the orientation of astigmatism is between 60 and 120 degrees. The superior and inferior segments of the bowties have similar power, size, and shape, and there is no skew in their alignment, indicating regular astigmatism in these eyes. Please, note the presence of corneal enantiomorphism which means mirror symmetry in topographic patterns between the right and left corneas.

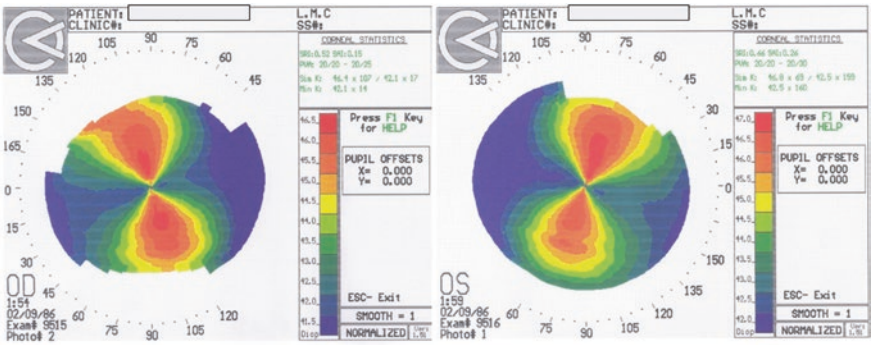

Case 2

A 54 year-old man has a manifest refraction of -1.75 $-2.0 \times 100°$ OD and -2.0 $-1.5 \times 80°$ OS. Best-spectacle corrected visual acuity is 20/20 OU. Corneal astigmatism is oriented horizontally (against-the-rule astigmatism). The corneal topography demonstrates an asymmetric bowtie pattern as the size of the temporal segment is greater than that of the nasal segment. Please, note the presence of corneal enantiomorphism which means mirror symmetry in topographic patterns between the right and left corneas.

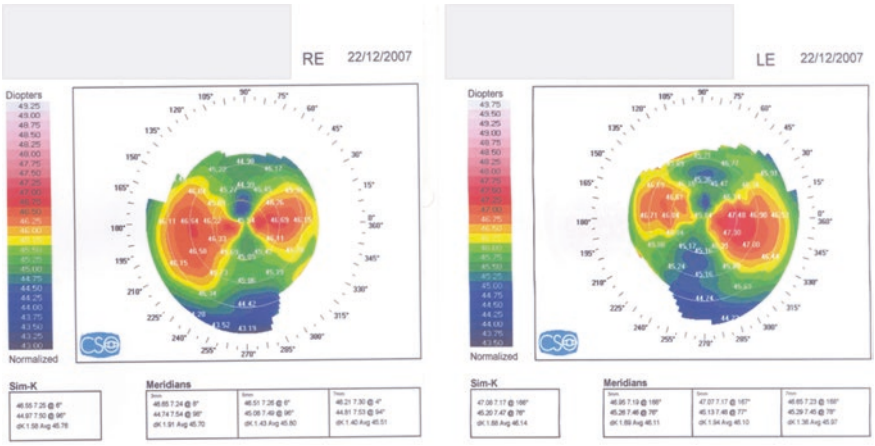

Case 3

A 30 year-old woman was examined for refractive surgery. Best-spectacle corrected visual acuity was 20/20 OD with $-4.25\ -0.50 \times 110°$. Central corneal thickness measured using an ultrasonic pachymetry was 498 microns in this eye. In the corneal topography, keratometric measurements are normal and all simple and combined indices, except for different sector index, are within the normal range; however, an inferior steepening is evident in the color-coded map. Similar findings were found in the fellow eye. The patient was diagnosed with keratoconus suspect and the surgery was cancelled.

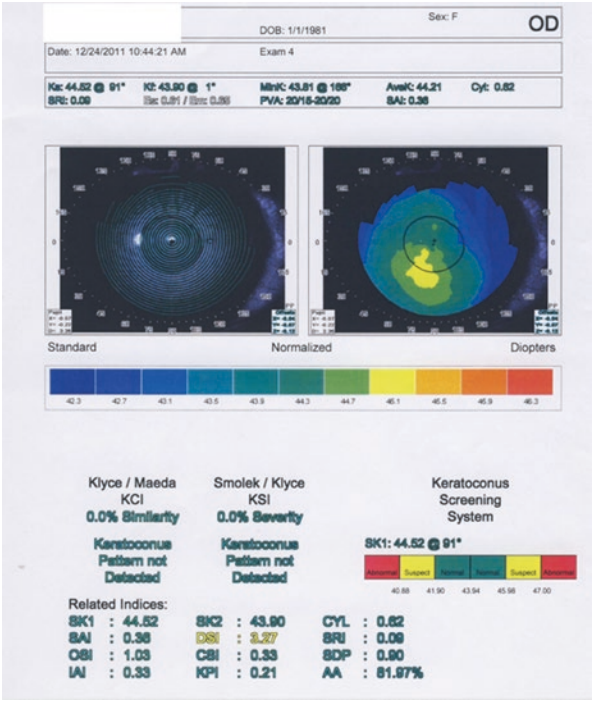

Case 4

A 36 year-old woman has a manifest refraction of $-6.0\ -1.0 \times 25°$ OD and -5.75 OS with a best-spectacle corrected visual acuity of 20/20 OU. Topographic patterns are asymmetric bowtie without SRAX. Please, note some indices are suspect (highlighted in yellow) and some indices are abnormal (highlighted in red).

Despite these findings, keratoconus index and keratoconus severity index are interpreted normal. The patient is diagnosed with keratoconus suspect.

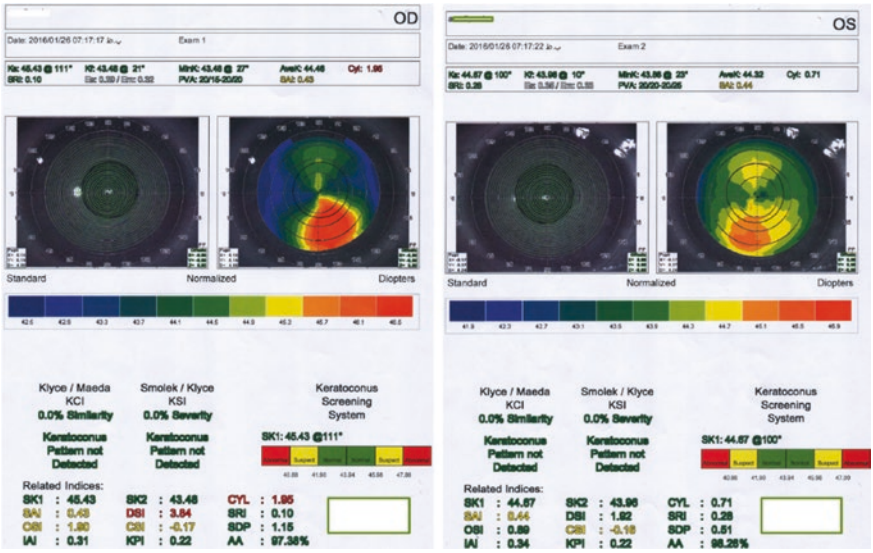

Case 5

A 21 year-old woman has a manifest refraction of $-4.75\ -2.50 \times 20°$ with a best-spectacle corrected visual acuity of 20/20 OS. Corneal topography demonstrates asymmetric bowtie with superior steepening. Some statistical indices are suspect and some are abnormal. Please, note keratoconus suspect is interpreted by the keratoconus severity index.

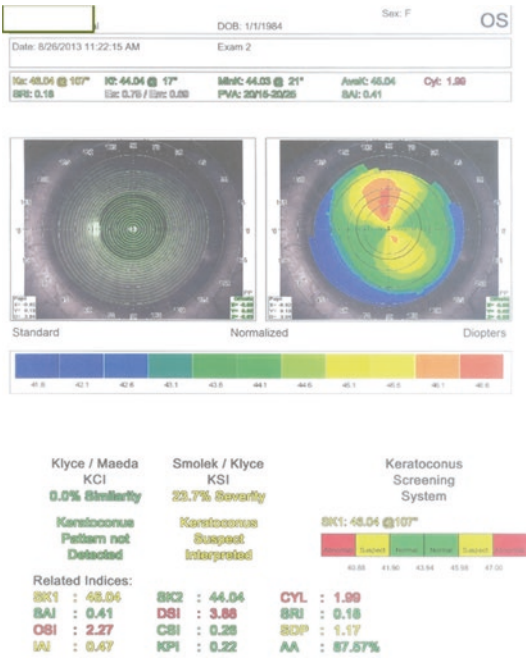

Case 6

A 24 year-old keratoconus-affected woman has a manifest refraction of −5.0 −7.5 × 30° and best-spectacle corrected visual acuity of 20/60 OD. Corneal topography reveals that all keratometric measurements and statistical indices are abnormally high. Topographic pattern is asymmetric bowtie with inferior steepening. Please, note the presence of SRAX

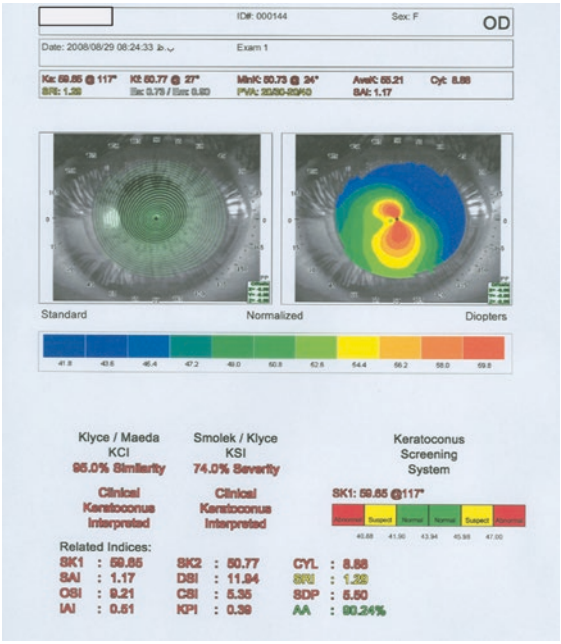

Case 7

A 51 year-old man has a manifest refraction of $-3.0\ -5.75 \times 70^{\circ}$ with a best-corrected visual acuity of 20/60 OD. The corneal topography demonstrates an against-the-rule irregular astigmatism with a crab claw pattern. The patient is diagnosed with pellucid marginal degeneration.

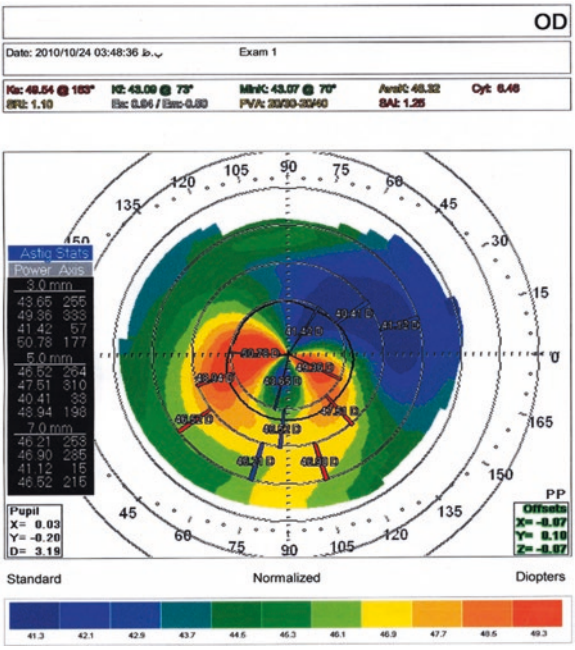

References

1. Anderson D, Kojima R. Topography: A clinical pearl. Optom Manag. 2007;42:35.
2. de Sanctis U, Aragno V, Dalmasso P, Brusasco L, Grignolo F. Diagnosis of subclinical keratoconus using posterior elevation measured with 2 different methods. Cornea. 2013;32:911–5.
3. Gatinel D. Corneal topography and wave front analysis. In: Albert & Jakobiec's principles & practice of ophthalmology, 3rd ed. Philadelphia, PA: Saunders/Elsevier; 2008. p. 921–963.
4. Gatinel D, Malet J, Hoang-Xuan T, Azar DT. Corneal elevation topography: best fit sphere, elevation distance, asphericity, toricity and clinical implications. Cornea. 2011;30:508–15.
5. Kanellopoulos AJ, Asimellis G. OCT-derived comparison of corneal thickness distribution and asymmetry differences between normal and keratoconic eyes. Cornea. 2014;33:1274–81.
6. Kim E, Weikert MP, Martinez CE, Klyce SD. Keratometry and topography. In: Cornea, 4th ed. Holland: Elsevier; 2017. p. 144–153.
7. Martínez-Abad A, Piñero DP. New perspectives on the detection and progression of keratoconus. J Cataract Refract Surg. 2017;43:1213–27.
8. Muftuoglu O, Ayar O, Ozulken K, Ozyol E, Akıncı A. Posterior corneal elevation and back difference corneal elevation in diagnosing forme fruste keratoconus in the fellow eyes of unilateral keratoconus patients. J Cataract Refract Surg. 2013;39:1348–57.
9. Naroo SA, Cervino A. Corneal topography and its role in refractive surgery. In: Refractive surgery: a guide to assessment and management. London, UK: Elsevier; 2004. p. 9–16.

10. Placido A. Novo instrumento per analyse immediate das irregularitades de curvatura da cornea. Periodico Oftalmol Practica. 1880;6:44–9.
11. Prakash G, Agarwal A, Mazhari AI, Kumar G, Desai P, Kumar DA, Jacob S, Agarwal A. A new, pachymetry-based approach for diagnostic cutoffs for normal, suspect and keratoconic cornea. Eye. 2012;26:650–7.
12. Rabinowitz YS. Videokeratographic indices to aid in screening for keratoconus. J Refract Surg. 1995;11:371–9.
13. Rabinowitz YS1, Yang H, Brickman Y, Akkina J, Riley C, Rotter JI, Elashoff J. Videokeratography database of normal human corneas. Br J Ophthalmol. 1996;80:610–6.
14. Randleman JB, Russell B, Ward MA, Thompson KP, Stulting RD. Risk factors and prognosis for corneal ectasia after LASIK. Ophthalmology. 2003;110:267–75.
15. Randleman JB, Woodward M, Lynn MJ, Stulting RD. Risk assessment for ectasia after corneal refractive surgery. Ophthalmology. 2008;115:37–50.
16. Reddy JC, Rapuano CJ, Cater JR, Suri K, Nagra PK, Hammersmith KM. Comparative evaluation of dual Scheimpflug imaging parameters in keratoconus, early keratoconus, and normal eyes. J Cataract Refract Surg. 2014;40:582–92.
17. Salz JJ, Trattler W. Patient evaluation and selection in refractive surgery. In: Cornea, 4th ed. Holland: Elsevier; 2017. p. 1719–27.
18. Santhiago MR, Smadja D, Gomes BF, Mello GR, Monteiro ML, Wilson SE, Randleman JB. Association between the percent tissue altered and post-laser in situ keratomileusis ectasia in eyes with normal preoperative topography. Am J Ophthalmol. 2014;158:87–95.
19. Schallhorn JM, Tang M, Li Y, Louie DJ, Chamberlain W, Huang D. Distinguishing between contact lens warpage and ectasia: Usefulness of optical coherence tomography epithelial thickness mapping. J Cataract Refract Surg. 2017;43:60–6.
20. Smadja D. Topographic and tomographic indices for detecting keratoconus and subclinical keratoconus: a systematic review. Int J Keratoconus Ectatic Corneal Dis. 2013;2:60–4.
21. Tanuj D, Neha M, Tarun A. New investigations in ophthalmology, vol. 3, 2nd ed. 2017. p. 30.
22. Taravella M, Davidson RS. Corneal topography and Wavefront Imaging. In: Ophthalmology, 4th ed. Philadelphia, PA: Saunders/Elsevier; 2014. p. 168–73.
23. Toprak I, Yaylalı V, Yildirim C. A combination of topographic and pachymetric parameters in keratoconus diagnosis. Cont Lens Anterior Eye. 2015;38:357–62.
24. Yeu E, Belin MW, Khachikian SS. Topographic analysis in keratorefractive surgery. In: Cornea, 4th ed. Holland: Elsevier; 2017. p. 1728–35.

Orbscan

Mehrdad Mohammadpour and Zahra Heidari

Introduction

Orbscan is the slit scanning corneal topographer can measure anterior curvature, anterior and posterior elevation, corneal pachymetry, anterior lens, anterior iris (anterior chamber depth), pupil size and white to white corneal diameter. The overwhelming advantage of slit-scan systems is that they measure multiple ocular surfaces (Fig. 1).

There are 3 generations of Orbscan:

Orbscan I → Only slit-scan topography.
Orbscan II → The Placido disk is added.
Orbscan IIz → Wavefront analysis is added (Zywave).
Orbscan III → The advance Placido system.

The second generation of Orbscan (IIz) combines a slit scanning and a Placido disc (40 rings) with tracking systems measures spontaneous eye movement. The Placido disk used for kerotometric analysis and the location of Placido rings related to the camera position and the radial gradient of the surface at the reflection point are determined by ray tracing (Fig. 2).

Orbscan measures more than 240 points in each slit scanning in 1–5 s. Orbscan IIz provides 40 slit images including:

– 20 from left, 20 from right projections.
– 45° beams projected.
– 20 image duration: 0.7 s each.

M. Mohammadpour (✉)
Faculty of Medicine, Department of Ophthalmology, Farabi Eye Hospital and Eye Research Center, Tehran University of Medical Sciences, Tehran, Iran
e-mail: mahammadpour@yahoo.com

Z. Heidari
Noor Ophthalmology Research Center, Noor Eye Hospital, Tehran University of Medical Sciences, Tehran, Iran
e-mail: zahra.heidari77@yahoo.com

M. Mohammadpour (ed.), *Diagnostics in Ocular Imaging*,
https://doi.org/10.1007/978-3-030-54863-6_2

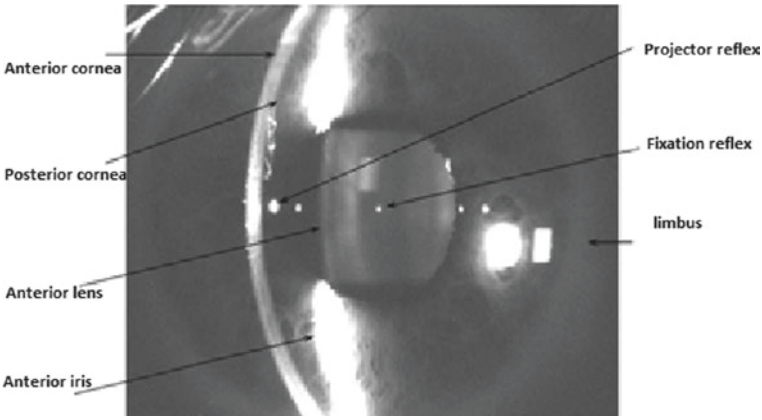

Fig. 1 Ocular measurement surfaces [1] (*With permission from Bausch and Lomb Incorporated*)

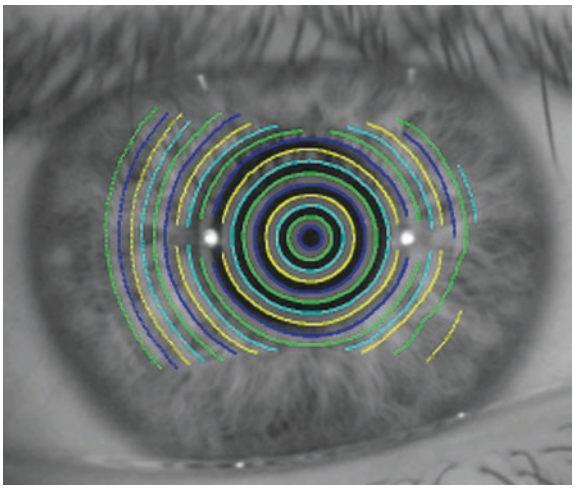

Fig. 2 Verification image of the Placido ring on the corneal surface [1] (*With permission from Bausch and Lomb Incorporated*)

Orbscan IIz measures the surface elevation directly with a triangle of backscattered slit beams. It measures surface slope directly using specular reflection, with a triangular height. Then combine the triangular and reflection data to obtain accurate surfaces of elevation, slope, and curvature. It measures more than 240 points in each slit scanning in 1–5 s (Fig. 3).

The new generation of Orbscan (Orbscan 3) is a third-generation anterior segment corneal imaging which provides a detailed analysis of both anterior and posterior surfaces of the cornea by calculating 23,000 points of the entire cornea based on the analysis of the reflected image of the Placido rings and the scanning optical slit method. The new software provides the analysis of the elevation and

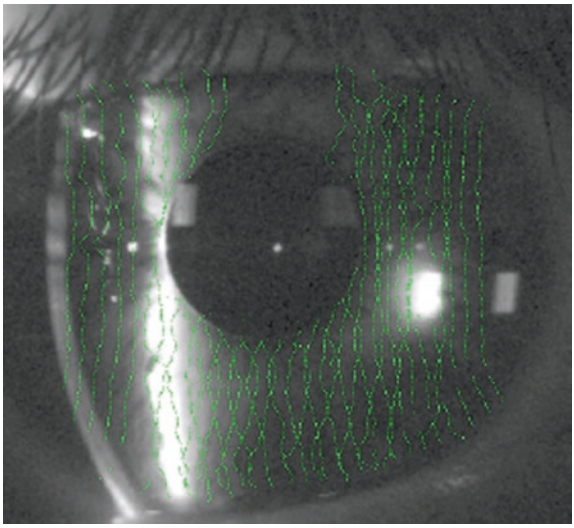

Fig. 3 The complete slit beam processing of the whole eye in the Orbscan system [1] (*With permission from Bausch and Lomb Incorporated*)

curvature measurements, full pachymetry, anterior chamber depth (ACD), and angle kappa, and white-to-white measurements.

Zywave 3 is the latest version of Zywave, which in addition to analyzing high and low order aberrations, also provides important information about iris recognition.

Zywave 3 can analyze 9 times more than the previous model by using an integrated HD camera and fast data transfer capability. A combination of Orbscan 3 and Zywave 3 is known as ZYOPTIX Diagnostic Workstation 3 (ZDW 3) platform, which can be compatible with the TECHNOLAS® TENEO 317 excimer laser and enable fast data exchange. This diagnostic platform is appropriate for customized wavefront-guided refractive surgery with iris registration (Fig. 4).

A study compared the Orbscan 3 with Pentacam recently and reported there was a low agreement in terms of anterior and posterior elevation from the best fit sphere. However, there was high agreement between two devices in pachymetry on the corneal apex. They suggested that generally, the indices measured by these devices are not comparable together [2].

Maps in Orbscan

There are different maps in Orbscan such as Quad map, Dual map, 3-D map, and difference map. The Quad map shows 4 maps including anterior and posterior float maps, Curvature (Axial) map, and pachymetry map (Fig. 5).

Float maps show the elevation of the anterior and posterior corneal surface compared with the best fit sphere (BFS). It is worth noting that these maps do not

Fig. 4 Old generation (left image) and new ZYOPTIX (right image) Diagnostic Workstation 3 platform (a combination of Orbscan 3 and Zywave 3) [1] [With permission from Bausch and Lomb Incorporated]

calculate curvature and only show elevations that can be either complete bridge, incomplete bridge, or central island. If the height is higher than the BFS, the color code will be yellow to red, and if it is less than BFS, the color code will be green to blue, and if it is the same level of BFS will be green.

Elevation Map

The elevation map displays the height of the cornea related to a spherical reference surface (Fig. 6).

The computer calculates an area as much as possible to measure the true shape of the cornea (best-fit sphere). Then compares the actual surface with a hypothetical sphere (BFS) and show areas above the sphere in hot colors and areas below the surface in cool colors. The elevation rate is not directly related to corneal strength at that point and does not indicate a steeping or a flattening surface. The difference in height of the surface with its corresponding BFS is shown as the surface difference. The below Schematic images illustrate the 'best-fit' sphere to a centrally flat cornea (top), as well as the 'best-fit' sphere to a centrally steep cornea (bottom). Blue areas will show negative values on an elevation map and red areas will show positive values on an elevation map.

Points above the BFS are shown in plus values, and those below the BFS are shown in minus values. In corneal astigmatism, one meridian is steeper than the other and is placed under the BFS taking minus values, opposite the flatter meridian which takes plus values (Fig. 7).

Orbscan has defined a separate BFS for anterior and posterior corneal surface, respectively. The difference of height (elevation) between each BFS with the

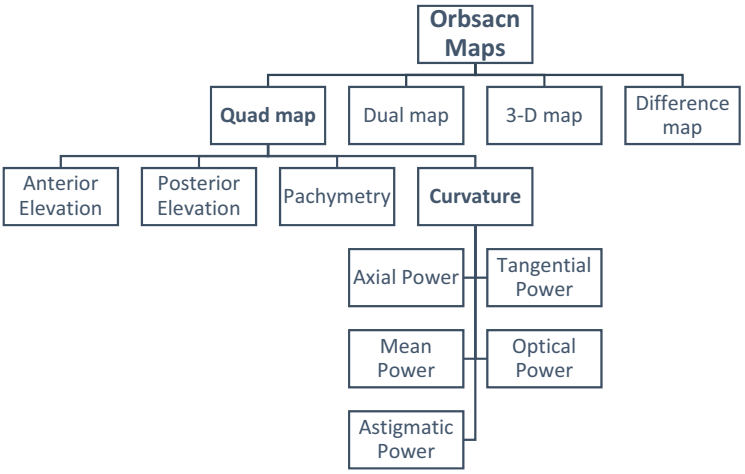

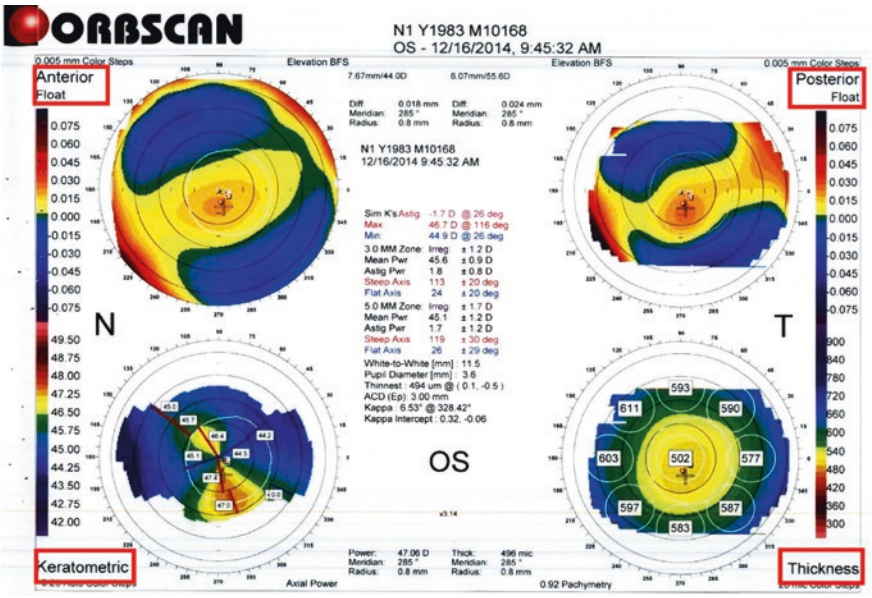

Fig. 5 Quad map of Orbscan

anterior and posterior corneal surface at the maximum point of corneal elevation in microns has been defined as anterior and posterior Diff., respectively. These two Diffs especially the posterior Diff. are very important indices that have an invaluable role in detecting early keratoconus. Their normal and pathologic values are mentioned in Table 1.

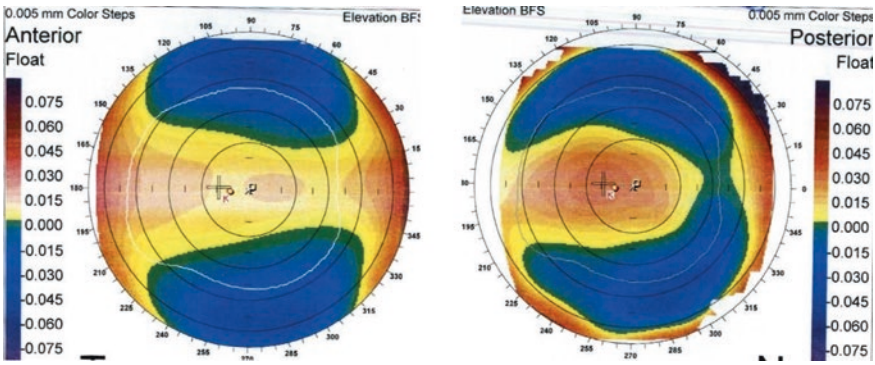

Fig. 6 Anterior and posterior elevation maps

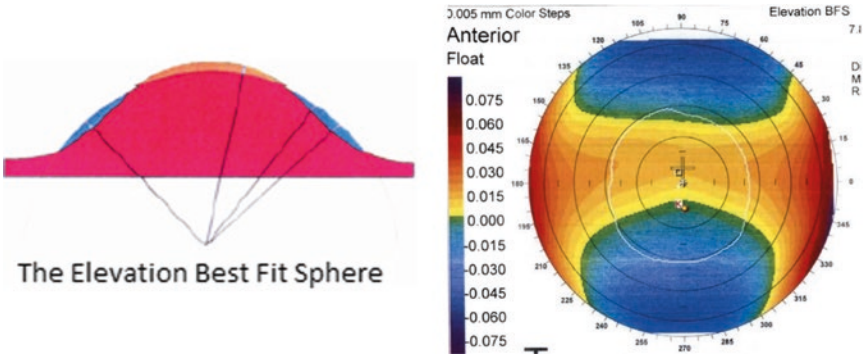

Fig. 7 Elevation map in corneal astigmatism based on best fit sphere reference, cool colors (blue) identify the flat area and hot colors (orange/red) identify the steep area [1] (*With permission from Bausch and Lomb Incorporated*)

Pachymetry Map

Orbscan measures the total corneal thickness from the tear film layer and shows the thinnest point of the cornea which may not correspond to the center of the cornea. This is useful for detecting thin cornea for estimating residual stromal bed thickness before refractive surgery (Fig. 8).

Studies shown that Orbscan provides overestimate pachymetry in comparison with ultrasound pachymetry (US) as a gold standard [3] and comparison of the repeatability of corneal thickness measurements with Pentacam and Orbscan at different grades of keratoconus indicated that in all grades of keratoconus, repeatability of CCT measurements with Pentacam was better than Orbscan [4].

To reduce this error, a correction factor called Acoustic factor (AF) was added to the second generation of Orbscan. This factor set to 0.92, which can be changed

Table 1 The author's (Mehrdad Mohammadpour) suggestive diagnostic criteria for normal, keratoconus suspect (SKCN), and definite Keratoconus (KCN) for Orbscan

Criteria	Normal	SKCN	KCN
Anterior corneal curvature (D)	<47.2	47.2–49	>49
Anterior BFS (D)	<47.8	47.8–50	>50
Posterior BFS (D)	<50	50–52	>52
Ratio of anterior/posterior curvature (Efkarpides)	<1.21	1.21–1.27	>1.27
Difference most anterior elevated point to BFS (μm)	<25	25–30	>30
Difference most posterior elevated point to BFS (μm)	<35	35–50	>50
Axial anterior corneal curvature (D)	<47.2	47.2–48.7	>48.7
Difference of mean K of two eyes (D)	<1	1–2	>2
Skewed Steepest Radial Axis (SRAX)	<10	10–20	>21
Inferior-Superior difference (IS value) at 3 mm (D)	<1.4	1.4–1.9	>1.9
Inferior-Superior difference (IS value) at 5 mm (D)	<1.4	1.4–2.5	>2.5
Irregularity difference in central 3 mm	<1.5	1.5–3	>3 D
Thinnest point (μm)	>500	470–500	<470

*There are no definite criteria for inclusion or exclusion of keratoconus

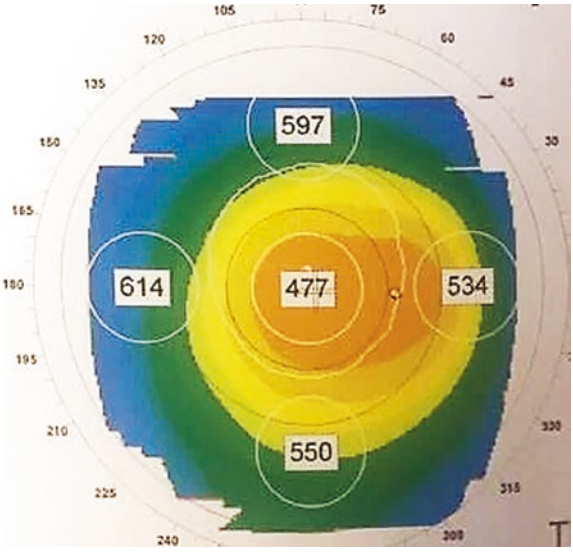

Fig. 8 Pachymetry map

in a thin or thick cornea. We found Pentacam had better agreement than Orbscan with US pachymetry in the normal thin cornea. The results obtained by Orbscan using AF 0.94 correspond to a better consistency. We proposed that a dynamic AF grading inversely with CCT provides a better approach for correcting Orbscan measurements [5].

Curvature Maps

Axial Power Map

This map calculated based on Placido data only and it is a familiar map and comfortable transition for the new user (Fig. 9).

Mean Power Map

This map shows the variation of corneal spherical power and the location of the corneal abnormality. It is very useful for the eye with advanced abnormalities (Fig. 10).

Astigmatic Power Map

Astigmatic power maps indicate local astigmatism in the corneal surface and its direction depends on corneal curvature (Fig. 11).

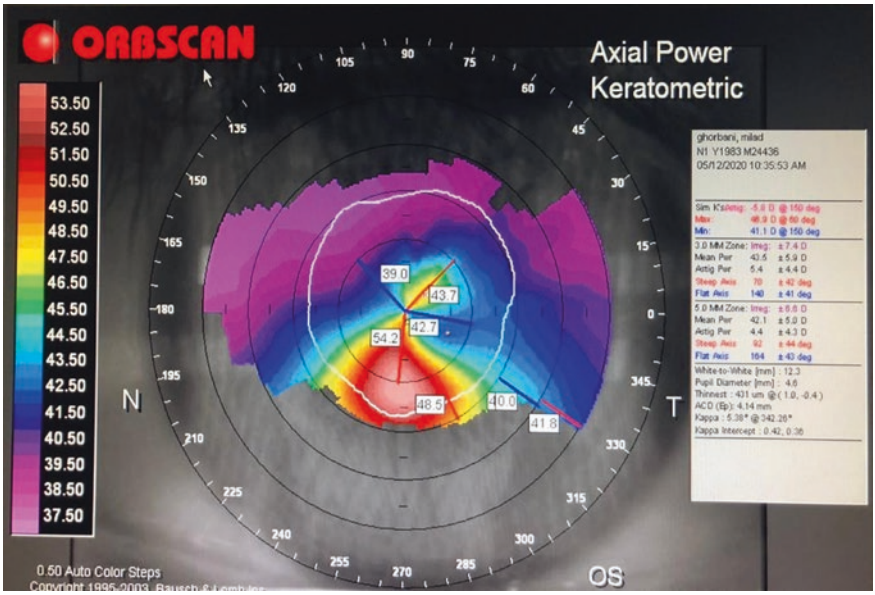

Fig. 9 Axial power map

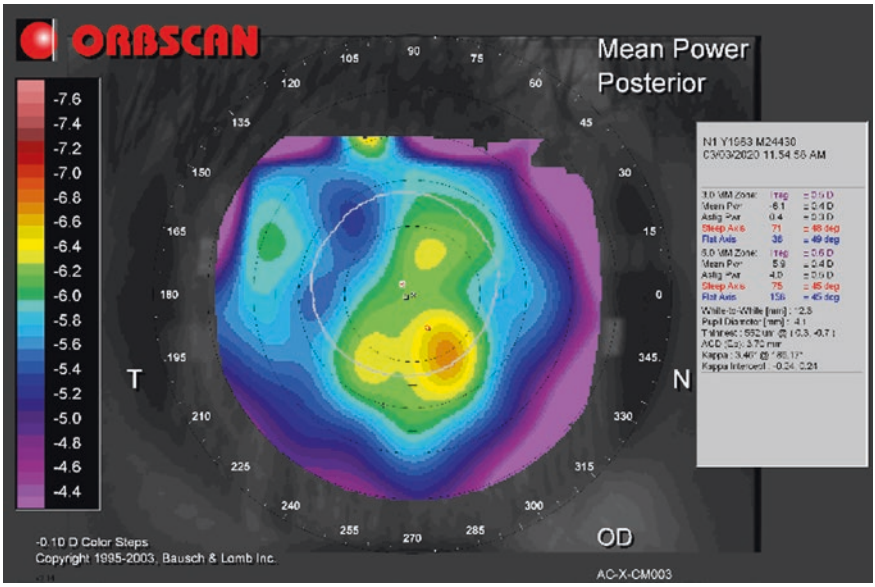

Fig. 10 Mean power map of Orbscan

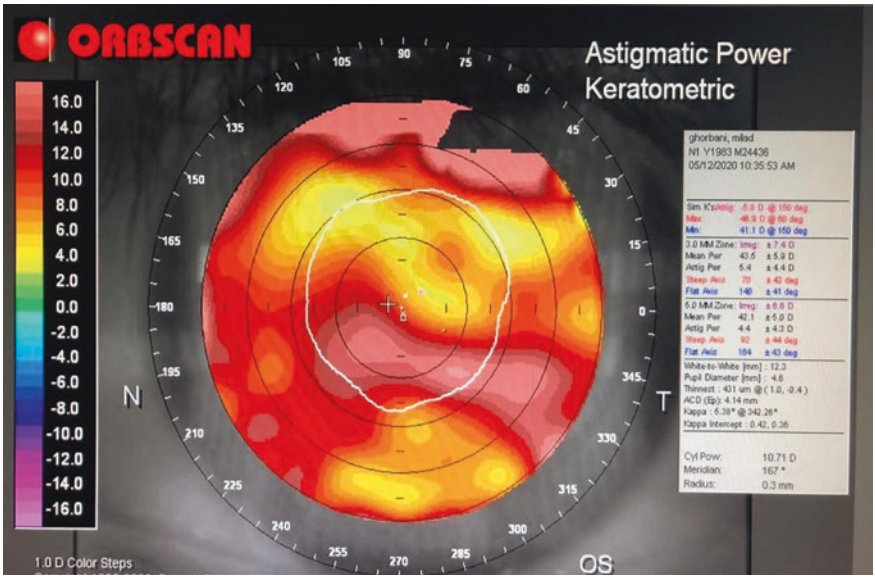

Fig. 11 Astigmatic power map

Tangential Power Map

Tangential power maps analyze the curvature of the cornea and convert these data into diopters and show total astigmatism with the tangential method (Fig. 12).

Optical Map

Optical or refractive power maps also known as Snell power maps and show the true optical power (Fig. 13).

There is the Normal band (NB) map on the Orbscan and shows all points in the normal range in green, and the elevation or depression distance from the BFS is in the normal range. This map helps people who are not familiar with normal and abnormal values with valuable indices in four maps of Orbscan (Fig. 14).

1. Sim K's (simulated K-Reading) and corneal astigmatism
2. Irregularity index at 3.00 mm zone and 5.00 mm zone
3. White to white
4. Pupil diameter
5. Thinnest point of the cornea
6. Anterior chamber depth (ACD)
7. Angle kappa.

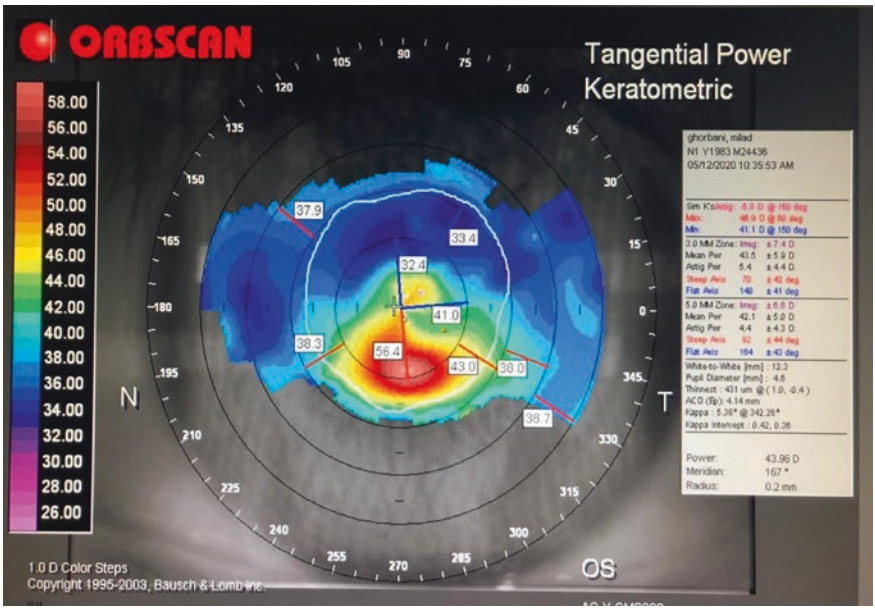

Fig. 12 Tangential power map

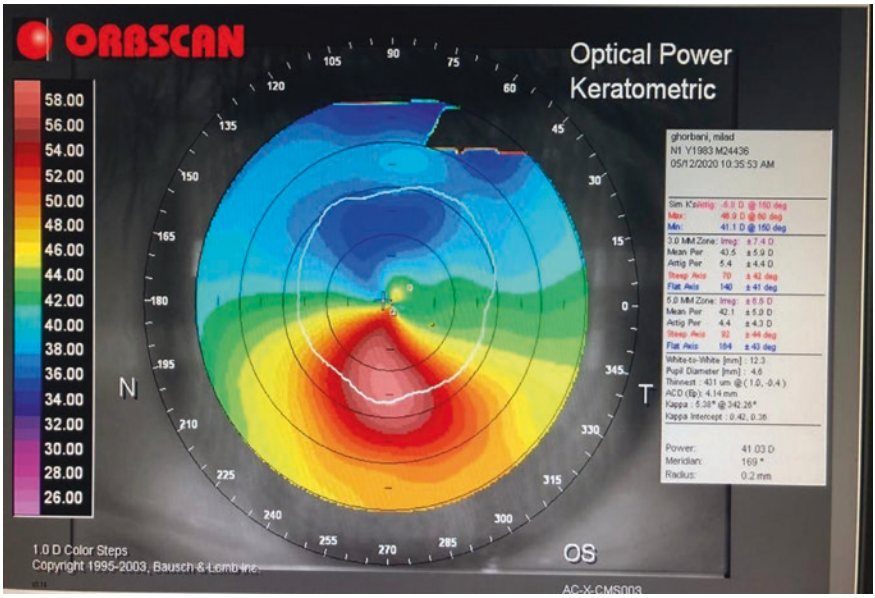

Fig. 13 Optical power map

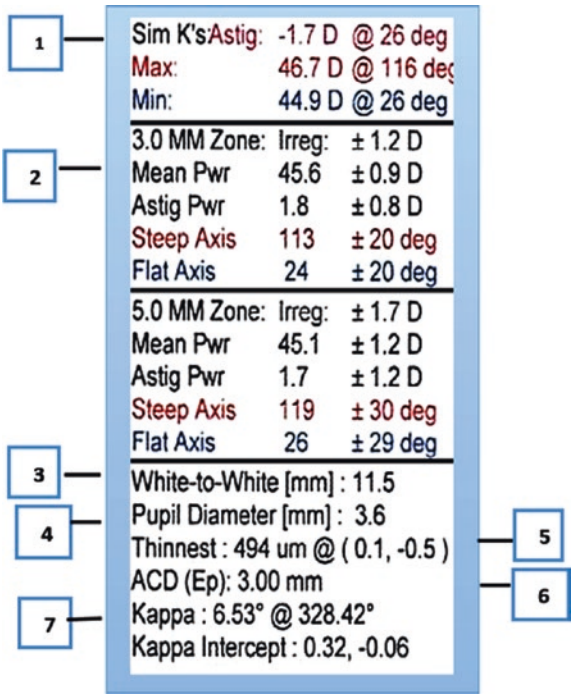

Fig. 14 An overview of the reports of the Orbscan four maps

Orbscan Indices for Risk of Keratoconus

There are some important indices for ectasia detection by Orbscan such as the number of abnormal maps, posterior surface float, irregularity, peripheral thickness changes, astigmatism variance between two eyes, and steep K (mean power map). The diagnostic range of the most important criteria is shown in Table 1.

Recently, Saad and Gatinel [6] developed a new Score analyzer, this software has been added to the Orbscan to calculate quantitative indices. The purpose of SCORE analysis is to compute the unique number of indices for accurate examination of suspected corneal. This software provides 3 additional graphs to the quad map of Orbscan: a Score bar which located the Score value on a linear color scale bar, and the RADAR map display which is a helpful map for the clinician for suspected case detection, and the average pachymetry and pachymetric thinning curves show meridionally corneal thickness profile. The score of zero is the optimal cut-off value. A score higher than zero (positive score) is predicted as a keratoconus-suspect, while a score lower than zero (negative score) is predicted as a normal cornea (Fig. 15).

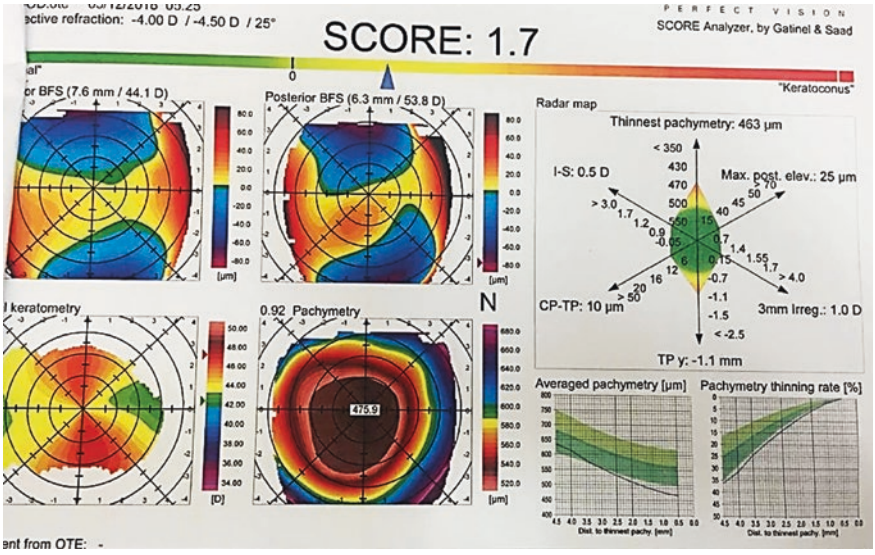

Fig. 15 SCORE software with a positive number

RADAR Map

The radar map shows 6 of the most important topographic, tomographic and pachymetric indices to calculate Score. The color scale, from green to red, allows quick visual analysis of the results. The yellow color corresponds to the cut value.

RADAR map consisted of 6 variables:

1. Pachymetry of the thinnest point (microns): The minimum thickness of the cornea
2. Maximum posterior elevation (microns)
3. Irregularity (diopters) in the central 3 mm
4. Vertical decentration (mm): Displacement of the thinnest point corresponds to the geometrical center of the cornea
5. CP-TP: Difference between mean central pachymetry (CP) and the pachymetry of the thinnest point (TP).
6. I-S value (diopters): Related to the vertical asymmetry of the anterior corneal surface. It is the difference between mean keratometric values of 5 points on the superior (S) and inferior (I) (Fig. 16).

Orbscan Pearls and Pitfalls

Orbscan is very sensitive to any abnormal increase in corneal elevation or a decrease in corneal thickness and has good sensitivity for the diagnosis of early keratoconus. Its false-negative rate is also low with a good topographic Placido based map.

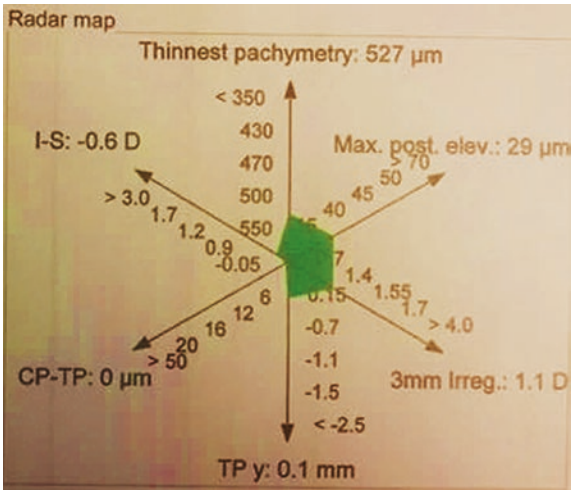

Fig. 16 The RADAR map shows the certain parameters used in the score function

However, it may overestimate the corneal thickness in normal and thick cornea and underestimate the corneal thickness in thin cornea and in the case of corneal haze. The manufacture (Bausch & Lomb) is recommended a correction factor (AF) of 0.92 to correct this error. In fact, the thickness value at the center of the thickness map is measured by the correction factor. This means that if the thickness value was 500 microns, the computer first calculates 544 microns and then shows the final thickness by affecting the correction factor. Therefore, the measured thickness in Orbscan is approximate, and in refractive surgery candidates with borderline corneal thickness, US pachymetry measurement is necessary for accurate measurement of corneal thickness. A special Nomogram can be obtained by using the ultrasound and Orbscan pachymetry with including regression analysis and a specific correction factor for more reliable thickness values.

Posterior corneal elevation measurement in Orbscan is not performed directly and it is provided by anterior surface data. The measurement of the posterior map in Orbscan is less accurate than Pentacam and the results should be interpreted with caution. Orbscan may overestimate posterior elevation in cases with normal values and abnormal elevation and especially following refractive surgery. In patients who underwent refractive surgery previously (especially LASIK), Orbscan measurements, especially posterior values, are also unreliable, and pseudo keratectasia may be seen. This can be stressful for both the surgeon and the patient. Therefore, we recommended Pentacam or other Scheimpflug-based imaging that directly measure the posterior corneal surface to confirm or reject the posterior corneal pathology. However, the manufacturer has recently declared that Orbscan 3 can measure the posterior surface of the cornea directly, and these limitations have been reduced in the new generation of Orbscan 3.

Case Study

Case 1

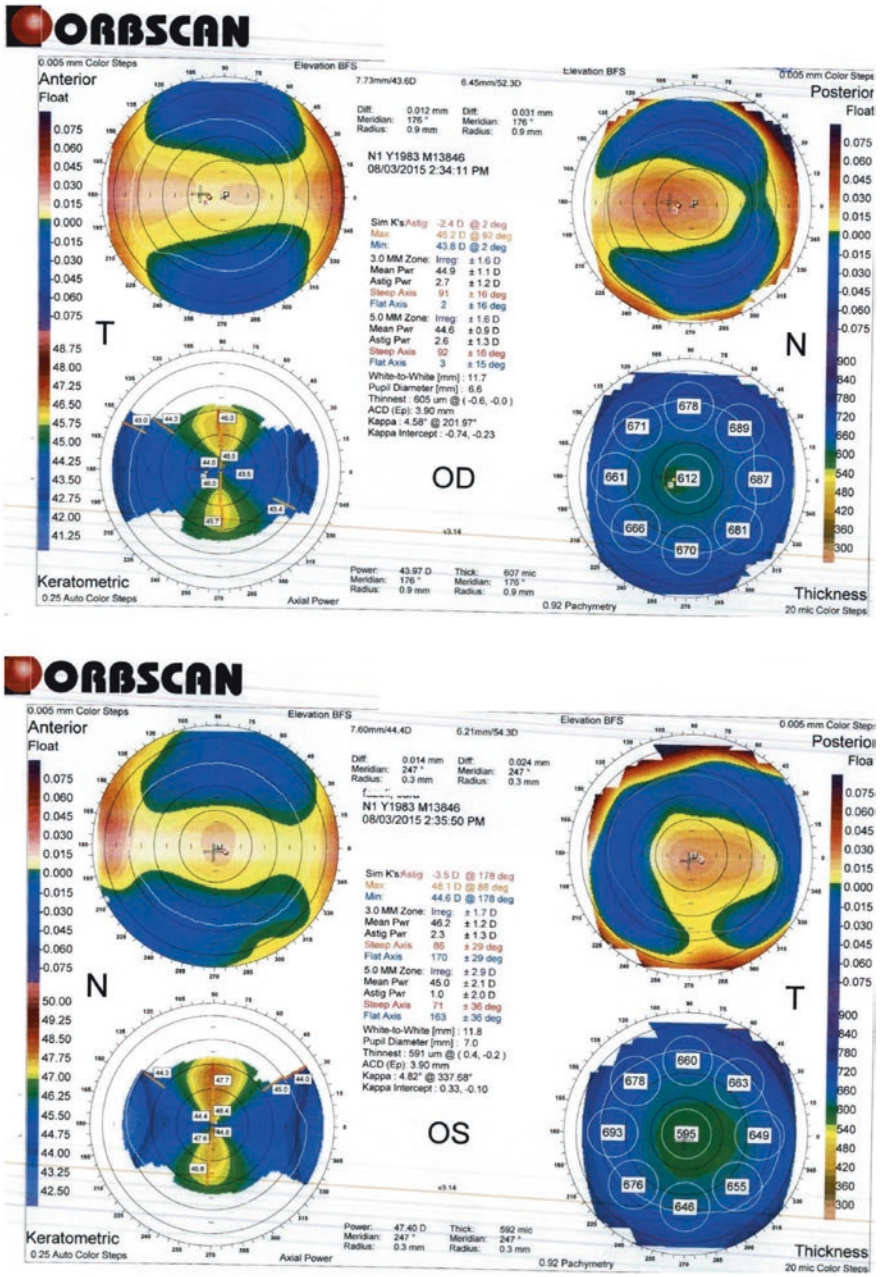

Fig. 17 A 24-year-old woman with the normal cornea and moderate astigmatism who was a candidate for refractive surgery. There is symmetric bow tie with normal diagnostic criteria in elevation and pachymetry maps

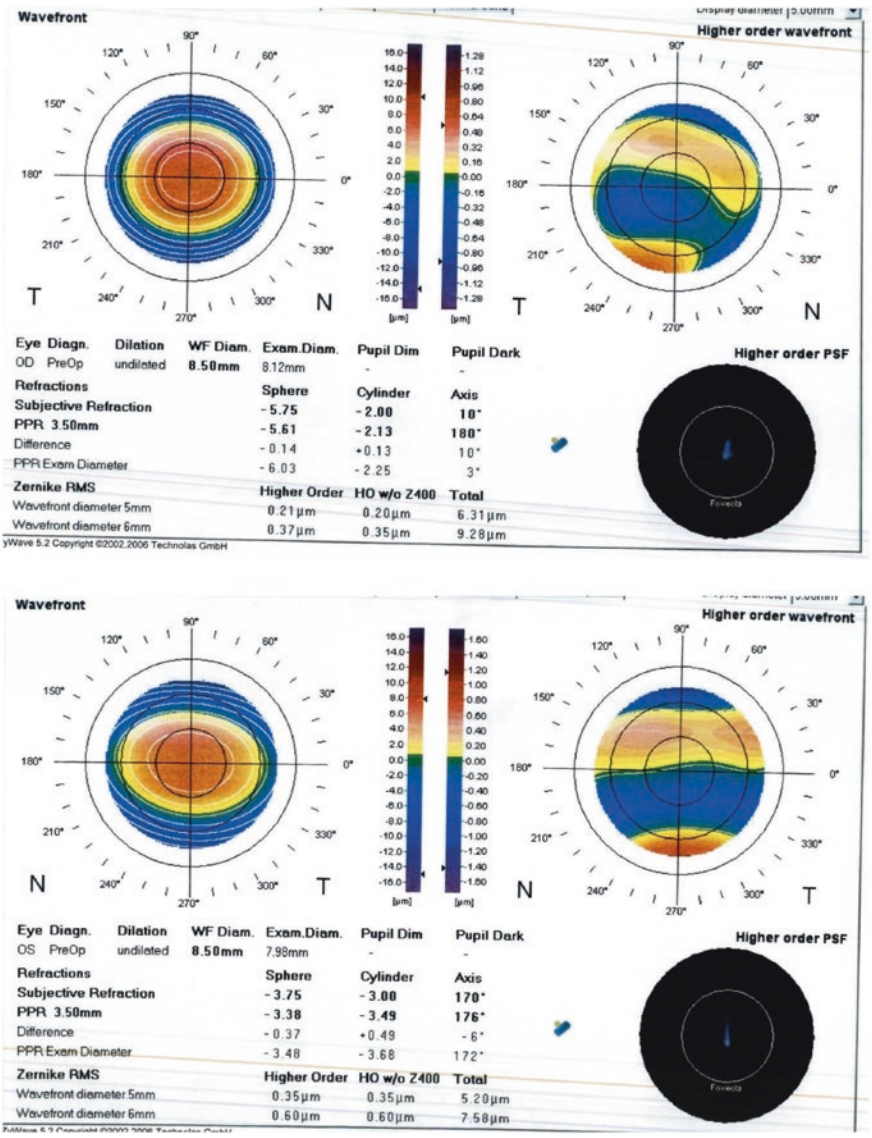

Fig. 18 Zywave aberrometry of the same patient

Case 2

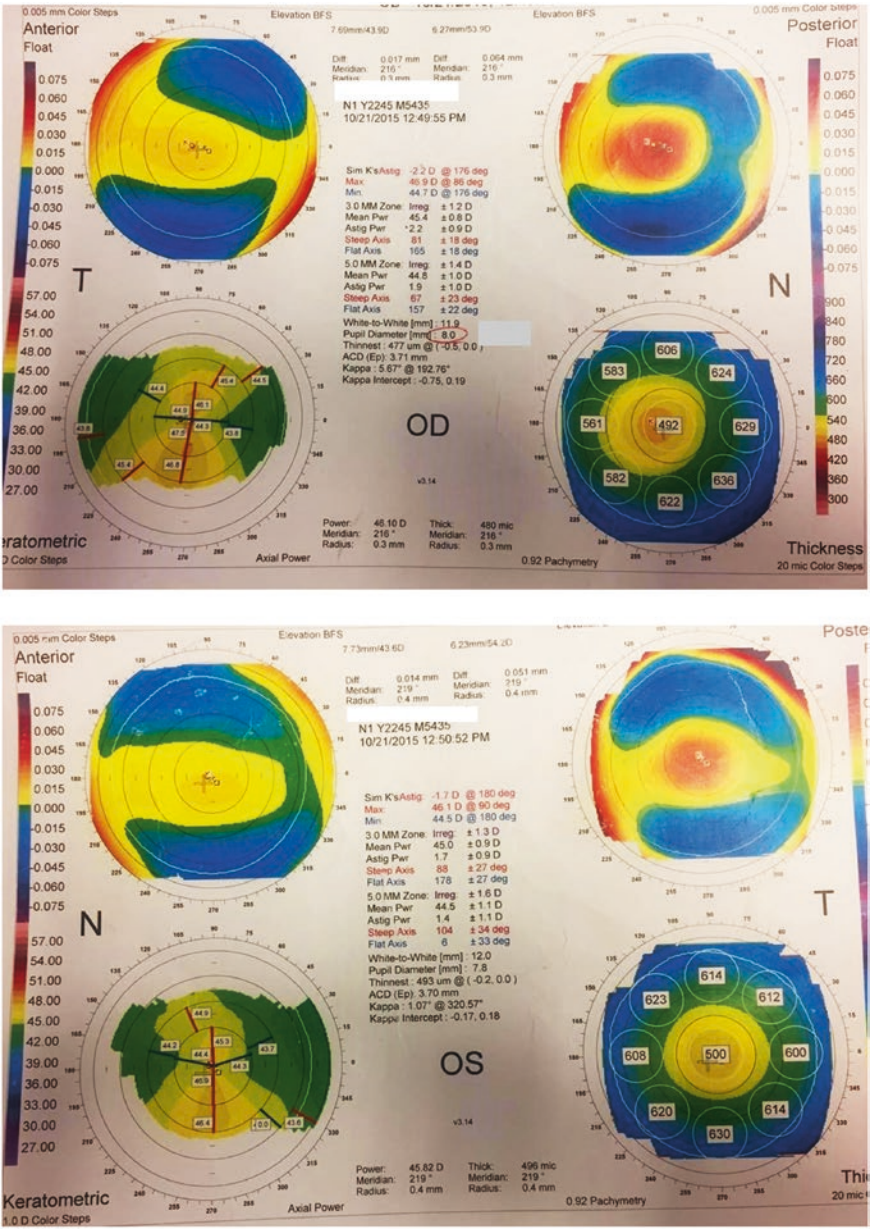

Fig. 19 A refractive surgery candidate with keratoconus suspect and asymmetric bow tie, EfKarpides index (ratio of radii of anterior to posterior curvature of the cornea) = 1.22, inferior steepening and abnormal posterior elevation values and thin cornea in both eyes

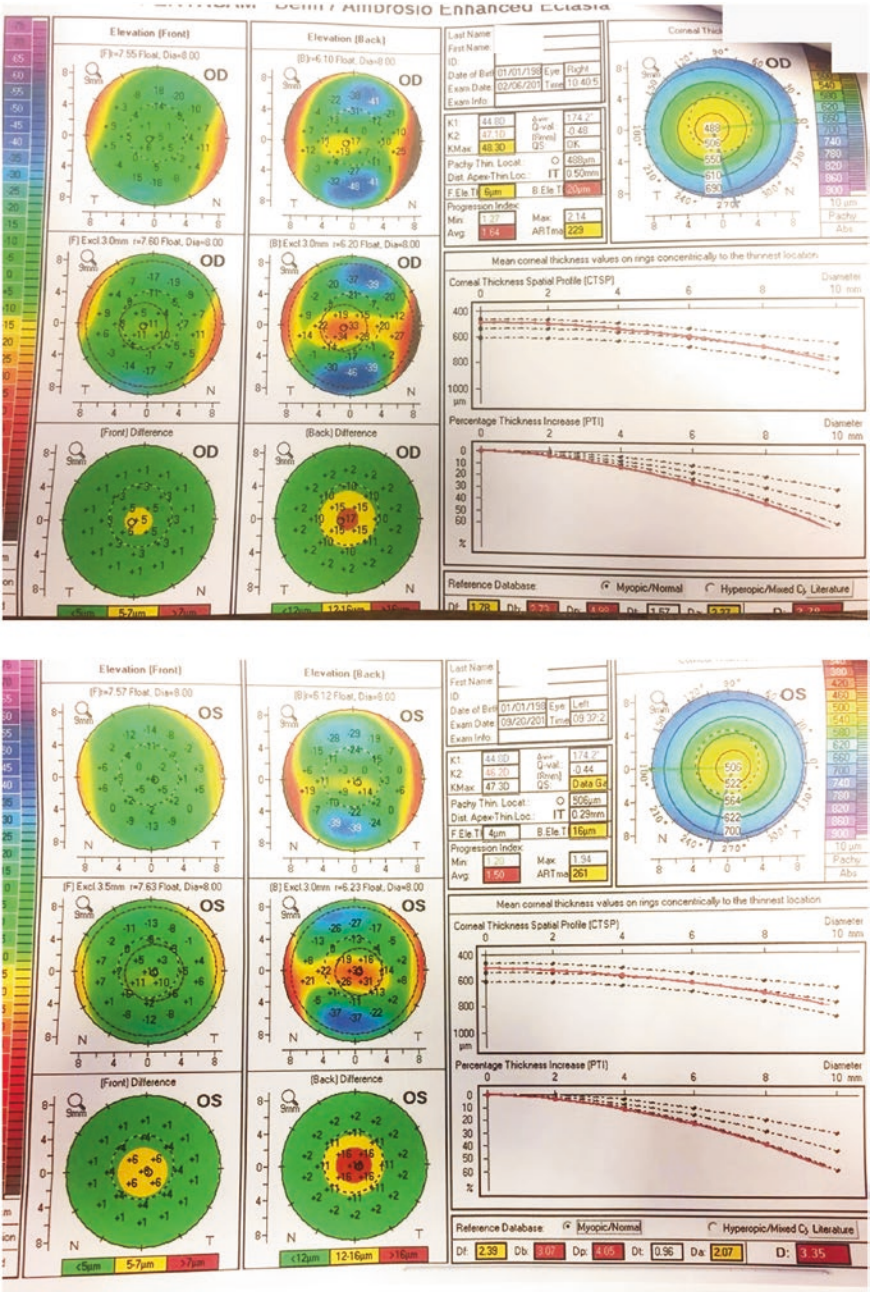

Fig. 20 These findings based on Orbscan maps correspond with the Pentacam parameters of the same patient (abnormal elevations and BADD values)

Case. 3

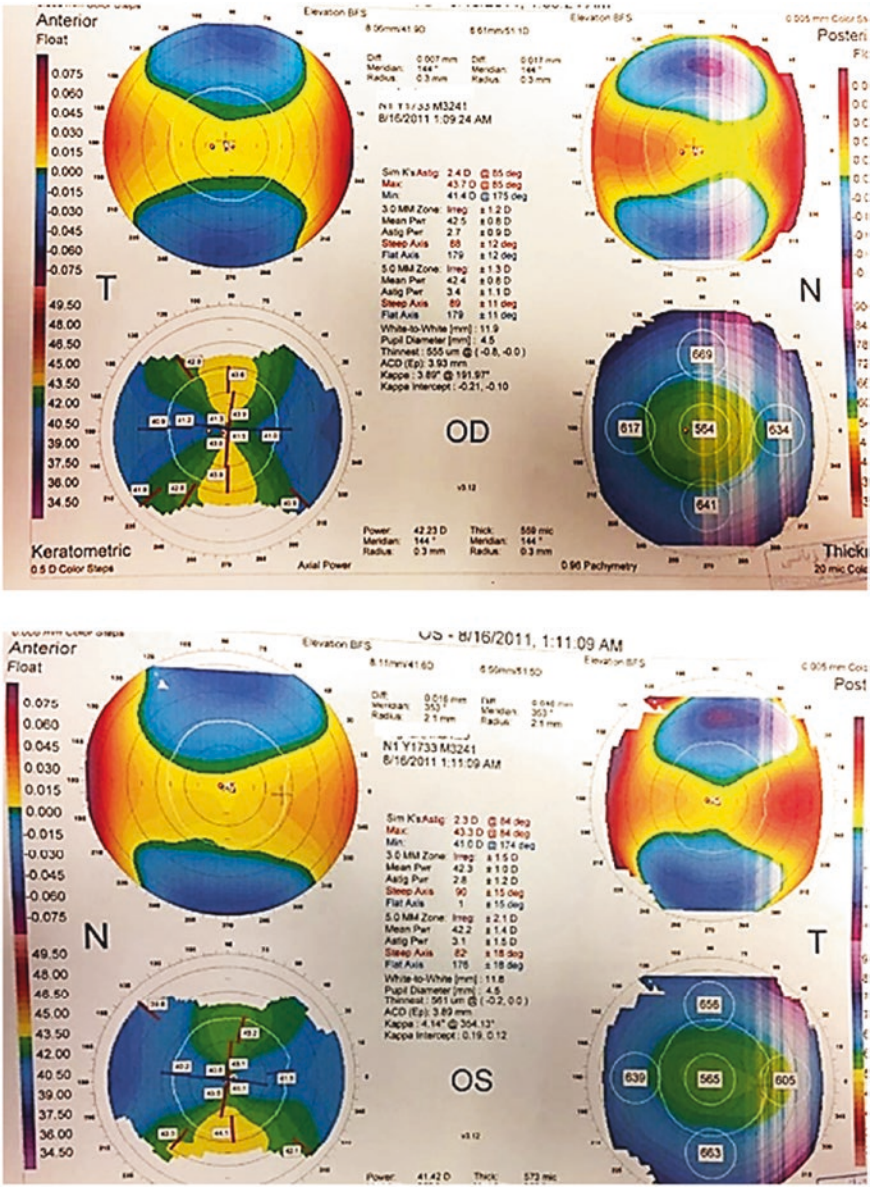

Fig. 21 A 28-year-old woman with the normal eye in right and keratoconus suspect in the left eye with symmetric bow tie, normal values in the right eye, and inferior steepening in the left eye

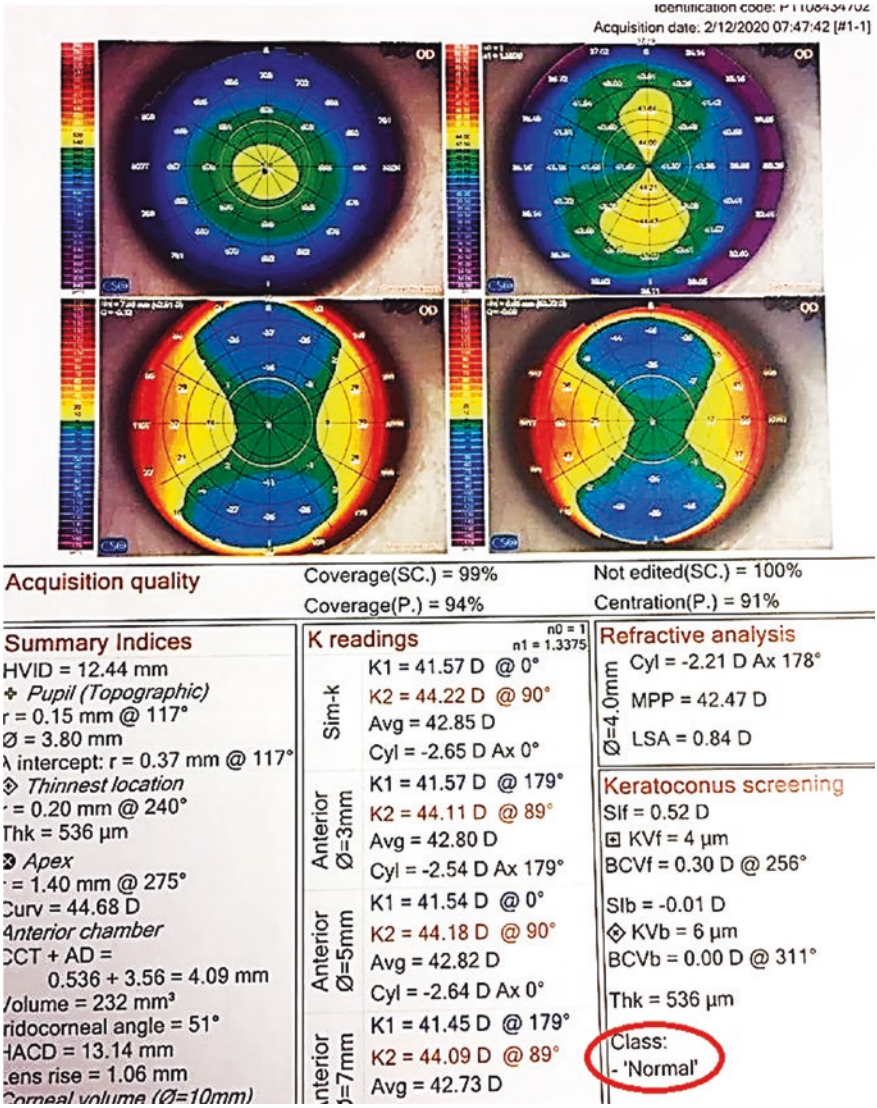

Fig. 22 These findings based on Orbscand are consistent with the artificial intelligence calculations in the Sirius classification as shown in the following images with the red circles

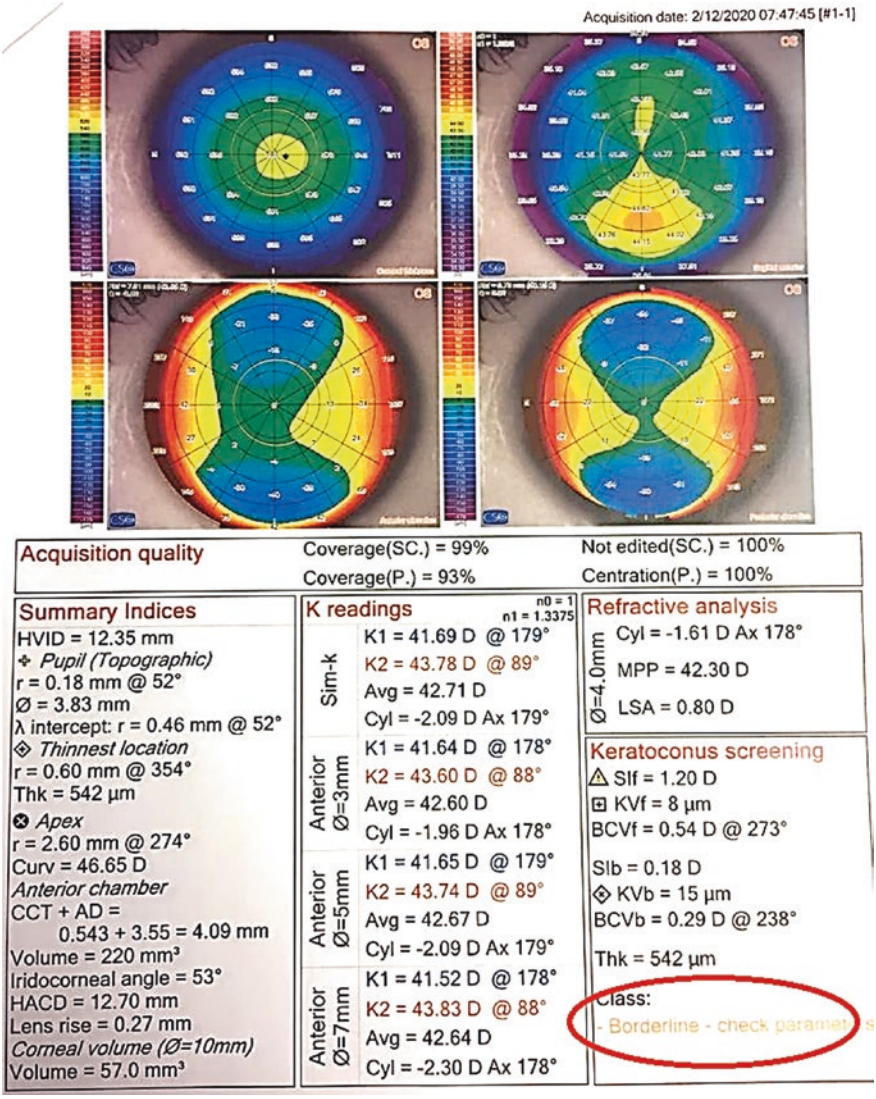

Fig. 22 (continued)

Case 4

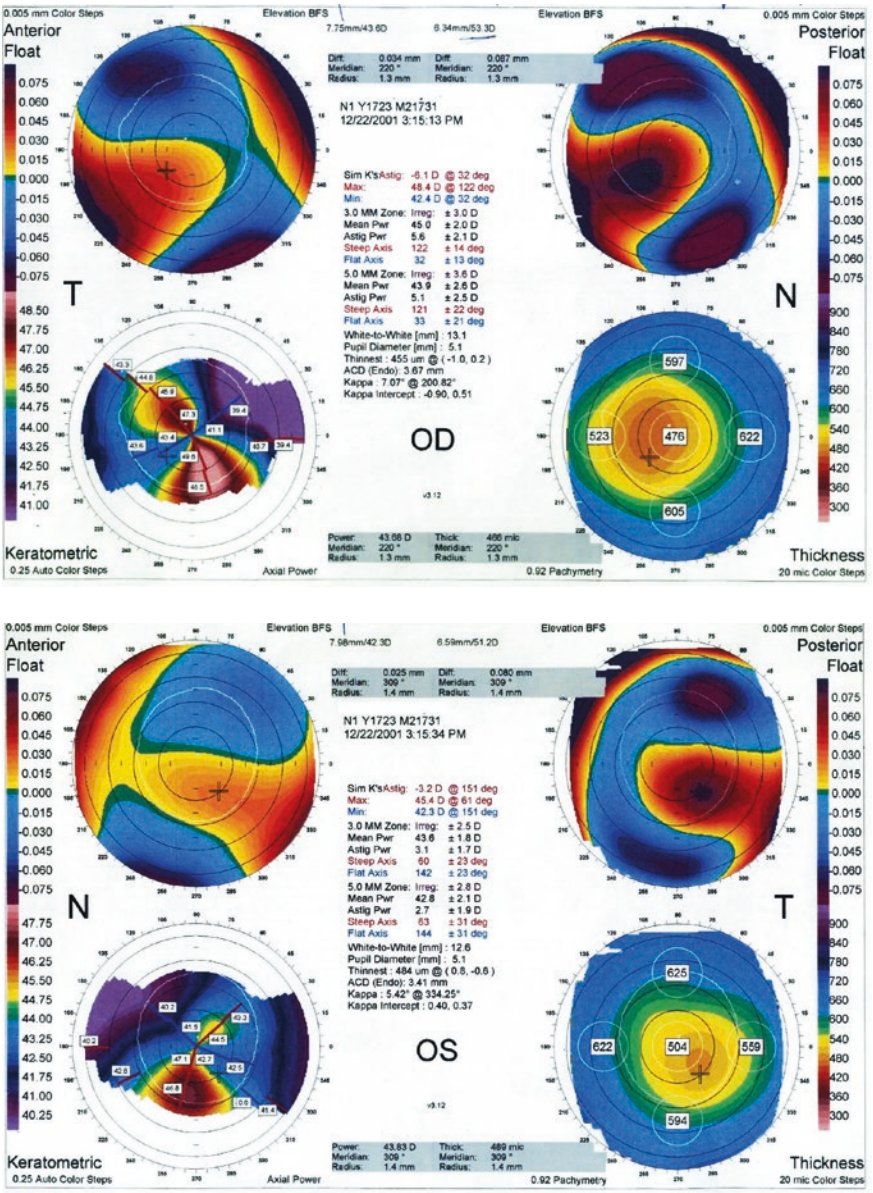

Fig. 23 A 34-year-old woman with refractive errors: OD = −3.25/−3.50~5 VA = 3/10 and OS = −3.50/−5.50~30 VA = 5/10 and inferior steepening diagnosed as definite keratoconus

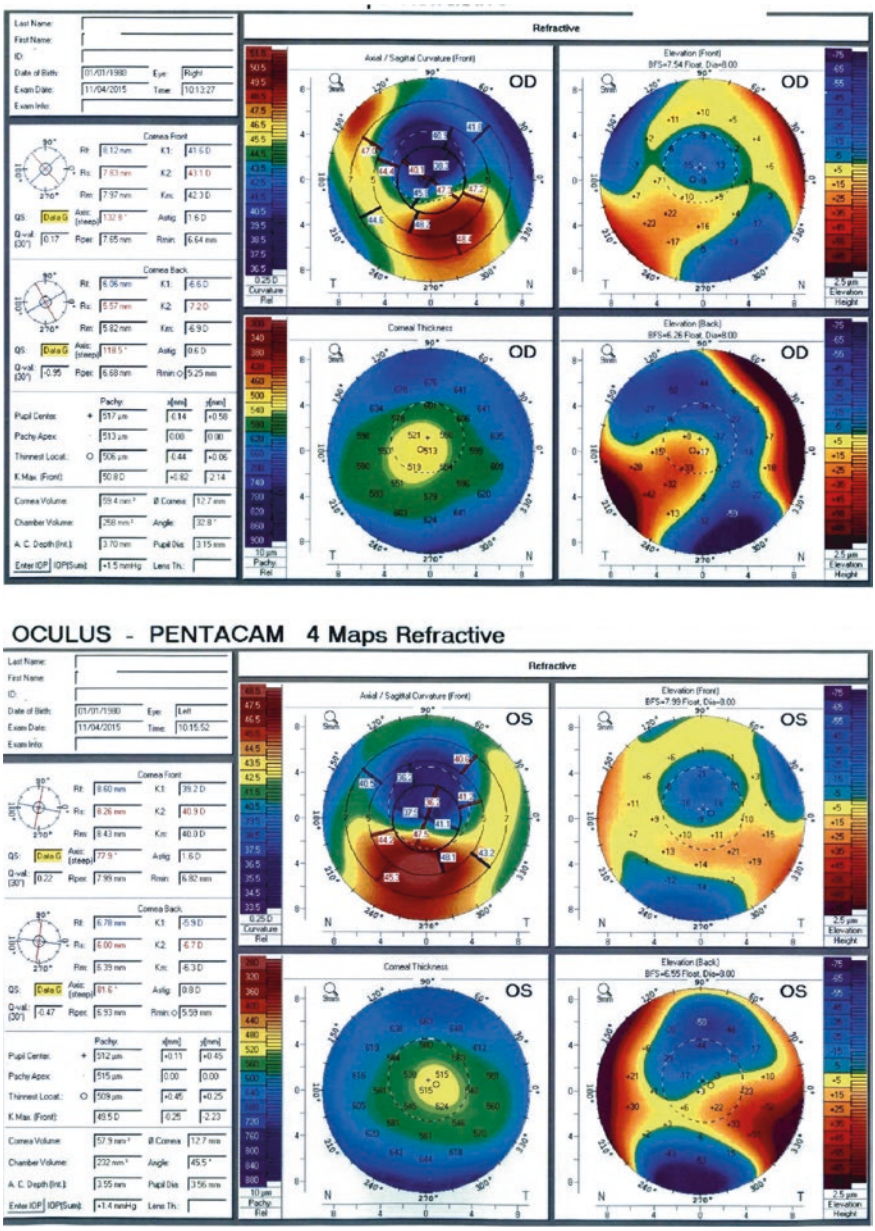

Fig. 24 She was a candidate for intrastromal corneal ring implantation and after Myoring (a 360° complete ring) implantation the center of the cornea was flattened and the visual acuity increased in both eyes, however, the periphery of both cornea shows significant corneal elevation and steepness which compatible with keratoconus. Post-refractive errors: OD = −1.5/−2.5~90 corrected distance visual acuity (CDVA) = 9/10 and OS = −2.50/−1.5~105 CDVA = 9/10

Case 5

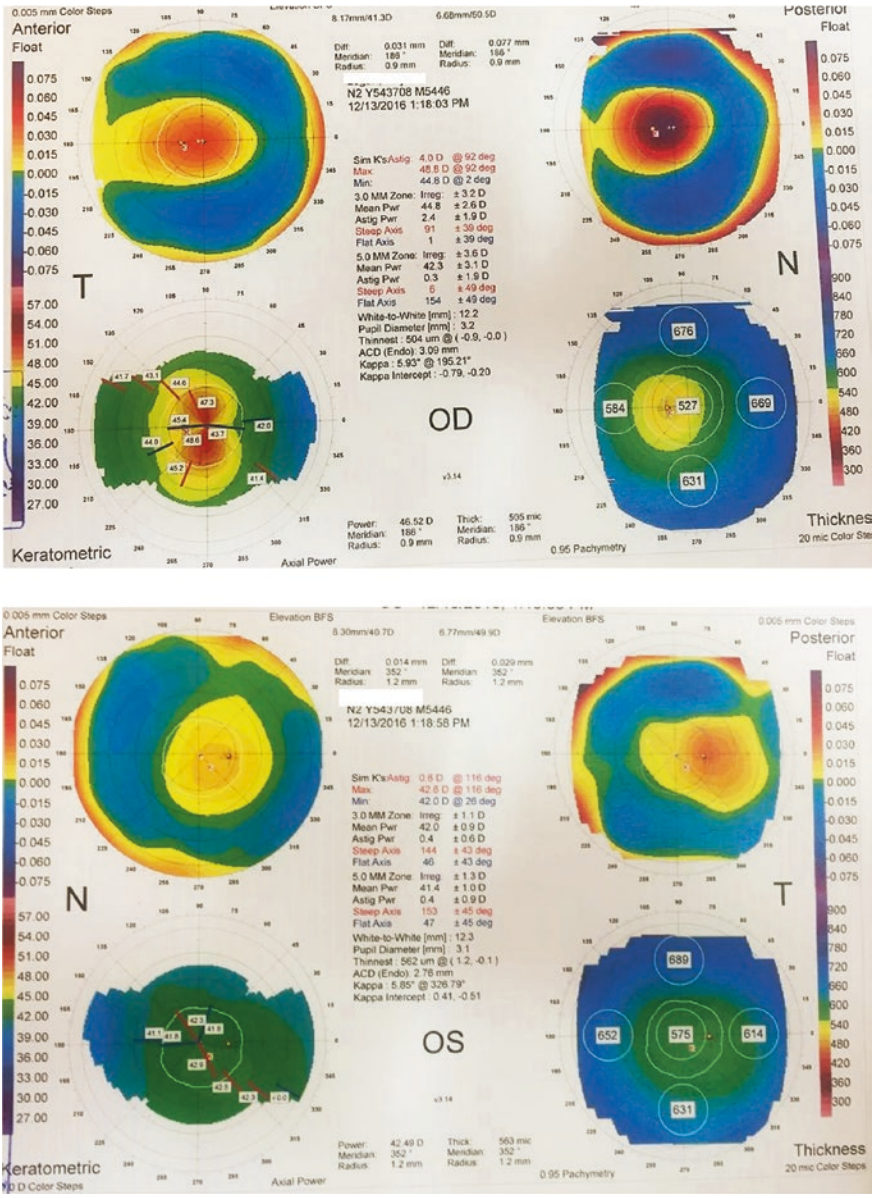

Fig. 25 A young man with central keratoconus in the right eye and forme fruste keratoconus in the left eye with refractive errors: OD = −1.25/−2.5~15 CDVA = 9/10 and OS = −1.75 sphere CDVA = 10/10 with abnormal values on posterior elevation (high posterior difference) and abnormal pattern on axial curvature map only in the right eye and with abnormal higher-order aberrations in both eyes

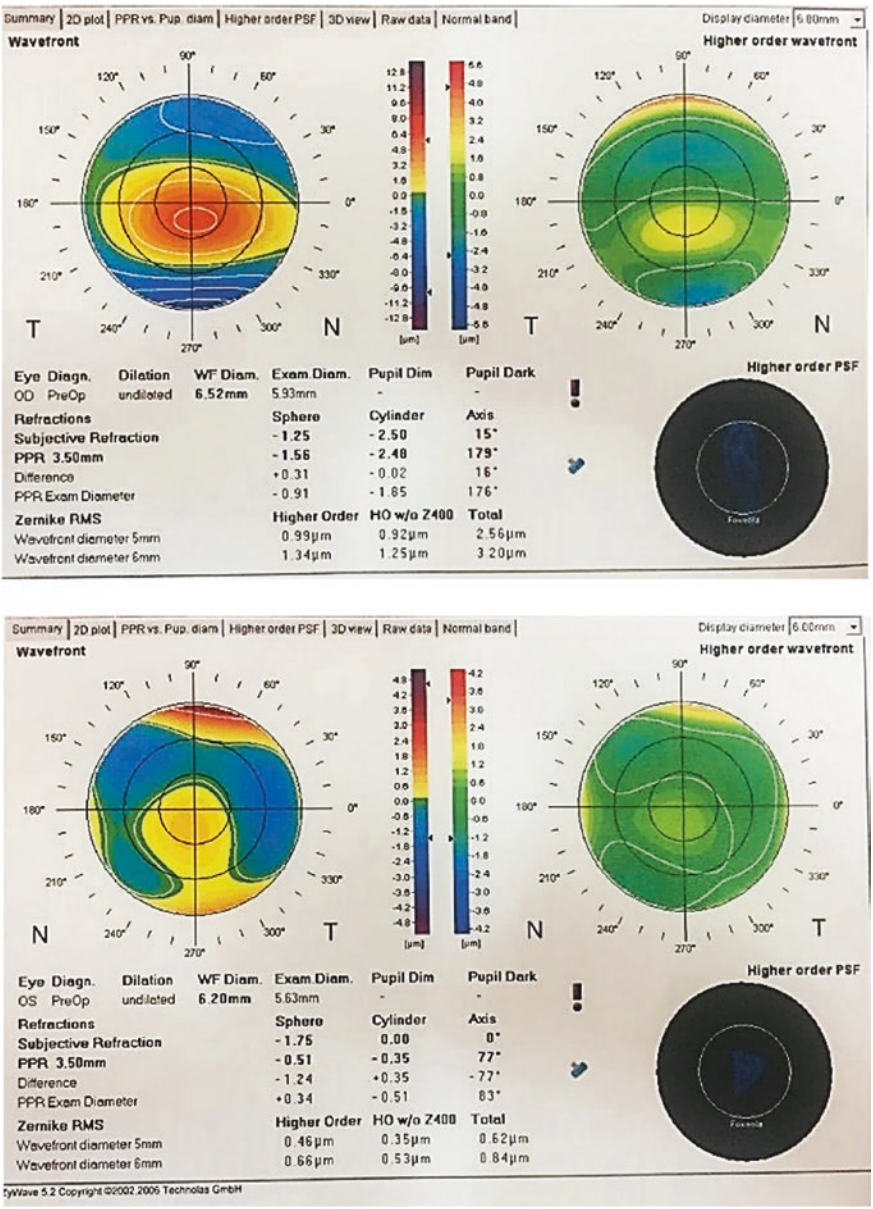

Fig. 26 The Coma aberration increased in both eyes (>0.3 µ) especially in eyes with definite keratoconus, so this index could be a good diagnostic parameter for early keratoconus detection

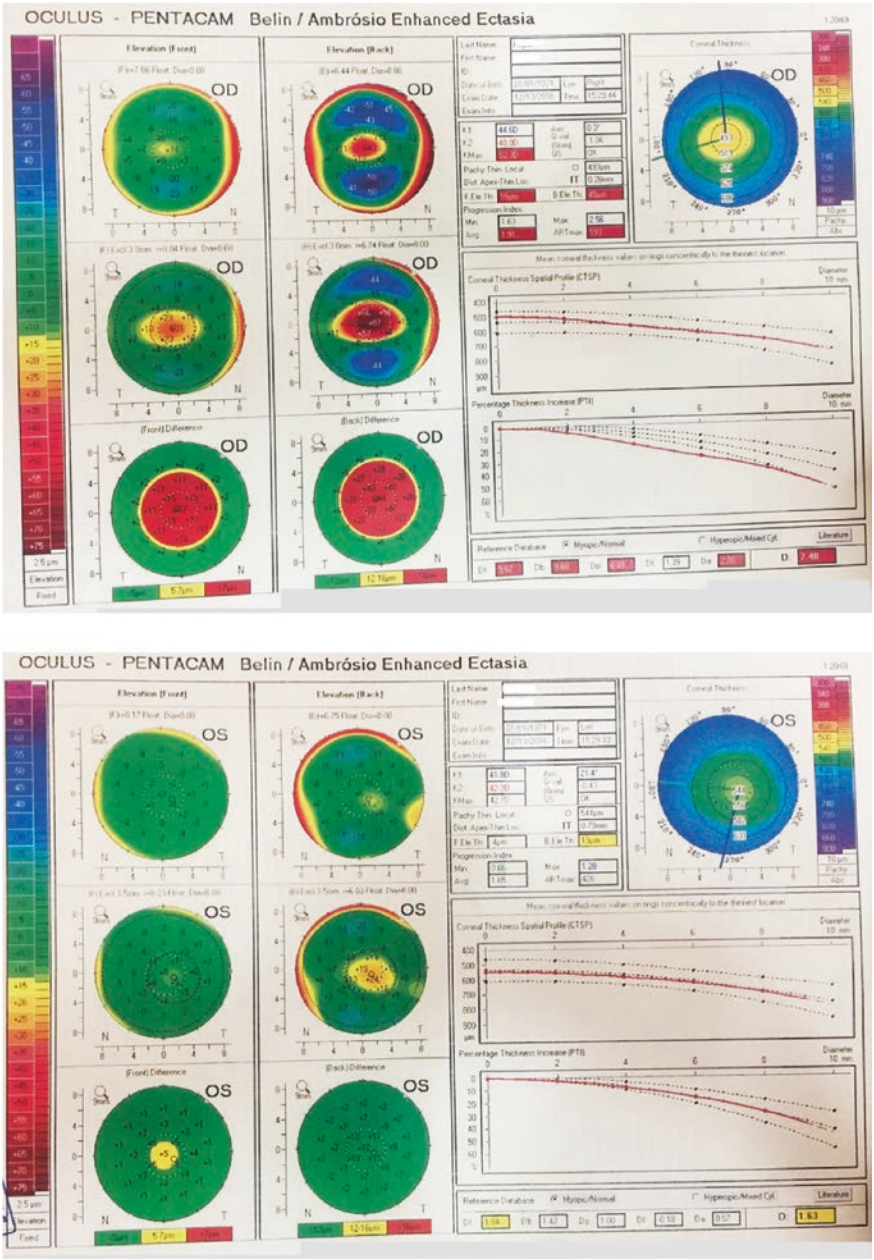

Fig. 27 These findings based on Orbscan data compatible with the Pentacam findings of the same patient (abnormal BADD)

Case 6

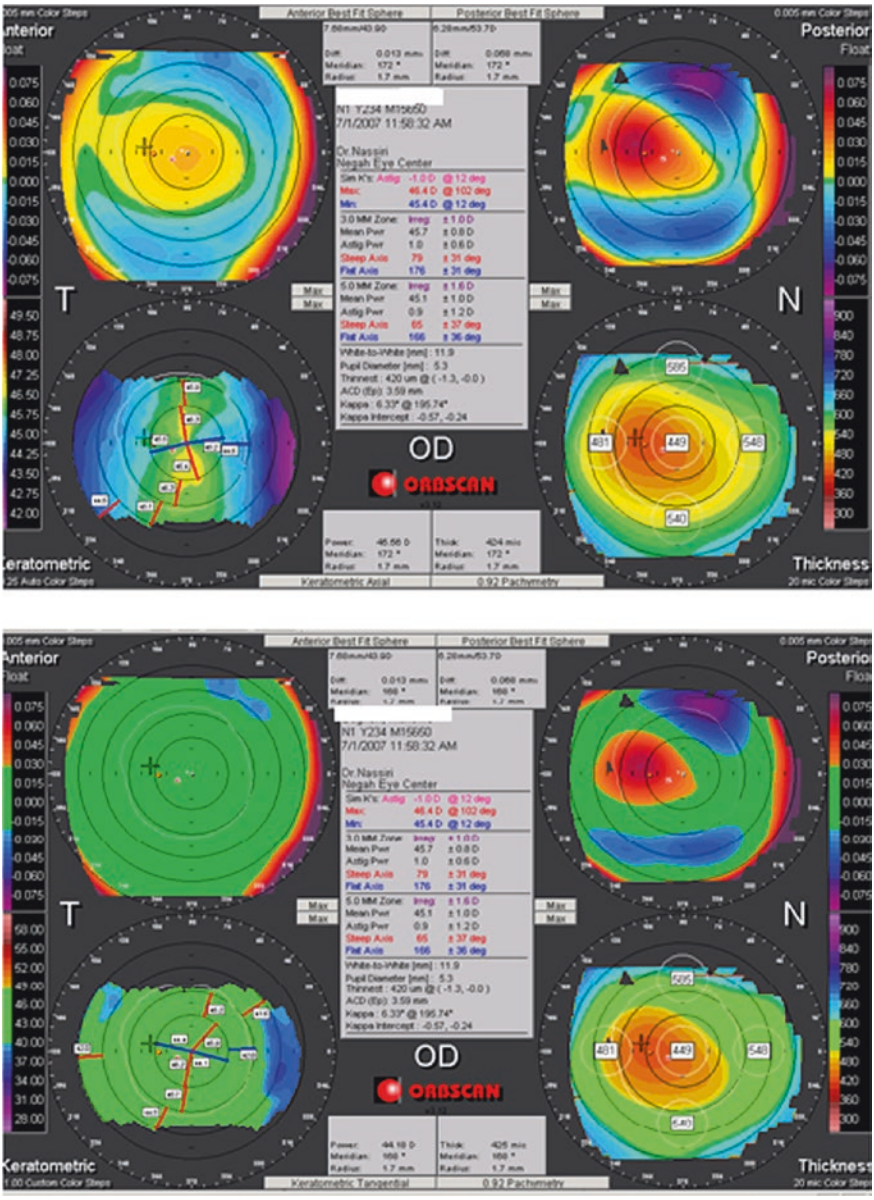

Fig. 28 A young man with posterior keratoconus and normal anterior surface elevation and abnormal posterior elevation. The normal pattern in the lower image due to 1.0 diopter scale. When the color steps scale change from 0.25 diopter (upper map) in auto color steps to 1.00 diopter (lower map) in custom color steps, the pachymetry and elevation maps have not changed and only the topographic pattern changed from symmetric bow tie in the upper map to the normal pattern in the lower map, while this is not a true normal case

Case 7

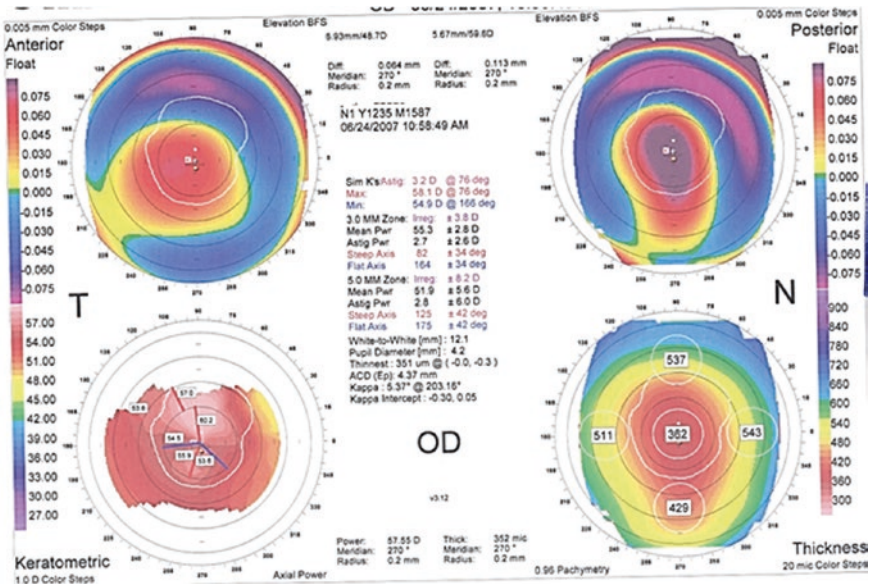

Fig. 29 A young man with generalized corneal thinning and steepening, irregularity more than 3 diopters diagnosed as keratoglobus

Case 8

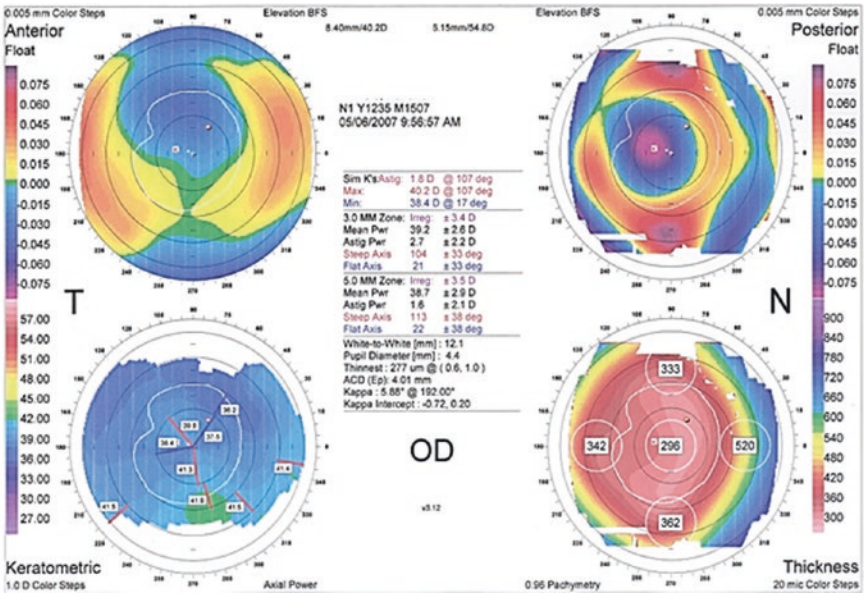

Fig. 30 A 35-year-old woman with a normal anterior elevation but posterior bulging with the thin cornea is present and misdiagnosed as post-refractive surgery ectasia. The topographic map shows corneal flattening and an oblate post PRK pattern. However, this case had corneal haze after PRK and Orbscan underestimates corneal thickness in thin cornea especially when corneal haze is present and it overestimates posterior elevation after refractive surgery

Case 9

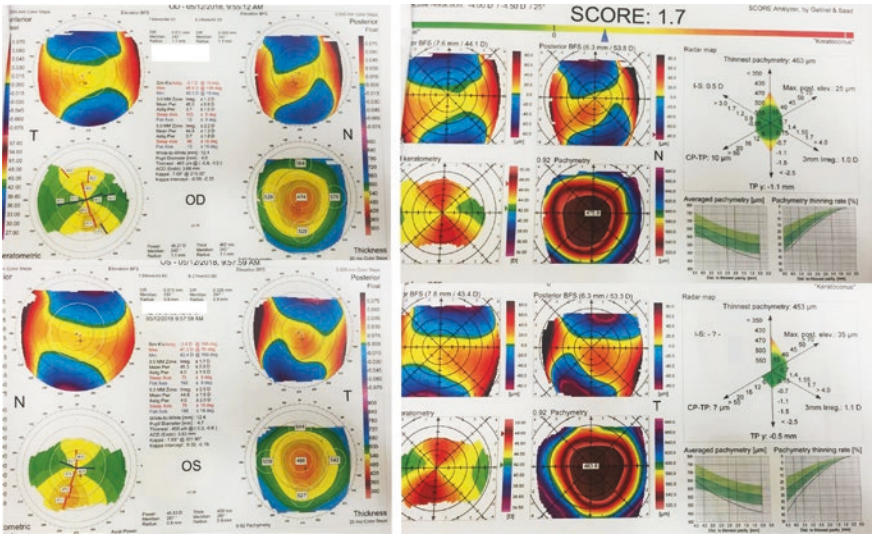

Fig. 31 A 33-year-old man with the thin cornea and high astigmatism in both eyes with borderline RADAR map and without keratoconus. Refractive errors: OD −3.50/−4.5~11, OS −2.50/−5.25~162 VA 20/25 OU. The RADAR map shows positive SCORE in both eyes and abnormal pachymetry thinning rate

Case 10

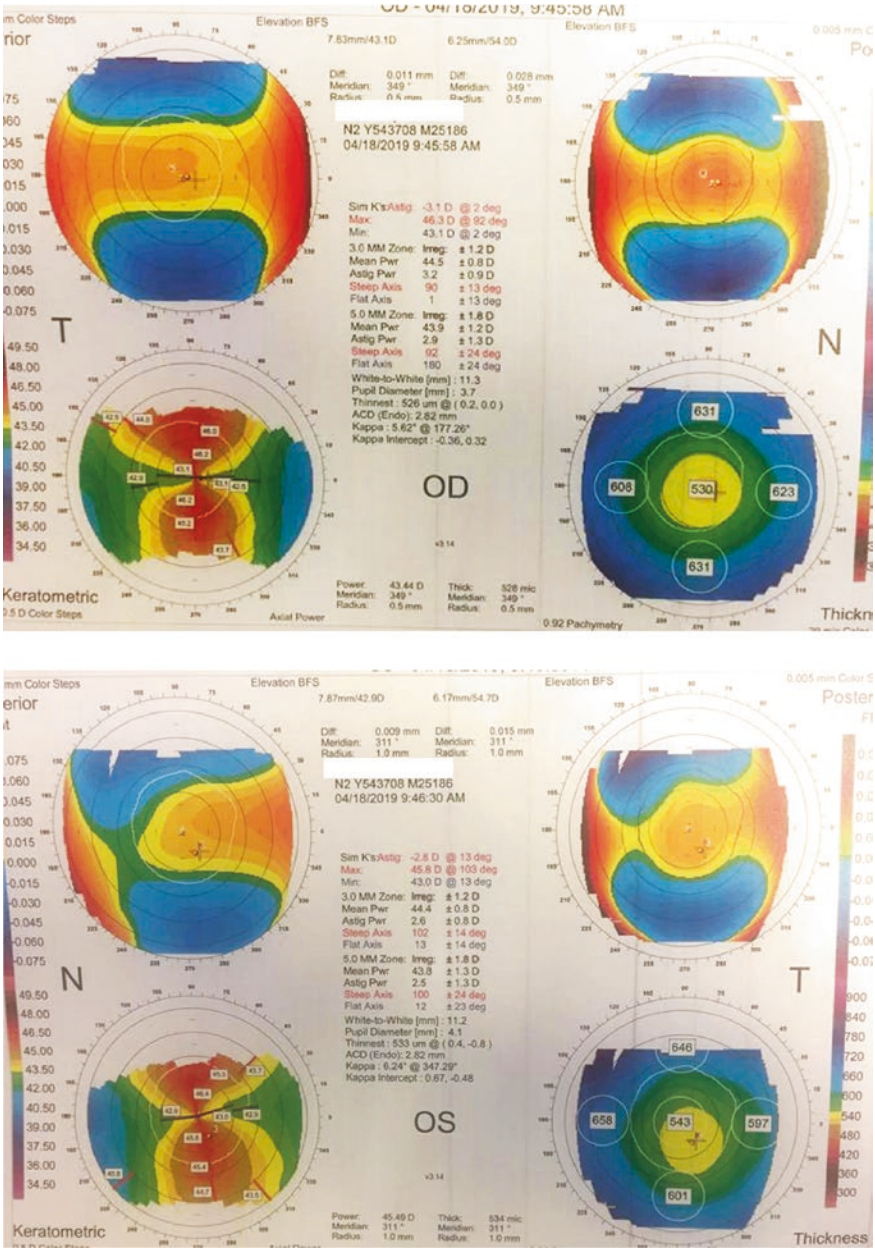

Fig. 32 A 33-year-old woman with high astigmatism and refractive errors: OD −6.75/−3.25~177 and OS −6.50/−2.75~4 and normal Orbscan Quad map in both eyes

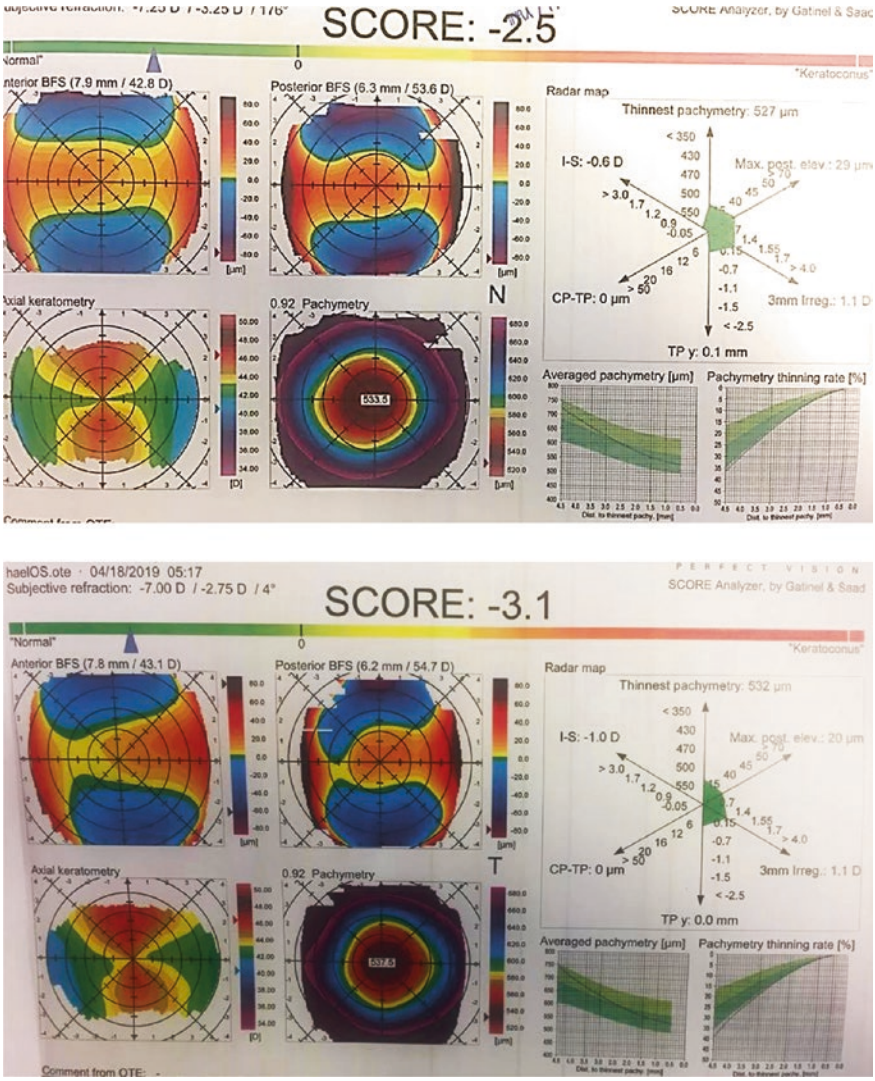

Fig. 33 The RADAR map shows a negative SCORE. This is a sample of true-negative diagnosis of SCORE analyzer software

Case 11

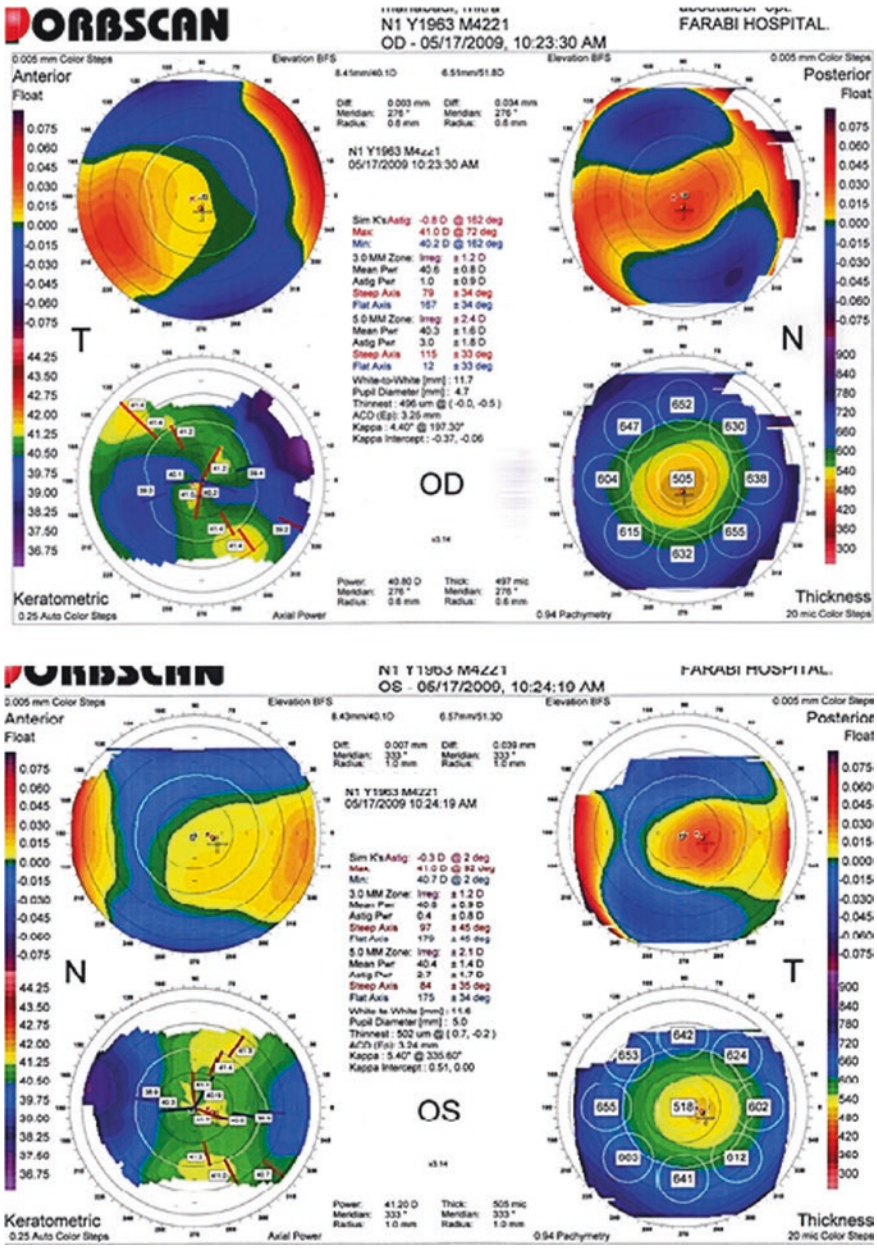

Fig. 34 A case of postoperative PRK with broken bow tie and abnormal values on elevations. Although the refractive errors reduced significantly, Orbscan shows peripheral steepening that indicating the ablation in the center of the cornea

Case 12

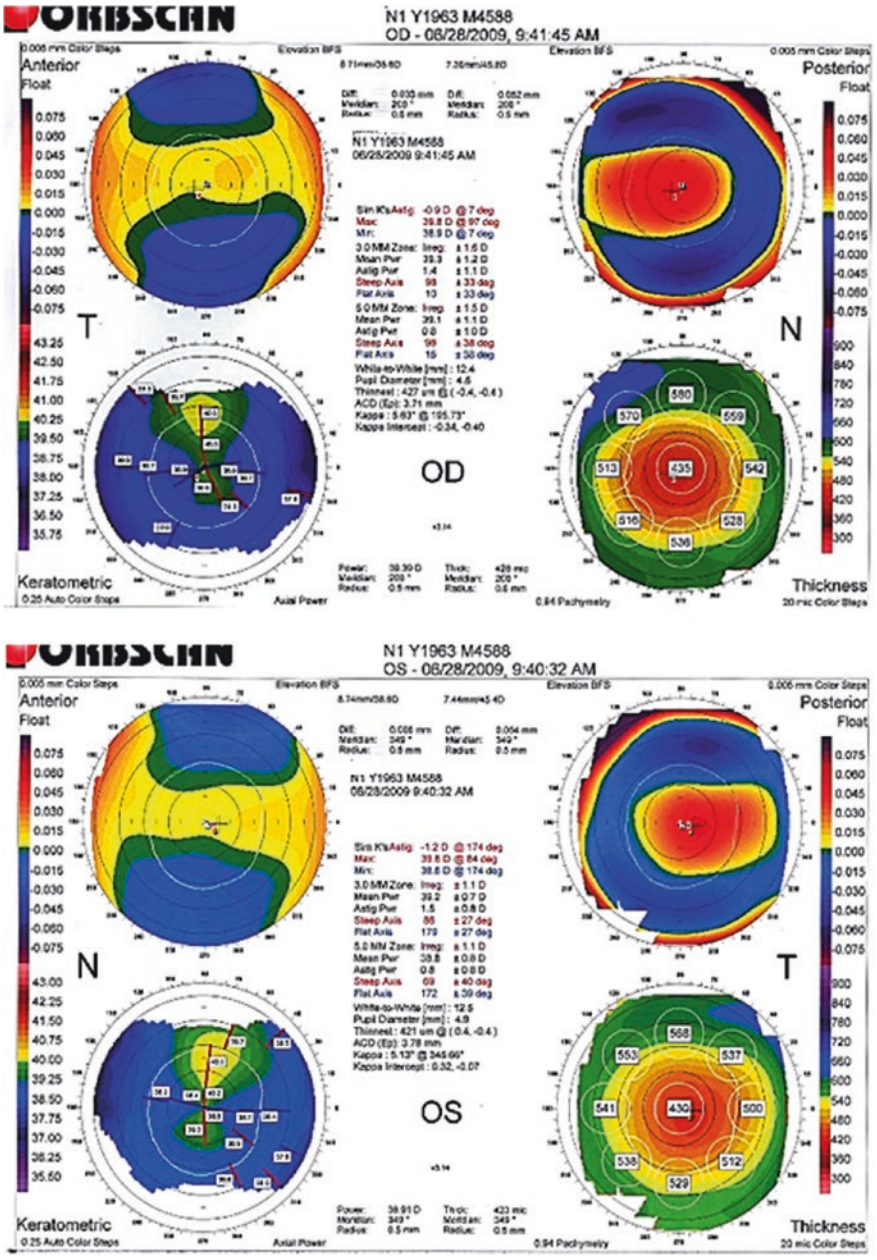

Fig. 35 A 29-year-old man following PRK with superior steepening and central corneal thinning on both corneas diagnosed as decentered ablation. However, the patient has an oblate corneal pattern and should not be treated as post-refractive surgery keratectasia

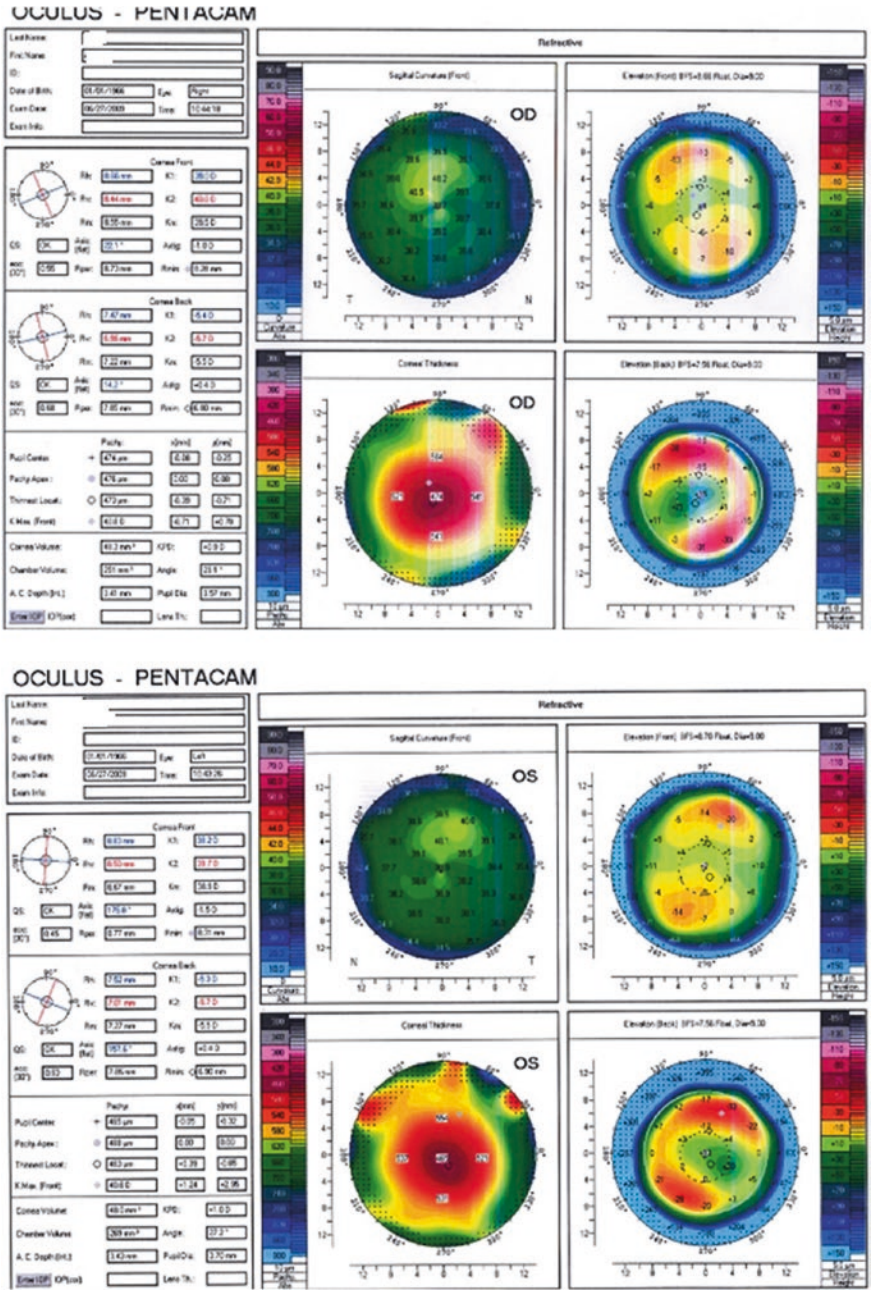

Fig. 36 These findings based on Orbscan data correspond with the Pentacam parameters of the same patient

Case 13

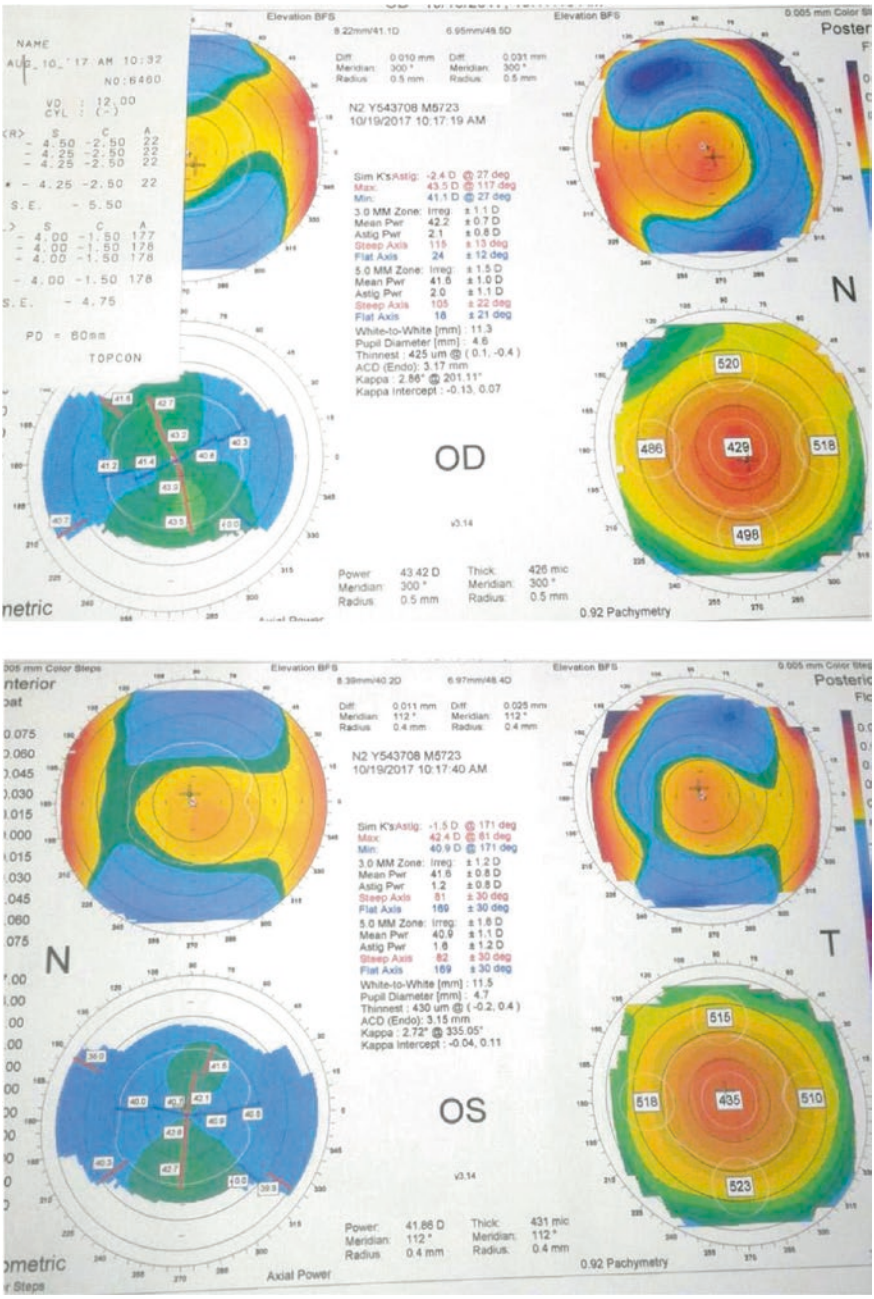

Fig. 37 A 32-year old woman with isolated corneal thinning and the refractive errors: OD = −4.25/−2.50~22 and OS = −4.00/−1.50~180 with normal elevation values and normal Efkarpides index and slight inferior steepening in the right eye and normal elevation and curvature values with asymmetric bow tie in the left eye with the central thin cornea in both eyes not compatible with keratoconus criteria

Case 14

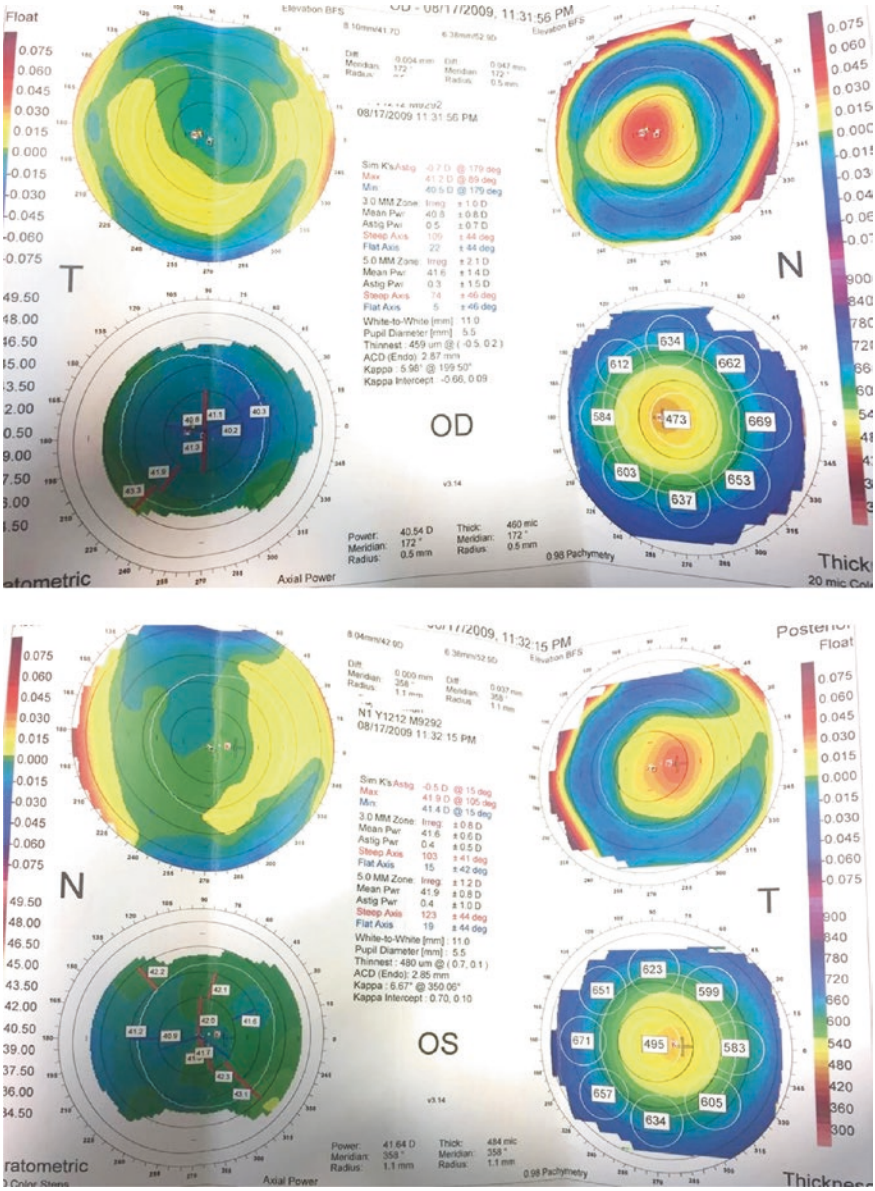

Fig. 38 A 31-year-old man with decentered ablation with a history of refractive surgery and refractive errors: OD = −2.50/−0.50~15 CDVA = 7/10 and OS = −2.00/−0.25~10 CDVA = 9/10 and abnormal values on posterior elevation. That is not well shown in the topographic map of Orbscan. However, it is well shown in the Pentacam topographic map

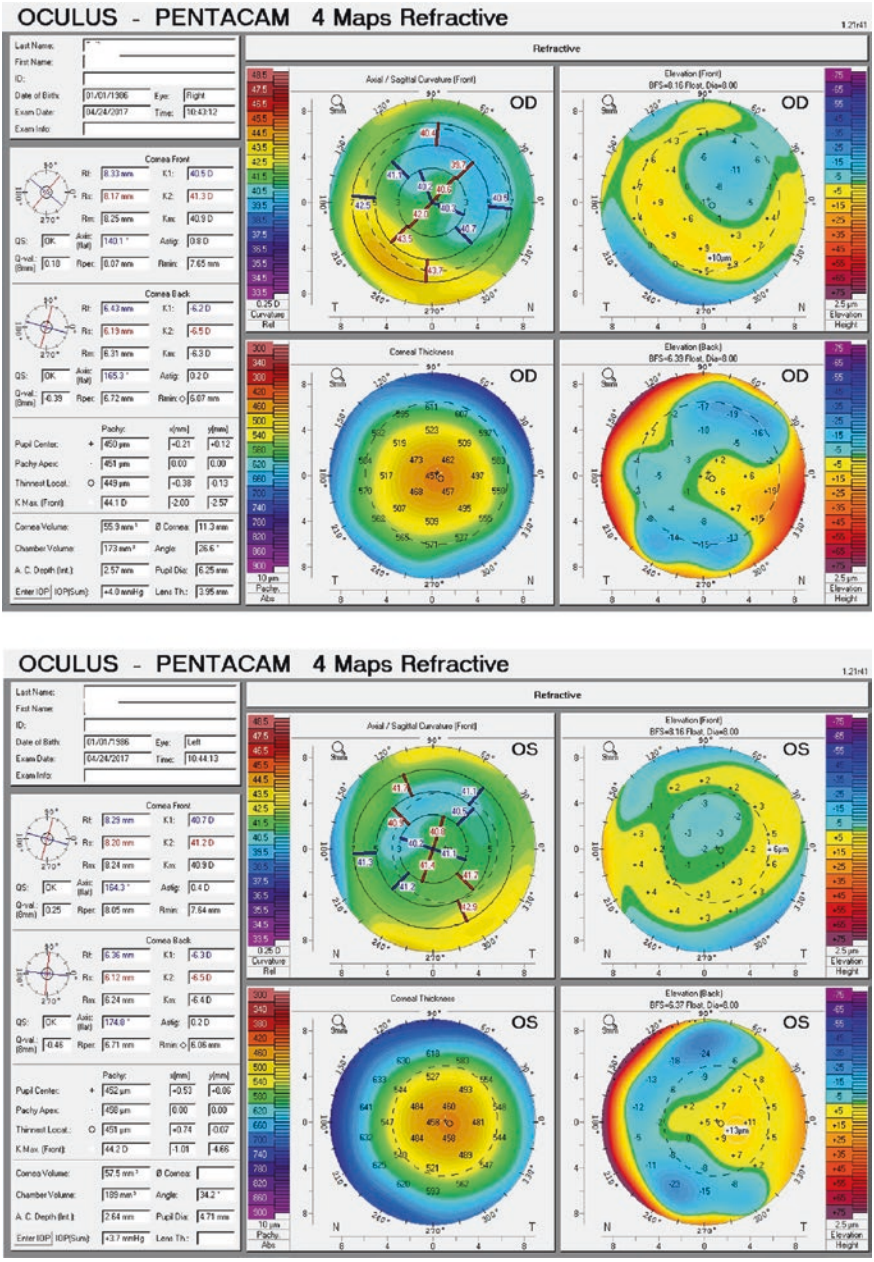

Fig. 38 (continued)

Case 15

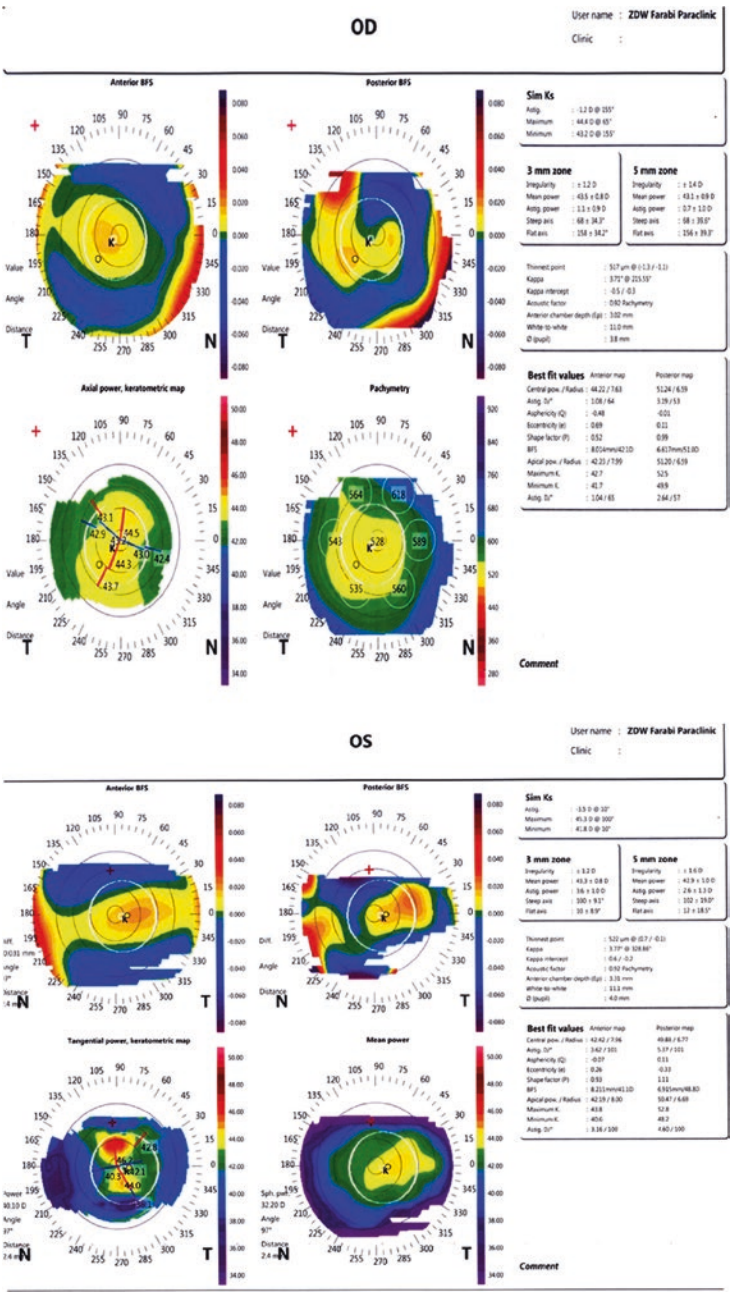

Fig. 39 A 32-year-old woman with forme fruste keratoconus in the right eye and superior steepening less than 20 degrees SRAX, and subclinical keratoconus in the left eye with significant superior steepening of 2.7 diopter with more than 20 degrees SRAX taken with Orbscan 3

Case 16

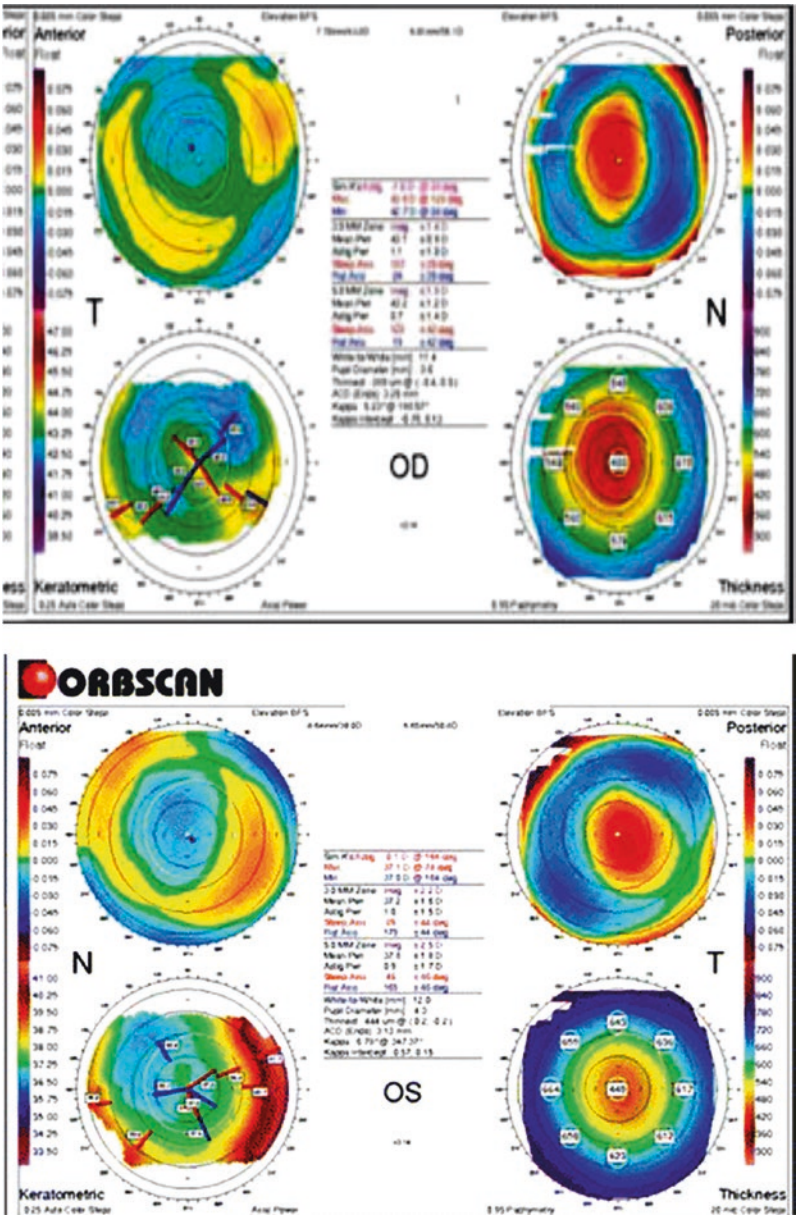

Fig. 40 A case with compound myopic astigmatism following SMILE surgery in two different lenticule depths (160 and 140 μm). The right eye with 160 um cap and left eye with 140 um cap. There was no difference in Postoperative outcomes in terms of uncorrected visual acuity through one year follow up. There were no significant differences in terms of visual acuity and refractive errors between the uses of lenticule at two different depths [7] (With permission from Springer, Cham)

References

1. Orbscan Operator's manual version 2.4 A Z. Rochester, NY 14609 USA: Bausch and Lomb Incorporated; 2008. p. 10, 11, 43–45, 51.
2. Gharieb HM, Othman IS, Elkitkat RS. Orbscan 3 Versus Pentacam HR: Evaluating the possible interchangeable use of various parameters. Cornea; 2020.
3. Marsich MW, Bullimore MA. The repeatability of corneal thickness measures. Cornea. 2000;19(6):792–5.
4. Aghazadeh Amiri M, Hashemi H, Ramin S, Yekta A, Taheri A, Nabovati P, et al. Corneal thickness measurements with Scheimpflug and slit scanning imaging techniques in keratoconus. J Curr Ophthalmol. 2017;29(1):23–7.
5. Mohammadpour M, Mohammad K, Karimi N. Central corneal thickness measurement using ultrasonic pachymetry, rotating scheimpflug camera, and scanning-slit topography exclusively in thin non-keratoconic corneas. J Ophthalmic Vis Res. 2016;11(3):245–51.
6. Saad A, Gatinel D. Validation of a new scoring system for the detection of early forme of keratoconus. Int J Keratoconus Ectatic Corneal Diss. 2012;1(2):100–8.
7. Güell JL, Verdaguer P, Pallás H, Elies D, Gris O, Manero F. Advantages and disadvantages of different cap thicknesses. In: Sekundo W (ed) Small Incision Lenticule Extraction (SMILE). Cham: Springer; 2015. p. 116.

Pentacam

Mehrdad Mohammadpour and Zahra Heidari

Introduction

Pentacam® (Oculus Optikgeräte GmbH, Wetzlar, Germany) is a rotating Scheimpflug camera that takes images in 3 dimensions in 2 s from 25.000 (HR/AXL: 138.000) points for providing complete images from corneal surfaces. It can be evaluated the cornea from limbus to limbus. The analysis of the ocular anterior segment consists of the calculation of the ocular chamber angle, volume, and height.

Images can be taken from the anterior and posterior surface of the cornea, the iris and the both surfaces of the lens, also the densitometry of the lens and cornea is automatically measured. All images transferred to the computer and several data derived from information. The new Pentacam AXL measures the axial length of the eye from the anterior surface of the cornea to the retina and calculates the IOL power for surgery planning. This measurement is performed by partial coherence interferometry (PCI) before the rotating Scheimpflug measuring procedure.

M. Mohammadpour (✉)
Department of Ophthalmology, Faculty of Medicine, Farabi Eye Hospital and Eye Research Center, Tehran University of Medical Sciences, Tehran, Iran
e-mail: mahammadpour@yahoo.com

Z. Heidari
Noor Ophthalmology Research Center, Noor Eye Hospital & Tehran University of Medical Sciences, Tehran, Iran
e-mail: zahra.heidari77@yahoo.com

M. Mohammadpour (ed.), *Diagnostics in Ocular Imaging*,
https://doi.org/10.1007/978-3-030-54863-6_3

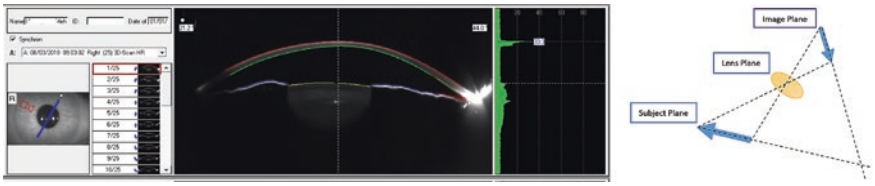

Fig. 1 Display of Scheimpflug images and its principle

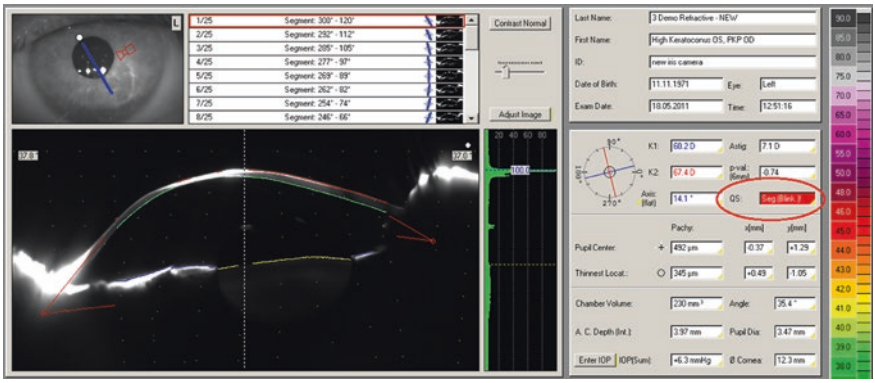

Fig. 2 Pentacam program for QS evaluation (*With permission from Oculus Pentacam*) [1]

Scheimpflug Image

Pentacam provides an overview of Scheimpflug and iris imagery. The advantage of Scheimpflug over the conventional method is that the object, lens, and image planes are not parallel to each other, but intersect in a common straight line, thereby increasing the depth of focus (Fig. 1).

Quality Specifications

The quality specification (QS) should be checked after each examination and in a perfect exam, it will be "OK" in the white color. If the QS item was yellow or red, the test should be repeated (Fig. 2).

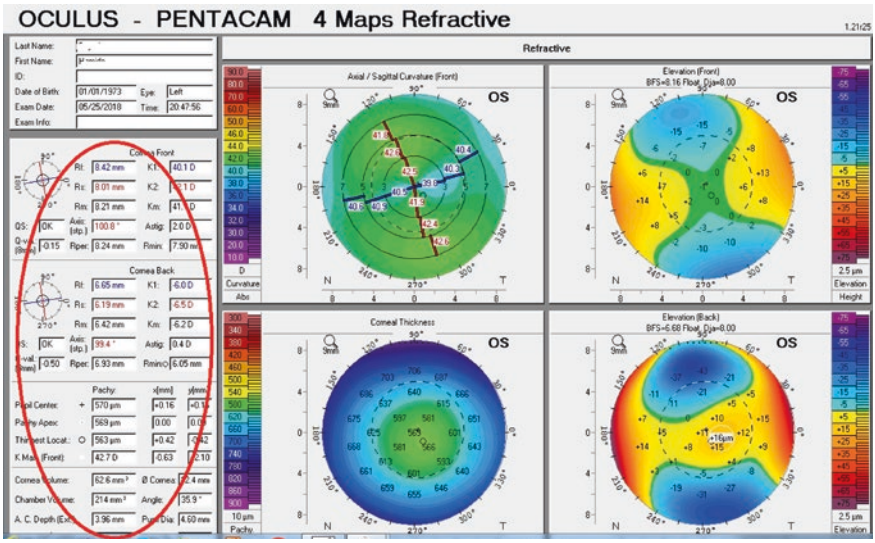

Fig. 3 Four maps display

The Various Topography and Tomography Maps of Pentacam

There are important topographic and tomographic maps in Pentacam, and both patterns and indices should be studied for the comprehensive evaluation of the cornea.

Refractive Maps

This display shows the pachymetry, topography and elevation maps of both anterior and posterior surfaces of the cornea, which are very useful maps for screening the patients for refractive surgery. The anterior surface, posterior surface, thickness, and anterior chamber information are also available in the refractive map (Fig. 3).

The curvature powers of the flat meridian (K1) and steep meridian (K2) in 3 mm zone, mean curvature power at 3 mm zone (SimK), maximum keratometry (Kmax), amount of corneal astigmatism, Axis of corneal astigmatism in 3 mm

Table 1 The author's (Mehrdad Mohammadpour) suggestive diagnostic criteria for normal, keratoconus suspect (SKCN) and definite keratoconus (KCN) for Pentacam

	Normal	SKCN	KCN
K max (D)	<47.2	47.2- 49	> 49
Against the rule astigmatism (D)	<1	1 - 2	>2
Corneal astigmatism (D)	<6	6 – 7	>7
Thinnest point (μm)	>500	470 - 500	< 470
Difference between Pachy Apex and Thinnest location (μm)	< 10	10 - 20	>20
Difference central thickness between two eyes (μm)	<10	10-30	>30
Displacement of the thinnest point from the center (mm)	<0.5	0.5 – 1	>1
Skewed Steepest Radial Axis (SRAX) (degrees)	<10	10-20	>21
IS value (Inferior- Superior difference at the 3 mm) (D)	<1.4	1.4 – 1.9	>1.9
IS value (Inferior- Superior difference at the 5 mm) (D)	<1.4	1.4 - 2.5	>2.5
Anterior elevation (μm)	<10	10 - 12	>12
Posterior elevation (μm)	<15	15 - 17	>17

There are no definite criteria for inclusion or exclusion of keratoconus.

Table 2 Amsler-Krumeich Keratoconus classification system [2, 3]

Stage I	Eccentric steepening Induced myopia and/or astigmatism of ≤5.0 D K-reading ≤48.00 D Vogt's lines, typical topography
Stage II	Induced myopia and/or astigmatism between 5.00 and 8.00 D K-reading ≤53.00 D Pachymetry ≥400 μm
Stage III	Induced myopia and/or astigmatism between 8.01 and 10.00 D K-reading >53.00 D Pachymetry 200–400 μm
Stage IV	Refraction not measurable K-reading >55.00 D Central scars Pachymetry ≤200 μm

zone, the corneal thickness at the apex (Pachy Apex), corneal thickness compatible with pupil center location (Pupil Center), the diameter of the pupil, the location of the thinnest point and corneal chamber data are the parameters in the refractive map. The normal and pathological values of some important parameters are shown in Table 1.

Keratoconus classification based on topographic data are displayed in Amsler-Krumeich criteria (Table 2).

There are other definitions for ectasia based on clinical examination and topographic criteria. Forme fruste keratoconus (FFKCN) is defined as eyes with apparently normal corneal topographic patterns with definite keratoconus in the fellow eye.

Table 3 New keratoconus spectrum classification (Mohammadpour classification)

Examination	Normal	KCN Suspect	Subclinical KCN	Forme Fruste KCN	Definite KCN
Slit-lamp	-	-	-	-	+
Retinoscopy	-	-	-	- (+) in fellow eye	+
Topography	-	Suspect (Subtle changes)	+	- (+) in fellow eye	+
Tomography	-	±	+	± (+) in fellow eye	+
Aberrometry	-	- (Subtle changes)	+	± (+) in fellow eye	+
Epithelial thickness map	-	- (Subtle changes)	+	± (+) in fellow eye	+
Biomechanics	-	±	+	± (+) in fellow eye	+

Minus sign (-) stands for negative or no sign(s) of keratoconus (KCN).
Positive sign (+) stands for positive sign(s) of keratoconus (KCN).

Eyes with abnormal topographic pattern compatible with early keratoconus and no clinical sign in slit lamp or retinoscopy examinations are considered as subclinical keratoconus (SCKCN).

Keratoconus suspect is defined as eyes with completely normal clinical examination and subtle topographic changes that are not completely compatible with definite KCN pattern (Table 3). The schematic presentation of these groups based on optimum cut off on topographic indices values are shown in Fig. 4. Corneal judgment only based on the cutoff point may compatible with true keratoconus, normal cornea (false positive), or true subclinical keratoconus (true positive).

Thickness Map

The distribution of corneal thickness in the absolute pachymetry map shows the thickness of the cornea across the entire surface of the cornea from limbus to the limbus, and the related color bar shows the corresponding values. The relation of current corneal thickness to the normal range is shown with the relative pachymetry map and the corneal evaluation is based on thinnest point location (Fig. 5). In low central corneal thickness (CCT) eye with low refractive error, the

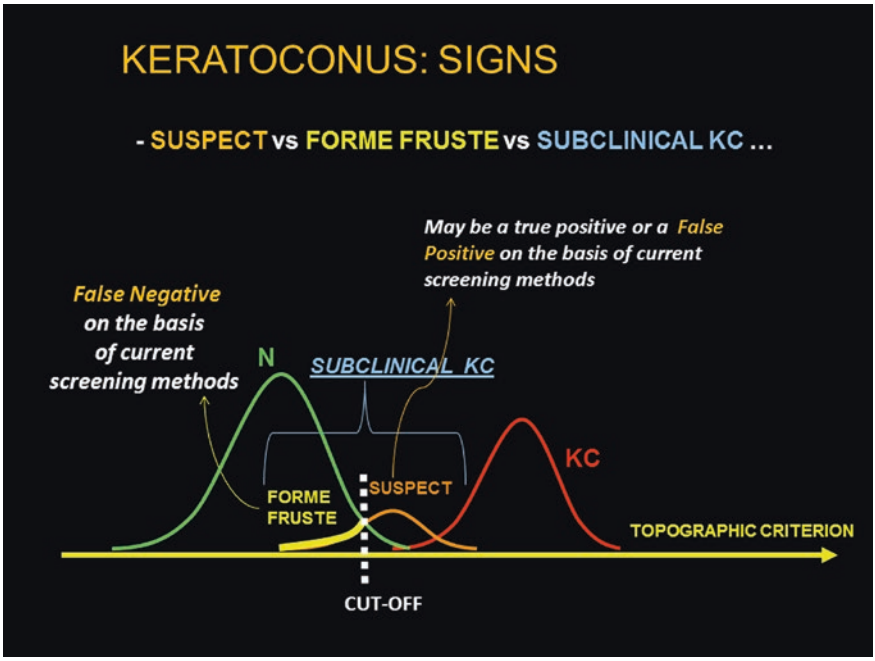

Fig. 4 Schematic images for signs of ectatic corneas (*Courtesy to Dr. Gatinel with permission for Springer Nature*) [4]

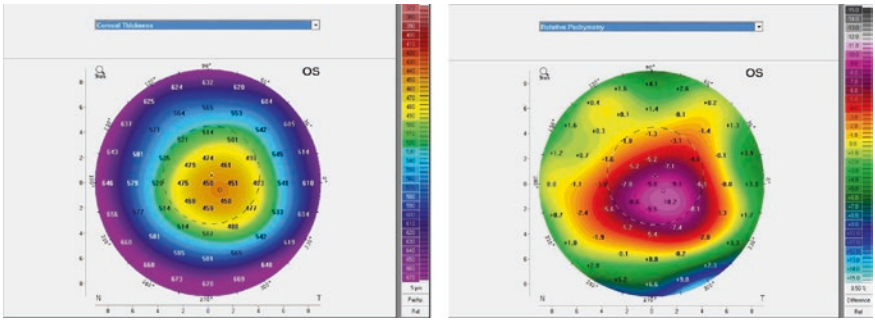

Fig. 5 Absolute and relative pachymetry maps

photorefractive keratectomy (PRK) could be the better approach for refractive surgery than laser-assisted in situ keratomileusis (LASIK) [5].

There are three important landmarks in the thinnest map including corneal apex, thinnest location (TL) and two opposite superior and inferior points at the central 5 mm diameter and the concentric shape is a normal pachymetry pattern

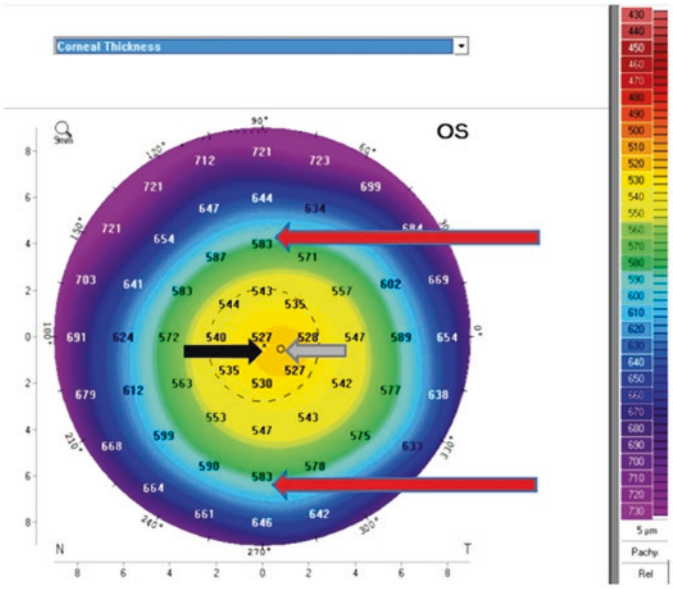

Fig. 6 The concentric shape with apex (black arrow), thinnest location (gray arrow), and two opposite points in superior and inferior (red arrows) part of the cornea

in thickness map (Fig. 6). Thickness difference less than 30 μm is the normal values for S-I difference. Difference between Pachy Apex and the thinnest location is <10 in the normal eye and difference thickness between two eyes more than 30 is compatible with pathological criteria (Table 1). Horizontal displacement, Dome shape, Bell shape, and keratoglobus are abnormal patterns correlated with abnormal corneal thickness. In central corneal thickness measurement in the thin cornea with normal topography, Pentacam had a better agreement with ultrasound (US) pachymetry than the Orbscan [6]. In eyes with refractive surgery (LASIK), Pentacam and Galilei are comparable with US pachymetry and Orbscan has a thinner measurement [7].

Corneal Power Map

Corneal curvature values including axial (sagital) curvature or instantaneous (tangential) curvature, are measured based on a geometrical corneal slope. Geometrical radii (mm) values are converted into refractive power values and are shown in diopters (D) according to the formula of $D = (1.3375 - 1) * (1000)/Rmm$.

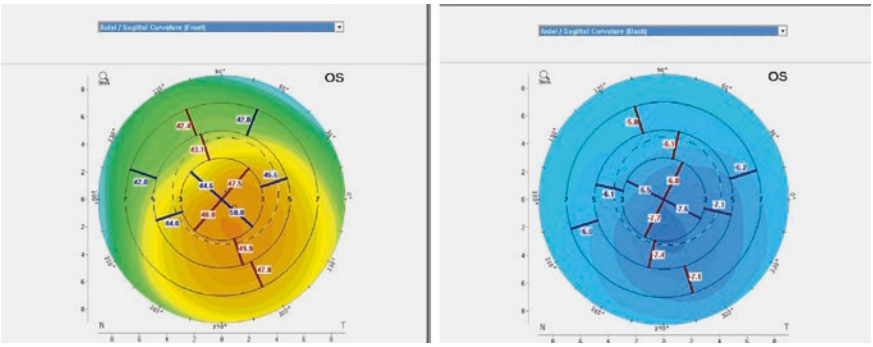

Fig. 7 Display of sagittal (axial) curvature for the anterior and posterior surface

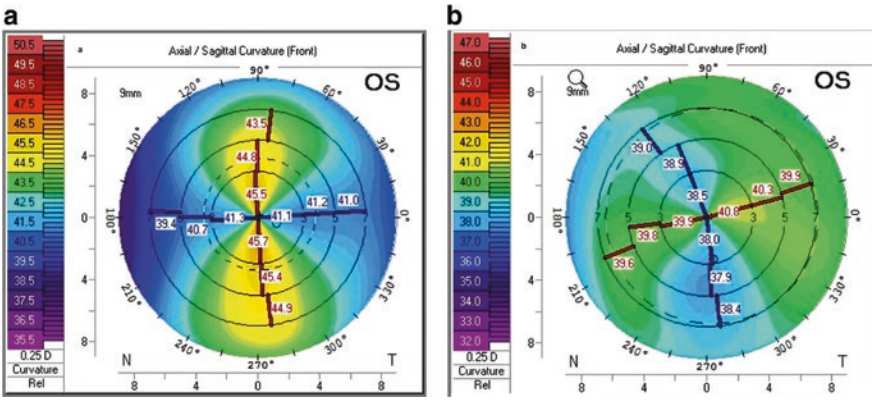

Fig. 8 Sagital curvature map for the normal cornea. The vertical SB demonstrated with the rule astigmatism (**a**) and horizontal SB (**b**) indicates against the rule astigmatism

Sagital Curvature Map

This map shows the curvature value of the cornea and depend on the slope of the measuring point and optical axis relationship. Steep areas are shown with hot color and flat areas are displayed with cold color (Figs. 7 and 8).

The normal pattern is symmetric bow tie (SB) with aligning and equal size in two segments. The skewed radial axis (SRAX) is the angle between the axes of the two segments, and any amount of SRAX is abnormal and more than 21 degrees is compatible with keratoconus (Table 1 and Fig. 9).

Abnormal patterns in the sagittal map are shown in Fig. 10. The different bow tie patterns indicate the irregularity of the curvature and shape of the cornea and these patterns contribute to the degree of astigmatism, however, there is a subtle amount of astigmatism in most of the human eyes. Different patterns of an axial map of Pentacam allow easy interpretation of different sources of astigmatism.

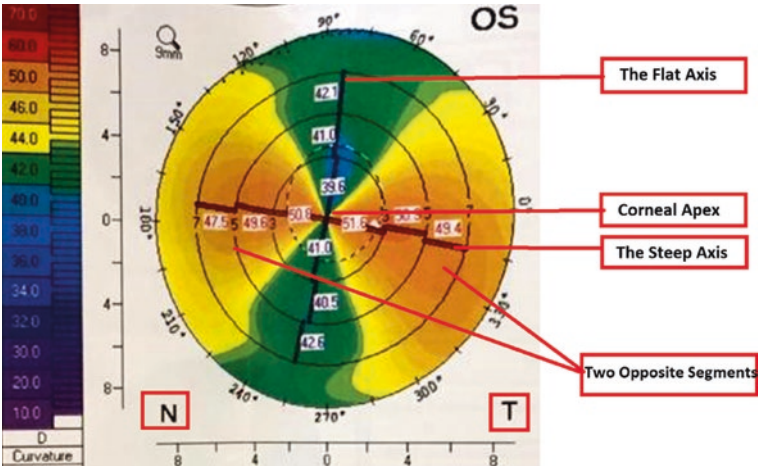

Fig. 9 The symmetric bow ties are characteristic in the sagital map

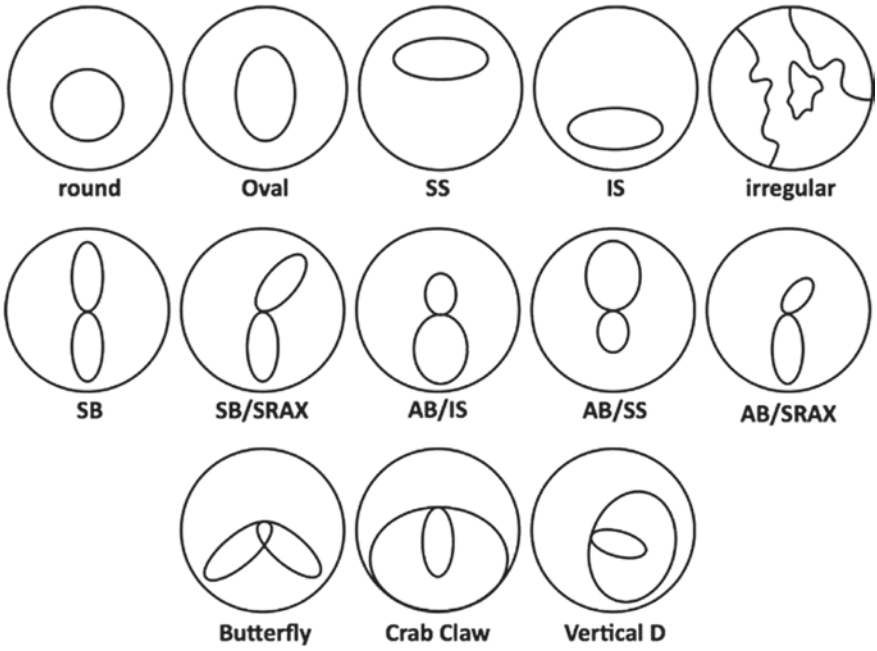

Fig. 10 Normal and abnormal corneal curvature patterns in the axial map (*With permission from Springer Nature*) [10]

Total corneal astigmatism (refractive astigmatism) includes anterior corneal astigmatism and ocular residual astigmatism (ORA). Understanding the different types of astigmatism is important before refractive surgery.

We studied the correlation of astigmatism components in 376 refractive surgery candidate eyes and found that there were good correlations between refractive astigmatism and corneal and residual astigmatism, however, the correlation between corneal astigmatism and ORA was weak [8]. Corneal astigmatism contributes more than 80% of refractive astigmatism [9].

Tangential Curvature

This display show the true corneal irregularities and compatible to the cornea curvature in measuring point (Fig. 11).

True Net Power Map

The optical power of the cornea is calculated based on the aggregated data of the anterior (corneal tissue: 1.376) and the posterior refractive surfaces (aqueous humor: 1.336) (Fig. 12).

The underlying equation is [1]:

$$\text{True Net Power} = \frac{1.376 - 1}{\text{anterior surface radius}} * 1000 + \frac{1.336 - 1.376}{\text{posterior surface radius}} * 1000$$

Keratometric Power Deviation Map

The difference between true net power map and anterior sagital map is the keratometric power deviation (KPD) map. This map indicates the effect of the posterior corneal surface (Fig. 13).

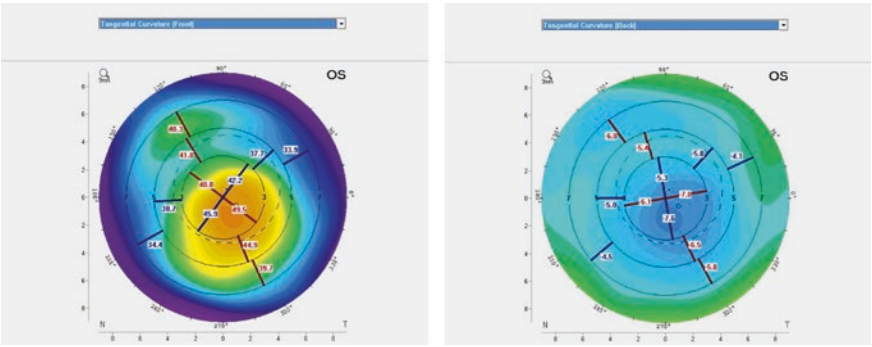

Fig. 11 Display of tangential curvature for the anterior and posterior surface

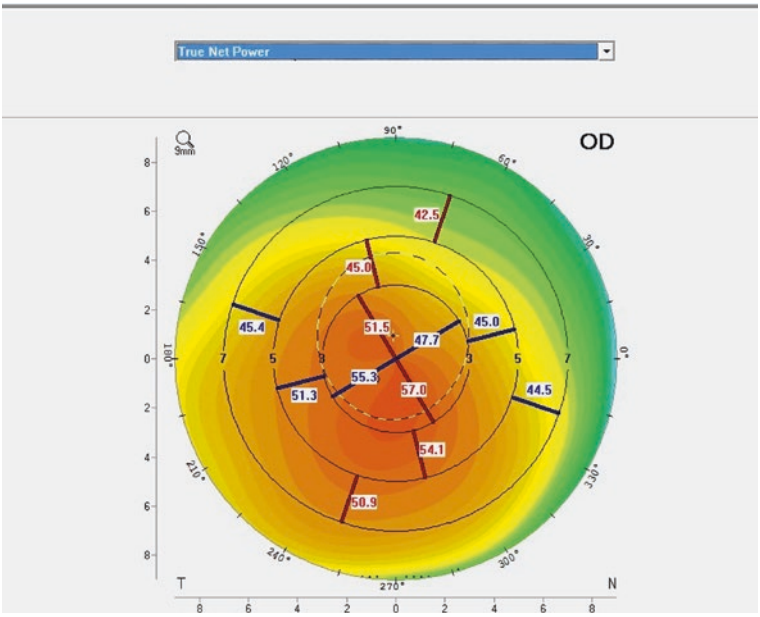

Fig. 12 True net power map for the keratoconus

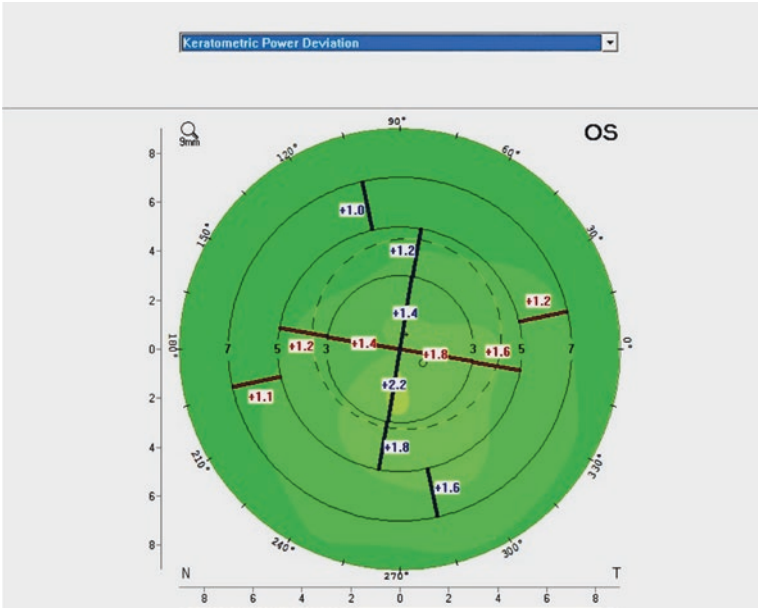

Fig. 13 Keratometric power deviation map

Equivalent Keratometer Readings Power Map

This map is known as Equivalent Keratometer Readings (EKR) and computed based on Snell's law by including the refractive indices of corneal tissue and aqueous humor and anterior and posterior power values (Fig. 14).

Total Cornea Refractive Power Map

This map shows the refractive power of the cornea which calculates based on the ray-tracing method (Fig. 15).

The Fast Screening Report Maps

This is a very important display for a quick overview of the cornea. This map shows the routine examination such as the anterior chamber, the pachymetry and the elevation data of the anterior or posterior surface of the cornea, and the patient's corneal densitometry of the cornea. The normal distribution is shown in the green and pathologic condition is shown in red color.

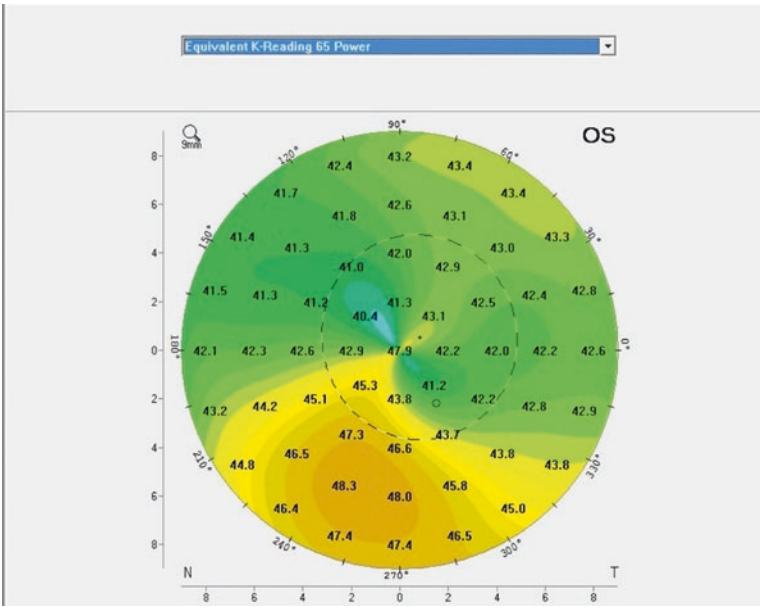

Fig. 14 EKR power map for the keratoconus

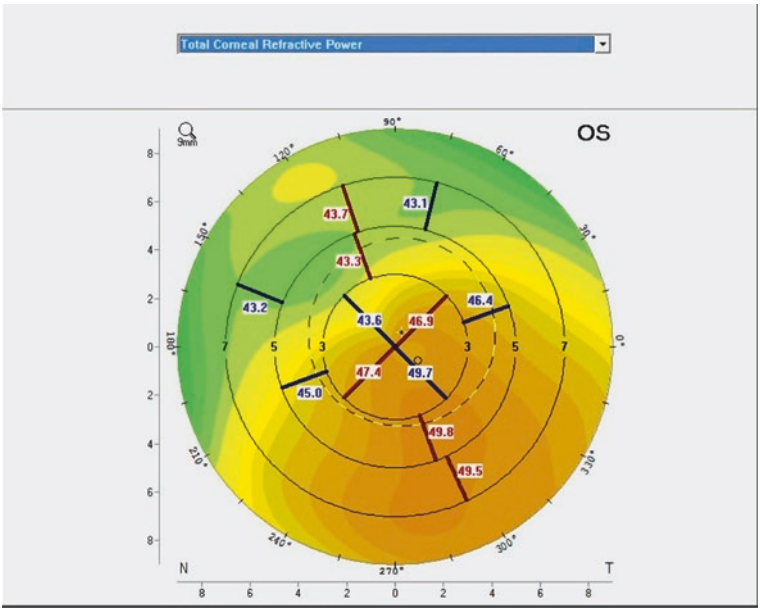

Fig. 15 Total corneal refractive power map

The bottom of the map is shown screening reports based on elevation data (BADD), the degree of the disease (TKC) and the degree of nuclear opacity (PNS) if the cataract is available (Fig. 16).

Corneal Thickness Spatial Profile (CTSP)

Corneal thickness values at the thinnest point are calculated based on the average of 22 rings centered on the thinnest point at 0.4 mm steps. The calculated values are shown in a progression graph as the CTSP line which starting from the thinnest point. Data is displayed at a 95% confidence interval from a normal population and helps clinicians to compare the profile of each eye with a normal population. The thin cornea or ectatic eyes shows abrupt and abnormal profiles, out of the 95% CI. The X-axis in a CTSP diagram shows the distance to the thinnest position on the cornea and Y-axis represents the absolute value of the corneal thickness (Figs. 17 and 18).

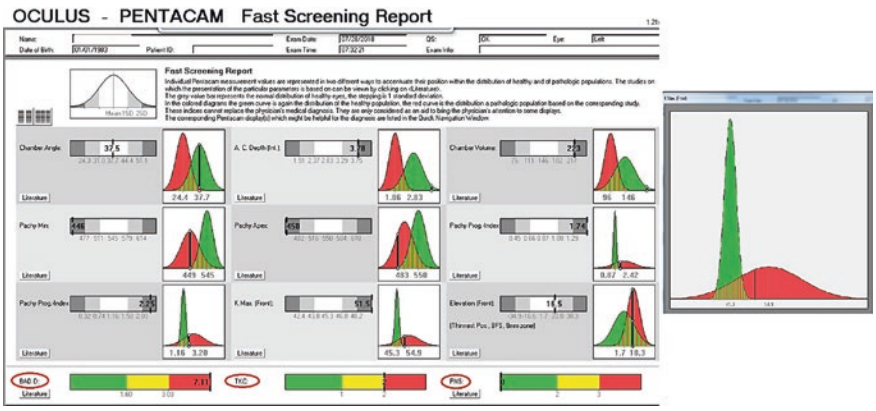

Fig. 16 The fast screening report display

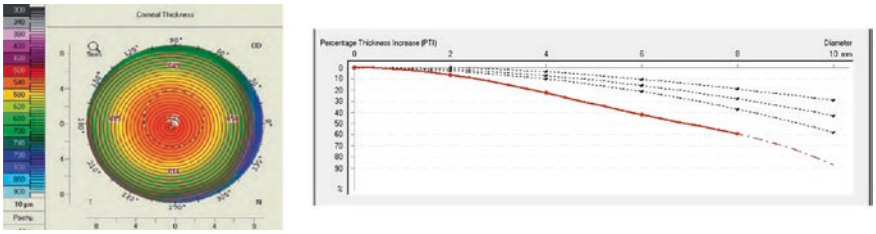

Fig. 17 The corneal thickness spatial profile (CTSP) in keratoconus, calculated based on the average of the concentric rings with the thinnest point (*With permission from Oculus Pentacam*) [1]

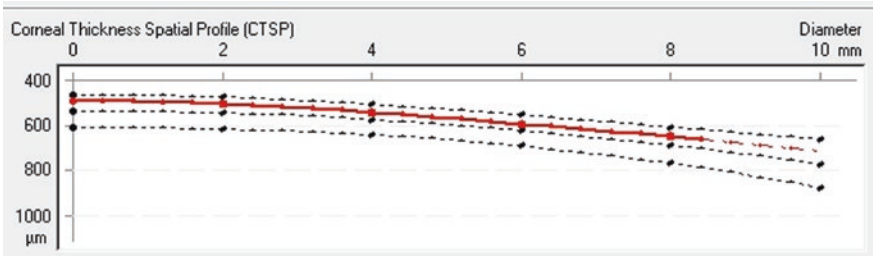

Fig. 18 Thickness profile in an ectatic eye

Percentage Thickness Increase (PTI)

Progression of corneal thickness is identified with PTI index which calculated according to the below formula [1]:

$$\text{PTI} = \frac{(\text{mean corneal thickness in the ring} - \text{thinnest corneal thickness})}{\text{thinnest corneal thickness}}$$

CTSP and PTI are powerful discriminant factors for keratoconus detection from the normal cornea. The normal average of profiles is 0.8–1.2. Abnormal profiles

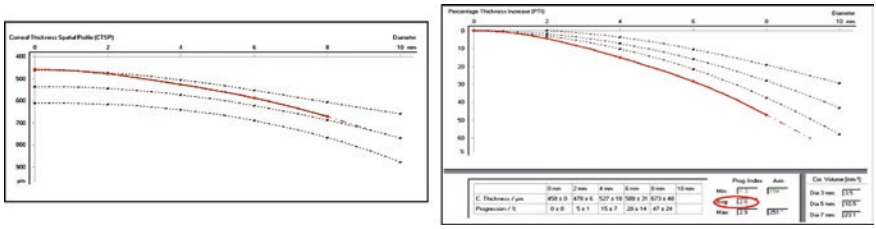

Fig. 19 Quick slop profile (*With permission from Springer Nature*) [11]

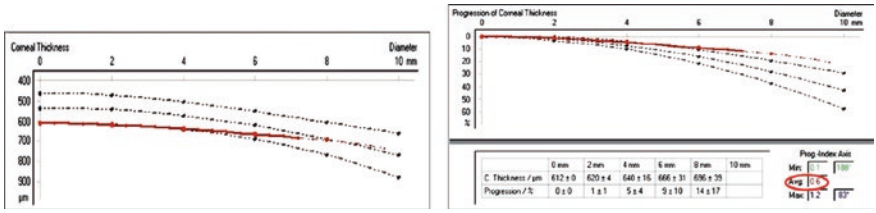

Fig. 20 Flat shape profile (*With permission from Springer Nature*) [11]

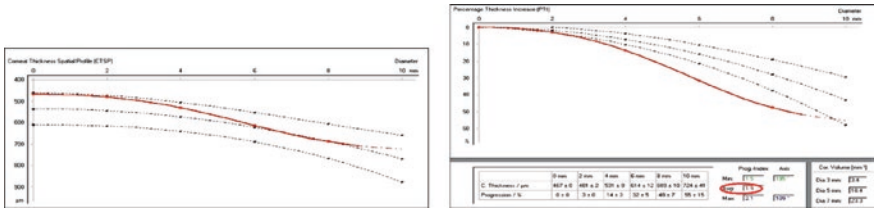

Fig. 21 S shape profile (*With permission from Springer Nature*) [11]

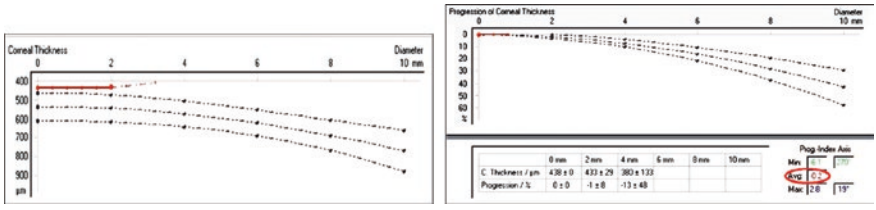

Fig. 22 The inverted shape profile (*With permission from Springer Nature*) [11]

include quick slope, flat shape, S shape, and inverted profile. In a quick slope profile, the red line leaves its direction before the 6 mm zone. It is compatible with the subclinical keratoconus pattern. The average is higher than 1.2 [11] (Fig. 19).

In the flat profile, the red line takes a straight direction. It is compatible with the thickened cornea such as the oedematous condition in Fuch's dystrophy. The average is low (<0.8) (Fig. 20).

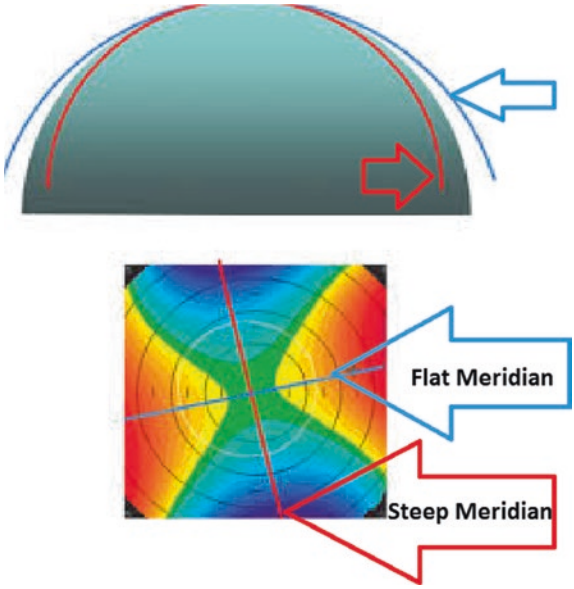

Fig. 23 The shape of the elevation map with the best fit sphere reference (*With permission from Springer Nature*) [10]

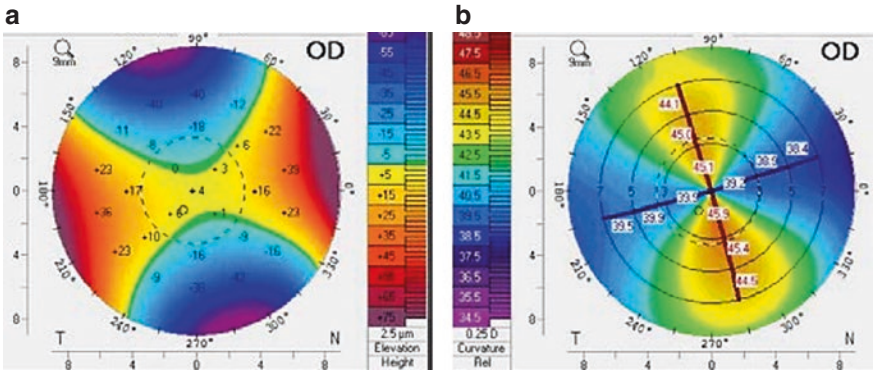

Fig. 24 A normal pattern of elevation map based on best fit sphere reference (**a**), which is compatible with orthogonal symmetric bow-tie with the rule astigmatism in curvature map (**b**)

In S shape the red line curved as "S". It is compatible with ectatic disorders and FFKCN. The average is high (>1.2) (Fig. 21).

In an inverted profile, the red line curved follows an upward direction. It is compatible with some pellucid marginal degeneration (PMD) cases. The average is very low (<0.8) (Fig. 22).

Elevation Maps

The elevation values are obtained from the height data compared with the reference surface. Points above the reference surface indicated plus values and points below the reference surface indicated minus values (Fig. 23).

The normal shape of the cornea in the elevation map is symmetric hourglass (sandy watch) pattern (Fig. 24). There are some abnormal corneal shapes in the elevation map which are considered the abnormality in corneal surfaces. Abnormal shapes including skewed hourglass, tongue-like and isolated island.

The Pentacam using a cross-sectional technique to recognize the anterior and posterior corneal surface, the anterior iris, and both surfaces of the lens. Measurement of these surfaces and their relative positional data can provide anterior and posterior elevation maps as well as complete corneal thickness maps. Elevation values could helpful for screening abnormal eyes. Elevation difference less than 10 μm is considered normal cornea for anterior surface and difference less than 15 μm is considered normal cornea for posterior surface. Elevation differences more than 12 μm or 17 μm is considered as keratoconus for anterior and posterior, respectively. The difference between 10–12 μm for the anterior surface and 15–17 μm for the posterior surface is considered suspicious cornea (Table 1) (Fig. 25).

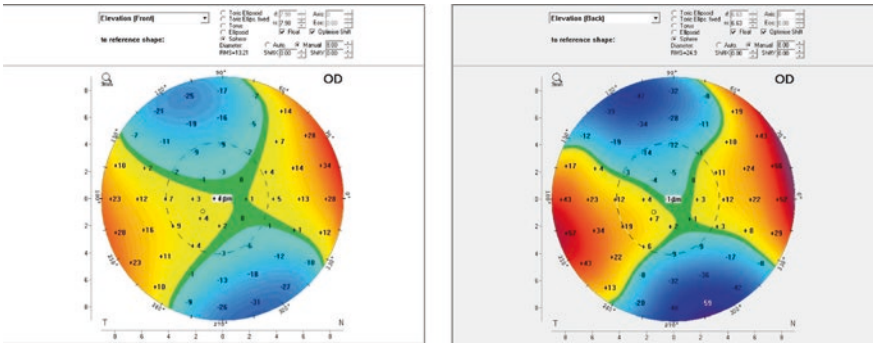

Fig. 25 Front and back elevation maps of a keratoconic cornea related to the best fit sphere

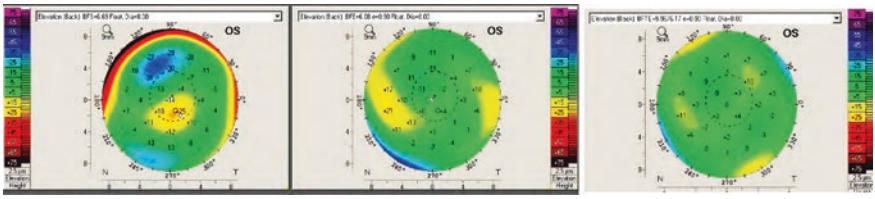

Fig. 26 Elevation maps based on different reference shapes, BFS, BFE, and BFTE, respectively (*With permission from Oculus Pentacam*) [1]

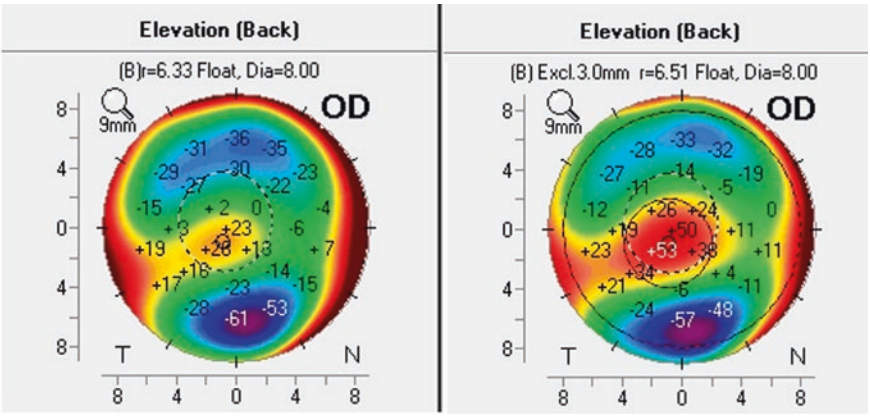

Fig. 27 Standard BFS and enhanced reference surface in the case of FFKCN

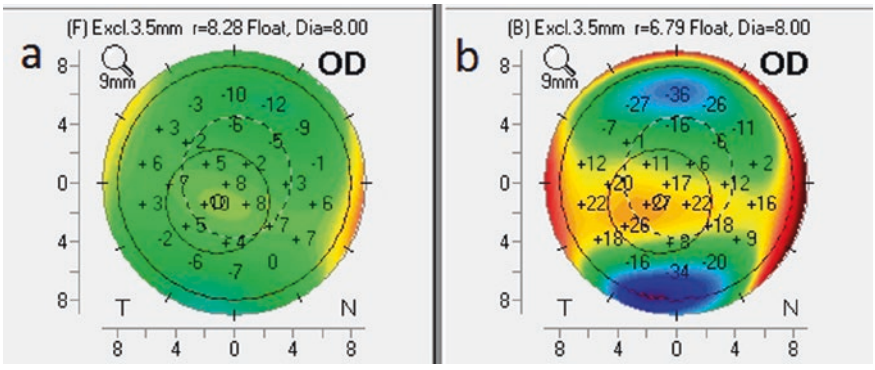

Fig. 28 Front (**a**) and back (**b**) elevation maps of a keratoconic cornea using an enhanced reference shape with an exclusion zone

There are 3 important reference shapes in Pentacam including best fit sphere (BFS), best-fit ellipse (BFE), best fit toric ellipse (BFTE). The BFE is perfect for the real shape of the cornea, and BFTE is considered for the astigmatic cornea (Fig. 26).

The float mode of the BFS in 8 mm diameter is the useful reference shape which provides simple interpretable information about corneal surfaces, however, it is influenced by the ectatic area and leads to the BFS steepening and partially masking the cone. The enhanced reference surface (ERS) solves this problem. It is a modified BFS which uses the same 8.0 mm central optical zone and removes a 3.50–4.00 mm area around the thinnest point in BFS calculation, so the impact of the cone at the best fit reference surface is minimized effectively (Fig. 27).

The ERS is important for preoperative refractive surgery screening to differentiate forme fruste keratoconus and subclinical keratoconus from normal eyes (Fig. 28).

In addition to BFS and ERS, there are two difference maps on the Belin display that indicate elevation changes from the standard map (baseline) to the exclusion

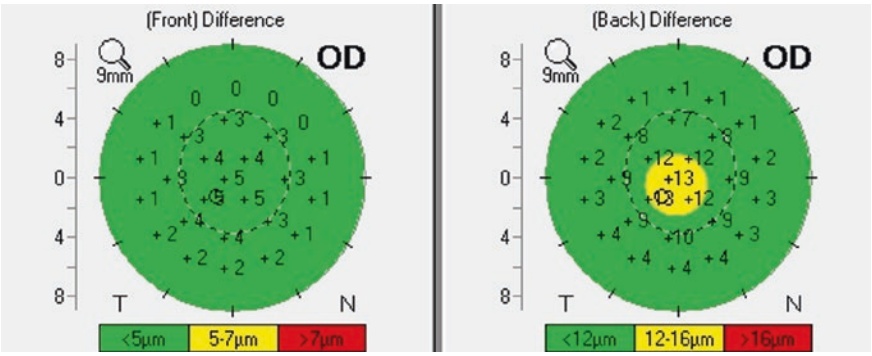

Fig. 29 Belin/Ambrósio Enhanced Ectasia Display (version III) difference maps on anterior and posterior surfaces

map (Fig. 29). These maps correspond to three-color scales that determine the amount of elevation change. In the normal cornea, the green color on the difference map indicates a change in elevation (from baseline to exclusion map) less than 6 μm on the anterior surface and 8 μm on the posterior surface of the cornea.

In the suspicious cornea, the yellow color indicates a change of between 6 and 12 μm for the front surface and 8–20 μm for the posterior surface. In eyes with keratoconus, red color is seen and indicates areas where the elevation difference between the two maps is 12 μm anterior or 20 μm posterior [1].

While, the front surface does not show much change from the baseline to the exclusion elevation map (the map is all green), the posterior surface shows a significant change (yellow central area).

The Belin/Ambrósio Enhanced Ectasia Display

This display designed by a Pentacam rotating Scheimpflug camera and provides extensive screening for subclinical ectatic disease. This display shows the anterior and posterior elevation and pachymetric data into one display, allowing us to quickly screening of refractive surgery candidates with an overview of the corneal shape. The changes in elevation values from BFS to ERS could effective for differentiation ectatic corneas from normal corneas.

There are important indices on the new version of Belin/Ambrósio Enhanced Ectasia Display (third version) such as curvature parameters (K1, K2, and Kmax), pachy thin location, elevation thickness at the front and the back surfaces of the cornea (F.Ele.Th and B.Ele.Th), progression thickness indices (PPI and ARTmax), and BADD indices (Fig. 30). The average of all parameters with pachymetric graphs (CTSP and PTI) allow the early keratoconus detection accurately. The average of PTI in normal cornea is less than 1.2 μm and if it is more

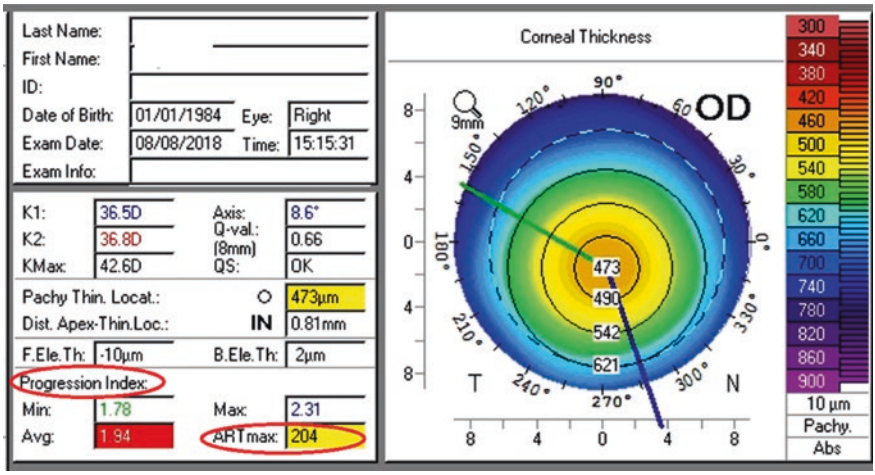

Fig. 30 Important keratoconus diagnostic indices in the Ambrósio display

Table 4 Suggestive relational and combined pachymetric indices for diagnosis of normal, keratoconus suspect (SKCN) and definite keratoconus (KCN)

	Normal	SKCN	KCN
Pachymetric Progression Index average (PPI-Ave)	<1.0	1.0 – 1.2	>1.2
Maximum Pachymetric Progression Index (PPI-Max)	<1.2	1.2 – 1.4	> 1.4
Ambrosio relational thickness average (ART-Ave)	>430	400 - 430	<400
Maximum Ambrosio relational thickness (ART-Max)	>340	300 - 340	< 300
Belin/Ambrosio enhanced ectasia total deviation value (BADD)	<1.6	1.6 – 2.6	> 2.6

There are no definite criteria for inclusion or exclusion of keratoconus.

than 1.2 µm compatible with abnormal cornea. A pachymetric progression index (PPI) is calculated from the thinnest point for every one degree meridian along the complete 360°. We found the averages and the standard deviation (SD) of PPI of the maximum meridians are 1.287 ± 0.204, 1.658 ± 0.415, and 2.710 ± 0.835 in normal, keratoconus suspect and definite suspect, respectively and PPImax had good accuracy (AUC > 0.8) for subclinical and definite KCN detection (AUC: 0.82 and 0.98, respectively) [12].

One of the important parameters in the Ambrósio display is the Ambrosio relational thickness (ARTmax) index, which facilitates the identification of abnormal

corneas. This index is calculated with the thinnest pachymetric value divided by the pachymetric progression. Ambrósio et al. [13] reported The ART-Mid and ART-Max have AUC of 0.98 and 0.99, with cut-offs of 426 μm and 339 μm, respectively for the normal cornea. They suggested if ARTMax < 400 μm do not perform LASIK. The author's suggestive criteria for new tomographic indices are presented in Table 4.

The BADD index (final D) is calculated by regression analysis and comparison between normal and keratoconic eyes. It is consists of five individual parameters: Df (front), Db (back), Dp (pachymetric progression), Dt (thinnest value), and Da (ARTmax).

These numerical values report the SD from the population mean for these individual parameters. These numbers are yellow in color code if ≥1.6 SD from the mean and red if ≥2.6 SD from the mean and are white if <1.6 SD [1].

Both the anterior and posterior surface elevations, progression indices, and final D are normal (white) (Fig. 31).

Both the anterior and posterior surfaces elevation values and D values are outside the normal ranges (yellow and red) (Fig. 32).

The anterior surface elevations are nearly normal (green) and the posterior elevations and thickness values are abnormal and final D value (=1.94) is highlighted (yellow) (Fig. 33).

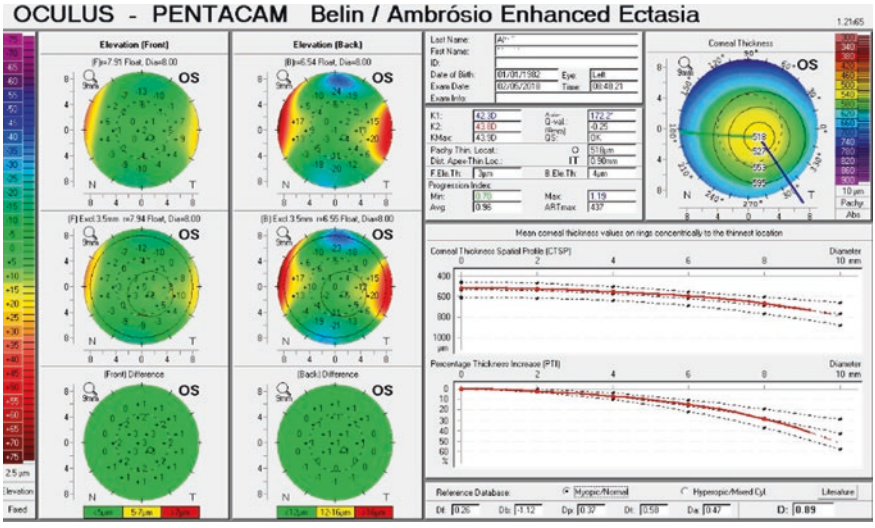

Fig. 31 Belin/Ambrósio Enhanced Ectasia Display (version III) of a normal eye

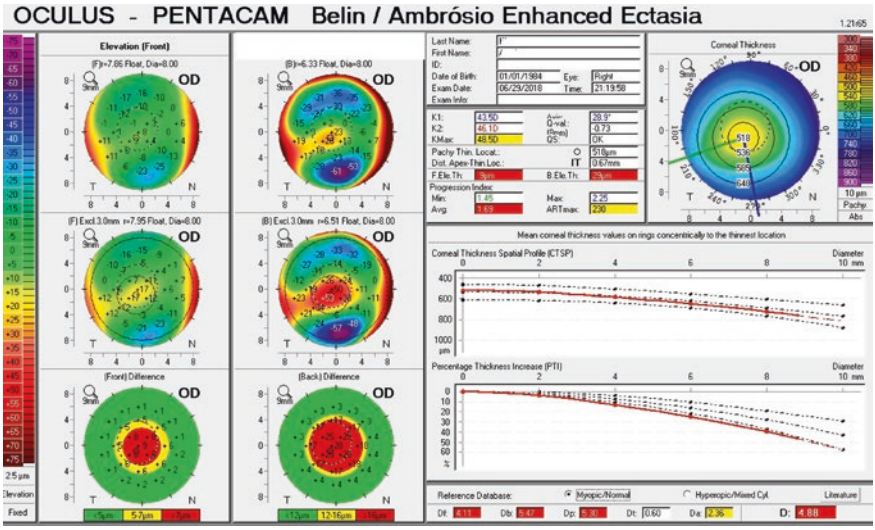

Fig. 32 Definite keratoconus example of the value of the Belin/Ambrósio Enhanced Ectasia Display (version III) and the "D" values

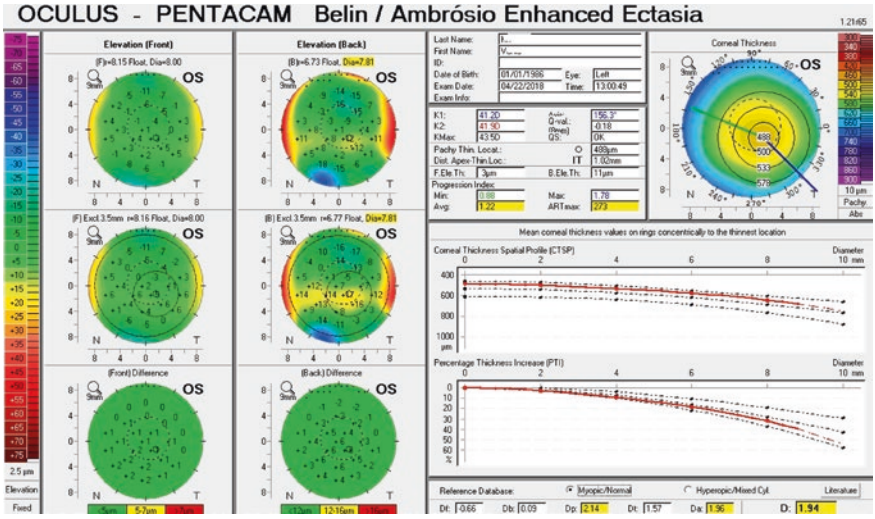

Fig. 33 Belin/Ambrósio Enhanced Ectasia Display (version III) with a suspicious area on the posterior corneal surface and thickness progression

Topometric KC Staging Map

This map is suitable for ectasia screening and including topometric and tomographic information (Fig. 34).

The difference between the mean of the five superior points and the five inferior points in the 3 mm central cornea in each 30 degrees is shown with the IS value

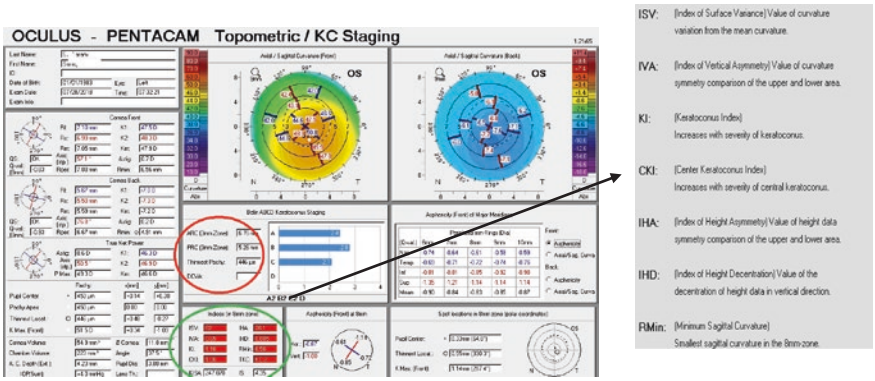

Fig. 34 The topometric KC staging map and its related indices for the detection of corneal ectasia

Table 5 Keratoconus screening values [1, 14]

Indices	abnormal	pathological
TKC	≥ 1.00	≥2.00
ISV	≥37	≥41
IVA	≥0.28	≥0.32
KI	-	>1.07
CKI	-	≥1.03
Rmin	-	<6.71
IHA	≥19	>21
IHD	≥0.014	≥0.016
IS value	1.4-1.9	>1.9
KISA	60%-100%	>100%

index. Another index of keratoconus screening that has recently been added to the Pentacam KC staging map is the KISA index. This indicates corneal asymmetry and includes IS value, SRAX, AST values, and central K. The abnormal range of indices is shown in Table 5 [1, 14]. The KISA index is calculated based on the following formula [14]: KISA = ((K)×(I-S)×(AST)×(SRAX)×100) /300

$$\text{KISA\%} = \frac{(\text{K}) \times (\text{I} - \text{S}) \times (\text{AST}) \times (\text{SRAX}) \times 100}{300}$$

In the prospective diagnostic test study, we evaluated 217 eyes including 70 KCN, 79 SKCN, and 68 normal and assessed the diagnostic ability of Pentacam parameters for distinguishing SKCN and KCN eyes compared with the control group, and found IS value was most sensitive parameter (AUC = 862; Sensitivity 80.1, Specificity 79.2) for early detection of KCN and IHD had the highest diagnostic ability (AUC = 0.999; Sensitivity 98.6, Specificity 100) for KCN detection [12].

Biomechanical parameters as a new factor may differentiate keratoconic cornea from normal eyes [15–17]. Also, there are modern manages for frank keratoconus

Table 6 Algorithm of Keratoconus Classificatin and Surgical Management. Adopted from: Mohammadpour M, Heidari Z, Hashemi H. Updates on Managements for Keratoconus. J Curr Ophthalmol, 2018. 30:110–124 [18]

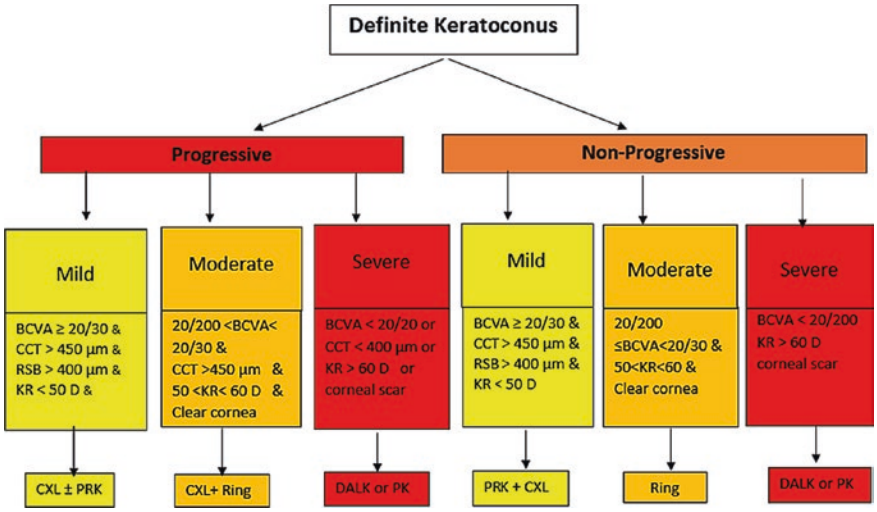

Surgical algorithm for management of keratoconus. Age <25 years should be considered as progressive keratoconus. Rigid gas permeable (RGP) lenses should be considered in any case if tolerant. Photorefractive keratectomy (PRK) is only recommended for age >25 years and in conjunction with corneal crosslinking (CXL). BCVA: Best corrected visual acuity, CCT: Central corneal thickness, RSB: Residual stromal bed, KR: Keratometry reading, D: Diopter, CXL: Cross-linking, PRK: Photorefractive keratectomy, DALK: Deep anterior lamellar keratoplasty, PK: Penetrating keratoplasty

based in new corneal imaging systems which may eliminate the corneal keratoplasty in severe cases [18], algorithm of keratoconus classification and surgical management identifies a new perspective on the classification of keratoconus (Table 6).

Belin ABCD Progression Display

The progress of four important parameters including (A) The anterior radius of curvature (ARC), (B) Posterior radius of curvature (PRC), (C) Thinnest pachymetry and (D) Best-corrected distance visual acuity (BDVA) is shown in the specific bar charts. Every diagram in a different color belongs to the respective examination and at the top of each bar is the absolute ABCD values (Fig. 35). The absolute values of the parameters from the baseline and post-treatment examinations and their progression are shown in this display. Keratoconus is also classified based on the ABCD classification system (Table 7).

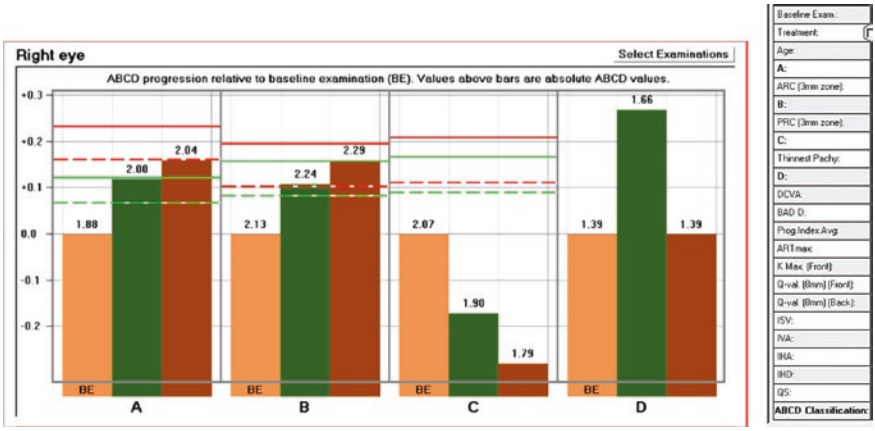

Fig. 35 Detail "Progression analyses" with related criteria (*Permission from Oculus Pentacam*) [1]

Table 7 ABCD keratoconus grading system (*With permission from Oculus Pentacam*) [1]

ABCD criteria	A	B	C	D
	ARC (mm)	PRC (mm)	Thinnest pachymetry (μm)	BDVA
Stage 0	>7.25	>5.9	>490	≥20/20
Stage I	>7.05	> 5.7	>450	<20/20
Stage II	>6.35	>5.15	>400	<20/40
Stage III	>6.15	>4.95	>300	<20/100
Stage IV	<6.15	<4.95	≤300	<20/400

Optical Densitometry Display

Corneal densitometry display is a screening map with respect to scattering data over a curved plane between the front and back surfaces of the cornea. This is a suitable map for evaluating the depth and location of scattering phenomena that may happen within the cornea. It could be effective for following up on the corneal haze in post-refractive surgery (PRK/LASIK) and keratoconus or corneal infection disease, cross-linking follow up, pre to post-operation compare, and for evaluating the position and depth of INTACS rings (Fig. 36).

Corneal densitometry map shows the densitometry values at each position of the cornea. The maximum and average of the mean values in Z direction from anterior and posterior surface are shown in Cornea Densito Maximum and average displays (Fig. 37).

Graph of the average optical densitometry in different zones and layers are shown in corneal optical densitometry display (Fig. 38).

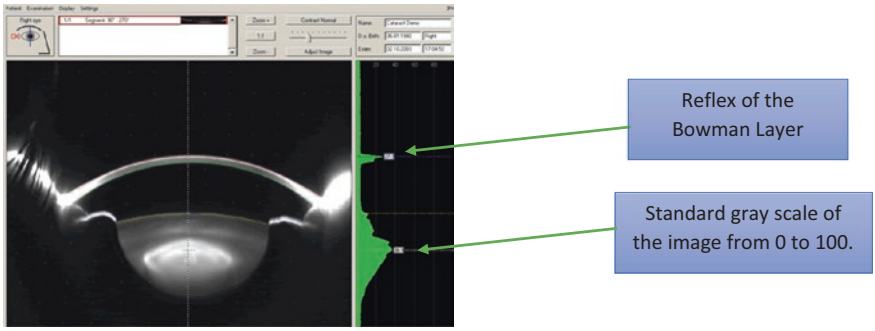

Fig. 36 Corneal optical densitometry (*With permission from Oculus Pentacam*) [1]

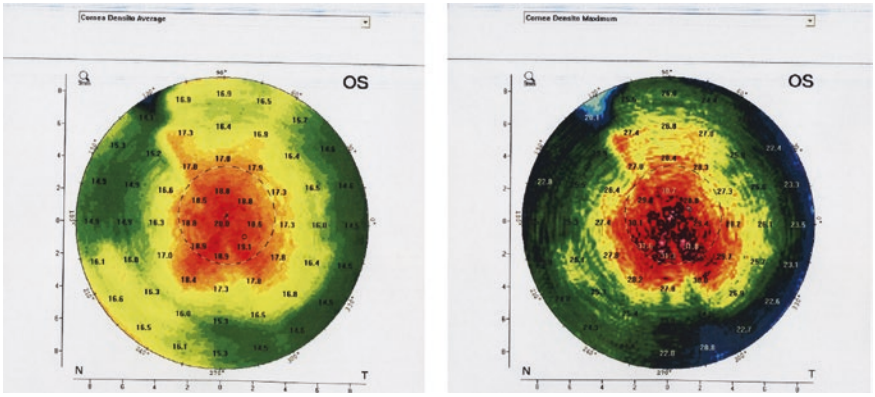

Fig. 37 Cornea Densito average and maximum displays

4 Maps Selectable

You can select the desired map through the drop-down list above the individual maps (Fig. 39).

Show Two Exam Mode

The Pentacle allows us to evaluate two examinations together and compare the two eyes. The patient's examination can be selected. A good comparison is possible from pachymetry, topography, tomography or ABCD progression images (Fig. 40).

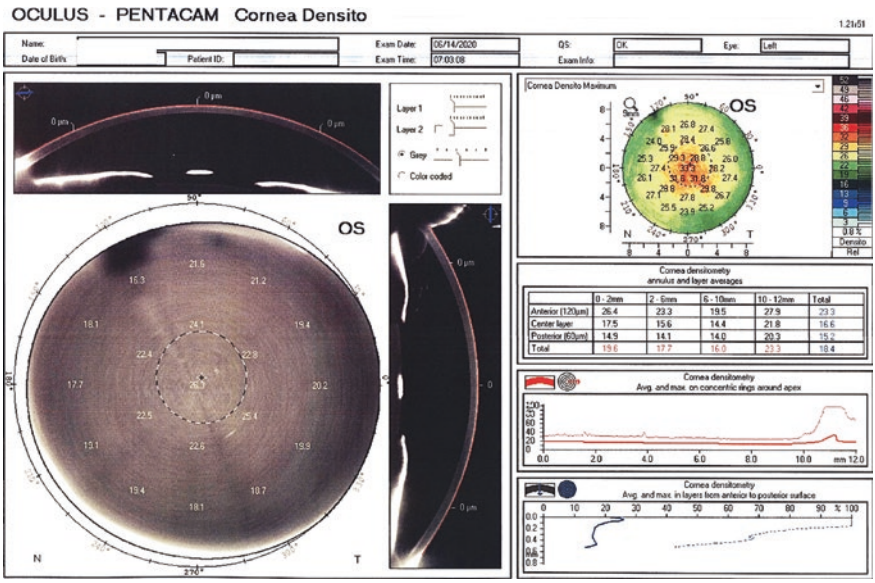

Fig. 38 Corneal optical densitometry display

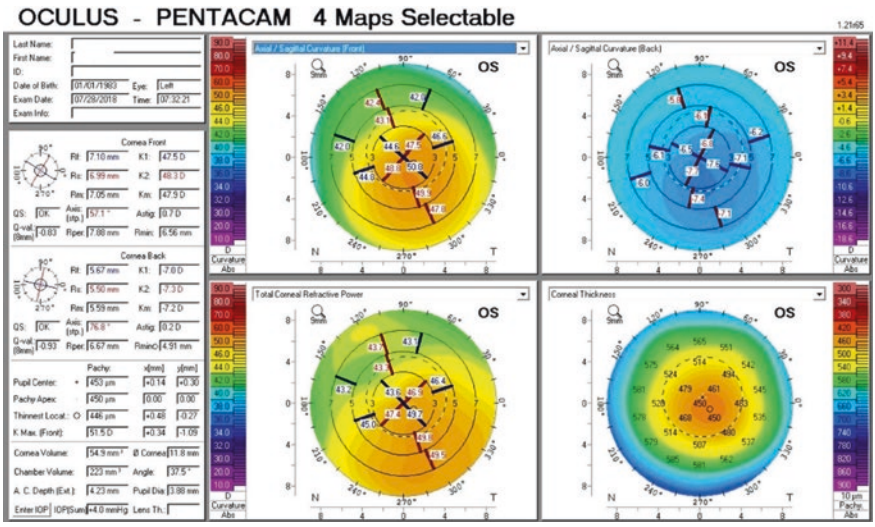

Fig. 39 4 maps selectable

Holladay Report

This display provides important information for treating and screenings the ectatic cornea and it can be useful for calculating IOL implantation. It is not possible to calculate posterior corneal curvature with Placido-based topography or manual keratometry, and the anterior curvature can be converted to refractive power

using a refractive index of 1.3375. Corneal refractive surgery changes the radii ratio between the posterior and the anterior corneal surface and the EKR in the Holladay Report considers these effects and it can be used for patients with history of refractive surgery. Also, this display can determine the subject's refraction stability, check the pupil diameters, and evaluate the corneal shape and condition.

This display shows the patient's general data at the left box and the Equivalent K-Readings 65 (EKR65) at the 4.5 mm zone, astigmatism amount, Q value, and spherical aberration (SA), RMS wavefront aberration and radius ratio (back/front) at the center box. The EKR65 values show optimal values for IOL power calculations.

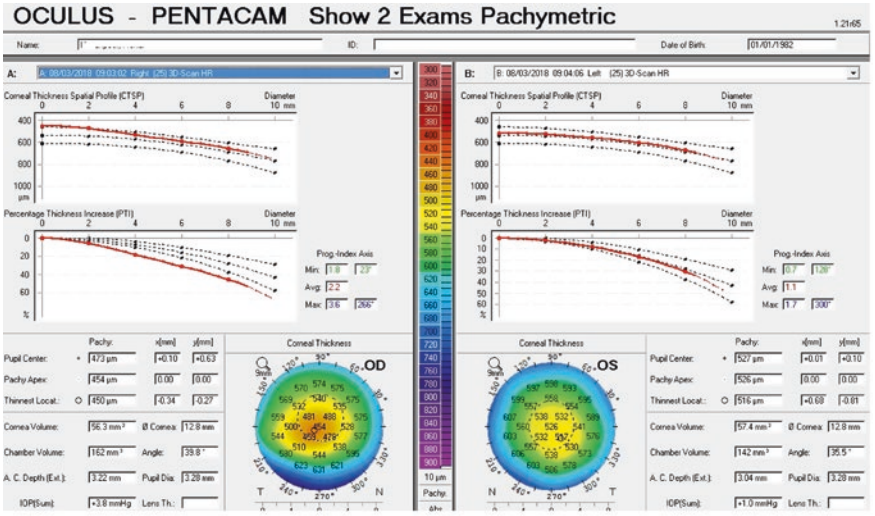

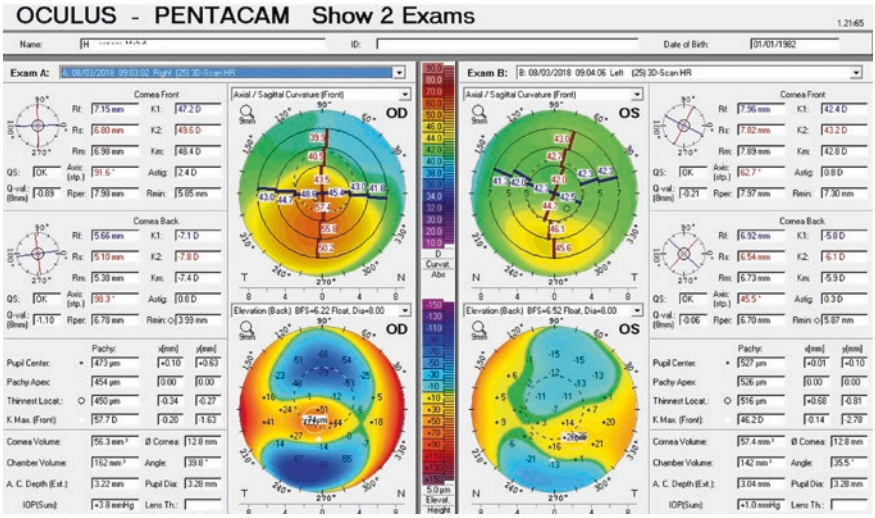

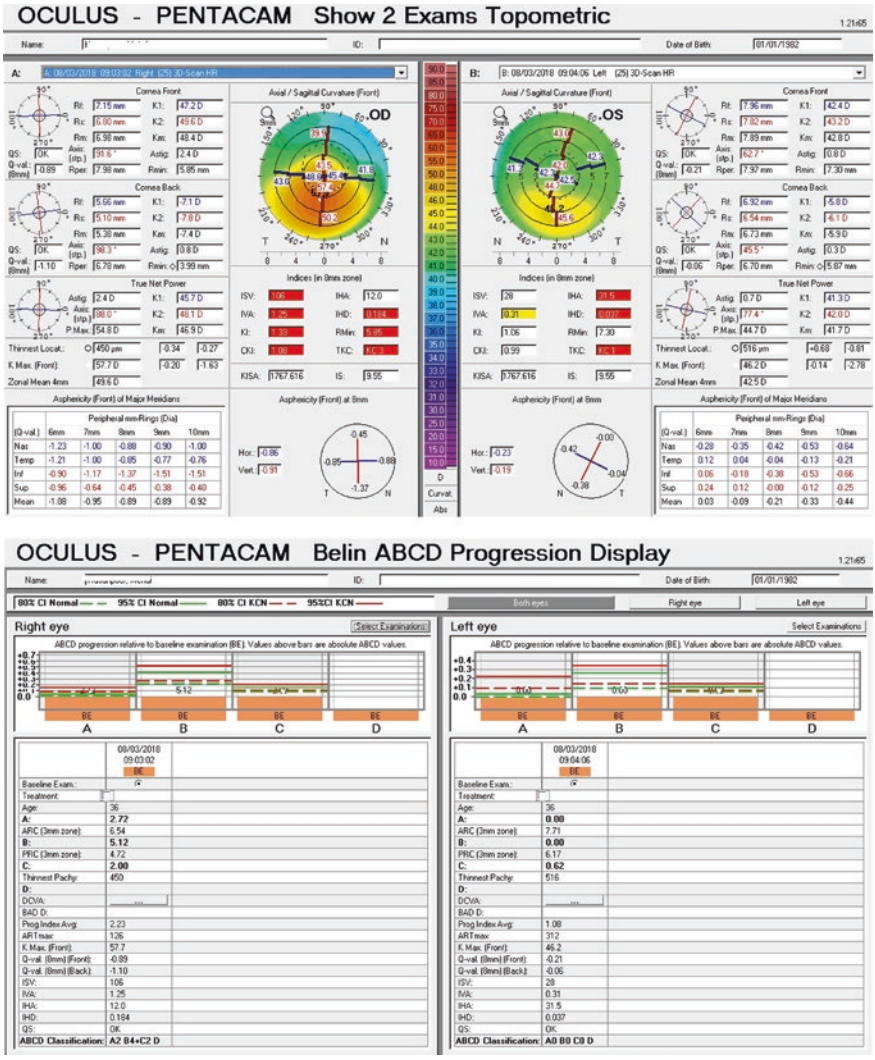

Fig. 40 The display shows 2 exams pachymetric, topographic, tomographic and ABCD progression, respectively

The upper right box shows pupil diameters and horizontal white to white corneal diameter, minimum pachymetry, estimated pre refractive mean keratometry and anterior chamber depth. In addition, Chord μ on this display indicates the distance between the intercept of the pupillary axis with the cornea and vertex normal and its normal range is less than 0.30 ± 0.15 mm.

The Hexamap presented in this display includes axial/sagital curvature (front), tangential curvature (front), corneal thickness, relative pachymetry, and elevation (front/back) (Fig. 41).

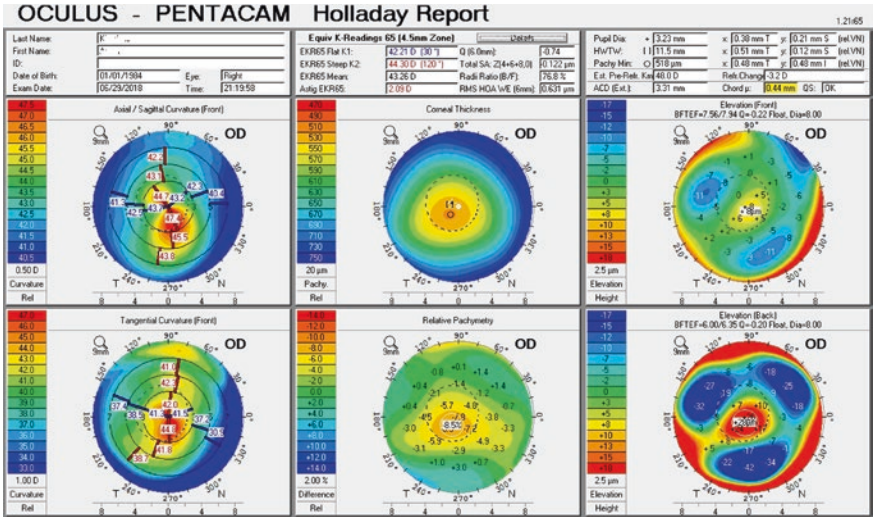

Fig. 41 Holladay report of a keratoconus eye

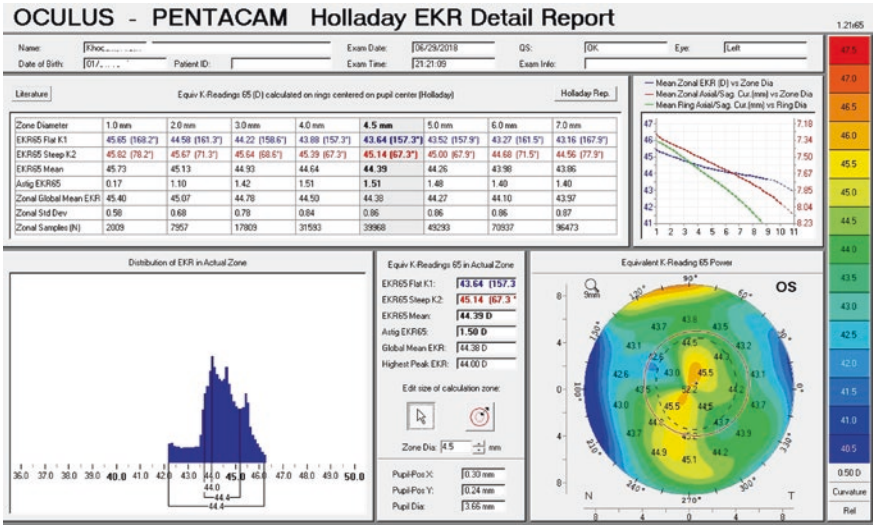

Fig. 42 Holladay EKR65 detail report of a keratoconus eye

Holladay EKR65 Detail Report

This reports the general information of the patients and the EKR65 (D) various parameters for from 1.0 to 7.0 mm which calculated from the pupil center and it indicates both front and back corneal power as the EKR power map in Snell's law and shows the appropriate values for IOL power calculations. The hot spot area is shown in curvature and elevation maps (Fig. 42).

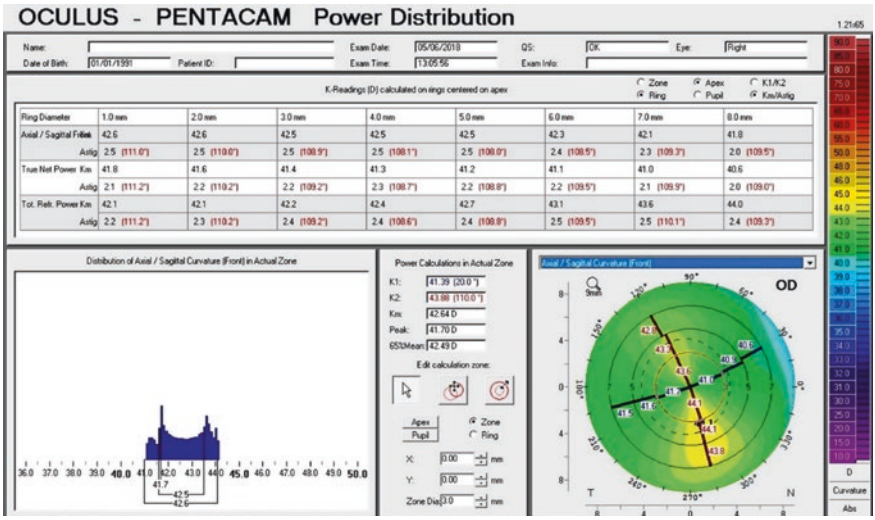

Fig. 43 The calculation of IOL power is done by k-reading based on true net power map following laser refractive surgery in ASCRS IOL calculation software

Calculating the power of the IOLs based on the true net power map (TNP) values give more accurate power of the IOLs, recently. This map calculates the data based on the anterior and posterior surface of the cornea and provides a true k reading (Fig. 43).

The free online service from the American Society of Cataract and Refractive Surgery (ASCRS) is available at http://iol.ascrs.org/. This online calculator can be used to provide IOL power calculations for eyes that have undergone myopic and hyperopic LASIK or PRK with the TNP measured at 4.0 mm.

Cataract Pre OP

This display consisted of three maps including axial curvature, total corneal refractive power and thickness maps, Scheimpflug images and quantitative data (Fig. 44).

Phakic IOL Simulation

Pentacam AXL had a module for phakic IOL (pIOL) simulation and determine the pre-surgical planning for iris-supported phakic anterior chamber lens and simulate the pIOL in the anterior chamber. This program could stimulate the growth of age-related lenses and the position of the anterior chamber lenses result from this. After selecting the pIOL from the Pentacam database the position of the lens is simulated. The minimum distance between the pIOL and the crystalline lens (lens rise) and between the pIOL and the endothelium, is computed and displayed in both color and numerical terms (Fig. 45). This information facilitates patient selection.

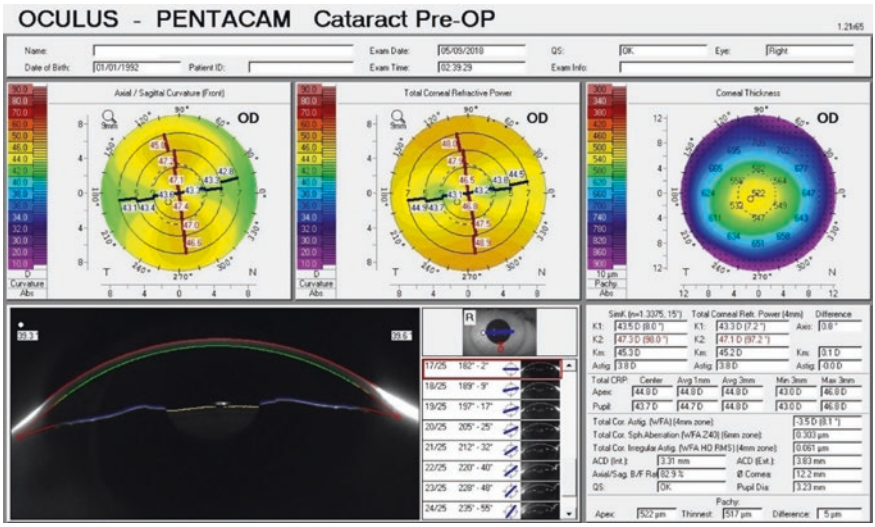

Fig. 44 Display Cataract-Pre-OP

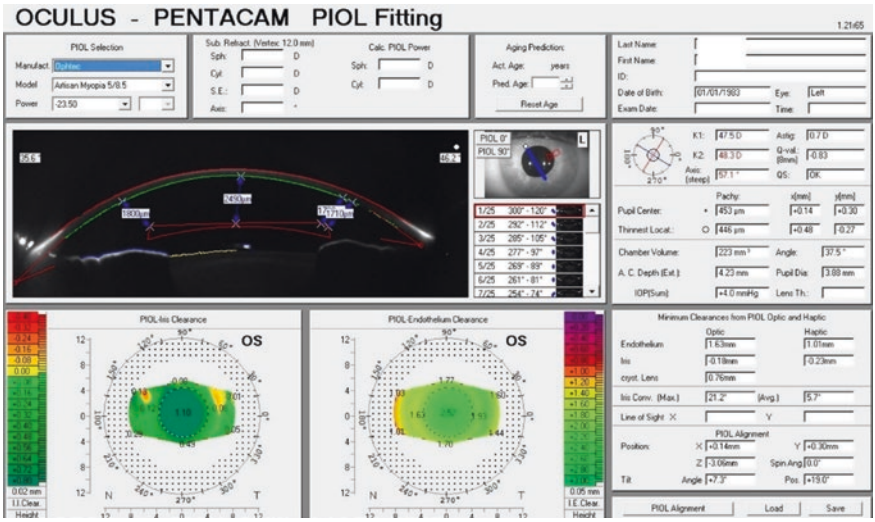

Fig. 45 Phakic IOL simulation with Pentacam

The Zernike Analysis Maps

The wavefront aberration (WFA) parameters derived from Pentacam are calculated based on height data in the 3D model and ray-tracing calculations. Polynomials are represented by the Zernike coefficient. Low order aberrations (LOA) including 1 and 2 orders, higher-order aberrations (HOA) including 3–8 orders, and all total aberrations (TOTAL) are presented on Zernike maps. We found HOA increased

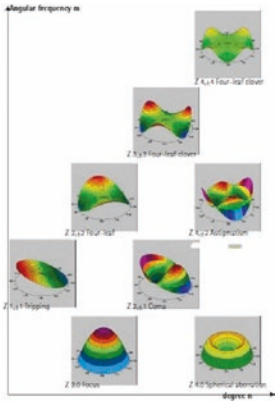

Z 0,0	Elevation constant, central height of the surface
Z 1, ±1	Tilt
Z 2,0	Focus, respective surface in the form of a conical section
Z 2, ±2	Astigmatism
Z 3, ±1	Coma
Z 3, ±3	Trefoil
Z 4,0	Spherical aberration
Z 4, ±2	Higher (4th) order astigmatism
Z 4, ±4	Four-lobed defect
Z 5, ±1	Higher (5th) order coma
Z 5, ±3	Higher (5th) order trefoil
Z 5, ±5	Five-lobed defect
Z 6,0	Higher (6th) order spherical aberration
Z 6, ±2	Higher (6th) order astigmatism
Z 6, ±4	Higher (6th) order four-lobed defect
Z 6, ±6	Six-lobed defect

Fig. 46 Overview of Zernike polynomials (*With permission from Oculus Pentacam*) [1]

with the increase of ocular astigmatism [19]. The zerrnike polynomials's names are related to their order and are shown in Fig. 46.

Zernike components are shown in two forms, pyramid and list presentation which are compared to healthy populations. Pentacam corneal wavefront independent of the pupil diameter and it is not only related to the anterior surface, and it can be suitable even for post-refractive eyes. We compared the diagnostic accuracy of wavefront parameters with Pentacam and found vertical coma (Z^{-13}) was a sensitive parameter for subclinical cornea (sensitivity = 75%, specificity = 100%, AUC = 0.857) [20] (Fig. 47).

The coefficient of Zernike polynomial units can be seen individually in the Z separate or Z vector modes, this provides an easier assessment of a single polynomial. (Fig. 48)

Fourier Analysis

Fourier analysis is a mathematical process, which breaks down a periodic function into a number of sine and cosine waves. The topographic map of Pentacam can be broken down into individual components using Fourier analysis. The original image is first divided into concentric rings, then the curvature of each ring is broken by sinusoidal or cosine waves (Fig. 49).

Corneal Asphericity (Q-Value)

Pentacam provides the asphericity of the anterior surface of the cornea in the 6 mm zone (or any selected zone) around the corneal apex with Q value. The Q value less than zero is considered normal cornea and the value of more than 1.0 is considered treated cornea. The average of the normal range is 0 to −1.00 (Fig. 50).

Corneal Rings

This display contains important information for preoperative planning depending on the technique of ring implantation. Recommendation values for ring implantation are given based on the incision depth nomogram and manual or femtosecond laser dissection technique (Fig. 51).

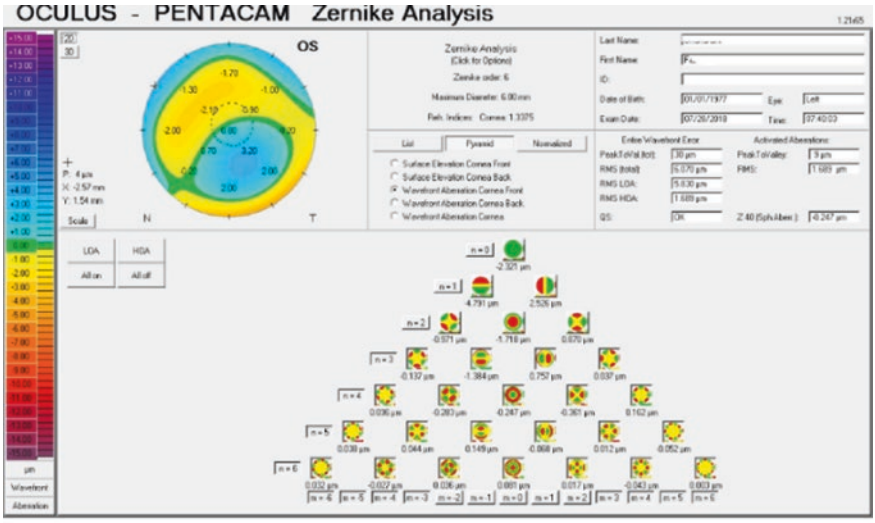

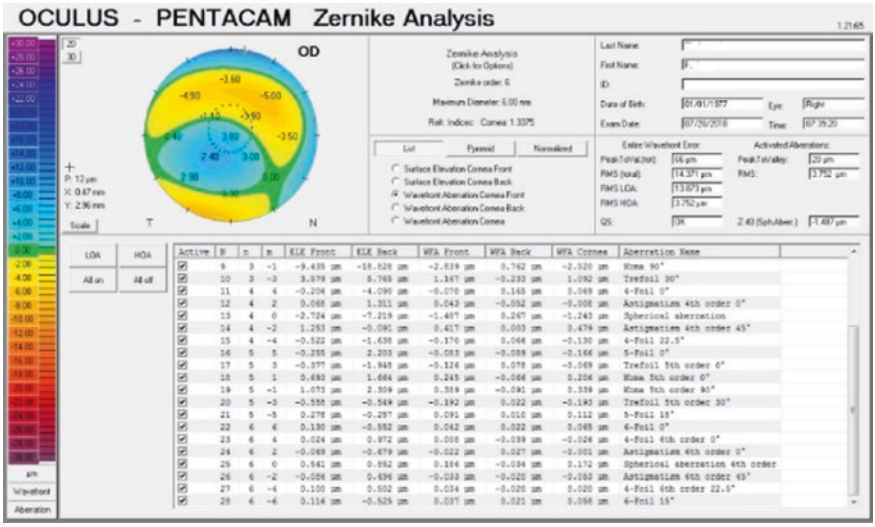

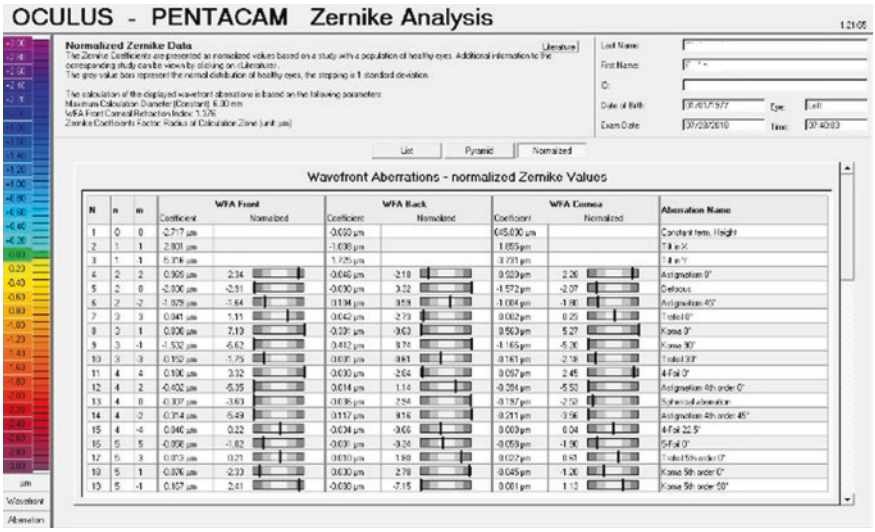

Fig. 47 Zernike coefficients are shown in keratoconus cornea including pyramid presentation, Table presentation, and normalized Zernike values

Contact Lens Fitting

This display contains important parameters for better contact lens fitting with a good perception of the total shape of the cornea. The Pentacam based on corneal geometry measurement suggests contact lenses from well-known companies. The soft contact lenses list is the bottom of the table. The distance values between the cornea and contact lens are presented in the fluorescent image simulation (Flo image) section (Fig. 52).

Anterior Chamber Depth and Glaucoma Screening

Pentacam calculates the anterior chamber depth (ACD), anterior chamber angle (ACA), and anterior chamber volume (ACV) in one examination. Anterior chamber depth display shows the range of the anterior chamber (Fig. 53).

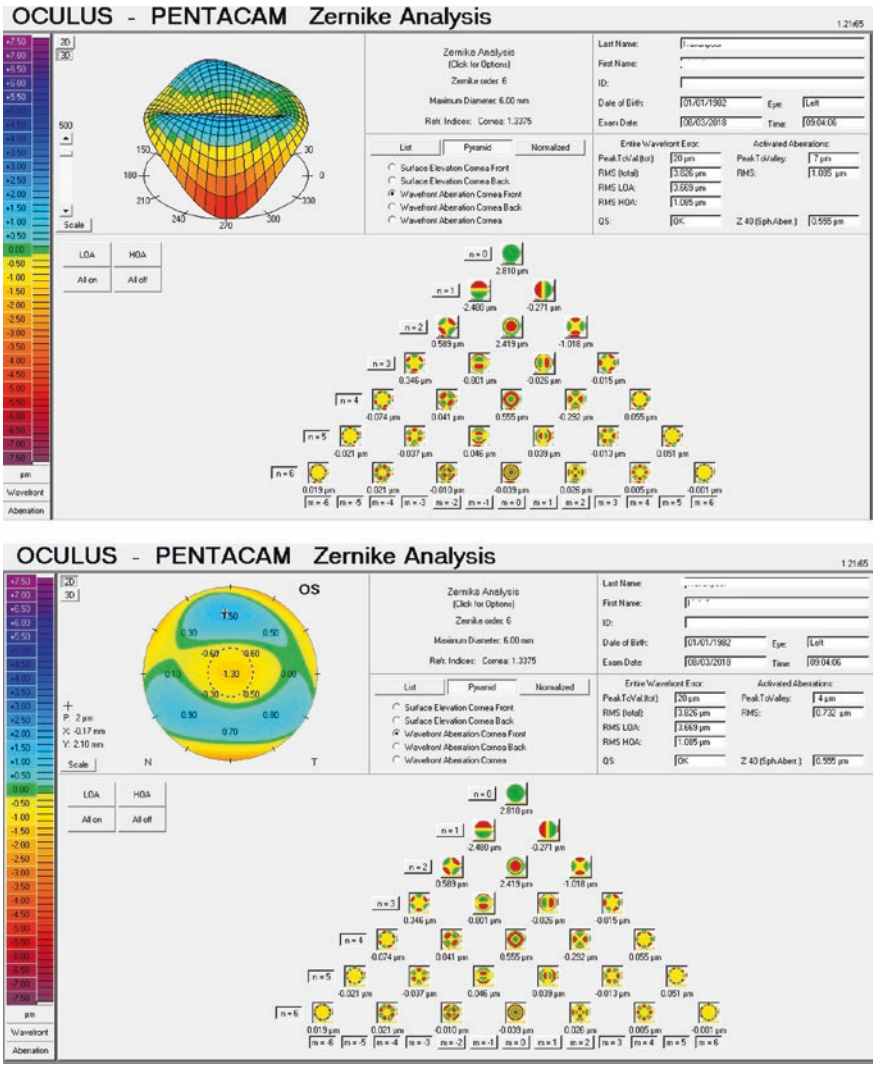

Fig. 48 Different modes of the single Zernike coefficient are shown from the same patient (first; Z separate and second; Z vector)

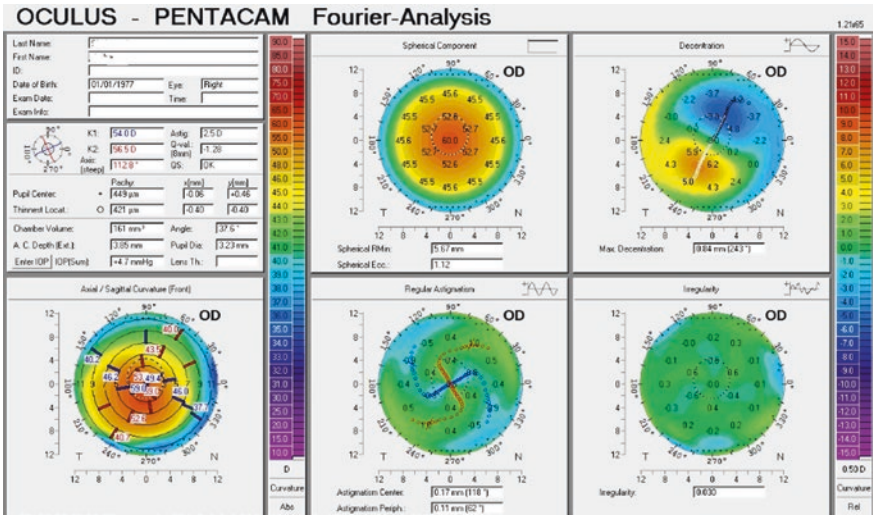

Fig. 49 "Fourier Analysis" of the sagital (axial) curvature map of a patient with keratoconus

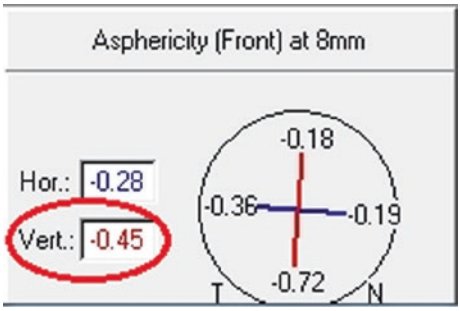

Fig. 50 Ashpericity front at 8 mm zone

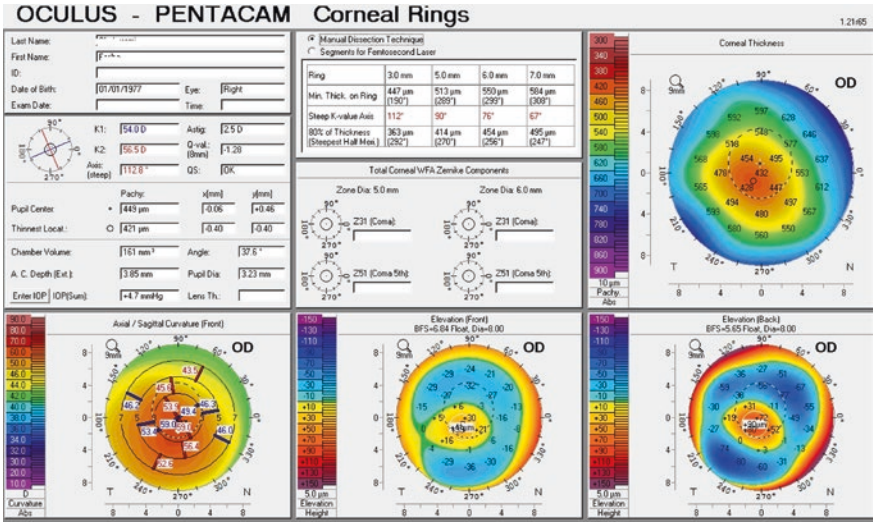

Fig. 51 Display "Corneal Rings" for the keratoconus eye

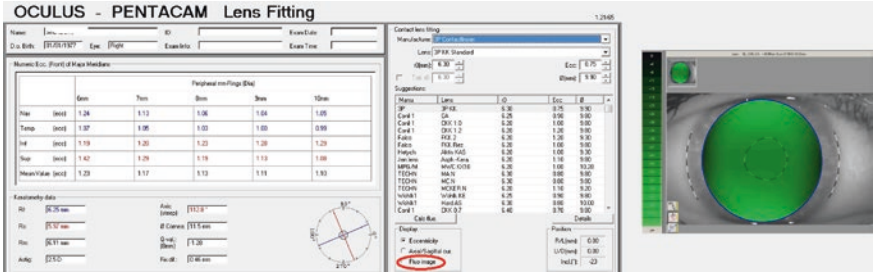

Fig. 52 Displays "Contact Lens Fitting" and "Fluo Image" (*With permission from Oculus Pentacam*) [1]

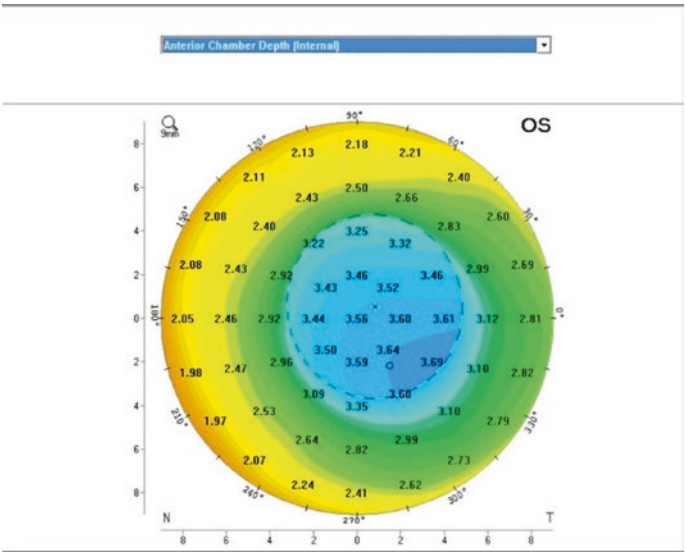

Fig. 53 Anterior chamber depth display

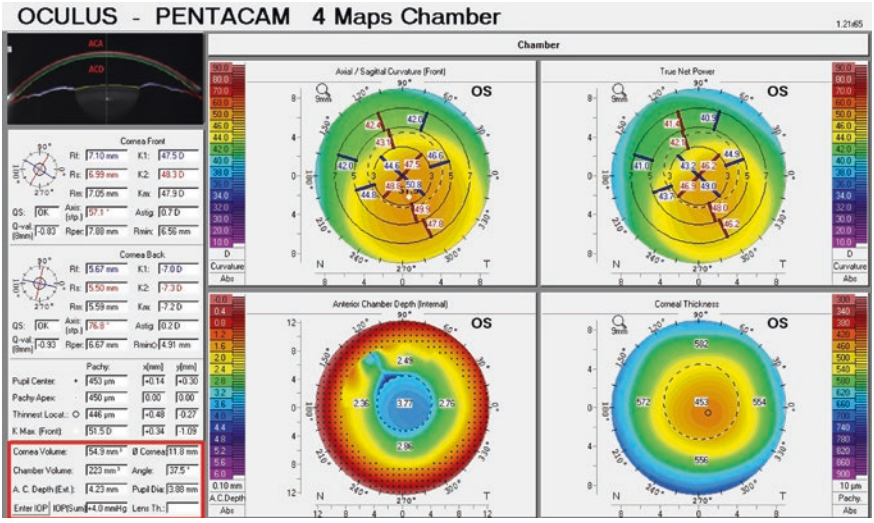

Fig. 54 Display of 4 maps chamber

These data have high sensitivity for detecting narrow-angle and are useful for following up after Iridectomy or even mild and moderate keratoconus detection [21]. By entry IOP manually, the modified IOP value is automatically corrected based on the thickness of the cornea. Pentacam provides 4 maps chamber for implantation of intraocular lenses to prevent glaucoma (Fig. 54).

Case Study

Case 1.

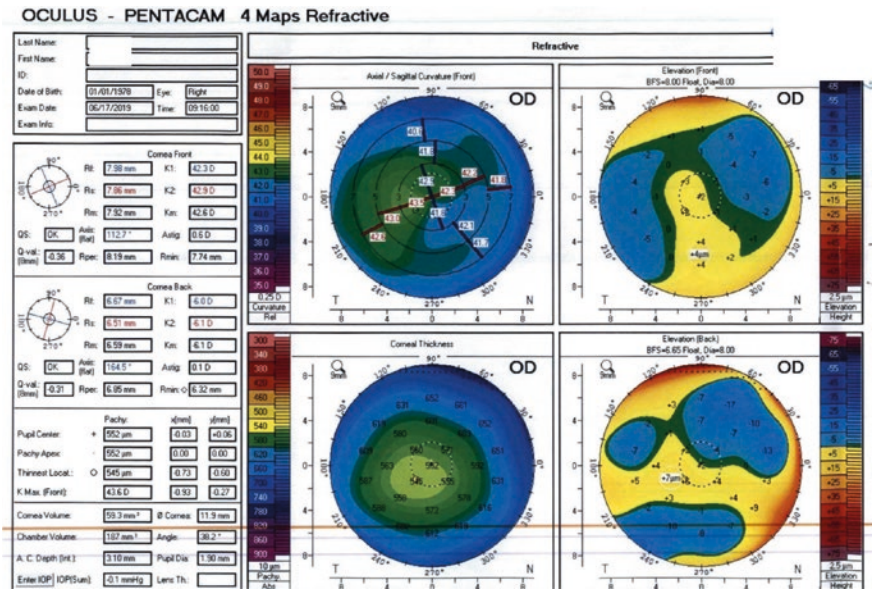

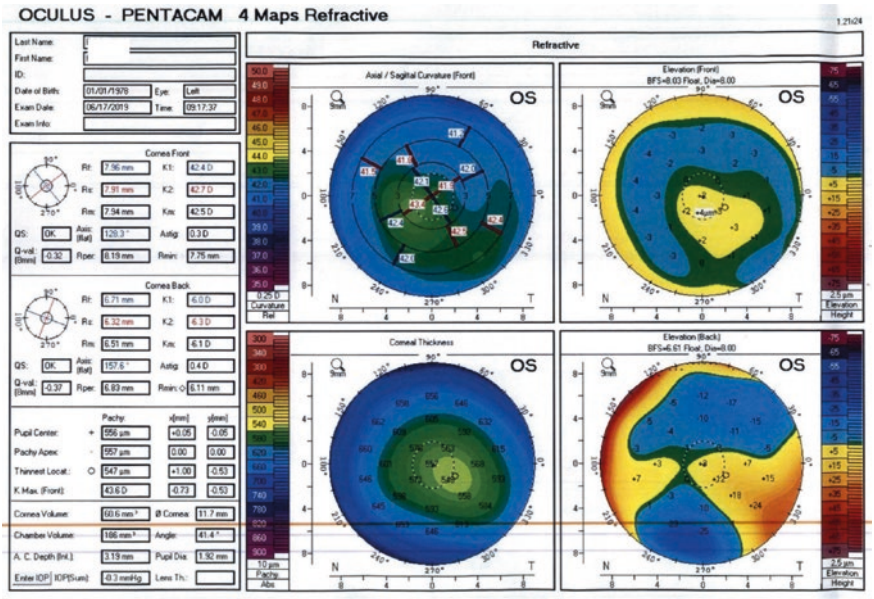

Fig. 55 A 38-year-old female with the inferior steepening in both eyes and subtle abnormal findings in the posterior elevation in the left eye. Refractive errors: OD Plano/−1.00~90 and OS −0.75 sphere; Corrected distance visual acuity (CDVA) 10/10 OU. There are normal pachymetric values in both eyes without keratoconus

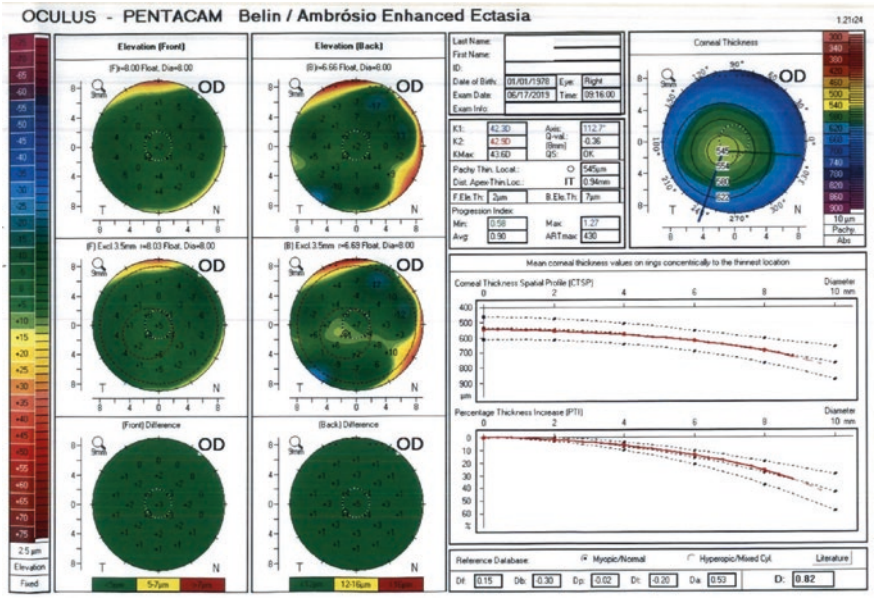

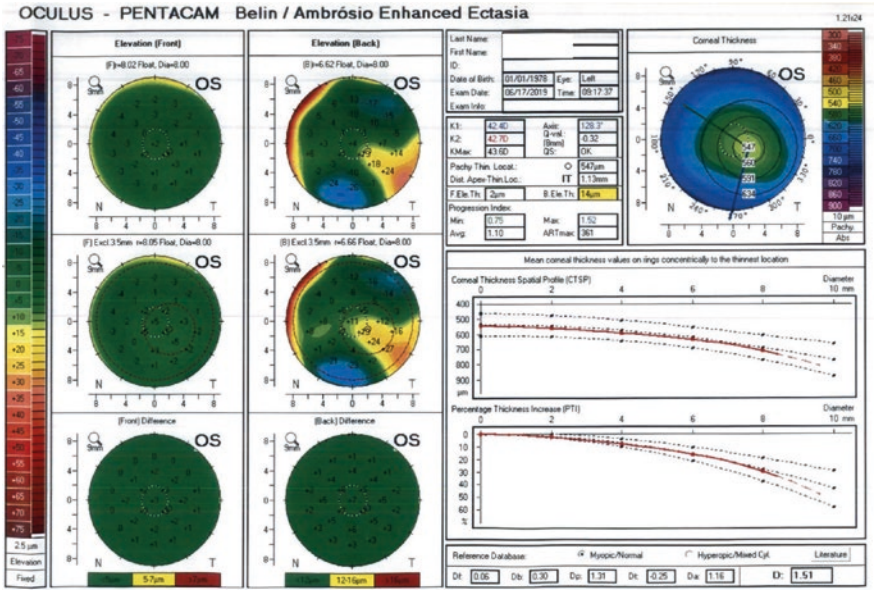

Fig. 56 Belin/Ambrosio display shows normal difference maps and normal values in D index and thickness graphs in both eyes and subtle changes of posterior elevation in the left eye

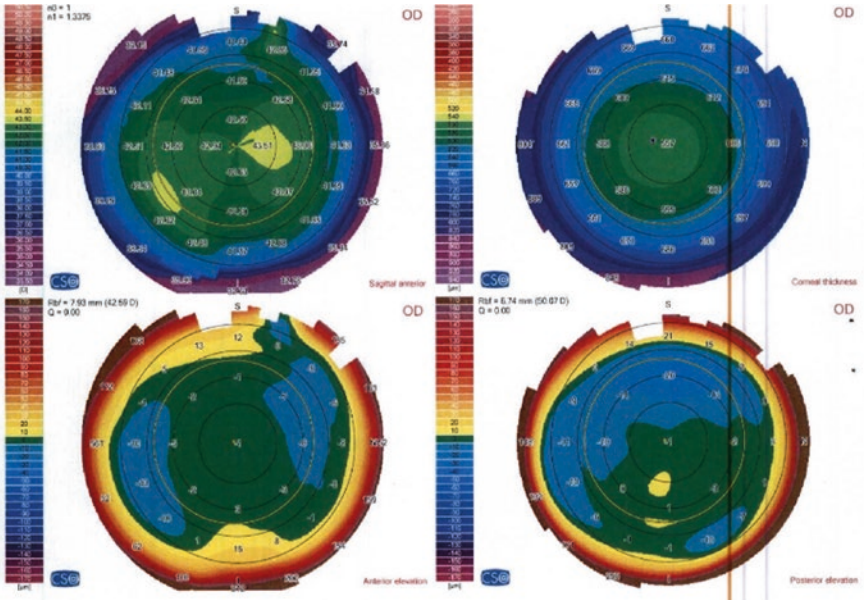

Acquisition quality	Coverage(SC.) = 99%	Not edited(SC.) = 100%
	Coverage(P.) = 81%	Centration(P.) = 98%

Summary Indices

HVID = 11.84 mm
Pupil (Topographic)
r = 0.17 mm @ 158°
Ø = 6.15 mm
λ intercept: r = 0.39 mm @ 158°
Thinnest location
r = 0.60 mm @ 167°
Thk = 555 µm
Apex
r = 3.40 mm @ 74°
Curv = 44.69 D
Anterior chamber
CCT + AD =
0.557 + 3.27 = 3.83 mm
Volume = 190 mm³
Iridocorneal angle = 46°
HACD = 12.53 mm
Lens rise = 0.16 mm
Corneal volume (Ø=10mm)
Volume = 57.7 mm³

K readings (n0 = 1, n1 = 1.3375)

Sim-k	K1 = 42.50 D @ 99°
	K2 = 43.19 D @ 9°
	Avg = 42.84 D
	Cyl = -0.68 D Ax 99°
Anterior Ø=3mm	K1 = 42.59 D @ 99°
	K2 = 43.23 D @ 9°
	Avg = 42.91 D
	Cyl = -0.64 D Ax 99°
Anterior Ø=5mm	K1 = 42.48 D @ 98°
	K2 = 43.19 D @ 8°
	Avg = 42.83 D
	Cyl = -0.70 D Ax 98°
Anterior Ø=7mm	K1 = 42.35 D @ 100°
	K2 = 43.08 D @ 10°
	Avg = 42.71 D
	Cyl = -0.73 D Ax 100°

K readings (n1 = 1.376, n2 = 1.336)

Posterior Ø=3mm	K1 = -5.98 D @ 6°
	K2 = -6.07 D @ 96°
	Avg = -6.02 D
	Cyl = +0.09 D Ax 6°
Posterior Ø=5mm	K1 = -5.98 D @ 1°
	K2 = -6.07 D @ 91°
	Avg = -6.03 D
	Cyl = +0.08 D Ax 1°
Posterior Ø=7mm	K1 = -6.01 D @ 10°
	K2 = -6.02 D @ 100°
	Avg = -6.02 D
	Cyl = +0.02 D Ax 10°

Refractive analysis

Ø=4.0mm
Cyl = -0.81 D Ax 98°
MPP = 42.41 D
LSA = 0.64 D

Keratoconus screening

SIf = 0.56 D
⊞ KVf = 3 µm
BCVf = 0.24 D @ 252°
SIb = 0.09 D
◈ KVb = 8 µm
BCVb = 0.16 D @ 259°
Thk = 555 µm
Class:
'Normal'

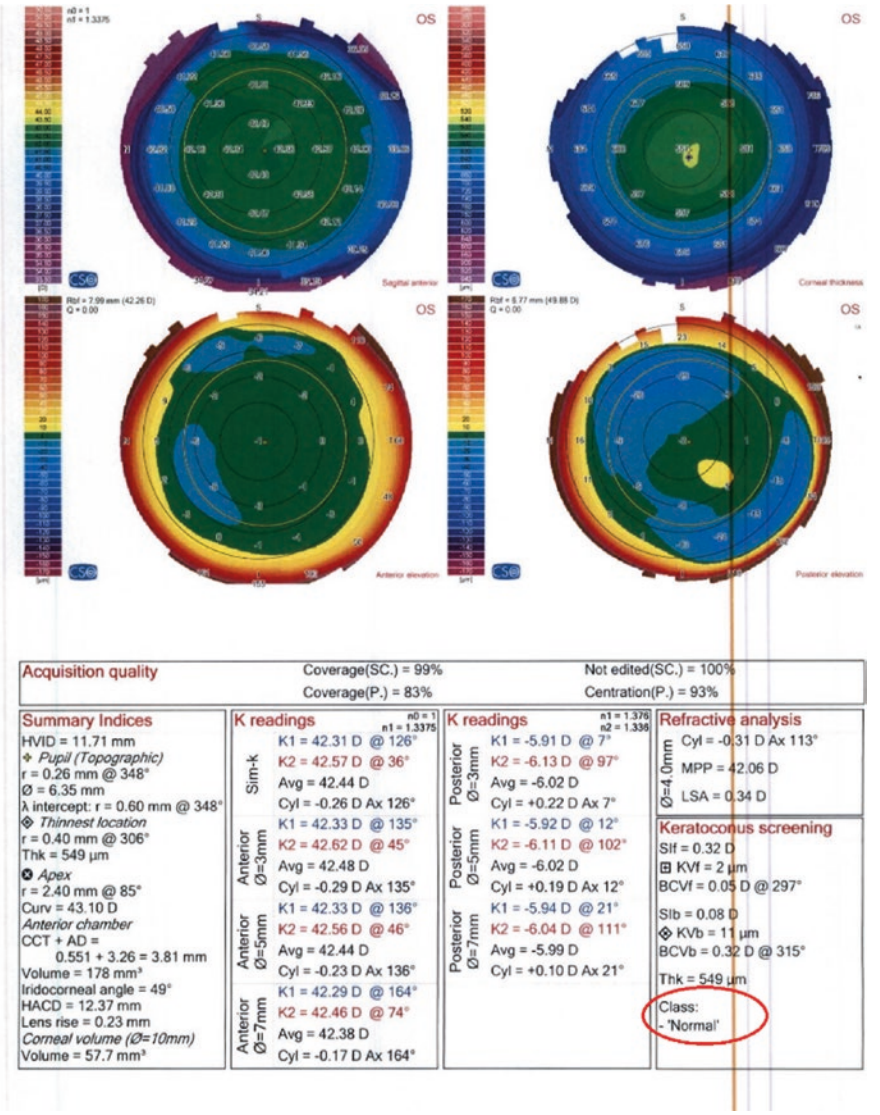

Fig. 57 These findings compatible with keratoconus screening indices of Sirius in the same patient which indicate normal class

Case 2.

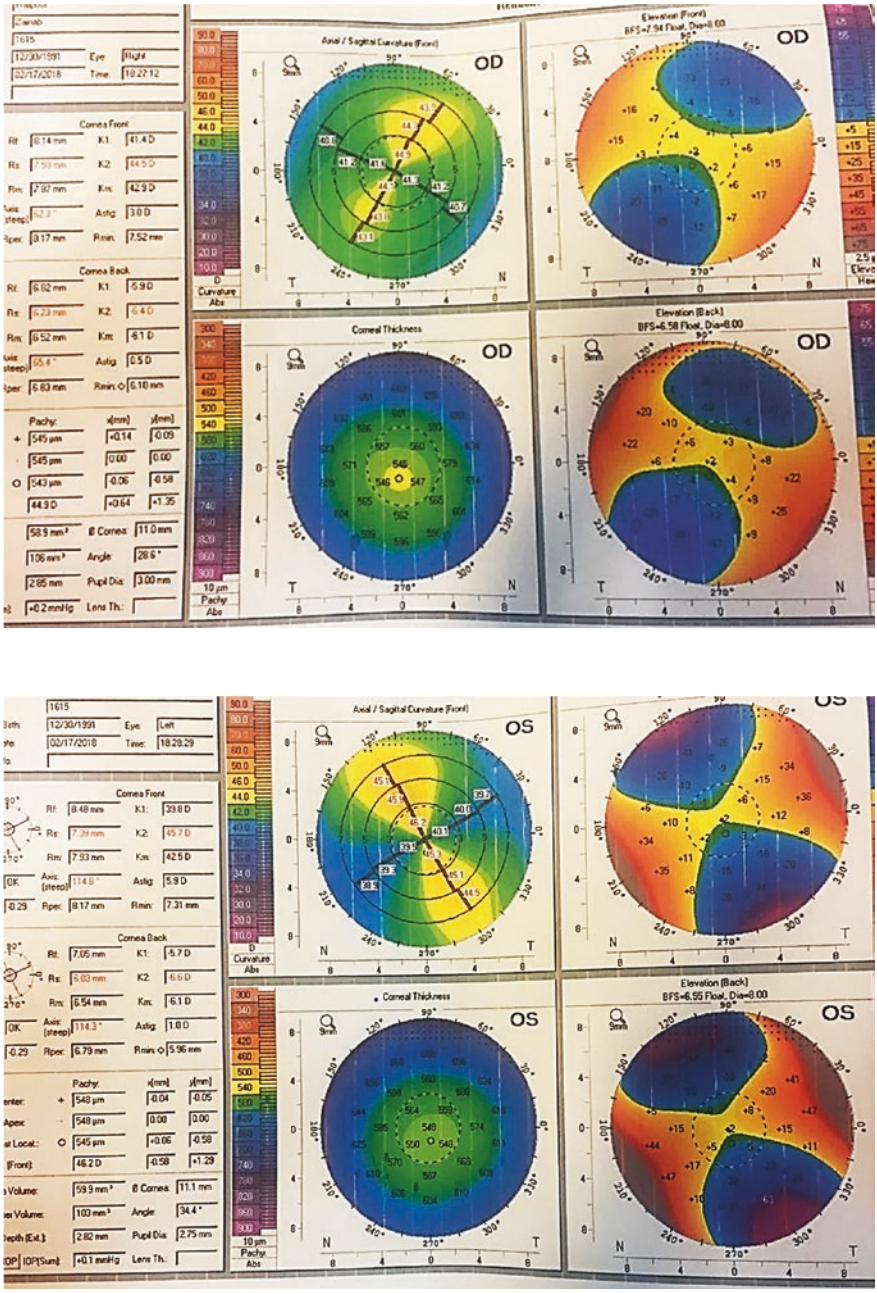

Fig. 58 A 30-year-old woman with refractive errors: OD = −0.25/−3.75~143 CDVA = 10/10 and OS = +4.00/−8.00~30 CDVA = 2/10 with enantiomorphism (mirror-image symmetry) pattern of astigmatism in topography in both eyes. Approximately all indices are at the normal range. Anisometropia and high astigmatism caused amblyopia and decreased the vision. So, this is not a case of keratoconus and any keratoconus treatment like cross-linking should not be performed

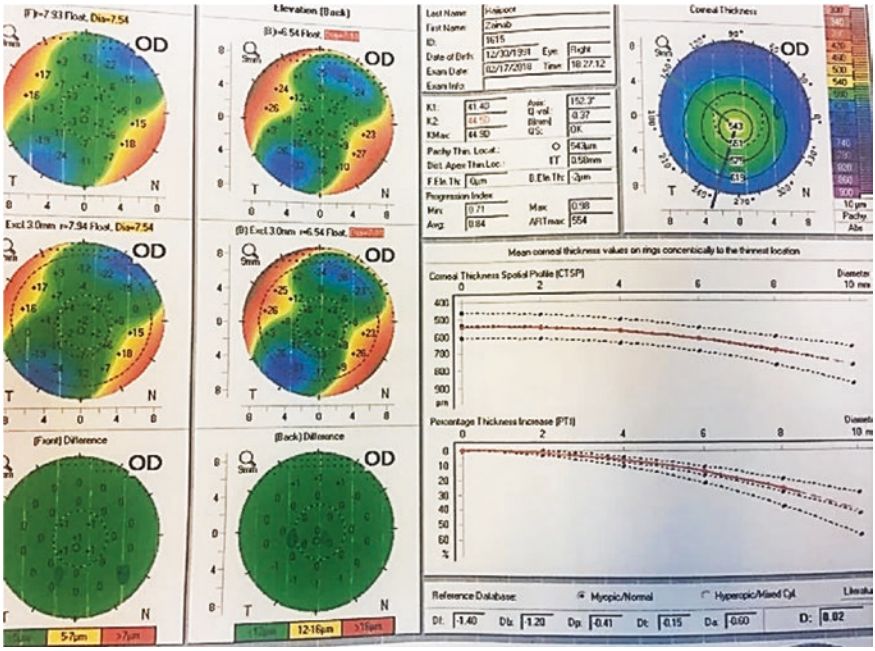

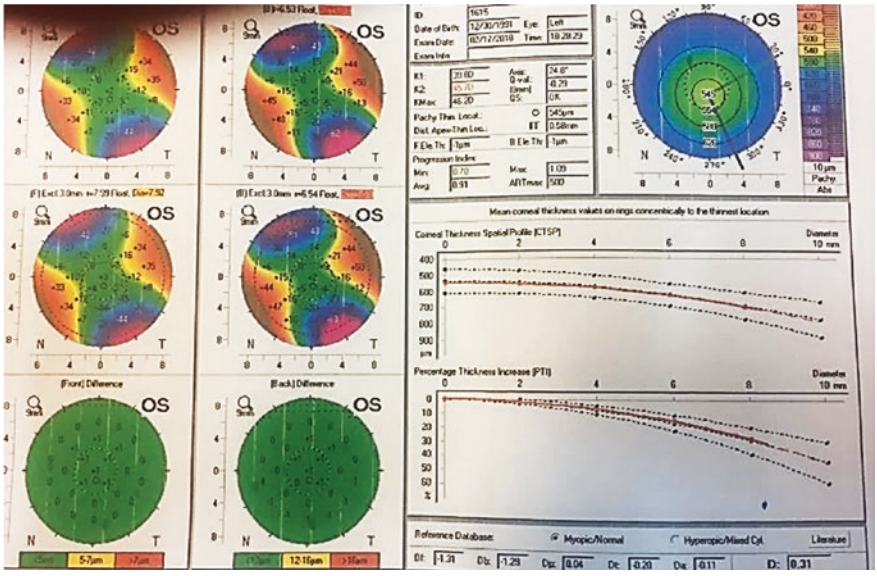

Fig. 59 These findings corresponded with Blin/Ambrosio display maps. The D index, difference maps, and pachymetric graphs are normal

Case 3.

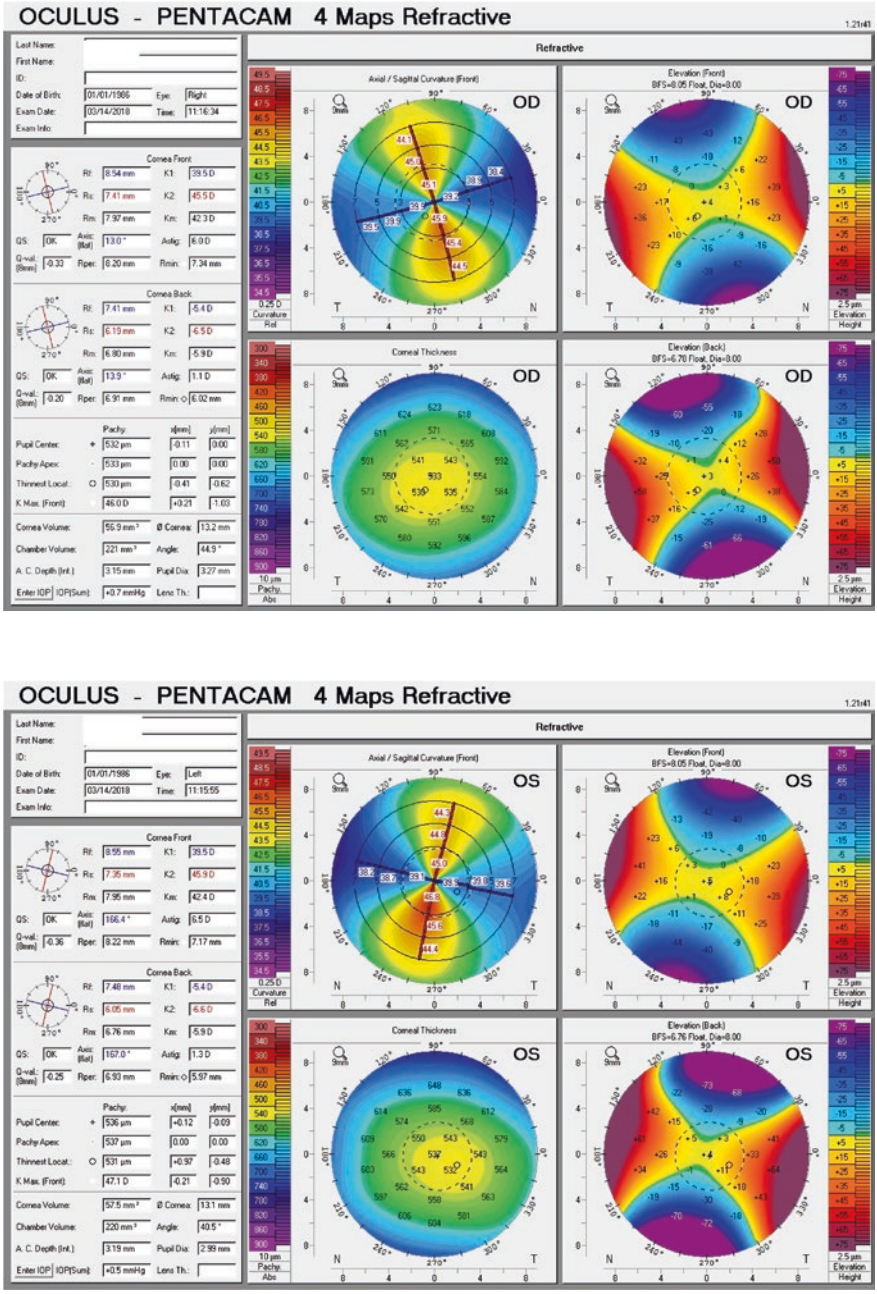

Fig. 60 A young man with high astigmatism and enantiomorphism (mirror-image symmetry) in topographic pattern in both eyes with refractive errors: OD = Plano/−7.00~10 and OS = Plano/−7.00~180 and CDVA = 7/10 who had blurred vision due to amblyopia. Symmetric bow tie and normal pachymetric indices with abnormal findings in anterior and posterior elevations were observed in tomography imaging. The patient has no keratoconus and should be followed up next year

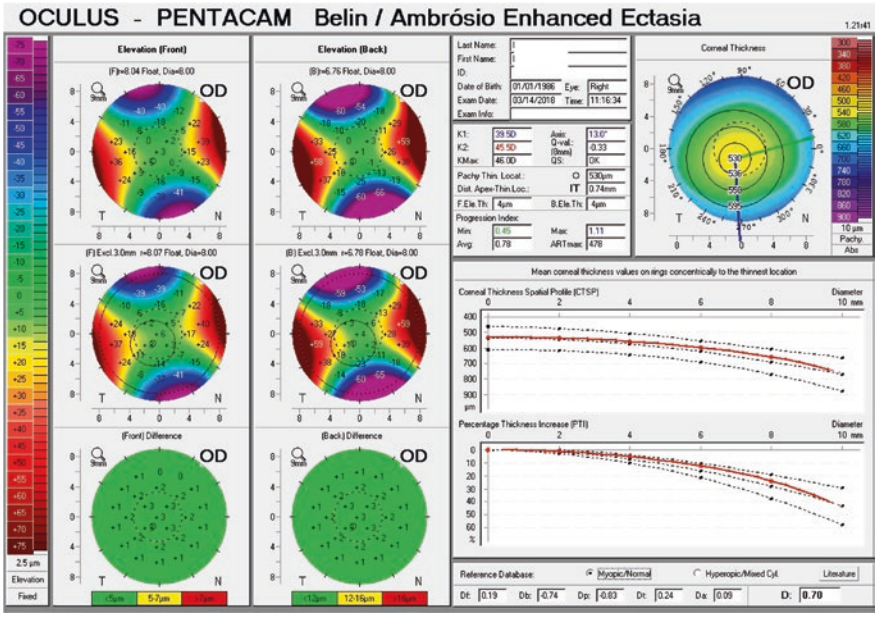

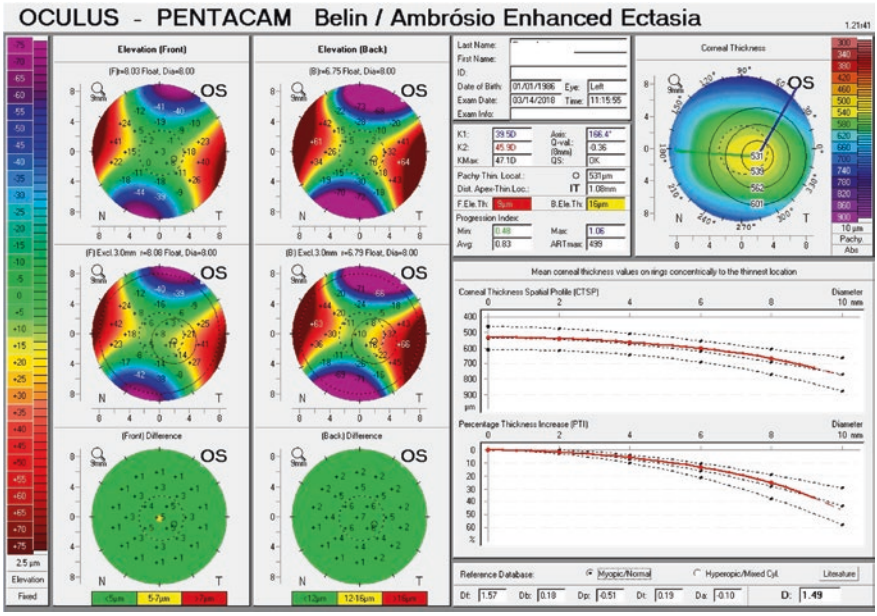

Fig. 61 There are normal values in pachymetric and Keratometric values. Keratoconus indices are at the normal range

Case 4.

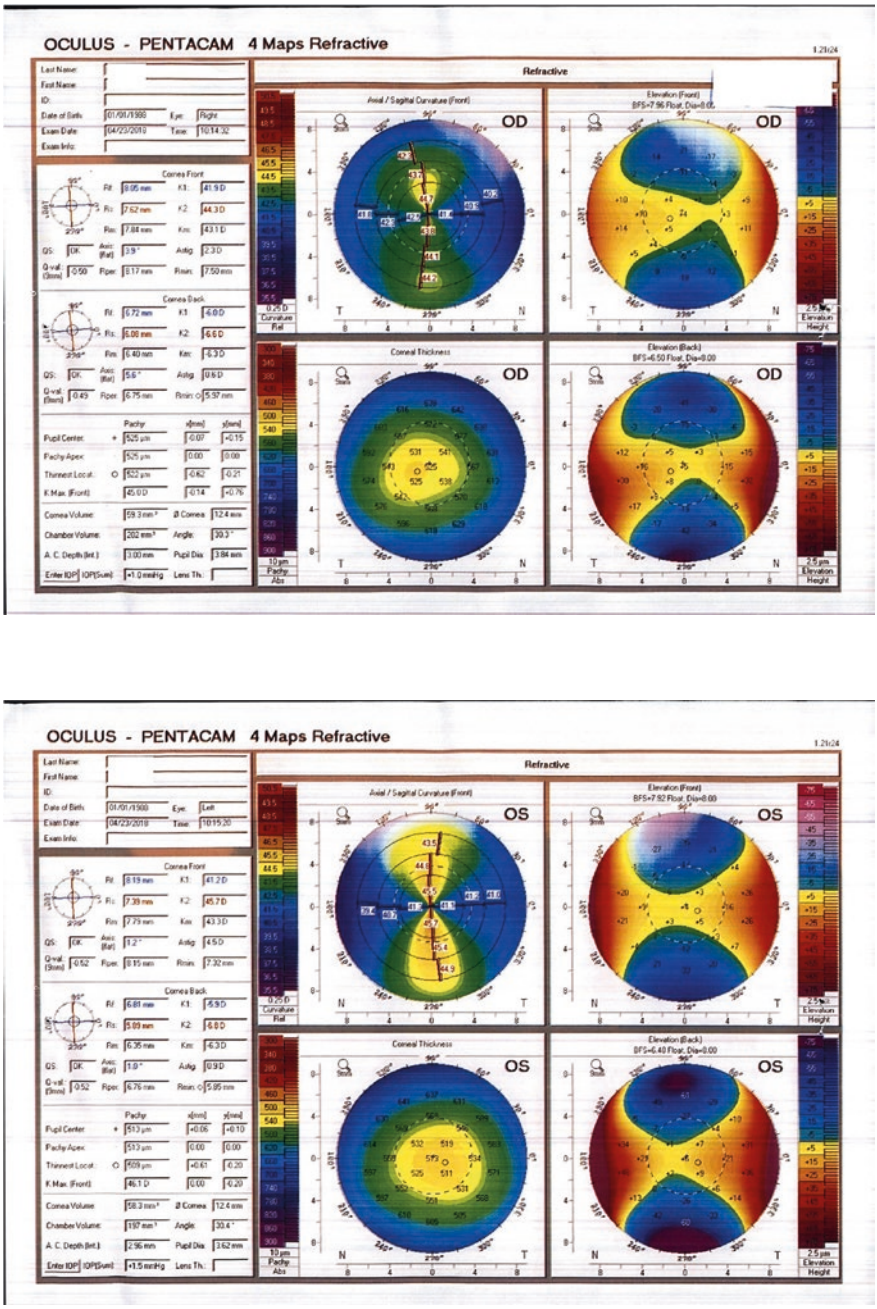

Fig. 62 A 29-year-old woman with ptosis and refractive errors: OD = −2.00/−1.75~180 CDVA = 10/10 and OS = −1.25/−4.25~5 CDVA = 10/10. There is superior steepening with normal topographic and tomographic values in the right eye and symmetric bow tie pattern in the left eye. This is not a keratoconus case and ptosis led to superior steepening

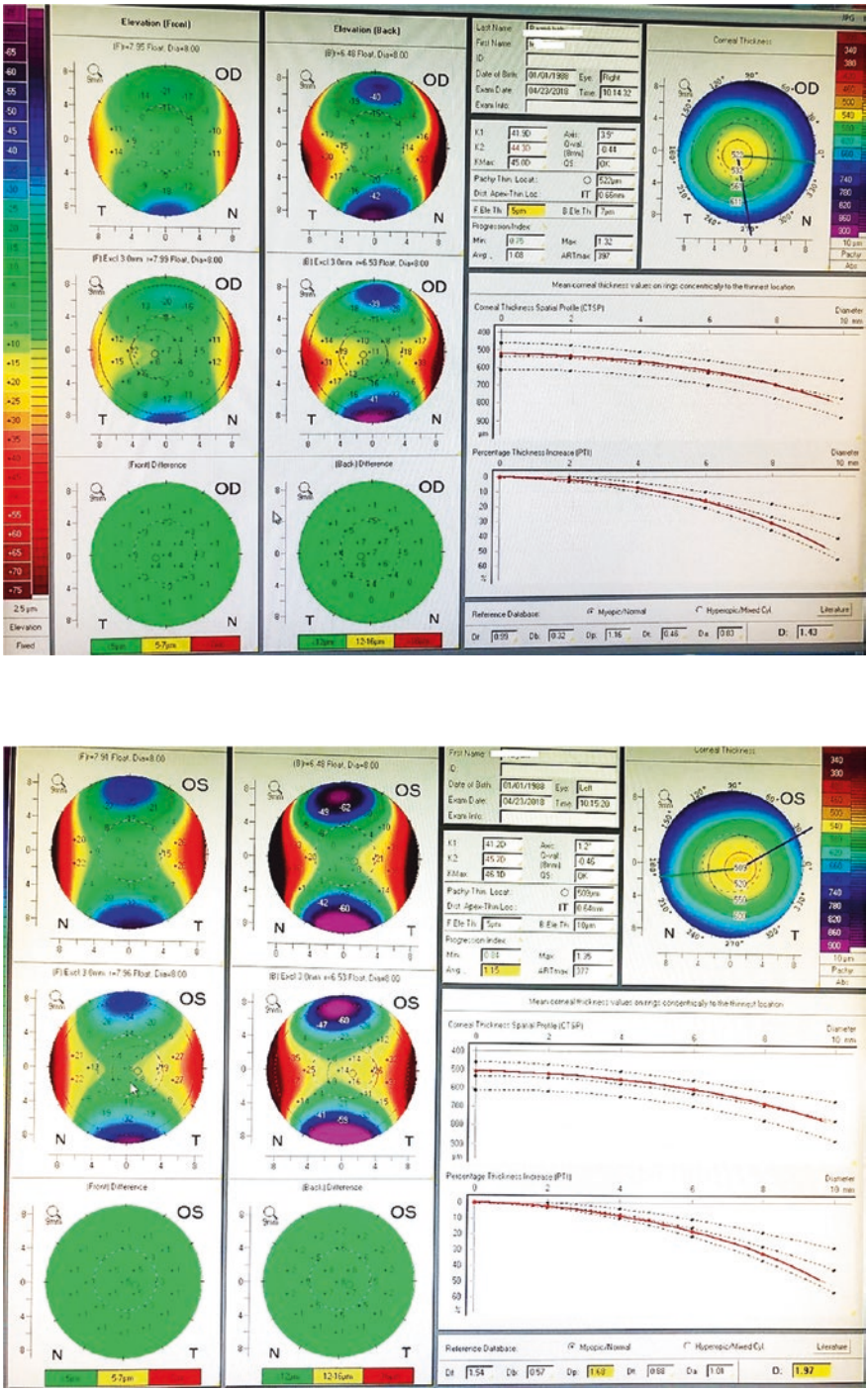

Fig. 63 These findings corresponded to Blin/Ambrosio display parameters. Average thickness progression are abnormal due to the presence of ptosis

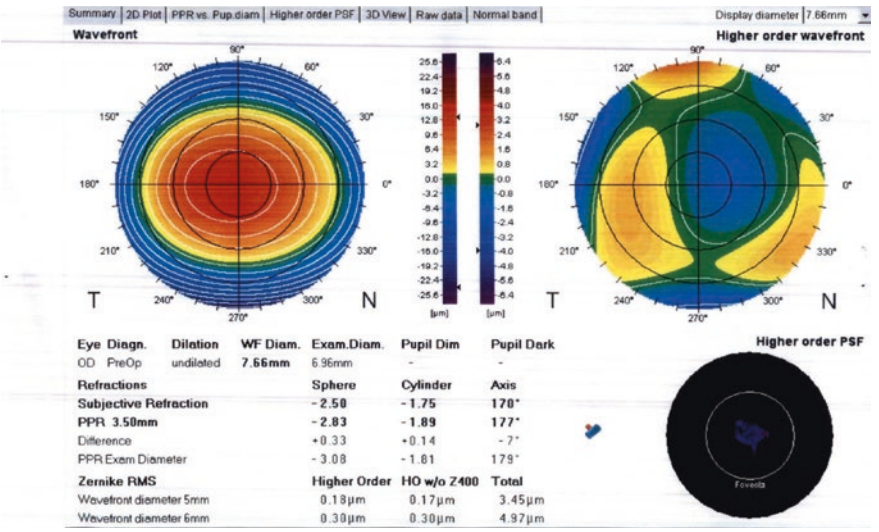

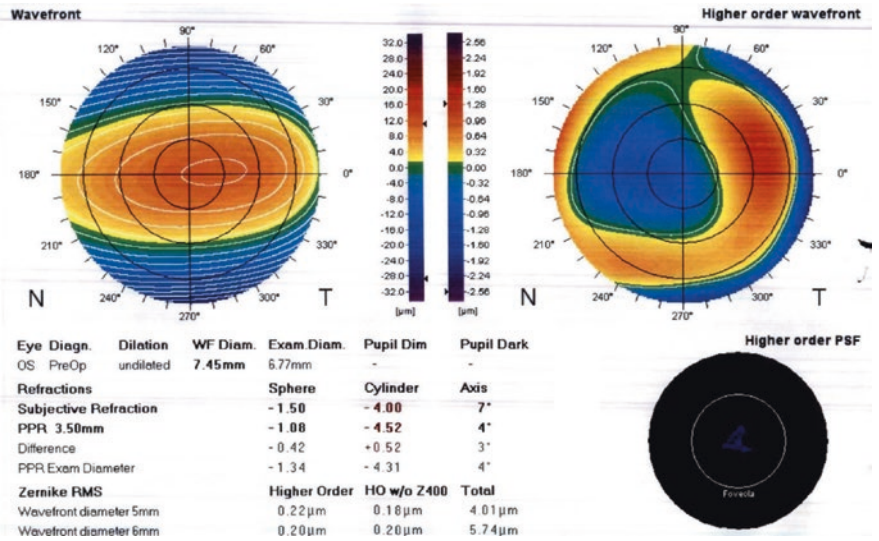

Fig. 64 There are normal higher-order aberrations (<0.30 µm) of the same patient in both eyes in wavefront maps

Case 5.

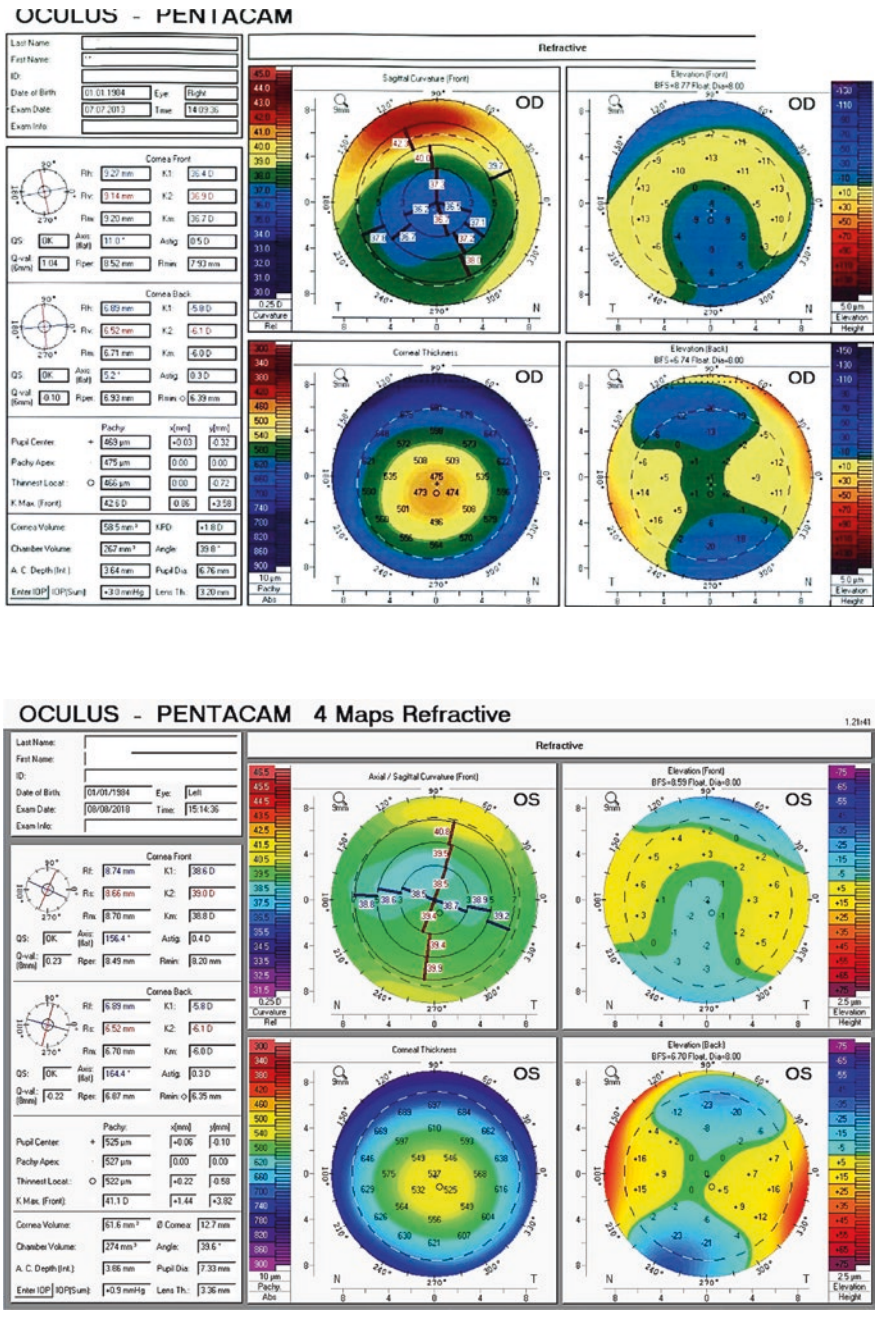

Fig. 65 A 34-year-old woman with a history of LASIK in the right eye and PRK in the left eye. There is decentered ablation in LASIK in the right eye and centered ablation in the PRK on the left eye. The patient has regression of the refractive error after decentered LASIK in the right eye 10 years after LASIK while there was no regression after PRK in the left eye

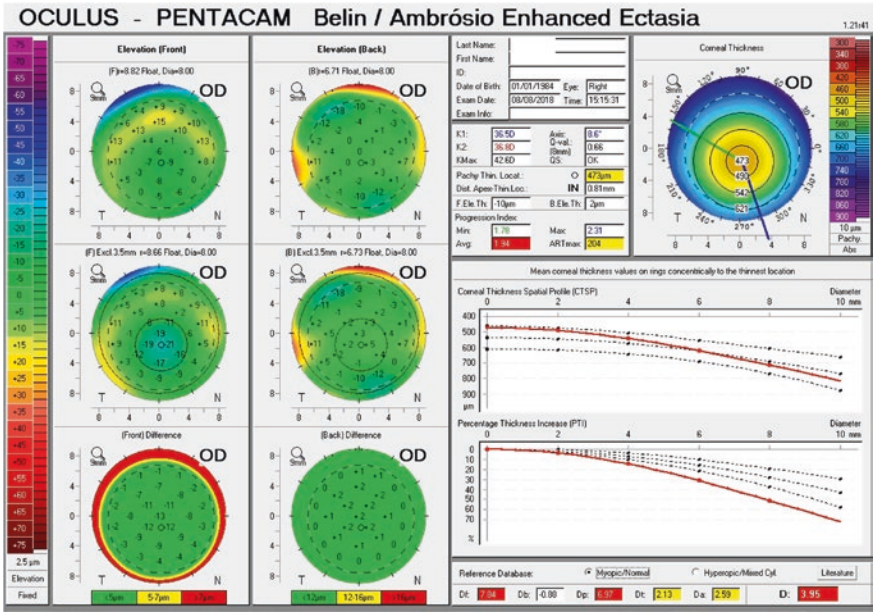

Fig. 66 Belin-Ambrosio display shows the abnormal range of D index and pachymetric values in the right eye, however, these indices are normal in the left eye

Case 6.

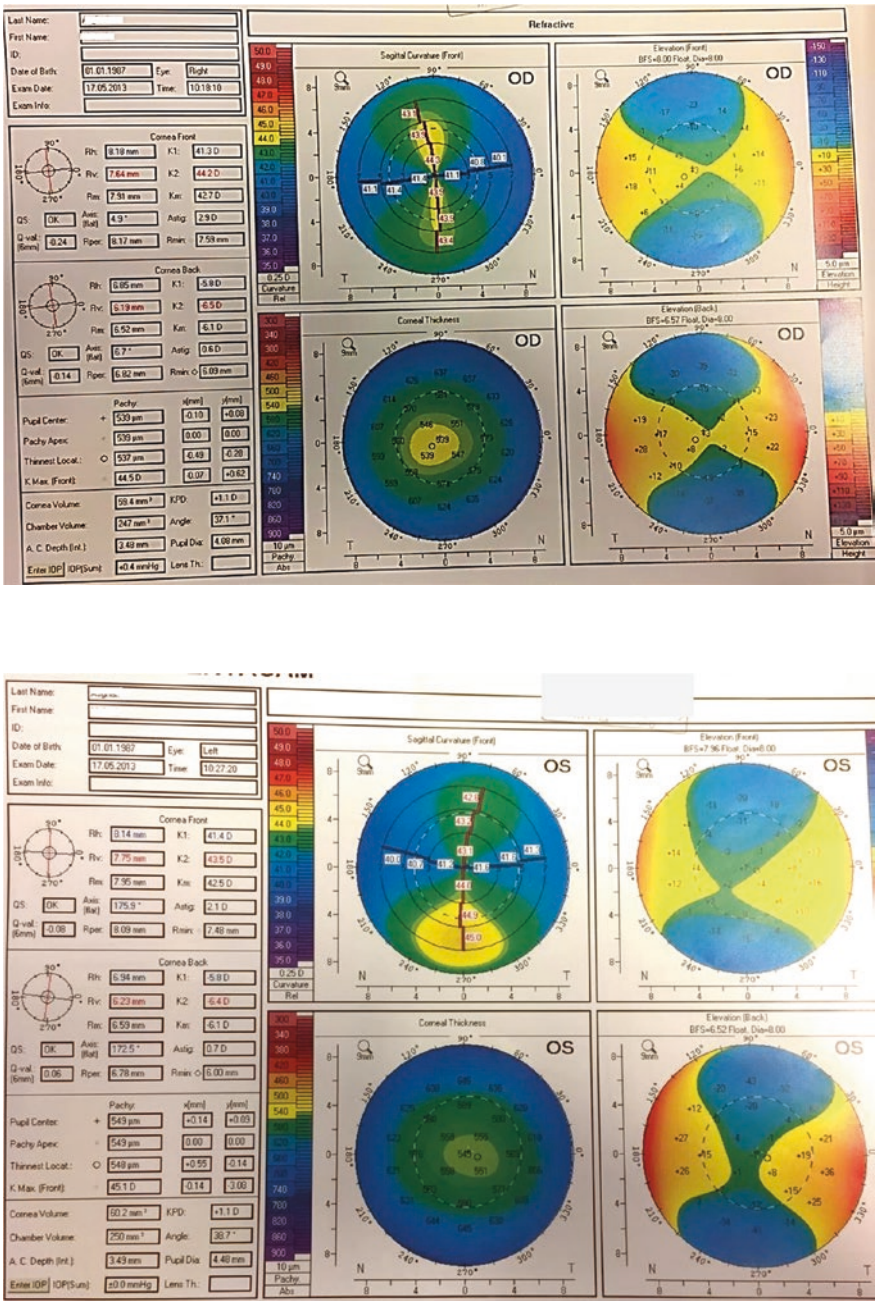

Fig. 67 A young woman with the normal cornea in the right eye and subclinical keratoconus in the left eye. Inferior steepening and abnormal elevation values are presented in the left eye

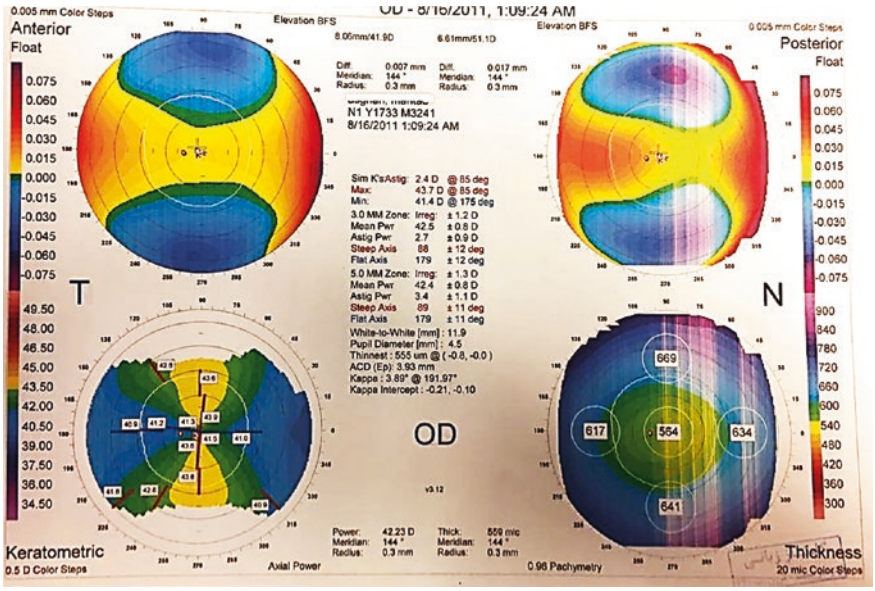

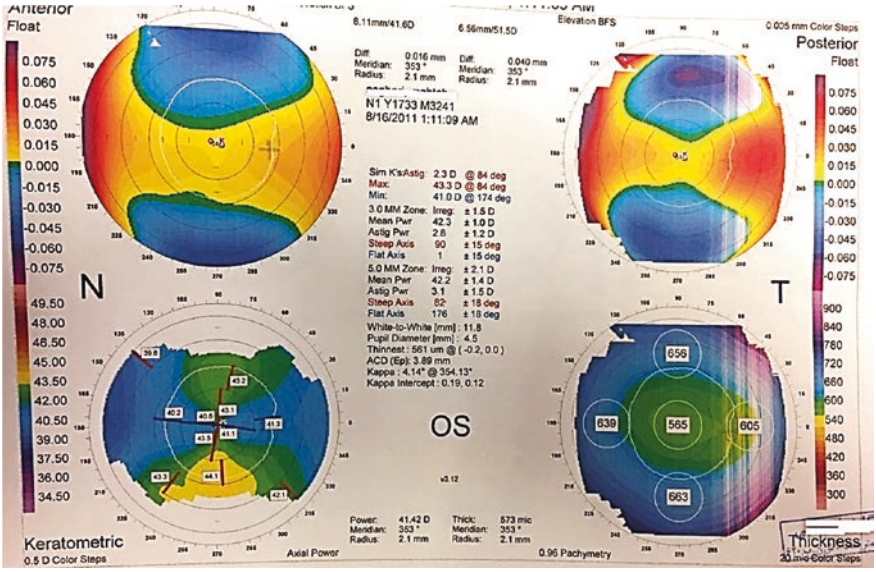

Fig. 68 These findings are compatible with Orbscan patterns in axial maps and Efkarpides (ratio of anterior/posterior curvature) values in both eyes, with normal range 1.2 in the right eye and more than 1.2 in the left eye of the same patient

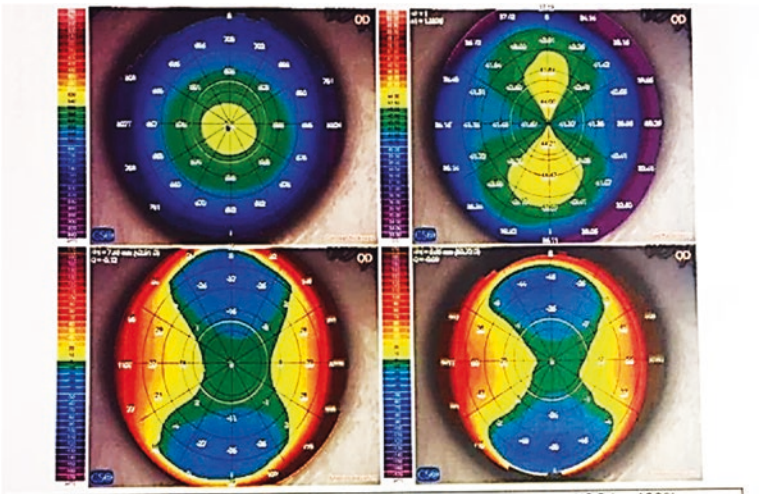

Acquisition quality	Coverage(SC.) = 99%	Not edited(SC.) = 100%
	Coverage(P.) = 94%	Centration(P.) = 91%

Summary Indices

HVID = 12.44 mm
Pupil (Topographic)
r = 0.15 mm @ 117°
Ø = 3.80 mm
λ intercept: r = 0.37 mm @ 117°
Thinnest location
r = 0.20 mm @ 240°
Thk = 536 µm
Apex
r = 1.40 mm @ 275°
Curv = 44.68 D
Anterior chamber
CCT + AD =
0.536 + 3.56 = 4.09 mm
Volume = 232 mm³
Iridocorneal angle = 51°
HACD = 13.14 mm
Lens rise = 1.06 mm
Corneal volume (Ø=10mm)
Volume = 56.6 mm³

K readings n0 = 1, n1 = 1.3375

Sim-k	K1 = 41.57 D @ 0°	
	K2 = 44.22 D @ 90°	
	Avg = 42.85 D	
	Cyl = -2.65 D Ax 0°	
Anterior Ø=3mm	K1 = 41.57 D @ 179°	
	K2 = 44.11 D @ 89°	
	Avg = 42.80 D	
	Cyl = -2.54 D Ax 179°	
Anterior Ø=5mm	K1 = 41.54 D @ 0°	
	K2 = 44.18 D @ 90°	
	Avg = 42.82 D	
	Cyl = -2.64 D Ax 0°	
Anterior Ø=7mm	K1 = 41.45 D @ 179°	
	K2 = 44.09 D @ 89°	
	Avg = 42.73 D	
	Cyl = -2.64 D Ax 179°	

Refractive analysis

Ø=4.0mm
Cyl = -2.21 D Ax 178°
MPP = 42.47 D
LSA = 0.84 D

Keratoconus screening

Sif = 0.52 D
KVf = 4 µm
BCVf = 0.30 D @ 256°
Sib = -0.01 D
KVb = 6 µm
BCVb = 0.00 D @ 311°
Thk = 536 µm
Class:
- 'Normal'

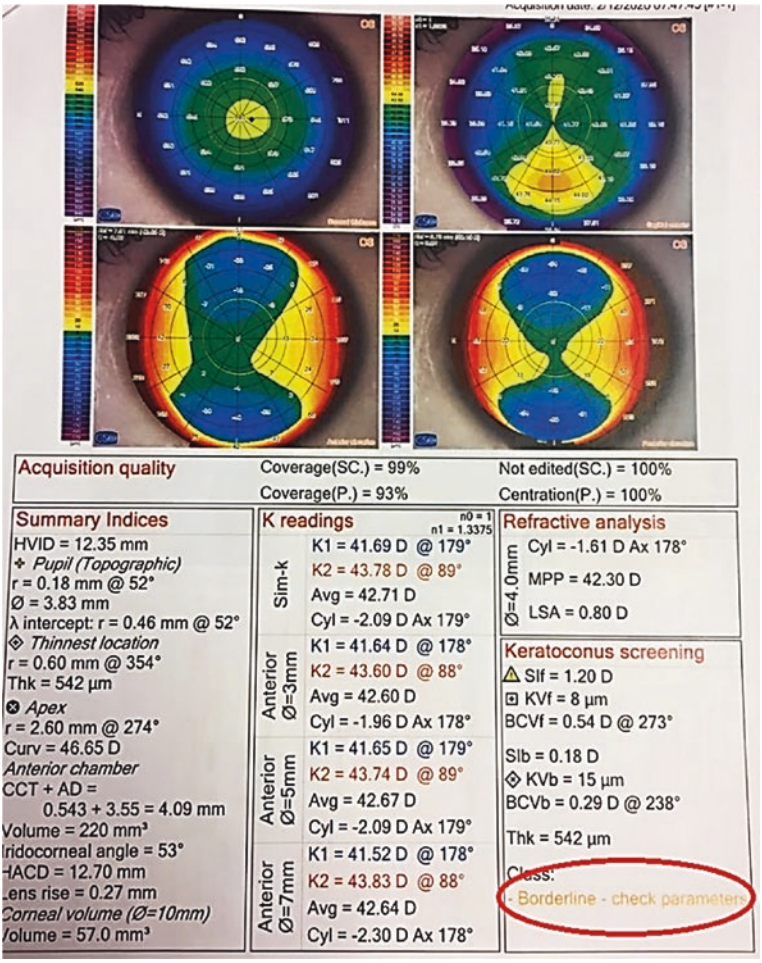

Fig. 69 These findings are compatible with normal and borderline in Sirius classifier in the right and left eye of the same patient, respectively

Case 7.

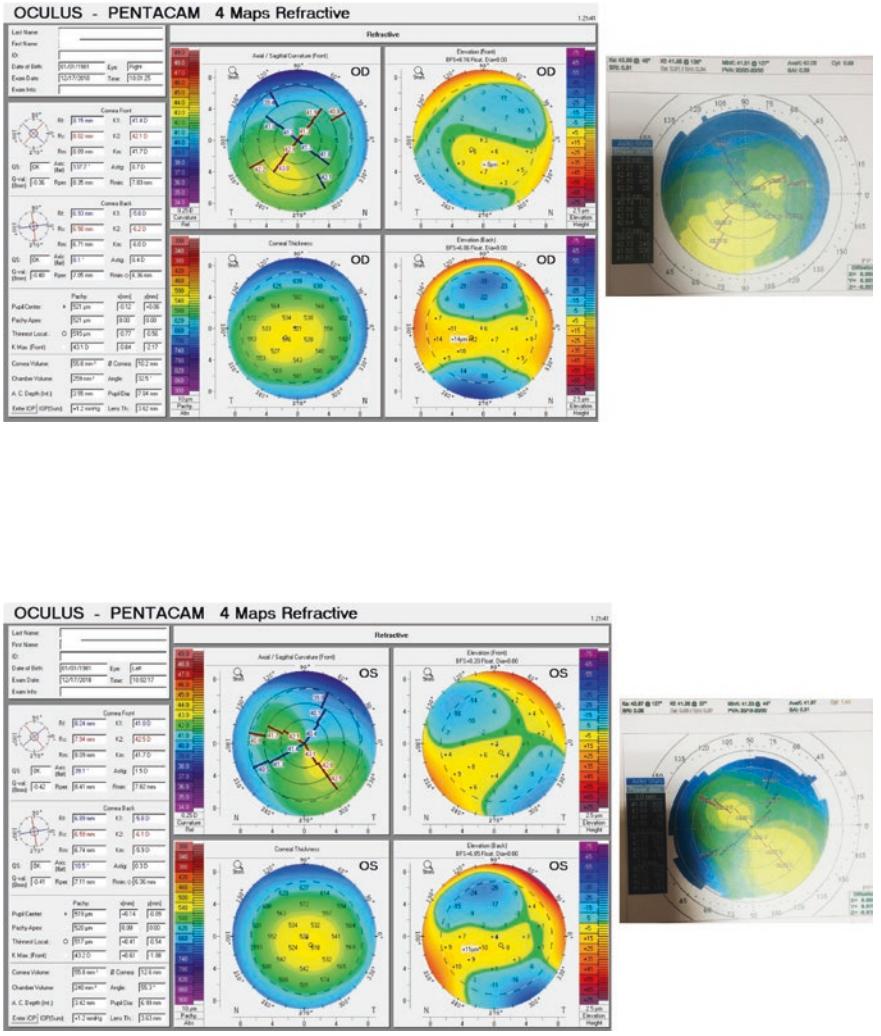

Fig. 70 A 34-years-old man with keratoconus suspect, and inferior steepening in both eyes in refractive and topographic maps. Normal pachymetric and elevation values are also shown in the quad maps of Pentacam

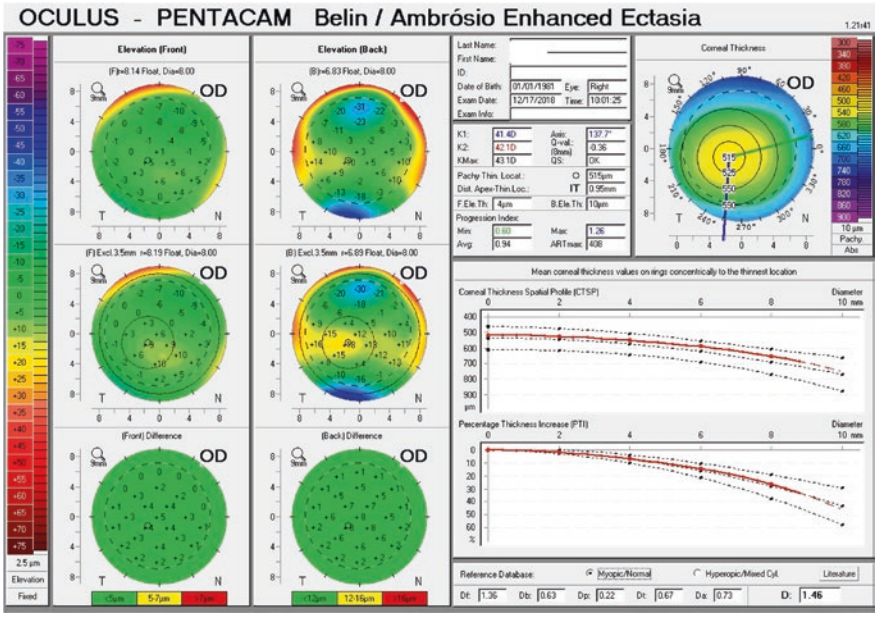

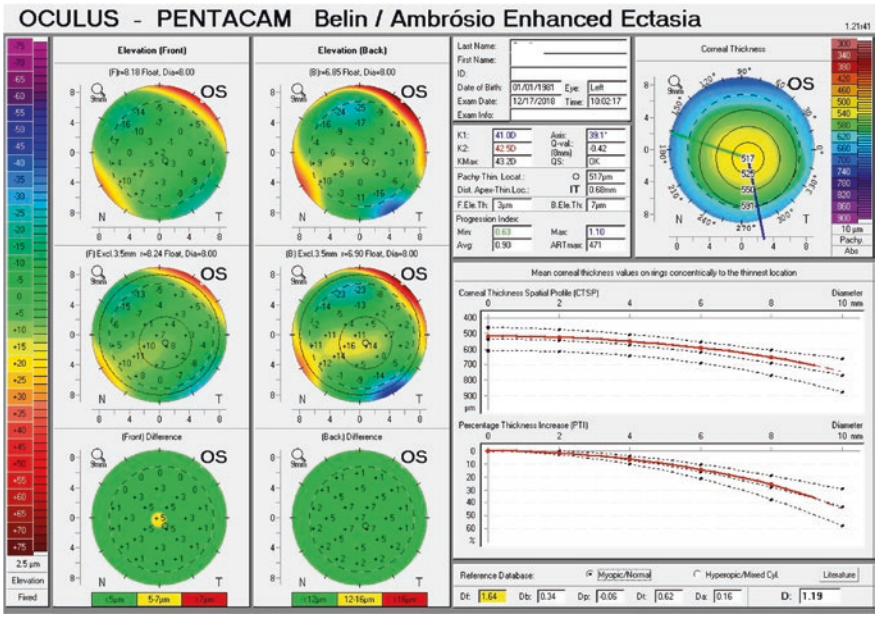

Fig. 71 There are normal values in Blin-Ambrosio display maps, D index and pachymetric graphs of the same patient in both eyes of the same patient, however, front D of the left eye is showing subtle abnormal changes

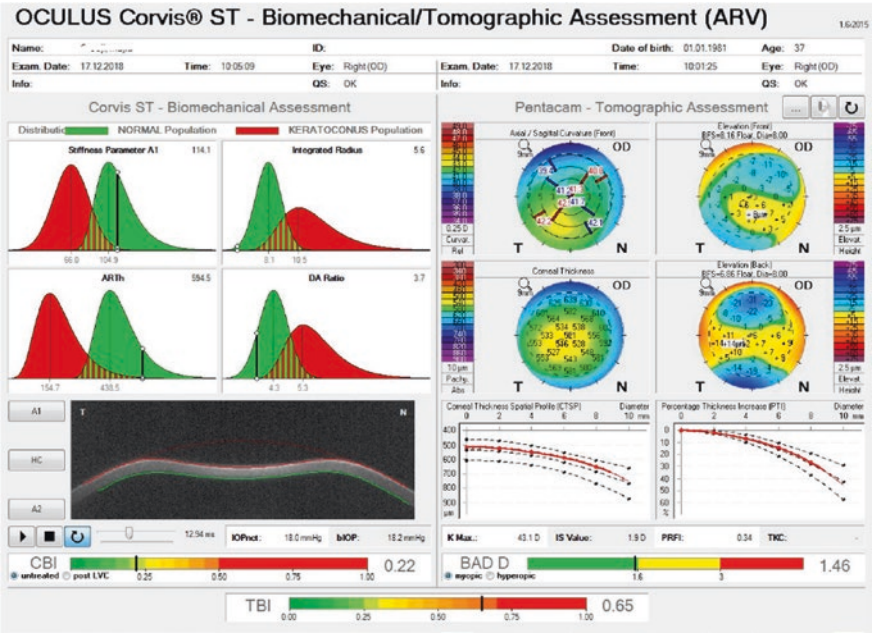

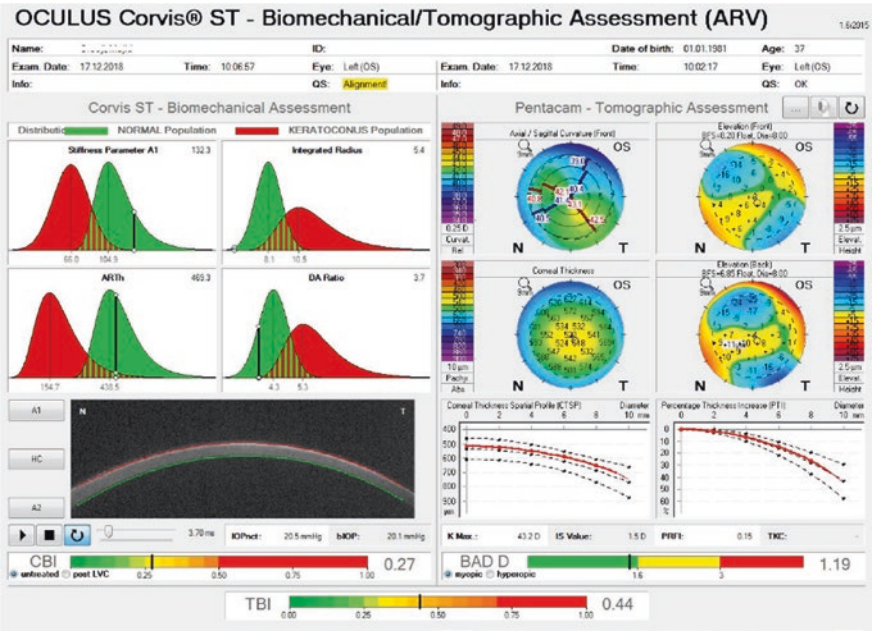

Fig. 72 The range of Corvis biomechanical index (CBI) and combined topographic and biomechanical index (TBI) is abnormal in both eyes of the same patient. TBI is a more sensitive index than CBI and D index parameters for keratoconus suspect detection

Case 8.

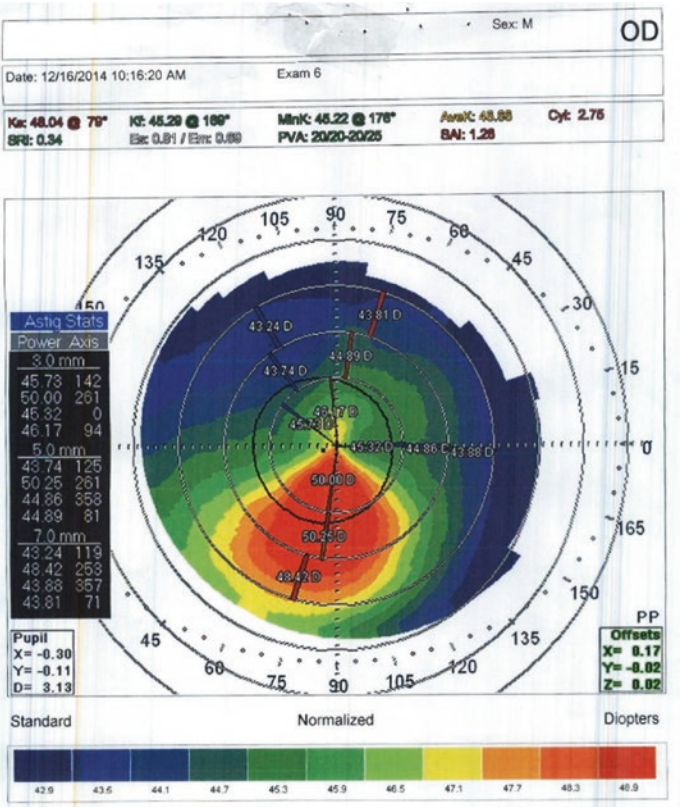
Sex: M
OD
Date: 12/16/2014 10:16:20 AM
Exam 6
Ks: 48.04 @ 79°
SRI: 0.34
Kt: 45.29 @ 169°
Ele: 0.81 / Em: 0.89
MinK: 45.22 @ 176°
PVA: 20/20-20/25
AvgK: 48.88
BAI: 1.26
Cyl: 2.75
Astig Stats
Power Axis
3.0 mm
45.73 142
50.00 261
45.32 0
46.17 94
5.0 mm
43.74 125
50.25 261
44.86 358
44.89 81
7.0 mm
43.24 119
48.42 253
43.88 357
43.81 71
Pupil
X= -0.30
Y= -0.11
D= 3.13
PP
Offsets
X= 0.17
Y= -0.02
Z= 0.02
Standard
Normalized
Diopters

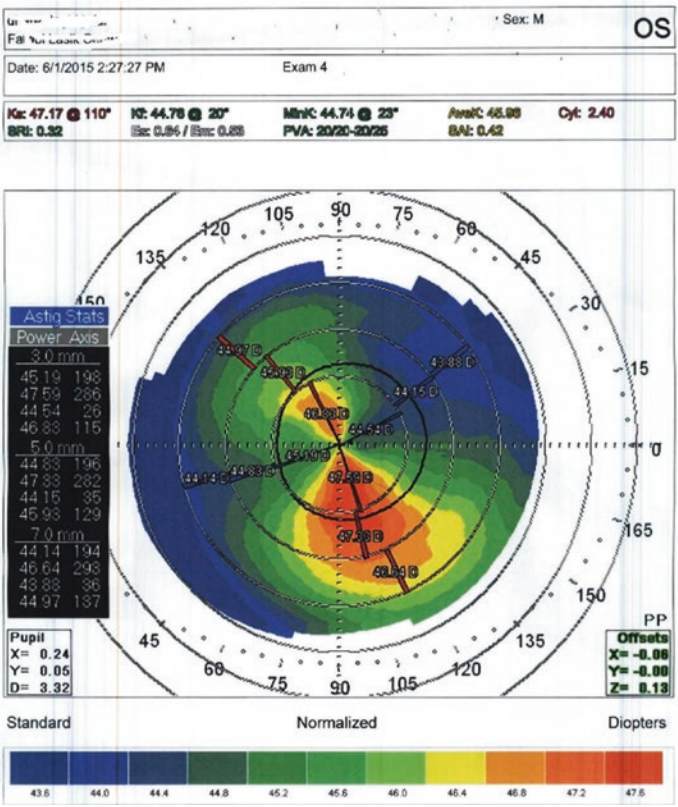

Fig. 73 A 30-year-old man with subclinical keratoconus and hyperopic astigmatism who had stable refraction for at least 5 years. The left eye underwent combined hyperopic photorefractive keratectomy (PRK) plus corneal cross-linking (CXL). Following surgery a hyper-prolate region created to increase the central corneal power and resulting in a pseudo-keratectasia pattern with stable round symmetric axial curvature and normal anterior and posterior elevations that rules out ectasia

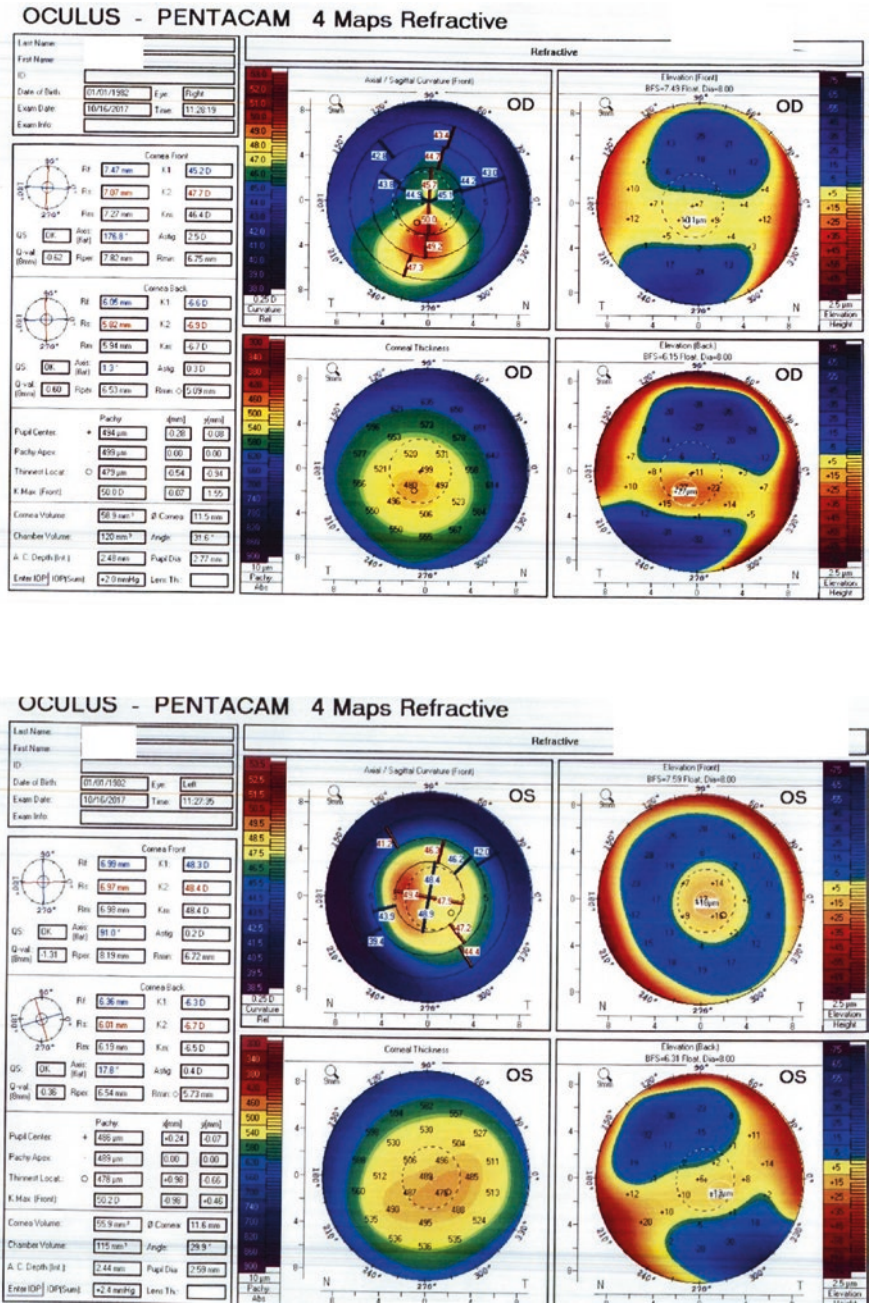

Fig. 74 There is inferior steepening in the right eye and stable refractive outcomes in the left eye of the same patient, including regular Keratometric values and subtle amount of astigmatism with normal elevation values after surgery. So, this case is a hyper prolate cornea due to hyperopic refractive surgery, not post-refractive ectasia

Case 9.

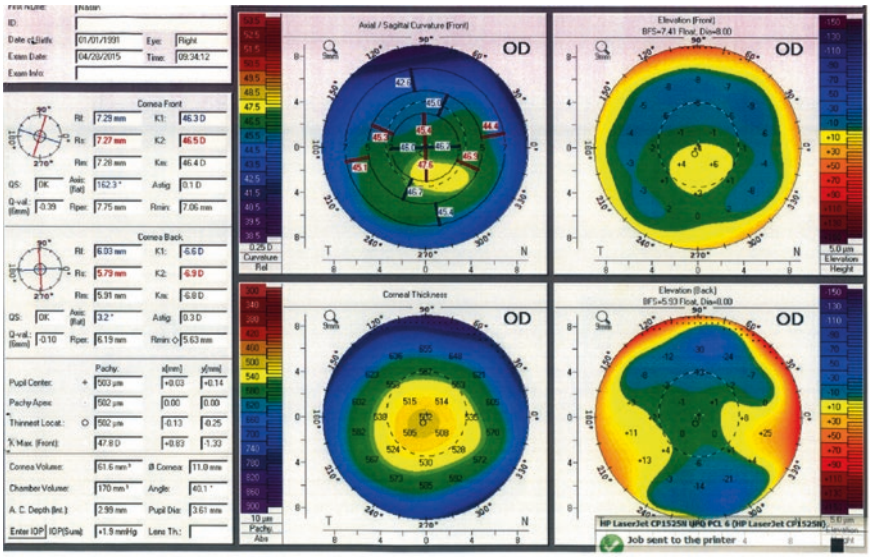

Fig. 75 A 35-year-old woman with mild keratoconus, thin cornea and low myopia and stable refraction for at least 5 years with significant inferior steepening on sagital curvature map of Pentacam [23]

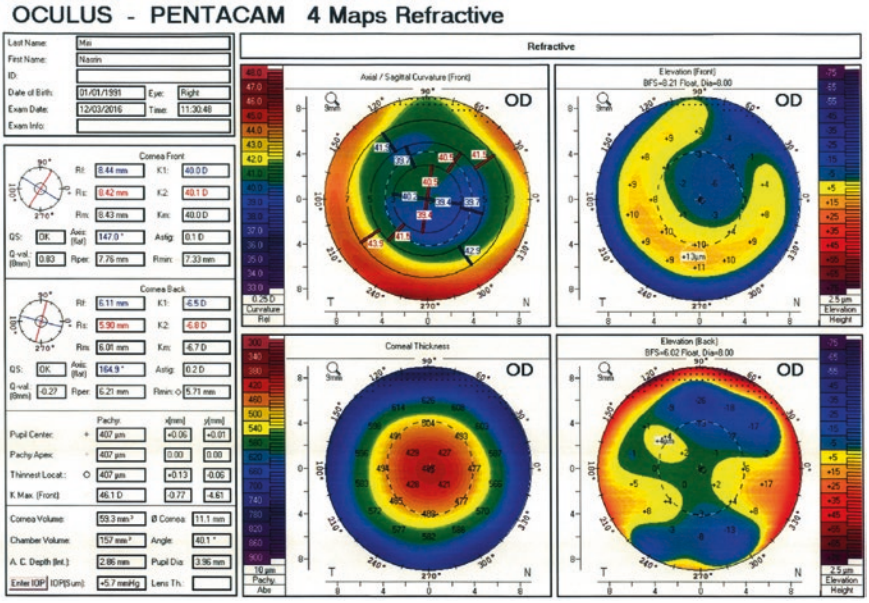

Fig. 76 The right eye of the same patient underwent combined customized PRK and CXL and stable excellent refractive outcomes were obtained during serial follow up examinations up to 5 years postoperatively

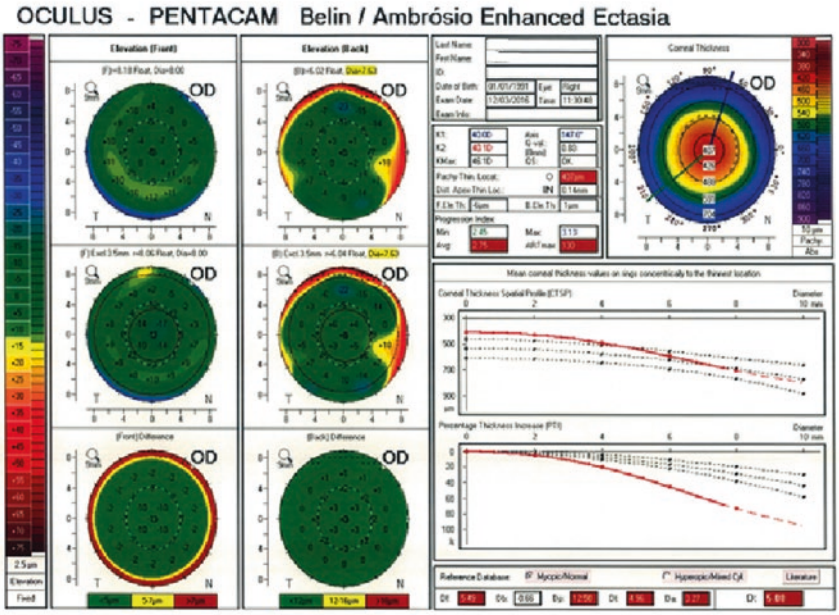

Fig. 77 There are normal elevation values in difference maps in Belin display, however, there are abnormal values in pachymetric values and D index in Ambrosio display. The Belin/Ambrosio display designed for virgin eye and distorted relationship can be seen in operated eyes

Case 10.

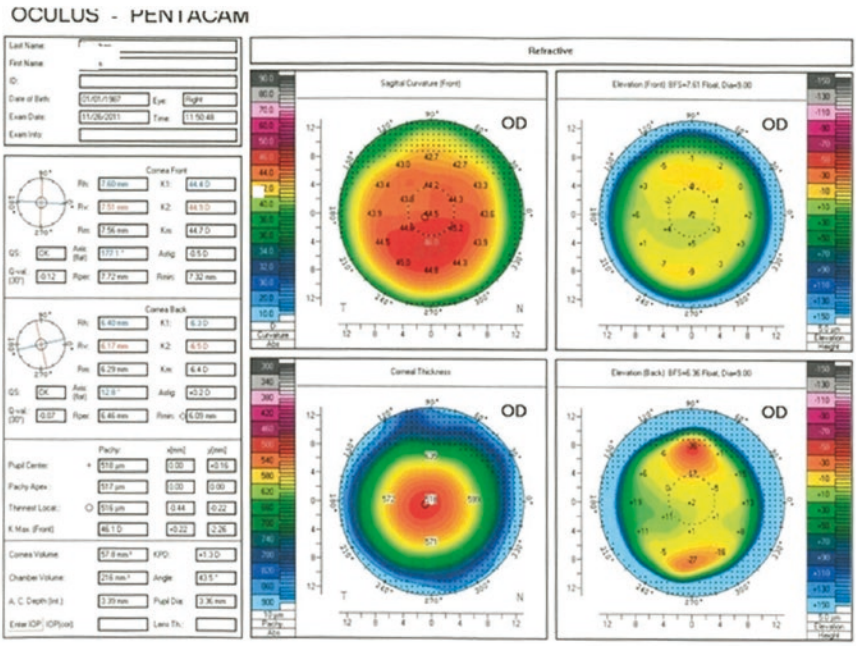

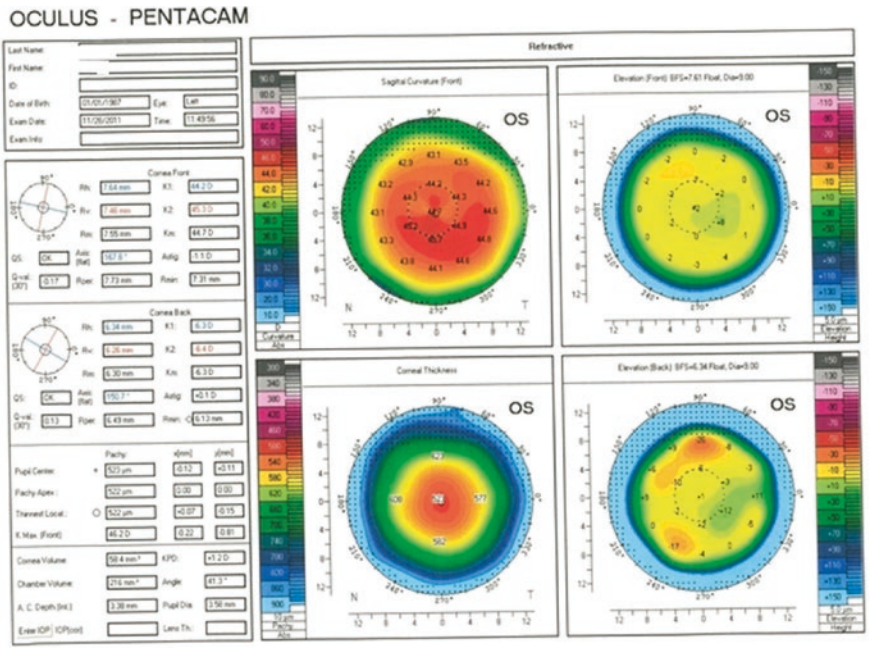

Fig. 78 A 25-year-old woman with subclinical keratoconus. She was scheduled by other surgeons for refractive surgery with refractive errors: OD = −1.50/−0.5~100, CDVA 10/10 and OS = −1.75/−0.75~90, CDVA 10/10. There is inferior steepening in axial maps and normal thickness values in both eyes and the corneas are apparently normal

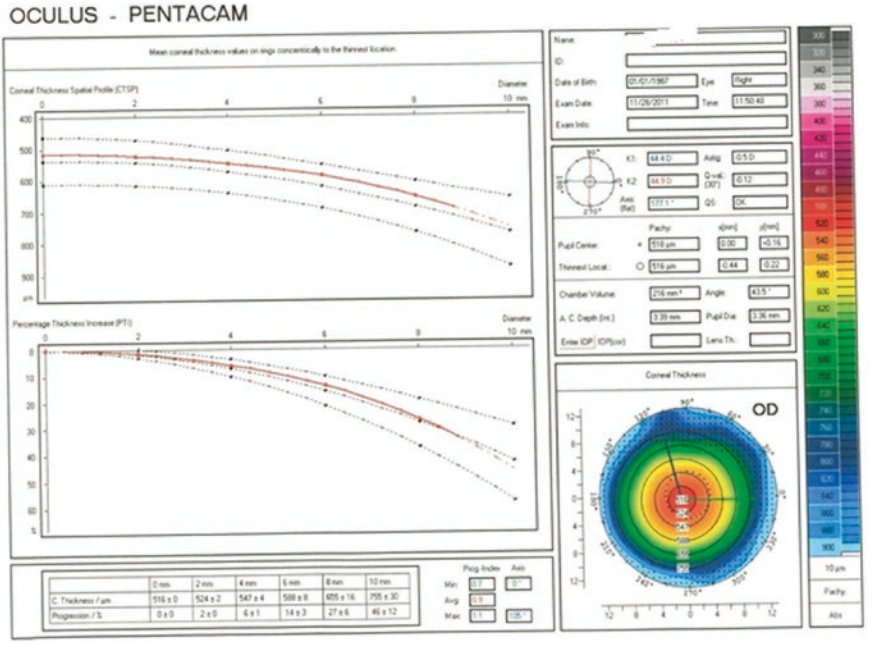

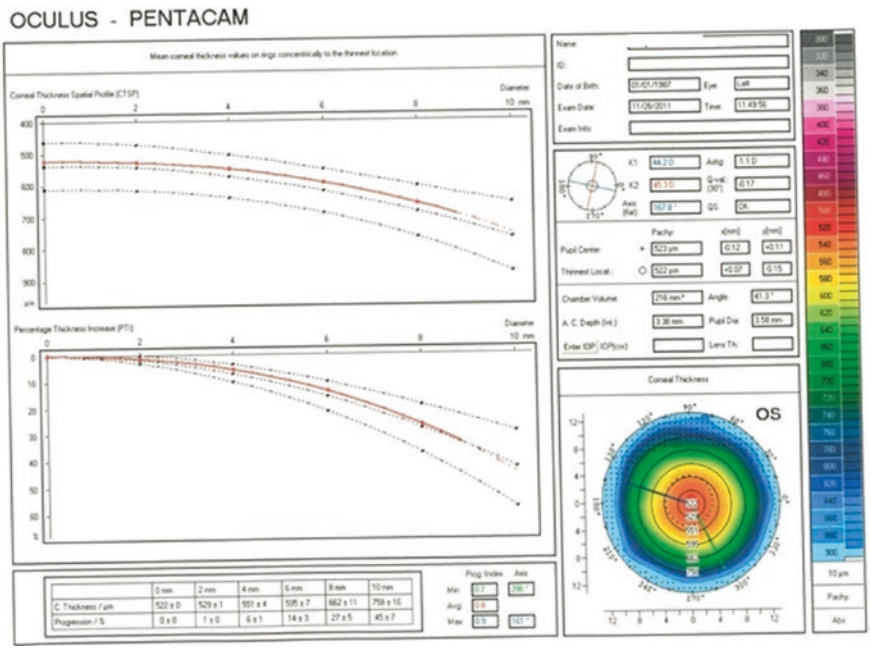

Fig. 79 There is a normal progression in thickness parameters in Pentacam of the same patient

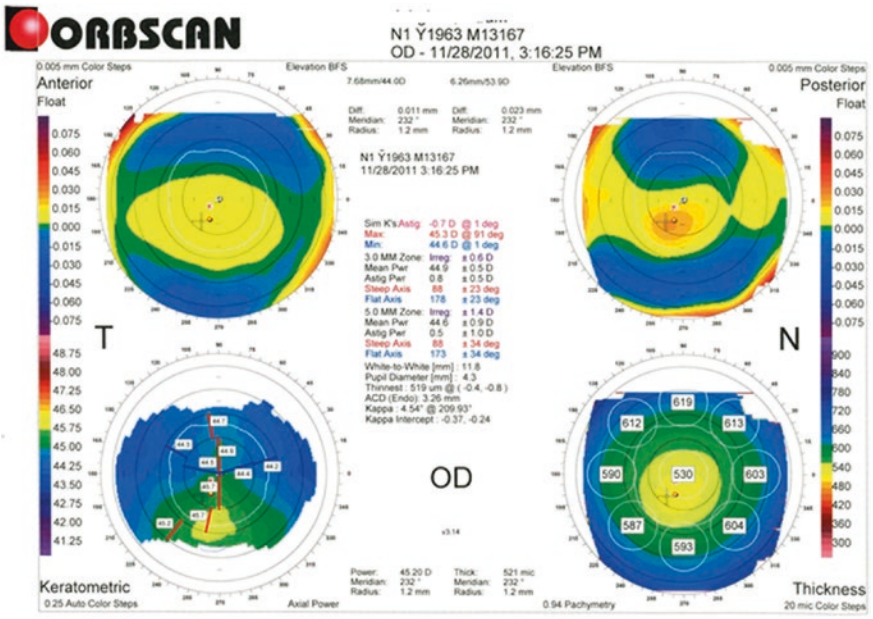

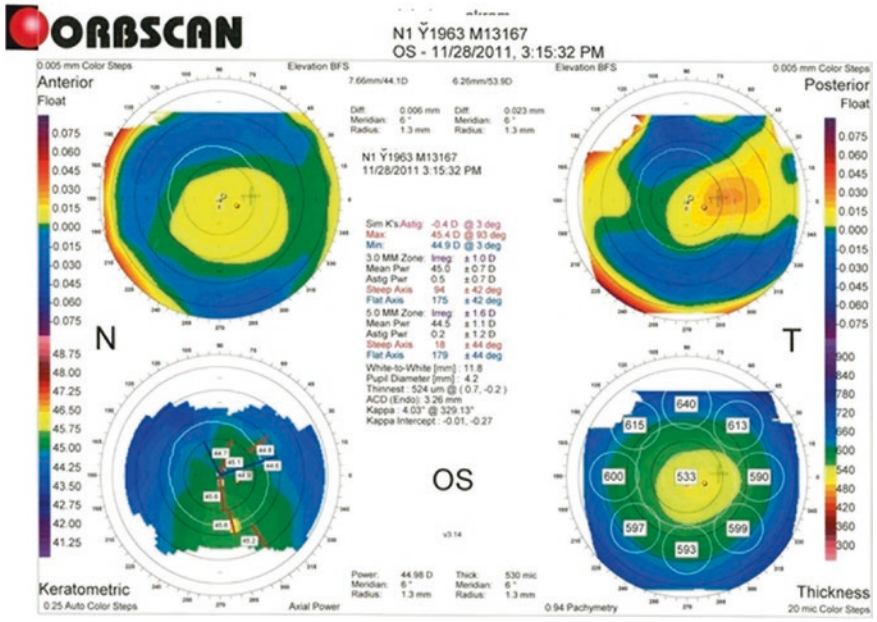

Fig. 80 There are inferior steepening in sagital maps with normal keratoconus screening values in Orbscan imaging for the same patient in both eyes

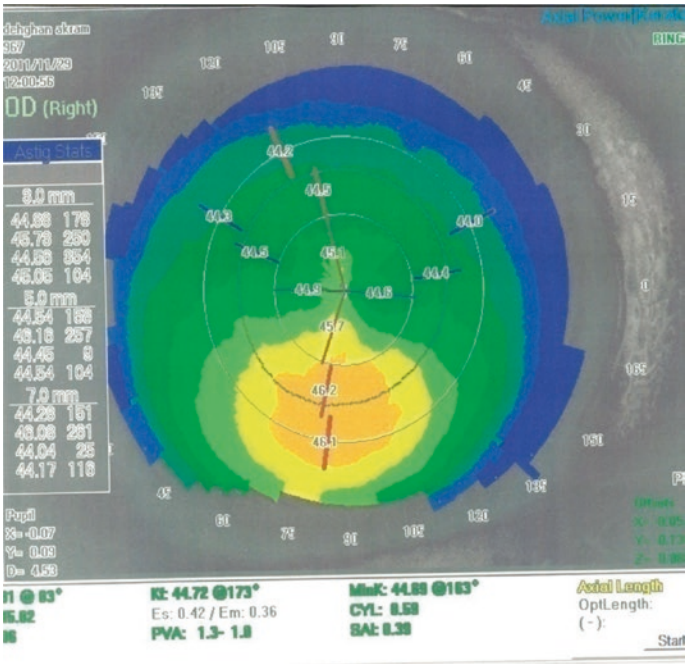

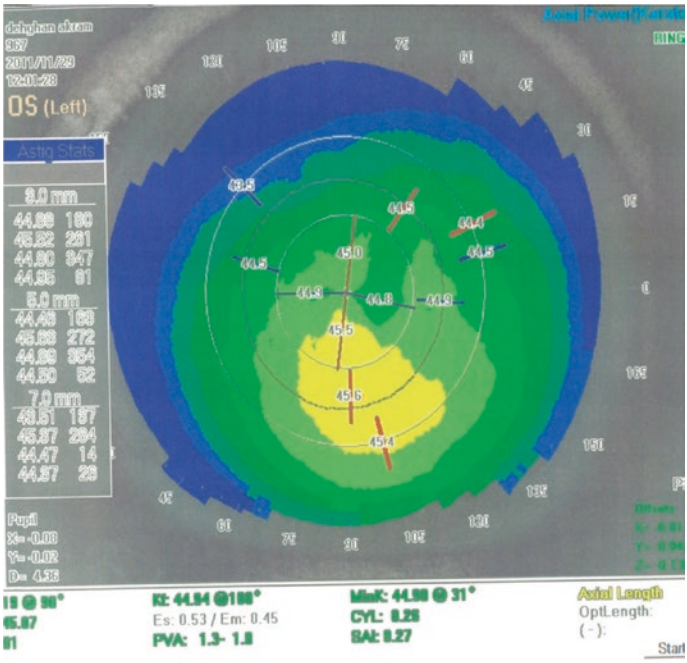

Fig. 81 In topographic imaging with a Placido-based system for the same patient, a significant SRAX with a sharper bottom is seen. This is a false-negative diagnosis of keratoconus in the Pentacam. It is strongly recommended that Placido topography be performed in patients with inferior steepening in Pentacam (or Scheimpflug based systems) with no clinical sign

Case 11.

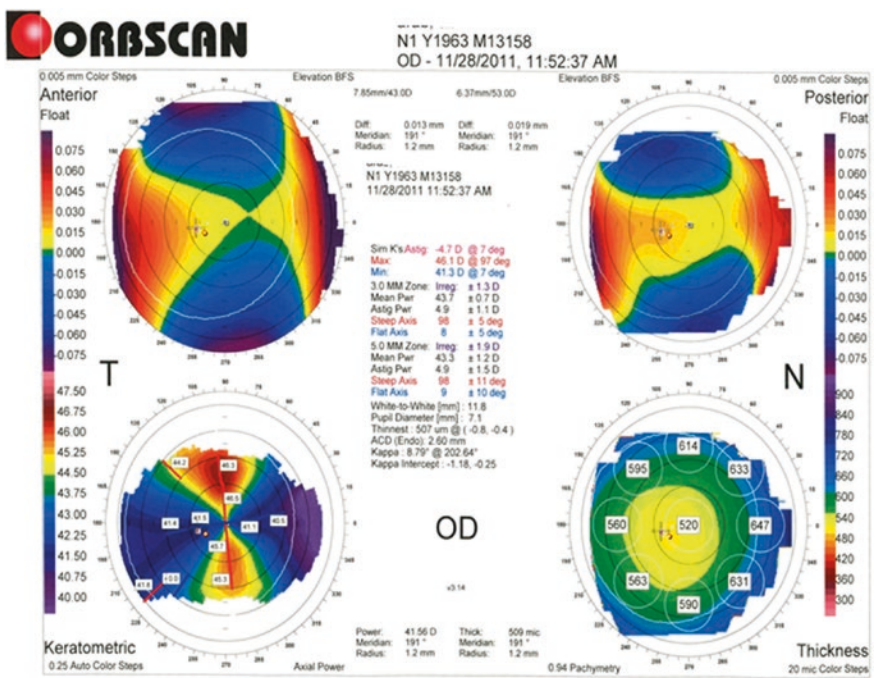

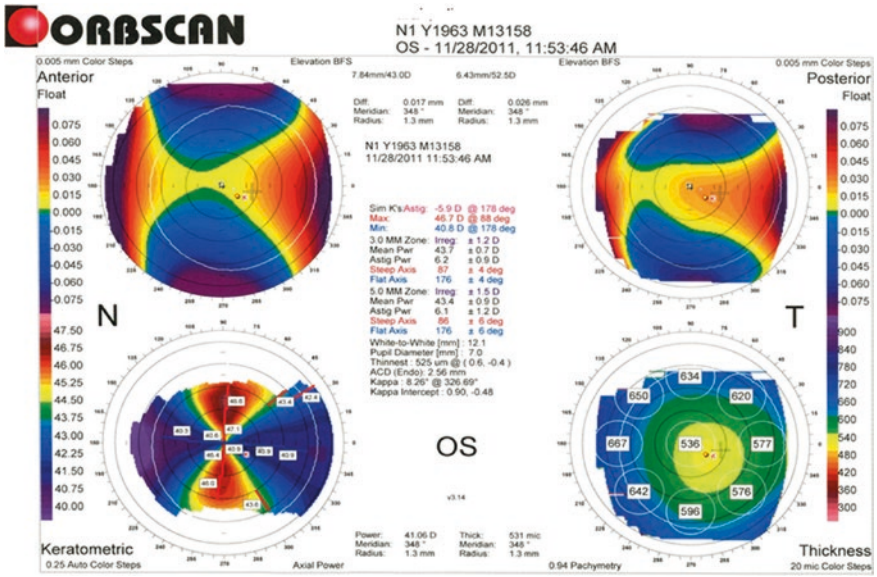

Fig. 82 A 21-year-old man with high astigmatism (mixed astigmatism) referred for keratoconus screening. There is an orthogonal symmetric bow tie pattern with no SRAX in Orbscan

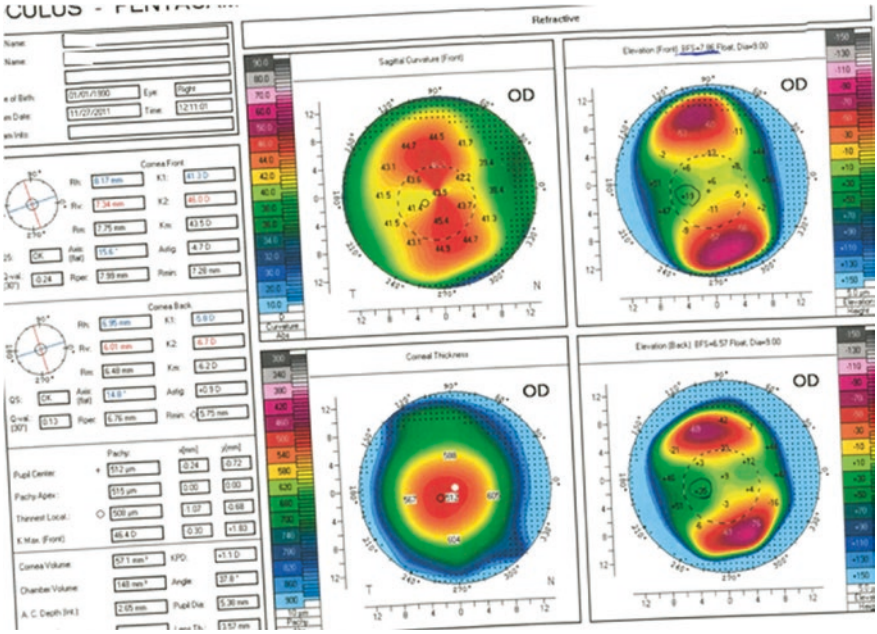

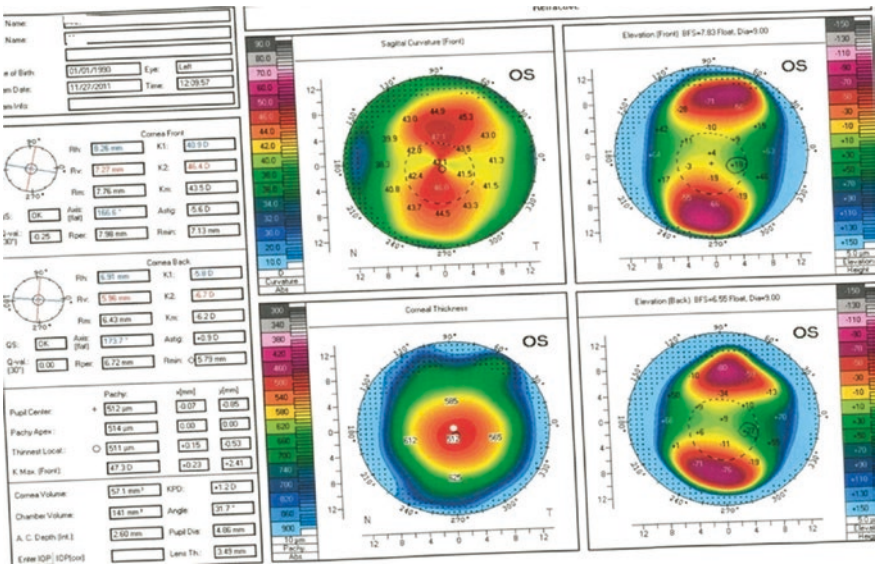

Fig. 83 There are abnormal elevation patterns in the same patient in Pentacam based on best-fit sphere reference (BFS)

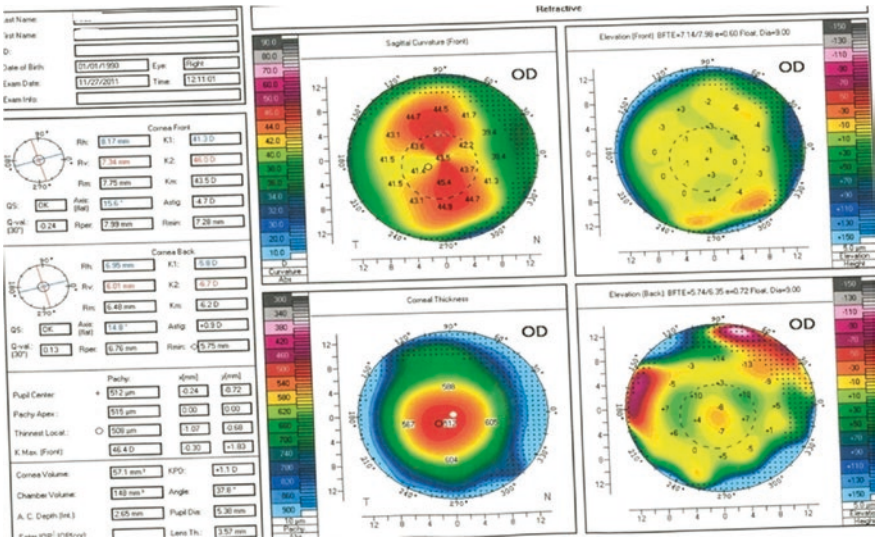

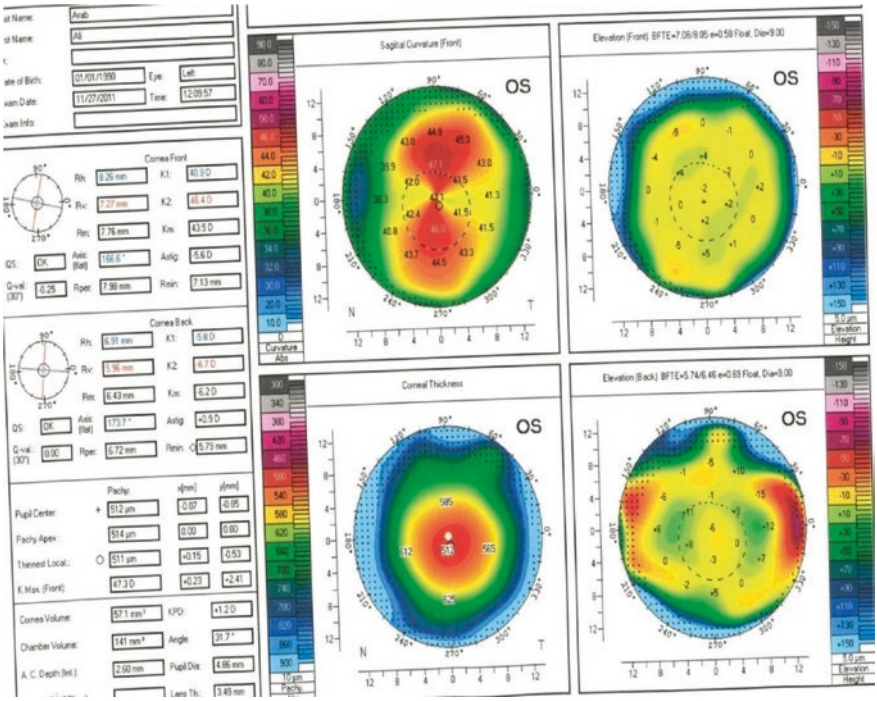

Fig. 84 There are normal elevation patterns in the best-fit toric ellipsoid of the same patient. This is a false-positive diagnosis of keratoconus in the Pentacam

In the case of corneal irregularity or suspicious value on elevation maps with the BFS, it is recommended to evaluate the elevation maps with the best fit toric ellipsoid (BFTE). When the irregularity due to the real corneal surface, the BFTE eliminates the effect of corneal astigmatic slope on the elevation maps and matches with astigmatic cornea perfectly.

Case 12.

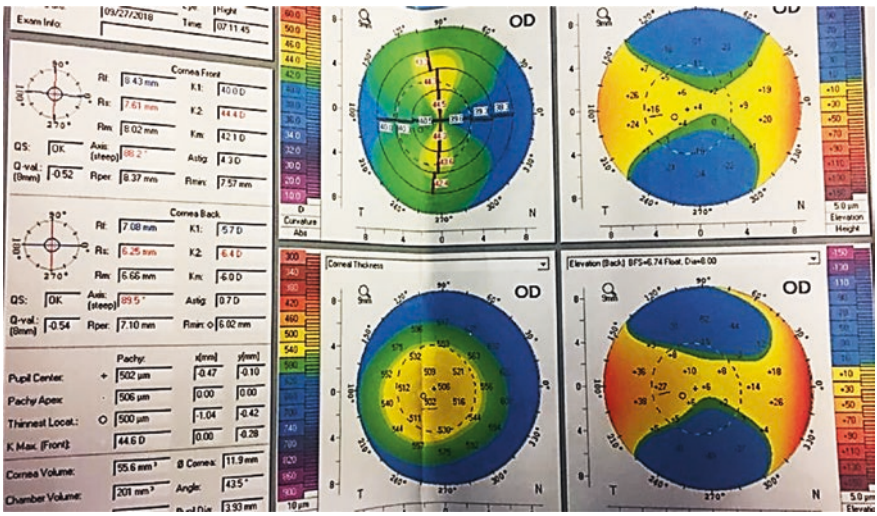

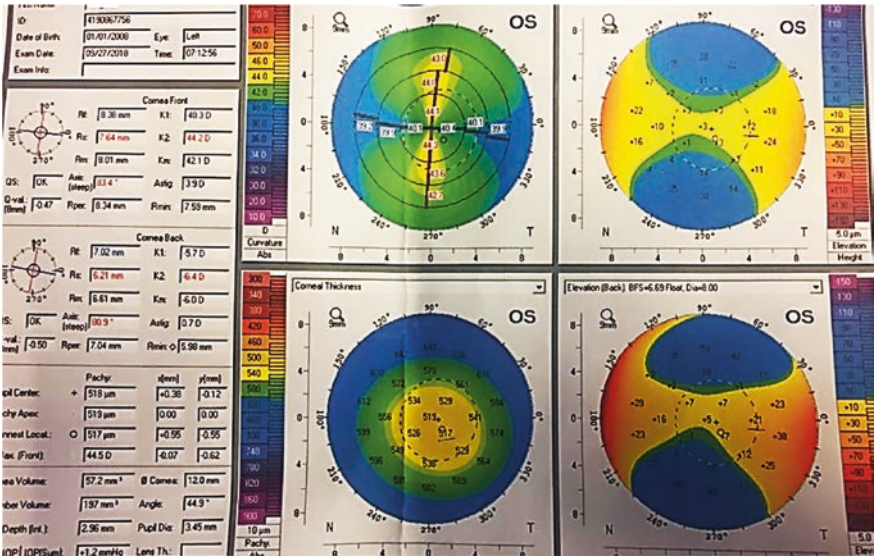
OS
Corneal Thickness
Elevation (Back) BFS=6.69 Float, Dia=8.00

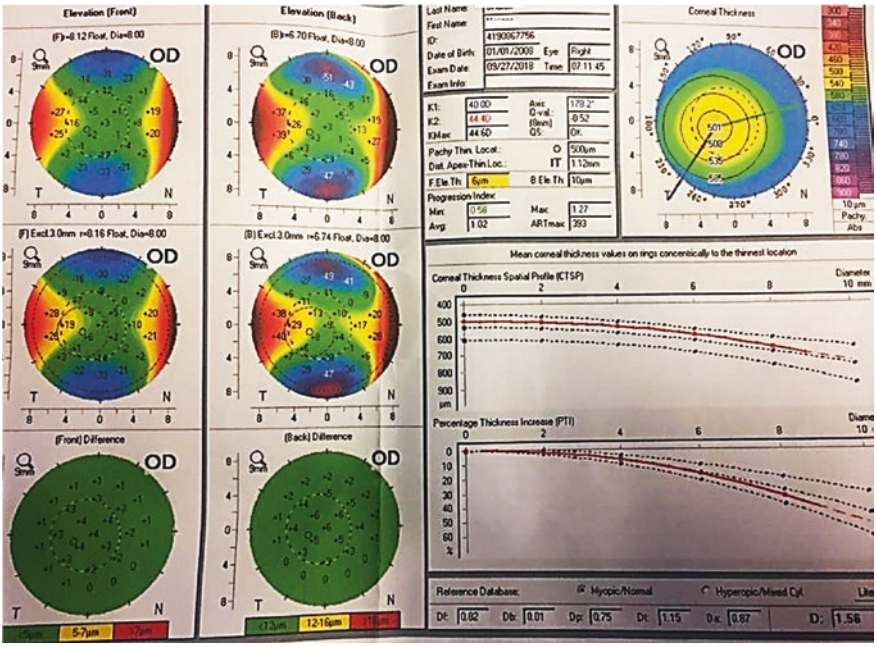
Elevation (Front)
Elevation (Back)
Corneal Thickness
OD
Mean corneal thickness values on rings concentrically to the thinnest location
Corneal Thickness Spatial Profile (CTSP)
Percentage Thickness Increase (PTI)
(Front) Difference
(Back) Difference

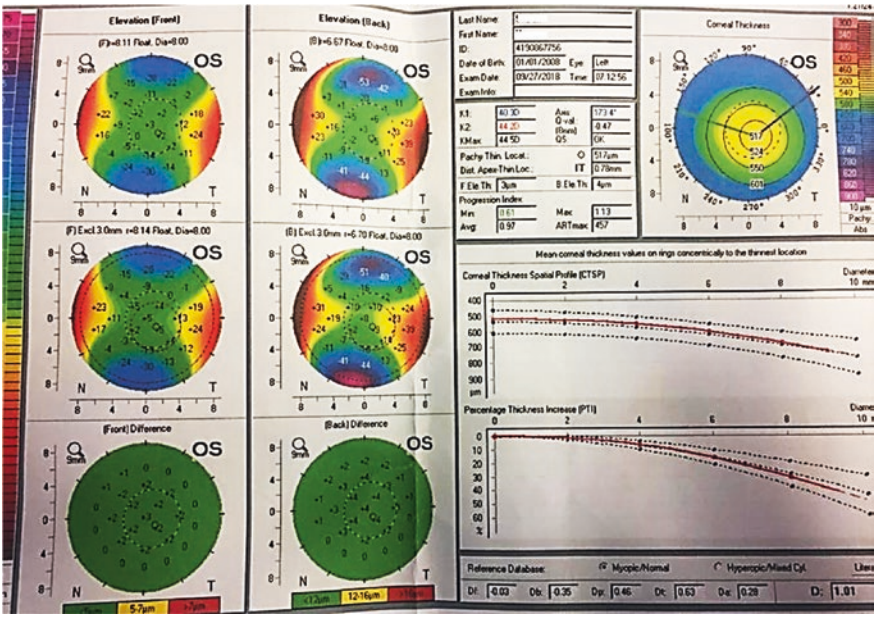

Fig. 85 A 14-year-old teenager was referred for treatment of keratoconus. Refractive errors: +2.00/−4.00~180 OU and DCVA 7/10 OU. The anterior and posterior elevations were higher than normal limit however, the axial map showed symmetric orthogonal with the rule astigmatism not compatible with keratoconus. This case shows a false positive case of high elevations due to the evaluation of a case with high astigmatism with BFS. It is recommended that cases with high astigmatism be evaluated with the BFTE reference plane and not with BFS

Case 13.

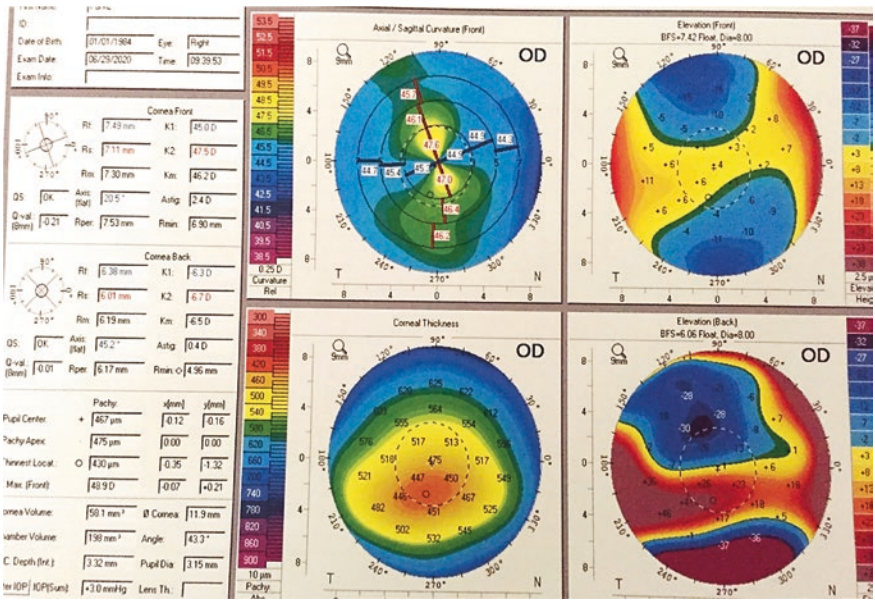

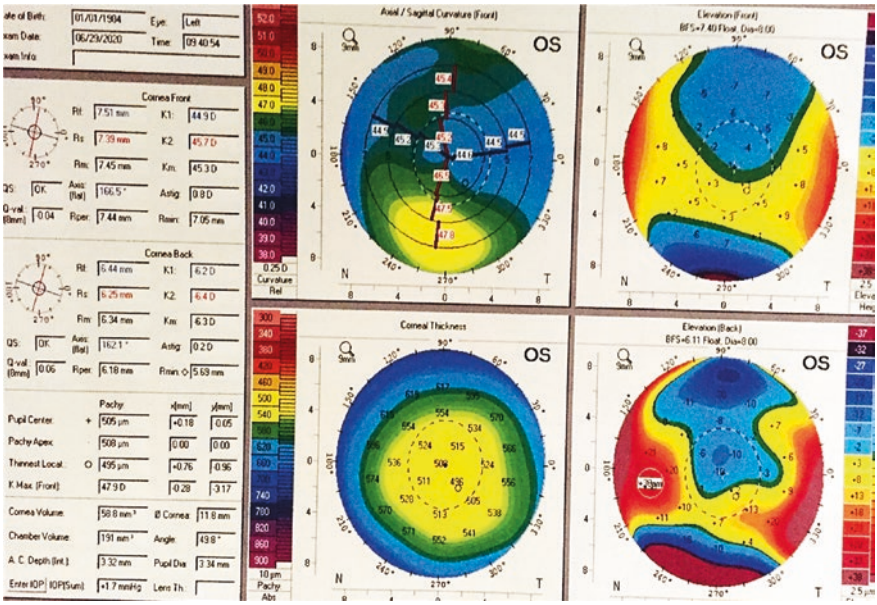

Fig. 86 A 36-year-old man with definite keratoconus and small central bowtie in the axial map in the right eye and inferior steepening in the left eye with kmax > 47 D in both eyes with clinical sign in slit lamp bio-microscopy and retinoscopy

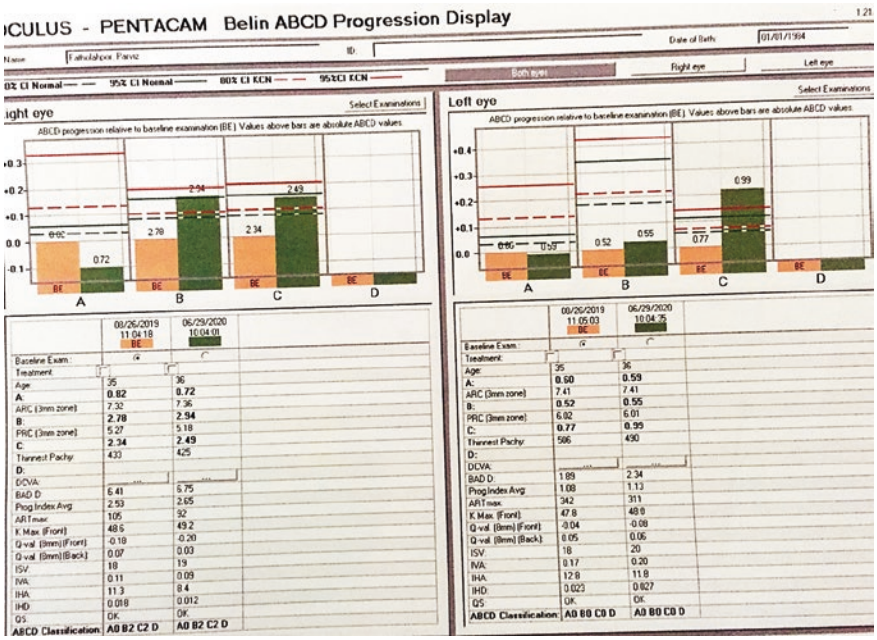

Fig. 87 The examinations of the same patient in 2019 and 2020 can be seen on the ABCD maps. The left orange bar information is for 2019 and the right green bar is for 2020. There are important changes in thickness in 2020 data. The thickness of the cornea in both eyes is significantly reduced in 2020. Evaluation of the progression of the disease helps clinicians to make a decision for cross-linking in keratoconus cornea in early stages

Case 14.

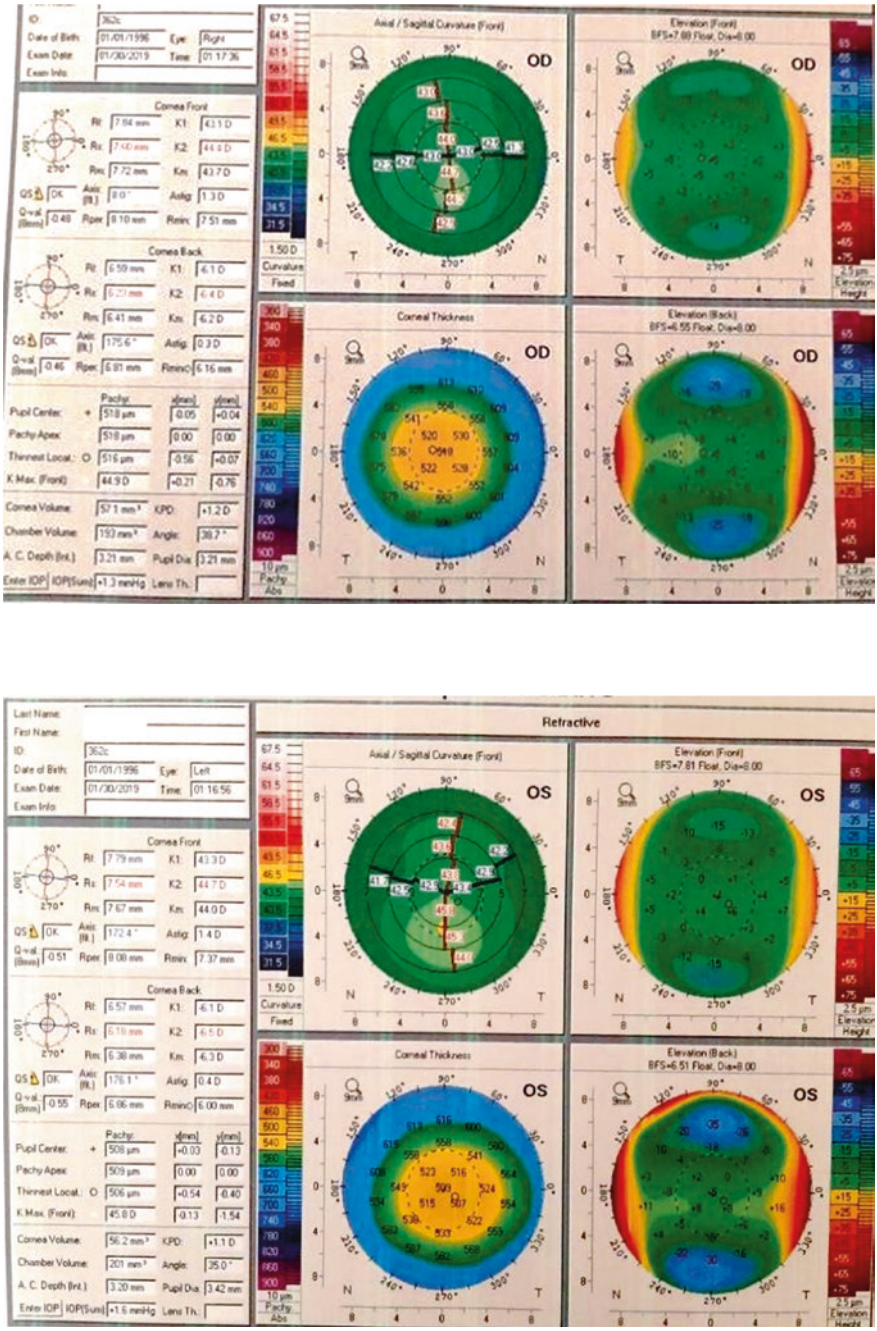

Fig. 88 A 24-year-old woman with early keratoconus in her left eye. The 4 maps refractive display of Pentacam in her left eye seems apparently normal due to a fixed 1.5 diopter scale and subsequent 30–67.50 range in color code scale caused to miss an early form of keratoconus

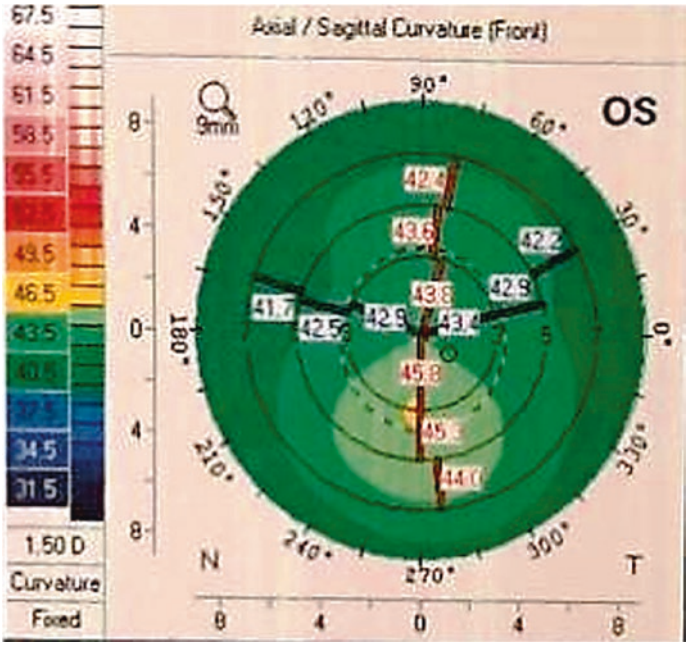

Fig. 89 By exact looking at the sagital map of the left eye of the same patient, you can see 2 diopters of inferior steepening

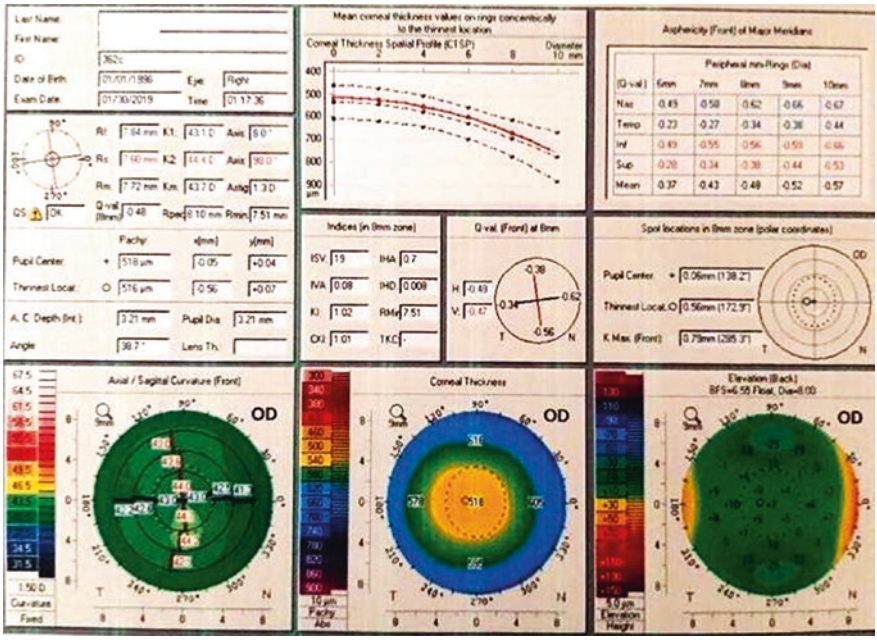

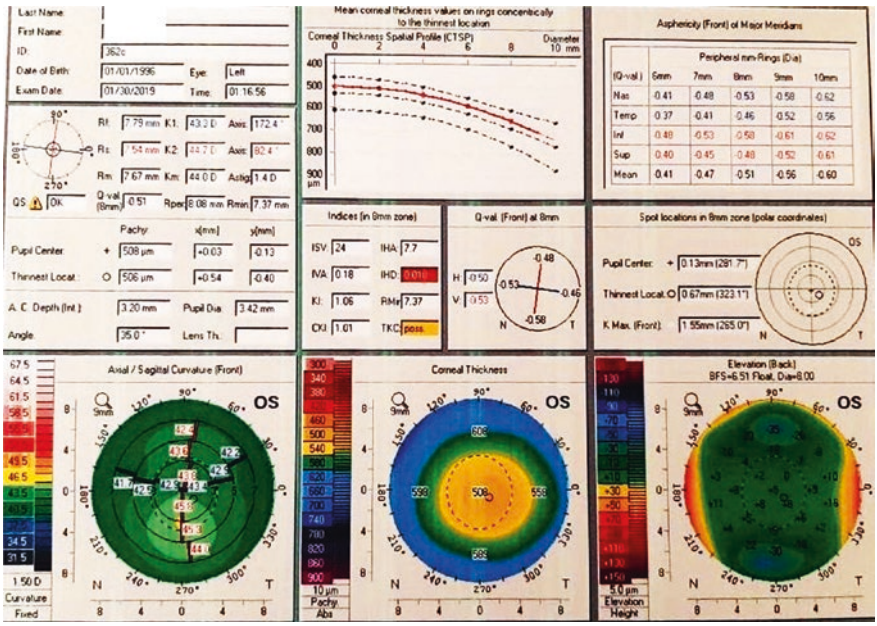

Fig. 90 IHD and TKC indices in KC staging display are normal in the right eye and abnormal in the left eye in the same patient

Case 15.

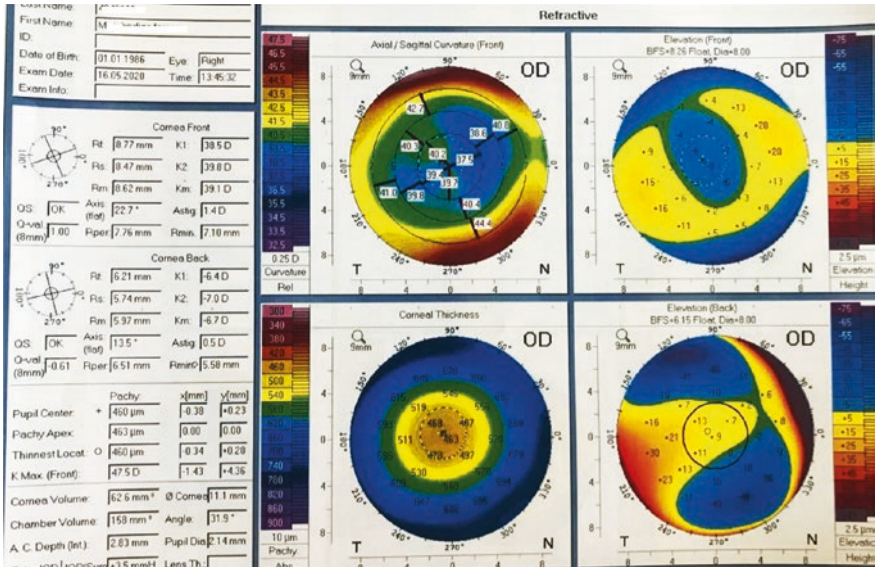

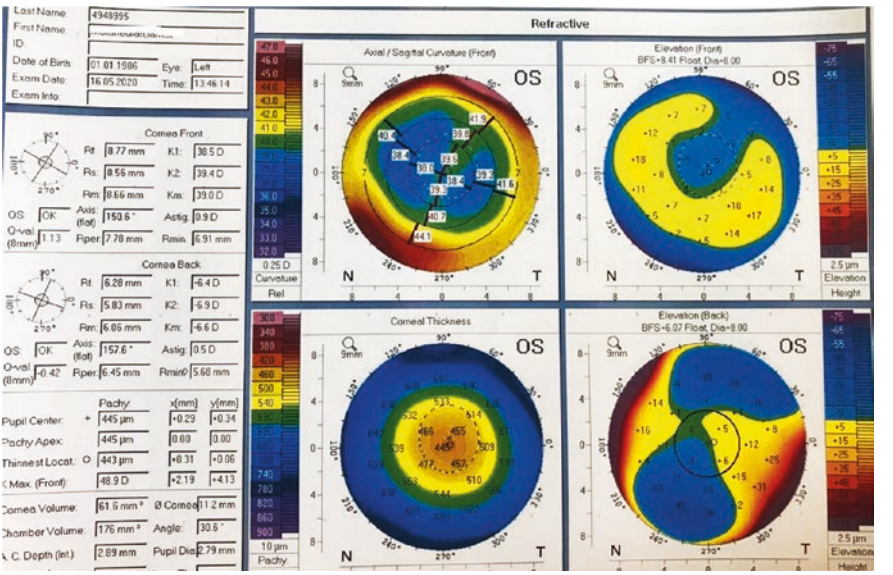
Refractive
Axial / Sagittal Curvature (Front)
Elevation (Front)
Corneal Thickness
Elevation (Back)
OS

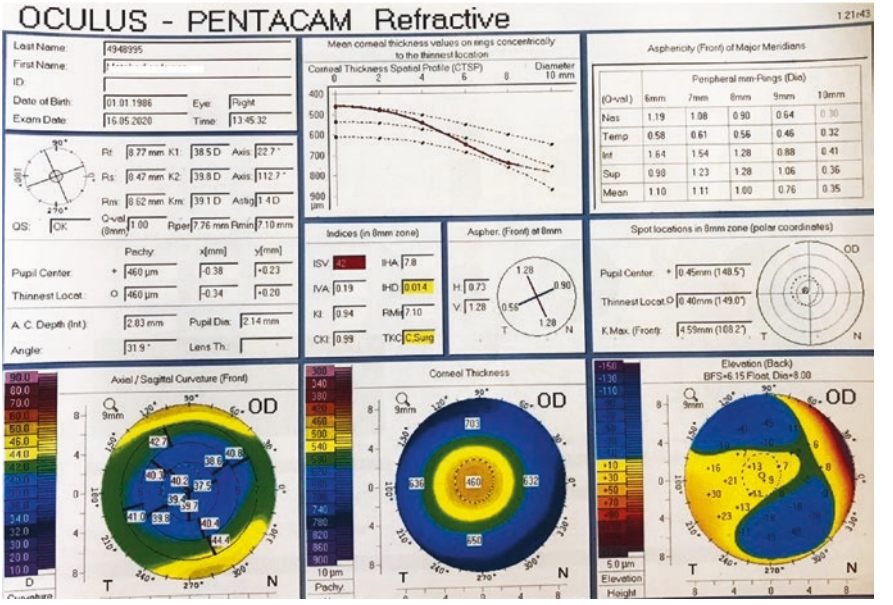
OCULUS - PENTACAM Refractive
Mean corneal thickness values on rings concentrically to the thinnest location
Corneal Thickness Spatial Profile (CTSP)
Asphericity (Front) of Major Meridians
Indices (in 8mm zone)
Aspher. (Front) at 8mm
Spot locations in 8mm zone (polar coordinates)
Axial / Sagittal Curvature (Front)
Corneal Thickness
Elevation (Back)
OD

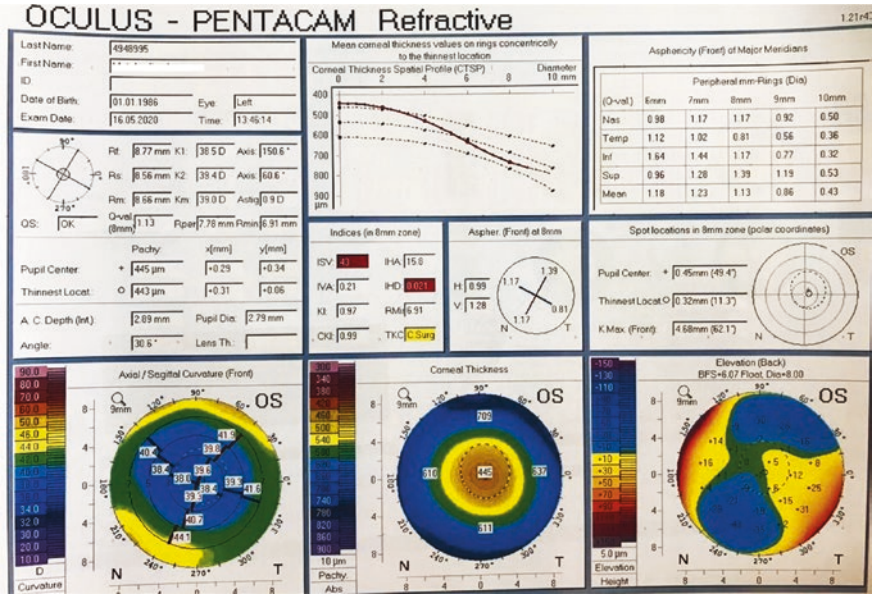

Fig. 91 A 34-year-old woman with a history of PRK 15 years ago. Uncorrected distance visual acuity (UDVA): OD 1/10 and OS 3/10; Refractive errors: OD −2.00/−1.00~50, BCVA 10/10 and OS −2.75 sphere, Corrected distance visual acuity (CDVA) 10/10. The refractive maps of Pentacam compatible with regression with centered ablation without ectasia

Case 16.

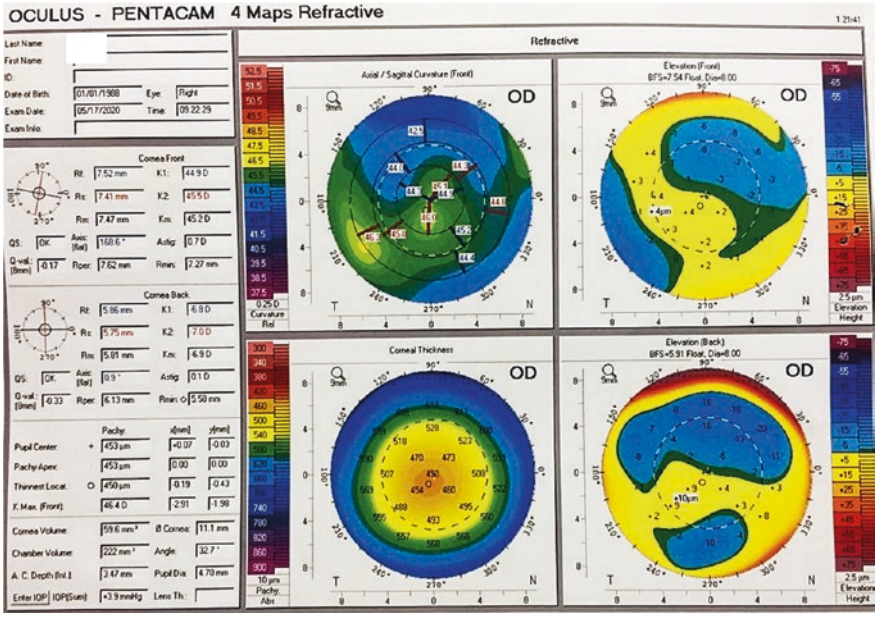

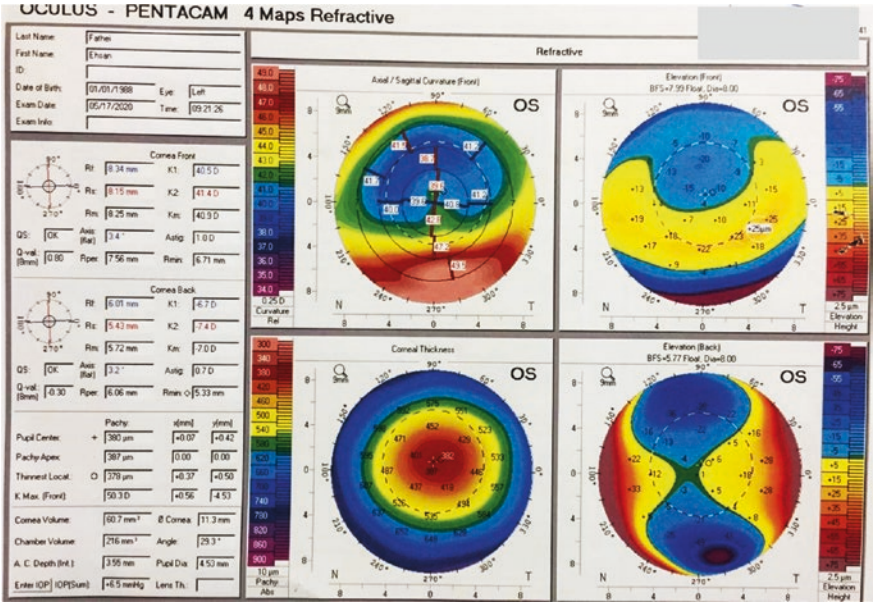
OCULUS - PENTACAM 4 Maps Refractive
Refractive
Axial / Sagittal Curvature (Front)
Elevation (Front)
Corneal Thickness
Elevation (Back)
OS

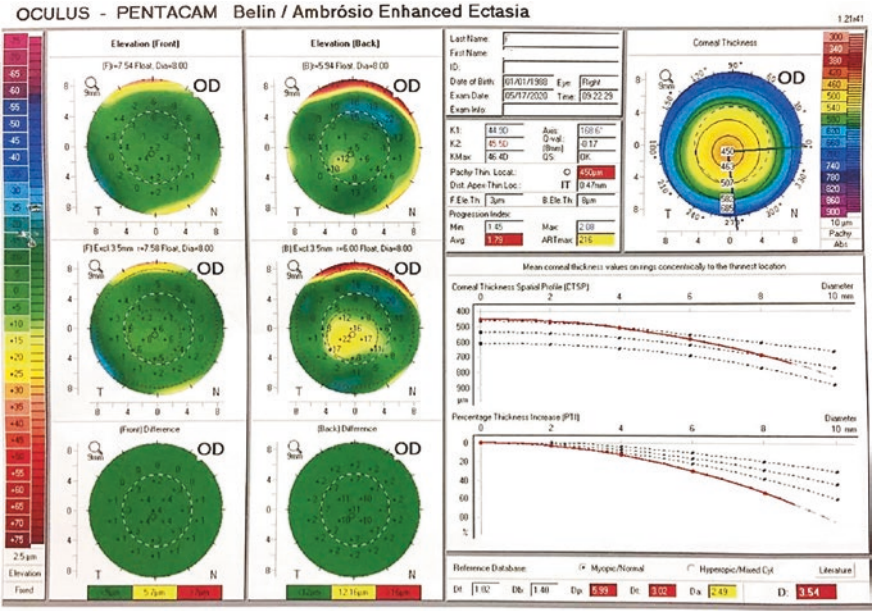
OCULUS - PENTACAM Belin / Ambrósio Enhanced Ectasia
Elevation (Front)
Elevation (Back)
Corneal Thickness
(Front) Difference
(Back) Difference
OD

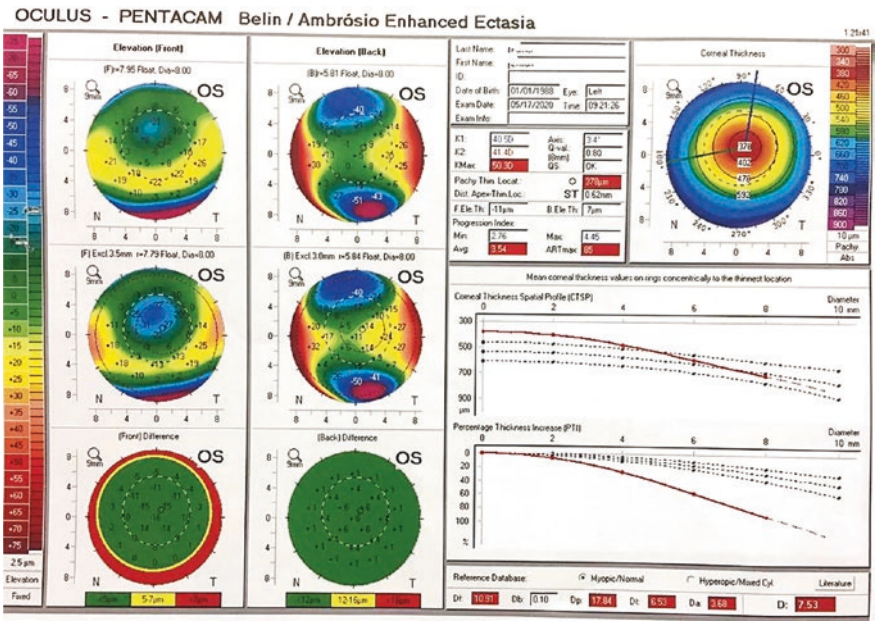

Fig. 92 A 33-year-old man with a history of PRK 4 years ago was referred for a gradual loss of vision in his left eye. CDVA of the right eye was 10/10 however, the left eye best corrected visual acuity (BCVA) did not increase more than 4/10 with Plano −0.75~135. The Pentacam of the left eye was compatible with both decentered ablation and post-refractive surgery ectasia with Kmax over than 50 diopters and significant inferior steepening and corneal thinning. This case suggests the hypothesis that decentered ablation may be a predisposing factor for keratectasia

Case 17.

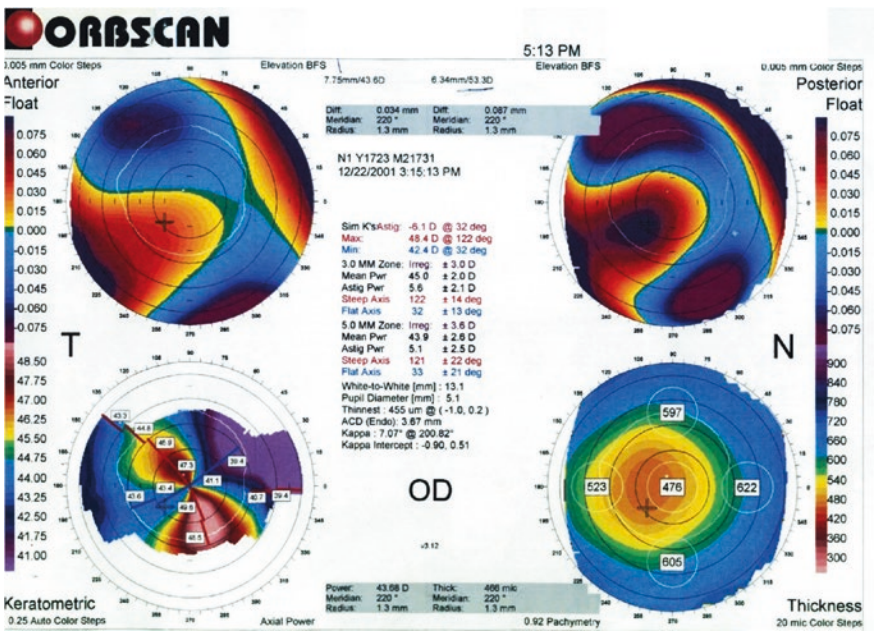

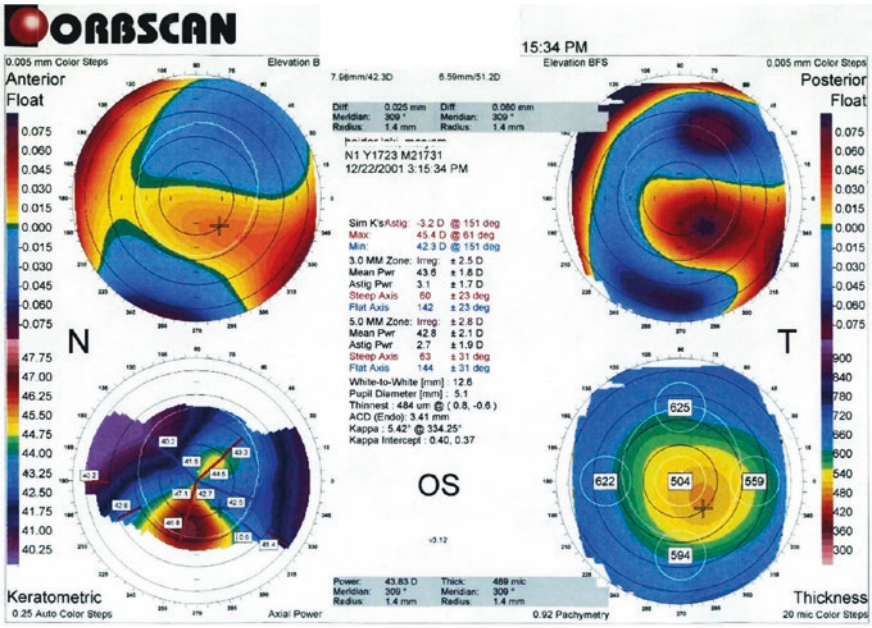

Fig. 93 A patient with definite keratoconus scheduled for intrastromal ring implantation with asymmetric bow tie in the right eye and inferior steepening in the left eye. Abnormal pachymetric and elevation values are seen in both eyes

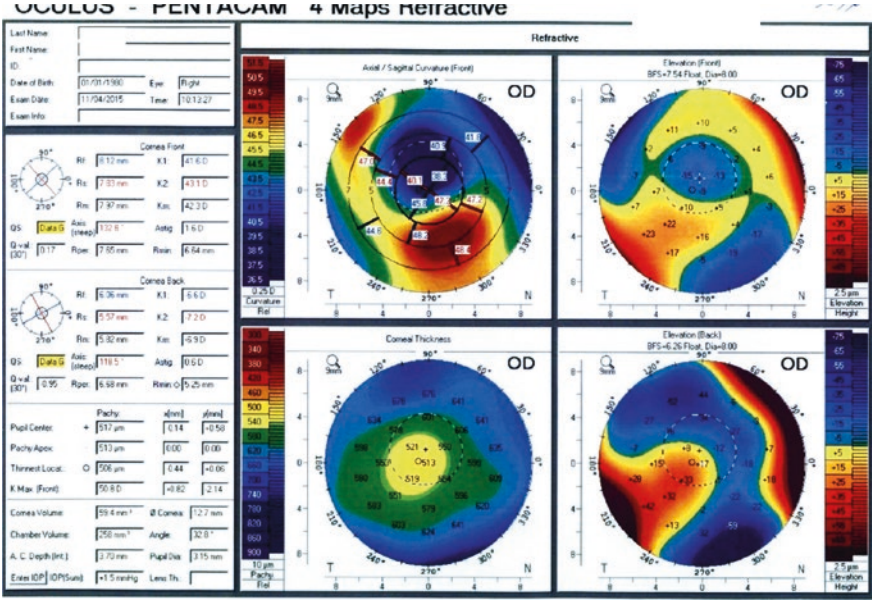

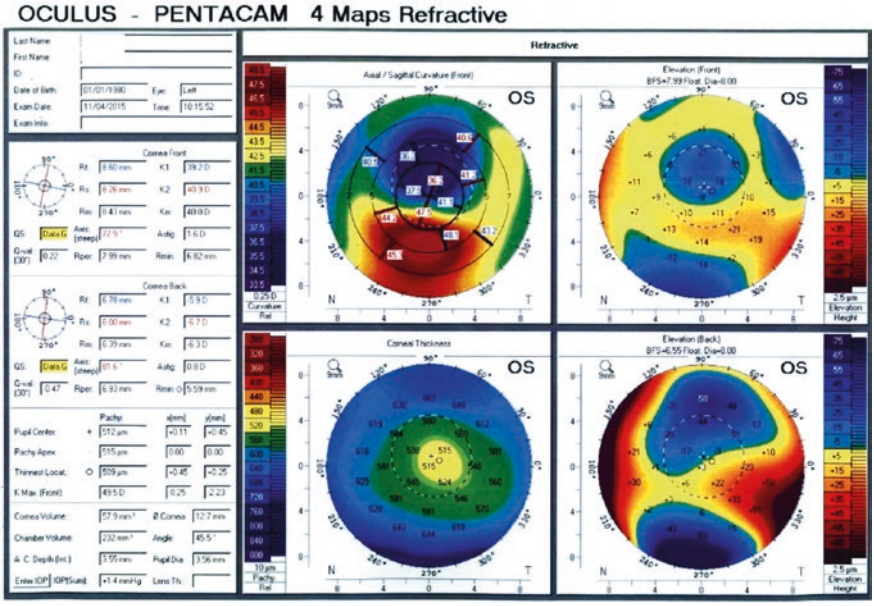

Fig. 94 The patient treated with intrastromal complete Myoring implantation plus cross-linking (CXL) in the right eye and Myoring implantation in the left eye. Both eyes had stable refraction after Myoring implantation and indicate that CXL is not mandatory for cases with Myoring implantation. However, our results showed CXL had adjustment and synergistic effect in long term outcomes of Myoring implantation

Case 18.

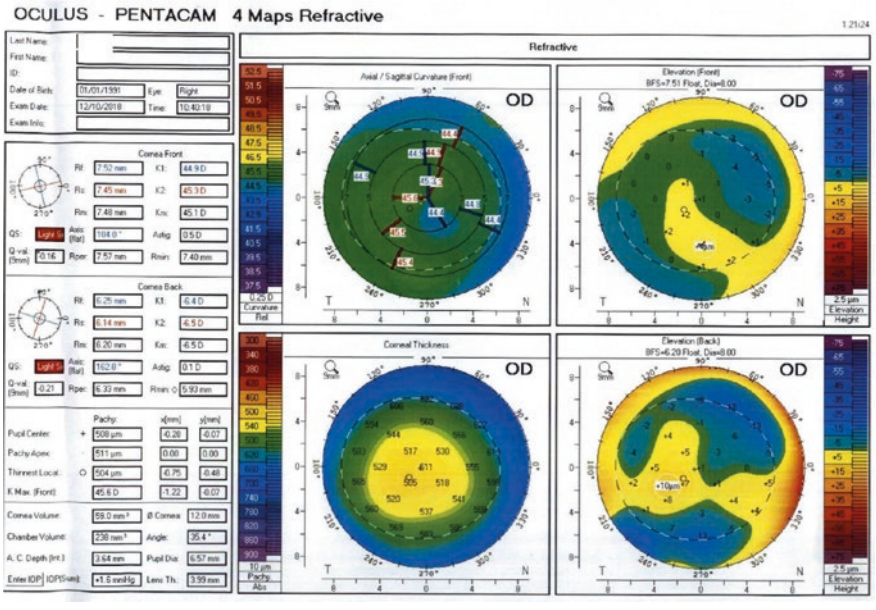

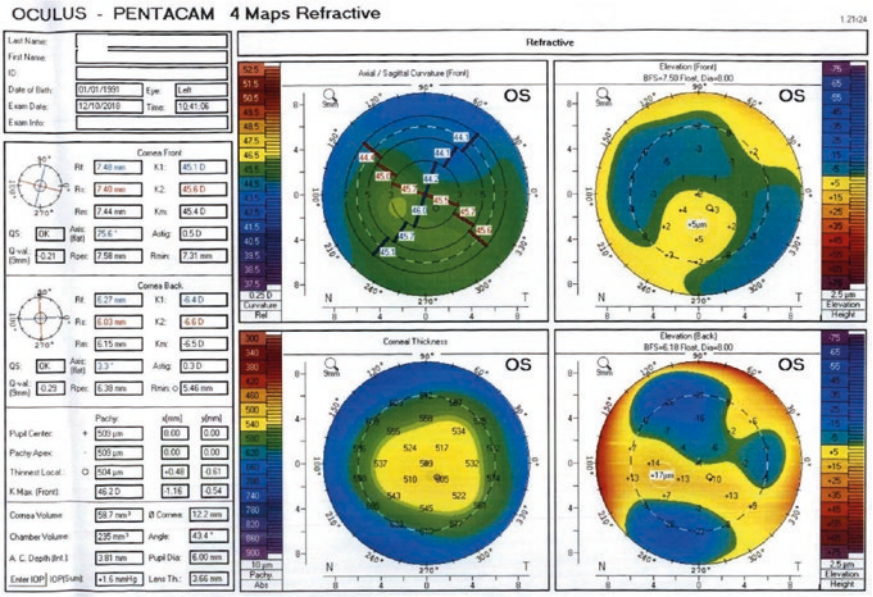

Fig. 95 A 26-year-old woman with early PMD. The refractive errors: OD = −3.00/−0.50~95 CDVA = 10/10 and OS = −2.50/−1.00~80 CDVA = 10/10 with normal thickness values and crab claw pattern on refractive maps of Pentacam

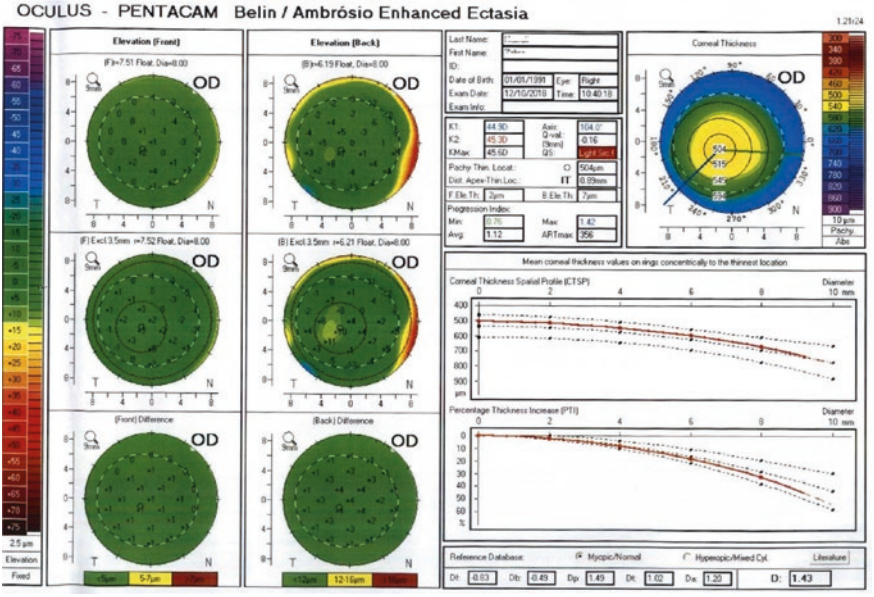

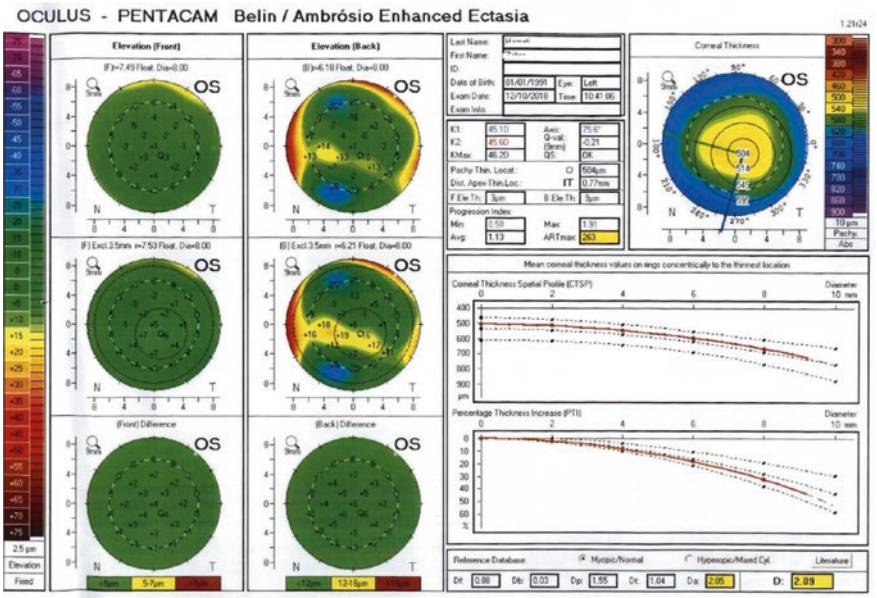

Fig. 96 There are normal Belin-Ambrosio display values on the right eye. There are normal anterior but tongue-like posterior and abnormal D index on the left eye (suspect ARTmax index) in the same patient

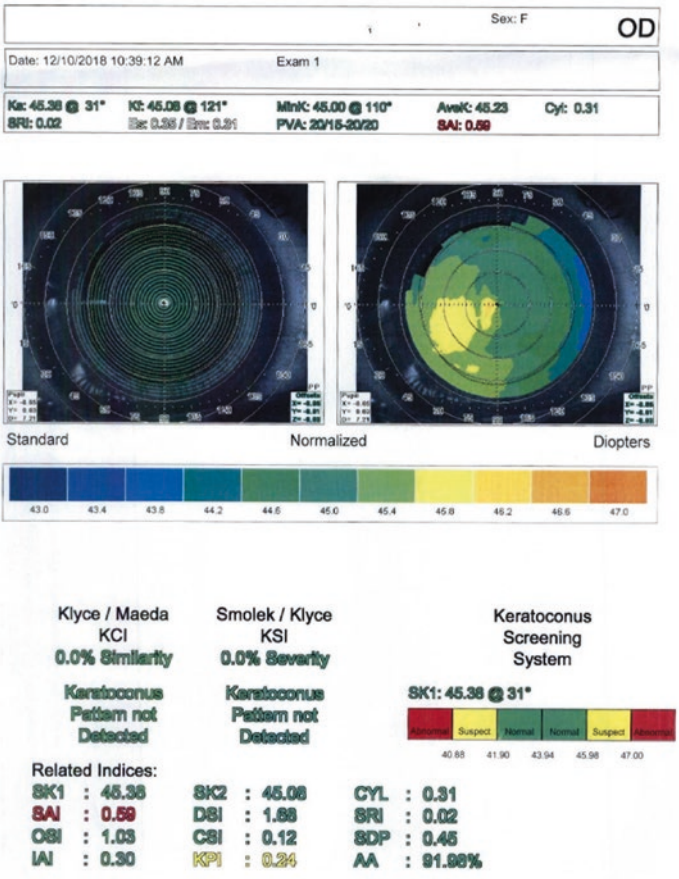
Sex: F
OD
Date: 12/10/2018 10:39:12 AM
Exam 1
Standard
Normalized
Diopters
43.0
43.4
43.8
44.2
44.6
45.0
45.4
45.8
46.2
46.6
47.0
Klyce / Maeda
KCI
0.0% Similarity
Keratoconus
Pattern not
Detected
Smolek / Klyce
KSI
0.0% Severity
Keratoconus
Pattern not
Detected
Keratoconus
Screening
System
SK1: 45.38 @ 31°
Abnormal
Suspect
Normal
Normal
Suspect
Abnormal
40.88
41.90
43.94
45.98
47.00
Related Indices:
SK1 : 45.38
SAI : 0.59
OSI : 1.03
IAI : 0.30
SK2 : 45.08
DSI : 1.68
CSI : 0.12
KPI : 0.24
CYL : 0.31
SRI : 0.02
SDP : 0.45
AA : 91.98%

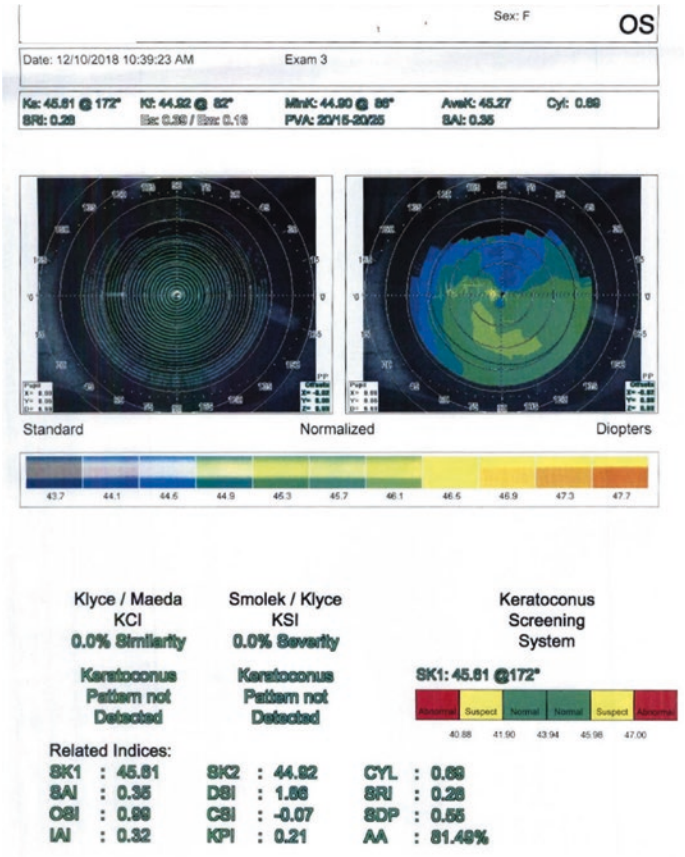

Fig. 97 These findings based on Pentacam derived data, compatible with crab claw patterns on the left eye in the topographic map with abnormal values in the right eye

Case 19.

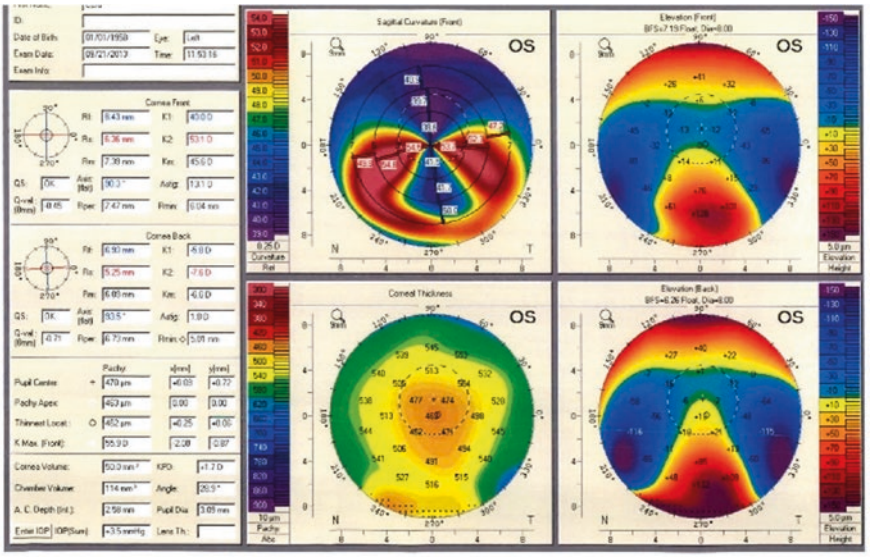

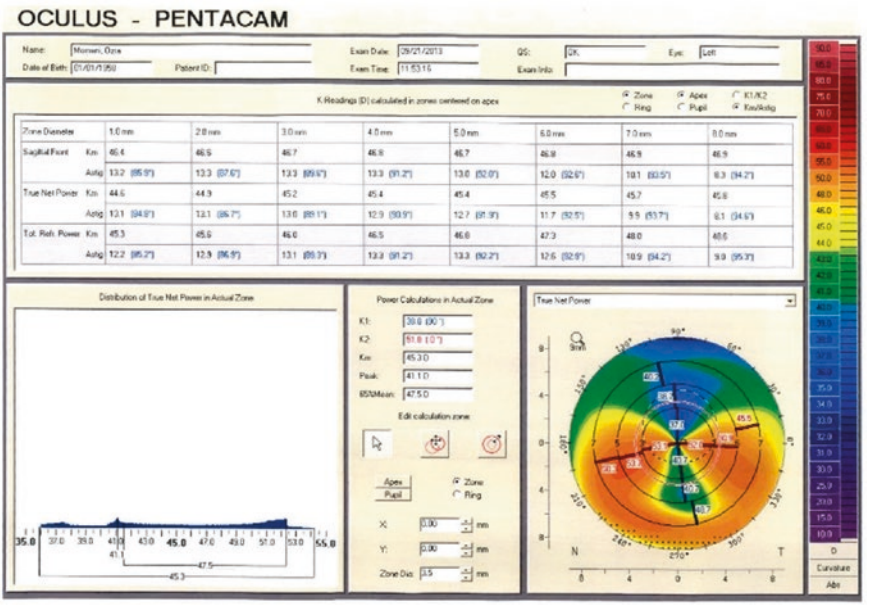

Fig. 98 A 63-year-old woman with cataract and against-the-rule astigmatism that led to decreased vision. This case also had pellucid marginal corneal degeneration that after cataract surgery the vision did not improve significantly. It must be noticed before cataract surgery in patients with any against the rule astigmatism. In these cases, make sure to take complete corneal imaging before cataract surgery

Case 20.

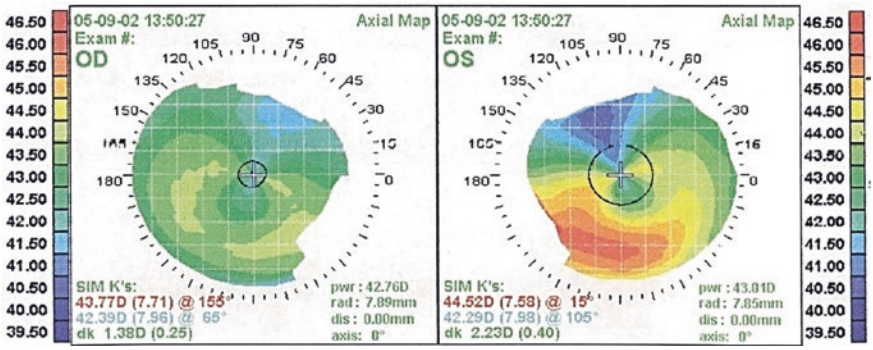

Fig. 99 A patient with a history of laser vision correction 20 years ago, there was a pattern of crab claw and low against the rule astigmatism in topographic map before refractive surgery (OD = 1.38 D cylinder and OS = 2.23 D cylinder), and note that these cases with against the rule astigmatism are a contraindication for LASIK

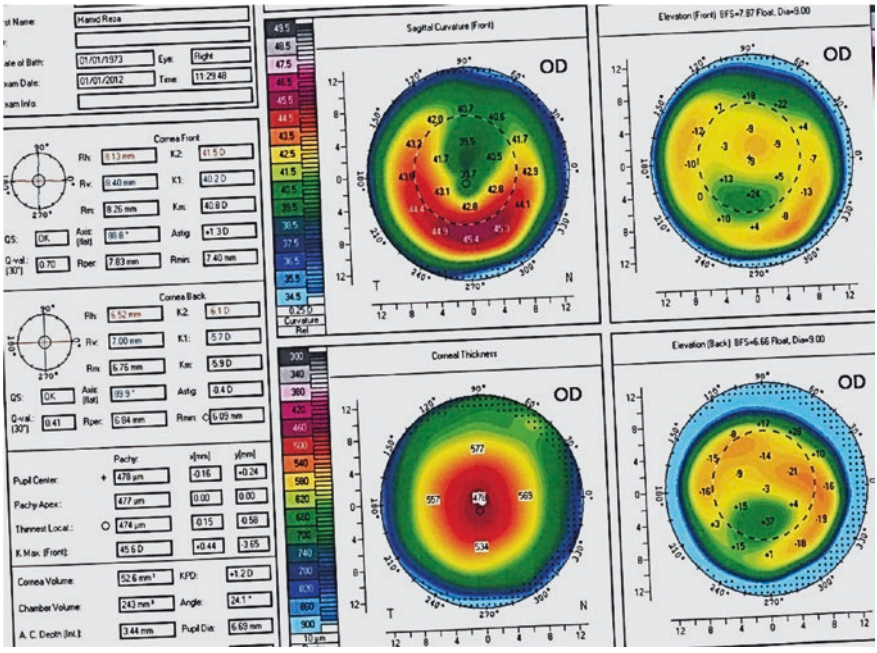

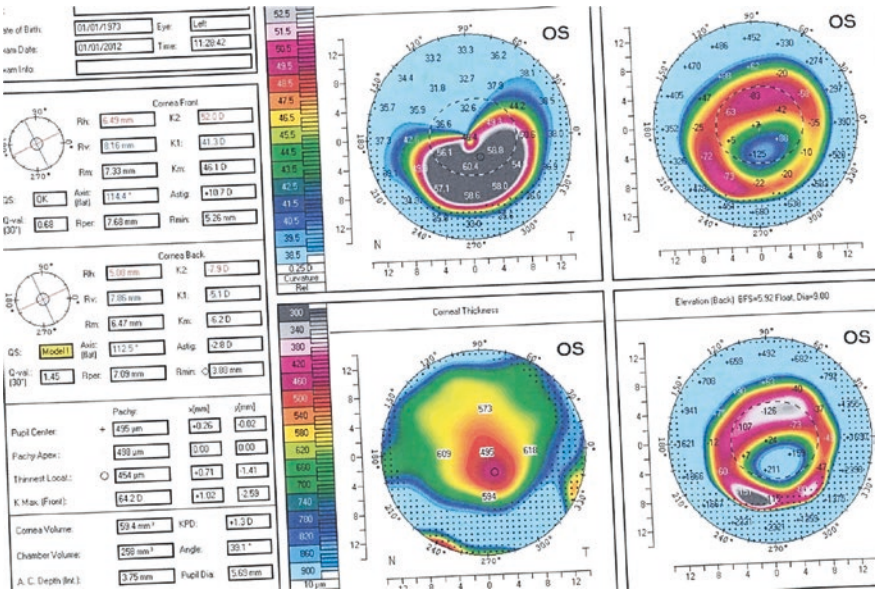

Fig. 100 There are high against the rule astigmatism and progressive PMD after LASIK with a microkeratome which are seen in refractive maps of Pentacam in the same patient

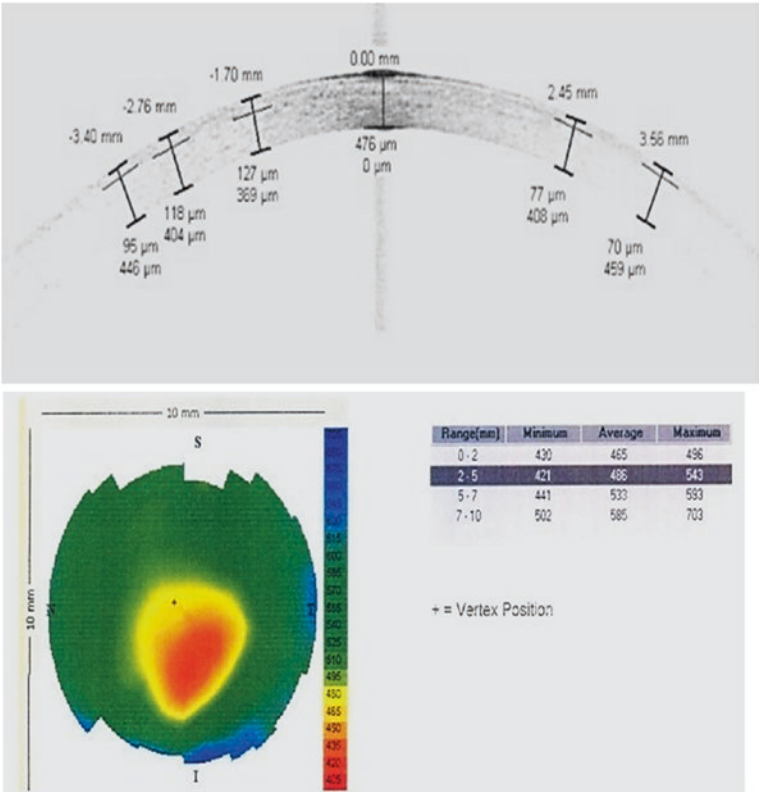

Fig. 101 Post-operative AS-OCT in the same patient shows localized corneal thinning with irregular thin LASIK flap created by Moria microkeratome

Case 21.

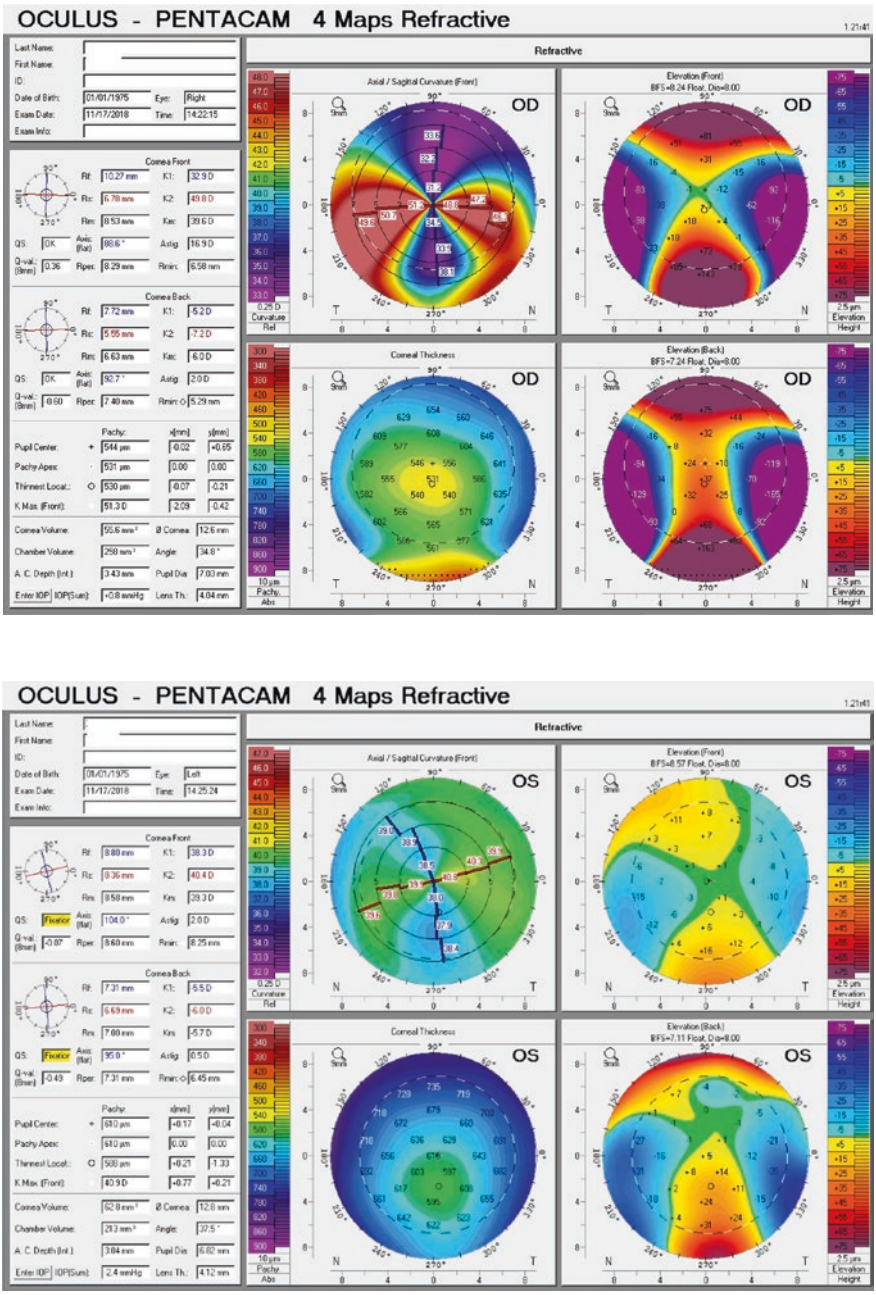

Fig. 102 A patient with PMD in the right and forme fruste keratoconus (FFKCN) in the left eye. The right eye shows a kissing bird pattern on topography with pathological values on tomography, and the left eye seems normal patterns but the Kmax and posterior elevation had abnormal range

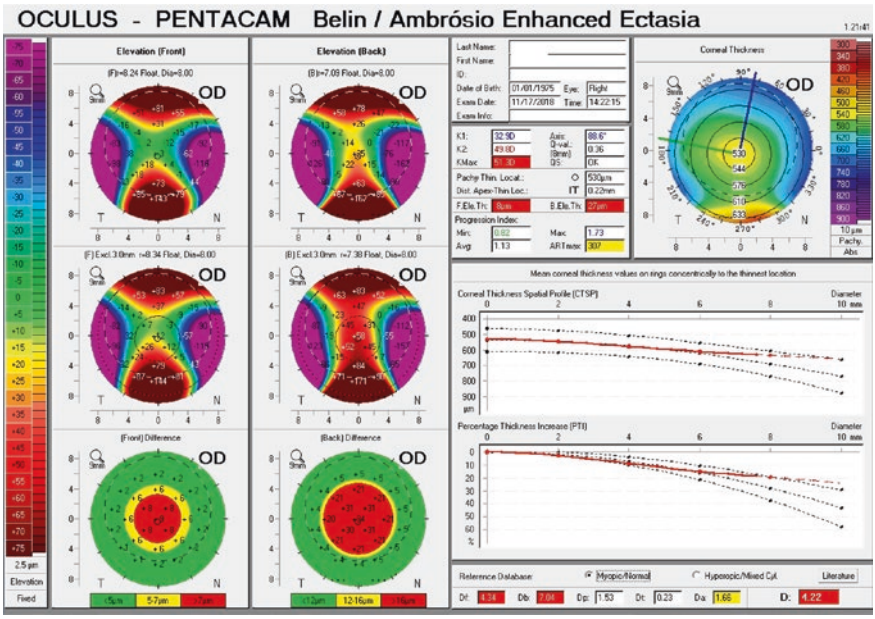

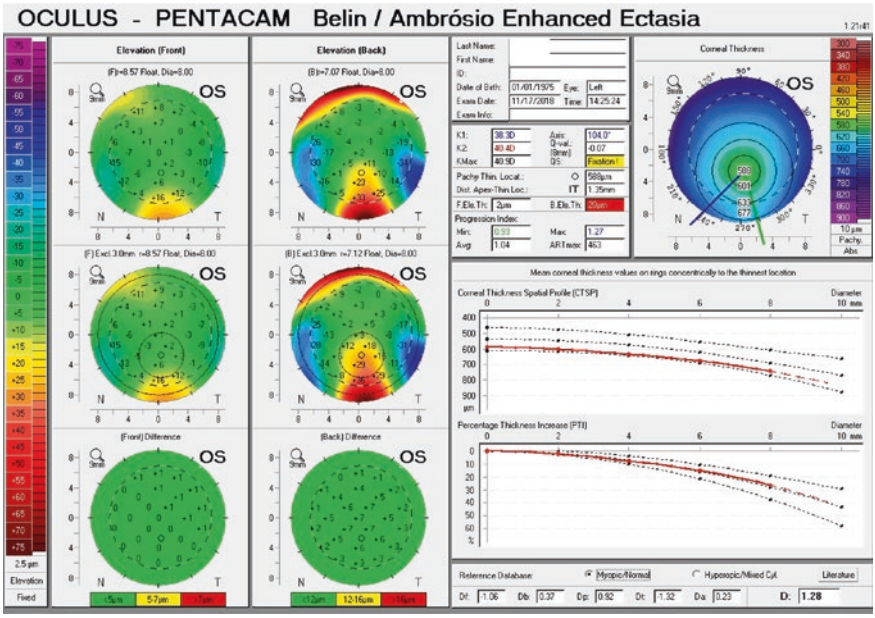

Fig. 103 These findings corresponded with the Blin/Ambrosio display parameters of the same patient. There are normal D index, normal difference maps and normal pachymetric graphs in the left eye and these items are abnormal in the right eye

Case 22.

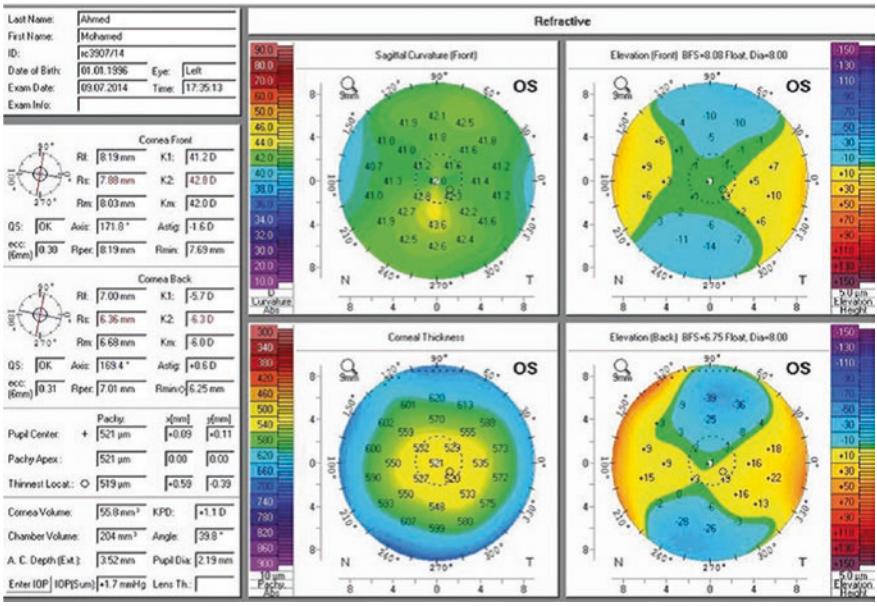
Last Name: Ahmed
First Name: Mohamed
ID: ic3907/14
Date of Birth: 01.01.1996 Eye: Left
Exam Date: 09.07.2014 Time: 17:35:13
Exam Info:
Refractive
Cornea Front
Rf: 8.19 mm K1: 41.2 D
Rs: 7.88 mm K2: 42.8 D
Rm: 8.03 mm Km: 42.0 D
QS: OK Axis: 171.8 ° Astig: -1.6 D
ecc: 0.30 Rper: 8.19 mm Rmin: 7.69 mm
Cornea Back
Rf: 7.00 mm K1: -5.7 D
Rs: 6.36 mm K2: -6.3 D
Rm: 6.68 mm Km: -6.0 D
QS: OK Axis: 169.4 ° Astig: +0.6 D
ecc: 0.31 Rper: 7.01 mm Rmin: 6.25 mm
Pachy x[mm] y[mm]
Pupil Center: 521 µm +0.09 +0.11
Pachy Apex: 521 µm 0.00 0.00
Thinnest Locat.: 519 µm +0.59 -0.39
Cornea Volume: 55.8 mm³ KPD: +1.1 D
Chamber Volume: 204 mm³ Angle: 39.8 °
A. C. Depth (Ext.): 3.52 mm Pupil Dia: 2.19 mm
Enter IOP IOP(Sum): +1.7 mmHg Lens Th.:
Sagittal Curvature (Front)
Elevation (Front) BFS+8.08 Float, Dia+8.00
Corneal Thickness
Elevation (Back) BFS+6.75 Float, Dia+8.00
OS
N
T

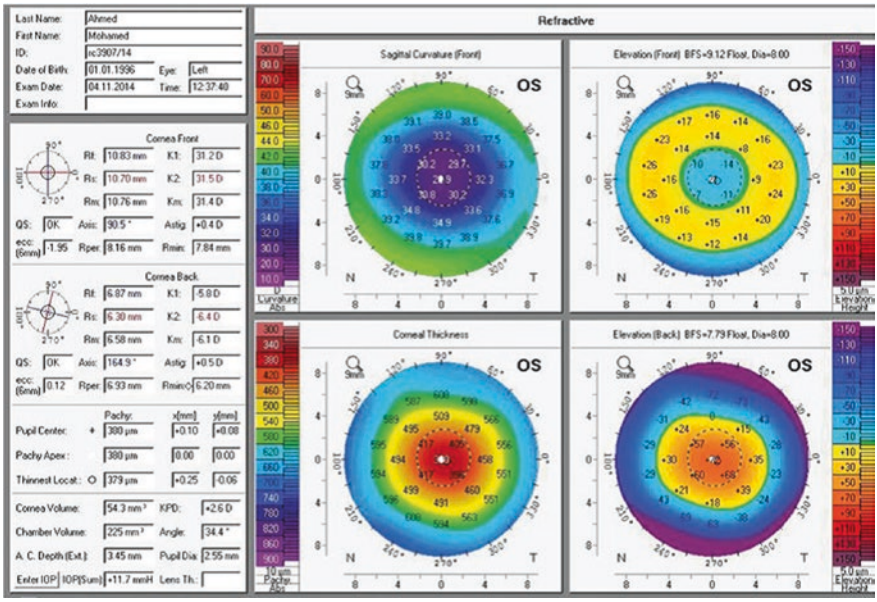

Fig. 104 A 26-year-old man with high myopia and astigmatism and refractive error of −12.00/−1.00~165 underwent SMILE surgery. The refractive error decreased significantly (+0.25/−0.50~120) and both refractive and topographic data remain unchanged for 3 months of follow up. (Curtesy to Dr. Ibrahim et al. in SMILE for Correction of Very High Myopia (Higher than −10 D), in Sekundo W. (ed.) *Small Incision Lenticule Extraction* (*SMILE*) with permission from Springer) [22]

Case 23.

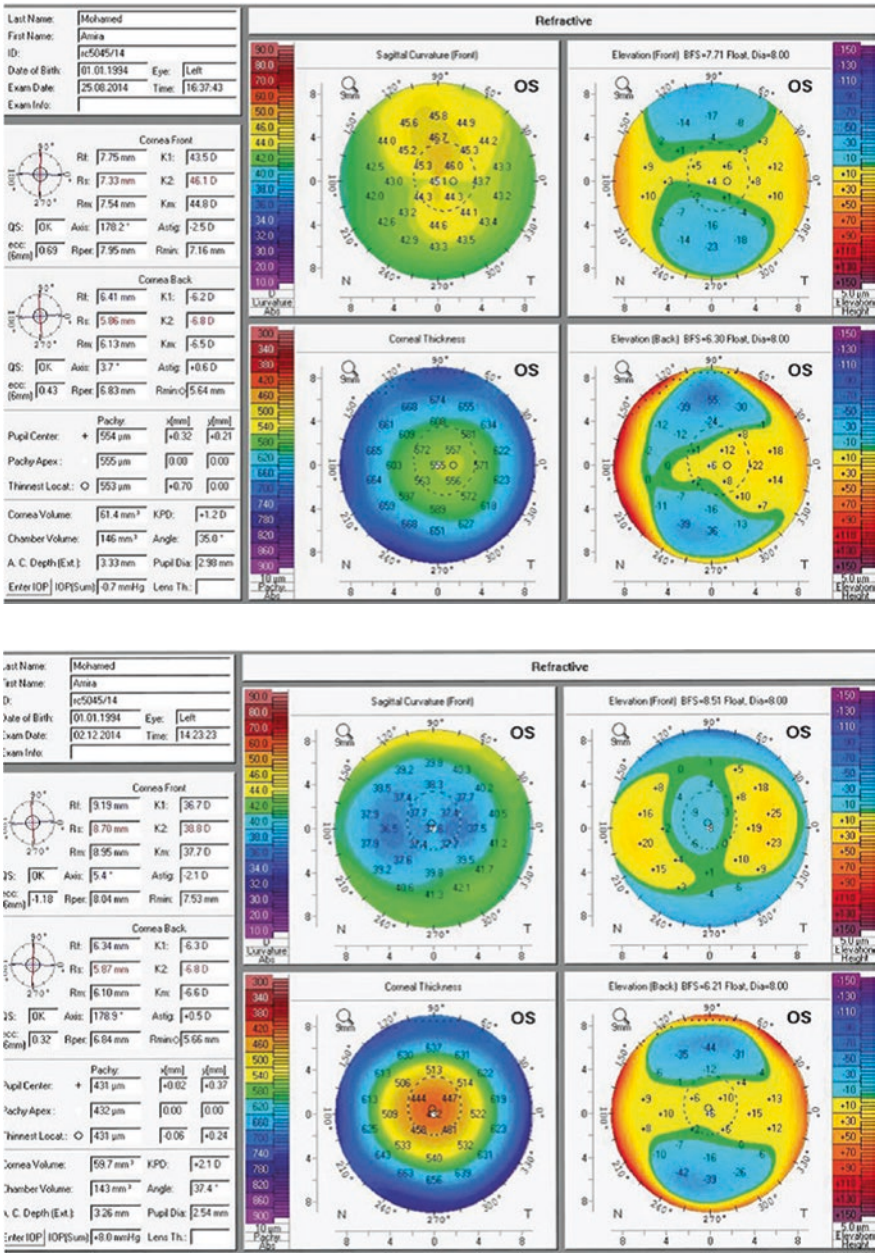

Fig. 105 A case of extreme high compound myopic astigmatism with refractive error of −14.00/−2.00~10 considered for refractive surgery underwent SMILE procedure. Three months after surgery the refractive error decreased to −2.00/−1.25~30 and posterior elevation unchanged. Despite high refractive error correction, the postoperative anterior corneal power is more than 37 diopters which is well acceptable for this amount of correction. (Curtesy to Dr. Ibrahim et al. in SMILE for Correction of Very High Myopia (Higher than −10 D), in Sekundo W. (ed.) *Small Incision Lenticule Extraction* (*SMILE*), with permission from Springer) [22]

References

1. Oculus Pentacam, Interpretation Guideline, 3rd. https://www.pentacam.com/fileadmin/user_upload/pentacam.de/downloads/interpretations-leitfaden/interpretation_guideline_3rd_edition_0915.pdf. User Guide Pentacam®/Pentacam® HR/Pentacam® AXL (UG/70700/0118/en). [Last accessed 2020-4-13].
2. Krumeich JH, Daniel J, Knulle A. Live-epikeratophakia for keratoconus. J Cataract Refract Surg. 1998;24(4):456–63.
3. Krumeich JH, Kezirian GM. Circular keratotomy to reduce astigmatism and improve vision in stage I and II keratoconus. J Refract Surg. 2009;25(4):357–65.
4. Gatinel D. Indices and screening tests for subclinical keratoconus. 2017. https://www.gatinel.com/recherche-formation/keratocone-2/indices-and-screening-tests-for-subclinical-keratoconus/. [Last accessed 2020-4-13].
5. Javadi MA, Mohammadpour M, Rabei HM. Keratectasia after LASIK but not after PRK in one patient. J Refract Surg. 2006;22(8):817–20.
6. Mohammadpour M, Mohammad K, Karimi N. Central corneal thickness measurement using ultrasonic pachymetry, rotating scheimpflug camera, and scanning-slit topography exclusively in thin non-keratoconic corneas. J Ophthalmic Vis Res. 2016;11(3):245–51.
7. Park SH, Choi SK, Lee D, Jun EJ, Kim JH. Corneal thickness measurement using Orbscan, Pentacam, Galilei, and ultrasound in normal and post-femtosecond laser in situ keratomileusis eyes. Cornea. 2012;31(9):978–82.
8. Mohammadpour M, Heidari Z, Khabazkhoob M, Amouzegar A, Hashemi H. Correlation of major components of ocular astigmatism in myopic patients. Cont Lens Anterior Eye. 2016;39(1):20–5.
9. Heidari Z, Mohammad-Rabie H, Mohammadpour M, Jafarzadehpur E, Khabazkhoob M, Mahmoud J, et al. Correlation between refractive, corneal and residual astigmatism in refractive surgery candidates. J Mazandaran Univ Med Sci. 2014;23(110):38–43.
10. Sinjab MM. Patterns and classifications in ectatic corneal diseases. In: Sinjab M, Cummings A, editors, Corneal collagen cross linking. Springer: Cham; 2017. p. 31, 34–6.
11. Sinjab MM. Introduction to astigmatism and corneal irregularities. In: Sinjab M, Cummings A, editors. Customized laser vision correction. Springer: Cham; 2018. p. 27–30.
12. Heidari Z, Hashemi H, Mohammadpour M. Evaluation of corneal topographic, tomographic and biomechanical indices for detecting clinical and subclinical keratoconus: a comprehensive three device study. Int J Ophthalmol. 2021;14(2); (In Press).
13. Ambrosio R Jr, Caiado AL, Guerra FP, Louzada R, Sinha RA, Luz A, et al. Novel pachymetric parameters based on corneal tomography for diagnosing keratoconus. J Refract Surg. 2011;27(10):753–8.
14. Rabinowitz YS, Rasheed K. KISA% index: a quantitative videokeratography algorithm embodying minimal topographic criteria for diagnosing keratoconus. J Cataract Refract Surg. 1999;25(10):1327–35.
15. Mohammadpour M, Etesami I, Yavari Z, Naderan M, Abdollahinia F, Jabbarvand M. Ocular response analyzer parameters in healthy, keratoconus suspect and manifest keratoconus eyes. Oman J Ophthalmol. 2015;8(2):102–6.
16. Roberts CJ, Mahmoud AM, Bons JP, Hossain A, Elsheikh A, Vinciguerra R, et al. Introduction of two novel stiffness parameters and interpretation of air puff-induced biomechanical deformation parameters with a dynamic scheimpflug analyzer. J Refract Surg. 2017;33(4):266–73.
17. Vinciguerra R, Ambrosio R Jr, Elsheikh A, Roberts CJ, Lopes B, Morenghi E, et al. Detection of keratoconus with a new biomechanical index. J Refract Surg. 2016;32(12):803–10.
18. Mohammadpour M, Heidari Z, Hashemi H. Updates on managements for keratoconus. J Curr Ophthalmol. 2018;30(2):110–24.

19. Mohammadpour M, Heidari Z, Mohammad-Rabei H, Jafarzadehpur E, Jabbarvand M, Hashemi H, et al. Correlation of higher order aberrations and components of astigmatism in myopic refractive surgery candidates. J Curr Ophthalmol. 2016;28(3):112–6.
20. Heidari Z, Mohammadpour M, Hashemi H, Jafarzadehpur E, Moghaddasi A, Yaseri M, et al. Early diagnosis of subclinical keratoconus by wavefront parameters using Scheimpflug, Placido and Hartmann-Shack based devices. Int Ophthalmol 2020;40(7):1659–1671.
21. Fallah Tafti M, Heidarian S, Kiarudi MY, Mohammadpour M, Majdi Nasab M. The role of corneal volume distribution and percentage increase in volume in detection of mild and moderate keratoconus. Iranian J Ophthalmol. 2010;22(4):49–58.
22. Ibrahim O, Abdalla M, Saeed A, Mohammed K, Ahmed I. SMILE for correction of very high Myopia (higher than −10 D). In: Sekundo W, editor. Small incision lenticule extraction (SMILE). Springer: Cham; 2015. p. 187–90.
23. Mohammadpour M, Farhadi B, Mirshahi R, Masoumi A, Mirghorbani M. Simultaneous photorefractive keratectomy and accelerated collagen cross-linking in high-risk refractive surgery (Tehran protocol): 3-year outcomes. Int Ophthalmol. 2020. [published online ahead of print, 2020 Jun 30].

Galilei Dual Scheimpflug Analyzer

Sepehr Feizi

Introduction

Corneal topography is the most commonly used imaging technology for evaluating the anterior corneal surface. Scheimpflug imaging is a newer technology that permits evaluation of both the anterior and posterior surfaces of the cornea and provides three-dimensional reconstruction of the cornea. The Galilei dual Scheimpflug analyzer (software version 5.2, Ziemer Ophthalmic Systems AG, Port, Switzerland) incorporates two important diagnostic modalities, including Placido imaging which supplies high precision curvature data and a revolving dual channel Scheimpflug camera which is optimal for the accurate acquisition of elevation data. The combination of Placido topography with Scheimpflug imaging improves the accuracy of the central anterior corneal curvature measurement and provides an accurate three dimensional analysis of the cornea and anterior eye segment. The Galilei device employs two opposing Scheimpflug cameras, each rotating 180 degrees apart. Therefore, the device captures slit images from opposite sides of the illuminated slit and the reciprocal relationship of the dual views allows simple averaging of the corresponding thickness values and the elevation data, compensating for unintentional x–y decentration, cyclotorsion, or misalignment through a software algorithm (Fig. 1). This is an important feature, particularly as living human eyes are always in motion even under perfect fixating conditions, and averaging the corresponding height and thickness values reduces the deviation by a factor of ten without needing to correct for decentration (Fig. 2). On the contrary, single Scheimpflug systems should make estimations on the variable surface inclination for calculating correct thicknesses or posterior heights. The other benefits of the Galilei are its short image acquisition time and independence on the examiner's expertise.

S. Feizi (✉)
Shahid Beheshti University of Medical Sciences, Tehran, Iran
e-mail: sepehrfeizi@yahoo.com

M. Mohammadpour (ed.), *Diagnostics in Ocular Imaging*,
https://doi.org/10.1007/978-3-030-54863-6_4

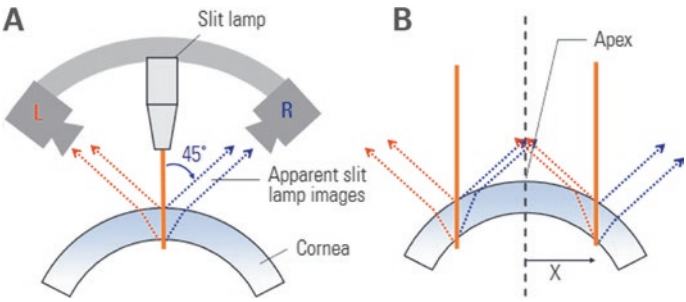

Fig. 1 **a** When the eye is appropriately aligned, the slit light is perpendicular to the corneal surface, the viewing angles for both cameras are equal, and the apparent slit images in both Scheimpflug views are identical. **b** In the decentered condition, depending on the direction of decentration to the left or right, the apparent slit image is either thicker or thinner in the left view as compared to the right view. Simple averaging of the thicknesses in the two corresponding Scheimpflug views reduces error by a factor of 10 without the need for correcting the decentration. Therefore, a misalignment of up to 1.0 mm results in a 30-micron error in corneal thickness measurement

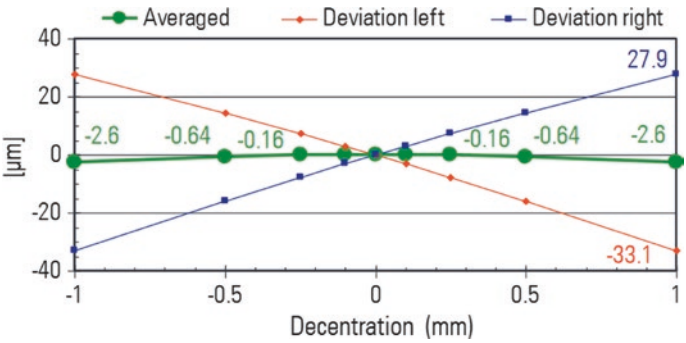

Fig. 2 This graphic simulates the apparent thickness deviation of a spherical cornea with a thickness of 500 µm and a decentration of up to ±1 mm. The thickness deviations from the true value are represented in red and blue, as detected from the left view and from the right view, respectively. The average values are represented in green

Scheimpflug Principle

The Scheimpflug principle, introduced by Theodor Scheimpflug in 1904, is the geometric rule that defines the orientation of the subject plane, the lens plane, and the plane of focus of an optical system. Scheimpflug imaging technique differs from conventional imaging techniques in which the planes of object, lens, and image are parallel. In the Scheimpflug principle, however, the object plane, lens plane, and image plane are not parallel to each other, but intersect in a common point (Fig. 3). In the standard imaging technique, if a planar subject is parallel to

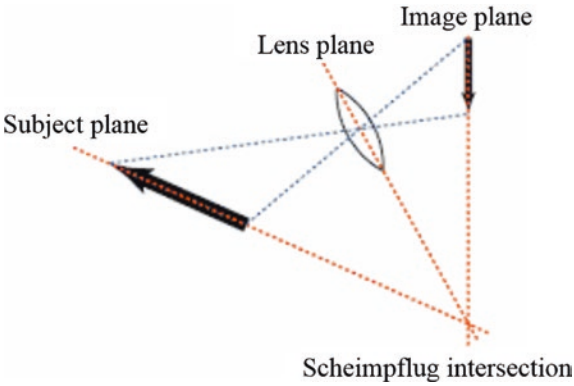

Fig. 3 The Scheimpflug principle. The object plane, lens plane, and image plane intersect each other in a common point

the image plane, it can coincide with the plane of focus, and the entire subject can be rendered sharply. If the subject plane is not parallel to the image plane, it will be in focus only along a line where it intersects the plane of focus. However, when a lens is tilted with respect to the image plane, an oblique tangent extended from the image plane and another extended from the lens plane meet at a line through which the plane of focus also passes. With this condition, a wide depth of focus is achieved, and a planar subject that is not parallel to the image plane can be completely in focus. It provides direct evaluation of the posterior corneal surface, which is in contrast to the Orbscan IIz (Bausch & Lomb, Rochester, NY), which derives its posterior elevation map mathematically. The Scheimpflug principle has been applied in ophthalmology to obtain optical sections of the entire anterior segment of the eye, from the anterior surface of the cornea to the posterior surface of the lens. This type of imaging allows assessment of anterior and posterior corneal topography, anterior chamber depth, as well as anterior and posterior topography of the lens.

Combination of Placido Topography with Scheimpflug Imaging

The resolution of Scheimpflug images is high and can accurately deliver profile data. The accuracy of the Scheimpflug images from the corneal periphery is very high and has a resolution of <1 pixel. Its accuracy, however, is insufficient to measure central corneal curvature since elevation differences in the center of the cornea are very small. Galilei solves this limitation by acquiring simultaneously Placido and Scheimpflug data and merging data generated by both methods into a comprehensive single set of data that describes corneal and anterior chamber geometry. Placido topography is the classical form of imaging the surface of the cornea with the aim of determining the corneal shape. The concentric rings of a Placido Disk are projected onto the anterior corneal surface to be evaluated,

and the image reflected back from the cornea is captured and measured. Geometric analysis of the captured data allows to measure the power of any given point on the corneal surface, and hence to provide a curvature map. The limitation of Placido topography, however, is that it cannot obtain data about the thickness and elevation of the cornea. Scheimpflug images can precisely supply thickness and elevation data of the cornea.

Clinical Applications

Scheimpflug analysis generates images of the anterior segment in 3 dimensions which can be used to diagnose and monitor corneal diseases (keratoconus, pellucid marginal degeneration, and post-refractive surgery ectasia), make a plan for refractive surgery, evaluate anterior chamber angle opening, and calculate intraocular lenses (IOLs) power. The achieve data can also be used for guiding of surgical plans and longitudinal follow-up of patients with known disease. For example, it is important to the refractive surgeon to precisely measure the anterior chamber depth prior to phakic refractive implant surgery. Other data that can be obtained by the Galilei include simulated keratometry, pachymetric map, anterior and posterior corneal elevation, keratoconus screening, anterior chamber depth, anterior chamber volume, anterior chamber angle opening, lens topography, crystalline lens thickness, corneal and lens densitometry, pupillometry, corneal diameter, total corneal wavefront, modulation transfer function, point spread function, and image formation on point spread function. The Galilei use ray tracing, which refracts incoming parallel rays through the anterior and posterior corneal surface, to calculate total corneal power. The Galilei can measure wavefront aberrations for the cornea independent of aberrations from the crystalline lens. This data is then displayed alongside root mean square indices calculated over a 6.0-mm optical zone centered over the pupil. Galilei's output reports consist of four reports, including the refractive report, the keratoconus report, the wavefront report, and the IOL power report.

The Refractive Report

The refractive report is the most commonly printed report used for preoperative refractive surgery screening. Refractive report contains four maps and several indices that evaluate corneal shape (Fig. 4). The maps include anterior axial curvature map, corneal pachymetry map, anterior elevation (best fit sphere [BFS]) map, and posterior elevation (BFS) map that are illustrated in clockwise order. The posterior

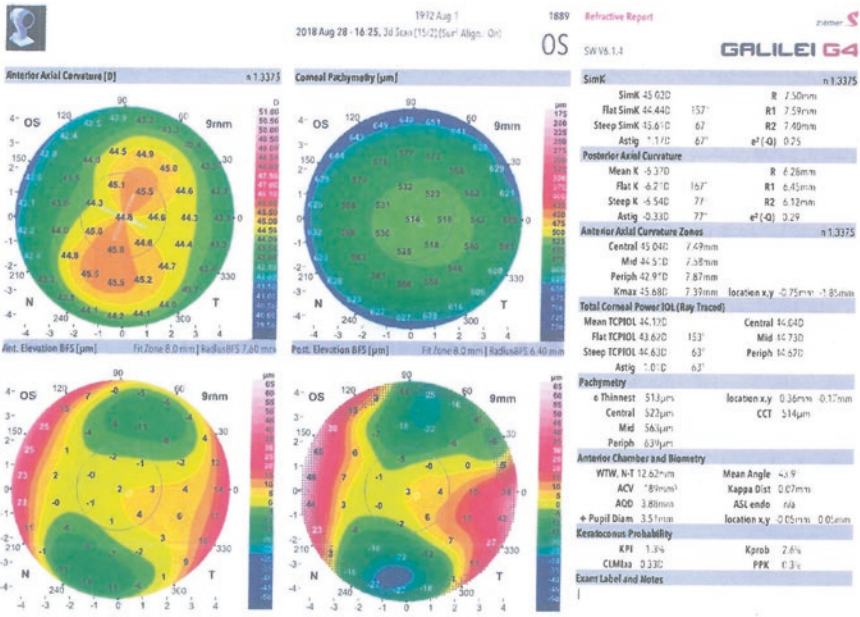

Fig. 4 The refractive report. Please, see the text

surface curvature map, which can be more informative for the early diagnosis of corneal diseases, is not exhibited in this report. The anterior axial curvature map is displayed with the default 1 D color scale, although the larger or smaller color scales can be selected. The corneal curvature is calculated based on the keratometric index (1.3375). Steep simulated keratometry and flat simulated keratometry are measured at the steep and flat meridians 0.5–2.0 away from the corneal center. The difference between these two powers is astigmatism and the average of these two powers is mean simulated keratometry. The astigmatism magnitude from the axial map is relative to the center of the map. Posterior curvature indices are calculated based on the difference between the refractive index of the cornea (1.376) and that of the aqueous humor (1.336). The pachymetry map of Galilei gives much more information than ultrasonic pachymetry. It shows the value and location of CCT and the thinnest corneal pachymetry, the central, paracentral, and peripheral average thickness.

In the anterior BFS elevation fitted for 8-mm-diameter central zone, the normal maximum peak of anterior elevation BFS is less than 10–12 microns within a 5-mm-diameter central region of interest. In the posterior BFS elevation fitted for 7.8-mm-diameter central zone, the normal maximum peak of posterior elevation BFS is less than 15–16 microns within a 5-mm-diameter central region of interest.

Indices Displayed with the Refractive Report

Several numerical data corresponding to the maps are presented in millimeters and diopters in the right column of the refractive report. These indices include those from anterior axial curvature map, (SimK values, SimK steep, SimK flat, and steeper astigmatism with angle), posterior axial curvature (K steep, K flat, and steeper astigmatism with angle), total corneal power (TCP) by ray tracing (TCP steep, TCP flat, and TCP astigmatism with angle), and eccentricity.

The average normal anterior axial curvature has a power of 41 D to 47 D using the keratometric index (1.3375). The axial anterior curvature is shown from the central (0–4 mm), mid-peripheral (4–7 mm) and peripheral (7–10 mm) regions. Kmax is the maximum power in the anterior axial curvature map and is determined by extracting the steepest single value within the 2 mm cone location and magnitude index (CLMI) spot on the anterior axial map. Cartesian coordinates (x, y) are used to demonstrate the location of the steepest point in relation to the reference point. This index is used to determine the severity and progression of keratoconus.

Mean posterior corneal power is the arithmetic mean of the pair of meridians 90° apart with the greatest difference in average power, from a 0.5 to 2.0 mm distance from the center. The power of the posterior steep and flat meridian is calculated using the corneal (1.376) and aqueous humor (1.336) refractive indexes. The average normal posterior axial curvature has a power of −5.50 D to −6.80 D.

Eccentricity (ε^2): This index reflects the shape of the cornea and is one of the four parameters that are used to describe the shape of a conic section. These parameters include Q (asphericity), p-value, E (corneal shape factor), and ε^2 (eccentricity). Galilei calculates ε^2 of the surface within a central diameter of 8 mm averaged over all meridians. The normal value of eccentricity is between 0 and 1.0, indicating the prolate profile of the cornea (steeper at the center and flatter at the periphery). $\varepsilon^2 > 1.0$ indicates a hyperprolate profile which is seen in keratoconus and after corneal refractive surgery performed for hyperopia and $\varepsilon^2 < 0$ indicates an oblate surface, for example, after corneal refractive surgery performed for myopia. $\varepsilon^2 = 1$ is an important cutoff value for the diagnosis of keratoconus. This measurement is performed for the anterior and posterior surface. The posterior surface is more prolate than anterior surface ($\varepsilon^2 = +0.20 \pm 0.16$) and typically precedes the anterior surface to show a parabolic shape in early keratoconus.

The Galilei uses ray tracing of the anterior surface, posterior surface, and pachymetry data to calculate the total corneal power (TCP) over a central 4.0-mm zone. Measurements of the power of the anterior and posterior corneal surfaces are obtained through ray tracing rather than the Gaussian optics formula. For each point on the map, the angle of incidence is calculated relative to the anterior surface normal for incoming parallel rays. The angle of refraction is calculated using the Snell law with air refractive index (1.0) and corneal refractive index (1.376). This angle of refraction is used to determine the nonparallel direction of incoming rays relative to the posterior surface normal and is used to calculate the angle

of incidence for the posterior surface. A new angle of refraction is calculated for the posterior surface using the Snell law with cornea (1.376) and aqueous (1.336). This final angle of refraction is used to calculate the intersection of the ray along the (0.0) axis and the resultant focal length that is used to determine total power for that point on the map. This method is used to measure TCP over steep (TCP steep) and flat (TCP flat) meridians. The averaged value is mean TCP and the difference between TCP-steep meridian and TCP-flat meridian is TCP astigmatism. TCP has excellent reproducibility and is a reliable index. The calculated corneal power from these measurements are extremely useful in IOL power calculation, especially for the calculation of the toric IOL power and in patients who undergo corneal refractive surgery.

The pachymetry map of Galilei gives much more information than ultrasound pachymetry. It shows the value and location of central corneal thickness (CCT) and the thinnest corneal pachymetry, the central, paracentral, and peripheral average thickness. CCT is measured in the central 0–4-mm area and the thinnest pachymetry is the thickness of the thinnest point located in the central 9.0 mm. The location of these points are determined by the Cartesian coordinates (x, y). The normal distance difference between CCT and the thinnest corneal point thickness should always be less than 25 microns. Dislocation of the thinnest point, usually temporal-inferior and more than 1 mm from the pupil center, is a sign of keratoconus. Normally, there is less than 200 microns of thickness difference between the CCT or thinnest corneal point and the periphery of the map at 4.5 mm of distance. Therefore, a normal thickness progression should have less than 10 color steps with a 20 microns scale. More steps indicate thinning of the center as in keratoconus or thickening of the periphery as in peripheral corneal edema. The mid-peripheral and peripheral corneal thickness are automatically measured and reported in the mid-peripheral zone (4–7 mm) and peripheral zone (7–10 mm), respectively. Corneal thickness can be measured at any point by manually placing the cursor at that point.

For measuring WTW distance, the limbus is fitted with a best-fit-ellipse in the top reference view image, which is provided by top view camera (1024×786 pixels CCD). The maximum length in the horizontal direction of the ellipse (not the ellipse long or short axis) is taken as the naso-temporal limbus parameter with a resolution of 0.01 mm. The same ellipse is used to measure the superior-inferior (vertical) limbus diameter. The central anterior chamber depth is calculated as the distance between the corneal endothelium and the crystalline lens' anterior surface, with a resolution of 0.01 mm.

The anterior chamber angle (ACA) measurements are performed by extrapolating the posterior corneal surface and the smoothed surface of the iris, to the point where both curves intersect. This angle of intersection is taken as the ACA, with a resolution of 0.10 degrees. Anterior chamber volume (ACV) is calculated between the posterior surface of the cornea (12.0 mm around the corneal vertex) and the iris and lens.

To measure angle kappa, the device measures automatically the distance between the pupil center and the center of the reflection of the four Purkinje dots,

which corresponds to the first Purkinje reflex in the cornea, with a measure resolution of 0.01 mm.

To measure mean pupil diameter, the pupil is fitted with a best-fit-circle and the averaged diameter of this circle in millimeter is considered as the pupil diameter. Cartesian coordinates (x, y) are used to characterize the location of the pupil center in relation to the corneal center.

The Keratoconus Report

In this report, the anterior axial curvature map is replaced with the anterior instantaneous (tangential) curvature map. The other maps are the same exhibited in the refractive report and consist of the anterior elevation (BFS) map, posterior elevation (BFS) map, and pachymetry map, illustrated in clockwise order (Fig. 5). The anterior instantaneous curvature map focuses on the localized curvature and every point correlates better with its real anatomical location on the corneal surface. Therefore, smaller details, which are smoothed out in the axial map, are accentuated in instantaneous map. The numerical indices of axial curvature and limbus measurements in the refractive map are replaced with the anterior surface keratoconus indices in the keratoconus reports, including surface asymmetry index, surface regularity index, inferior-superior index, irregular astigmatism index,

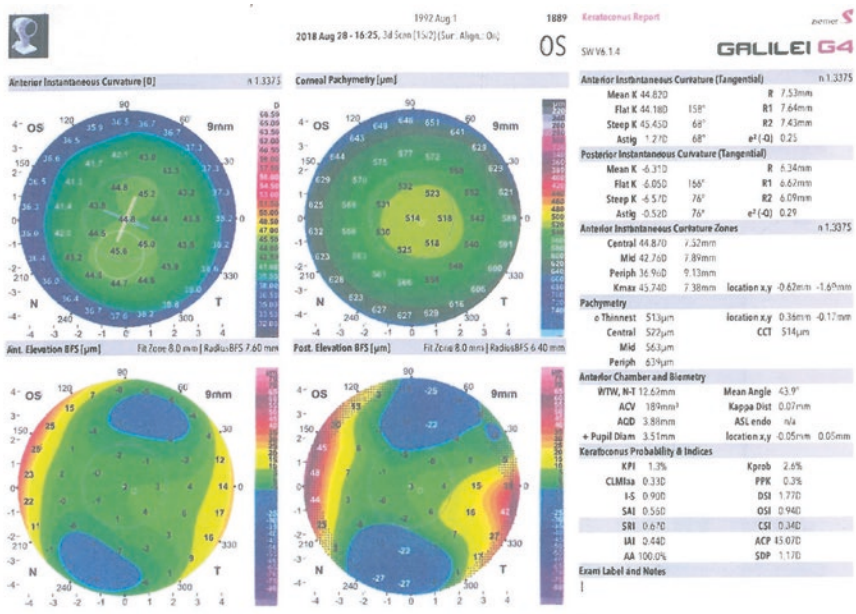

Fig. 5 The keratoconus report. Please, see the text

asphericity asymmetry index, center/surround Index, differential sector index, opposite sector index, cone location and magnitude index, keratoconus prediction index, keratoconus probability, and percentage probability of keratoconus.

Indices Displayed with the Keratoconus Report

The surface asymmetry index (SAI), which illustrates the average of differences in corneal power, is determined by the differences in keratometric power between opposite points distributed on 128 meridians. SAI >0.50 is abnormal. This index has been found the best parameter to discriminate clinical keratoconus among all Galilei indices. SAI may play a role in the diagnosis of subclinical keratoconus alongside other indices such as posterior best-fit sphere.

The surface regularity index (SRI) characterizes the local irregularities of the corneal surface. SRI is calculated as the sum of power variation along 256 semi-meridians on ten central rings over the corneal surface. A value of SRI below 1.0 is generally accepted as normal. This index approaches zero in spherical surfaces, and any increase in irregularity of corneal surface will manifest as an increase in this index. When the SRI value equals zero, the corneal surface is perfectly smooth. SRI has excellent diagnostic sensitivity and accuracy for identification of both subclinical and clinical keratoconus.

The inferior-superior (I-S) index calculates the dioptric asymmetry between the inferior and superior hemispheres. This index is a valuable diagnostic parameter for keratoconus and an I-S index $\geq$ 1.4 D is suspect for the disease. For early stage of the disease, however, the I-S index has limited sensitivity (10.8%) which indicates the limitation of the index in screening cases with subclinical keratoconus. Interestingly, its high specificity (90.7%) suggests that I-S index may be better for the confirmation of the disease.

The irregular astigmatism index (IAI) defines variation in measured axial power between central rings along any given meridian. This index, which is calculated as the average sum of area-corrected keratometric power variations along every meridian for the entire analyzed corneal surface, has excellent diagnostic accuracy for the detection of clinical keratoconus. Its accepted abnormality threshold is >0.50. IAI, however, should be used with caution for the diagnosis of subclinical keratoconus and a combination of indices should be considered when screening refractive surgery candidates.

The asphericity asymmetry index (AAI) quantifies the asymmetry of asphericity over the corneal surface. This index is measured as the magnitude of difference between the maximum negative best-fit toric aspheric (BFTA) reference surface value and the maximum positive BFTA elevation value. Posterior AAI is calculated as the absolute value of the highest negative and positive elevations within the posterior corneal zone. The AAI index is 10.72 ± 5.72 microns (maximum BFTA limit 25–30 microns) for the anterior surface and 22.49 ± 9.29 microns (limit 40–45 microns) for the posterior surface. A higher value of AAI correlates

with increased rates of curvature change and corresponds well with the amount of corneal coma. Posterior AAI may be a valuable index for the detection of early keratoconus as posterior corneal changes may occur first in the development of this disease. In addition, posterior AAI has a sensitivity of 100% and specificity of 99.5% in the detection of clinical keratoconus.

The center/surround Index (CSI) quantitatively characterizes the difference in corneal power between two areas of the cornea. The corneal surface is first divided into 8 arbitrary sectors measuring a 45° angle. Then, the mean axial keratometric power is calculated for each sector. This process repeats itself until each possible pattern of sector distribution has been applied to the corneal surface. Therefore, CSI represents the difference in the average area-corrected corneal power between a central area (3.0-mm diameter) and an annulus surrounding the central area (3.0–6.0-mm diameter). In normal eyes CSI value is <1.0, whereas in keratoconus CSI is >1.0. CSI is, especially, a sensitive index for identification of centrally located keratoconus. Moreover, CSI has a significant association with visual function, making it a valuable parameter in assessing overall visual acuity. Although CSI achieved by Galilei has an excellent diagnostic accuracy in discriminating keratoconus-affected eyes, it fails as an individual parameter in distinguishing early keratoconus, and should not be used as a standalone index when diagnosing subclinical keratoconus.

The differential sector index (DSI) is related to the degree of asymmetry of the corneal surface. Similar to CSI, DSI is measured based on the 8-sector pattern of the corneal surface and characterizes the maximum difference between any two sectors. Therefore, this index increases with an increase in surface irregularity. DSI >3.50 is a sensitive index for the detection of peripherally located cone and in corneas with regular astigmatism. DSI is a highly accurate index in the detection of clinical keratoconus. However, it is not a reliable parameter for the identification of the early stage of the disease.

The opposite sector index (OSI) is calculated based on the greatest difference between any two opposite sectors, divided in 45°. OSI has been found sensitive in identifying peripherally located corneal steepening. Although OSI >2.10 is a valuable screening index for frank keratoconus, it is not a reliable parameter for distinguishing eyes with subclinical keratoconus and should not be used alone when considering the early stage of the disease.

The cone location and magnitude index (CLMI) characterizes the steepest area of curvature, and the magnitude of the index identifies the difference between the steepest area and the rest of the curvature map. This index, which has good repeatability among various devices, relies on an area-corrected average steepest 2 mm-diameter circle within the central 8 mm-diameter anterior curvature map. From this, a difference between all points outside the circle and all points inside the circle is calculated. Similar analyses were performed for a second circle that is centered 180 degrees away in angular position. CLMI is then calculated based on these two differences, which aims to characterize the steepest area of curvature relative to the rest of the corneal surface map. Posterior CLMI may serve as a valuable measure of asymmetric corneal steepening.

The keratoconus prediction index (KPI), which simulates the percent probability of keratoconus, is a linear discriminate analysis of eight quantitative topographic indices from videokeratography to detect keratoconus. These indices include simulated K1, simulated K2, SAI, CSI, DSI, OSI, IAI and AA. Based on the Galilei system, KPI from 0 to 10% corresponds to normal or suspicious corneas; KPI from 10 to 20% corresponds to suspicious or borderline keratoconic corneas, KPI from 20 to 30% corresponds to keratoconic or perhaps still suspicious corneas, and KPI>30% is indicative of pellucid marginal degeneration or keratoconus. This index has a sensitivity of 100% and a specificity of 96% for the detection of keratoconus. The discriminant functions of this index are chiefly due to this fact that it is a multivariate parameter, including a variety of tomographic data. However, it is not always useful for the screening of keratoconus suspect because it has a significant overlapping between keratoconus suspect and keratoconus in its scoring system. Therefore, it should not be used alone in screening patients and should be confirmed by clinical diagnosis. KPI is capable of discriminating keratoconus from other corneal surface abnormalities, including corneal irregularities after radial keratotomy, photorefractive keratectomy, and keratoplasty as well as corneal warpage due to contact lens wear.

The keratoconus probability (Kprob) characterizes sensitivity and specificity of the reported KPI value on the basis of a normative and keratoconic database. This index has an inverse relationship with visual acuity. Kprob has an excellent accuracy for discrimination of keratoconus from normal cornea; this index, however, is not sensitive when distinguishing of eyes with subclinical keratoconus. Therefore, Kprob is only suitable for discriminating frank keratoconus.

Percentage probability of keratoconus (PPK) is defined as the optimal threshold for detecting keratoconus. The PPK is calculated from a validated equation that incorporates CLMI using axial data. The cutoff values of 45.0% and 20.0% are considered for the diagnosis of clinical and subclinical keratoconus, respectively. Like the other probability indices, PPK can distinguish keratoconus with excellent accuracy but fails in discrimination of eyes with subclinical keratoconus from normal eyes.

The Wavefront Report

The Galilei system uses the corneal elevation profile to automatically compute corneal wavefront data and higher order aberrations (HOAs) in microns (at left) and in diopters (at right). The wavefront map in microns is similar to that in diopters, however, the colors are inverted (Fig. 6). The Galilei system has an excellent repeatability in measuring corneal aberrations in any region of interest from 3 to 6 mm. Compared to single Scheimpflug systems, the Galilei system has less variability in measured Zernike terms, probably secondary to the added benefit of having a dual-channel camera.

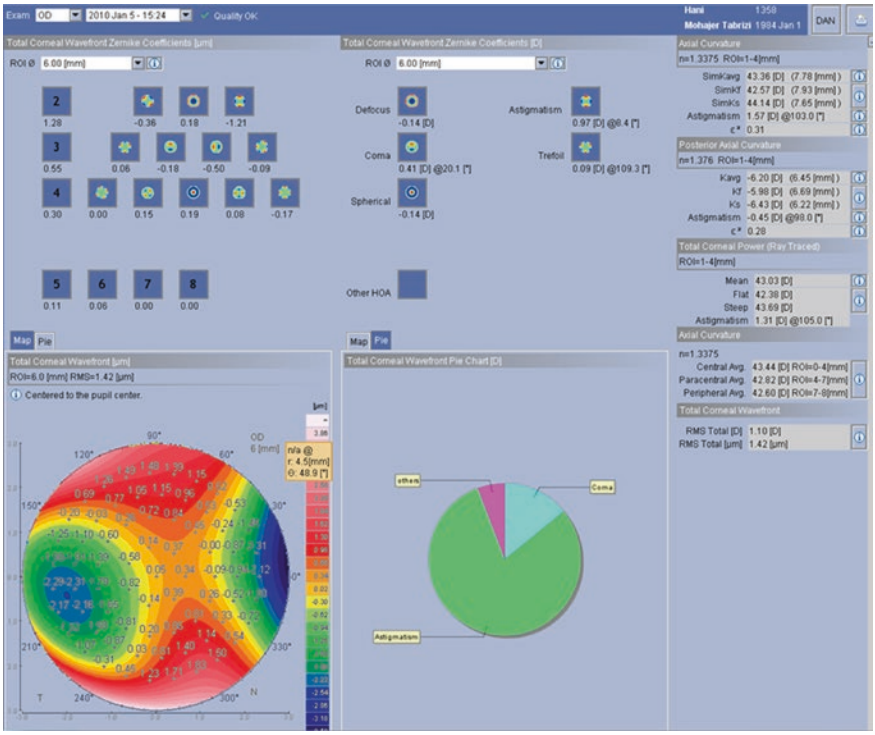

Fig. 6 The wavefront report. Please, see the text

The total HOAs are displayed in the wavefront report, which is automatically calculated by the Galilei system. The second-order (lower order) corneal aberrations include the Zernike coefficients for defocus and vertical and oblique astigmatism which are demonstrated in the first row of the wavefront report. These second-order corneal aberrations are related to the corneal components of manifest refractive error. Third-order aberrations consist of the vertical and horizontal coma and trefoil. Vertical coma, which reflects early changes in the corneal surface, is probably the most important HOA for the detection of keratoconus and monitoring the progression of the disease over time. Fourth-order aberrations are spherical aberration, vertical and horizontal quatrefoil, and vertical and horizontal secondary astigmatism, which can increase (>0.30 μm) in corneal diseases. Total root mean square (RMS) in diopters and microns is also exhibited at the bottom right of the numerical indices. The RMS for 3rd-, 4th-, 5th-, 6th-, and total higher-order aberrations has been found useful indicators for the screening of keratoconus. However, the RMS of vertical coma has acceptable sensitivity and specificity for differentiating between normal eyes and eyes with early stage of keratoconus.

The IOL Power Report

This report demonstrates the anterior axial curvature map, the total corneal power map by ray tracing from an 8-mm-diameter data zone, the total wavefront HOA map from a 6-mm-diameter data zone, and a top view of the Placido ring pattern reflected on the cornea. The indices included in this report are SimK values, total corneal power calculated at the central zone (0–4 mm), paracentral zone (4–7 mm), and peripheral zone (7–10 mm), RMS HOA, spherical aberration, ACD, ACV for an 8-mm-diameter central zone, the chamber angles in degrees at the superior, temporal, inferior, and nasal direction, horizontal and vertical limbus diameter, the pupil diameter (approximately mesopic) and the Cartesian location of the pupil centroid relative to the center of the map. The average anterior segment length (ASL), distance from the posterior corneal surface to the posterior lens, requires measurement with a dilated pupil.

The amount of spherical aberration can be used to select one of the aspheric IOL to compensate for corneal spherical aberration postoperatively. Currently available aspheric IOLs have negative spherical aberration (−0.27 microns for the AMOTecnis Multifocal IOL or −0.20 microns for the Alcon Acrysoft IQ IOL) or neutral (zero) spherical aberration (the Bausch and Lomb SofPort IOL or Mediphacos IOL). It has been demonstrated that IOL power calculation using the ray traced TCP from a central 4-mm-diameter data zone is more accurate for eyes that have undergone corneal refractive surgery. The use of SimK to calculate toric IOLs is a common practice worldwide. However, these values are derived from only the anterior corneal surface and hence do not take into account the curvature of the posterior corneal surface. The corneal astigmatism magnitude and direction derived from TCP can provide better postoperative results.

Case Presentation

Case 1

A 28-year-old man has refractive errors of $-2.0\ -1.75 \times 145$ OD and plano OS with a best spectacle-corrected visual acuity 9/10 OD and 10/10 OS. In the Galilei map of the right eye, anterior BFS fitted for central 8.0-mm area has a diameter of 7.54 mm and the anterior maximum elevation is 5 microns (within normal limit). Posterior elevation map exhibits a hot point with the maximum elevation of 15 microns (borderline) that corresponds to the maximum elevation in the anterior elevation map. The axial curvature map shows a small, central, oblique bowtie pattern in the 3-mm central area that corresponds to the thinnest corneal thickness (486 microns). I-S value is 0.34 D (within normal limit); however, SRI (1.87) and

SAI (0.93) are abnormal and KPI (17.8%) is borderline. The Galilei map of the left eye (not shown) is normal. This patient is keratoconus suspect and should not be considered for corneal refractive surgery.

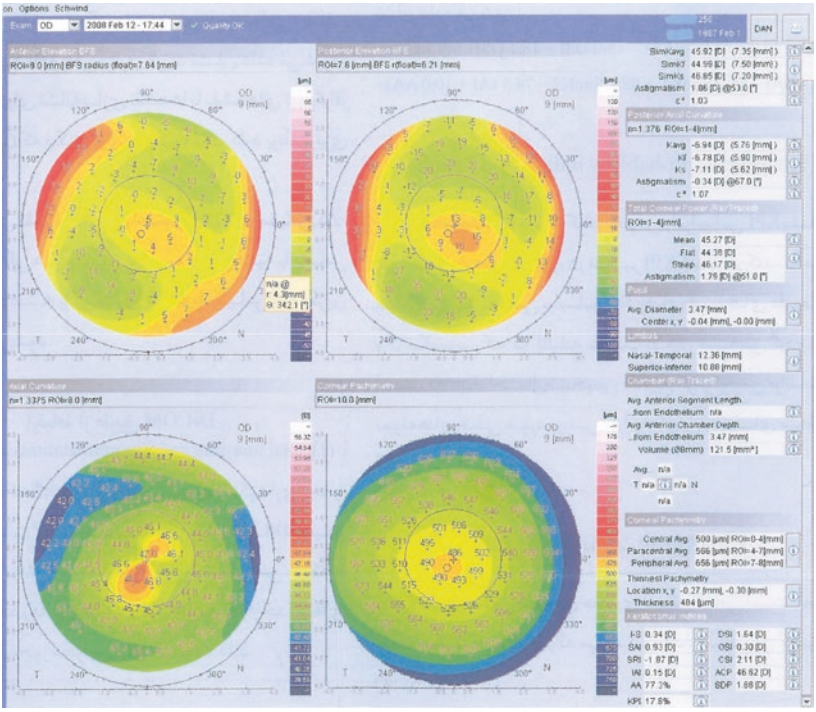

Case 2

An 18-year-old woman has refractive errors of $-3.0\ -0.75 \times 150$ OD and $-2.75\ -1.25 \times 60$ OS with a best spectacle-corrected visual acuity 10/10 OU. There is no remarkable finding in the anterior and posterior elevation maps. The anterior curvature map shows inferior steepening in the right eye; the area of maximum steepening coincides with the thinnest point (481 microns). SAI (0.98), SRI (0.81), and I-S value (2.11 D) are abnormal, and KPI (12.3%) is borderline. The anterior and posterior elevation maps of the left eye are normal. The anterior curvature map exhibits an inferior steepening pattern despite the keratometric values are within normal limit in the left eye. SAI (0.98), I-S value (2.28 D), and ACP (44.42 D) are abnormally high, and KPI (15.4%) is borderline. This patient is diagnosed with early stage of keratoconus.

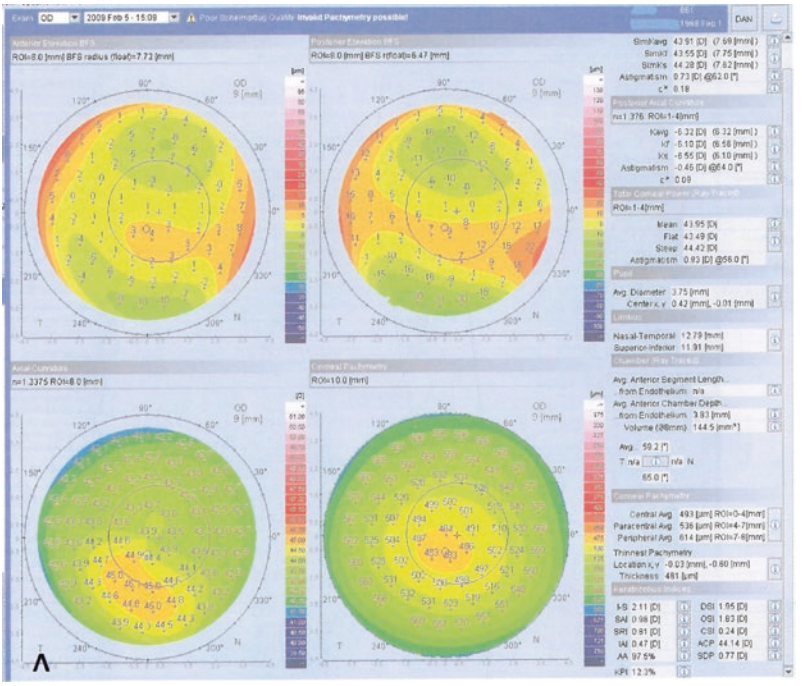
A

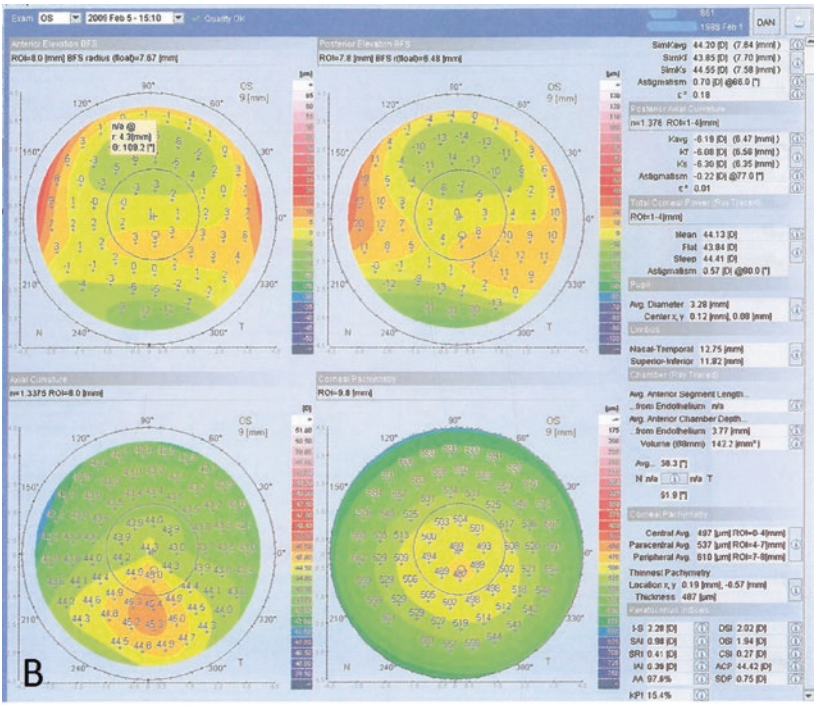
B

Case 3

A 39-year-old man presents with a progressive reduction in visual acuity. He underwent LASIK for a myopia of −5.0 D 15 years ago. Manifest refractive error is −5.0 −4.0 × 50 OD with a best spectacle-corrected visual acuity of 5/10 OD. Both anterior and posterior elevation maps demonstrate abnormally elevated areas in the inferior cornea. The anterior curvature map shows corneal flattening in the superior part, indicating decentered ablation. The maximum curvature in the inferior cornea is 51.6 D. These findings suggest that the patient develops post-LASIK ectasia in addition to receiving decentered ablation. The thinnest point is located superior to the hot areas observed in other three maps. All of the keratoconus indices are abnormally high and KPI is 98.1%, confirming the diagnosis of post-LASIK ectasia.

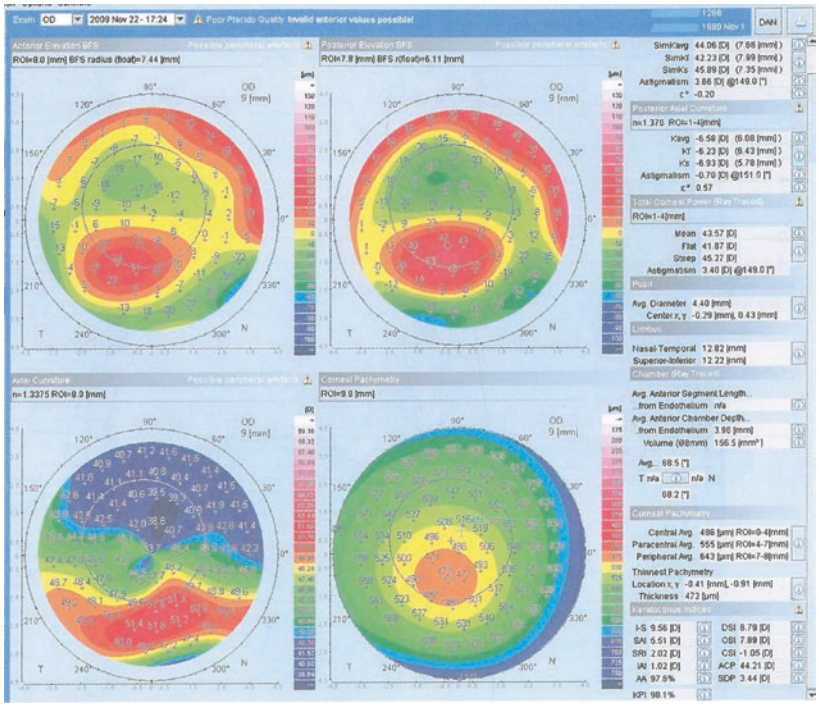

Case 4

A 25-year-old refractive surgery candidate has a manifest refraction of −3.0 D OU and best spectacle-corrected visual acuity of 10/10 OU. The refractive error was stable during 1 year and there is no family history of keratoconus. The anterior and posterior elevation maps are normal. The anterior curvature map demonstrates

superior steepening; the area of steepening does not coincide with the thinnest point which is located at the corneal center. Keratoconus indices are within normal limit and KPI is zero. Therefore, he does not have keratoconus and the hot spot observed in the curvature map is probably due to the accumulation of tear film. Corneal refractive surgery can be considered for this case.

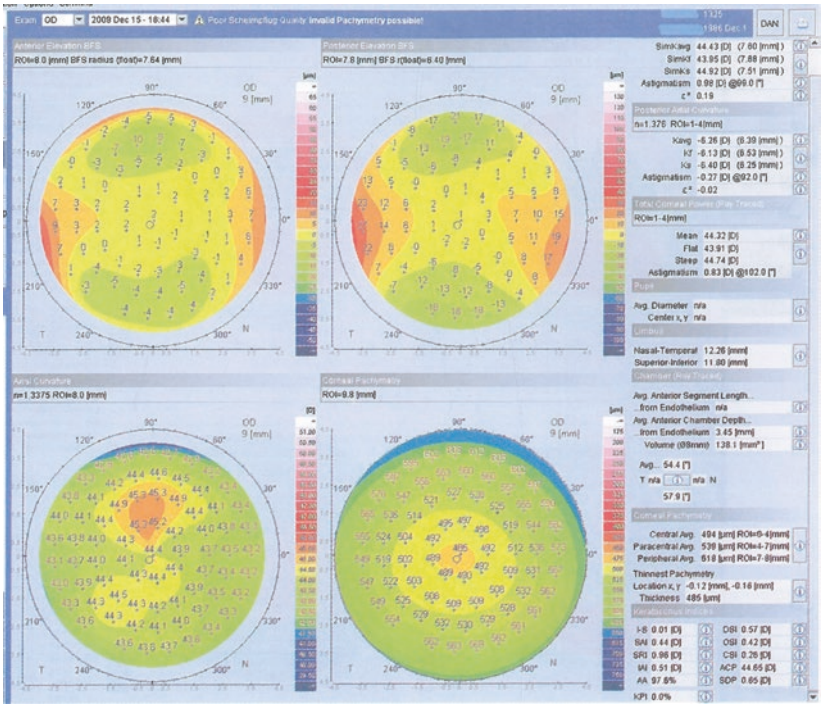

Case 5

A 23-year-old man complains of a gradual decrease in visual acuity OD. Manifest refraction is $-3.0\ -1.5 \times 20$ with a best spectacle-corrected visual acuity of 20/50 in this eye. The visual acuity increases to 10/10 with a rigid gas-permeable contact lens. The anterior elevation map demonstrates a bridge pattern with a maximum elevation of 8.0 microns, and the posterior elevation map exhibits an island pattern with a maximum elevation of 19 microns. The anterior curvature map demonstrates inferior steepening with a maximum curvature of 48.9 D. The thickness of the thinnest point is 447 microns. Despite keratometric readings, including flat SimK (44.34 D) and steep SimK (46.29 D), are within normal limit, the patient is diagnosed with keratoconus, based on the elevation maps. All of the keratoconus indices are abnormal and KPI is 48.1%, confirming the diagnosis of keratoconus.

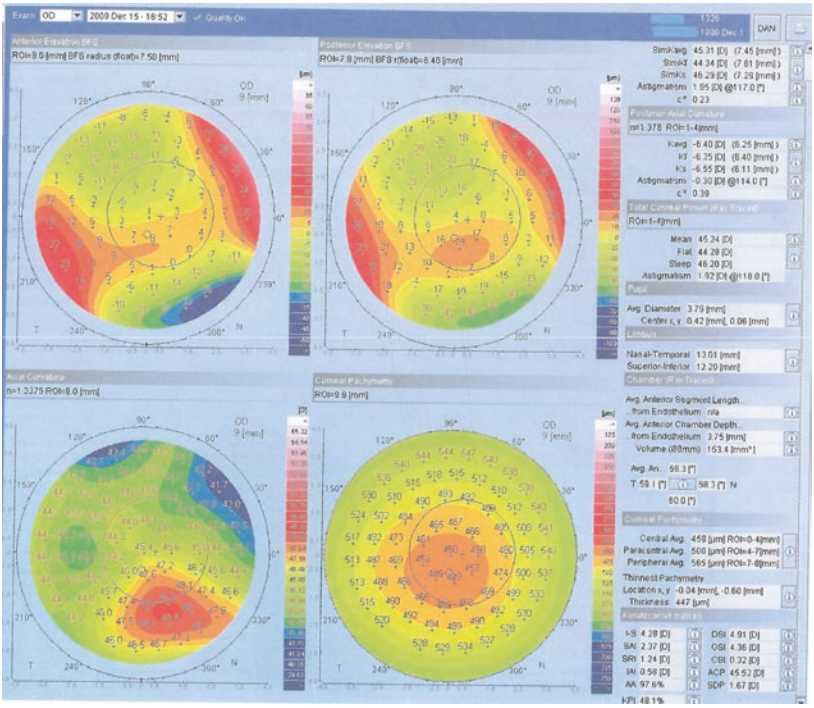

Case 6

A 42-year-old man has a manifest refraction of $-5.0\ -0.75 \times 110$ OD and $-4.75\ -1.50 \times 90$ OS. Best spectacle-corrected visual acuity is 10/10 OU. Refraction has slightly increased since last year. The examination of two eyes is unremarkable. The anterior and posterior elevation maps demonstrate a hot area in the inferior portion of both corneas. The anterior curvature map illustrates an against-the-role astigmatism and kissing bird pattern with the maximum elevation in the inferior cornea which is compatible with the elevation areas in the elevation map. SimK measurements and the pachymetry map are within normal limit. The majority of keratoconus indices and KPI (14.8%) are borderline. The Galilei map of the left eye is very similar to that of right eye. These finding are compatible with the diagnosis of early pellucid marginal degeneration.

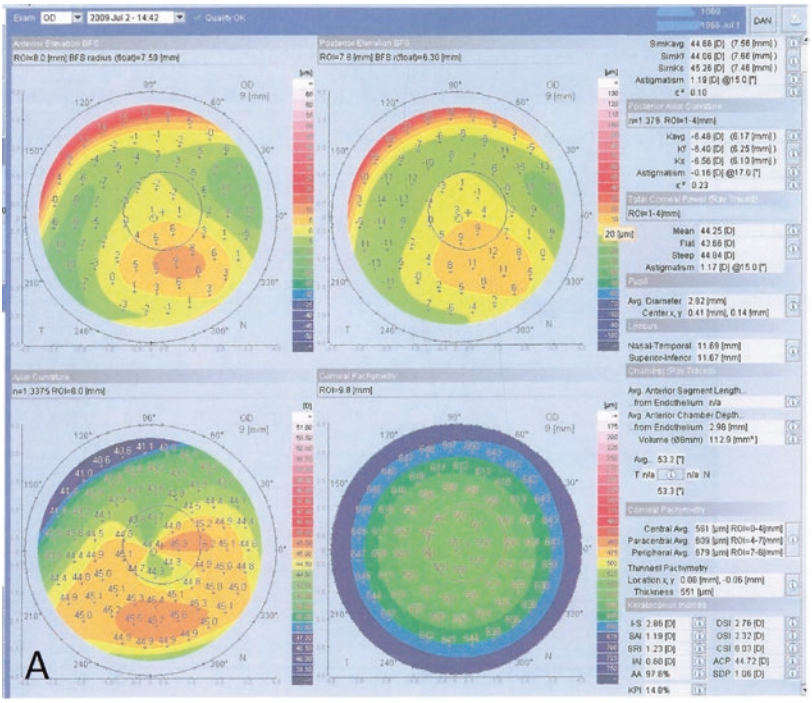
A

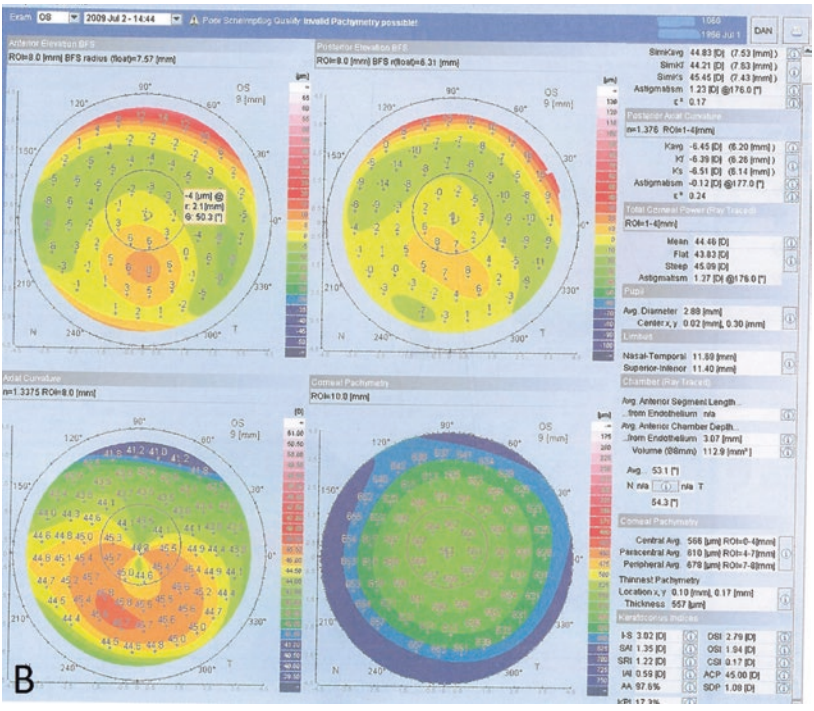
B

References

1. Anayol MA, Guler E, Yagci R, Sekeroglu MA, Ylmazoglu M, Trhs H, et al. Comparison of central corneal thickness, thinnest corneal thickness, anterior chamber depth, and simulated keratometry using galilei, Pentacam, and Sirius devices. Cornea. 2014;33(6):582–6.
2. Galilei AC. Map interpretation guide. Software V. Port. Switzerland: Zeimer Ophthalmic Systems AG; 2011.
3. Crawford AZ, Patel DV, McGhee CN. Comparison and repeatability of keratometric and corneal power measurements obtained by Orbscan II, Pentacam, and Galilei corneal tomography systems. Am J Ophthalmol. 2013;156(1):53–60.
4. Roberts CJ, Züger BJ. The advantage and principle of Dual Scheimpflug imaging for analyzing the anterior segment of the human eye. SIS Surgical Instrument Systems AG Port, Switzerland, Apr 2006
5. Demir S, Sonmez B, Yeter V, Ortak H. Comparison of normal and keratoconic corneas by Galilei Dual-Scheimpflug Analyzer. Cont Lens Anterior Eye. 2013;36(5):219–25.
6. Feizi S, Yaseri M, Kheiri B. Predictive ability of Galilei to distinguish subclinical keratoconus and keratoconus from normal corneas. J Ophthalmic Vis Res. 2016;11(1):8–16.
7. Galilei G4 Operator Manual. Port, Switzerland: Zeimer Ophthalmic Systems AG; 2016.
8. Golan O, Piccinini AL, Hwang ES, De Oca Gonzalez IM, Krauthammer M, Khandelwal SS, et al. Distinguishing highly asymmetric keratoconus eyes using Dual Scheimpflug/Placido analysis. Am J Ophthalmol. 2019;201:46–53.
9. Hsieh YH, Weng TH, Chou YC, Wu KL, Liang CM, Tai MC. Agreement of post-LASIK corneal power and corneal thickness measurements by pentacam and GALILEI corneal tomography systems. J Chin Med Assoc. 2018. https://doi.org/10.1016/j.jcma.2018.07.005, pmid: 30268641.
10. Jahadi Hosseini HR, Katbab A, Khalili MR, Abtahi MB. Comparison of corneal thickness measurements using Galilei, HR Pentacam, and ultrasound. Cornea. 2010;29(10):1091–5.
11. Park SH, Choi SK, Lee D, Jun EJ, Kim JH. Corneal thickness measurement using Orbscan, Pentacam, Galilei, and ultrasound in normal and post-femtosecond laser in situ keratomileusis eyes. Cornea. 2012;31(9):978–82.
12. Salouti R, Nowroozzadeh MH, Zamani M, Ghoreyshi M, Salouti R. Comparison of anterior chamber depth measurements using Galilei, HR Pentacam, and Orbscan II. Optometry. 2010;81(1):35–9.
13. Smadja D, Touboul D, Cohen A, Doveh E, Santhiago MR, et al. Detection of subclinical keratoconus using an automated decision tree classification. Am J Ophthalmol. 2013;156(2):237–46 e1.
14. Smadja D, Touboul D, Colin J. Comparative evaluation of elevation, keratometric, pachymetric and wavefront parameters in normal eyes, subclinical keratoconus and keratoconus with a Dual Scheimpflug analyzer. Int J Kerat Ect Cor Dis. 2012;1(3):158–66.
15. Menassa N, Kaufmann C, Goggin M, Job OM, Bachmann LM, Thiel MA. Comparison and reproducibility of corneal thickness and curvature readings obtained by the Galilei and the Orbscan II analysis systems. J Cataract Refract Surg. 2008;34(10):1742–7.
16. Moshirfar M, Motlagh MN, Murri MS, Momeni-Moghaddam H, Ronquillo YC, Hoopes PC. Galilei corneal tomography for screening of refractive surgery candidates: a review of the literature, part II. Med Hypothesis Discov Innov Ophthalmol. 2019;8(3):204–18.

SIRIUS®

Mehrdad Mohammadpour and Zahra Heidari

Introduction

Sirius® (Costruzione Strumenti Oftalmici, Florence, Italy) is a corneal tomographer device that consists of both Placido and Scheimpflug systems (a hybrid device). The combination of two technologies allows accurate corneal topography, corneal pachymetry, anterior and posterior elevations of the cornea, and contact lens fitting and dry eye detection with high-speed analysis of the entire cornea and anterior segment.

Scheimpflug images with 3D (dimensional) analysis, give accurate corneal elevation data for the anterior segment elevation and Arc-Step (Placido disk) with 2D corneal maps gives a better assessment of corneal curvature and refractive power. Arc step algorithm is a recent generation reflection-based topographer that calculates curvature and elevation simultaneously. Twenty-five Scheimpflug images at higher than 100,000 points and 1 Placido disk image are taken in 1 second (Fig. 1).

Sirius provides complete information about corneal pachymetry, elevation, curvature, wavefront analysis, and dioptric power of both anterior and posterior surfaces over 12 diameters. Anterior chamber biometric indices calculated based on 25 sections from the cornea. Accurate measurement with high speed reduces eye movement, static cyclotorsion correction (SCC) software in Sirius, provides a link between Excimer laser in patients undergoing refractive surgery, and adjusts static cyclotorsion and the pupil size during surgery. This mechanism is a helpful tool to reduce wavefront and improve the quality of vision through less

M. Mohammadpour (✉)
Department of Ophthalmology, Faculty of Medicine, Farabi Eye Hospital and Eye Research Center, Tehran University of Medical Sciences, Tehran, Iran
e-mail: mahammadpour@yahoo.com

Z. Heidari
Noor Ophthalmology Research Center, Noor Eye Hospital & Tehran University of Medical Sciences, Tehran, Iran
e-mail: zahra.heidari77@yahoo.com

M. Mohammadpour (ed.), *Diagnostics in Ocular Imaging*,
https://doi.org/10.1007/978-3-030-54863-6_5

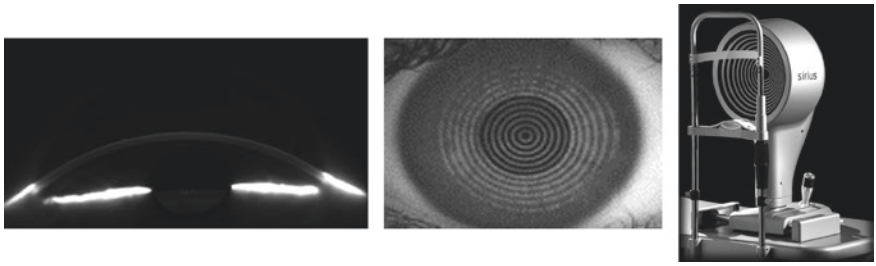

Fig. 1 Sirius with the combination of Scheimpflug and Placido (*With permission from Costruzione Strumenti Oftalmici* (*CSO*)) [1]

Table 1 Technical data of Sirius [1]

Specifications	
Operation distance	80 mm from corneal vertex
Number of rings	22
Number of measuring points	21632 front 1600 rear
Number of points analyzed	Over 100,000
Diameter of the corneal area covered	0.4 to over 9.6 mm of diameter
Diopters measuring Arc	1–100 D
Measurement range	0/80 mmHG (0/10,64 kPa)
Size (H × W × D) mm	105 × 110 × 30 mm
Wight	7 kg
Base movement	74 mm
Placido's LED lighting	White LED
Fluorescein led lighting	Blue LED 460 nm
Pupillometry	LED lighting IR LED 875 nm
Accuracy and repeatability	Class A as per IOS 19980;2005 (E)
Power supply	24 V DC external power supply unit
Input power supply unit	90–264 V AC; −47/63 Hz Max 0.9 A OUTPUT; 24 V DC–2A
Power frequency	(50/60 Hz) magnetic field IEC 6 1000-4-8
Power cable	Four-core cable conductors
Computer connection	USB3 Type A cable

variability of refractive errors. Sirius could measure the anterior segment with high repeatability [2].

Other anterior segment indices measured by Sirius include the IOL calculation module, measurement of pupil diameter in scotopic, mesopic and photopic condition, also there are some important maps for refractive surgery screening and follow up and evaluation of the progression of corneal ectatic disorders. The technical data is shown in Table 1.

Pupillography

The pupil size is measured in different conditions including scotopic, mesopic, and photopic based on light conditions. The pupil diameter is important for improving vision quality in clinical procedures. Sirius could detect the change of the pupillary center location with offset parameters in keratoconic patients which is an important factor for corneal surgeries [3] (Fig. 2).

Tear Film Evaluation

Sirius provides a comprehensive analysis of tear film, including a dynamic view of non-invasive break-up time (NIBUT) with TearScope examination and meibography with 5 step classification. Placido disk system allows advance assessment of tear film based on the ocular surface disease index (OSDI) questionnaire, tear osmolarity, meibomian gland analysis for the detection of dry eye disease. When the image is taken, the meibomian glands can be seen under infrared light, and software to help analyze the gland's status. The Sirius no-contact meibography is a simple, cost-effective, and reliable tool for evaluating meibomian gland functions [4, 5] (Fig. 3).

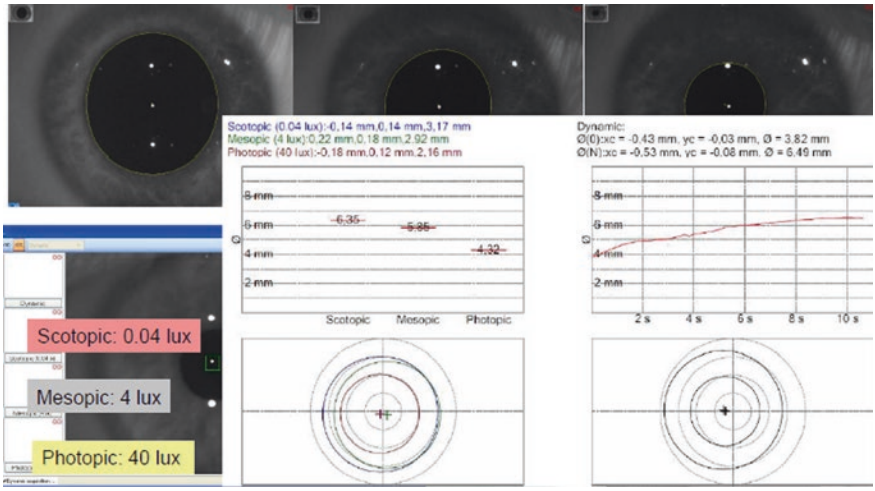

Fig. 2 Pupil measurement with Sirius (*With permission from CSO*)

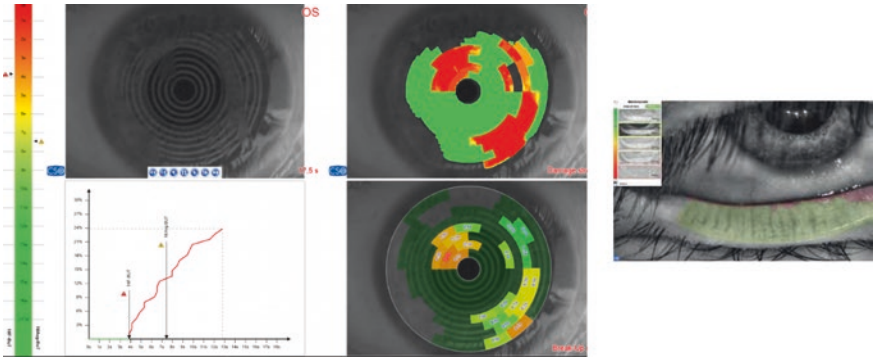

Fig. 3 Tear film map (*With permission from CSO*)

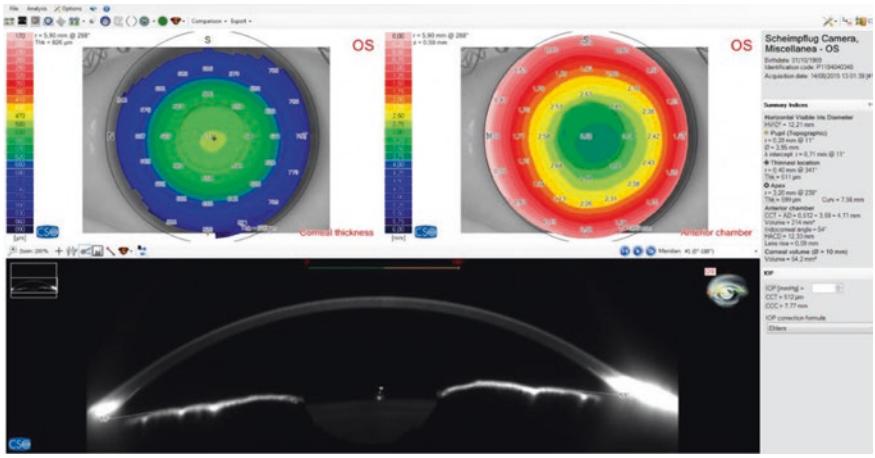

Fig. 4 Iridocorneal angles well demonstrated in the Scheimpflug image (*With permission from CSO*)

Glaucoma Screening

Sirius provides repeatable Iridocorneal angles and pachymetry measurements which are useful for the diagnosis of glaucoma [6] and calculation of corrected intraocular pressure (IOP) (Fig. 4).

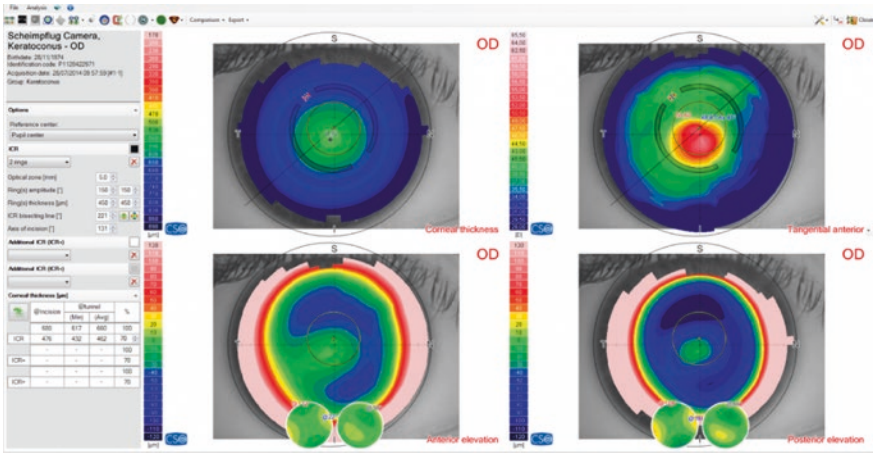

Fig. 5 Intrastromal ring planning for the management of keratoconus (*With permission from CSO*)

Corneal Intrastromal Rings

Corneal Intrastromal ring planning based on data derived from the pachymetry map is an option for the management of mild to moderate keratoconus. Long time follow up has shown that Intrastromal rings can reduce refractive errors and improve visual acuity [7]. This display on Sirius shows the topographic flat and steep meridians and offers the appropriate rings position and depth for corneal implantation (Fig. 5).

Corneal Aberrometry

The optical path distance and wavefront error (OPD/WFE) maps and the visual simulations (PSF, MTF, image convolution with optotype) offers a comprehensive analysis of wavefront aberrations and can help the ophthalmologist for better measurement of the quality of vision. It is possible to select anterior, posterior, and total corneal aberrometry for different pupil diameters (Fig. 6).

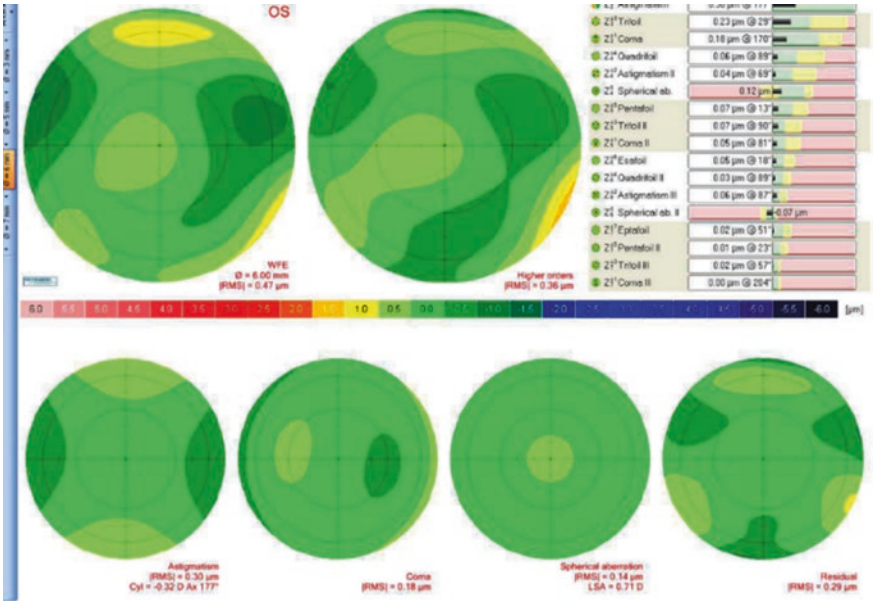

Fig. 6 Wavefront aberration maps

IOL Calculation

Although traditional devices use axial length and keratometry reading for IOL calculation, Sirius uses Ray tracking technology based on Snell's law at each optical interface to calculate the predicted lens position (PLP), implanted IOL power, predicted refractive errors and predicted wavefront errors. This module offers the calculation of spherical or toric lenses and regards the previous condition of the cornea (untreated or previously treated) accurately [8] (Fig. 7).

Contact Lens Application Module

An auto fit rigid contact lens module is available to find the best contact lens curvature and diameter in a database containing most of the international contact lens manufacturers (Fig. 8).

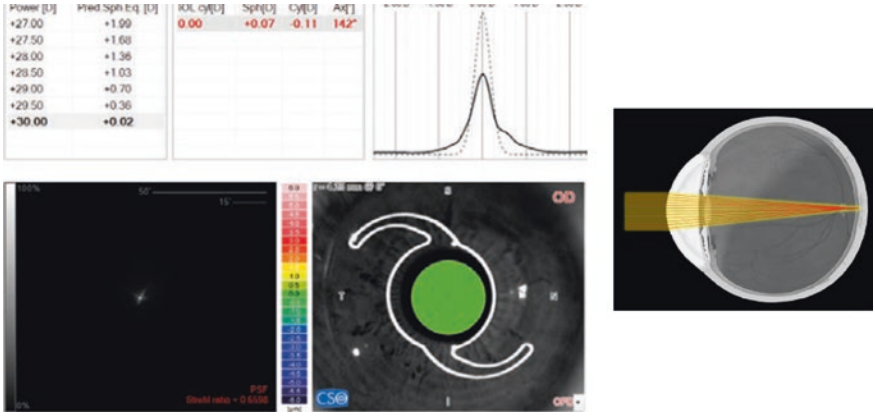

Fig. 7 IOL power calculations are estimated based on Ray tracking technology (*With permission from CSO*)

Fig. 8 Contact lens map helps the correct fitting (*With permission from CSO*)

Phoenix Software

PHOENIX is an advance software in Sirius which examines and documents Keratoconus Summary, Corneal Aberrometry, Glaucoma Summary, Tear Film Analysis, Meibography, Pupillography, Densitometry, and Videokeratoscope. The phoenix software algorithm let us to save patient data for future reviewing and follow-ups (Fig. 9).

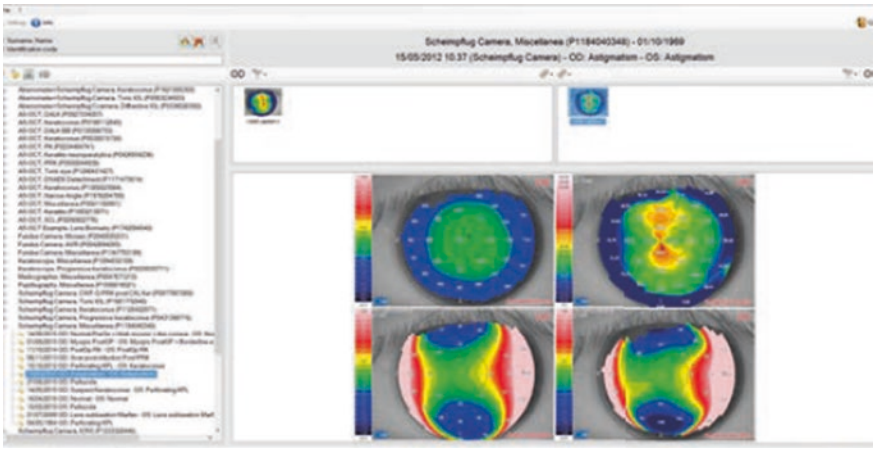

Fig. 9 Documenting the patient's corneal data with Phoenix software (*With permission from CSO*)

Diagnostic Tools

Summary indices: including an overview of the thinnest location, iris diameter, and anterior chamber data.

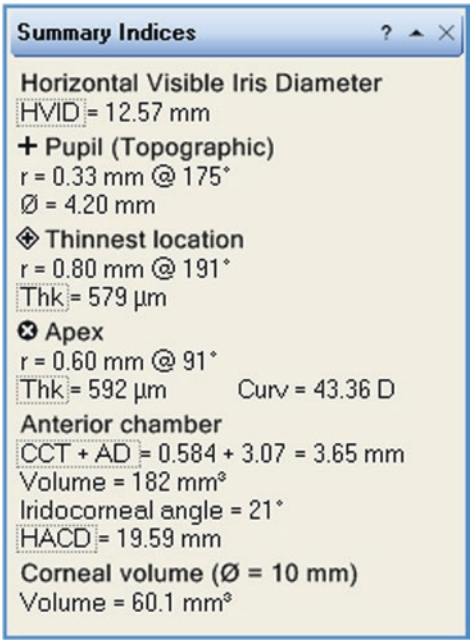

- HVID: Horizontal Visible Iris Diameter size
- Pupil: Topographic pupil size with information about the decentration to the vertex (=pupil offset)
- Thinnest location: Location and pachymetry of the thinnest point
- Apex: Location, pachymetry, and curvature of the steepest point (anatomical) of the cornea
- Anterior chamber: Anterior chamber depth
  CCT + AD (Central Corneal Thickness + Aqueous depth).

Corneal Thickness

SIRIUS provides essential information about the corneal thickness and comprehensive diagnostic assistance (Fig. 10).

Axial Curvature

Axial (or sagital) curvature algorithm measures the curvature at a specific point on the corneal surface in the axial direction with respect to the corneal optical axis (Fig. 11). It calculates the perpendicular distance from the tangent line to a point on the optical axis. This map is designed to evaluate corneal qualitatively through colors and facilitate the interpretation of results by inexperienced users [9].

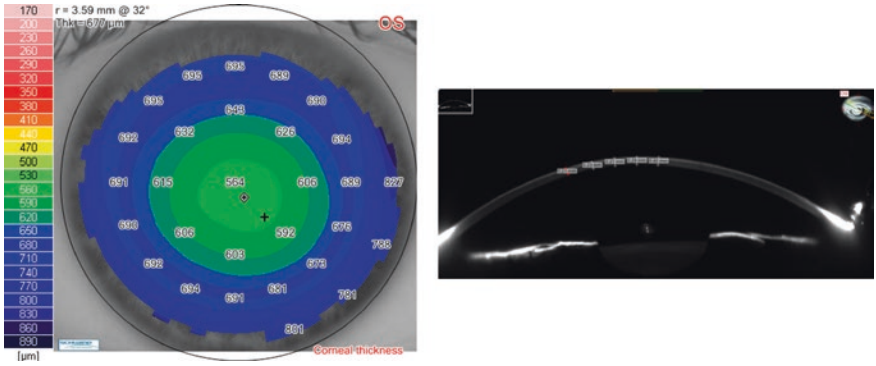

Fig. 10 Pachymetric distribution (*With permission from CSO*)

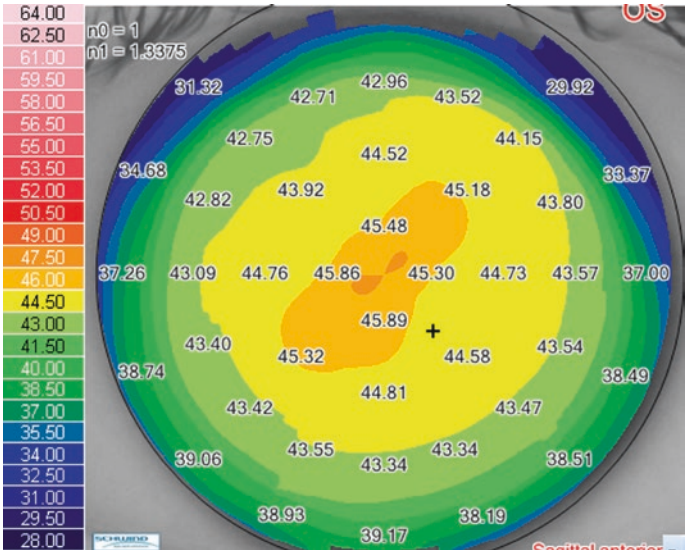

Fig. 11 Corneal curvature distribution with an axial map (*With permission from CSO*)

Tangential Curvature

Tangential (or instantaneous) curvature algorithm does not reconstruct the corneal surface by connecting to the optical axis. The radius of the tangent circle is considered as the radius of curvature. This map shows the curvature of the peripheral cornea more accurately than the axial map and suitable for monitoring the conical shape of ecstatic disease. However, its interpretation may be more complex [9] (Fig. 12).

Altimetric Elevation

Spherical reference:

- Value > 0, steeper than the reference
- Value < 0, flatter than the reference (Fig. 13).

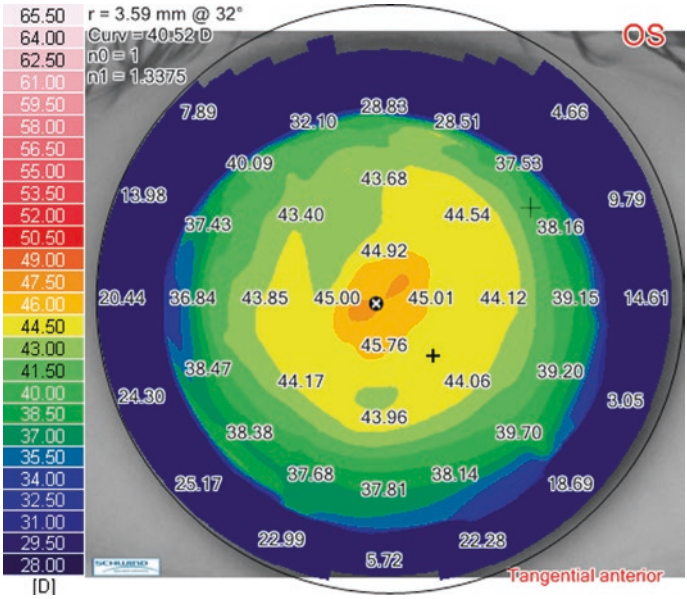

Fig. 12 Corneal curvature distribution with tangential map (*With permission from CSO*)

Keratoconus Screening

This display contains important information about the patient's cornea using neural network artificial intelligence software (**Phoenix software**) to prevent post-surgery ectasia. This combines a suite of diagnostic equipment including:

- **SIf**: (Symmetry Index front) The Symmetry Index of the anterior curvature
- **SIb**: (Symmetry Index back) The Symmetry Index of the posterior curvature
- **KVf**: (Keratoconus Vertex front) the Highest point of ectasia on the anterior corneal surface.
- **KVb**: (Keratoconus Vertex back) the Highest point of ectasia on the anterior corneal surface
- **BCVf/b**: Baiocchi Calossi Versaci (HOAs)
- **ThkMin**: Thinnest pint of the cornea (Fig. 14).

Based on the analysis of the 3502 maps including 1280 healthy (normal) eyes, 877 keratoconus eyes, 426 subclinical keratoconus eyes, and 940 eyes with a history of refractive surgery and using artificial intelligence software, the corneas into one of the following 5 categories with high accuracy (>90%): Normal eye, suspect keratoconus (Borderline—check parameters), keratoconus compatible, abnormal or treated and myopic post-operation

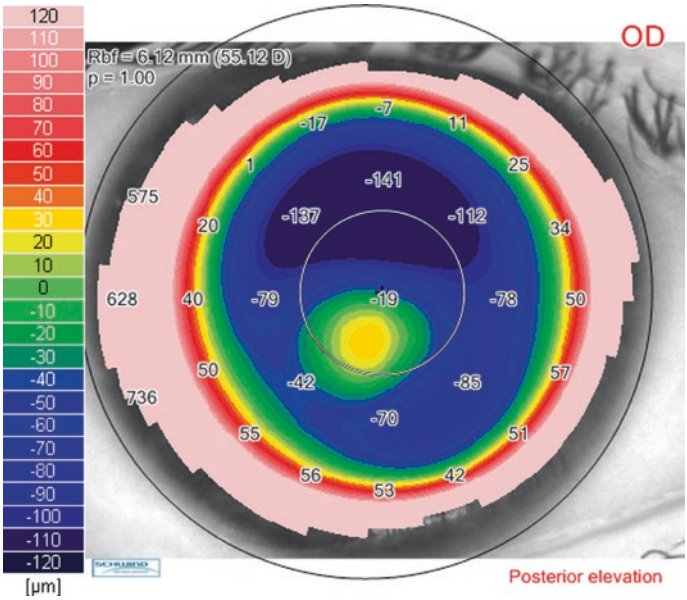

Fig. 13 Corneal curvature distribution based on spherical reference (*With permission from CSO*)

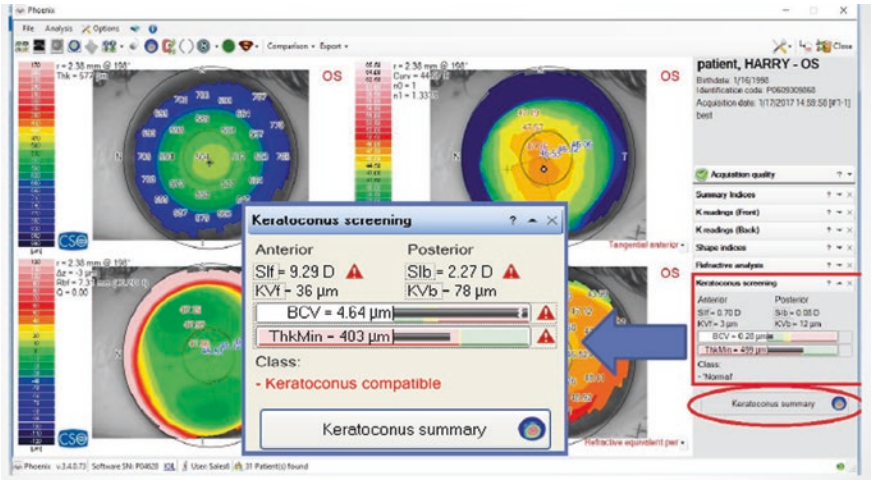

Fig. 14 Keratoconus screening Summary (*With permission from CSO*)

SI_f and SI_b

Curvature-based information is extracted by drawing a circle with a radius of 1.5 mm and centers of (0, +1.5) and (0, −1.5) mm. The presence of keratoconus is shown by determining the difference of average size in the superior and inferior hemispheres.

In the keratoconus eye, due to anatomic corneal deformity, it is expected higher curvature in the inferior half compared with the superior half, which this difference is very small for the healthy cornea. These measurements are performed for both the anterior and posterior cornea. We found SI_b is a sensitive parameter for subclinical keratoconus (SKCN) diagnosis [10], however, another study reported this index had high diagnostic ability among Sirius indices for the KCN detection [11] (Fig. 15).

KV_f and KV_b

Best Asphero-toric is used as a reference level to calculate the keratoconus vertex indices. This surface is used as a reference for modeling Elevation Information of Anterior and posterior Corneal within 8 mm Radius (Fig. 16). We evaluated 70 eyes with definite KCN and found KV_b had the perfect diagnostic ability (AUC ≥ 0.999) to distinguish KCN from normal corneas [10].

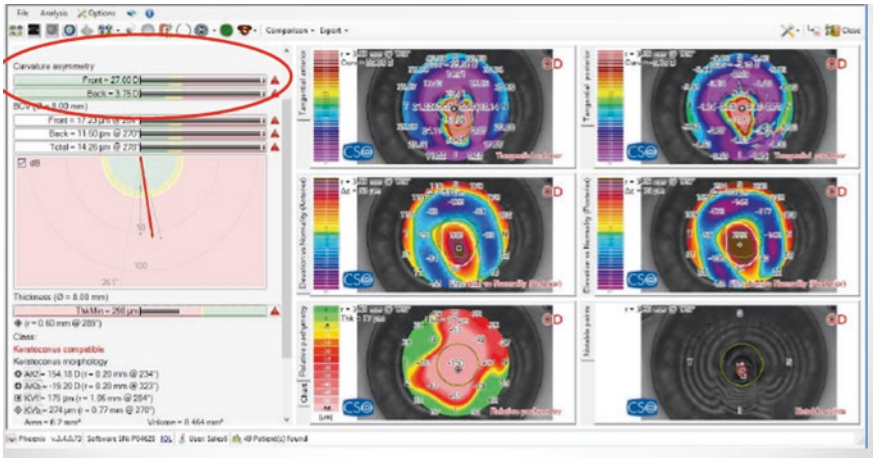

Fig. 15 Anterior and posterior corneal curvature information (*With permission from CSO*)

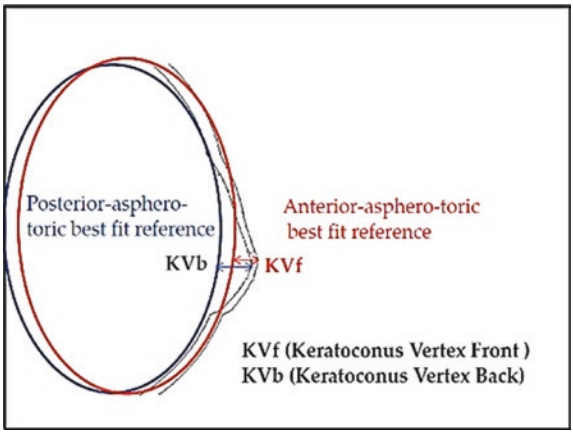

Fig. 16 Anterior and Posterior elevations from asphero-toric best fit reference (*With permission from Bahermahd Company*)

BCV

The BCV parameter is taken from the beginning of the name 3 scientists named Baiocchi, Calossi, Versaci who have conducted the research. Since the keratoconus statistically occurs in the infero-temporal part of the cornea, it is expected that the highest aberration will be observed in this area. The following HOA components are used in the calculation of the BCV index:

Vertical trefoil Z_3^{-3}
Vertical coma Z_3^{-1}
Horizontal coma Z_3^{+1}
Primary spherical aberration Z_0^4
Second-order vertical coma Z_5^{-1}.

The BCV parameter for the anterior and posterior corneal surfaces is calculated vectorially. In healthy corneas, the value of parameters is usually close to zero, or even if there are values greater than zero for the BCVf and BCVb, the total result will cer tainly be close to zero. We compared the accuracy of three devices (Pentacam, Sirius and OPD-Scan III) to differentiate SKCN from normal corneas by wavefront parameters, and found the front BCV of Sirius was the most accurate parameter in all 3 devises [12] (Fig. 17).

ThkMin

One of the important keratoconus characteristics is corneal thinning. The software analyzes the entire surface of the cornea and detects the thinnest corneal thickness in the 8 mm zone. The corneal thickness is assessed by analyzing the whole corneal surface and comparing it with the thinnest normal healthy cornea (Fig. 18).

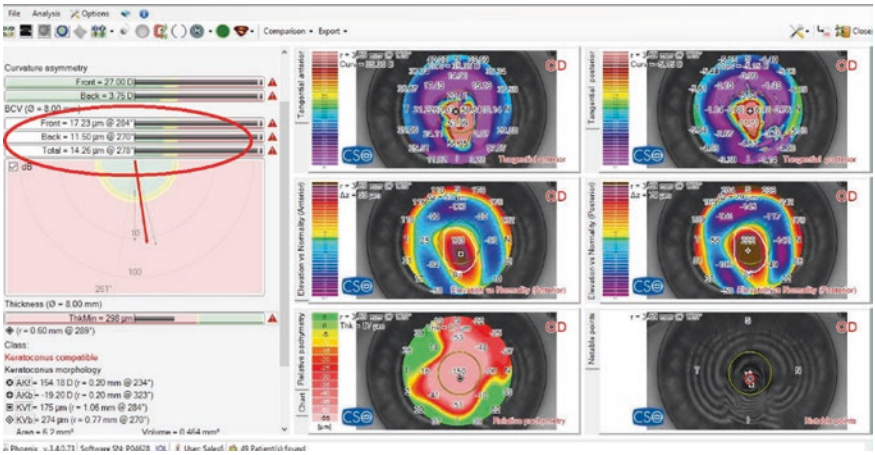

Fig. 17 Main aberrometric corneal wave-front deviation (*With permission from CSO*)

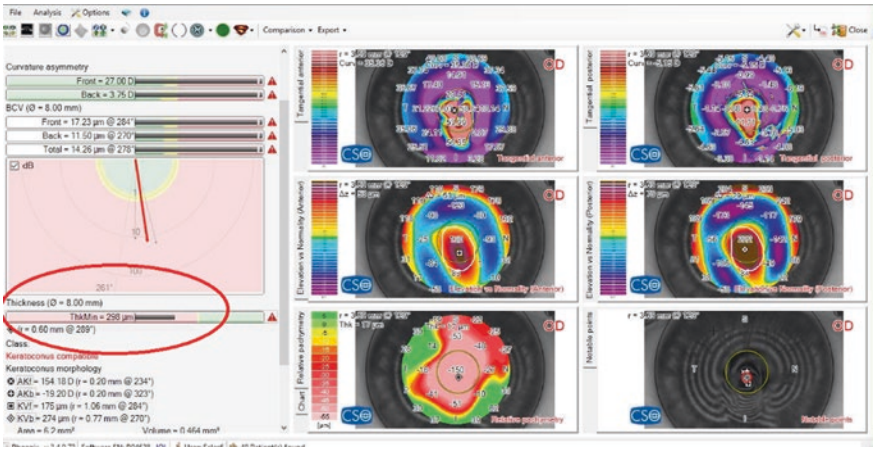

Fig. 18 Minimal Corneal Thickness (*With permission from CSO*)

Anterior and posterior tangential map, anterior and posterior elevation map and pachymetric map are visible on one page. The cone for each of the maps is displayed along with the thinnest point (Fig. 19).

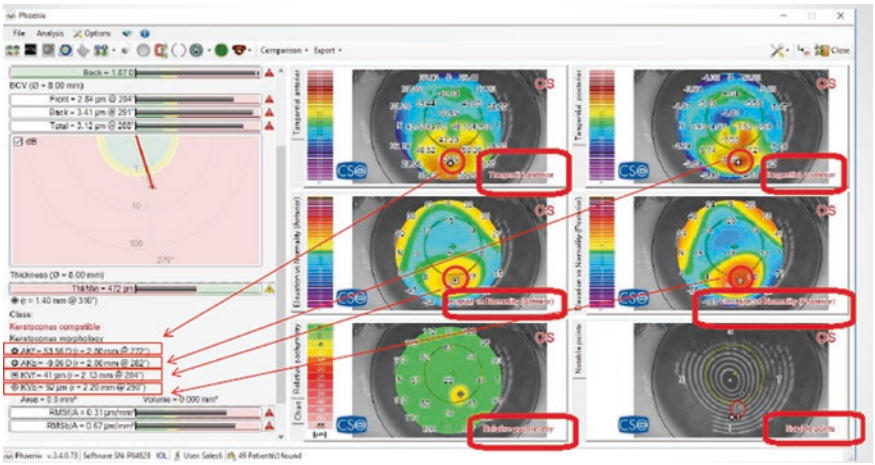

Fig. 19 Curvature, elevation, and pachymetric information in one map (*With permission from CSO*)

AKf—Apical Keratoscopy Front; the Steepest point of the anterior corneal surface

AKb—Apical Keratoscopy Back; the Steepest point of the posterior corneal surface

KVf—Keratoconus Vertex Front; The highest point of ectasia on the anterior corneal surface

KVb—Keratoconus Vertex Back; The highest point of ectasia on the posterior corneal surface

Thinnest point of the cornea (ThkMin—Minimum Thickness).

In suspect keratoconus cases, these points are close to each other and the red circle will have a smaller radius (Fig. 20). The Sirius keratoconus screening parameters could classify SKCN and KCN corneas effectively [13].

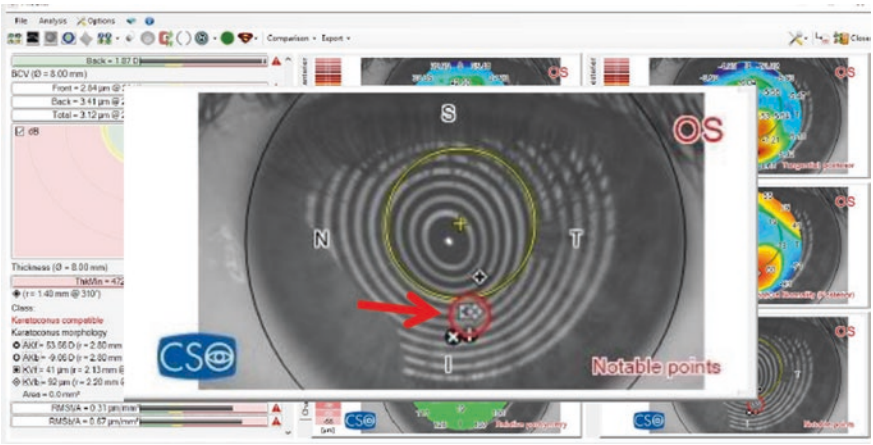

Fig. 20 The coincidence of abnormal indices in keratoconus (*With permission from CSO*)

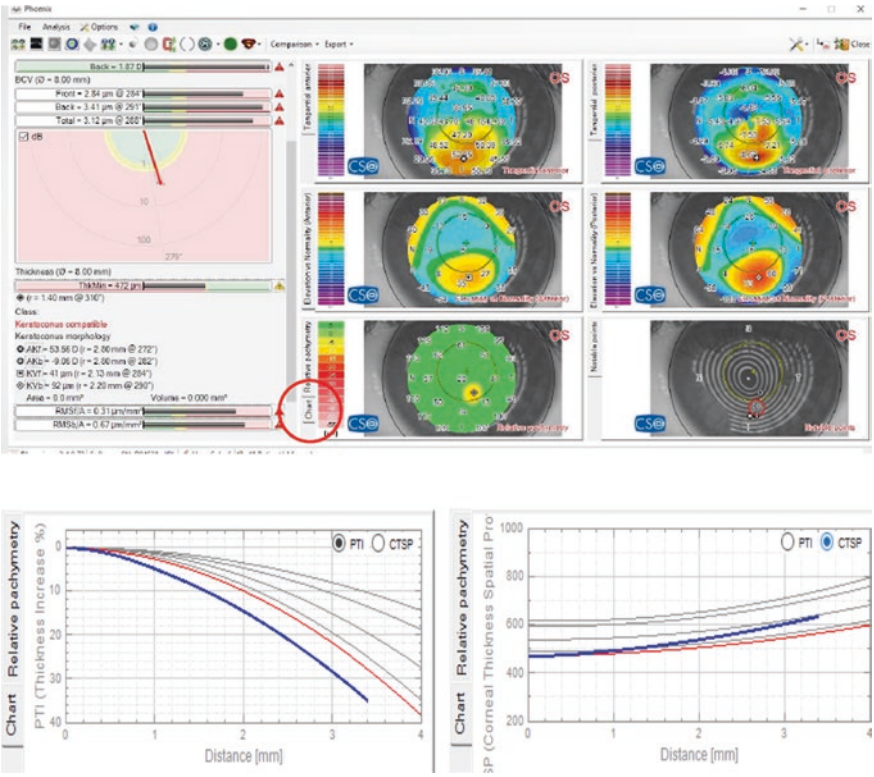

Fig. 21 Corneal Thickness spatial profile and percentage thickness increase diagrams (*With permission from CSO*)

PTI and CTSP

The corneal thickness is illustrated in the corneal thickness spatial profile (CTSP) and percentage thickness increase (PTI) diagrams. The location of the PTI and CTSP diagrams at different radii is shown in the figure with a red circle (Fig. 21).

Case Study

Case 1.

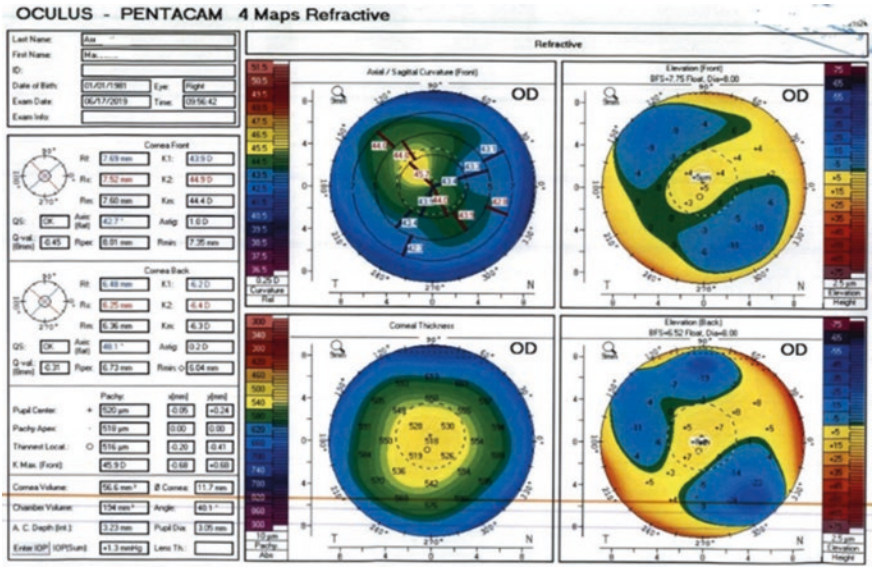

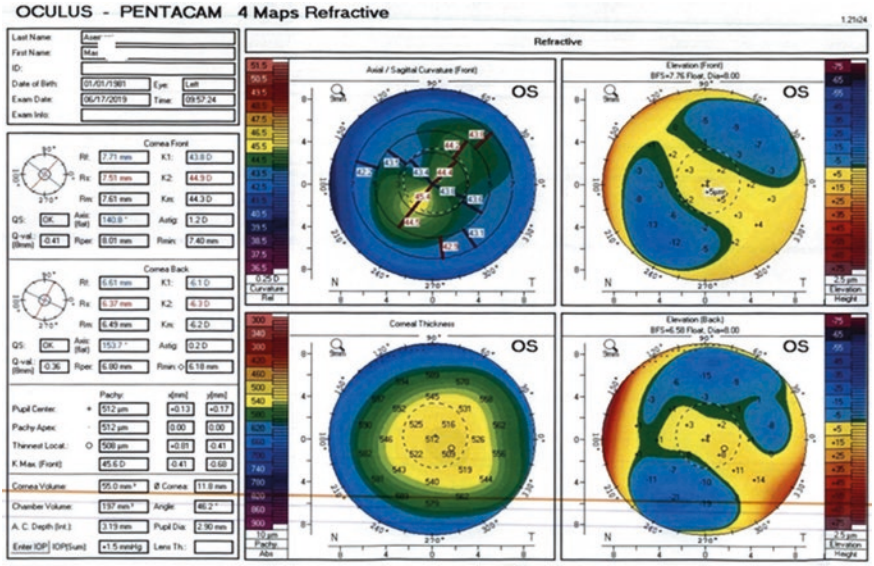

Fig. 22 A 37-year woman with the clear cornea, and manifest refractive error: OD = −7.25/−1.00~50 corrected distance visual acuity (CDVA) = 9/10 and OS = −6.00/−0.75~145 CDVA = 9/10. There are superior steepening in the right eye and inferior steepening in the left eye in Pentacam axial maps with normal pachymetric and elevation maps

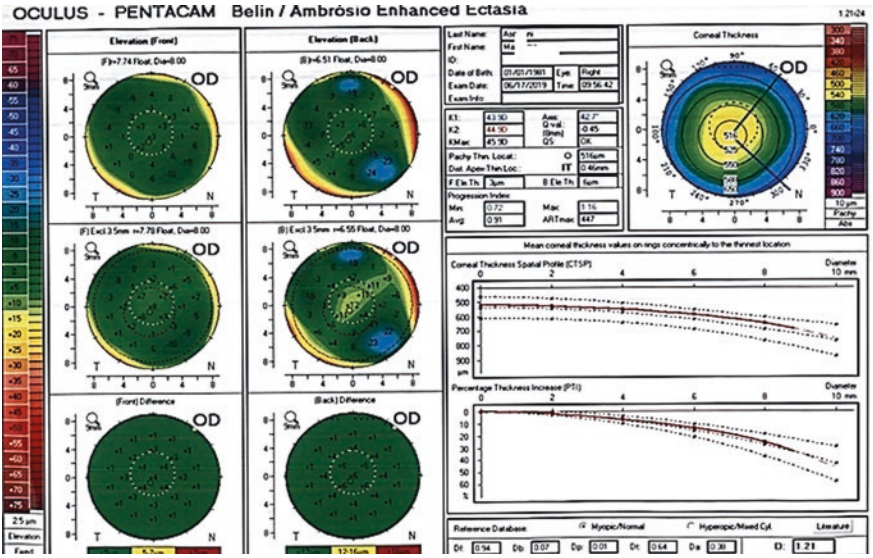

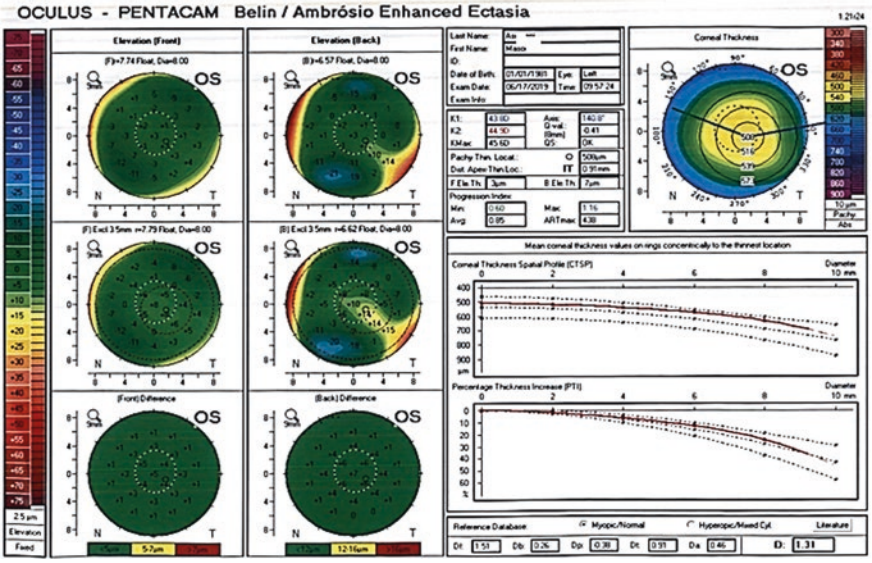

Fig. 23 Belin-Ambrosio display including D index, thickness and difference maps are normal in both eyes of the same patient

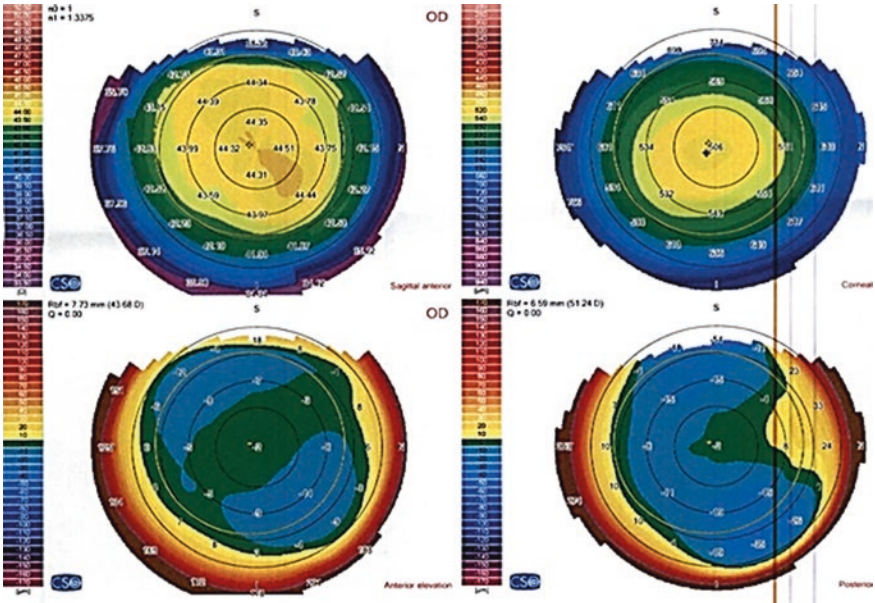

Acquisition quality	Coverage(SC.) = 97%	Not edited(SC.) = 100%
	Coverage(P.) = 84%	Centration(P.) = 93%

Summary Indices

HVID = 11.84 mm
Pupil (Topographic)
= 0.31 mm @ 151°
Ø = 6.82 mm
intercept: r = 0.73 mm @ 151°
Thinnest location
= 0.40 mm @ 210°
Thk = 505 µm
Apex
= 0.60 mm @ 329°
Curv = 45.12 D
Anterior chamber
CCT + AD =
0.506 + 3.25 = 3.76 mm
Volume = 154 mm³
Iridocorneal angle = 50°
HACD = 12.06 mm
Lens rise = 0.21 mm
Corneal volume (Ø=10mm)
Volume = 54.7 mm³

K readings n0 = 1 n1 = 1.3375

Sim-k	K1 = 43.86 D @ 37°
	K2 = 44.71 D @ 127°
	Avg = 44.28 D
	Cyl = -0.85 D Ax 37°
Anterior Ø=3mm	K1 = 44.06 D @ 44°
	K2 = 44.72 D @ 134°
	Avg = 44.39 D
	Cyl = -0.66 D Ax 44°
Anterior Ø=5mm	K1 = 43.91 D @ 39°
	K2 = 44.67 D @ 129°
	Avg = 44.29 D
	Cyl = -0.77 D Ax 39°
Anterior Ø=7mm	K1 = 43.72 D @ 39°
	K2 = 44.38 D @ 129°
	Avg = 44.05 D
	Cyl = -0.66 D Ax 39°

K readings n1 = 1.376 n2 = 1.336

Posterior Ø=3mm	K1 = -6.07 D @ 18°
	K2 = -6.35 D @ 108°
	Avg = -6.21 D
	Cyl = +0.28 D Ax 18°
Posterior Ø=5mm	K1 = -6.06 D @ 17°
	K2 = -6.28 D @ 107°
	Avg = -6.17 D
	Cyl = +0.22 D Ax 17°
Posterior Ø=7mm	K1 = -6.06 D @ 20°
	K2 = -6.24 D @ 110°
	Avg = -6.15 D
	Cyl = +0.18 D Ax 20°

Refractive analysis

Ø=4.0mm
Cyl = -0.62 D Ax 49°
MPP = 43.93 D
LSA = 0.89 D

Keratoconus screening

SIf = -0.16 D
KVf = 3 µm
BCVf = 0.00 D @ 108°
SIb = -0.04 D
KVb = 13 µm
BCVb = 0.00 D @ 252°
Thk = 505 µm
Class:
- 'Normal'

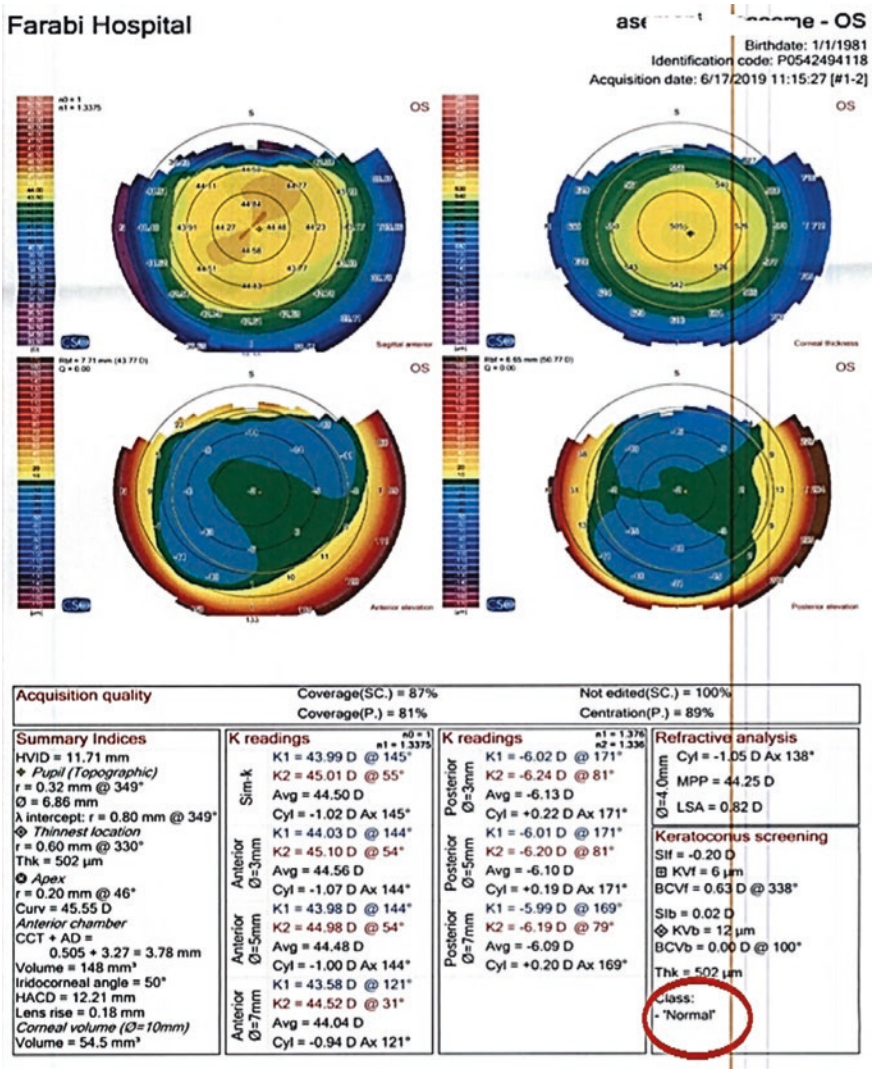

Fig. 24 The Sirius keratoconus screening software of the same patient shows normal classification in both eyes

Case 2.

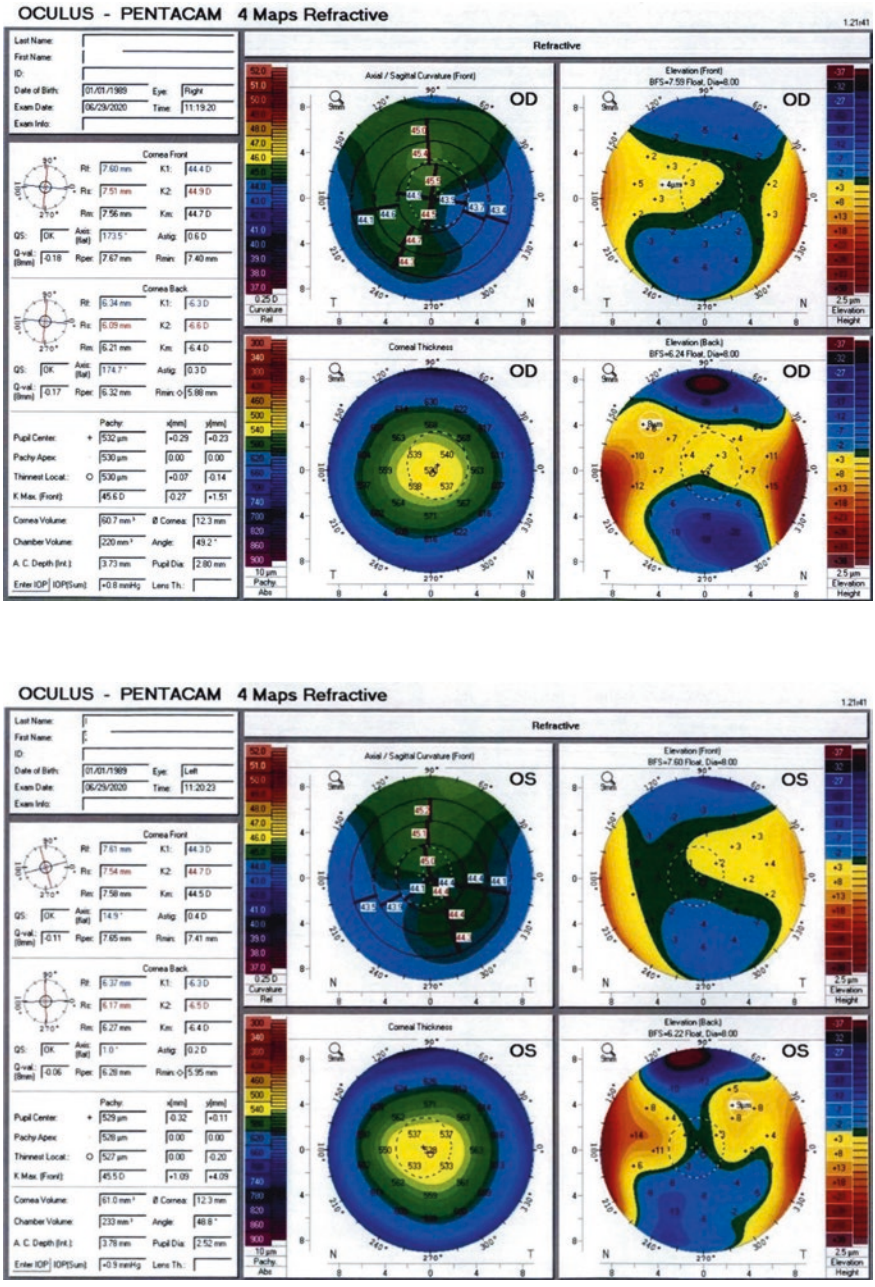

Fig. 25 A 29-year-old woman with family history of keratoconus and refractive errors: OD −5.50/−0.75~100 and CDVA = 10/10, OS −5.50/−0.75~90 and CDVA = 10/10. There are superior steepening in both eyes in Pentacam axial maps with normal pachymetric and elevation values

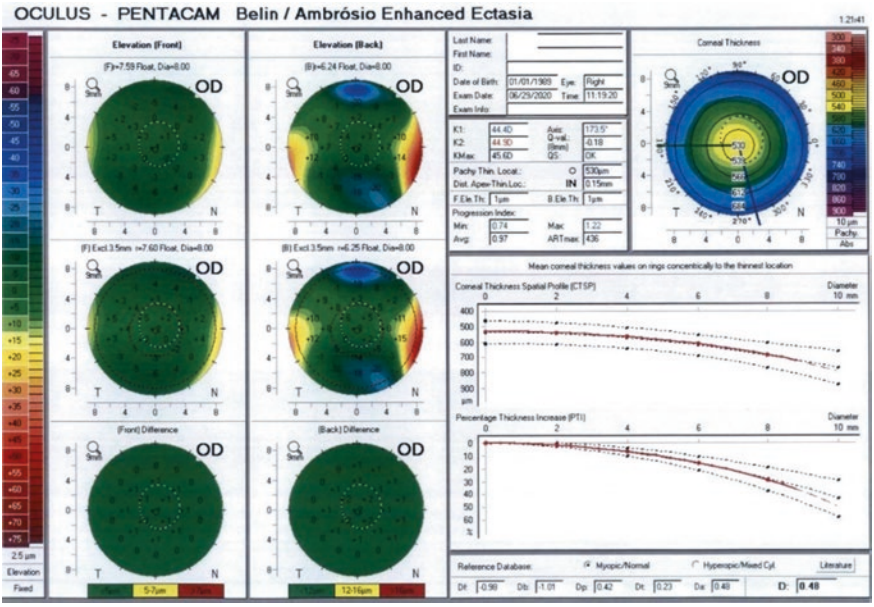

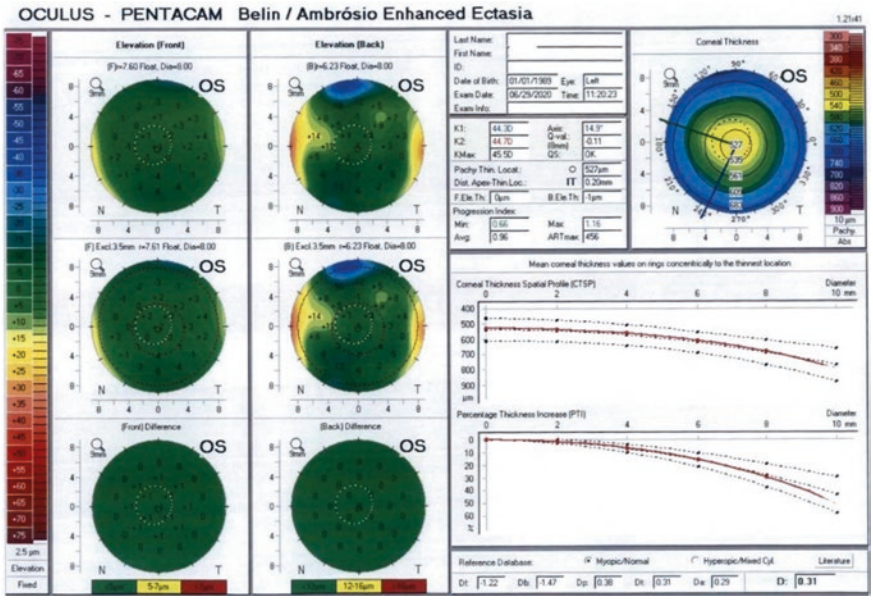

Fig. 26 Belin-Ambrosio display including D index, thickness and difference maps are normal in both eyes of the same patient

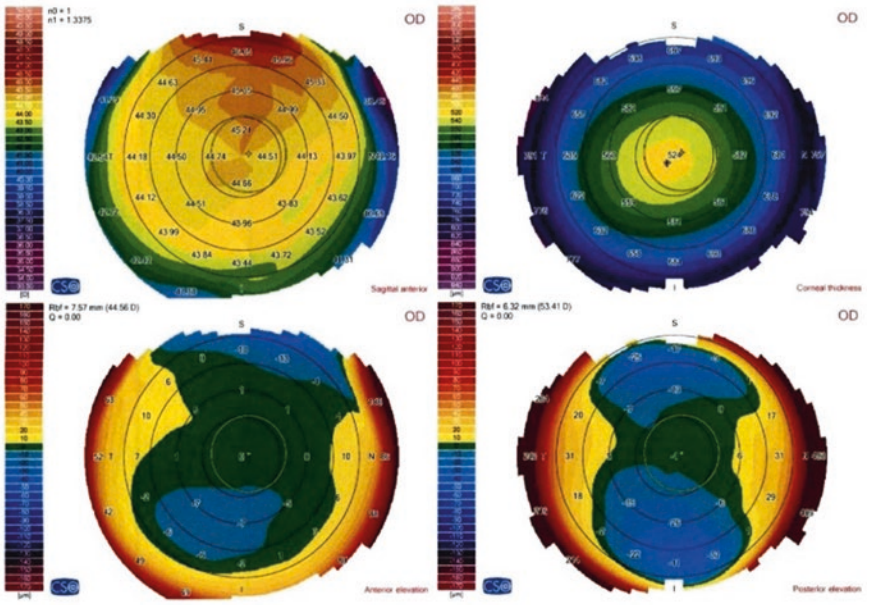

Acquisition quality	Coverage(SC.) = 99%	Not edited(SC.) = 100%
	Coverage(P.) = 84%	Centration(P.) = 90%

Summary Indices

HVID = 12.63 mm
Pupil (Topographic)
r = 0.29 mm @ 22°
Ø = 2.86 mm
λ intercept: r = 0.81 mm @ 22°
Thinnest location
r = 0.40 mm @ 223°
Thk = 523 µm
Apex
r = 3.40 mm @ 87°
Curv = 46.74 D
Anterior chamber
CCT + AD =
0.524 + 3.73 = 4.25 mm
Volume = 209 mm³
Iridocorneal angle = 53°
HACD = 12.40 mm
Lens rise = 0.05 mm
Corneal volume (Ø=10mm)
Volume = 58.5 mm³

K readings (n0 = 1, n1 = 1.3375)

Sim-k	K1 = 44.43 D @ 156°
	K2 = 44.90 D @ 66°
	Avg = 44.66 D
	Cyl = -0.47 D Ax 156°
Anterior Ø=3mm	K1 = 44.53 D @ 157°
	K2 = 44.99 D @ 67°
	Avg = 44.76 D
	Cyl = -0.47 D Ax 157°
Anterior Ø=5mm	K1 = 44.44 D @ 156°
	K2 = 44.91 D @ 66°
	Avg = 44.68 D
	Cyl = -0.47 D Ax 156°
Anterior Ø=7mm	K1 = 44.35 D @ 159°
	K2 = 44.88 D @ 69°
	Avg = 44.61 D
	Cyl = -0.53 D Ax 159°

K readings (n1 = 1.376, n2 = 1.336)

Posterior Ø=3mm	K1 = -6.24 D @ 177°
	K2 = -6.57 D @ 87°
	Avg = -6.40 D
	Cyl = +0.32 D Ax 177°
Posterior Ø=5mm	K1 = -6.23 D @ 177°
	K2 = -6.56 D @ 87°
	Avg = -6.40 D
	Cyl = +0.33 D Ax 177°
Posterior Ø=7mm	K1 = -6.25 D @ 178°
	K2 = -6.54 D @ 88°
	Avg = -6.39 D
	Cyl = +0.29 D Ax 178°

Refractive analysis

Ø=4.0mm
Cyl = -0.49 D Ax 148°
MPP = 44.19 D
LSA = 0.71 D

Keratoconus screening

Slf = -1.06 D
KVf = 4 µm
BCVf = 0.00 D @ 111°
Slb = -0.13 D
KVb = 11 µm
BCVb = 0.00 D @ 69°
Thk = 523 µm
Class:
Normal

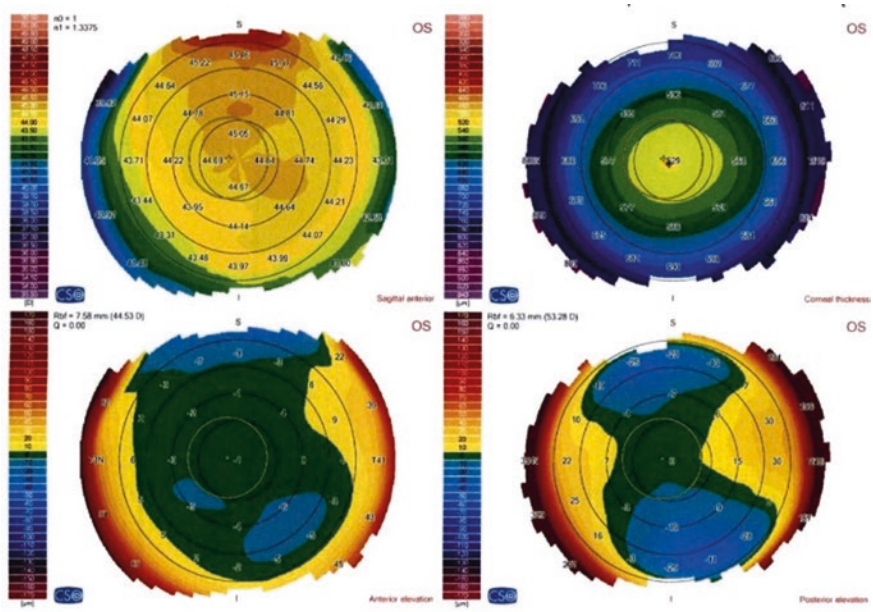

Acquisition quality	Coverage(SC.) = 99%	Not edited(SC.) = 100%
	Coverage(P.) = 89%	Centration(P.) = 88%

Summary Indices

HVID = 12.67 mm
Pupil (Topographic)
r = 0.39 mm @ 166°
Ø = 3.02 mm
λ intercept: r = 1.13 mm @ 166°
Thinnest location
r = 0.20 mm @ 208°
Thk = 529 µm
Apex
r = 3.40 mm @ 88°
Curv = 45.61 D
Anterior chamber
CCT + AD =
0.529 + 3.81 = 4.34 mm
Volume = 208 mm³
Iridocorneal angle = 55°
HACD = 12.33 mm
Lens rise = 0.07 mm
Corneal volume (Ø=10mm)
Volume = 59.0 mm³

K readings (n0 = 1, n1 = 1.3375)

Sim-k	K1 = 44.50 D @ 40°
	K2 = 44.85 D @ 130°
	Avg = 44.68 D
	Cyl = -0.34 D Ax 40°
Anterior Ø=3mm	K1 = 44.67 D @ 44°
	K2 = 44.96 D @ 134°
	Avg = 44.81 D
	Cyl = -0.29 D Ax 44°
Anterior Ø=5mm	K1 = 44.55 D @ 40°
	K2 = 44.87 D @ 130°
	Avg = 44.71 D
	Cyl = -0.32 D Ax 40°
Anterior Ø=7mm	K1 = 44.45 D @ 32°
	K2 = 44.80 D @ 122°
	Avg = 44.63 D
	Cyl = -0.35 D Ax 32°

K readings (n1 = 1.376, n2 = 1.336)

Posterior Ø=3mm	K1 = -6.14 D @ 10°
	K2 = -6.49 D @ 100°
	Avg = -6.31 D
	Cyl = +0.35 D Ax 10°
Posterior Ø=5mm	K1 = -6.16 D @ 12°
	K2 = -6.51 D @ 102°
	Avg = -6.33 D
	Cyl = +0.34 D Ax 12°
Posterior Ø=7mm	K1 = -6.19 D @ 13°
	K2 = -6.50 D @ 103°
	Avg = -6.34 D
	Cyl = +0.31 D Ax 13°

Refractive analysis

Ø=4.0mm
Cyl = -0.28 D Ax 59°
MPP = 44.26 D
LSA = 0.52 D

Keratoconus screening

Sif = -0.73 D
KVf = 4 µm
BCVf = 0.00 D @ 37°
Sfb = -0.12 D
KVb = 10 µm
BCVb = 0.00 D @ 9°
Thk = 529 µm
Class:
Normal

Fig. 27 These findings are consistent with the diagnosis of Phoenix Sirius software, which shows normal corneas in both eyes of the same patient

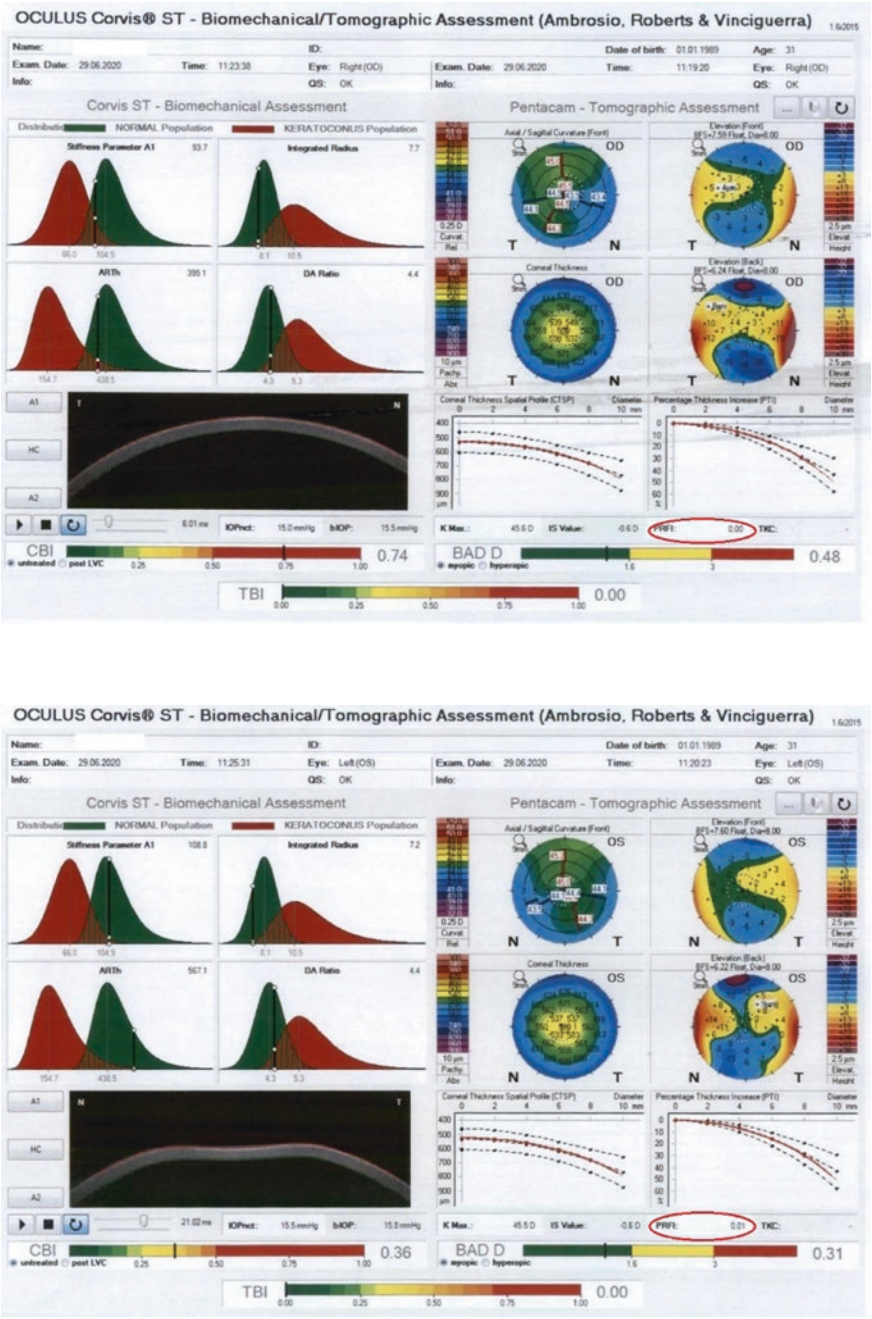

Fig. 28 Combined biomechanical and topographical indices including TBI and BADD and new Pentacam random forest index (PRFI) are normal in both eyes of the same patient, however the Corvis biomechanical indices (CBI) are abnormal in both eyes. Regular follow-up is recommended for KCN family history and possibly poor corneal biomechanics

Case 3.

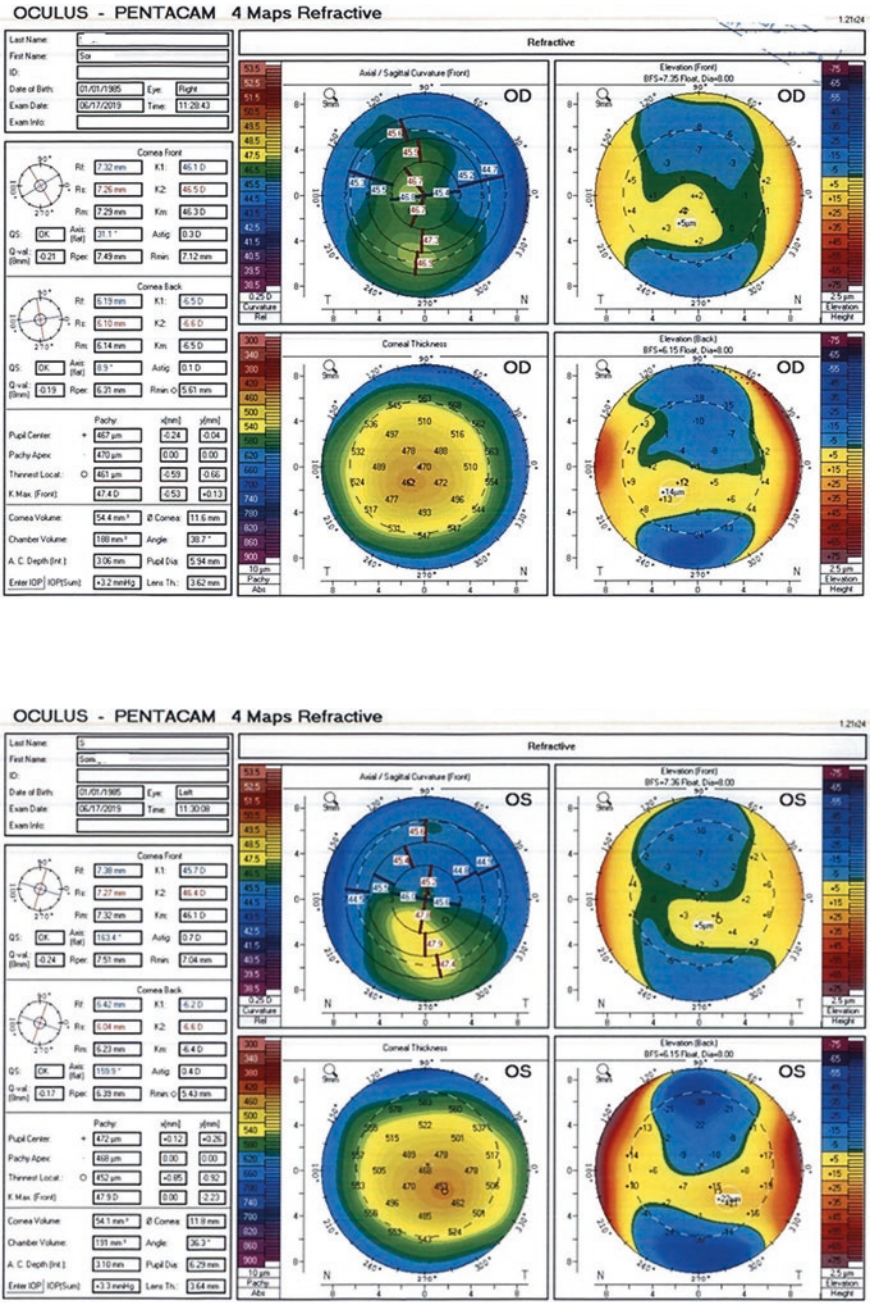

Fig. 29 A 34-year-old woman with subclinical keratoconus and refractive error OU = −3.00/−0.50~180 and CDVA = 10/10 OU. Pentacam Quad maps indices are in normal range with an inferior steepening pattern in axial maps

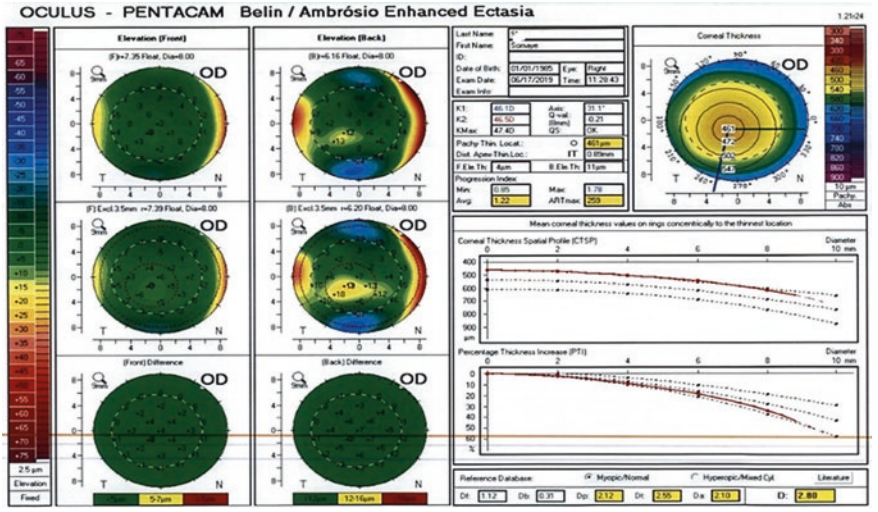

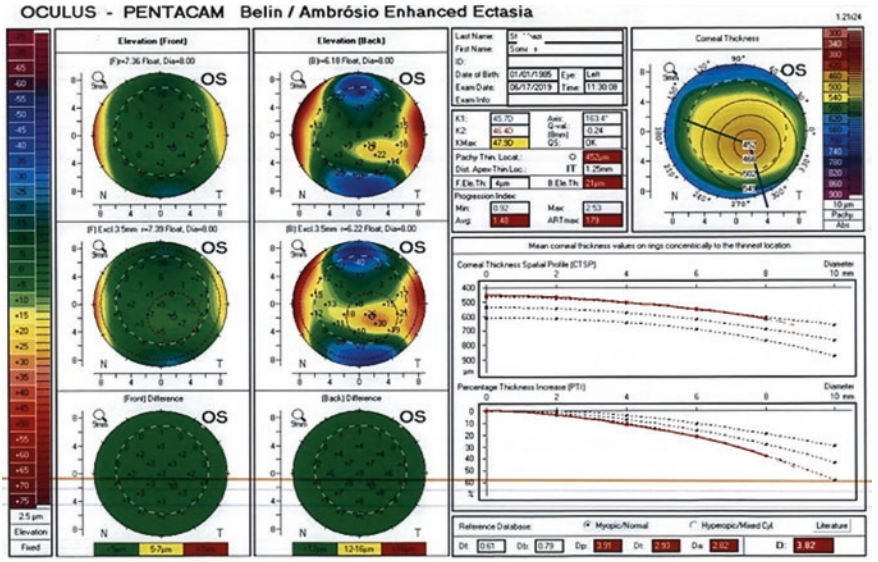

Fig. 30 Belin/Ambrosio display of the same patient shows normal difference maps and abnormal values in D index and thickness graphs

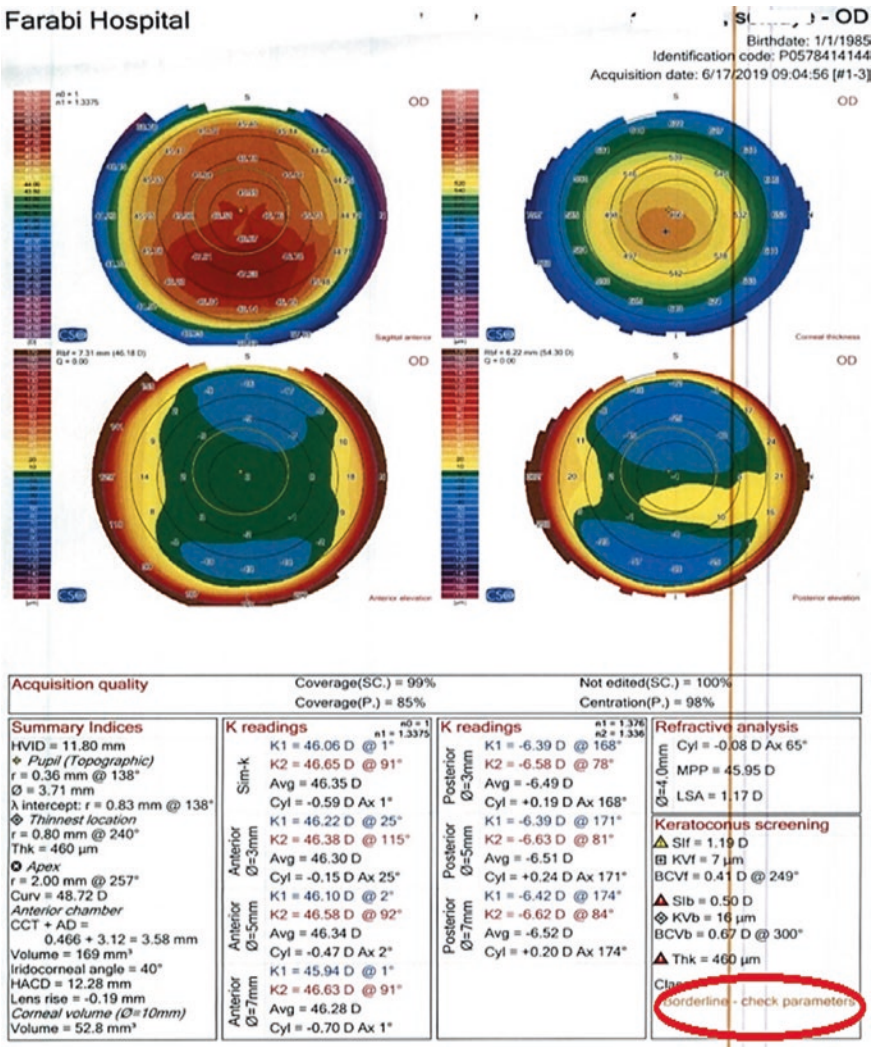
Farabi Hospital
- OD
Birthdate: 1/1/1985
Identification code: P0578414144
Acquisition date: 6/17/2019 09:04:56 [#1-3]
OD
Sagittal anterior
Corneal thickness
Anterior elevation
Posterior elevation
Acquisition quality
Coverage(SC.) = 99%
Coverage(P.) = 85%
Not edited(SC.) = 100%
Centration(P.) = 98%
Summary Indices
HVID = 11.80 mm
Pupil (Topographic)
r = 0.36 mm @ 138°
Ø = 3.71 mm
λ intercept: r = 0.83 mm @ 138°
Thinnest location
r = 0.80 mm @ 240°
Thk = 460 µm
Apex
r = 2.00 mm @ 257°
Curv = 48.72 D
Anterior chamber
CCT + AD =
0.466 + 3.12 = 3.58 mm
Volume = 169 mm³
Iridocorneal angle = 40°
HACD = 12.28 mm
Lens rise = -0.19 mm
Corneal volume (Ø=10mm)
Volume = 52.8 mm³
K readings
Sim-k
K1 = 46.06 D @ 1°
K2 = 46.65 D @ 91°
Avg = 46.35 D
Cyl = -0.59 D Ax 1°
Anterior Ø=3mm
K1 = 46.22 D @ 25°
K2 = 46.38 D @ 115°
Avg = 46.30 D
Cyl = -0.15 D Ax 25°
Anterior Ø=5mm
K1 = 46.10 D @ 2°
K2 = 46.58 D @ 92°
Avg = 46.34 D
Cyl = -0.47 D Ax 2°
Anterior Ø=7mm
K1 = 45.94 D @ 1°
K2 = 46.63 D @ 91°
Avg = 46.28 D
Cyl = -0.70 D Ax 1°
K readings
Posterior Ø=3mm
K1 = -6.39 D @ 168°
K2 = -6.58 D @ 78°
Avg = -6.49 D
Cyl = +0.19 D Ax 168°
Posterior Ø=5mm
K1 = -6.39 D @ 171°
K2 = -6.63 D @ 81°
Avg = -6.51 D
Cyl = +0.24 D Ax 171°
Posterior Ø=7mm
K1 = -6.42 D @ 174°
K2 = -6.62 D @ 84°
Avg = -6.52 D
Cyl = +0.20 D Ax 174°
Refractive analysis
Ø=4.0mm
Cyl = -0.08 D Ax 65°
MPP = 45.95 D
LSA = 1.17 D
Keratoconus screening
Sif = 1.19 D
KVf = 7 µm
BCVf = 0.41 D @ 249°
Sib = 0.50 D
KVb = 16 µm
BCVb = 0.67 D @ 300°
Thk = 460 µm
Cla
Borderline - check parameters

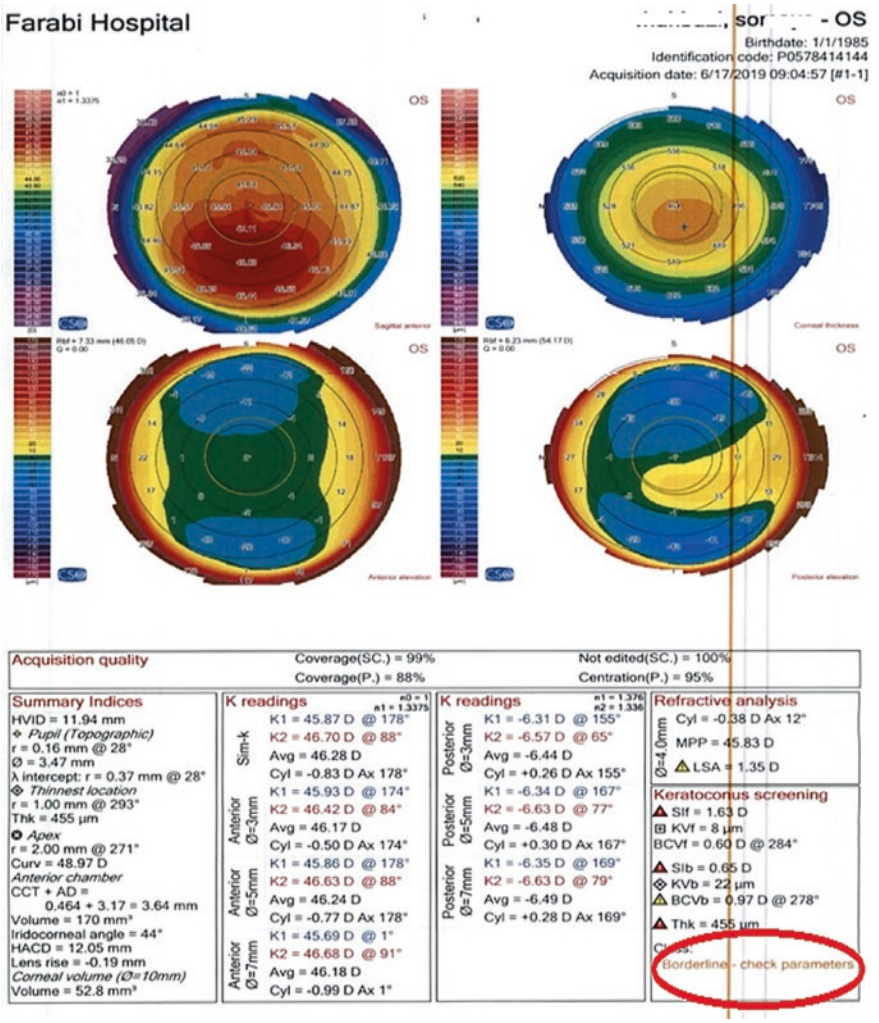

Fig. 31 These findings are consistent with the diagnosis of Phoenix Sirius software in the same patient, which shows borderline parameters and indicates corneal abnormalities

Case 4.

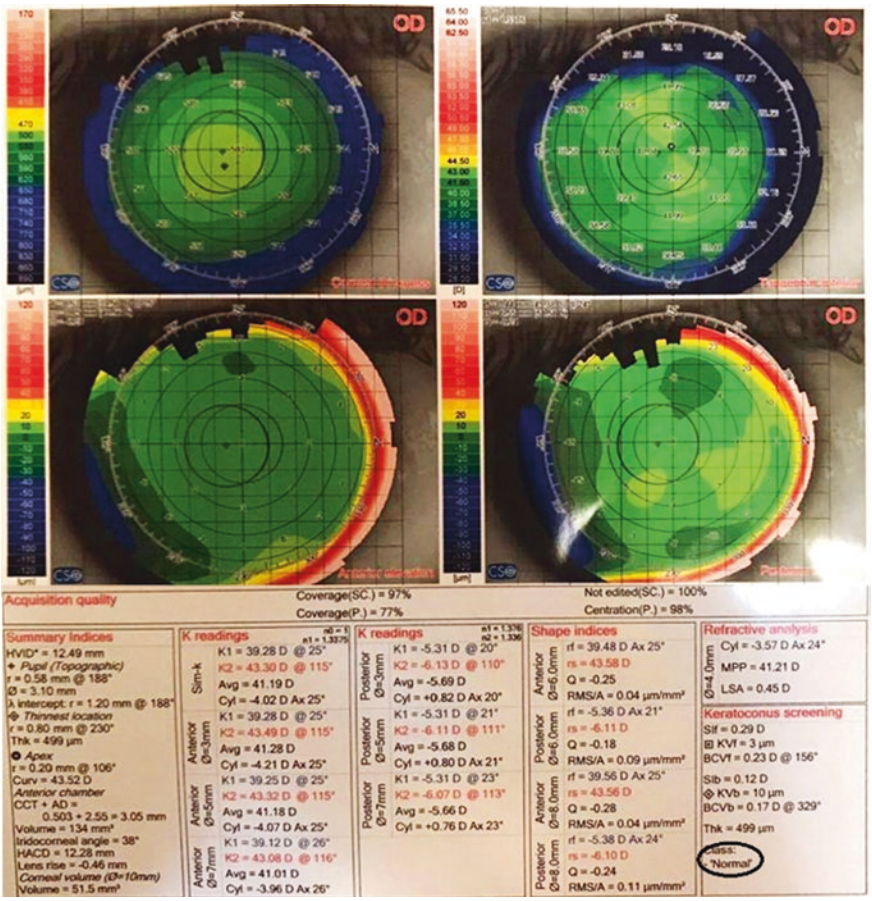
OD
OD
OD
OD
Acquisition quality
Coverage(SC.) = 97%
Coverage(P.) = 77%
Not edited(SC.) = 100%
Centration(P.) = 98%
Summary Indices
HVID* = 12.49 mm
✦ Pupil (Topographic)
r = 0.58 mm @ 188°
Ø = 3.10 mm
λ intercept: r = 1.20 mm @ 188°
✧ Thinnest location
r = 0.80 mm @ 230°
Thk = 499 µm
◉ Apex
r = 0.29 mm @ 106°
Curv = 43.52 D
Anterior chamber
CCT + AD =
0.503 + 2.55 = 3.05 mm
Volume = 134 mm³
Iridocorneal angle = 38°
HACD = 12.28 mm
Lens rise = -0.46 mm
Corneal volume (Ø=10mm)
Volume = 51.5 mm³
K readings
Sim-k
K1 = 39.28 D @ 25°
K2 = 43.30 D @ 115°
Avg = 41.19 D
Cyl = -4.02 D Ax 25°
Anterior Ø=3mm
K1 = 39.28 D @ 25°
K2 = 43.49 D @ 115°
Avg = 41.28 D
Cyl = -4.21 D Ax 25°
Anterior Ø=5mm
K1 = 39.25 D @ 25°
K2 = 43.32 D @ 115°
Avg = 41.18 D
Cyl = -4.07 D Ax 25°
Anterior Ø=7mm
K1 = 39.12 D @ 26°
K2 = 43.08 D @ 116°
Avg = 41.01 D
Cyl = -3.96 D Ax 26°
K readings
Posterior Ø=3mm
K1 = -5.31 D @ 20°
K2 = -6.13 D @ 110°
Avg = -5.69 D
Cyl = +0.82 D Ax 20°
Posterior Ø=5mm
K1 = -5.31 D @ 21°
K2 = -6.11 D @ 111°
Avg = -5.68 D
Cyl = +0.80 D Ax 21°
Posterior Ø=7mm
K1 = -5.31 D @ 23°
K2 = -6.07 D @ 113°
Avg = -5.66 D
Cyl = +0.76 D Ax 23°
Shape indices
Anterior Ø=6.0mm
rf = 39.48 D Ax 25°
rs = 43.58 D
Q = -0.25
RMS/A = 0.04 µm/mm²
Posterior Ø=6.0mm
rf = -5.36 D Ax 21°
rs = -6.11 D
Q = -0.18
RMS/A = 0.09 µm/mm²
Anterior Ø=8.0mm
rf = 39.56 D Ax 25°
rs = 43.56 D
Q = -0.28
RMS/A = 0.04 µm/mm²
Posterior Ø=8.0mm
rf = -5.38 D Ax 24°
rs = -6.10 D
Q = -0.24
RMS/A = 0.11 µm/mm²
Refractive analysis
Ø=4.0mm
Cyl = -3.57 D Ax 24°
MPP = 41.21 D
LSA = 0.45 D
Keratoconus screening
Sif = 0.29 D
KVf = 3 µm
BCVf = 0.23 D @ 156°
Sib = 0.12 D
KVb = 10 µm
BCVb = 0.17 D @ 329°
Thk = 499 µm
Class:
'Normal'

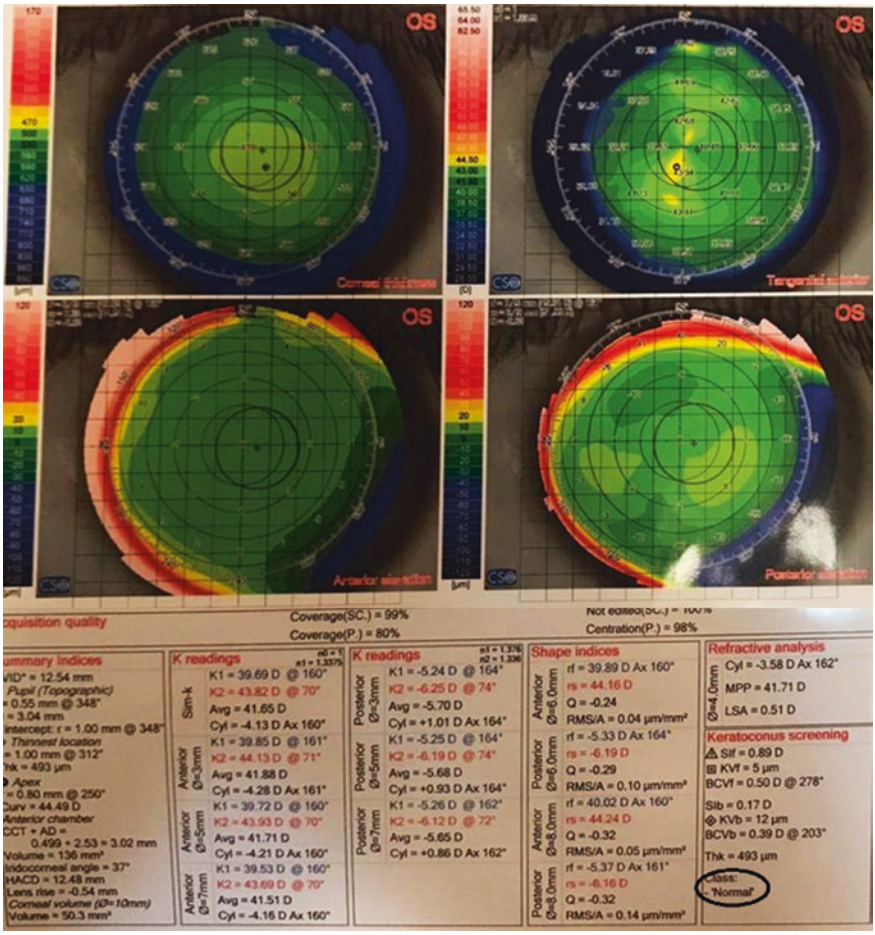

Fig. 32 A 45-year-old man with keratoconus suspect in his both eyes and refractive errors OD +2.50/−5.00~25 and OS +2.5/−5.00~158. He is a candidates for refractive surgery. The classification of Sirius Phoenix software seems to be normal due to the fixed 1.5 drop scale, which results in the loss of the true shape of the cornea and miss the early form of keratoconus

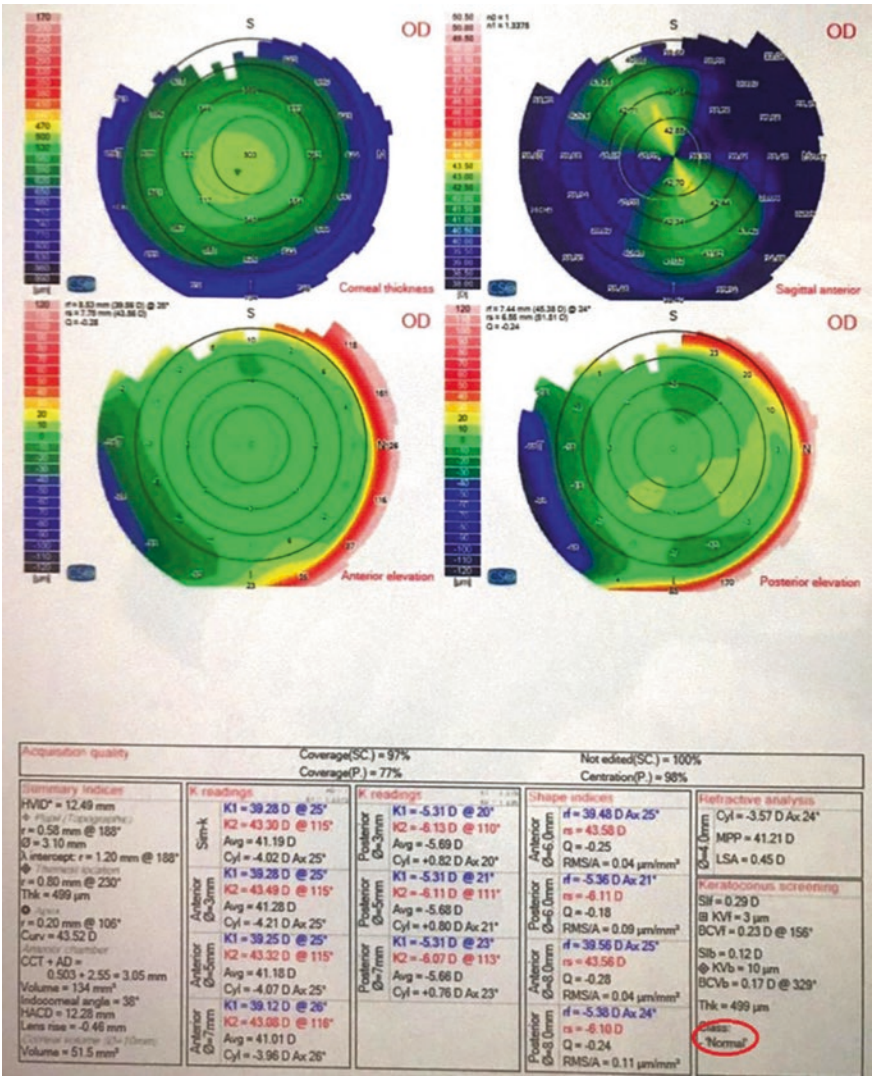
S
OD
Corneal thickness
Sagittal anterior
Anterior elevation
Posterior elevation
Acquisition quality
Coverage(SC.) = 97%
Coverage(P.) = 77%
Not edited(SC.) = 100%
Centration(P.) = 98%
Summary indices
HVID* = 12.49 mm
r = 0.58 mm @ 188°
Ø = 3.10 mm
λ intercept: r = 1.20 mm @ 188°
r = 0.80 mm @ 230°
Thk = 499 µm
r = 0.20 mm @ 106°
Curv = 43.52 D
CCT + AD = 0.503 + 2.55 = 3.05 mm
Volume = 134 mm³
Iridocorneal angle = 38°
HACD = 12.28 mm
Lens rise = -0.46 mm
Volume = 51.5 mm³
K readings
Sim-k
K1 = 39.28 D @ 25°
K2 = 43.30 D @ 115°
Avg = 41.19 D
Cyl = -4.02 D Ax 25°
Anterior Ø=3mm
K1 = 39.28 D @ 25°
K2 = 43.49 D @ 115°
Avg = 41.28 D
Cyl = -4.21 D Ax 25°
Anterior Ø=5mm
K1 = 39.25 D @ 25°
K2 = 43.32 D @ 115°
Avg = 41.18 D
Cyl = -4.07 D Ax 25°
Anterior Ø=7mm
K1 = 39.12 D @ 26°
K2 = 43.08 D @ 116°
Avg = 41.01 D
Cyl = -3.96 D Ax 26°
K readings
Posterior Ø=3mm
K1 = -5.31 D @ 20°
K2 = -6.13 D @ 110°
Avg = -5.69 D
Cyl = +0.82 D Ax 20°
Posterior Ø=5mm
K1 = -5.31 D @ 21°
K2 = -6.11 D @ 111°
Avg = -5.68 D
Cyl = +0.80 D Ax 21°
Posterior Ø=7mm
K1 = -5.31 D @ 23°
K2 = -6.07 D @ 113°
Avg = -5.66 D
Cyl = +0.76 D Ax 23°
Shape indices
Anterior Ø=6.0mm
df = 39.48 D Ax 25°
ds = 43.58 D
Q = -0.25
RMS/A = 0.04 µm/mm²
Posterior Ø=6.0mm
df = -5.36 D Ax 21°
ds = -6.11 D
Q = -0.18
RMS/A = 0.09 µm/mm²
Anterior Ø=8.0mm
df = 39.56 D Ax 25°
ds = 43.56 D
Q = -0.28
RMS/A = 0.04 µm/mm²
Posterior Ø=8.0mm
df = -5.38 D Ax 24°
ds = -6.16 D
Q = -0.24
RMS/A = 0.11 µm/mm²
Refractive analysis
Ø=4.0mm
Cyl = -3.57 D Ax 24°
MPP = 41.21 D
LSA = 0.45 D
Keratoconus screening
Sif = 0.29 D
KVf = 3 µm
BCVf = 0.23 D @ 156°
Sib = 0.12 D
KVb = 10 µm
BCVb = 0.17 D @ 329°
Thk = 499 µm
Class:
'Normal'

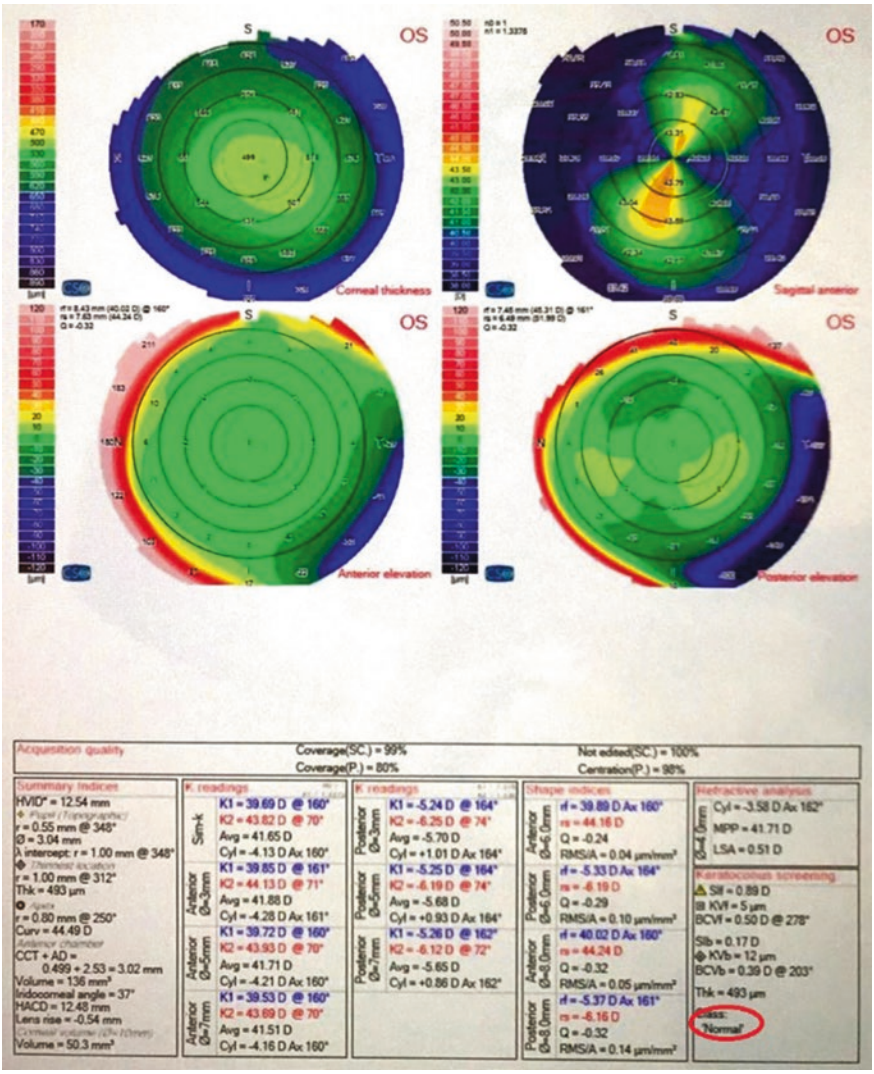

Fig. 33 Small central bow-tie better seen with 0.5 diopter scale

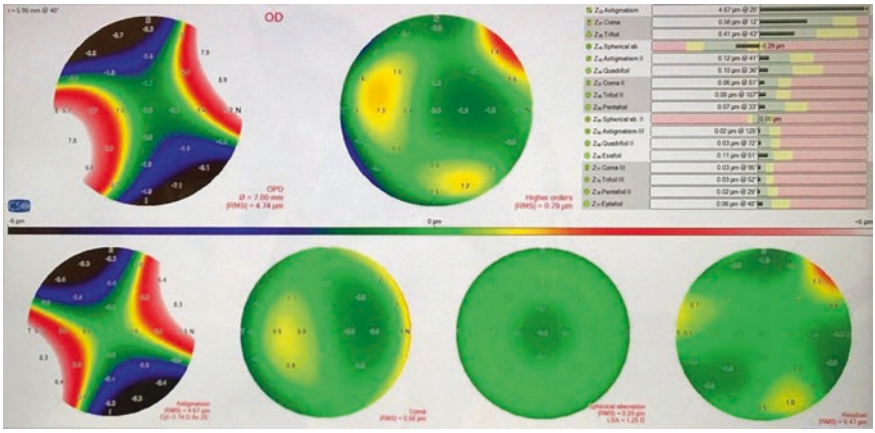

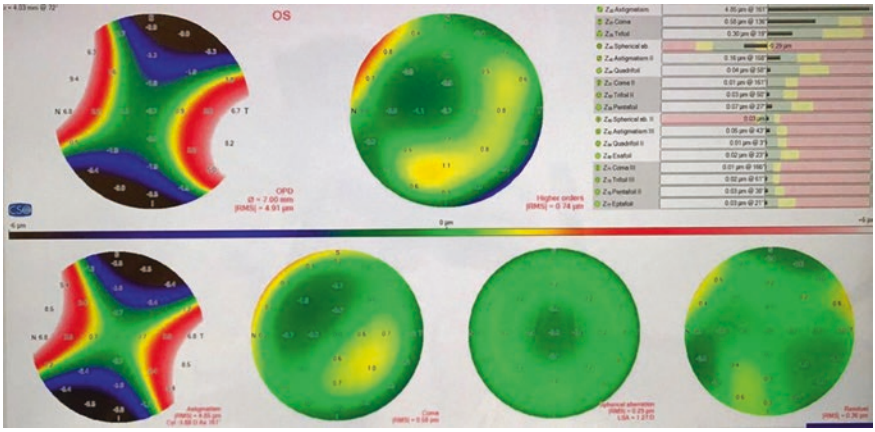

Fig. 34 Significant HOA mostly Coma in this case (case number 4) suggest early form of keratoconus

Case 5.

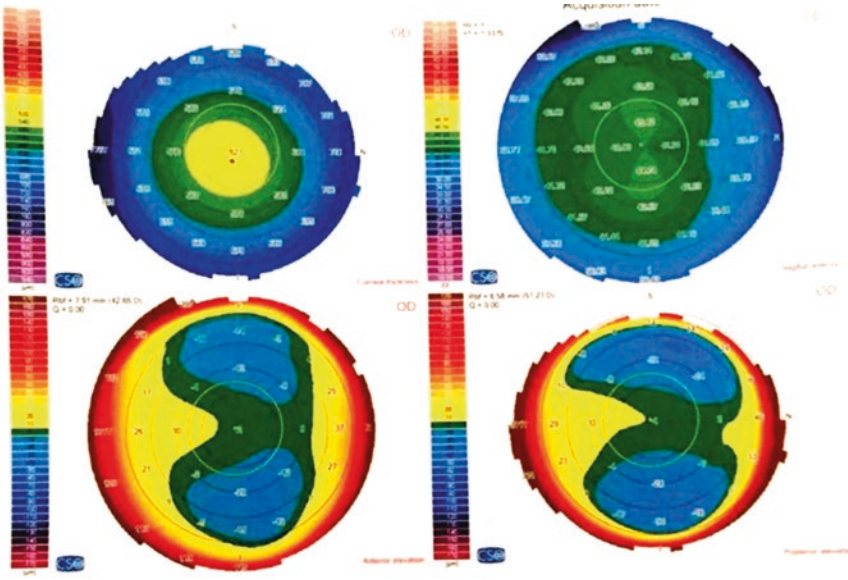

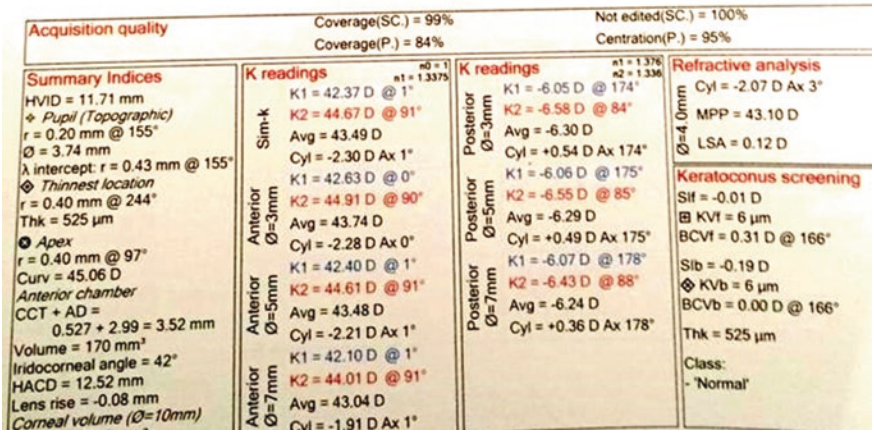
Acquisition quality
Coverage(SC.) = 99%
Coverage(P.) = 84%
Not edited(SC.) = 100%
Centration(P.) = 95%
Summary Indices
HVID = 11.71 mm
Pupil (Topographic)
r = 0.20 mm @ 155°
Ø = 3.74 mm
λ intercept: r = 0.43 mm @ 155°
Thinnest location
r = 0.40 mm @ 244°
Thk = 525 µm
Apex
r = 0.40 mm @ 97°
Curv = 45.06 D
Anterior chamber
CCT + AD =
0.527 + 2.99 = 3.52 mm
Volume = 170 mm³
Iridocorneal angle = 42°
HACD = 12.52 mm
Lens rise = -0.08 mm
Corneal volume (Ø=10mm)
K readings
n0 = 1
n1 = 1.3375
Sim-k
K1 = 42.37 D @ 1°
K2 = 44.67 D @ 91°
Avg = 43.49 D
Cyl = -2.30 D Ax 1°
Anterior Ø=3mm
K1 = 42.63 D @ 0°
K2 = 44.91 D @ 90°
Avg = 43.74 D
Cyl = -2.28 D Ax 0°
Anterior Ø=5mm
K1 = 42.40 D @ 1°
K2 = 44.61 D @ 91°
Avg = 43.48 D
Cyl = -2.21 D Ax 1°
Anterior Ø=7mm
K1 = 42.10 D @ 1°
K2 = 44.01 D @ 91°
Avg = 43.04 D
Cyl = -1.91 D Ax 1°
K readings
n1 = 1.376
n2 = 1.336
Posterior Ø=3mm
K1 = -6.05 D @ 174°
K2 = -6.58 D @ 84°
Avg = -6.30 D
Cyl = +0.54 D Ax 174°
Posterior Ø=5mm
K1 = -6.06 D @ 175°
K2 = -6.55 D @ 85°
Avg = -6.29 D
Cyl = +0.49 D Ax 175°
Posterior Ø=7mm
K1 = -6.07 D @ 178°
K2 = -6.43 D @ 88°
Avg = -6.24 D
Cyl = +0.36 D Ax 178°
Refractive analysis
Ø=4.0mm
Cyl = -2.07 D Ax 3°
MPP = 43.10 D
LSA = 0.12 D
Keratoconus screening
Sif = -0.01 D
KVf = 6 µm
BCVf = 0.31 D @ 166°
Sib = -0.19 D
KVb = 6 µm
BCVb = 0.00 D @ 166°
Thk = 525 µm
Class:
- 'Normal'

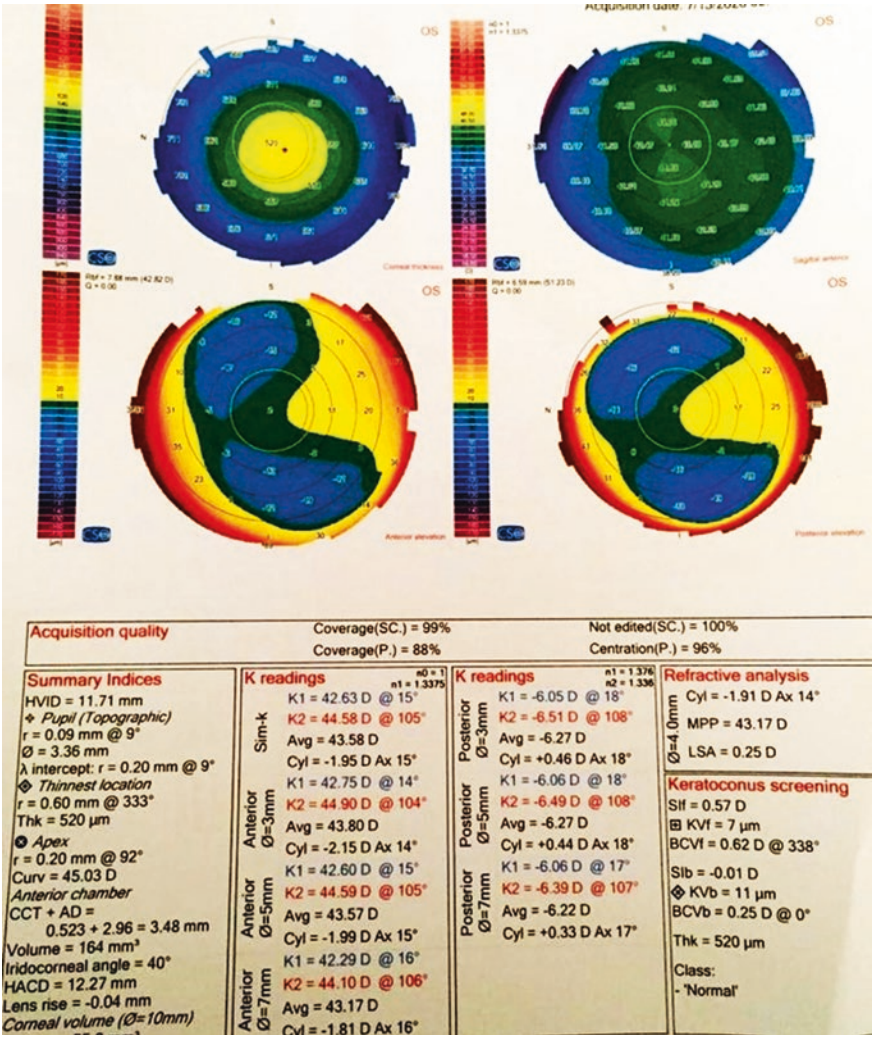

Fig. 35 A 24-year-old woman scheduled for refractive surgery with refractive errors: OD −4.75/−2.00~180 CDVA 10/10 and OS −4.50/−2.25~15 CDVA 10/10. The corneas are apparently normal and there are a normal axial maps on the 1.50 diopter scale. Note that 1.50 diopter scale masks the details and pattern of corneal astigmatism on the sagital curvature map

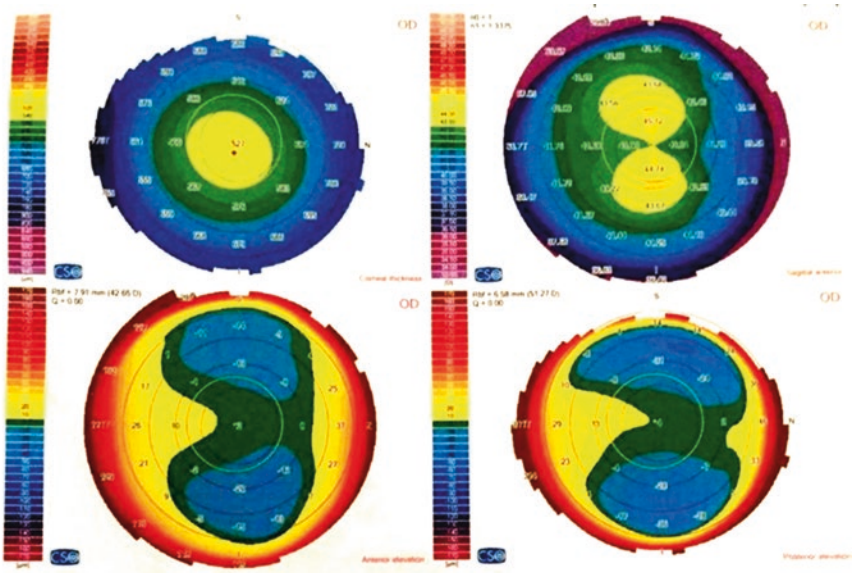

Acquisition quality	Coverage(SC.) = 99%	Not edited(SC.) = 100%
	Coverage(P.) = 84%	Centration(P.) = 95%

Summary Indices

HVID = 11.71 mm
Pupil (Topographic)
r = 0.20 mm @ 155°
Ø = 3.74 mm
λ intercept: r = 0.43 mm @ 155°
Thinnest location
r = 0.40 mm @ 244°
Thk = 525 µm
Apex
r = 0.40 mm @ 97°
Curv = 45.06 D
Anterior chamber
CCT + AD =
0.527 + 2.99 = 3.52 mm
Volume = 170 mm³
Iridocorneal angle = 42°
HACD = 12.52 mm
Lens rise = -0.08 mm
Corneal volume (Ø=10mm)

K readings (n0 = 1, n1 = 1.3375)

Sim-k	K1 = 42.37 D @ 1°
	K2 = 44.67 D @ 91°
	Avg = 43.49 D
	Cyl = -2.30 D Ax 1°
Anterior Ø=3mm	K1 = 42.63 D @ 0°
	K2 = 44.91 D @ 90°
	Avg = 43.74 D
	Cyl = -2.28 D Ax 0°
Anterior Ø=5mm	K1 = 42.40 D @ 1°
	K2 = 44.61 D @ 91°
	Avg = 43.48 D
	Cyl = -2.21 D Ax 1°
Anterior Ø=7mm	K1 = 42.10 D @ 1°
	K2 = 44.01 D @ 91°
	Avg = 43.04 D
	Cyl = -1.91 D Ax 1°

K readings (n1 = 1.376, n2 = 1.336)

Posterior Ø=3mm	K1 = -6.05 D @ 174°
	K2 = -6.58 D @ 84°
	Avg = -6.30 D
	Cyl = +0.54 D Ax 174°
Posterior Ø=5mm	K1 = -6.06 D @ 175°
	K2 = -6.55 D @ 85°
	Avg = -6.29 D
	Cyl = +0.49 D Ax 175°
Posterior Ø=7mm	K1 = -6.07 D @ 178°
	K2 = -6.43 D @ 88°
	Avg = -6.24 D
	Cyl = +0.36 D Ax 178°

Refractive analysis

Ø=4.0mm
Cyl = -2.07 D Ax 3°
MPP = 43.10 D
LSA = 0.12 D

Keratoconus screening

Sif = -0.01 D
⊞ KVf = 6 µm
BCVf = 0.31 D @ 166°
Sib = -0.19 D
◈ KVb = 6 µm
BCVb = 0.00 D @ 166°
Thk = 525 µm
Class:
- 'Normal'

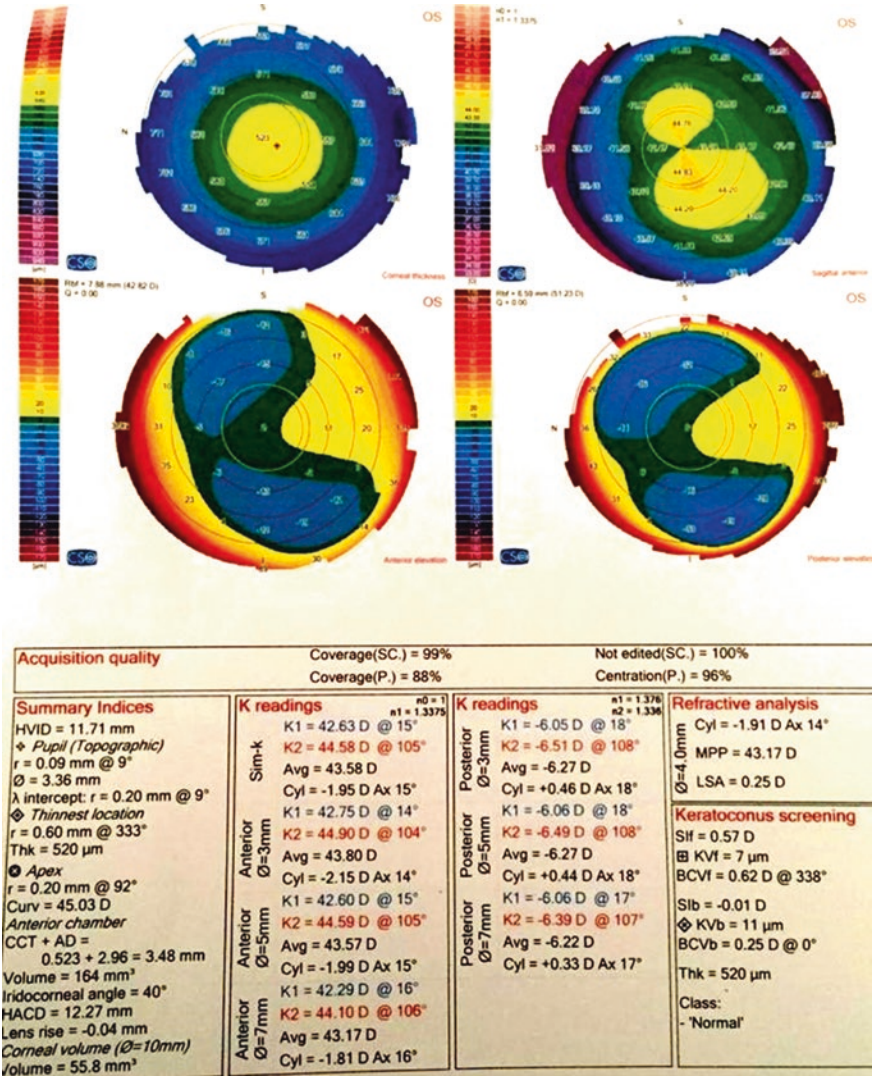

Fig. 36 However, 0.5 diopter scale shows details of sagital curvature precisely in the same patient

Case 6.

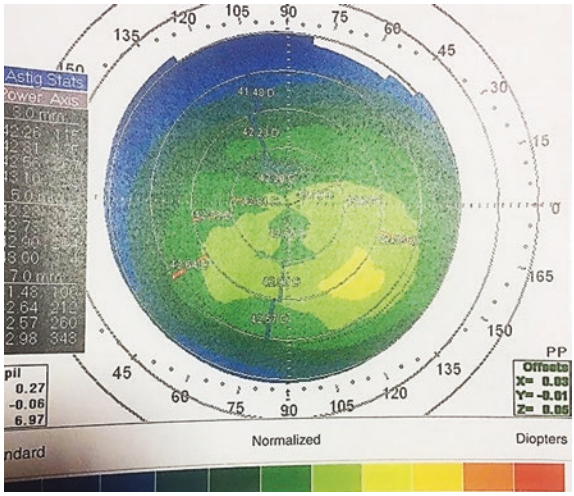

Fig. 37 A 34-year-old man with early stage of PMD on the left eye, and refractive error OD = −3.25/−0.75~55 CDVA = 10/10 and OS = −3.00/−1.00~90 CDVA = 10/10. There is the localized steepening with a crab claw pattern on Placido topography

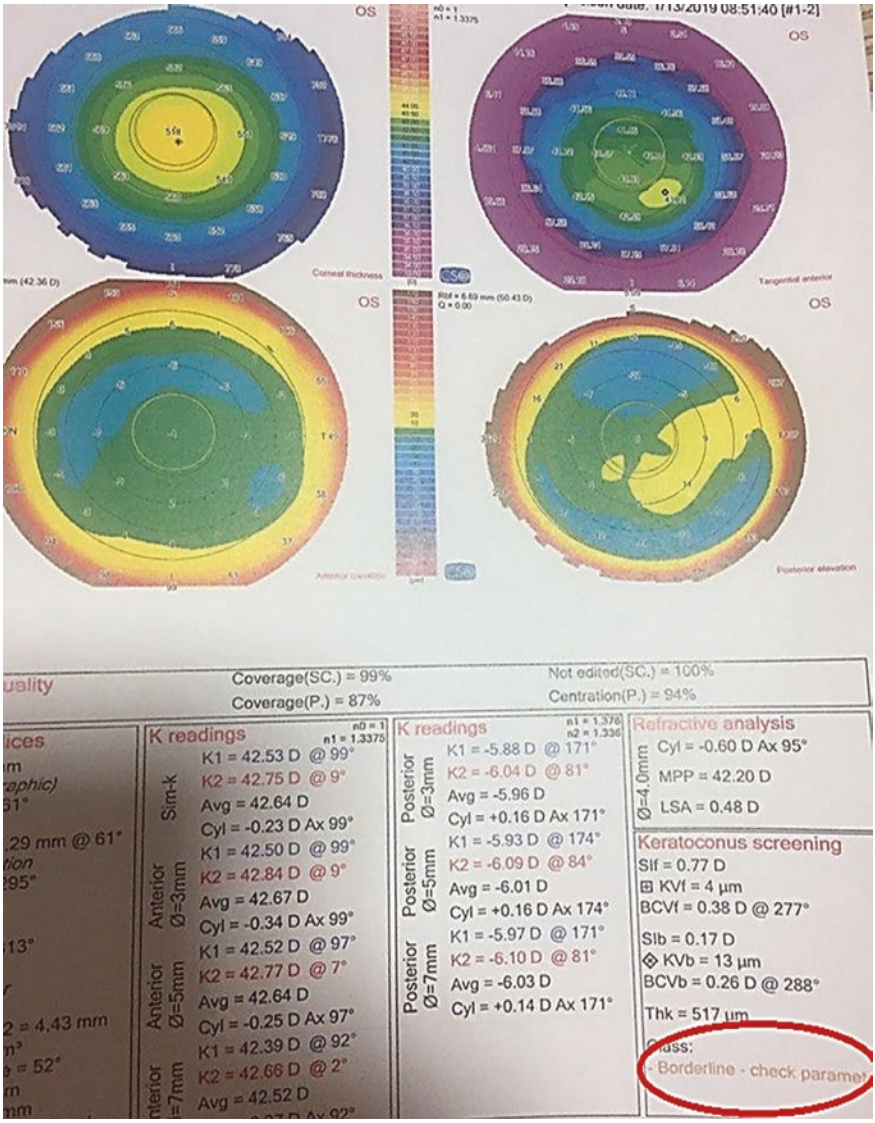

Fig. 38 The Sirius screening software also diagnosed the Borderline-check parameter in the same patient which indicates the abnormality of the cornea

Case 7.

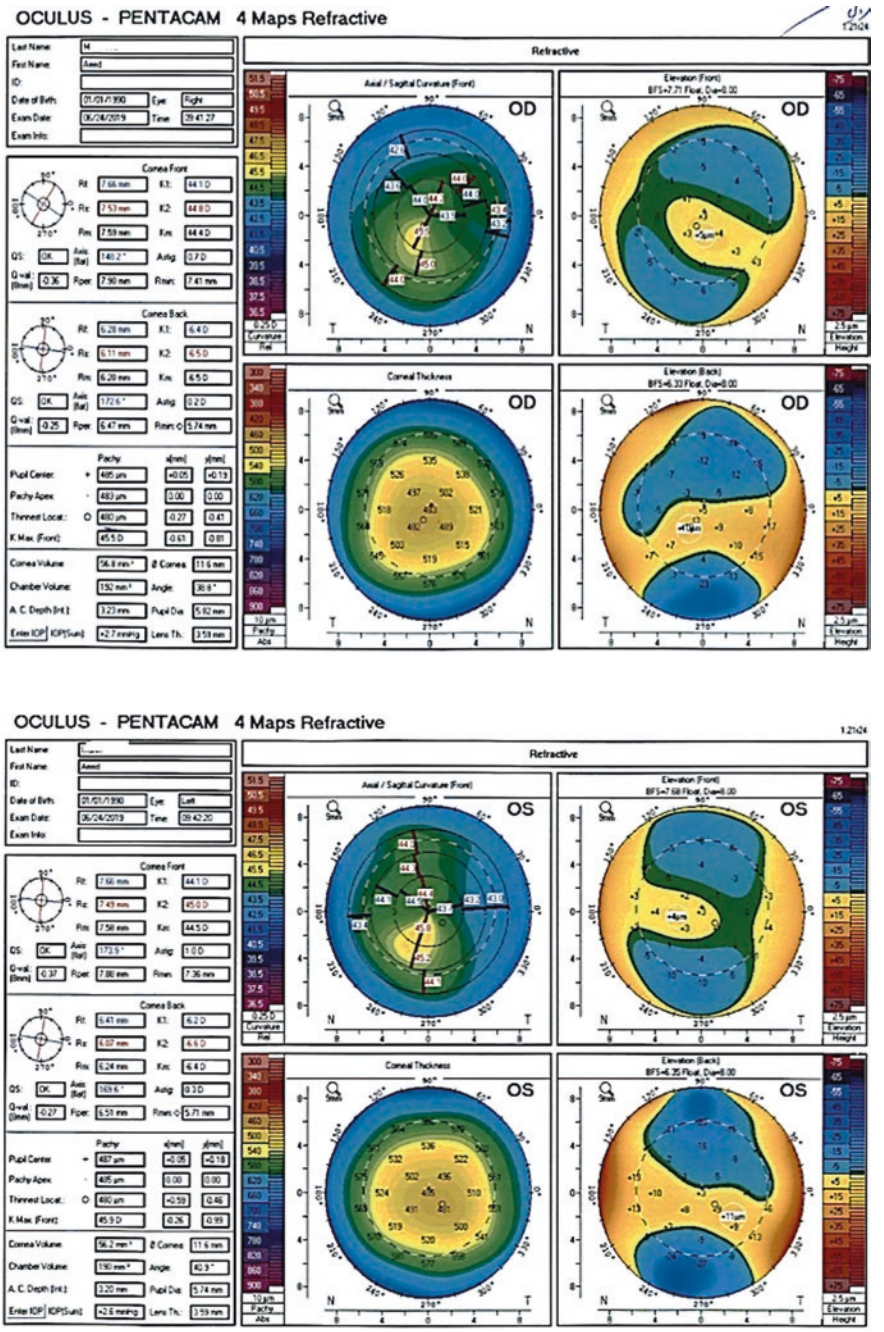

Fig. 39 A 29-year-old man with subclinical keratoconus, and refractive errors: OD = −3.00/−0.75~130 CDVA = 10/10 and OS = −3.00/0.50~10 CDVA = 10/10. There is inferior steepening on both eyes in axial maps of Pentacam

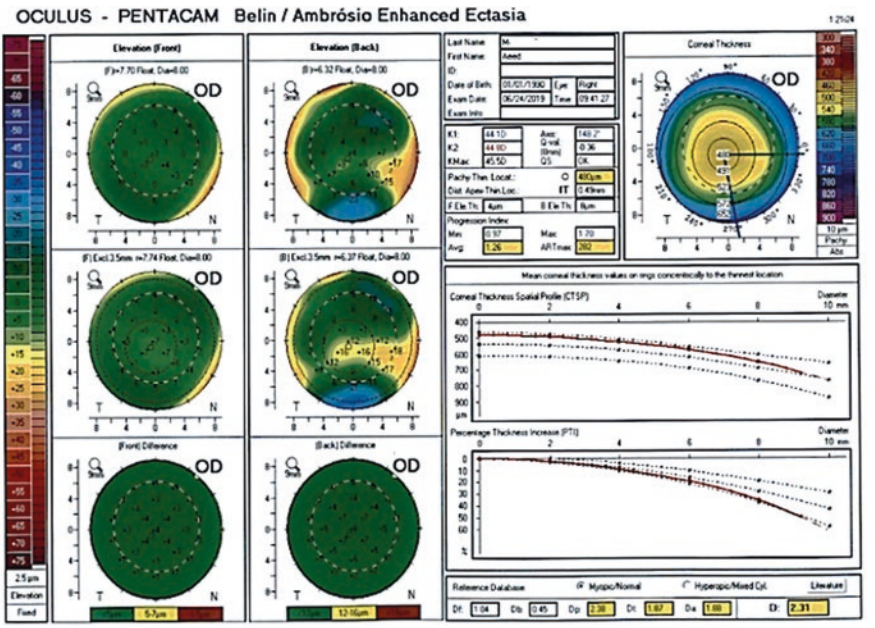

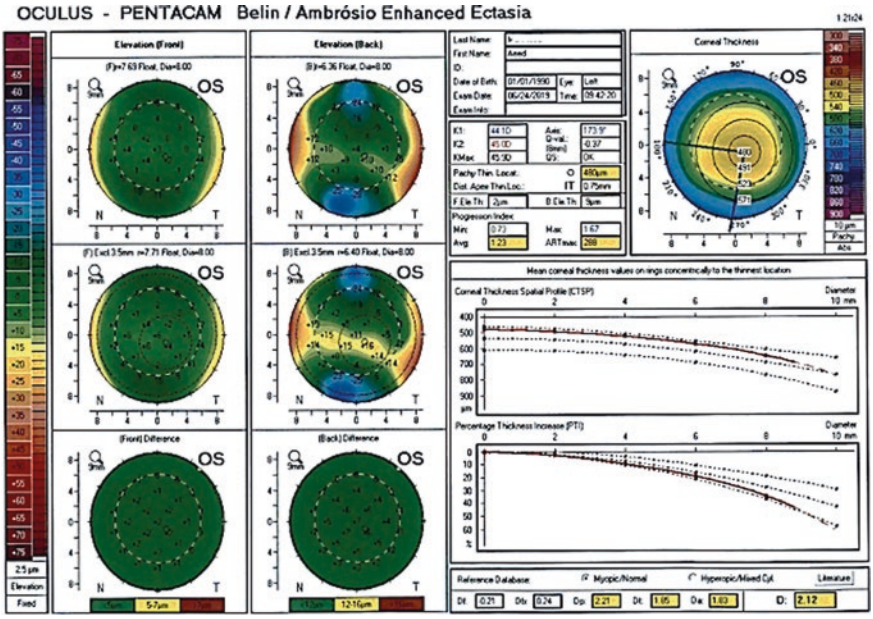

Fig. 40 These findings consisted with abnormal pachymetric progression and D index value in Belin-Ambrosio display maps of the same patient

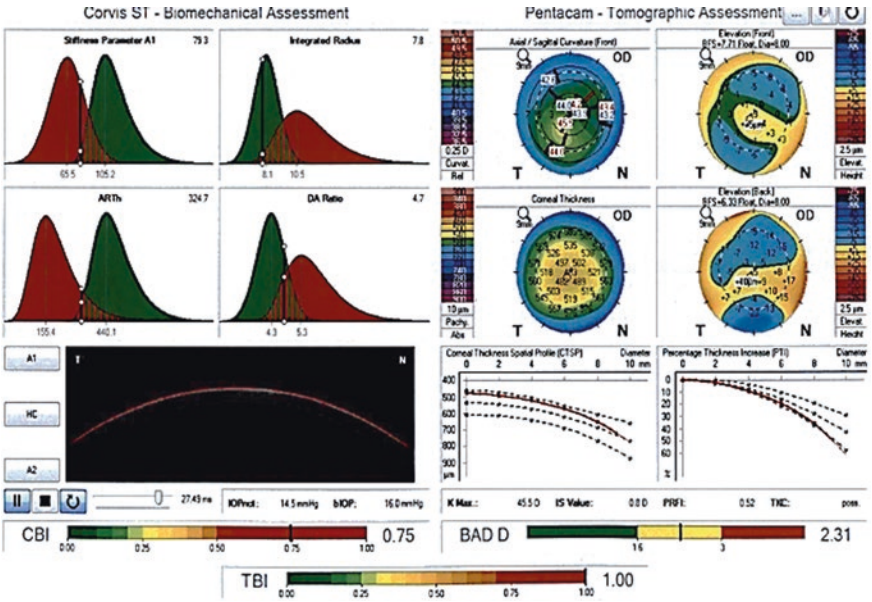

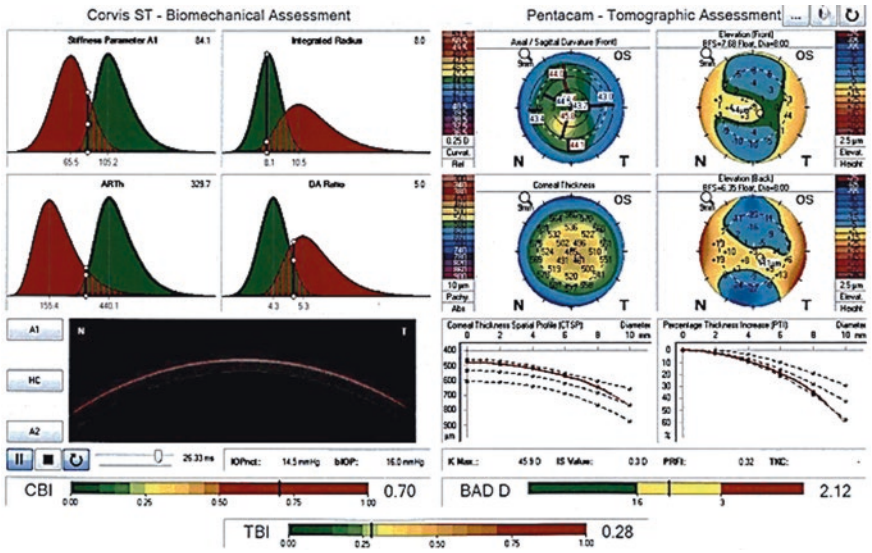

Fig. 41 Biomechanical and combined biomechanical and topographical indices including CBI and TBI are abnormal in both eyes of the same patient

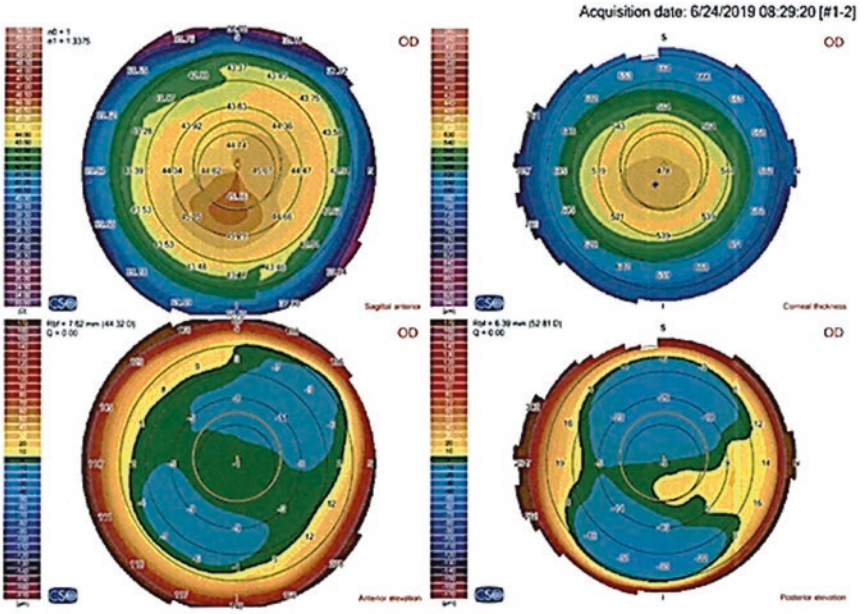

Acquisition quality	Coverage(SC.) = 99%	Not edited(SC.) = 100%
	Coverage(P.) = 74%	Centration(P.) = 99%

Summary Indices

HVID = 11.75 mm
Pupil (Topographic)
r = 0.25 mm @ 83°
Ø = 3.39 mm
λ intercept: r = 0.58 mm @ 83°
Thinnest location
r = 0.60 mm @ 237°
Thk = 472 µm
Apex
r = 1.00 mm @ 274°
Curv = 46.55 D
Anterior chamber
CCT + AD =
0.478 + 3.13 = 3.60 mm
Volume = 163 mm³
Iridocorneal angle = 44°
HACD = 11.87 mm
Lens rise = 0.07 mm
Corneal volume (Ø=10mm)
Volume = 53.8 mm³

K readings (n0 = 1, n1 = 1.3375)

Sim-k	K1 = 44.53 D @ 152°	
	K2 = 45.28 D @ 62°	
	Avg = 44.90 D	
	Cyl = -0.75 D Ax 152°	
Anterior Ø=3mm	K1 = 44.69 D @ 150°	
	K2 = 45.41 D @ 60°	
	Avg = 45.05 D	
	Cyl = -0.72 D Ax 150°	
Anterior Ø=5mm	K1 = 44.54 D @ 150°	
	K2 = 45.25 D @ 60°	
	Avg = 44.89 D	
	Cyl = -0.70 D Ax 150°	
Anterior Ø=7mm	K1 = 44.31 D @ 145°	
	K2 = 44.95 D @ 55°	
	Avg = 44.63 D	
	Cyl = -0.64 D Ax 145°	

K readings (n1 = 1.376, n2 = 1.336)

Posterior Ø=3mm	K1 = -6.26 D @ 172°	
	K2 = -6.59 D @ 82°	
	Avg = -6.42 D	
	Cyl = +0.33 D Ax 172°	
Posterior Ø=5mm	K1 = -6.22 D @ 171°	
	K2 = -6.55 D @ 81°	
	Avg = -6.38 D	
	Cyl = +0.33 D Ax 171°	
Posterior Ø=7mm	K1 = -6.24 D @ 172°	
	K2 = -6.49 D @ 82°	
	Avg = -6.36 D	
	Cyl = +0.25 D Ax 172°	

Refractive analysis

Cyl = -0.71 D Ax 137°
Ø=4.0mm
MPP = 44.37 D
LSA = 0.56 D

Keratoconus screening

△ Sif = 1.00 D
⊞ KVf = 3 µm
BCVf = 0.45 D @ 270°
△ Sib = 0.58 D
◈ KVb = 14 µm
BCVb = 0.76 D @ 297°
△ Thk = 472 µm

ABSS:
- Borderline - check parameter

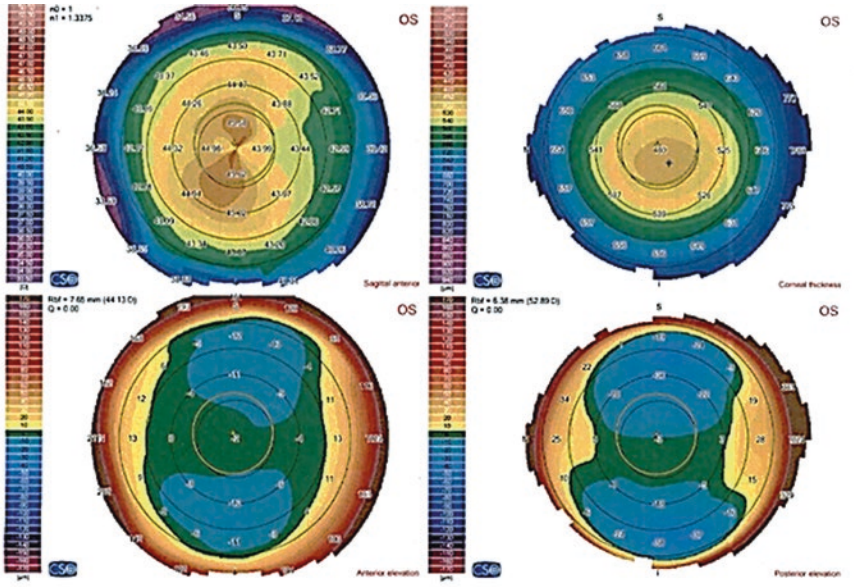

Acquisition quality	Coverage(SC.) = 99%	Not edited(SC.) = 100%
	Coverage(P.) = 76%	Centration(P.) = 99%

Summary Indices

HVID = 11.89 mm
Pupil (Topographic)
r = 0.24 mm @ 112°
Ø = 3.12 mm
λ intercept: r = 0.55 mm @ 112°
Thinnest location
r = 0.60 mm @ 306°
Thk = 476 µm
Apex
r = 0.80 mm @ 236°
Curv = 46.07 D
Anterior chamber
CCT + AD =
0.480 + 3.10 = 3.58 mm
Volume = 157 mm³
Iridocorneal angle = 44°
HACD = 11.77 mm
Lens rise = 0.00 mm
Corneal volume (Ø=10mm)
Volume = 54.7 mm³

K readings (n0 = 1, n1 = 1.3375)

Sim-k	K1 = 44.11 D @ 174°
	K2 = 45.21 D @ 84°
	Avg = 44.65 D
	Cyl = -1.09 D Ax 174°
Anterior Ø=3mm	K1 = 44.27 D @ 171°
	K2 = 45.54 D @ 81°
	Avg = 44.90 D
	Cyl = -1.27 D Ax 171°
Anterior Ø=5mm	K1 = 44.13 D @ 172°
	K2 = 45.25 D @ 82°
	Avg = 44.68 D
	Cyl = -1.13 D Ax 172°
Anterior Ø=7mm	K1 = 43.92 D @ 172°
	K2 = 44.94 D @ 82°
	Avg = 44.42 D
	Cyl = -1.03 D Ax 172°

K readings (n1 = 1.376, n2 = 1.336)

Posterior Ø=3mm	K1 = -6.25 D @ 179°
	K2 = -6.64 D @ 89°
	Avg = -6.44 D
	Cyl = +0.39 D Ax 179°
Posterior Ø=5mm	K1 = -6.21 D @ 178°
	K2 = -6.58 D @ 88°
	Avg = -6.39 D
	Cyl = +0.38 D Ax 178°
Posterior Ø=7mm	K1 = -6.21 D @ 178°
	K2 = -6.53 D @ 88°
	Avg = -6.36 D
	Cyl = +0.32 D Ax 178°

Refractive analysis

Ø=4.0mm
Cyl = -0.96 D Ax 176°
MPP = 44.23 D
⚠ LSA = 0.01 D

Keratoconus screening

Sif = 0.52 D
⊞ KVf = 3 µm
BCVf = 0.26 D @ 207°
⚠ Sib = 0.52 D
◈ KVb = 11 µm
BCVb = 0.69 D @ 259°
⚠ Thk = 476 µm
Cl...
- Borderline - check parameters

Fig. 42 Sirius screening software of the same patient also diagnosed Borderline-check parameters which indicate the abnormality of the cornea

Case 8.

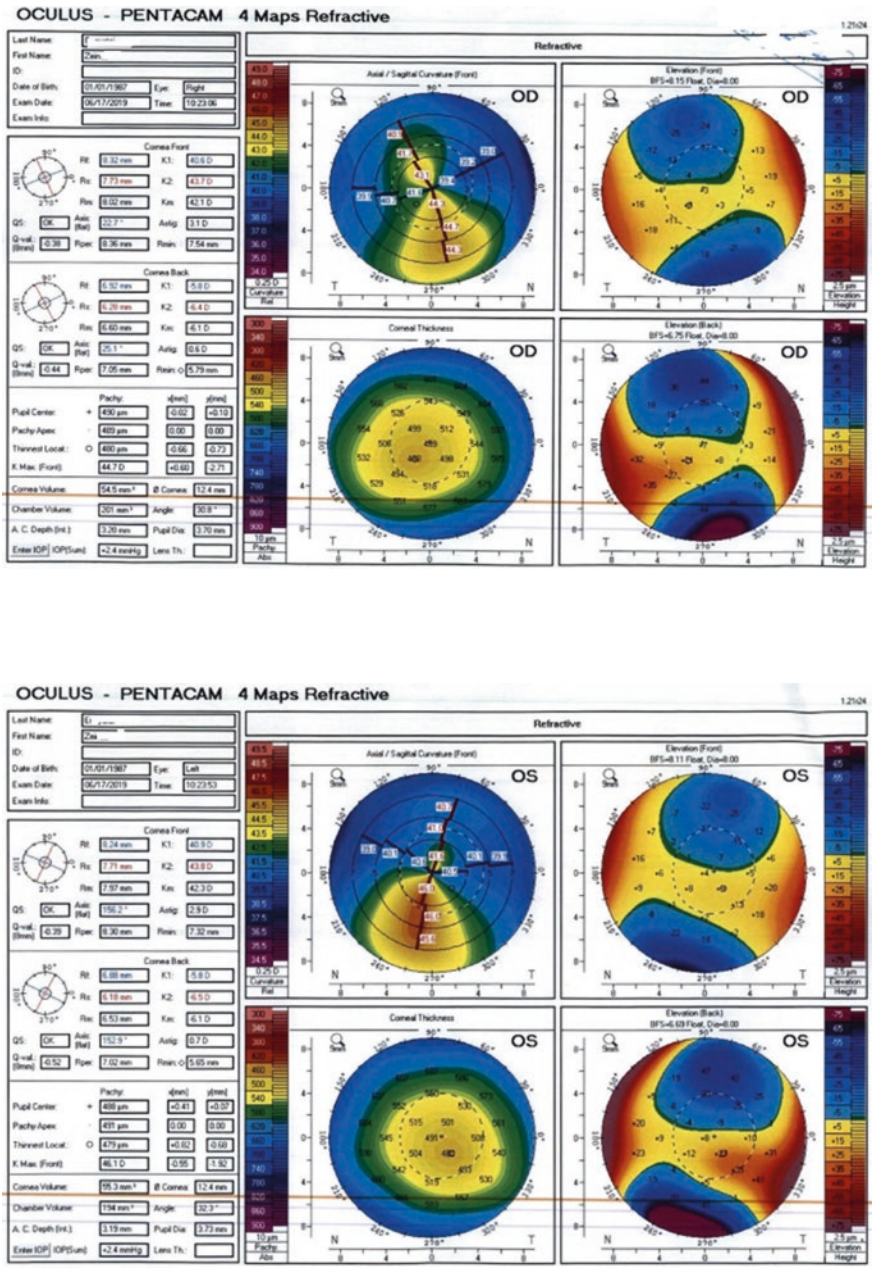

Fig. 43 A 32-year-old woman with early keratoconus, and refractive errors: OD = −3.25~15 CDVA = 9/10 and OS = −0.75/−3.00~160 CDVA = 9/10 and present of scissor motions and inferior steepening in both eyes, more advanced in the left eye

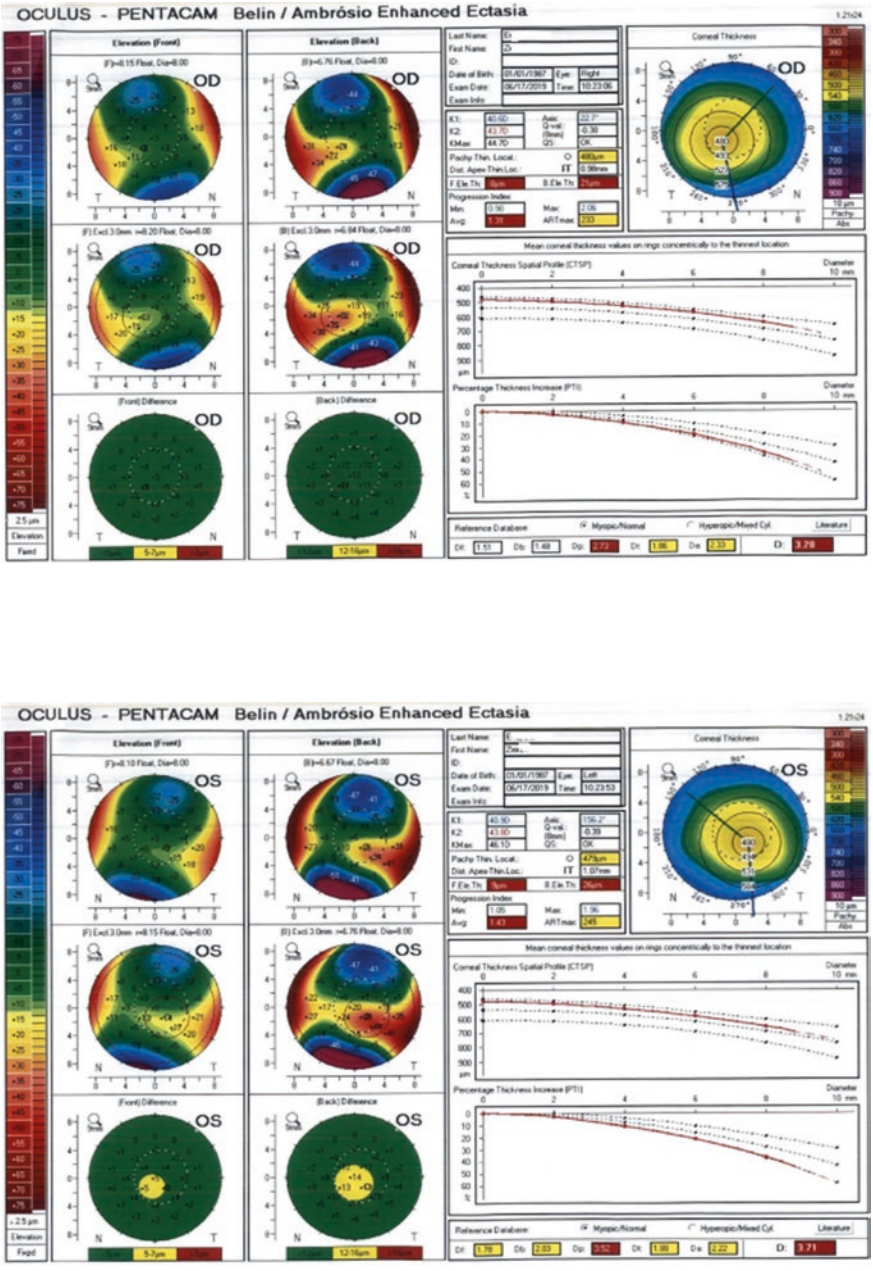

Fig. 44 These findings consisted with abnormal pachymetry, elevation, and D index values in Belin-Ambrosio display maps of the same patient

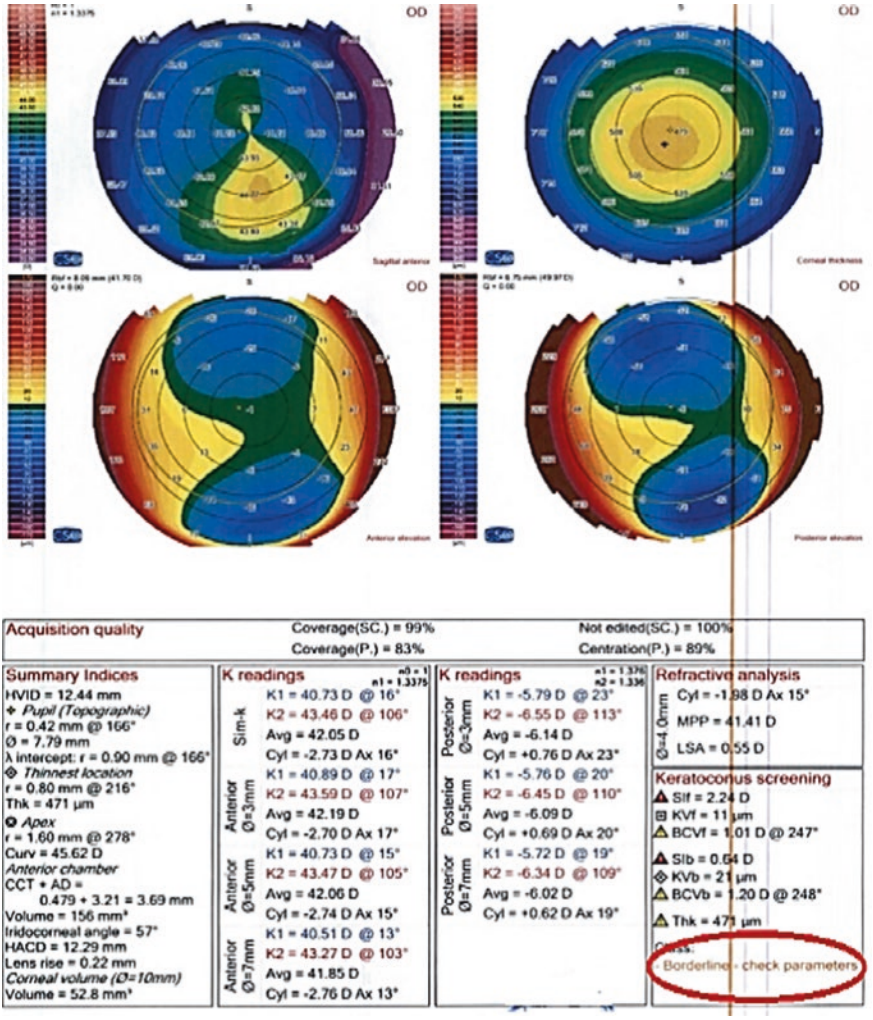
OD
OD
OD
OD
Sagittal anterior
Corneal thickness
Anterior elevation
Posterior elevation
Acquisition quality
Coverage(SC.) = 99%
Coverage(P.) = 83%
Not edited(SC.) = 100%
Centration(P.) = 89%
Summary Indices
HVID = 12.44 mm
Pupil (Topographic)
r = 0.42 mm @ 166°
Ø = 7.79 mm
λ intercept: r = 0.90 mm @ 166°
Thinnest location
r = 0.80 mm @ 216°
Thk = 471 µm
Apex
r = 1.60 mm @ 278°
Curv = 45.62 D
Anterior chamber
CCT + AD =
0.479 + 3.21 = 3.69 mm
Volume = 156 mm³
Iridocorneal angle = 57°
HACD = 12.29 mm
Lens rise = 0.22 mm
Corneal volume (Ø=10mm)
Volume = 52.8 mm³
K readings
Sim-k
K1 = 40.73 D @ 16°
K2 = 43.46 D @ 106°
Avg = 42.05 D
Cyl = -2.73 D Ax 16°
Anterior Ø=3mm
K1 = 40.89 D @ 17°
K2 = 43.59 D @ 107°
Avg = 42.19 D
Cyl = -2.70 D Ax 17°
Anterior Ø=5mm
K1 = 40.73 D @ 15°
K2 = 43.47 D @ 105°
Avg = 42.06 D
Cyl = -2.74 D Ax 15°
Anterior Ø=7mm
K1 = 40.51 D @ 13°
K2 = 43.27 D @ 103°
Avg = 41.85 D
Cyl = -2.76 D Ax 13°
K readings
Posterior Ø=3mm
K1 = -5.79 D @ 23°
K2 = -6.55 D @ 113°
Avg = -6.14 D
Cyl = +0.76 D Ax 23°
Posterior Ø=5mm
K1 = -5.76 D @ 20°
K2 = -6.45 D @ 110°
Avg = -6.09 D
Cyl = +0.69 D Ax 20°
Posterior Ø=7mm
K1 = -5.72 D @ 19°
K2 = -6.34 D @ 109°
Avg = -6.02 D
Cyl = +0.62 D Ax 19°
Refractive analysis
Ø=4.0mm
Cyl = -1.98 D Ax 15°
MPP = 41.41 D
LSA = 0.55 D
Keratoconus screening
Sif = 2.24 D
KVf = 11 µm
BCVf = 1.01 D @ 247°
Sib = 0.64 D
KVb = 21 µm
BCVb = 1.20 D @ 248°
Thk = 471 µm
Borderline - check parameters

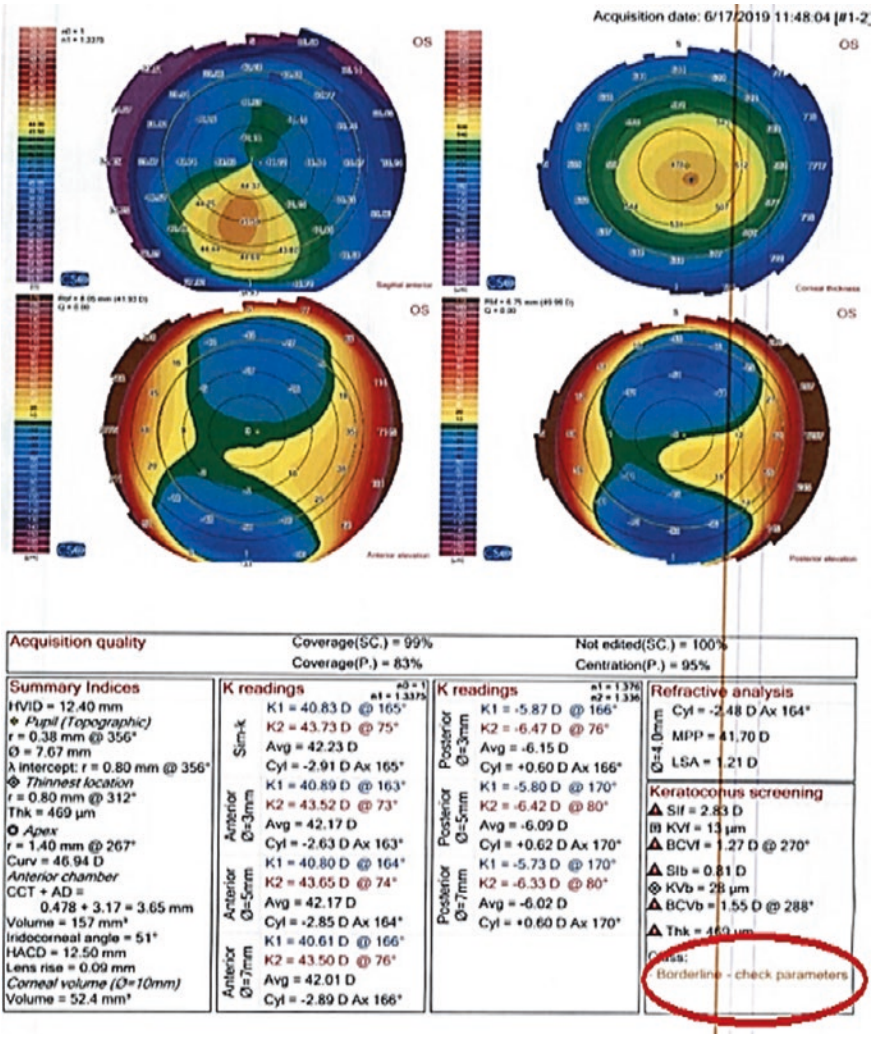

Fig. 45 The Sirius keratoconus screening software of the same patient shows Borderline-check parameters which indicate the abnormal cornea

Case 9.

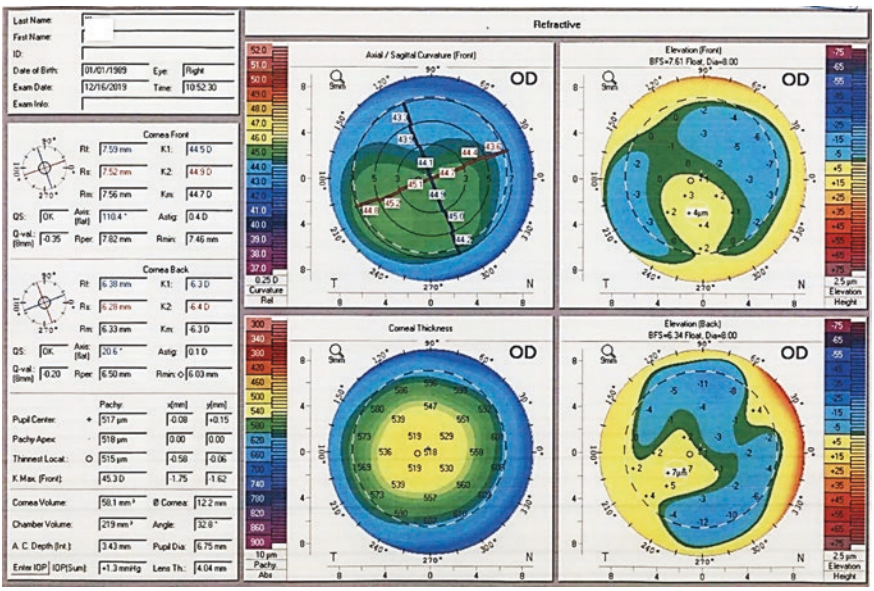

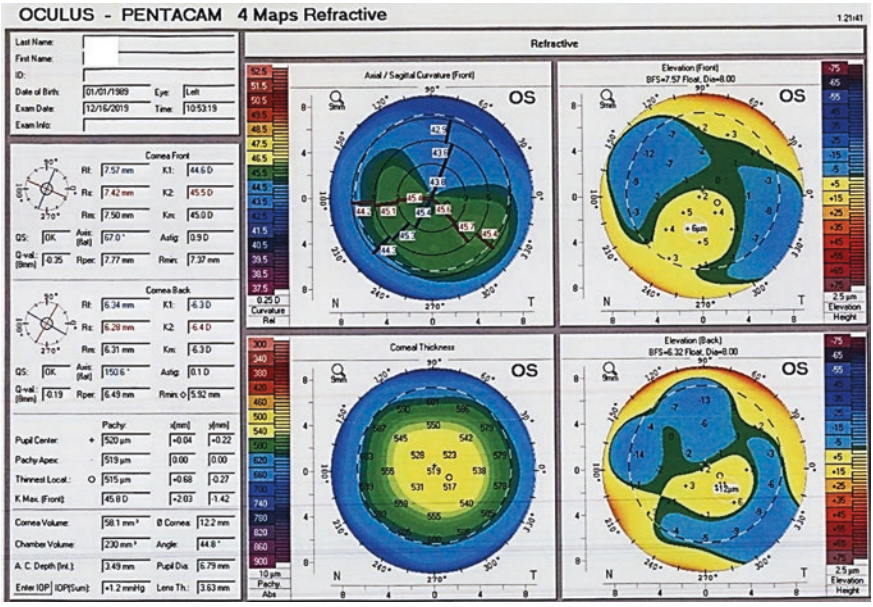

Fig. 46 A 30-year-old man with the normal cornea in the right eye and early PMD in the left eye. Refractive errors: OD = −0.50/−1.25~100 CDVA = 10/10 and OS = −0.75/−1.75~85 CDVA = 10/10 with normal thickness values and crab claw pattern on refractive maps of Pentacam

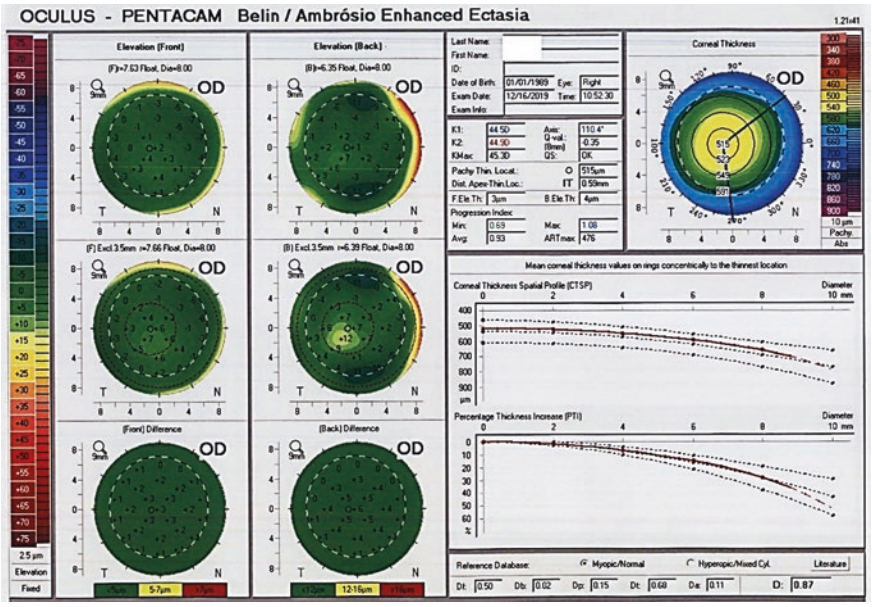

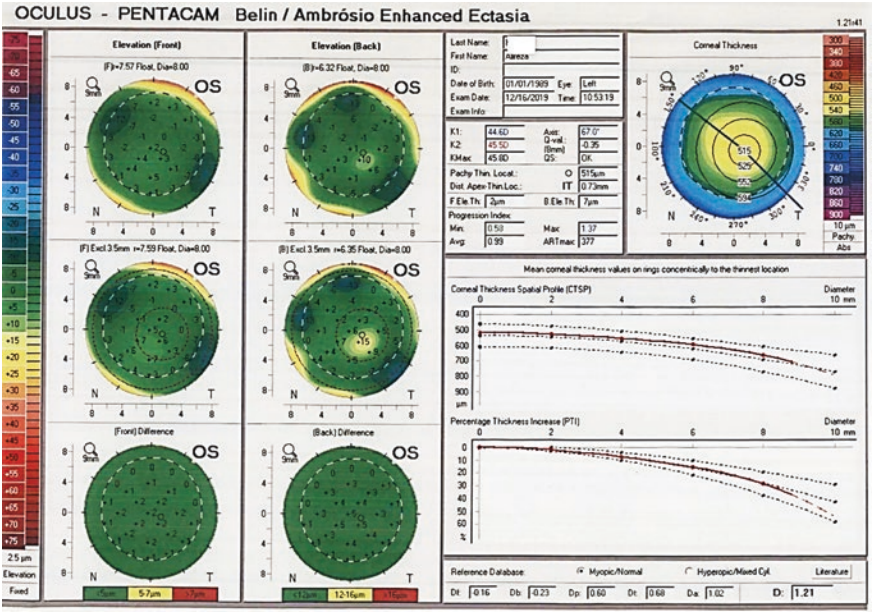

Fig. 47 There are normal values in Blin-Ambrosio display maps in both eyes of the same patient

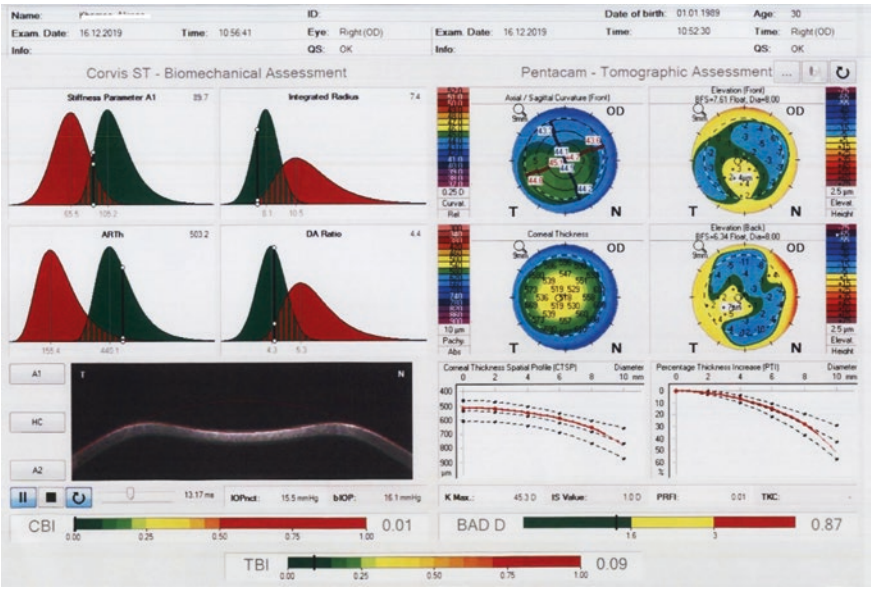

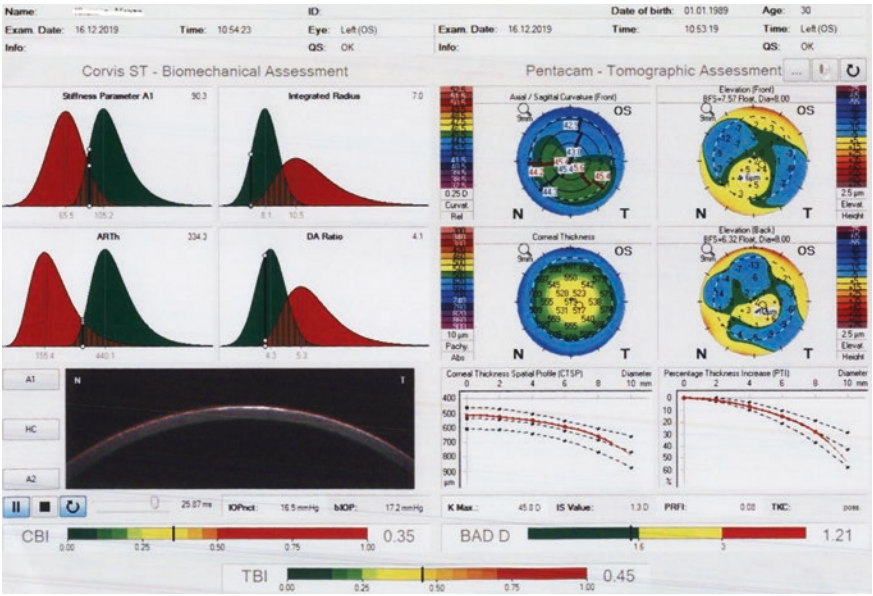

Fig. 48 Corneal biomechanical index (CBI) and combined topographic and biomechanical index (TBI) of the same patient are normal in the right eye and abnormal in the left eye

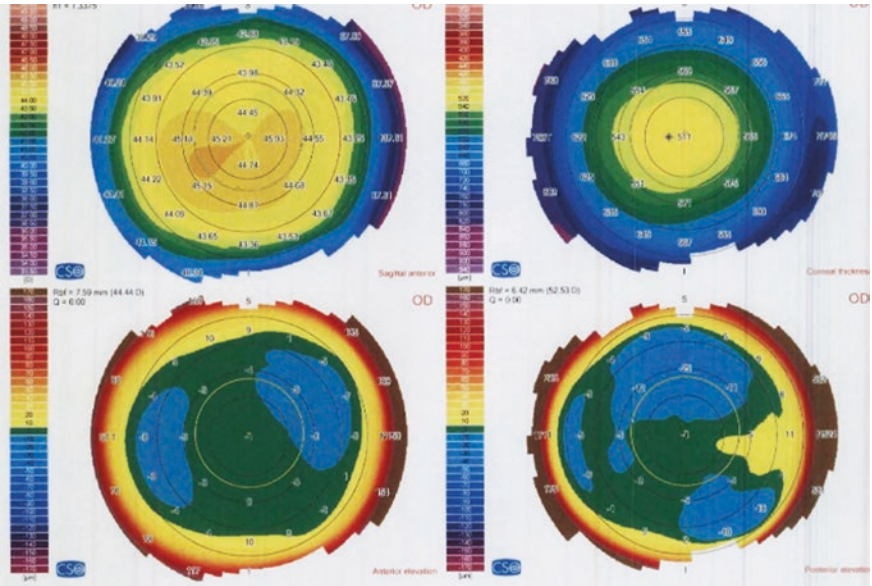

Acquisition quality	Coverage(SC.) = 99%	Not edited(SC.) = 100%
	Coverage(P.) = 80%	Centration(P.) = 95%

Summary Indices

HVID = 12.53 mm
Pupil (Topographic)
r = 0.12 mm @ 87°
Ø = 4.11 mm
λ intercept: r = 0.31 mm @ 87°
Thinnest location
r = 0.60 mm @ 180°
Thk = 510 µm
Apex
r = 1.40 mm @ 206°
Curv = 45.45 D
Anterior chamber
CCT + AD =
0.511 + 3.43 = 3.94 mm
Volume = 189 mm³
Iridocorneal angle = 47°
HACD = 12.35 mm
Lens rise = -0.04 mm
Corneal volume (Ø=10mm)
Volume = 56.2 mm³

K readings n0 = 1 n1 = 1.3375

Sim-k	K1 = 44.53 D @ 105°
	K2 = 45.09 D @ 15°
	Avg = 44.81 D
	Cyl = -0.55 D Ax 105°
Anterior Ø=3mm	K1 = 44.57 D @ 104°
	K2 = 45.13 D @ 14°
	Avg = 44.85 D
	Cyl = -0.56 D Ax 104°
Anterior Ø=5mm	K1 = 44.53 D @ 105°
	K2 = 45.07 D @ 15°
	Avg = 44.80 D
	Cyl = -0.54 D Ax 105°
Anterior Ø=7mm	K1 = 44.41 D @ 104°
	K2 = 44.91 D @ 14°
	Avg = 44.66 D
	Cyl = -0.50 D Ax 104°

K readings n1 = 1.376 n2 = 1.336

Posterior Ø=3mm	K1 = -6.21 D @ 1°
	K2 = -6.43 D @ 91°
	Avg = -6.32 D
	Cyl = +0.22 D Ax 1°
Posterior Ø=5mm	K1 = -6.22 D @ 4°
	K2 = -6.40 D @ 94°
	Avg = -6.30 D
	Cyl = +0.18 D Ax 4°
Posterior Ø=7mm	K1 = -6.25 D @ 15°
	K2 = -6.35 D @ 105°
	Avg = -6.30 D
	Cyl = +0.10 D Ax 15°

Refractive analysis

Ø=4.0mm
Cyl = -0.89 D Ax 100°
MPP = 44.37 D
LSA = 0.71 D

Keratoconus screening

Sif = 0.74 D
KVf = 3 µm
BCVf = 0.28 D @ 236°
Sib = 0.10 D
KVb = 14 µm
BCVb = 0.19 D @ 343°
Thk = 510 µm
Class:
- 'Normal'

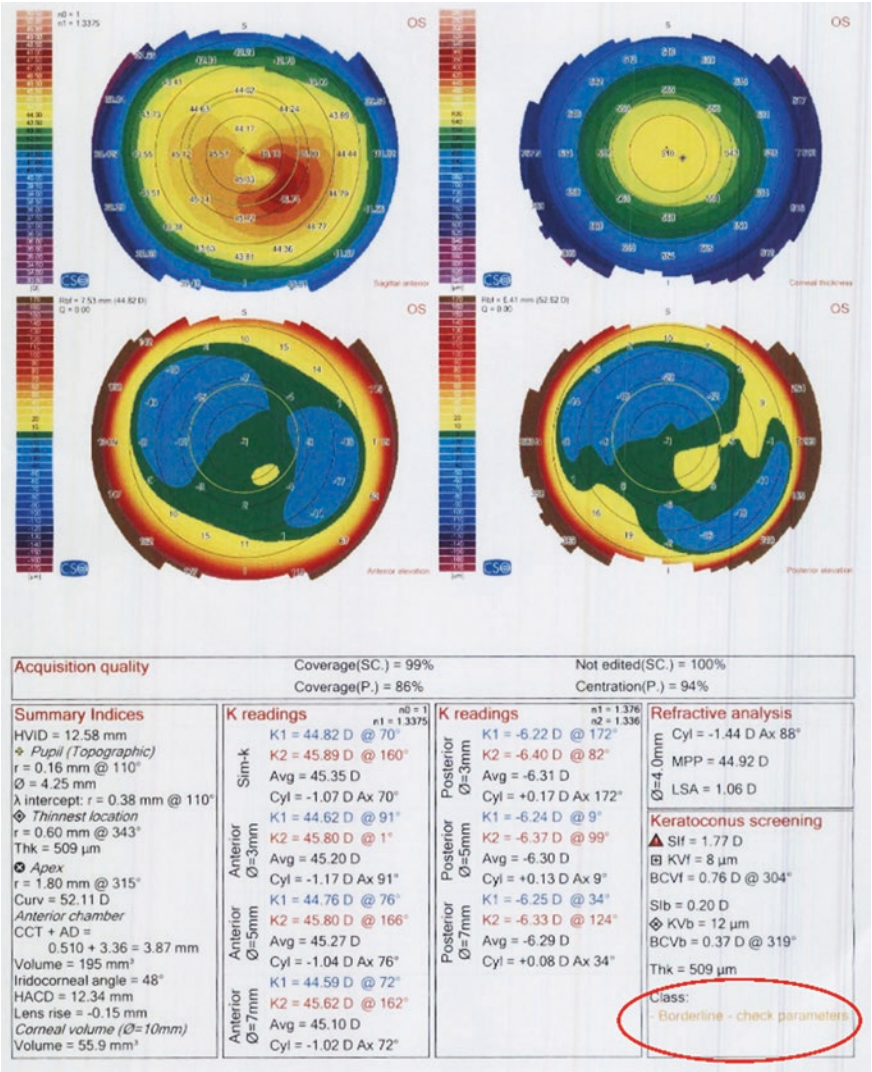

Fig. 49 These findings consisted with the Sirius keratoconus screening phoenix software of the same patient which shows normal class in the right eye and abnormal parameters in the left eye

Case 10.

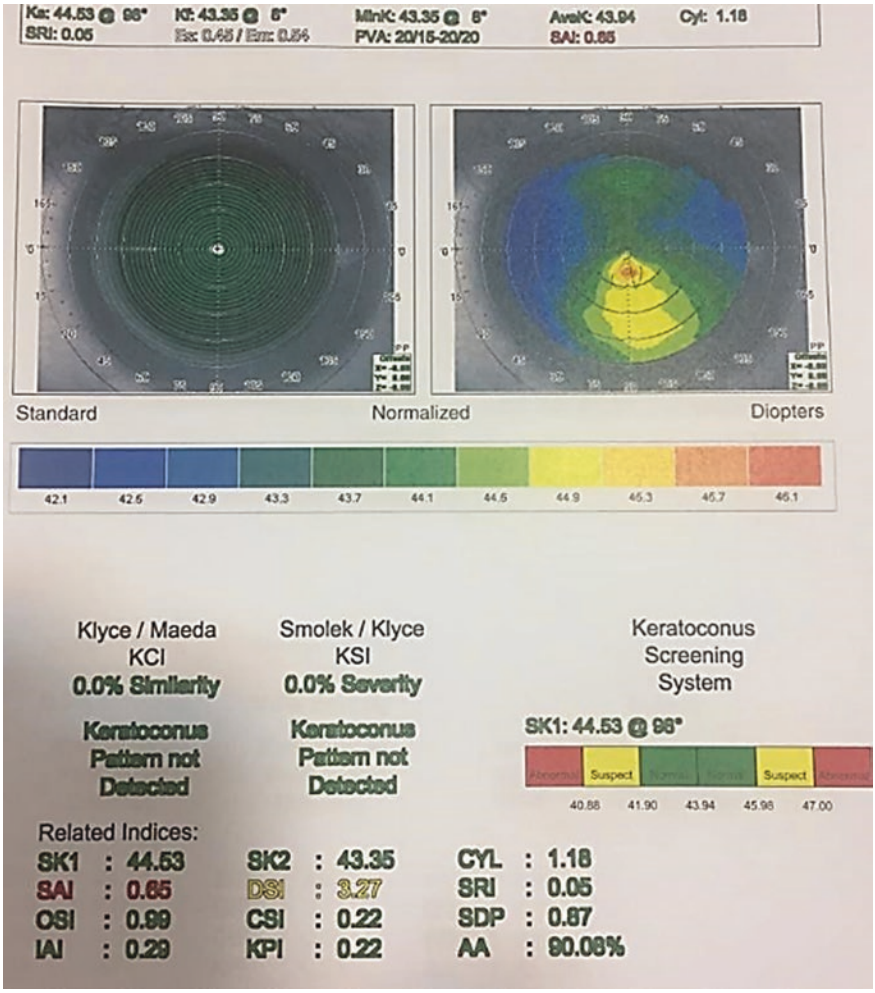
Standard
Normalized
Diopters
42.1
42.5
42.9
43.3
43.7
44.1
44.5
44.9
45.3
45.7
46.1
Klyce / Maeda
KCI
0.0% Similarity
Keratoconus
Pattern not
Detected
Smolek / Klyce
KSI
0.0% Severity
Keratoconus
Pattern not
Detected
Keratoconus
Screening
System
SK1: 44.53 @ 96°
Suspect
Suspect
40.88
41.90
43.94
45.98
47.00
Related Indices:
SK1 : 44.53
SAI : 0.65
OSI : 0.99
IAI : 0.29
SK2 : 43.35
DSI : 3.27
CSI : 0.22
KPI : 0.22
CYL : 1.18
SRI : 0.05
SDP : 0.87
AA : 90.08%

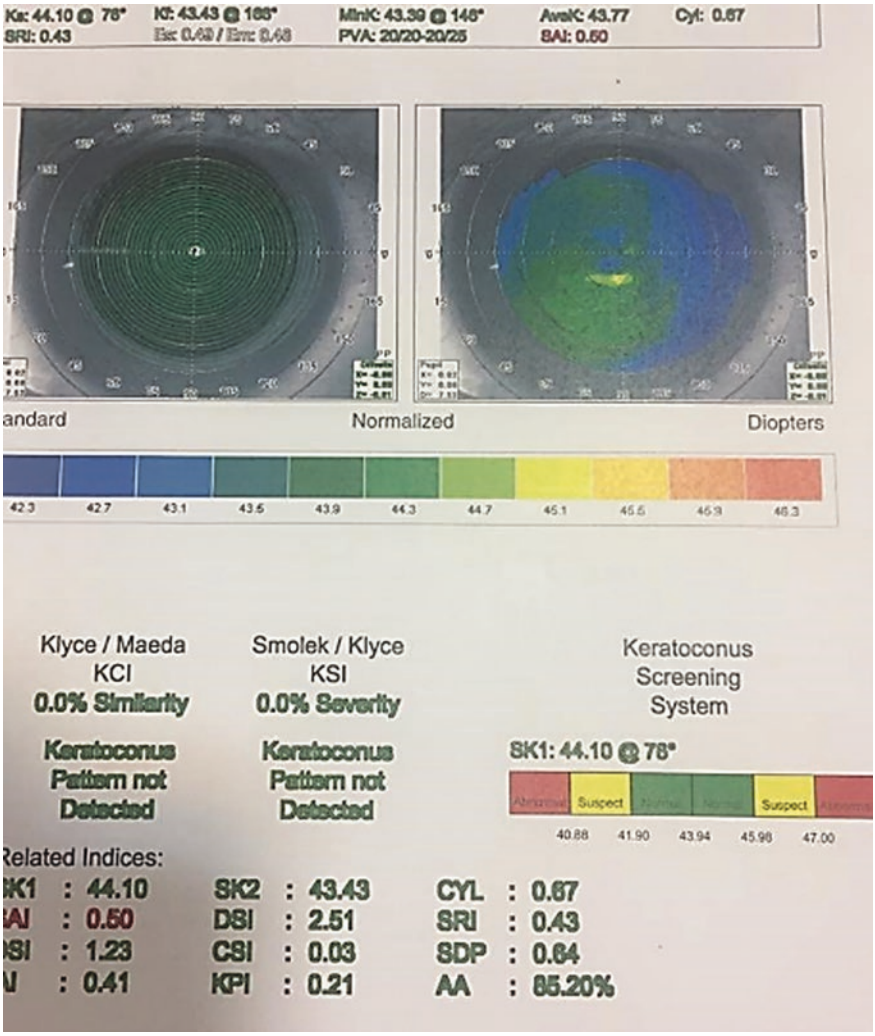

Fig. 50 A young woman with subclinical keratoconus and inferior steepening and borderline KCN related indices in Placido topography, however, the Sirius parameters are normal and show that this type of steepening may be related to normal variations

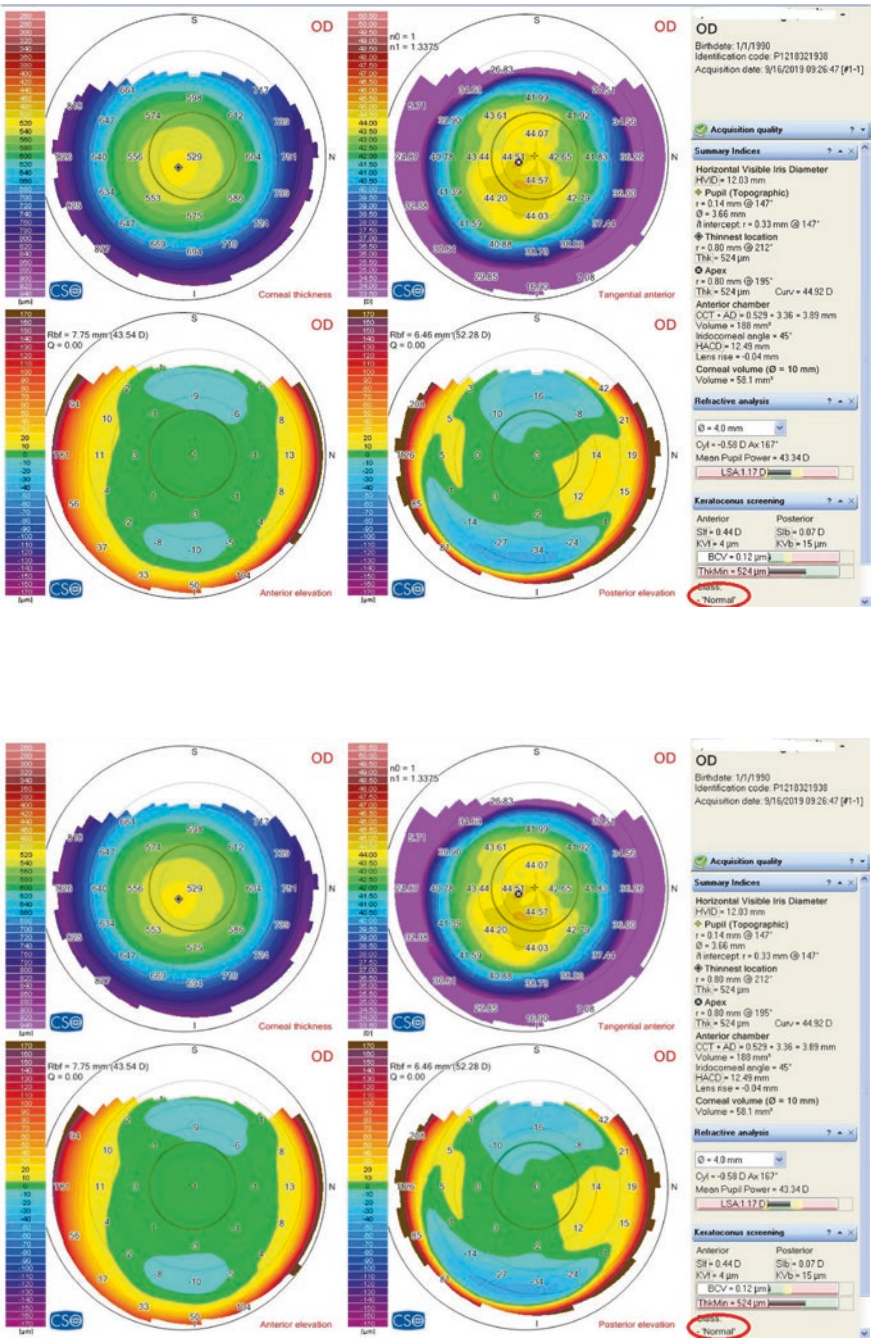

Fig. 51 The Sirius keratoconus screening software of the same patient shows normal cornea

Case 11.

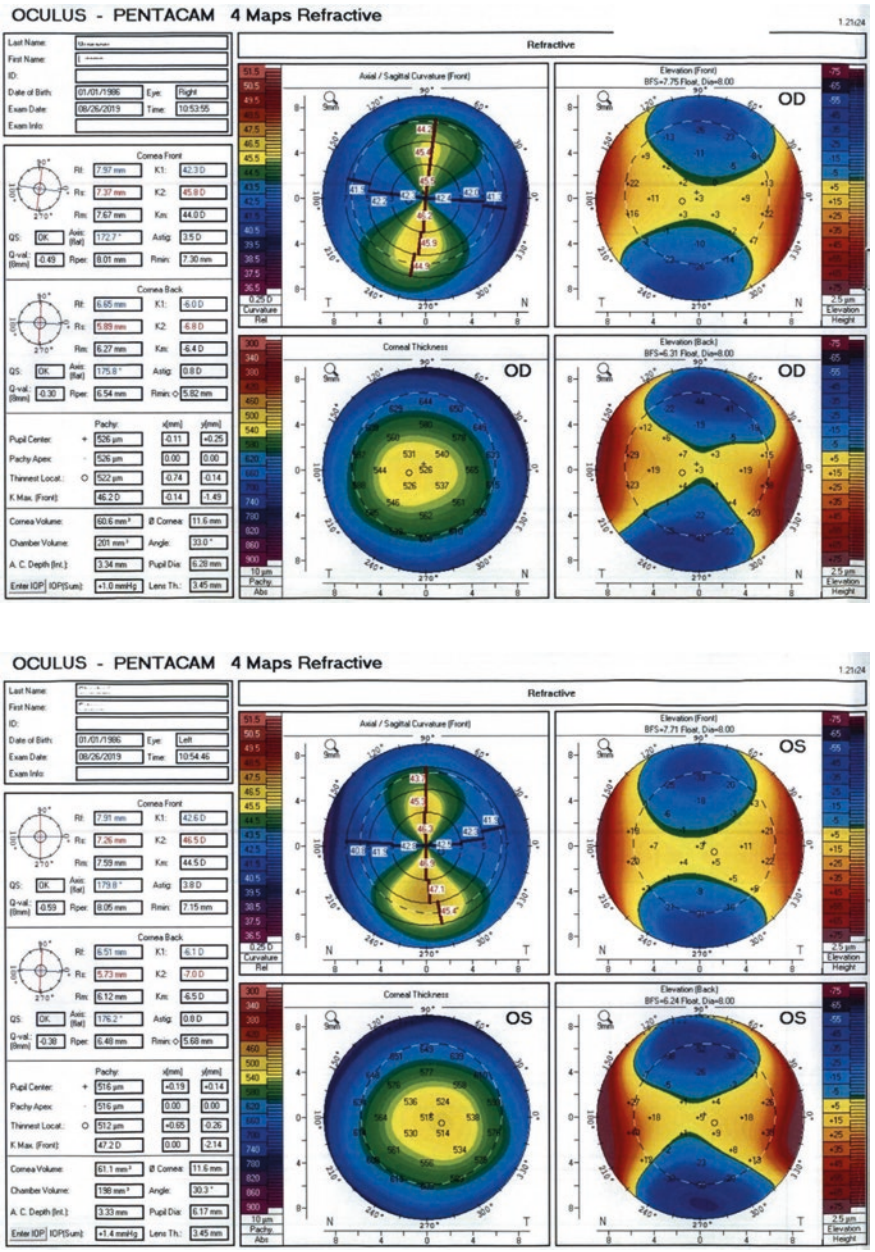

Fig. 52 A 28-year-old woman with the normal cornea in the right eye and keratoconus suspect in the left eye and refractive errors: OD = −4.25~180 CDVA = 10/10 and OS = −0.50/−4.25~180 CDVA = 10/10. There are symmetric bow tie pattern and normal values in Quad maps of Pentacam in both eyes and abnormal BADD and TBI only in the left eye. The Sirius screening values are abnormal in the left eye. The 4 maps cannot detect early stages of KCN, however artificial intelligence indices could detect correctly early KCN

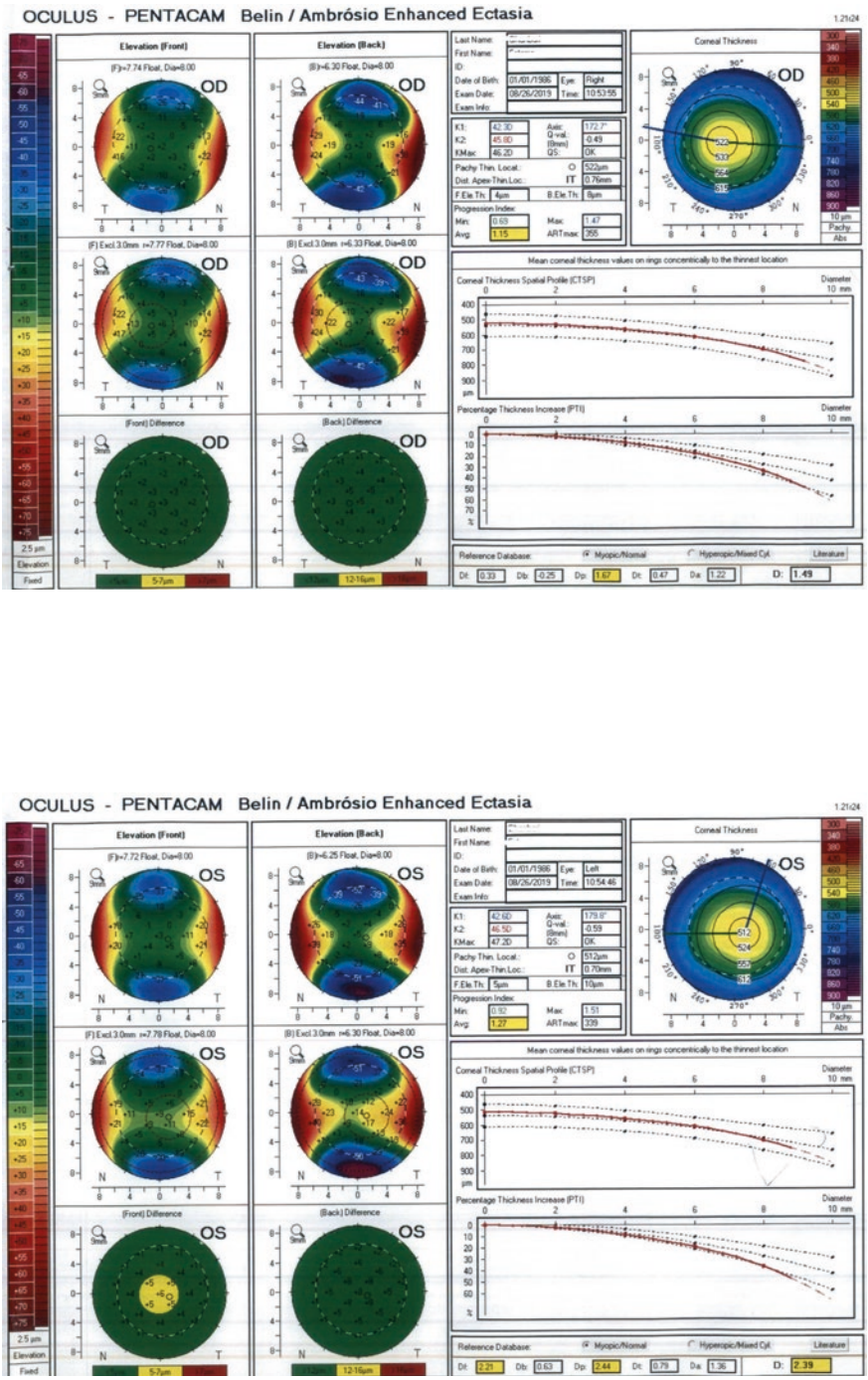

Fig. 53 There are abnormal findings in the D index in the left eye of the same patient

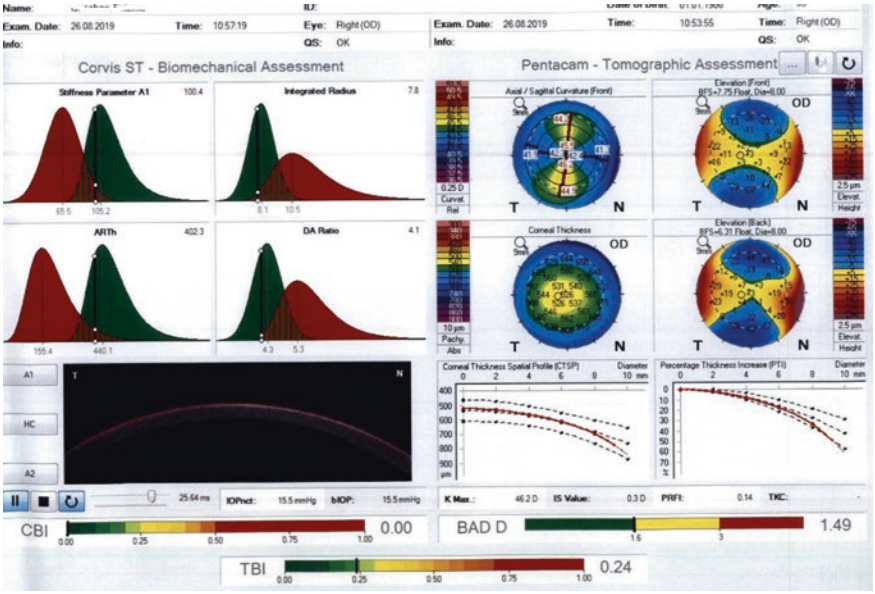

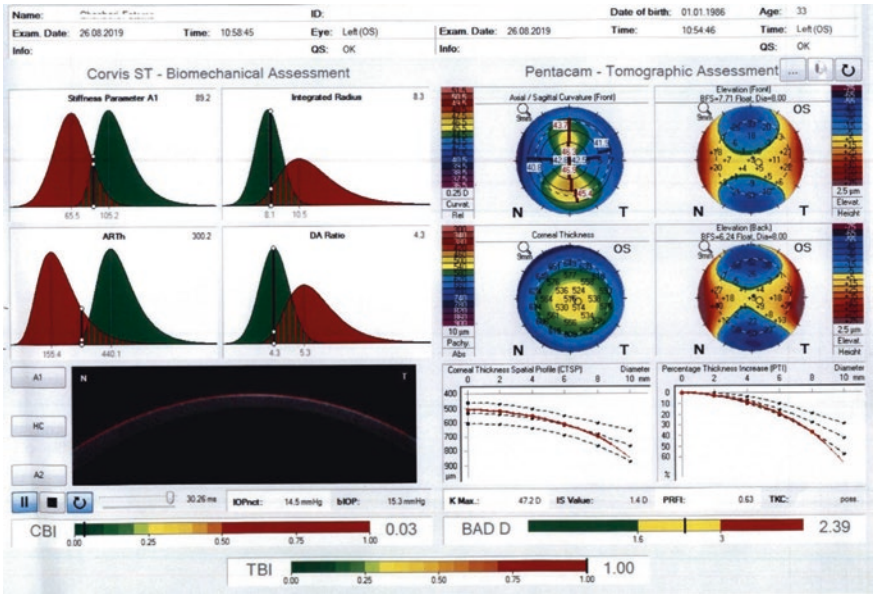

Fig. 54 There is normal CBI on both eyes of the same patient and normal TBI and BADD values in the right eye and abnormal TBI and BADD values in the left eye

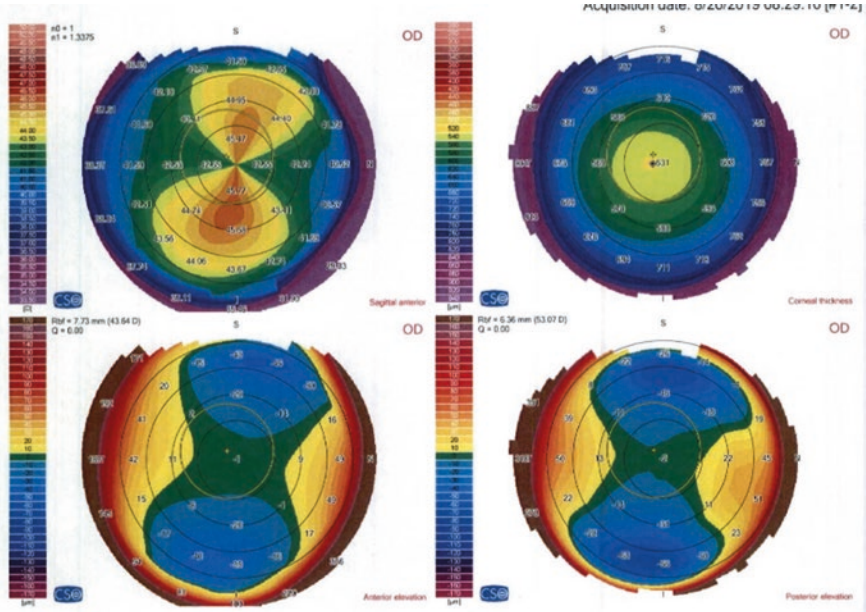

Acquisition quality	Coverage(SC.) = 99%	Not edited(SC.) = 100%
	Coverage(P.) = 86%	Centration(P.) = 93%

Summary Indices

HVID = 11.80 mm
Pupil (Topographic)
r = 0.49 mm @ 139°
Ø = 3.61 mm
λ intercept: r = 1.14 mm @ 139°
Thinnest location
r = 0.40 mm @ 182°
Thk = 529 µm
Apex
r = 1.60 mm @ 261°
Curv = 46.61 D
Anterior chamber
CCT + AD =
0.531 + 3.31 = 3.84 mm
Volume = 176 mm³
Iridocorneal angle = 44°
HACD = 12.18 mm
Lens rise = 0.18 mm
Corneal volume (Ø=10mm)
Volume = 59.9 mm³

K readings (n0 = 1, n1 = 1.3375)

Sim-k	K1 = 42.47 D @ 170°
	K2 = 45.80 D @ 80°
	Avg = 44.07 D
	Cyl = -3.33 D Ax 170°
Anterior Ø=3mm	K1 = 42.54 D @ 170°
	K2 = 45.80 D @ 80°
	Avg = 44.11 D
	Cyl = -3.26 D Ax 170°
Anterior Ø=5mm	K1 = 42.47 D @ 170°
	K2 = 45.75 D @ 80°
	Avg = 44.05 D
	Cyl = -3.28 D Ax 170°
Anterior Ø=7mm	K1 = 42.30 D @ 169°
	K2 = 45.58 D @ 79°
	Avg = 43.88 D
	Cyl = -3.28 D Ax 169°

K readings (n1 = 1.376, n2 = 1.336)

Posterior Ø=3mm	K1 = -6.04 D @ 173°
	K2 = -6.78 D @ 83°
	Avg = -6.39 D
	Cyl = +0.74 D Ax 173°
Posterior Ø=5mm	K1 = -6.05 D @ 172°
	K2 = -6.78 D @ 82°
	Avg = -6.39 D
	Cyl = +0.73 D Ax 172°
Posterior Ø=7mm	K1 = -6.11 D @ 171°
	K2 = -6.69 D @ 81°
	Avg = -6.39 D
	Cyl = +0.59 D Ax 171°

Refractive analysis

Ø=4.0mm
Cyl = -2.85 D Ax 167°
MPP = 43.53 D
LSA = 0.68 D

Keratoconus screening

SIf = 0.52 D
KVf = 4 µm
BCVf = 0.22 D @ 240°
SIb = -0.16 D
KVb = 14 µm
BCVb = 0.00 D @ 326°
Thk = 529 µm
Class:
- 'Normal'

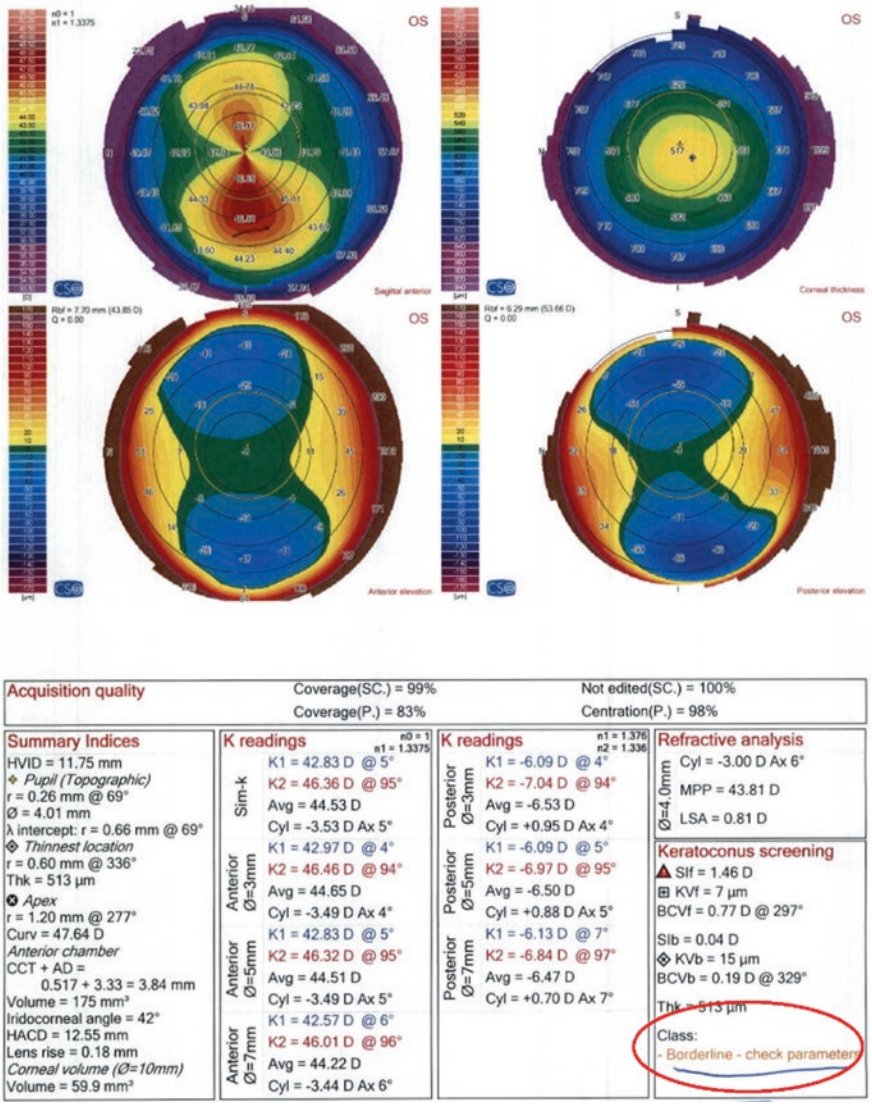

Fig. 55 The Sirius keratoconus screening software has classified both eyes of the same patient correctly: OD; normal and OS; borderline-check parameter which indicates the abnormal cornea in the left eye

Case 12.

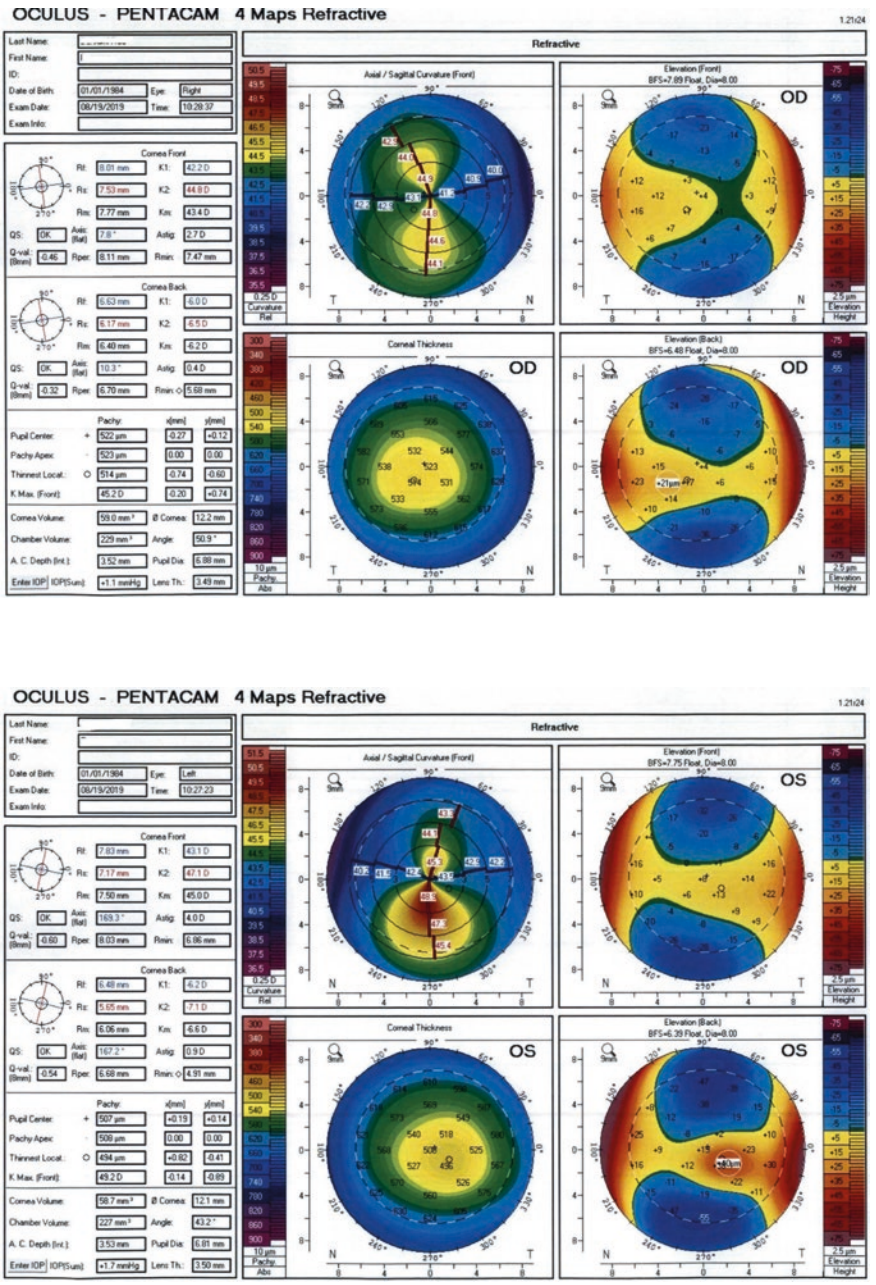

Fig. 56 A 34-year-old woman with forme fruste keratoconus (FFCN) in the right eye and subclinical keratoconus in the left eye and refractive errors: OD = −0.75/−1.75~175 CDVA = 10/10 and OS = −2.25/−4.00~172 CDVA = 10/10 with asymmetric bow tie and abnormal values in the left eye on Pentacam. There is apparently normal cornea in the right eye on the topography map

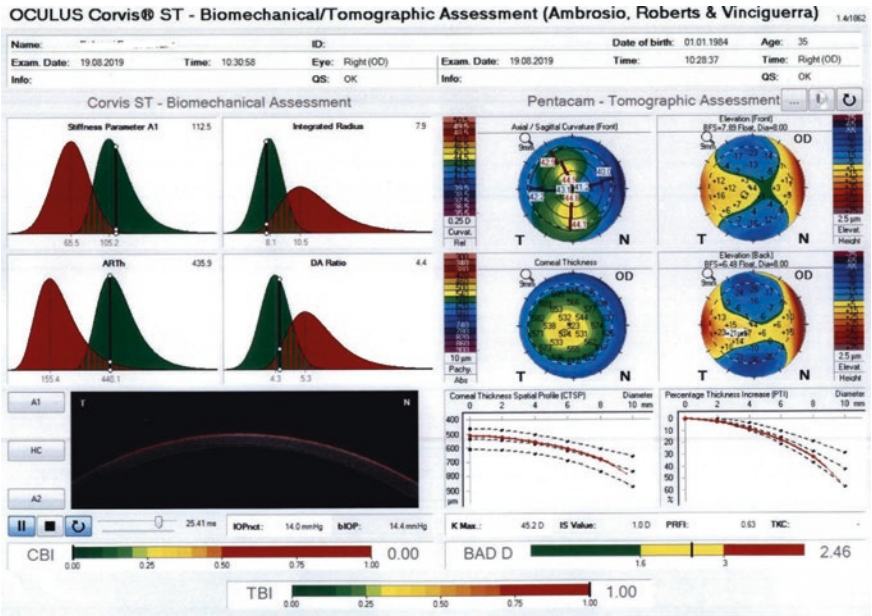

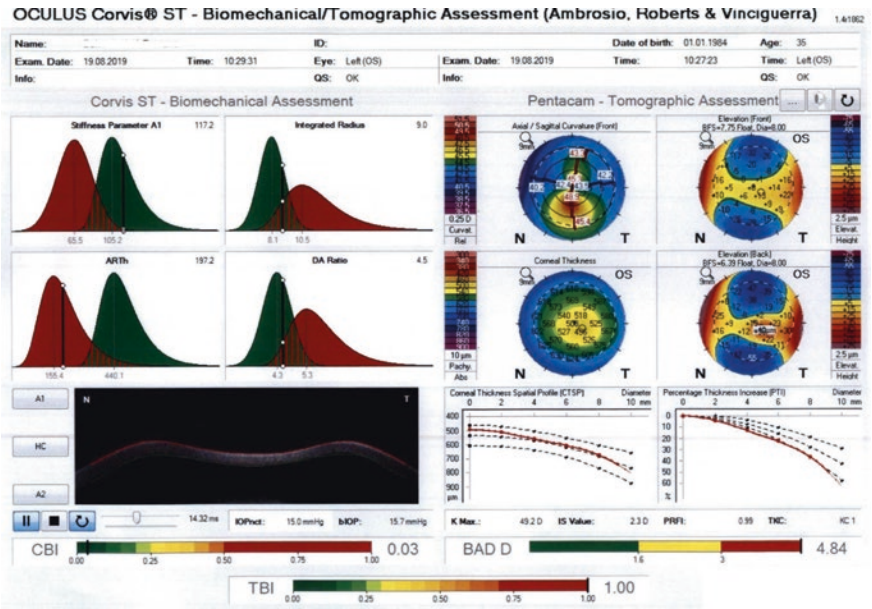

Fig. 57 There are abnormal findings in BADD and TBI values in combined biomechanical and topographical assessments, however, the corneal biomechanical index (CBI) shows normal values in both eyes

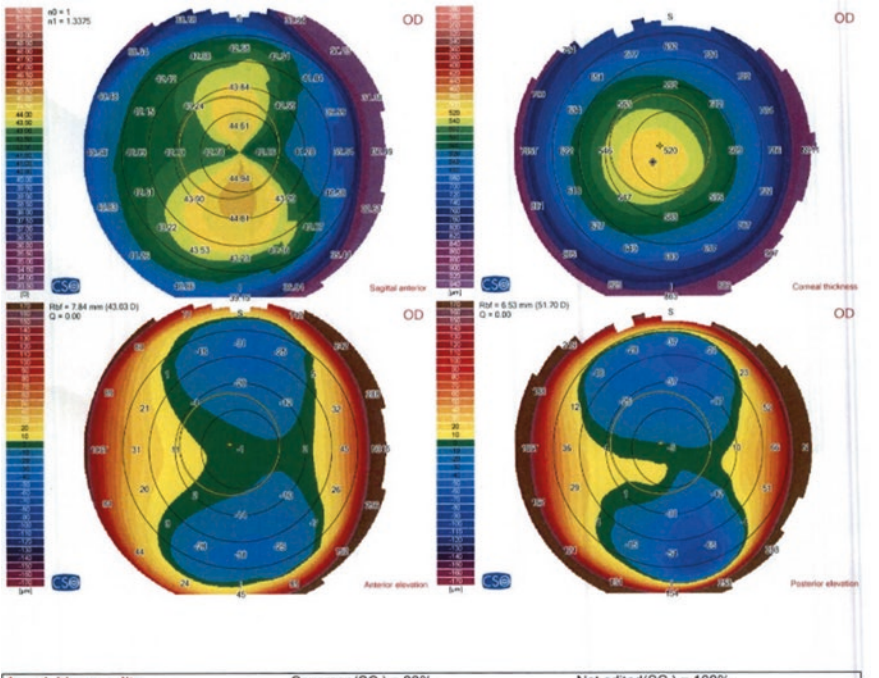

Acquisition quality	Coverage(SC.) = 99%	Not edited(SC.) = 100%
	Coverage(P.) = 85%	Centration(P.) = 98%

Summary Indices

HVID = 12.49 mm
Pupil (Topographic)
r = 0.45 mm @ 154°
Ø = 3.85 mm
λ intercept: r = 1.10 mm @ 154°
Thinnest location
r = 0.80 mm @ 210°
Thk = 513 µm
Apex
r = 1.40 mm @ 270°
Curv = 45.22 D
Anterior chamber
CCT + AD =
0.520 + 3.47 = 3.99 mm
Volume = 205 mm³
Iridocorneal angle = 52°
HACD = 12.33 mm
Lens rise = 0.11 mm
Corneal volume (Ø=10mm)
Volume = 57.5 mm³

K readings n0 = 1, n1 = 1.3375

Sim-k	K1 = 42.34 D @ 2°	
	K2 = 44.71 D @ 92°	
	Avg = 43.49 D	
	Cyl = -2.37 D Ax 2°	
Anterior Ø=3mm	K1 = 42.48 D @ 4°	
	K2 = 44.79 D @ 94°	
	Avg = 43.60 D	
	Cyl = -2.31 D Ax 4°	
Anterior Ø=5mm	K1 = 42.34 D @ 2°	
	K2 = 44.68 D @ 92°	
	Avg = 43.48 D	
	Cyl = -2.35 D Ax 2°	
Anterior Ø=7mm	K1 = 42.09 D @ 2°	
	K2 = 44.46 D @ 92°	
	Avg = 43.25 D	
	Cyl = -2.37 D Ax 2°	

K readings n1 = 1.376, n2 = 1.336

Posterior Ø=3mm	K1 = -6.03 D @ 9°	
	K2 = -6.59 D @ 99°	
	Avg = -6.30 D	
	Cyl = +0.56 D Ax 9°	
Posterior Ø=5mm	K1 = -6.01 D @ 6°	
	K2 = -6.53 D @ 96°	
	Avg = -6.26 D	
	Cyl = +0.52 D Ax 6°	
Posterior Ø=7mm	K1 = -5.99 D @ 6°	
	K2 = -6.46 D @ 96°	
	Avg = -6.22 D	
	Cyl = +0.47 D Ax 6°	

Refractive analysis

Ø=4.0mm
Cyl = -2.04 D Ax 180°
MPP = 43.13 D
LSA = 0.40 D

Keratoconus screening

Sif = 0.82 D
KVf = 6 µm
BCVf = 0.50 D @ 236°
Sib = 0.42 D
KVb = 15 µm
BCVb = 0.53 D @ 333°
Thk = 513 µm
Class:
- Borderline - check parameters

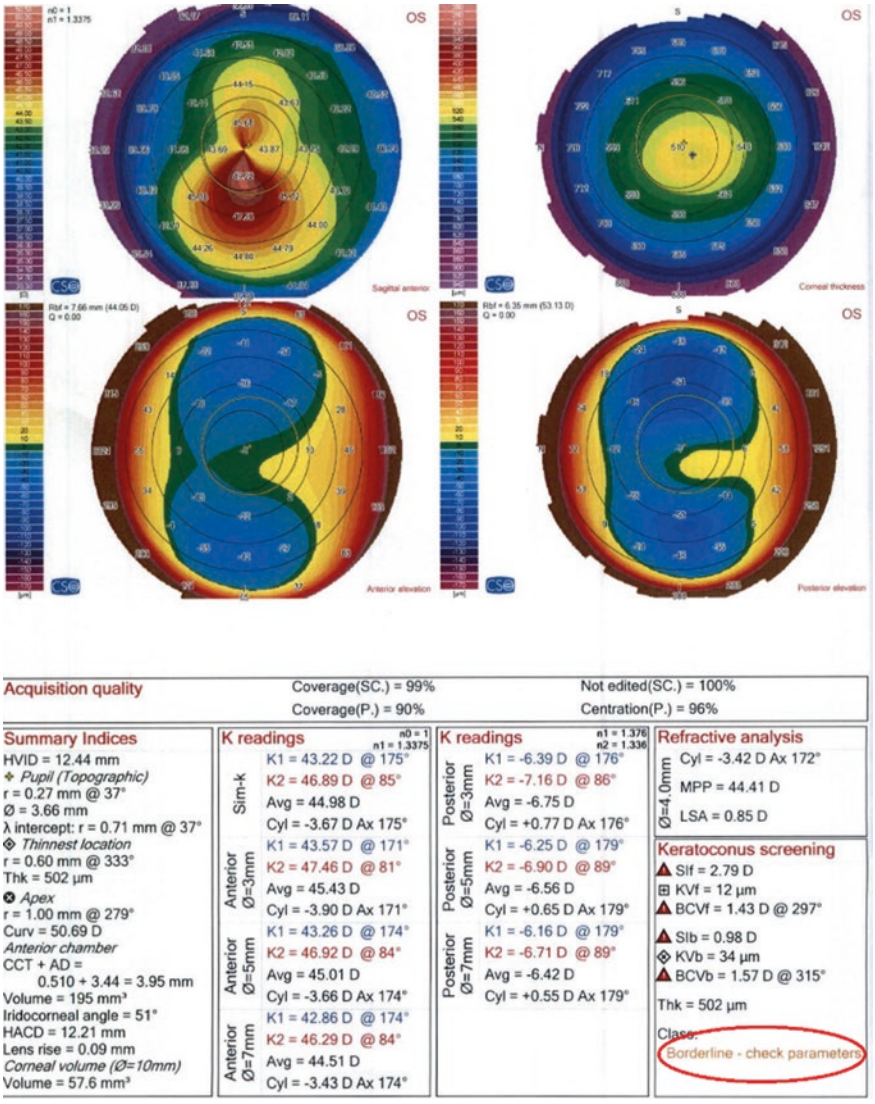

Fig. 58 These findings consisted with the Sirius keratoconus screening phoenix software which shows abnormal-check parameter classifications in both eyes

Case 13.

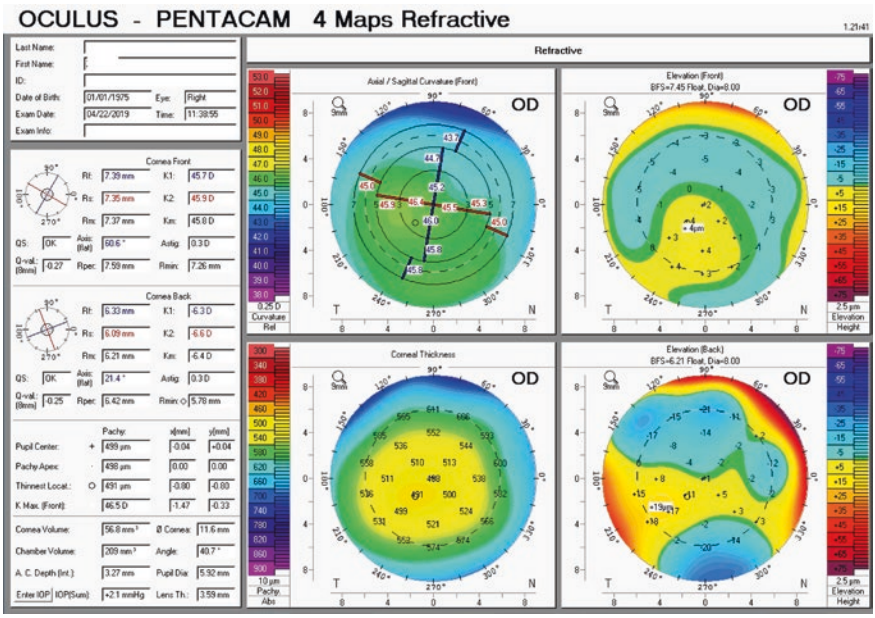

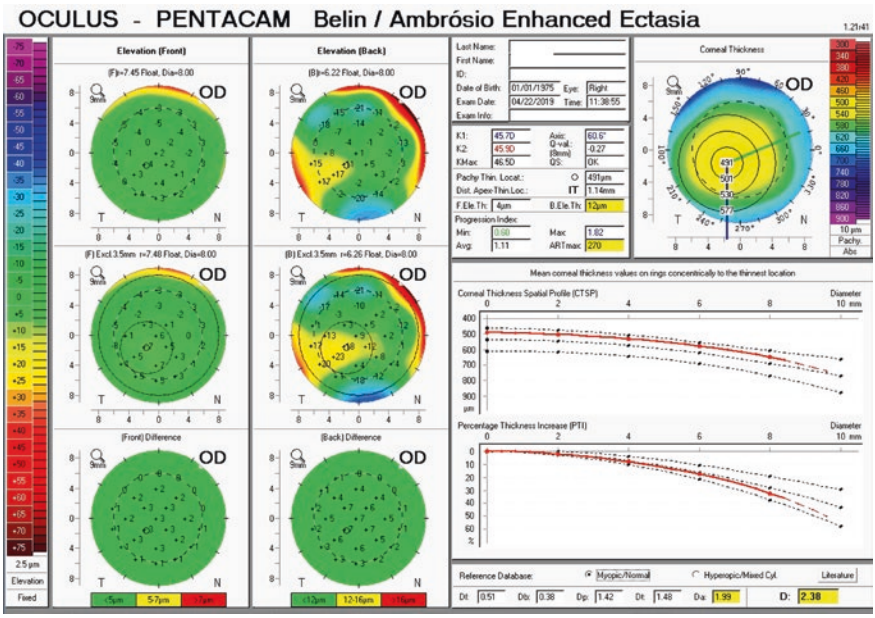

Fig. 59 A 30-year-old woman with early PMD and refractive errors: OD = −3.50/−0.50~20 CDVA = 20/20 and OS = −3.50/−0.25~160 CDVA = 20/20. There are normal thickness values and crab claw pattern on refractive maps of Pentacam

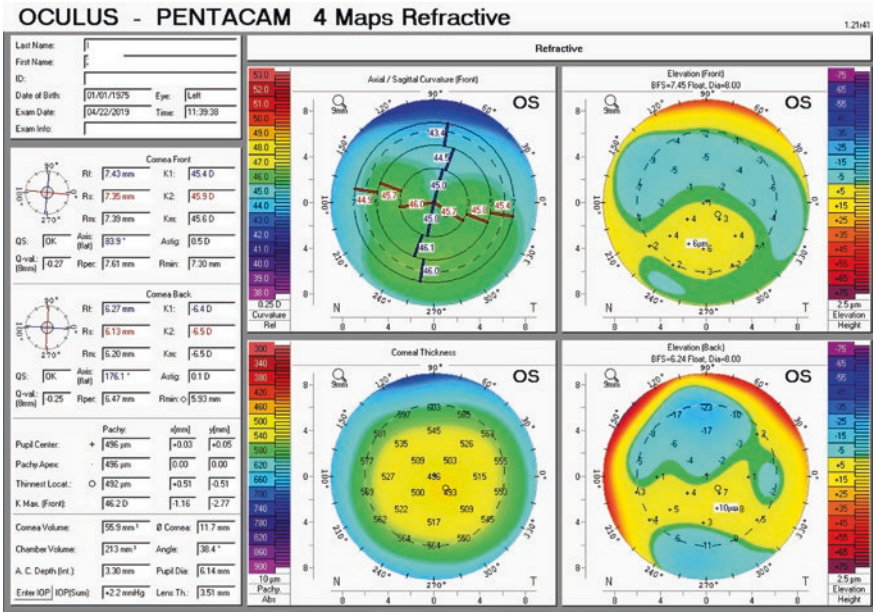

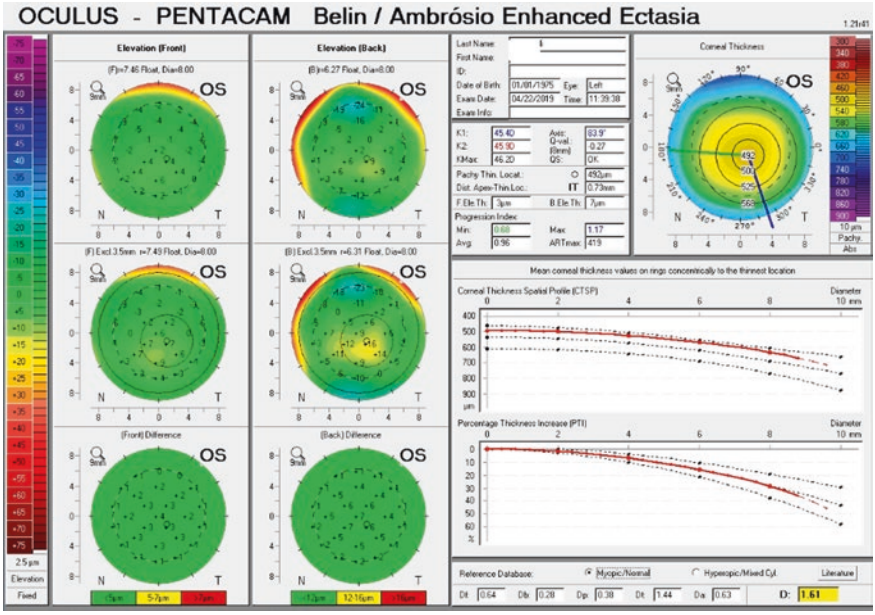

Fig. 60 The D index shows borderline values in both eyes of the same patient

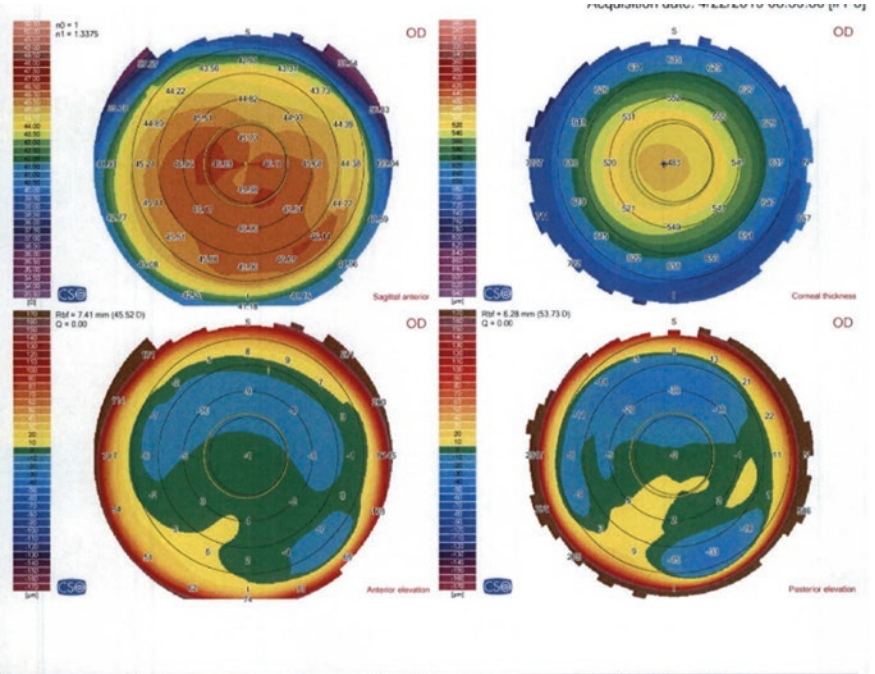

Acquisition quality	Coverage(SC.) = 99%	Not edited(SC.) = 100%
	Coverage(P.) = 92%	Centration(P.) = 94%

Summary Indices

HVID = 11.89 mm
Pupil (Topographic)
r = 0.08 mm @ 170°
Ø = 3.25 mm
λ intercept: r = 0.20 mm @ 170°
Thinnest location
r = 0.40 mm @ 185°
Thk = 481 µm
Apex
r = 1.00 mm @ 182°
Curv = 46.91 D
Anterior chamber
CCT + AD =
0.483 + 3.16 = 3.64 mm
Volume = 168 mm³
Iridocorneal angle = 41°
HACD = 12.31 mm
Lens rise = -0.28 mm
Corneal volume (Ø=10mm)
Volume = 54.1 mm³

K readings (n0 = 1, n1 = 1.3375)

Sim-k	K1 = 45.64 D @ 68°
	K2 = 46.18 D @ 158°
	Avg = 45.91 D
	Cyl = -0.54 D Ax 68°
Anterior Ø=3mm	K1 = 45.70 D @ 66°
	K2 = 46.29 D @ 156°
	Avg = 45.99 D
	Cyl = -0.59 D Ax 66°
Anterior Ø=5mm	K1 = 45.62 D @ 69°
	K2 = 46.17 D @ 159°
	Avg = 45.90 D
	Cyl = -0.54 D Ax 69°
Anterior Ø=7mm	K1 = 45.47 D @ 71°
	K2 = 45.97 D @ 161°
	Avg = 45.72 D
	Cyl = -0.50 D Ax 71°

K readings (n1 = 1.376, n2 = 1.336)

Posterior Ø=3mm	K1 = -6.37 D @ 177°
	K2 = -6.54 D @ 87°
	Avg = -6.46 D
	Cyl = +0.17 D Ax 177°
Posterior Ø=5mm	K1 = -6.39 D @ 3°
	K2 = -6.52 D @ 93°
	Avg = -6.45 D
	Cyl = +0.13 D Ax 3°
Posterior Ø=7mm	K1 = -6.40 D @ 23°
	K2 = -6.50 D @ 113°
	Avg = -6.45 D
	Cyl = +0.09 D Ax 23°

Refractive analysis

Ø=4.0mm
Cyl = -0.79 D Ax 70°
MPP = 45.52 D
LSA = 0.79 D

Keratoconus screening

⚠ SIf = 0.93 D
⊞ KVf = 5 µm
BCVf = 0.45 D @ 240°
SIb = 0.18 D
KVb = 13 µm
BCVb = 0.35 D @ 326°
⚠ Thk = 481 µm
Class:
- Borderline - check parameters

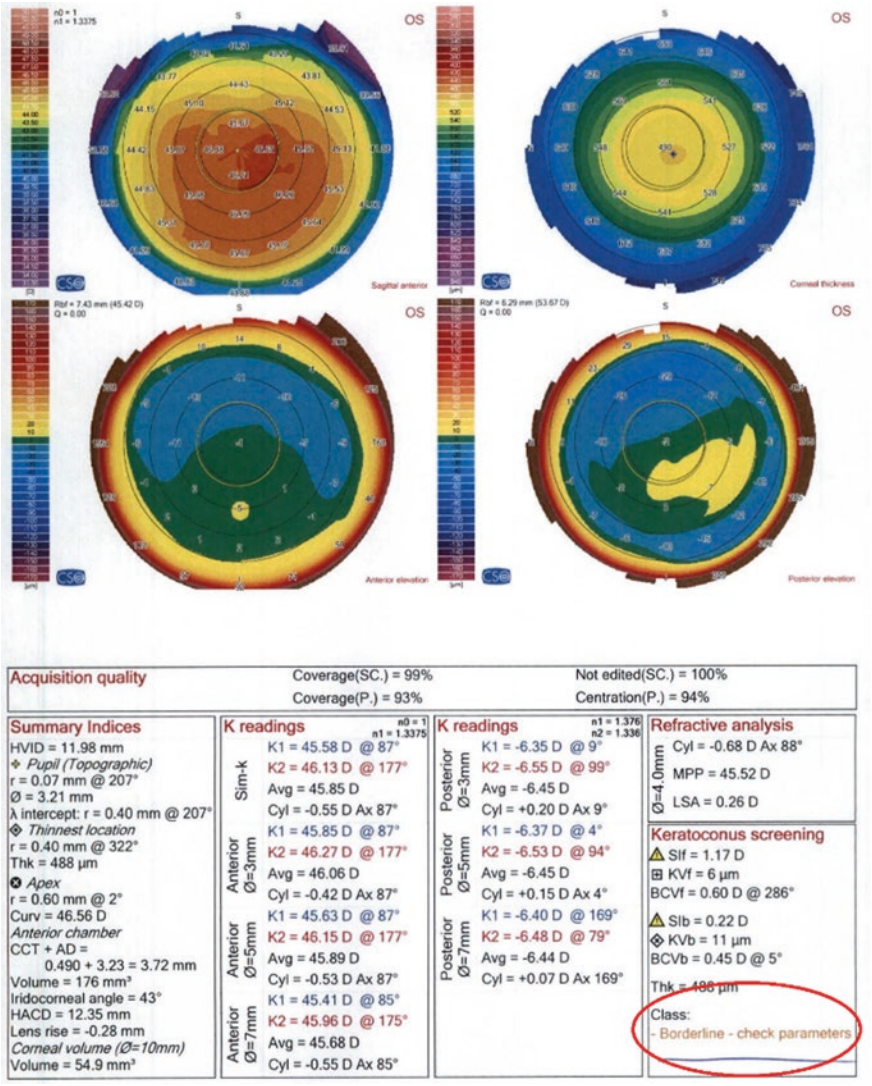

Fig. 61 The Sirius phoenix software keratoconus detection classified both eyes of the same patient correctly as borderline-check parameters

Case 14.

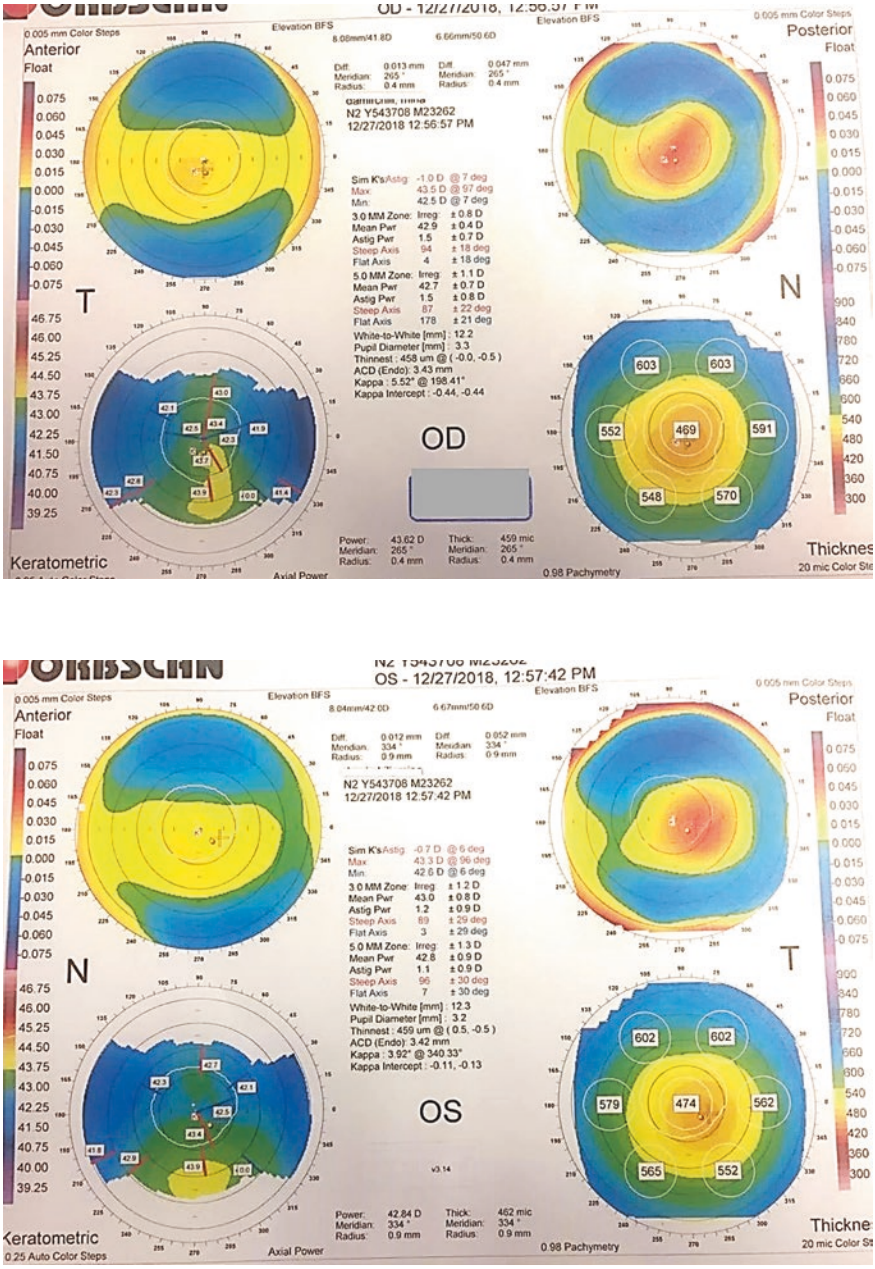

Fig. 62 A 27-year-old woman with the subtle topographic changes with corneal thinning in the right eye and subclinical keratoconus in the left eye and refractive errors: OD = −3.25/−0.75~55 CDVA = 10/10 and OS = −3.00/−1.00~90 CDVA = 10/10 with abnormal values in Orbscan in both eyes. In the early stages of keratoconus, corneal changes may be very mild and may not even be seen in OCT

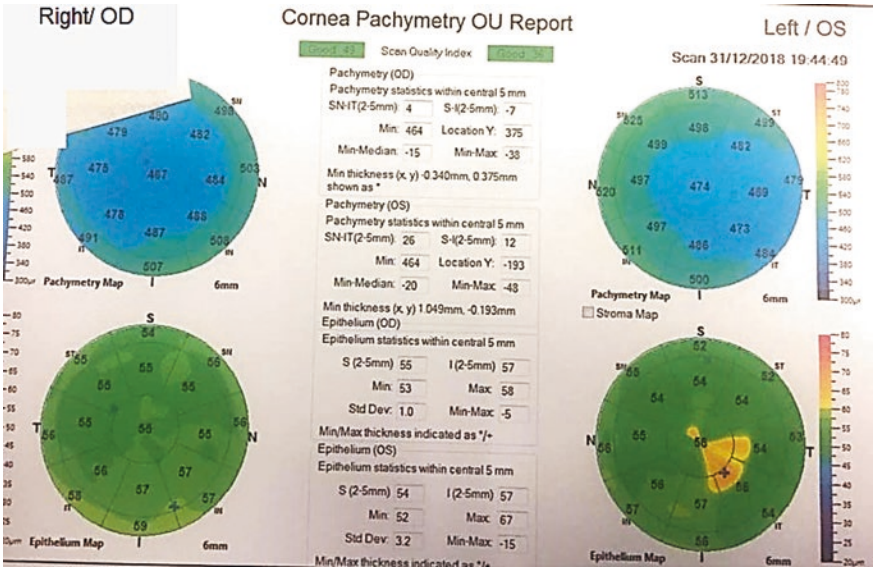

Fig. 63 The epithelial thickness map in OCT (Optovue) shows normal values in the right eye and abnormal values in the left eye

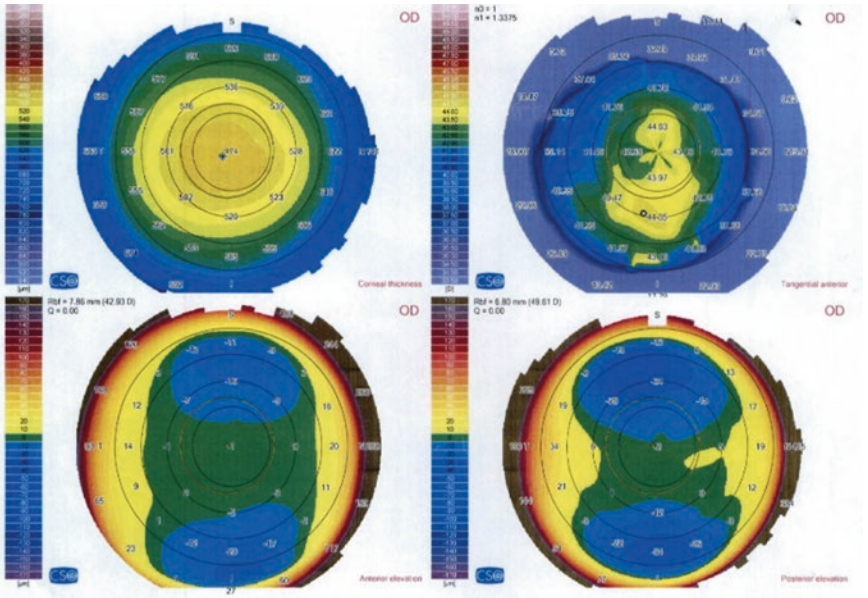

Acquisition quality	Coverage(SC.) = 99%	Not edited(SC.) = 100%
	Coverage(P.) = 89%	Centration(P.) = 88%

Summary Indices

HVID = 12.67 mm
Pupil (Topographic)
r = 0.17 mm @ 165°
Ø = 3.62 mm
λ intercept: r = 0.41 mm @ 165°
Thinnest location
r = 0.40 mm @ 208°
Thk = 473 µm
Apex
r = 2.40 mm @ 257°
Curv = 44.50 D
Anterior chamber
CCT + AD =
0.474 + 3.52 = 4.00 mm
Volume = 210 mm³
Iridocorneal angle = 49°
HACD = 12.72 mm
Lens rise = 0.17 mm
Corneal volume (Ø=10mm)
Volume = 49.8 mm³

K readings (n0 = 1, n1 = 1.3375)

Sim-k	K1 = 42.81 D @ 4°
	K2 = 43.89 D @ 94°
	Avg = 43.34 D
	Cyl = -1.08 D Ax 4°
Anterior Ø=3mm	K1 = 42.98 D @ 5°
	K2 = 43.93 D @ 95°
	Avg = 43.45 D
	Cyl = -0.95 D Ax 5°
Anterior Ø=5mm	K1 = 42.84 D @ 4°
	K2 = 43.87 D @ 94°
	Avg = 43.35 D
	Cyl = -1.03 D Ax 4°
Anterior Ø=7mm	K1 = 42.63 D @ 2°
	K2 = 43.75 D @ 92°
	Avg = 43.18 D
	Cyl = -1.13 D Ax 2°

K readings (n1 = 1.376, n2 = 1.336)

Posterior Ø=3mm	K1 = -5.78 D @ 5°
	K2 = -6.19 D @ 95°
	Avg = -5.98 D
	Cyl = +0.40 D Ax 5°
Posterior Ø=5mm	K1 = -5.80 D @ 5°
	K2 = -6.16 D @ 95°
	Avg = -5.97 D
	Cyl = +0.36 D Ax 5°
Posterior Ø=7mm	K1 = -5.81 D @ 6°
	K2 = -6.09 D @ 96°
	Avg = -5.95 D
	Cyl = +0.28 D Ax 6°

Refractive analysis

Ø=4.0mm
Cyl = -0.70 D Ax 3°
MPP = 43.01 D
LSA = 0.73 D

Keratoconus screening

Sif = 0.60 D
KVf = 5 µm
BCVf = 0.33 D @ 243°
Sib = 0.18 D
KVb = 9 µm
BCVb = 0.36 D @ 311°
Thk = 473 µm
Class:
Borderline - check parameters

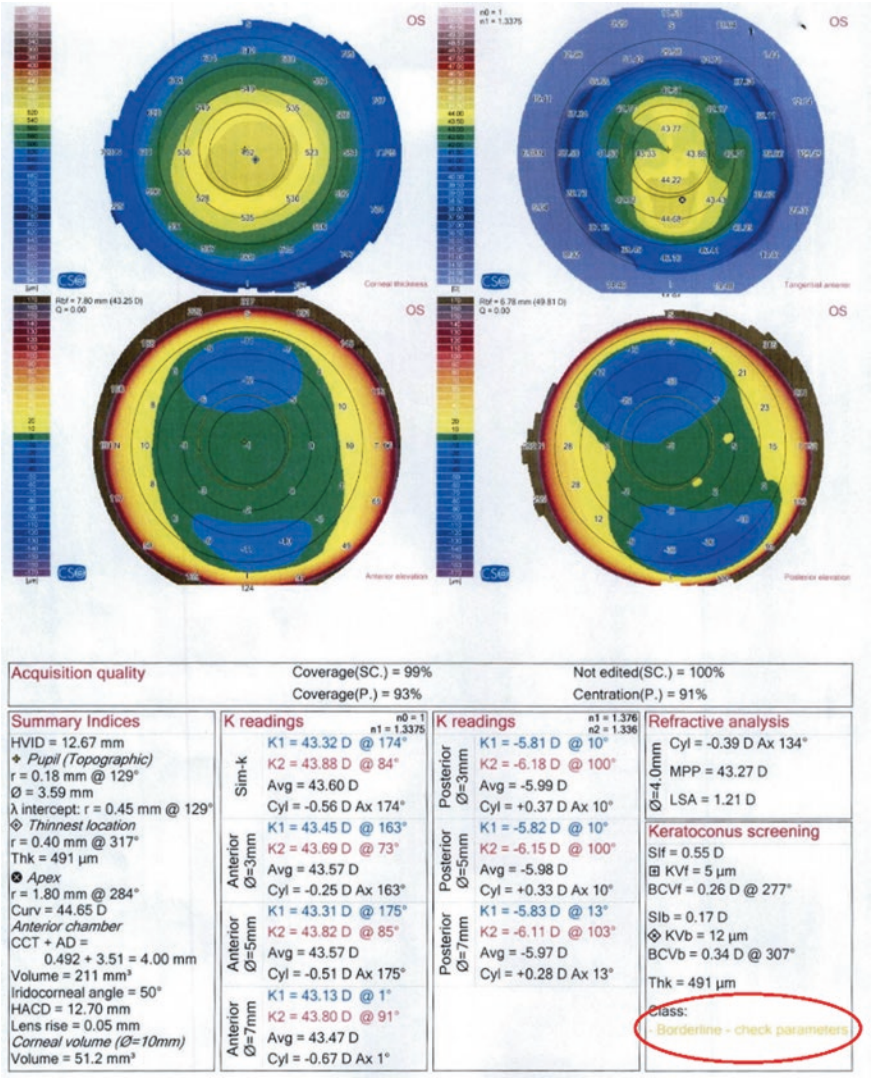

Fig. 64 These findings are consistent with the Sirius keratoconus screening software in recognizing both eyes as borderline-checking parameters

Case 15.

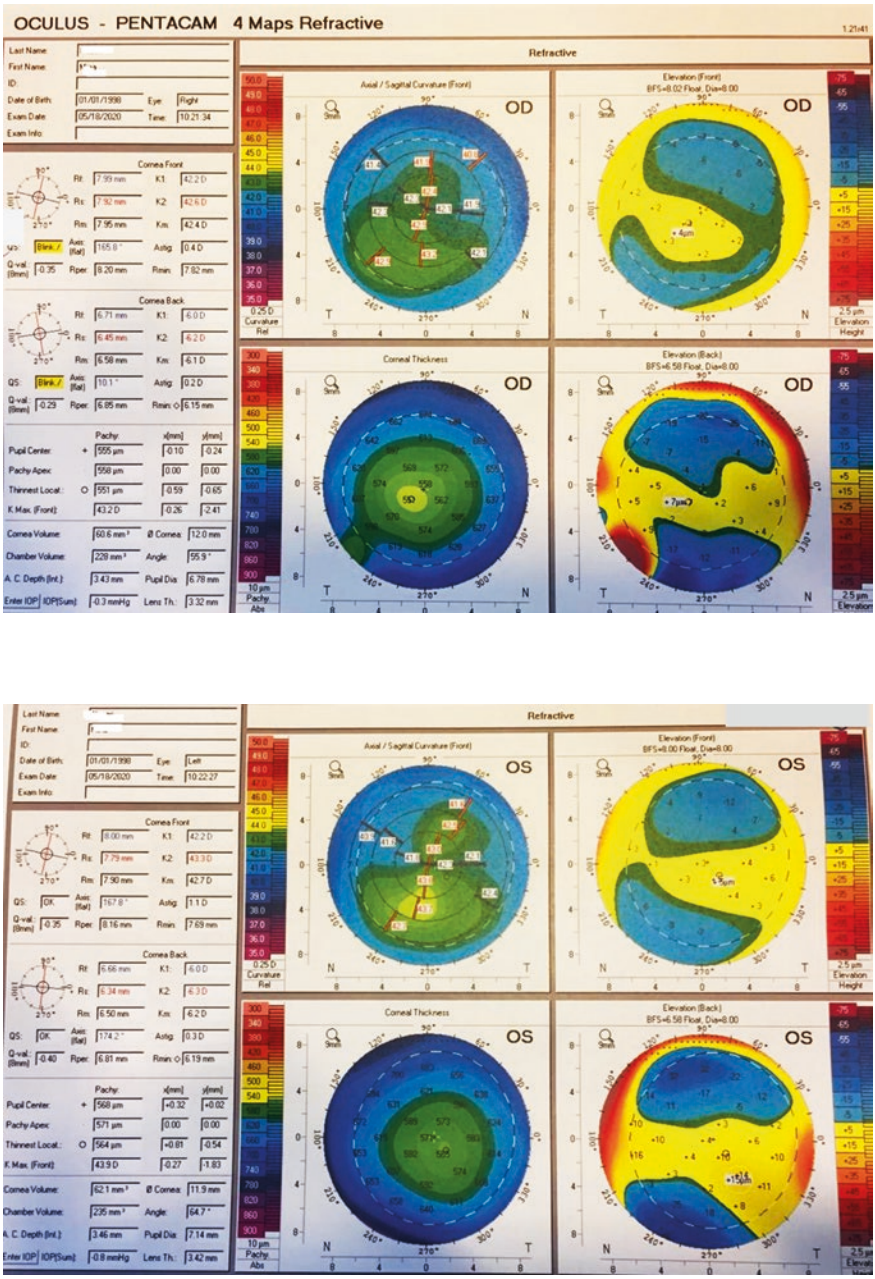

Fig. 65 A 20-year-old candidate for laser vision correction. Refractive errors in both eyes: −2.00/−0.50~180 and CDVA 10/10 OU. Four Refractive maps of Pentacam and Sirius seems normal. However, topometric keratoconus staging and Placido based topography maps both shows subclinical form of keratoconus

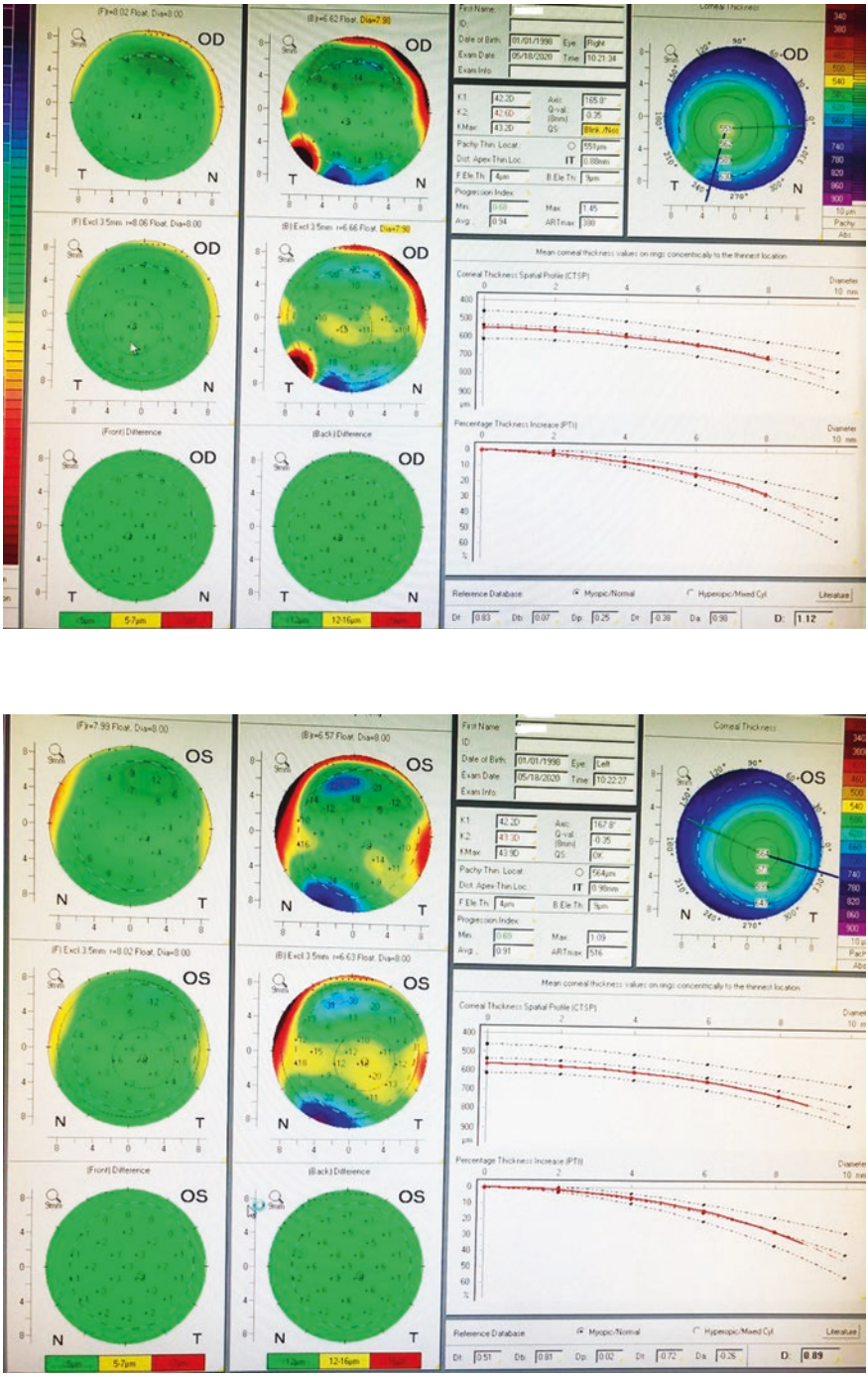

Fig. 66 The D index and pachymetric progression are in normal range in the same patient

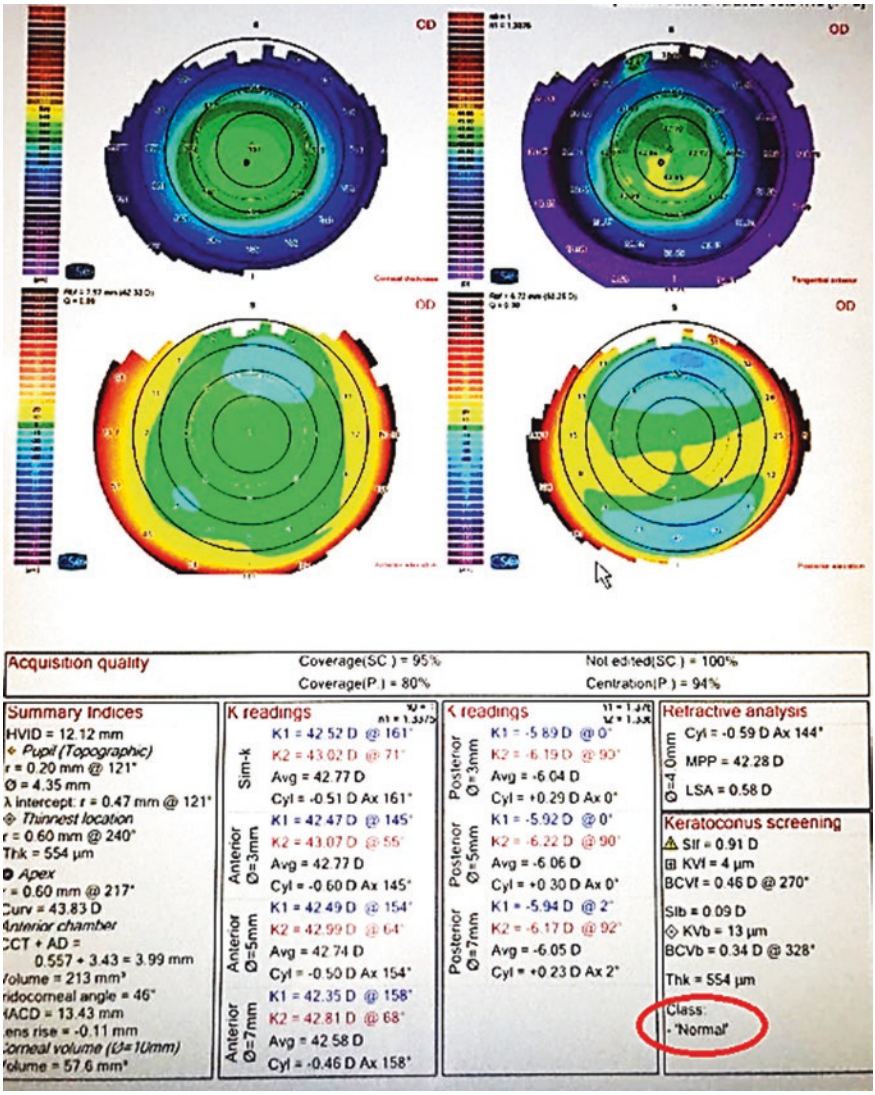
OD
OD
OD
OD
Acquisition quality
Coverage(SC) = 95%
Coverage(P) = 80%
Not edited(SC) = 100%
Centration(P) = 94%
Summary Indices
HVID = 12.12 mm
Pupil (Topographic)
r = 0.20 mm @ 121°
Ø = 4.35 mm
λ intercept: r = 0.47 mm @ 121°
Thinnest location
r = 0.60 mm @ 240°
Thk = 554 µm
Apex
r = 0.60 mm @ 217°
Curv = 43.83 D
Anterior chamber
ACT + AD =
0.557 + 3.43 = 3.99 mm
Volume = 213 mm³
Iridocorneal angle = 46°
ACD = 13.43 mm
Lens rise = -0.11 mm
Corneal volume (Ø=10mm)
Volume = 57.6 mm³
K readings
Sim-k
K1 = 42.52 D @ 161°
K2 = 43.02 D @ 71°
Avg = 42.77 D
Cyl = -0.51 D Ax 161°
Anterior Ø=3mm
K1 = 42.47 D @ 145°
K2 = 43.07 D @ 55°
Avg = 42.77 D
Cyl = -0.60 D Ax 145°
Anterior Ø=5mm
K1 = 42.49 D @ 154°
K2 = 42.99 D @ 64°
Avg = 42.74 D
Cyl = -0.50 D Ax 154°
Anterior Ø=7mm
K1 = 42.35 D @ 158°
K2 = 42.81 D @ 68°
Avg = 42.58 D
Cyl = -0.46 D Ax 158°
K readings
Posterior Ø=3mm
K1 = -5.89 D @ 0°
K2 = -6.19 D @ 90°
Avg = -6.04 D
Cyl = +0.29 D Ax 0°
Posterior Ø=5mm
K1 = -5.92 D @ 0°
K2 = -6.22 D @ 90°
Avg = -6.06 D
Cyl = +0.30 D Ax 0°
Posterior Ø=7mm
K1 = -5.94 D @ 2°
K2 = -6.17 D @ 92°
Avg = -6.05 D
Cyl = +0.23 D Ax 2°
Refractive analysis
Ø=4.0mm
Cyl = -0.59 D Ax 144°
MPP = 42.28 D
LSA = 0.58 D
Keratoconus screening
Sif = 0.91 D
KVf = 4 µm
BCVf = 0.46 D @ 270°
Sib = 0.09 D
KVb = 13 µm
BCVb = 0.34 D @ 328°
Thk = 554 µm
Class:
- 'Normal'

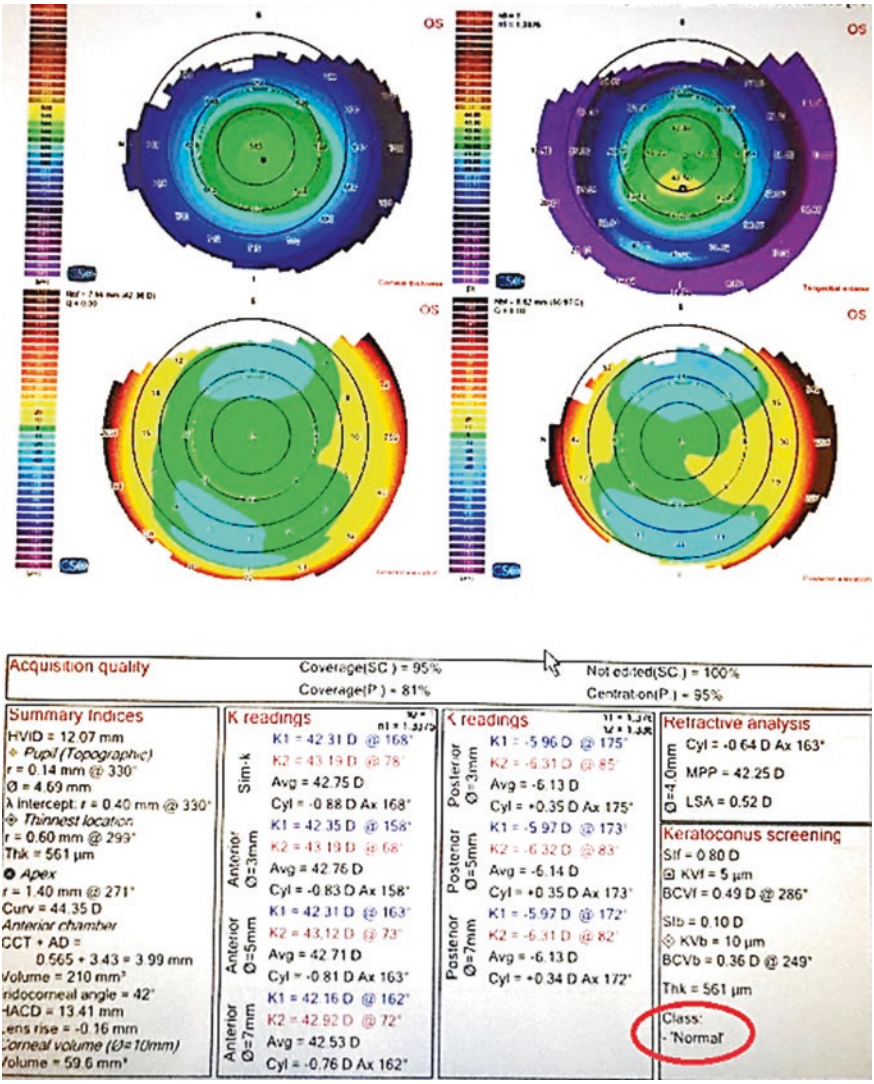

Fig. 67 Phoenix screening software in Sirius indicates normal class in the same patient

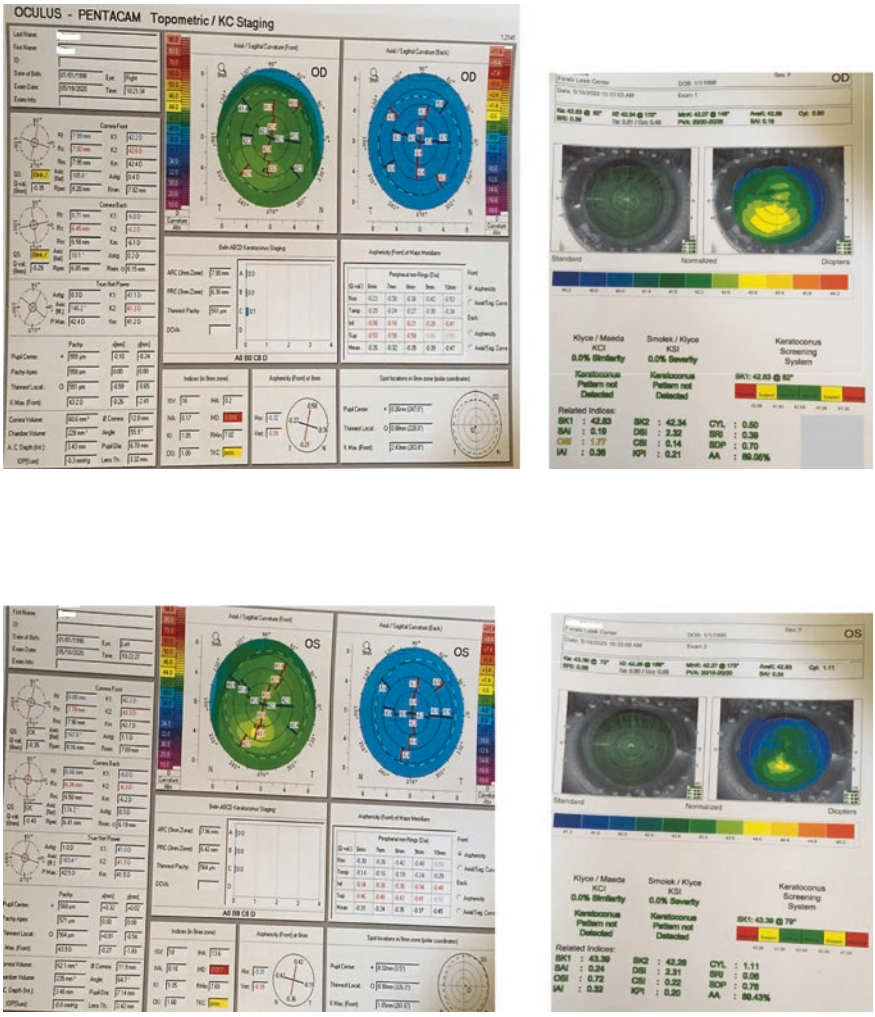

Fig. 68 There are inferior steepening and abnormal findings in topometric indices which show the eyes with subclinical keratoconus

References

1. Sirius CSO Guidelines. https://www.csoitalia.it/en/prodotto/info/47-sirius and Distributor Meeting Sirius.pdf (CSO R&D department). Last accessed 13 April 2020.
2. Savini G, Barboni P, Carbonelli M, Hoffer KJ. Repeatability of automatic measurements by a new Scheimpflug camera combined with Placido topography. J Cataract Refract Surg. 2011;37(10):1809–16.
3. Hondur G, Cagil N, Sarac O, Ozcan ME, Kosekahya P. Pupillary offset in keratoconus and its relationship with clinical and topographical features. Curr Eye Res. 2017;42(5):708–12.
4. Gulmez Sevim D, Gumus K, Unlu M. Reliable, noncontact imaging tool for the evaluation of meibomian gland function: sirius meibography. Eye Contact Lens. 2020;46(Suppl 2):135–40.
5. Mohamed Mostafa E, Abdellah MM, Elhawary AM, Mounir A. Noncontact meibography in patients with keratoconus. J Ophthalmol. 2019;2:2965872.
6. Mansoori T, Balakrishna N. Anterior segment morphology after laser iridotomy in primary angle closure suspects. Clin Exp Optom. 2018;101(3):333–8.
7. Fernandez-Vega Cueto L, Lisa C, Madrid-Costa D, Merayo-Lloves J, Alfonso JF. Long-term follow-up of intrastromal corneal ring segments in paracentral keratoconus with coincident corneal keratometric, comatic, and refractive axes: stability of the procedure. J Ophthalmol. 2017;2017:4058026.
8. Savini G, Bedei A, Barboni P, Ducoli P, Hoffer KJ. Intraocular lens power calculation by ray-tracing after myopic excimer laser surgery. Am J Ophthalmol. 2014;157(1):150–3.
9. Cavas-Martinez F, De la Cruz Sanchez E, Nieto Martinez J, Fernandez Canavate FJ, Fernandez-Pacheco DG. Corneal topography in keratoconus: state of the art. Eye Vis. 2016;3:5.
10. Heidari Z, Hashemi H, Mohammadpour M. Evaluation of corneal topographic, tomographic and biomechanical indices for detecting clinical and subclinical keratoconus: a comprehensive three device study. Int J Ophthalmol. 2021; 14(2) (In Press).
11. Shetty R, Rao H, Khamar P, Sainani K, Vunnava K, Jayadev C, Kaweri L. Keratoconus screening indices and their diagnostic ability to distinguish normal from ectatic corneas. Am J Ophthalmol. 2017;181:140–8.
12. Heidari Z, Mohammadpour M, Hashemi H, Jafarzadehpur E, Moghaddasi A, Yaseri M, Fotouhi A. Early diagnosis of subclinical keratoconus by wavefront parameters using Scheimpflug, Placido and Hartmann-Shack based devices. Int Ophthalmol. 2020;40(7):1659-1671.
13. Zhang Y, Chen YG, Yang HY, Xia YJ, Zhao R. Analysis on the role of Sirius combined topography and tomography system in screening for suspect keratoconus. Zhonghua Yan Ke Za Zhi. 2018;54(1):33–8.

MS-39®

Mehrdad Mohammadpour and Zahra Heidari

Introduction

MS-39® (Costruzione Strumenti Oftalmici, Florence, Italy) is a spectral-domain (SD) anterior segment optical coherence tomography (ASOCT) (845 nm) combined with 22 rings of Placido disk which provides anterior chamber tomography, anterior and posterior topography and high-resolution corneal imaging. The MS-39 shows cross-sectional images with a 16 mm diameter. New ASOCT with high repeatability is reliable for clinical use [1] (Fig. 1).

This machine provides complete information about anterior and posterior corneal curvature and elevation as well as pachymetry and corneal dioptric power of both surfaces. In addition to the clinical diagnosis of the anterior segment, it can be assessed the corneal surgery planning, an IOL calculation, pupil diameter measurements and the advanced analysis of tear film. Corneal aberrometry, glaucoma screening, keratoconus screening, crystalline biometry and features of Phoenix software are available in new AS-OCT (Fig. 2 and Table 1).

Since scheimpflug imaging suffers from scattering and reflected halos lead to inaccurate measurements, AS-OCT images provide excellent high-resolution imaging to allow for epithelial thickness measurement (Fig. 3).

Compared to retinal OCT with an adaptive lens for measuring the anterior segment, the MS-39 AS-OCT with the same axial resolution (3.5 μm) allows wider area measurements (16 mm) (Figs. 4 and 5).

M. Mohammadpour (✉)
Department of Ophthalmology, Faculty of Medicine, Farabi Eye Hospital and Eye Research Center, Tehran University of Medical Sciences, Tehran, Iran
e-mail: mahammadpour@yahoo.com

Z. Heidari
Noor Ophthalmology Research Center, Noor Eye Hospital & Tehran University of Medical Sciences, Tehran, Iran
e-mail: zahra.heidari77@yahoo.com

M. Mohammadpour (ed.), *Diagnostics in Ocular Imaging*,
https://doi.org/10.1007/978-3-030-54863-6_6

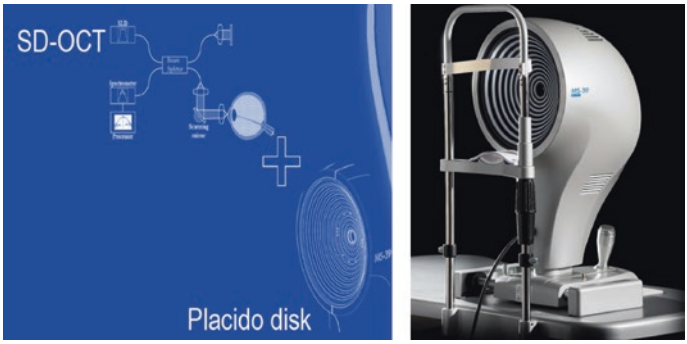

Fig. 1 Combination of ASOCT and Placido disc in MS39 (*With permission from Costruzione Strumenti Oftalmici* (*CSO*)) [2]

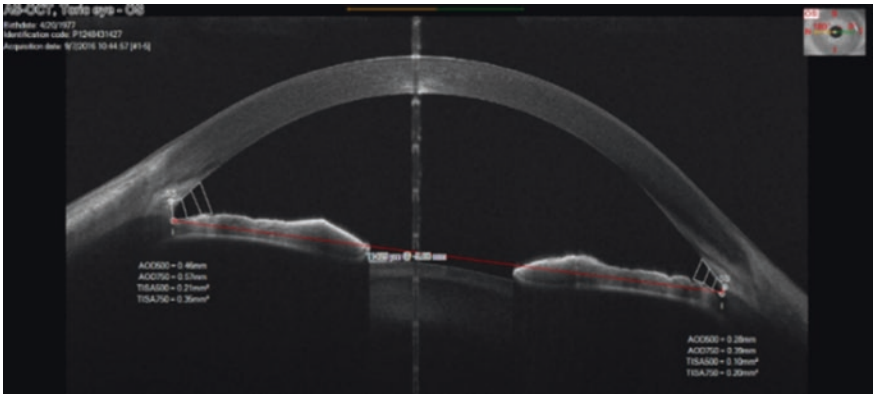

Fig. 2 Anterior segment OCT view (*With permission from CSO*) [2]

Topographic/tomographic evaluations including:

Maps:
- Tangential curvature
- Sagital curvature
- Elevation
- Refractive power
- Corneal thickness
- Epithelial thickness
- Anterior chamber depth

Advanced analysis:
- Customizable summaries
- Keratoconus summary
- ICRS summary
- Optical corneal analysis
- Follow up summaries

Indices:
- Summary indices
- K-readings
- Epithelial thickness indices
- Shape indices
- Refractive analysis indices
- Keratoconus screening

Infrared pupillography:
- Scotopic (0.04 lx)
- Mesopic (4 lx)
- Photopic (50 lx)
- Dynamic light conditions

Table 1 Technical data of MS-39 OCT [2]

Specifications	
Data transfer	USB 3.0
Power supply	External power source 24 VCC in: 100–240 Vac 50/60 Hz – 2A Out: 24 Vdc – 100 W
Power net cable	IEC C14 plug
Dimensions (H × W × D)	505 × 315 × 251 mm
Weight	10.4 kg
Chinrest movement	70 mm ± 1 mm
Chin up height from the table	23 cm
Base movement (xyz)	105 × 110 × 30 mm
Working distance	74 mm
Placido's disk illuminations	Led@635 nm
OCT source	Led@845 nm
Pupillographic illumination	Led@950 nm
Placido disk rings	22
Measured points	31,232 (anterior surface) 25,600 (posterior surface) from 1 D to 100 D
Topographic covering	10 mm
Measurement accuracy	Class A according to UNI EN ISO 19980-2012
Image field	16 mm × 8 mm
Image(s) resolution	Keratoscopy (640 × 480) + 25 radial scans on a 16 mm transversal field (1024 A-scan) Section: 0n 16 mm (1600 A-Scan) on 8 mm
Axial resolution	3.6 µm in tissue
Transversal resolution	35 µm (in air)
Operating system	Windows 10 (64 bit)

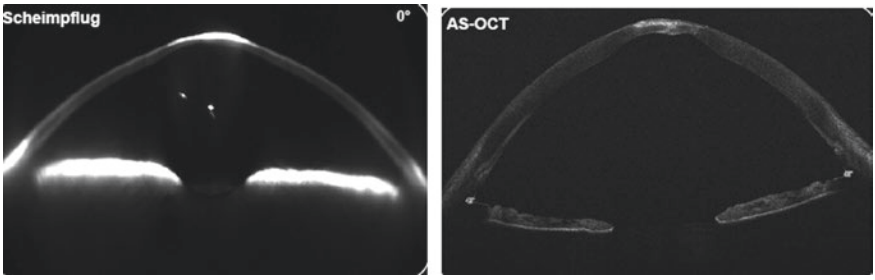

Fig. 3 MS-39 AS-OCT provides better imaging with higher resolution than scheimpflug imaging systems (*With permission from CSO*) [2]

The keratoconus eye with steepening in the bulging area is shown. Tangential curvature is measured at each point of each meridian. Asymmetry indices of the anterior and posterior cornea (SIf and SIb) are defined as the difference of the

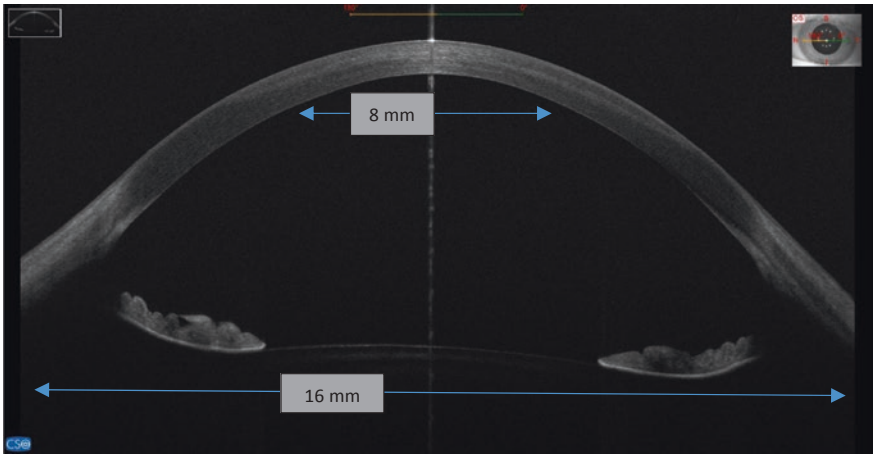

Fig. 4 Wider area measurement in a single step in MS-39 AS-OCT (*With permission from CSO*) [2]

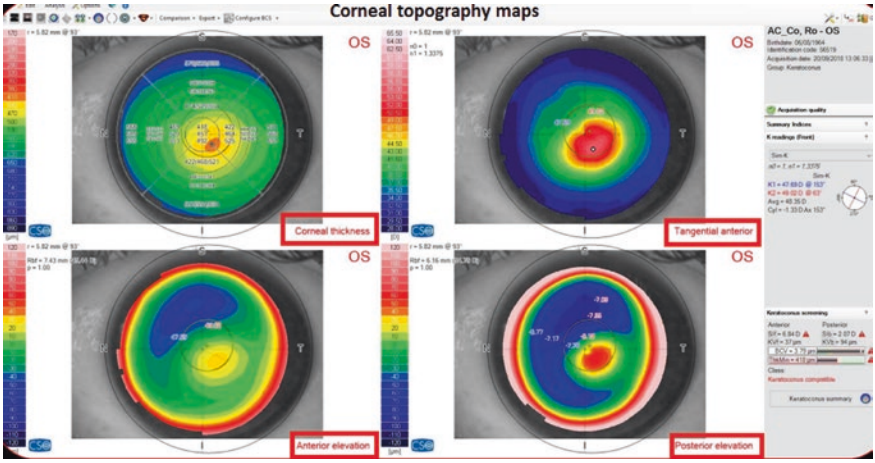

Fig. 5 Curvature, elevation and pachymetric evaluation summary in 4 maps (*With permission from CSO*) [2]

mean anterior tangential curvature expressed in diopters of two circular zones centered on the vertical axis in the inferior and superior hemispheres is helpful for ectasia detection in keratoconus corneas as shown in Fig. 6.

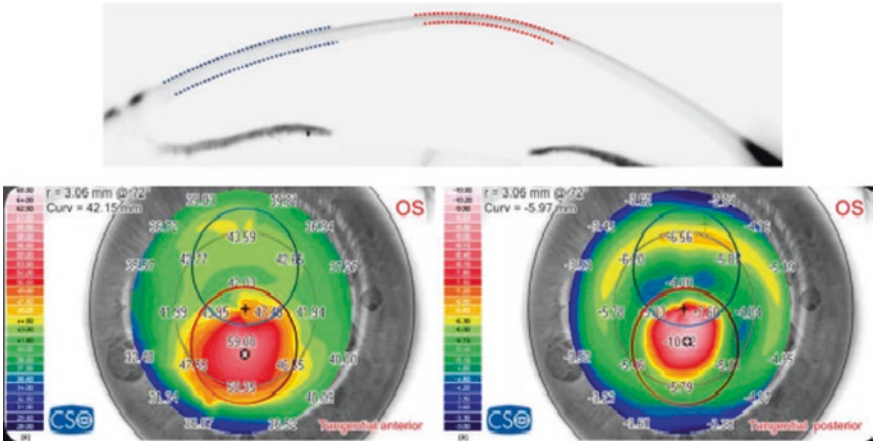

Fig. 6 Keratoconus steepening area and Tangential curvature maps (*With permission from CSO*) [2]

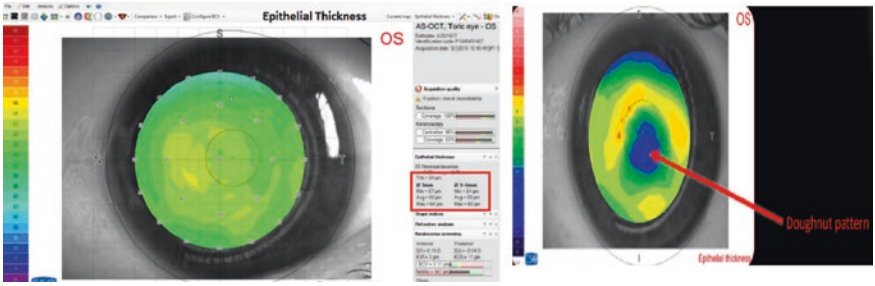

Fig. 7 Epithelial thickness map, and doughnut pattern of epithelial thickness map in keratoconus (*With permission from CSO*) [2]

Epithelial Thickness Map

The epithelial layer masking effect is known for its morphology and MS-39-OCT provides useful information about the corneal surface abnormalities with high repeatability of epithelial thickness measurements in both keratoconic and normal corneas [3]. It can also measure the stromal layer accurately. Epithelial thinning on the cone surrounded by thickening epithelium forms a donut pattern in keratoconic cornea (Fig. 7).

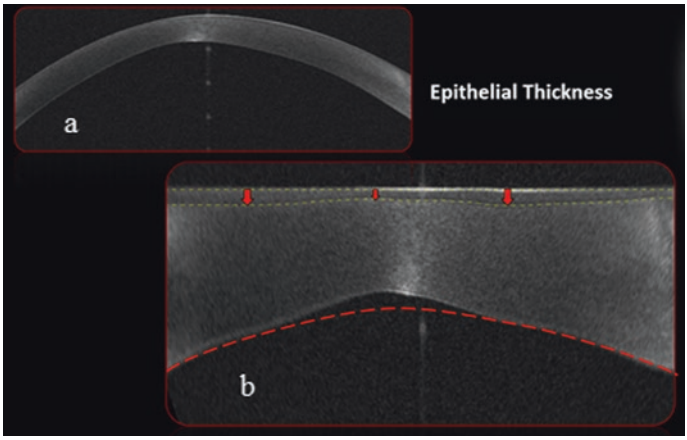

Fig. 8 The normal view (**a**) and straightened view (**b**); epithelium thinning is seen in a straightened view with more detail (*With permission from CSO*) [2]

The normal view and straightened corneal OCT view are shown. In the straightened view the bulged part of the stromal layer becomes thinner in the same part of the epithelial layer as shown in Fig. 8.

Stromal Thickness Map

Stromal layer evaluation provides structural information of the eye. Cross-sectional OCT images create corneal thickness and elevation maps for accurate assessment of ectasia and/or refractive surgery planning (Fig. 9).

Glaucoma Screening

The new OCT provides a glaucoma summary based on stromal spur distance AOD (Angle Opening Distance) and Trabecular Iris Space Area (TISA). Also, intraocular pressure (IOP) correct by adjusting to the corneal thickness (Fig. 10).

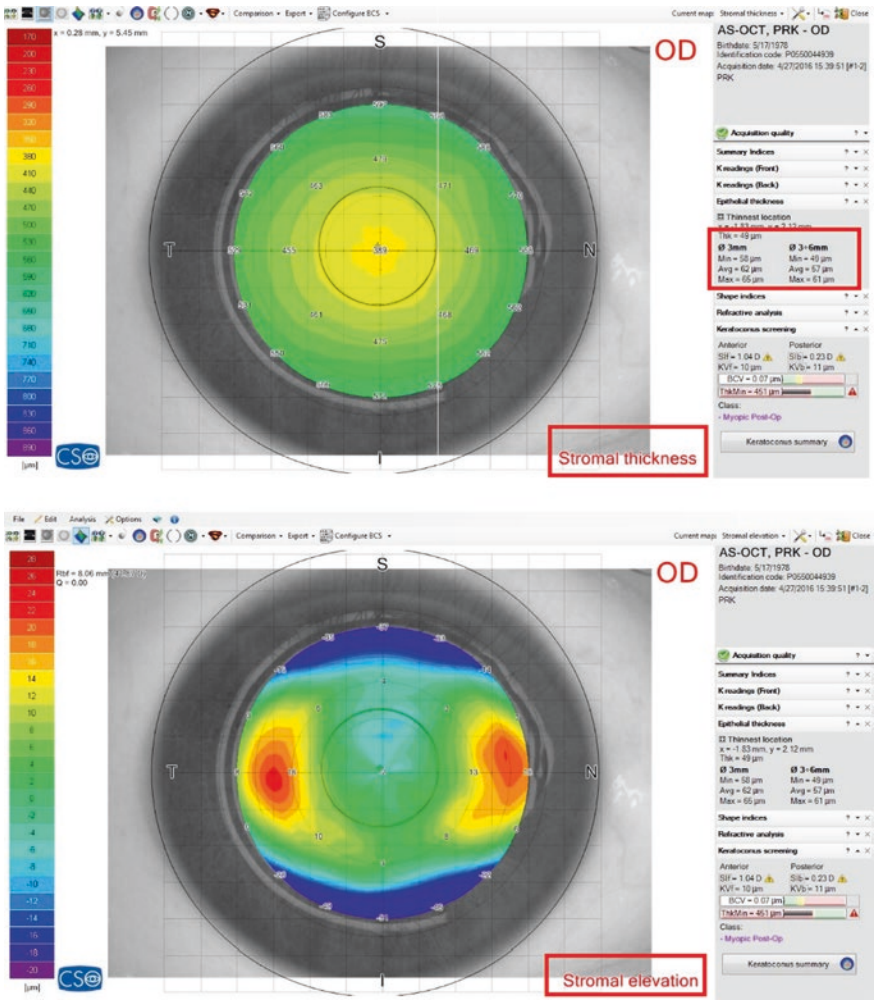

Fig. 9 Stromal thickness and Stromal elevation maps for spherical and toric ablations after photorefractive keratectomy (*With permission from CSO*) [2]

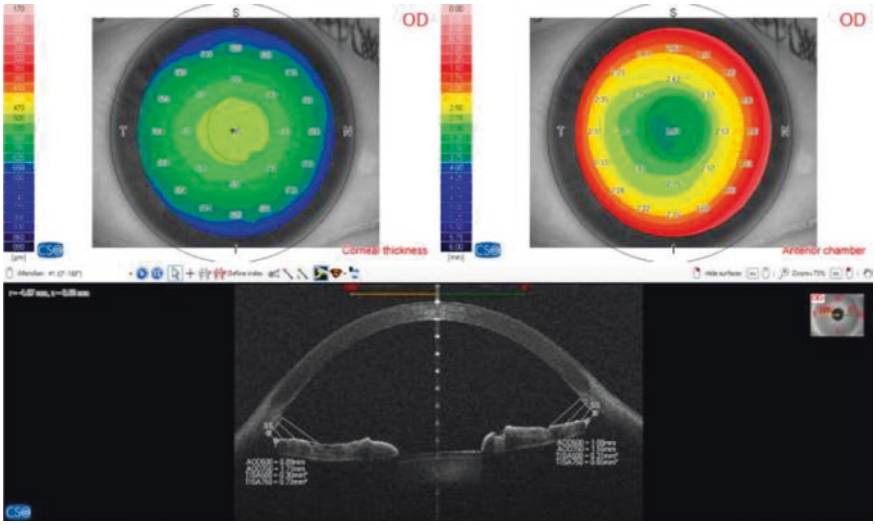

Fig. 10 Glaucoma summary well demonstrated in MS-39 (*With permission from CSO*) [2]

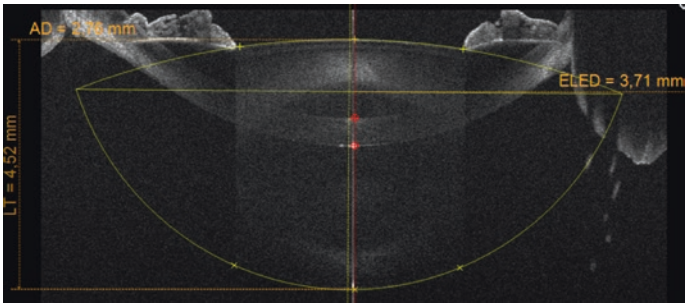

Fig. 11 Estimation of the lens equator distance for phakic intraocular lens implantation (*With permission from CSO*) [2]

Crystalline Biometry

To determine more accurately expected lens equator distance (ELED), followed by the calculation of the distance between phakic intraocular lenses (pIOLs) and crystalline lens before implanting the IOL. The MS-39 provides an acquisition mode to measure the thickness of the crystalline lens, its distance from the cornea to the equator, crystalline lens rise (CLR) and predicted lens position (PLP) (Fig. 11).

Case Study

Case 1.

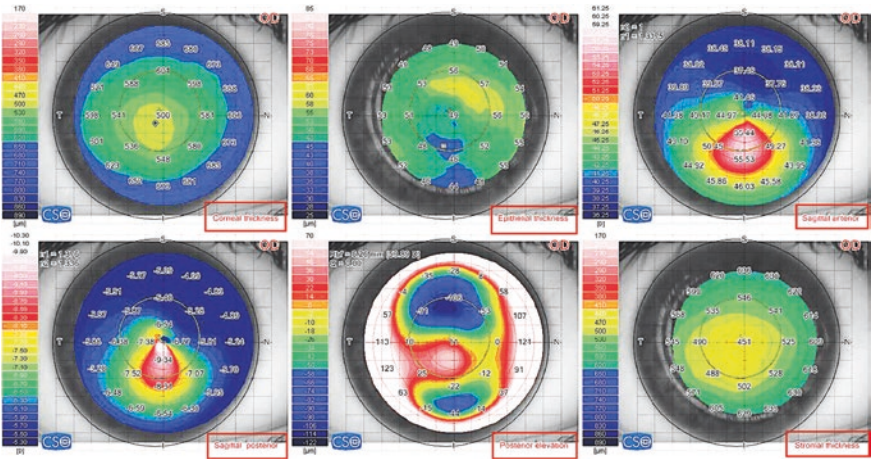

Fig. 12 Hexa maps (including corneal and epithelial thickness, anterior and posterior sagital, posterior elevation, and stromal thickness) of a patient with definite keratoconus and inferior steepening and abnormal epithelial and stromal thickness maps (*with permission from Costruzione Strumenti Oftalmici* (*CSO*))

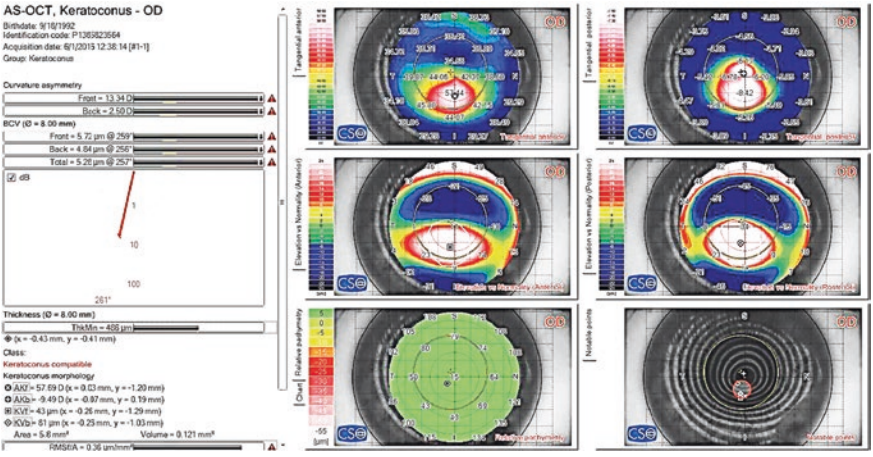

Fig. 13 Phoenix software keratoconus detection parameters have an abnormal range in keratoconus maps of the same patient. Also, the relative pachymetry chart is out of the normal range

Case 2.

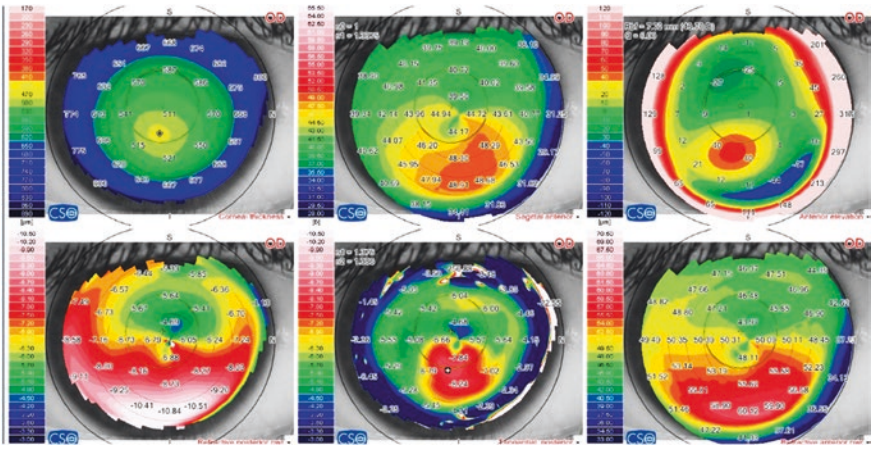

Fig. 14 Another form of Hexa maps in a patient with pellucid marginal degeneration (PMD) with crab claw pattern and inferior steepening (*with permission from CSO*)

Case 3.

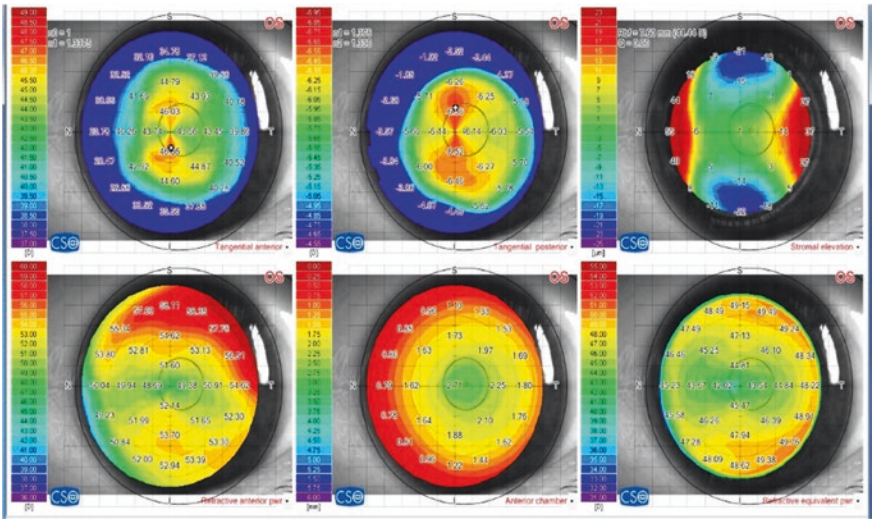

Fig. 15 A phakic IOL candidate without keratoconus. Hexa maps show regular orthogonal symmetric bow tie pattern. The anterior chamber depth (ACD) was measured for phakic intraocular implantation, and this patient was not a suitable candidate for phakic intraocular lens surgery due to ACD of 2.7 mm (*with permission from CSO*)

Case 4.

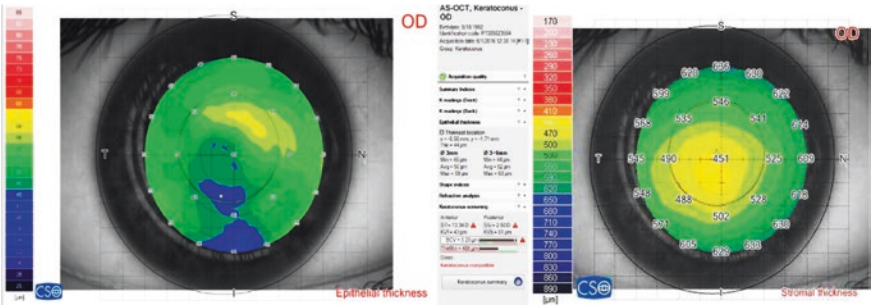

Fig. 16 A patient with advanced keratoconus and inferior steepening that shows epithelial thinning in the inferior part of the cornea and corresponds to anterior bulging of the stroma and the stromal thinning (*with permission from CSO*)

Case 5.

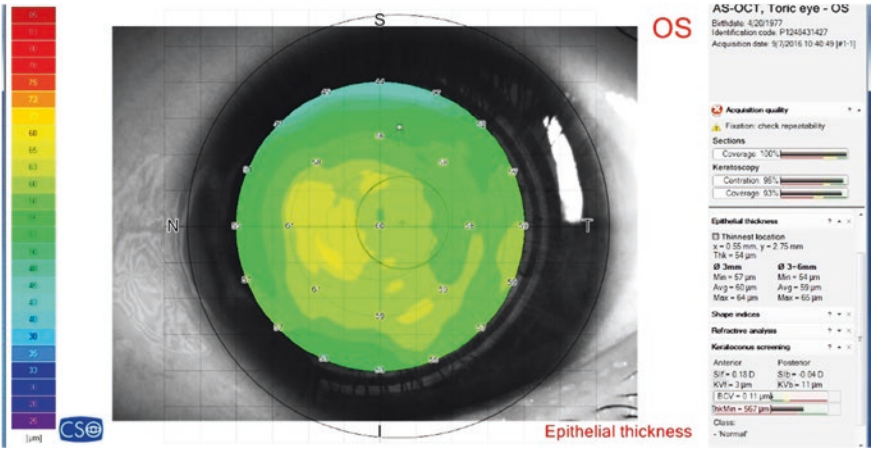

Fig. 17 A patient with the toric cornea without keratoconus and fairly even distribution of epithelium is seen in the epithelial thickness map (*with permission from CSO*)

Case 6.

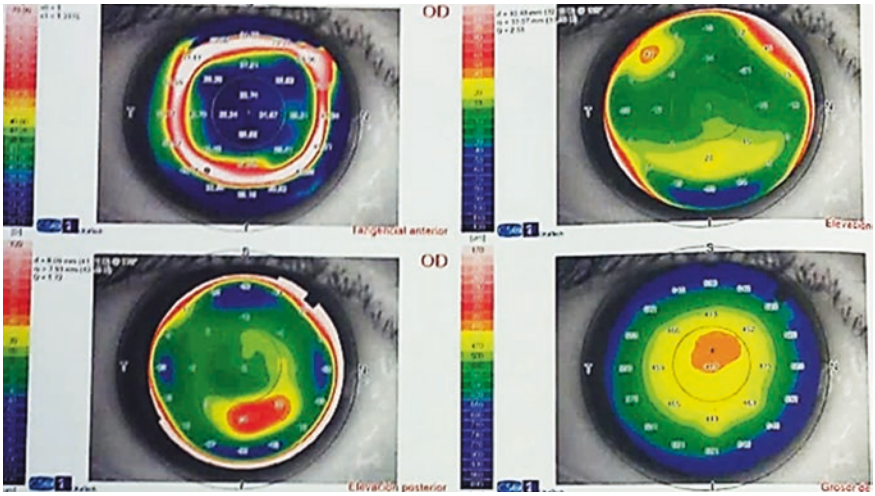

Fig. 18 A patient with a history of radial keratotomy who is a candidate for cataract surgery. Aberrated anterior and posterior surfaces with very oblate anterior corneal shape are seen in Quad maps. AS-OCT can estimate IOL power calculation by measuring true anterior and posterior curvature and ray-tracing software more accurately. (*Reprint with permission from Atlas of anterior segment OCT, CSO, 2019*) [4]

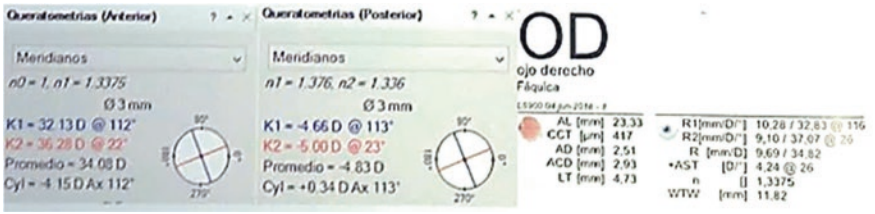

Fig. 19 Anterior and posterior keratometry and biometric measurements are shown

Case 7.

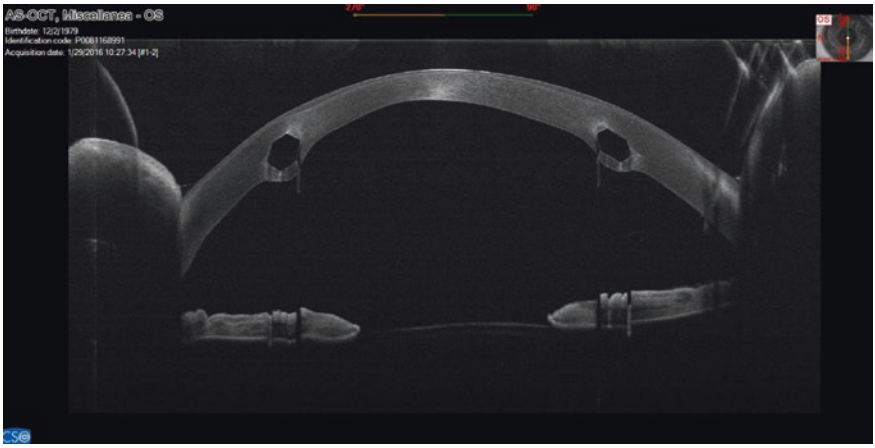

Fig. 20 A case with definite keratoconus which managed with an Intacs intrastromal corneal ring segment. The OCT provides a suitable position and depth of intrastromal ring implantation (*with permission from CSO*)

Case 8.

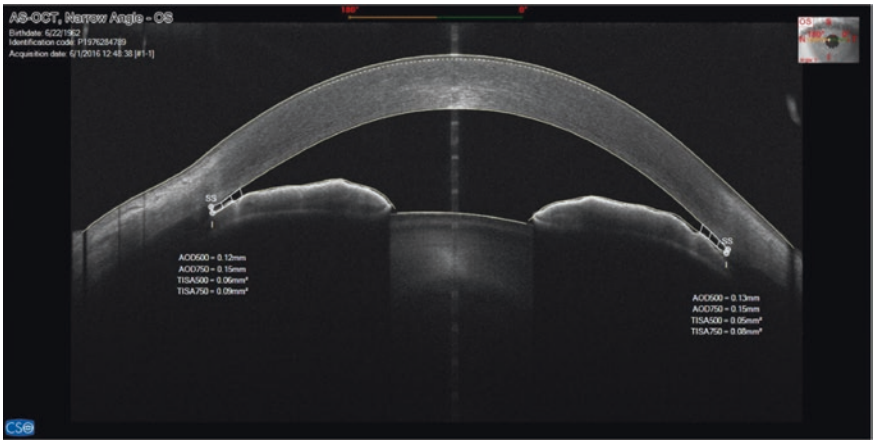

Fig. 21 A case with the thick cornea and occludable iridocorneal angle (*with permission from CSO*)

Case 9.

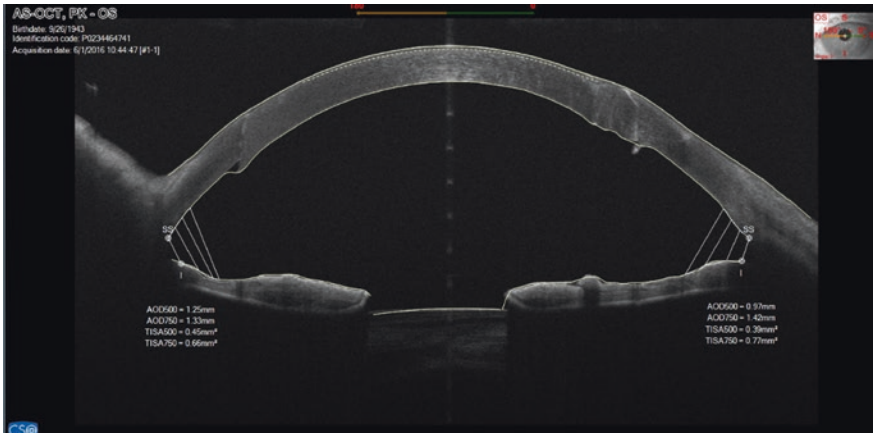

Fig. 22 A case with a history of penetrating keratoplasty (PK). MS39 OCT could show the posterior wound healing (*with permission from CSO*)

Case 10.

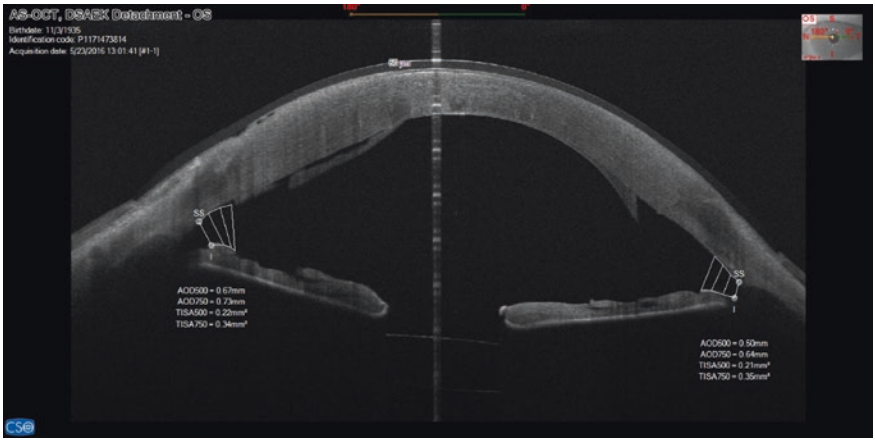

Fig. 23 A case with the partial detachment of posterior lenticule following DSEAK and an increase in corneal thickness next to it (*with permission from CSO*)

Case 11.

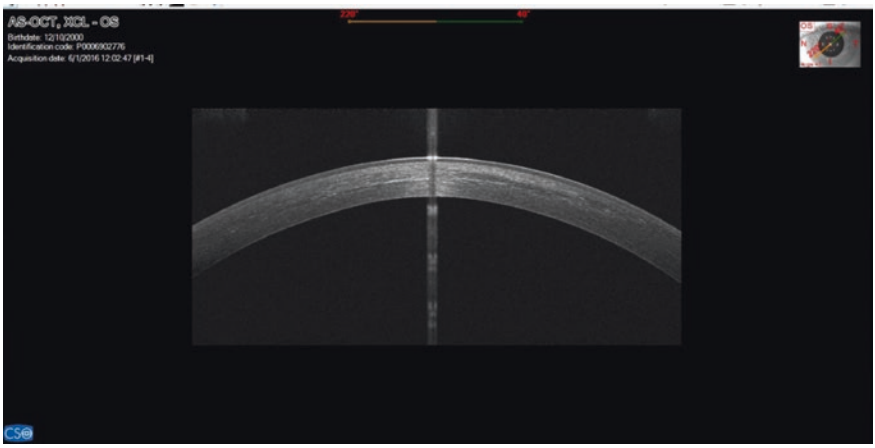

Fig. 24 Cross-linking (CXL) demarcation line after LASIK in a patient with post LASIK ectasia due to thick LASIK flap (*with permission from CSO*)

Case 12.

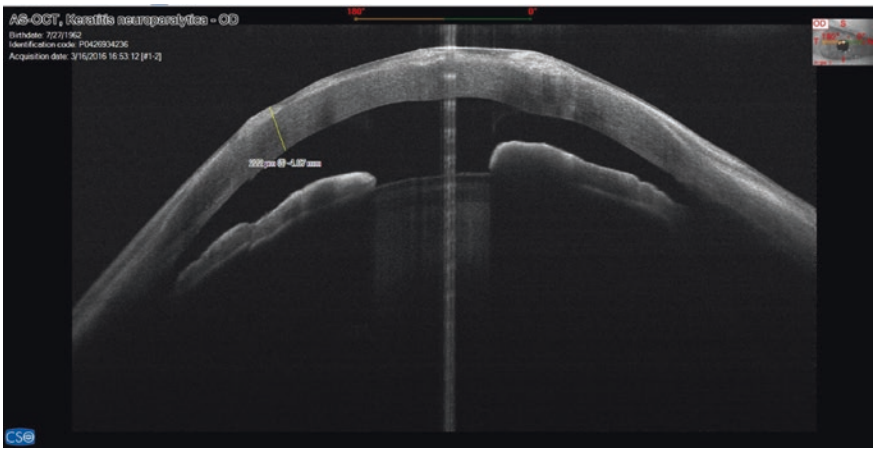

Fig. 25 A case with neurotrophic ulcer following herpetic keratitis (*with permission from CSO*)

Case 13.

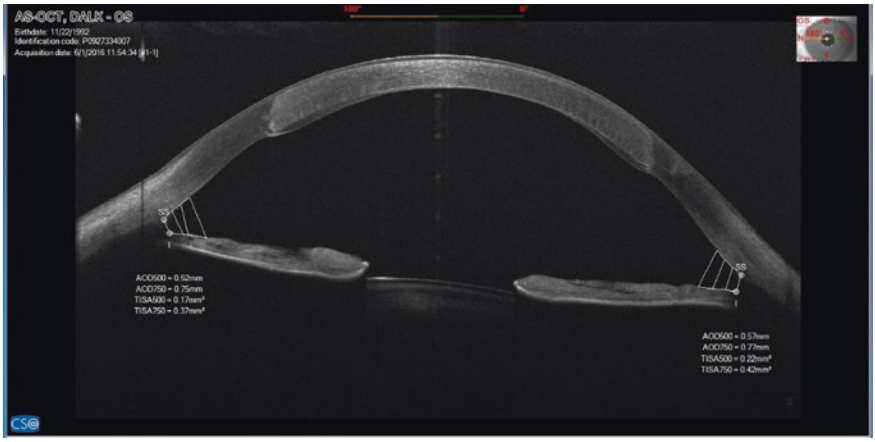

Fig. 26 A case with a history of DALK by Melles Technique which shows acceptable wound healing. However, a slight internal wound mismatch between donor and recipient corneal tissues can be seen (*with permission from CSO*)

Case 14.

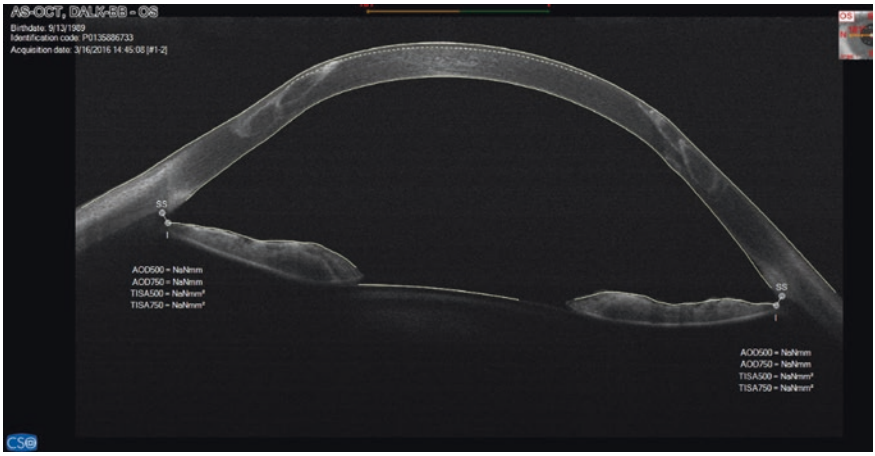

Fig. 27 A case with a history of DALK by Big Bubble Technique which shows well wound healing and without any internal wound mismatch between donor and recipient corneal tissues (*with permission from CSO*)

Case 15.

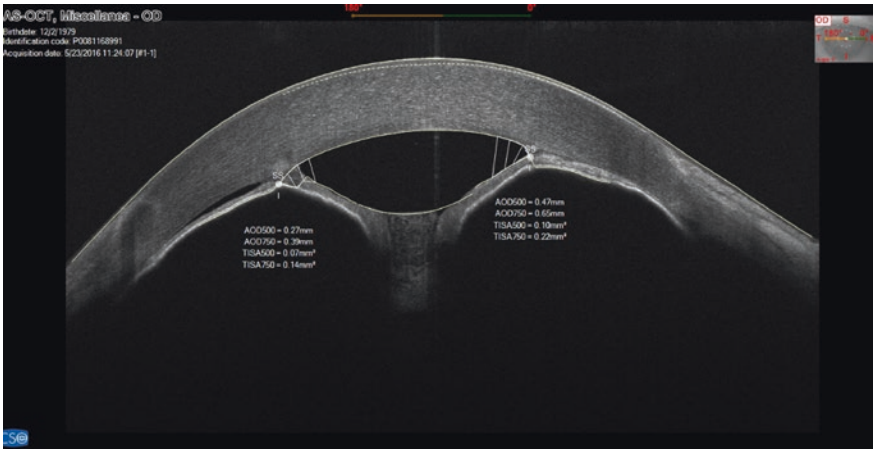

Fig. 28 A case with anterior segment dysgenesis with iridocorneal adhesion (*with permission from CSO*)

Case 16.

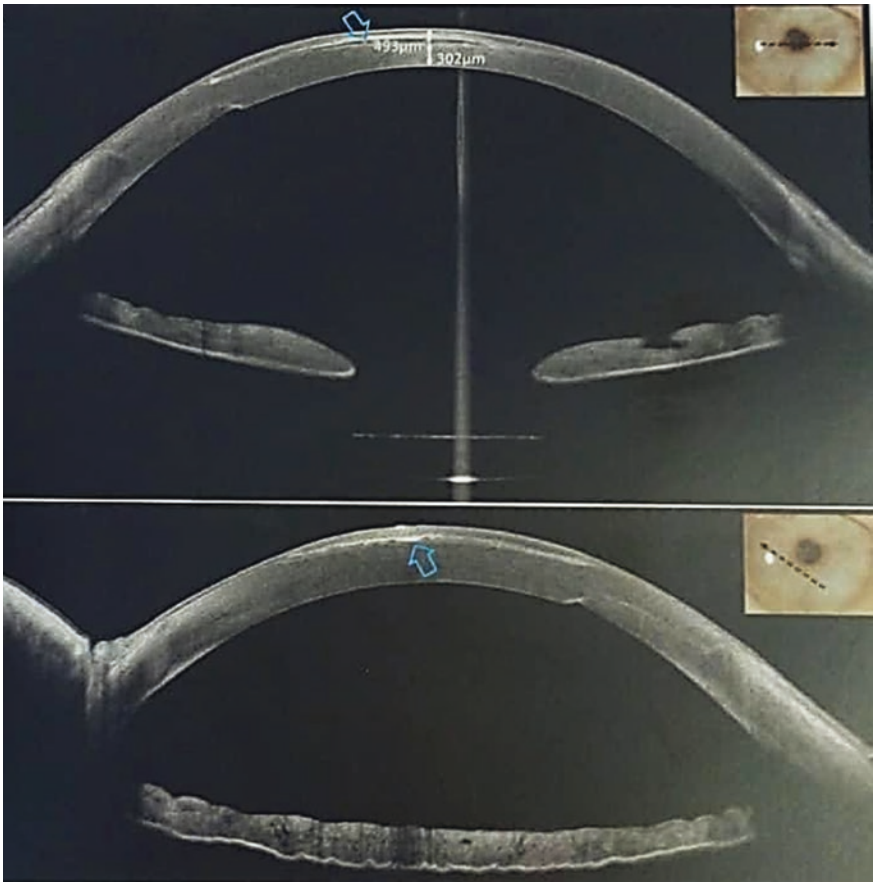

Fig. 29 MS-39 can show the LASIK flap and epithelial ingrowth as well as individual corneal layers. The epithelial ingrowth under the corneal flap indicates with a blue arrow that appears as a hyperreflective band. The depth of epithelial ingrowth can be measured with MS-39 AS-OCT, accurately. (*Reprint with permission from Atlas of anterior segment OCT, CSO, 2019*) [4]

Case 17.

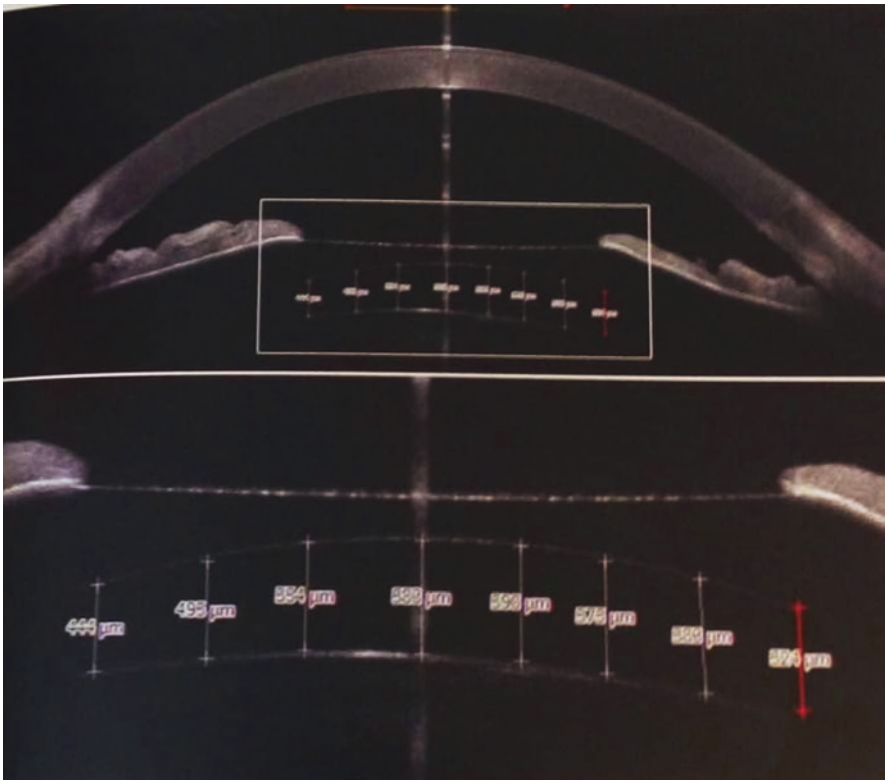

Fig. 30 A 28-year-old man with −9.00 D myopia who underwent implantation of Implantable Collamer Lens (ICL, STARR). The measurement of the scotopic ICL vault is shown in a wide view with a large magnification. (*Reprint with permission from Atlas of anterior segment OCT, CSO, 2019*) [4]

References

1. Savini G, Schiano-Lomoriello D, Hoffer KJ. Repeatability of automatic measurements by a new anterior segment optical coherence tomographer combined with Placido topography and agreement with 2 Scheimpflug cameras. J Cataract Refract Surg. 2018;44(4):471–8.
2. MS39 CSO Guidelines. https://www.csoitalia.it/en/prodotto/info/63-ms-39-as-oct. Distributor Meeting MS39.pdf (CSO R&D department). Last Accessed 13 April 2020.
3. Vega-Estrada A, Mimouni M, Espla E, Alio Del Barrio J, Alio JL. Corneal epithelial thickness intrasubject repeatability and its relation with visual limitation in keratoconus. Am J Ophthalmol. 2019;200:255–62.
4. Atlas of anterior segment OCT, CSO, 2019; ISBN: 978-88-31256-02-5.

Nontopographic Corneal Imaging

Anterior Segment Optical Coherence Tomography

Golshan Latifi and Parisa Abdi

Introduction

Optical coherence tomography (OCT) was first introduced in 1991 for imaging the retina [9] and 3 years later in 1994 the first anterior segment OCT (AS-OCT) was proposed for imaging the anterior segment of the eye [9].

OCT imaging is based on measuring the echo time delay of light (typically infrared) reflected from tissue structures [7]. Light from a low-coherence light source is splited into two arms: In the reference arm, a mirror reflects the light, while in the sample arm the light is back scattered by the tissue. Light is backscattered at interfaces between variably reflective tissue layers of the eye. The light returning from the two arms are collected to create the interference pattern. The instrument creates a series of A-scans; which are combined into a B-scan. Each A-scan is related to the strength of the reflected signal as a function of depth [7, 9].

OCT systems are characterized by wavelength of their light sources [3]. Shorter wavelengths as used in retinal OCTs (800–900 nm, near infrared system), provide higher axial resolutions, but their imaging depth is limited. On the other hand, the longer wavelength systems like AS-OCTs (1,050–1,310 nm) provide a deeper tissue penetration [6]. Image resolution is compromised to some extent by longer wavelengths, but axial resolutions have been improved as 1–5 μm in the new generations of OCT.

G. Latifi · P. Abdi (✉)
Department of Ophthalmology, Farabi Eye Hospital, Tehran University of Medical Sciences, Tehran, Iran
e-mail: paris.abdi@gmail.com

G. Latifi
e-mail: golshan24@yahoo.com

M. Mohammadpour (ed.), *Diagnostics in Ocular Imaging*,
https://doi.org/10.1007/978-3-030-54863-6_7

There are two major types of OCTs:

- Time domain OCT: a moving reference mirror is used to obtain cross sectional images. Therefore it is limited by the time taken for the reference mirror to scan the tissue plane [12].
- Frequency-domain OCT:
  - Fourier domain OCT or spectral-domain OCT: the reference mirror is fixed and generates varying wavelengths of light to cause an interference pattern between the tissue sample of interest and the reference arm. So this system has faster acquisition times than time domain systems and its higher resolution allows visualization of more details [12].
  - Swept source OCT: a longer wavelength is used to increase penetration, so better signals are provided from deeper regions [11]. A narrow-band source is used to sweep across a broad optical bandwidth [2].
  - Ultra-high-resolution OCT: precise imaging is provided by axial resolution of 1–4 μm [11].

Finally, an OCT is called en face OCT, when it produces coronal scans (rather than axial scans). These scans can be generated by both frequency-domain and spectral domain OCTs [12].

Time-domain OCT systems include:

- Visante OCT (Carl Zeiss Meditec, Oberkochen, Germany): has a wavelength of 1,310 nm, a 16 mm scan width, and 6 mm scan depth [4].
- Heidelberg slit lamp OCT (Heidelberg Engineering GmbH, Heidelberg, Germany): has a 1,310 nm wavelength, as well as a 15 mm scan width, and 7 mm scan depth [12].

Spectral-domain OCT systems include [1]:

- Spectralis (Heidelberg Engineering GmbH)
- Cirrus OCT (Carl Zeiss Meditec).
- RTVue (Optovue, Inc., Fremont, California, USA): it can image both the anterior and posterior segments. A short wavelength (830 nm) is used, so the axial resolution is as high as 4–7 μm. The capture speed of its camera is 26,000 A-scans per second (13 times faster than the Visante). [2, 13–1] its limitations is shorter depth of scans and lower widths of horizontal scans (3–6 mm) [4].

Swept-source OCTs include:

- Casia SS-1000 OCT (Tomey, Nagoya, Japan): has a scan speed of 30,000 A-scans per second, a 1,310 nm wavelength, horizontal scan width of 16 mm, and axial resolution of 10 μm [4].
- DRI Triton swept-source OCT (Topcon, Tokyo, Japan): has a scan speed of 100,000 A-scans per second, a 1,050 nm wavelength, a horizontal scan width of 3–12 mm, and an axial resolution of 5 μm [10].

Ultra-high resolution OCTs, include:

- Copernicus HR (Optopol Technologies SA, Zawiercie, Poland).
- Bioptigen Envisu (Bioptigen Inc., Morrisville, North Carolina, USA) [4, 11].

The main limitation of AS-OCT is imaging structures past the iris pigment epithelium, as the infrared light has poor penetration past this pigmented structure [12].

Characteristics of commercially available AS-OCT machines:

Instrument	Company	Measurement type	Axial resolution (μm)	Scan depth (mm)	Scanning speed per minute
Visante	Carl Zeiss Meditec	Time-domain	18	6	2000 A scans
Slit lamp	Heidelberg	Time-domain	25	7	2000 A scans
Spectralis	Heidelberg	Spectral-domain	4–7	2	40,000 A scans
Cirrus	Carl Zeiss Meditec	Spectral-domain	5	2	27,000 A scans
RTVue	Optovue	Spectral-domain	5	2–2.3	26,000 A scans
Casia SS-1000	Tomey	Spectral-domain (swept source)	10	6	30,000 A scans
Ultra-high resolution	Custom build device	Spectral-domain	~3	6	24,000–26,000 A scans

Clinical Applications of AS-OCT [7, 9, 12]

AS-OCT is widely used in clinical practice in evaluation of the anterior segment of the eye. Some of its various clinical applications are as the followings:

- Tear Meniscus Measurement
- Conjunctiva: conjunctivochalasis, pterygium, pinguecula
- Sclera: scleral thinning, scleromalacia, scleritis
- Refractive Surgery: thickness of the LASIK flap and remaining stromal bed, interface complications after LASIK surgery
- Ectatic Disorders: detection of thinning in keratoconus, keratoglobus, pellucid marginal degeneration, detection of stromal demarcation line after Corneal collagen cross-linking, evaluation of the cornea before and after implantation of ring segments

- Corneal transplantation: evaluation of depth of dissection in deep anterior lamellar keratoplasty, graft apposition, evaluation of complications like pupillary block, visualization of wound interface pattern
- Assessment of Descemet's Membrane: Descemet's Membrane detachment after cataract surgery, evaluation of Descemet's Membrane after various keratoplasty operations including penetrating keratoplasty (PKP), Descemet's membrane endothelial keratoplasty (DMEK), and Descemet's membrane stripping automated endothelial keratoplasty (DSAEK)
- Corneal opacities, deposits, degenerations and dystrophies
- Evaluation of Corneal thinning or thickening: corneal edema, corneal thinning like descemetocele
- Crystalline lens: detection of different types of cataract, lenticonus, lens subluxations, capsular rupture
- Cataract surgery: visualization of cataract clear corneal incisions, detection of postoperative complications such as Descemet'smembrane detachment, evaluation of intraocular lens like subluxation and capture
- Tumours: non-pigmented anterior iris tumours, lesions of the ocular surface, ocular surface squamous neoplasia
- Phakic intraocular lenses: position and complications of iris claw, angle support and posterior chamber phakic IOLs Figs. 1, 2, 3, 4, 5, 6, 7, 8, 9 10, 11, 12, 13, 14, 15, 16, 17, 18, 19, 20, 21, 22, 23, 24, 25, 26, 27, 28, 29 and 30.
- Epithelial thickness measurement: Figs. 31, 32 and 33.

Role of OCT in Biometry

For more than 50 years, the only available tool to measure axial length was ultrasound biometry. Nowadays optical biometry has largely replaced ultrasound and is the technique of choice in biometry.

Available Optical biometers use one of the following technologies [8]:

1. Partial coherence interferometry (PCI): IOL Master 500 (Carl Zeiss), the AL-Scan (Nidek) and Pentacam AXL (Oculus).
2. Optical low coherence reflectometry (OLCR): Lenstar LS900 (Haag-Streit), Aladdin (Topcon) and Galilei G6 (Zeimer).
3. SS-OCT: IOL Master 700 (Carl Zeiss), Argos (Movu), OA 2000 (Tomey) and the Eyestar 900 (Haag-Streit).

IOL Master 700

It performs rapid scanning at a speed of 2000 scans per second. The device provides a full length longitudinal cut through the eye and can image the various ocular structures. This helps in identification of abnormalities such as lens tilt,

posterior polar cataracts, and macular pathologies to some extent. The OCT image provides a fixation check by showing the pit of the fovea. The IOL Master 700 measures the curvature of the anterior corneal surface using telecentric keratometry. It can also measure the posterior corneal curvature and gives a new parameter called total keratometry (TK). It provides anatomic measurements required for modern IOL power calculation formulas including anterior chamber depth, lens thickness, axial length and central corneal thickness [5].

All the modern IOL power calculation formulae including the Barret suite (Barret Universal 2, the Barrett True K, and the Barrett Toric) are available on board the IOL Master 700. Barrett TK Universal II and the Barrett TK Toric, which utilize TK are also available.

The IOL Master 700 can captures a high-resolution image of the eye and could be linked with the Callisto eye system for markerless toric IOL implantation [8].

Argos

Argos uses SS-OCT technology and can measure Keratometry, AL, CCT, ACD, WTW, LT, CCT, and pupil size. Like the IOL Master 700, the argos can make measurements through dense cataracts using SS-OCT technology. All popular IOL power calculation formulae are incorporated in the device [8].

OA-2000

OA 2000 combines a placido disc topographer with an SS-OCT biometer. It measure keratometry, CCT, ACD, AL, LT, WTW, pupillometry, and corneal topography. All modern IOL power calculation formulae including ones based on ray tracing (e.g. Okulix) are available on board [8].

Eyestar 900

Eyestar 900 is not commercially available yet. Haag-Streit claims that it can provide biometric analysis of the entire eye from the cornea to the retina, including elevation-based corneal topography [8]

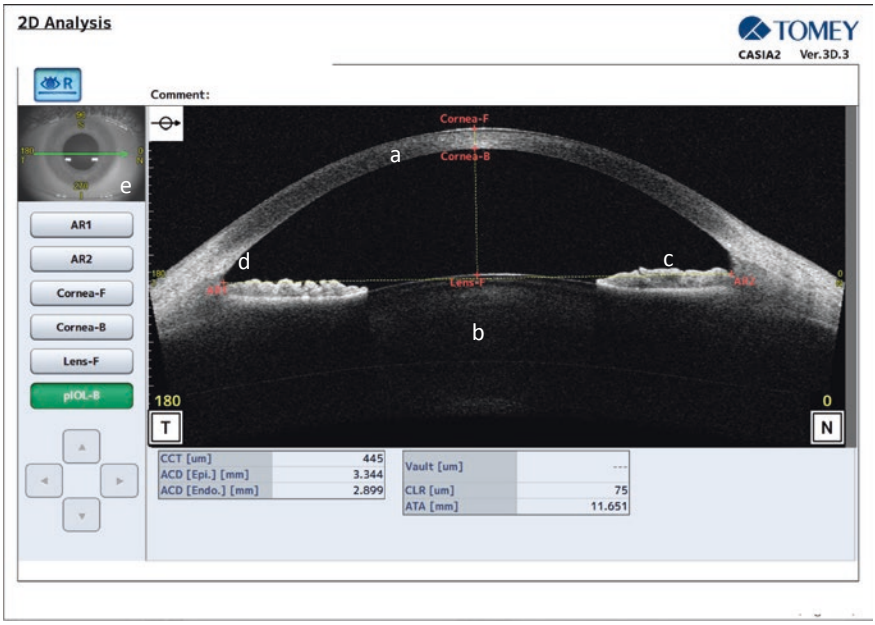

Fig. 1 Normal AS-OCT. cornea (a); lens (b); iris (c); scleral spur (d); en face image (the arrow shows the position and the direction of image acquisition) (e). (CASIA 2, Tomey, Japan)

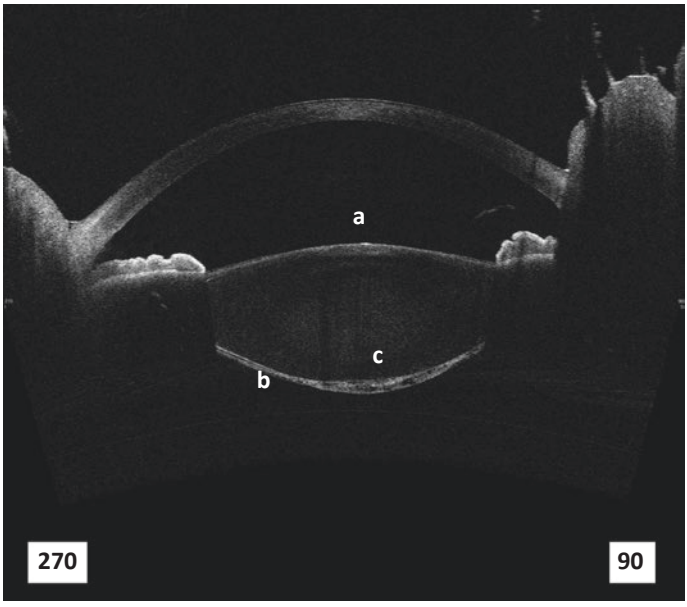

Fig. 2 Posterior subcapsular cataract. anterior lens capsule (a); posterior lens capsule (b); Plaque of posterior subcapsular opacity (c) AS-OCT (CASIA 2, Tomey, Japan)

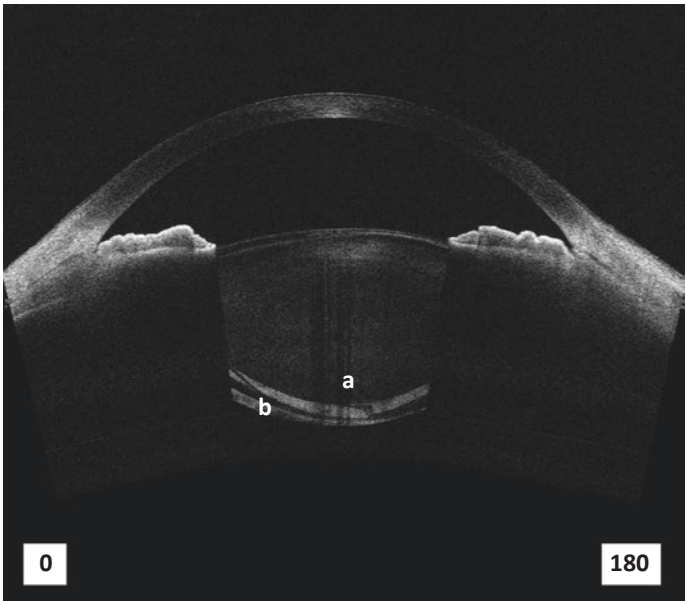

Fig. 3 Traumatic cataract. Note the posterior cortical opacity (a); posterior lens capsule is intact (b). AS-OCT (CASIA 2, Tomey, Japan)

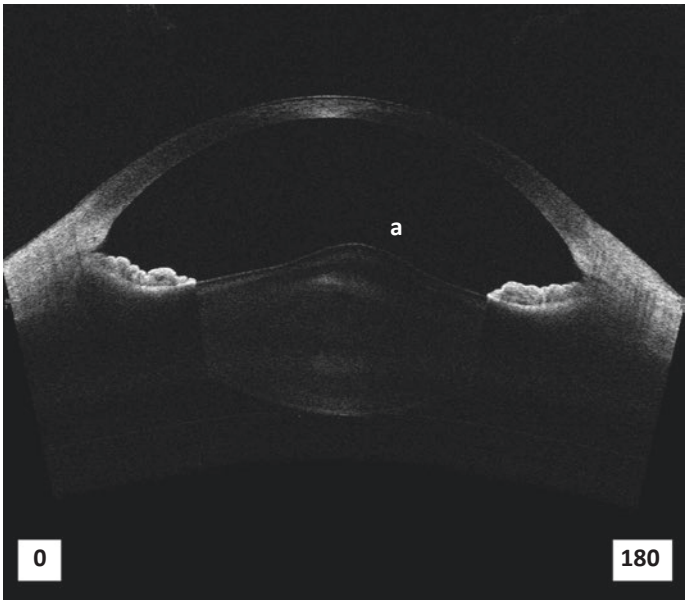

Fig. 4 Anterior lenticonus. Note the anterior conical protrusion of the central lens surface (a). AS-OCT (CASIA 2, Tomey, Japan)

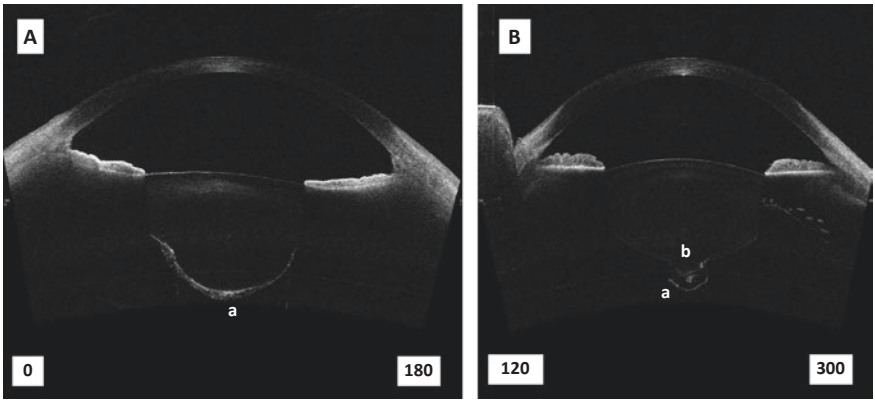

Fig. 5 Posterior polar cataract. **A** and **B** ectatic posterior capsule (a); posterior subcapsular/cortical opacity (b). AS-OCT (CASIA 2, Tomey, Japan)

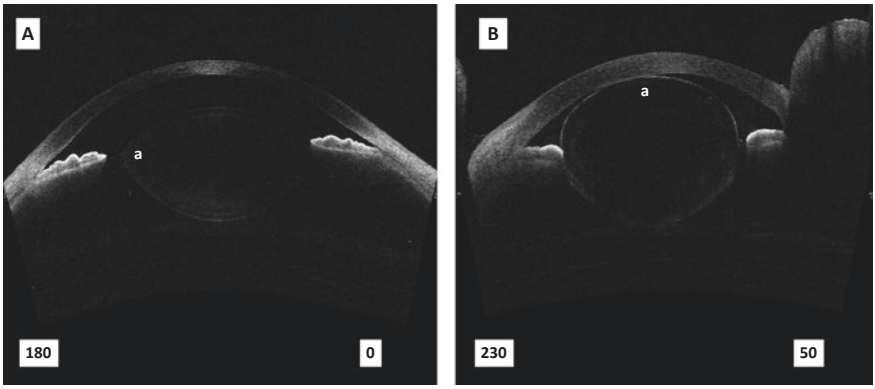

Fig. 6 Microspherophakia. Small diameter spherical lens with large anteroposterior diameter. **A** Note the lens equator being within pupillary area after dilation (a) and shallow AC. AS-OCT (CASIA 2, Tomey, Japan). **B** Crystalline lens is dislocated into AC. Note the anterior capsule of the lens is in touch with the cornea (a). AS-OCT (CASIA 2, Tomey, Japan)

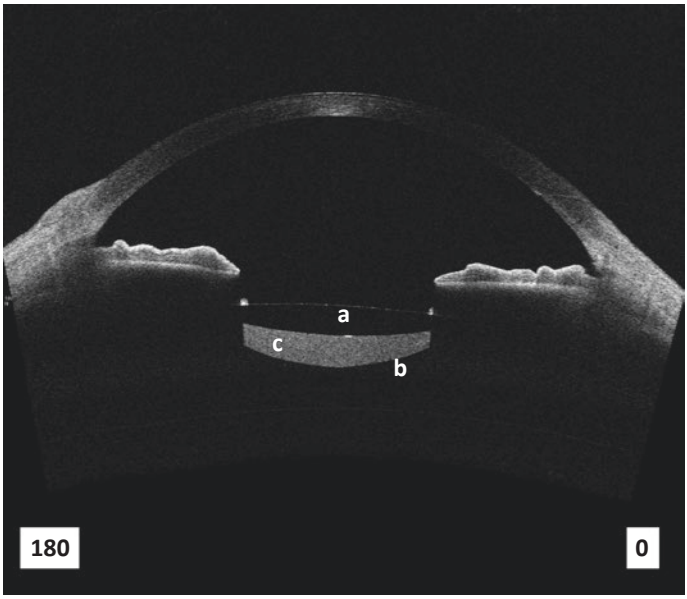

Fig. 7 Capsular block after cataract surgery. intraocular lens (a); posterior capsule (b); hyper-reflective material trapped inside the capsular bag (c). AS-OCT (CASIA 2, Tomey, Japan)

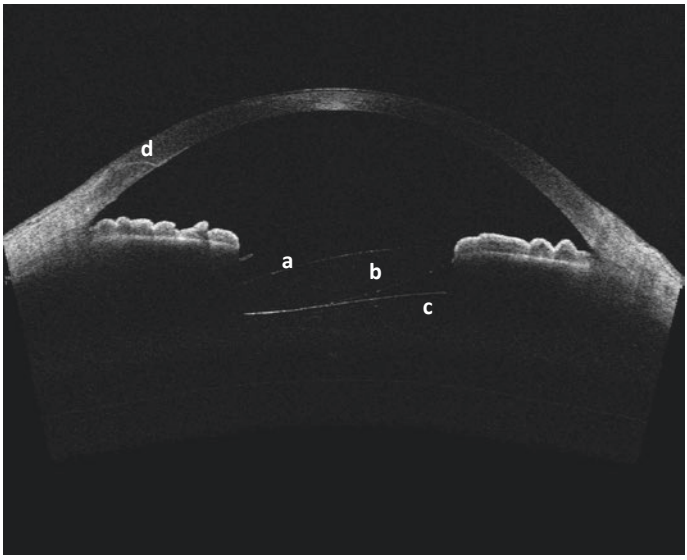

Fig. 8 Tilted posterior chamber intraocular lens (IOL). The IOL is implanted with one haptic in the bag and the other in ciliary sulcus. Anterior border of IOL (a); posterior border of IOL (b); capsular bag (c); temporal clear cornea incision in cataract surgery (d) AS-OCT (CASIA 2, Tomey, Japan)

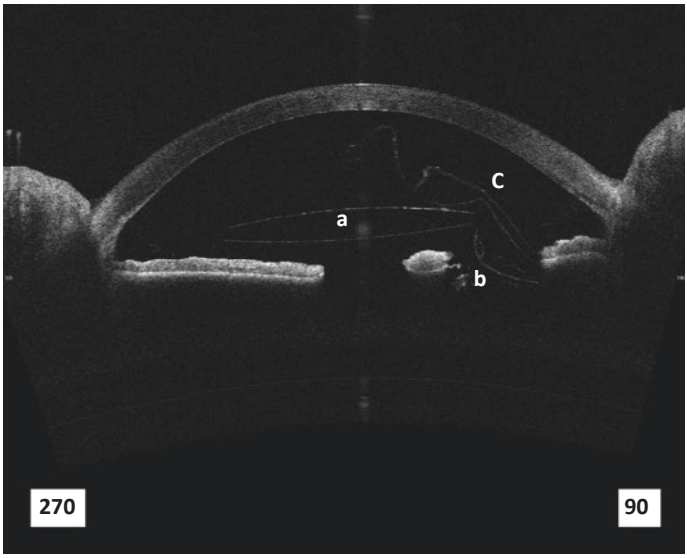

Fig. 9 Vitreous prolapse through laser peripheral iridotomy (LPI) after Artisan implantation. Iris claw IOL (Artisan) (a); large LPI (b); vitreous strands in anterior chamber (c). AS-OCT (CASIA 2, Tomey, Japan)

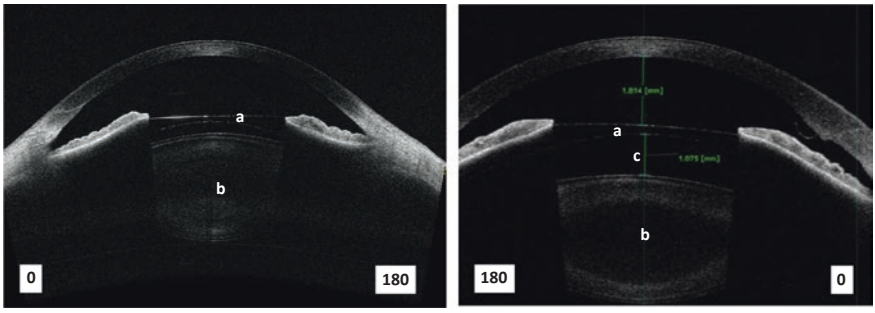

Fig. 10 Implantable collamer lenses (ICL) AS-OCT (CASIA 2, Tomey, Japan). **A** Normal vault (Distance between the back surface of ICL and the front surface of the lens). ICL (a); crystalline lens (b). **B** High vault (c). ICL (a); crystalline lens (b); Note shallow anterior chamber

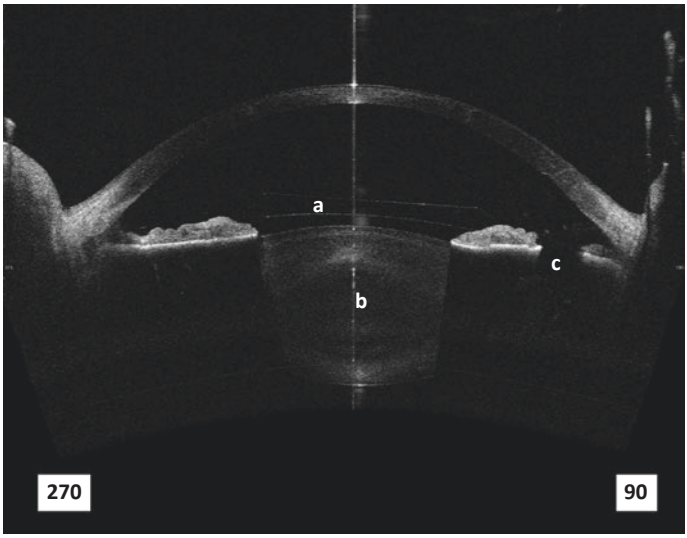

Fig. 11 Phakic Artisan. Artisan lens (a); crystalline lens (b); Laser peripheral iridotomy (LPI) (c). AS-OCT (CASIA 2, Tomey, Japan)

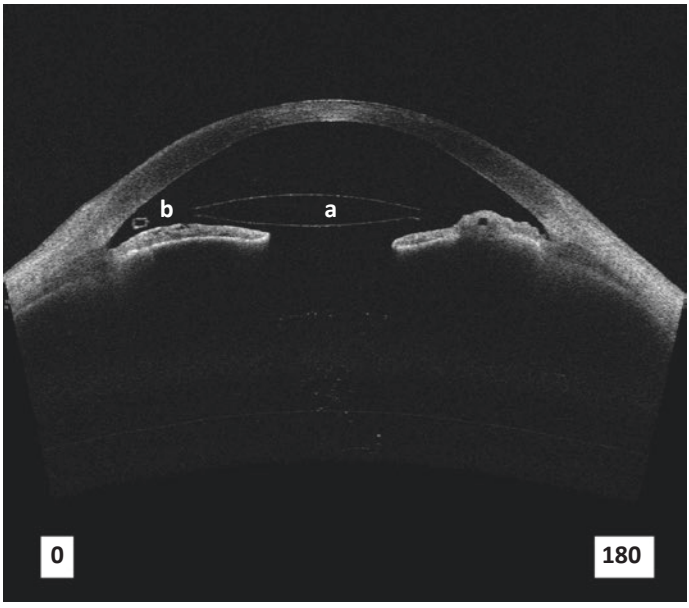

Fig. 12 Angle support anterior chamber lens (AC-IOL) in an aphakic eye. AC-IOL (a); lens haptic in the angle (b). AS-OCT

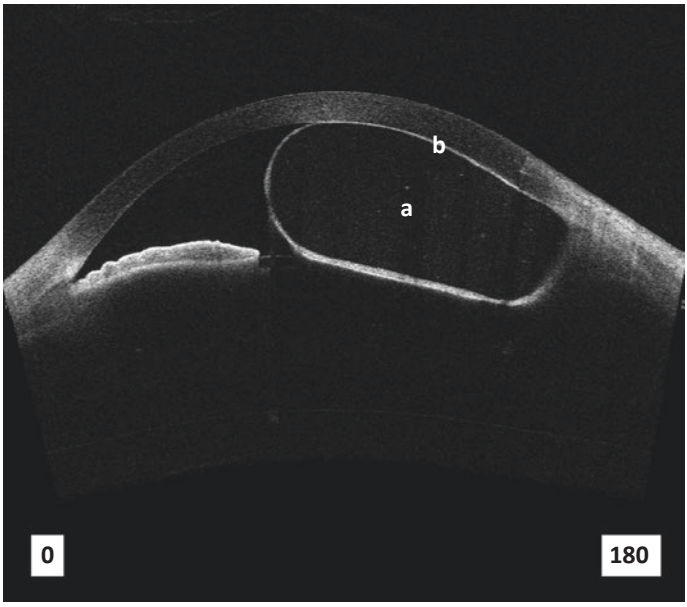

Fig. 13 Large iris cyst (a). The cyst has a hyper-reflective wall (b); Note that the cyst has obliterated the angle; cyst wall is in touch with corneal endothelium; and details of iris are not visible. AS-OCT (CASIA 2, Tomey, Japan)

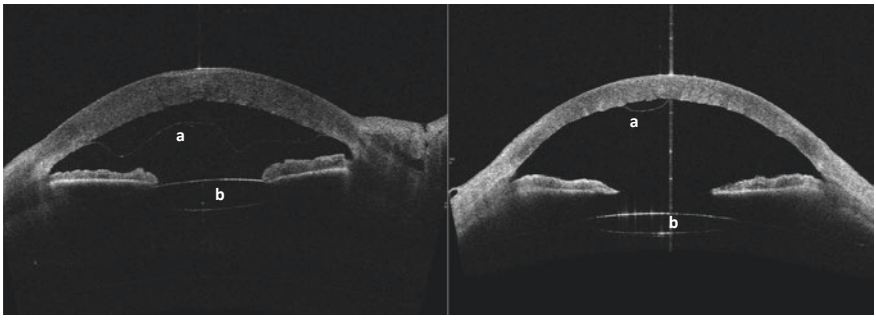

Fig. 14 Descemet's membrane(DM) detachment. AS-OCT (CASIA 2, Tomey, Japan). **A** Total detachment after cataract extraction. Note diffuse corneal thickening (edema). DM (a); Intraocular lens (b). **B** localized detachment. DM (a); Intraocular lens (b)

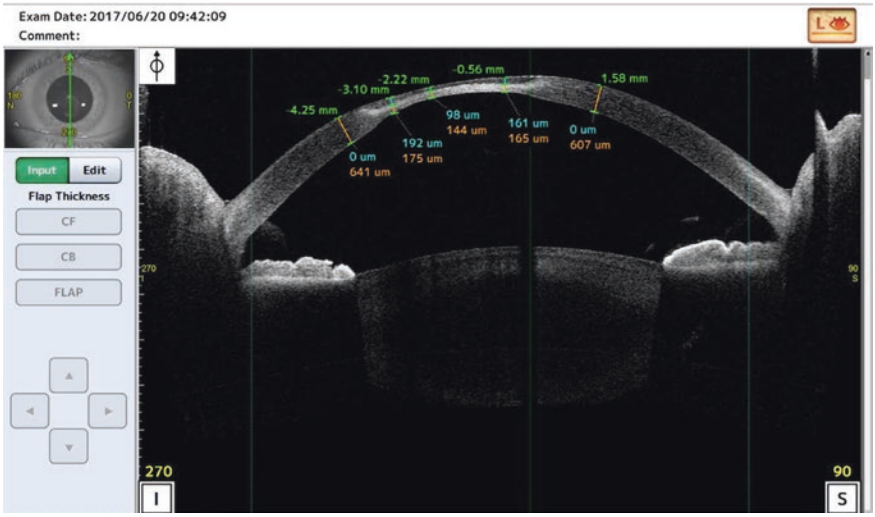

Fig. 15 Inferior paracentral corneal scar (Hyper-reflective lesion extended deeply up to the DM) (a); The cornea is thinned in the area of scar. Epithelial thickening for regularizing anterior corneal surface is evident (hypo-reflective area overlying the hyper-reflective scar) (b). AS-OCT (CASIA 2, Tomey, Japan)

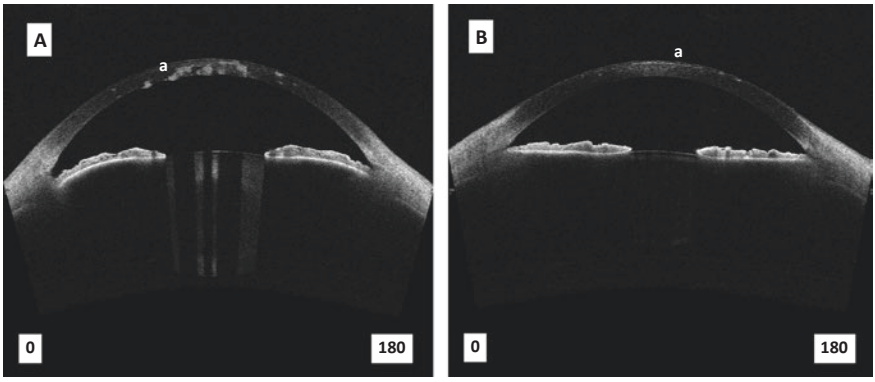

Fig. 16 AS-OCT (CASIA 2, Tomey, Japan). **A** Granular corneal dystrophy. Multiple discrete hyper-reflective areas in central cornea, extended into deep stroma (a); Note the dark shadows with sharp borders exactly underneath each opacity obscuring lens details. **B** Reis-buckler corneal dystrophy. Note the superficial location of the opacities in bowman layer (a)

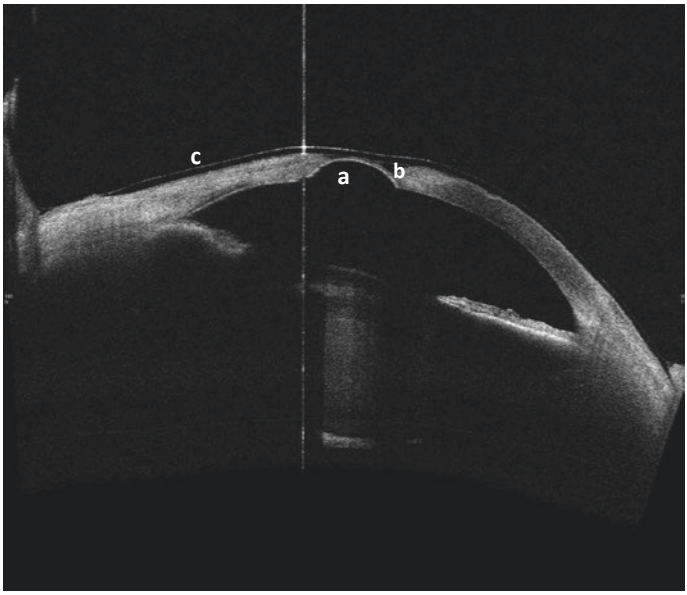

Fig. 17 Descemetocele. DM is protruded through the defect (a); only a thin layer of epithelium covers the DM (b); there is no stroma. Contact lens (c). AS-OCT (CASIA 2, Tomey, Japan)

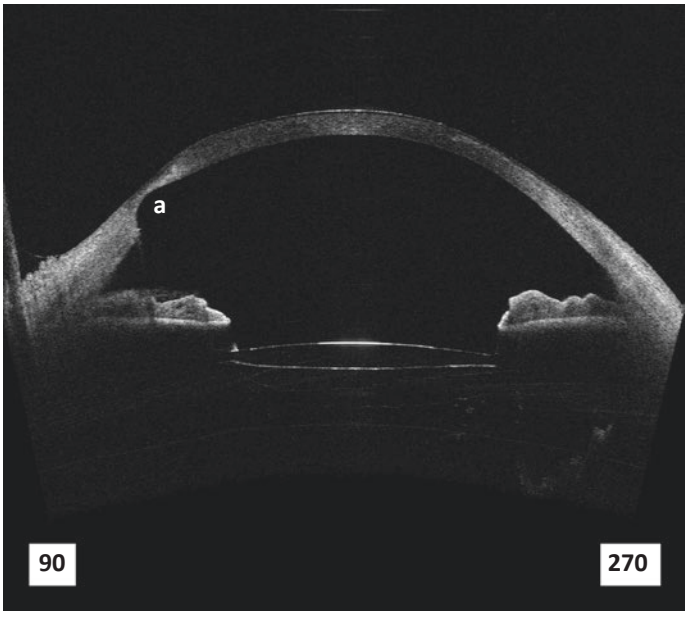

Fig. 18 Terrien marginal degeneration. Note the marked peripheral thinning in the superior portion of the cornea (a). AS-OCT (CASIA 2, Tomey, Japan)

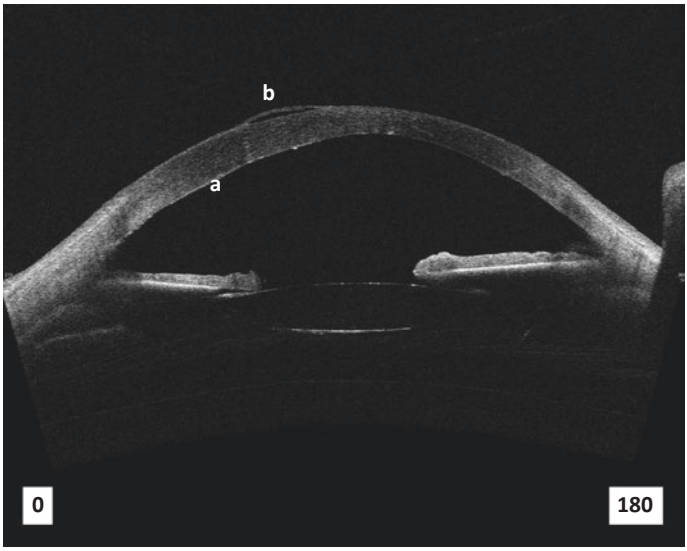

Fig. 19 Fuchs corneal endothelial dystrophy. Corneal thickness is increased in inferior parts. The patient is pseudophakic. Note the thick hyper-reflective DM (a); epithelial bullae (b). AS-OCT (CASIA 2, Tomey, Japan)

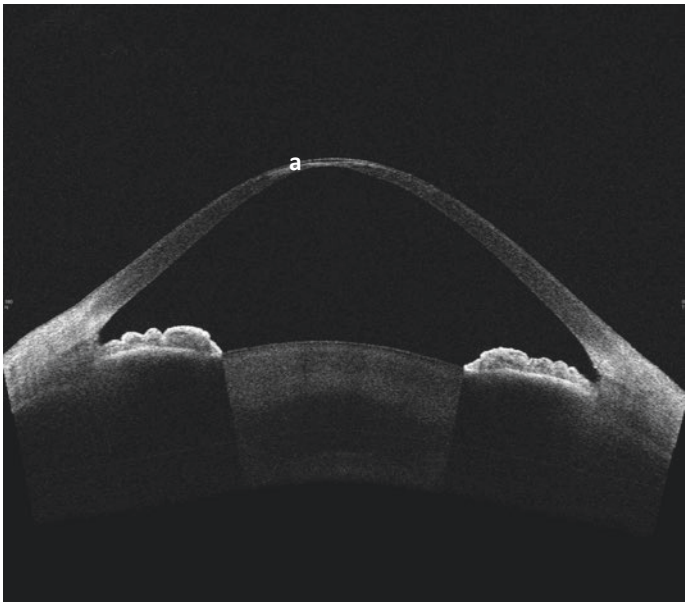

Fig. 20 Advanced keratoconus. Central thinning and bulging of the cornea in central part. Note the stromal scars at the apex of the cone (a). AS-OCT (CASIA 2, Tomey, Japan)

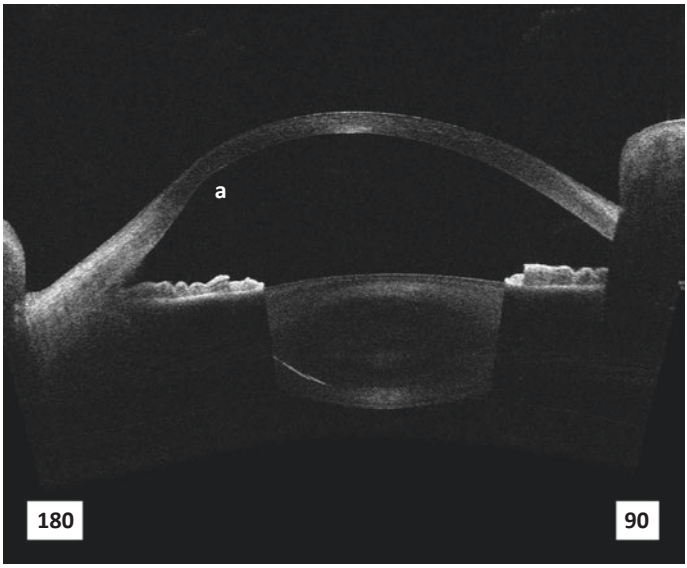

Fig. 21 Pellucid marginal degeneration. Corneal thinning and bulging in inferior part of the cornea (a). AS-OCT (CASIA 2, Tomey, Japan)

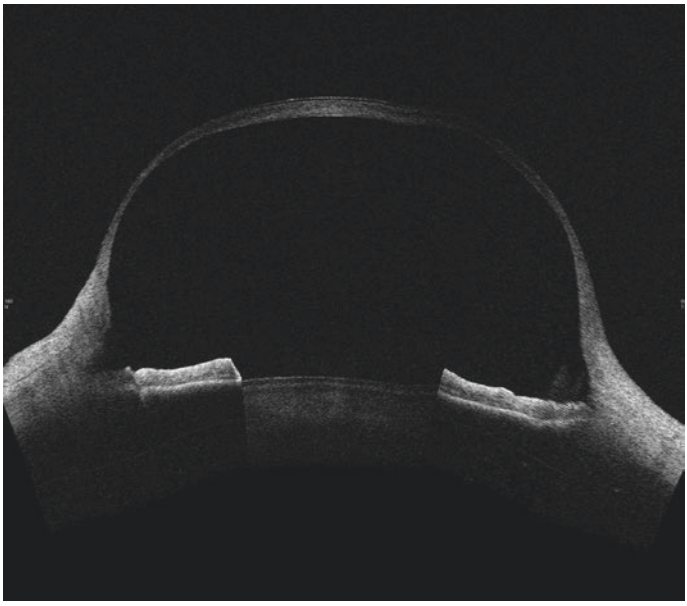

Fig. 22 Keratoglobus. Global thinning and bulging of the cornea. Note the very deep AC. AS-OCT (CASIA 2, Tomey, Japan)

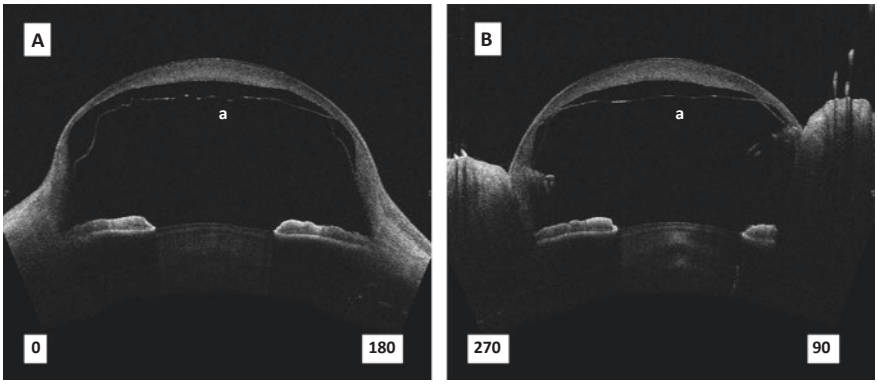

Fig. 23 Spontaneous DM detachment in Keratoglobus. DM is visible as a thin layer separate from cornea (a); The extent of detachment is from nasal to temporal (**A**) and from superior to inferior (**B**) cornea. Note the high arching ectatic cornea with the maximum thinning at mid-periphery and the increased central thickness due to edema. AS-OCT (CASIA 2, Tomey, Japan)

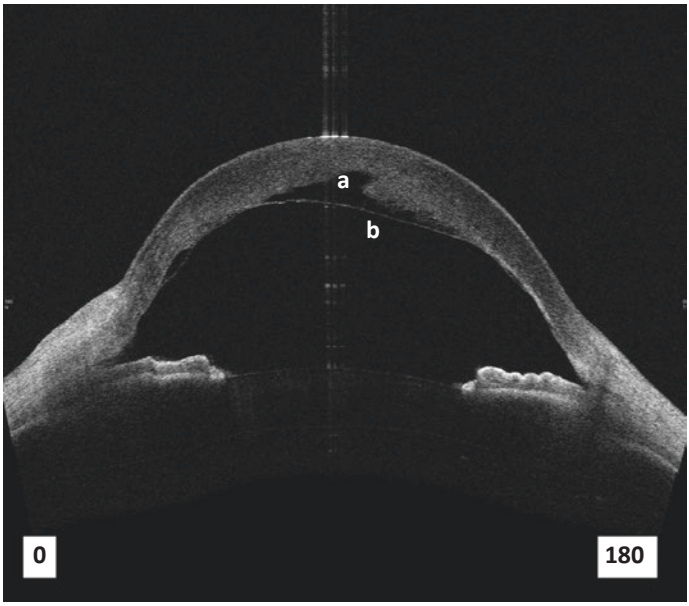

Fig. 24 Keratoconus hydropse. Significant corneal edema with large intrastromal cysts (a); DM (b). AS-OCT (CASIA 2, Tomey, Japan)

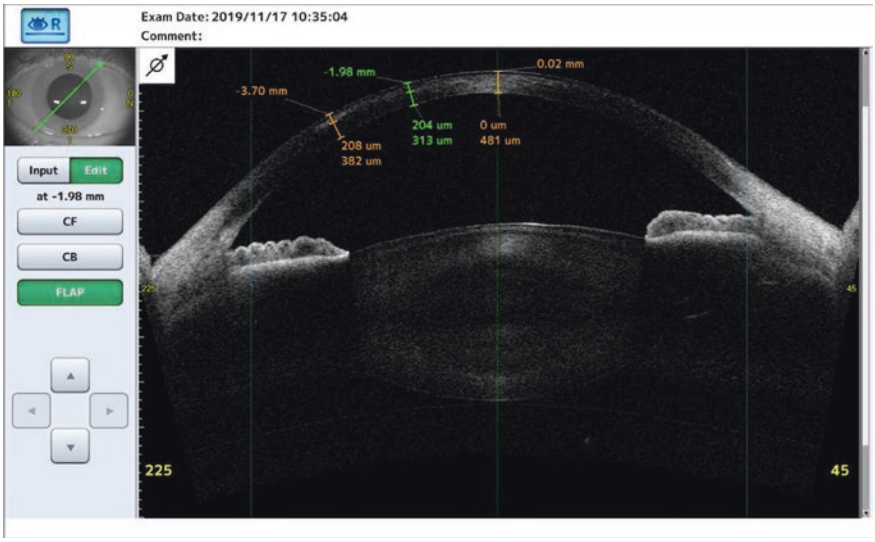

Fig. 25 Demarcation line after corneal crosslinking (CXL) (a); A transition zone between the cross-linked anterior corneal stroma and the untreated posterior corneal stroma. It is a measure of effectiveness of the CXL. AS-OCT (CASIA 2, Tomey, Japan)

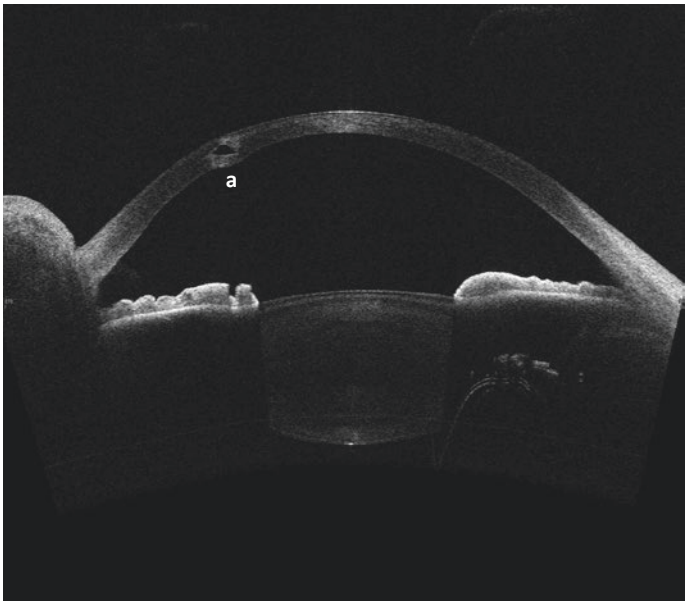

Fig. 26 Intracorneal ring segments (ICRS). Keraring with triangular cross section (a). AS-OCT (CASIA 2, Tomey, Japan)

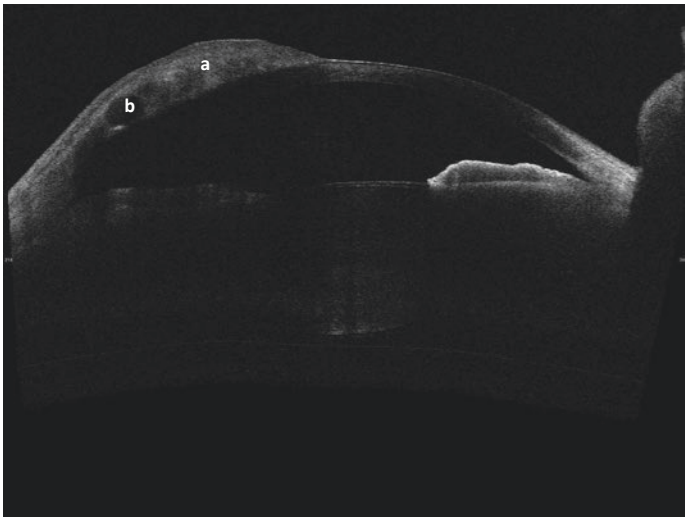

Fig. 27 Pterygium. Hyper-reflective non-homogenous mass (a) with cysts inside (b) extending to the cornea, and obscuring the cornea itself. AS-OCT (CASIA 2, Tomey, Japan)

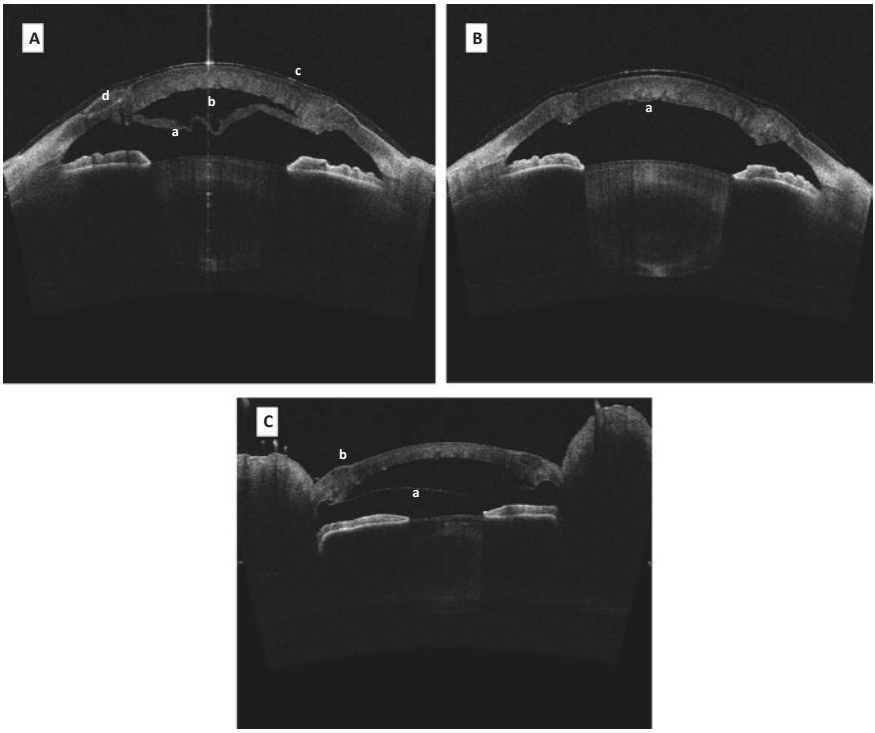

Fig. 28 **A** Deep anterior lamellar keratoplasty (DALK) double anterior chamber. Posterior lamella from recipient bed with irregular thickness prepared by layer by layer dissection (pre-descemet DALK) (a) is unattached to anterior lamella from donor and a fluid filled space (second chamber) (b) is formed in between. Note the graft edema. Bandage contact lens (c); suture line (d). AS-OCT (CASIA 2, Tomey, Japan). **B** Same patient after air injection into anterior chamber and reattachment of the two lamellas. Graft edema is decreased. Posterior lamella from the recipient bed could still be recognized (a); Its thickness is <80 μm which makes the visual outcome of pre-descemet DALK comparable to big bubble DALK. AS-OCT (CASIA 2, Tomey, Japan). **C** Double anterior chamber after big bubble DALK. DM (a); Graft-host junction (b). AS-OCT (CASIA 2, Tomey, Japan)

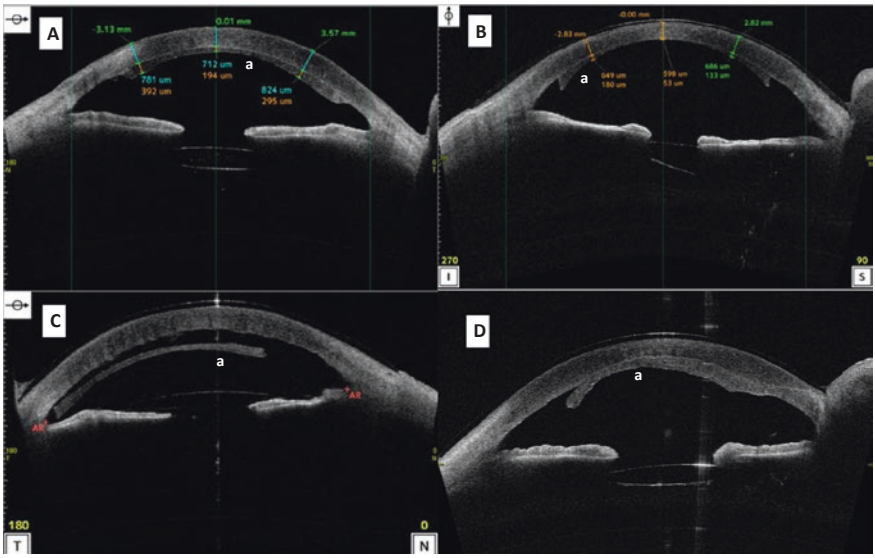

Fig. 29 Descemet striping automated endothelial keratoplasty (DSAEK). **A** Attached graft (a) with a central thickness of 194 µm and peripheral thickness of 392 µm. The graft is meniscus shaped, peripherally thicker. **B** thin DSAEK. Note the central graft thickness of about 50 µm. **C** the graft is completely unattached and dislocated temporally (a). **D** thick edematous DSAEK graft partially detached at inferior part (a)

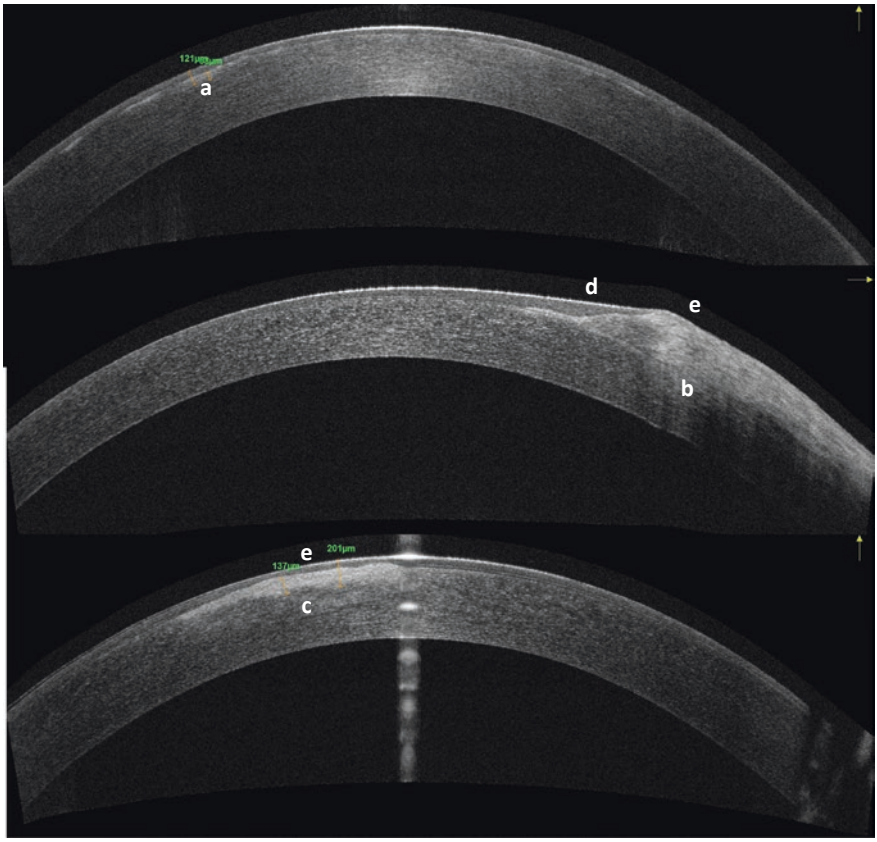

Fig. 30 RTVue anterior segment OCT (Optovue, Fremont, CA) superficial corneal scar. Note the higher resolution (axial resolution 5 μm), and the shallower depth of the scan compared to Casia 2 (swept source OCT with axial resolution of 10 μm; the epithelium could not be distinguished, but the scan width and depth makes the entire AC, iris, and even lens can be visualized in one picture) (Figs. 1, 2, 3, 4, 5, 6, 7, 8, 9 10, 11, 12, 13, 14, 15, 16, 17, 18, 19, 20, 21, 22, 23, 24, 25, 26, 27, 28, 29) the boundaries of scar could sharply be recognized (a, b, c), and corneal epithelium could be clearly distinguished from stroma (epithelial thickening adjacent to the elevated scar (d) and thinning at the top of elevated scar (e); the smoothening effect of the epithelium for irregular scars of bowman layer) Only the cornea and not the anterior chamber could be pictured with this OCT

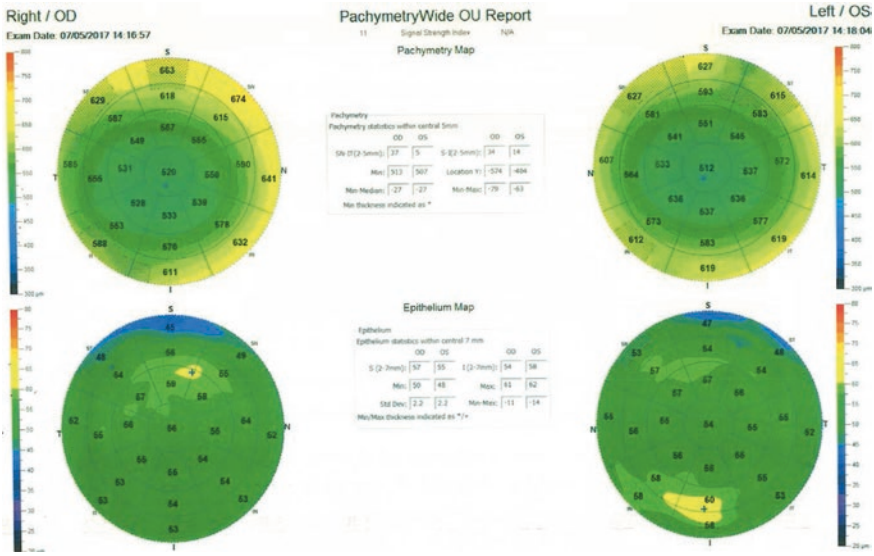

Fig. 31 Normal RTVue anterior segment OCT epithelial thickness map (Inferior row maps) (Optovue, Fremont, CA) Normal central epithelial thickness is 54 ± 5 μm. Upper epithelium is slightly thinner than inferior due to the effect of blinking

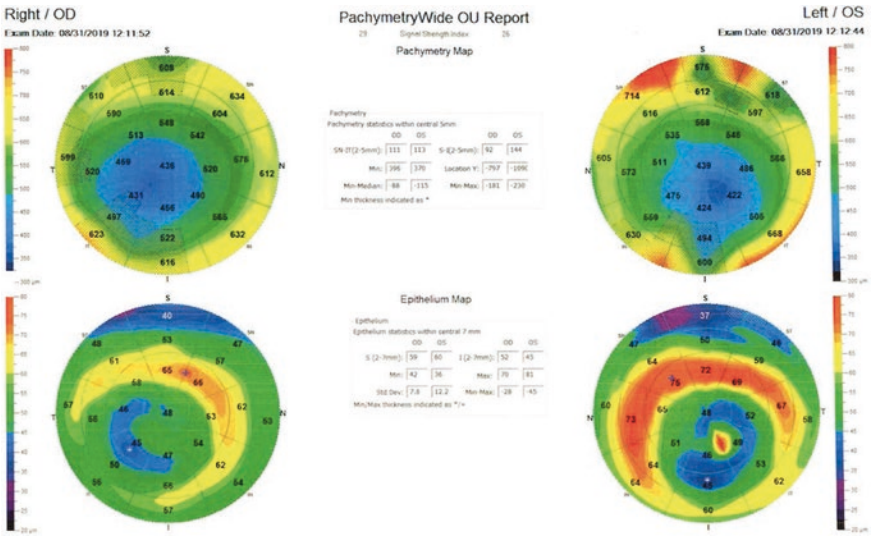

Fig. 32 Epithelial thickness map. Severe keratoconus Epithelial thinning at the cone location (a) and a ring shaped thickening of the epithelium around it (b) (donut pattern) RTVue (Optovue, Fremont, CA) AS-OCT

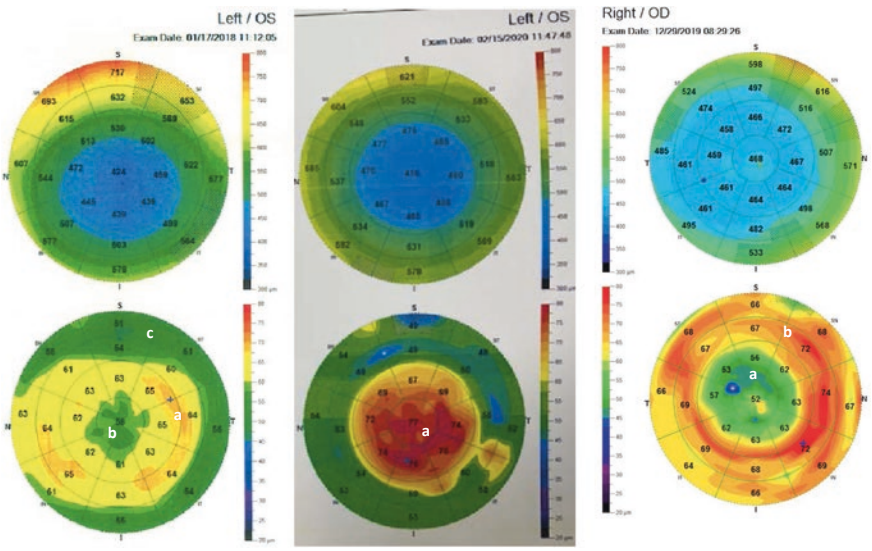

Fig. 33 Epithelial thickness map post refractive surgery. RTVue (Optovue, Fremont, CA) AS-OCT. **A** Myopic laser ablation. Central thickening of the epithelium where the curvature has rendered flat (the degree of epithelial hyperplasia is higher at the edges of the ablation zone (a) where the curvature change is abrupt compared to more central parts (b) and peripheral thinning (c). **B** Regression after myopic photorefractive keratectomy. Note significant epithelial thickening at the center (a). **C** Hyperopic laser ablation. Central thinning of epithelium where the curvature is steep (a) and epithelial thickening at the ablated annular zone (b)

Acknowledgments We would like to thank Maryam kasiri, BS and Pouran Fadakar, BS imaging technicians of cornea imaging unit at Farabi eye hospital, Tehran University of Medical Sciences, Tehran, Iran for their great contribution in image acquisition and data collecting.

References

1. Bald M, et al. Anterior chamber angle evaluation with fourier-domain optical coherence tomography. J Ophthalmol. 2012.
2. Choma MA, et al. Sensitivity advantage of swept source and Fourier domain optical coherence tomography. Opt Express. 2003;11(18):2183–9.
3. Gumus K, Pflugfelder SC. Anterior segment optical coherence tomography (AS-OCT) in the management of dry eye. Int Ophthalmol Clin. 2017;57(2):13–22.
4. Han SB, et al. Applications of anterior segment optical coherence tomography in cornea and ocular surface diseases. J Ophthalmol. 2016.
5. Kurian M, et al. Biometry with a new swept-source optical coherence tomography biometer: repeatability and agreement with an optical low-coherence reflectometry device. J Cataract Refract Surg. 2016;42(4):577–81.
6. Lim S-H. Clinical applications of anterior segment optical coherence tomography. J Ophthalmol. 2015.

7. Marcus Anga MB, Werkmeisterd RM. Anterior segment optical coherence tomography. Prog Retin Eye Res. 2018;66:132–ss56.
8. Mohan P, Chakrabarti A. Intraocular lens power calculation in 2019: the cutting edge. Kerala J Ophthalmol. 2019;31(3):191.
9. Sridhar MS, Martin R. Anterior segment optical coherence tomography for evaluation of cornea and ocular surface. Indian J Ophthalmol. 2018;66(3):367.
10. Tatham AJ. Clinical advantages of swept-source OCT and new non-damaging laser treatments. Rev Ophthalmol. 2014.
11. Thomas BJ, et al. Ultra high-resolution anterior segment optical coherence tomography in the diagnosis and management of ocular surface squamous neoplasia. Ocular Surface. 2014;12(1):46–58.
12. Wang SB, et al. Anterior segment optical coherence tomography and its clinical applications. Clin Exp Optom. 2019;102.

Corneal Biomechanics

Mahmoud Jabbarvand, Hesam Hashemian, Mehdi Khodaparast, Mohammadreza Aghamirsalim and Peiman Mosaddegh

A healthy cornea generates about 70% of the total eye refractive power of about 60 diopters [1]. Consequently, variations in biomechanical and geometrical properties of cornea can intensely affect corneal refractive power and may interrupt the eye vision.

Evaluation of corneal biomechanical properties is essential for different ophthalmological operations such as refractive surgeries [2] and for accurate measurement of intraocular pressure (IOP) [3]. Changes in mechanical properties of the cornea result in corneal diseases, such as corneal ectasia, as well as cornea refractive problems [4]. So, evaluation of corneal material properties can be used as a beneficial tool for recognizing the corneal diseases such as keratoconus [5]. Moreover, accurate estimation of IOP makes detection of pathological diseases, such as glaucoma, more feasible [6].

Ocular Response Analyzer® (ORA) is an older biomechanical evaluation device which evaluated intraocular pressure as well as corneal hysteresis (CH) and corneal resistance factor (CRF) as corneal biomechanical properties.

Luce studied the results of ORA tonometry test to estimate biomechanical properties of the cornea and their relationship to IOP [7]. He expressed that corneal hysteresis measured by ORA provides valuable data for qualification of refractive surgery outcomes.

M. Jabbarvand (✉) · H. Hashemian · M. Khodaparast · M. Aghamirsalim
Ophthalmology Department, Farabi Eye Hospital, Tehran University of Medical Sciences, Tehran, Iran
e-mail: ma.jabarvand@gmail.com

H. Hashemian
e-mail: h-hashemian@tums.ac.ir

M. Khodaparast
e-mail: khodaparastzavareh@yahoo.com

P. Mosaddegh
Mechanical Engineering, Isfahan University of Technology, Isfahan, Iran

M. Mohammadpour (ed.), *Diagnostics in Ocular Imaging*,
https://doi.org/10.1007/978-3-030-54863-6_8

For instance, post-LASIK eyes showed low corneal hysteresis. Assessment of the biomechanical properties of cornea in normal and keratoconus eyes was conducted by Shah et al. [8].

Corvis ST is another non-contact tonometer recently used for assessing biomechanical properties of cornea. Corvis ST tonometer applies a metered air puff in about 32 ms with a maximum amplitude of 25 kPa [9]. Due to the applied pressure, cornea deforms, it passes through the first applanation and reaches the highest concavity configuration. Then, by reducing the amount of applied pressure, cornea begins to return to its natural shape by passing through the second applanation. This tonometer uses an ultrahigh-speed camera capturing more than 4300 images per second to record cornea deformation during tonometry test. These images provide an efficient tool for assessing cornea biomechanical material properties.

What can Corvis do?

The information obtained on the biomechanical response of the cornea is used to calculate a biomechanically corrected IOP (bIOP). The first print out of Corvis is 1-IOP/Pachy Display.

IOP correction is based on corneal thickness, age and the biomechanical response of the cornea. When calculated this way IOP is less influenced by corneal properties and thickness than it is with other measurement methods. As the Corvis ST measures both biomechanical response and corneal thickness with high precision, the device is able to correct for both factors at the same time.

Due to the measurement principle, the IOP measurements are not influenced by tear film. This, and the fast auto tracking and auto release, ensure highly repeatable IOP and thickness readings, completely user independent.

Figure 1 is IOP/Pachy map of a 14 year old keratoconus patient. Upper box is name, and specifications of the patient. Quality score (QS) shows the quality of the imaging. Here it is marked as “Ok”. Intraocular pressure (IOP) as well as CCT (Central corneal thickness) is in the left upper box. In the left lower chart we can see IOP follow up. Right upper scheimpflug image is the biomechanical response video which can be played and viewed. Right lower chart is the pachymetry progression chart from periphery to center compared to the normal population range.

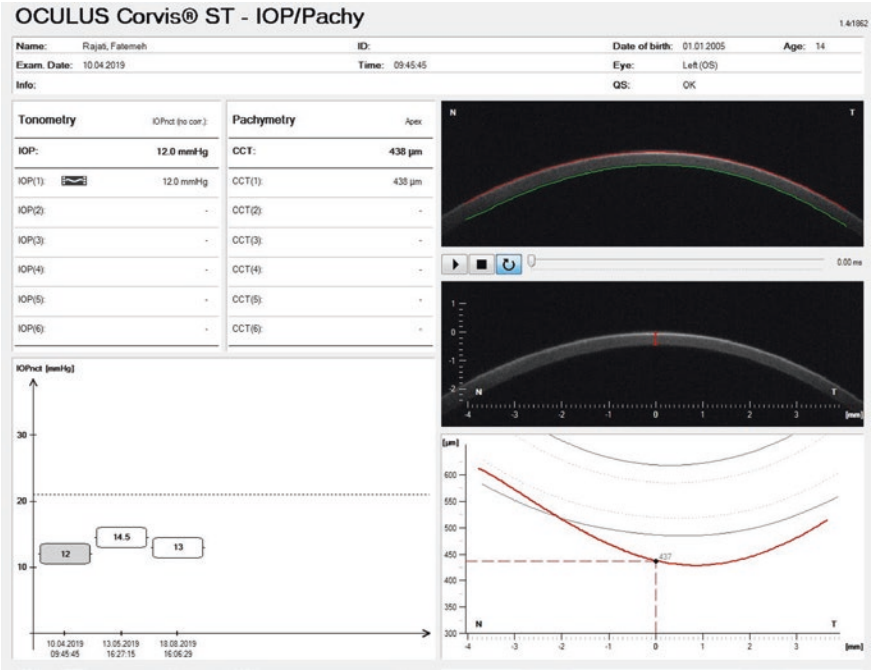

Fig. 1 IOP/Pachy map of a 14 year old keratoconus patient

Next map is Dynamic corneal response map.

In the upper left part there are six charts:

1. Deformation amplitude: It shows deformation amplitude at the corneal apex from the start to the end of the measurement. Y is the deformation of apex and X is the time.
2. Applanation length: shows how much the cornea is applanated in each time point. Y is the applanation length and X is the time.
3. Corneal velocity (Apex): Y axis displays the speed in which corneal apex moves at each time point (X axis) of measurement.
4. The delta arc length represents the change of the arc length during the measurement in a defined 7 mm zone.

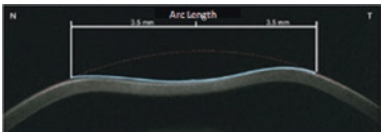

5. DA ratio 2 mm: the deformation amplitude ratio between the apex and at 2 mm from the apex: the ratio between the deformation amplitude at the apex and the average deformation amplitude at a 2 mm nasal and temporal zone.
6. The inverse concave radius (1/R): the integrated radius of corneal curvature between the first and second applanations.
7. The bottom left table displays applanation length and velocity (speed) of apex movement at two applanation times.

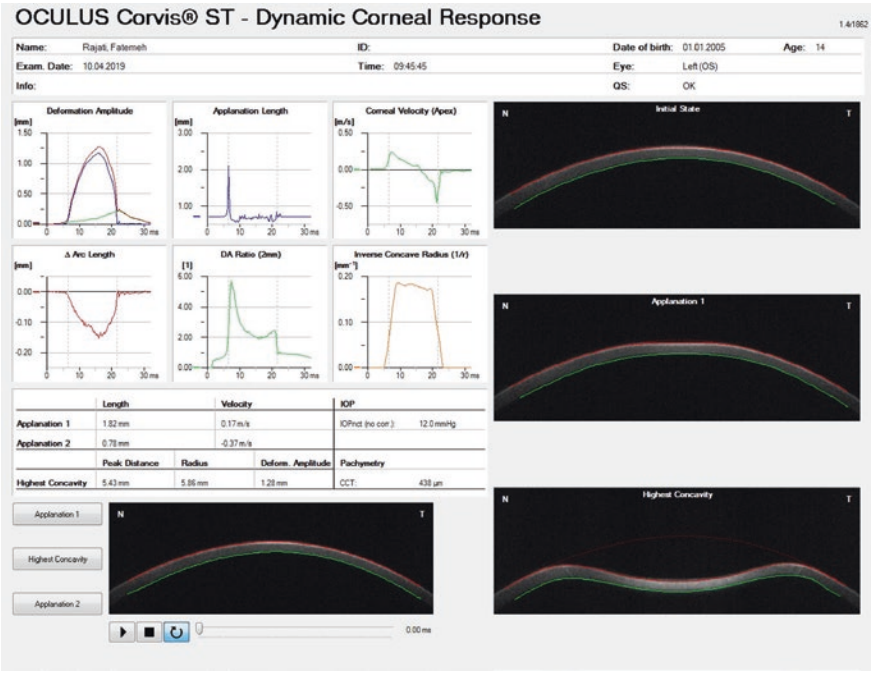

Next map is Vinciguerra Screening Report.

You can see four selectable chart plotting different variables versus time. This variables may be the variables mentioned in dynamic corneal response map mentioned in previous page or some other variables including:

1. Whole eye movement: As the cornea deforms and approaches maximum displacement, the whole eye displays a slow linear motion in the anterior–posterior direction.
2. Deflection amplitude: displacement of corneal apex in reference to the cornea's initial state.
   Therefore, the deformation amplitude is the sum of corneal deflection amplitude and whole eye movement.
3. Deflection area: describes the "displaced" area of the cornea in the analyzed horizontal sectional plane.

4. Inverse concave radius: The inverse concave radius (1/R) is plotted over the duration of the air pulse and the integrated sum is calculated between the first and second applanation events.
5. The peak distance: describes the distance between the two highest points of the cornea's temporal-nasal cross-section at the highest concavity moment.

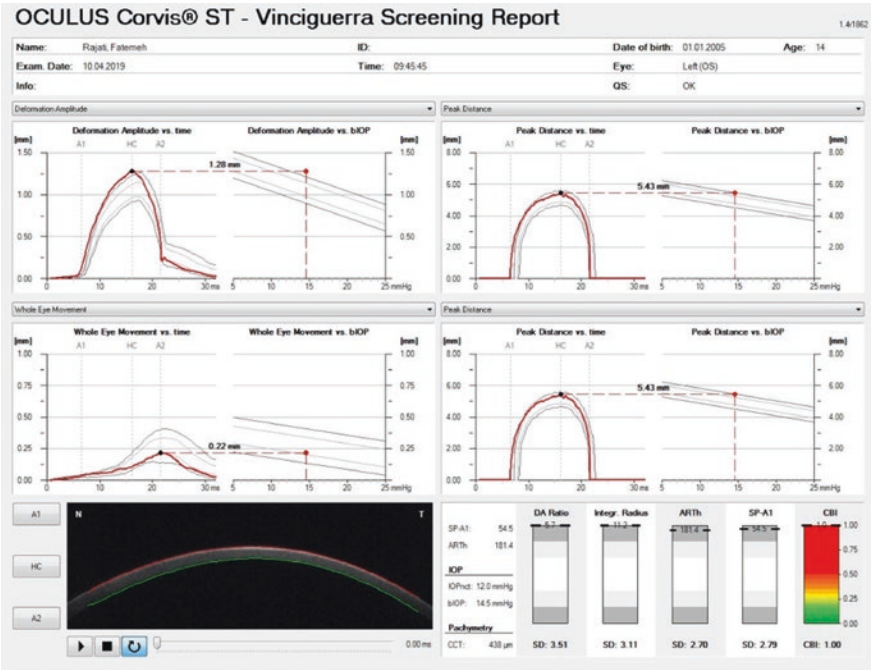

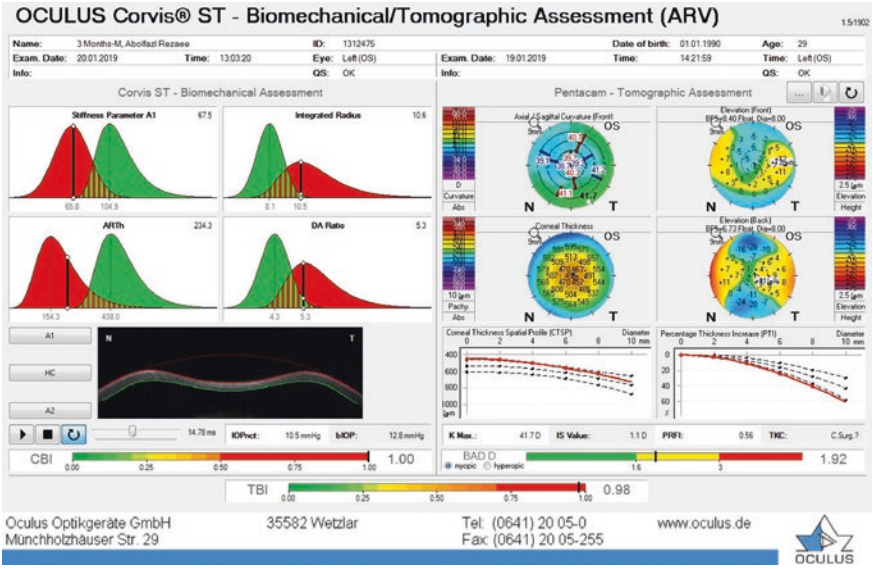

In the following section we would present corneal biomechanical changes in some cases.

Biomechanical changes after refractive surgery and intracorneal ring segment implantation

Figure 2—a 20 year old female refractive surgery candidate. Following printout is Integration of Pentacam and Corvis data for a combined tomographic and biomechanical analysis. Final: **TBI is calculated using an artificial intelligence approach to optimize ectasia detection**.

The quality score was OK. The patient was found to have a normal topographic pattern in left eye. The front sagittal curvature findings using Pentacam® HR revealed with-the-rule astigmatism with Kmax of 49.6D. Pachymetric progression indices were normal. Normal anterior and posterior curvature were demonstrated in Tomographic evaluation. The BAD-D was 1.42, under the cut-off value of normality; CBI was 0, and TBI values were 0.02, which are within normal values.

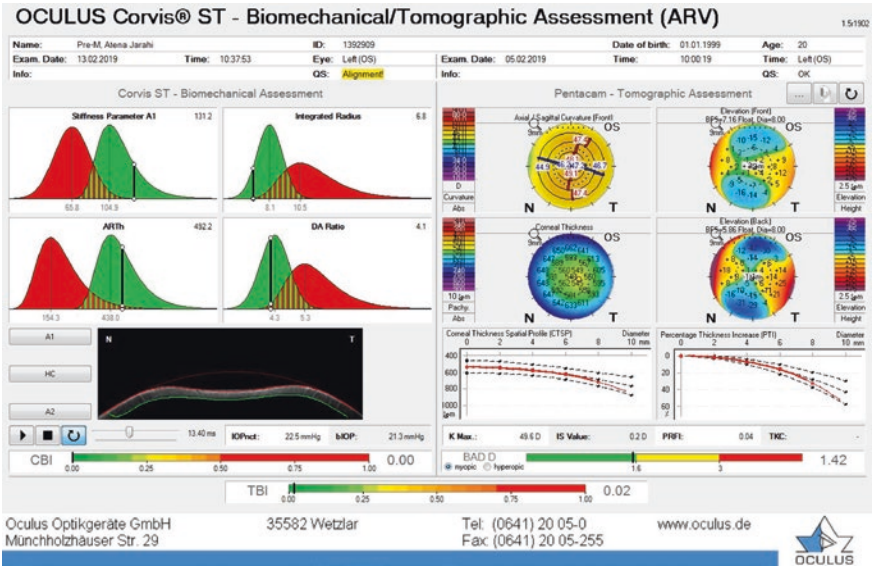

Fig. 2 Integration of pentacam and corvis data for a combined tomographic and biomechanical analysis of a 20 year old patient

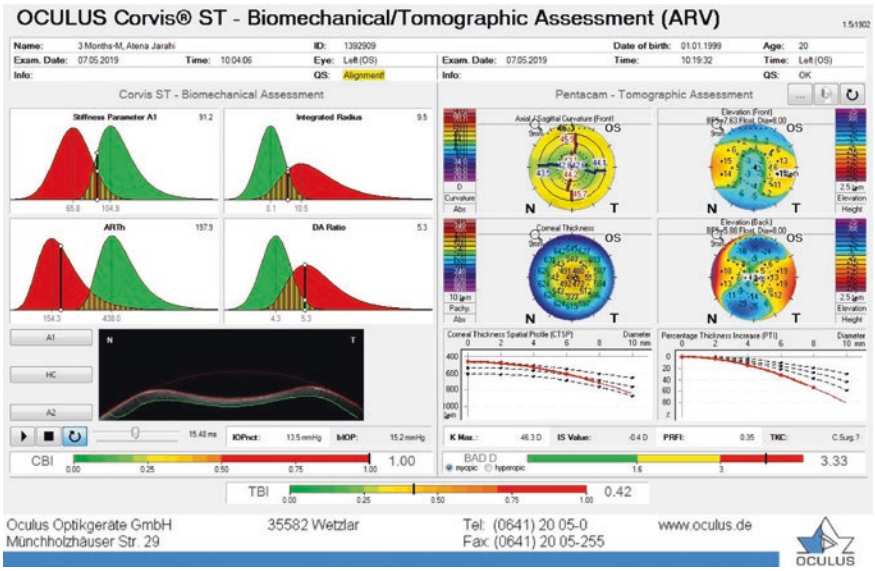

Fig. 3 Integration of pentacam and corvis data for a combined tomographic and biomechanical analysis of a 20 year old female candidate for PRK

Post PRK

Figure 3—A 20 year old female without history of any significant eye disease who had undergone PRK 3 months ago. Normal topographic pattern was found in both eyes of this patient. The front sagittal curvature measured using Pentacam® HR demonstrated flatness with Kmax of 46.3D due to history of surface ablation surgery. Tomographic evaluation demonstrated abnormal anterior and posterior curvature. The BAD-D was 3.33, over the cut-off value of normality; CBI was 1 in abnormal range, and TBI values was 0.42 in borderline range. Stiffness Parameter and Integrated Radius were in borderline value in addition ARTh and DA Ratio were abnormal.

Pre F-LASIK

A 34-year-old male scheduled an appointment to enquire about F-LASIK.He had no prior history of any major underlying eye diseases or surgeries. The central corneal thickness was circa 543 μm. The front sagittal curvature measured using Pentacam® HR demonstrated a orthogonal with-the-rule astigmatism with Kmax of 43.9D and normal anterior and posterior curvature in front and back elevation maps Pachymetric progression indices and biomechanical assessment were normal. The BAD-D was 0.37, under the cut-off value of normality; CBI and TBI values were 0.00 and 0.03 respectively.

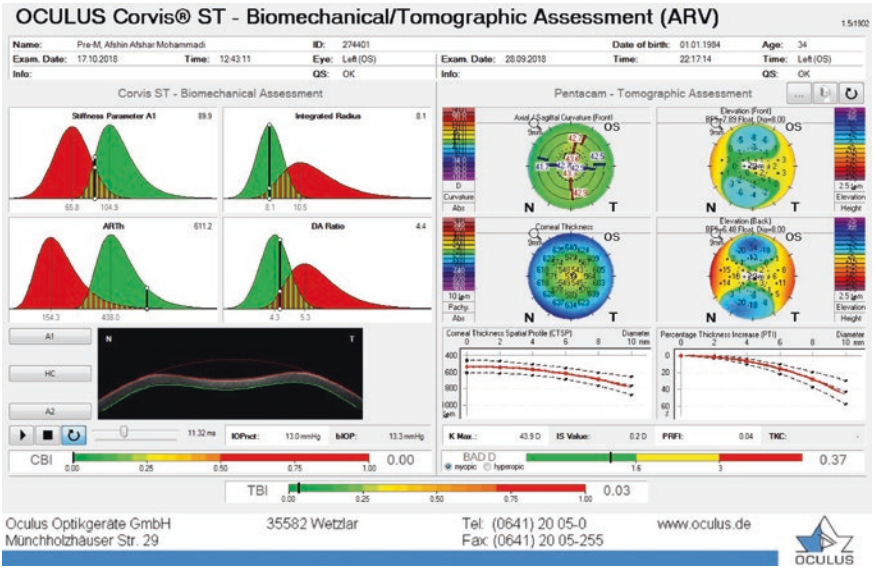

3 months after F-LASIK sagittal curvature demonstrated flattening with decrease of Kmax(42.4) and centeral cornea thickness duo to ablation surgery.

In addition to significant Biomechanical assessment changes, increased of CBI, TBI, and BAD D to abnormal rang were detectable.

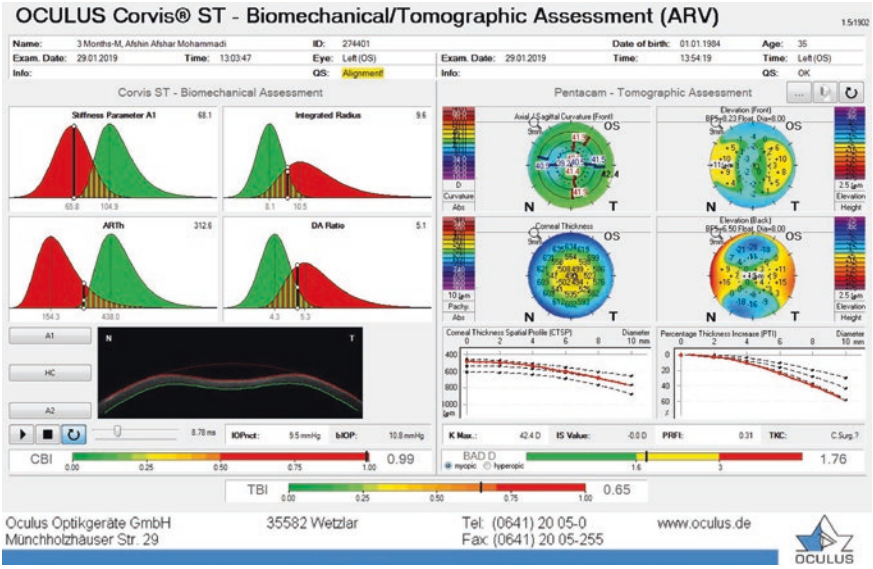

Pre Smile

A 32-year-old male who uses soft contact lenses scheduled an appointment to enquire about SMILE surgery.

He had not worn soft contact lenses for more than4 weeks prior to the appointment. He had no history of significant eye problem other than conjunctivitis during childhood.

The patient presented with a normal Biomechanical/tomographic assessment pattern in both eyes before refractive surgery.

The front sagittal curvature was found normal with Kmax of 45.1D. Normal anterior and posterior curvatures were demonstrated in Tomographic evaluation. The CBI and TBI values were 0.00 in addition to BAD-D value which was 0.22, acceptable in the cut-off value of normality. After 3 months post smile surgery central flattening was detected in front sagittal curvature map. TBI and CBI change 1.00 and BAD-D was in borderline cut-off limit in 3 months after SMILE surgery.

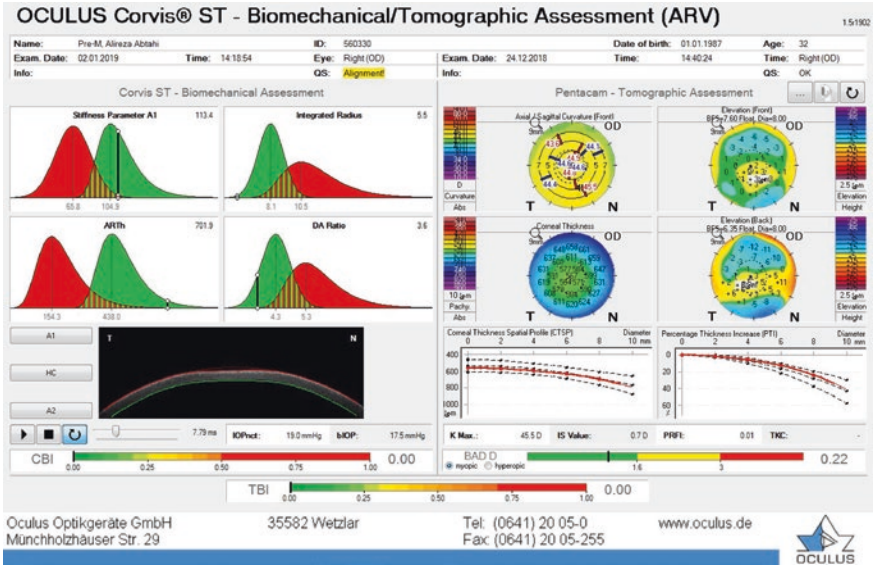

3m After Smile

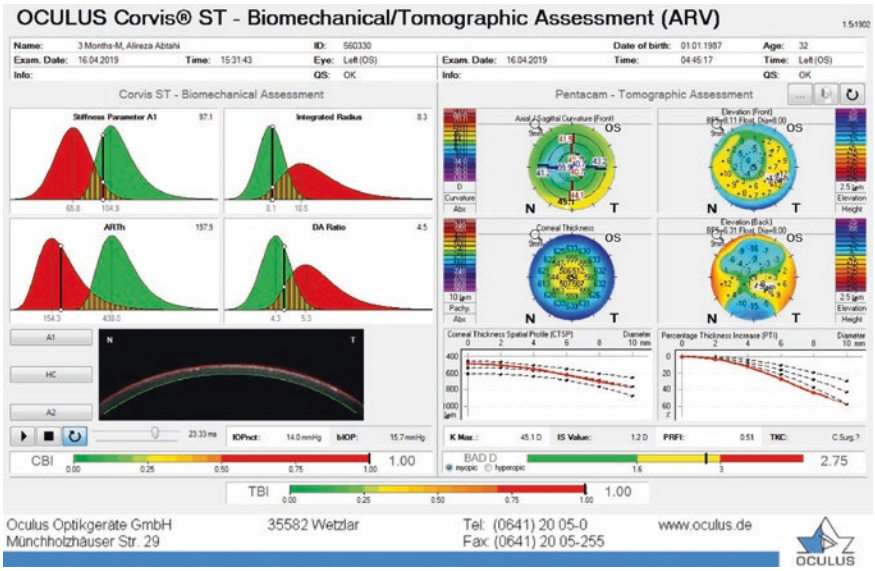

Pre ICRS

A 24-year-old male known case of keratoconus in the both eye presented for keratoconus evaluation complaining of progressive vision loss in the right eye. He was candidate for ICRS.

The front sagittal curvature demonstrated asymmetrical bow tie with inferioir steepening and STRAX.Kmax was 56.1D.anterior and posterior elevation maps and Pachymetric progression indices were abonmal. The BAD-D was 6.93, over the cut-off value of normality.CBI was 0.89, and TBI values was 1.00 which were in abnormality cut off limit.3 months after ICSR implantion the front sagittal curvature showed topometric pattern of keratoconus with Kmax 49.7 D and inferior–superior asymmetry of 3.1D. No significant changes were detected in the BAD-D, TBI, and CBI values in 3 months after ICSR implantion.

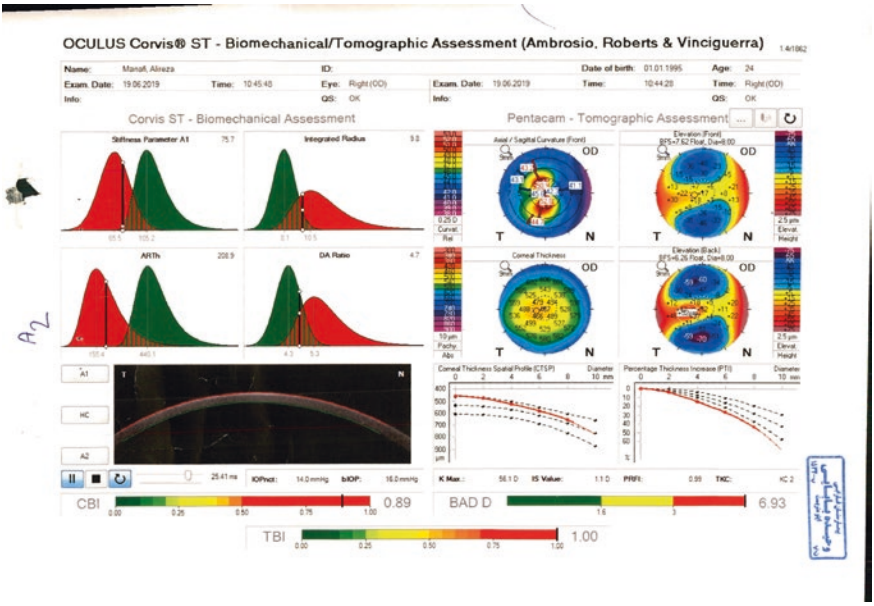
OCULUS Corvis® ST - Biomechanical/Tomographic Assessment (Ambrosio, Roberts & Vinciguerra)
Corvis ST - Biomechanical Assessment
Pentacam - Tomographic Assessment
CBI 0.89
BAD D 6.93
TBI 1.00

Post ICRS

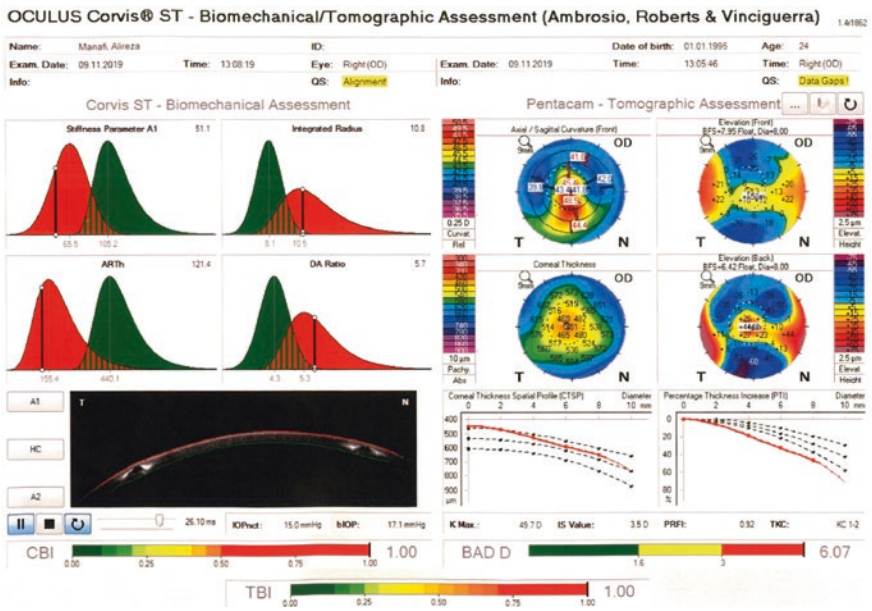
OCULUS Corvis® ST - Biomechanical/Tomographic Assessment (Ambrosio, Roberts & Vinciguerra)
Corvis ST - Biomechanical Assessment
Pentacam - Tomographic Assessment
CBI 1.00
BAD D 6.07
TBI 1.00

References

1. Picero DP, Alcyn N. In vivo characterization of corneal biomechanics. J Cataract Refract Surg. 2014;40(6). https://doi.org/10.1016/j.jcrs.2014.03.021.
2. Bryant MR, McDonnell PJ. Constitutive laws for biomechanical modeling of refractive surgery. J Biomech Eng. 1996;118(4):473–481. https://doi.org/10.1115/1.2796033.
3. Liu J, Roberts CJ. Influence of corneal biomechanical properties on intraocular pressure measurement: quantitative analysis. J Cataract Refract Surg. 2005; 31(1):146–155. https://doi.org/10.1016/j.jcrs.2004.09.031.
4. Piñero DP, Alcón N. In vivo characterization of corneal biomechanics. J Cataract Refract Surg. 2014;40(6):870–887. https://doi.org/10.1016/j.jcrs.2014.03.021.
5. Shah S, Laiquzzaman M, Bhojwani R, Mantry S, Cunliffe I. Assessment of the biomechanical properties of the cornea with the ocular response analyzer in normal and keratoconic eyes. Investig Ophthalmol Vis Sci. 2007;48(7):3026–31. https://doi.org/10.1167/iovs.04-0694.
6. Farandos NM, Yetisen AK, Monteiro MJ, Lowe CR, Yun SH. Contact lens sensors in ocular diagnostics. Adv Healthc Mater. 2015;4(6):792–810. https://doi.org/10.1002/adhm.201400504.
7. Luce DA. Determining in vivo biomechanical properties of the cornea with an ocular response analyzer. J Cataract Refract Surg. 2005; 31(1). https://doi.org/10.1016/j.jcrs.2004.10.044.
8. Shah S, Laiquzzaman M, Bhojwani R, Mantry S, Cunliffe I. Assessment of the biomechanical properties of the cornea with the ocular response analyzer in normal and keratoconic eyes. Invest Ophthalmol Vis Sci. 2007;48(7). https://doi.org/10.1167/iovs.04-0694.
9. Ambrysio JR R, Ramos I, Luz A, Faria FC, Steinmueller A, Krug M, Belin MW, Roberts CJ. Dynamic ultra high speed Scheimpflug imaging for assessing corneal biomechanical properties. Rev Bras Oftalmol. 2013;72(2). https://doi.org/10.1590/s0034-72802013000200005.

Ultrasound Biomicroscopy (UBM)

Leila Ghiasian and Seyed Javad Hashemian

Introduction

Ultrasound Bio Microscopy (UBM) is a high-resolution ultrasound technique that allows noninvasive, in vivo imaging of anterior segment details at near microscopic resolution. It is a diagnostic and treatment method used for anterior segment visualization of the eye [3]. UBM allows qualitative and quantitative evaluation of the anterior chamber anatomy and many pathologies of the conjunctiva, cornea, anterior chamber, iridocorneal angle, iris, zonules, ciliary body, lens and vitreous base which gives many information for clinical application. In addition, UBM has been used for evaluating corneal dystrophies, scars, cysts, changes after excimer laser photokeratectomy and LASIK procedures, intraocular lens implants and their positions (tilt, haptic location), the angle for glaucoma diagnosis (open-angle glaucoma, primary angle closure glaucoma included plateau iris syndrome, pigmentary glaucoma pupillary block glaucoma and pseudoexfoliation syndrome), anterior segment tumors and some other rare eye diseases (such as ICE syndrome, phakomatoses, and metabolic disorders), the anterior chamber depth, sulcus-to-sulcus diameter, capsular bag thickness and diameter, ciliary ring diameter, ciliary process-capsular bag distance and ciliary apex-capsular bag plane. The important advantage of UBM compare to anterior segment optical coherence tomography is to create better images from structures that located posterior to the iris [4].

The first UBM system for clinical usage introduced by Foster and Pavlin in the early 1990s.

After that, Coleman et al. invented another UBM system suitable for 3-D analysis that gives many information especially from the cornea. During the time, UBMs

L. Ghiasian (✉)
Eye Research Center, The Five Senses Institute, Rassoul Akram Hospital,
Iran University of Medical Science, Tehran, Iran
e-mail: leilaghiasian@gmail.com; ghiasian.l@iums.ac.ir

S. J. Hashemian
Iran University of Medical Science, Tehran, Iran
e-mail: sj_hashemian@yahoo.com

M. Mohammadpour (ed.), *Diagnostics in Ocular Imaging*,
https://doi.org/10.1007/978-3-030-54863-6_9

upgraded with higher scan rate images and more compact handheld probes compare to the original. High-frequency digital UBM or very high-frequency digital UBM is a newer technology that gives corneal epithelium and stromal measurements and corneal flap and residual stromal bed evaluation in post-LASIK corneas. It uses as an important tool in keratoconus screening and staging [2].

Principle

UBM has much higher frequency transducer (35–80 MHz) compared to regular ultrasound modalities such as A-scan or B scan (10 MHz) [5]. This technique upgrades the resolution results up to 30u axially and 50u laterally which comes at the expense of reduced depth of penetration (4–5 mm for 50 MHz) and smaller angular field. According to the principles of ultrasound, high frequency and short focal length are associated with high image resolution and poor penetration. The second part of this devise is computer monitor which records the real-time images for later analysis. Because of close interface between transducer and object and protect image distortion, filled eye-cup devices must be used for creation of an offset distance [6]. The images are based on the reflection from an interface due to the change in the medium's impedance [7]. The most important advantage of ultrasound over all optically based systems is that they are not affected by opaque intervening mediums [8].

Technique

The UBM examination technique is similar to immersion B-scan ultrasonography. The process is done with the examined patient in a supine or sitting position after applying topical anesthetic. A plastic or silicone eyecup (22–24 mm) is placed within palpebral fissure to separate the eyelids and form a water bath environment. This filled with methylcellulose solution (1–2.5%) or normal saline. In comparison to methylcellulose, normal saline generates better image quality [9]. The transducer should be placed within the small water bath solution in such a way that the scanning beam strikes the target perpendicularly to maximize the detection of reflected signals and the examiner should not give undue pressure that may distort the structures. UBM also could be used in sitting or prone position with keeping its image quality. This can be examined any anatomical alternation in different positions [10].

Types of Scans

The white line on the side of the probe body indicates the direction of the linear movement of the transducer.

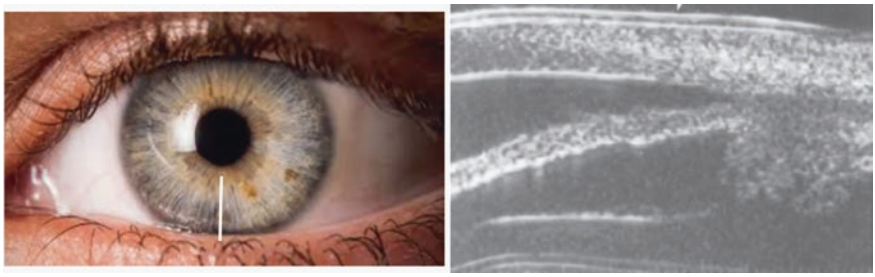

Fig. 1 Radial (longitudinal) scan. Slit lamp photograph of the anterior segment of the eye showing the plane of a radial scan. The probe is placed perpendicular to the limbus with the marker towards the pupil and corresponding UBM image. Right picture: Reuse from Springer [1]

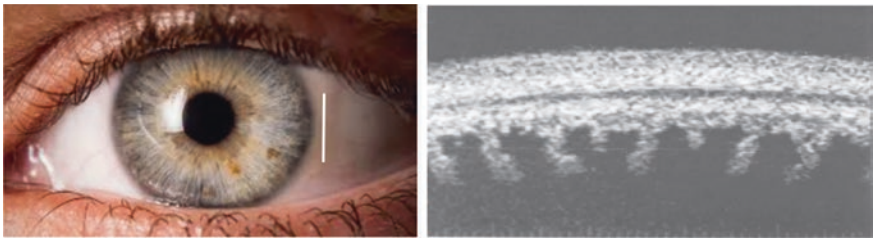

Fig. 2 Peripheral transverse scan. Slit lamp photograph of the anterior segment showing the plane of a transverse scan. The probe is placed over the sclera slightly posterior and parallel to the limbus and corresponding UBM image showing the ciliary body processes. Right image: Reuse from Springer [1]

Radial/Longitudinal scan: UBM transducer is held perpendicular to the limbus with the marker towards the pupil. Image in this position shows the cornea and central iris on the left side of the display, and the limbus, ciliary body, and sclera on the right side. This type of scan is the most common scan used in UBM examinations and especially useful for angle evaluation (Fig. 1).

Transverse scan: UBM transducer is held parallel to the limbus over the iris center with the marker oriented towards the superior or nasal hemispheres. The resulting scan shows a section of the cornea and central iris of approximately 20°. For the peripheral structures, the probe must be moved posteriorly towards the fornix to get an image of the peripheral iris, ciliary body processes and ora serrata. This type of scan is ideal for the evaluation of iris and ciliary body masses and their lateral extentions (Fig. 2).

***Sulcus to sulcus scan* (*Axial scan*)**: UBM transducer is held perpendicular to the cornea directly over the pupil. The resulting scan shows the anterior segment from front to back. The probe should be placed in the center of the cornea with the patient looking in the primary gaze. If the marker line pointing in the superior position, it gives a vertical axial scan and if the marker is in the nasal position, it gives the horizontal scan. This type of scan is ideal for assessing the anterior chamber depth and the orientation of intraocular lenses (Fig. 3).

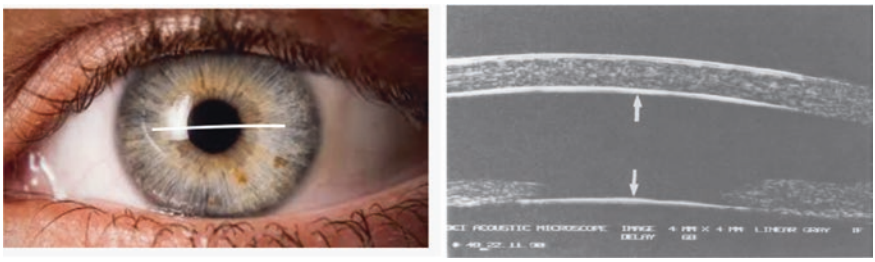

Fig. 3 Axial scan. Slit lamp photograph of the anterior segment showing the plane of an axial horizontal scan. The probe is placed perpendicular to the cornea directly over the pupil and corresponding UBM image. Right image: Reuse from Springer [1]

Normal Corneal Structures in UBM

Before any introduction about corneal pathologies, it is necessary to know the normal appearance of cornea in ultrasound biomicroscopy.

The Cornea

The cornea is the first structure seen on UBM. The corneal layers are well-differentiated with this device. The reflection from the epithelium create a smooth, regular and superficial line in a normal eye. The Bowman's membrane forms a highly dense reflective line just beneath the epithelial surface. The distance between these two lines is the epithelial thickness. The corneal stroma reveals a low internal reflectivity that is lower than sclera that contains more irregular collagen distribution. The 3rd high reflective line is the Descemet's membrane and endothelial layer [11]. These two layers are usually difficult to differentiate in UBM imaging and form a single highly reflective line that located at the posterior corneal margin (Fig. 4). The corneoscleral junction can also be recognized due to the lower internal reflectivity of the cornea in comparison to the sclera because of the structural differences. The change zone from the cornea to the sclera is not an obvious line and it is a gradual transition area similar to slow histological change. The inner part of this junction compatible to Schwalbe's line. The surgical limbus is located approximately 1 mm anterior to the scleral spur that is representing the transition between conjunctiva and corneal epithelium [12].

The Sclera

The normal sclera has a relatively high reflective area compared to the cornea, episclera, ciliary body and peripheral choroid so UBM can detect it for

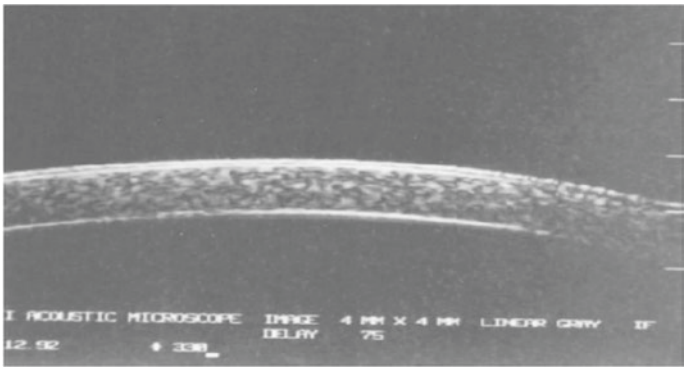

Fig. 4 Ultrasound biomicroscopic image of normal cornea. The top echo is from the epithelial surface. The second echo below the previous one and is from Bowman's membrane layer. The corneal stroma shows weak backscatter. The endothelium-Descemet's layer provides a bright echo at the interface with aqueous. Reuse from Springer [1]

differentiate the scleral structural abnormalities. In addition, it is a practical device for the assessment of treatment and outcome of these abnormalities [13]. UBM is only able to examine the anterior scleral equator. The scleral spur is the thickest part of the sclera that forms a constant landmark allowing image interpretation and it is the important key for find out any angle pathology. Scleral spur identified in the area where the radiopaque shadow of the sclera converges with the radiolucent shadow of the cornea. The thinnest part of the sclera is located under the muscle insertion [3].

Anterior Chamber

This chamber is an echo free area between the cornea and the iris. UBM can measure the anterior chamber depth from the posterior surface of the cornea to the anterior lens capsule (normal AC depth is about 2.5–3.0 mm). The margins of the iris can show the best orientation for measuring this chamber from the center of pupillary space. Measurement of anterior chamber depth can be taken from any point on the endothelial surface to any point on the iris or on the lens surface and create an anterior chamber profile that is important for many clinical issues [14].

The Iris

The iris is a relative flat structure with a uniform echogenicity that meet the ciliary body at the iris recess and attach to the scleral spur [15]. The space between iris

periphery and the ciliary processes named as ciliary sulcus. The normal iris profile is straight compare to anterior bowing in pupillary block glaucoma [16] and posterior bowing in pigment dispersion glaucoma [17].

The iris shows some variations at its surface. The iris stroma has a relatively low reflectivity compare to iris epithelium that forms a thick high reflective layer at the posterior surface and useful for differentiation of intra and extra iris lesions. The normal iris shows thickness variations in different regions. The thinnest part is generally located at its root and the thickest part is near the pupillary margin.

The Angle

The angle can be studied in a cross-section by putting the probe in a radial orientation at the limbus. The corneoscleral junction and scleral spur can be distinguished in many cases. Accurate angle analysis depends on precise localization of the structures and UBM could be used as a qualitative device for angle appositional closure, existence of ciliary rotation and identify other abnormalities in this area. Quantitative analysis of the geometric angle width is not a practical process and usually employed as a research tool [11].

UBM Limitations

1. Inability to visualize structures deeper than 4 mm
2. It is an immersion technique (compare to non-contact scanning method in AS-OCT) and needs an experienced operator
3. Needs direct contact so it is not useful in eyes with an open eye and postoperative evaluation (at least at early postoperative days)
4. It needs supine position in most cases while performing the scan
5. Difficulty in children
6. Possibility of causing injury to cornea with the eyecup while performing UBM

Although newer techniques such as anterior segment optical coherence tomography (AS-OCT) and Scheimflug imaging have the advantage of being noncontact and also better resolution of anterior structures but UBM still stands superior because of the deeper penetration and better visualization of some structures like ciliary body, zonules and lens. The role of UBM in corneal pathologies as a non-topographic corneal imaging is limited and summarized in this chapter.

UBM and Corneal Pathologies

In general, corneal pathologies can be assessed directly by slit lamp examination. In the presence of relatively clear cornea, most pathologies can be seen and the depth can be measured. With a dense corneal opacity or a covered cornea, UBM could be an important role to evaluate the cornea and underlying anterior chamber pathologies [1]. Newer UBM, very high-frequency (VHF) digital ultrasound, can measure the corneal epithelial thickness and create an epithelial thickness profile [18] for many clinical purposes that summarized later in this chapter.

Corneal Edema

The most common causes of corneal edema is related to any endothelial disorders secondary to inflammatory processes, ocular surgery, trauma and toxins. Corneal edema can affect the epithelium or stroma or both. With UBM, in majority of cases, it is possible to detect the cause of corneal edema and find out any interference of anterior segment structures that may help us to planning a better surgical approach if needed.

The typical features of corneal edema in UBM [7, 11, 15] (Fig. 5).

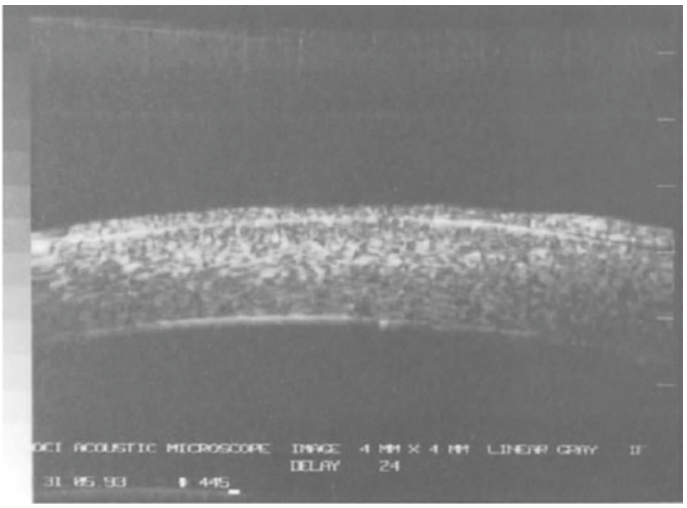

Fig. 5 Ultrasound biomicroscopic image of an edematous cornea. The epithelium is thickened and irregular. The stroma is thickened with increased reflectivity

1. Epithelium: Thickend with irregular echo and internal reflectivity
2. Stroma: Thickened and increased reflectivity, can be localized or diffused
3. Bulla may be visible on anterior surface line specially in some severe corneal edema as a separation of the epithelium from underlying Bowman's membrane.

Blood Staining of the Cornea

Consider a traumatic total hyphema with suspicious corneal staining and invisible anterior chamber that is full of blood. UBM image in this condition may be helpful for diagnosis and also planning for probable surgery. UBM may show these signs [19]:

1. Epithelial edema
2. High reflection in stroma
3. Blood filled anterior chamber with various densities

Descemet's Membrane Detachment

DMD can easily be overlooked or misdiagnosed especially after ocular surgeries. It could be seen just as a corneal edema and should be considered as a differential diagnosis in cases of corneal edema after any intraocular surgery. UBM could be helpful in diagnosis and treatment planning in the presence of corneal edema [20].

UMB shows the normally thin transparent Descemet's membrane detached from the back of the edematous cornea. It can describe the location and extension of this detached membrane [11] (Figs. 6 and 7).

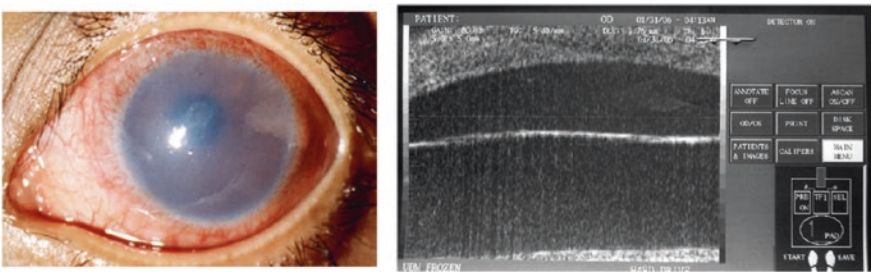

Fig. 6 Severe corneal edema and corresponding UBM image showing total Descemet's detachment. Reuse from Springer [20]

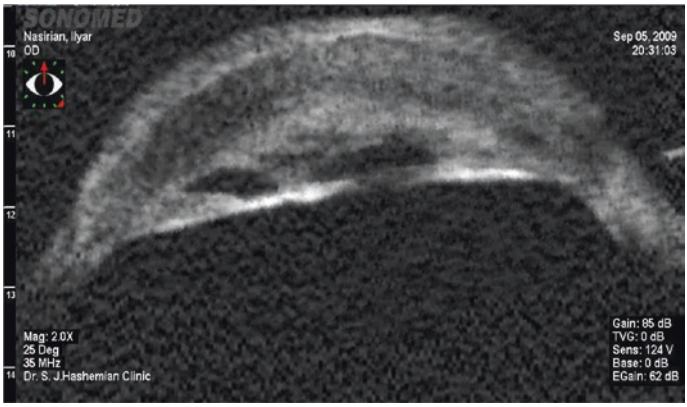

Fig. 7 Descemet's membrane detachment in postoperative follow up after lamellar graft

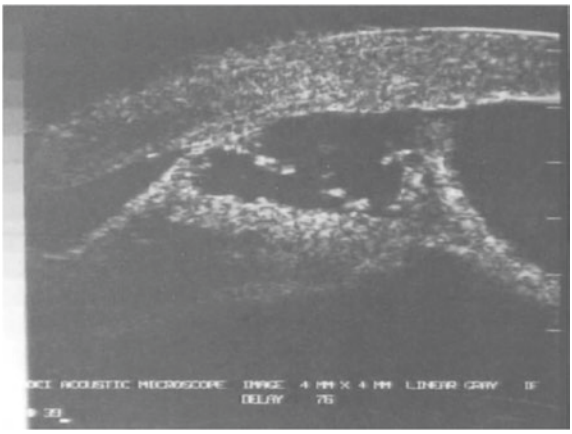

Fig. 8 Adherent leukoma. Strands of iris tissue extend anteriorly and attach to the posterior corneal surface

Corneal Opacification and Underlying Changes

There are multiple causes of corneal opacities secondary to different types of corneal pathologies. UBM gives quantitative information from the opacity (depth, thinning) and it enable to give an additive information about any underlying anterior segment changes [1] (Fig. 8). UBM could offer an objective way to measure the depth of corneal opacities and bypass a dense opacity and get an image from other layers of the cornea and anterior segment [21]. In general, a corneal scar creates a higher reflectivity compare to surrounding normal cornea (Fig. 9).

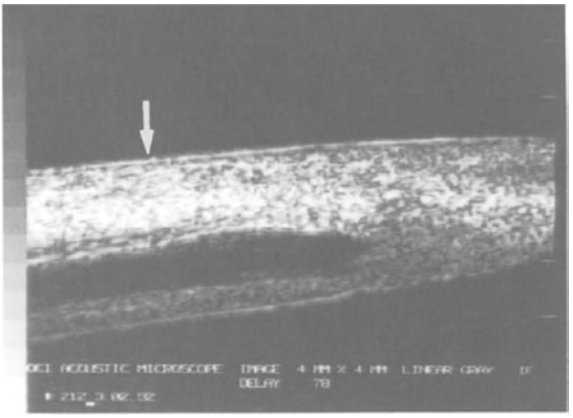

Fig. 9 Scarred cornea secondary to inflammation shows increased stromal reflectivity

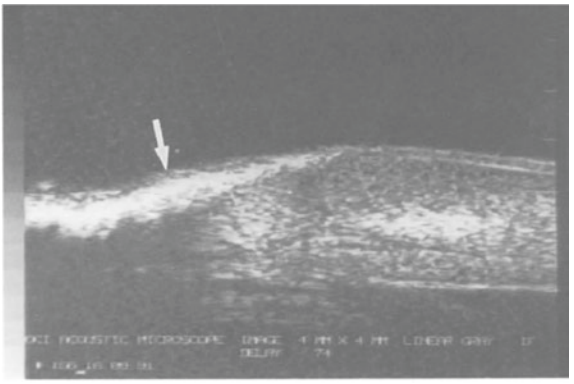

Fig. 10 Scarred thick cornea with an area of calcification (arrow) and complete shadowing of structures behind it. Reuse from Springer [1]

If any calcification present at the site of scar, the reflectivity increases to a very high levels and creates shadowing of posterior structures due to absorption of sound by the site of calcification [1] (Fig. 10). In central corneal opacities versus in off-center area, UBM may shows a sharper interface between opaque cornea and adjacent normal tissue compare to AS-OCT due to back-scattering of light from deep opacities that merged with reflection from normal posterior cornea [21]. Comparing to OCT, UBM give a slightly higher reading for corneal opacity depth measurments [21]. Considering a corneal scar that is denser than normal cornea, it creates a higher optical index and appear thicker in OCT but due to higher ultrasound velocity it would appear thinner in UBM. These changes are ignorable and the findings in both devices agreed very well. It seems that AS-OCT and UBM can be used interchangeably for measuring both total corneal thickness and corneal opacity depth in patient with corneal opacity.

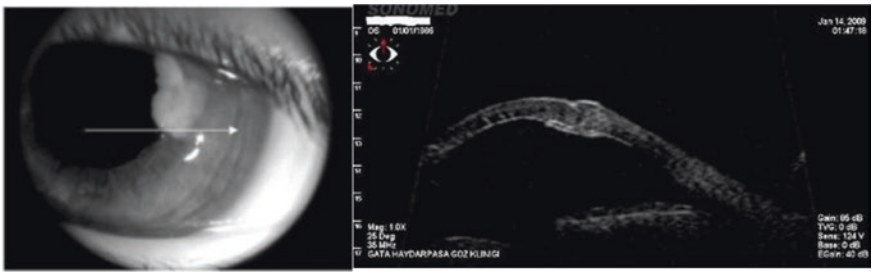

Fig. 11 Previous history of uneventful DALK surgery for keratoconus with creamy-colored deposit at interface and clinical suspicion of fungal keratitis with corresponding UBM image. Reuse from Springer [23]

Corneal Infection

UBM can be used to assess the severity of corneal infections. In opacified corneas due to any type of keratitis, the severity and extent of corneal thinning and risk of probable perforation can be assessed with UBM during the follow ups [22] (Fig. 11).

Conjunctival Flaps

After a conjunctival flap procedure for any reason, it is difficult to assess the covered cornea and the underlying anterior chamber. Conjunctival flap can be differentiated from the corneal tissue and also it evaluates the corneal thickness beneath the conjunctiva [1] (Fig. 12). Also, it can give a clue for planning any future surgery for visual rehabilitation.

Corneal Grafts

UBM shows edema and thickening of the corneal stroma and epithelium independently and also it can assess the graft-host junction alignment. At this junction, it may show an irregular reflectivity due to step in apposition of posterior surface of graft-host junction (Fig. 13).

Any posterior step or gap can also visible in UBM imaging and at the same time any underlying abnormalities at anterior chamber can be recognize [24]. In addition, UBM is a useful tool in the preoperative planning of the patient before

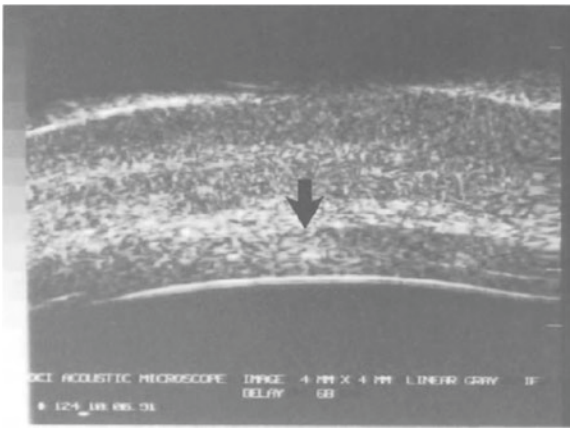

Fig. 12 Conjunctival flap. The cornea (arrow) can be differentiated beneath the conjunctival tissue with a relatively normal thickness

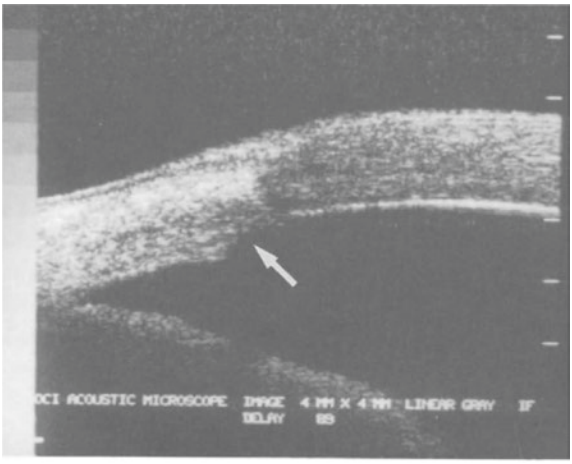

Fig. 13 Graft-host junction shows a step on the graft side. Reuse from Springer [1]

keratoplasty and can help to confront the possible difficulties before the operation. A visible extensive synechia in UBM can predispose the patient to graft rejection and elevated IOP that may increase the chance of graft failure and propose a higher risk graft for the patient [25] (Fig. 14).

After DSAEK (Fig. 15), UBM and VHF digital UBM can be used to visualize and assess host and donor cornea thickness profiles and give a sublayer anatomy information specially when the corneal edema is existing and obscure the clear visualization. Donor lenticules made with microkeratomes, create a nonuniform thickness profiles that thinner at center compare to peripheral part (Fig. 16).

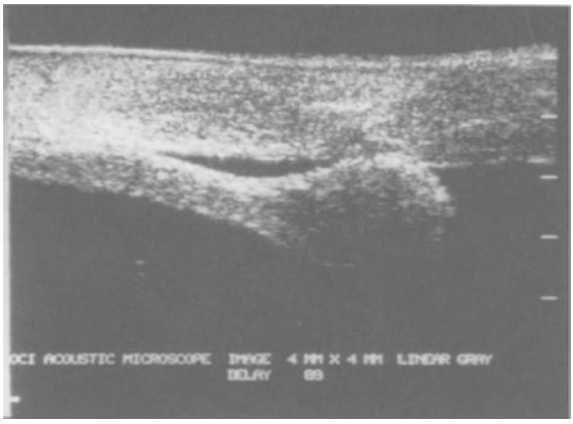

Fig. 14 Iris beneath the graft has closed the angIe and is adherent to the graft-host junction. Reuse from Springer [1]

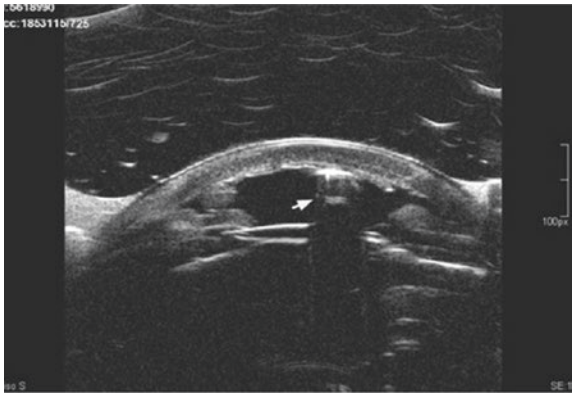

Fig. 15 Air bubble after DSAEK surgery. A 75-year-old man underwent Descemet's stripping automated endothelial keratoplasty (DSAEK) for decompensated cornea in his right eye, with an uneventful surgical course. An ultrasound biomicroscopic scan demonstrates a small air bubble in the anterior chamber (white arrow). The iris inferiorly is elevated, almost touching the cornea. Reuse from Springer [26]

Corneal Dystrophies

Ultrasound biomicroscopy can give an information about the depth and extension of reflective changes due to multiple precipitate and changes in stromal lamellas in some corneal dystrophies.

Granular dystrophy: Localized hyperechoic dots and flakes against the normal stroma specially at the superficial stroma [1, 11] (Fig. 17).

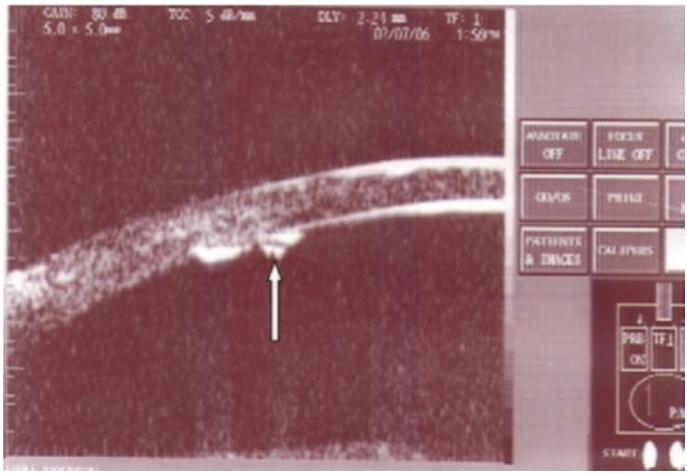

Fig. 16 UBM picture of a cornea after penetrating keratoplasty with inflammatory deposits on the sutures. Arrow is at the inflammatory deposits. Reuse from Springer [27]

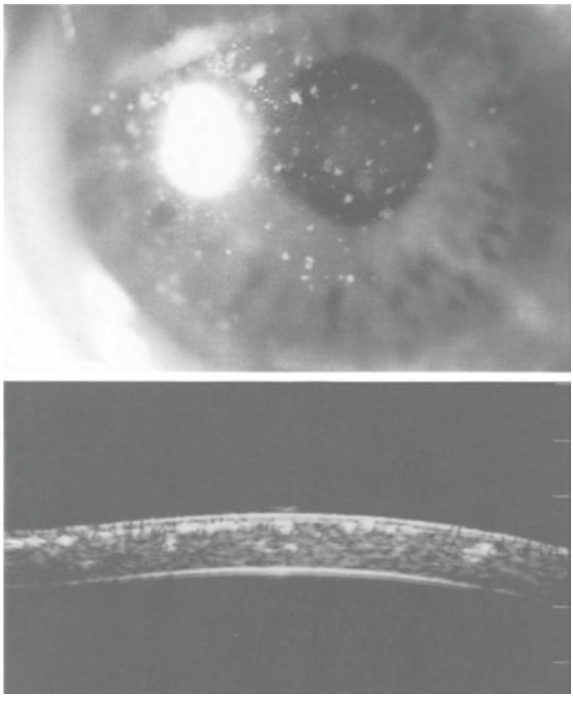

Fig. 17 Clinical appearance of a granular dystrophy and corresponding UBM image that shows highly reflective hyaline bodies are outlined against the stroma in the superficial cornea. Reuse from Springer [1]

Macular dystrophy: In advanced cases it may shows diffuse hyper reflection signal in the stroma without relative clear zones between them [21].

Lattice dystrophy: Diffuse and homogeneous hyper reflection in the corneal stroma that may notify a dark band at the depth of the pathology to separate normal part of stroma from involved area [21].

Acute Corneal Hydrops

Ultrasound biomicroscopy is a useful device for quantitative and qualitative measurement of features in acute corneal hydrops [28]. It is a diagnostic and also prognostic tool for this situation.

Morphologic characteristics of acute hydrops in UBM:

1. Increase corneal thickness due to epithelial and stromal edema.
2. DM tear: UBM can localized the tear and measure the size of tear under the edematous cornea, usually it located under the most edematous area of the cornea. When the tear is larger, we expect more extensive corneal edema and it usually compatible to the size of the tear. It may appear as a defect in the DM with rolled edges and the loss of continuity of bright and intense reflectivity due to DM at the posterior surface of the cornea.
3. Intrastromal cysts or clefts: they may communicating with anterior chamber [29].

UBM can also be used as a follow up device to see any resolution of corneal edema in various location in patient without treatment or for detection of treatment effect in patient with any type of procedure. This is especially useful to document the morphometric changes at multiple follow-up points.

UBM can also help in planning for early penetrating keratoplasty in poor outcome cases in which there is a very large DM tear or a large intrastromal cyst that may cause intrastromal migration of the tamponade and preventing the tear closure [28].

Photoablative Corneal Surgery

After photorefractive keratectomy, UBM reveals the change in surface configuration and the normal double-layered superficial appearance is replaced by a less clear single-layer due to loss of Bowman's Membrane [1] (Fig. 18).

VHF digital ultrasonography can detect any irregularities in the epithelial and stromal thickness profiles in candidates for phototherapeutic keratectomy [30]

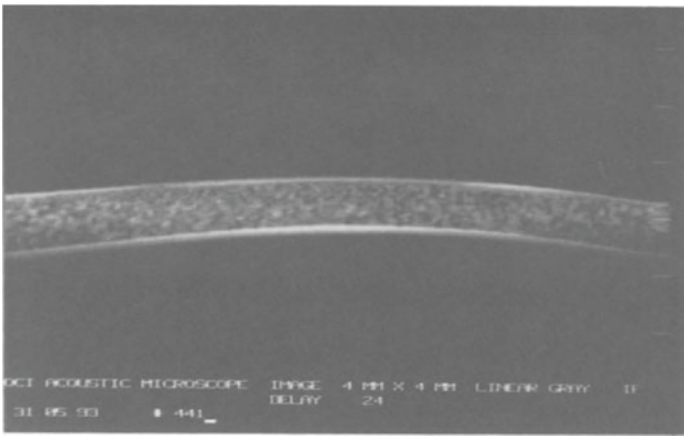

Fig. 18 Excimer laser treated cornea shows only a single reflection from the epithelial surface. The echo from Bowman's membrane is absent. Reuse from Springer [1]

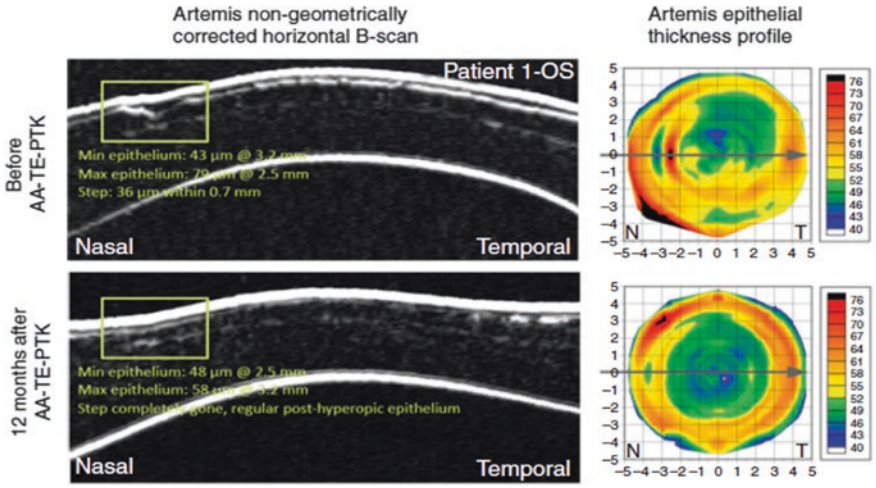

Fig. 19 A 50-year-old male was referred with complaints of severe visual disturbances after LASIK years ago for low hyperopia, Left column: Artemis non-geometrically corrected horizontal B-scans before and after the Trans-epithelial Phototherapeutic Keratectomy procedure. The yellow box highlights the nasal region where the flap interface stops abruptly. In this area, there is a crevice on the stromal surface with overlying thick epithelium and thin epithelium on the adjacent ridge. Right column: Artemis epithelial thickness maps before and after the Trans-epithelial Phototherapeutic Keratectomy procedure plotted on the same scale. These show the nasal step in epithelial thickness which has been completely smoothed after the procedure. Reuse from Springer [33]

and also as a guide for repositioning of a dislocated flap ("free cap") after LASIK [31] and assess the postoperative changes in the corneal epithelial thickness profile induced by myopic LASIK and PRK to find out the sources of regression or residual refractive error or any visual disturbances (Fig. 19) in patients for an accurate planning for further enhancement procedures [32, 33].

Corneal Thickness Measurement

Measurement of central corneal thickness was previously carried out by use of contact ultrasound pachymeters. Several studies have reported multiple reason for variation in handheld pachymetry, wrong probe position, compression of the cornea by the probe, displacement of the tear film by the probe, and not placing the probe perpendicularly on the cornea. In comparison to the UBM images, as an immersion technique, contact pachymetry showed thicker result that may due to decentration or oblique diffusion. In comparison to AS-OCT and Scheimflug images, UBM may show a slightly thicker corneal pachymetry measurements [8].

Ciliary Sulcus Measurements

VHF ultrasound is useful in providing accurate measurement of the anterior chamber depth, angle to angle and sulcus to sulcus measurements which helps selecting a suitable size for phakic intraocular lenses (especially posterior phakic IOLs). Ciliary sulcus-to-sulcus (STS) diameter is most accurately measured by UBM. Optical instruments cannot be measuring the sulcus diameter directly because the optical path is blocked by the iris pigment epithelium.

A weak correlation was found between 0˚ STS and 0˚ white-to-white (WTW) with partial coherence interferometry biometry and scanning-slit topography in emmetropic eyes. However, the correlation was weaker in myopic eyes and in general UBM is the most accurate way to measure sulcus diameter specially for preoperative evaluation to choose an appropriate posterior chamber phakic intraocular lens (PC pIOL) diameter, especially in myopic eyes [34]. With the aid of software calipers, vertical and horizontal CSDs (ciliary sulcus diameter) can be measured. The vertical diameter measure from the superior iris root at the ciliary process to the inferior iris root. The horizontal diameter is measured from the nasal iris root at the ciliary process to the temporal side (Fig. 20).

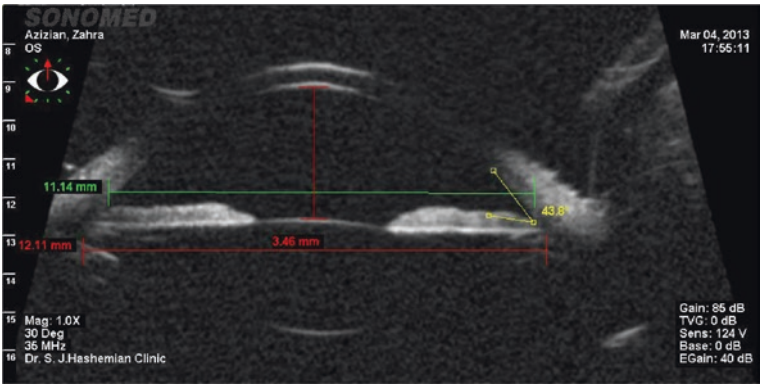

Fig. 20 Sulcus-to-sulcus measurement. An ultrasound biomicroscopic scan shows sulcus to-sulcus and anterior chamber measurements before ICL implantation surgery

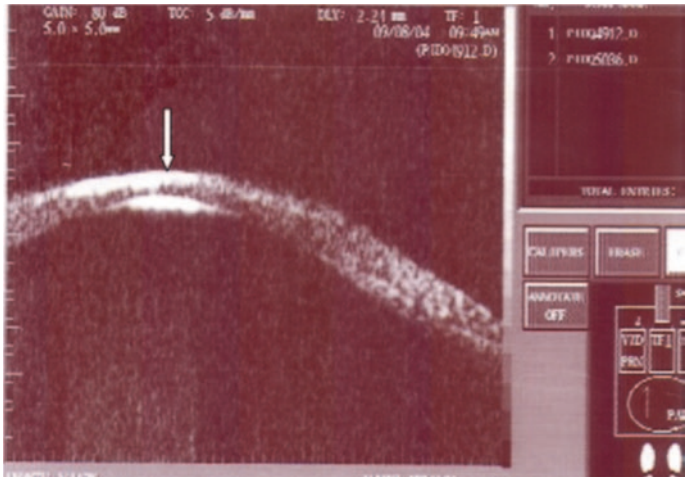

Fig. 21 Paracentral coning has a widened highly reflective epithelium. Stroma is extremely thinned. The structure of the cornea is unrecognizable at the ectatic part of the cornea. Reuse from Springer [27]

Corneal ectasia: The dynamic visualization of the cornea can localized and quantify the thinnest part of the cornea in ectatic cornea [35] (Fig. 21). It could be useful for identify the band of thinning in terrain marginal degeneration [36, 37], find out the localized posterior excavation in posterior keratoconus [38] or as a diagnostic tool in congenital corneal staphyloma [39].

Generally, in the ectatic area the epithelium shows higher reflectivity and the underlying stroma thinned significantly. Also, it can determine the width, depth, extension, thickness and structure of the cornea at the ectatic part (Figs. 22, 23, 24 and 25).

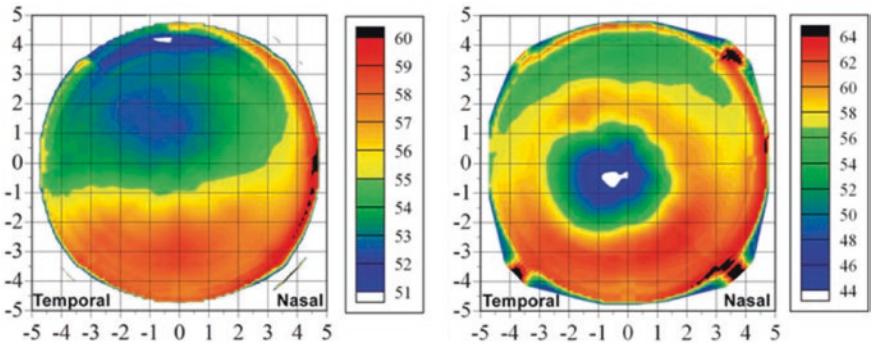

Fig. 22 Mean epithelial thickness profile for normal eyes and keratoconic eyes. The color scale represents epithelial thickness in microns. A Cartesian 1-mm grid is superimposed with the origin at the corneal vertex. Reuse from Springer [2]

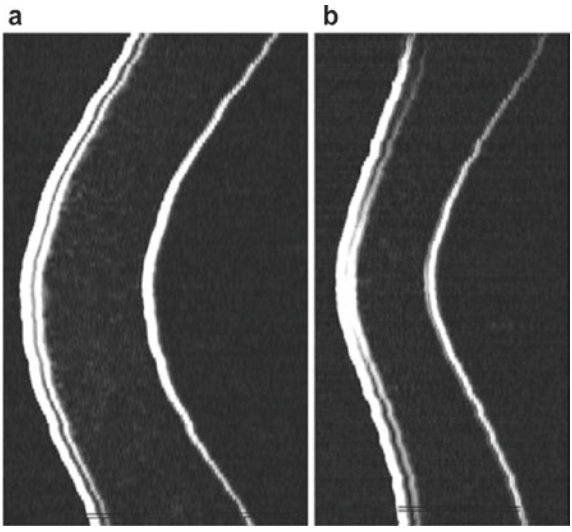

Fig. 23 **a** (left) B-scan of a normal cornea using the Artemis very high-frequency digital ultrasound arc scanner. The epithelium appears uniform in thickness across the 10 mm diameter of the scan. **b** (right) B-scan of a keratoconic cornea using the Artemis very high-frequency digital ultrasound arc-scanner. The epithelium appears very thin centrally coincident with a visible cone on the back surface. The epithelium is clearly thicker either side of the cone. The central epithelium is much thinner and the peripheral epithelium is much thicker compared to normal eye. Reuse from Springer [2]

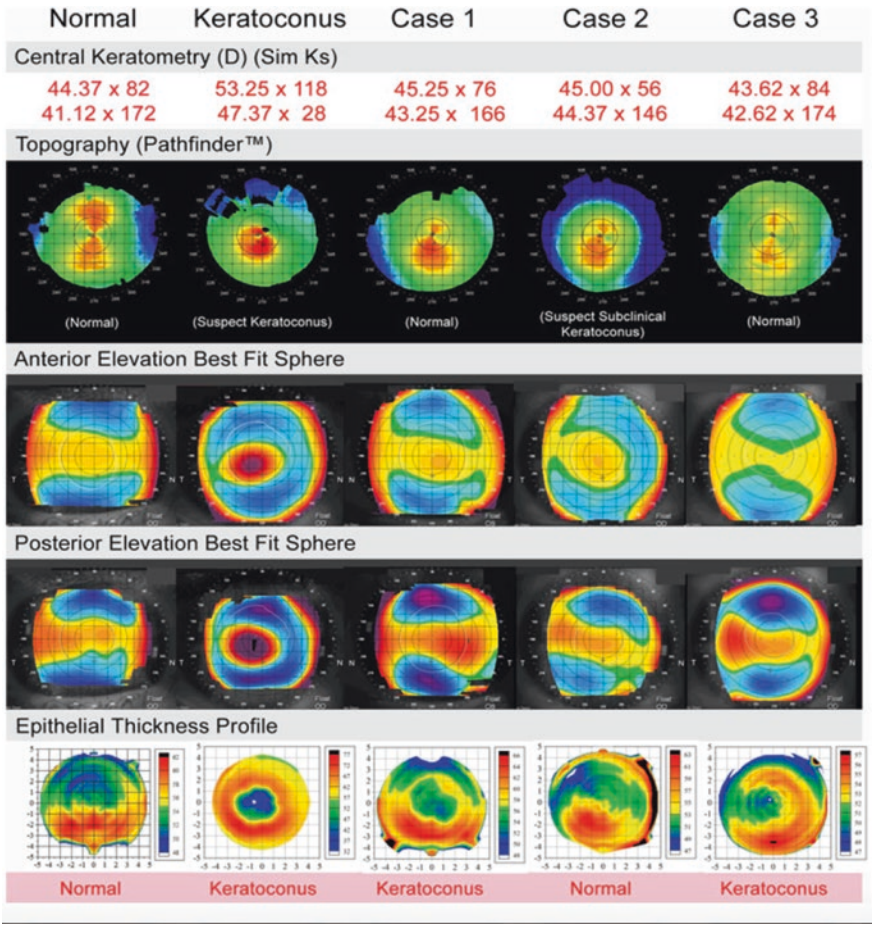

Fig. 24 Central keratometry, Atlas corneal topography and PathFinder™ corneal analysis, Orbscan anterior and posterior elevation BFS and Artemis epithelial thickness profile for one normal eye, one keratoconic eye, and three example eyes in which the diagnosis of keratoconus might be misleading by topography. The final diagnosis based on the epithelial thickness profile is shown at the bottom of each example. Reuse from Springer [2]

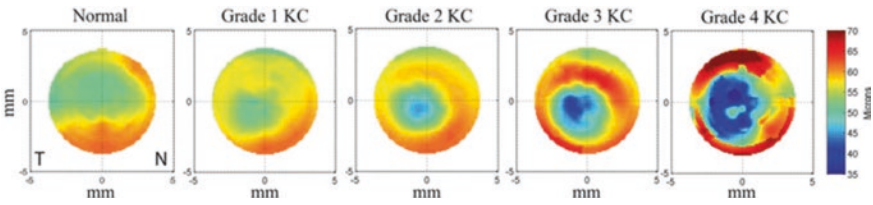

Fig. 25 Epithelial thickness maps. The departure from the normal epithelial distribution is evident even in grade 1 keratoconus but becomes more obvious with severity. Reuse from Springer [2]

Pachymetric Maps

After use of conventional UBM for years, Reinstein and Silverman using very high-frequency (VHF) digital showed Pachymetric maps that are representing of each corneal layer's thickness using very high-frequency (VHF) digital ultrasound biomicroscopy. Then they use an arc-scanner for creation of a full width of the cornea and showed a different visualization of cornea after LASIK surgery and demonstrated the flap (flap thickness profile), residual stromal thickness and also documented the epithelial compensation induced by ablation of underlying stromal tissue. Then they reported the use of UBM for detecting the changes in distribution of epithelial thickness in keratoconic patients and suggest that as a screening device in ectatic corneas. Generally, the epithelial thickness map shows thicker epithelium inferiorly than superiorly and also thicker temporally than nasally [18]. This irregularity may due to the effect of eyelid mechanics and blinking [40].

Indication for epithelial map thickness:

1. Keratoconus screening
2. Diagnosis of stromal surface irregularity and compensatory epithelial irregularity
3. Application of trans-epithelial PTK: It is important in complicated cases after refractive surgery
4. An indicator to measure probability of steepening in hyperopic patient after corneal refractive surgery

Changes in epithelial thickness profile have been described in many situation like, myopic excimer laser ablation [32, 41], hyperopic excimer laser ablation [42], radial keratotomy [43], intra-corneal ring segments [44] and in ectasia [45, 46]. In these cases, without any doubt the changes in epithelial thickness are a compensatory response to the change in stromal surface.

The epithelium being thicker over the "valleys" and thinner over the "hills", where the stroma protrudes.

Compensatory epithelial thickness changes can be summarized by the following rules [2]:

1. The epithelium thickens over the areas where tissue has been removed or the curvature has been flattened: Central epithelial thickening After myopic ablation or radial keratotomy and peripheral epithelial thickening after hyperopic ablation.
2. The epithelium thins over the areas that are relatively elevated or the curvature has been steepened: Central thinning in keratoconus and ectasia over the area of elevation and also after hyperopic ablation due to corneal steepening.
3. The magnitude of epithelial changes secondary to the corneal curvature is correlated to the magnitude of corneal curvature change: In a higher ablation

in high myopic or high hyperopic patients, we expected the more epithelial thickening.

4. The amount of epithelial remodeling is limited by the speed of change in corneal curvature: More epithelial remodeling for a more localized irregularity. In the local changes with a high curvature gradient, the epithelial remodeling is almost complete but in a cornea with global change in its curvature, epithelial remodeling is just a partially smoothing the process. With a hyperopic ablation the epithelial compensation is about twice compare to myopic ablation due to more localized area of treatment and there is almost total epithelial compensation.

For a very localized stromal loss due to a previous corneal ulcer.

Corneal stroma represents approximately 90% of the total corneal thickness and it represents a central thickness about 478–500 μm [47]. Stromal thickness map shows that the corneal stroma is thinner in the central cornea and become progressively thicker towards the peripheral cornea in all directions. The thinnest central region was slightly displaced inferiorly and temporally with reference to the corneal vertex. This finding might be useful for keratoconus screening for detection of any deviation from the normal.

Indication for stromal map thickness: (include bowman's layer, Descemet's and endothelium).

1. Exclude the variable changes in epithelial layer after corneal refractive surgery and show the stromal thickness without the epithelial impression
2. Keratoconus screening: Deviation from the normal stromal thickness
3. Corneal refractive surgery retreatment: Provide the residual stromal map

Epithelium in Keratoconus

Generally, the corneal epithelium has the ability to change its thickness over the cornea to recreate a smooth and relatively regular corneal surface and hide the presence of any irregularity at the stromal level [48]. Therefore, in a keratoconic patient, the epithelial profile must have a specific feature that could be a compensatory for cone. In keratoconus, epithelial thickness profile is clearly different. Whereas the epithelium in normal eyes was relatively homogeneous in thickness with a pattern of slightly thicker epithelium inferiorly than superiorly, the epithelium in keratoconic eyes is irregular and also showing a doughnut shape pattern, and a significant difference in thickness between the thin epithelium at the center of the doughnut and the surrounding annulus of thick epithelium. This type of epithelial thickness profile advances along with the progression of keratoconus and shows more irregularity with progression of the disease. In an advance stage of KCN, epithelial map may show excessive epithelial thinning that lead to a breakdown in the epithelium. The epithelial thickness map in these corneas shows the thinnest part of itself at the apex of the cone and surrounded by a ring of thickened epithelium. So, the central epithelium is much thinner and the peripheral

epithelium is much thicker compared to normal. In addition, whenever the cornea became steeper the area of minimum thickness in epithelium became thinner. When thinning in the epithelial map is more significant, there is also an increase in the irregularity of the epithelial thickness profile and it is an indicative factor for the severity of the keratoconus. The thinning location in epithelial map also displace to inferior and temporal. Epithelial thickness changes in keratoconus also proved the role of epithelium for surface stromal irregularity compensation. So, epithelial thickness mapping appears to be an additional informative and useful tool for diagnosis of keratoconus when topographical changes are relatively ambiguous. Changes in epithelial thickness could potentially compensate the small amount of stromal surface irregularity and produce a completely normal anterior elevation, while the ectasia would be manifest on the posterior surface elevation in topography. In the other hand, not all of the posterior elevations shows the diagnosis of keratoconus and it must be confirmed by a diagnostic tool in eyes with an eccentric posterior elevation [2, 27, 35].

Epithelial Profile After Ectasia

Epithelial changes in ectatic process is similar to keratoconus patient with a donut shape pattern that the thin area cover the ectatic cone and surrounded by an annulus of thicker epithelium [46].

Epithelial Changes After Refractive Surgery

Significant and important changes demonstrated in epithelial thickness profiles after both myopic and hyperopic PRK and LASIK. After myopic ablation, a central compensated thickening of epithelium is clear [32]. After radial keratotomy, a similar compensation epithelial thickness changes secondary to curvature change without any tissue removal occur [43].

Compensatory epithelial thickness changes are also occurred after hyperopic laser ablation and in this situation, the profile shows central epithelial thinning and paracentral epithelial thickening that cover the location of maximum ablation [42].

Stromal Thickness Change After Refractive Surgery

Many methods that use for measuring postoperative corneal thickness will be compromised by the compensated epithelial changes that are known to occur after excimer laser ablations and intraoperative stromal thickness measurements are somehow unreliable due to changing in tissue hydration at that time [49]. UBM scans are centered on the corneal vertex, so the same fixed location can be found more confidently before and after surgery, improving the easier finding for the same measurement location. Errors caused by intraoperative hydration

and refractive index changes are also avoided [50]. One of the interesting findings from this layered pachymetry analysis in a patent after myopic LASIK is that in the periphery of the cornea that no ablation was done, the stroma became thicker. The LASIK flaps and also, ablation itself separate anterior lamellae that can reduce the strain acting on the anterior peripheral lamellae and the distance between lamellae expands allowing them to separate and causing thickening [51].

Flap

Studies have demonstrated the use of VHF digital UBM for measuring the flap thickness and residual stromal thickness (RST) for assessing further enhancement [52]. VHF digital UBM can be used to present the anatomy and thickness of flap. Some clinical application of flap image:

1. Evaluating microfolds
2. Epithelial ingrowth diagnosis
3. Cryptic buttonholes diagnosis
4. Planning for a new flap creation if needed

Due to its ability to differentiate both Bowman's interface and the flap interface, the thickness of the stromal component of the flap can be detected (flap thickness without the epithelium) (Fig. 26).

In conclusion, although newer techniques such as anterior segment optical coherence tomography and Scheimflug devices have the advantage of being non-contact with better resolution of anterior structures, UBM still have its advantage

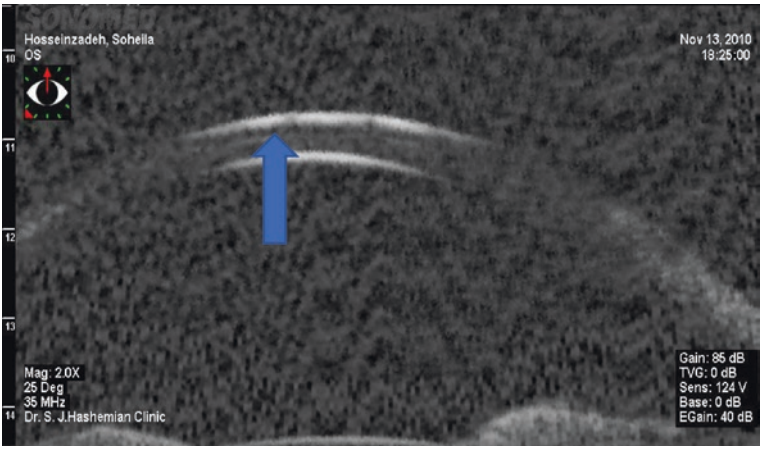

Fig. 26 LASIK flap (blue arrow)

of deeper penetration and better visualization of ciliary body, zonules, and lens and also has its superiority in a patient with opaque cornea. The future prospect of three-dimensional-UBM imaging system that create volumetric images looks so attractive.

References

1. Pavlin CJ, Foster FS. Ultrasound biomicroscopy of the eye: Springer Science & Business Media; 2012.
2. Alio JL. Keratoconus. Recent Advances in Diagnosis and Treatment Alicante: Springer. 2017.
3. Pavlin CJ, Sherar MD, Foster FS. Subsurface ultrasound microscopic imaging of the intact eye. Ophthalmology. 1990;97(2):244–50.
4. Martin R. Cornea and anterior eye assessment with slit lamp biomicroscopy, specular microscopy, confocal microscopy, and ultrasound biomicroscopy. Indian J Ophthalmol. 2018;66(2):195.
5. Kumar RS, Anegondi N, Chandapura RS, Sudhakaran S, Kadambi SV, Rao HL, et al. Discriminant function of optical coherence tomography angiography to determine disease severity in glaucoma. Invest Ophthalmol Vis Sci. 2016;57(14):6079–88.
6. Rosen DB, Conway MD, Ingram CP, Ross RD, Montilla LG. A brief overview of ophthalmic ultrasound imaging. Novel Diagnostic Methods in Ophthalmology: IntechOpen; 2019.
7. Avitabile T, Russo V, Ghirlanda R, Castiglione F, Marino A, Reibaldi A. Corneal oedemas: diagnosis and surgical planning with ultrasound biomicroscopy. Ophthalmologica. 1998;212(Suppl. 1):13–6.
8. Kanellopoulos AJ, Asimellis G. Comparison of high-resolution Scheimpflug and high-frequency ultrasound biomicroscopy to anterior-segment OCT corneal thickness measurements. Clin Ophthalmol (Auckland, NZ). 2013;7:2239.
9. Kapetansky FM. A new water bath for ultrasonic biomicroscopy. Ophthalm Surg Lasers Imaging Retina. 1997;28(7):605–6.
10. Esaki K, Ishikawa H, Liebmann JM, Ritch R. A technique for performing ultrasound biomicroscopy in the sitting and prone positions. Ophthalm Surg Lasers Imaging Retina. 2000;31(2):166–9.
11. He M, Wang D, Jiang Y. Overview of ultrasound biomicroscopy. J Curr Glaucoma Prac. 2012;6(1):25.
12. Pavlin CJ, Ritch R, Foster FS. Ultrasound biomicroscopy in plateau iris syndrome. Am J Ophthalmol. 1992;113(4):390–5.
13. Zur D, Neudorfer M, Shulman S, Rosenblatt A, Habot-Wilner Z. High-resolution ultrasound biomicroscopy as an adjunctive diagnostic tool for anterior scleral inflammatory disease. Acta Ophthalmol. 2016;94(6):e384–9.
14. Pavlin CJ, Simpson ER, Foster FS. Ultrasound biomicroscopy. Ultrasound Clin. 2008;3(2):185–94.
15. Bhatt DC. Ultrasound biomicroscopy: an overview. J Clin Ophthalmol Res. 2014;2(2):115.
16. Huang EC, Barocas VH. Active iris mechanics and pupillary block: steady-state analysis and comparison with anatomical risk factors. Ann Biomed Eng. 2004;32(9):1276–85.
17. Liu L, Ong EL, Crowston J. The concave iris in pigment dispersion syndrome. Ophthalmology. 2011;118(1):66–70.
18. Reinstein DZ, Gobbe M, Archer TJ, Silverman RH, Coleman DJ. Epithelial thickness in the normal cornea: three-dimensional display with Artemis very high-frequency digital ultrasound. J Refract Surg. 2008;24(6):571–81.
19. Yan H, Yan Li. Atlas of ocular trauma. Springer; 2019.

20. Osman EA. The benefit of ultrasound biomicroscopy (UBM) in management of total Descemet's membrane detachment after deep sclerectomy surgery. Int Ophthalmol. 2011;31(4):345.
21. Zhou S-y, Wang C-x, Cai X-y, Huang D, Liu Y-z. Optical coherence tomography and ultrasound biomicroscopy imaging of opaque corneas. Cornea. 2013;32(4):e25.
22. Guerriero S, La Tegola MG, Monno R, Apruzzese M, Cantatore A. A case of descemet's membrane rupture in a patient affected by Acanthamoeba Keratitis. Eye Contact Lens. 2009;35(6):338–40.
23. Bahadir AE, Bozkurt TK, Kutan SA, Yanyali CA, Acar S. Candida interface keratitis following deep anterior lamellar keratoplasty. Int Ophthalmol. 2012;32(4):383–6.
24. Pavlin CJ, Harasiewicz K, Sherar MD, Foster FS. Clinical use of ultrasound biomicroscopy. Ophthalmology. 1991;98(3):287–95.
25. Dada T, Aggarwal A, Vanathi M, Gadia R, Panda A, Gupta V, et al. Ultrasound biomicroscopy in opaque grafts with post-penetrating keratoplasty glaucoma. Cornea. 2008;27(4):402–5.
26. Algaeed AH, Kozak I. Clinical atlas of ophthalmic ultrasound. Springer; 2019.
27. Sohar N, Skribek A, Fulop Z, Kolozsvari L. The success of treating keratoconus: visual acuity and follow-up with ultrasound biomicroscopy. Spektrum der Augenheilkunde. 2012;26(3):159–64.
28. Sharma N, Mannan R, Jhanji V, Agarwal T, Pruthi A, Titiyal JS, et al. Ultrasound biomicroscopy-guided assessment of acute corneal hydrops. Ophthalmology. 2011;118(11):2166–71.
29. Nakagawa T, Maeda N, Okazaki N, Hori Y, Nishida K, Tano Y. Ultrasound biomicroscopic examination of acute hydrops in patients with keratoconus. Am J Ophthalmol. 2006;141(6):1134–6.
30. Reinstein DZ, Archer T. Combined Artemis very high-frequency digital ultrasound-assisted transepithelial phototherapeutic keratectomy and wavefront-guided treatment following multiple corneal refractive procedures. J Cataract Refract Surg. 2006;32(11):1870–6.
31. Reinstein DZ, Rothman RC, Couch DG, Archer TJ. Artemis very high-frequency digital ultrasound-guided repositioning of a free cap after laser in situ keratomileusis. J Cataract Refract Surg. 2006;32(11):1877–83.
32. Reinstein DZ, Srivannaboon S, Gobbe M, Archer TJ, Silverman RH, Sutton H, et al. Epithelial thickness profile changes induced by myopic LASIK as measured by Artemis very high-frequency digital ultrasound. J Refract Surg. 2009;25(5):444–50.
33. Alió JL, Azar DT, Abbouda A, El Aswad A. Difficult and complicated cases in refractive surgery. Springer; 2015.
34. Ahn ES. Ophthalmic Ultrasonography, Singh AD, Hayden BC (eds). BMJ Publishing Group Ltd; 2012.
35. Avitabile T, Marano F, Castiglione F, Reibaldi A. Keratoconus staging with ultrasound biomicroscopy. Ophthalmologica. 1998;212(Suppl. 1):10–2
36. Skribek A, Sohár N, Gyetvai T, Nógrádi A, Kolozsvári L. Role of ultrasound biomicroscopy in diagnosis and treatment of Terrien disease. Cornea. 2008;27(4):427–33.
37. Berrocal AM, Chen PC, Soukiasian SH. Ultrasound biomicroscopy of corneal hydrops in Terrien's marginal degeneration. Ophthalm Surg Las Imag Retina. 2002;33(3):228–30
38. Silas MR, Hilkert SM, Reidy JJ, Farooq AV. Posterior keratoconus. Br J Ophthalmol. 2018;102(7):863–7.
39. Zhang Y, Zhou J, Zhu D. Ultrasonographic characteristics of congenital corneal staphyloma. J Med Ultrason 2016;43(2):291–3
40. Reinstein DZ, Silverman RH, Coleman DJ. High-frequency ultrasound measurement of the thickness of the corneal epithelium. J Refract Surg. 1993;9(5):385–7.
41. Reinstein DZ, Archer TJ, Gobbe M. Change in epithelial thickness profile 24 hours and longitudinally for 1 year after myopic LASIK: three-dimensional display with Artemis very high-frequency digital ultrasound. J Refract Surg. 2012;28(3):195–201.

42. Reinstein DZ, Archer TJ, Gobbe M, Silverman RH, Coleman DJ. Epithelial thickness after hyperopic LASIK: three-dimensional display with Artemis very high-frequency digital ultrasound. J Refract Surg. 2010;26(8):555–64.
43. Reinstein DZ, Archer TJ, Gobbe M. Epithelial thickness up to 26 years after radial keratotomy: three-dimensional display with Artemis very high-frequency digital ultrasound. J Refract Surg. 2011;27(8):618–24.
44. Reinstein DZ, Srivannaboon S, Holland SP. Epithelial and stromal changes induced by intacs examined by three-dimensional very high-frequency digital ultrasound. J Refract Surg. 2001;17(3):310–8.
45. Kanellopoulos AJ, Aslanides IM, Asimellis G. Correlation between epithelial thickness in normal corneas, untreated ectatic corneas, and ectatic corneas previously treated with CXL; is overall epithelial thickness a very early ectasia prognostic factor? Clin Ophthalmol (Auckland, NZ). 2012;6:789.
46. Reinstein DZ, Gobbe M, Archer TJ, Couch D. Epithelial thickness profile as a method to evaluate the effectiveness of collagen cross-linking treatment after corneal ectasia. J Refract Surg. 2011;27(5):356–63.
47. Reinstein DZ, Archer TJ, Gobbe M, Silverman RH, Coleman DJ. Stromal thickness in the normal cornea: three-dimensional display with Artemis very high-frequency digital ultrasound. J Refract Surg. 2009;25(9):776–86.
48. Reinstein DZ, Archer TJ, Gobbe M. Rate of change of curvature of the corneal stromal surface drives epithelial compensatory changes and remodeling. J Refract Surg. 2014;30(12):800–5.
49. Silverman RH, Patel MS, Gal O, Sarup A, Deobhakta A, Dababneh H, et al. Effect of corneal hydration on ultrasound velocity and backscatter. Ultrasound Med Biol. 2009;35(5):839–46.
50. Chakrabarti HS, Craig JP, Brahma A, Malik TY, McGhee CN. Comparison of corneal thickness measurements using ultrasound and Orbscan slit-scanning topography in normal and post-LASIK eyes. J Cataract Refract Surg. 2001;27(11):1823–8.
51. Roberts C. The cornea is not a piece of plastic. J Refract Surg. 2000;16(4):407–13.
52. Reinstein DZ, Couch DG, Archer T. Direct residual stromal thickness measurement for assessing suitability for LASIK enhancement by Artemis 3D very high-frequency digital ultrasound arc scanning. J Cataract Refract Surg. 2006;32(11):1884–8.

Confocal Scan

Mohammad Soleimani

Introduction

In Vivo Confocal Microscopy (IVCM) is one of the most useful imaging techniques uniquely for studying intact living cornea. The principles of this rapid and minimally invasive modality were described for the first time by Hans Goldmann in 1940s and patented by Marvin Minsky in 1950s [1–4]. Unlike other anterior segment imaging techniques, such as Ultrasound Biomicroscopy (UBM) and anterior segment optical coherence tomography (ASOCT), IVCM provides high-resolution en face images of all the corneal layers in both healthy and pathological states, parallel to the epithelial surface [4, 5]. Highly-contrast images, imaging of the living cornea at the cellular level and the ability to evaluation structures through corneal opacities are the advantages of IVCM over the slit lamp examination which enable clinicians and scientists gain information for their clinical and research purposes [6–8]. In addition to qualitative uses, like diagnosis of Acanthamoeba keratitis by an expert observer, nowadays several software applications are designed for quantifying IVCM images and a variety of image parameters for quantitative analysis are available [9] (Fig. 1).

The most important applications of ICVM include:

- Studying of normal cornea [10]
- Early detection and diagnosis of infectious pathogens [5, 11, 12]
- Monitoring the cellular events of wound healing following incisional surgery, endothelial keratoplasty, corneal crosslinking procedures, and refractive surgery procedures [13–18]
- Evaluation of changes in the corneal nerve plexus due to injury or disease
- Understanding of the ocular surface alteration in conditions such as dry eye disease, contact lens wearing and glaucomatous patients [19].

M. Soleimani (✉)
Farabi Eye Hospital, Tehran University of Medical Sciences, Tehran 1336616351, Iran
e-mail: soleimani_md@yahoo.com

M. Mohammadpour (ed.), *Diagnostics in Ocular Imaging*,
https://doi.org/10.1007/978-3-030-54863-6_10

Fig. 1 Confocal microscope

It is notable although confocal microscopy is designed for ocular surface structures, it is well useful for evaluation other surfaces of human body such as skin and oral mucosal membrane. So this technology is applicable not only in ophthalmology, but also in other medical fields like dermatology and otorhinolaryngology for diagnosis of different lesions, detection and staging of cancers and management of patients [20].

Principles

The basic principle of IVCM is optical sectioning of a thick, light-scattering object, such as the cornea that allows providing images from different depths [4, 21]. Light beam pass through a pinhole aperture and focused by a condenser lens onto a small area of the examined specimen. Then the reflected lightbeam from the specimen pass through a second objective lens and focuses on a second pinhole aperture and electronic detectors capture produced signals of reflected light beam. The term "confocal" is used because of the conjugation of the illumination and detection paths with the same point [21]. Unlike other conventional light microscopes, this property eliminates the reflected light outside the focal point and improves image resolution and contrast [5] (Fig. 2).

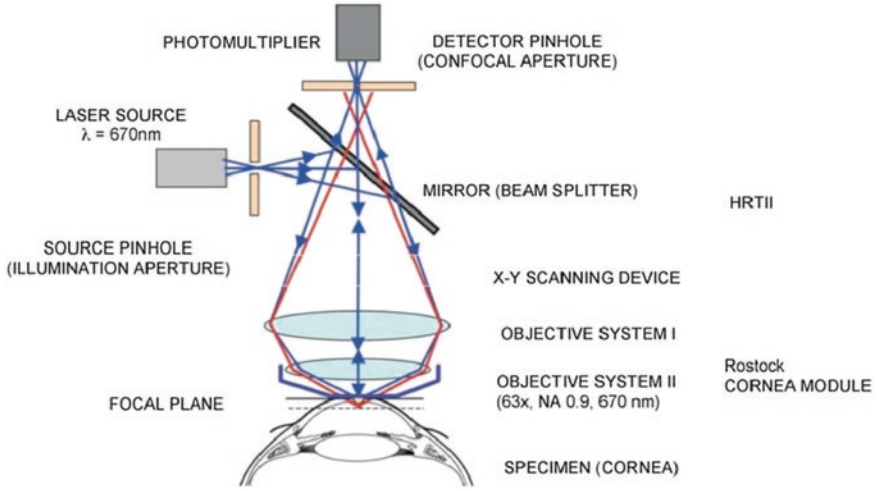

Fig. 2 Schematic principle of In Vivo Confocal Microscopy of cornea. light passes through the first pinhole and focuses on the focal plane in the cornea by the condenser lens. Reflected light passes through the objective lens and a conjugate exit pinhole and is detectable by the observer or camera. Scattered light outside the focal point (broken lines) is greatly limited by the pinholes and does not reach the observation system

There are three classes of IVCM according to type and intensity of illumination, magnification, image contrast and image resolution;

1. The Tandem Scanning Confocal Microscope (TSCM) uses a spinning Nipkow disc with multiple conjugate sets of pinhole, but this instrument is no longer produced. The axial resolution in this system is 9 mm [22–24].
2. The Slit Scanning Confocal Microscope (SSCM) uses two conjugate slits, so reduces scanning time. However images captured by this system are sharper, brighter and present greater detail, but it has lower axial resolution (24 mm) than the TSCM, and the subbasal nerve plexus is not as clearly identified [25, 26].
3. The Laser Scanning Confocal Microscope (LSCM), which uses a coherent high-intensity light source and laser beam scanning with a set of galvanometer scanning mirrors. This technique produces 400 times magnification and better contrast and axial resolution (7.6 mm) than other in vivo confocal systems [24, 27, 28].

Normal Cornea in IVCM

As mentioned before, IVCM is a useful tool for studying normal cornea. The epithelium,corneal nerves, Bowman's membrane, all stromal layers, and the endothelium are visible in IVCM with specific characteristics as discussed below [28] (Fig. 3).

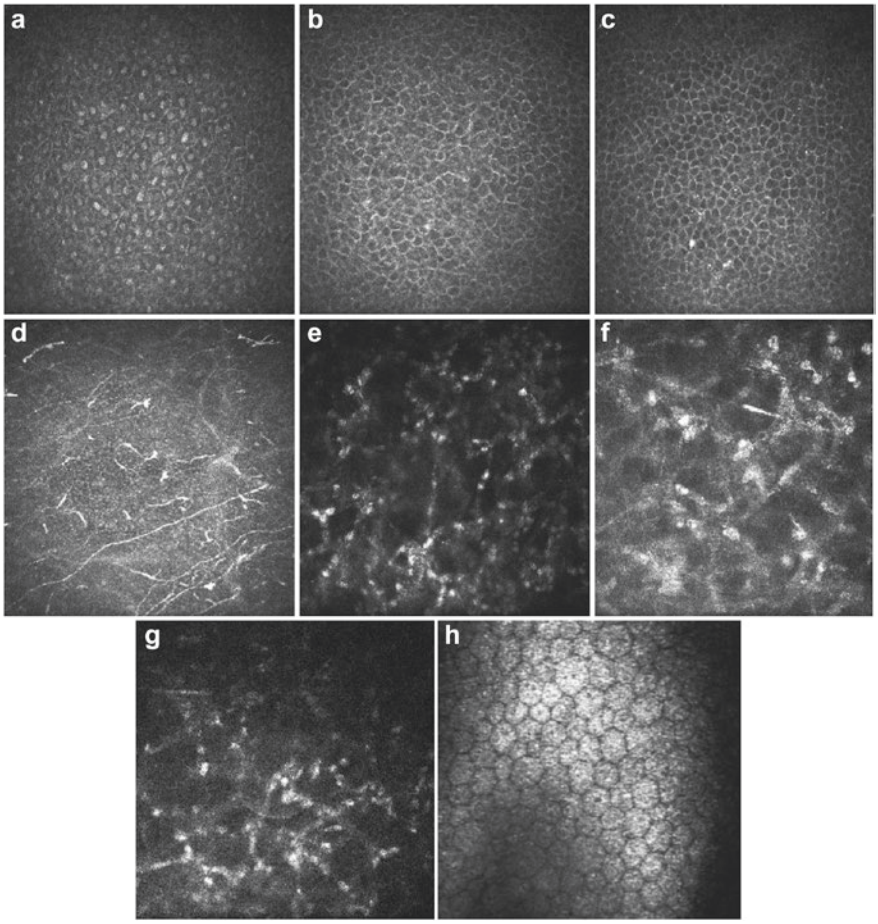

Fig. 3 IVCM images with LSCM technique of the normal cornea. **a** Superficial epithelial cells. **b** Intermediate epithelial (wing) cells. **c** Basal epithelial cells. **d** Bowman's layer with subbasal nerves. **e** Anterior stroma with hyper-reflective keratocyte nuclei. **f** Posterior stroma. **g** Endothelium. **h** Oblique section showing the epithelium, Bowman's layer, and anterior stroma

Normal epithelium typically consists of five to seven layers of cells, including superficial epithelial cells, intermediate or wing cells, and basal epithelial cells. Superficial epithelial cells are arranged in a polygonal cell pattern with shiny cytoplasm and reflecting nucleus surrounded by perinuclear dark halo. These cells could be large up to 50 mm in diameter [29]. Wing cells have regular mosaic shape with reflecting cellular borders. The wing cells are smaller in size (about 20 mm but regular in form. They can also be subdivided into upper and lower wing cells; the latter are smaller [30]. Basal epithelial cells have a smaller diameter (8–10 mm), cylindrical appearance and indistinctive nuclei in absence of reflecting border [31]. Notable point is that basal epithelial cells are the most

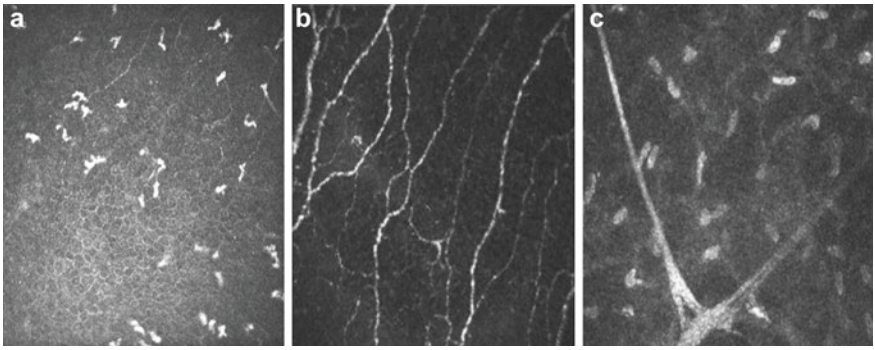

Fig. 4 Laser scanning confocal microscope images of **a** Sub-basal nerve plexus. **b** Subepithelial nerve (arrows). **c** stromal nerve (arrow)

easily visible cells of the epithelial layers as the result of their location immediately anterior to Bowman layer [31–34].

The cornea is the most densely innervated tissue in the human body with a density of nerve endings 200–300 times greater than the skin. The most important roles of corneal nerves include regulation of corneal sensation and tear secretion in addition to promotion of wound healing and epithelial integrity. Corneal nerves consist of sub-basal corneal nerves, subepithelial nerve plexus and stromal nerves. IVCM allows studying morphology, density and disease-induced or surgically induced alterations of corneal nerves. The sub-basal corneal nerve plexus is located between the Bowman layer and the basal epithelium and characterized by hyper-reflective fibers of 4–8 mm length with homogeneous reflectivity. Also anastomoses and organized connecting fibers make Y-shaped and H-shaped patterns [35, 36]. The subepithelial nerve plexus placed between the Bowman layer and the anterior stroma. The properties of this plexus include patchy distribution, limitation to the mid periphery of cornea and possibly absent in the central cornea, and low contrast nerves with irregular edges [37]. Stromal nerves appear as thick, reflective linear structures which run along a straight pathway, although it is sometimes possible to find dichotomous branches (T and Y shapes).They are present only in the anterior and mid stroma but not in the posterior stroma [37, 38] (Fig. 4).

The Bowman's layer which lies at between the basal cells and the stroma, is a 8–10 mm thick area organized by randomly arranged collagen fibrils. Corneal stroma forms above 80%of the whole corneal thickness. It consists of egg-shaped hyper-reflective structures as keratocyte nuclei with a dark background of the connective lamellae in between [39]. Also interconnected cell processes of the keratocytes appear under certain pathologic events such as corneal edema [40]. Keratocyte density is higher in the anterior stroma just under Bowman's layer in comparison to the middle and deeper stroma, which show a progressive decreasing trend in cell density [19]. The endothelium is a single layer tissue consist of honeycomb regular mosaic of hexagonal cells with similar size and shape [10].

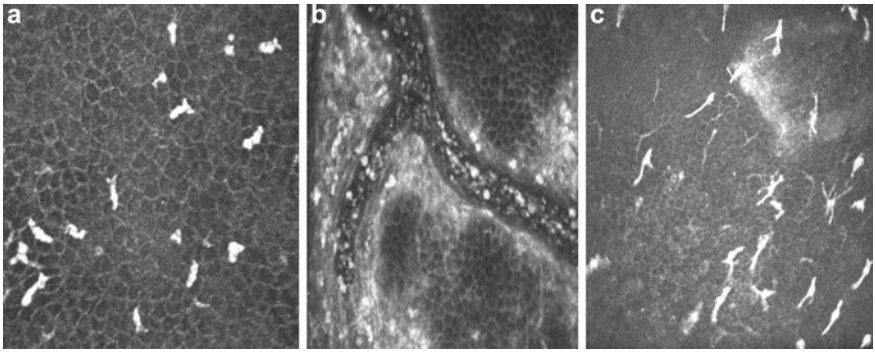

Fig. 5 confocal images of cell types. **a** Leucocytes are hyper-reflective cells, located at the level of the basal cells and sub-basal nerve plexus. **b** Red Blood Cells in the vascularized cornea which are hyper- reflective structures. **c** Dendritic cells with typical spider-like structure at the level of basal cells or the sub basal nerve plexus.

Moreover, different cell types could be differentiated according to their morphologies; Leucocytes appear as hyper-reflective oval-round cell bodies, lied at the level of the wing or basal cells or sub basal nerve plexus [41]. Erythrocytes are 7 mm in diameter rbiconcave discs with central hyper-reflective reflex as a typical finding [30]. Dendritic cells or Langerhans cells are typically spider-like structures at the level of basal cells or the sub basal nerve plexus of the corneal epithelium [8, 42–44] (Fig. 5).

Keratitis

Microbial keratitis is an emerging condition that can lead to irreversible and severe complications like blindness. Different pathogens, including bacteria, viruses, fungi, and parasites may play a role. Contact lens wearing is the major risk factor of microbial keratitis. Early diagnosis and initiation of appropriate therapy targeted at causative agent is associated with better outcomes. Although microbiologic studies are still gold standard for detection of organisms, but many factors such as high false-negative rate, inadequate sampling, delay in culture, and previous treatments with antibiotics limit their uses [45, 46].

Diagnosis of corneal ulcer is one of the most important uses of IVCM as a rapid and repeatable technique with acceptable sensitivity and specificity rate. Although IVCM is a helpful imaging technique in the diagnosis and management of Acanthamoeba and filamentous fungal keratitis, the current resolution of this modality limits its use in cases of bacterial and viral keratitis, diagnosis of small infective organisms (<10 μm) and morphological analysis except in pathogens with characteristics morphology that differentiate them from other structures.

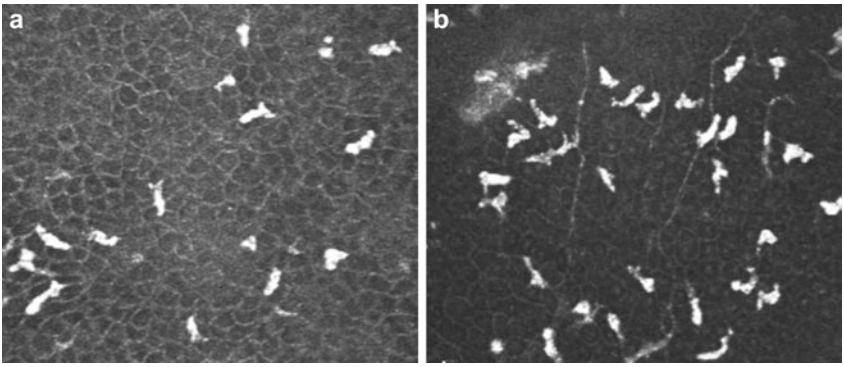

Fig. 6 Confocal scanning of bacterial ulcer shows hyper-reflective cell bodies, most probably leukocyte infiltration in the epithelial layers. (Reproduced with permission from R.F. Guthoff • C.Baudouin • J.Stave. Atlas of Confocal Laser Scanning In-vivo Microscopy in Opthalmology – Principles and Applications in Diagnostic and Therapeutic Ophtalmology. Springer. 2006)

Despite these disadvantages, IVCM is a useful tool in the follow-up of infectious keratitis patients for evaluation the healing process and response to treatment [5].

Bacterial Keratitis

Bacteria are common cause of infectious keratitis in temperate climates [46, 47]. Accurate and rapid diagnosis and antibiotic selection is so necessary in these cases [5]. Although smear and culture of cornea is still the basic diagnostic tool in infectious keratitis, but sometimes IVCM findings can guide physicians (Fig. 6). Results of some previous studies are mentioned below.

Bacillus cereus: These large bacteria (approximately 10 μm in diameter) appear as small, round, hyper-reflective bodies within the anterior stroma [48].

Borrelia burgdorferi: This tick-borne spirochete and causative agent of Lyme borreliosis appears as 36 μm long hyper-reflective structure in the epithelium. Interestingly these structures consist of eight consecutive reflective dots in a straight row pattern that may show irregular coiling pattern of a spirochete [49].

Streptococcus viridians: IVCM shows 1.5- to 2-μm-diameter spherical hyper-reflective bodies under the epithelium that resemble to intracellular structure fragments which make difficult differentiation between them. It is noticeable Staphylococcus werneri has equal morphology in IVCM too [50].

Nocardia: This microorganism is a thin (<1.5 μm in diameter) and branching filamentous bacteria that reveals as multiple thin (<1 μm) and short beaded filamentous structures surrounded by inflammatory cells [51].

Viral Keratitis

Prevalence of viral keratitis like HSV keratitis is high even in developed countries and sometimes nonspecific clinical findings make the diagnosis challenging and the requirement of diagnostic procedures necessary. As with bacterial keratitis, effectiveness of IVCM in evaluation structural corneal changes and monitoring patient follow-up during viral keratitis are more than diagnosis.

Herpes Simplex Virus: Dense fibrosis in the anterior stroma, highly reflective dendritic structures in the basal epithelial cells near to areas of stromal fibrosis, nerve plexus alterations in the scarred areas and enlargement of epithelial cells are visible in HSV keratitis [52, 53].

Adenovirus: IVCM in these patients shows clusters of hyper-reflective cells in the basal epithelial layer with multiple dendritic cells in the Bowman's layer beneath these areas. Clusters of highly reflective irregularly shaped cells, probably activated keratocytes are also detectable in anterior stroma. During the course of the disease, the density of dendritic cell clusters decline, and the hyper-reflectivity begin fade in anterior stroma but not in the mid-stroma. Cluster formation and delayed hyper-reflectivity in the mid-stroma are characteristic findings in Adenovirus infection that differentiate it from HSV keratitis withthe linear foci [54].

Fungal Keratitis

Fungal keratitis is a sight threatening condition usually occurs in hot and humid climates [55–58]. Prevalence of fungal keratitis especially Fusarium keratitis is increasing in industrialized countries, where it is becoming a public health problem. Risk factors of fungal keratitis include contact lens wearing, long-term steroid and antibiotic use, trauma with vegetative material, and chronic ocular surface disease [59]. Filamentous fungi are the major cause of fungal keratitis with Fusarium and Aspergillus species, but yeast, and, in particular, Candida, are not uncommon cause of keratitis. Unfortunately the diagnosis is frequently missed because of nonspecific clinical manifestations, so noninvasive and rapid imaging techniques, such as IVCM, are beneficial for diagnostic goals, follow-up and treatment monitoring [5]. This is a remarkable point although smears and cultures are the gold standard tests, IVCM has a sensitivity about 90% and a specificity about 80% for the diagnosis of fungal keratitis [60]. However IVCM cannot differentiate between fungus types but some data can be helpful before fungal cultures become positive [5].

Filamentous Fungi: Aspergillus is a filamentous fungus that consists of septate hyphae with dichotomous branches that are oriented at a 45° angle and are 5–10 μm in diameter. Interlocking white lines approximately 6 μm wide and 200–400 μm long in the superficial stroma, and with branching at a 45° angle are characteristic features of Aspergillus keratitis [61–63] (Fig. 7). It is noticeable

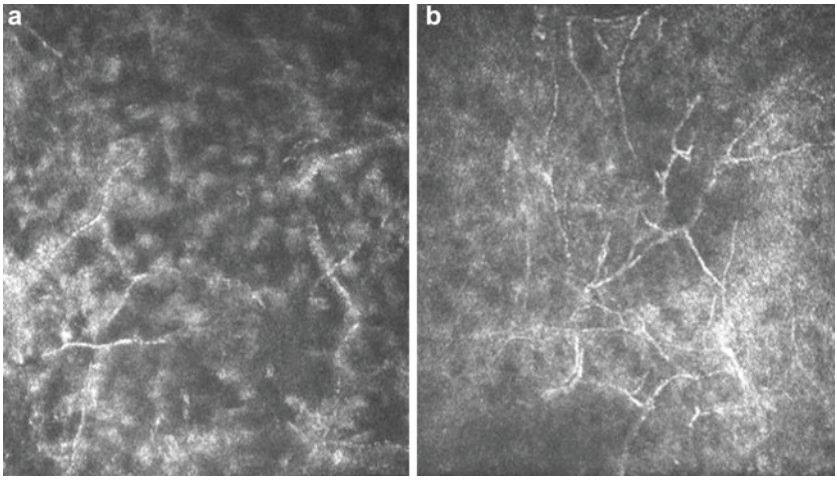

Fig. 7 LSCM of Images of *Aspergillus fumigatus* keratitis

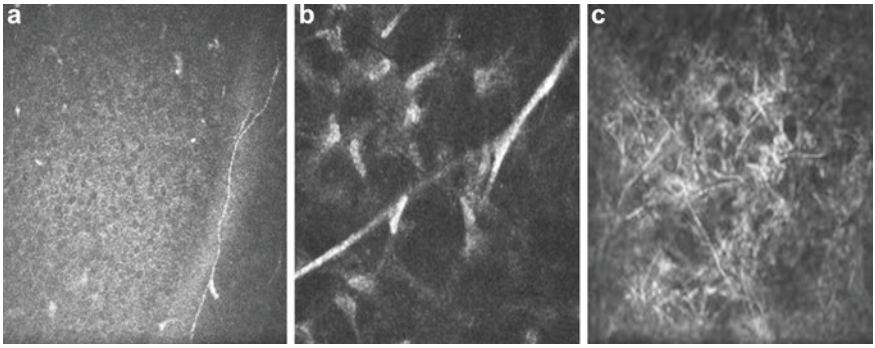

Fig. 8 LSCM of linear hyper-reflective structures within the cornea. **a** Corneal nerve plexus within the Bowman's layer. **b** Corneal nerve within the anterior stroma. **c** Filamentous fungi within the anterior stroma in a case of Fusarium keratitis

degree of branch orientation is not a definitive finding for differentiation between Aspergillus and Fusarium which branches at a 90° angle. Aspergillus hyphae are distinct from stromal nerves which have less branches, larger diameter [25–50 μm) and deeper location in stroma [61] (Fig. 8).

Like Asergillus, Fusarium is also a septate filamentous fungus but its hyphae branches at a 90° angle [61]. Fusarium is visible in IVCM as hyper-reflective lines 200–300 μm long and 3–5 μm wide with branches at a 90° angle in the anterior stroma[63] (Fig. 9).

Yeast: Candida albicans is example of a yeast which consisted of round, budding structures that may form pseudohyphae. In an infected cornea by this pathogen IVCM reveals multiple, high-contrast elongated particles 10–40 μm long and 5–10 μm wide in the anterior stroma [63].

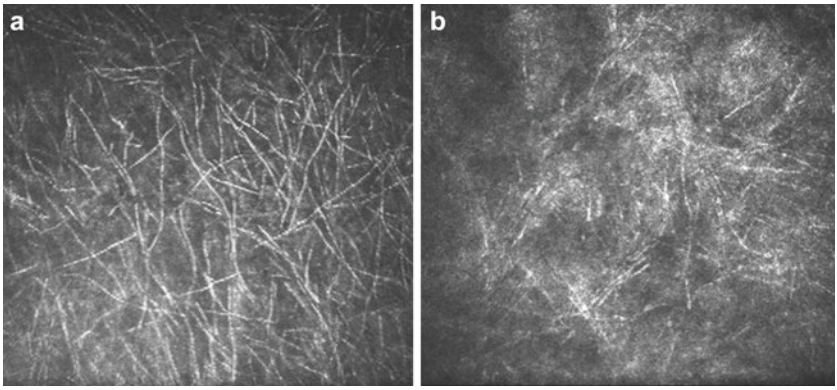

Fig. 9 Confocal scanning of Fusarium keratitis. A. Interlocking and branching hyphae. B. Decrease in hyphae density during appropriate treatment

Microsporidium: The IVCM appearance of this obligate intracellular microorganism is still controversial because the size of Microsporidia (1 and 2 μm) is close to the current resolution of IVCM [64, 65].

Depth of invasion is an important prognostic factor in fungal keratitis; involvement of anterior chamber is associated with a very poor prognosis. IVCM is the currently the only method that allows determination of the depth of infection. IVCM could aid the clinician in deciding the timing for surgical intervention when the disease is progressing despite medical treatment [66].

Acanthamoeba Keratitis

Acanthamoeba is a ubiquitous protozoan found in water, air, and soil, with a 2-stage life cycle including: active trophozoites and non-active cysts. The infection rate is 1.2 per million adults and between 0.2 and 1 per 10,000 contact lens wearers per year in the United Kingdom, Hong Kong, Europe, and the USA [5]. Acanthamoeba keratitis is a severe, potentially blinding eye disease usually occurs in contact lens users especially who had exposure to water. Misdiagnosis of patients as a bacterial corneal ulcer is common because initial clinical signs are often nonspecific. This latency in diagnosis leads to advanced stages of disease associated with a fairly guarded prognosis. So diagnostic tools are frequently needed [67–69]. Conventional laboratory microbiological procedures such as corneal smears, culture, and PCR have variable degrees of sensitivity. Also cultures take about 2 weeks to become positive and PCR is not available in all of the centers [70, 71]. IVCM is another diagnostic tool not only for more rapid identification of both Acanthamoeba cysts and trophozoites, but also for monitoring the treatment. According to some studies IVCM has above 90% sensitivity and 80% specificity in comparison to corneal smears for diagnosing Acanthamoeba keratitis [60, 72].

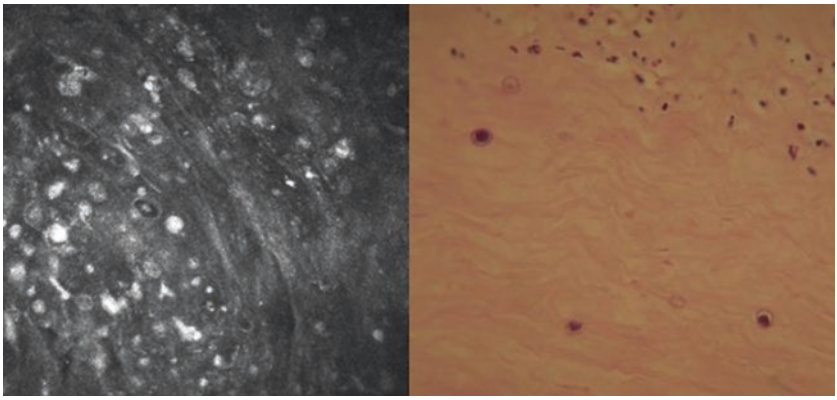

Fig. 10 A. Confocal scanning of Acanthamoeba keratitis which shows characteristic target pattern of Acanthamoeba cysts and multiform hyper-reflective structures as trophozoites. B. Representative feature in pathological section

Cysts: The cysts are inactive form of Acanthamoeba, measuring 15–28 μm with a double wall corresponding to an outer ecocyst and an inner endocyst [70]. Acanthamoeba cysts are visible with IVCM in the epithelium and the stroma as spherical, occasionally ovoid, or pear- or egg-shaped hyper-reflective structures, sometimes with a double-wall appearance depending on the plane of the images and their obliqueness [48, 73–81]. The differentiation between cysts from leukocyte or epithelial nuclei, or even cellular debris may be difficult in clinical practice when the characteristic double-walled feature is not visible. Despite the size, the higher reflectivity and contrast of cysts may help in this situation. Clustering and rows of cysts are typically suggestive of active proliferative disease [73, 75] (Fig. 10).

Trophozoites: Trophozoites are the active form of Acanthamoeba, measuring 25–40 μm in diameter [70]. They observe with IVCMashyper-reflective structures with variable size, from 15 to more than 100 μm, and shape. Pseudopodia extensions is a differentiating feature of trophozoites from other corneal cell [82].

Also radial keratoneuritis appears in IVCM with irregularly thickened nerves [60, 73, 76, 78, 83]. Not only diagnosis, but also treatment of Acanthamoeba keratitis is challenging. Throughout the prolonged course of pharmaco-therapy with toxic drugs, distinction between toxicity from persistent infection gets difficult. In these cases, IVCM is very helpful and can exhibit the presence or absence of Acanthamoeba.

Limitations

IVCM is a contact diagnostic procedure so in the case of infectious keratitis may cause ocular irritation and pain resulting undesirable eye movements that may blur the images. Thus a high degree of cooperation is necessary to capture high-quality

images. Also IVCM is an operator dependent procedure because of the small field of view that makes right selection of involved area critical. At last interpretation requires an experienced and well-trained observer [5].

IVCM in Surgical Procedures of Cornea

IVCM is a helpful tool for evaluation alteration in cornea such as innervations and cellularity after transplantation or keratorefractive surgeries.

Corneal Transplantation

Lamellar keratoplasty has become popular over the last years for the treatment of localized corneal disease [84]. Currently, the most common lamellar keratoplasty procedure is endothelial keratoplasty (EK), specifically, Descemet's stripping endothelial keratoplasty (DSEK), in which Descemet's membrane and endothelium of donor is transplanted to the host cornea. IVCM has provide information on the residual changes in the host cornea after EK. After DSEK for Fuchs' dystrophy, corneal backscatter (scattered light toward observer from the cornea which is associated with decreased postoperative visual acuity) from the surgical interface is significant in the early period, but declines progressively over the first 2 years after surgery. Contrary to popular belief, backscatter from this region has not been associated with changes in visual acuity or disability glare after EK, but backscattering from the subepithelial and anterior stroma is more and associated with disability glare. It could be mention even preoperatively (in Fuchs' dystrophy) backscattering from subepithelial and anterior stroma is high due to subtle basal epithelial edema which declines over the first 6 months after DSEK, mainly because of resolution of edema, but thereafter persists and remains elevated in comparison to normal eyes through 2 years after surgery [85–89].

Corneal nerves are not damaged by EK procedures except those passing through the site of the incision, whereas all the corneal nerves are injured severely during penetrating keratoplasty (PK) [90, 91]. IVCM has showed pathologic findings of sub-basal and stromal nerves before and after EK for Fuchs' dystrophy. An abnormal subbasal nerve plexus is associated with decreased corneal sensitivity and stromal nerves are frequently tortuous [91, 92]. Also abnormality of subepithelial cells and keratocytes before and after DSEK for Fuchs' dystrophy has been shown by IVCM. Pathologic subepithelial cells are hyper-reflective cells, which possibly responsible for corneal backscatter and increased anterior surface aberrations. Keratocyte numbers of anterior cornea are reduced in Fuchs' dystrophy, and remain reduced through 3 years after DSEK which possibly results in impaired repair of the anterior after EK [88, 93]. Moreover, uniquely examination of endothelium after EK is available by IVCM even in opaque corneas; for

example microfolds of the posterior donor cornea after EK are visible in confocal microscopy,however these folds have not been contributed with postoperative visual acuity [94, 95].

Keratorefractive Surgery

Laser-assisted in situ keratomileusis (LASIK) and photorefractive keratectomy (PRK) are the most common refractive surgery procedures. Both involve tissue removal by excimer photoablation [96]. Long-term changes in corneal backscatter and cellularity in both procedures have been studied by IVCM.

IVCM shows transient increases in corneal backscatter in the early period after excimer keratorefractive Surgery, whereas it decreases over the time [97, 98]. However regeneration of corneal sub basal nerves after these surgical procedures take several years, but decreased corneal sensitivity remains for months [99, 100]. Although keratocyte density declines after LASIK and PRK but it does not affect on visual outcomes, backscatter or anterior surface aberrations [98, 101]. No long-term detrimental effects have been observed in the corneal endothelium by IVCM [102, 103].

IVCM Imaging of Nerves in Several Corneal and Systemic Diseases

IVCM allows imaging corneal nerves in different ocular surface diseases and conditions, including post-LASIK dysesthesia) and neurotrophic epitheliopathy [99, 104–109].

Post-LASIK Hypoesthesia or Dysesthesia

“Keratoneuralgia” is an uncommon condition of developing neurotrophic epitheliopathy or chronic pain Following LASIK [110–112]. IVCM can visualize loss of corneal innervation or the presence of abnormal nerve regeneration. Confocal microscopy of the cornea after LASIK reveals depletion in corneal nerve density in the early postoperative period that increases with time, however it will be very low for up to 6 months post-LASIK, and even 1 year after LASIK, the number of subbasal and stromal nerves in the corneal flap won’t be more than 50% of the preoperative density [99, 104, 105]. On the other hand not only nerve density but also nerve morphology is associated with corneal sensation, short nerves and loss of connections between nerve bundles may lead to corneal hyposensitivity. Despite abnormal feature of corneal nerves, it seems normal sensation returns to eyes by 6 months after LASIK [106, 108] (Fig. 11).

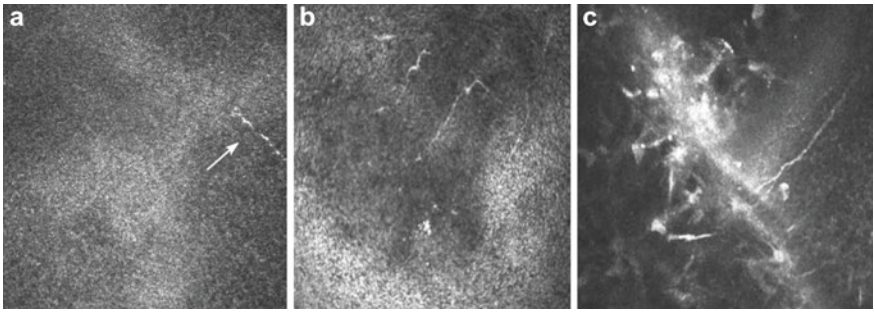

Fig. 11 Subbasal corneal re-innervation after laser-assisted in situ keratomileusis (LASIK). Regenerating nerve fibers in the central cornea, *a* two months, **b** six months and **c** eight months after LASIK

Neurotrophic Keratopathy

Neurotrophic Keratopathy may occur after several conditions such as herpes simplex keratitis (HSK) and herpes zoster ophthalmicus (HZO) [113–117]. In these cases confocal microscopy may demonstrate enlargement of superficial epithelial cells and depletion in density in both HSK and HZO [114, 118]. Area of scar in subbasal nerves and decrease in subbasal nerve fibers are the other findings [113, 114].

Keratoconus

IVCM has been increasingly help to better understanding of pathophysiology, corneal changes, severity, progression, and possibly the development of neurotrophic ulcers in the keratoconus patients. Epithelial cell and subbasal nerve density may decrease whereas tortuousity of nerves increase in addition toabnormal architecture of nerves in the region of the cone [119–123].

Corneal collagen cross-linking (CXL) is one of the available procedures to strengthen of the cornea and thus slow the progression of keratoconus by combining the use of riboflavin and ultraviolet light type A (UVA) [124]. Conventional methods of CXL include transepithelial approach (“epi-on”) and after epithelium-removal to increase penetration of riboflavin to stroma (“epi-off”). IVCM reveals immediately disappearance of sub basal and anterior stromal nerves after CXL in “epi-off” approach while in “epi-on” method corneal nerves and keratocytes damage less. In both approaches corneal sensation decreases but in “epi-on” approach recovery period is faster (1 month in “epi-on” approach in comparison to 3 months for “epi-off” approach) [124–127].

Diabetes

Diabetes is one of the biggest global concerns in healthcare systems because of its high prevalence and disabling complications. Microvascular involvement of diabetes may lead to multi organ damages such as nephropathy, retinopathy, and neuropathy (known clinical triad of diabetes) [128, 129]. Examination of corneal nerves in patients with diabetic neuropathy is one of the applications of IVCM. Confocal microscopy reveals significant reduction in sub basal nerve density and increase in nerve fiber tortuosity in patients with type 1 or type 2 diabetes. Interestingly, 50% of patients who had no clinical signs of diabetic neuropathy exhibit abnormal corneal sub basal nerve plexus changes, which may show corneal changes are prior to clinically peripheral nerve changes [129–131].

Rheumatologic Disorders

Several rheumatologic disorders such as Systemic lupus erythematosus (SLE), Rheumatoid arthritis (RA) and Sjögren's syndrome may affect the eyes. Keratoconjunctivitis sicca is one of the most common ocular manifestations in these situations and visualize in IVCM by significant raise in the Langerhans cell numbers within the central cornea [44, 132–134]. Other findings in Sjögren's disease include Meibomian gland and conjunctival goblet cell density decrease [135, 136].

IVCM in Dry Eye

Dry eye disease is a common disorder of ocular surface, which can be disabling through adverse effects on the quality of life patients and economic costs for health care providers [137–139]. This entity includes several clinical subtypes which discussion about them is out of border of this book. IVCM is applicable to examine the Meibomian glands including their acinar unit diameter and density, orifice diameter, periglandular inflammatory cells density and changes associated with Sjogren's syndrome, graft-versus-host disease, contact lens wear and aging [135, 140–145]. In addition confocal microscopy is a valuable imaging modality for evaluation both dry eye severity and monitoring the response to treatment [146, 147].

IVCM studies show dry eye-related changes occur in different layers of cornea including epithelium, sub basal nerve plexus and stroma; In the epithelium superficial epithelial cell numbers decrease and inflammatory dendritic cells increase, however alteration in number of basal cells or stromal keratocytes is controversial [148–155]. Interestingly the dramatic rise of dendritic cells in the corneal epithelium is thought to be associated with dry eye pathogenesis. In sub basal nerve

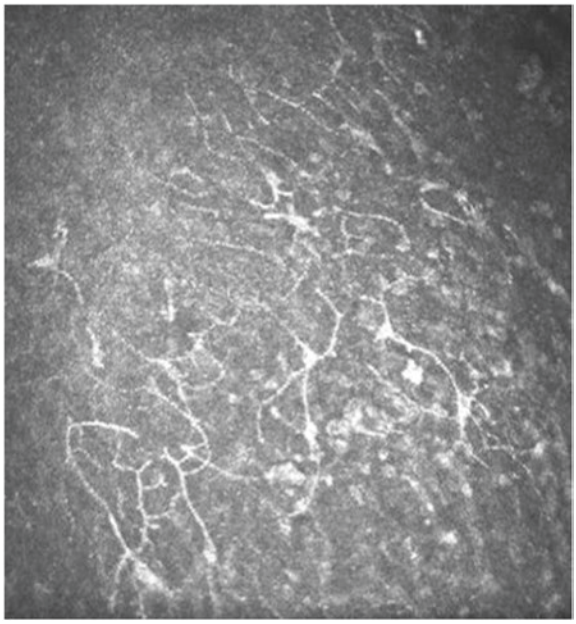

Fig. 12 Infiltration of elongated dendritic cells in dry eye disease

plexus tortuosity and beading of neural fibers increase but similar changes for density are not indicated in different studies [150, 155–157]. The changes in corneal endothelial cell density in dry eye are not yet clear [155]. IVCM of conjunctiva in dry eye patients may show depleted epithelial cell density of temporal bulbar conjunctiva and increased number of conjunctival epithelial microcysts, dendritic cells, and lymphocytes [158]. In follow-up of these patients decreasing in dendritic cells and keratocytes density and tortuosity of nerves with appropriate treatment may appear in IVCM [159, 160] (Fig. 12).

Also confocal microscopy is useful for evaluation of patients with Meibomian Gland Dysfunction and show dilation and obstruction of meibomian gland ducts, depletion in acinar unit density o the glands and great density of inflammatory cells [141, 143, 161].

IVCM in Ocular Allergy

Ocular allergy is a multifactorial disorder of the ocular surface with several presentations and severities. Ocular allergy may lead to inflammatory involvement of ocular surface structures, including corneal and conjunctival epithelia. IVCM is a helpful imaging modality to assess physiopathology, changes in ocular surface structures and management of patients [162]. This section will focuses on atopic

keratoconjunctivitis (AKC) and vernal keratoconjunctivitis (VKC) as severe, vision threatening and challenging subtypes of ocular allergy.

AKC

IVCM of AKC patients shows a significant decrease in basal epithelial cell density and the ratio of basal epithelial to superficial epithelial cell density in the central corneal [163]. Confocal microscopy reveals increased numbers of tarsal conjunctival inflammatory cells in AKC patients. Feature of corneal nerves may alter as decrease in length and branch density of sub-basal nerve plexusand increase in thickness and of bifurcation formation of stromal nerves [163]. IVCM can visualize changes of Meibomian glands such as severe Langerhans cell infiltration around the Meibomian glands in these patients [164].

VKC

Basal epithelial cell numbers of VKC patients are decreased, but other changes may occur too, including: enlargement, hyper-reflectivity and abnormal nucleocytoplasmic ratio of superficial epithelial cells. Limbal morphology of VKC patients may show atrophy in palisades of vogt, loss of bright basal cells, infiltration of Langerhans cells and vessel dilation [164]. Inflammatory findings of these patients include increased presence of activated keratocytes and stromal dendritic cells and also bulbar and tarsal conjunctival dendritic cells as spherical hyper- reflective inflammatory cells [164, 165]. Sub basal nerve plexus shows depleted nerve fiber density, bead-like formations, and increased nerve tortuosity. Also thickness, tortuosity and branching of stromal nerves increase [165]. Extensive fibrosis and depletion in Meibomian gland acinar units, and also periglandular inflammation occur of AKC patients [166].

IVCM in Contact Lens Wearing

IVCM has clearly provided new information about the ocular surface alteration in contact lens wearing and become a valuable tool for evaluation and management of these patients. Contact lenses may affect different parts of ocular surface as discussed below [19].

Silicone hydrogel lenses may lead to formation mucin balls in the tear layer of patients. IVCM visualizes them as 40–80 μm structures with central high reflectivity and peripheral translucency. Mucin balls may penetrate the full thickness

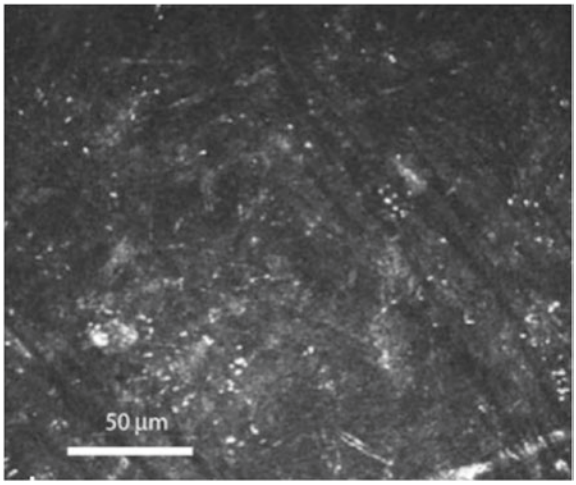

Fig. 13 Microdots in the corneal stroma of a rigid lens wearer

of the epithelium and activate the keratocytes of the underlying anterior stroma [167–169]. All forms of lenses especially rigid lenses may lead to enlargement of epithelial cells. The degree of epithelial disturbance in response to various concentrations of preservatives used in contact lens disinfecting solutions depends on the duration of lens wear. Also numbers of dendritic cells increase in the layer of the sub basal nerve plexus in both the central and peripheral cornea in association with various combinations of soft contact lenses and lens care solutions [170, 171]. Although corneal sensation decreases in prolonged use of contact lenses, but IVCM shows no changes in number, distribution or morphology of corneal nerves. These results suggest that functional disturbance but not structural may play role in corneal hypoesthesia of these patients.

Corneal edema due to contact lens wearing may formation dark lines and folds in IVCM. Typical stromal change is the presence of hyper-reflective panstromal microdot deposits presumed as granules of lipofuscin-like material (Fig. 13). This event has been associated with the duration of contact lens wear [8, 172, 173]. Also microdots appear in other disorders such as chloroquine-induced keratopathy, exfoliation syndrome and mucopolysaccharidoses [174–176].

Endothelial blebs are an acute response to lens wear which appear in IVCM bright centrally and dark annular surrounding. Chronic response of the endothelium to lens wear observes with IVCM as increased polymegethism and light scatter [177, 178]. Corneal limbus and conjunctiva are also affected by long-term use of soft contact lens. Microcystic formations in epithelial cells, microdot deposits in corneal stroma, increased Langerhans cell density and decreased of keratocyte density are features of corneal limbus due to contact lens wear [179]. In the bulbar conjunctiva epithelial thinning, accelerated formation and enlargement of microcysts, and increased epithelial cell density occur. In addition Meibomian glands changes include decreased basal epithelial cell numbers and acinar unit diameters, higher glandular orifice diameters, and greater secretion reflectivity [142, 180].

IVCM for Evaluation of the Ocular Surface in Glaucomatous Patients

IVCM is applicable to evaluate filtering blebs to better understand the conjunctival wound healing process and getting information about ocular surface changes due to topical anti glaucoma medications and their preservatives in glaucomatous patients [19].

Function of filtering bleb is a determining factor of the long-term success of glaucoma filtering surgery. In condition which the appearance of the bleb is not correlated to intraocular pressure control and the reason of failure is unclear IVCM could be useful. In functional blebs IVCM shows a normal conjunctival epithelium with several microcysts and a loose hypo-reflective sub-epithelial tissue with a high number of optically clear spaces. In contrast, in non-functional blebs number of microcysts is minimal, subepithelial tissue shows hyper-reflectivity, and dense connective tissue with numerous blood vessels exists [181–184].

On the other hand, long-term use of topical anti glaucoma drops and their preservatives is a challenging issue due to their significant effects on the ocular surface. Confocal microscopy shows reduced density of superficial epithelial cells and sub basal nerves, activation of stromal keratocytes, and an increase in sub basal nerve tortuosity in glaucomatous patients under treatment with benzalkonium chloride (BAK)-containing eye drops chronically [185, 186].

Acknowledgement I would like to express my special thanks to Dr. Kasra CHeraqpour for his effort in preparation of this chapter.

References

1. Minsky M. Memoir on inventing the confocal scanning microscope. Scanning. 1988;10(4):128–38.
2. Egger MD, Petran M. New reflected-light microscope for viewing unstained brain and ganglion cells. Science. 1967;157(3786):305–7.
3. Petroll WM, Jester JV, Cavanagh HD. In vivo confocal imaging. Int Rev Exp Pathol. 1996;36:93–129.
4. Petroll WM, Robertson DM. In vivo confocal microscopy of the cornea: new developments in image acquisition, reconstruction, and analysis using the HRT-Rostock corneal module. Ocular Surface. 2015;13(3):187–203.
5. Labbé A, Khammari C, Dupas B, Gabison E, Brasnu E, Labetoulle M, et al. Contribution of in vivo confocal microscopy to the diagnosis and management of infectious keratitis. Ocular Surface. 2009;7(1):41–52.
6. Jalbert I, Stapleton F, Papas E, Sweeney D, Coroneo M. In vivo confocal microscopy of the human cornea. Br J Ophthalmol. 2003;87(2):225–36.
7. Leduc C, Dupas B, Ott-Benoist A, Baudouin C. Advantages of the in vivo HRT2 corneal confocal microscope for investigation of the ocular surface epithelia. J Fr Ophtalmol. 2004;27(9 Pt 1):978–86.
8. Zhivov A, Stachs O, Kraak R, Stave J, Guthoff RF. In vivo confocal microscopy of the ocular surface. Ocular Surface. 2006;4(2):81–93.

9. Patel DV, McGhee CN. Quantitative analysis of in vivo confocal microscopy images: a review. Surv Ophthalmol. 2013;58(5):466–75.
10. Guthoff RF, Zhivov A, Stachs O. In vivo confocal microscopy, an inner vision of the cornea–a major review. Clin Exp Ophthalmol. 2009;37(1):100–17.
11. Efron N, Morgan PB, Makrynioti D. Chronic morbidity of corneal infiltrative events associated with contact lens wear. Cornea. 2007;26(7):793–9.
12. Vaddavalli PK, Garg P, Sharma S, Sangwan VS, Rao GN, Thomas R. Role of confocal microscopy in the diagnosis of fungal and Acanthamoeba keratitis. Ophthalmology. 2011;118(1):29–35.
13. Kobayashi A, Mawatari Y, Yokogawa H, Sugiyama K. In vivo laser confocal microscopy after Descemet stripping with automated endothelial keratoplasty. Am J Ophthalmol. 2008;145(6):977–85. e1.
14. Bouheraoua N, Jouve L, El Sanharawi M, Sandali O, Temstet C, Loriaut P, et al. Optical coherence tomography and confocal microscopy following three different protocols of corneal collagen-crosslinking in Keratoconus. Invest Ophthalmol Vis Sci. 2014;55(11):7601–9.
15. Petroll WM, Cavanagh HD, Jester JV. Clinical confocal microscopy. Curr Opin Ophthalmol. 1998;9(4):59–65.
16. Tervo T, Moilanen J. In vivo confocal microscopy for evaluation of wound healing following corneal refractive surgery. Prog Retinal Eye Res. 2003;22(3):339–58.
17. Kaufman SC, Kaufman HE. How has confocal microscopy helped us in refractive surgery? Curr Opin Ophthalmol. 2006;17(4):380–8.
18. Jester JV, Petroll WM, Cavanagh HD. Corneal stromal wound healing in refractive surgery: the role of Myofibroblasts. Prog Retinal Eye Res. 1999;18(3):311–56.
19. Villani E, Baudouin C, Efron N, Hamrah P, Kojima T, Patel SV, et al. In vivo confocal microscopy of the ocular surface: from bench to bedside. Curr Eye Res. 2014;39(3):213–31.
20. Ulrich M, Lange-Asschenfeldt S. In vivo confocal microscopy in dermatology: from research to clinical application. J Biomed Optics. 2013;18(6):061212.
21. Mazzotta C, Hafezi F, Kymionis G, Caragiuli S, Jacob S, Traversi C, et al. In vivo confocal microscopy after corneal collagen crosslinking. Ocular Surface. 2015;13(4):298–314.
22. Lemp MA, Dilly PN, Boyde A. Tandem-scanning (confocal) microscopy of the full-thickness cornea. Cornea. 1985;4(4):205–9.
23. Cavanagh HD, Jester JV, Essepian J, Shields W, Lemp MA. Confocal microscopy of the living eye. The CLAO J. 1990;16(1):65–73.
24. Petroll WM, Cavanagh HD, Jester J. Three-dimensional imaging of corneal cells using in vivo confocal microscopy. J Microsc. 1993;170(3):213–9.
25. Masters BR, Thaer AA. Real-time scanning slit confocal microscopy of the in vivo human cornea. Appl Opt. 1994;33(4):695–701.
26. Brakenhoff G, Visscher K. Confocal imaging with bilateral scanning and array detectors. J Microsc. 1992;165(1):139–46.
27. Erie EA, McLaren JW, Kittleson KM, Patel SV, Erie JC, Bourne WM. Corneal subbasal nerve density: a comparison of two confocal microscopes. Eye Contact Lens. 2008;34(6):322.
28. Zhivov A, Stachs O, Stave J, Guthoff RF. In vivo three-dimensional confocal laser scanning microscopy of corneal surface and epithelium. Br J Ophthalmol. 2009;93(5):667–72.
29. Wilson T. Confocal microscopy. Microanalysis of Solids: Springer; 1994. p. 219–32.
30. Guthoff RF, Baudouin C, Stave J. Atlas of confocal laser scanning in-vivo microscopy in ophthalmology: Springer Science & Business Media; 2007.
31. Eckard A, Stave J, Guthoff RF. In vivo investigations of the corneal epithelium with the confocal Rostock Laser Scanning Microscope (RLSM). Cornea. 2006;25(2):127–31.
32. del Castillo JMBt, Wasfy MA, Fernandez C, Garcia-Sanchez J. An in vivo confocal masked study on corneal epithelium and subbasal nerves in patients with dry eye. Investigative ophthalmology & visual science. 2004;45(9):3030–5.

33. Ceresara G, Fogagnolo P, De Cillà S, Panizzo V, Danelli PG, Orzalesi N, et al. Corneal involvement in Crohn's disease: an in vivo confocal microscopy study. Cornea. 2011;30(2):136–42.
34. Patel D, Ku J, Johnson R, McGhee C. Laser scanning in vivo confocal microscopy and quantitative Aesthesiometry reveal decreased corneal innervation and sensation in Keratoconus. Eye. 2009;23(3):586.
35. Matsuda H. Electron microscopic study of the corneal nerve with special reference to the nerve endings. Nippon Ganka Gakkai Zasshi. 1968;72(7):880–93.
36. Ueda S, del Cerro M, LoCascio JA, Aquavella JV. Peptidergic and catecholaminergic fibers in the human corneal epithelium: an immunohistochemical and electron microscopic study. Acta Ophthalmol. 1989;67(S192):80–90.
37. Auran JD, Koester CJ, Kleiman NJ, Rapaport R, Bomann JS, Wirotsko BM, et al. Scanning slit confocal microscopic observation of cell morphology and movement within the normal human anterior cornea. Ophthalmology. 1995;102(1):33–41.
38. Oliveira-Soto L, Efron N. Morphology of corneal nerves using confocal microscopy. Cornea. 2001;20(4):374–84.
39. Patel DV, McGhee CN. Contemporary in vivo confocal microscopy of the living human cornea using white light and laser scanning techniques: a major review. Clin Exp Ophthalmol. 2007;35(1):71–88.
40. Jester JV, Moller-Pedersen T, Huang J, Sax CM, Kays WT, Cavangh HD, et al. The cellular basis of corneal transparency: evidence for 'corneal crystallins.' J Cell Sci. 1999;112(5):613–22.
41. Zhivov A, Stachs O, Kraak R, Guthoff R. Cellular laser microscopy of corneal ulcer and infiltrate. Klin Monatsbl Augenheilkd. 2008;225(1):86–90.
42. Mastropasqua L, Nubile M, Lanzini M, Carpineto P, Ciancaglini M, Pannellini T, et al. Epithelial dendritic cell distribution in normal and inflamed human cornea: in vivo confocal microscopy study. American journal of ophthalmology. 2006;142(5):736–44. e2.
43. Zhivov A, Stave J, Vollmar B, Guthoff R. In vivo confocal microscopic evaluation of Langerhans cell density and distribution in the normal human corneal epithelium. Graefe's Arch Clin Exp Ophthalmol. 2005;243(10):1056–61.
44. Zhivov A, Stave J, Vollmar B, Guthoff R. In vivo confocal microscopic evaluation of langerhans cell density and distribution in the corneal epithelium of healthy volunteers and contact lens wearers. Cornea. 2007;26(1):47–54.
45. Thomas PA, Geraldine P. Infectious keratitis. Curr Opin Infect Dis. 2007;20(2):129–41.
46. Keay L, Edwards K, Naduvilath T, Taylor HR, Snibson GR, Forde K, et al. Microbial keratitis: predisposing factors and morbidity. Ophthalmology. 2006;113(1):109–16.
47. Pachigolla G, Blomquist P, Cavanagh H. A 5-year review of 132 cases of microbial keratitis at a major urban county hospital. Eye Contact Lens. 2007;33(4):207.
48. Chew S-J, Beuerman RW, Assouline M, Kaufman HE, Barron BA, Hill JM. Early diagnosis of infectious keratitis with in vivo real time confocal microscopy. The CLAO J. 1992;18(3):197–201.
49. Linna T, Mikkilä H, Karma A, Seppälä I, Petroll WM, Tervo T. In vivo confocal microscopy: a new possibility to confirm the diagnosis of Borrelia keratitis? Cornea. 1996;15(6):639.
50. Kaufman SC, Laird JA, Cooper R, Beuerman RW. Diagnosis of bacterial contact lens related keratitis with the white-light confocal microscope. The CLAO J. 1996;22(4):274–7.
51. Vaddavalli PK, Garg P, Sharma S, Thomas R, Rao GN. Confocal microscopy for Nocardia keratitis. Ophthalmology. 2006;113(9):1645–50.
52. Cavanagh HD, Petroll WM, Alizadeh H, He Y-G, McCulley JP, Jester JV. Clinical and diagnostic use of in vivo confocal microscopy in patients with corneal disease. Ophthalmology. 1993;100(10):1444–54.

53. Rosenberg ME, Tervo TM, Müller LJ, Moilanen JA, Vesaluoma MH. In vivo confocal microscopy after herpes keratitis. Cornea. 2002;21(3):265–9.
54. Dosso AA, Rungger-Brändle E. Clinical course of epidemic keratoconjunctivitis: evaluation by in vivo confocal microscopy. Cornea. 2008;27(3):263–8.
55. Asbell P, Stenson S. Ulcerative keratitis: survey of 30 years' laboratory experience. Arch Ophthalmol. 1982;100(1):77–80.
56. Leck A, Thomas P, Hagan M, Kaliamurthy J, Ackuaku E, John M, et al. Aetiology of suppurative corneal ulcers in Ghana and south India, and epidemiology of fungal keratitis. Br J Ophthalmol. 2002;86(11):1211–5.
57. Upadhyay MP, Karmacharya PC, Koirala S, Tuladhar NR, Bryan LE, Smolin G, et al. Epidemiologic characteristics, predisposing factors, and etiologic diagnosis of corneal ulceration in Nepal. Am J Ophthalmol. 1991;111(1):92–9.
58. Liesegang TJ, Forster RK. Spectrum of microbial keratitis in South Florida. Am J Ophthalmol. 1980;90(1):38–47.
59. Patel A, Hammersmith K. Contact lens-related microbial keratitis: recent outbreaks. Curr Opin Ophthalmol. 2008;19(4):302–6.
60. Kanavi MR, Javadi M, Yazdani S, Mirdehghanm S. Sensitivity and specificity of confocal scan in the diagnosis of infectious keratitis. Cornea. 2007;26(7):782–6.
61. Winchester K, Mathers WD, Sutphin JE. Diagnosis of Aspergillus keratitis in vivo with confocal microscopy. Cornea. 1997;16(1):27–31.
62. Avunduk A, Beuerman R, Varnell E, Kaufman H. Confocal microscopy of *Aspergillus fumigatus* keratitis. Br J Ophthalmol. 2003;87(4):409–10.
63. Brasnu E, Bourcier T, Dupas B, Degorge S, Rodallec T, Laroche L, et al. In vivo confocal microscopy in fungal keratitis. Br J Ophthalmol. 2007;91(5):588–91.
64. Sagoo MS, Mehta JS, Hau S, Irion LD, Curry A, Bonshek RE, et al. Microsporidium stromal keratitis: in vivo confocal findings. Cornea. 2007;26(7):870–3.
65. Shah GK, Pfister D, Probst LE, Ferrieri P, Holland E. Diagnosis of microsporidial keratitis by confocal microscopy and the chromatrope stain. Am J Ophthalmol. 1996;121(1):89–91.
66. Kumar RL, Cruzat A, Hamrah P, editors. Current state of in vivo confocal microscopy in management of microbial keratitis. Semin Ophthalmol. 2010, Taylor & Francis.
67. Foulks GN. Acanthamoeba keratitis and contact lens wear: static or increasing problem? Eye Contact Lens. 2007;33(6):412–4.
68. Mathers WD. Acanthamoeba: a difficult pathogen to evaluate and treat. LWW. 2004.
69. Claerhout I, Goegebuer A, Van Den Broecke C, Kestelyn P. Delay in diagnosis and outcome of Acanthamoeba keratitis. Graefe's Arch Clin Exp Ophthalmol. 2004;242(8):648–53.
70. Awwad ST, Petroll WM, McCulley JP, Cavanagh HD. Updates in Acanthamoeba keratitis. Eye Contact Lens. 2007;33(1):1–8.
71. Mathers WD, Nelson SE, Lane JL, Wilson ME, Allen RC, Folberg R. Confirmation of confocal microscopy diagnosis of Acanthamoeba keratitis using polymerase chain reaction analysis. Arch Ophthalmol. 2000;118(2):178–83.
72. Tu EY, Joslin CE, Sugar J, Booton GC, Shoff ME, Fuerst PA. The relative value of confocal microscopy and superficial corneal scrapings in the diagnosis of Acanthamoeba keratitis. Cornea. 2008;27(7):764–72.
73. Kobayashi A, Ishibashi Y, Oikawa Y, Yokogawa H, Sugiyama K. In vivo and ex vivo laser confocal microscopy findings in patients with early-stage Acanthamoeba keratitis. Cornea. 2008;27(4):439–45.
74. Auran JD, Starr MB, Koester CJ, LaBombardi VJ. In vivo scanning slit confocal microscopy of Acanthamoeba keratitis. A case report. Cornea. 1994;13(2):183–5.
75. Winchester K, Mathers WD, Sutphin JE, Daley TE. Diagnosis of Acanthamoeba keratitis in vivo with confocal microscopy. Cornea. 1995;14(1):10–7.
76. Pfister DR, Cameron JD, Krachmer JH, Holland EJ. Confocal microscopy findings of Acanthamoeba keratitis. Am J Ophthalmol. 1996;121(2):119–28.
77. Cho B-J, Holland EJ. In vivo tandem scanning confocal microscopy in Acanthamoeba keratitis. Korean J Ophthalmol. 1998;12(2):112–207.

78. Bourcier T, Dupas B, Borderie V, Chaumeil C, Larricart P, Baudouin C, et al. Heidelberg retina tomograph II findings of Acanthamoeba keratitis. Ocular Immunol Inflam. 2005;13(6):487–92.
79. Matsumoto Y, Dogru M, Sato EA, Katono Y, Uchino Y, Shimmura S, et al. The application of in vivo confocal scanning laser microscopy in the management of Acanthamoeba keratitis. Mol Vis. 2007;13(7):1319–26.
80. Mathers WD, Sutphin JE, Folberg R, Meier PA, Wenzel RP, Elgin RG. Outbreak of keratitis presumed to be caused by Acanthamoeba. Am J Ophthalmol. 1996;121(2):129–42.
81. Parmar DN, Awwad ST, Petroll WM, Bowman RW, McCulley JP, Cavanagh HD. Tandem scanning confocal corneal microscopy in the diagnosis of suspected Acanthamoeba keratitis. Ophthalmology. 2006;113(4):538–47.
82. Su P-Y, Hu F-R, Chen Y-M, Han J-H, Chen W-L. Dendritiform cells found in central cornea by in-vivo confocal microscopy in a patient with mixed bacterial keratitis. Ocular Immunol Inflam. 2006;14(4):241–4.
83. Nakano E, Oliveira M, Portellinha W, de Freitas D, Nakano K. Confocal microscopy in early diagnosis of Acanthamoeba keratitis. J Refract Surg. 2004;20(5):S737–40.
84. Tan DT, Mehta JS. Future directions in lamellar corneal transplantation. Cornea. 2007;26:S21–8.
85. McLaren JW, Patel SV. Modeling the effect of forward scatter and aberrations on visual acuity after endothelial keratoplasty. Invest Ophthalmol Vis Sci. 2012;53(9):5545–51.
86. Baratz KH, McLaren JW, Maguire LJ, Patel SV. Corneal haze determined by confocal microscopy 2 years after Descemet stripping with endothelial keratoplasty for Fuchs corneal dystrophy. Arch Ophthalmol. 2012;130(7):868–74.
87. Patel SV, Baratz KH, Hodge DO, Maguire LJ, McLaren JW. The effect of corneal light scatter on vision after Descemet stripping with endothelial keratoplasty. Arch Ophthalmol. (Chicago, Ill: 1960). 2009;127(2):153–60.
88. Patel SV, McLaren JW. In vivo confocal microscopy of Fuchs endothelial dystrophy before and after endothelial keratoplasty. JAMA Ophthalmol. 2013;131(5):611–8.
89. Van Der Meulen IJ, Patel SV, Lapid-Gortzak R, Nieuwendaal CP, McLaren JW, Van Den Berg TJ. Quality of vision in patients with Fuchs endothelial dystrophy and after Descemet stripping endothelial keratoplasty. Arch Ophthalmol. 2011;129(12):1537–42.
90. Patel SV, Erie JC, McLaren JW, Bourne WM. Keratocyte density and recovery of subbasal nerves after penetrating keratoplasty and in late endothelial failure. Arch Ophthalmol. 2007;125(12):1693–8.
91. Ahuja Y, Baratz KH, McLaren JW, Bourne WM, Patel SV. Decreased corneal sensitivity and abnormal corneal nerves in Fuchs endothelial dystrophy. Cornea. 2012;31(11):1257.
92. Al-Aqaba M, Alomar T, Lowe J, Dua HS. Corneal nerve aberrations in bullous keratopathy. Am J Ophthalmol. 2011;151(5):840–9. e1.
93. Patel SV, Baratz KH, Maguire LJ, Hodge DO, McLaren JW. Anterior corneal aberrations after Descemet's stripping endothelial keratoplasty for Fuchs' endothelial dystrophy. Ophthalmology. 2012;119(8):1522–9.
94. Raecker ME, McLaren JW, Kittleson KM, Patel SV. Endothelial image quality after descemet stripping with endothelial keratoplasty: a comparison of three microscopy techniques. Eye Contact Lens. 2011;37(1):6–10.
95. Seery LS, Nau CB, McLaren JW, Baratz KH, Patel SV. Graft thickness, graft folds, and aberrations after Descemet stripping endothelial keratoplasty for Fuchs dystrophy. Am J Ophthalmol. 2011;152(6):910–6.
96. Shortt AJ, Allan BD, Evans JR. Laser-assisted in-situ keratomileusis (LASIK) versus photorefractive keratectomy (PRK) for myopia. Cochrane Database Systemat Rev. 2013(1).
97. McLaren JW, Bourne WM, Patel SV. Stromal reflectance after photorefractive keratectomy: a paired comparison between epithelial removal by rotary brush and excimer laser-scrape. Invest Ophthalmol Visual Sci. 2012;53(14):1469.
98. McLaren JW, Bourne WM, Patel SV. Standardization of corneal haze measurement in confocal microscopy. Invest Ophthalmol Vis Sci. 2010;51(11):5610–6.

99. Erie JC, McLaren JW, Hodge DO, Bourne WM. Recovery of corneal subbasal nerve density after PRK and LASIK. Am J Ophthalmol. 2005;140(6):1059–64. e1.
100. Patel SV, McLaren JW, Kittleson KM, Bourne WM. Subbasal nerve density and corneal sensitivity after laser in situ keratomileusis: femtosecond laser vs mechanical microkeratome. Arch Ophthalmol. 2010;128(11):1413–9.
101. Calvo R, McLaren JW, Hodge DO, Bourne WM, Patel SV. Corneal aberrations and visual acuity after laser in situ keratomileusis: femtosecond laser versus mechanical microkeratome. Am J Ophthalmol. 2010;149(5):785–93.
102. Klingler KN, McLaren JW, Bourne WM, Patel SV. Corneal endothelial cell changes 5 years after laser in situ keratomileusis: femtosecond laser versus mechanical microkeratome. J Cataract Refract Surg. 2012;38(12):2125–30.
103. Patel SV, Bourne WM. Corneal endothelial cell loss 9 years after excimer laser keratorefractive surgery. Arch Ophthalmol. 2009;127(11):1423–7.
104. Lee SJ, Kim JK, Seo KY, Kim EK, Lee HK. Comparison of corneal nerve regeneration and sensitivity between LASIK and laser epithelial keratomileusis (LASEK). Am J Ophthalmol. 2006;141(6):1009–15. e1.
105. Lee BH, McLaren JW, Erie JC, Hodge DO, Bourne WM. Reinnervation in the cornea after LASIK. Invest Ophthalmol Vis Sci. 2002;43(12):3660–4.
106. Kallinikos P, Berhanu M, O'Donnell C, Boulton AJ, Efron N, Malik RA. Corneal nerve tortuosity in diabetic patients with neuropathy. Invest Ophthalmol Vis Sci. 2004;45(2):418–22.
107. Stapleton F, Hayward KB, Bachand N, Trong PH, Teh DW, Deng KM, et al. Evaluation of corneal sensitivity to mechanical and chemical stimuli after LASIK: a pilot study. Eye Contact Lens. 2006;32(2):88–93.
108. Stachs O, Zhivov A, Kraak R, Hovakimyan M, Wree A, Guthoff R. Structural-functional correlations of corneal innervation after LASIK and penetrating keratoplasty. J Refract Surg. 2010;26(3):159–67.
109. Tuisku IS, Lindbohm N, Wilson SE, Tervo TM. Dry eye and corneal sensitivity after high myopic LASIK. J Refract Surg. 2007;23(4):338–42.
110. Ambrósio R Jr, Tervo T, Wilson SE. LASIK-associated dry eye and neurotrophic epitheliopathy: pathophysiology and strategies for prevention and treatment. J Refract Surg. 2008;24(4):396–407.
111. Rosenthal P, Baran I, Jacobs DS. Corneal pain without stain: is it real? Ocular Surface. 2009;7(1):28–40.
112. Nettune GR, Pflugfelder SC. Post-LASIK tear dysfunction and dysesthesia. Ocular Surface. 2010;8(3):135–45.
113. Hamrah P, Cruzat A, Dastjerdi MH, Zheng L, Shahatit BM, Bayhan HA, et al. Corneal sensation and subbasal nerve alterations in patients with herpes simplex keratitis: an in vivo confocal microscopy study. Ophthalmology. 2010;117(10):1930–6.
114. Hamrah P, Cruzat A, Dastjerdi MH, Prüss H, Zheng L, Shahatit BM, et al. Unilateral herpes zoster ophthalmicus results in bilateral corneal nerve alteration: an in vivo confocal microscopy study. Ophthalmology. 2013;120(1):40–7.
115. Rosenberg ME, Tervo TM, Immonen IJ, Müller LJ, Grönhagen-Riska C, Vesaluoma MH. Corneal structure and sensitivity in type 1 diabetes mellitus. Invest Ophthalmol Vis Sci. 2000;41(10):2915–21.
116. Martone G, Alegente M, Balestrazzi A, Nuti E, Traversi C, Pichierri P, et al. In vivo confocal microscopy in bilateral herpetic keratitis: a case report. London, UK: SAGE Publications; 2008.
117. Patel DV, McGhee CN. Laser scanning in vivo confocal microscopy demonstrating significant alteration of human corneal nerves following herpes zoster ophthalmicus. Arch Neurol. 2010;67(5):640–1.
118. Hamrah P, Schrems W, Hoesl L, Dastjerdi M, Dana R, Pavan-Langston D. Corneal epithelial and stromal changes in patients with herpes simplex keratitis: An in vivo confocal microscopy study. Invest Ophthalmol Visual Sci. 2009;50(13):2389.

119. Patel DV, Tavakoli M, Craig JP, Efron N, McGhee CN. Corneal sensitivity and slit scanning in vivo confocal microscopy of the subbasal nerve plexus of the normal central and peripheral human cornea. Cornea. 2009;28(7):735–40.
120. Mocan MC, Yilmaz PT, Irkec M, Orhan M. In vivo confocal microscopy for the evaluation of corneal microstructure in keratoconus. Curr Eye Res. 2008;33(11–12):933–9.
121. Patel DV, McGhee CN. Mapping the corneal sub-basal nerve plexus in keratoconus by in vivo laser scanning confocal microscopy. Invest Ophthalmol Vis Sci. 2006;47(4):1348–51.
122. Niederer RL, Perumal D, Sherwin T, McGhee CN. Laser scanning in vivo confocal microscopy reveals reduced innervation and reduction in cell density in all layers of the keratoconic cornea. Invest Ophthalmol Vis Sci. 2008;49(7):2964–70.
123. Mannion LS, Tromans C, O'Donnell C. An evaluation of corneal nerve morphology and function in moderate keratoconus. Contact Lens and Anterior Eye. 2005;28(4):185–92.
124. Spoerl E, Huhle M, Seiler T. Induction of cross-links in corneal tissue. Exp Eye Res. 1998;66(1):97–103.
125. Wollensak G, Spoerl E, Seiler T. Riboflavin/ultraviolet-A–induced collagen crosslinking for the treatment of keratoconus. Am J Ophthalmol. 2003;135(5):620–7.
126. Al-Aqaba M, Calienno R, Fares U, Otri AM, Mastropasqua L, Nubile M, et al. The effect of standard and transepithelial ultraviolet collagen cross-linking on human corneal nerves: an ex vivo study. Am J Ophthalmol. 2012;153(2):258–66. e2.
127. Spadea L, Salvatore S, Paroli MP, Vingolo EM. Recovery of corneal sensitivity after collagen crosslinking with and without epithelial debridement in eyes with keratoconus. J Cataract Refract Surg. 2015;41(3):527–32.
128. Dyck PJ, Overland CJ, Low PA, Litchy WJ, Davies JL, Dyck PJB, et al. Signs and symptoms versus nerve conduction studies to diagnose diabetic sensorimotor polyneuropathy: Cl vs. NPhys Trial. Muscle Nerve. 2010;42(2):157–64.
129. Petropoulos IN, Green P, Chan AW, Alam U, Fadavi H, Marshall A, et al. Corneal confocal microscopy detects neuropathy in patients with type 1 diabetes without retinopathy or microalbuminuria. PLoS ONE. 2015;10(4):e0123517.
130. Misra SL, Craig JP, Patel DV, McGhee CN, Pradhan M, Ellyett K, et al. In vivo confocal microscopy of corneal nerves: an ocular biomarker for peripheral and cardiac autonomic neuropathy in type 1 diabetes mellitus. Invest Ophthalmol Vis Sci. 2015;56(9):5060–5.
131. Bitirgen G, Ozkagnici A, Malik R, Kerimoglu H. Corneal nerve fibre damage precedes diabetic retinopathy in patients with type 2 diabetes mellitus. Diabet Med. 2014;31(4):431–8.
132. Palejwala NV, Walia HS, Yeh S. Ocular manifestations of systemic lupus erythematosus: a review of the literature. Autoimmune Dis. 2012;2012.
133. Marsovszky L, Resch MD, Németh J, Toldi G, Medgyesi E, Kovács L, et al. In vivo confocal microscopic evaluation of corneal Langerhans cell density, and distribution and evaluation of dry eye in rheumatoid arthritis. Innate Immun. 2013;19(4):348–54.
134. Mohsenin A, Huang JJ. Ocular manifestations of systemic inflammatory diseases. Conn Med. 2012;76(9):533–44.
135. Villani E, Beretta S, De Capitani M, Galimberti D, Viola F, Ratiglia R. In vivo confocal microscopy of meibomian glands in Sjögren's syndrome. Invest Ophthalmol Vis Sci. 2011;52(2):933–9.
136. Hong J, Zhu W, Zhuang H, Xu J, Sun X, Le Q, et al. In vivo confocal microscopy of conjunctival goblet cells in patients with Sjögren's syndrome dry eye. Br J Ophthalmol. 2010;94(11):1454–8.
137. Enríquez-de-Salamanca A, Bonini S, Calonge M. Molecular and cellular biomarkers in dry eye disease and ocular allergy. Curr Opin Allergy Clin Immunol. 2012;12(5):523–33.
138. Kari O, Saari KM. Diagnostics and new developments in the treatment of ocular allergies. Curr Allergy Asthma Rep. 2012;12(3):232–9.
139. Miljanović B, Dana R, Sullivan DA, Schaumberg DA. Impact of dry eye syndrome on vision-related quality of life. Am J Ophthalmol. 2007;143(3):409–15. e2.

140. Matsumoto Y, Sato EA, Ibrahim OM, Dogru M, Tsubota K. The application of in vivo laser confocal microscopy to the diagnosis and evaluation of meibomian gland dysfunction. Mol Vision. 2008;14:1263.
141. Ibrahim OM, Matsumoto Y, Dogru M, Adan ES, Wakamatsu TH, Goto T, et al. The efficacy, sensitivity, and specificity of in vivo laser confocal microscopy in the diagnosis of meibomian gland dysfunction. Ophthalmology. 2010;117(4):665–72.
142. Villani E, Ceresara G, Beretta S, Magnani F, Viola F, Ratiglia R. In vivo confocal microscopy of meibomian glands in contact lens wearers. Invest Ophthalmol Vis Sci. 2011;52(8):5215–9.
143. Matsumoto Y, Shigeno Y, Sato EA, Ibrahim OM, Saiki M, Negishi K, et al. The evaluation of the treatment response in obstructive meibomian gland disease by in vivo laser confocal microscopy. Graefe's Arch Clin Exp Ophthalmol. 2009;247(6):821–9.
144. Ban Y, Ogawa Y, Ibrahim OM, Tatematsu Y, Kamoi M, Uchino M, et al. Morphologic evaluation of meibomian glands in chronic graft-versus-host disease using in vivo laser confocal microscopy. Mol Vis. 2011;17:2533.
145. Villani E, Canton V, Magnani F, Viola F, Nucci P, Ratiglia R. The aging Meibomian gland: an in vivo confocal study. Invest Ophthalmol Vis Sci. 2013;54(7):4735–40.
146. Villani E, Galimberti D, Papa ND, Nucci P, Ratiglia R. Inflammation in dry eye associated with rheumatoid arthritis: cytokine and in vivo confocal microscopy study. Innate Immun. 2013;19(4):420–7.
147. Alhatem A, Cavalcanti B, Hamrah P, editors. In vivo confocal microscopy in dry eye disease and related conditions. Semin Ophthalmol. 2012, Taylor & Francis.
148. Cruzat A, Witkin D, Baniasadi N, Zheng L, Ciolino JB, Jurkunas UV, et al. Inflammation and the nervous system: the connection in the cornea in patients with infectious keratitis. Invest Ophthalmol Vis Sci. 2011;52(8):5136–43.
149. Tuominen IS, Konttinen YT, Vesaluoma MH, Moilanen JA, Helintö M, Tervo TM. Corneal innervation and morphology in primary Sjogren's syndrome. Invest Ophthalmol Vis Sci. 2003;44(6):2545–9.
150. Villani E, Galimberti D, Viola F, Mapelli C, Ratiglia R. The cornea in Sjogren's syndrome: an in vivo confocal study. Invest Ophthalmol Vis Sci. 2007;48(5):2017–22.
151. Zhang X, Chen Q, Chen W, Cui L, Ma H, Lu F. Tear dynamics and corneal confocal microscopy of subjects with mild self-reported office dry eye. Ophthalmology. 2011;118(5):902–7.
152. Efron N. Contact lens-induced changes in the anterior eye as observed in vivo with the confocal microscope. Prog Retinal Eye Res. 2007;26(4):398–436.
153. Villani E, Viola F, Sala R, Salvi M, Mapelli C, Curro N, et al. Corneal involvement in Graves' orbitopathy: an in vivo confocal study. Invest Ophthalmol Vis Sci. 2010;51(9):4574–8.
154. Lin H, Li W, Dong N, Chen W, Liu J, Chen L, et al. Changes in corneal epithelial layer inflammatory cells in aqueous tear–deficient dry eye. Invest Ophthalmol Vis Sci. 2010;51(1):122–8.
155. Matsumoto Y, Ibrahim OM. Application of in vivo confocal microscopy in dry eye disease. Invest Ophthalmol Visual Sci. 2018;59(14):DES41–DES7.
156. Benítez-del-Castillo JM, Acosta MC, Wassfi MA, Díaz-Valle D, Gegúndez JA, Fernandez C, et al. Relation between corneal innervation with confocal microscopy and corneal sensitivity with noncontact esthesiometry in patients with dry eye. Invest Ophthalmol Vis Sci. 2007;48(1):173–81.
157. Villani E, Galimberti D, Viola F, Mapelli C, Del Papa N, Ratiglia R. Corneal involvement in rheumatoid arthritis: an in vivo confocal study. Invest Ophthalmol Vis Sci. 2008;49(2):560–4.
158. Wakamatsu TH, Sato EA, Matsumoto Y, Ibrahim OM, Dogru M, Kaido M, et al. Conjunctival in vivo confocal scanning laser microscopy in patients with Sjögren syndrome. Invest Ophthalmol Vis Sci. 2010;51(1):144–50.
159. Iaccheri B, Torroni G, Cagini C, Fiore T, Cerquaglia A, Lupidi M, et al. Corneal confocal scanning laser microscopy in patients with dry eye disease treated with topical cyclosporine. Eye. 2017;31(5):788.

160. Levy O, Labbé A, Borderie V, Hamiche T, Dupas B, Laroche L, et al. Increased corneal sub-basal nerve density in patients with Sjögren syndrome treated with topical cyclosporine A. Clin Exp Ophthalmol. 2017;45(5):455–63.
161. Messmer E, Torres ES, Mackert M, Zapp D, Kampik A. In vivo confocal microscopy in blepharitis. Klin Monatsbl Augenheilkd. 2005;222(11):894–900.
162. Irkec MT, Bozkurt B. Molecular immunology of allergic conjunctivitis. Curr Opin Allergy Clin Immunol. 2012;12(5):534–9.
163. Hu Y, Matsumoto Y, Adan ES, Dogru M, Fukagawa K, Tsubota K, et al. Corneal in vivo confocal scanning laser microscopy in patients with atopic keratoconjunctivitis. Ophthalmology. 2008;115(11):2004–12.
164. Le Q, Hong J, Zhu W, Sun X, Xu J. In vivo laser scanning confocal microscopy of vernal keratoconjunctivitis. Clin Exp Ophthalmol. 2011;39(1):53–60.
165. Leonardi A, Lazzarini D, Bortolotti M, Piliego F, Midena E, Fregona I. Corneal confocal microscopy in patients with vernal keratoconjunctivitis. Ophthalmology. 2012;119(3):509–15.
166. Ibrahim OM, Matsumoto Y, Dogru M, Adan ES, Wakamatsu TH, Shimazaki J, et al. In vivo confocal microscopy evaluation of meibomian gland dysfunction in atopic-keratoconjunctivitis patients. Ophthalmology. 2012;119(10):1961–8.
167. Ladage PM, Petroll WM, Jester JV, Fisher S, Bergmanson JP, Cavanagh HD. Spherical indentations of human and rabbit corneal epithelium following extended contact lens wear1. Eye Contact Lens. 2002;28(4):177–80.
168. Craig JP, Sherwin T, Grupcheva CN, McGhee CN. An evaluation of mucin balls associated with high-DK silicone-hydrogel contact lens wear. Springer: Lacrimal Gland, Tear Film, and Dry Eye Syndromes 3; 2002. p. 917–23.
169. Millar TJ, Papas EB, Ozkan J, Jalbert I, Ball M. Clinical appearance and microscopic analysis of mucin balls associated with contact lens wear. Cornea. 2003;22(8):740–5.
170. Ladage PM, Yamamoto K, Ren DH, Li L, Jester JV, Petroll WM, et al. Effects of rigid and soft contact lens daily wear on corneal epithelium, tear lactate dehydrogenase, and bacterial binding to exfoliated epithelial cells. Ophthalmology. 2001;108(7):1279–88.
171. Sindt CW, Grout TK, Critser DB, Kern JR, Meadows DL. Dendritic immune cell densities in the central cornea associated with soft contact lens types and lens care solution types: a pilot study. Clin Ophthalmol (Auckland, NZ). 2012;6:511.
172. Böhnke M, Masters BR. Long-term contact lens wear induces a corneal degeneration with microdot deposits in the corneal stroma. Ophthalmology. 1997;104(11):1887–96.
173. Hollingsworth JG, Efron N. Confocal microscopy of the corneas of long-term rigid contact lens wearers. Contact Lens Anterior Eye. 2004;27(2):57–64.
174. Ma X, He L, He D, Xu J. Chloroquine keratopathy of rheumatoid arthritis patients detected by in vivo confocal microscopy. Curr Eye Res. 2012;37(4):293–9.
175. Sbeity Z, Palmiero PM, Tello C, Liebmann JM, Ritch R. Non-contact in vivo confocal scanning laser microscopy in exfoliation syndrome, exfoliation syndrome suspect and normal eyes. Acta Ophthalmol. 2011;89(3):241–7.
176. Mocan MC, Eldem B, Irkec M. In vivo confocal microscopic findings of two siblings with Maroteaux-Lamy syndrome. Cornea. 2007;26(1):90–3.
177. Efron N, Mutalib HA. Confocal microscopy observations of the cornea in response to contact lens wear. Die Kontaktlinse. 2001;35(1):4–16.
178. Nagel S, Wiegand W, Thaer A, Geyer O. Light scattering study of the cornea in contact lens patients. In vivo studies using confocal slit scanning microscopy. Der Ophthalmologe: Zeitschrift der Deutschen Ophthalmologischen Gesellschaft. 1996;93(3):252–6.
179. Rong B, Yan X. Changes of corneal limbus in long-term soft contact lens wearers by using laser confocal microscope. [Zhonghua yan ke za zhi] Chin J Ophthalmol. 2007;43(6):514–8.
180. Efron N, Al-Dossari M, Pritchard N. Confocal microscopy of the bulbar conjunctiva in contact lens wear. Cornea. 2010;29(1):43–52.
181. Labbé A, Dupas B, Hamard P, Baudouin C. In vivo confocal microscopy study of blebs after filtering surgery. Ophthalmology. 2005;112(11):1979. e1–e9.

182. Guthoff R, Klink T, Schlunck G, Grehn F. In vivo confocal microscopy of failing and functioning filtering blebs: results and clinical correlations. J Glaucoma. 2006;15(6):552–8.
183. Messmer EM, Zapp DM, Mackert MJ, Thiel M, Kampik A. In vivo confocal microscopy of filtering blebs after trabeculectomy. Arch Ophthalmol. 2006;124(8):1095–103.
184. Amar N, Labbé A, Hamard P, Dupas B, Baudouin C. Filtering blebs and aqueous pathway: an immunocytological and in vivo confocal microscopy study. Ophthalmology. 2008;115(7):1154–61. e4.
185. Martone G, Frezzotti P, Tosi GM, Traversi C, Mittica V, Malandrini A, et al. An in vivo confocal microscopy analysis of effects of topical antiglaucoma therapy with preservative on corneal innervation and morphology. American journal of ophthalmology. 2009;147(4):725–35. e1.
186. Baratz KH, Nau CB, Winter EJ, McLaren JW, Hodge DO, Herman DC, et al. Effects of glaucoma medications on corneal endothelium, keratocytes, and subbasal nerves among participants in the ocular hypertension treatment study. Cornea. 2006;25(9):1046–52.

Aberration, Aberrometry and Aberrometers

Hossein Aghaei

Introduction

There are two main theories regarding nature of the light:

1. Ray theory 2. Wave theory.

In the XIth century, the thesis of the visual ray was definitively abandoned in favor of Ibn al-Haytham's waork [1] which revolutionized the optics [2].

He claimed that "each point of the object emits an infinity of rays a part of which enters the optical system of the eye. This system modifies rays to reconstruct an image. In a perfect optical system this image is a point, called image point, which all rays entering the system of the eye converge to".

Stated in wave optics, the system of the eye should transform the input wavefront [A wavefront is a surface over which an optical disturbance has a constant phase. Rays and wavefronts are two mutually complementary approaches to light propagation. Wavefronts are always normal (perpendicular) to the rays] into a perfect convergent spherical wavefront that has the image point as center.

In a real aberration-affected optical system the rays adjusted by the optical system do not converge entirely to a fix point image. So, for one object point conform more than one image points that make a blurred image. This deviation from the ideal state is named "aberration" and is a portion of the optical quality of the system. Aberration can be quantified either with respect to the expected image point or to the wavefront corresponding to this ideal point. Compare the real output wavefront to the ideal one, is referred as "wavefront aberration" [3, 4].

H. Aghaei (✉)
Eye Research Center, The Five Senses Institude, Rassoul Akram Hospital, Iran
University of Medical Sciences, Tehran, Iran
e-mail: aghaee.h1376@yahoo.com

M. Mohammadpour (ed.), *Diagnostics in Ocular Imaging*,
https://doi.org/10.1007/978-3-030-54863-6_11

Aberration

Definition
The term aberration is from the Latin word ab-erratio mean: Going off-track or deviation.

Aberration is defined as the difference that exists between the ideal image that we would expect to see when luminous rays are refracted in the perfect optical system (Snell's law) and what is actually achieved. These differences vary from simple defocus to highly aberrated wavefronts. Aberrations in the human eye are as unique as a person's fingerprints.

Aberrations can be divided into two categories:

1. **Chromatic**
2. **Monochromatic**.

Chromatic aberrations are caused by the difference in distribution of incident polychromatic radiation throughout a medium and depend on the wavelength of the light that penetrates the eye. Refractive index of a material and wavelength of the light that proceed through it are two factors that determine magnitude of chromatic aberration.

Monochromatic aberrations are related to a specific wavelength and include spherical refractive error (defocus), cylindrical refractive errors (astigmatism), and high-order aberrations (HAO) such as spherical aberrations and coma. When we discuss wavefront aberrations, we usually refer to monochromatic aberrations. The optical quality of the eye can be assessed through the shape of the wavefront and its aberrations.

Aberrations also can categorize in two orders:

Low-order aberrations

Low-order aberrations consist of:
Zero order: These aberrations are characterized by axial symmetry and a flat wavefront.

First-order: These linear aberrations correspond to tilting around a horizontal (x) or vertical (y) axis. They describe the tilt or prismatic error of the eye.

Second-order: Spherical defocus and astigmatism describe the spherical error and astigmatic component and its orientation or axis. These components are similar to measurements found with basic refraction. These optical errors can correct by using of spectacles and contact lenses. This aberrations make major amount of total aberrations.

High-order aberrations
Higher order aberrations (HOA) are all those aberrations that fall within the third order and above. These aberrations can negatively affect the vision of seemingly

healthy eyes and typically cannot be easily corrected with non-invasive procedures or devices such as spectacles and contact lenses [5].

Higher-order aberrations consist of:
Third-order aberrations correspond to horizontal and vertical coma and triangular astigmatism with the base along the x- or y-axis (trefoil).

Fourth-order: aberrations contain spherical aberration, tetrafoil and secondary astigmatism.

Fifth-tenth order: aberrations are important only when the pupil is greatly dilated.

Ocular higher order aberrations can be expanded as far as the instrument will allow in terms of order. However, those of main interest and importance are the third and fourth orders, as the fifth and sixth order aberrations are usually very small in magnitude and therefore negligible [6].

Clinically relevant aberrations are as follows:
Defocus (spherical refractive error). This low-order aberration is observed in the presence of myopic and hyperopic ametropia where the light rays focus at a different focal point than emmetropia.

Astigmatism. These low-order aberrations demonstrate different meridian focuses at different focal planes and make a toric wavefront.

Coma. Coma exists because of misalignment of the centres of the pupil, cornea and lens. This high-order aberration of the optic system is produced when light rays form an angle with the optical axis, or when some peripheral light rays do not focus on the same retinal plane but are focused at different distances from the retina. The image of the retinal focal point has a comet-like appearance.

Spherical aberration. This high-order aberration is produced in a spherical optical medium where peripheral rays focus before or after the paraxial rays. The wavefront modifies its curvature as it approaches the pupil edge. It can be measured by determining the distance between the focus of these two rays. In a normal eye, it is approximately 0.50 D. All spherical surfaces give rise to spherical aberrations, which are not generated from planar surfaces where the dioptric power is equal at all points of the surface.

Aberrometry

Wavefront Sensing Devices

Aberration can be measured as the test beam move into the eye (ingoing aberrometry) or as the wavefront emerges from the eye (outgoing aberrometry).

Ingoing aberrometers operate by examining how wavefronts external to the eye are changed as they pass through the optics of the eye. Ingoing aberrometers typically measure the transverse ray error. In other words, in the ideal case, a ray of

light entering the eye focuses to the fovea. When aberrations are present, the ray strikes the retina at a point away from the fovea. Ingoing aberrometers measure the distance between the fovea and the point where the ray strikes the retina. This distance is proportional to the slope of the wavefront and can eventually be used to reconstruct the shape of the wavefront.

Outgoing aberrometers measure the slope or direction of travel of the wavefront at a series of points across the pupil.

Aberrations can be described quantitatively using Zernike polynomials, named after Frits Zernike, a Dutch mathematician and astronomer who won the Nobel Prize for his invention of phase contrast microscopy.

Zernike Polynomials

Aberrations can be described quantitatively using Zernike polynomials.

Polynomials are mathematical equations that usually contain multiple terms and variables [7]. Zernike polynomials are one of the mathematical representations that can be used to describe wavefront errors.

The shape of the wavefront is illustrated in the x and y coordinates; the third dimension, height, is illustrated in the z-axis. The final figure is obtained from the sum of the Zernike polynomials describing all types of deformation (Fig. 1).

Z_n^m or double indexing system displays both the order (n) and frequency (m) of the wavefront error [8]. This method of Zernike expression also allows easier

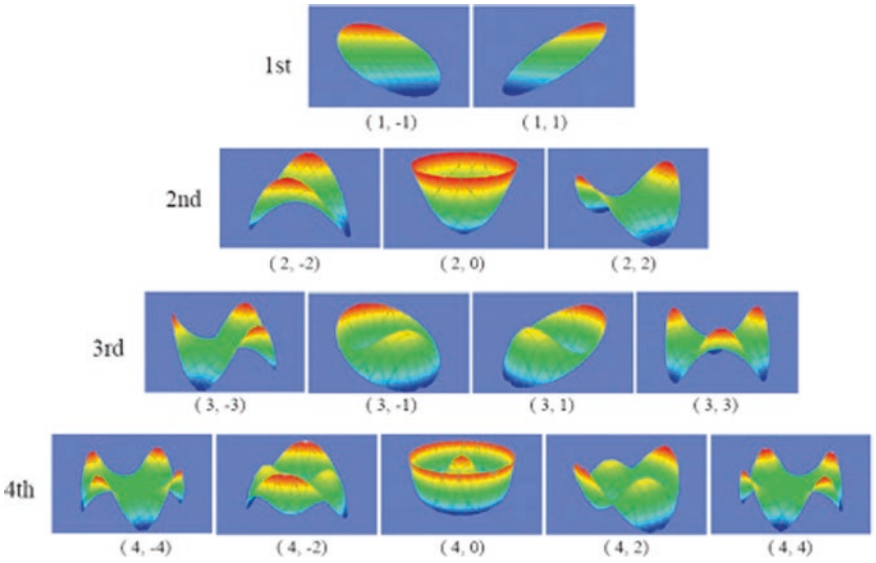

Fig. 1 Zernike polynomials

comparison of wavefront errors as aberrations with the same frequency have similar shapes (Fig. 2).

There are other equations, such as the Taylor polynomials; however, they are not orthogonal, which creates practical problems in data fitting.

The information from the wavefront aberrometer can also be given in the form of *Zernike coefficients* (C_n^m) that reflect the same order and frequency as the corresponding Zernike polynomials, measured in micrometers (μm) (Fig. 2) [8].

Wavefront aberrations can be further classified based on their Zernike order as lower ($n \leq 2$) or higher order aberrations, with lower order aberrations extending from the zero to the second order, whilst the higher order aberrations ($n \geq 3$) are all those above the second order.

The zero order has only 1 term that represents a constant. The 1st order has 2 terms, which represent the tilt for the x and y axes. The 2nd order has 3 terms, which represent the defocus and regular astigmatism in vertical and horizontal axes. The 3rd order shows coma and trefoil in 4 terms. In a similar way, the 4th order represents spherical aberration, secondary astigmatism, and tetrafoil in 5 terms [9].

Polynomials can be expanded up to any arbitrary order if sufficient numbers of measurements for calculation are made [10].

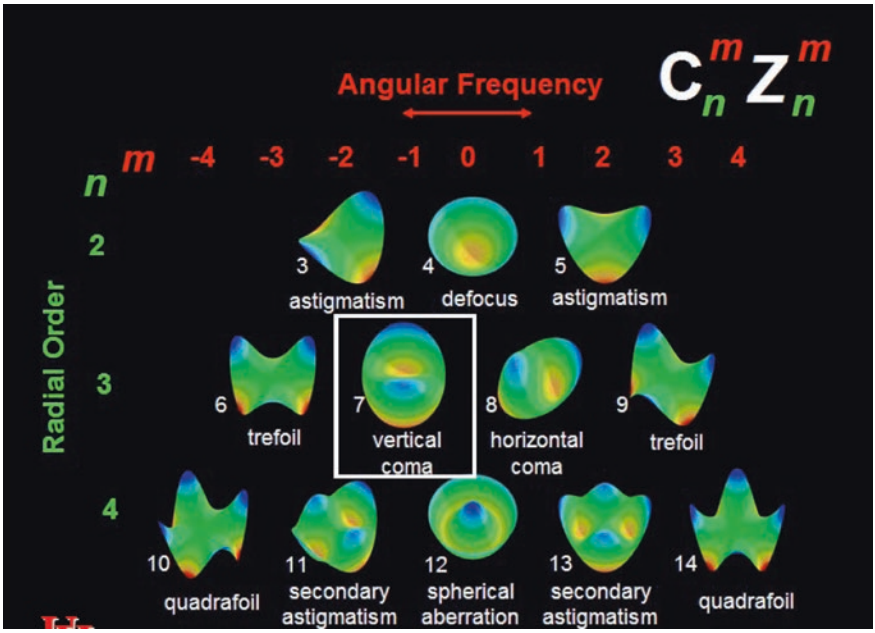

Fig. 2 Zernike polynomials; Z_n^m and C_n^m

Wavefront aberration data is collected and measured by different principles:

1. Outgoing refractive aberrometry (Hartmann-Shack)
2. Retinal imaging aberrometry (Tscherning)
3. Incoming Adjustable Refractometry (Scheiner)
4. Double pass aberromety (Slit Skiascopy)
5. Optic path difference (combined retinoscopy and topography)
6. Retinal ray tracing.

Hartmann-Shack (HS) Aberrometer

The most commonly used apparatus measuring aberrations of human eye objectively are based on the Hartmann Shack principle.

Light with a flat wavefront passing through a perfect eye coincides exactly in one point on the retina (the second focal point of the eye). Conversely, light from a point on the retina leaves the eye with a perfect flat wavefront.

The principle of a HS aberrometer is simple (Fig. 3).

A narrow laser beam (around 1 mm wide) is sent via a beam splitter BS into the eye and makes a point on the retina. Some of the light is scattered and propagates back through the lens and pupil, as if coming from a point-source on the retina. This light bundle then falls upon a regular planar array of identical converging micro-lenses (typically of the order of 0.5 mm diameter). Each micro-lens focuses its part of the light on a charge-coupled device (CCD) camera placed on the focal plane of the lenslet array. If the eye is free of aberration, the overall wavefronts leaving the eye are plane (parallel rays); each lens will focus the light on the focal point of its optical axis. Therefore, the overall set of point images (spots) on the CCD camera, matches the regular grid pattern of the lenses (Fig. 4).

If, however, the wavefronts leaving the eye are not plane, the parts of wavefront entering each micro lens will, in general, be tilted with respect to the lens' axis, so

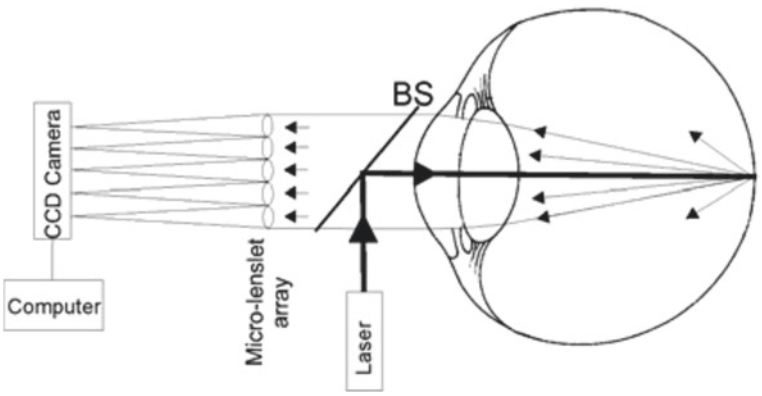

Fig. 3 Hartmann–Shack aberrometer

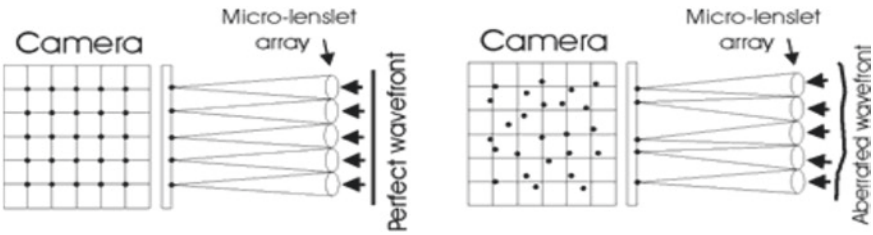

Fig. 4 Planar (left) and aberrated (right) wavefront

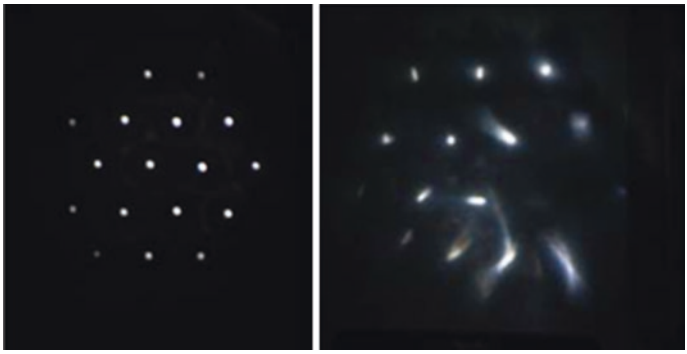

Fig. 5 Light on the screen in perfect eye (left) and aberrated eye (right)

that the point image in its focal plane is not on its optical axis, but is displaced (by an amount and direction) depending on the local tilt of the wavefront (Fig. 5) [11].

The Hartmann–Shack devices usually determine aberrations in the form of Zernike polynomials. Although the Shack-Hartmann method of wavefront aberrometry is a very accurate one, the level of accuracy is dependent on the number of spots that are collected within a 7-mm pupil area. In general, it appears that >100 spots within a 7-mm pupil area is sufficient for accurately measuring up to eighth-order aberrations [12].

Retinal Imaging Aberrometry (Tscherning)

The Tscherning system is similar to the Hartmann- Shack system; however, the incident light beam passes through a perforated lens. It uses a frequency- doubled neodymium: yttrium–aluminum-garnet (Nd:YAG) laser emitting light at 532 nm. A video recorder registers any deformation of the reflected pattern, analyzes it, and returns the image to a reticulum. Analyzing the image and comparing the aberrated retinal grid pattern with the ideal grid positioning measures the optical

aberrations at the level of the entrance of the pupil. The slope of the difference between the actual images compared with the ideal grid represents the wavefront error [13].

Tscherning aberrometry is used in the Allegretto WaveLight Analyzer distributed by WaveLight Laser Technologie AG (Erlangen, Germany). The Tscherning's principle is also utilized in a retinal tracing method applied with the Tracey technology.

Tracey System

This device measures an ingoing light that transfers through the optical system of the eye and forms an image on the retina. It measures one ray at a time in the entrance pupil rather than measuring all of the rays at the same time like previously mentioned devices. This design decreases the chance of crossing the rays in highly aberrated eyes. In the retinal raytracing aberrometer, a narrow laser beam scans across the pupil. Aberrations cause this beam to strike the retina away from the fovea. A position sensor is used to record the deviation of the beam from the fovea. Rapid-scanning and position-sensing technology is required with this technique to ensure that eye motion effects are negligible. The total scanning time is 10–40 ms [14].

Optic Path Difference (Combined Retinoscopy and Topography)

This technology duplicates the examination in a skiascope. The system scans a large number of points and, different from other systems, examines the relationship between the light source and the reflected component. In the dynamic skiascopy wavefront sensor, the retina is scanned with a slit-shaped light beam and the reflected light is captured by an array of rotating photodetectors over a 360-degree area. The system scans a large number of points and investigates the relationship between the light source and the reflected component. The time difference of the reflected light is used to determine the aberrations [15]. This diagnostic instrument combines autorefractometry, corneal topography, and analysis of the wavefront to create a single map of the corneal surface's refractive power. This principle is used in the Nidek OPD-Scan distributed by Nidek.

Series Measurements and Parallel Measurements in Aberrometry

The preceding wavefront technologies take two separate approaches to measuring aberrations. The Shack-Hartmann and the Tscherning devices measure wavefront aberrations in *parallel*, meaning that many different pupil entry positions are measured simultaneously. The retinal raytracing and spatially resolved refractometer techniques, conversely, measure in *series*, meaning that a single pupil entry

point is measured in a given instant and measurements at different pupil entry points are made sequentially.

The advantage of parallel measurement is that hundreds of points can be captured at the same time to avoid errors caused by eye motion and fluctuations in tear film and accommodation. Typically, measurements with the Shack-Hartmann and Tscherning systems can be made in a single video frame, which is equivalent to 25–30 milliseconds. The retinal raytracing system operates on the order of 50 ms for 64 pupil points. The spatially resolved refractometer operates on the order of several minutes for 36 pupil points. The drawback to systems that measure in parallel is that there is a limit to how densely measurements can be made within the pupil. In the Shack-Hartmann system, fabrication of the lenslet array is the limiting factor. As the diameter of the lenslets decreases, the cost of fabrication of the lenslet arrays increases dramatically. The lower limit for lenslet arrays found today is around 200 μm between each lenslet. In the Tscherning system, the limitation on sampling the pupil is determined by the spacing of spots on the retina that can be reliably resolved.

The advantage of systems that measure wavefront aberrations in series is that the number of samples within the pupil and the measurement region within the pupil are customizable. Thus, the pupil can be sampled with arbitrary resolution. If a patient has a high level of aberration in a localized region of the pupil, the series system can focus on and perform high-resolution measurement of this region. The drawback to these systems is that as the number of measurement points increases, so does the duration of the examination.

Following analysis, all of the systems produce a graphical image with chromatic scales—the aberrometric maps. These images resemble topographical maps. They describe the difference in microns between a light wavefront and a reference wavefront.

Information Presented by the Maps Includes the Following

Modulation transfer function (MTF). The MTF is a method to describe the contrast sensitivity of a lens. Modulation transfer is the ability of a lens system to transfer an object's contrast to its image. Modulation is therefore a ratio of image contrast to object contrast. Ideally, it would be one, or 100%. This parameter is the objective equivalent of the contrast sensitivity and provides a measurement of the quality of the image.

Point spread function (PSF). This parameter expresses the effect of the aberrations on the retinal image and consequently on the quality of the image. It is limited by diffraction and optical aberrations. The smaller and the sharper the better.

Phoropter predicted refraction (PPR). This parameter corresponds to a translation of the wavefront into a spherocylindrical value similar to the refraction obtained with the phoropter.

Root mean square (RMS) or mean sum of the square. Wavefront aberrations depicted with Zernike polynomials and coefficients can be difficult to understand and interpret, and therefore the *root mean square* (RMS) can be valuable when assessing the wavefront error [16].

This parameter represents the mean residual square root of the total aberration and permits numerical quantification of the error and calculation of to what degree the surface examined deviates from the perfect reference surface; this allows the wavefront error to be represented as a single number that is more straightforward and easily interpreted [16].

Image quality decreases with the RMS value if the aberration form is maintained. However, it is not obvious that two wavefront aberrations with the same RMS error but with different types produce the same degradation of image quality [17].

Aberrometers

There are a number of different types of wavefront measurement devices available on the market. Although some of them may not present in the market. Although (while) it is often difficult to adequately categorize new products in an understandable fashion, there appear to be four different principles by which wavefront aberration information is collected and measured (Table 1).

Zywave Aberrometer

The Zywave aberrometer in the Zyoptix system uses the Hartman-Shack method of analysis of the outgoing wavefront that measures up to fifth-order Zernike aberrations, including coma, trefoil, and spherical aberrations.

The Zywave software (version 5.2 of the Zyoptix Evolution Package) for Zyoptix produces a composite aberration map from the best three of five aberration maps. The Zywave can give an estimate of refractive error, representing

Table 1 List of some wavefront devices

Outgoing reflection aberrometry(Shack Hartmann)	Retinal imaging aberrometry (Tscherning)	Ray tracey	Ingoing adjustable refractometry (Scheiner)	Double pass aberrometry (Slit skiascopy)
Alcon LADARWave VisX Wavescan B&L Zywave Meditec WASCA	WaveLight Analyzer Schwind Aberrometer	iTrace	InterWave SSR	Nidek OPD scan

the second-order aberrations of the eye (PPR: Phoropter Predicted Refraction). The Zywave was designed to measure refractive errors over a range of +6.00 to −12.00 Ds and up to 5.00 D of cylinder. The Zywave is part of the Zyoptix Diagnostic Workstation (along with the Orbscan II/IIIz corneal topographer) for wavefront-guided refractive surgery (Fig. 6).

In new version of the ZYWAVE^3 has nine times the number of data points (lenslets/centroids) than the previous generation model, plus an HD camera with high-speed data transfer technology (Fig. 7).

With regards to higher-order aberrations, there are many factors one must examine as sources for differences in repeatability data. For example, instrument alignment, [18] time between measurements, [19] and biological variables (ocular optics, tears, accommodation, pupil size) [20] among others must be considered.

One important difference between the Zywave and other clinical aberrometers is the relatively low spatial resolution of its Shack-Hartmann grid. The Zywave has 76 spots on its centroid pattern while others such as the LADARWave (Alcon Labs, Inc, Fort Worth, TX) has 204–213, the Wavescan (VISX, Santa Clara, CA) has 240 and the COAS (AMO-Wavefront Sciences, Albuquerque, NM) has 1,452 sampling points [21] (Table 2).

The Zywave is first measured on the undilated pupil. If the patient accepts the Zywave refraction in the Phoropter, dilated Zywave examinations are performed, and the acceptance of the measurement is checked. If the patient does not accept the Zywave refraction, Zyoptix LASIK is not performed.

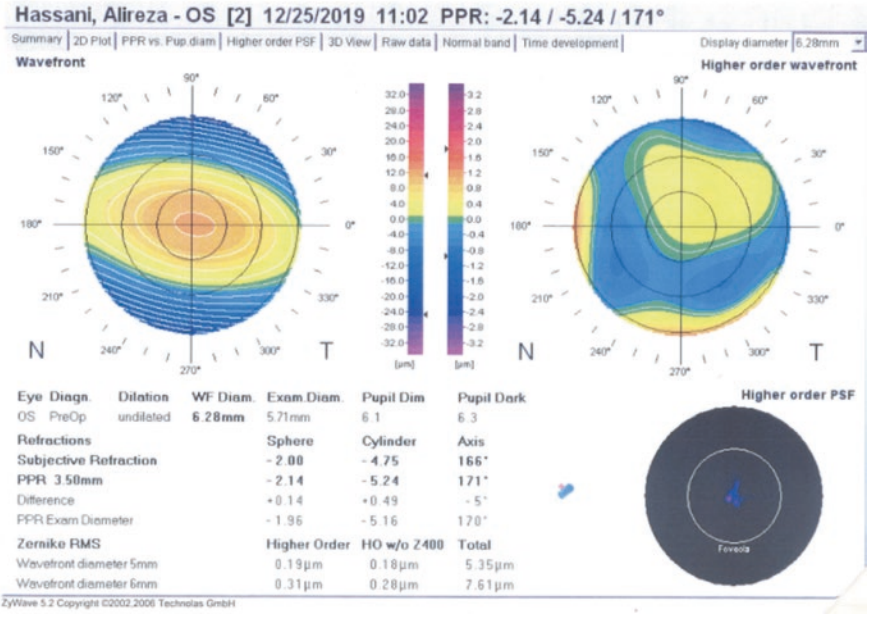

Fig. 6 Zywave II map

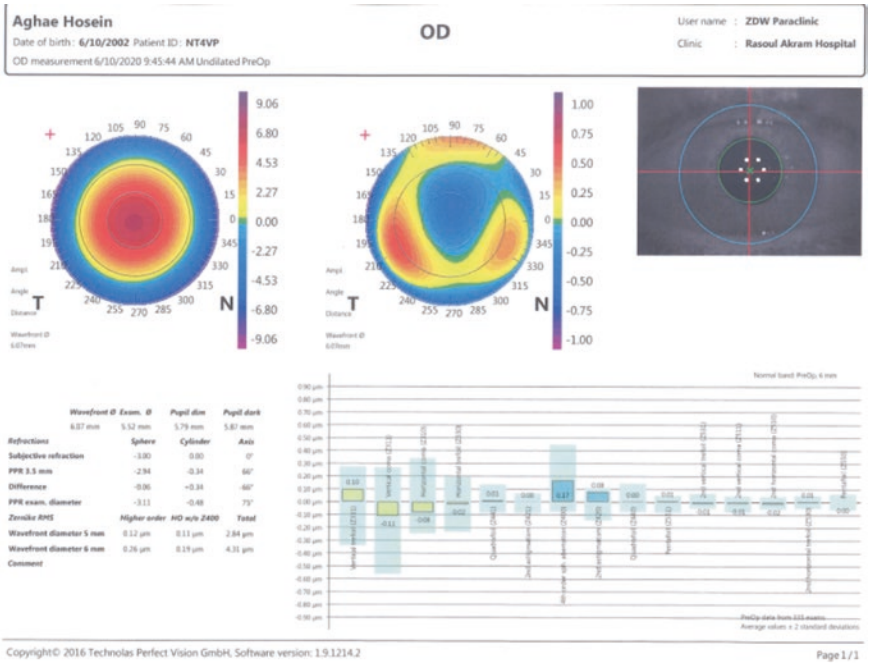

Fig. 7 Zywave[3] display

Table 2 Comparison of commercially available aberrometers with respect to the number of lenslets (or equivalent) collecting light within a 7-mm entrance pupil

System name (manufacturer)	Type	Spots in 7-mm pupil[a]	Lenslet pitch (resolution)/mm
WASCA/COAS (Carl Zeis Meditec)	Shack-Hartmann	800	210
Wavescan (VISX)	Shack-Hartmann	222	400
LADARwave Custom Cornea LADARwave Custom Cornea	Shack-Hartmann Shack-Hartmann	172	450
Wavefront Analyser (Wavelight)	Tscherning	98	600
Zywave (Bausch & Lomb)	Shack-Hartmann	74	700
KR-9000 (TOPCON)	Shack-Hartmann	74	700
VFA (Tracey)	Retinal Ray-Tracing	80	Variable

[a]Calculated from the lenslet pitch and obtained from published sources

OPD-Scan

The OPD-Scan (Optical Path Difference Scanning System) is a combination aberrometer and topographer that uses the principle of spatial dynamic skiascopy to calculate the aberrations of the eye and placido disk topography to measure the corneal shape. The unit uses over 8000 data points to plot the aberrations of the eye and the corneal topography. In addition to aberrometry and topography, the OPD-Scan provides autorefractometry, keratometry, and pupillometry functions integrated into one unit, allowing accurate data registration between the different types of examinations.

The aberrometry measuring method consists of an infrared light-emitting diode housed within a chopper wheel with slit apertures. The receiving system consists of a photodetector array that converts the time differences of stimulation into dioptric power maps, which correlate the refractive error in a two-dimensional map at the entrance pupil. The dioptric power maps or refractive maps are displayed as ''OPD maps'' from which traditional Zernike-based maps out to the eighth order can be derived.

The OPD-Scan has a comparatively wide measuring range of −20 to +22 D of sphere and up to 12 D of cylinder. An added benefit is that aberrometry and topography are performed on the one instrument; therefore, the axis of alignment is the same with accurate registration of data.

Unique to the OPD-Scan are refractive diopter maps termed internal OPD and OPD maps. The OPD map displays the spatially resolved refractive and aberrometric status of the entire optical path of the eye. The OPD internal map displays the refractive status of the eye due to internal aberrations by subtracting the effects of the corneal front surface from the total aberrometry.

This map allows the surgeon to identify whether the source of the aberrations is corneal, internal, or a combination of them. The source can be an important factor in the clinical outcome of refractive surgery. For refractive surgery, various indices allow determination of the corneal vertex, the pupil center, and the photopic and mesopic pupil centers. Preoperatively, this information is essential to determine the center of the treatment; postoperatively, these indices can be used to determine the centration of the procedure.

OPD-Scan III Specifications

Wavefront aberrometer: Measurement principle is Automated objective refraction (dynamic skiascopy). Spherical power range is from −20.00 to+22.00 D. Cylindrical power range is from 0 to ±12.00 D and axis range from 0 to 180°. Measurement area is from 2.0 to 9.5 mm (7 zone measurement). It analyzes 2,520 points (7 × 360). OPD, Internal OPD, Wavefront, Zernike graph, PSF, MTF graph, Visual Acuity are different maps of OPD III.

1. Irregularity: With separation into Total, Corneal and Internal components allows determination of the source of the optical problems.
2. PSF images of OPD, Axial and Internal OPD map simulate objective retinal visual quality from each component of the eye.
3. Corneal Spherical Aberration aids in the selection of aspheric IOLs and contact lenses.
4. Color coded Classification Indices help identify post-LASIK corneas and Keratoconus.
5. The Astigmatism index aids the implantation of toric IOLs such as incision placement and lens alignment.
6. A retroillumination image of cataracts captured during the OPD exam allows better understanding of pupillary effects on vision (Fig. 8).

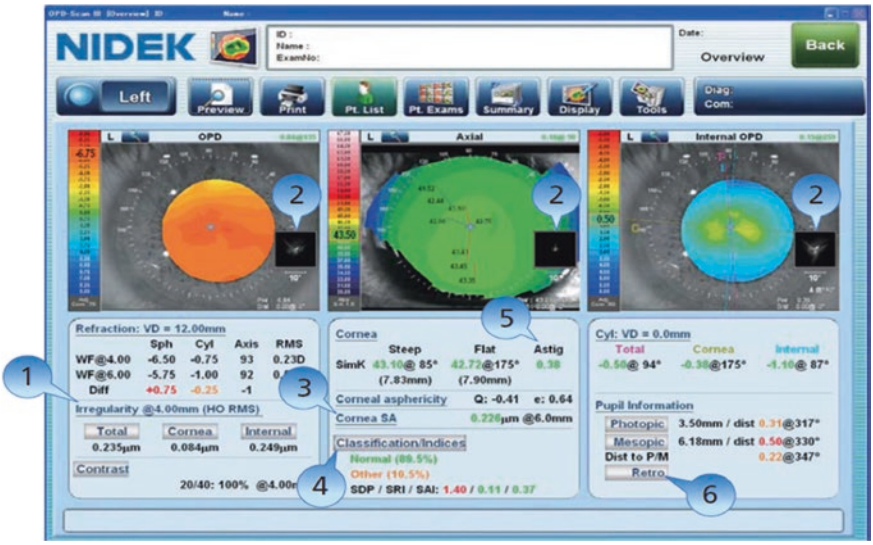

Fig. 8 An overwiew map of OPD scan III

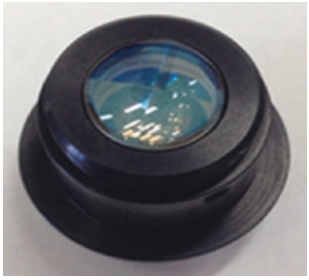

Fig. 9 Pyramidal optical component

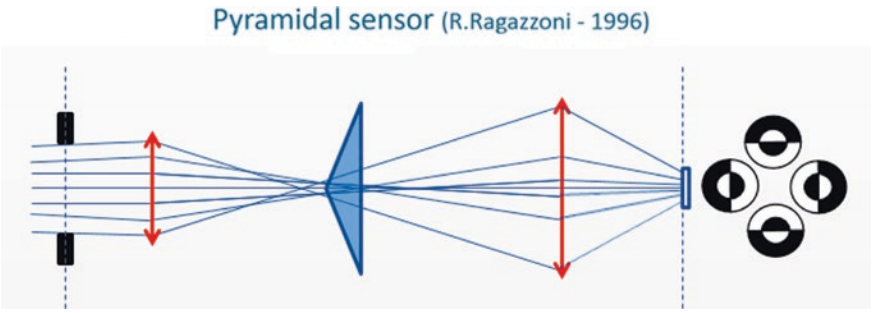

Fig. 10 Pyramid wavefront sensor

PERAMIS Aberrometer

SCHWIND PERAMIS is a multifunctional combination of a state-of-the-art topograph and aberrometer. The measurement of the cornea and total eye are analyzed in a single measuring procedure.

PERAMIS (perami) comes from the old Egyptian language and means PYRAMID. The measuring principle of the new SCHWIND PERAMIS is a **pyramidal** wavefront sensor that measures with 45.000 measuring points the ocular wavefront aberrations (Fig. 9).

The Pyramid Wavefront Sensor (PWS) is based on an oscillating pyramidic optical component, placed at the focal plane of the aberrated optical system e.g., a telescope in astronomical adaptive optics (Fig. 10).

A **pyramid wavefront sensor** is a type of a wavefront sensor. It measures the optical aberrations of an optical wavefront. This wavefront sensor uses a pyramidal prism with a large apex angle to split the beam into multiple parts at the geometric focus of a lens. A four-faceted prism, with its tip centered at the peak of the point spread function, will generate four identical pupil images in the absence of optical aberrations. In the presence of optical aberrations, the intensity distribution among the pupils will change. The local wavefront gradients can be obtained

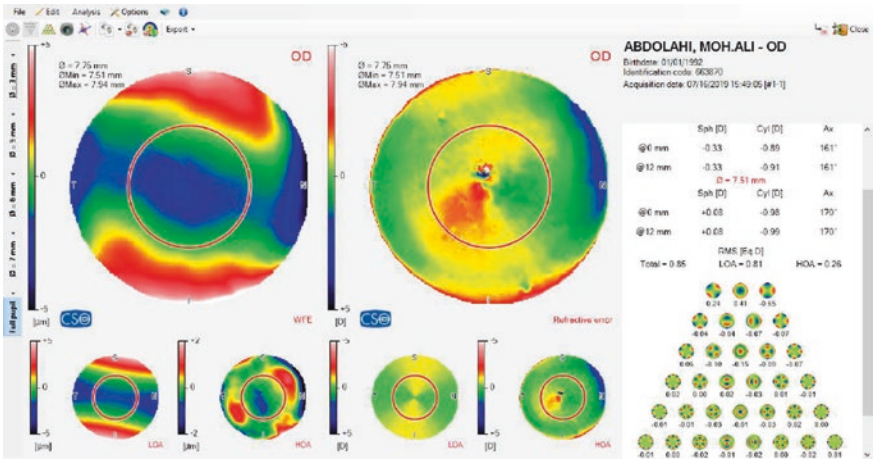

Fig. 11 PERAMIS wavefront display

by recording the distribution of intensity in the pupil images. The wavefront aberrations can be evaluated from the estimated wavefront gradients (Fig. 10) [22].

An important advantage of this sensor for the eye is the easy adaptability to the variations in the range of the aberrations one can expect in the human eye optics: from very little aberrated normal eyes to extremely aberrated eyes in patients with pathological corneas. The dynamic range of the sensor can be modified simply by changing the extension of the source on the retina. The traditional Zernike-based maps out to the eighth order can be derived (Fig. 11).

Sirius

This device combines Scheimpflug and Placido ring information for evaluating the cornea and anterior segment. It analyses more than 100,000 points in 22 rings in 12 mm of cornea only in one second. It evaluates corneal aberrations and show them by zernike polynomials. Corneal aberration is shown in normative data for each HOA and by green, yellow and red colours (Fig. 12).

The normative data is shown in different pupil size. By using of optical quality summary menu, data related to MTF and PSF depending on amount of HOA are shown (Fig. 12).

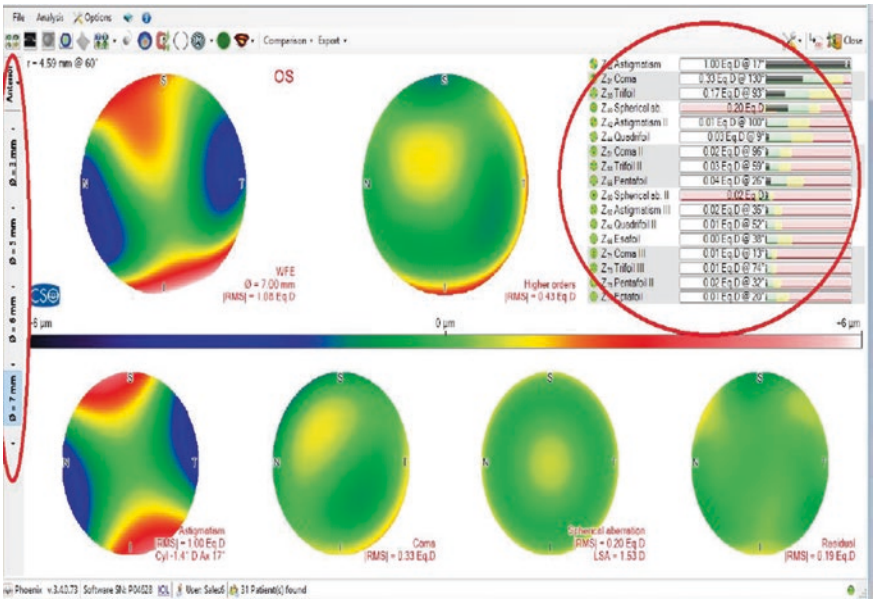

Fig. 12 Sirius corneal aberration of a keratoconus patient that has high RMS of coma

iTrace Aberrometer (Tracey Technologies, Houston, Tx)

The iTrace System (Tracey Technologies, Houston, Tx) is uniquely designed to combine Placido corneal topography with a ray tracing aberrometer to measure quality of vision in a patient [23].

The ray tracing method uses a laser beam parallel to the line of sight through the pupil. Local aberrations in the path of the laser beam through the cornea and the internal structures like crystalline lens cause a shift in the location of image on the retina [14, 24, 25].

The iTrace (Tracey Technologies, Houston, Tx) uses this fundamental principle of Ray Tracing where a sequential series of infrared beams on the order of 100 microns and a 785 nm wavelength each is projected into the entrance pupil parallel to the eye's line of sight. Once the position of point 1 has been determined the laser beam is shifted to another position, and the localization of the next point in the retina is registered. This process continues until 64 laser beams have been projected through the entrance pupil 4 times each (256 points) at high speed (approximately 250 milliseconds) [26].

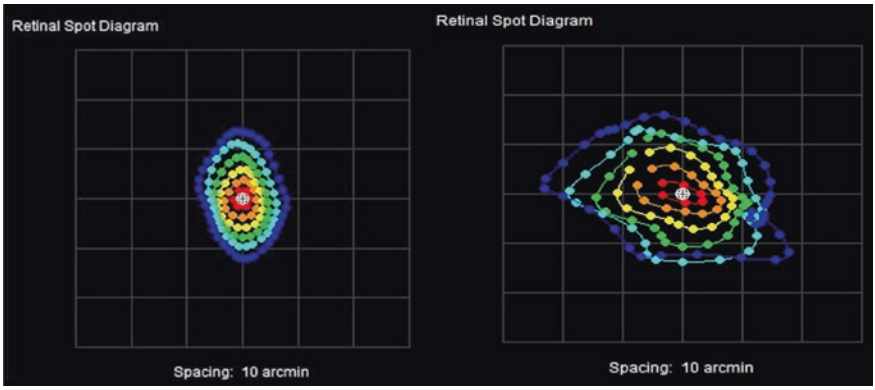

Fig. 13 RSD in a normal patient (left) and another Pellucid Marginal Degeneration patient (right)

Local aberrations at the beam's entry point on the cornea or the lens cause a shift in the location on the retina with respect to a position of reference. When a set of points is sequentially projected in the entrance pupil a **retinal spot diagram** (RSD) is created (Fig. 13). The RSD contains all the information related to the patient's refraction, aberrations and point spread function(PSF) and MTF (Modulation Transfer Function) maps. Analyzing the RDS's morphology, we obtain an idea of the degree of the wavefront's qualitative aberration. The smaller the RSD the higher the concentration of laser beams that reaches any point of the retina (Fig. 13).

From RSD, PSF and MTF maps can be calculated.

There are different maps in iTrace aberrometer that determine optical quality of the patients [26].

Overview Screen of the WF Verification Display

The WF Verification Display shows all the patient's data on limbal diameter, pupil size and scan diameter (Fig. 14).

This screen shows the number of non-measure points. If they are less than nine they are displayed in yellow and if they are more than nine they appear in red and the exam is invalid. Occasionally, those unmeasured points are due to an opacification (corneal scar or cataract). Horizontal and Vertical Point Profile show the position of each point that reflects on the retina, taking the centre of each profile in the X and Y-axis. It gives us an image of the quality of the laser's signal captured in our measurement; if the profile is irregular the measurement is incorrect. Distorted RSD in this map indicates an error in the measurement or presence of a high-aberrated eye [26].

Fig. 14 Overview screen of the WF verification display

Multi-zone Refraction Analysis

Based on Zernike coefficients, conventional refractive indexes (sphere and cylinder) are calculated by iTrace. It determines sphere and cylinder of the patient in different pupillary diameter (Multi-zone refraction analysis). The value displayed in green (Tracey Refraction Number) is achieved from the measurement at 4 mm or the greatest measurement if the pupil is less than 4 mm (Fig. 15) [23]. The smaller the HOA, the more homogeneous is the multi-zone refraction analysis in the different optic zones. The iTrace measurement range is of –15 D to +15 D sphere and 10 D cylinder.

Wavefront map Total and High-order Aberrations (HOA) (Wavefront Total and Wavefront HOA): These maps show colour-coded wavefront aberrations of the eye measured in microns of error. The error can be positive or negative. Measurements are taken from the entrance pupil.

Warm colours indicate that the wavefront is in front of the reference plane and blue colours indicate that the wavefront is retarded in relation to this plane reference (Fig. 16).

RMS (Root Mean Square) map: A total RMS value for the total aberration of the eye and a specific value of RMS for each Zernike term of the eye aberrations can be achieved (Fig. 17).

Total refractive and HOA refractive mapss These measurements show the whole eye and not only to the corneal power. Emmetropia is represented in green. Myopia in red and hypermetropia in blue (Fig. 18). This map in combination with

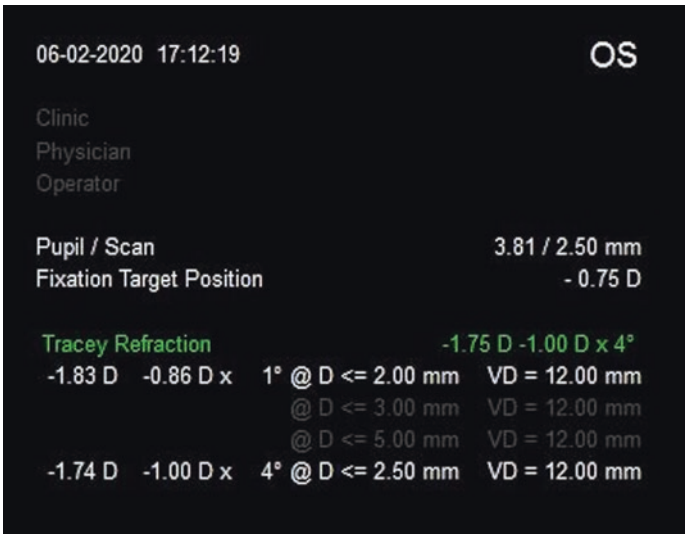

Fig. 15 Multi-zone refraction analysis

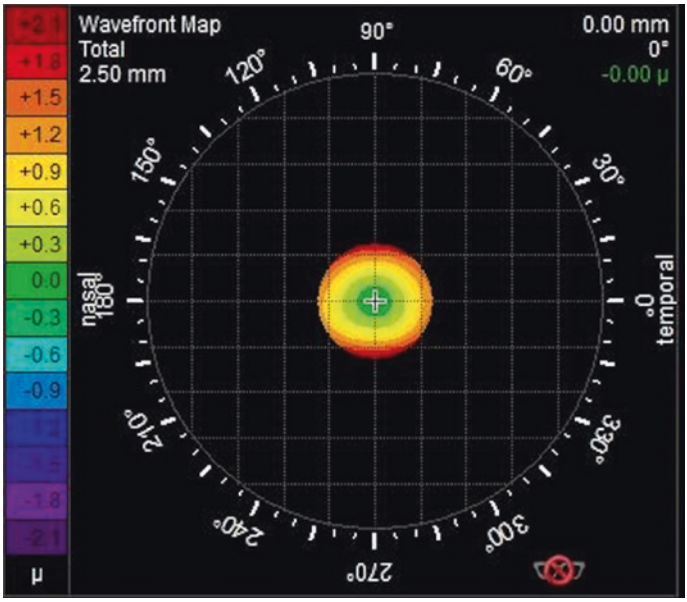

Fig. 16 Wavefront map total

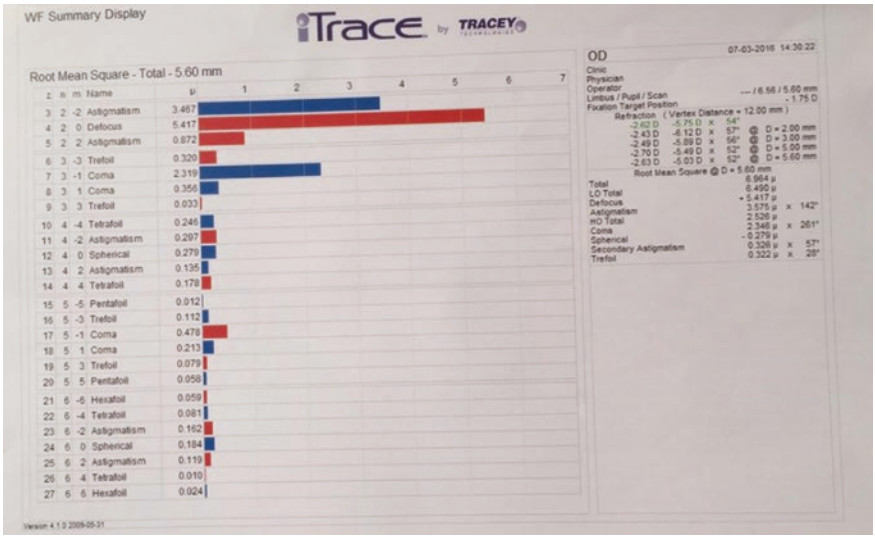

Fig. 17 RMS display

the topographic data can indicate if the astigmatism is totally corneal or if it has a lenticular component.

Zernike polynomials: This map shows a detailed analysis of the specific aberrations in an eye. The iTrace shows the Zernike polynomials up to the 6th order (27 terms) and can show the totals for the eye («Total»), only the corneal and the difference between the corneal and the totals (internal optics) (Fig. 19).

Aberration of internal optics analysis. Wavefront combined analysis and corneal topography: Through corneal topography the corneal aberrations map can be mathematically generated and these aberrations can be adequately subtracted from the total aberrations of the entire eye (Fig. 20). The resulting difference mainly represents the aberrations of the internal optics; in this way aberrations from the cornea can be separated from those from the internal part of the eye. Most of the aberrations of the internal optics are induced by the crystalline lens.

These differentiation can help us in some clinical subjects. For example: If a patient has high total aberrations we can identify if the refractive procedure we are planning is better in the cornea or in the crystalline lens, depending on which one is more.

With the iTrace system we able to analyse topographic and aberrometric data.

Wavefront analysis: There are two displays: (1) Visual Function Analysis (VFA Summary Display) shows the Refraction Map HO Total or the Wavefront HO Total (depending on which one we select). This map shows refraction in different diameters, the RMS, PSF, Snellen letter and Potential Visual Complaints

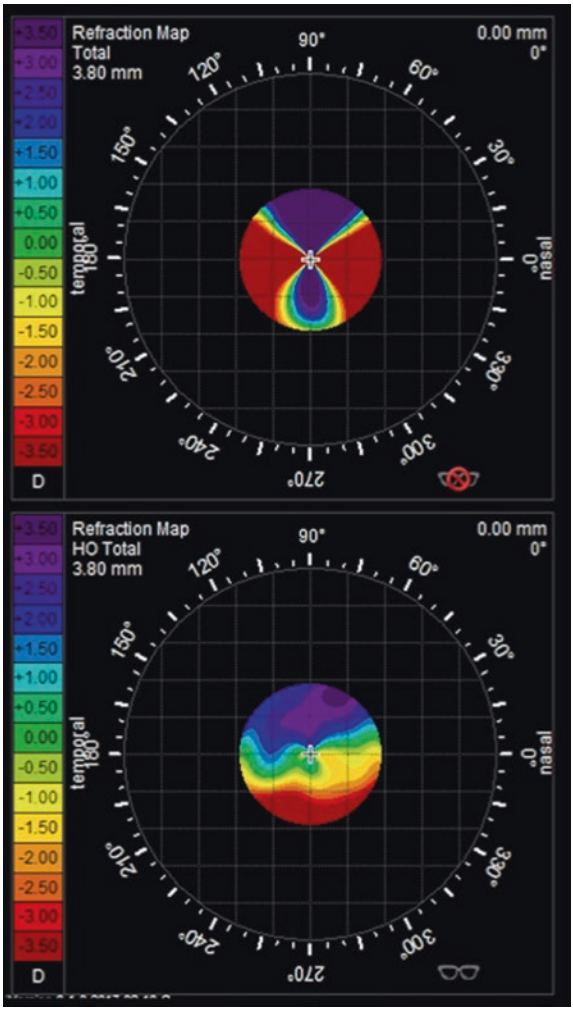

Fig. 18 Total refractive and HOA refractive map

(nocturnal myopia, halos, glare, defocus, double vision). These symptoms are measured with 1–3 crosses depending on their intensity (Fig. 21).

(2) **Wavefront comparison map**: It compares two wavefront maps in one patient in different time. We can compare two wavefront maps in one patient, especially when we want to compare the status of the aberrations before and after the surgery (Fig. 22).

iDesign Aberrometer (AMO company): The Hartmann-Shack sensor measures the refractive error of the eye. The instrument evaluates the deflection of rays emanating from a small beam of light projected onto the retina. The system incorporates a fogged fixation target to control the eye's natural accommodation during the imaging.

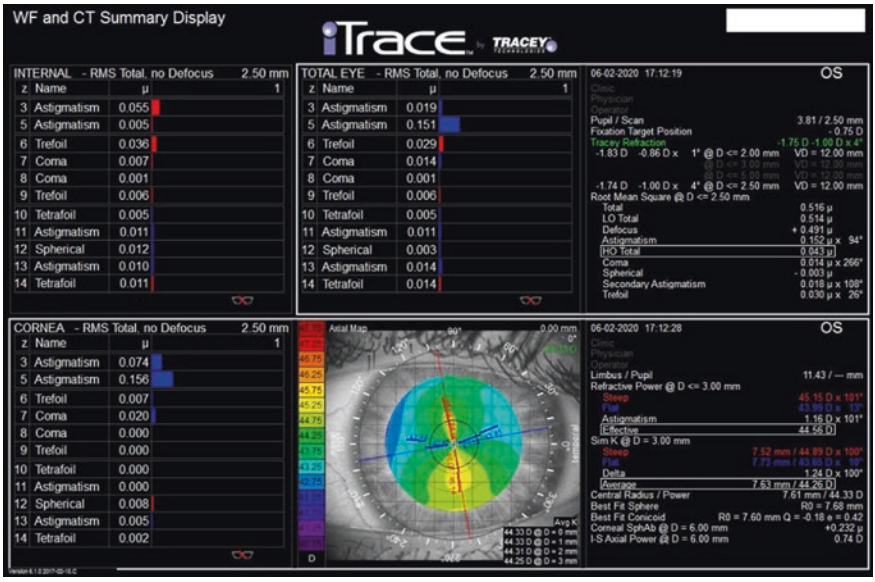

Fig. 19 Zernike polynomials display

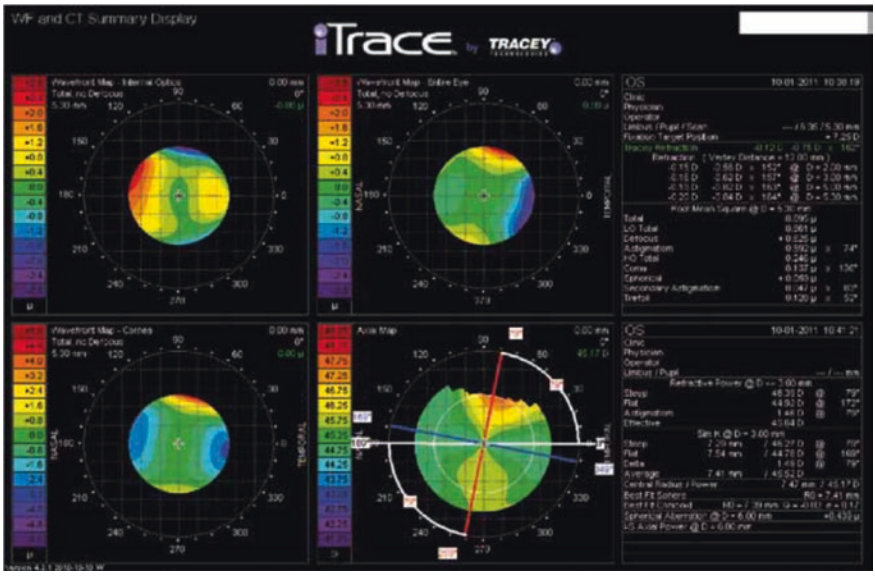

Fig. 20 Wavefront combined analysis and corneal topography

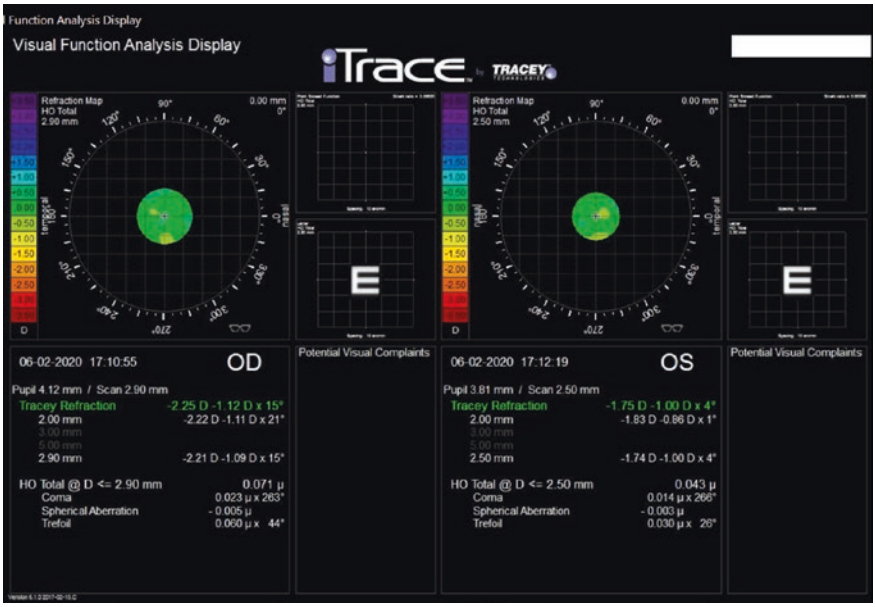

Fig. 21 Visual function analysis display

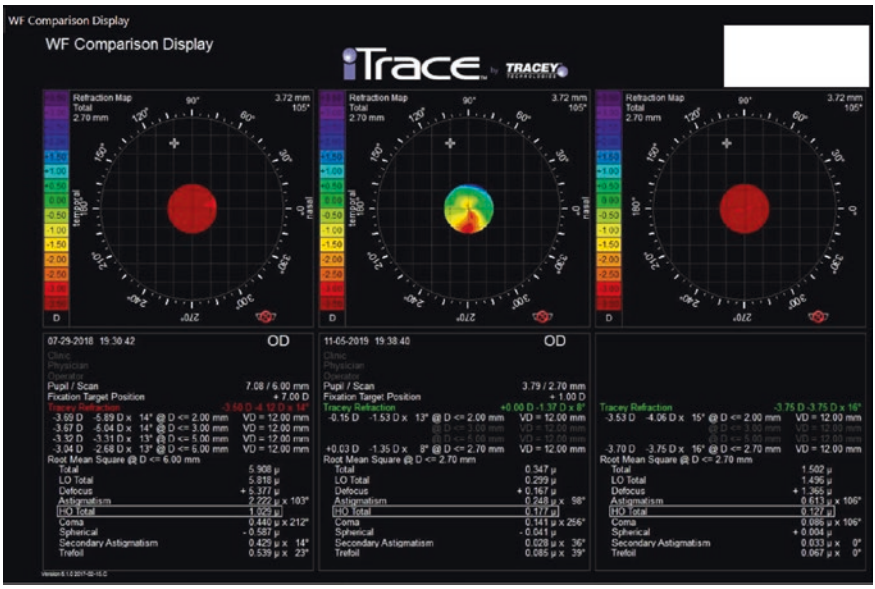

Fig. 22 Wavefront comparison display

The corneal topography function applies a spot reflection-based approach where the ***iDesign***System analyzes the spot pattern image on the cornea and computes the corneal elevation and corneal power. The system displays the refractive errors and wavefront aberrations as the optical path difference (OPD) between the measured outgoing wavefront and the ideal plane wave. The ***iDesign***System software subtracts the sphero-cylindrical refractive errors from the wavefront errors map and displays the higher order aberrations as OPD errors. Regions of the pupil with positive OPD are in front of the ideal plane wave and areas with negative OPD are behind the ideal plane wave.

View options can be set for the following maps/images:

- Eye Image (Scotopic and Photopic Iris images with Pupilometry data)
- Wavefront Error and Wavefront Correction Maps
- Wavefront Difference Maps
- Point Spread Functions Image
- Zernike Coefficients and Differences Table
- Corneal Topography Maps
- Corneal Topography Difference Maps
- Custom View (displays up to four views associated with one exam).

References

1. Mugler C. Les origines de la science grecque chez Homère, Paris; 1964.
2. R. Rashed. Le “Discours de la lumière” d’Ibn al-Haytham (Alhazen): Traduction française critique. Rev Histoire Sci Appl.1968;21:197-24.
3. Cade F, Cruzat A, Paschalis EI, Santo LE, Pineda R. Analysis of four aberrometers for evaluation lower and higher order aberrations. Public Lib Sci ONE. 2013;8:1–7.
4. Lin HZ, Chen C, Lee Y Effect of pharmacologic pupil dilation with tropicamide and phenylephrine on wavefront measurements. Taiwan J Ophthal. 2013;3:62–6.
5. Yanoff M, Duker JS Ophthalmology, 3rd ed. Beijing: Elsevier Heath Sciences; 2009. p. 33, 53, 132, 166.
6. Phillip K, Martinez A, Ho A, et al. Total ocular, anterior corneal and lenticular higher order aberrations in hyperopic, myopic and emmetropic eyes. Vis Res. 2012;52:31–37.
7. Barnes-Svarney P. The handy math answer book. Michigan: Visible Ink Press p; 2000. p. 150.
8. Dai G Wavefront optics for vision correction. Washington: SPIE Press; 2008. p. 26, 43–53.
9. Roorda A. A review of basic wavefront optics. In: Krueger RR, Applegate RA, MacRae SM, editors. Wavefront Customized Visual Correction; the Quest for Super Vision II. NJ, Slack: Thorofare; 2004. p. 9–18.
10. Thibos LN. Wavefront data reporting and terminology. J Refract Surg. 2001;17(5):S578–83.
11. Thibos LN. Principles of Hartmann-Shack aberrometry. J Refract Surg. 2000;16:S563–5.
12. Durrie DS, Stahl ED. Comparing wavefront devices. In: Krueger RR, Applegate RA, MacRae SM, editors. Wavefront customized visual correction: The quest for super-vision II. Thorofare (NJ): Slack; 2004. p. 161–8, 18.
13. Mrochen M, Kaemmerer M, Mierdel P, et al. Principles of Tscherning aberrometry. J Refract Surg. 2000;16:S570–1.

14. Molebny VV, Panagopoulou SI, Molebny SV, Wakil YS, Pallikaris IG. Principles of ray tracing aberrometry. J Refract Surg. 2000;16:S572–5.
15. Gualdi L, Cappello V, Giordano C. The use of NIDEK OPD Scan II wavefront aberrometry in toric intraocular lens implantation. J Refract Surg. 2009; 25(suppl 1):S110–5.
16. Bille JF, Harner CFH, Lösel F. Aberration-free surgery: New frontiers in vision. Heidelberg: Springer; 2004. p. 7–8.
17. Hamam H. New metric for optical performance. Opt Vis Sci. Applet: https://www.umoncton.ca/genie/electrique/Cours/Hamamh/Optics/Aber/Illustrations.htm (to appear).
18. Liang CL, Juo SH, Chang CJ. Comparison of higher-order wavefront aberrations with 3 aberrometers. J Cataract Refract Surg. 2005;31:2153–6.
19. Cheng X, Himebaugh NL, Kollbaum PS, Thibos LN, Bradley A. Test-retest reliability of clinical Shack-Hartmann measurements. Invest Ophthalmol Vis Sci. 2004;45:351–60.
20. Radhakrishnan H, Charman WN. Age-related changes in ocular aberrations with accommodation. J Vis. 2007;7:111–21.
21. Cervino A, Hosking SL, Montes-Mico R, Bates K. Clinical ocular wavefront analyzers. J Refract Surg. 2007;23:603–16.
22. Ragazzoni R. Pupil plane wavefront sensing with an oscillating prism. J Mod Opt. 1996;43(2):289–93.
23. Wakil JS, Padrick TD, Molebny S. The iTrace combination corneal topography and wavefront system by Tracey technologies. In: Corneal topography in the wavefront era. SLACK Inc. p. 177–188
24. Molebny VV, Pallikaris IG, Naoumidis LP, et al. Retinal tray tracing technique for eye refraction mapping. Proc SPIE. 1997;2971:175–83.
25. Molebny VV, Pallikaris IG, Panagopoulou SI, Brandau J, Wakil JS. Tracey retinal ray tracing technology. In: Customized corneal ablation. The quest for supervision. SLACK Inc. p. 193–6.
26. Alfredo Castillo Gómez, MD, PhD; Antonio Verdejo del Rey, OD et al. Principles and clinical applications of ray-tracing aberrometry (Part I). J Emmetropia. 2012;3:96–110.

Retina Imaging

Optical Coherence Tomography (OCT)

Fedra Hajizadeh and Mohammad Zarei

Optical coherence tomography (**OCT**) is an imaging technic that was first applied for eye length measurements in 1988 and then in 1991 for creating in vivo retinal images. During ensuing years, it became an essential part of ocular examination in most eye clinics. It uses low coherence interferometry technique to create two or three-dimensional in vivo images of ocular structures. Optical coherence tomography utilizes near infrared laser waves that can penetrate ocular media with minimal scattering to achieve high quality images. The axial resolution is high enough (2–3 microm) to make OCT the imaging method of choice for evaluating retinal microanatomy in many conditions. Using near infrared light and being a noninvasive technique, OCT is generally considered a harmless imaging method.

Introduction of OCT has revolutionized the diagnosis and classification of retinal diseases as well as glaucoma and—to some extent—anterior segment diseases. All parts of retina and optic disc, some parts of choroid, and even sclera can be visualized by OCT.

Similar to ultrasound imaging, OCT imaging works by sending waves through the eye and then studying the pattern of reflected waves. However, in contrast to ultrasound, electromagnetic waves travel so fast that direct measurement of time-delay of waves reflected from a surface (to measure the depth of the reflecting surface) is impossible. To circumvent this problem, OCT technology uses interferometry to measure the depth of reflecting surface. An interferometer, splits the light from a single source into two beams and send each of them into a separate path. One beam—the reference beam—is sent to a mirror with a known distance from the splitter. The second beam—the probe beam—is sent into the eye to

F. Hajizadeh (✉)
Noor Ophthalmology Research Center, Noor Eye Hospital, Tehran, Iran
e-mail: fhajizadeh@noorvision.com; fedra_hajizadeh@yahoo.com

M. Zarei
Farabi Eye Research Center, Tehran University of Medical Sciences, Tehran, Iran
e-mail: mzareiran81@gmail.com

M. Mohammadpour (ed.), *Diagnostics in Ocular Imaging*,
https://doi.org/10.1007/978-3-030-54863-6_12

be reflected from ocular surfaces. Back-reflected beams from both arms meet each other in the interferometer and "interfere" with each other, forming the interference fringe. Based on degree of phase difference, interference between two beams can be constructive (forming bright bands in fringe), destructive (forming dark bands in fringe), or anything in between. The key point is that the degree of phase difference between two beams is a function of difference between the length of reference path (which is known) and the depth of reflecting ocular surface (which is not known). This means that by analyzing the interference pattern and considering the known length of reference path, the depth of reflecting surface can be calculated.

The first generation of OCT devices used time-domain (TD) technology. In this technology, the reference mirror moves to modulate the length of reference path, which leads to changes in the interference pattern. By analyzing these changes, the depth of a reflecting ocular surface and intensity of reflected light from that surface can be measured.

Although revolutionary for its time, TD-OCT could not provide the clinicians with details needed in many clinical conditions. Next generation of OCT was developed based on Fourier-domain technology (FD-OCT). Unlike TD-OCT, instead of mechanical scanning by a mirror, FD-OCT uses spectral information to obtain data regarding depth of reflecting tissues and intensity of reflected light (Fig. 1). This technology is used in spectral-domain OCT (SD-OCT) and swept source OCT (SS-OCT) devices.

Spectral-domain OCT uses superluminescent diodes (wavelength of 800–870 nm). By changing the zero point (**point** of maximum sensitivity) in SD-OCT machines toward RPE and choroid (enhanced depth imaging) better images of deeper structures such as choroid can be obtained. Brightest or most reflective surface on OCT images lies at the level of zero point. So we can guess the zero point location in OCT images.

Swept source OCT (SS-OCT) is the next generation of OCT technology, which uses longer wavelength (>1000 nm). By using longer wavelength visualization of deeper structures is improved. It seems that EDI-SD-OCT and SS-OCT have similar tissue depth penetration (around 500 μm).

Interpretation of a Retinal OCT Image

Normal OCT

Having a good knowledge of normal retinal OCT is a prerequisite for interpretation of abnormal retinal OCT.

Figure 2 demonstrates a SD-OCT image of normal macula.

The inner most layer is internal limiting membrane (ILM) formed by the end-feet of Müller cells and astrocytes. Retinal nerve fiber layer (RNFL)—the second most inner layer—is formed by axons of ganglion cells; with the thickest part

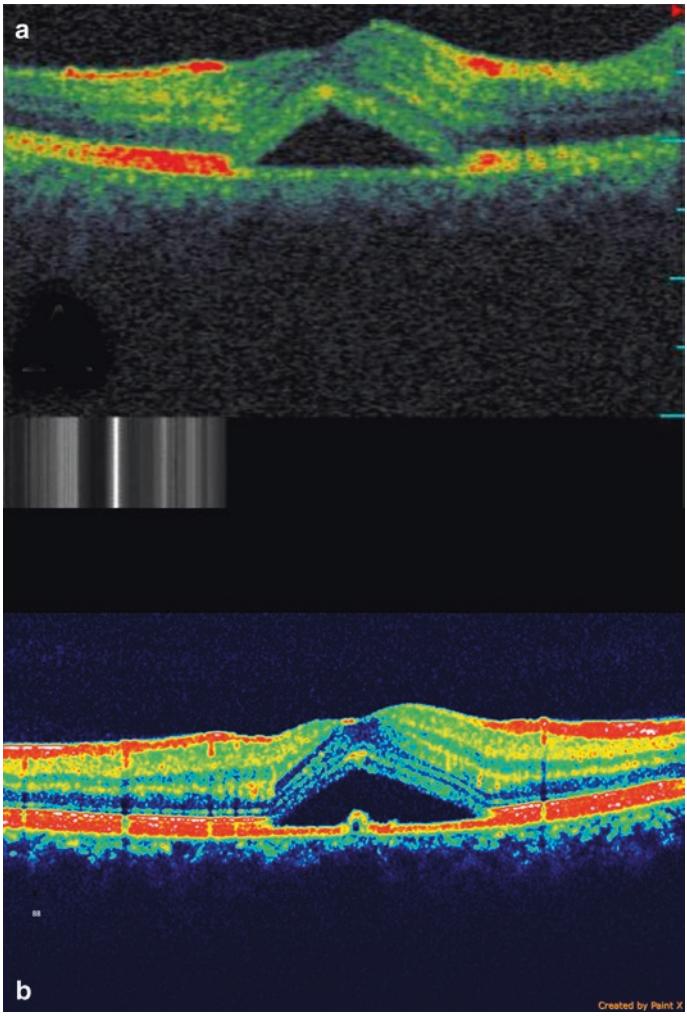

Fig. 1 **a** TD-OCT of a patient with CSR. **b** FD-OCT of the same condition

adjacent to optic disc. These axons are main constituent of optic nerve, optic tract and chiasm.

Retinal nerve fiber layer thickness profile is a circular scan around optic disc. In normal eyes, the thickest part is the inferior temporal part, followed by the superior temporal, superior nasal, and inferior nasal, respectively. Assessment of RNFL is helpful for detection of early glaucoma or diagnosis of other optic neuropathies and monitoring their progression. Outside the RNFL, lies ganglion cell layer (GCL); a neuronal layer that receives visual signals from photoreceptors via amacrine and bipolar cells. It has been suggested that evaluation of macular GCL may

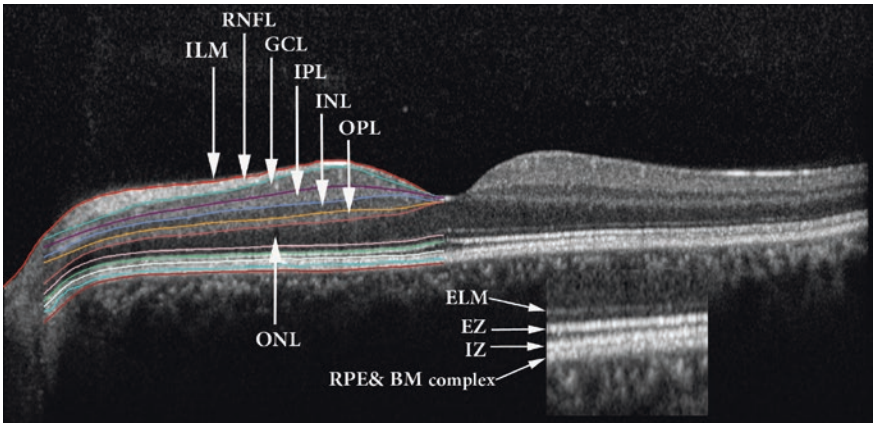

Fig. 2 Spectral domain OCT image of normal macula. ILM = Internal limiting membrane, RNFL = Retinal nerve fiber layer, GCL = Ganglion cell layer, IPL = Inner plexiform layer, INL = Inner nuclear layer, OPL = Outer plexiform layer, ONL = Outer nuclear layer, ELM = External limiting layer, EZ = Ellipsoid zone, IZ = Interdigitation zone, RPE&BM complex = Retinal pigmented epithelium and Bruch's membrane complex

find applications in diagnosis and monitoring of glaucoma and some neurological diseases, e.g. multiple sclerosis.

Inner plexiform layer (IPL) is a crowded networks dendrites of ganglion cells, making connections to inner nuclear layer cells. Inner plexiform layer appears as a band of medium reflectivity beneath the GCL (Fig. 2). IPL evaluation along with GCL proved to be useful in diagnosis and follow-up of patients with glaucoma and other neurological disorders. The IPL is the outermost part of ganglion cell complex (GCC) which is defined as three innermost retinal layers together: RNFL, GCL and IPL. Changes in GCC may be good indicators for early detection of glaucoma, especially in atypical conditions.

Inner nuclear layer (INL) is a hyporeflective layer outside the IPL and is made by the bipolar, horizontal and amacrine cells. Predictive value of microcystic edema and other changes in this layer have been studied in neurological diseases and optic neuritis. Outer plexiform layer (OPL)-a band of medium reflectivity beneath IPL-consists of a dense arrangement of synapses between horizontal cells and photoreceptor inner segments. Outer nuclear layer (ONL) contains nuclei of rods and cones; Its health is directly related to visual performance.

Outside the ONL, there are three to four discrete hyper-reflective bands on OCT (small magnified islet in Fig. 2). The innermost band-the least hyperreflective—is external limiting membrane (ELM). External limiting membrane is not a true membrane but a fine line of medium reflectivity formed by numerous desmosomes between photoreceptors and Müller cells. Integrity of ELM is associated with visual acuity.

Outside the ELM, is the ellipsoid zone (EZ) which is assumed to correspond to inner segment/outer segment (IS/OS) junction. The health of this zone is also strongly related to visual acuity.

Interdigitation zone (IZ) is the third band. Whether or not this zone corresponds to tips of cone outer segments or is equivalent to "Verhoeff membrane" (consisting of zonulae occludentes of apical regions of RPE cells), is not established. However, this zone is linked to photoreceptors function and visual acuity.

The outermost band is RPE and Bruch's membrane complex.

There is a hyporeflective zone between the ELM and EZ that is called myoid zone, which is assumed to comprise of abundant mitochondria.

To present a topographic representation of macular thickness, it is usual to use an ETDRS grid overlay. In a normal OCT-derived topographic maps of macula, foveal center is the thinnest point. The thickest macular zone is a ring of 3 mm diameter off the foveal center. From this ring toward periphery, retinal thickness is progressively reduced. The temporal quadrant is thinner than the nasal quadrant. Normal mean values of retinal thicknesses in topographic OCT maps, varies between different OCT devices: foveal center point (FCP) thickness, average macular thickness (average macular thickness over the ETDRS grid area) and central subfield mean thickness has been reported to be 141–225 μm, 260–280 μm, and 193–271 μm, respectively (Fig. 3).

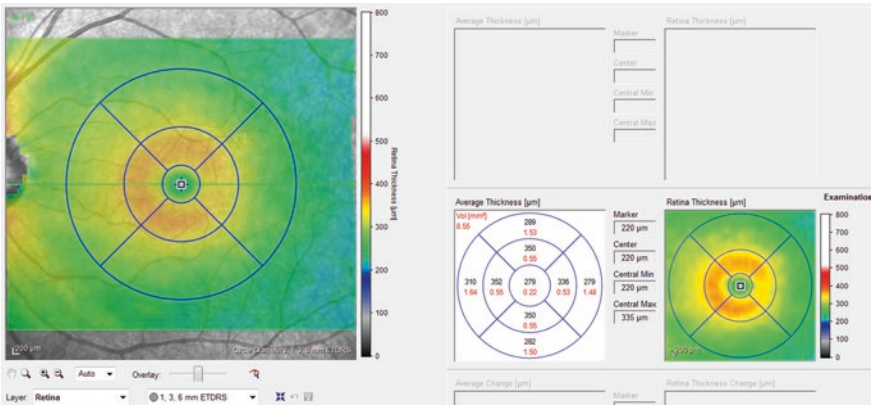

Fig. 3 Demonstrates a normal macular topographic map. Central subfield thickness is equal to mean retinal thickness in the central 1 mm-diameter circle (the small central circle) and foveal central point (FCP) thickness is thickness at the center of central circle

Basics in OCT Image Interpretation

While examining a macular OCT image, first thing to find is the foveal center. In normal subjects, it is the thinnest point and is expected to be found at the bottom of foveal depression (Fig. 4).

An efficient approach to evaluate macula with OCT is to get a raster and a radial scan as well as wide field scan and check all scans to rule out any abnormality. Familiarity with different parts of normal OCT image of posterior fundus is of utmost importance (Fig. 5).

After finding the fovea, integrity of all retinal layers and RPE in all sections should be checked. Choroid should also be searched for any pathology.

In new generation OCT machines, obtaining wide field images (55° rather than 30°) is possible (Fig. 6). The advantages of wide field OCT are the ability to measure and demonstrate large, elevated lesions, especially in choroid and more peripheral retina.

In contrast with normal fundus, locating the fovea in OCT of pathologic conditions may not be easy. There are some clues to find the central fovea in abnormal subjects. If the foveal depression cannot be detected in the first attempt, it should be checked if the scan line has truly crossed through the foveal center. Then the area with the thickest ONL should be located which usually corresponds to centeral fovea (Fig. 7).

With the advent of new softwares, almost all new versions of OCT devices can segment all retinal layers separately and provide thickness maps for each layer (Fig. 8).

Clinically speaking, ganglion cell layer and retinal nerve fiber layer thickness maps maybe the most important (Figs. 9 and 10).

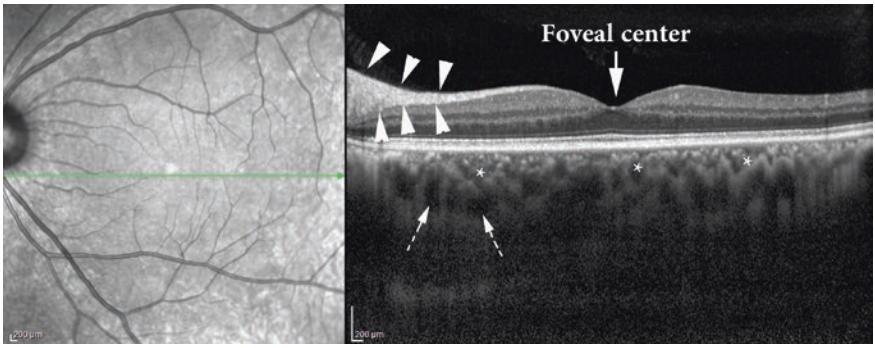

Fig. 4 The normal fovea with marked central foveal depression. Even without SLO image, in horizontal cross-sectional OCT, the laterality of the image can be easily guessed by evaluating the thickness of RNFL layer (between arrowheads). The thickest RNFL is near the optic disc; therefore, this image belongs to the left eye. This image also shows the small choroidal vessel layer (Sattler layer; Stars) and large choroidal vessel layer (Haller layer; dashed arrows)

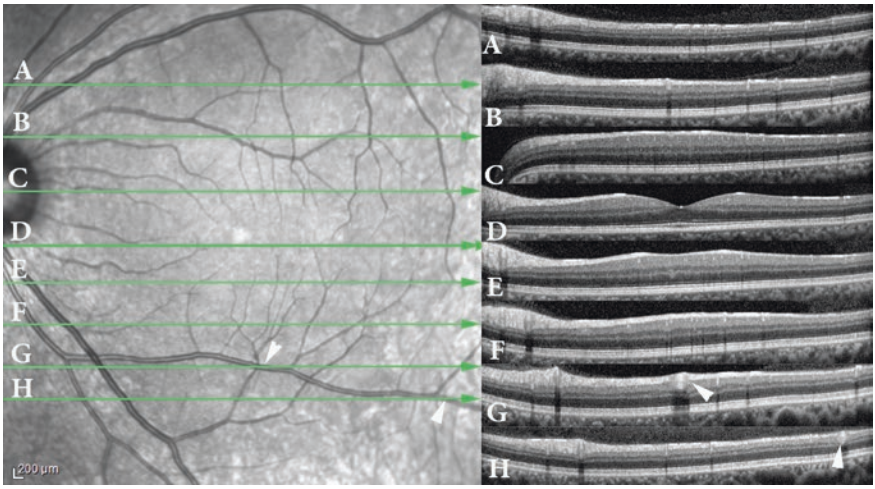

Fig. 5 Raster cross sectional images of the posterior pole. Note the differences between various sections of macula. Retinal vessels crossing the OCT section create small vertical hyper-reflective foci (white arrowheads) with dark shadowing over the underlying retina

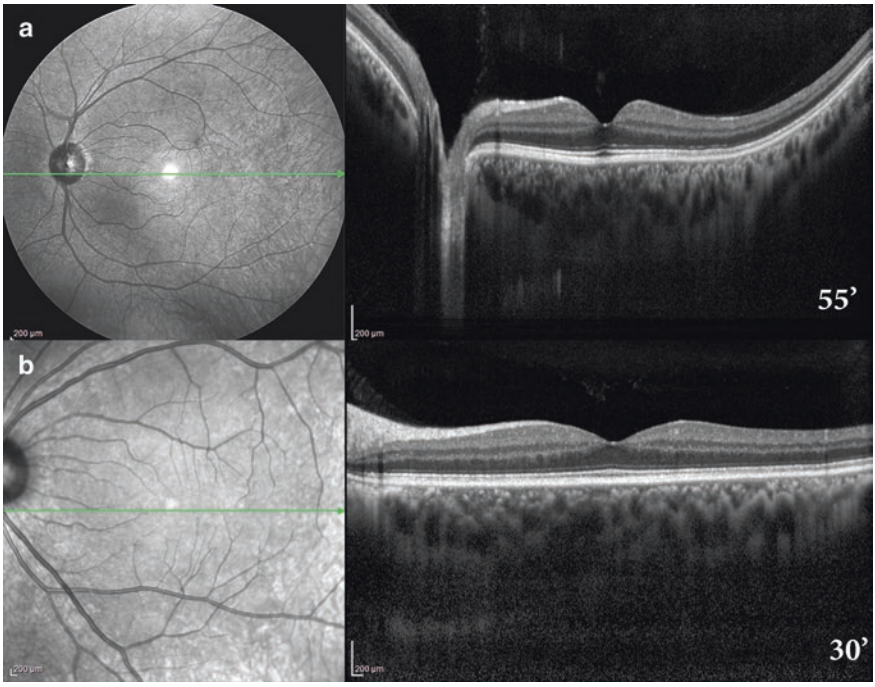

Fig. 6 **a** Wide field (55°) versus **b** conventional field (30°) OCT images

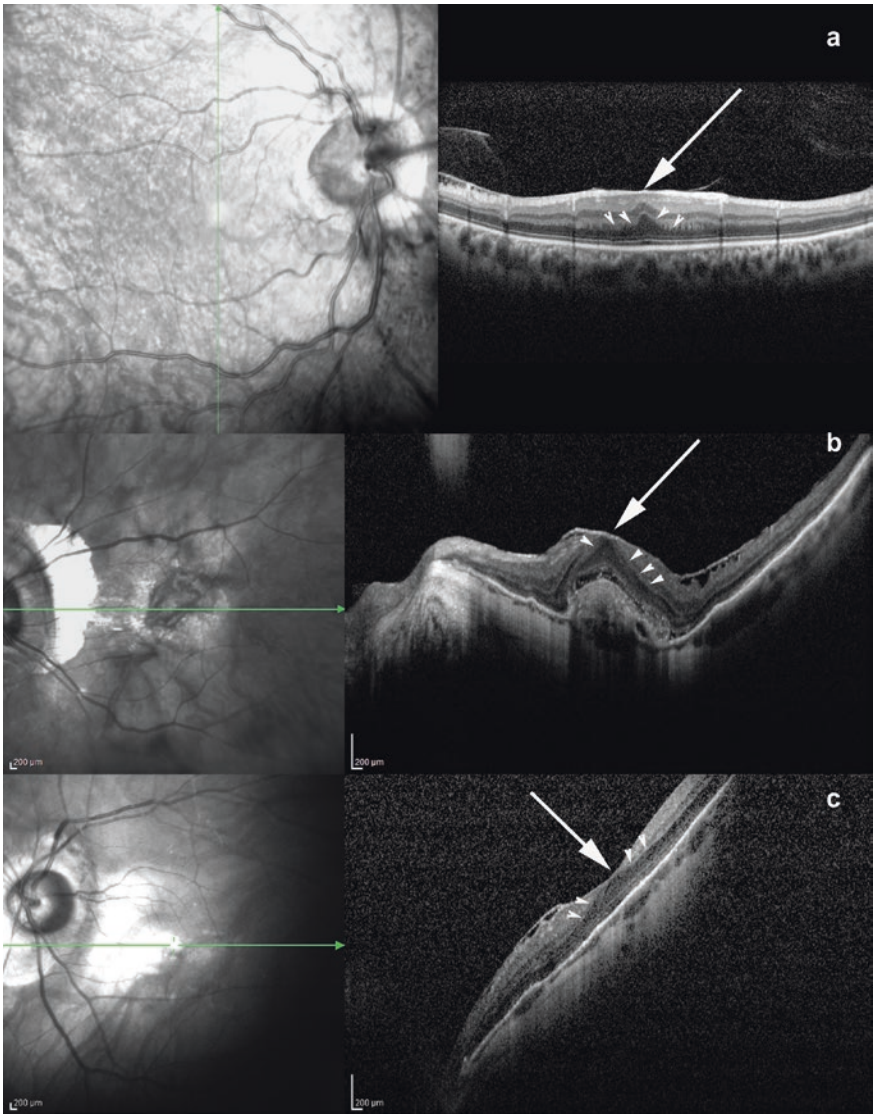

Fig. 7 **a** In tractional maculopathy and epiretinal membrane sometimes the foveal center cannot be found in the first attempt. The location with the thickest ONL (white arrow) usually corresponds to central fovea. **b** In the presence of central foveal lesion such as neovascular membrane by trailing the inner aspect of ONL (white arrowheads) and finding its thickest point, fovea can be localized. **c** In high myopic eyes, distortion and thinning of retinal layer may sometimes result in foveal flattening. In such cases, by following the inner aspect of ONL, foveal center can be found, even in the presence of a fine epiretinal membrane

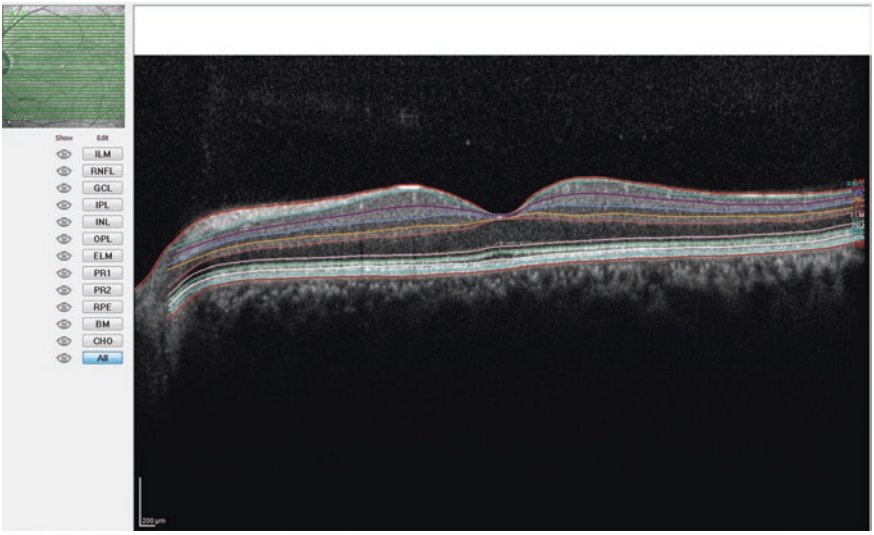

Fig. 8 Segmentation of each retinal layers with differentiating color-coding

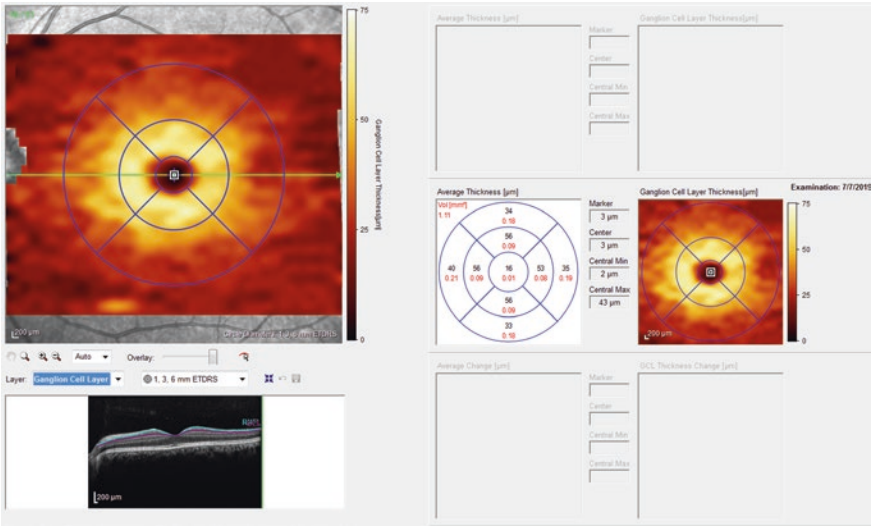

Fig. 9 Ganglion cell layer thickness map in a normal subject (Heidelberg Engineering Spectralis SD-OCT). The doughnut pattern, centered at fovea is characteristic. Parafoveal region is the thickest zone. Some OCT devices (Carl Zeiss Meditech Cirrus HD-OCT 5000) provides a multicolor map that highlights the potential changes

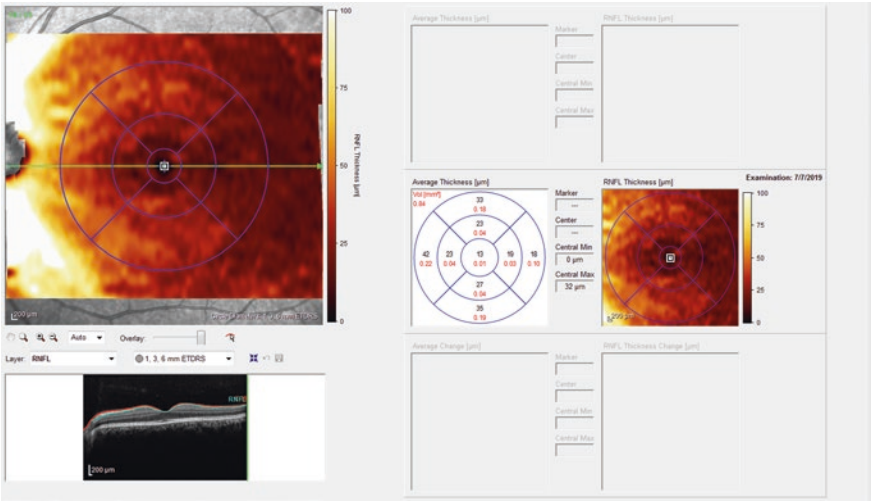

Fig. 10 The retinal nerve fiber layer map. The thickest areas are superior and inferior peripapillary regions

The ganglion cell map and retinal nerve fiber layer map are mostly useful in the fields of glaucoma and neurological disorders and will be discussed in Chap. 25.

Suggested Reading

1. Thomas D, Duguid G. Optical coherence tomography—a review of the principles and contemporary uses in retinal investigation. Eye. 2004;18(6):561–70.
2. Waldstein S, Faatz H, Szimacsek M, Glodan AM, Podkowinski D, Montuoro A, Simader C, Gerendas B, Schmidt-Erfurth U. Comparison of penetration depth in choroidal imaging using swept source vs spectral domain optical coherence tomography. Eye (London, England). 2015;29. https://doi.org/10.1038/eye.2014.319.
3. Mwanza JC, Budenz DL. New developments in optical coherence tomography imaging for glaucoma. Curr Opin Ophthalmol. 2018;29:121–9.
4. Kim KE, Park KH. Macular imaging by optical coherence tomography in the diagnosis and management of glaucoma. Br J Ophthalmol. 2018;102(6):718–24.
5. Alonso R, Gonzalez-Moron D, Garcea O. Optical coherence tomography as a biomarker of neurodegeneration in multiple sclerosis: a review. Mult Scler Relat Disord. 2018;22:77–82.
6. Sudhakar P. Commentary: ganglion cell complex of retinal layer thickness by optical coherence tomography in cases of multiple sclerosis without optic neuritis compared to healthy eyes. Indian J Ophthalmol. 2019;67:653–4.
7. Lotfy NM, Alasbali T, Khandekar R. Macular ganglion cell complex parameters by optical coherence tomography in cases of multiple sclerosis without optic neuritis compared to healthy eyes. Indian J Ophthalmol. 2019;67(5):648–53.
8. Kim NR, Lee ES, Seong GJ, et al. Comparing the ganglion cell complex and retinal nerve fibre layer measurements by Fourier domain OCT to detect glaucoma in high myopia. Br J Ophthalmol. 2011;95:1115–21.

9. Chhablani JK, Kim JS, Cheng L, Kozak I, Freeman W. External limiting membrane as a predictor of visual improvement in diabetic macular edema after pars plana vitrectomy. Graefes Arch Clin Exp Ophthalmol. 2012;250:1415–20. https://doi.org/10.1007/s00417-012-1968-x.
10. Staurenghi G, Sadda S, Chakravarthy U, Spaide RF. International nomenclature for optical coherence tomography P. Proposed lexicon for anatomic landmarks in normal posterior segment spectral-domain optical coherence tomography: the IN*OCT consensus. Ophthalmology. 2014;121:1572–8
11. Spaide RF, Christine AC. Anatomical correlates to the bands seen in the outer retina by optical coherence tomography: literature review and model. Retina. 2011;31(8):1609–19.
12. Roh YR, Park KH, Woo SJ. Foveal thickness between Stratus and Spectralis optical coherence tomography in retinal diseases. Korean J Ophthalmol. 2013;27:268–75.
13. Grover S, Murthy RK, Brar VS, Chalam KV. Comparison of retinal thickness in normal eyes using stratus and spectralis optical coherence tomography. Invest Ophthalmol Vis Sci. 2010;51:2644–7.
14. yYanni SE, Wang J, Cheng CS, Locke KI, Wen Y, Birch DG, Birch EE. Normative reference ranges for the retinal nerve fiber layer, macula, and retinal layer thicknesses in children. Am J Ophthalmol. 2013;155(2):354–60 e1.

OCT Angiography (OCT-A)

Fedra Hajizadeh and Nazanin Ebrahimiadib

OCT-A is a novel imaging technique that extracts volumetric images of microvascular circulation from the data of OCT images. A high speed OCT obtains densely sampled volume and with the technique of "decorrelation", the amplitude or intensity of the backscattered signal in sequential B-scan OCTs, at the same cross section will be compared. As the only factor that can create a fluctuation in amplitude or density would be blood flow, by RBC entering and exiting a particular voxel, a signal will be detected by OCT A. Conceivably, greater fluctuation means greater flow. In this way, OCT A construct a three-dimensional angiographic map in a non-invasive manner. It isolates retinal vascular network into superficial and deep retinal vascular plexus and gives a separate map for choroidal vessels as well. Additionally, it provides information about structure of retina and choroid. However, it is still in its infancy and there are still many unanswered questions in this field.

In brief, OCT A has three advantages over fluorescein angiography (FA) and indocyanine green angiography (ICGA):

1. It does not need injection of dye.
2. It provides structural and functional information simultaneously.
3. It illustrates the superficial, deep vascular networks of retina in addition to peripapillary and choroid map separately.
4. It creates 3 dimensional and en-face images.

Disadvantages include:

1. OCT-A is more likely to have artifact compared to FA and ICGA. Motion artifact is one of the most common ones.

F. Hajizadeh (✉)
Noor Ophthalmology Research Center, Noor Eye Hospital, Tehran, Iran
e-mail: fedra_hajizadeh@yahoo.com; fhajizadeh@noorvision.com

N. Ebrahimiadib
Retina Department, Farabi Eye hospital, Tehran University of Medical Sciences, Tehran, Iran
e-mail: nazanin.ebrahimiadib@gmail.com

M. Mohammadpour (ed.), *Diagnostics in Ocular Imaging*,
https://doi.org/10.1007/978-3-030-54863-6_13

2. OCT-A usually misses the vessels with low blood flow (micro-aneurysms and fibrotic CNV).
3. Hemorrhages, pigmentation and PED can preclude laser wave penetration so that underlying structures could not be visualized. However, this can be seen with FA as well.

Vascular Layers with OCT-A

The Retinal Vessels

In OCT-A the retinal vascular plexus may be separated into the following.

1. Superficial capillary plexus (SCP) (Fig. 1)
2. Middle capillary plexus (MCP) (Fig. 2)
3. Deep capillary plexus (DCP) (Fig. 3)
4. Radial peripapillary capillary plexus (RPCP) (Fig. 5).

Due to close proximity of MCP and DCP, they often categorized as deep vascular complex (DVC).

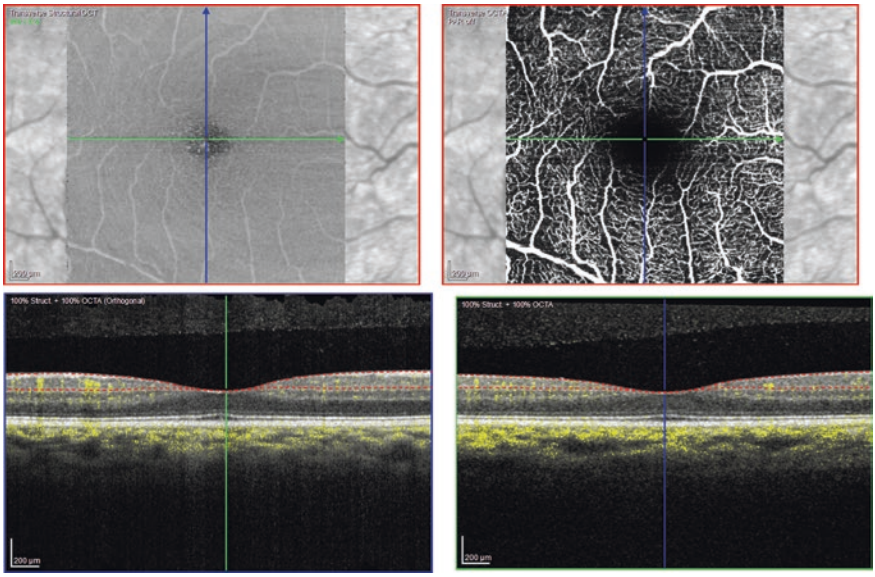

Fig. 1 OCT A: Superficial capillary plexus arranged in a centripetal pattern in the macula that converge in parafoveal capillary ring. The superficial and deep circulations join as interlocked pattern in the periphery. The SCP is a compressed network of vessels located within the ganglion cell complex

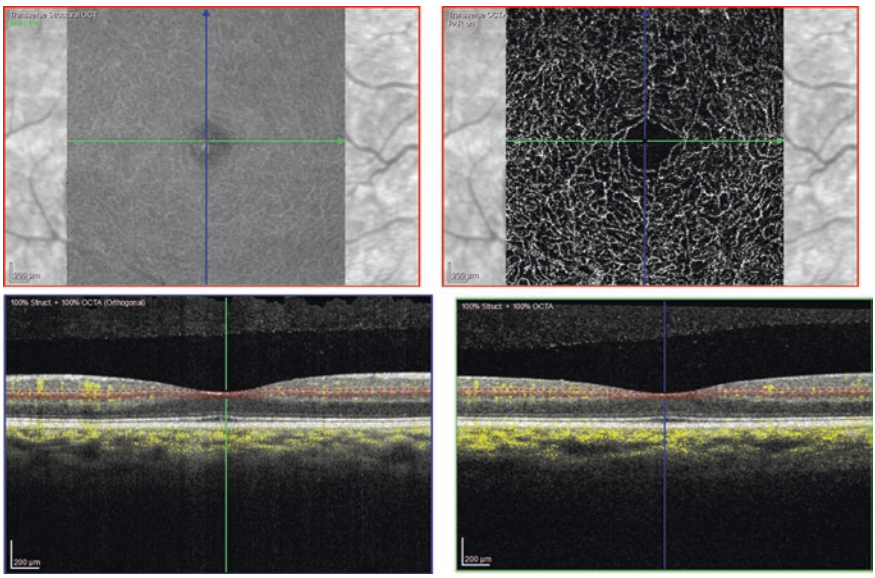

Fig. 2 OCT A: Middle capillary plexus located in the amacrine cells and bipolar cell processes, and connected to SCP at the border of inner plexiform layer/inner nuclear layer

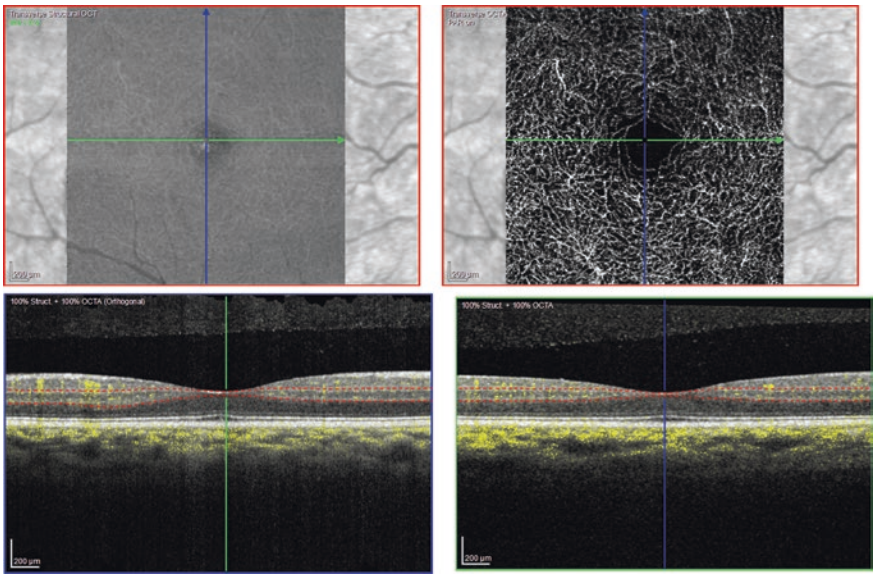

Fig. 3 OCT A: Deep capillary plexus located in horizontal cell area and connected with SCP at the border of inner nuclear layer/outer plexiform layer

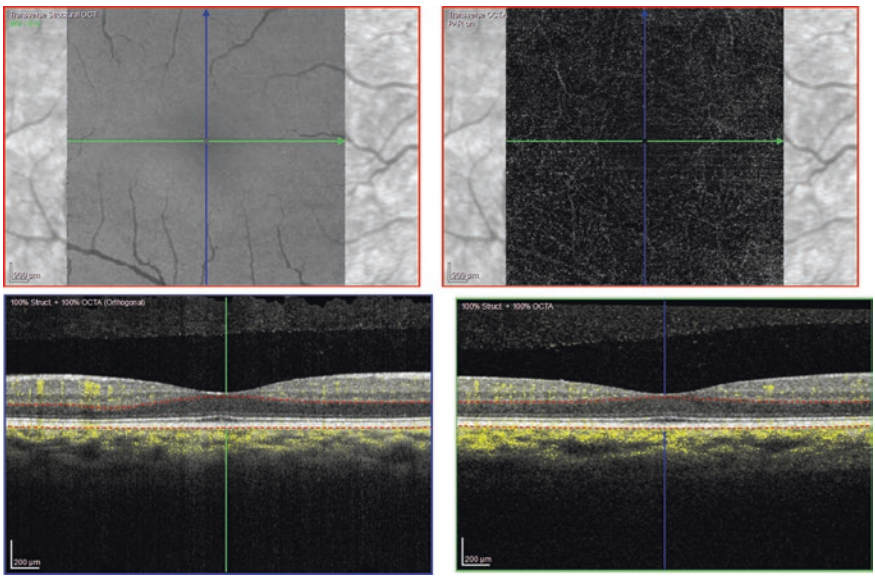

Fig. 4 Avascular area sandwiched between DCP and RPE, which is void of retinal vessels

Avascular area is an area beneath DCP and above RPE layer that is void of retinal vessels (Fig. 4). Existence of any vessel in that area is considered pathologic.

Three retinal capillary plexuses merge into a single capillary loop at foveal avascular zone (FAZ). Elderly people as well as patients with diabetes, myopia and hypertension show FAZ enlargement (Fig. 5).

Despite this vascular conjunction each of three vascular plexus has its own arteriolar supply and venous drainage.

Choroidal Vascular Plexus

The innermost part of choroid that named choriocapillaris can be illustrated by OCT-A (Fig. 6). OCT-A can also provide en face images of choriocapillaris with thin slab of 10–30 microns.

Due to scattering of laser light by RPE and choriocapillaris, OCT-A cannot demonstrate larger sized vessels of choroid (Fig. 7). SS OCT-A reduces this limitation by deeper penetration of beams. Removal of projection artifacts can also increase choroidal blood flow visibility.

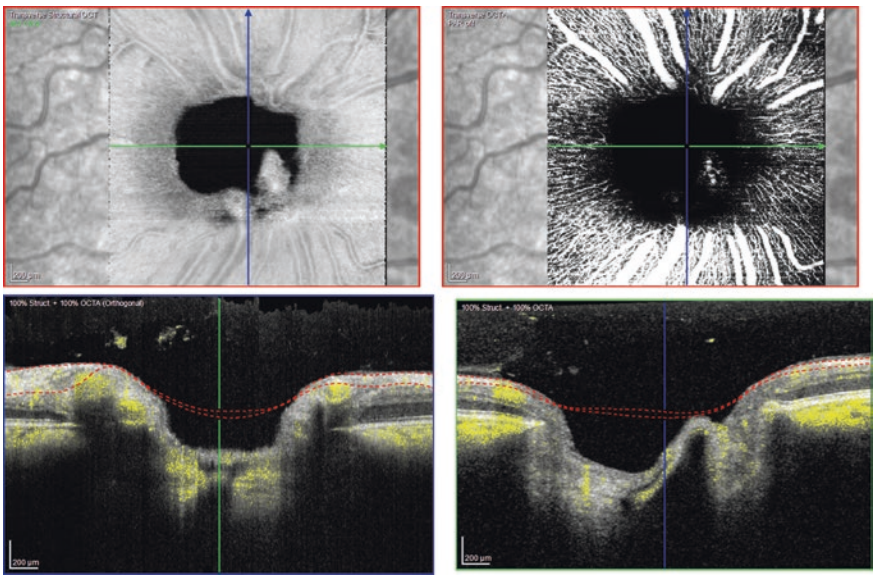

Fig. 5 OCT A: Radial peripapillary capillary plexus (RPCP) is a unique capillary meshwork surrounding the optic disc and is mainly located within the retinal nerve fiber layer (RNFL). This plexus supplies metabolites and oxygen to optic nerve axons. There is an association between perfusion in RPCP and RNFL thickness

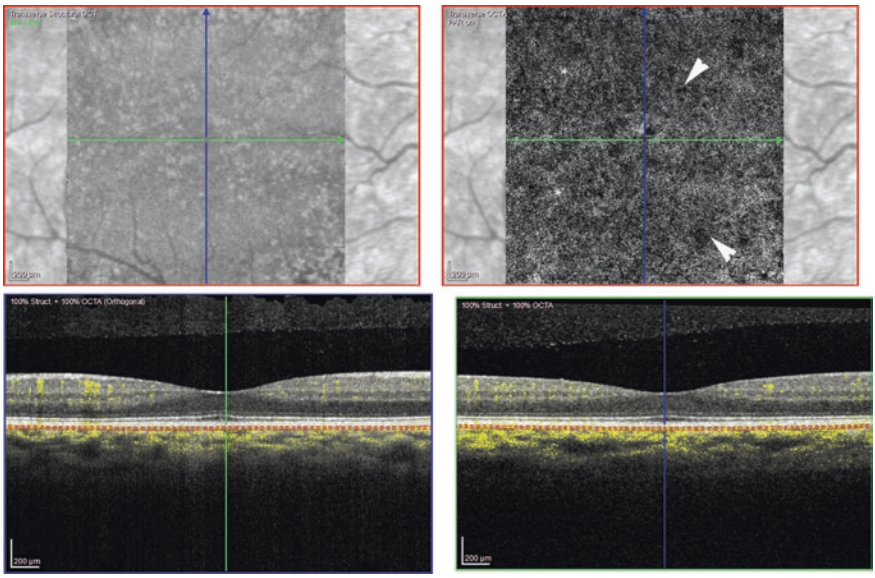

Fig. 6 OCT-A, Choriocapillaris layer appears with a granular pattern that has small dark "flow voids" regions (white arrowheads) representing the inter-capillary spaces and "bright areas" (asterisks) representing vascular flow

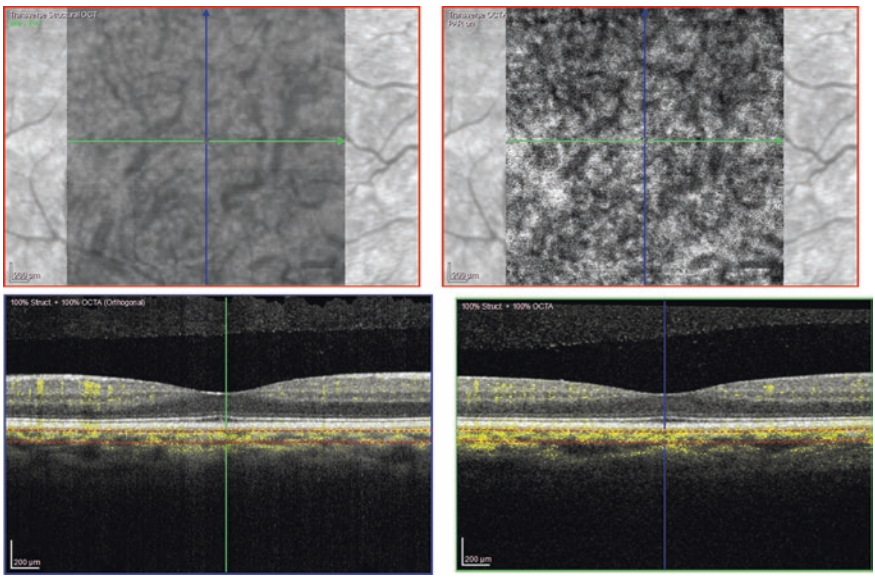

Fig. 7 OCT A: Medium sized vessels of choroidal stroma are visible in a normal subject

Pearls, Pitfalls, and Artifacts

Low signal strength, hazy media, considerable noise and patient movement can affect the quality of OCT-A images.

Here, we name some artifacts in OCT-A:

Segmentation artifact is a common problem that is defined as the error in layer delineation by apparatus software. It occurs most commonly in distorted retina (such as: high myopia, neovascular ARMD, …). Projection artifact is commonly associated with this type of artifact.

Projection artifacts is characterized by visualization of superficial vascular layer in the vascular map of deeper layers. It is produced by part of the OCT beam that passes through deeper retinal layers and creates the image of superficial vascular plexus in that deeper layer. Subtraction of en face superficial capillary plexus OCT-A from the deeper layer may be a simple strategy to eliminate this artifact.

Shadowing artifact occurs when different obstacles such as vitreous opacities, pigments, hemorrhage or druse prevent the OCT beam from reaching and reflecting from deeper layers of the retina and choroid.

Eye movement triggers ***displacement artifact*** and it results in an image with mismatched sections; i.e. one part of the image is an area of the eye, while the outstanding slice is from another region. The section of image that is lost due to eye movement is called "**gap defect**". The lost data may be present in raw images or in images that the software tried to repair the eye movement.

False negative flow: When the decorrelation values are low but a flow exists. This leads to false impression of no flow. In cases of lesions that cast a shadow such as drusen, this artifact may develop.

False positive flow: When the decorrelation is sufficient to produce the signal of flow while there is no or little flow. Noise in the image or eye movement can produce this condition.

Stretch artifact is secondary to software correction of eye movement. In this type of artifact, part of the image seems to have been extended, usually in a non-uniform way.

Quilting defect or checkerboard defect is straight line pattern of stretch artifacts, distortion and displacement artifacts. It occurs when software correction of several vertical and horizontal saccades of eye motion are not repaired adequately, so that a rectilinear pattern of stretch artifact will form. Ensuing image resembles a quilt.

Suggested Readings

1. Kim DY, Fingler J, Zawadzki RJ, Park SS, Morse LS, Schwartz DM, et al. Optical imaging of the chorioretinal vasculature in the living human eye. Proc Natl Acad Sci. 2013;110:14354–9.
2. Choi W, Mohler KJ, Potsaid B, Lu CD, Liu JJ, Jayaraman V, et al. Choriocapillaris and choroidal microvasculature imaging with ultrahigh speed OCT angiography. PLoS ONE. 2013;8:e81499.
3. Schwartz DM, Fingler J, Kim DY, Zawadzki RJ, Morse LS, Park SS, et al. Phase-variance optical coherence tomography: a technique for noninvasive angiography. Ophthalmology. 2014;121:180–7.
4. Spaide RF, Klancnik JM, Cooney MJ. Retinal vascular layers imaged by fluorescein angiography and optical coherence tomography angiography. JAMA Ophthalmol. 2014;E1–6. https://doi.org/10.1001/jamaophthalmol.2014.3616.
5. Nesper PL, Fawzi AA. Human parafoveal capillary vascular anatomy and connectivity revealed by optical coherence tomography angiography. Investig Ophthalmol Vis Sci. 2018;59:3858–67.
6. Campbell JP, Zhang M, Hwang TS, Bailey ST, Wilson DJ, Jia Y, et al. Detailed vascular anatomy of the human retina by projection-resolved optical coherence tomography angiography. Sci Rep. 2017;7:42201.
7. Garrity ST, Paques M, Gaudric A, Freund KB, Sarraf D. Considerations in the understanding of venous outflow in the retinal capillary plexus. Retina. 2017;37:1809–12.
8. Savastano MC, Lumbroso B, Rispoli M. In vivo characterization of retinal vascularization morphology using optical coherence tomography angiography. Retina. 2015;35:2196–203.
9. Campbell JP, Zhang M, Hwang TS, Bailey ST, Wilson DJ, Jia Y, et al. Detailed vascular anatomy of the human retina by projection-resolved optical coherence tomography angiography. Sci Rep. 2017;7:42201. pmid:28186181.
10. Jia Y, Simonett JM, Wang J, Hua X, Liu L, Hwang TS, et al. Wide-field OCT angiography investigation of the relationship between radial peripapillary capillary plexus density and nerve fiber layer thickness. Investig Ophthalmol Vis Sci. 2017;58:5188–94.
11. Borrelli E, Lonngi M, Balasubramanian S, et al. Macular microvascular networks in healthy pediatric subjects [published online ahead of print February 22, 2018]. Retina.

12. Garrity ST, Iafe NA, Phasukkijwatana N, Chen X, Sarraf D. Quantitative analysis of three distinct retinal capillary plexuses in healthy eyes using optical coherence tomography angiography. Investig Ophthalmol Vis Sci. 2017;58:5548–55.
13. Al-Sheikh M, Phasukkijwatana N, Dolz-Marco R, Rahimi M, Iafe NA, Freun KB, et al. Quantitative OCT angiography of the retinal microvasculature and the choriocapillaris in myopic eyes. Invest Ophthalmol VIs Sci. 2017;58(4):2063–9.
14. Lee WH, Park J-H, Won Y, Lee M-W, Shin Y-I, Jo Y-J, et al. Retinal microvascular change in hypertension as measured by optical coherence tomography angiography. Sci Rep [Internet]. Nature Publishing Group; 2019;9:156.
15. Ghasemi Falavarjani K, Al-Sheikh M, Akil H, Sadda SR. Image artefacts in swept-source optical coherence tomography angiography. Br J Ophthalmol [Internet]. 2016.
16. Spaide RF, Fujimoto JG, Waheed NK. Image artifacts in optical coherence tomography angiography. Retina [Internet]. 2015;35:2163–80.

Fluorescein Angiography

Elias Khalilipour and Fedra Hajizadeh

Fundus Fluorescein Angiography (FFA) has become an indispensable and essential tool in the diagnosis and management of many retinal conditions e.g. retinovascular disease, inflammatory conditions, and tumors since 1961 when fluorescein angiography was presented in ophthalmic imaging by Novotny and Alvis.

FFA takes about 15–20 minutes and is based on the principle of "fluorescence" that is defined as the ability of a cold body to emit the light with a higher wavelength when stimulated by the light with a shorter wavelength.

During FFA, the intravenous fluorescein dye entering the retinal circulation is excited at a wavelength between 465 and 490 nm (with blue light stimulation) and after that emits yellowish-green light (between 520 and 530 nm).

Sodium fluorescein is a molecule of low molecular weight (367 Da) bound to plasma proteins by 60–80%. Such dye does not cross the outer blood-retinal barrier (BRB) formed at the retinal pigment epithelial (RPE). Nevertheless, the choroidal capillary fenestrations allow free leakage of the dye into the extracellular choroidal space.

Preceding to injection, red-free and fundus photos are taken. These are valuable for recognizing landmarks and associating zones of clinically apparent pathology with their angiographic features. Sodium fluorescein is delivered in a bolus manner during fluorescein angiography with sufficient speed using either 2–3 mL of 25% solution or 5 mL of 10% solution.

Fundus angiography snapshots are captured just after dye injection, primarily at 0.5 seconds intervals for the first 5 seconds, then with five to ten seconds pauses for the following few minutes. Late phase snapshots must be captured at

F. Hajizadeh (✉)
Noor Ophthalmology Research Center, Noor Eye Hospital, Tehran, Iran
e-mail: fedra_hajizadeh@yahoo.com; fhajizadeh@noorvision.com

E. Khalilipour
Farabi Eye Hospital, Tehran University of Medical Sciences, Tehran, Iran
e-mail: ekhalilipour@gmail.com

M. Mohammadpour (ed.), *Diagnostics in Ocular Imaging*,
https://doi.org/10.1007/978-3-030-54863-6_14

10–12 minutes or later. The time that fluorescein spreads in retinal circulation depend on the "arm-to-retina" passage time lasts about 12–15 seconds and is influenced by factors like age, cardiac output, blood viscosity, and speed of dye injection.

The primary fluorescence is called the "choroidal flush," and patchy choroidal filling will follow soon. If there is a cilioretinal artery (approximately 30% of the general population), it will fill with the choroid (Fig. 1a).

The fine characteristics of the choriocapillaris are not visible in most fluorescein angiography snapshots, and only choroidal flush can appear on the angiogram. Before fluorescein appears in the retinal circulation within 10–15 seconds following dye injection, it usually appears in the choroidal circulation about 1 seconds earlier. Due to abundant melanin, xanthophylls, and lipofuscin pigments, the tall retinal pigment epithelium blocking choroidal fluorescence, and the foveal avascular zone (FAZ) of the macula, the central area of the macula at this phase may be hyper-fluorescent (Fig. 1b).

The retinal veins appear black, with choroidal fluorescence silhouetting them. The capillary phase happens shortly afterward, about 13 seconds after the injection of the dye.

One to three seconds after the appearance of fluorescein in choroidal circulation, fluorescein will appear in the arteries that point to the start of the arterial phase, which spreads till the arteries are fully filled.

The arteriovenous phase is marked by the complete filling of the arteries and capillaries and laminar flow in the veins (Fig. 1c).

The laminar flow is due to two reasons: (1) a faster vascular stream in the middle of the vessel relative to the walls of the vessel and (2) the fluorescein dye entering veins from smaller venules.

During the venous phase, dye completely fills the entire lumen at about 16 seconds after the injection of the dye.

The greatest fluorescence of the vessels occurs around 30 seconds after the dye has been injected, at that time it is possible to visualize the fine perifoveal capillaries.

The transit phase is the first full passage of fluorescein-containing blood through the retina and choroid.

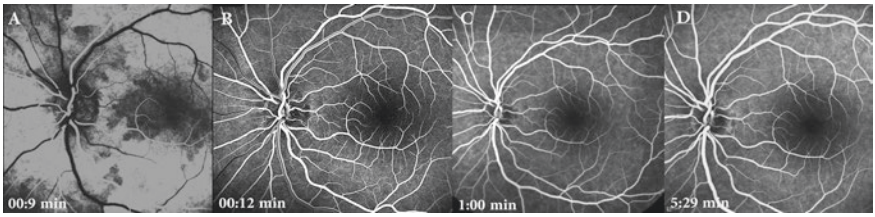

Fig. 1 **a** Patchy choroidal filling in the early arterial phase of the angiogram and **b** Arteriovenous phase (laminar filling of veins can be seen), **c** recirculation phase **d** the late phase of angiography

At the end of the transit cycle, owing to leakage from choriocapillaris, fluorescein persists in the choroid and sclera. There is also a small volume of fluorescein in the optic nerve head and retinal vessels, but there is no leakage.

The recirculation phase happens approximately 30 seconds after dye injection, as blood with lower fluorescein concentration (due to excretion of fluorescein by the kidney) returns to the retinal blood vessels and this phase lasts about 2–3 minutes (Fig. 1c).

And finally, in the late phase of angiography, 3–5 minutes following injection, retinal and choroidal vessels with reduced fluorescein concentration become gray as they slowly begin to empty of fluorescein (Fig. 1d).

Fluorescein is not leaked by the large choroidal vessels and the retinal vessels. Though, the choriocapillaris leaks fluorescein due to large openings in its endothelium so the extravasated fluorescein spreads through the choroidal tissue, Bruch's membrane, and sclera.

Abnormal Fluorescein Angiogram

Depending on the grade of fluorescence, it is classified as hyper-fluorescence and hypo-fluorescence. Diagram 1 and 2 classifies and describes several retinochoroidal conditions that abnormal fluorescence in fundus fluorescein angiography are seen (Figs. 2 and 3).

Fluorescein Angiography Adverse Reactions

Although angiography is a relatively safe imaging technique, some abnormal reactions to injected fluorescein should be considered. These include itching, nausea, and vomiting, which are usually transient and do not require treatment.

Severe reactions include severe urticaria, syncope, and dye extravasation from injected the vein, resulting in pain and local irritation of the skin and, in rare cases, local necrosis of the tissue during the injection. In these cases, topical and systemic antihistamines and cold compresses can be used.

Transient discoloration of the skin after dye injection occurs in many patients may cause these patients to be sensitive to sunlight, which requires no further treatment except avoiding severe exposure to sunlight.

Anaphylaxis shock and cardiovascular or respiratory system suppression are among the rare reactions in angiography that should prompt cardiovascular resuscitation in these cases.

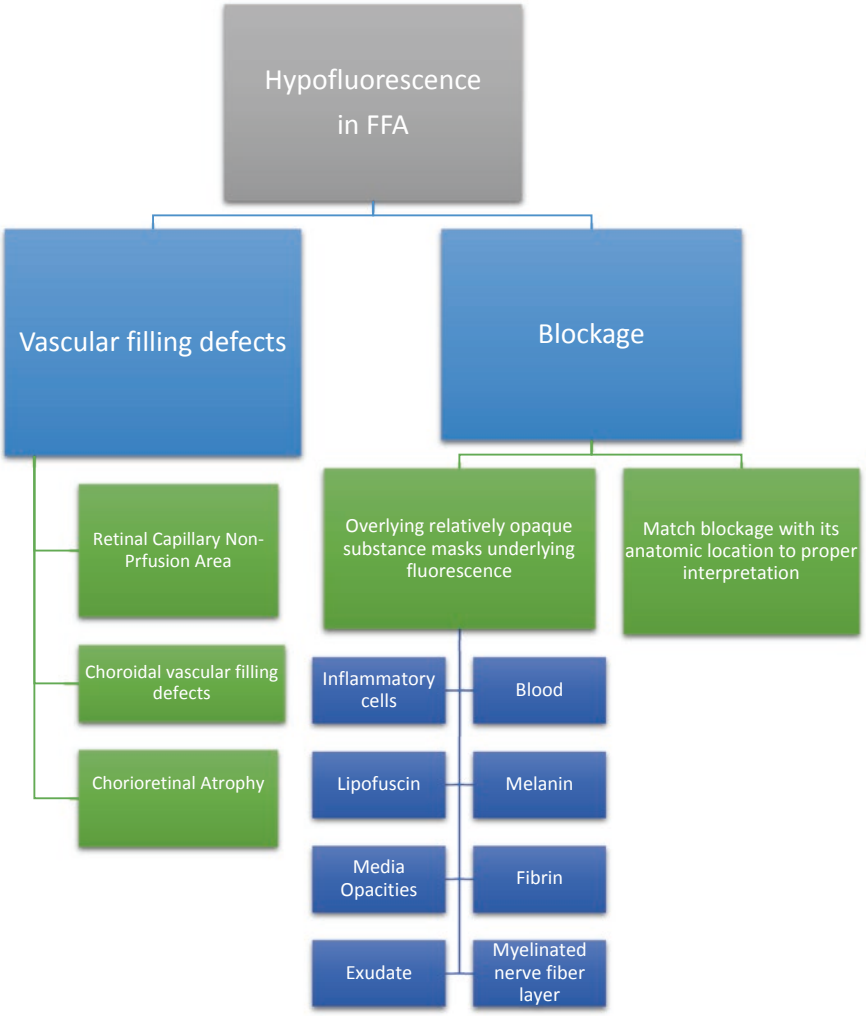

Fig. 2 Causes of abnormal hypofuorescence in fundus fluorescein angiography (FFA)

Confocal Scanning Laser Ophthalmoscope (cSLO)

Confocal Scanning Laser Ophthalmoscope (cSLO) is a device used for stereoscopic high-contrast retinal imaging with or without dyes and used for multiple retinal imaging such as fluorescein angiography, auto-fluorescence or ICG.

Unlike techniques like conventional fundus photography that use white light for retinal imaging, in this method, the monochromatic laser is exposed to the surface of the retina in a raster pattern and the reflected light passes through a confocal optical system to a photodiode detector that is conjugate to the retinal plane. This

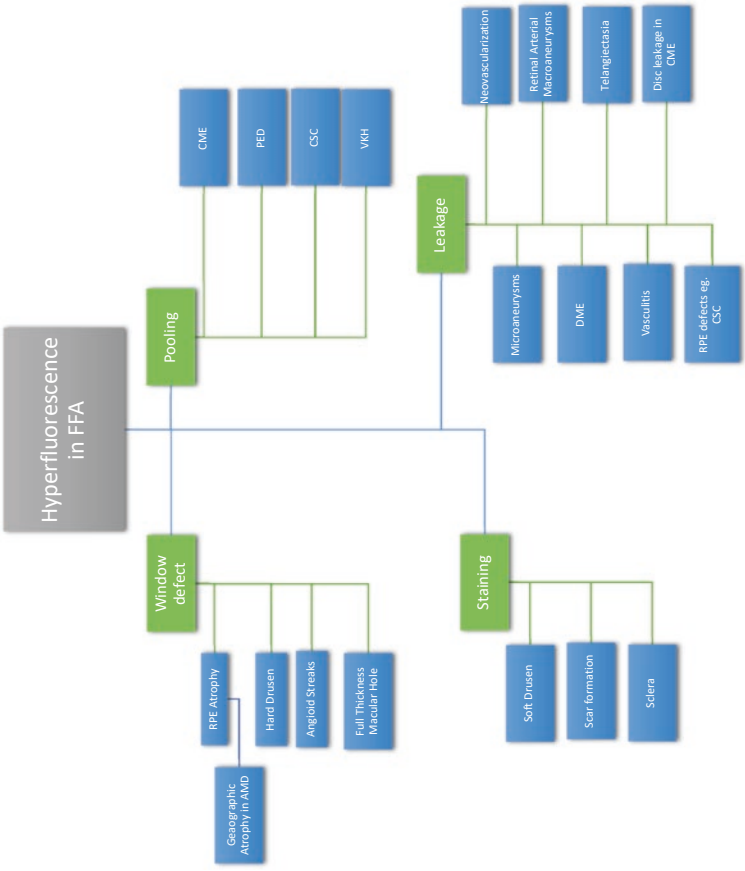

Fig. 3 Causes of abnormal hyper florescence in fundus fluorescein angiography (FFA). *CME* Cystoid Macular Edema, *PED*Retinal pigment epithelial detachment, *CSC* Central serous chorioretinopathy, *VKH* Vogt-Koyanagi-Harada, *DME* Diabetic Macular Edema

confocal system features a series of apertures that allow the system to suppresses light reflected or scattered from outside of the intended focal plane to remove optical aberrations and therefore high-contrast and high detailed images can be captured.

Because of laser light used in this device has less intensity in comparison to white light used in conventional fundus photography, patients are more comfortable with this method, and also fundus imaging is possible through poorly dilated pupils. Another advantage of this method is the ability of monochromatic laser light to pass through media opacities such as cataracts. Since it uses monochromatic light, it cannot capture full-color images. With 32 successive and equidistant optical section images attained from the SLO, a topographic 3-dimensional map with optical slices can be made digitally.

Confocal scanning laser ophthalmoscope carries a significant improvement in imaging of the retina. While white light scatters in ocular media the use of infrared and other visible wavelengths through confocal modifiable apertures offers improved imaging at different depths of the retina. Most SLO devices use four color-channels including blue 532 nm, green 660 nm, red and 790 nm near-infrared wavelengths to achieve this purpose (Fig. 4).

The blue channel principally allows details of the inner retina and the vitreoretinal interface such as the retinal nerve fiber layer and the epiretinal membrane (Fig. 5). The green channel specifies details of deeper retinal layers such as retinal blood vessels and intra-retinal lipid exudation. Near-infrared principally depicts

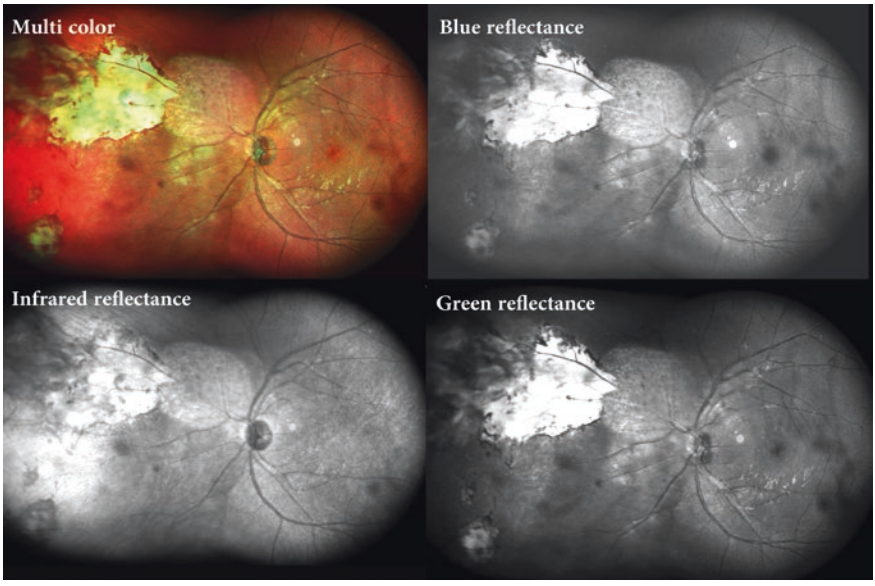

Fig. 4 Multicolor composite cSLO retinal image of the left eye of a patient with three different channels (Blue, Green and Infrared channel)

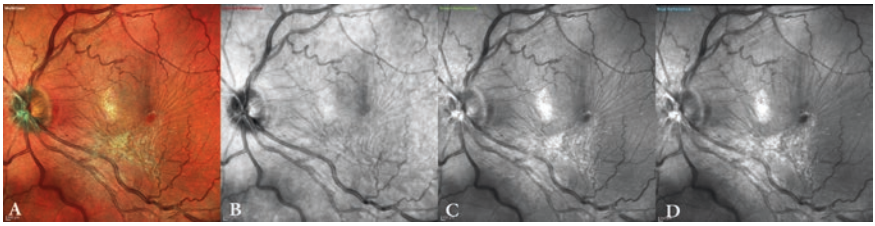

Fig. 5 The epiretinal membrane in the left eye of a patient in multicolor (**a**), infrared (**b**), green (**c**) and blue channel (**d**). Extent and details of ERM are best seen in Blue channel

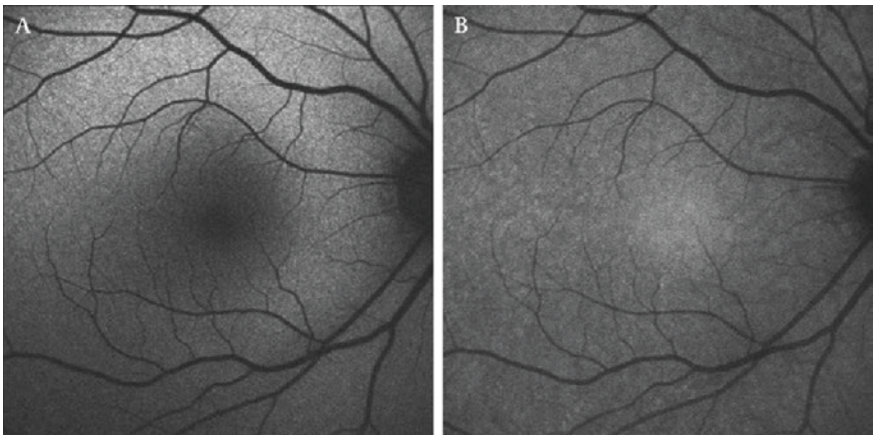

Fig. 6 The blue- auto-fluorescence (BAF) (**A**) and the near-infrared AF (NIA) (**B**) confirmed hypo-autofluorescence caused by the main retinal vessels and the optic disc. In the BAF, the FAF from the central fovea is covered by the macular pigment, which absorbs short-wavelength light, whereas the NIA showed delicate hyper-autofluorescence in the central macula

the outer retinal and choroidal structures like drusen and retinal pigmentary epithelium changes. The so-called 'multicolor' mode, technologically advanced for SPECTRALIS Optical Coherence Tomography SD-OCT (SPECTRALIS SD-OCT, Heidelberg Engineering, Heidelberg, Germany), employs cSLO to capture three concurrent laser reflections by means of three monochromatic sources.

Fundus Auto-fluorescence (FAF)

Lipofuscin (LF) accumulation is a hallmark of normal aging in many cells including RPE cells

In RPE, LF accumulation is mainly due to incomplete degradation of photoreceptor outer segments by lysosomes. Over the age of 70, 1/4 of the cytoplasmic

space of RPE of cells is occupied by lipofuscin and melano-lipofuscin (product of LF and melanin). Excessive LF accumulation may be a pathologic and common downstream pathogenic mechanism in various retinal degenerative diseases like age-related macular degeneration (AMD).

Origin of Fundus Autofluorescence

Auto-fluorescence from RPE is correlated with LF content and accumulation. Fundus Auto-fluorescence (FAF) is increased with RPE dysfunction that cannot digest LF but may be decreased with photoreceptor loss (ie, no outer segments for LF accumulation) and RPE loss.

Major components of LF include A2E (Bis-retinoid N-retinyl-N-retinylidene ethanolamine), peroxidation products of proteins and lipids and more than ten different fluorophores.

LF has a broad range of excitation (300 to 600 nm) and can be excited by visible light. The emission spectrum is also broad (480 to 800 nm) but maximum emission is in 600 to 640 nm region. There are some challenges in recording fundus auto-fluorescence images. For example, the auto-fluorescence signal from the human retina is quite weak so powerful detectors need to record these signals. The other challenge is the crystalline lens does auto-fluoresce especially when it has nuclear sclerosis cataract.

Confocal SLO addresses some of these issues: Focused low-power laser is swept across fundus in a raster pattern. Confocal nature of cSLO ensures reflectance and fluorescence are from the same optical plane (“conjugate”) and suppresses AF from sources anterior to the retina—so AF from the crystalline lens is rejected. To reduce background noise and increase image contrast, several single FAF images can be averaged (usually 4 to 16 frames), So FAF imaging can be done at low intensities.

LF is a mixture/collection of fluorophores so different wavelengths used by cSLO and Fundus camera systems may mean they are exciting and recording from different components of LF, for example, Blue auto-fluorescence (BAF) is the conventional fundus auto-fluorescence images used commonly by ophthalmologists uses the same excitation and barrier filters of FFA for FAF. However, morerecently, the green light was presented for clinical use in commercial confocal scanning laser ophthalmoscopes (cSLO). In addition to theoretically exciting different fluorophores, the green light is less absorbed by macular pigments compared to blue light and enhances the LF signal in the macula. Near-Infrared Auto-fluorescence (NIA) instead of using FA filters to acquire short-wavelength FAF or blue auto-fluorescence (BAF) uses near-infrared (i.e. ICG) filters (Excitation: 787 nm—Emission: >800 nm). NIA is very comfortable for patients in comparison to BAF. Near-Infrared Autofluorescence (NIA) appears to correspond to melanin (mostly from RPE and some from choroid) as opposed to lipofuscin.

Normal Blue Auto-fluorescence (BAF)

- Optic nerve head is dark (no RPE and no LF)
- Blood vessels are dark due to absorption by blood
- In the macular area, the FAF signal is reduced by absorption by the luteal pigment (blue light FAF) (Fig. 6)

Abnormal Blue Auto-fluorescence (BAF)

- Due to
  - Change in the amount or composition of LF
  - Presence of absorbing or auto-fluorescent material anterior to the RPE
  - Abnormal tissue with fluorophores similar to RPE LF at the level of the choroid
  - Vitreous, lens, cornea opacities may affect detected AF

Clinical Applications of Blue Auto-fluorescence (BAF)

- Retinal Dystrophies
  - Best's Disease (yellowish material in vitelliform lesions are intensely hyper-autofluorescent properties and during atrophic stages become hypo-autofluorescent)
  - Stargardt's (fundus flecks represent areas of LF accumulation so they are hyper-autoflurescent)
  - Cone Dystrophy
  - Retinitis Pigmentosa
  - Pattern Dystrophies
- CSC
- Hydroxychloroquine toxicity
- Parafoveal Telangiectasis
- Age-related Macular Degeneration (AMD)
  - Areas of decreased auto-fluorescence appear to be most important and correspond with geographic atrophy and areas of increased auto-fluorescence around the geographic atrophy appear to represent areas of "sick " RPE and are suggestive of areas of future GA growth.

Suggested Readings

1. Adl MA, LeHoang P, Bodaghi B. Use of fluorescein angiography in the diagnosis and management of uveitis. Int Ophthalmol Clin. 2012;52(4):1–12.
2. Berkow JW, Kelly JS, Orth DH. Fluorescein angiography. A guide to the interpretation of fluorescein angiograms. 2nd ed. San Francisco: American Academy of Ophthalmology; 1984. p. 9–16.
3. Gupta V, Gupta P, Herbort C, et al. Fluorescein angiography. Uveitis: text and imaging. New Delhi: Jaypee Brothers Medical Publishers (P) Ltd; 2009. p. 61–87.
4. Patel M, Kiss S. Ultra-wide-field fluorescein angiography in retinal disease. Curr Opin Ophthalmol. 2014;25(3):213–20.
5. Yannuzzi LA, Rohrer KT, Tindel LJ, Sobel RS, Costanza MA, Shields W, Zang E. Fluorescein angiography complication survey. Ophthalmology. 1986;93(5):611–7.
6. Khochtali S, Khairallah-Ksiaa I, Yahia S. Normal fundus fluorescein angiography. 2020. https://doi.org/10.1007/978-81-322-2410-5_5.
7. Haug S, Fu AD, Johnson RN, et al. Fluorescein angiography: basic principles and interpretation. In: Ryan SJ, editor. Retina. 6th ed. St. Louis: Elsevier; 2017. p. 1–45.
8. Lumbroso B, Rispoli M. Practical handbook of fluorescein angiography. 1st ed. New Delhi: Jaypee Brothers Medical Publishers; 2014.

Indocyanine Green Angiography (ICGA)

Elias Khalilipour and Fedra Hajizadeh

Indocyanine green (ICG) is a high-molecular-weight (775 Da), water-soluble dye with dark green color and has maximum optical absorption at 800 nm and maximum emission at 835 nm in the near-infrared wavelength. ICG's unique features that make it different from FFA include:

- More than 98% of this dye binds to serum proteins and hence it passes in a very small amount from choriocapillaris fenestrations and remains in the blood vessels.
- Fluorescence properties in the near infra-red wavelength with the ability to pass through blood, the macular pigments, and the RPE. Infrared is scattered fewer than visible light, so will be appropriate in eyes with media opacities.

These exclusive properties make this dye suitable for choroidal vascular imaging, details of pigment epithelial detachments (PEDs), the presence of pachyvessels, and focal areas of choroidal vascular hyper-permeability (CVH) and choroidal neovascularization (CNV). Unlike fluorescein, which is excreted by the kidneys, the liver metabolizes this dye, so urine discoloration will not occur in patients undergoing ICG angiography. Furthermore, the effective first-pass effect in the liver decreases the recirculation phenomenon that occurs with FFA.

Due to the low fluorescence efficacy of ICG dye (about 4% of fluorescein), a scanning laser ophthalmoscope (SLO) detects ICG fluorescence better than conventional fundus camera (SLO section).

At the beginning of imaging, 25 mg of this dye is injected into the cubital vein in a bolus fashion after fluorescein injection or in the same syringe simultaneously after having been mixed. By using confocal scanning laser ophthalmoscopy and

E. Khalilipour
Farabi Eye Hospital, Tehran University of Medical Sciences, Tehran, Iran
e-mail: ekhalilipour@gmail.com

F. Hajizadeh (✉)
Noor Ophthalmology Research Center, Noor Eye Hospital, Tehran, Iran
e-mail: fhajizadeh@noorvision.com; fedra_hajizadeh@yahoo.com

M. Mohammadpour (ed.), *Diagnostics in Ocular Imaging*,
https://doi.org/10.1007/978-3-030-54863-6_15

advanced filters, indocyanine green angiography can be done simultaneously with fluorescein angiography. ICG is occasionally used to complement fluorescein angiography.

This dye is better tolerated than fluorescein and has a higher safety profile. Side effects of ICG infusion are rare, but since this dye contains iodine compounds, it is forbidden in patients with a history of increased sensitivity to iodine or shellfish, and should also be avoided in patients with liver pathologies.

In the initial phase of ICG injection, which contains the first 6 min after dye injection the highest fluorescence of the retinal and choroid vessels is observed and unlike the FFA here the details of the large and medium choroid vessels are well characterized (Fig. 1 and 2).

As the middle phase progresses from about 6 min to about 15 min, the choroid fluorescence begins to fade and shows any abnormalities that result in dye absorption resulting in hyper-fluorescence in the mid-phase.

The late phase begins after 15 min and the choroidal vessels are often hypo-fluorescent, but the choriocapillaris is nearly uniform and mildly hyper-fluorescent and the retinal vessels are indistinguishable and the optic disc is black. In this phase, the hyper-fluorescent regions in the underlying hypo-fluorescent background exhibit a good contrast (Fig. 1).

This dye is capable of extravasation from the choroidal vessels into the choroidal stroma and the RPE and is usually well stained in the late stages after 30 min and the pathologies leading to hypo-fluorescent are well tolerated in the late phases. They show themselves (Fig. 1).

Meanwhile, fluorescence becomes very weak after 30 min, the early phase can be repeated by ICG reinjection.

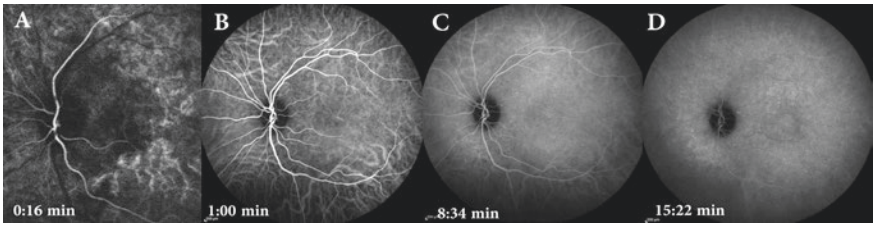

Fig. 1 Normal ICG-angiography: the initial phase of ICG (**a**), early phase (**b**), middle phase (**c**) and late phase (**d**)

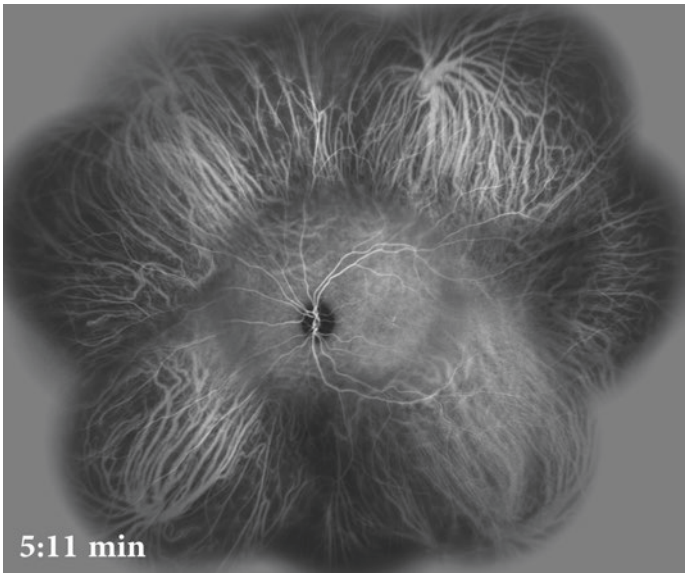

Fig. 2 Montage early phase of ICGA in a healthy subject

Abnormal ICG

Hypo-fluorescent anomalies signify vascular filling defects or areas of blockage by pigment, blood, or tissue overlying fluorescence.

Due to less than a natural overlying blockage, hyper-fluorescent anomalies illustrate either areas with increased ICG dye amounts or regions with diminished ICG signal transmission.

The hyper-fluorescent regions in the ICG can be divided into “plaque” and “focal hotspot”. Plaques often appear better in the late phases and are greater than one disc diameter in size and usually correspond to occult CNVs, but focal hotspots are usually less than one disc diameter, with relatively distinct margins and are visible more in the context of retinal angiomatous proliferation (RAP) and polypoidal vasculopathy.

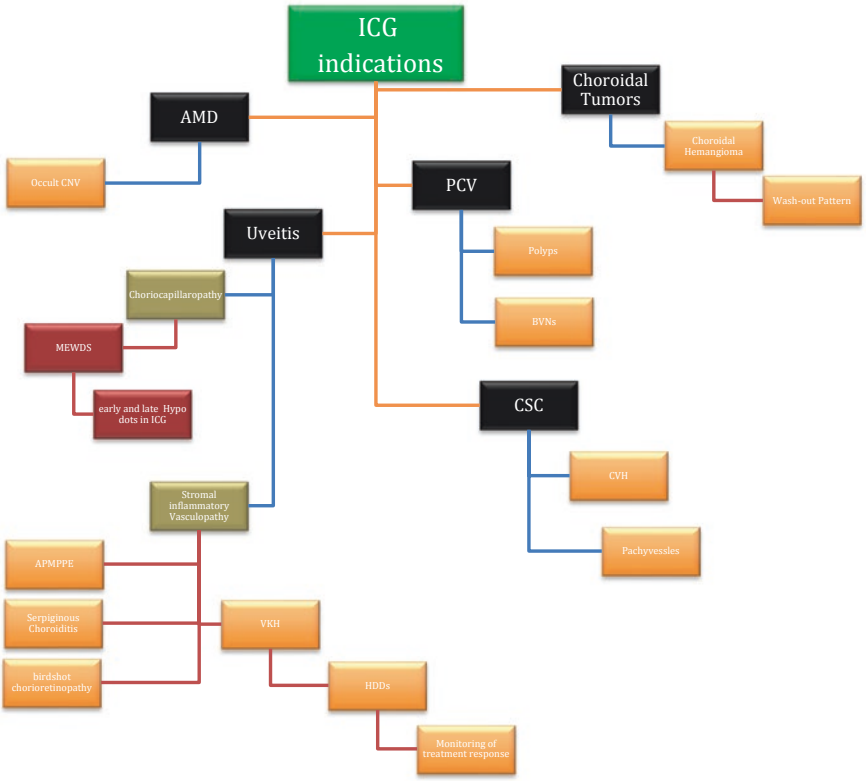

Fig. 3 Some indications of ICG angiography in ophthalmology. AMD: age-related macular degeneration), CNV: Choroidal neovascularization, MEWDS: Multiple evanescent white dot syndrome, APMPPE: Acute posterior multifocal placoid pigment epitheliopathy, VKH: Vogt-Koyanagi-Harada, HDDs: hypo-fluorescent dark dots, CVH: choroidal vascular hyper-permeability, PCV: polypoidal choroidal vasculopathy BVNs: Branching vascular networks

ICG Indications

Figure 3 shows some indications of ICG angiography in ophthalmology.

Suggested Readings

1. Bischoff PM, Flower RW. Ten years' experience with choroidal angiography using indocyanine green dye: a new routine examination or an epilogue? Doc Ophthalmol. 1985;60:235–91.
2. Fox IJ, Wood EH. Indocyanine green: physical and physiologic properties. Proc Mayo Clin. 1960;35:732–44.

3. Hayashi K, Hasegawa Y, Tokoro T. Indocyanine green angiography of central serous chorioretinopathy. Int Ophthalmol. 1986;9:37–41.
4. Kogure K, Choromokos E. Infrared absorption angiography. J Appl Physiol. 1969;26(1):154–7.
5. Flower RW, Hochheimer BF. Indocyanine green dye fluorescence and infrared absorption choroidal angiography performed simultaneously with fluorescein angiography. Johns Hopkins Med J. 1976;138:33–42.
6. Destro M, Puliafito CA. Indocyanine green angiography of choroidal neovascularization. Ophthalmology. 1989;96:846–53.
7. Cherrick GR, Stein SW, Leevy CM, Davidson CS. Indocyanine green: observations on its physical properties, plasma decay, and hepatic extraction. J Clin Invest. 1960;39(4):592–600.
8. Staurenghi G, Bottoni F, Giani A. Clinical applications of diagnostic indocyanine green angiography. In: Ryan SJ, editor. Retina. 6th ed. St. Louis: Elsevier; 2017. p. 46–76.

Ultrasonography (B-Scan) and Ultrasound Biomicroscopy (UBM)

Fariba Ghassemi

Ultrasonography (B-Scan) in Retinal Disease

Ocular structure can be properly evaluated by clinical inspection, ophthalmoscopy, and slit-lamp examination. B-scan ultrasonography is an important adjuvant especially in opaque media for the clinical assessment of various ocular and orbital diseases. Ultrasonography or B-mode scan may be used to rule out retinal, vitreous, and choroidal detachments, tumors, and other pathologies that affect the posterior segment of the eye.

Ultrasonography with proper examination technique could collect more information than clinical examination alone in some cases. B-scan as a two dimensional image differs from A-scan by generating a photograph by using both the vertical and horizontal dimensions to show configuration and location.

An oscillating sound beam is generated in B-scan ultrasonography probe, passing through the eye and rebounding back to the receiver in the probe and the analysis process is performed and a number of dots appear on the screen. The more strong the echo, the brighter the dot.

For example, the dots that make up the posterior vitreous hyaloid face are not as bright as the dots that form the preretinal membrane or retina.

This is very helpful in differentiating a posterior vitreous detachment (benign condition) from a more highly reflective retinal detachment, because the retina is more dense than vitreous.

Diagnostic B-scan ultrasound can accurately used in the detection and differentiation of:

- Some iris or ciliary body lesions
- Lens condition and location
- Vitreous abnormalities as opacities (Fig. 1)

F. Ghassemi (✉)
Farabi Eye Hospital, Tehran University of Medical Sciences (TUMS), Tehran, Iran
e-mail: fariba.ghassemi@gmail.com

M. Mohammadpour (ed.), *Diagnostics in Ocular Imaging*,
https://doi.org/10.1007/978-3-030-54863-6_16

- Rhegmatogenous (RRD) or tractional versus exudative retinal (TRD vs. ERD) detachments (Fig. 2, 3)
- Serous versus hemorrhagic choroidal detachments (Fig. 4)
- Intraocular tumors (Figs. 5, 6, 7, 8, 9, 10, 11, 12, 13)
- Disc drusen versus papilledema (Fig. 14).

Dynamic examination (moving the eye at the time of scanning) is vital for distinguishing certain pathologic conditions as detachments and differentiating it from more benign condition as posterior vitreous detachment (Fig. 1).

Pearls

*The ultrasound pattern of a vitreous hemorrhage depends on its stage and extend.

New and minor hemorrhages are expressed as small dots or linear areas of low reflective mobile vitreous opacities. Severe and older hemorrhages are more echogenic due to vitreous opacities or shaped membranes.

In some sections, the retina was isolated from the choroid and choroid from the sclera. Dual portion may be detectable of separation of bullous and dome shaped choroidal detachment from the overlying retina. At the periphery (by end gaze echography) multiple choroidal mounds protrude to vitreous cavity causing half closed umbrella like appearance (Fig. 4).

Pearls

*Vitreous hemorrhage layering the posterior vitreous face forming membrane like echogenicity should be separated from detached retina by observing the after

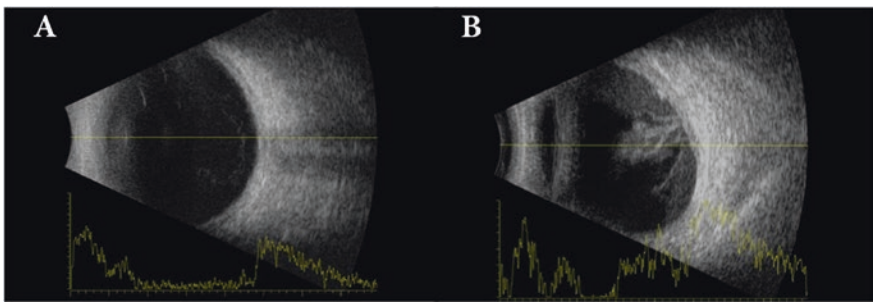

Fig. 1 **A** B-scan examination illustrates some vitreous hemorrhage in a 20 years old male with recent blunt trauma history. Fundus examination is not possible due to hazy media. New vitreous hemorrhage is hypo-echoic. **B** Another patient with 2 weeks history of blunt trauma to the eye. Old vitreous hemorrhage is more echogenic than new hemorrhage

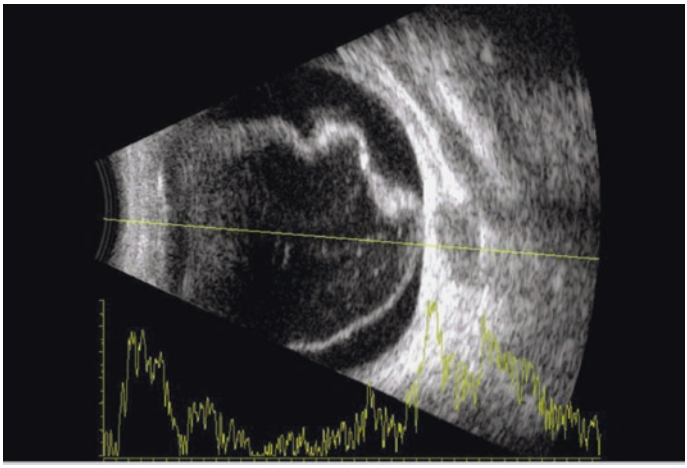

Fig. 2 Total retinal detachment and vitreous hemorrhage. The retinal detachment appears as a curly membrane of high reflectivity in an open-funnel configuration, connecting to the optic disc and to the ora serrata at periphery

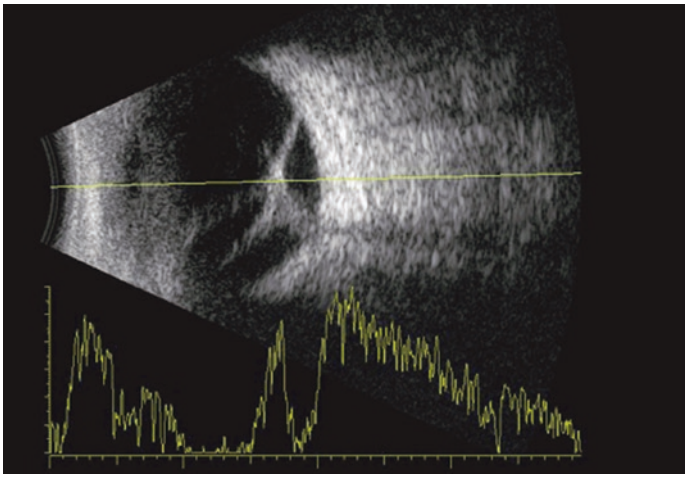

Fig. 3 Tractional retinal detachment. The b-scan shows a straightened and tight retina due to traction of membranes. The posterior pole is totally detached with a closed funnel

movement of retina. The first will have wavy movement and the retina will have jerky, rebound limited vertical movement.

*Membrane formation may also occur following inflammation, long standing RD, and diabetes. The membrane may cause retinal stiffness, which may restrict its movement. Depending on the direction of friction vector, the retinal surface in TRD is smooth or concave.

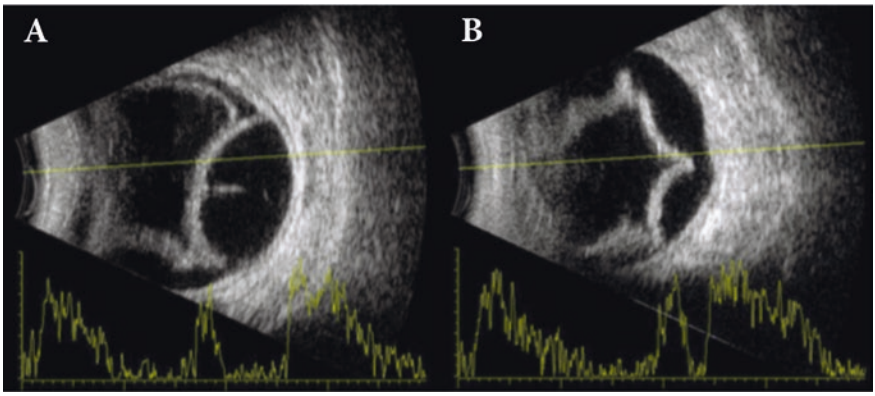

Fig. 4 Acute spontaneous supra-choroidal effusion. The b-scan shows a thick chorioretinal complex detachment with some septa inside it (**A**). The A scan passing perpendicularly the choroidal mound shows a wide bifid (M) spike (**B**)

*In cases of bullous retinal detachments with 'shifting fluid' an exudative retinal detachment (ERD) should be rule out. ERD typically has subretinal echoes, a choroidal mass can be observed, and the ultrasound may also reveal the cause of ERD (e.g. posterior scleritis, Vogt-Koyanagi-Harada syndrome, choroidal tumor, granuloma).

B-scan ultrasonography is widely used for the initial and follow-up evaluation of intraocular tumors. Using this valuable imaging technique allows the physician to know the size, consistency and quality of the ocular tumor.

Retinoblastoma is a highly malignant retinal cancer that is commonly found in infants and young children, and has focal areas of calcification within the tumor. Ultrasound as a safe and cost effective way to easily detect the calcium, characterized as highly reflective foci within the tumor or vitreous (Fig. 5).

Pearls

The presence of calcium in the intraocular mass, which confirmed with lower gain of the b-scan, denotes retinoblastoma mainly unless proven otherwise.

Pearls

*Choroidal melanoma may be associated with extra-scleral extension (acoustic hollowness in orbital fat tissue) and rarely subretinal or supra-choroidal hemorrhage.

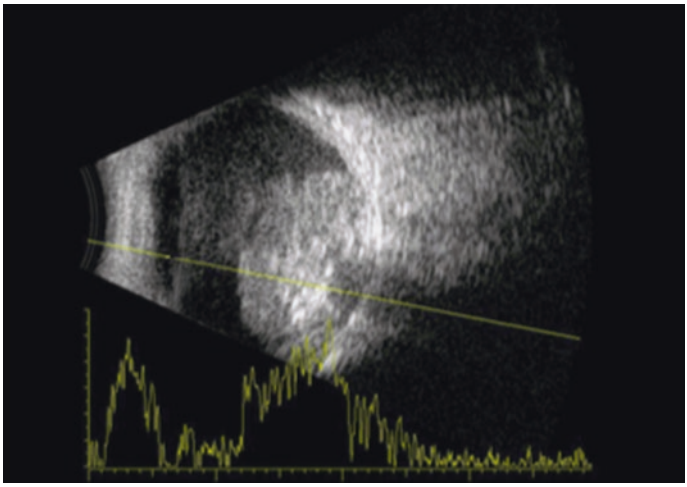

Fig. 5 A highly reflective dome shaped large intraocular mass of the 13 months old female baby has been shown. Multiple stippled and conglomerate echogenic, calcified content with acoustic shadowing is visible inside the lesion and are characteristic for retinoblastoma

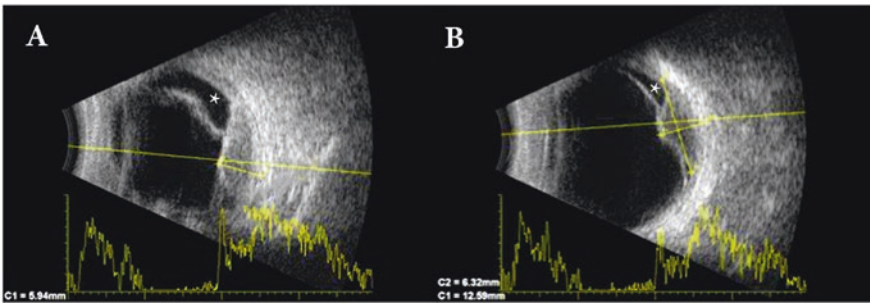

Fig. 6 Choroidal melanoma. Oval homogenous dome shaped mass with acoustic hollowness inside. A: Note the low to medium internal reflectivity and rapid sound attenuation inside the tumor (red arrow) in A-scan. **A** and **B** The exudative retinal detachment is visible (asterisks)

*The choroidal excavation is evident in some choroidal melanoma cases, indicating a tumor that invades the deeper choroidal structures (Fig. 6).

*Large sized choroidal melanoma may have higher internal reflectivity due to edema and necrosis inside the tumor. The high internal pulsation and sound attenuation are preserved as small choroidal melanoma tumors.

*Sometimes there is heterogeneity in the reflectivity of the tumor in large scale melanoma due to necrosis and potential edema and hemorrhage inside the tumor (Fig. 7).

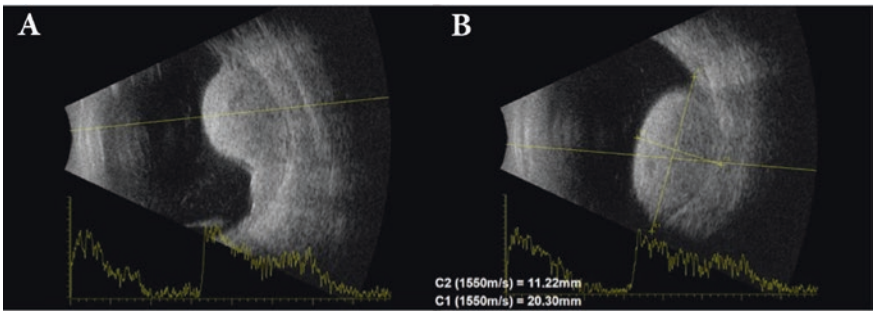

Fig. 7 **A** and **B** Large sized choroidal melanoma. The b-scan revealed an enormous sized choroidal melanoma with medium to high internal reflectivity proven to be choroidal melanoma with pathology after enucleation

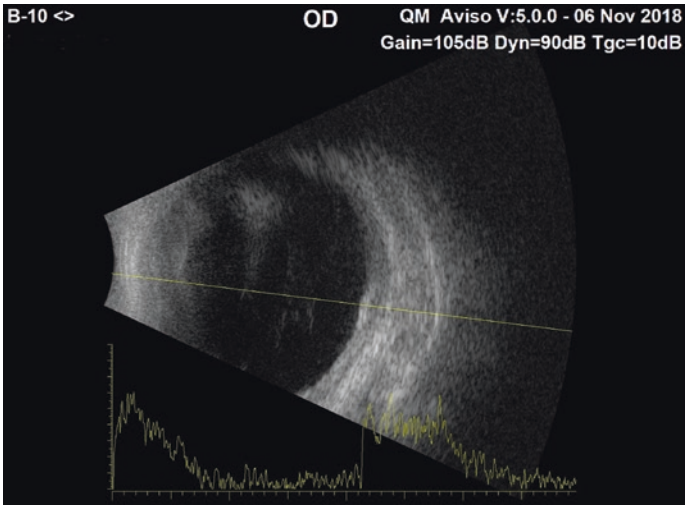

Fig. 8 Choroidal nevus. A small dome shaped or flat melanocytic lesion with medium to high internal reflectivity

Pearls

*The phthisic eyes may have stippled calcified hyper-reflective spots (but not plaque like) in the sclera and chorioretinal boundary. The key indicator for diagnosis is the short axial length and low intraocular pressure in these cases.

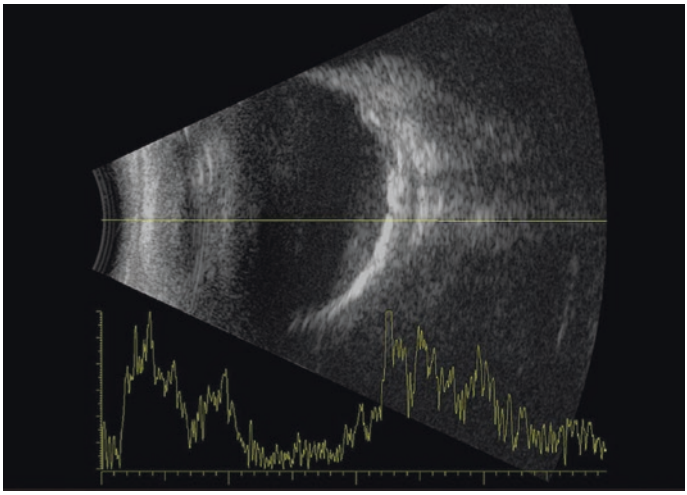

Fig. 9 Choroidal osteoma. A dense hyper- reflective, plaque like, flat lesion with severe back shadowing indicating; the calcium content of the tumor. The tabletop high internal reflectivities of the lesion at the tumor in A scan showing the hard consistency and dense calcium nature of the mass

Pearls

*Echographically, choroidal metastatic tumors usually have an irregular plaque-like sometimes lumpy bumpy contour, an irregular internal structure, a medium-to-high internal reflectivity, and little evidence of internal vascularity. The subretinal fluid is often more than that expected due to the size and volume of the tumor.

Pearls

*Retinal dysplasia may have similar B-scan as severe PHPV (Fig. 12) and non-attachment (Fig. 13). However cystic changes in the tissue supposed to be retina may be detected in B-scan.

In conclusion, by knowing the ultrasound characteristics of different intraocular pathologies and its limitations and advantages, we will have a low cost tool in our hands for diagnosis and the management of ocular disease with B-scan ultrasonography.

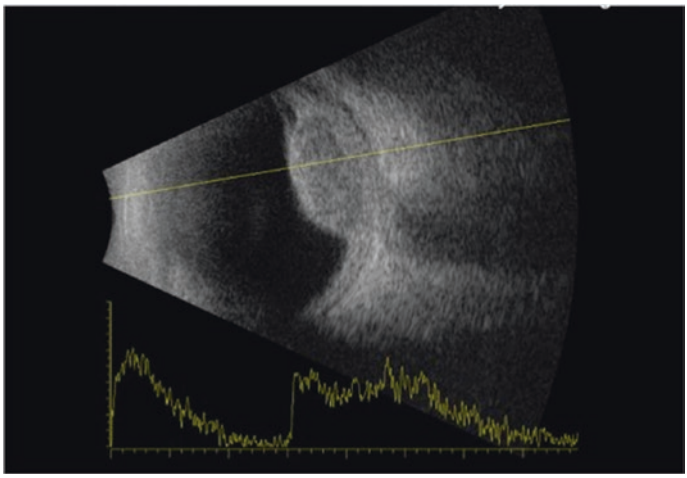

Fig. 10 A dome shaped heterogeneous mass with high internal reflectivity in the A-scan originating from the metastatic renal cell carcinoma in a female patient with past history of renal cell carcinoma 2 years ago

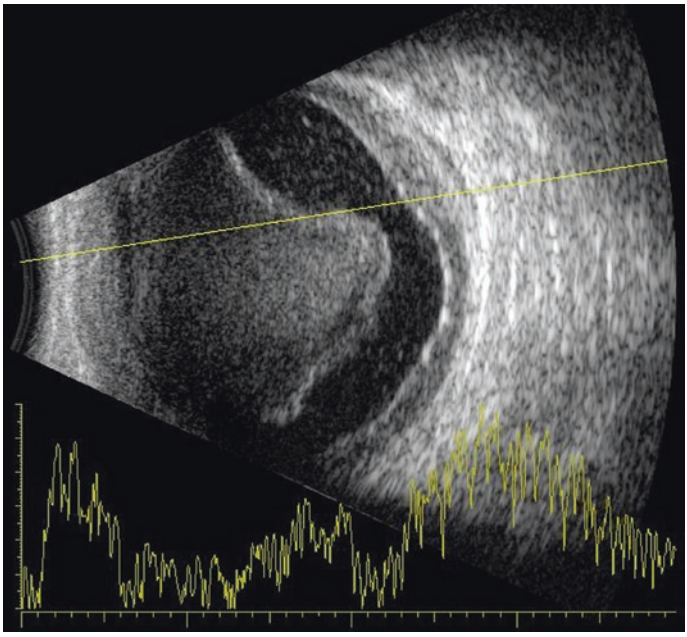

Fig. 11 Choroidal metastasis from breast cancer origin. Plaque like flat extensive tumor with irregular internal reflectivity, total retinal detachment and severe vitreous opacity. Subretinal fluid appears to have some reflectivity due to viscous or hemorrhagic nature

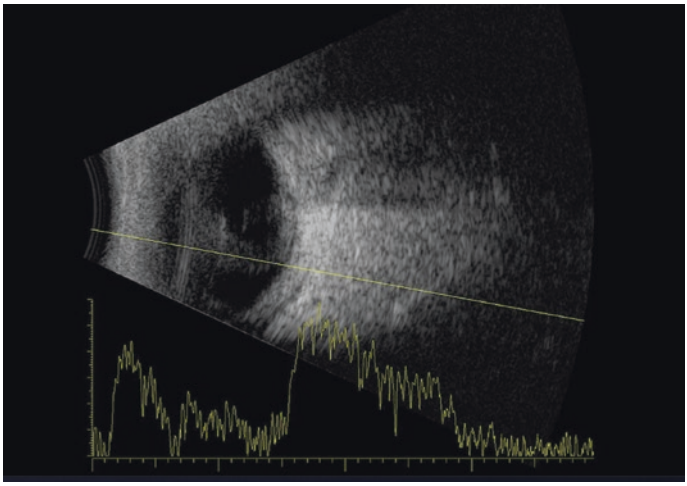

Fig. 12 Persistent hyperplastic primary vitreous (PHPV). An 8 month-old male baby with lack of eye contact and nystagmus in both eyes. The b-scan illustrates total retinal detachment with thick choroid possibly secondary. Small axial length is remarkable. The echography showed total detachment indicates the poor chance for operation

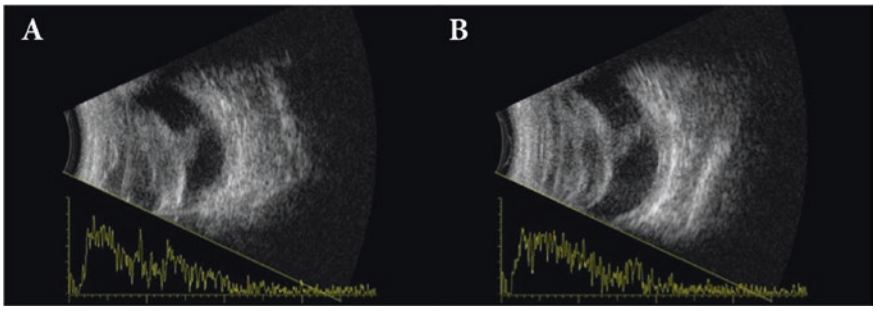

Fig. 13 A 24 month-old male baby with lack of eye contact and nystagmus in both eyes. The B-scan displays a thick stalk originating from optic nerve head and, attaching to the retrolental fibrotic mass. Axial length and choroidal thickness are normal. This patient could be a poor chance candidate for a lensectomy and vitrectomy

Suggested Readings

1. He M, Wang D, Jiang Y. Overview of ultrasound biomicroscopy. J Curr Glaucoma Pract. 2012;6(1):25–53.
2. De La Hoz Polo M, Torramilans Lluís A, Pozuelo Segura O, Anguera Bosque A, Esmerado Appiani C, Caminal Mitjana JM. Ocular ultrasonography focused on the posterior eye segment: what radiologists should know. Insights Imaging. 2016;7(3):351–64.

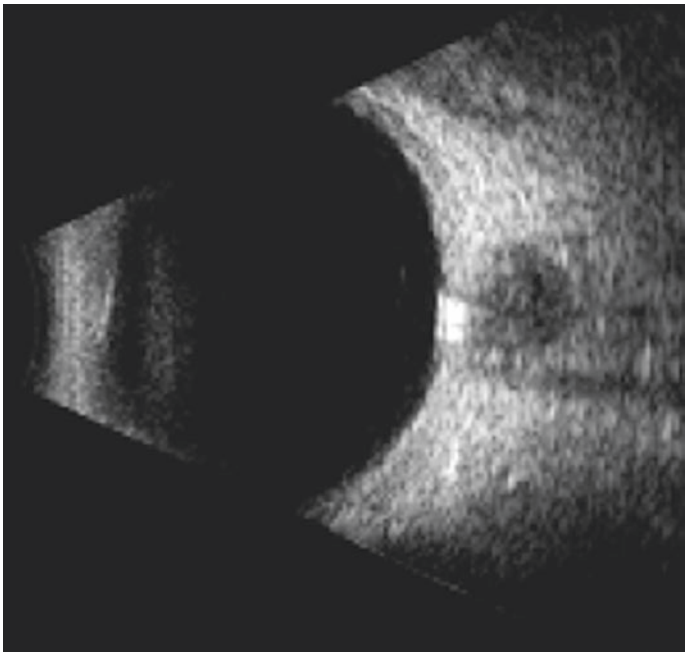

Fig. 14 Optic nerve head drusen. The presence of a reflective material on the disc with some calcified content causing some elevation and swelling of the disc

3. Green RL, Byrne SF. Diagnostic ophthalmic ultrasound. In: Ryan SJ, editor. Retina. Philadelphia: Elsevier/Mosby 2006. p. 265–350.
4. Kendall CJ, Prager TC, Cheng H, Gombos D, Tang RA, Schiffman JS. Diagnostic ophthalmic ultrasound for radiologists. Neuroimaging Clin N Am. 2015;25(3):327–65.
5. Harrie RP. Clinical ophthalmic echography: a case study approach. New York, NY: Springer Science + Business Media, LLC; 2008.

Ultrasound Biomicroscopy (UBM)

An Effective Anterior Segment and Posterior Segment Diagnostic Tool

Ultrasound biomicroscopy (UBM) is a noninvasive technique used to illustrate the structures of anterior segment of the eye, using a high-frequency (20–100 MHz) ultrasound transducer. UBM, which was first presented, by Charles Pavlin and Stuart Foster in 1989 provides detailed two-dimensional in vivo gray scale images

of the various anterior segment structures, making it ideal to visualize and evaluate the entire anterior segment.

UBM has been broadly used as a method of imaging and qualitative and quantitative evaluation of various ocular pathologies of adnexa, conjunctiva, sclera, cornea, anterior chamber, ciliary body, anterior vitreous and retina (Fig. 15).

The principal components of UBM are the transducer as a critical component and image processing part. The probe, which contains the transducer, is small and light handheld or mounted on a gantry device. Computer monitor with the main processing unit records and saves real-time images displayed on the monitor, for later analysis.

According to the principles of ultrasound physics, image quality depends on the frequency of the ultrasound, the ratio of the focal length to the transducer diameter (f-number) and the length of the pulse. Higher frequency and shorter focal length are typically associated with higher image resolution but lower penetration.

Ultrasound biomicroscopy (UBM) has considerably improved the resolution of anterior segment tumors, from 300–400 μm with traditional 10 MHz ultrasonography, to 20–50 μm, with tissue penetration up to 4–5 mm.

Higher frequency transducers provide finer resolution of more superficial structures, whereas lower frequency transducers have higher perception depth with less resolution.

Lower-frequency transducers (up to 50 MHz) are used where penetration depth is important.

Higher-frequency transducers (80–100 MHz) are used for more superficial structures by improved resolution.

Limitation

- The most significant limitation of UBM is restricted penetration in large lesions.
- Limitation related to immersion technique and a skilled operator to perform the scan.
- The other limitation is the need for the supine position when scanning.

UBM Applications

Iris

- Iris cyst (**central, mid-zonal, peripheral, and dislodged types of** iris pigment epithelial- IPE-cysts or inclusion cysts due to trauma)
- Iris tumors (melanoma, nevus)
- Iris anterior and posterior synechia (pupillary margin and peripheral iris)
- Iris congenital anomalies (Figs. 16 and 17).

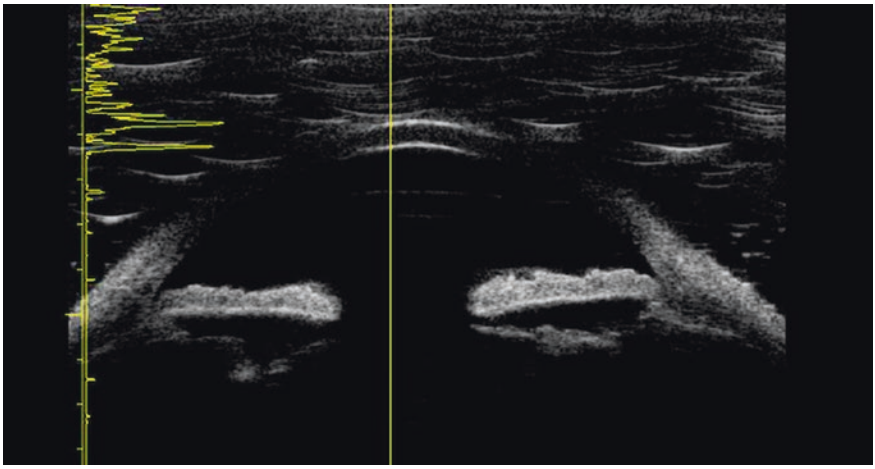

Fig. 15 A normal UBM image. The cornea and anterior chamber with open angle, pupil border and the anterior capsule just in the back of pupil. The ciliary body cross section is visible on the back of the iris root

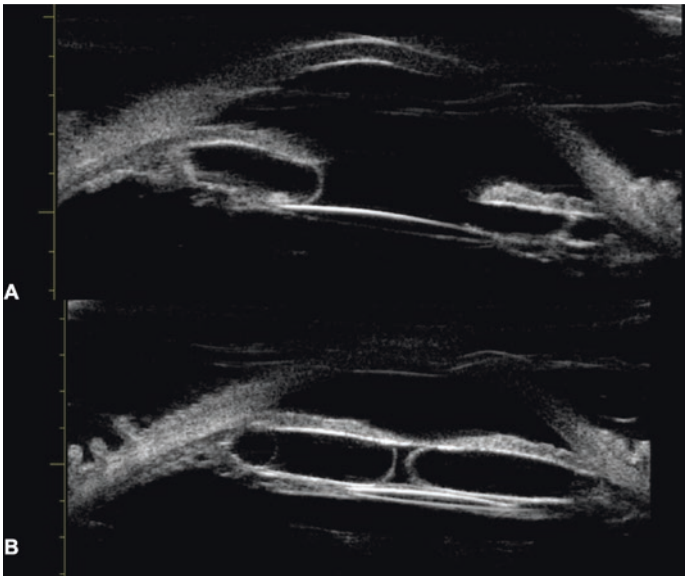

Fig. 16 The image shows a large mid-zonal iris cyst in the back of the iris originating from iris pigment epithelium at the base of the iris on the axial (**A**) and transverse (**B**) cuts. The iris was extensively involved in the both side of the pupil

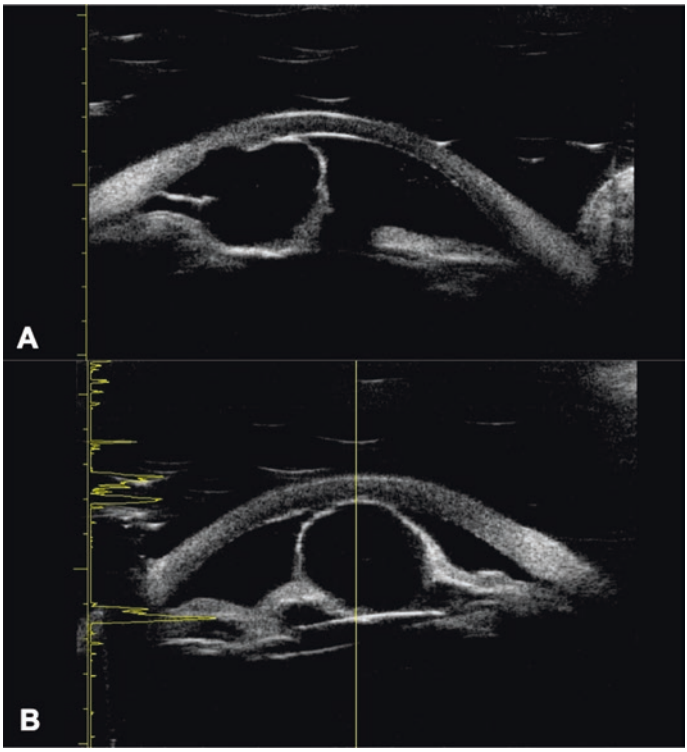

Fig. 17 Large iris cyst. A cystic iris mass arises from the iris stroma from the angle up to the pupil and abutting the posterior surface of cornea. Axial (**A**) and transverse (**B**) cuts. Ciliary body is spared. The cyst of the iris caused iris stromal atrophy especially at the pupil border. The cross section shows the extent and multiplicity of the cyst

Ciliary Body (CB)

- CB tumors (melanoma, nevus)
- CB cysts
- Detachment (Figs. 18, 19 and 20).

All the ciliary body cysts with any solid part should be considered suspicious for the development of ciliary body melanoma (Fig. 21).

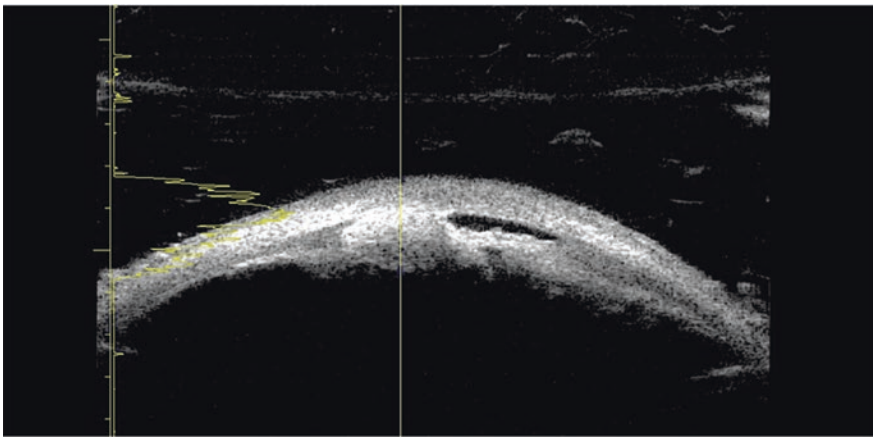

Fig. 18 Involvement of the ciliary body with a highly reflective, smooth solid lesion with no high internal reflectivity, located at the ciliary body in the longitudinal scan. It is proved to be by the same size in the follow up examinations (ciliary body melanocytoma or nevus)

Uveitis/Scleritis

- Localization of IOL implants in suspected uveitis-glaucoma-hyphema syndrome
- Finding the cause of hypotonia (ciliary body detachment, ciliary body atrophy due to uveitis or trauma) (Fig. 22).

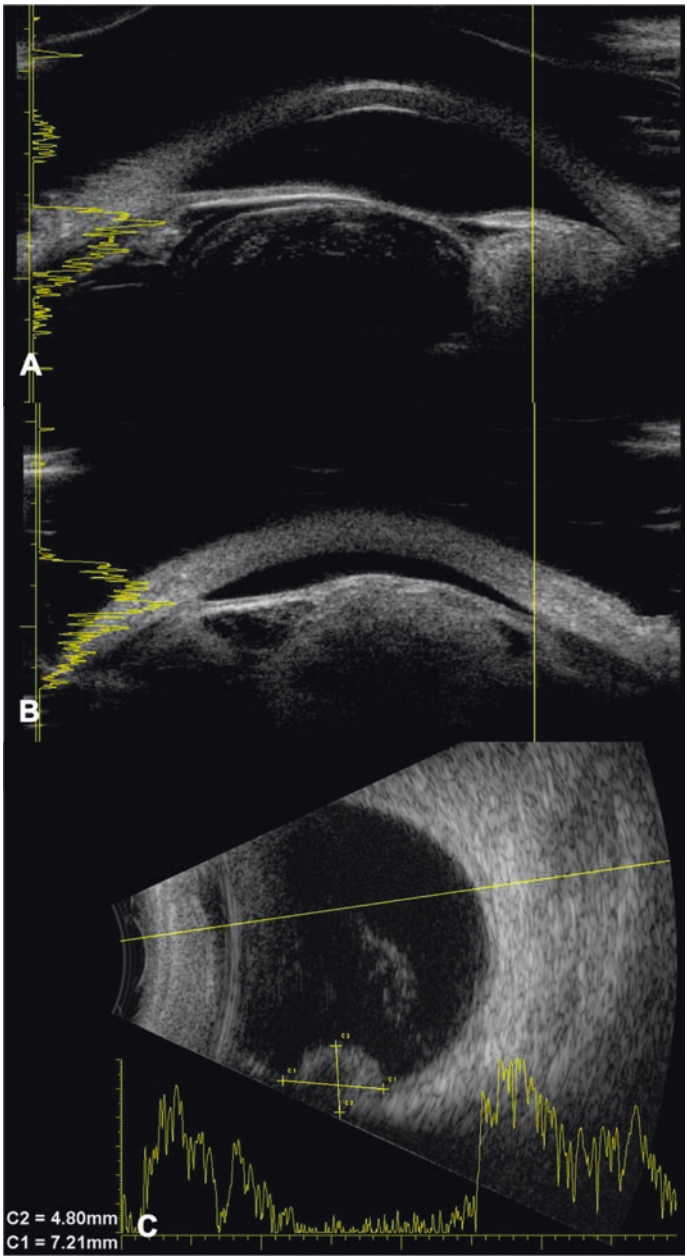

Fig. 19 Ciliary body melanoma. The figure shows ciliary body solid mass with medium internal reflectivity with iris root involvement in the longitudinal (**A**) and transverse (**B**) scan. The tumor top is not visible well because of the limitation of UBM (50 MHz) in penetrance of more than 4–5 mm. The B-scan is used for more accurate thickness measurement (**C**)

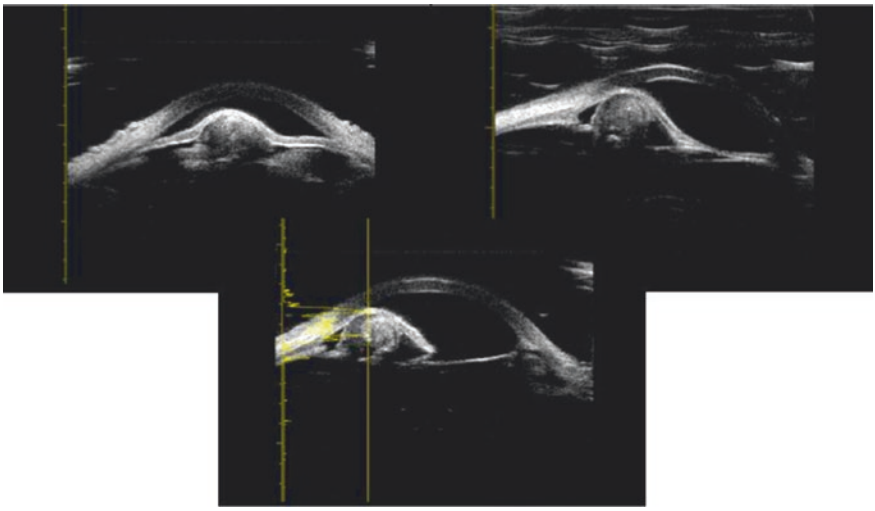

Fig. 20 A round heterogeneous mass in the back of the iris with different reflectivity mimicking the ciliary body melanoma clinically

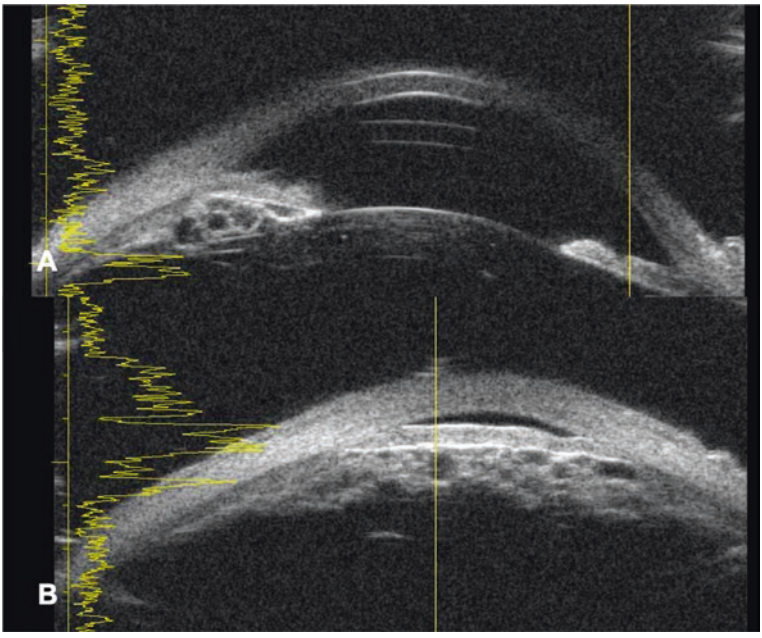

Fig. 21 Multiple ciliary cysts. The figure shows congenital ciliary cysts with multiple sized cysts in the axial (**A**) and transverse (**B**) scans. These cysts have variable sizes with significant changes during the time. Ciliary body has porous and spongiform pattern in this case

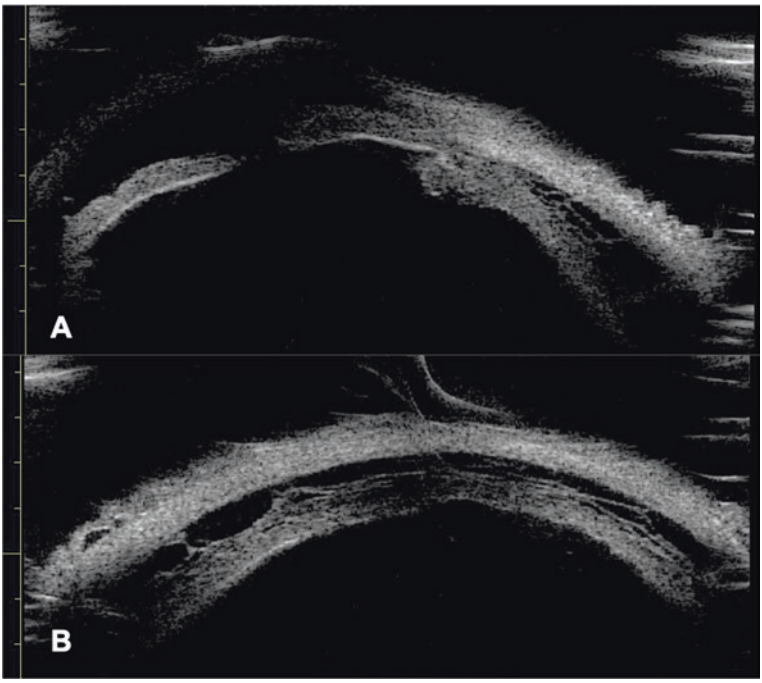

Fig. 22 Refractory hypotonia. The figure shows the detachment of the ciliary body with thin ciliary body approximately in 180 degree shown on longitudinal (up) and transverse (down) cuts. On the upper figure we see an peripheral anterior synechia caused by old uveitis

Suggested Reading

1. He M, Wang D, Jiang Y. Overview of ultrasound biomicroscopy. J Curr Glaucoma Pract. 2012;6(1):25–53.
2. Liebmann JM, Ritch R. Ultrasound biomicroscopy of the anterior segment. J Am Optom Assoc. 1996;67(8):469–79.
3. Dada T, Gadia R, Sharma A, Ichhpujani P, Bali SJ, Bhartiya S, Panda A. Ultrasound biomicroscopy in glaucoma. Surv Ophthalmol. 2011;56(5):433–50.

Age-Related Macular Degeneration (ARMD)

Hamid Riazi Esfahani and Fedra Hajizadeh

Age-related macular degeneration (ARMD) is the main cause of irreversible visual loss affecting 10–15% of adults over 65 years of age in developed countries. In individuals over the age of 75, the incidence is approximately 30%. It has traditionally been categorized into two major types: non-exudative or "dry" AMD, and exudative or "wet" AMD.

Dry AMD: Eyes with drusen, non-neovascular pigment epithelial detachments (PEDs),macular pigmentary alterations and migrations and geographic or non-geographic atrophy.

Wet AMD: Eyes with neovascularization, which are subdivided into type 1, 2, and 3 neovascularization based on the spectral-domain optical coherence tomography (SD-OCT) findings.

Non-exudative AMD

Drusen

Different types of drusen have been defined, including hard drusen, soft drusen, cuticular drusen and calcified drusen.

Small drusen, also called hard drusen, are defined as small yellow lesions (less than 63 μm in size) with distinct borders. Medium-sized drusen are 63–124 μm in size. Large drusen, also termed soft drusen, are 125 μm or greater in size and often have indistinct borders. Large drusen may combine with each other to form a drusenoid PED, which is generally considered to be 350 μm or greater in size.

F. Hajizadeh (✉)
Noor Ophthalmology Research Center, Tehran, Iran
e-mail: fhajizadeh@noorvision.com; fedra_hajizadeh@yahoo.com

H. Riazi Esfahani
Farabi Eye Hospital, Tehran University of Medical Sciences, Tehran, Iran
e-mail: amidriazi@gmail.com

M. Mohammadpour (ed.), *Diagnostics in Ocular Imaging*,
https://doi.org/10.1007/978-3-030-54863-6_17

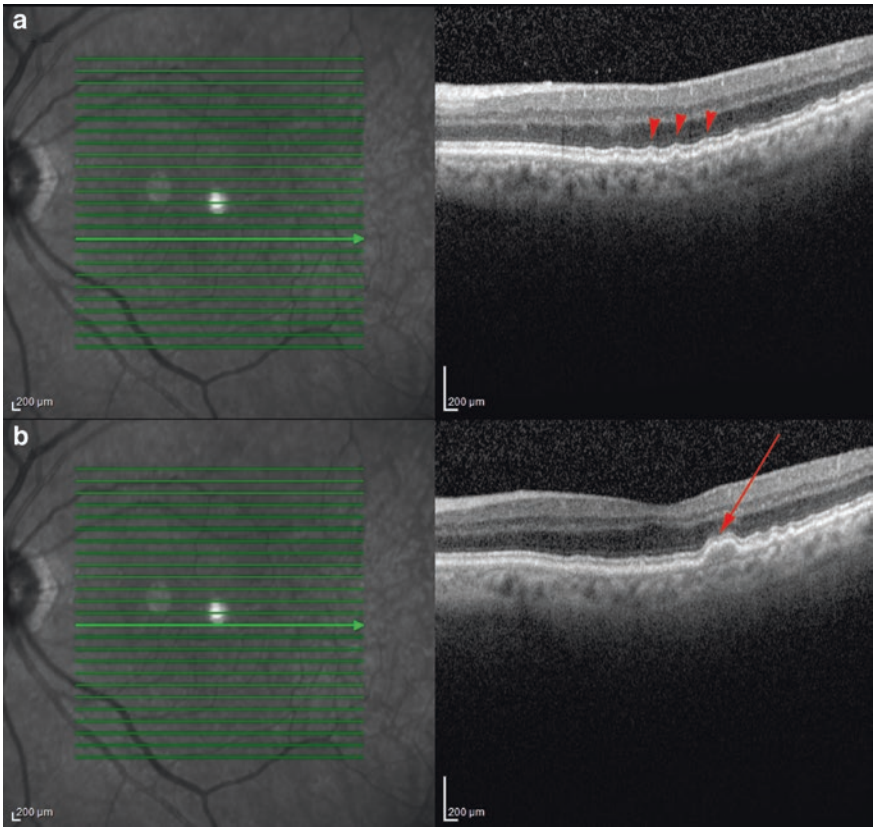

Fig. 1 **a** The SD-OCT display a cluster of hard drusen (red arrowheads). **b** A single medium soft drusen as a dome-like elevations of the pigment epithelium (red arrow) with multiple hard drusen

Drusen development and resorption can occur simultaneously in patients with AMD. Large drusen resorption, may be lead to geographic atrophy.

Cuticular drusen (basal laminar deposits) seem as numerous identical tiny, yellow round accumulations under the RPE in young to middle age patients.

With fluorescein angiography in early phases, they reveal a "starry-sky" appearance with multiple pinpoint hyper-fluorescent dots against a dark setting.

In OCT imaging, a characteristic "sawtooth" pattern may be observed. Acquired vitelliform lesions may be developed in these eyes in subretinal space. Also, these eyes may develop large drusen or choroidal neovascularization (CNV) later in their course (Fig. 1).

Subretinal Drusenoid Deposit (Reticular Pseudodrusen)

Subretinal Drusenoid Deposit (SDD) is defined as an interlocking pattern of yellowish deposits above the RPE that appears whiter than typical drusen. They are primarily appeared in the superior outer macula and may progress to involve the central macula.

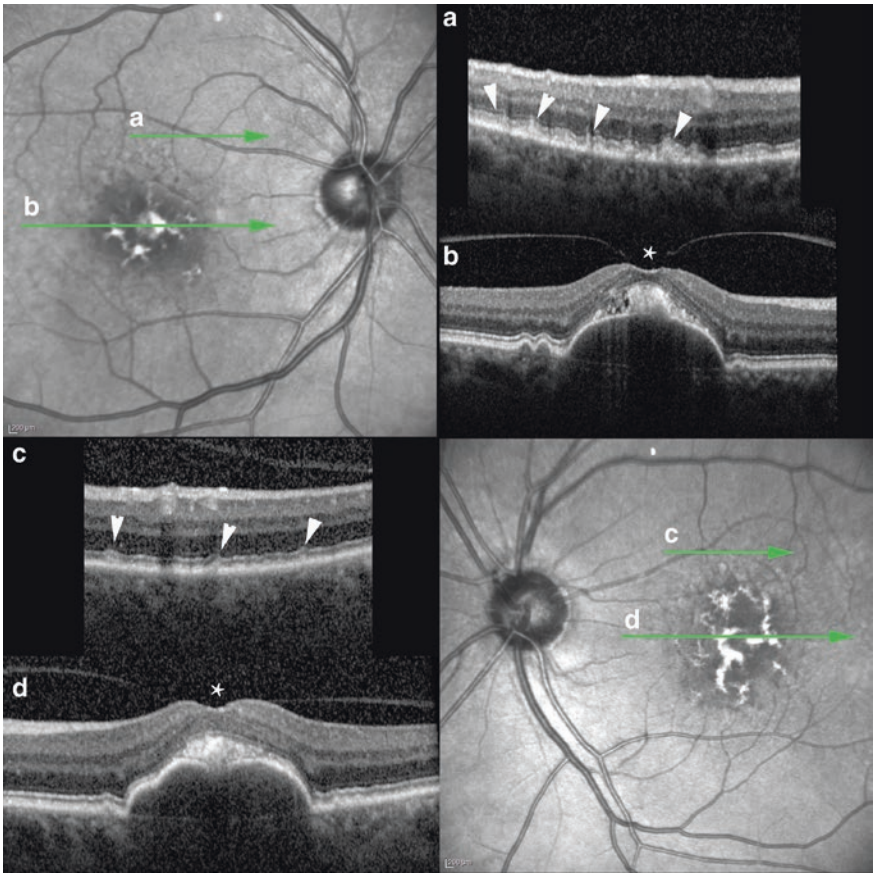

Fig. 2 This patient has Subretinal Drusenoid Deposit (SDD) or reticular pseudodrusen throughout the superior part of the fundus in both eyes. SDD have a predilection for the superior paramacular in most cases (**a**). In SD-OCT, SDD situated above the RPE band in subretinal space that may violate the external limiting membrane (ELM) (**a** and **c**). The SD-OCT from central macula shows large drusenoid PED with a hyper-reflective materials due to pigment clumping lying immediately at the of top the drusenoid PED with some posterior shadowing (**b** and **d**)

Although these lesions may be missed with fluorescein angiography, but are best visualized with near infrared scanning laser ophthalmoscopy or blue light reflectance imaging.

They are accompanying with a higher risk of type 2 neovascularization than are other types of drusen (Fig. 2).

Atrophy

Although drusen are the hallmark for Dry AMD, but other abnormalities including RPE atrophy, RPE hyperplasia and PED may be observed. RPE atrophy associated with outer retina and choriocapilaries atrophy in well-defined areas larger than 175 μm is called geographic atrophy.

These areas are often oval or round with a predilection for the central macula. The state of the RPE can be evaluated with Fundus auto-fluorescence in marginal zone of the atrophic area. Indeed, the areas without RPE and overlying outer retina look hypo-autofluorescent with this imaging technique. While, the margin of the atrophic area may be hyper-autofluorescence that may indicate the cells that are at risk for becoming atrophic in the future. With fluorescein angiography, early hyper-fluorescence, representing a transmission defect. Although, if there is choriocapillaries loss, only large choroidal vessels will be seen coursing through the stained sclera in atrophic zone in the late phases of the study.

Pigmentary Changes

Pigmentary changes, either hyperpigmentation or hypopigmentation may occur in dry AMD. These changes may be an indicator for progression to geographic atrophy and wet type disease.

AMD classification	Definition
No obvious age related changes	Without any drusen or pigmentary abnormality
Normal aging changes	Only small drusen (drupelets) with no other RPE changes including pigmentary changes or geographic atrophy
Early AMD	Medium drusen or other RPE changes including pigmentary changes or geographic atrophy
Intermediate AMD	Large drusen with or without pigmentary changes
Advance AMD	Wet AMD with or without geographic atrophy, geographic atrophy alone

Acquired Vitelliform Lesions

These round lesions are collections of extracellular photoreceptors derived yellow materials in the subretinal space that may occur in association with a variety of entities, including dry type AMD. These material originated from photoreceptor

outer segment shedding that accumulate in the subretinal space due to loss of apposition between the photoreceptor tips and the RPE apical surface or RPE dysfunction.

As these materials contain variable amounts of lipofuscin and melanin, they revealed hyper-autofluorescence and hyper-reflectance appearance on fundus auto-fluorescence and infrared reflectance imaging.

Histopathologic studies have revealed varying degrees of RPE, ellipsoid zone, external limiting membrane (ELM) and outer nuclear layer attenuation; intraretinal migration of pigment-laden cells. Eyes with acquired vitelliform lesions are also at risk of developing geographic atrophy or choroidal neovascularization.

Pigment Epithelial Detachment

The Retinal pigment epithelial detachment (PED) is a separation between retinal pigment epithelium (RPE) and the underlying Bruch layer. The PEDs can be categorized into drusenoid, serous, vascularized, or mixed subtypes.

Drusenoid PED

They usually occur in accompanying with large confluent drusen. OCT imaging usually shows PED with or without undulating surface with an underlying moderate to high reflectivity.

It is common to see hyper-reflective materials due to pigment clumping laying immediately at top the drusenoid PED with some posterior shadowing. Subretinal fluid is not typical for drusenoid PEDs although, the presence of hypo-reflective area in sub-retina does not necessarily reflect that there is a related CNV. It can be due to a sick RPE that lead to subretinal fluid formation or an acquired vitelliform lesion. These PEDs may be collapsed and RPE atrophy may be formed.

No abnormal choroidal flow or vascular tangled should be detected beneath the PED on en face OCTA.

However, some artefacts on OCT-A of Drusenoid PEDs may mimic the CNV features. These artefacts may be due to vessel projection from the more superficial retinal vessels or unmasking artefacts from overlying RPE atrophy.

There is no consensus on a size to distinguish drusenoid PEDs from a large drusen, although many specialists have defined a drusenoid PED as measuring 350 μm or more in height (Fig. 3).

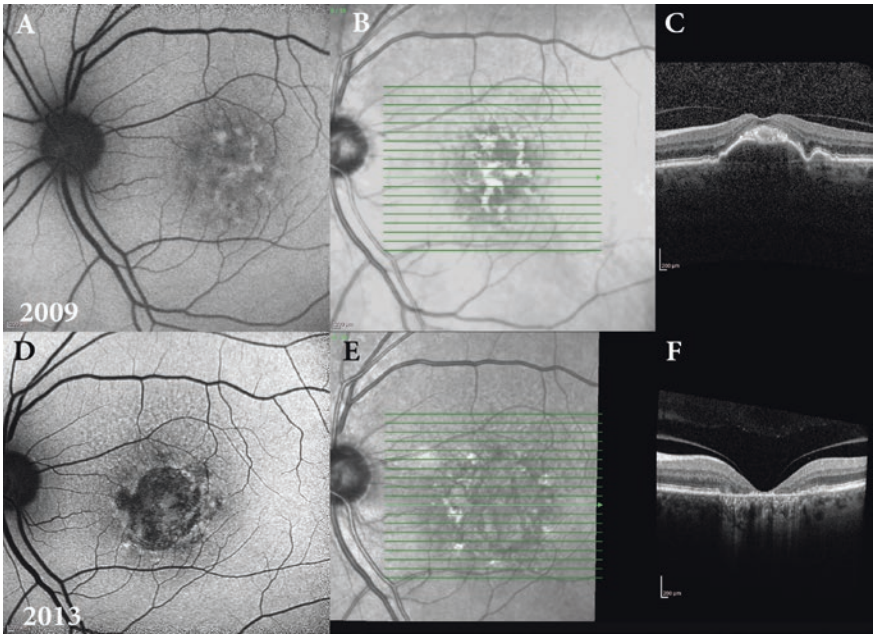

Fig. 3 Imaging of a patient with a drusenoid PED and overlying acquired vitelliform lesion due to abnormal RPE function at the top of the RPE. (upper images: fundus autofluorescence (**a**), scanning laser ophthalmoscopy (**b**) and SD-OCT (**c**), respectively). The lesion resolves completely over 4 years (**d**, **e**, **f**), leaving a geographic atrophy of the RPE and outer retina with outward disfiguration of the retina

Serous PED

Serous PED is a well-demarcated RPE elevation without any obvious notch. It contains a homogenously hyporeflective space.

OCTA confirms a non-vascularized nature of theses PEDs, with no signs of abnormal flow beneath the RPE. Any irregular border or notching of the serous PED may be an indicator for CNV formation. (vascularized serous PED) (Fig. 4).

Wet AMD

Wet AMD is characterized by the presence of choroidal or sometimes intraretinal neovascularization with associated subretinal and/or intraretinal fluid or haemorrhages. In Type 1 neovascularization, the tangle of the vessels proliferates under

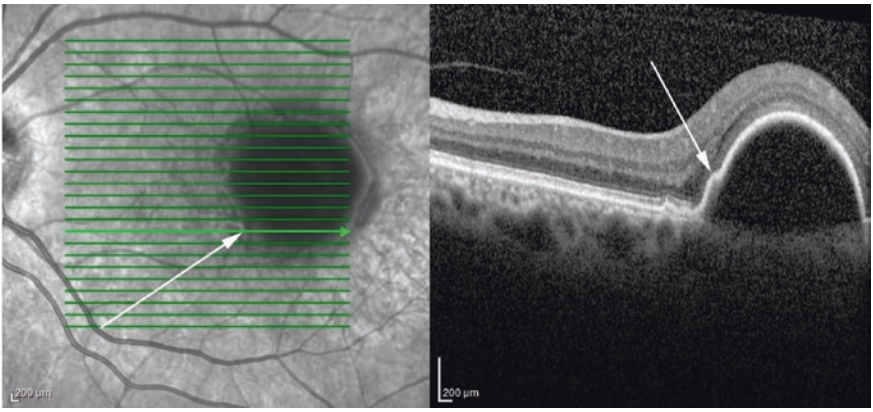

Fig. 4 SD-OCT of left eye shows serous PED with a notching (white arrows) compatible with vascularized serous PED. The Scanning laser ophthalmoscopy of the left eye reveals irregular PED with a notching at the site of neovascularization

the RPE. Type 2 neovascularization, in which choroidal vessels have perforated the RPE complex reaching to the subretinal space.

Third subtype of neovascularization (type 3) in AMD that also referred to as retinal angiomatous proliferation(RAP) is recognized with proliferation of new vessels within the retina itself. This type of neovascularization may, have simultaneous choroidal CNV, although the main feature is active proliferation within neurosensory retina originated from deep retinal capillary plexiform.

Another form of neovascularization is polypoidal choroidal vasculopathy (PCV), which is a subgroup of the type 1 neovascularization, as it is located beneath the RPE. With PCV, there may be a branching vascular network (BVN) with terminal polypoidal changes.

Type 1 Neovascularization

The most common type of CNV in AMD is vascularized PED (type 1 NV). It originates from the choroid and extends under the RPE that causes vascularized serous PED with uneven surfaces and an irregular shape.

This form of neovascularization is poorly delineated with fluorescein angiography and reveals irregular stippled areas of leakage in the late phase (Fig. 5).

A notch at the edge of an otherwise regular serous PED is highly suspicious of an underlying vascularization either in angiography or OCT (Fig. 4).

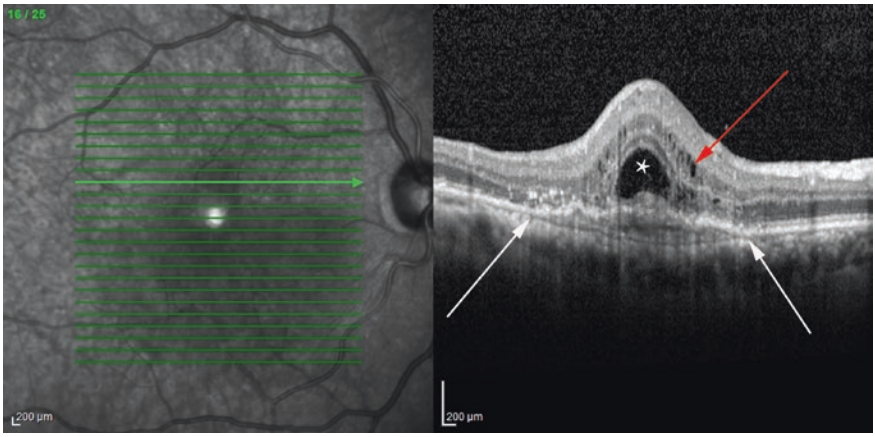

Fig. 5 A fibrovascular PED (between white arrows) accompanied with macular thickening, subretinal (asterix) and intra retinal fluid (red arrow)

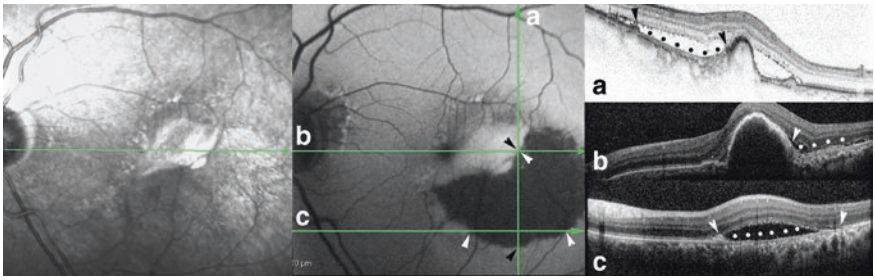

Fig. 6 RPE tear: There is pigment epithelial clumping due to consolidation of the ripped RPE layer (flap of preserved pigment epithelium) that cause hyper reflective and hyper autofluorescence appearance in fundus scanning laser ophthalmoscopy and autofluorescence (the left and middle images). Also, there is an area without RPE (between the arrow heads). Fundus scanning laser ophthalmoscopy and autofluorescence show hypo reflective and hypoautofluorescence lesions corresponding to these bare areas. SD-OCT reveals RPE void areas that indicated with dot line between the arrowheads. (Right image)

Retinal Pigment Epithelium Tears

RPE tears can occur as the natural course of the fibrovascular PEDs in neovascular AMD. The risk of RPE tear is known to be 15% greater in those with tall PED who receiving anti-VEGF therapy.

Large RPE tears may lead to severe visual loss, but visual acuity may be preserved in eccentric small RPE tear (Fig. 6).

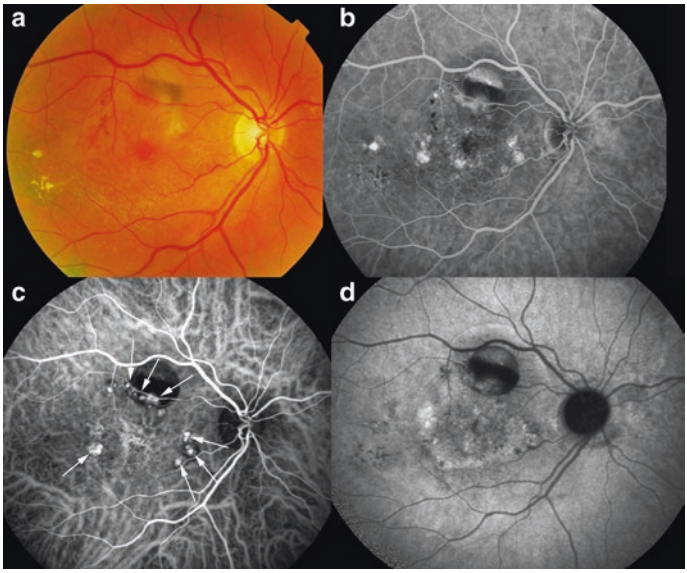

Fig. 7 **a** Hemorrhagic detachments of the pigment epithelium and neurosensory retina with prominent intra and subretinal exudation are the hallmarks for PCV. **b** Fluorescein angiography shows an area of hyperfluorescence corresponding to the vascular abnormality, but the ICG angiogram clearly explains the features. **c**, **d** ICG angiography on the bottom images shows a branching vascular network with polypoidal elements (arrows)

Polypoidal Choroidal Vasculopathy

PCV as a subtype of type 1 neovascularization is associated with choroidal abnormalities such as increased thickness, hyperpermeability, and pachyvessels and absence of the typical AMD clinical findings (such as drusen or pigmentation).

Polypoidal neovascularization is a recently defined Type 1 neovascularization with polyps, in the absence of other phenotypic and demographic features characteristic of PCV like pachychoroid.

OCT usually demonstrates a shallow irregular PED that contains BVN, called "double layer sign". These shallow irregular PED usually located beside one or more thumb shaped PED or large notched serous PED. Polyps could be identified as a String of round structures below the surface of a large thumb shaped PED ("pearls on string appearance") (Fig. 7C) or as solitary round lesion beneath smaller peaked PED (at the area of the notch) (Fig. 8).

Although the BVN is detected on en face OCT-angiography in nearly all cases, the polyps are not readily visible on the en face OCT-A images. Static properties due to partial obstruction of lumen and low flow velocity are the presumed reasons for this pattern. Although, swept sourse (SS) OCT-A may have advantage over

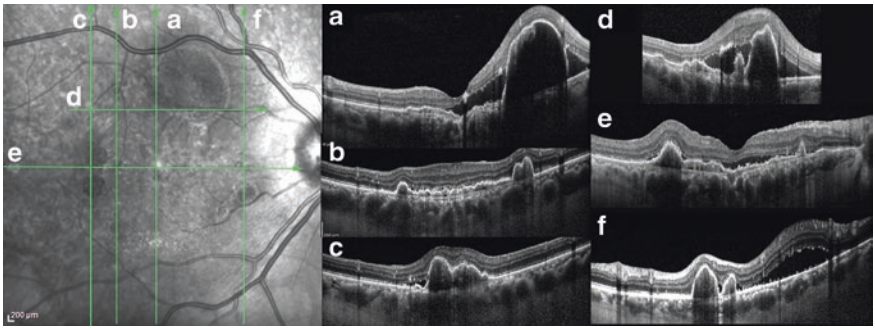

Fig. 8 OCT of the same patient demonstrates, shallow irregular PED called "double layer sign" (**b**, **c**) beside one or larger peaked PED or large notched serous PED (**a**, **d**). The shallow irregular PEDs usually contain BVNs between elevated RPE and Bruch's membrane. Polyps could be detected underneath the surface of a large thumb shaped PED (**e**, **f**) or notched PED

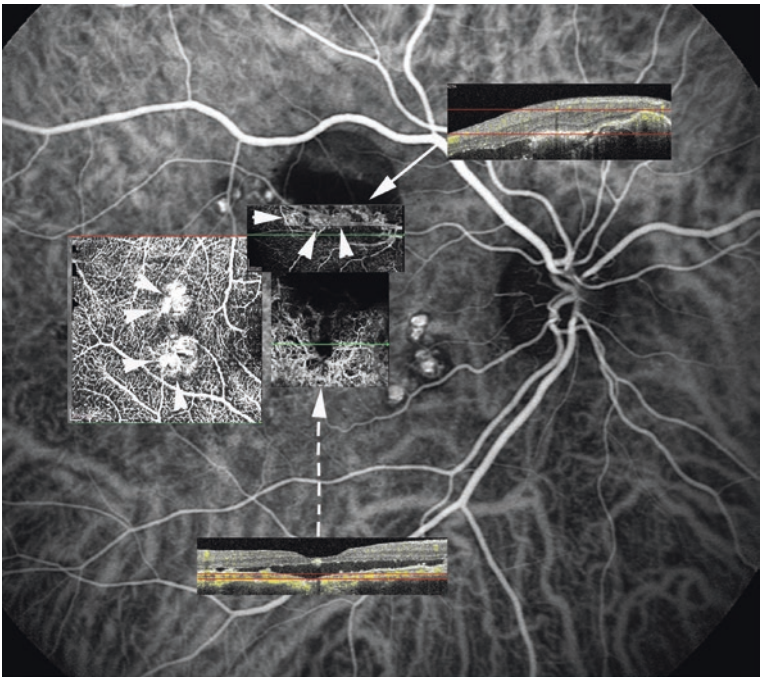

Fig. 9 ICGA of the same patient with overriding en-face OCT-angiography. OCT-A from polyps in various area at macula(white arrowheads) and large choroidal vessels at foveal center(dashed arrow) are notable

other OCT-A systems to detect polyps but ICGA is still a gold standard imaging to detect polyps. (Fig. 9).

Type 2 Neovascularization

This form of neovascularization penetrates the RPE – Bruch membrane complex and proliferates above the RPE in the subretinal space. In FA, it demonstrates well-defined early vascular pattern with late leakage.

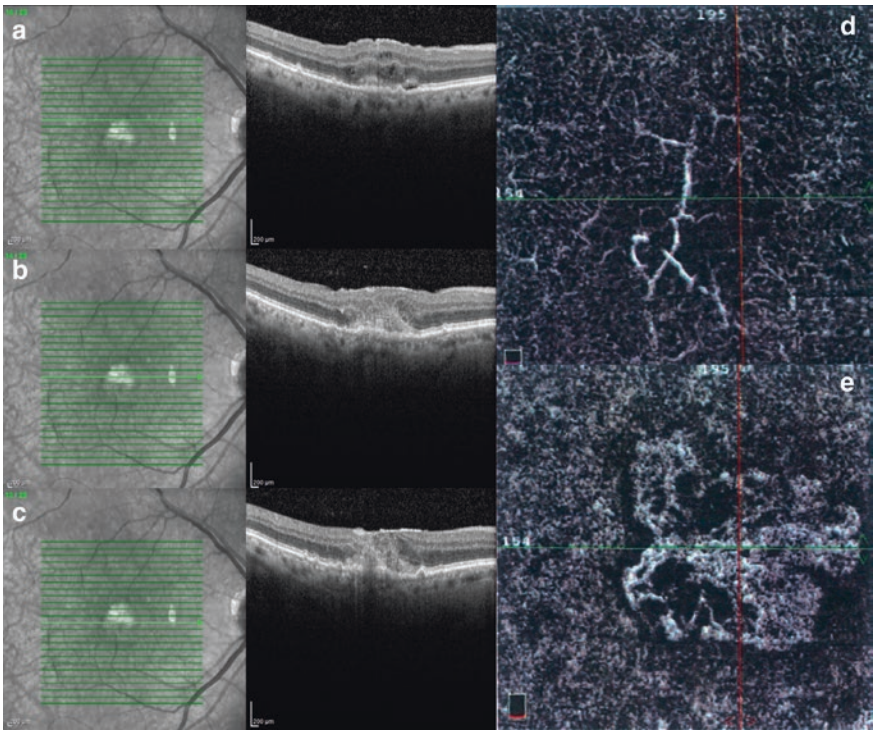

Fig. 10 The SD-OCT of the type 3 neovascularization (left column). **a** Small intraretinal fluid with minimal subretinal fluid in SD-OCT. **b** Intraretinal funnel shape hyper-reflective lesion at the level of the inner nuclear layer representing type 3 neovessels overlying a PED with RPE erosion. **c** Growing intraretinal type 3 lesion. **d**, **e** Corresponding en-face OCT angiography at the level of deep retina that shows intraretinal abnormal vessels arising from deep retinal capillary plexus at the level of the inner nuclear layer (**d**), there is usually clew-like vascular lesion at the level of the choriocapillaris (**e**)

Pure type 2 neovascular lesions is not common feature. But type 2 is the most common lesion type in other circumstances including pathological myopia, angioid streaks, multifocal choroiditis.

Type 3 Neovascularization (Retinal Angiomatous Proliferation (RAP))

Type 3 Neovascularization is characterized by the formation of predominantly intra-retinal vascularization originated from deep retinal capillary plexus that can be accompanied with a vascularized PED.

In contrast to type 1 or type 2 neovascularization, Type 3 lesions are typically associated with prominent intraretinal edema or haemorrhage and rarely subretinal fluid.

In this circumstance, PEDs are usually smaller than other type 1 neovascularisations including PCV-related vascularized PEDs. In OCT, in earlier stages there is focal RPE erosion over a small PED. Later, inverted funnel-shaped inner retinal lesion joining a small,elevated PED usually without obvious subretinal fluid

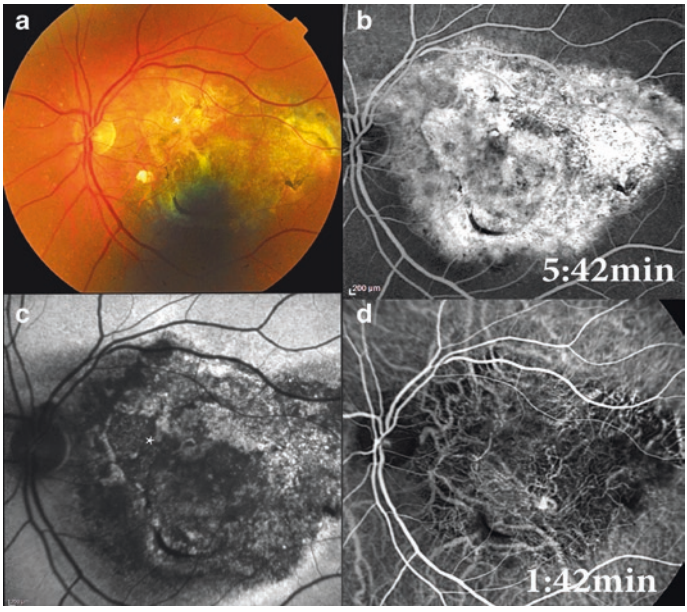

Fig. 11 **a** Color fundus of a patient with disciform scar.Sub-retinal scar and fibrosis are remarkable(asterix). **b** FA at late stage shows prominent and severe staining of scar tissue. **c** FAF illustrates considerable hyporeflectivity secondary to widespread RPE disruption. **d** ICG in mid phase shows loss of chriocapillaris and dark area in macula due to tick scar and fibrous tissue

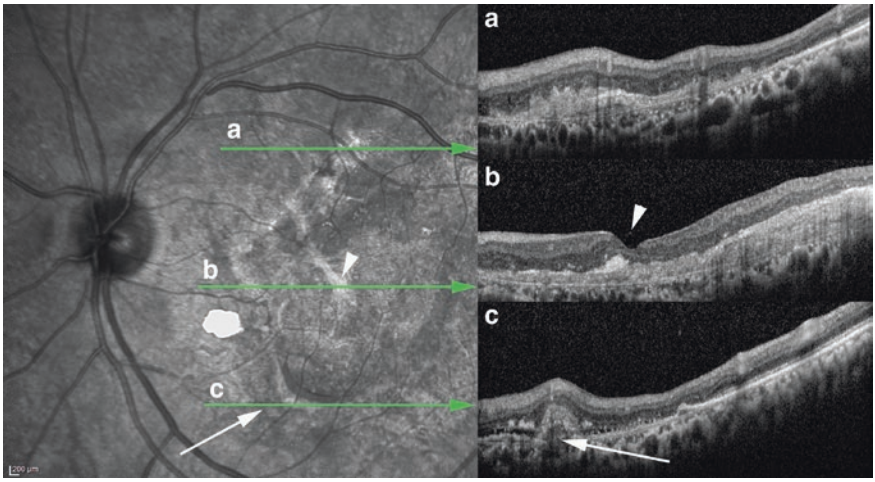

Fig. 12 SLO-OCT of the same patient in Fig. 11. Prominent sub-retinal scaring from advance CNV, the arrow shows the residual active CNV site with sub-retinal fluid (white arrow).Significant photoreceptor disruption in fovea (white arrowhead) predicts poor vision in this case

("kissing sign") is formed. In contrast to other types of CNV in which the external limiting membrane (ELM) may remain intact, disruption of the external limiting membrane on top of the PED is prominent feature from earlier stages in this type of CNV Fig. 10.

Disciform Scarring

Patients with advance wet type AMD may develop disciform scarring from any type of neovascularization. In this situation, there is no way to differentiate the type of neovascularization due to prominent sub-retinal and sub RPE fibrous formation (Figs. 11 and 12).

Suggested Reading

1. Spaide RF, Curcio CA. Drusen characterization with multimodal imaging. Retina. 2010;30(9):1441–54.
2. Roquet W, Roudot-Thoraval F, Coscas G, Soubrane G. Clinical features of drusenoid pigment epithelial detachment in age related macular degeneration. Br J Ophthalmol. 2004;88:638–42.
3. Lima LH, Laud K, Freund KB, Yannuzzi LA, Spaide RF. Acquired vitelliform lesion associated with large drusen. Retina. 2012;32(4):647–51.
4. Zweifel SA, Spaide RF, Yannuzzi LA. Acquired vitelliform detachment in patients with subretinal drusenoid deposits (reticular pseudodrusen). Retina. 2011;31(2):229–34.

5. Sarraf D, Reddy S, Chiang A, et al. A newgrading system for retinal pigment epithelial tears. Retina. 2010;30(7):1039–45.
6. Constantinides G. Relation between retinal pigment epithelial detachment and dye leakage in central serous retinopathy. J Fr Ophtalmol. 2000;23(7):649–54.
7. Spaide RF. Enhanced depth imaging optical coherence tomography of retinal pigment epithelial detachment in age-related macular degeneration. Am J Ophthalmol. 2009;147(4):644–52.
8. Rahimy E, Freund KB, Larsen M, Spaide RF, Costa RA, Hoang Q, et al. Multilayered pigment epithelial detachment in neovascular age-related macular degeneration. Retina. 2014;34(7):1289–95.
9. Coscas GJ, Lupidi M, Coscas F, Cagini C, Souied EH. Optical coherence tomography angiography versus traditional multimodal imaging in assessing the activity of exudative age-related macular degeneration: a new diagnostic challenge. Retina. 2015;35(11):2219–28.
10. Miller AR, Roisman L, Zhang Q, et al. Comparison between spectral-domain and swept-source optical coherence tomography angiographic imaging of choroidal neovascularization. Invest Ophthalmol Vis Sci. 2017;58(3):1499–505. https://doi.org/10.1167/iovs.16-20969.
11. Cheung CMG, Yanagi Y, Mohla A, Lee SY, Mathur R, Chan CM, et al. Characterization and differentiation of polypoidal choroidal vasculopathy using swept source optical coherence tomography angiography. Retina. 2017;37(8):1464–74.
12. Inoue M, Balaratnasingam C, Freund KB. Optical coherence tomography angiography of polypoidal choroidal vasculopathy and polypoidal choroidal neovascularization. Retina. 2015;35(11):2265–74.
13. Kuehlewein L, Dansingani KK, de Carlo TE, Bonini Filho MA, Iafe NA, Lenis TL, et al. Optical coherence tomography angiography of type 3 neovascularization secondary to age-related macular degeneration. Retina. 2015;35(11):2229–35.
14. Freund KB, Ho IV, Barbazetto IA, et al. Type 3 neovascularization: the expanded spectrum of retinal angiomatous proliferation. Retina. 2008;28:201–11.

Central Serous Chorioretinopathy (CSC)

Fatemeh Bazvand and Fariba Ghassemi

Definition and Pathophysiology

Central serous chorioretinopathy (CSC, CSCR), the fourth most common non-surgical retinopathy is characterized by serous retinal detachment with or without pigment epithelial detachment (PED). The acute CSC is a self-limiting disease in general; however, sequel such as recurrence of diffuse retinal pigment epitheliopathy (DRPE) and choroidal neovascular membrane (CNVM) can occur. Primary pathology was reported to be prominently in RPE and choroid. CSC has recently been shown to be a part of the spectrum of pachychoroid diseases including pachychoroid pigment epitheliopathy, CSC, pachychoroidneovasculopathy (PNV) and polypoidal choroidal vasculopathy (PCV).

Epidemiology, Demography and Risk Factors

CSC is more common in males (male/female: 2.6–6/1) and between 20 and 64 years age. Bilateral CSC can occur in 14–40% of cases and is higher in Asian. Some conditions including poorer visual acuity, DPRE changes and secondary CNVM are more frequent in the elderly patients than young cases.

Probable risk factors include steroid usage, autoimmune disease, psychopharmacologic medication use, Helicobacter pylori infection, Type A behavior, sleeping disturbance, hypertension, sympathomimetic agents (pseudoephedrine, oxymetazoline, 3,4 methylenedioxymethamphetamine, and ephedra), phosphodiesterase-5

F. Bazvand · F. Ghassemi (✉)
Tehran University of Medical Sciences (TUMS), Tehran, Iran
e-mail: fariba.ghassemi@gmail.com

F. Bazvand
e-mail: ft1_bazvand@yahoo.com

M. Mohammadpour (ed.), *Diagnostics in Ocular Imaging*,
https://doi.org/10.1007/978-3-030-54863-6_18

inhibitors (ie sildenafil and tadalafil) and familial predisposition. Some situation like polymorphisms in Complement factor H and Cathedrin and probable inherited thick choroid with dilated outer choroidal vessels (pachyvessels) can be categorized as familial predisposition.

In cases of CSC, hyperpermeable choroid is seen as a result of inflammation, ischemia, or choroidal circulation stasis.

Clinical Features

The presenting symptoms include metamorphopsia, micropsia, central scotoma or blurred vision.

The features of CSC can be classified as acute (generally resolved within 3–4 months) or chronic disease (at least duration: 4–6 months). In acute phase, typically a serous macular detachment is seen. Fibrin as yellowish subretinal material also could be seen. Retinal pigmentary epithelium (RPE) defects may be seen clinically. RPE degeneration and atrophy, cystoid and schitic retinal edema and choroidal neovascularization (CNV) are observed in chronic stage or DRPE.

Multimodal Imaging of CSC

Different image modalities can be used in CSC. The findings of these images are summarized in Table 1.

Sub-Retinal Fluid (SRF) (Figs. 1, 2, 3, 4, 5, 6, 7, 8, 9)

In acute CSC, SRF appears to be hypoautofluorescence and in chronic CSC to be hyperfluorescence in FAF. The latter one is due to presence of sub-retinal precipitates in SRF. In location of SRF, dark area at the choriocapillaris is observed in OCTA as diffuse or focal ill-defined area.

Pigment Epithelial Detachment (PED) (Figs. 1, 2 and 9)

As a common finding in CSC PED may be noted in more than 50% of cases and is located within or outside the SRF. Serous type of PED is common in CSC. Usually, PED could be localized at the area of choroidal vascular hyperpermeability in ICGA (indocyanine green angiography) and pachychoroid in EDI-OCT (enhanced depth OCT). PED shows foci as early hyper-cyanescence that changes

Table 1 Findings of multimodal imaging in acute and chronic central serous chorioretinopathy (CSC)

Image	General	Acute CSC	Chronic CSC
OCT	– Subretinal fluid (SRF) – Microrips – PED – A clump or band-like fibrin deposits in subretinal space	– Intact neurosensory retina – Photoreceptors outer segment elongation in longer time – Focal erosion of photoreceptor outer segment – Intraretinal HRD	– HRDs – RPE layer irregularity – A double layer sign – Permanent subretinal deposits – Complete disappearance of outer segments
EDI-OCT	– Increased choroidal thickness – Dilated vessels of outer layer of choroid – Choriocapillaris atrophy	– Increased choroidal thickness – Dilated vessels of outer layer of choroid – Choriocapillaris atrophy	– Increased choroidal thickness – Dilated vessels of outer layer of choroid – Choriocapillaris atrophy
Enface OCT	– Thinning of the inner choroidal layer – Focal or diffuse outer choroidal vessel dilatation – Hyperreflective areas at level of Bruch's membrane and choriocapillaris complex – Absence of a signal at the RPE level	Thinning of the inner choroidal layer – Focal or diffuse outer choroidal vessel dilatation – Hyperreflective areas at level of Bruch's membrane and choriocapillaris complex – Absence of a signal at the RPE level	– HRD in inner choroid – Hyperreflectivity of wall of dilated vessels – CNV
FAF	– NIR-FAF may be more sensitive than SW-FAF to detect outer retinal changes in CSC – Combining the two methods of autofluorescence imaging, SW-FAF and NIR-FAF, can better predict recent or resolved CSC episodes	– Hypoautofluorescence dot and area in SW-FAF – Hypoautofluorescence dot and area like SW-FAF in NIR-FAF – Granular hyperautofluorescence in NIR-FAF	– Hypoautofluorescence at the point of leakage in most cases – Hyperautofluorescence at the previous leakage point – Punctate or granular hyperautofluorescence – Mixed FAF patterns – Granular hyperautofluorescence
FFA	– To establish the diagnosis – To rule out other differential conditions. – To determine the type of leakage pattern – To localize the leakage point	– Leakage point: a single point or multifocal points	– Multifocal leakage or diffuse oozing as granular or mottled hyperfluorescence – Window defect – Leaking scar, or blowout leak
ICGA	– Dilated choroidal vessels – Choroidal hyperpermeability – Congested vortex vein ampullas – PED	– Choroidal filling delay in early phase – Focal choroidal hyper-cyanescence – Wash-out, or centrifugal displacement of hyper-cyanescence in the late phase	– CNV – Area of RPE atrophy

(continued)

Table 1 (continued)

Image	General	Acute CSC	Chronic CSC
OCTA	– Dark area and spot – Focal choroidal ischemia with surrounding hyperperfusion – Dilated choriocapillaris	– Dark areas at the choriocapillaris – Dark spots at the choriocapillaris – Abnormal choroidal vessels	– CNV – Abnormal choroidal vessels

CSC Central serous chorioretinopathy, *CNV* Choroidal neovascularization, *OCT* optical coherence tomography, *EDI-OCT* enhanced depth optical coherence tomography, *FAF* Fundus autofluorescence, *FFA* Fundus Fluorescein Angiography, *HRD*: Hyperreflective dots**,** *ICG* indocyanine green, *NIR* Near infrared, *OCTA* optical coherence tomography angiography, *SW-FAF* Short wave fundus autofluorescence

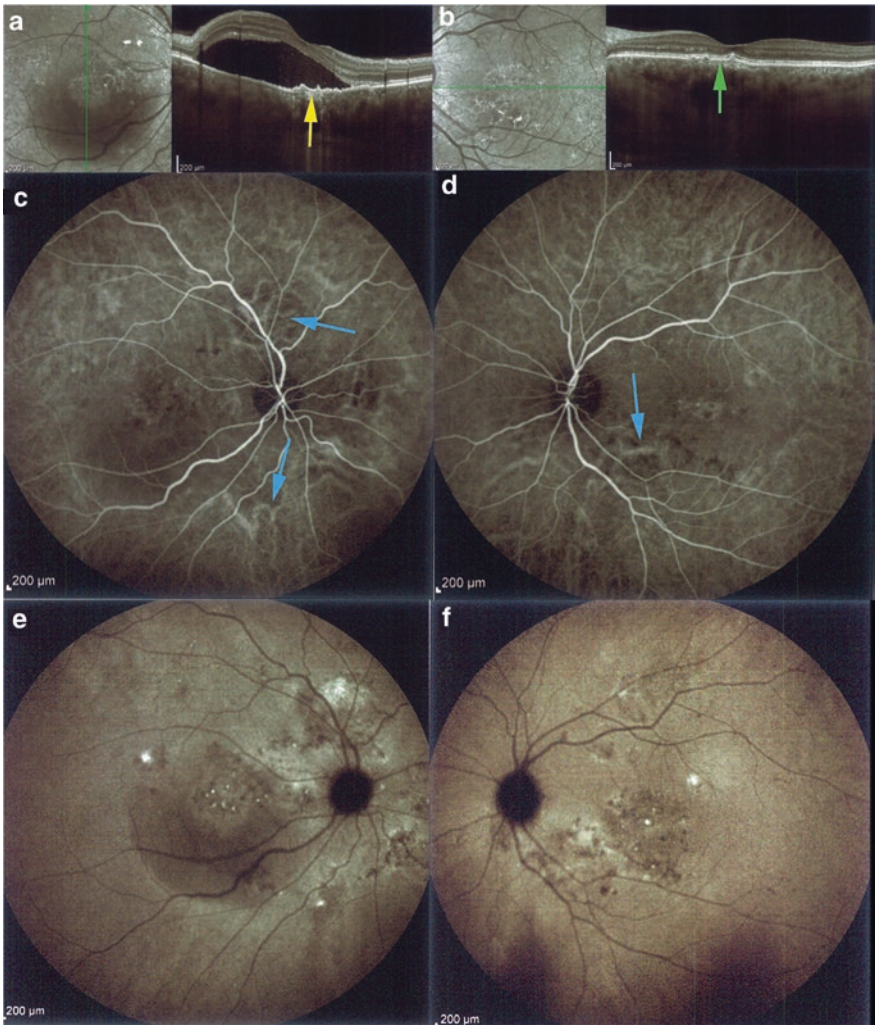

Fig. 1 Chronic CSC. **a** and **b** Optical coherence tomography (OCT) in right and left eye shows sub-retinal fluid, shallow irregular PED (pigment epithelial detachment)(yellow arrow) and hyper-reflective dots (HRD) in right eye and irregular RPE (retinal pigment epithelium) in left eye (green arrow). **c** and **d** Dilated choroidal vessels and hyper-permeability (blue arrow) in both eyes are observed in ICGA (Indocyanine angigraphy). **e** and **f** FAF (fundus auto-flourescence) reveals mix pattern of hyper and hypo-fluorescence in both eyes due to chronic CSC

hypo-cyanescence surrounded by a ring of hypercyanescence in late phase. Wash-out, (Fig. 9) or centrifugal displacement of hyperfluorescence in the late phase of ICGA could observe at this site. PED is observed as dark spot at the chorio-capillaris (Fig. 9) level in OCTA as single or multiple, well-defined areas with no detectable flow.

Hyper-Reflective Dot (HRD) or Precipitates (Figs. 1 and 3)

The origin of these HRD is not clear. The suggested probable origins are shed photoreceptor outer segments, activated microglia and macrophages, or concentrated fibrin or lipid compounds. HRDs (hyperreflective dots) increase in number with time, indicating the chronicity of SRF. Sometimes, HRD may be noted

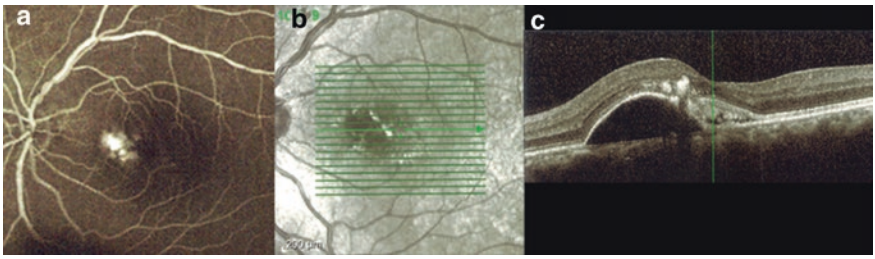

Fig. 2 Pigment epithelial detachment and accumulation of vitelliform lesion in chronic CSC. **a** FFA (fundus fluorescein angiography) of left eye shows irregular staining (other scans don't reveal here) in nasal part of macula. **b** IR (infrared image) reveals hypo-reflective area in macula in association with reticular hyper-reflective lines. **c** OCT shows sub-retinal fluid with hyper-reflective lesions in SRF and inner retina and PED

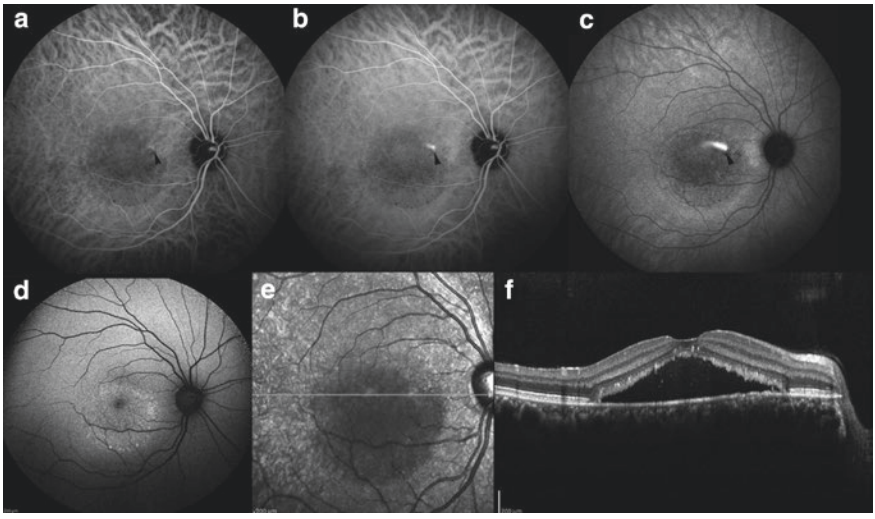

Fig. 3 Precipitates in chronic CSC. **a**, **b** and **c**ICGAs reveal a leakage site with smokestack pattern (black arrowhead) from the early to the late phases, hypo- cyanecence dots that are compatible with hyper-autofluorescent spot in FAF in area of SRF, and a ring of hyper-autofluorescence around the area of SRF (**d**). **e** IR shows hypo-reflective area consistent with SRF. **f** OCT reveals SRF with hyper-reflective precipitates inside it and elongated outer segment of photoreceptors. HRD on the top of SRF area and irregular RPE surface in nasal site of fovea also are visible

in acute CSC. In chronic and recurrent CSC, HRD is more common. HRD in inner choroid may be seen in active chronic CSC. The precipitates are hyper-autofluorescent in FAF and hypo-cyanecent in ICGA.

RPE Layer Irregularity (Fig. 1)

RPE layer irregularity is seen due to RPE atrophy as a result of prolonged detachment. FAF pattern is hypo-autofluorescence in acute CSC afterward it shows mix pattern of hypo (location of RPE atrophy and gravity-driven descending tracts of RPE atrophy) and hyper (precipitates) fluorescence. Descending tracts (Figs. 5 and 7) are hyper-autofluorescent, and after RPE damage, these tracts become hypo-autofluorescent. Area of RPE atrophy show hypercyanescence in the early phase and hypo-cyanescence in the late phase of ICGA. Fundus fluorescein angiography (FFA) shows window defect in the location of RPE atrophy in resolved CSC. In the location of diffuse RPE defect, multifocal leakage or diffuse oozing as granular or mottled hyper-fluorescence are observed.

A Double Layer Sign and Choroidal Neovascularization (CNV) (Fig. 7)

A double layer sign defined as undulated RPE layer with hyporeflective content over the intact underlying Bruch's membrane has been described in chronic CSC. A choroidal neovascularization (CNV) is sometimes present at the position of a shallow irregular PED (double layer sign).

OCTA (optical coherence tomography angiography) could show CNV in chronic CSC. The other diagnostic tool in detection of CNV is ICGA, which is an important diagnostic tool for the detection of CNV in chronic CSC.

Intra-retinal Cysts or Schitic Spaces

Intra-retinal cysts are often observed in OCT after several years due to fluid passage through damaged RPE function.

Pachychoroid (Figs. 4, 6, 8 and 11)

The choroidal vessels show abnormalities in CSC. Choroidal thickness increase and/or dilated vessels of outer layer of choroid as pachychoroid may be observed in CSC. ICGA could document abnormality of choroidal vasculature

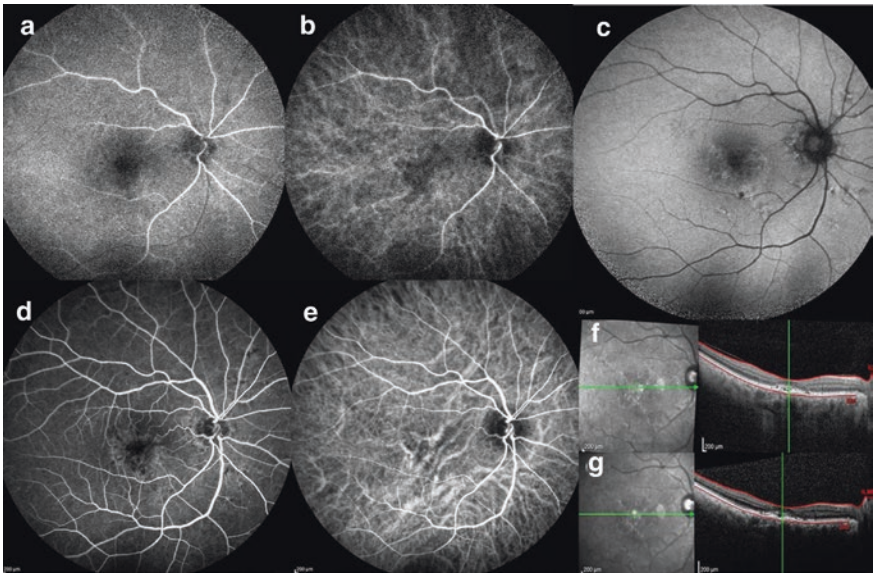

Fig. 4 Choroidal hyper-permeability. **a**, **b**, **d**, **e** ICGAs show hyper-permeability of choroidal vessels and dilated choroidal vessels from early to late phases. **c** A mixed pattern (hypo- and hyper-autofluoecent) is observed in FAF. **f** and **g** Irregularity of RPE with mottling pattern of ellipsoid zone are observed in OCT of right eyes

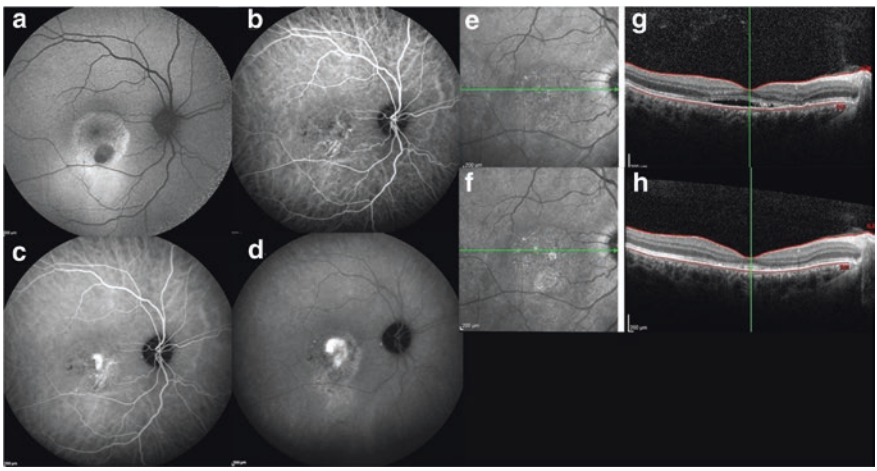

Fig. 5 **a** Descending tract in chronic CSC. FAF reveals hyper-fluorescence area in macula with hyper-autofluorescence descending tract. **b**, **c**, **d** ICGAs show dilated choroidal vessels with a plaque of hypercyanescence with smokestack pattern from the early to the late phases and producing hypercyanescent ring. **e–h** SRF with irregular and focal erosion of outer segment of photoreceptors are observed in OCT of right eye that resolved after a single session of half dose photodynamic therapy

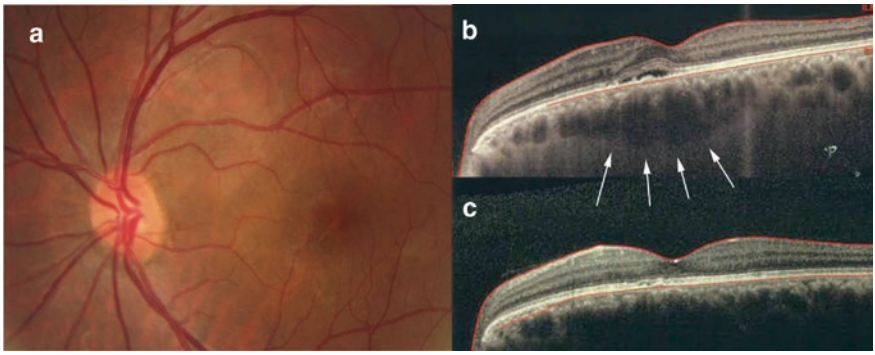

Fig. 6 **a** SRF is revealed in fundus photograph. **b** SRF in OCT over the thicker part of choroid that resolved after 3 months spontaneously (**c**). Pachychoroid vessels (white arrow) are visible

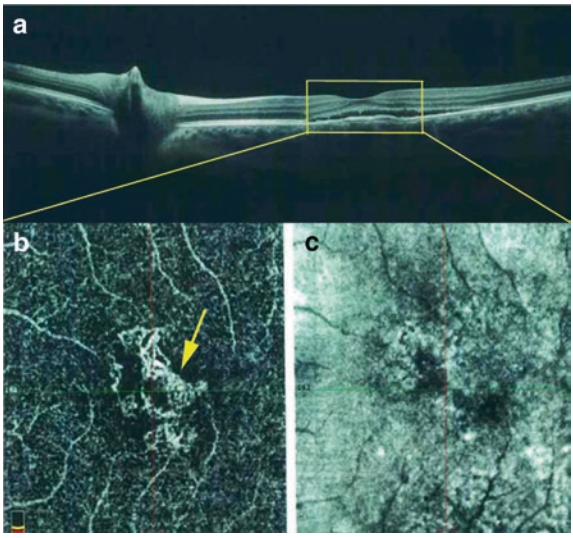

Fig. 7 Double layer sign. **a** Shallow irregular PED with SRF in OCT of left eye is visible. **b** The CNV is observed in OCT-A in the location of double layer sign (yellow arrow). Hyperreflective areas at the level of Bruch's membrane and choriocapillaris complex in enface OCT is visible (**c**)

and differentiate CSC from CNV or polypoidal choroidal vasculopathy. Choriocapillaris atrophy could occur in CSC. Choroidal filling delay in early phase, choroidal hyperpermeability and congested vortex vein ampullas could be observed in ICGA. Focal choroidal ischemia with surrounding hyperperfusion corresponding to the ICGA findings is observed in OCTA.

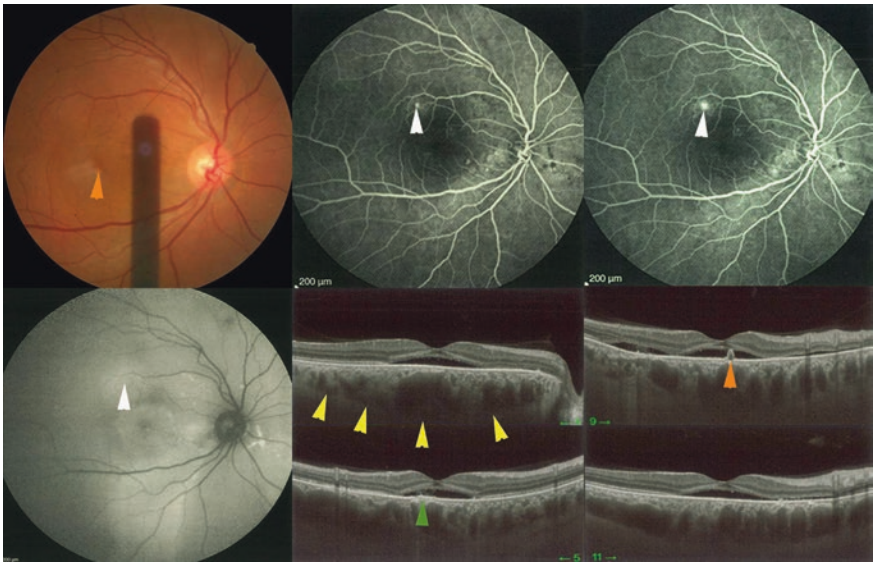

Fig. 8 Leakage site. SRF and a small PED (orange arrowhead) in fundus photograph of right eye are visible. The leakage site showed an ink-blot pattern in fluorescein angiography and hyper-autofluorescence in FAF. Mix pattern and hyper-autofluorescence descending tract of RPE observed in FAF. Dilated choroidal vessels (yellow arrowhead), SRF, PED (orange arrowhead) and irregular RPE (green arrowhead) are visible in OCT

Leakage Point

Microrip in Bruch's membrane and RPE could be seen in OCT that is compatible with the site of CSC leak. FFA could be used to determine the leakage pattern and localization the leakage point. Leakage point in FFA could be divided into a single point (most frequent) or multifocal points (less common). The typical point leakage could show ink-blot or smoke-stack pattern (Figs. 3 and 8). A bridging tissue, extending from outer retinal layers to RPE, may cause atypical leakage pattern on FFA. The leakage point is observed as hypoautofluorescence dot in FAF due to RPE defect and hyperautofluorescence (at the previous leakage point) due to RPE hyperplasia in chronic CSC (Figs. 10 and 11).

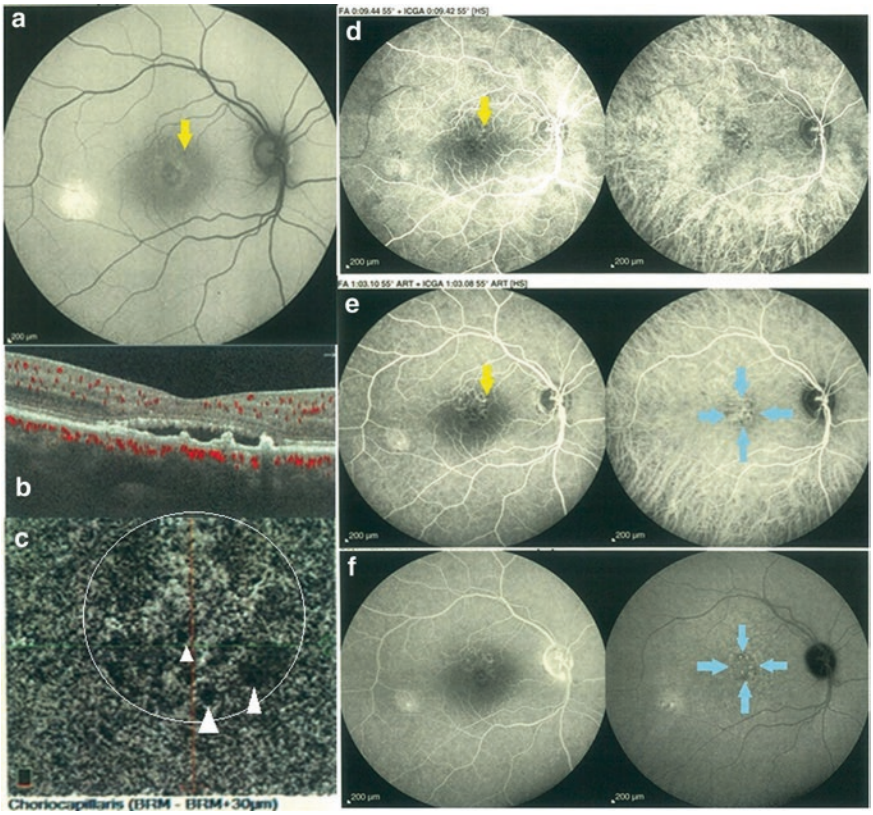

Fig. 9 Washout pattern and dark area and spot. Granular hyper-autofluorescence with hypo-autofluorescence spot at the leakage point in FAF (yellow arrows show leakage point in FAF and FFA [**d–f** the left images]) is observed in right eye. Dark area (white circle) with dark spot (with arrowheads), compatible with SRF and PED respectively, are observed in OCTA. Wash-out, or centrifugal displacement of hyper-fluoresence in the late phase with a ring of hyper-fluorescence (blue arrows) is visible in ICG from early phase to late phase (**d–f** the right images are ICG)

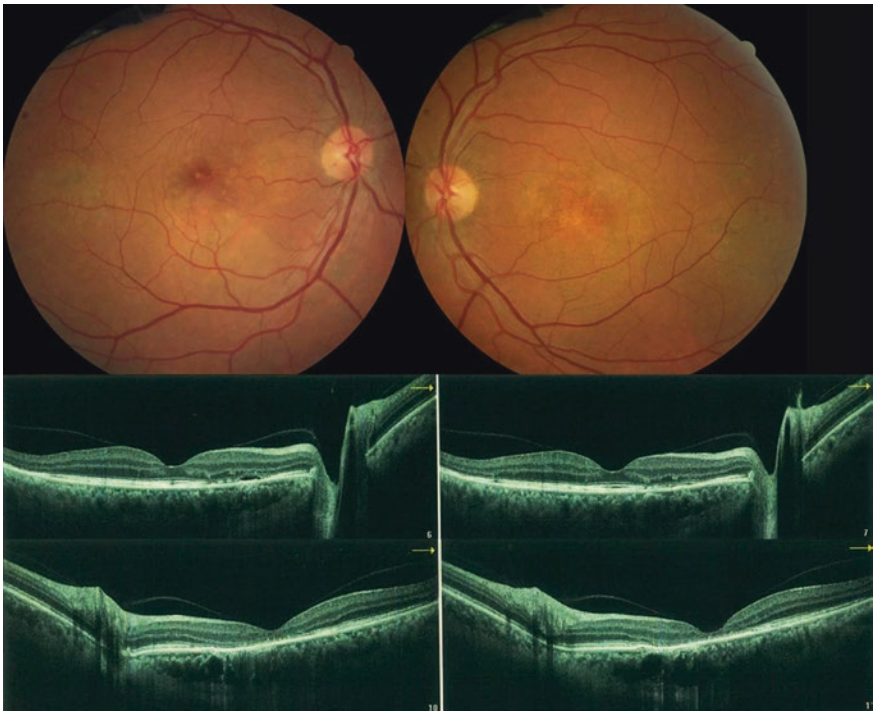

Fig. 10 Yellowish deposits with outer retina atrophy, RPE atrophy and irregularity in both eyes and a small SRF in nasal part of macula in right eye are observed in fundus photograph and OCT of a patient with chronic CSC

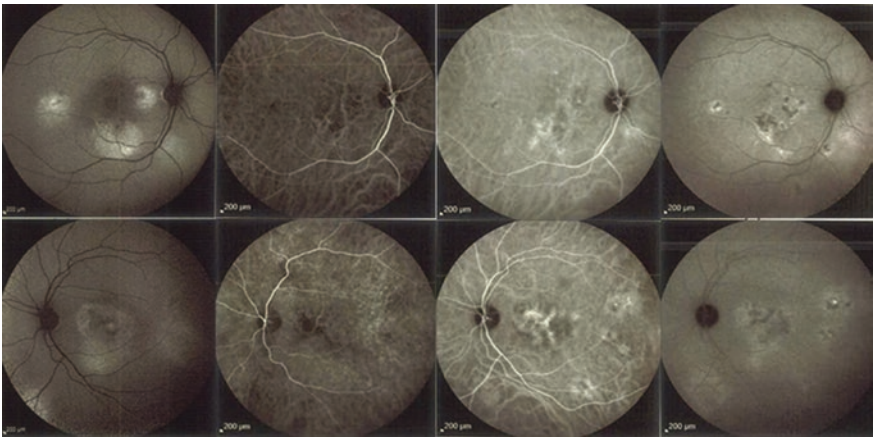

Fig. 11 FAF and ICG of the same patient (Fig. 10). Multiple hyper-fluorescence with granular pattern is visible in FAF (top left and bottom left) of both eyes. Choroidal vessels hyper-permeability and dilated choroidal vessels are observed in the ICG

Suggested Reading

1. Wang M, Munch IC, Hasler PW, Prünte C, Larsen M. Central serous chorioretinopathy. Acta Ophthalmol. 2008;86:126–45.
2. Nicholson BP, Atchison E, Idris AA, Bakri SJ. Central serous chorioretinopathy and glucocorticoids: an update on evidence for association. Surv Ophthalmol. 2018;63(1):1–8.
3. Nicholson B, Noble J, Forooghian F, Meyerle C. Central serous chorioretinopathy: update on pathophysiology and treatment. Surv Ophthalmol. 2013;58:103–26.
4. Dansingani KK, Balaratnasingam C, Klufas MA, Sarraf D, Freund KB. Optical coherence tomography angiography of shallow irregular pigment epithelial detachments in pachychoroid spectrum disease. Am J Ophthalmol. 2015;160(6):1243–54.e2.

Vitreoretinal Interface Abnormality

Nazanin Ebrahimiadib, Mohammadreza Ghahari and Fedra Hajizadeh

Vitreomacular interface is the plane where the posterior vitreous cortex attaches the inner limiting membrane (ILM). These two tissues have distinct characteristics, as they are composed of two different types of collagen fibers. With the aid of OCT images, vitreoretinal interface abnormalities can be identified easily. In 2013, the international VMT study group classified vitreoretinal interface abnormalities into six category including (1) vitreomacular adhesion (VMA), (2) vitreomacular traction (VMT), (3) full thickness macular hole (FTMH), (4) lamellar macular hole (LMH), (5) pseudohole (PH) and (6) epiretinal membrane (ERM).

Assessment of thinning, thickening, intraretinal cyst or subretinal fluid and ellipsoid zone disruption in the central 1 mm of the fovea is crucial in determining the functional and structural outcome. These abnormalities can be focal or >1000 μm.

VMA, by definition, is the separation of posterior hyaloid from parafoveal area while attachment persists within 3 mm from the center of the fovea without causing any change in configuration of macula and fovea. If bonding of posterior hyaloid cause any change in foveal contour, it is called VMT. VMT can cause a vertical traction or a combination of tangential and vertical traction. Intra-retinal changes or foveal elevation has been observed. VMT can be divided in two types: focal (≤1500 μm) and broad (>1500 μm). Spontaneous separation of VMT is rare and progression of VMT is associated with metamorphopsia and visual acuity worsening.

VMA does not cause any visual symptom and is part of a normal process of posterior vitreous detachment (PVD). If VMT partially detaches from fovea, it can produce FTMH, LMH, macular schisis, or inner retina distortion. LMH is defined

N. Ebrahimiadib · M. Ghahari
Farabi Eye Hospital, Tehran University of Medical Sciences, Tehran, Iran
e-mail: nazanin.ebrahimiadib@gmail.com

M. Ghahari
e-mail: mrghary@gmail.com

F. Hajizadeh (✉)
Noor Eye Hospital, Noor ophthalmology research center, Tehran, Iran
e-mail: fhajizadeh@noorvision.com; fedra_hajizadeh@yahoo.com

M. Mohammadpour (ed.), *Diagnostics in Ocular Imaging*,
https://doi.org/10.1007/978-3-030-54863-6_19

by an irregular foveal contour and a shallow defect of the inner retina tissue. The inner retina tissue may be missed or not.

In a FTMH, all the retinal layers from ILM to RPE are lost at the foveal center. Usually, FTMH is the result of tractional forces induced by VMT, whereas LMH ensues secondary to stretches induced by ERM.

PH develops secondary to tractions of ERM. They have a good visual acuity and a normal thickness at the foveal center because there is no tissue loss. It has a smaller opening (200–400 μm) compared to LMH. Tractional LMH are considered a division of PH, although controversy and overlapping exist. There is a steep foveal contour compared to LMH. The ERM has a central opening that forms PH and piles up at the edges of the fovea and folds back to the pouch of the PH. The course of PH is usually stable (Fig. 19.1).

The traction induced by VMT can affect fovea only in inner layers or deeper and cause subretinal fluid and elevation at the level of RPE (Figs. 19.2, 19.3, 19.4).

Vertical and tangential tractions induced by VMT have role in formation of a FTMH (Fig. 19.5).

Diagnosis of macular hole can be made with the aid of OCT and usually needs radial scans, as it may easily be missed with horizontal scans (Fig. 19.6). In this situation, only retinal cysts adjacent to macular hole may be evident, therefore all the radial scans should be reviewed meticulously. Single cysts in the walls of the hole are circular, clustered cysts are irregular and angular in shape. Paravascular cysts are adjacent to large retinal vessels.

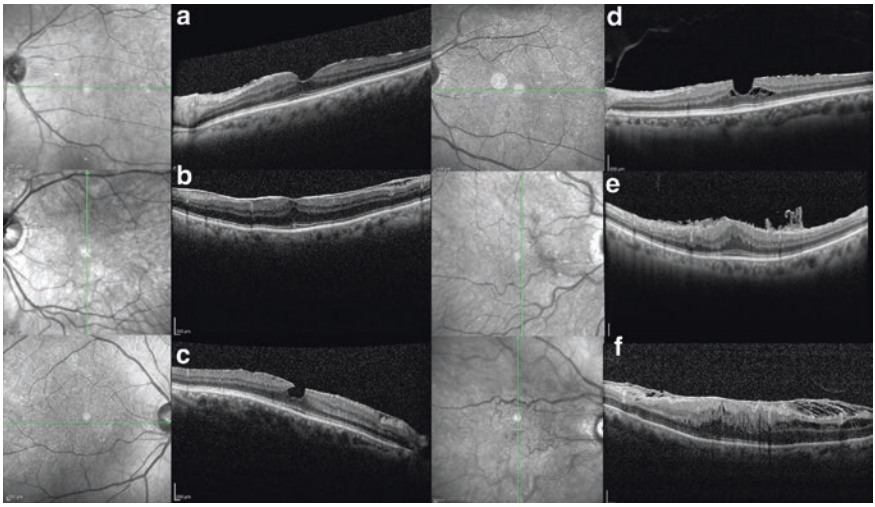

Fig. 19.1 A: OCT: Adherent ERM involving macula with few or no plication of retinal surface. B: ERM with blunting of foveal pit C: pseudohole with ERM D: LMH, tractional type with microfolds on the inner retina surface and hyporeflective intraretinal cystoid changes adjacent to the hole, Vitreopapillary attachment is present. E: ERM with central foveal thickening and ILM wrinkling are evident. F: ERM and schisis of ILM, disorganized inner retina and ellipsoid zone

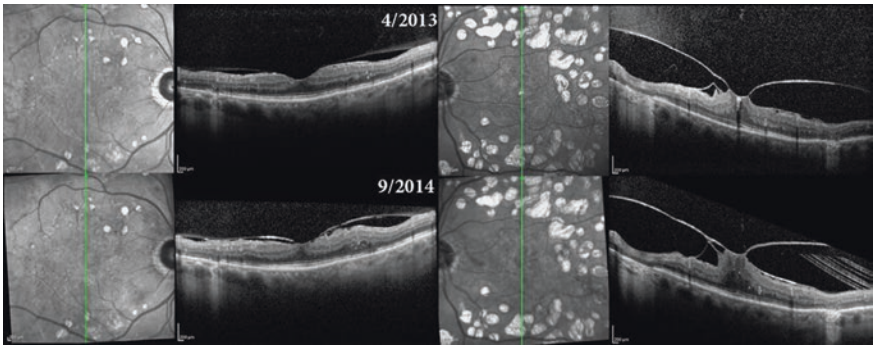

Fig. 19.2 OCT: VMA in the right and VMT in the left eye of a diabetic patient. VMA is relatively stable in 17 months follow up while VMT shows increased traction and viteroschisis in the same time period observation. A mirror artifact is present in the lower right image

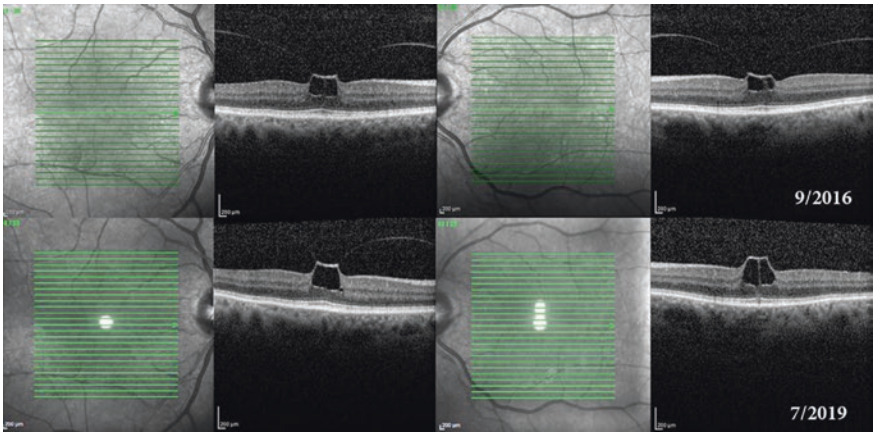

Fig. 19.3 A stable VMT during 3 years are demonstrated in the right and left eye. Primarily, inner retinal layers are involved

ERM is a semitransparent proliferation in the surface of retina that can be eccentric or involving macula. It occurs secondary to an incomplete PVD and appears as a hyper-reflective band in OCT that can cause plication of inner retina with bridging the ILM and/or penetration into deeper layers of retina. Its tangential tractions and contractive forces cause retina thickening and disfigurement at the foveal contour (Figs. 19.7, 19.8, 19.9). Frequency of ERM increases with age and can cause retinal vascular tortuosity. It can become opaque progressively, causing obscuration of retinal details, intraretinal fluid collection and leakage in fluorescein angiography.

ERM can form secondary to retinal vascular accident, diabetes, intraocular inflammation, intraocular tumor, retinal dystrophy and trauma. ERM is one of the

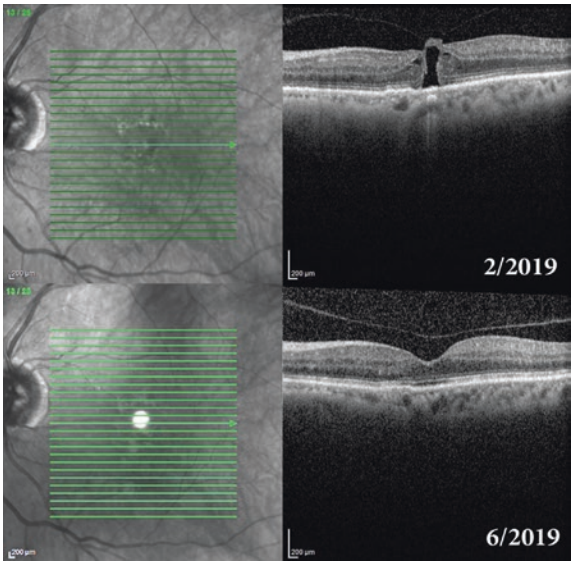

Fig. 19.4 OCT: Top: VMT and impending macular hole in a diabetic patient; Bottom: one month after intravitreal bevacizumab injection, separation of posterior hyaloid and resuming of outer retinal layers are evident

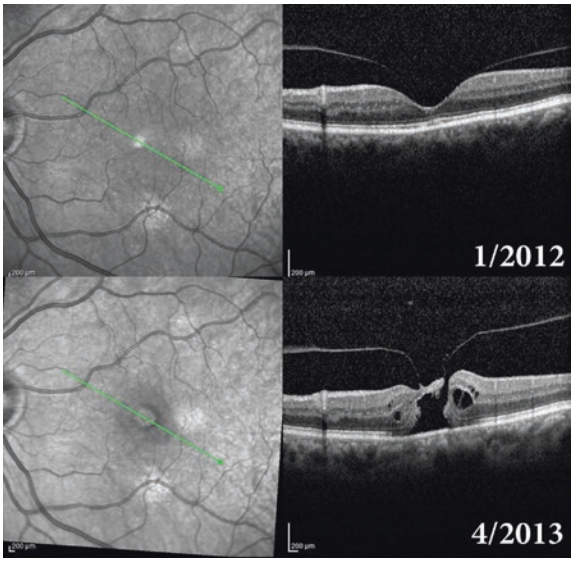

Fig. 19.5 Top: VMA and outer retina atropy. Detachment of posterior hyaloid from surface of retina in perifoveal and parafoveal area while is still adhered to the foveal center with no change in foveal contour is demonstrated. Bottom: In 15 months follow up, VMA evolve into VMT which caused full thickness macular hole. In SLO image, the hole is hyper-reflective with a sharp border that has some hypo-reflective dots within the hole. A halo of hypo-reflectivity pertinent to cysts and retinal edema in the wall of the hole are evident as well

components of combined hamartoma of retina and RPE (Fig. 19.10). The ERM is usually pigmented in this disease.

Lamellar macular hole is a partial thickness defect in fovea with part of outer nuclear layer remaining on top of the RPE and a split in the walls of the hole.

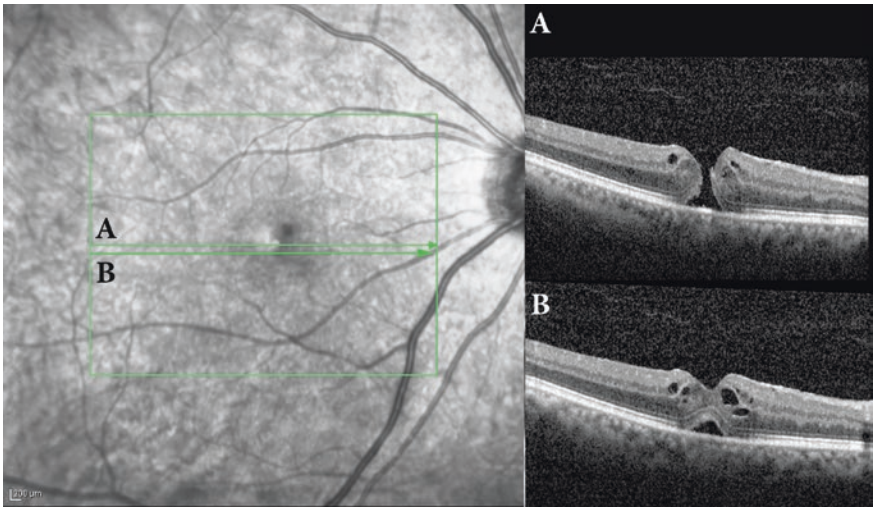

Fig. 19.6 A: OCT Line A scan shows a full thickness macular hole with small diameter (<400 μm). Small parafoveal cysts are present. Line B scan with SRF and parafoveal cysts adjacent to the macular hole. FTMH is not evident in this line of scan.)

Fig. 19.7 Enface OCT of an epiretinal membrane. Tension lines affect the foveal center

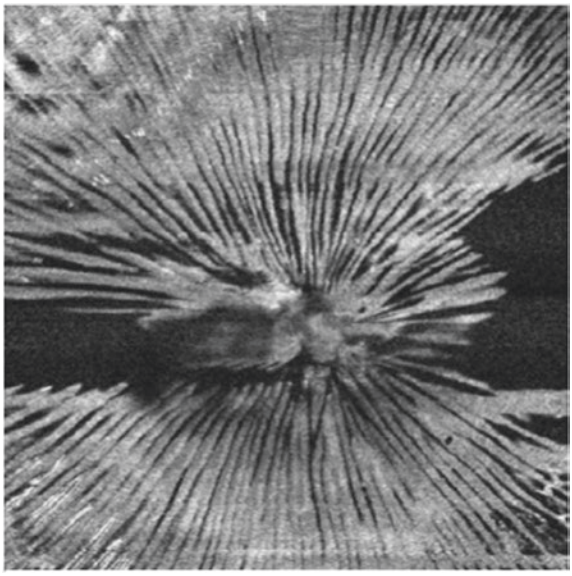

LMH is usually associated with ERM and has been divided into two subtypes: tractional and degenerative.

Tractional form has an ERM inducing tractional forces that cause a separation between outer nuclear and outer plexiform layer of retina. Some vertical

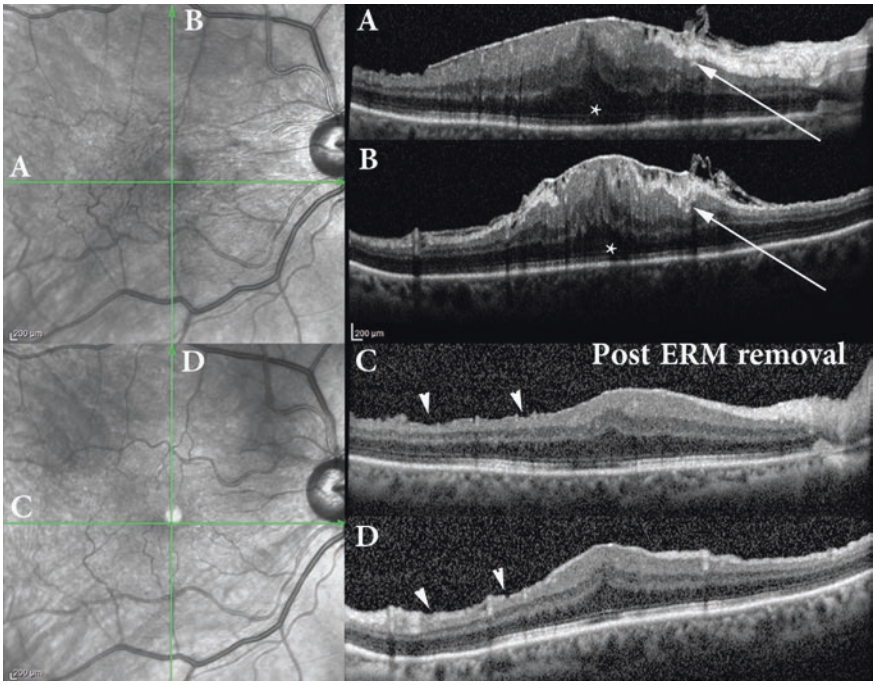

Fig. 19.8 OCT of the right eye, A: horizontal and B: Vertical scans of macula, Epiretinal membrane (ERM) appears as a hyper-reflective band involving macula with distortion of foveal contour and corrugation of inner layers of retina. ERM is penetrating into retinal layers. (white arrows). Ellipsoid zone is disrupted. (asterisk) C and D: Horizontal and vertical scans of macula of the same patient after ERM removal. Decreased thickening and restoration of ellipsoid zone are evident. Areas of pinching with forceps can be recognized with nerve fiber layer dimpling (arrowheads)

hyper-reflective bands from ERM proceed to bridge the split layers of retina and forming hypo-reflective spaces. Cystic changes may be present in inner plexiform layer. Photoreceptor layer is usually intact in tractional type while degenerative form has schisis areas with a defective photoreceptor layer and even RPE atrophy. Foveal edge in tractional form is often elevated as opposed to degenerative form that is usually round and wide. The ERM associated with degenerative type LMH, has a homogenous medium reflectivity with no contractile qualities. Lamellar hole associated epiretinal proliferation (LHEP) fills the space between the ERM and inner surface of retina leaving no area in between for vertical bands seen in tractional form. Foveal bump is sometimes present at the bottom of degenerative hole (Fig. 19.11). Sometimes, both features described are observed in a LMH.

The course of both types of LMH is usually slowly progressive and a few develop a full thickness macular hole formation. Tractional subtypes possibly benefit from surgery in contrast to degenerative forms. Usually, a complete PVD has

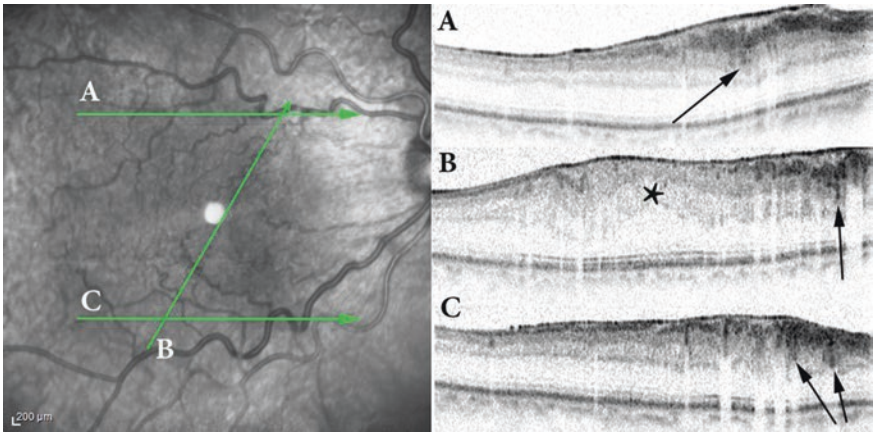

Fig. 19.9 A, B and C: ERM with penetrating pillars intraretinally (black arrows). Asterisk indicates foveal center with loss of contour due to tangential tractions of ERM. The thickened outer nuclear layer confirms that the location is at the foveal center

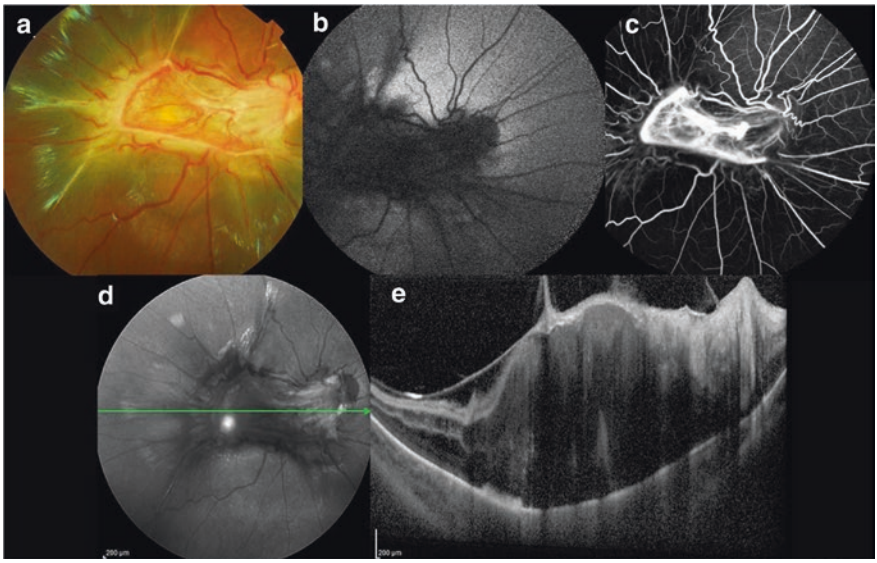

Fig. 19.10 Combined hamartoma of retina and RPE. Vascular tortuosity and fluorescein leakage are observed. Retinal layers in macula are disorganized and very thick

not occurred, therefore separation of posterior vitreous is important during vitrectomy. It is recommended that the epiretinal membrane be removed up to the rim of the hole, leaving the tissue consisting of macular pigment intact. Degenerative forms are better to be observed, although thinning of the remaining fovea and

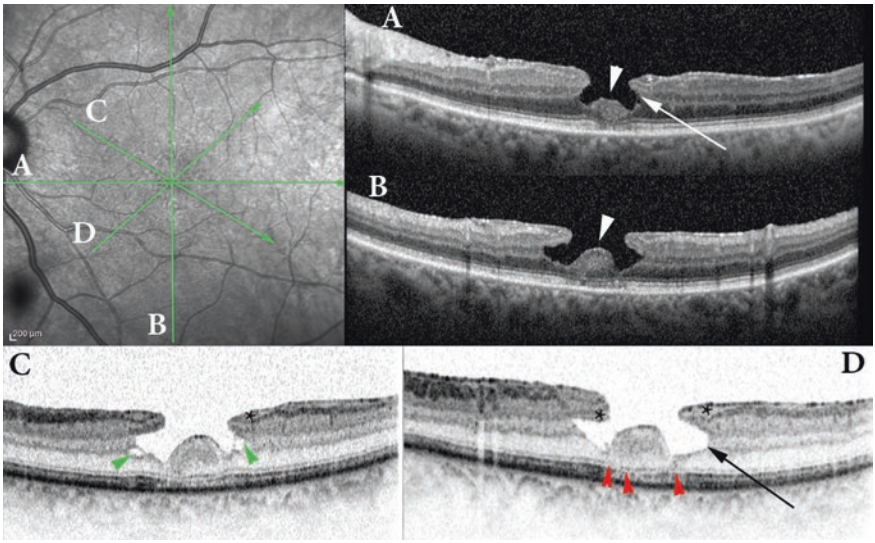

Fig. 19.11 Degenerative lamellar macular hole; SLO image show some reflectivity change with irregular borders corresponding to LMH. A and B: LMH has a wide opening and there is a cleft (white arrow) between inner nuclear and outer plexiform layers of fovea and a steep foveal contour. Partial thickness defect has a base, which has a larger diameter than the top. Foveal bump (white arrowheads) can be seen. C: Round edged cavitations(green arrowheads) in retinal layers are evident in LMH borders. D: Lamellar hole associated epiretinal proliferation (asterisk) is illustrated as a medium reflective line covering the area between ERM and RNFL. There is some disruption(red arrowheads) in photoreceptor layer

progressive disruption of ellipsoid zone may occur. In addition, expansion of the LHEP can occur which is correlated with widening of the hole and atrophy of outer retina and poor visual outcome.

Suggested Reading

1. Kulikoy AN, Sansovskii SV, Berezin RD, Maltsey DS, et al. Vitreoretinal interface abnormalities in diabetic macular edema and effectiveness of anti-VEGF therapy: an optical coherence tomography study. Clinical Ophthalmology; 2017.
2. Coassin M, Mori T, Di Zazzo A, Sgrulletta R, et al. Lamellar macular holes: monitoring and management strategies. Clin Ophthalmol. 2019;13:1173–82.
3. Haritoglou C, Tadayoni R, Hubschman J-P. Lamellar macular hole surgery – current concepts, future prospects. Clin Ophthalmol. 2019;13:143–6.

Diabetic Retinopathy and Retinal Vascular Diseases

Hassan Khojasteh, Hooshang Faghihi, Masoud Mirghorbani and Fedra Hajizadeh

Diabetic Retinopathy

Diabetic retinopathy is still one of the major causes of vision loss throughout the world. Small blood vessel damage is the basis of all retinal complications. Microaneurysms, cotton wool spots, retinal hemorrhage, retinal edema, and exudate are the features of the non-proliferative stage. New vessel formation is the hallmark of the proliferative phase, which results in further complications such as vitreous hemorrhage, tractional or combined retinal detachment, and neovascular glaucoma. Although the signs of diabetic retinopathy are usually evident through a dilated fundus examination, imaging tools still play a significant role in the diagnosis and planning of these patients.

Fluorescein angiography is mainly used to determine ischemia and neovascularization; however, other features such as microaneurysms and macular leakage are also detectable (Fig. 1).

OCT is a useful diagnostic tool for evaluating diabetic macular edema (DME). There are different classifications for DME based on OCT findings, including diffuse versus focal retinal thickening, sponge–like edema, cystoid edema, and tractional macular edema. The status of the external limiting membrane (ELM) and

H. Khojasteh · H. Faghihi · M. Mirghorbani
Farabi Eye Hospital, Tehran University of Medical Sciences, Tehran, Iran
e-mail: khojasthe63@gmail.com

M. Mirghorbani
e-mail: masoud_mirghorbani2016@yahoo.com

H. Faghihi
Noor Ophthalmology Research Center, Noor Eye Hospital, Tehran, Iran
e-mail: hfaghihi@yahoo.com

F. Hajizadeh (✉)
Noor Ophthalmology Research Center, Tehran, Iran
e-mail: fhajizadeh@noorvision.com; fedra_hajizadeh@yahoo.com

M. Mohammadpour (ed.), *Diagnostics in Ocular Imaging*,
https://doi.org/10.1007/978-3-030-54863-6_20

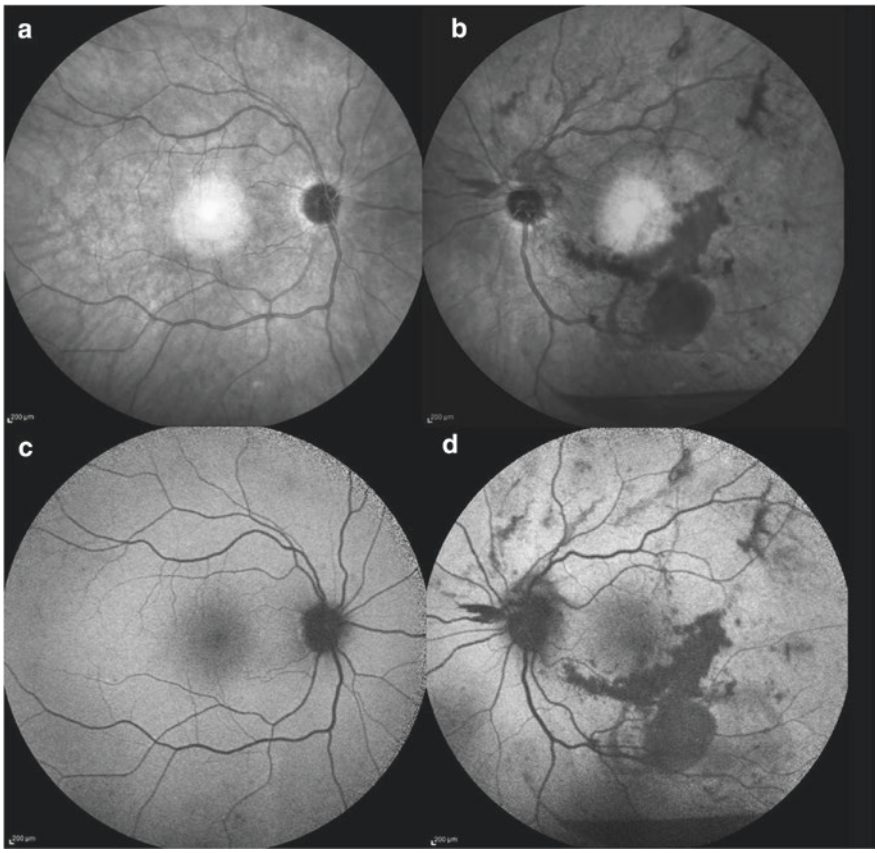

Fig. 1 A 58-year-old man with decreased vision in his left eye. Clinical examination revealed retinal and vitreous hemorrhage. In near infrared (NIR) image of the left eye (**b**), there are multiple dark areas related to hemorrhage, which also caused blocked autofluorescence in fundus autofluorescence modality (FAF) (**d**). The right eye (**a** and **c**) seems to be unremarkable

ellipsoid zone, which are visually predicting, can be studied by OCT. Recently, it was shown that hyper-reflective foci in outer layers were correlated with more photoreceptor destruction and low visual prognosis (Figs. 2, 3, 4, 5 and 6).

Retinal Vein Occlusion

Retinal vein occlusion (RVO) is a major cause of vision loss in the elderly and remains the second most common vascular accident after diabetic retinopathy.

According to the anatomical site of occlusion, it is classified in three groups:

1. Central retinal vein occlusion (CRVO) is typically caused by thrombosis of the main retinal vein, posterior to lamina cribrosa, of the optic nerve. Based on

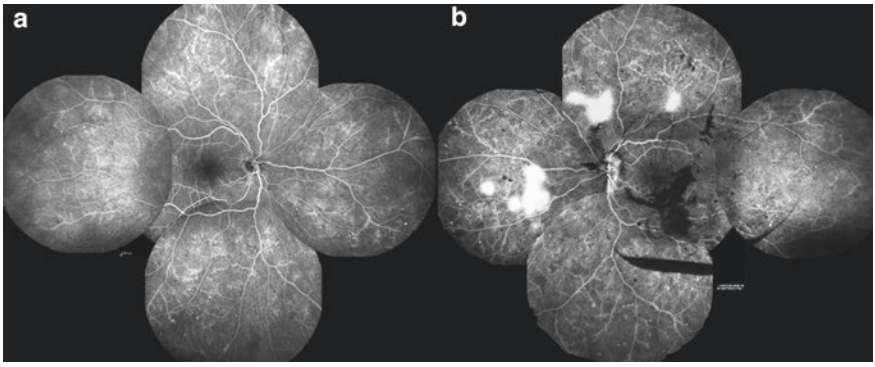

Fig. 2 Same patient as in Fig. 1. Fluorescein angiography in the right eye (**a**) shows microaneurysm, vessel staining, and intraretinal leakage as hyper-fluorescent lesions and also areas of hypofluorescent capillary non- perfusion. In the symptomatic left eye (**b**), fluorescein angiography illustrates the neovascularizations by prominent leakage. There are also areas of blocked fluorescence due to hemorrhage

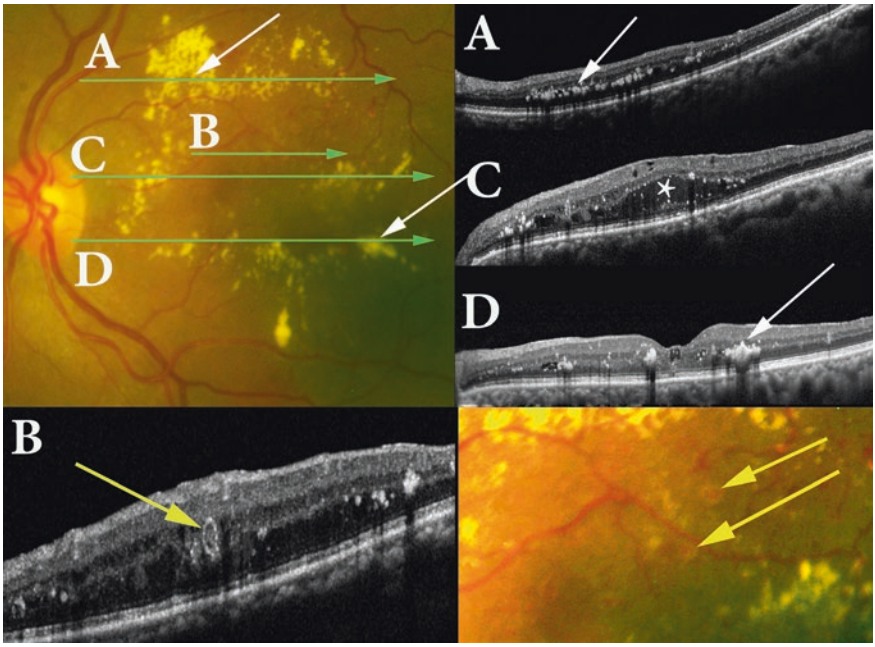

Fig. 3 Case of diabetic macular edema. Retinal thickening with diffuse exudates are shown in the color fundus photograph. OCT shows increased thickness, intraretinal fluid (asterisk), and hyperreflective deposits related to exudates (white arrows). Microaneurysm is shown as an oval hyper-reflective structure (yellow arrows)

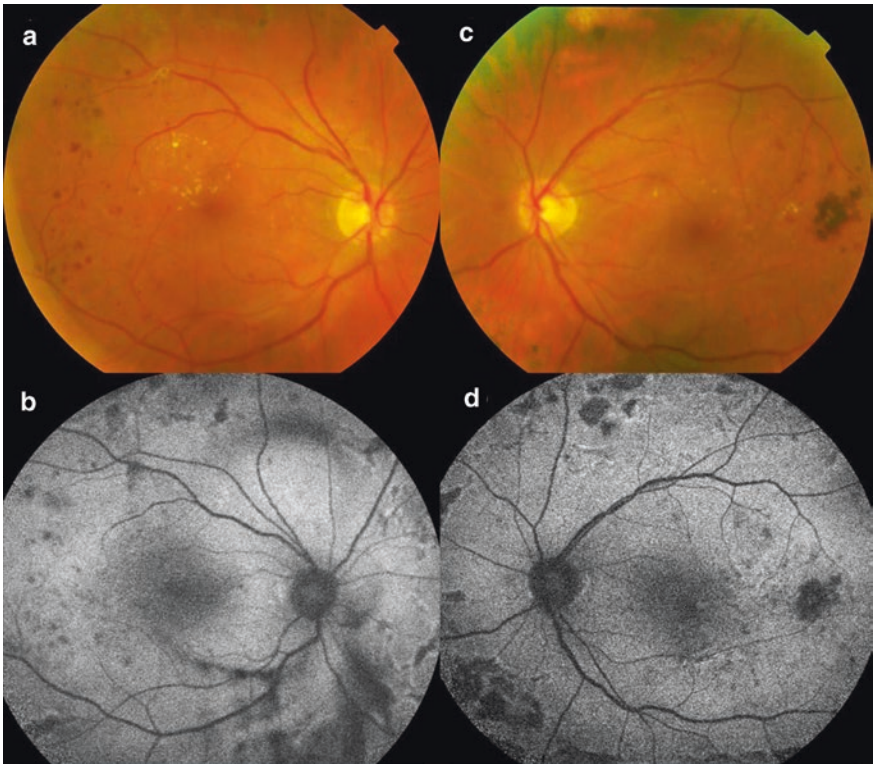

Fig. 4 A 65-year-old diabetic man with bilateral vision loss and a history of panretinal photocoagulation (PRP) in both eyes. Color fundus photographs reveal bilateral macular edema (**a** and **c**), and fundus autofluorescence images (**b** and **d**) shows dark areas due to hemorrhage and laser scars

ischemic damage, CRVO is categorized into ischemic (nonperfused) and nonischemic (perfused) types.

2. Hemi-retinal vein occlusion (HRVO) is caused by occlusion at major retinal vein bifurcation.
3. Branch retinal vein occlusion (BRVO) occurs when one of the branch retinal veins is occluded.

Clinical Features

Vascular tortuosity, retinal hemorrhages, cotton wool spots, and optic nerve edema are the results of increased intravenous pressure. Although the main cause of vision loss is cystoid macular edema (CME), other complications including macular ischemia, optic neuropathy, vitreous hemorrhage, tractional retinal detachment, and neovascular glaucoma might occur.

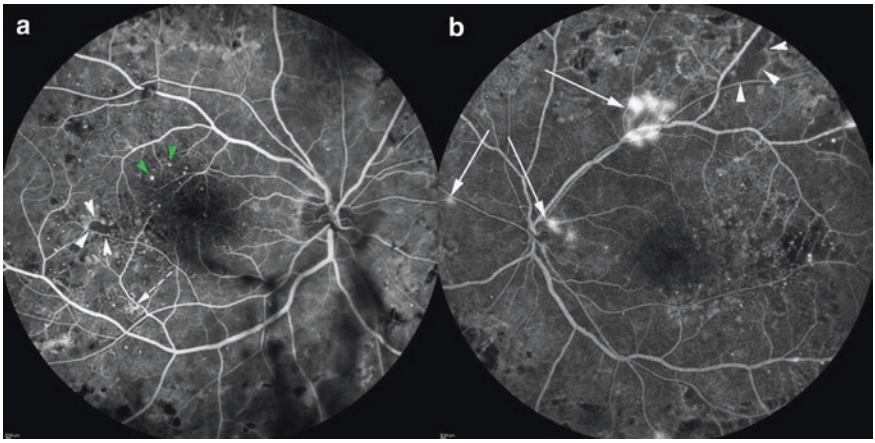

Fig. 5 The same patient as in Fig. 4. Fluorescein angiography shows still active disease. Leakage of neovascularization in the left eye (**b**) (white arrows), areas of capillary non-perfusion (white arrowheads), microaneurysms (green arrowheads), and intraretinal microvascular abnormality (IRMA) (dashed arrow) are illustrated

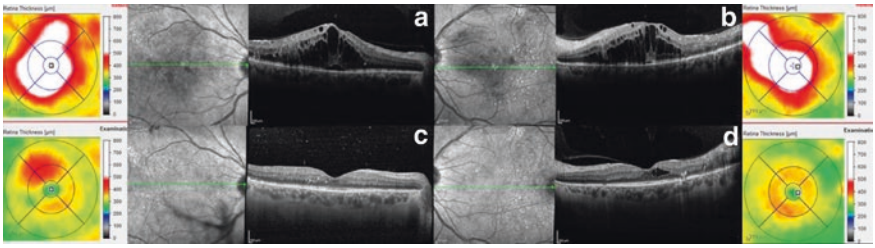

Fig. 6 Macular OCT of the same patient shows significant macular thickening and intraretinal and sub-retinal fluid, especially in the right eye (**a** and **b**). The post-treatment OCT images in the lower row (C and D) reveal marked improvement of macular edema

Diagnostic Imaging Test

RVO is actually a clinical diagnosis, but imaging tests may be helpful in revealing more details about the prognosis and treatment strategies. Fluorescein angiography (FA) can determine the amount of retinal ischemia which is so important in prognosis. FA can also easily detect any leakages due to edema or neovascularization.

Optical coherence tomography (OCT) is a noninvasive helpful modality for detecting any structural abnormalities of the macula. Intraretinal or subretinal fluid, vitreomacular traction, loss of outer retinal integrity, and atrophy of retinal layers are different OCT features seen in RVO patients (Figs. 7, 8, 9, 10 and 11).

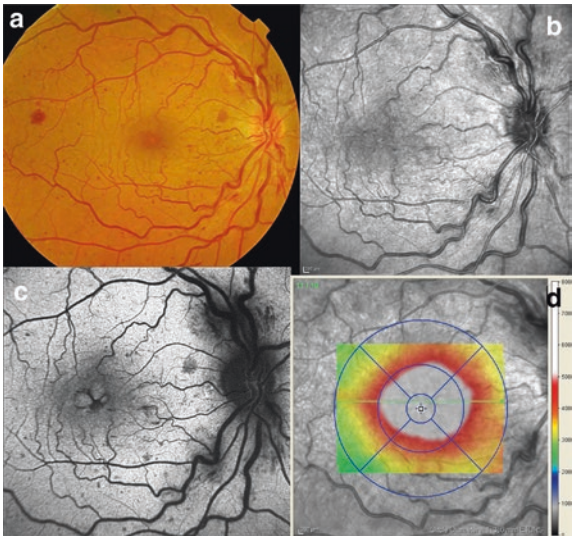

Fig. 7 A patient with perfused CRVO. Color fundus photograph (**a**) and near infrared reflectance image (**b**) shows diffuse retinal hemorrhage and vascular touristy. **c** Fundus autofluorescence (FAF) image shows multiple areas of blocked fluorescence due to hemorrhage and abnormally increased macular autofluorescence due to cystoid macular edema (CME). **d** Topographic map with marked increase in macular thickness

Retinal Artery Occlusion

Retinal artery occlusion (RAO) is one of the main causes of acute and painless visual loss, especially in older adults. The ophthalmic artery is the main artery of the eye, and occlusion of this artery causes profound visual loss. Blockage of the central retinal artery, the second most important artery, is called central retinal artery occlusion (CRAO). Although it usually causes severe vision loss, in some cases with a normal extra-artery (which is called cilioretinal artery), central vision may be preserved.

Branch retinal artery occlusion (BRAO) is the condition in which blockage occurs in any branches of the retinal artery. Symptoms are correlated with the location and amount of damage.

The diagnosis of RAO is clinical with particular retinal findings. Whitish discoloration of the retina in the affected area of the blocked vessel can be found in a dilated fundus examination. Outstanding reddish central fovea surrounded by pale and edematous retina results in the appearance of “cherry red spots” in CRAO. However, sometimes the fundus findings are subtle, and imaging can be helpful.

Fluorescein angiography may reveal filling delay. However, it might be unremarkable because of reopening of the vessel and recirculation.

Optical coherence tomography (OCT) is a sensitive diagnostic tool, and it shows the changes of inner retinal layers as increased reflectivity and thickness in the acute phase, which turns into inner retinal atrophy in chronic stages. The severity of OCT changes may be related to the visual prognosis (Figs. 12, 13 and 14).

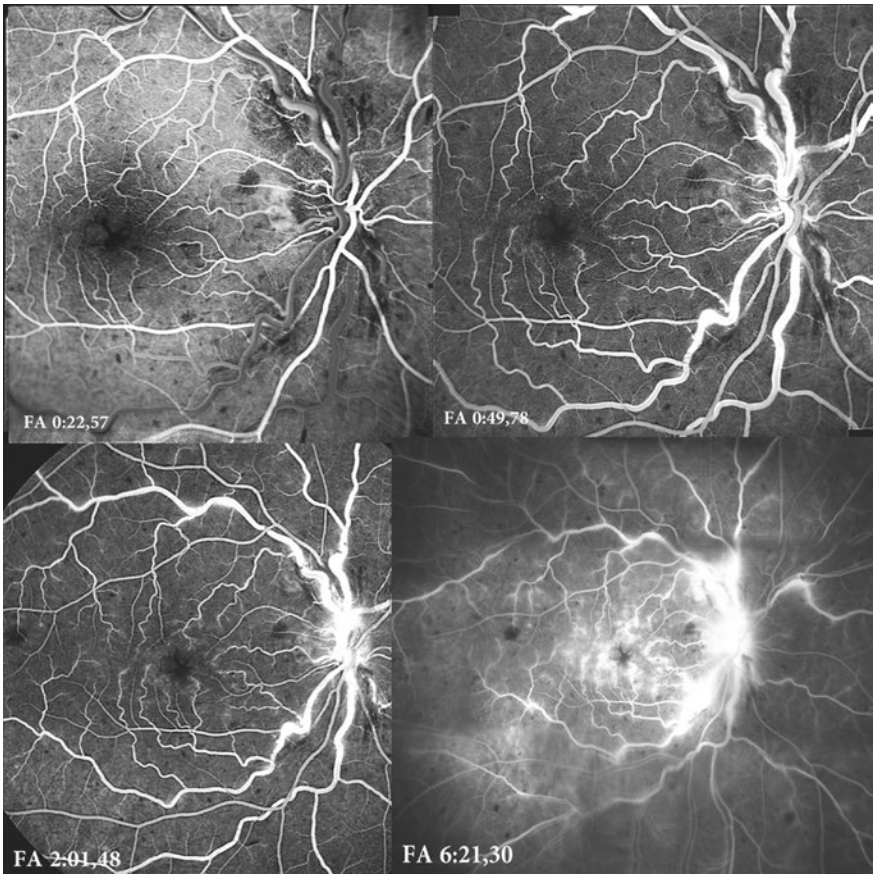

Fig. 8 Fluorescein angiography of the same case as in Fig. 7. Early angiogram (upper row) indicates delayed arteriovenous transit time and blockage by retinal hemorrhage. In the late phase (lower row), some leakage in the macula due to cystoid macular edema and also vessel wall staining are evident

Other Features of Vascular Insufficiency and Abnormality

Cotton Wool Spots

Cotton wool spots (CWS) are seen as small (usually less than 1/3 disc diameter) and yellowish-white lesions located in the superficial retina. The underlying mechanism for CWS formation is thought to be occlusion of the pre-capillary arteriole which causes nerve fiber layer infarcts. However, any factor that interferes with the axoplasmic flow in the retinal nerve fiber layer may also result in similar lesions.

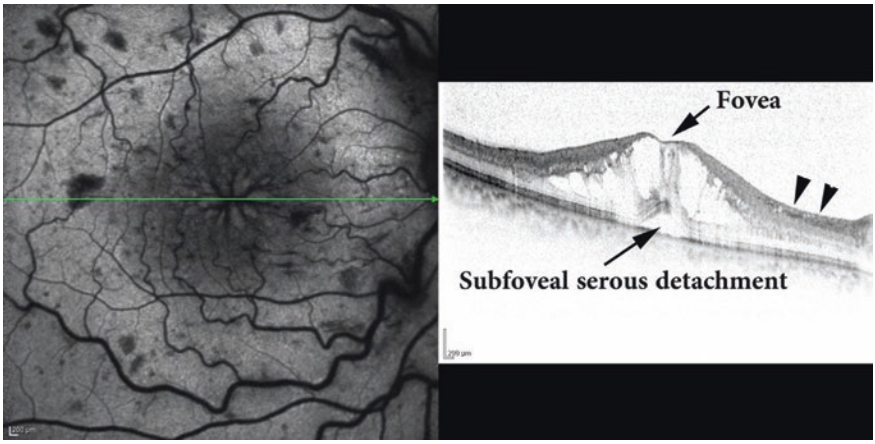

Fig. 9 Cross-sectional macular OCT of the same patient as in Fig. 7. The OCT is shown in a black and white pattern. A typical cystoid macular edema with diffuse intraretinal fluid/cysts and a localized subfoveal serous detachment are shown

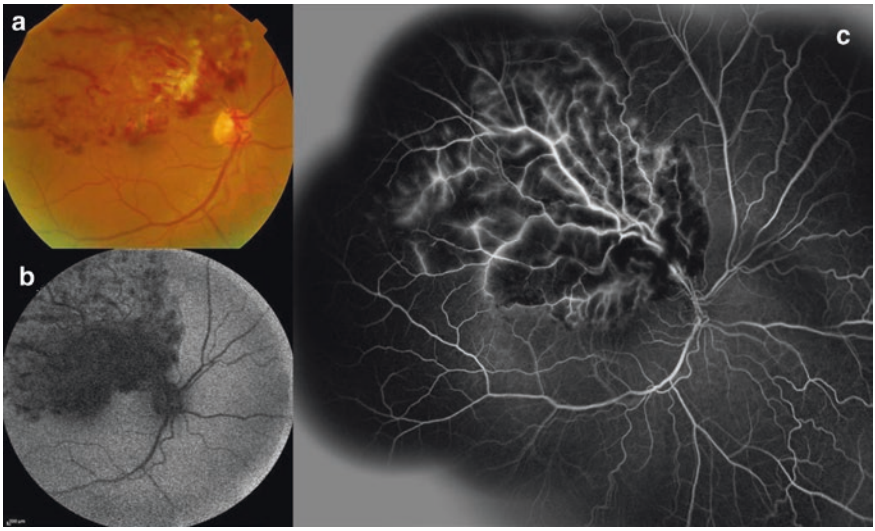

Fig. 10 Color fundus photograph of a patient with BRVO (**a**) shows diffuse retinal thickening, flame shape hemorrhage, and cotton wool spots in the supratemporal region with macular involvement which blocked the normal retinal autofluorescence (**b**). Fluorescein angiography reveals hyperfluorescent stained ischemic vessel walls and hypofluorescent areas due to either blockage or hypoperfusion

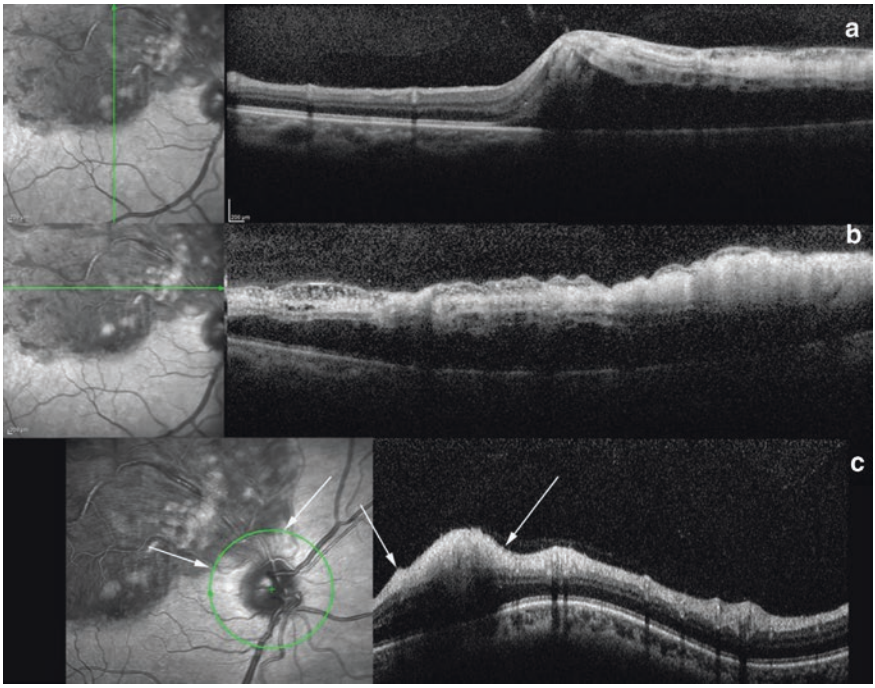

Fig. 11 Various OCTs of the same patient as in Fig. 10. Vertical cross-sectional OCT (**a**) shows increased retinal thickness and inner retinal hyper-reflectivity in the involved area. In horizontal OCT (**b**) of the involved area, diffuse edema of inner retinal layers and sever hyper-reflectivity are illustrated. Edema is also involved in the peripapillary area (**c**) (white arrows)

Along with diabetes and hypertension as the main risk factors, many conditions may cause CWS, including immune processes such as systemic lupus erythematosus, infectious diseases (e.g., HIV retinopathy), and trauma. It can also be found in a neoplastic process such as lymphoma or leukemia.

In OCT images, CWS are shown as hyperreflective lesions in the inner retina. OCT can also aid the study of the chronicity of a lesion; in old lesions for which fundus findings are unremarkable or subtle, OCT can show atrophic changes of the retinal nerve fiber layer (Figs. 15, 16 and 17).

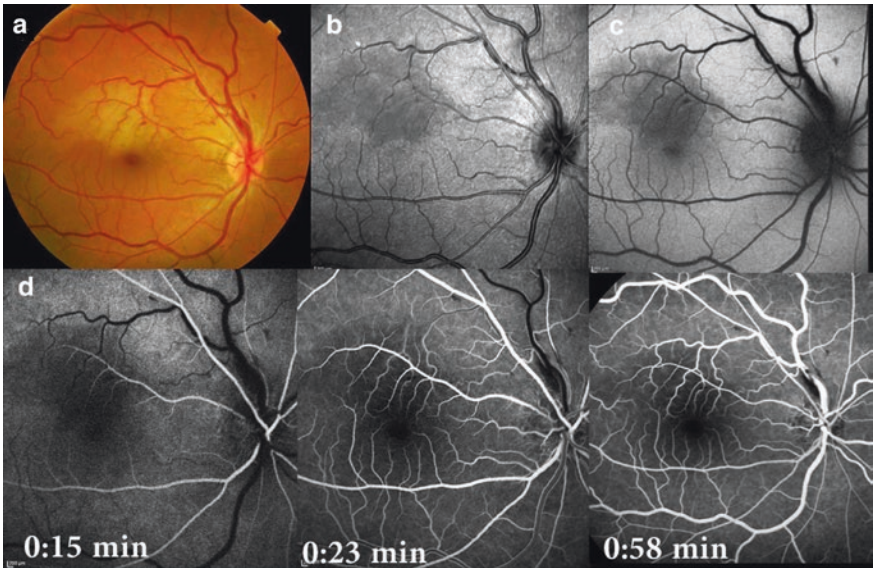

Fig. 12 A patient with the chief complaint of darkness in the inferior hemifield in his right eye. Color fundus photograph (**a**) in acute phase reveals whitish discoloration and edema in the superior part of the macula with foveal sparing. A distinct area of reduced reflectance and hypoautofluorescence is visible in NIR (**b**) and FAF (**c**). Fluorescein angiography in different time frames (**d**) represents the significant filling delay in the supratemporal branch of the retinal artery

Retinal Macroaneurysm

A retinal macroaneurysm is an acquired focal dilation of retinal arterioles that may range from 100 to 250 microns in diameter. Macroaneurysms are usually found within a third-degree branch in the supratemporal region.

As a risk factor, systemic hypertension can be detected in nearly 75% of patients. Bilateral involvement has been reported in 10% of cases. The patient might be asymptomatic or may complain of vision loss due to complications which can be classified into major types.

1. Hemorrhagic type: A macroaneurysm can rupture and cause a particular pattern of retinal hemorrhage. Hemorrhage in different levels (preretinal, intraretinal, subretinal, and sometimes vitreous hemorrhage) may raise the diagnosis of macroaneurysm (Fig. 18).
2. Exudative type: Vision loss occurs as a result of macular edema (Figs. 19 and 20).

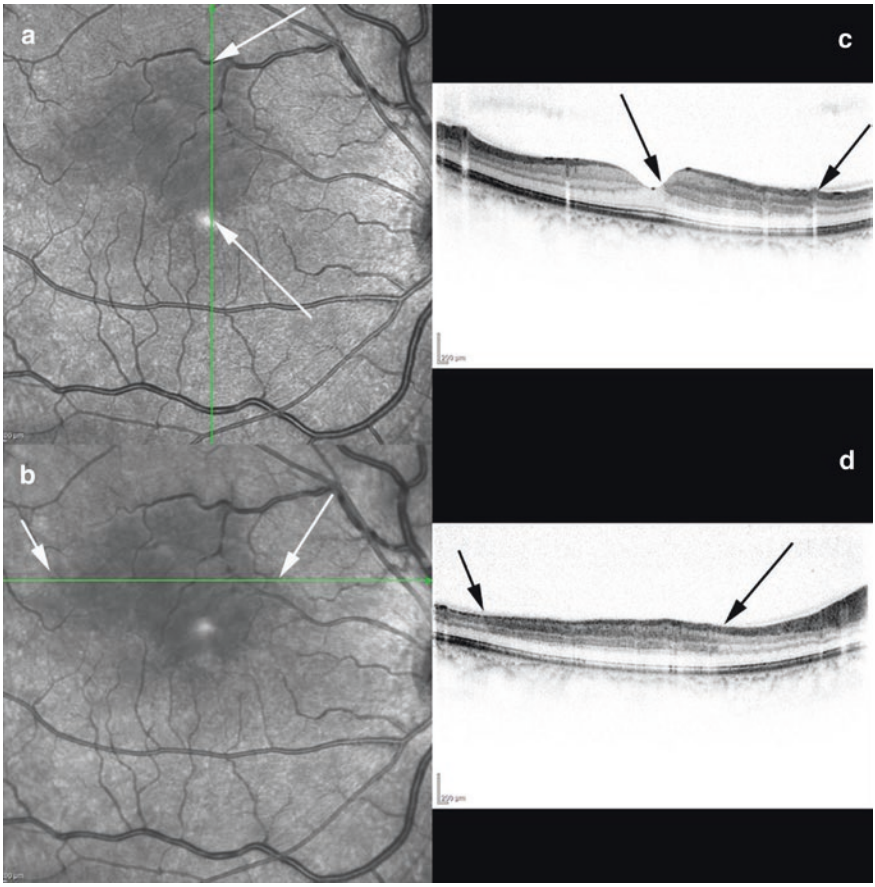

Fig. 13 SLO-OCT images of the same patient in vertical (**a** and **c**) and horizontal sections (**b** and **d**) demonstrate increased thickness and reflectivity in the corresponding ischemic retina. The boundaries of the damaged retina can be shown by OCT (black arrows) or SLO (white arrows)

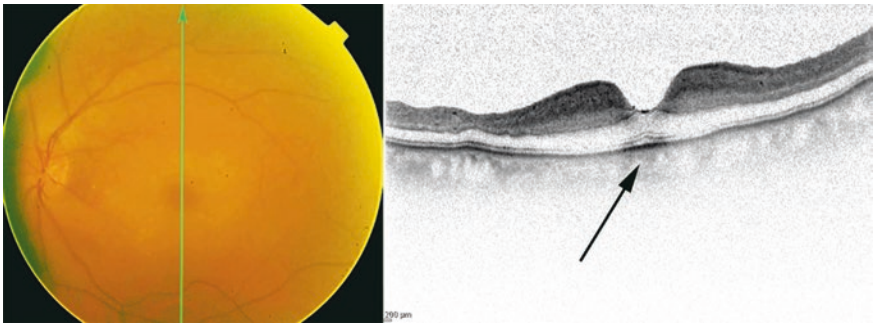

Fig. 14 Color fundus photograph in CRAO (**a**) shows retinal whitening and cherry red spot. Macular OCT reveals increased reflectivity of inner retinal layers and a corresponding decrease in reflectivity in outer layers. Reflectivity of subfoveal area is preserved as a result of lack of overlying inner layers (arrow)

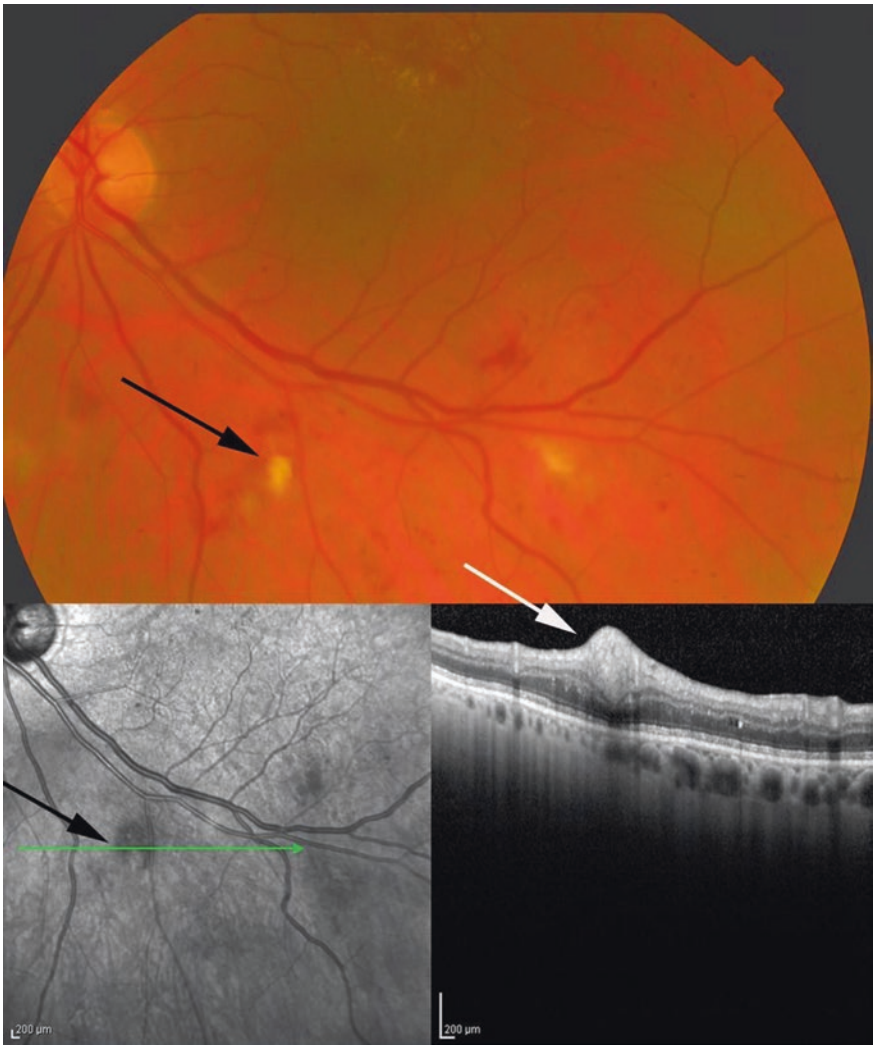

Fig. 15 Images of an elderly lady with uncontrolled hypertension. In the color fundus (upper row), the CWS is shown by the black arrow as a small yellow–white lesion. The cross-sectional OCT (lower row) of the corresponding lesion shows increased retinal thickness with marked hyperreflectivity, which is mainly located in the inner retinal layers

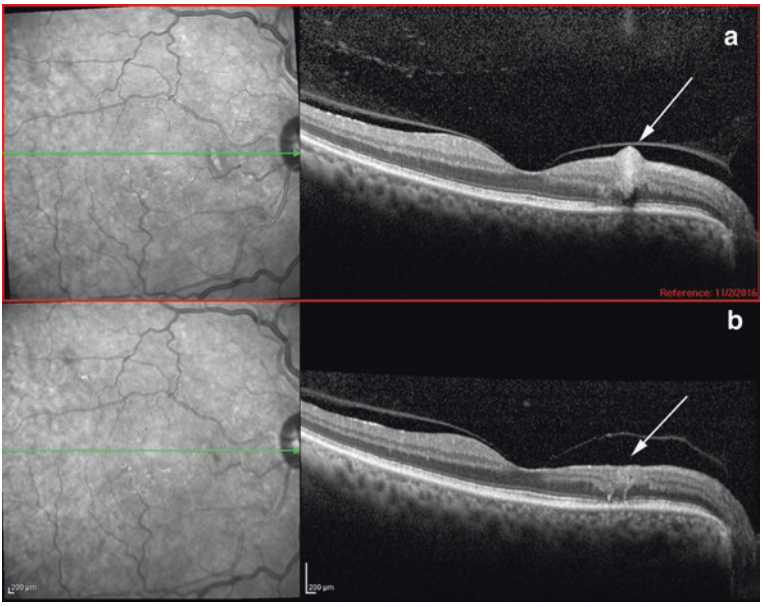

Fig. 16 Comparison of OCT features of a single CWS in acute and resolving phase in an elderly man with diabetes. In the acute phase (**a**), the lesion is shown as an elevated and hyperreflective area with posterior shadowing. Three months later, the cross-sectional OCT of the same area (**b**) shows significant atrophic changes throughout the retinal layers with more dominancy in the inner parts. The ellipsoid zone is also disrupted

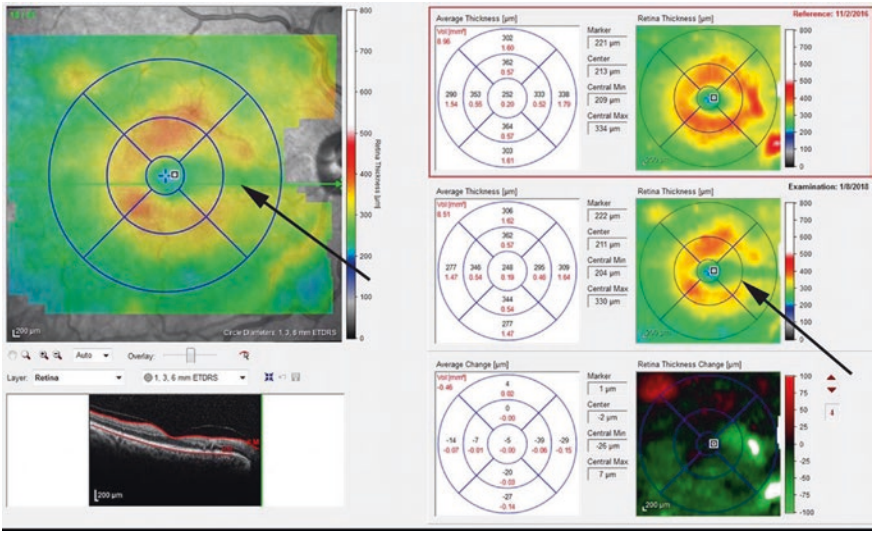

Fig. 17 Topographic maps of the case discussed above. Exchanges of colors by the cooler one (green) at the area of the prior lesion (black arrow) indicates atrophic changes of CWS and chronicity of lesion

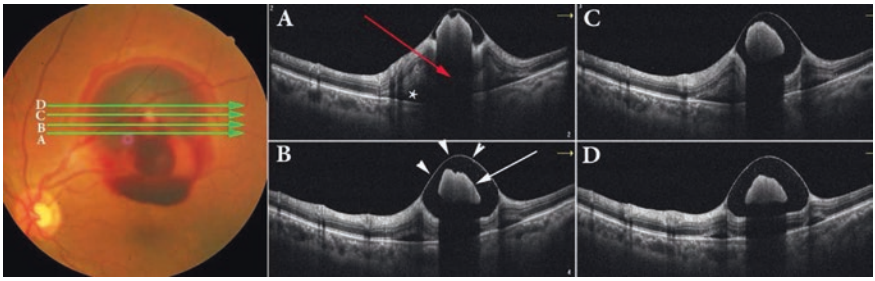

Fig. 18 Color fundus photograph and OCT in a hemorrhagic macroaneurysm. The lesion is located in the supratemporal area as its usual location. Hemorrhaging at different levels gives the lesion its typical features. The red arrow indicates the location of the macroaneurysm which is obscured by shadowing of the overlying hemorrhage (white arrow). Localized sub-retinal fluid is shown by an asterisk. The hyperreflective internal limiting membrane is pushed forward by fluid and hemorrhage (white arrowheads)

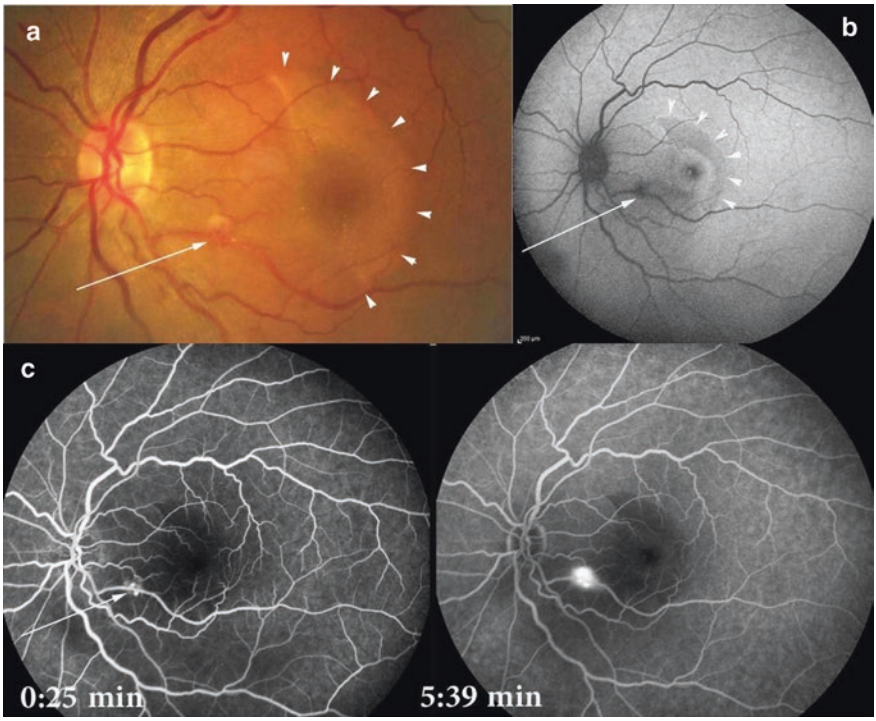

Fig. 19 A 71-year-old patient with decreased vision in her left eye. In the color fundus photograph (**a**), there are some degrees of vascular tortuosity and arterial narrowing which may indicate underlying systemic hypertension. The white arrow shows the abnormal focal dilation of a retinal arteriole with nearby exudation which extends towards the macula. The boundaries of macular edema, exudation, and fluid are shown by white arrowheads. In FAF (**b**), the macroaneurysm is shown as an area of blocked auto-fluorescence (white arrow). Alterations in macular auto-fluorescence are caused by edema and exudation (arrowheads). Fluorescein angiography (**c**) shows a hyperfluorescent area due to pooling of dye in the macroaneurysm which further increases as a result of leakage (**d**)

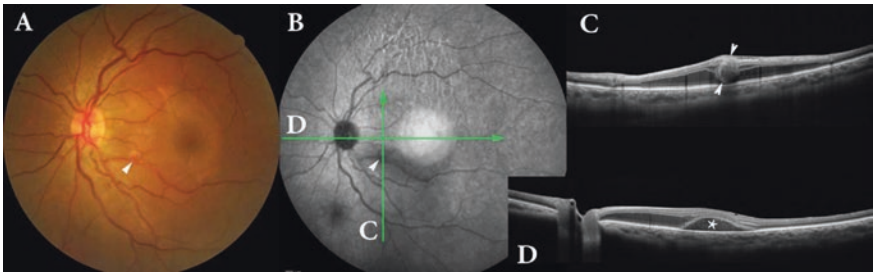

Fig. 20 Color fundus (**a**) and SLO-OCT images (**b**, **c**, and **d**) of the case discussed above. The cross-section from the macroaneurysm itself (**c**) shows a ring–like hyperreflective lesion within the inner retina with shadowing in the outer layers. In the OCT from the central macula (**d**), the accumulation of fluid is evident in both intraretinal and subretinal spaces

Paracentral Acute Middle Maculopathy

Paracentral acute middle maculopathy (PAMM) is a new entity first described in 2013 by Sarraf et al. The underlying pathophysiology seems to be vascular insufficiency and ischemia at the level of intermediate or deep capillary plexus which are located in the inner and outer boundaries of the inner nuclear layer (INL). In fundus examination, it appears as a gray–white retinal patch and might be isolated or in combination with other vascular accidents (Figs. 21 and 22).

It is characterized by a hyperreflective band at the level of INL. Intensity and extension of the lesion can be correlated with severity of ischemia.

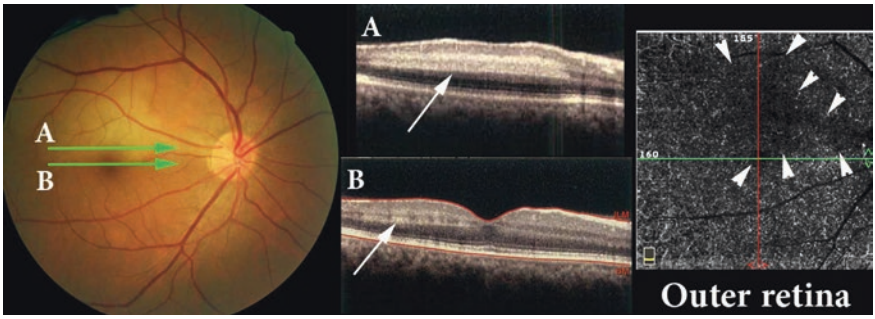

Fig. 21 Multimodal imaging of a patient with sudden vision loss in his right eye. Color fundus photograph shows whitish discoloration of macula in the corresponding area of the cilioretinal artery. **a**PAMM lesion is seen as a hyperreflective band at the level of the inner nuclear layer (white arrow). When the cross-sectional OCT cut is moved towards the margin of the less ischemic area, the intensity and continuity of the hyperreflective band is decreased (**b**). Optical coherence tomography angiography (OCT-A) reveals an area with reduced signal intensity (white arrowheads) due to vascular insufficiency and edema

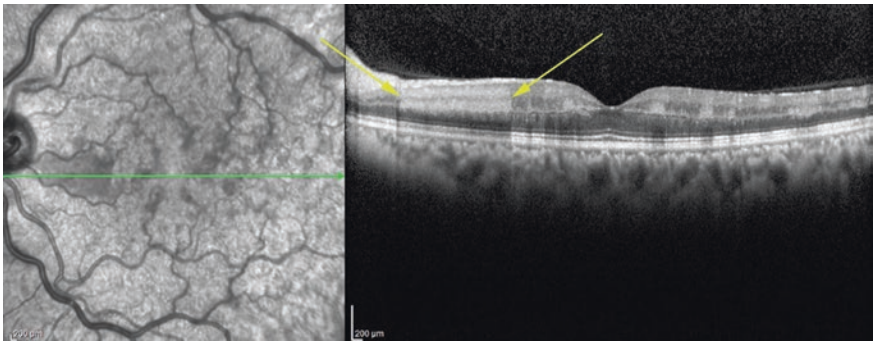

Fig. 22 A PAMM lesion is presented in a case of hypertensive retinopathy. Note the vascular tortuosity in the NIR image (left image). Multiple hyperreflective lesions at the level of the inner nuclear layer are evident in the OCT (right image), which are more prominent near the optic disc (yellow arrow)

Suggested Reading

1. Baskin DE. Optical coherence tomography in diabetic macular edema. Curr Opin Ophthalmol. 2010;21:172–7.
2. Goatman KA. A reference standard for the measurement of macular oedema. Br J Ophthalmol. 2006;90:1197–202.
3. Murakami T, Yoshimura N. Structural changes in individual retinal layers in diabetic macular edema. J Diabetes Res. 2013;2013:920713.
4. Otani T, Kishi S, Maruyama Y. Patterns of diabetic macular oedema with optical coherence tomography. Am J Ophthalmol. 1999;127:688–93.
5. Kim NR, Kim YJ, Chin HS, Moon YS. Optical coherence tomographic patterns in diabetic macular oedema: prediction of visual outcome after focal laser photocoagulation. Br J Ophthalmol. 2009;93:901–5.
6. Uji A, Murakami T, Nishijima K, Akagi T, Horii T, Arakawa N, Muraoka Y, Ellabban AA, Yoshimura N. Association between hyperreflective foci in the outer retina, status of photoreceptor layer, and visual acuity in diabetic macular edema. Am J Ophthalmol. 2012;153:710–7.
7. Sakimoto S, Gomi F, Sakaguchi H, Akiba M, Kamei M, Nishida K. Analysis of retinal nonperfusion using depth-integrated optical coherence tomography images in eyes with branch retinal vein occlusion. Invest Ophthalmol Vis Sci. 2015;8(56):640–6.
8. Spaide RF, Lee JK, Klancnik JK Jr, Gross NE. Optical coherence tomography of branch retinal vein occlusion. Retina. 2003;23:343–7.
9. Ahn SJ, Woo SJ, Park KH, Jung C, Hong JH, Han MK. Retinal and choroidal changes and visual outcome in central retinal artery occlusion: an optical coherence tomography study. Am J Ophthalmol. 2015 Jan 9. pii: S0002-9394(15)00005-7.
10. Coady PA, Cunningham ET, Vora RA, et al. Spectral domain optical coherence tomography findings in eyes with acute ischaemic retinal whitening. Br J Ophthalmol. Published Online First: 03 July 2014. https://doi.org/10.1136/bjophthalmol-2014-304900.
11. Arroyo, Jorge G. Cotton-wool spots may challenge diagnosis. Rev Ophthalmol. 2004:111–4.
12. Kozak I, Bartsch DU, Cheng L, Freeman WR. Hyperreflective sign in resolved cotton wool spots using high-resolution optical coherence tomography and optical coherence tomography ophthalmoscopy. Ophthalmology. 2007;114:537–43.

13. Schmidt D. The mystery of the cotton-wool spots a review of recent and historical descriptions. Eur J Med Res. 2008;13:231–66.
14. Goldenberg D, Soiberman U, Loewenstein A, Goldstein M. Heidelberg spectral-domain optical coherence tomographic findings in retinal artery macroaneurysm. Retina. 2012;32:990–5.
15. Moorsavi RA, Fong KC, Chopdar A. Retinal artery macroaneurysms: clinical and fluorescein angiographic features in 34 patients. Eye (Lond). 2006;20(9):1011–20.
16. Rahimy E, et al. Paracentral acute middle maculopathy what we knew then and what we know now. Retina J Retinal Vitr Dis. 2015;35:10.
17. Chen X, et al. Spectrum of retinal vascular diseases associated with paracentral acute middle maculopathy. Am J Ophthalmol. 2015;160(1):26–34.
18. Yu S, et al. The spectrum of superficial and deep capillary ischemia in retinal artery occlusion. Am J Ophthalmol. 2015;159(1):53–63.e1–2.
19. Rahimy E, et al. Paracentral acute middle maculopathy in nonischemic central retinal vein occlusion. Am J Ophthalmol. 2014;158:372–80.
20. Munk M, et al. New associations of classic acute macular neuroretinopathy. Br J Ophthalmol. 2015;306845.

Uveitis

Nazanin Ebrahimiadib, Fedra Hajizadeh and Marjan Imani Fooladi

Vogt-Koyanagi-Harada

Vogt Koyanagi Harada (VKH) has four stages; prodromal, uveitic, chronic and chronic recurrent. In uveitic phase, there is a diffuse inflammation and thickening of choroidal stroma with secondary multifocal exudative detachment in retina. Optic disc hyperemia is commonly observed and inflammation can spill over to the vitreous cavity and anterior chamber and give rise to a bilateral granulomatous panuveitis. There may be a delayed onset of presentation between the two eyes. Ciliary body effusion can develop which leads to shallow anterior chamber and myopic shift. Retinal vasculitis is absent, however, occasionally peripheral retinal vascular leakage with minimal severity can be seen. Extra-ocular manifestations include meningitis (cerebrospinal fluid pleocytosis), inner ear involvement (hearing loss of higher frequencies and tinnitus) and integumentary signs such as vitiligo, poliosis and alopecia. Inflammation targets melanocyte associated protein of choroidal stroma, skin and hair. Therefore, VKH is more common in pigmented races and loss of pigmentation in the eye, skin and hair is a manifestation of chronic stages of the disease. With continuous inflammation, sunset glow fundus (depigmentation of stroma) and Dalen Fuchs nodules appear in fundus. RPE clumps and areas of atrophy are findings of chronically active disease. Glaucoma and choroidal neovascularization are among long-term complications (Fig. 1).

As VKH is an inflammatory process originating from the choroidal stromal, invovlement of the optic nerve and vitreous may be absent in early phases of uveitic stage. The pattern of "Starry sky" is characteristic in fluorescein angiography during early phases of disease (Figs. 2 and 4). Treatment at this stage, within

N. Ebrahimiadib · M. I. Fooladi (✉)
Farabi Eye Hospital, Qazvin Square, Tehran University of Medical Sciences, South Kargar Street, 1336616351 Tehran, Iran
e-mail: mimanifo@gmail.com

F. Hajizadeh
Noor Ophthalmology Research Center, Noor Eye Hospital, Tehran, Iran

M. Mohammadpour (ed.), *Diagnostics in Ocular Imaging*,
https://doi.org/10.1007/978-3-030-54863-6_21

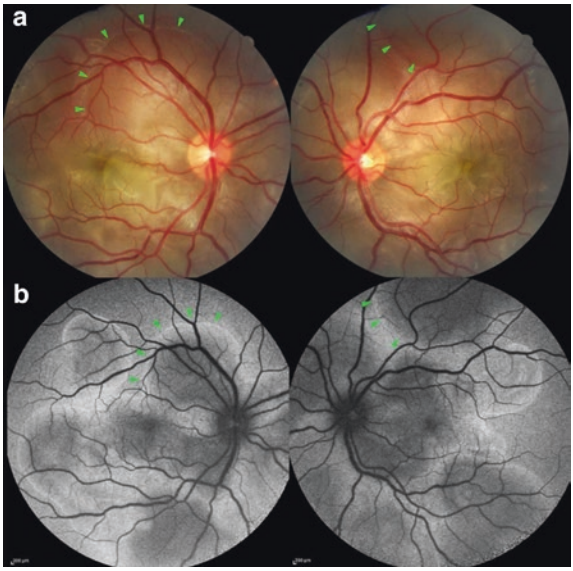

Fig. 1 Uveitic phase of Vogt-Koyanagi-Harada; A: Color retinal photographs of the right and left eye during the acute phase of VKH show multifocal serous retinal detachment (green arrowheads). Media seems to be clear. B: Fundus autofluorescence (FAF) clearly shows regions of serous detachment and their pockets of fluid correspondent to the areas with decreased autofluorescence in the center and a rim of hyperautofluorescence (green arrowheads)

3–4 weeks of disease onset, improves the visual outcome. Inflammation of the choroid causes an ischemia that manifest as hypofluorescent dark dots and choroidal stromal vasculitis (fuzzy vessels) in indocyanine green angiography (ICGA). Early and late choroidal hyperfluorescence and optic disc hyperfluorescence (in early phases of active disease) are other findings in ICGA.

EDI-OCT is a valuable method of imaging that gives information about the choroid. Diffuse choroidal thickening due to infiltration of inflammatory cells is the hallmark of acute phase of VKH. This thickening causes choroidal folds and RPE corrugations and anterior bulging of the choroid, RPE and retina. Sub-retinal fluid with hyper-reflective materials and septations bridging outer retina are common features in OCT. Ususally, there is no intra-retinal fluid (Figs. 3 and 4).

Toxoplasma Retinochoroiditis

Toxoplasmosis is the most frequent infectious cause of posterior uveitis. This protozoan never eradicate from the body and can recur every now and then. The “headlight in the fog” is characteristic for ocular toxoplasmosis. The presence of a focal necrotizing retinochoroiditis adjacent to an old scar is pathognomonic in fundoscopy of these patients. FA and ICG is usually of no value in the diagnosis, whereas, OCT features can be very helpful. This protozoan has a predilection for neural tissue, so ocular toxoplasmosis starts in inner retina from where it extends to involve full thickness retina, the vitreous and/or choroid. Retinal involvement in OCT, manifests as hyperreflectivity in retinal layers alongside with a disorganization so that retinal layers cannot be differentiated. This is called smudge effect.

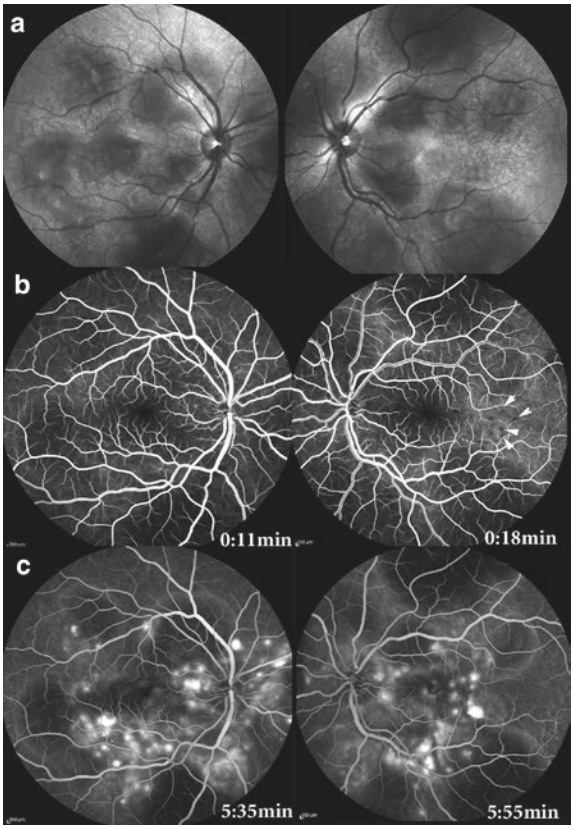

Fig. 2 Uveitic phase of Vogt-Koyanagi-Harada; A: Infrared images of both eyes depict multiple areas of decreased reflectivity due to blockage of serous detachments. B: early phases of fluorescein angiography (FA) in both eyes show small spots of hypofluorescence (white arrowheads) due to inflammatory choroidal ischemia (arrows). C: Later phases of FA illustrate pinpoint areas of leakage at the level of RPE. They subsequently expand and fill the areas of exudative retinal detachment homogenously (pooling). Optic nerve does not show leakage in this case

Retina becomes thickened during active inflammation and cast a posterior optical shadow in OCT. Segmental phlebitis is usually seen in the vicinity of the active patch of toxoplasmosis. Diffuse retinal vasculitis may occur as well. Although, veins are mostly involve in the ocular toxoplasmosis, arterioles can become inflamed and is called kyrieleis' plaque. Kyrieleis' plaque is the inflammation of the vascular endothelium and appear as a creamy exudate in retinal arteriole with a beaded or nodular configuration. It reflects the severity of ocular inflammation and can be seen in infectious uveitis with other etiologies such as syphilis, herpes zoster and rickettsia, as well.

Vitreous cells in addition to posterior hyaloid thickening can be appreciated in OCT. Additionally, vitreoretinal surface adjacent to active lesion show hyperreflective oval deposits.

Choroidal involvement, if present, manifests as an inflammatory granuloma that appears as a hyporeflective nodule in EDI-OCT. Haller's layer show dilated vessels in active phase which becomes constricted with healing. Upon scarification, vessels of Haller's and Sattler's layer cannot be distinguished. Inflammation

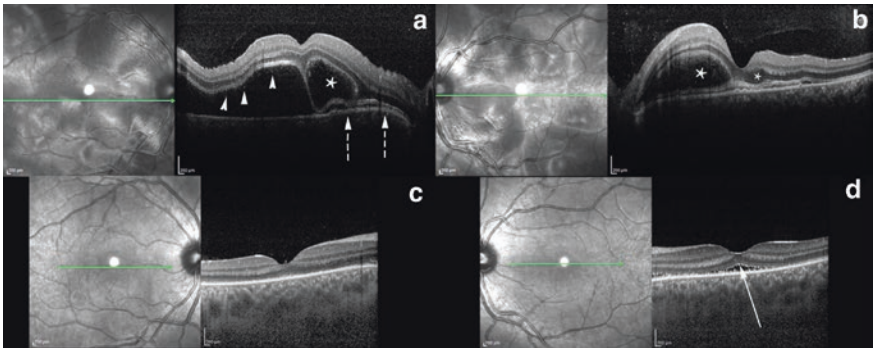

Fig. 3 EDI-OCT in Vogt-Koyanagi-Harada; A, B: acute phase in the right and left eye respectively, subretinal fluid with hyperreflective material (arrowheads); septations seem to delineate a pocket of fluid in outer retina space (asterisks). Inward bulging of the choroid (dashed arrows) and RPE is evident. Inner retina seems not affected. Vascular lumens of choriocapillaris is not recognizable. C, D: after starting immunosuppressive; substantial improvement occurred with resolution of subretinal fluid. Choriocapillaris pattern resumed, although it is still thick. Ellipsoid zone and RPE changes have not recovered completely. Residual subfoveal fluid is evident in the left eye (arrow). This indicates a persistent subclinical activity of the disease

destructs choroid and makes it thinner. In OCT, choroid and retina appears hyperreflective and an approximation of inner retina to outer part of the retina happens in inactive phase. An atrophic or elevated scar or a combination of these two can develop.

Remodeling of retinal vessels has been observed in acute phase, while shunt vessels between retina and choroid is the hallmark of healing phase. This shunt should be differentiated from a choroid neovascularization.

Increased thickness of RPE/Bruch complex in addition to serous retinal detachment can be seen. In addition to RPE hypertrophy, split of RPE/Bruch and disruption of RPE are among the OCT findings. A fine epiretinal membrane may develop after active ocular toxoplasmosis subsides (Figs. 5 and 12.6).

Acute Posterior Multifocal Placoid Pigment Epitheliopathy (APMPPE)

APMPPE is a form of posterior uveitis that primarily involves choriocapillaris. The common age of presentation is in the second to fourth decade with the chief complaint of photopsia and central or paracentral scotoma. It usually occurs bilaterally with a delay of several days to weeks to manifest in the other eye. There is usually a prodromal phase with flu like symptoms.

In slit lamp examination, a few cells may be seen in anterior chamber and more cells are present in the vitreous. In fundoscopy multiple lesions at the level of

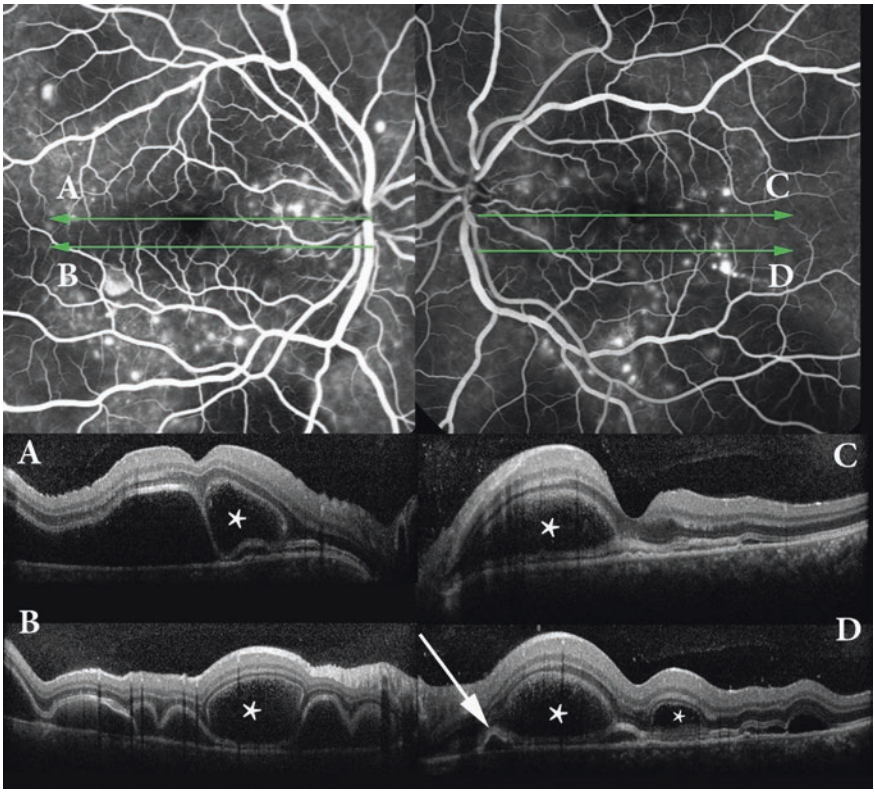

Fig. 4 Correspondence FA and OCT in acute uveitic phase of VKH: Late phase of fluorescein angiography shows classic pattern of starry sky. A, B, C and D: OCT scans corresponding to green lines shown in fluorescein angiography demonstrate undulations of RPE. Focal area of pigment epithelial detachment (arrow) can be seen. Choriocapillaris lumen cannot be recognized. Interestingly pockets of fluid in outer retina, outlined by septations are clearly depicted (asterisks)

RPE and choroid can be seen posterior to equator (Fig. 7). New lesions may recur in periphery within several weeks. Papillitis can be seen while cystoid macular edema is uncommon.

It is plausible that the occlusive nature of vasculitis cause a choriocapillaritis that manifests as confluent areas of hypo or non perfusion in ICG (Fig. 8). Choroidal thickening with overlying retinal involvement can be observed in EDI OCT (Fig. 9).

Lesions resolve spontaneously in 4–8 weeks. With healing, regions of RPE hyper and hypopigmentation (mottling) appear along with patchy areas of RPE and photoreceptor atrophy, while choroidal atrophy has not been reported. Some degree of ellipsoid zone restoration with thickening of the RPE can occur. Visual prognosis is good unless lesions involves the fovea.

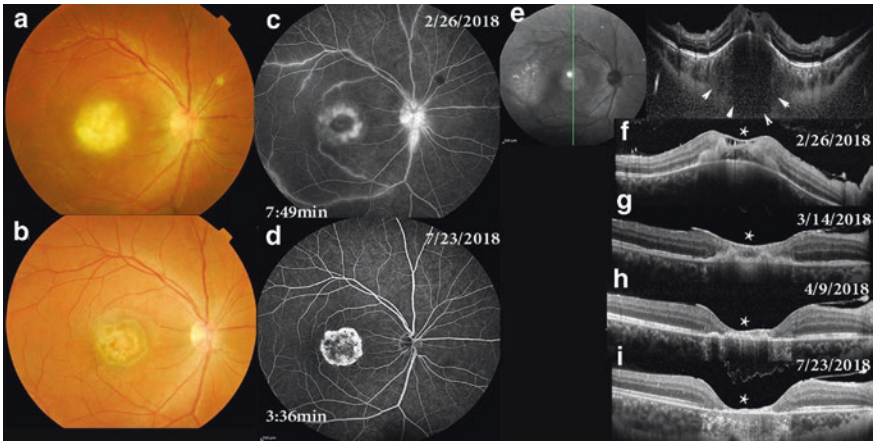

Fig. 5 A: fundus photo of active lesion of toxoplasma retinochoroiditis involving fovea. A creamy white lesion with indistinct border is evident. B: Atrophic scar of the same lesion. Border is sharp and pigmentation started to develop. C: FA shows active leakage of the lesion, in addition to optic nerve leakage and segmental phlebitis and arteriolitis adjacent and remote from the lesion. D: FA in healing phase shows staining of the lesion and improvement of optic nerve and retinal vascular inflammation. E to I: EDI-OCT of a lesion from active to atrophic phase. E: Choroidal nodule outer boundry is delimited with arrowheads. F: Retina is partially healed showing an atrophic disorganized hyperreflective retina that layers cannot be defined. RPE is hypertrophic and split from Bruch's membrane. A fine epiretinal membrane can be appreciated. Posterior optical shadowing is evident (asterisk show the location of fovea). G: approximation of inner and outer retina with healing of choroidal nodule is observed. H: Atrophy progressed and only a thin layer of retina remained. I: retina thinning advanced to mimic a macular hole. Increased transmission of light due to retina atrophy increased the visibility of choroid which is thin and hyperreflective with constricted Haller and Sattler

The most important extraocular manifestation is vasculitis of central nervous system.

Therefore, neuroimaging is required in all patients.

Ampiginous chorioretinitis is a variant of primary choriocapillaropathy that from the point of view of the course of disease stands between APMPPE and serpiginous choroiditis. There is bilateral involvement with numerous lesions and patients usually experience several relapses. Lesions of different stages can be seen; active lesions heal with fibrosis. Figure 10 illustrates advanced stages of disease. Chorioretinal scar involves macula in the right eye and there is partial fovea sparing in the left eye.

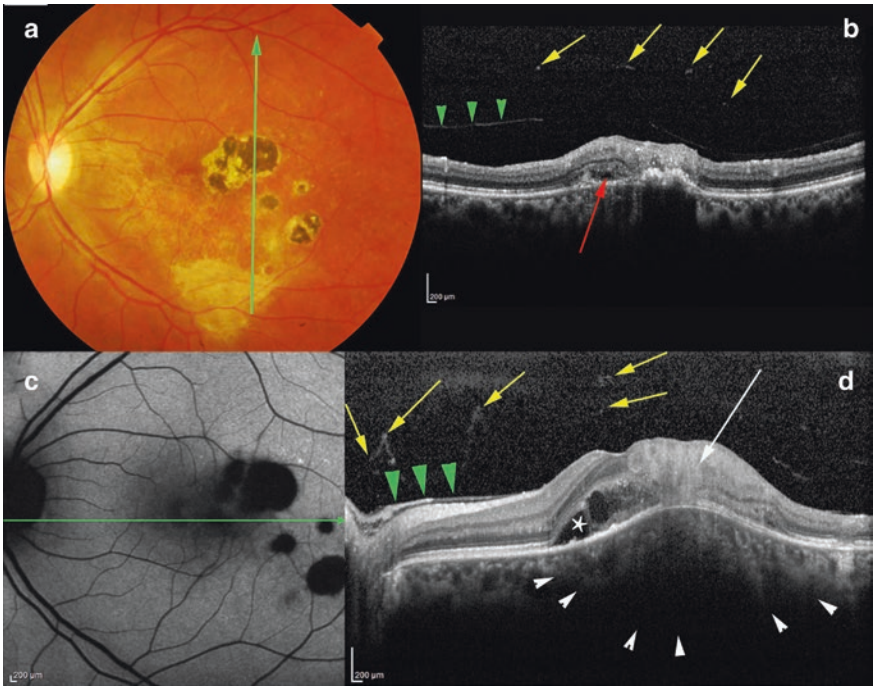

Fig. 6 Ocular toxoplasmosis. A: fundus photo shows stellate pigmented scar and an area of partially active patch of toxoplasmosis along the inferior arcade B: OCT scanning the scarified lesion with some active borders inferiorly (left part of the OCT). Thickening of posterior hyaloid face (green arrowheads) and vitreous cells (yellow arrows) are demonstrated. Hyperreflective and disorganized retina and choroid is evident in the hyperpigmented section. RPE is thickened and separated from Bruch's membrane at the right side of red arrow and outer and inner retina approximates in this region. However, in the inferior border of the lesion, the retina is still thick with a small pocket of subretinal fluid (red arrow). C: fundus autofluorescence depicted the area of scar as hypoautofluorescent. D: OCT scanning of the active part of the lesion. Smudge effect (white arrow) in retina and intraretinal and subretinal fluid (asterisk) in addition to choroid hyporeflective nodule (white arrowheads delineate the outer boundry) is clearly shown. Vitreous comprises hyperreflective deposits (yellow arrows) and posterior hyaloid face becomes thickened (green arrowheads) which is more visible at papillomacular bundle

Ocular Behcet's

Behcet's disease is a systemic autoinflammatory condition that has a chronic relapsing nature. Disease is more common along the Silk road. Occlusive vasculitis which primarily involve veins, can affect almost every organ, but the key features characteristic for diagnosis include recurrent oral aphthous ulcer, genital ulcer, skin lesions (erythema nodosum, pseudofolliculitis (nodules similar to

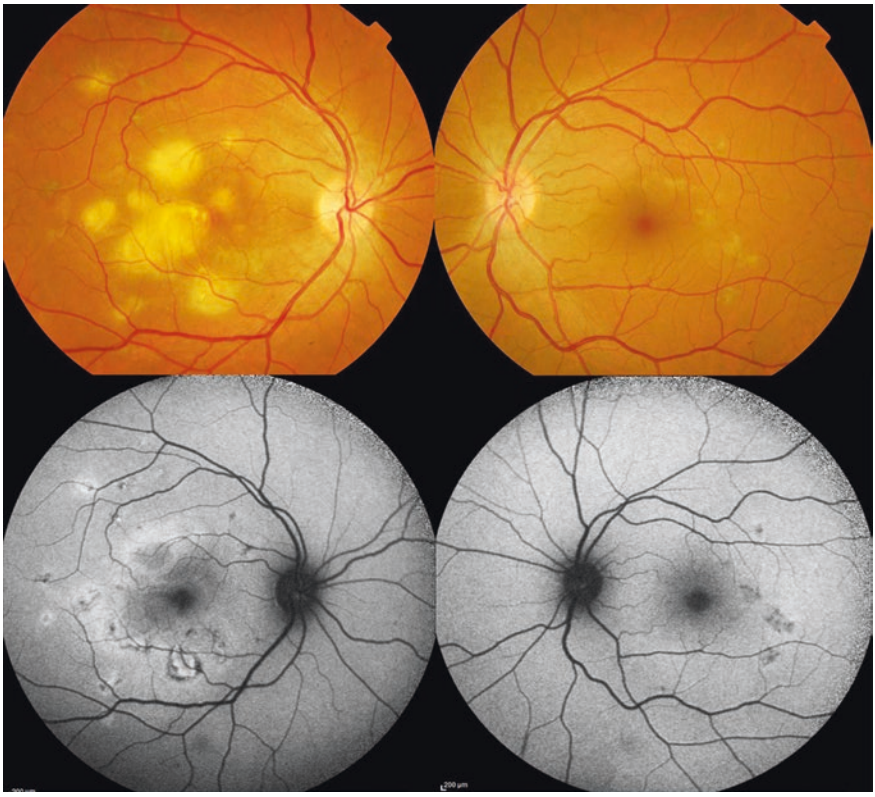

Fig. 7 APMPPE: Fundus photos of the right eye; multiple, creamy-white, flat lesions, sized 1–2 disc area are evident in deep layers at posterior pole; larger and more numerous in the right eye. FAF of the both eyes shows regions of hypo and hyper autoflluorescence. Compared to FA and ICG fewer lesions are evident in FAF and there is a lag for changes in RPE to occur and cause autofluorescent changes.

acne), positive pathergy test and uveitis. Ocular inflammation is the most common manifestation of Behcet's disease. It typically appears as a non granulomatous panuveitis that may present unilaterally at first. Disease is more severe in men.

Other common systemic manifestations include superficial migratory thrombophlebitis and joint inflammation. CNS involvement includes meningitis with or without involvement of the brain. Encephalitis and involvement of cerebral vessels (venous thrombosis or arteritis) may be misdiagnosed as a brain tumor. Gastro intestine, kidney, heart, testis and epididym have been reported to become involved during Behcet's disease.

Uveitis of Behcet's have several characteristics. First; Keratic precipitates of non-granulomatous type. Second, uveitis develop rapidly and resolves fast with or without treatment. Third, this disease may manifest with hypopyon. As the

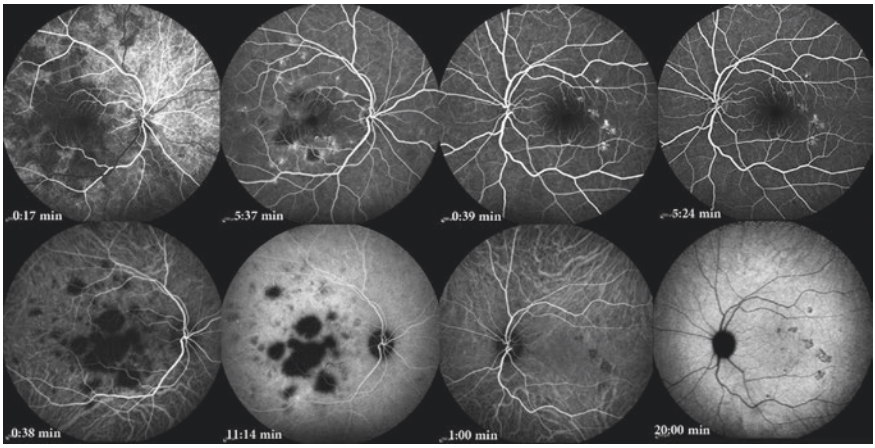

Fig. 8 APMPPE: upper row: FA of both eyes show early hypofluorescence with late staining correspondent to lesions in funduscophy, but more extensive than what observed in fundus photos. Lower row: ICG reveals even more extensive areas of involvement. The lesions are hypocyanescence from early to later phases of the ICG

fibrinous component is not prominent, hypopyon is shifting and there may be minimal ciliary flush. The presence of hypopyon reflects the severity of disease and involvement of posterior segment. Diagnosis of retinal vasculitis definitely need FA, preferably wide-field. Retinal vasculitis is usually associated with poorer visual outcome. Other factors such as being young at onset, male gender, skin lesions, joint inflammation, CNS findings and vascular thrombosis in addition to repeated attacks of posterior uveitis are associated with poorer visual outcome.

Vitreous exudate, a few days after the onset of attack, accumulates in inferior periphery posterior to vitreous base and is called "string of pearls" which is suggestive of Behcet's uveitis. These are different from snowballs seen in inferior periphery of intermediate uveitis. "String of pearls" resolves within several days. Occlusive vasculitis of retinal veins manifests as hemorrhage in deep retinal layers along with frosted branch angiitis. In addition to veins, capillaries are involved in inflammatory process. Diffuse capillaritis give rise to a fern like pattern in FA which is characteristic for Behcet's uveitis. Deep retinal capillary plexus is involved and shunts form to compensate for ischemia. FA is the only reliable method to investigate the capillary non perfusion of the retina. Neovascularization of disc and elsewhere in the periphery of retina can develop in Behcet's uveitis (Figs. 11 and 12). With severe peripheral retinal ischemia secondary to occlusive vasculitis, NVI and NVG may occur. Branch retinal vein occlusion in posterior pole of a young patient with no risk factor is strongly suggestive for behcet's disease and need investigation for other signs of Behcet's disease. Vitreous hemorrhage, tractional and exudative retinal detachment can be seen. Patches of retinitis are infiltration of inflammation in superficial layers of retina which is associated with retinal thickening. In OCT, they appear as hyperreflective foci with posterior

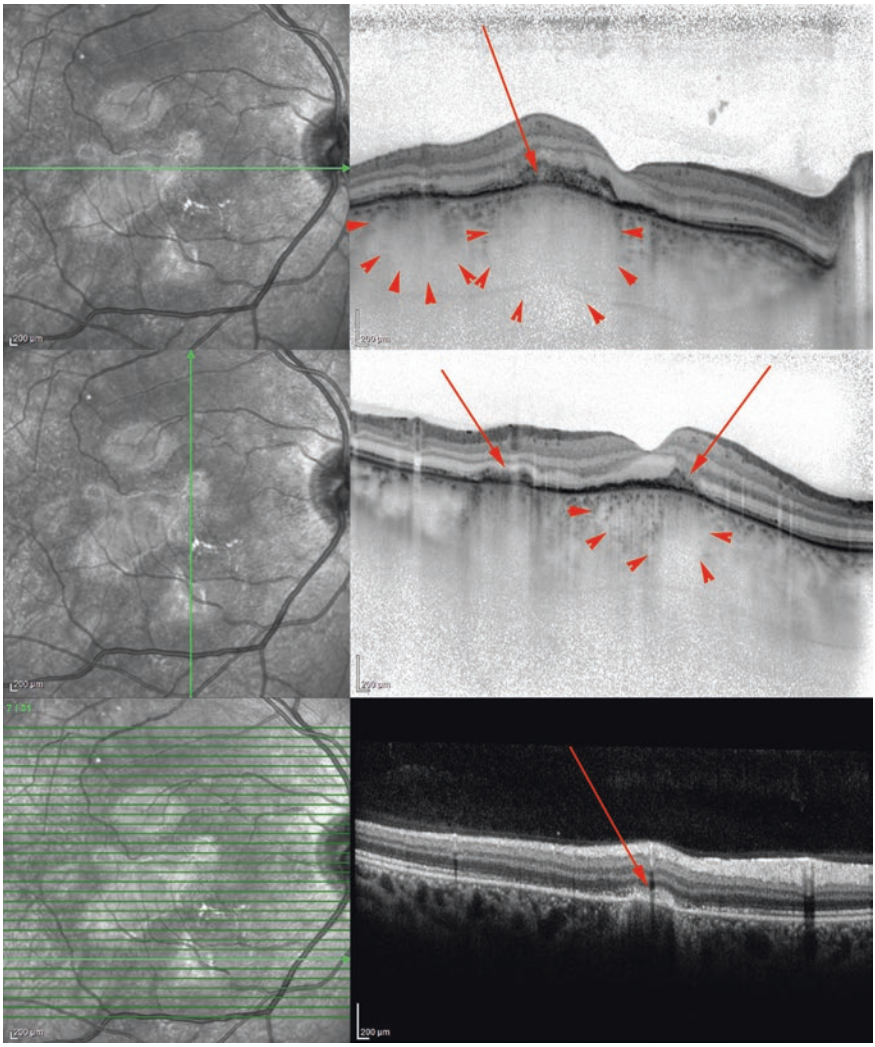

Fig. 9 APMPPE: EDI-OCT Dome shape elevation of retina due to choroidal inflammatory nodule (red arrowheads) is seen. Overlying outer retina shows hyperreflectivity (red arrows)

shadowing. It heals spontaneously within several days leaving no scar but a thinning of nerve fiber layer and inner retina.

With recurrences, posterior synechia, peripheral anterior synechia, cyclitic membrane, iris atrophy, cataract and glaucoma may develop. Optic atrophy and sclerosed vessels of retina indicate an end stage uveitis.

Rare ocular manifestations of Behcet's include scleritis, episcleritis, keratitis, conjunctival ulceration, orbital inflammation, optic neuritis and oculomotor pulsy.

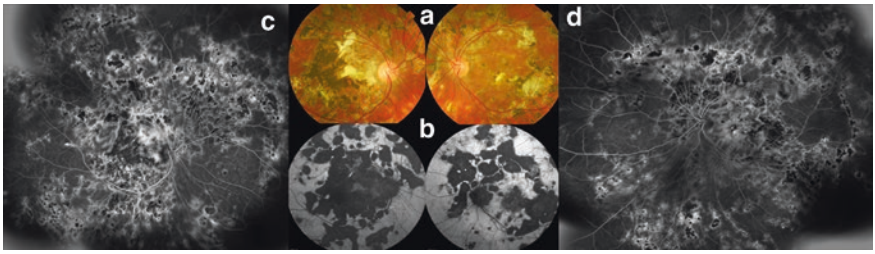

Fig. 10 Ampiginous chorioretinitis; A: Fundus photo of the right and left eye show diffuse patchy scar and fibrosis in addition to hyperpigmentation involving posterior pole, more extensive in the right eye. B: Fundus autofluorescence clearly shows hypoautofluorescent areas in regions with atrophic RPE. Posterior pole of the right eye is involved more extensively. C and D: Fluorescein angiography of the right and left eye shows area of choriocapillaris loss as hypofluorescent areas with staining at the edge of the lesions. There is blockage in pigmented areas

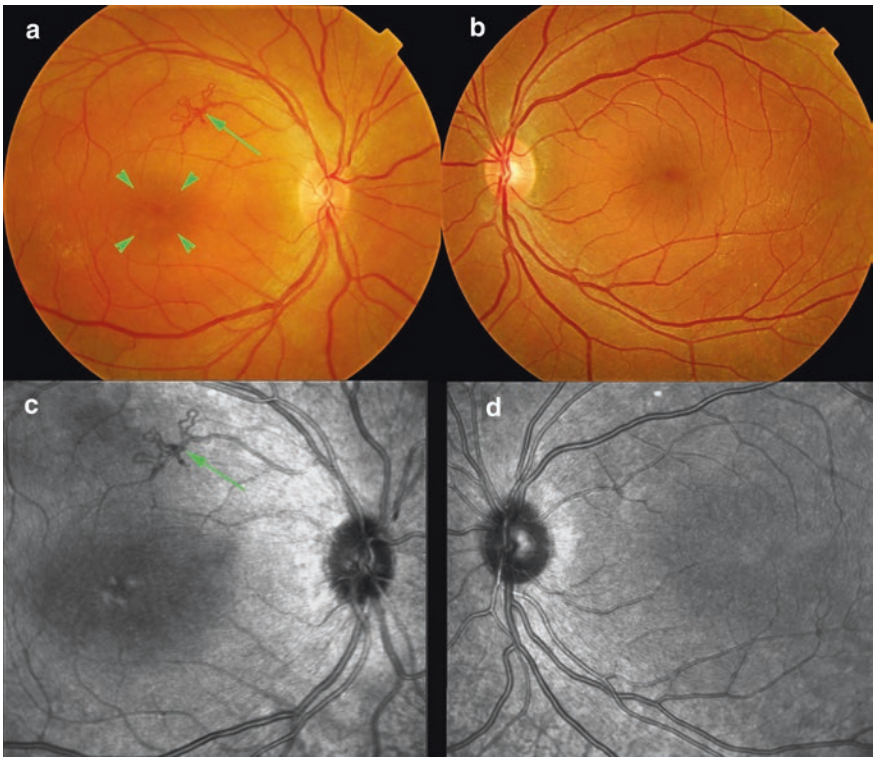

Fig. 11 Ocular involvement of Behcet's disease. A and B: Fundus photo of the right and left eye in a patients with Behcet's disease. Cystic macular edema (green arrowheads) and neovascularization of retina is evident in the right eye. Left eye looks normal. C and D: Infrared image of the left and right eye. In the right eye, cysts of macula appear hyperreflective with a hyporeflective NVE

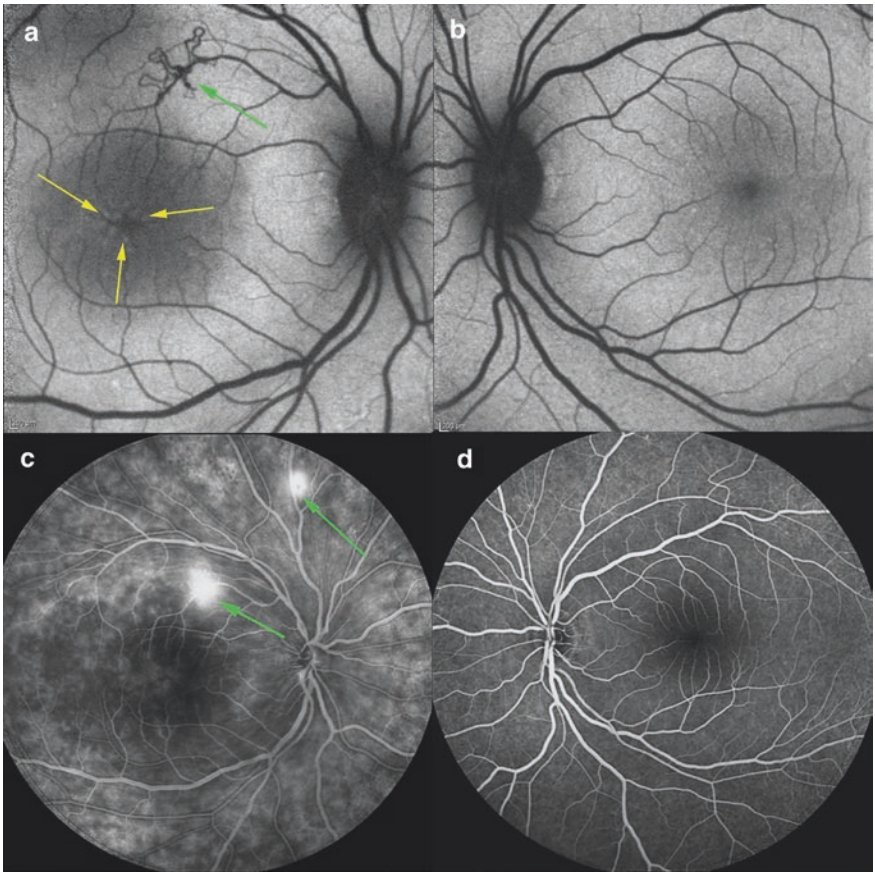

Fig. 12 Ocular involvement of Behcet's disease. A, B: Autofluorescence of the right and left eye. Neovascularization of retina (green arrow) has blocked the autofluorescence of the RPE. Cystoid macular edema appears as hyperfluorscent pockets in fovea (yellow arrows), because cysts push away the retinal pigments of fovea and unmask the lipofuscin of RPE. C: FA of the right eye shows increased vascular lumen and late staining and leakage of retinal vessels. Capillaries that normally are not visible, become clearly visible due to diffuse inflammation (fern like appearance). Inflammatory NVEs is evident in the right eye (green arrows). There is no area of capillary non perfusion in the right eye. D: FA of the left eye does not show any abnormality

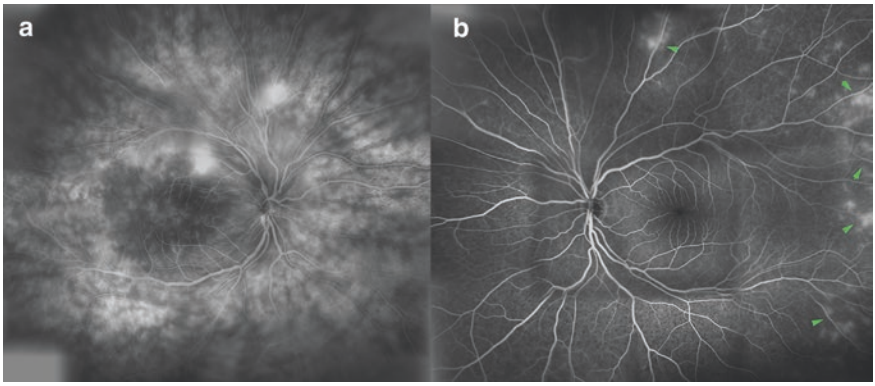

Fig. 13 A: late phase of wide field FA of the right eye shows severe fern like pattern involving posterior pole and periphery of the retina. Two spots of NVE are evident. Macular leakage represents CME. B: Wide field FA of the left eye. Areas of peripheral vascular inflammation (green arrowheads) is solely evident in this type of image

Obtaining wide field imaging especially wide field FA is informative in cases of uveitis. As criteria of some uveitic diseases such as Behcet's require bilateral involvement, documentation of subtle involvement in normal appearing eye is valuable. Composite photos can give a wide field view of fundus (Fig. 13).

Cystoid macular edema can be present and may be associated with vitreomacular traction, epiretinal membrane and macular hole in protracted cases (Figs. 14 and 15).

Neuroretinitis

There is an inflammation of optic nerve and adjacent vessel that subsequently involve neural retina (retinitis component). Leakage of the vessels of the optic disc lead to accumulation of exudate in retina and focal subretinal exudate. Lipid rich exudate penetrate retina deep down to outer plexiform layer and sit with a radial pattern relative to fovea. This forms a macular star which appears with a delay of 1–2 weeks following the optic nerve inflammation (Fig. 16). So in suspected

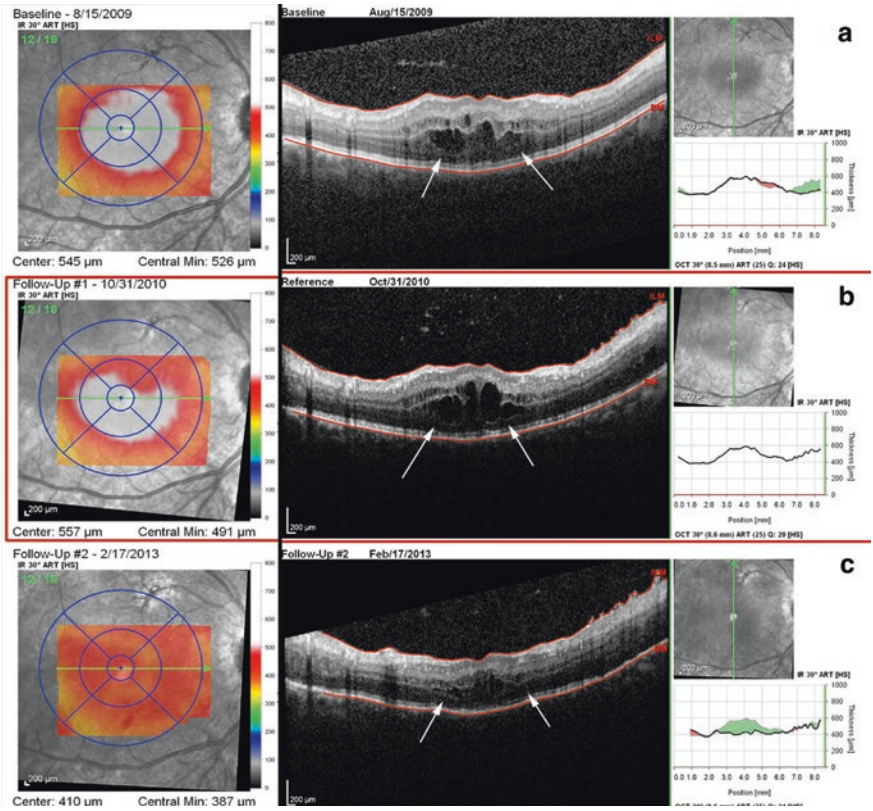

Fig. 14 Cystoid macular edema, OCT; A, B, C: Resolution of inflammatory cystoid macular edema of the right eye with local corticosteroid injections. Cystic spaces are mostly in inner plexiform and inner nuclear layer (IPL and INL). Cells in the vitreous cavity and ILM wrinkling can be appreciated. Ellipsoid zone disruption (white arrows) (A) becomes more pronounced with chronicity of CME (B) and persists despite resolution of edema (C). Of note is the red color of the area of macular thickening in superimposed map of the OCT in SLO images that shows decreased thickening from A to C

patients with optic disc edema, examination in 2 weeks in necessary to establish the correct diagnosis. Macrophages absorb these exudates. Aqueous part of the edema and exudation can infiltrate to external limiting membrane and reach subretinal space (Fig. 17). In a small proportion of patients, macular star never develop. Optic disc hemorrhage (splinter shaped or other forms) can be seen. Vitreous cells are commonly seen.

Patients with neuroretinitis usually present with dyschromatopsia and central or cecocentral scotoma. There is usually a positive RAPD in the side of involvement with subsequent optic atrophy. However, the foveal pathology is usually the underlying cause of decreased vision.

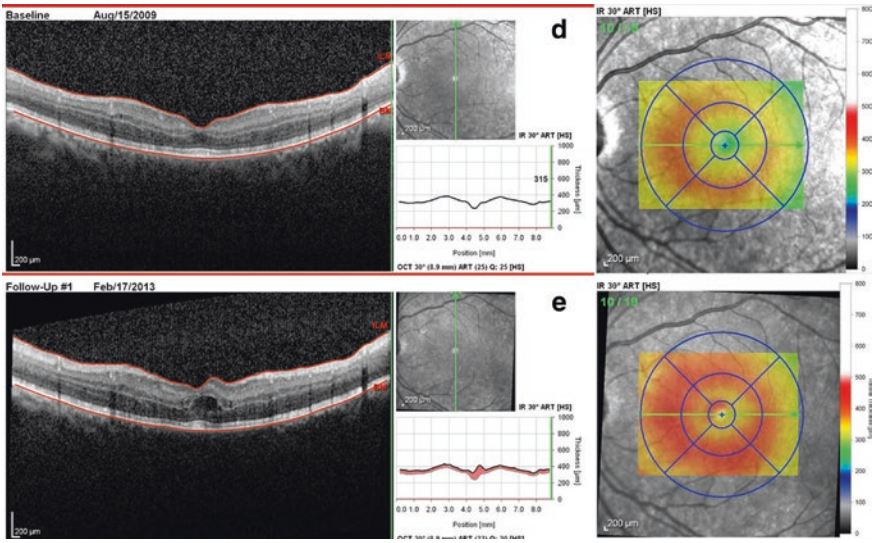

Fig. 15 D and E: OCT of the left eye. B scans confirms the presence of cysts in inner retinal layers (IPL and INL), with a quick review of the map on SLO, one understands macula becomes thickened subsequently (lower image) and there is less thickening compared to the left eye

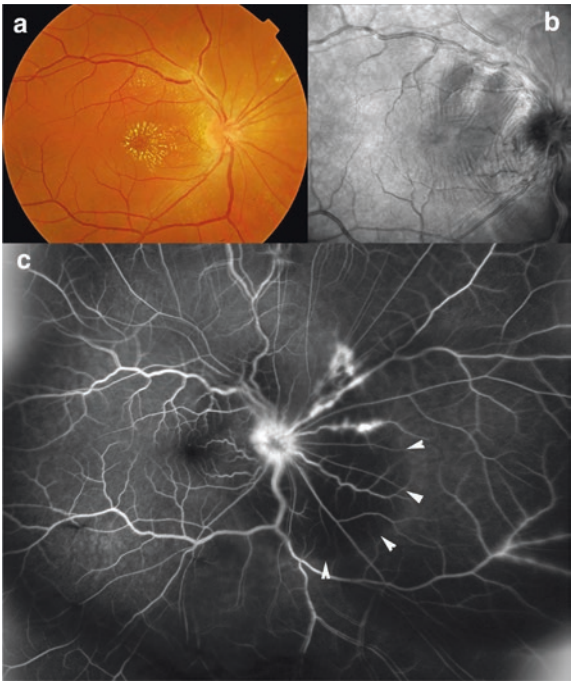

Fig. 16 Neuroretinitis A: Fundus photo illustrates blurring of the margin of optic nerve head. Exudates can be seen in fovea. B: Infrared imaging show hyporeflectivity in edematous areas. C: FA clearly depicts optic nerve leakage in addition to peripapillary segmental vasculitis especially in nasal part of the optic nerve. The area outlined with arrowheads represents blockage due to retinal adema secondary to inflammation of the optic nerve

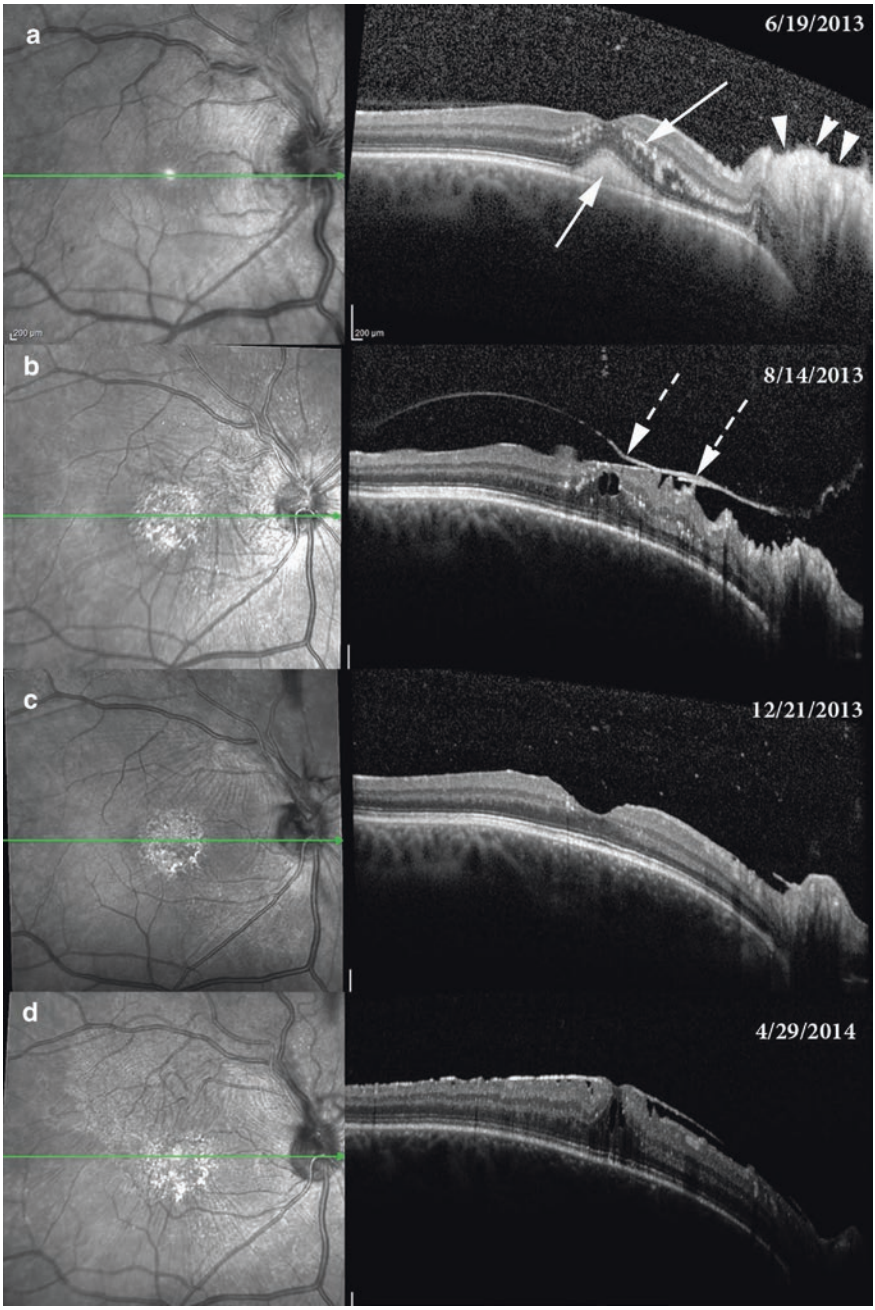

Fig. 17 Neuroretinitis; SLO-OCT images scanning fovea in acute, chronic, resolving and complication phase of neuroretinitis. A: location of exudates are in subretinal and outer plexiform layer (white arrows). Exudates appear as hyperreflective material. Inner retina in papillomacular bundle becomes thick and hyperreflective representing neural retinitis (white arrowheads). B: Two months later, accumulation of inflammatory debris lead to thickening of posterior hyaloid (dashed arrows), formation of inner retinal folds and intraretinal cysts. C: resolution of the inflammation and edema is clearly shown D: Epiretinal membrane with thickening and blunting of the foveal pit can be recognized. Ellipsoid zone disruption and some RPE changes are evident

Nearly 50% of cases of neuroretinitis are idiopathic. In those with an etiology, either infectious (such as cat scratch disease, herpes family, TB, toxoplasmosis, toxocara) or autoimmune (sarcoidosis, antiphospholipid syndrome) causes are responsible. It is usually unilateral with good visual recovery. Focal retinitis has been reported in cases with cat scratch disease. Recurrence has been observed more commonly in cases with autoimmune etiology and macular star may not develop in subsequent episodes.

References

1. Elahi S, Herbort CP Jr. Vogt-Koyanagi-Harada Disease and Birdshot Retinochoroidopathy, Similarities and Differences: A Glimpse into the Clinicopathology of Stromal Choroiditis, a Perspective and a Review. Klin Monbl Augenheilkd. 2019;236(4):492–510
2. Orefice JL, Costa RA, Scott IU, Calucci D, Orefice F; Grupo Mineiro de Pesquisa em Doencas Oculares Inflamatorias (MINAS). Spectral optical coherence tomography findings in patients with ocular toxoplasmosis and active satellite lesions (MINAS Report 1). Acta Ophthalmol. 2013; 91(1):e41–7
3. Xerri O, Salah S, Monnet D, Brezin AP. Untreated acute posterior multifocal placoid pigment epitheliopathy (APMPPE): a case series. BMC Ophthalmology. 2018; ;18(1):76
4. Ksiaa I, Abroug N, Kechiada M, Zina S, Jelliti B, Khochtali S, Attia S, Khairallah M. Eye and Behcet's disease. J Fr Ophthalmol. 2019;42(4):e133–46
5. Abdelhakim A, Rasool N. Neuroretinitis: a review. Curr Opin Ophthalmol. 2018;6:514–9. https://doi.org/10.1097/ICU.0000000000000527

Adult Intraocular Tumor

Babak Masoomian and Fariba Ghassemi

Uveal Melanoma

1. Introduction
   Approximately 5% of all melanoma tumors arise in ocular tissue. Most ocular melanoma (85%) is uveal (iris, ciliary body or choroid) in origin and it is the most common intraocular malignant tumor. Tumors arise from the pigment cells (melanocytes).
2. Incidence
   Incidence of posterior uveal melanoma (UM) is highest among people with light skin and blue eyes. Other risk factors have been suggested, such as blue light exposure and arc welding, but are still debated in the field. The cutaneous conditions associated with uveal melanoma are familial atypical mole and melanoma, cutaneous melanoma, and oculo-dermal melanocytosis (nevus of Ota). The reported incidence of UM was 4.3 case per million population with a higher rate in male than female (4.9 vs. 3.7 per million). It is more generally seen with peaks at the age 70 years in the older age group.
3. Clinical features
   Iris melanoma appears as a variably pigmented, usually well-defined mass in the iris stroma and has predilection to appear in the inferior portion of the iris. Less common iris melanoma has diffuse form with trabecular meshwork infiltration or tapioca melanoma that has the appearance a gelatinous nodular iris.
   Ciliary body melanoma can attain a larger size before it is recognized clinically. The patient is often asymptomatic. It can cause displacement of the lens,

B. Masoomian (✉) · F. Ghassemi
Farabi Eye Hospital, Tehran University of Medical Sciences (TUMS), Qazvin square, Kargar Street, Tehran, Iran
e-mail: dr.masoomian@yahoo.com

F. Ghassemi
e-mail: fariba.ghassemi@gmail.com

M. Mohammadpour (ed.), *Diagnostics in Ocular Imaging*,
https://doi.org/10.1007/978-3-030-54863-6_22

which results in an uncorrectable astigmatism. Signs include dilated episcleral vessels (sentinel vessels), segmental cataract and raised intraocular pressure. Usually the lesion has a dome-shaped configuration visualized after dilation of the pupil. Less often it can produce a circumferential ring pattern.

Choroidal melanoma may present with different symptoms. If it is located at the macula, it could produce decrease visual acuity or visual distortion. Peripheral choroidal melanoma tends to present with a visual field defect or flashing. If an exudative retinal detachment is present, the patient may meet first a retinal surgeon before the diagnosis of melanoma is made. It may be dome or mushroomed shaped with or without superficial orange pigment (lipofuscin) and associated subretinal fluid. Choroidal Melanoma is frequently pigmented, and an amelanotic melanoma must be distinguished from other simulating lesions.

4. Diagnosis

A-scan	Low to medium intensity echo spike
B-scan	An elevated dome-shaped, mushroom shaped more characteristics Acoustically partial hollowness and choroidal excavation
FA	No pathognomonic angiographic sign Early: A blockage of the background fluorescence, spotty hyperfluorescence due to changes in the pigment epithelium, an independent vascular network, "double circulation" pattern in dome-shaped melanomas Late: leakage from the tumor vessels can be observed
FAF	Hypoautofluorescence (39%), isoautofluorescence (6%), and hyperautofluorescence (55%)
ICG	The intrinsic choroidal vasculature of the tumor can be observed Tumor vessels are tortuous, have random direction, and show abnormal branching In pigmented tumors, in all frames the hypocyanescence is caused by blockage from the tumor pigment Early: filling of the tumor vascular channels, Late: diffuse hyperfluorescence due to vascular leakage, sometimes a three-ring pattern of staining
OCT	Serous retinal detachments around and overlying the tumor, intra-retinal cystic spaces in the overlying retina and loss of normal retinal architecture overlying the tumor
OCTA	Decreased flow rate of SMV of choroidal melanoma cases compared with nevi was a significant finding The presence of mural and piercing feeding vessels
MRI	• **T1**: hyperintense signal • **T2**: moderately low intensity • **T1 Gd**: shows enhancement
CT	Elevated, hyperdense sharply marginated lenticular or mushroom-shaped lesions, which enhance with the administration of contrast

FA: Fluorescein angiography, FAF: Fundus autofluorescence, OCT: Optical coherence tomography, OCTA: Optical coherence tomography angiography, MRI: Magnetic resonance imaging, CT: Computerized tomography

Iris melanoma is usually diagnosed with slit lamp biomicroscopy whereas ciliary body and choroidal melanoma are typically diagnosed with indirect ophthalmoscopy. Transillumination is a useful method of detecting ciliary body and anterior choroidal melanomas. It is also used for the delineation of the tumor margins intraoperatively. Mostly, the tumor shows up as a dark shadow with well-defined margins. Ocular ultrasound has been the simplest and the most reliable paraclinical test for evaluation of these patients. Other para clinical methods including fluorescein angiography and optical coherence tomography are of lesser value.

There are some risk factors for assessment of malignant behavior of small melanocytic choroidal lesions include: tumor thickness more than 2 mm at initial diagnosis, presence of symptoms, presence of sub retinal fluid, presence of orange pigment on the surface of the lesion, location of the tumor close to optic disc margin (less than 3 mm) and the presence of ultrasonographic hollowness of the lesion.

More recently, UM biopsy for genetic testing has become increasingly warranted due to the accuracy of cytogenetic prognostication and the landscape characterized by the emerging possibilities of personalized treatment regimens (Figs. 1, 2, 3, and 4).

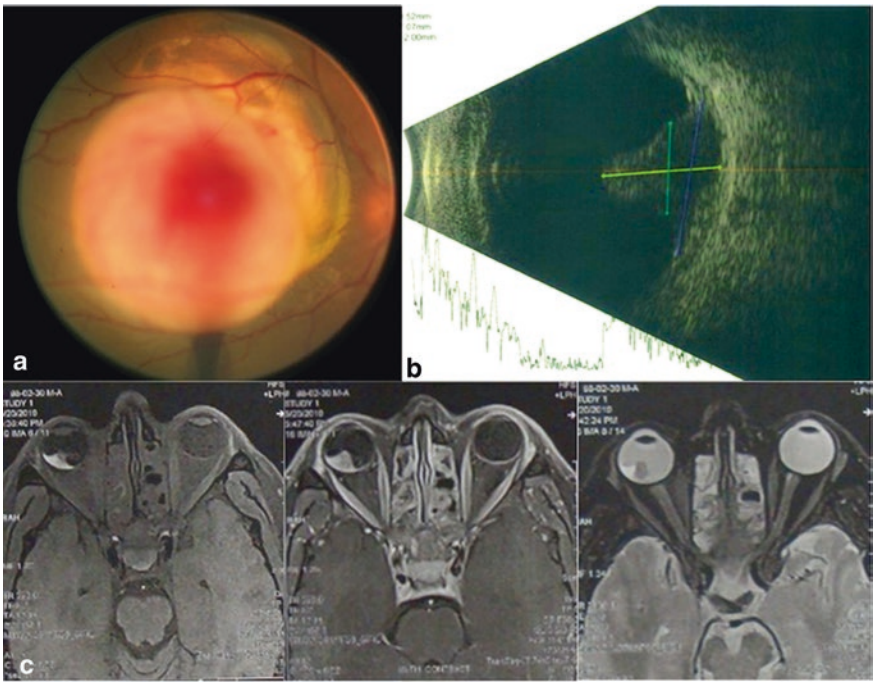

Fig. 1 **a** Fundus photo of a 60 years old male, shows a big posterior pole mushroom shaped mass with both melanotic and amelanotic portions of the tumor. Fresh hemorrhage probably due to Bruch's membrane rupture, limited to the top of the lesion is present. **b** B-scan revealed the mushroom shape of the lesion. **c** MRI revealed no extraocular extension. Unlike the usual T2 appearance of the choroidal melanoma, in this patient, the lesion is more reflective than vitreous (due to intra-lesion hemorrhage or edema)

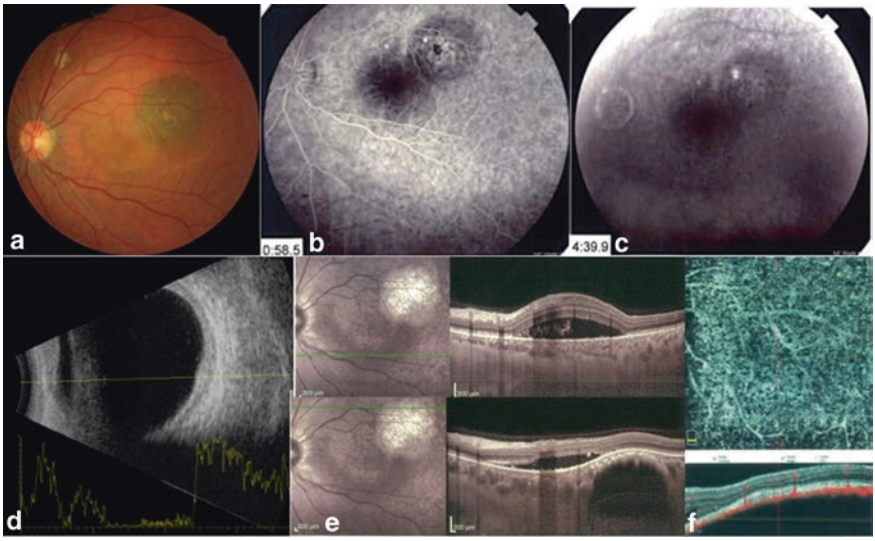

Fig. 2 **a** A small choroidal melanoma in 44 years old female developing from previous choroidal nevus showed recent growing. **b** and **c** show the early and late phase of fluorescein angiography with early hyper and late mild leakage of fluorescein and staining. **d** B scan shows dome shaped lesion without subretinal fluid. **e** The choroidal thick lesion with accompanying subretinal fluid with narrowed but still preserved choriocapillaris layer. The subretinal fluid is viscous with some reflectivities assumed to be fibrinous material. The OCTA image shows no significant vascular pattern

5. Treatment

Enucleation is the traditional treatment method of uveal melanomas. It is indicated for advanced melanomas that occupy most of the intraocular space, presence of severe secondary glaucoma and optic nerve invasion by tumors.

From the beginning of the seventies, *Plaque Brachytherapy* has been used for treatment of uveal melanoma (most commonly ruthenium-106 and iodine-125). Size of the plaque is selected to maintain a 2 mm safety margin around the base of the tumour and radiation emitted to the apex of the lesion is between 80 and 100 Gy, which is considered to be the effective tumoricidal dose. The complications of plaque brachytherapy include cataract, proliferative radiation retinopathy and radiation papillopathy.

Proton bean radiotherapy is other treatment modality that indicated for all melanomas (even large tumors) and standard treatment is fractionated four times; total dose of 60–70 cobalt Gy equivalents (c Gy) is administered.

Transpupillary thermotherapy (TTT) is a treatment method that induces hyperthermia to the tumor by delivering heat in the infrared range. Tumor is heated to a temperature of 60–65 degrees. It could be effective method for only small tumors or can be used in combination with other methods.

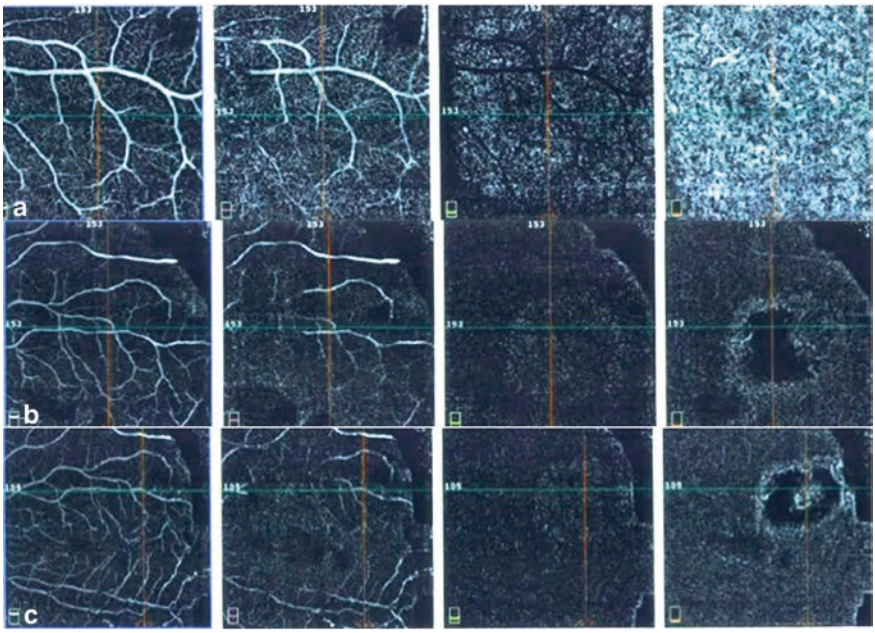

Fig. 3 The OCT-A images of the same patient in different scanning diameter shows different vascular pattern. **a** 3×3 mm with a near normal vascular pattern. **b** 6×6 mm window shows a circular vascular density with a hypovascular and hypo-reflective center. Two radial vascular patterns are piercing the medial and lateral border. **c** the 8×8 mm window shows the hyper-reflective border and a vascular center of the lesion

6. Prognosis

When eye melanoma spreads to distant parts of the body, the five-year survival rate is approximately 15%. Many clinical and pathological prognostic factors have been identified that are associated with higher risk of uveal melanomas metastasis. These include large tumor size, ciliary body involvement, presence and extent of cells with epithelioid morphology, and older patient age.

The survival rates of patients with uveal tract melanoma have not changed in the last 30 years. Cumulative metastasis rate were 25% and 34%, respectively, in the Collaborative Ocular Melanoma Study (COMS) at 5 and 10 years after treatment. Typical metastases sites include liver (90%), lung (24%), and bone (16%). As such, the bulk of surveillance strategies are concentrated on the liver. These include abdominal magnetic resonance imaging (MRI) and ultrasound and liver function tests.

Suggested Reading

1. Shields JA, Shields CL. Intraocular tumors: An atlas and text. 3rd ed. Philadelphia, PA: Lippincott Wolters Kluwer. 2016:45–59.

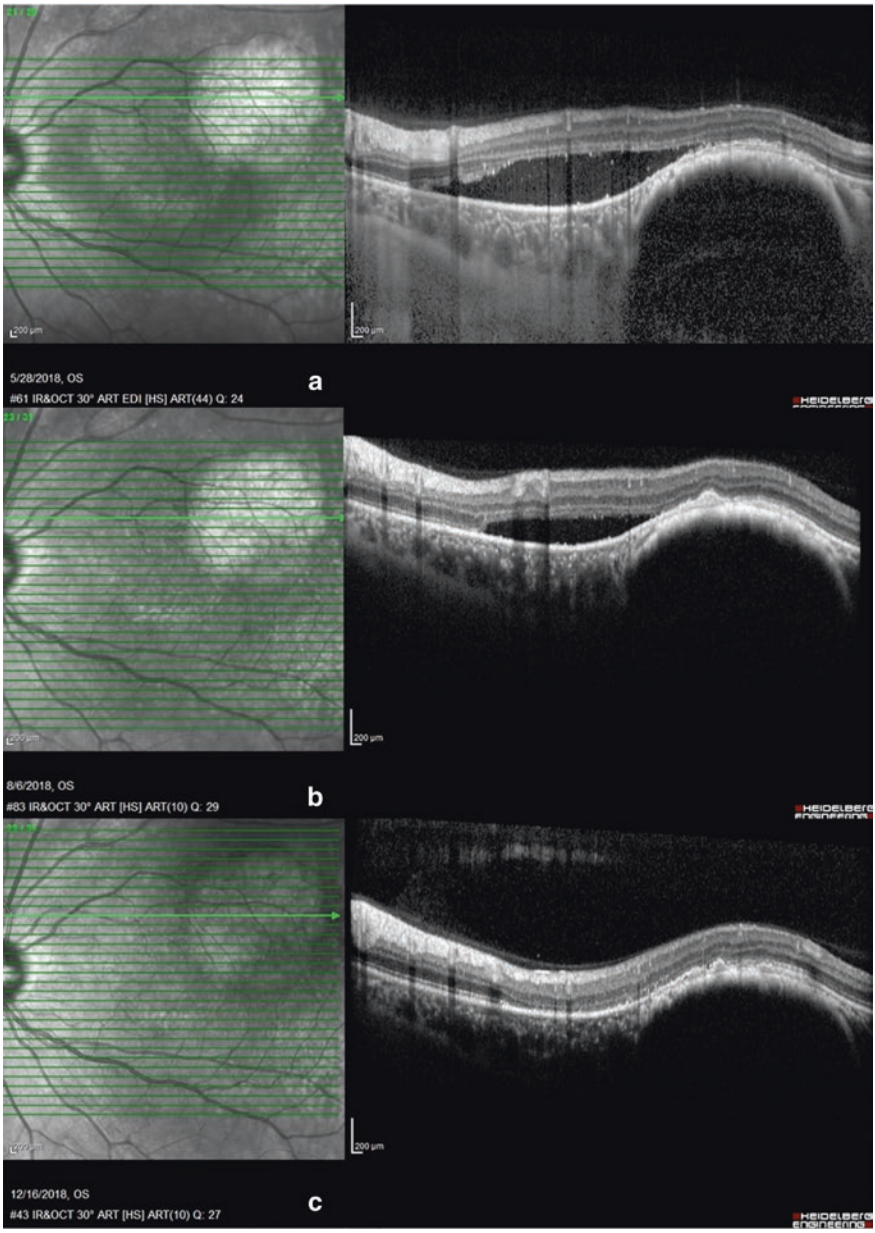

Fig. 4 The above lesion (Fig. 2) was treated with full dose and full power and fluence once. **a** to **c** show the disappearance of the subretinal fluid with the stabilized condition and size of the lesion

2. Singh D, Topham A. Incidence of Uveal Melanoma in the United States: 1973–1997". Ophthalmology. 2003;110(5): 956–61.
3. Shields JS, Shields CL. Posterior uveal melanoma: clinical and pathologic features. In: Shields JA, Shields CL, editors, Intraocular tumours—a text and Atlas. Philadephia Pa, USA: W.B. Saunders; 1992. p. 117–36.
4. Atmaca LS, Batioğlu F, Atmaca P. Fluorescein and Indocyanine Green Videoangiography of Choroidal Melanomas. Jpn J Ophthalmol. 1999;43(1):25–30.
5. Materin MA, Raducu R, Bianciotto C, Shields CL. Fundus Autofluorescence and Optical Coherence Tomography Findings in Choroidal Melanocytic Lesions. Middle East Afr J Ophthalmol. 2010;17(3): 201–6.
6. Ghassemi F, Mirshahi R, Fadakar K, Sabour S. Optical Coherence tomography angiography in choroidal melanoma and nevus. Clin Ophthalmol. 2018;12:207–14.
7. Hawkins BS. The COMS randomized trial of iodine 125 brachytherapy for choroidal melanoma, III: initial mortality findings: COMS report no. 18. Arch Ophthalmol. 2001;119(7):969–82.
8. Diener-West M, Reynolds SM, Agugliaro DJ, et al. Screening for metastasis from choroidal melanoma. The Collaborative Ocular Melanoma Study Group Report 23. J Clin Oncol. 2004;22(12):2438–44.
9. Feinstein EG, Marr BP, Winston CB, Abramson DH. Hepatic abnormalities identified on abdominal computed tomography at diagnosis of uveal melanoma. Arch Ophthalmol. 2010;128(3):319–23.

Choroidal Hemangioma

1. Introduction

is a hamartomatous benign congenital vascular tumor of the choroid. It can be subdivided into two types: circumscribed type and diffuse type. The circumscribed type usually involves a part of the choroid and is usually not associated with any systemic disease whereas the diffuse type involves large portions of the choroid and is commonly found in patients with Sturge–Weber syndrome.

2. Incidence

Choroidal hemangioma exact incidence is difficult to estimate since most circumscribed choroidal hemangiomas only come to medical attention if patients become symptomatic or if found incidentally; however, the disease is felt to be relatively rare. The mean age at diagnosis ranged from 38 years to 47 years, considerably

older than the mean age at diagnosis for diffuse choroidal hemangioma, which is typically in the first decade of life.

3. Clinical features

Circumscribed choroidal hemangiomas are orange-red colored, round lesions that located mostly in the posterior half of the fundus. Typical lesion ranges from 3 to 7 mm in diameter and 1 to 3 mm in thickness. They are associated with subretinal fluid or overlying intraretinal cysts. May be symptomatic, depending on their location. Serous retinal detachment occurs frequently as a complication, and can be mistaken for central serous retinopathy.

Diffuse choroidal hemangioma is generally identified ipsilaterally to a facial nevus flammeus. The fundus usually has a red hue that is much more saturated than that of the uninvolved side. The choroid tends to be thickened diffusely by the hemangiomatous vascular lesion, but it has more thickness around the optic disc. So, causes prominent disc cupping that resembles glaucomatous optic neuropathy. In some cases, elevated intraocular pressure usually is caused by elevated episcleral and orbital venous pressure, angle malformation or both; is a feature of many eyes that have diffuse choroidal hemangioma. Serous retinal detachment is an eventual complication. Clinically, choroidal hemangiomas are elevated and usually round or slightly oval lesions with flecks of pigment, splotchy yellow material, and/or orange pigments that may be develop over time.

4. Diagnosis

A-scan	High intensity echo spike
B-scan	An elevated dome-shaped, acoustically solid mass
FA	Very early hyperfluorescence of larger-caliber choroidal blood vessels. Late frames: stains with fluorescence and any associated subretinal fluid
FAF	
ICG	Early: filling of the tumor vascular channels, Intermediate: intense hypercyanescence of the lesion Late: washout of the tumor central portion.
OCT	The subretinal fluid accumulation along with cystic retinal degeneration that can occur overlying the lesion
OCTA	A dense irregular vascular network in the outer retinal and choroid capillary layers
MRI	• **T1**: hyperintense signal • **T2**: iso or hyperintensity • **T1 Gd**: shows early enhancement
CT	Moderate enhancement with contrast material

FA: Fluorescein angiography, FAF: Fundus autofluorescence, OCT: Optical coherence tomography, OCTA: Optical coherence tomography angiography, MRI: Magnetic resonance imaging, CT: Computerized tomographyDifferential diagnosis includes choroidal nevus, amelanotic choroidal melanoma, choroidal metastasis, choroidal osteomas and central serous chorioretinopathy (Figs. 5 and 6).

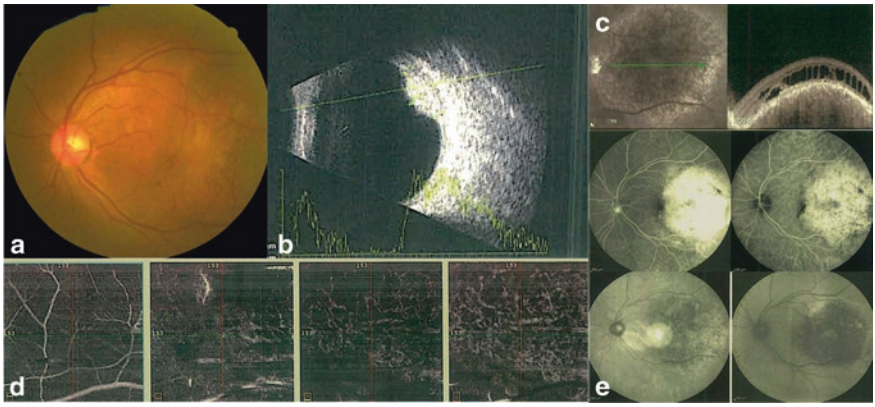

Fig. 5 **a** A pinkish choroidal lesion in 35 years old female complaint of decreased vision and mild hazy media due to mild posterior subcapsular cataract. **b** In B-scan a dome shaped mass with high internal reflectivity was shown. **c** In OCT, disclosed retinal cystic changes in outer nuclear and outer plexiform layer. **d** OCT-A showed superficial and deep capillary plexus are intact and vascular remodeling with some dilation. **e** Early and late phase of FA and ICG shows late washout of the dye from tumor vasculature

5. Treatment

Observation alone may be indicated in cases of asymptomatic hemangiomas. Photodynamic therapy (PDT) has been used with considerable success in the treatment of small to medium-size circumscribed choroidal hemangiomas.In patients who have an extremely thick choroidal hemangioma, extensive non-rhegmatogenous retinal detachment, low-dose ocular irradiation (e.g. plaque brachytherapy, external beam and proton beam radiation) appears to be effective.

Suggested Reading

1. Shields JA, Shields CL. Intraocular tumors: An atlas and text. 3rd ed. Philadelphia, PA: Lippincott Wolters Kluwer, 2016:45-59.
2. Shields CL, Honavar SG, Shields JA. Circumscribed choroidal hemangioma: Clinical manifestations and factors predictive of visual outcome in 200 consecutive cases. Ophthalmology. 2001;108: 2237–48.
3. Scott IU, Alexandrakis G, Cordahi GJ. Diffuse and circumscribed choroidal hemangiomas in a patient with Sturge-Weber syndrome. Arch Ophthalmol. 1999;117:406–7.
4. Singh AD, Kaiser PK. Choroidal hemangioma. Ophthalmol Clin North Am. 2005;18:151–61.
5. Jurklies B, Bornfeld N. The role of photodynamic therapy in the treatment of symptomatic choroidal hemangioma. Graefes Arch Clin Exp Ophthalmol. 2005;243:393–96.

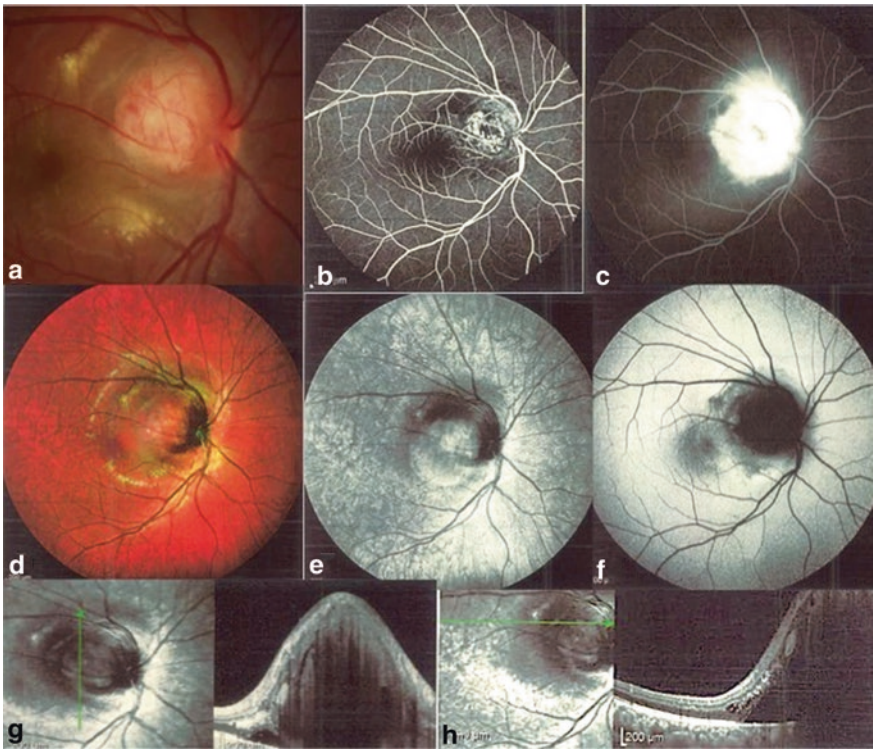

Fig. 6 Peripapillary . **a** Color fundus photography of peripapillary **b** and **c** Fluorescein angiography of hemangioma reveals hyperfluorescence in the early stage and late leakage. **d** Multicolor imaging shows an orange-red lesion encroaching the papillomacular bundle. **e** and **f** Infrared and autofluorescence showed hyporeflectivity. **g** and **f** EDI-OCT shows elevation of the retinal-choroid complex and photoreceptor loss. Multiple shadows cause the linear structure of the lesion

6. López-Caballero C, Saornil MA, De Frutos Jet al. High-dose iodine-125 episcleral brachytherapy for circumscribed choroidal haemangioma. Br J Ophthalmol. 2010; 94:470–3.

Choroidal Osteoma

1. Introduction

Choroidal osteoma is a benign tumor that is characterized by replacing choroid with mature bones tissue.

2. Incidence

Choroidal osteoma is a rare condition. Its precise frequency remains unknown but, predominantly affects young adults in their early twenties with a large range from

few months old to late sixties. It is unilateral in more than 80% of patients and has a predilection for women. It has been reported in races. No correlation was found between choroidal osteoma and metabolic and electrolytes abnormalities. Some reports have linked choroidal osteomas to Stargardt's maculopathy, polypoidal choroidal maculopathy, pregnancy, and intraocular inflammation.

3. Clinical features

Patients usually present with symptoms of blurred vision, metamorphopsia, or visual field defects. About 30 percent of cases remain asymptomatic. A choroidal neovascular membrane and decalcification in the subfoveal region is associated with poor vision. The description of choroidal osteoma given by J.D. Gass in 1978 still contains: (1) slightly and irregularly raised, yellow-white, juxtapapillary, choroidal tumor and well-defined geographic boundaries; (2) diffuse and mottled depigmentation of the overlying pigment epithelium; and (3) multiple small vascular networks on the tumor surface. Thin, atrophic, yellow-gray regions with associated RPE atrophy represent areas of decalcification. Choroidal neovascularization (CNV) can also be observed. It appears as elevated gray-green areas associated with subretinal fluid and subretinal hemorrhage.

4. Diagnosis

A-scan	• The highest intensity echo spike
B-scan	• Slightly elevated choroidal mass remains • Highly reflective even at lower scanning sensitivities (pseudo-optic nerve/ double optic nerve)
FA	• Early patchy hyperfluorescent choroidal filling pattern with late diffuse staining • CNV= leakage
FAF	• Various patterns have been detected depending on the level of decalcification • Lipofuscin accumulation, outer retina and RPE atrophy. • Calcified choroidal osteomas were shown to have relatively well preserved fluorescence on blue-FAF
OCT	• The overlying retina is preserved in architecture over the calcified areas while photoreceptor loss was noted over the decalcified areas.
OCTA	• Fine vascular network within tumor with its absence in some • Dark background where decalcification was present • Presence of a neovascular membrane • A dense irregular vascular network in the outer retinal and choroid capillary layers
MRI	• **T1**: hyperintense signal • **T2**: area of relative low intensity • **T1 C+ Gd**: shows enhancement
CT	Calcific curvilinear regions on the posterior aspect of the globe, usually sparing the optic disc.

FA: Fluorescein angiography, FAF: Fundus autofluorescence, OCT: Optical coherence tomography, OCTA: Optical coherence tomography angiography, MRI: Magnetic resonance imaging, CT: Computerized tomographyDifferential diagnosis includes choroidal metastasis, sclerochoroidal calcifications, amelanotic choroidal melanoma, amelanotic choroidal nevus, choroidal hemangioma, choroidal granuloma (TB, sarcoid), and phthisis (Figs. 7 and 8).

5. Treatment

Asymptomatic or stable choroidal osteoma can be observed. Transpupillary thermotherapy (TTT) has been tried on a limited number of patients but, Photodynamic therapy (PDT), a less RPE dependent form, has had promising results in both extrafoveal and subfoveal CNV. More recently, partially effective anti-VEGF treatments such an intravitreal ranibizumab and bevacizumab have been used.

6. Prognosis

At 10 years, 56–58% of patients have visual acuity less than or equal to 20/200. Long term impaired visual acuity in patients with choroidal osteoma is associated with subretinal fluid, RPE changes, and subretinal hemorrhage from choroidal

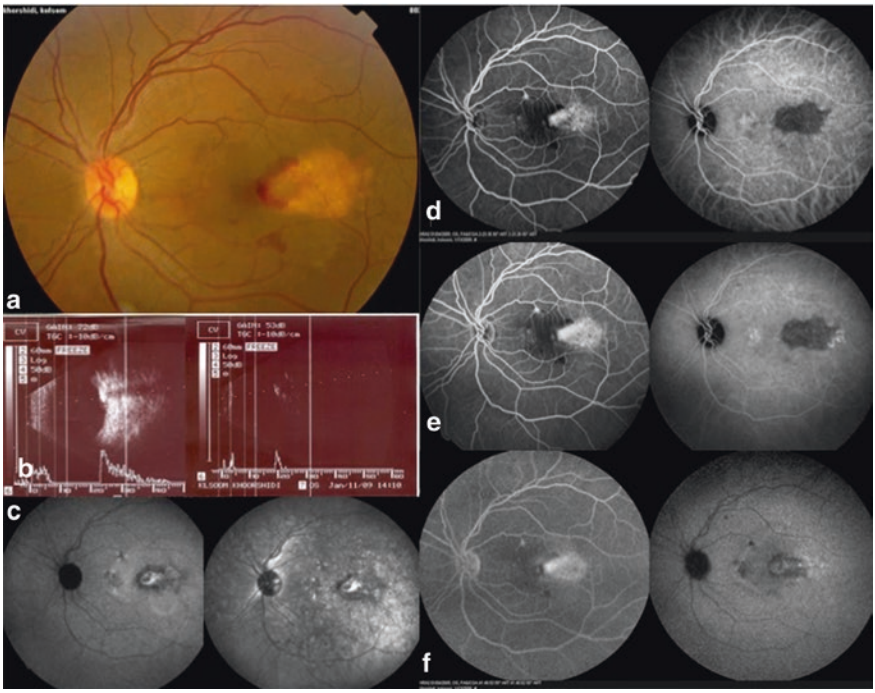

Fig. 7 Choroidal osteoma. **a** Color fundus photography shows a creamy- pink lesion at the temporal part of the macula. **b** B-scan echography shows a solid mass with acoustic shadowing. By lower gain the calcified part is persisted after disappearance of soft tissue signals. A-scan echography shows very high reflectivity. **c** The lesion has low reflectivity in Infrared and is hyper autofluorescent. **d–f** Fluorescein showed higher from early to mid and late phase. In indocyanine angiography hypo-cyanescens is present and persisted throughout the angiography and late hot spot appeared on the lesion

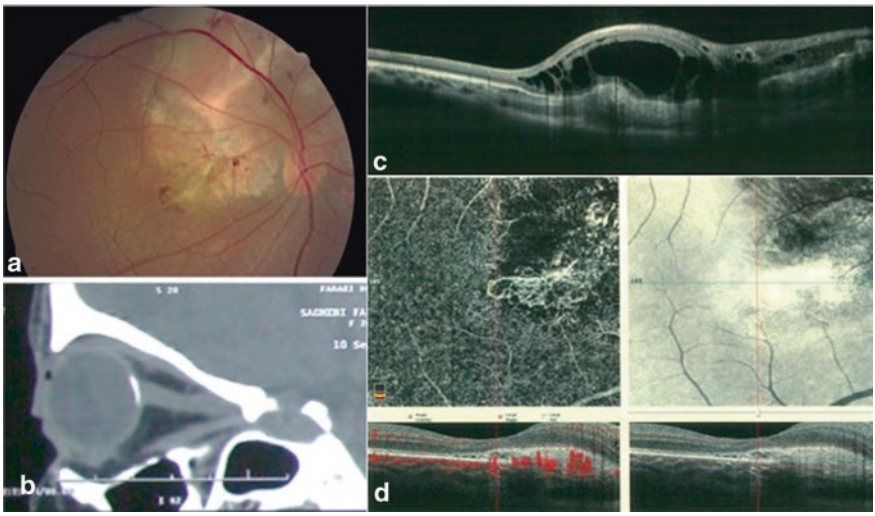

Fig. 8 Choroidal osteoma with neovascularization. **a** Color fundus photography show an orange-red color lesion with mottling. **b** CT scan has been performed for this 50 YO male. It revealed a plaque like highly reflective lesion in the posterior pole of the eye. **c** EDI-OCT shows horizontal lamellar lines, and speckled regions. The standard choroidal vasculature pattern is not visible. The cystic change over the lesion is noted. **d** OCT-angiography reveals a fine vascular network within or over the tumor

neovascularization. Decalcification has also recently emerged as a potential predictive factor for reduced visual acuity.

Suggested Reading

1. Kadrmas EF, Weiter JJ. Choroidal osteoma. Int Ophthalmol Clin. 1997; 37:171–82.
2. Shields CL, Sun H, Demirci H, Shields JA. Factors predictive of tumor growth, tumor decalcification, choroidal neovascularization,and visual outcome in 74 eyes with choroidal osteoma. Arch Ophthalmol. 2005;123:1658–66.
3. Figueira EC, Conway RM, Francis IC. Choroidal osteoma in association with Stargardt's dystrophy. Br J Ophthalmol. 2007;9:978–9.
4. Browning DJ. Choroidal osteoma: Observations from a community setting. Ophthalmology. 2003;110:1327–34.
5. Gass JD. New observations concerning choroidal osteomas. Int Ophthamol. 1979;1:71–84.
6. Song JH, Bae JH, Rho MI, Lee SC. Intravitreal bevacizumab in the management of subretinal fluid associated with choroidal osteoma. Retina. 2010;30: 945–51.

Intraocular Metastasis

1. Introduction

The uvea is the most common site for ocular metastasis. 88% of metastases are in the choroid as the main part of the uvea, , followed by metastases in the iris (9%) and ciliary body (2%). This large difference is thought due to the distribution of blood supply of choroid compared to iris or ciliary body.

2. Incidence

In a review of patients dying from the malignancy, 8% displayed choroidal metastases on autopsy. Lung (40%), gastrointestinal (9%), kidney (8%), and other are the most common primary cancer sites for uveal metastasis in males. For females , breast (68%) lung (12%) and others (4%) were the most common site of primary tumor. In 12% of females, the primary location was unknown at the time of presentation. Breast cancer is the most common cancer to metastasize to the choroid (47% total in men and women combined).

3. Clinical features

Given the site of involvement, most often seen in posterior equator, patients usually have blurred vision (70–81%). The other less common manifestations include flashes and floaters (5–12%), and pain (5–14%). Nontheless, on regular eye exam 9–11% of patients present with no symptoms the lesions may be found. In general, the lesions were located posterior to the equator in 88% of cases.

Choroidal metastases generally appear as a yellow subretinal mass (94%) combined with subretinal fluid (73%). Infrequently, the mass can appear with an orange color, typically with renal cell carcinoma, carcinoid tumor, or thyroid cancer metastases (3%) or brown-gray, usually with metastatic melanoma (3%). The majority of eyes (72%) had one focus, with mean number of tumors per eye being 1.6 (median: 1, range: 1–13).

4. Diagnosis

A-scan	Low to medium to high intensity echo spike, mostly high spike
B-scan	An elevated flat plaque like or rarely dome-shaped
FA	No pathognomonic angiographic sign A hypofluorescent pattern in early arterial phases, with hyperfluoresence in the late venous phases
FAF	Hypoautofluorescence of the tumor with overlying areas of bright 3+ hyperautofluorescence correlating to the deposits of lipofuscin and 2+ hyperautofluorescence of subretinal fluid
ICG	Early: subtle diffuse homogeneous cyanescence of the tumour and a blurred choroidal pattern Mid phase: ill defined isocyanescence without hyperfluorescence Late: in the late frames hypocyanescent overall

OCT (EDI)	Serous retinal detachments around and overlying the tumor, "lumpy bumpy" choroidal surface with compression of the overlying choriocapillaris irregularities of the outer retinal layer
OCTA	Not documented well
MRI	• **T1**: isointense signal • **T2**: hypointensity • **T1 Gd**: shows enhancement
CT	Elevated, hyperdense lesion, which enhance with the administration of contrast

FA: Fluorescein angiography, FAF: Fundus autofluorescence, OCT: Optical coherence tomography, OCTA: Optical coherence tomography angiography, MRI: Magnetic resonance imaging, CT: Computerized tomographyChoroidal metastases differential diagnosis includes choroidal hemangioma, granuloma, choroidal osteoma, choroidal melanoma and sclerochoroidal calcification. Choroidal metastases differ from other choroidal tumors by distinguishing features of ophthalmoscopy and different imaging methods.

Ultrasonography determines the size and echogenicity of the tumor and allows metastasis to be differentiated from other intraocular neoplasms, especially melanomas. Less than 0.5% of choroidal metastases present with a "mushroom" or "collar-button" features. The Mass thickness refers to root of the metastases, the mean breast tumor metastasis thickness is 2 mm, the lung and the prostate 3 mm, and the gastrointestinal and the kidney 4 mm.

FA typically displays a hypofluorescent pattern in early arterial phases, with hyperfluoresence in the late venous phases, later than most choroidal melanomas. Choroidal metastases also contain dilated retinal capillaries with a pinpoint leakage at the tumor border in 73% of cases as compared to melanoma in 16% of cases.

With enhanced depth imaging OCT (EDI-OCT) on patients with choroidal metastases, more than 70%, examiner could find a characteristic "lumpy bumpy" choroidal surface with compression of the overlying choriocapillaris in 93% of cases. In addition, defects in the outer retinal layer can be seen in 80% of cases.

For patients with unidentified primary source and indeterminate diagnostic findings, fine needle aspiration biopsy (FNAB) could be effective test for doing definite diagnosis.

5. Treatment

Systemic chemotherapy, immunotherapy and/or hormone therapy (based on primary tumor diagnosis) are the preferred treatments in patients with bilateral, multifocal choroidal metastases. The presence of fenestrated endothelium in the choriocapillaris allows drugs to penetrate the choroidal lesions.

External beam radiotherapy (EBRT) at a dose of 40–60 Gy induces tumor regression in 85–93% of patients with vision recovery or stabilization in 56% of eyes.

Plaque radiotherapy provides more focused, targeted radiotherapy than EBRT, resulting in good tumor control and fewer ocular complications.

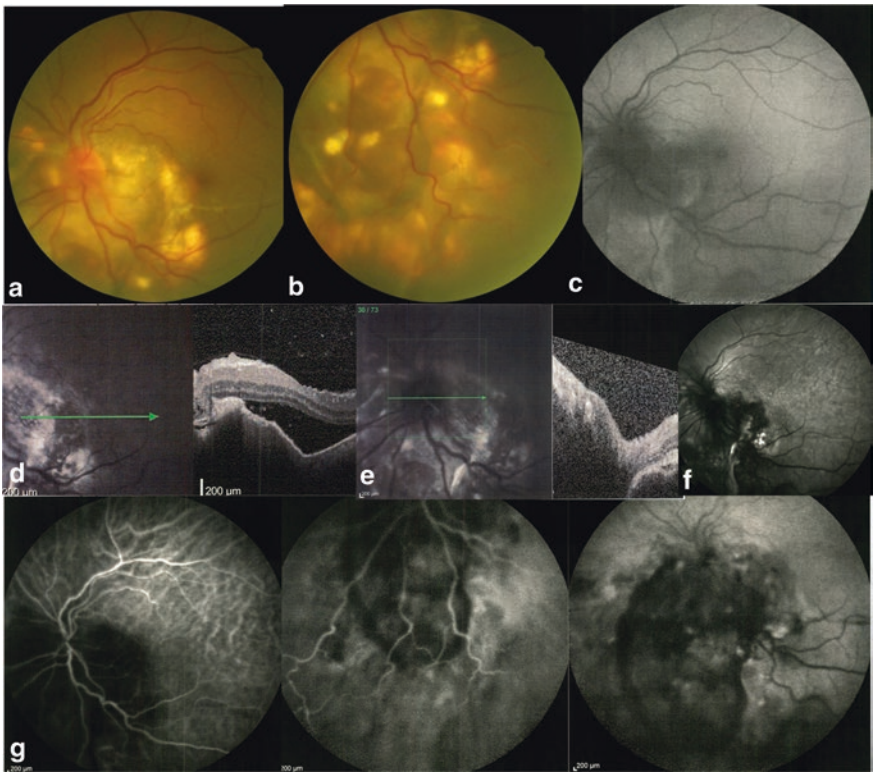

Fig. 9 The image shows a flat tumor originating from lung (small cell carcinoma) cancer with recent onset of chemotherapy (**a**, **b**). Infrared illustrates the heterogeneous hyper and hypo-intense consistency of the tumor. **c** The lumpy bumpy appearance of the choroid and occupied peripapillary choroid with overlying subretinal fluid was shown in OCT (**d**, **e**). Hypo-autofluosence of the entire lesion with pointy hyperautofluorescence at temporal border of the lesion is visible (**f**). Indocyanine green angiography shows the lesion to be hypocyanescent through the early to mid and late phase with small hot spots on it at the later frames (**g**)

Various laser modalities including transpupillary thermotherapy (TTT) and photodynamic therapy (PDT) using diode laser have been widely used with successful outcome for either primary or secondary treatment of choroidal metastases (Fig. 9).

Suggested Reading

1. Shields JA, Shields CL. Intraocular tumors: An atlas and text. 3rd ed. Philadelphia, PA: Lippincott Wolters Kluwer. 2016:45-59.
2. Bloch RS, Gartner S. The incidence of ocular metastatic carcinoma. Arch Ophthalmol. 1971;85:673–5.
3. Shields CL, Shields JA, Gross NE, Schwartz GP, Lally SE. Survey of 520 eyes with uveal metastases. Ophthalmology. 1997;104:1265–76.

4. Arevalo JF, Fernandez CF, Garcia RA. Optical coherence tomography characteristics of choroidal metastasis. Ophthalmology. 2005; 112:1612–9.
5. Ratanatharathorn V, Powers WE, Grimm J, Steverson N, Han I, Ahmad K, et al. Eye metastasis from carcinoma of the breast: Diagnosis, radiation treatment and results. Cancer Treat Rev. 1991;18:261–76.
6. Kaliki S, Shields CL, Al-Dahmash SA, Mashayekhi A, Shields JA. Photodynamic therapy for choroidal metastasis in 8 cases. Ophthalmology. 2012;119:1218–22.
7. Arepalli S, Kaliki S, Shields CL. Choroidal metastasis: origin, features, and therapy. Indian J Ophthalmol. 2015;63(2):122-7.

Childhood Intraocular Tumors

Hamid Riazi Esfahani and Fariba Ghassemi

Retinoblastoma

1. Introduction

Retinoblastoma is the most common intraocular malignancy of childhood; it represents approximately 4% of all pediatric malignancies. Retinoblastoma can occur as a somatic or germline mutation on chromosome 13q14 locus. It can be unilateral or bilateral. The bilateral cases and 10–15% of unilateral cases represent germinal mutations.

2. Incidence

It is estimated that 7,000 new cases of retinoblastoma are diagnosed annually worldwide. The incidence of retinoblastoma is estimated to be about 11 cases per million children younger than 5 years. Based on a study, 250–400 new cases of retinoblastoma are diagnosed in the United States each year. Mortality rate in developed countries is about 5%, in contrast in developing countries the mortality may reach to 50% or more.

3. Clinical features

They usually present with painless leukocoria or strabismus in children less than 5 years of age. In fundoscopy, a small retinoblastoma appears as a subtle, translucent lesion in the sensory retina. Slightly larger tumors lead to dilate retinal blood vessels that feed and drain the mass. Some foci of chalky white calcification may be occurred in larger tumors that may mimic cottage cheese appearance.

The growth patterns of the retinoblastoma are divided into endophytic, and exophytic and diffuse infiltrating types. Endophytic retinoblastoma grows from the retina toward the vitreous cavity and may cause a hazy mass with obscuration of

H. Riazi Esfahani · F. Ghassemi (✉)
Farabi Eye Hospital, Tehran University of Medical Sciences (TUMS), South Kargar Street, Qazvin square, Tehran, Iran
e-mail: fariba.ghassemi@gmail.com

M. Mohammadpour (ed.), *Diagnostics in Ocular Imaging*,
https://doi.org/10.1007/978-3-030-54863-6_23

the retina and retinal blood vessels. It can produce different types of seed in to vitreous cavity. An exophytic retinoblastoma grows from the retina outward into the subretinal space and causes an exudative retinal detachment, sometimes behind crystalline lens. The diffuse retinoblastoma infiltrating the retina and vitreous without a mass formation. It may be accompanied a lot of intraretinal and subretinal seeds.

Based on International Classification of Retinoblastoma, tumors are categorized based on the tumor size and location and also the extent of the seeding as follows:

-Group A—small tumor (s) less than 3 mm in size;
-Group B—tumor(s) more than 3 mm in size or location within 1.5 mm of the optic disc and/or foveola, or with subretinal fluid;
-Group C—tumor(s) with localized subretinal or vitreous seeding;
-Group D—tumor(s) with diffuse subretinal or vitreous seeding;
-Group E—massive tumor(s) filling >50% of the globe or iris neovascularization and/or with vitreous hemorrhage.

Diagnosis

A-scan	High intensity echo spike, higher intensity at the calcification sites
B-scan	An elevated dome-shaped, irregular, acoustically solid mass
FA	Dilated and torturous vessels, microaneurysms, intraretinal microvascular anomalies, and areas of retinal nonperfusion
ICG	Early: spots of hypercyanecence Late: slightly hyperfcyaescent with mottled areas surrounded by a hypofluorescent ring
OCT	intratumoral microcalcification, INL “fish tail” sign, and ONL “shark fin” sign
OCTA	Phase contrast method: Pretreatment: healthy network of blood vessels Post treatment: a dense system of blood vessels with abnormal branching patterns
MRI	• **T1**: mildly hyperintense signal • **T2**: hyperintensity **T1 Gd**: shows moderate to marked enhancement
CT	High density compared with the vitreous body, usually calcified and moderately enhancing after iodinated contrast medium administration

FA: Fluorescein angiography, FAF: Fundus autofluorescence, OCT: Optical coherence tomography, OCTA: Optical coherence tomography angiography, MRI: Magnetic resonance imaging, CT: Computerized tomography

Treatment

Remarkable progress has been achieved over the past decade in the management of retinoblastoma. There are numerous techniques for management of retinoblastoma including enucleation, thermotherapy, radiotherapy (external

beam radiotherapy or plaque radiotherapy) and chemotherapy by intravenous, intra-arterial, and intravitreal routes. Intra-arterial chemotherapy has improved the globe saving chance in eyes with group D retinoblastoma (Figs. 1 and 2).

Astrocytic Hamartoma

These tumors tend to occur in children and are usually asymptomatic. Unlike retinal capillary hemangioma, they have minimal potential for growth and exudation. These intraretinal tumors can appear in the optic disc area or any part of retina. The lesion may be homogeneous or it may contain glistening foci of calcification.

As most of them are non-progressive and asymptomatic, no intervention is necessary, although routine examination is indicated. If there is related serous retinal detachment, then an intervention may be employed. All the patients with astrocytic hamartoma of the retina should be evaluated for the tuberous sclerosis (Figs. 3 and 4).

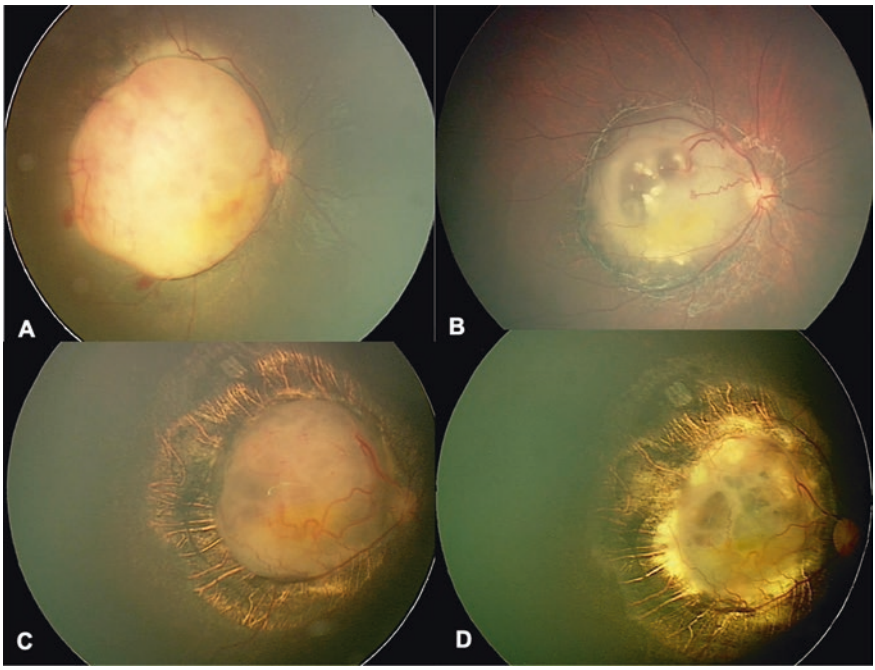

Fig. 1 The figure shows a group C endophytic retinoblastoma tumor in the posterior pole. Its regression pattern (type II) was noted and the regressed mass acquired the cystic and cavernous appearance during the follow up after receiving 3 sessions of intra-arterial chemotherapy

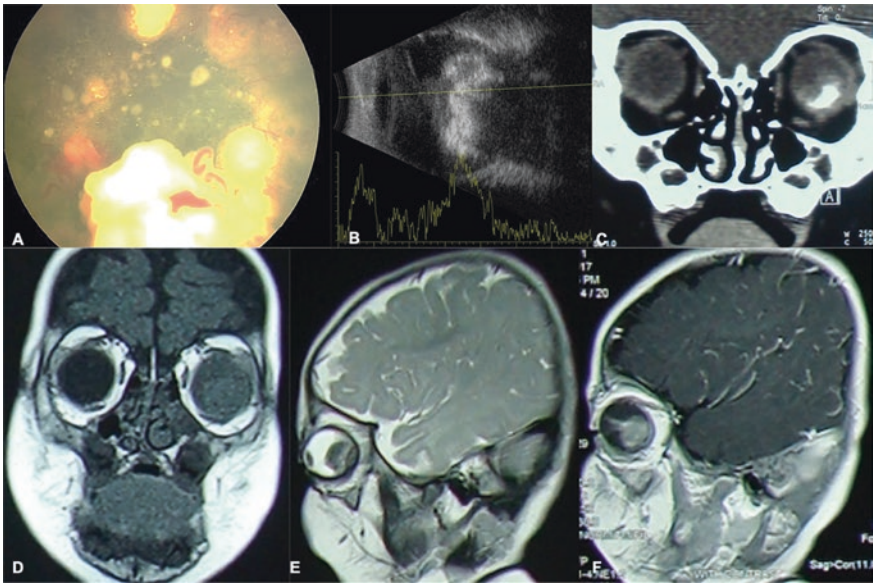

Fig. 2 **a**, **b** Mixed (endophytic and exophytic) large calcified retinoblastoma tumor with severe and extensive vitreous seeds. **c** The computerized scan showed the calcified mass. **d**, **e** Magnetic resonance imaging showed the higher than vitreous reflectivity on T1, lower reflectivity on T2 and enhancing of the lesion after injecting the contrast

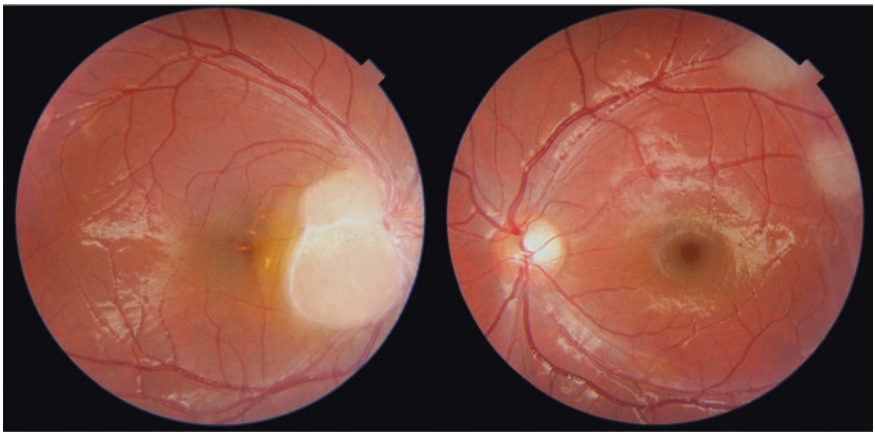

Fig. 3 Color fundus image shows a peripapillary elevated white calcified tumor with two flat and white masses on the superior arcade of the left eye. These appearances corresponds to the astrocytic hamartoma and the patient had no other organ involvement but a few ash leaf on the skin

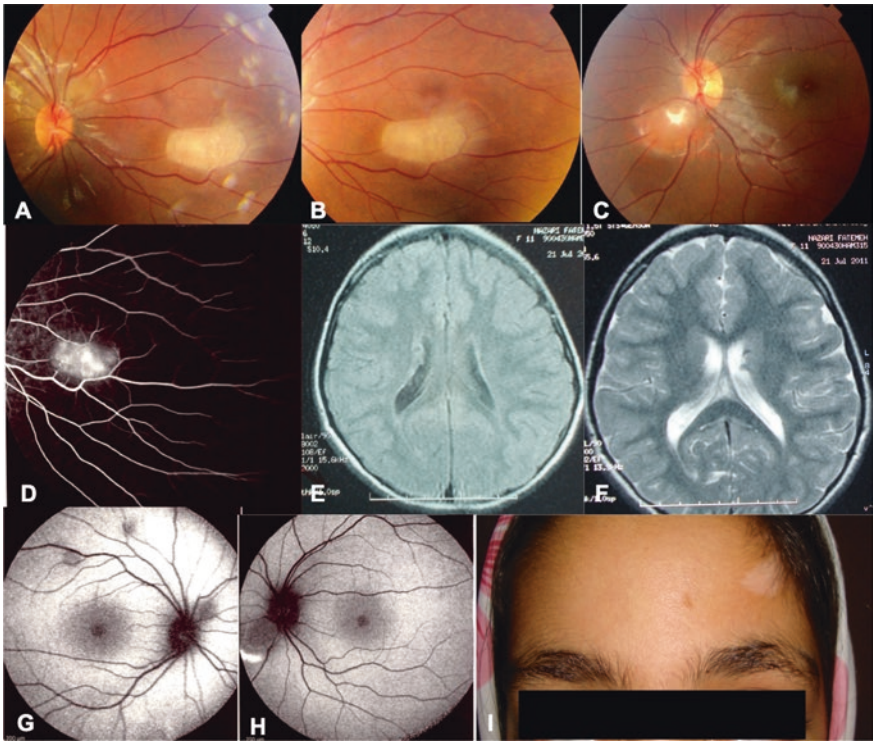

Fig. 4 **a**, **b**, **c** Multiple white slate grey and white preretinal lesions in color fundus images. **d** Fluorescein angiography revealed late leakage . **e**, **f** Brain MRI showed multiple brain astrocytoma. **g**, **h** Hypo-autofluorescent feature of lesions are remarkable. **i** The patient had many ash leaf macules on different parts of the body skin

Combined Hamartoma of the Retina and Retinal Pigment Epithelium (RPE)

This presumed congenital tumor is usually located in peripapillary area but occasionally in the macular region and less commonly in the periphery. The glial and fibrotic component of these tumors causes contraction of the inner retinal surface with some pigmentation.

OCT shows epiretinal membrane (ERM) associated with minor vertical vitreo-retinal traction (mini pick) and prominent vertical vitreo-retinal traction (maxi pick) in a saw tooth or folded pattern. Rarely, retinal exudation or hemorrhage can occur. These lesions can rarely be multiple and can be seen in association with neurofibromatosis type 2.

Medulloepithelioma

This tumor arises from the nonpigmented epithelium of the ciliary body. A small medulloepithelioma in the ciliary body is usually difficult to detect clinically. It can be benign or malignant but usually grows slowly. The distance metastasis is rare. Related features include lens displacement, cataract, neovascularization of the iris, and secondary glaucoma. A larger tumor appears as an amelanotic pink, often cystic, mass.

Retinal Hemangioblastoma

Retinal hemangioblastoma is a vascular hamartoma that usually is diagnosed in the first 2 decades of life. There is a strong association between retinal hemangioblastomas and Von Hippel–Lindau (VHL) syndrome, especially in bilateral or the cases with multiple lesions, and these patients should be evaluated for this condition with brain, spine and also renal imagings.

It appears as a reddish orange mass, randomly located in the fundus, and with dilated and tortuous feeding and draining vessels. Those tumors located beside or on the optic disc might not exhibit a feeding vessel. Regardless of the tumor location, these tumors produce subretinal fluid, subretinal and intraretinal exudation, and vitreoretinal fibrosis that may cause visual loss.

Ultra-wide field fluorescein angiography is the most efficient tool for detection of the subtle retinal hemangioblastoma.This test reveals rapid filling of the mass with fluorescein and usually shows leakage of the dye from the mass into the adjacent retina and vitreous cavity.

Optical coherence tomography (OCT) may represent the full thickness intraretinal tumor with related subretinal or intraretinal fluid and epiretinal membrane.

Retinal hemangioblastoma management consists of both systemic and eye monitoring. All hemangioblastoma lesions should be detected and considered for treatment. Laser photocoagulation, cryotherapy and photodynamic therapy can be used for the management.

Larger tumors usually require plaque radiotherapy or internal resection by pars plana vitrectomy (Fig. 5).

Retinal Racemose Hemangioma

The retinal racemose hemangioma is arteriovenous anastomoses that can occur as a solitary condition or as a manifestation of Wyburn-Mason syndrome as retino-encephalo-facial angiomatosis (Fig. 6). There is no hereditary tendency.

This vascular anomaly is characterized by a dilated, tortuous retinal artery emanating from the optic disc into the retina, with communication directly with

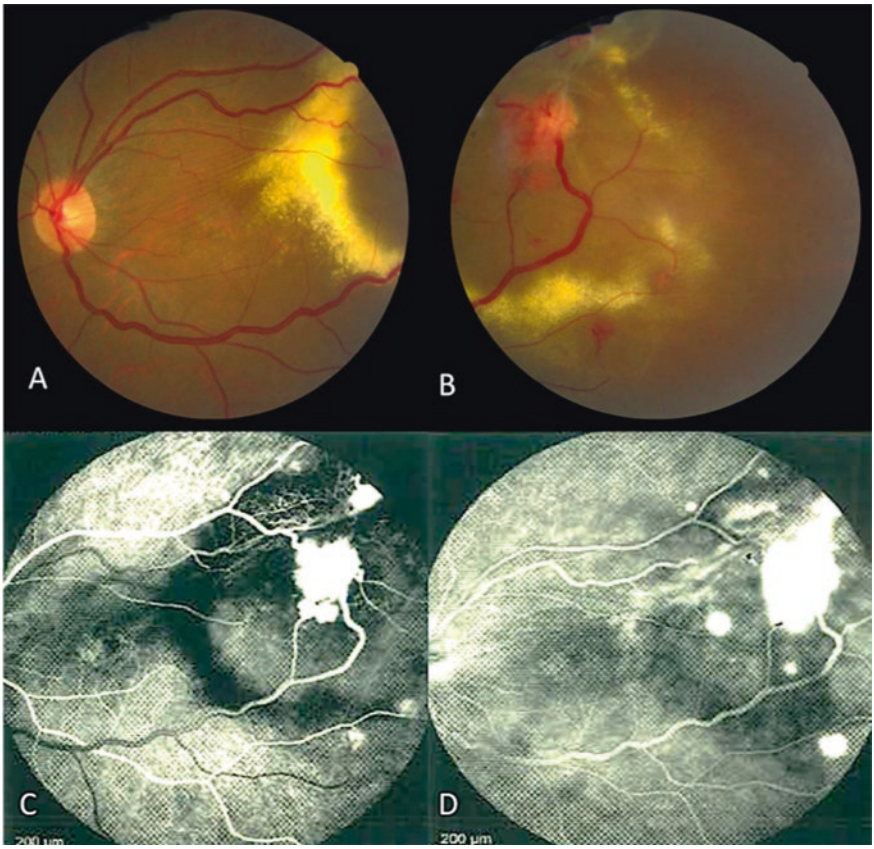

Fig. 5 **a**, **b** color fundus images of a patient with multiple different sized vascular lesions on the retina and hard exudate circinating the lesion with feeding vessels. **c**, **d** Fluorescein angiography illustrates prominent leakage

a dilated retinal vein that leaves the retina back into the optic disc. Retinal exudation or hemorrhages are rare findings unless a branch retinal vein obstruction occurs. This abnormality usually remains stable and treatment is rarely indicated. Although it is recommended that we do brain and facial imaging to rule out probable accompanying lesions.

Retinal Cavernous Hemangioma

This venous-fed vascular hamartoma typically appears as a protruded or sessile intraretinal lesion that is composed of multiple grapes like vascular channels. A grey-white fibrous tissue may be detected on the surface. The retinal exudation is rare.Concomitant intracranial vascular hamartomas may be detected. As a general rule, no active treatment is needed for retinal cavernous hemangioma.

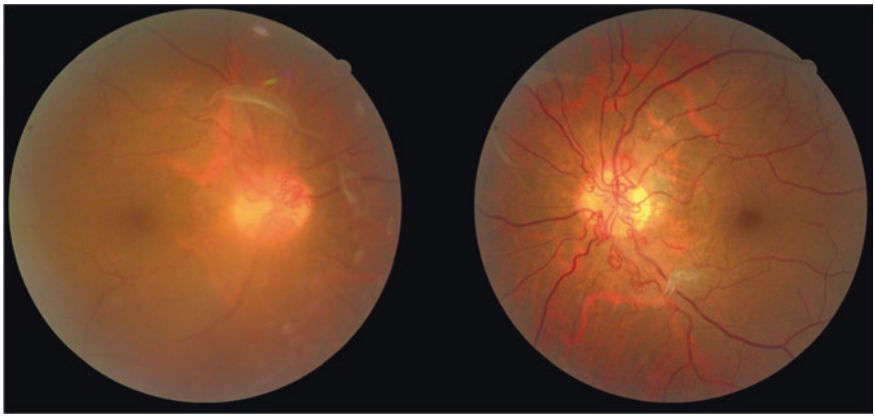

Fig. 6 Color fundus images of a patient with bilateral racemose angioma over the optic disc with hazy media (cataract) in right eye. Preretinal fibrous tissues were visible on the retina of both eyes

If vitreous hemorrhage occurs, ablative treatments to the tumor surface can be attempted. Vitrectomy may be necessary, if vitreous hemorrhage does not resolve.

Suggested Reading

1. Saktanasate J, Vongkulsiri S, Khoo CT. Invisible Retinoblastoma. JAMA Ophthalmol. 2015;133(7):e151123.
2. Park K, Sioufi K, Shields CL. Clinically Invisible Retinoblastoma Recurrence in an Infant. Retin Cases Brief Rep. 2019;13(2):108–10.
3. Rushlow DE, Mol BM, Kennett JY, et al. Characterisation of retinoblastomas without RB1 mutations: genomic, gene expression, and clinical studies. Lancet Oncol. 2013;14(4):327–34.
4. ElZomor H, Taha H, Aleieldin A, et al. High Risk Retinoblastoma: Prevalence and Success of Treatment in Developing Countries. Ophthalmic Genet. 2015;36(3):287–9.
5. Cassoux N, Lumbroso L, Levy-Gabriel C, Aerts I, Doz F, Desjardins L. Retinoblastoma: Update on Current Management. Asia-Pac J Ophthalmol (Philadelphia, Pa). 2017;6(3):290-5.
6. Scelfo C, Francis JH, Khetan V, et al. An international survey of classification and treatment choices for group D retinoblastoma. Int J Ophthalmol. 2017;10(6):961-7.
7. Davila JR, Mruthyunjaya P. Updates in imaging in ocular oncology. F1000 Res. 2019;8.
8. Welch RJ, Rao R, Gordon PS, Say EAT, Shields CL. Optical coherence tomography of small Retinoblastoma. Asia-Pac J Ophthalmol (Philadelphia, Pa). 2018;7(5):301–6.

9. Nadiarnykh O, Davidoiu V, Grafe MGO, Bosscha M, Moll AC, de Boer JF. Phase-based OCT angiography in diagnostic imaging of pediatric retinoblastoma patients: abnormal blood vessels in post-treatment regression patterns. Biomed Opt Express. 2019;10(5):2213–26.
10. Manjandavida FP, Stathopoulos C, Zhang J, Honavar SG, Shields CL. Intra-arterial chemotherapy in retinoblastoma—a paradigm change. Indian J Ophthalmol. 2019;67(6):740–54.
11. Ghassemi F, Shields CL. Intravitreal melphalan for refractory or recurrent vitreous seeding from retinoblastoma. Arch Ophthalmol (Chicago, Ill: 1960). 2012;130(10):1268–71.
12. Pichi F, Massaro D, Serafino M, et al. Retinal astrocytic hamartoma: optical coherence tomography classification and correlation with tuberous sclerosis complex. Retina (Philadelphia, Pa). 2016;36(6):1199–208.
13. Shields CL, Benevides R, Materin MA, Shields JA. Optical coherence tomography of retinal astrocytic hamartoma in 15 cases. Ophthalmology. 2006;113(9):1553–7.
14. Shields CL, Manalac J, Das C, Saktanasate J, Shields JA. Review of spectral domain-enhanced depth imaging optical coherence tomography of tumors of the retina and retinal pigment epithelium in children and adults. Indian J Ophthalmol. 2015;63(2):128–32.
15. Baskaran P, Shukla D, Shah P. Optical coherence tomography and fundus autofluorescence findings in presumed congenital simple retinal pigment epithelium hamartoma. GMS Ophthalmol Cases. 2017;7:Doc27.
16. Tadepalli SH, Shields CL, Shields JA, Honavar SG. Intraocular medulloepithelioma—a review of clinical features, DICER 1 mutation, and management. Indian J Ophthalmol. 2019;67(6):755–62.
17. Berdia J, Johnson BB, Hubbard GB, 3rd. Retinal hemangioblastoma and syrinx in von Hippel-Lindau Disease. Retina (Philadelphia, Pa). 2017;37(3):e29–30.
18. Wong WT, Agron E, Coleman HR, et al. Clinical characterization of retinal capillary hemangioblastomas in a large population of patients with von Hippel-Lindau disease. Ophthalmology. 2008;115(1):181–8.
19. Gorovoy IR, Duncan JL. Retinal hemangioblastoma. JAMA Ophthalmol. 2014;132(3):325.
20. Golas L, Skondra D, Ittiara S, et al. Efficacy of retinal lesion screening in Von Hippel-Lindau Patients with widefield color fundus imaging versus widefield FA. Ophthalmic Surg Lasers Imaging Retina. 2019;50(11):e260–5.
21. Sagar P, Shanmugam PM, Konana VK, Ramanjulu R, Mishra KCD, Simakurthy S. Optical coherence tomography angiography in assessment of response to therapy in retinal capillary hemangioblastoma and diffuse choroidal hemangioma. Indian J Ophthalmol. 2019;67(5):701–3.
22. Barreira AK, Jr., Nakashima AF, Takahashi VK, Marques GA, Minelli T, Santo AM. Retinal racemose hemangioma with focal macular involvement. Retin Cases Brief Rep. 2016;10(1):52–4.

23. Chaudhry R, Riaz A. Racemose Hemangioma of Retina with Vein Occlusion. Journal of the College of Physicians and Surgeons–Pakistan: JCPSP. 2019;29(10):1019–20.
24. Zheng A, Boss J, Rachitskaya AV. Noninvasive Structural Imaging of a Retinal Cavernous Hemangioma Using SS-OCTA and Correlation to Previously Reported Histopathology. Ophthalmic Surg Lasers Imaging Retina. 2019;50(11):e320–3.
25. Materin MA, Shields CL, Marr BP, Demirci H, Shields JA. Retinal racemose hemangioma. Retina (Philadelphia, Pa). 2005;25(7):936–7.

Degenerative Retinal Disorders

Narges Hassanpoor, Fedra Hajizadeh and Nazanin Ebrahimiadib

Pathologic Myopia

One of the most common degenerative retinal disorders is "pathologic myopia " that is defined by an axial length of more than 26.5 mm (high myopia) in the presence of posterior staphyloma. Posterior staphyloma is any related pathology in posterior pole development due to axial elongation. The prevalence of pathologic myopia is increasing and it is the 4th most common etiology of irreversible blindness in developed countries.

The main reasons for best corrected visual acuity loss in these patients are macular schisis, tractional maculopathy, choroidal neovascular membranes, progressive thinning and atrophy of retina and choroid resulting in photoreceptor loss, dome-shaped maculopathy, rhegmatogenous retinal detachment with and without macular hole and myopic optic neuropathy (or glaucoma). We discuss more about some of these complications.

Myopic Macular Schisis

The term "myopic macular schisis" or "myopic foveal schisis" was introduced in 1999 by Takano and Kishi to describe the splitting of the inner retinal layers at the macula in patients with posterior staphyloma. This entity is one of the major

N. Hassanpoor · N. Ebrahimiadib (✉)
Farabi Eye Hospital, Tehran University of Medical Sciences (TUMS), Tehran, Iran
e-mail: nazanin.ebrahimiadib@gmail.com

N. Hassanpoor
e-mail: nargeshassanpoor@gmail.com

F. Hajizadeh
Noor Ophthalmology Research Center, Noor Eye Hospital, Tehran, Iran
e-mail: fedra_hajizadeh@yahoo.com

M. Mohammadpour (ed.), *Diagnostics in Ocular Imaging*,
https://doi.org/10.1007/978-3-030-54863-6_24

causes of visual loss in highly myopic eyes. OCT is the most useful and reliable imaging modality for evaluation of early to advance myopic changes. Myopic foveo-schisis prevalence has been reported as high as 30–40% in 8–26 diopter myopic eyes. It is a slowly progressive condition leading to severe central visual loss in untreated cases. There is a spectrum for myopic macular schisis from mild cases with diffuse tiny cystic changes in outer nuclear layer with minimal effect on visual acuity, to severe ones with splitting of the neural retina into a thin outer layer and a thick inner layer connected by axially oriented fibers (Fig. 1). Their Natural history and visual prognosis are different and in some cases can even lead to lamellar hole, full thickness macular hole or even macular hole associated retinal detachment. There is an international grading system for myopic maculopathy by Ohno-Matsui K et al. in which category 0 is no macular lesion, category 1 is tessellated fundus, category 2 is diffuse chorioretinal atrophy, category 3 is patchy chorioretinal atrophy, category 4 is macular atrophy and plus lesions are lacquer cracks, choroidal neovascularization and fuchs spots.

In mild to moderate cases of myopic macular schisis, no treatment is needed. However, in severe cases with progressive visual loss, vitrectomy with and without ILM peeling and release of tractions can improve both anatomy and function. In some cases, spontaneous resolution of tractions can lead to significant anatomic and functional improvement (see Fig. 1).

Progressive Thinning and Atrophy of Retina and Choroid

Myopia is characterized by elongation of the axial length (AL). Pathologic elongation leads to staphyloma formation and related complications such as lacquer crack and progressive thinning and atrophy of retina and choroid (Fig. 2) Choroidal atrophy results in photoreceptor loss due to interruption of the oxygen and nutrition supply of outer retina by choroid. This eventually induce vision loss in pathologic myopic patients (Figs. 3 and 4).

Posterior Staphyloma

Posterior staphyloma is an outpouching of a circumscribed region of the posterior fundus and has been considered as a hallmark for pathologic myopia. Posterior staphyloma has different subtypes based on shape (wide versus narrow) and location (peripapillary, nasal, inferior, macular). Histologically, it is characterized by an abrupt thinning of sclera, a significant de-arrangement of scleral collagen fibers and a marked choroidal thinning, which is more prominent at the edge of the staphyloma. Another distinct mechanism for choroidal thinning is induced by axial elongation. Wide-field optical coherence tomography can best make the diagnosis of posterior staphyloma (Figs. 5 and 6).

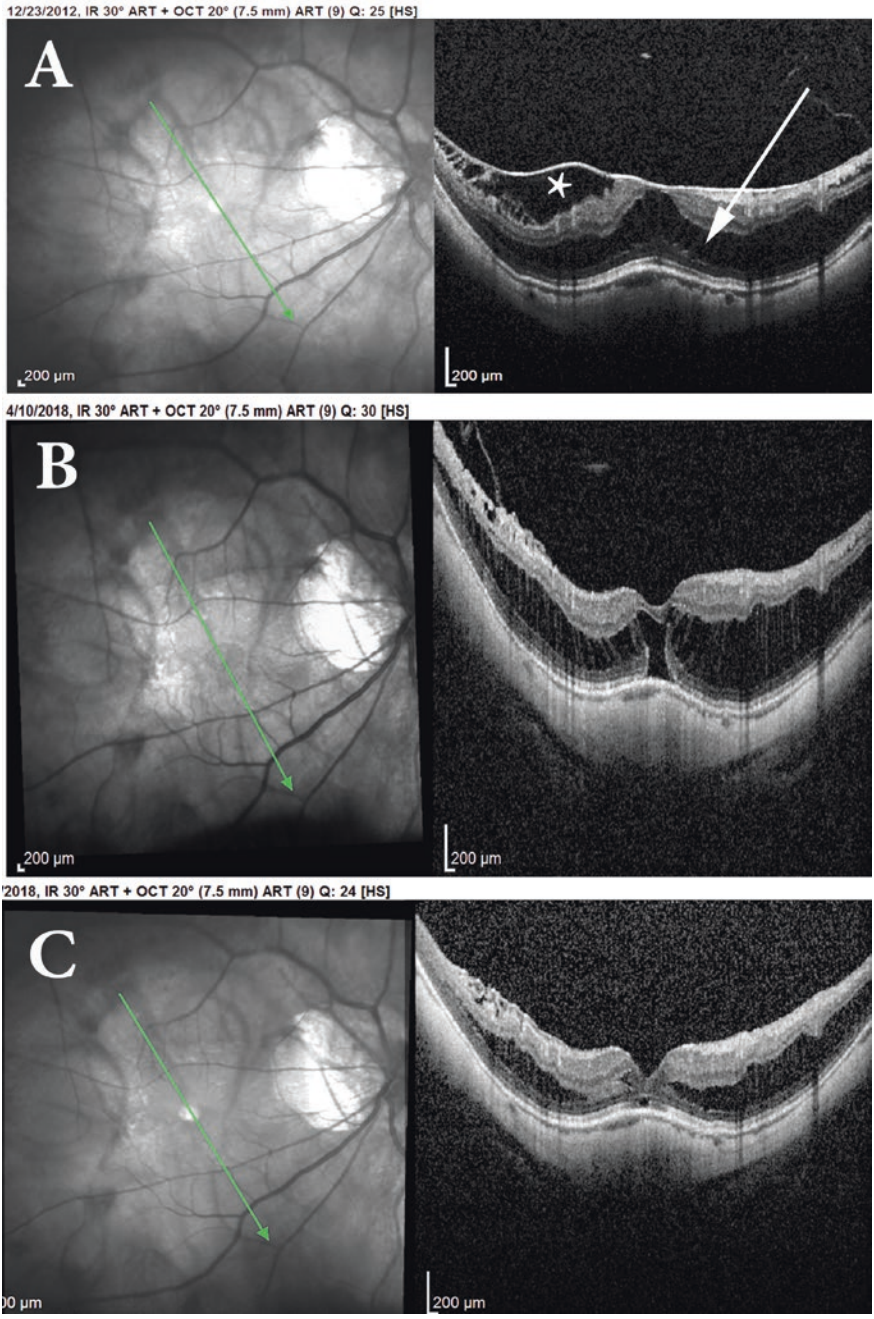

Fig. 1 **a** Compound myopic macular schisis. **a** Schisis in both inner retina (asterisk) and outer retinal layers (arrow). Fine vertical bridges are visible in schisis. **b** Six months and **c** one year follow up reveals spontaneous resolution of tractions and improvement of schisis

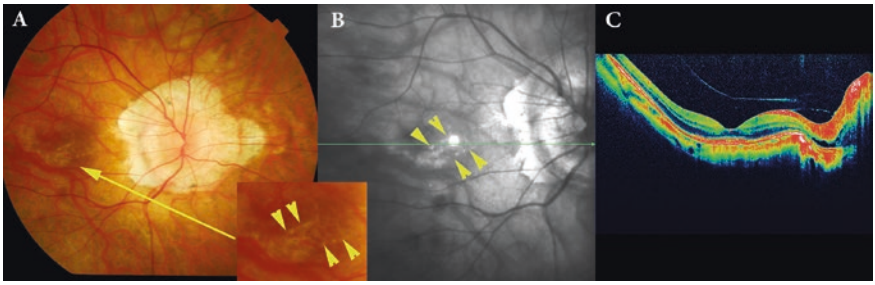

Fig. 2 Pathologic myopia **a** Color fundus photograph. Lacquer crack (yellow arrow) at the inferonasal aspect of fovea (magnified in inset and marked by yellow arrowheads) are notable. **b** SLO image. Lacquer cracks are visible as hyper-reflective lines (yellow arrowheads). **c** OCT does not clearly illustrate the lacquer crack. Thinning with mild RPE irregularity are the only finding in the scan of the lesion

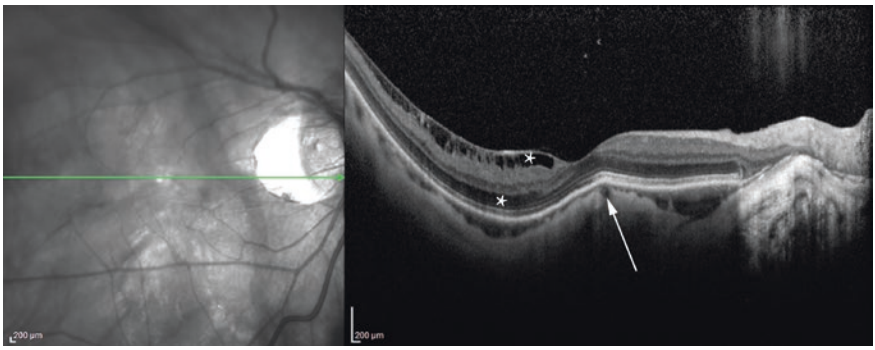

Fig. 3 Compound myopic macular schisis (asterisks) and extreme choroidal thinning in a pathologic myopia patient. In foveal region there is no choroidal tissue. Only one vascular lumen is visible (arrow). Visual acuity is 20/40. There is a moderate photoreceptor layer disruption due to choroidal thinning

Stargardt Disease

Stargardt disease is the most common inherited macular dystrophy that occurs due to the ABCA4 gene mutation and is most commonly inherited in an autosomal recessive pattern. In their fundus examination, the presence of “pisciform” flecks

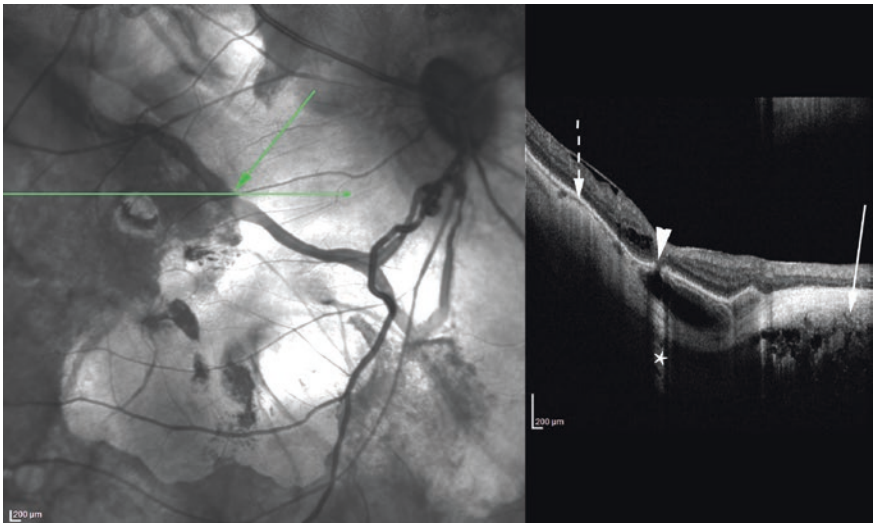

Fig. 4 Pathologic myopia; SLO image at the left side demonstrate a lacquer crack as a hypo-reflective line. OCT line of scan (green arrow) shows a focal loss of RPE and Bruch's membrane (arrowhead) and an increase in the light penetrance into the deeper tissues at the same spot (asterisk) are visible. Ciliary arteries penetrating the choroid in the vicinity of the optic nerve is shown (arrow). Note the extremely thin choroid (dashed arrow) and staphyloma in OCT

or yellow subretinal deposits are characteristic. Flecks may form individual or confluent patterns. Flecks are mostly populated in posterior pole and with time, mid-periphery can be involved with a centrifugal pattern. Peripapillary region is characteristically spared.

OCT shows numerous hyper-reflective deposits at the level of RPE and sub-RPE with diffuse disruption of outer retinal layers and prominent foveal atrophy. Fluorscein angiography (FA) and Fundus Auto-Fluorescence (FAF) can be helpful in diagnosis. FA show characteristic dark choroid choroid in around 80% of patients. FAF highlights flecks and RPE deposits and shows a characteristic pattern of older hypo-auto-fluorescence flecks at the center and newer hyper-auto-fluorescence flecks at the mid-periphery with a centrifugal pattern (Fig. 7).

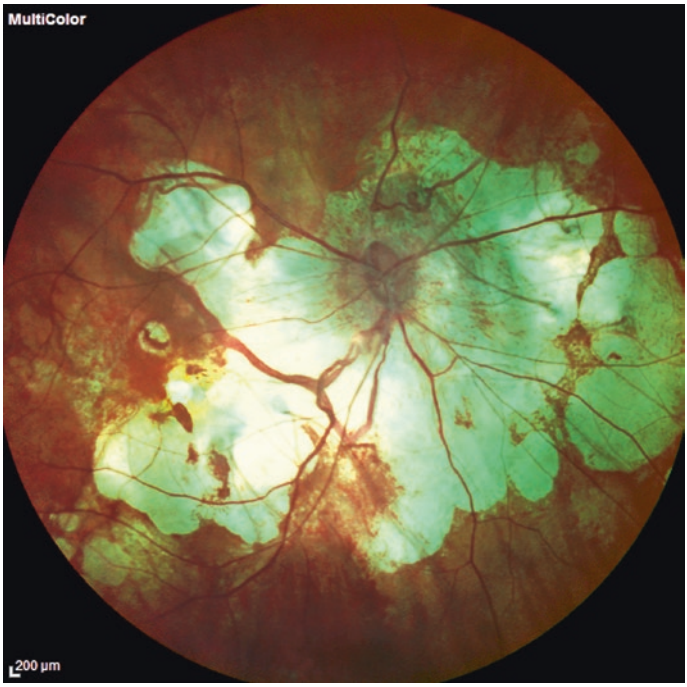

Fig. 5 Posterior staphyloma of peripapillary type in pathologic myopia**;** Color fundus photograph shows a severe patchy chorio-retinal atrophy along with diffuse pigmentary changes

Best Vitelliform Dystrophy

Mutations in the BEST1 gene cause a spectrum of clinical phenotypes known as the bestrophinopathy. They categorized into five groups.

- Best vitelliform macular dystrophy (BVMD)
- Autosomal recessive bestrophinopathy (ARB) disease
- Autosomal Dominant vitreoretinochoroidopathy (ADVIRC)
- Microcornea, rod-cone dystrophy, early-onset cataract, posterior staphyloma (MRCS) syndrome
- Atypical retinitis pigmentosa.

Best vitelliform macular dystrophy (BVMD) is the most common type. Typical stages of the disease include vitelliform, pseudohypopyon, scrambled egg, and atrophic phase. The disease-especially in autosomal recessive type- can be multifocal and asymmetric and this may cause diagnostic dilemma.

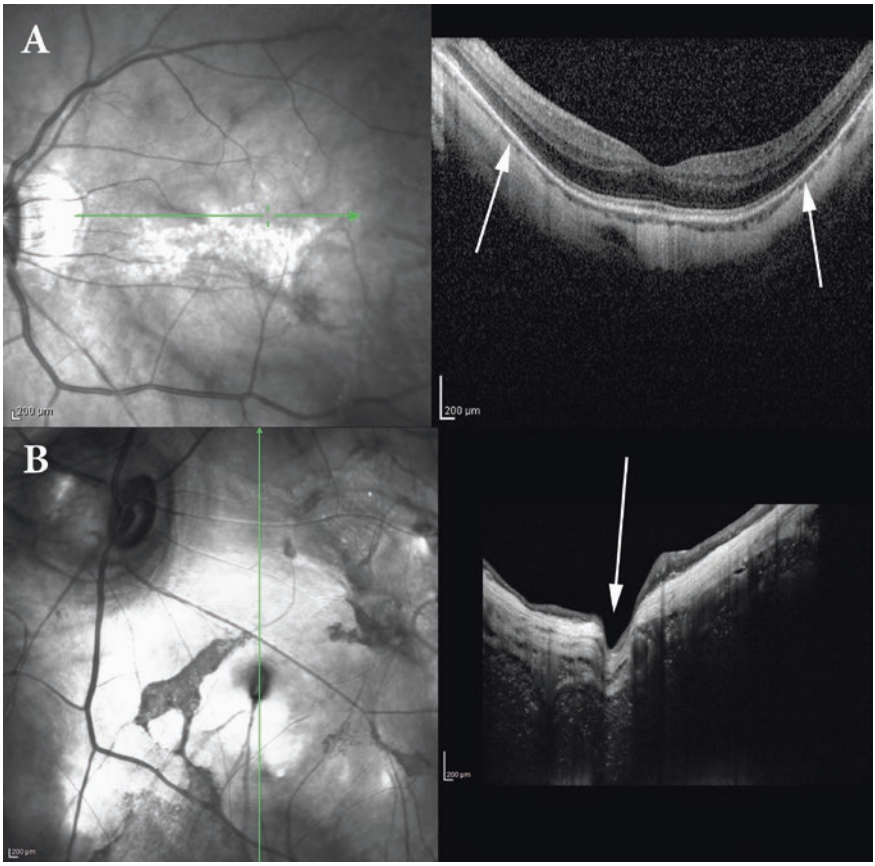

Fig. 6 Posterior staphyloma of peripapillary type in pathologic myopia; **a** OCT shows dramatic posterior bowing of the globe wall that is compatible with wide macular type staphyloma. Choroid is extremely thin. The thinnest part of the choroid is in staphyloma edges (arrows). Mild macular schisis is also visible. **b** a point of outpouching of the eye wall (retina, choroid and sclera) that is more visible in vertical OCT. It may be the site of penetration of globe by ciliary vessels

OCT in vitelliform stage shows a homogenous hyper-reflective material in subretinal space. In pseudohypopyon stage, a homogenous hypo-reflectivity can be seen in subretinal space that should not be mistaken with subretinal fluid secondary to CNV. In cases complicated with CNV, intra-retinal fluid or cystic changes are usually seen in OCT. As staining of the vitelliform material could be mistaken with leakage due to CNV in FA, OCTA is considered the best diagnostic method

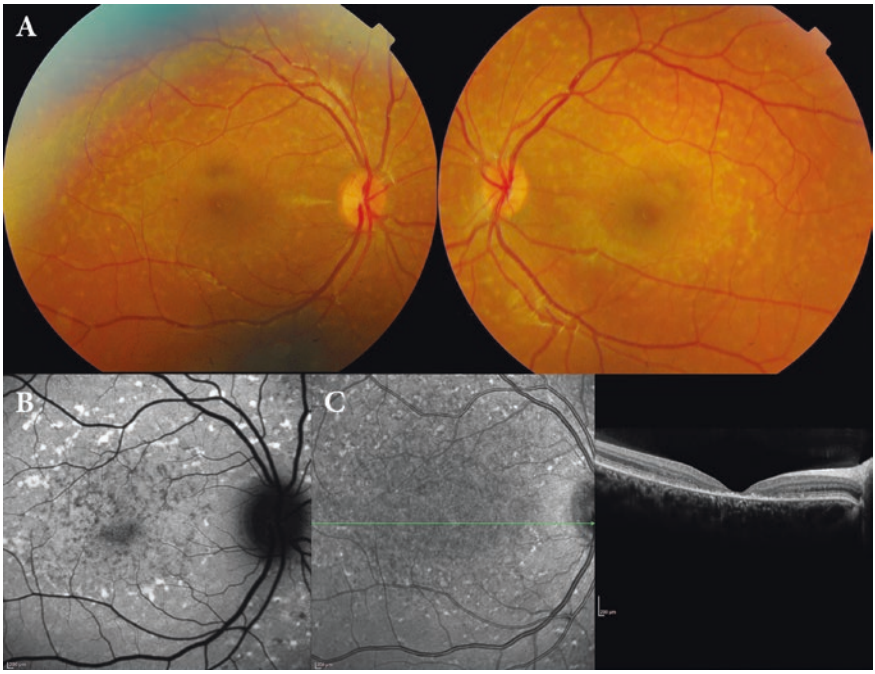

Fig. 7 Stargardt disease **a** Fundus photo shows numerous pisciform flecks in posterior pole with peripapillary sparing. **b** FAF highlights flecks and RPE deposits and shows a characteristic pattern of older hypo-auto-fluorescent flecks at the center and newer hyper- auto-fluorescent flecks at the mid-periphery appear with a centrifugal pattern. **c** SLO-OCT of the patient shows numerous hyper-reflective deposits at the RPE and sub-RPE level and diffuse disruption of outer retinal layers with prominent foveal atrophy

to show CNV in bestrophinopathy patients (Figs. 8 and 9). In advanced stages, Best vitelliform macular dystrophy exhibits central atrophy in OCT.

Fibrotic pillar can be seen occasionally in Best disease and has a dramatic appearance in OCT. It is a fibrotic pillar that develops in the sub-RPE space, usually within 100 μm of the foveal center. These lesions appear hyperreflective on spectral domain OCT and seem to elevate the retina like a circus tent such that they are usually surrounded by a hyporeflective subretinal space in OCT (Fig. 10).

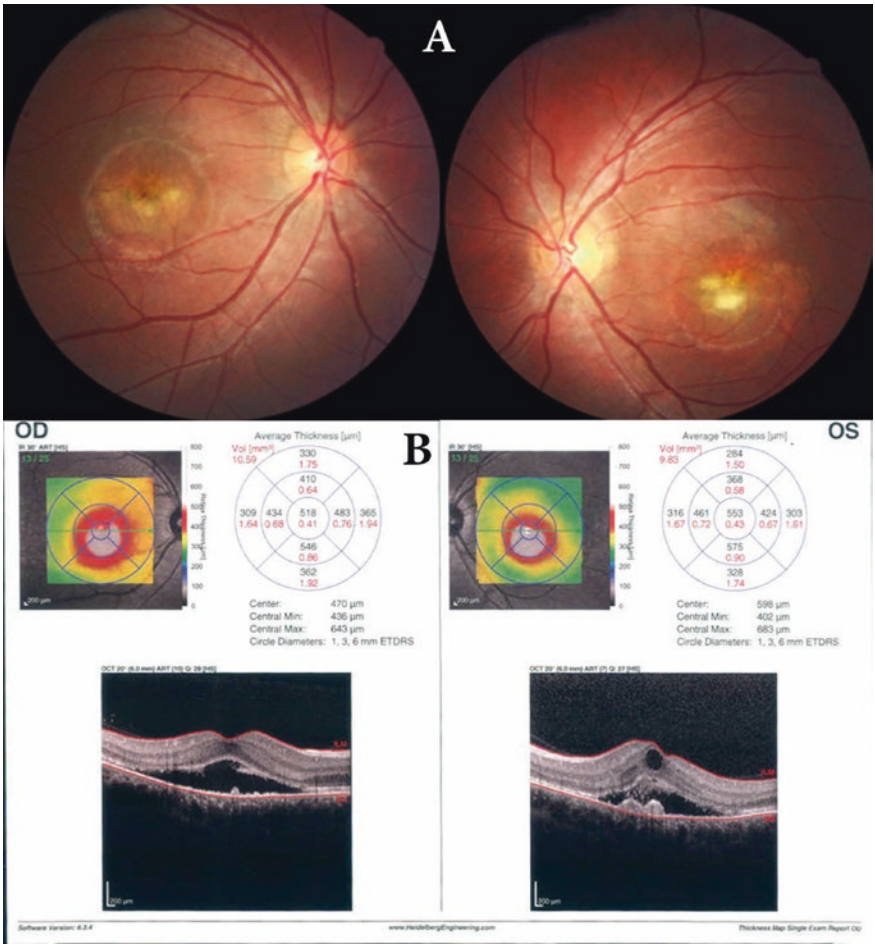

Fig. 8 **a** Fundus photo of the right and left eye. Yellow vitelliform deposition is illustrated in macula of both eyes. **b** OCT of both eyes depict the vitelliform deposition as subretinal hyporeflectivity. Of note is the presence of intraretinal cystic change, in addition to pronounced RPE changes in OCT of the left eye

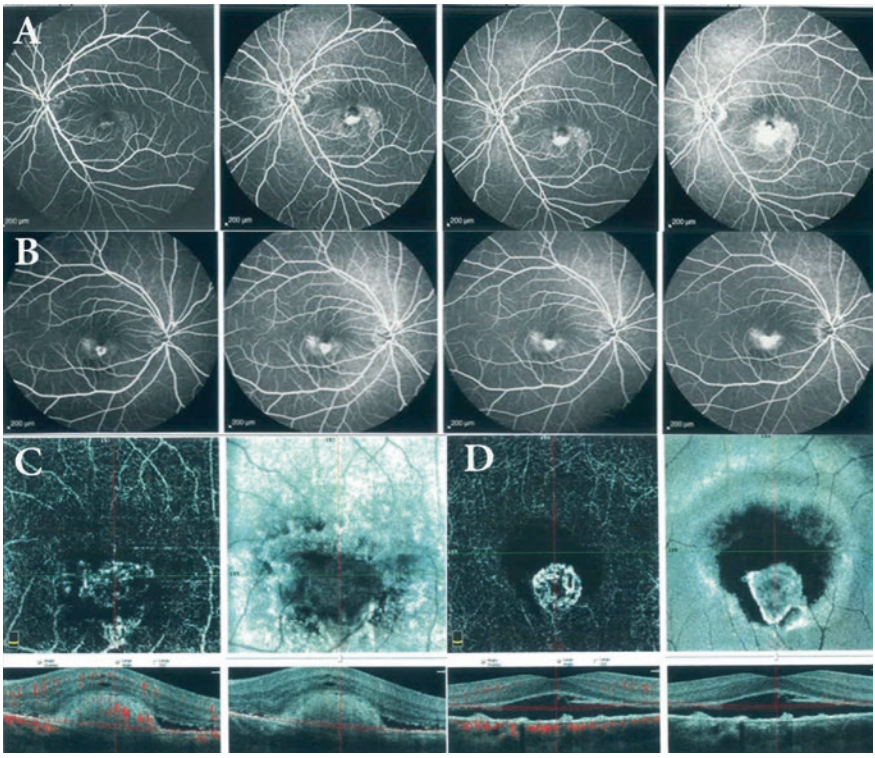

Fig. 9 Best vitelliform macular dystrophy. FA of the left (**a**) and the right (**b**) eye reveals leakage and staining in both eye, more pronounced in the left eye. Of note is that FA is not confirming the presence of CNV in these eyes. **c** and **d** OCTA documents secondary CNV in both eyes

Retinitis Pigmentosa

Retinitis Pigmentosa (RP) is clinically and genetically heterogenous group of inherited retinal disorders that result in loss of rod photoreceptors and therefore disease starts from peripheral retina. Nyctalopia and peripheral vision impairment are the most common symptoms. Central vision impairment can occur due to

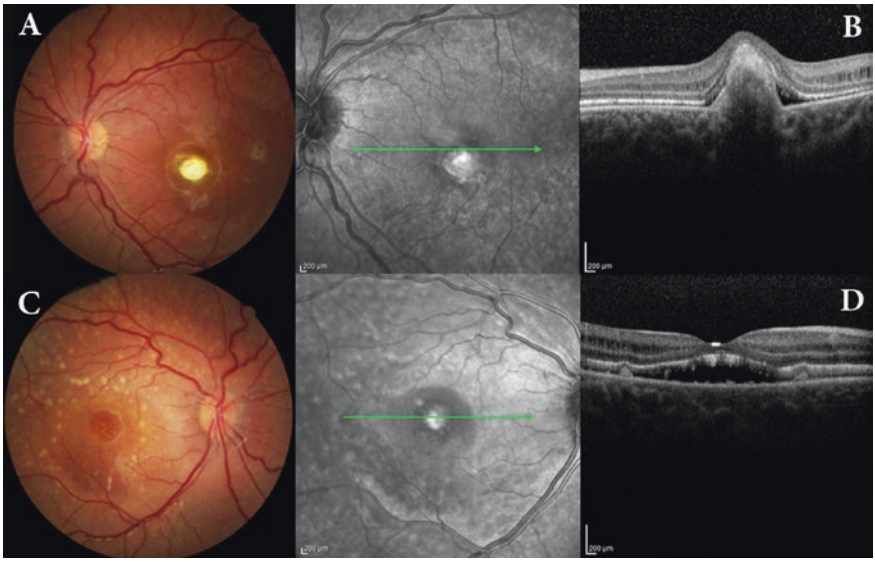

Fig. 10 Best vitelliform dystrophy. **a** Fundus photo of the left eye shows fibrotic pillar appearance in central fovea. **b** SLO and OCT reveals a hyperreflective thumb like lesion that cause a tent like elevation of its overlying retina and is surrounded by a minimal hyporeflective subretinal space. **c** Fundus photo of the right eye reveals multifocal area of vitelliorm deposition extending beyond macula. **d** SLO and OCT shows a hypo-reflectivity in sub-retinal area, compatible with vitelliform material accumulation

cystoid macular edema. This is manageable with topical, periocular, intra-vitreal and systemic treatments.

Other types of inherited disease of photoreceptors include rod-cone and cone-rod dystrophy that has different prognosis and symptoms.

OCT confirms that attenuation of outer retinal layers initiates from peripheral fovea which encroaches fovea in advanced cases. OCT is also helpful to detect cystoid macular edema. RP, in addition to other inherited retinal disorders, can be associated with uveitis and retinal vasculitis. FA is indispensable to search for vasculitis and disc leakage (Figs. 11, 12 and 13).

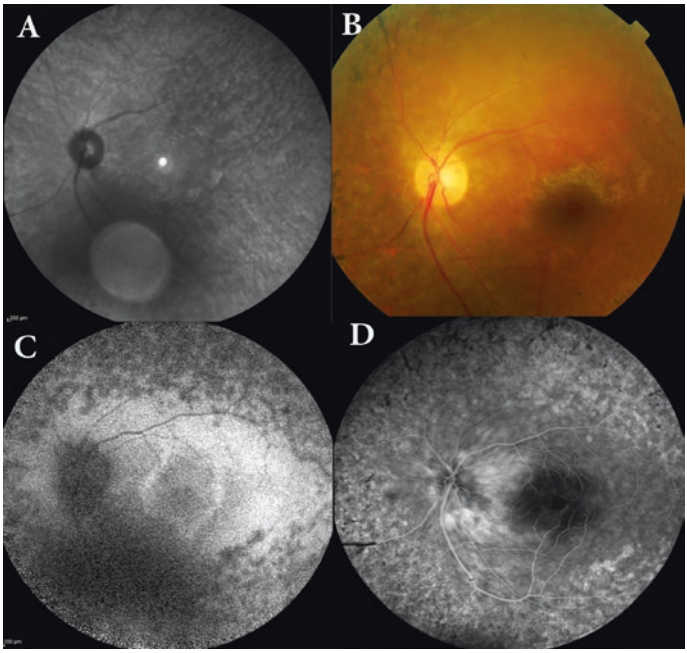

Fig. 11 Advanced retinitis pigmentosa; **a** Infrared image shows faint pigmentary change in peripheral retina. **b** Fundus photo reveals peripheral bone spicules, vascular attenuation and optic nerve head pallor (RP triad). **c** FAF shows a typical parafoveal ring of hyper-auto-fluorescence. A severely decreased FAF are seen at the location of bony spicules. **d** FA shows areas blockage and staining in correspondent areas related to bony spicules. Disc leakage is evident as well

Inherited retinal disorders are slowly progressive and do not have any widely applicable treatment. However, gene therapy for RPE 65 mutation variant and a retinal prosthetic called ARGUS II implant has been shown effective for end stage patients.

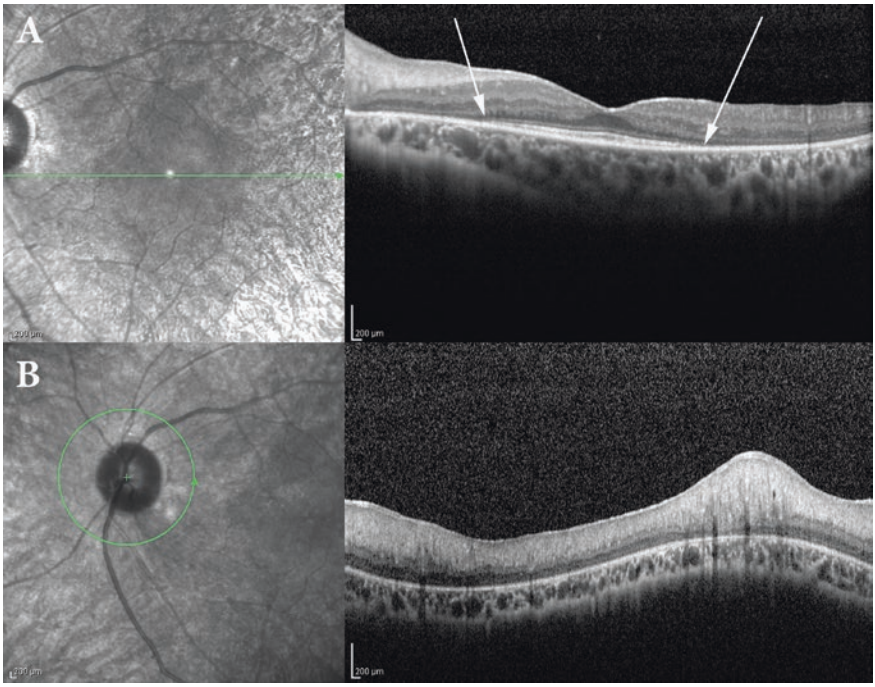

Fig. 12 Retinitis Pigmentosa; **a** OCT, in not very advanced cases disruption of outer retinal layers is evident at para-central macula (arrows) while central macula has preserved and make a flying saucer configuration. **b** RNFL OCT shows a marked amorphous thickening of optic nerve head that is characteristic in an RP patient and could be differentiated from inflammatory eye disease. Optic nerve head leakage in FA of the left eye was evident in Fig. 11

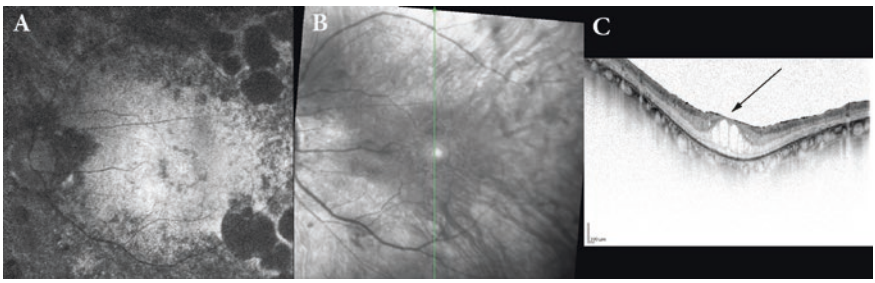

Fig. 13 Retinitis Pigmentosa; **a** Fundus autofluorecence shows area of patchy atrophy with relative preservation of macula. **b** SLO shows the line of OCT scanning **c** OCT illustrates cystoid macular edema (arrow). Note that despite the cystoid macular edema formation, the outer retinal layers are relatively preserved in central macular area but are markedly attenuated in para-central area

Suggested Readings

1. Ohno-Matsui K. Pathologic Myopia. Asia Pac J Ophthalmol (Phila). 2016 Nov/Dec;5(6):415–23.
2. Ruiz-Medrano J, Montero JA, Flores-Moreno I, Arias L, García-Layana A, Ruiz-Moreno JM. Myopic maculopathy: Current status and proposal for a new classification and grading system (ATN). Prog Retin Eye Res. 2019;69:80–115. https://doi.org/10.1016/j.preteyeres.2018.10.005 (Epub 2018 Nov 1).
3. Gohil R, Sivaprasad S, Han LT, Mathew R, Kiousis G, Yang Y. Myopic foveoschisis: a clinical review. Eye (Lond). 2015;29(5):593–601. https://doi.org/10.1038/eye.2014.311.
4. Ikuno Y, Fujimoto S, Jo Y, Asai T, Nishida K. Choroidal thinning in high myopia measured by optical coherence tomography. Clin Ophthalmol. 2013;7:889–93. https://doi.org/10.2147/OPTH.S44138.
5. Ohno-Matsui K, Jonas JB. Posterior staphyloma in pathologic myopia. Prog Retin Eye Res. 2019;70:99–109. https://doi.org/10.1016/j.preteyeres.2018.12.001 (Epub 2018 Dec 8).
6. Ohno-Matsui K, Kawasaki R, Jonas JB, et al. International photographic classification and grading system for myopic maculopathy. Am J Ophthalmol. 2015;159(5):877-83.e7. https://doi.org/10.1016/j.ajo.2015.01.022 (Epub 2015 Jan 26).

Glaucoma Imaging

OCT and Glaucoma: Interpretation

Sasan Moghimi, Mona SafiZadeh, Andrew Camp and Robert N. Weinreb

Introduction

The introduction of optical coherence tomography (OCT) into clinical practice in the 1990s has allowed a significant advance in glaucomatous structural assessment. OCT can help clinicians with both the diagnosis and monitoring of glaucoma. It utilizes a near-infrared superluminescent diode light in a fashion similar to the way B-mode ultrasound uses sound to generate two-dimensional images. OCT continues to evolve rapidly, providing clinicians with more detailed qualitative and quantitative information of both superficial and deep structures of the eye. In 2006, the first commercially available spectral-domain OCT (SDOCT) system was introduced. SDOCT employs detection of the light echoes simultaneously by measuring the interference spectrum, using an interferometer with a high-speed spectrometer [1]. Currently the most popular systems in OCT are Cirrus HD-OCT (Carl Zeiss Meditec (Dublin, CA)), Spectralis SDOCT (Heidelberg Engineering GmbH, Heidelberg, Germany), Optovue Inc. (Fremont, CA), and DRI OCT Triton (Topcon Medical Systems (Oakland, NJ)). Specifications of each instrument is out of the scope of this chapter. However, we included interpretations of printouts from each device in this chapter and give more details during case studies in chapter "OCT and Glaucoma: Case Review".

Figure 1 demonstrates the timeline of changes in glaucomatous eyes demonstrating disease progression. RNFL loss is the first sign of structural damage in preperimetric glaucoma and is followed or accompanied by optic nerve head (ONH) changes. Visual field (VF) changes start to appear as the disease progresses

S. Moghimi (✉) · A. Camp · R. N. Weinreb
Department of Ophthalmology, Hamilton Glaucoma Center, Shiley Eye Institute, University of California, San Diego, CA, US
e-mail: sasanimii@yahoo.com

M. SafiZadeh
Tehran University of Medical Sciences, Tehran, Iran

M. Mohammadpour (ed.), *Diagnostics in Ocular Imaging*,
https://doi.org/10.1007/978-3-030-54863-6_25

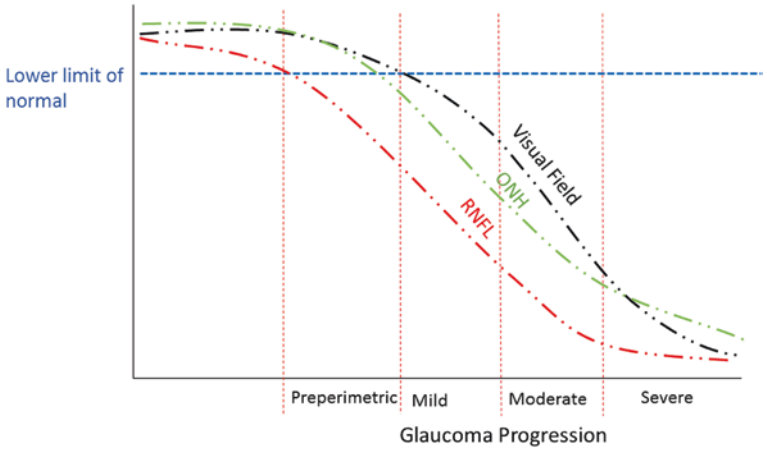

Fig. 1 Timeline of structural and functional progression in glaucoma

to the perimetric stage. Monitoring advanced glaucoma with OCT is difficult as most structural parameters reach their minimum value around -12 dB of VF loss, and beyond that there is little change in RNFL while the disease progresses [2, 3].

OCT was first used to obtain reproducible measures of the **circumpapillary retinal nerve fiber layer (RNFL) thickness** [4, 5]. Reliable **Ganglion Cell Analysis** became possible with the higher resolution and denser sampling capabilities of spectral domain OCT. SDOCT also allowed imaging **ONH anatomic features** with great precision and led to the development of novel measurements such as Bruch's membrane opening (BMO) and minimum rim width (MRW) [6].

RNFL Analysis

RNFL thickness measurements are the most widely studied of the three parameters that can be evaluated with OCT. OCT devices provide a three-dimensional map of the RNFL around the ONH (Cirrus, Optovue, DRI Triton) and/or measure the peripapillary RNFL thickness on a 3.46 mm scan circle centered on the ONH or BMO. A recent protocol from Heidelberg Spectralis OCT enables the measurement of two additional scan circles with 4.1 mm and 4.7 mm diameters. The 3.46 mm scan is most sensitive to glaucomatous changes but the larger scan diameters are helpful in cases of severe peripapillary atrophy (PPA).

Studies have shown RNFL change can be detected by OCT in glaucomatous patients before any change in visual field [7]. OCT has become the preferred technique for RNFL analysis in eyes with suspected or established glaucoma since it became available.

ONH Analysis

All OCT devices scan the ONH area and provide some information about ONH morphology. More recent SDOCT imaging studies challenge the importance of the clinical disc margin in glaucoma management and have considered BMO a better landmark for neuroretinal rim measurements. The BMO margin is a stable landmark that can be easily found in OCT images and corresponds to the anatomical border of neural tissue [6]. ONH parameters are very useful for differentiating glaucomatous and non-glaucomatous optic neuropathies, but their superiority to RNFL measurements for diagnosis of early glaucoma is still controversial.

Macular Ganglion Cell Analysis

The death of retinal ganglion cells (RGCs) is pathognomonic of glaucoma. RGC loss in the macula could be a sign of early glaucomatous damage because about 35% of total retinal thickness in the macula is constituted of these cells [8, 9]. Time-domain OCT was able to measure total macular retinal thickness but because of low resolution and poor sampling density the segmentation of the inner retina was not reliable. The diagnostic power of the macula thickness parameter was lower than the RNFL parameter for glaucoma diagnosis due to the poor resolution [10, 11]. However, performing macula OCT imaging is easier than ONH imaging because the optical axis of the eye is naturally aligned to the fovea, which allows easier gaze fixation. The macular area is also less affected by anatomical variations compared to ONH and RNFL parameters. There continued to be interest in improving measurement of macular thickness parameters because of these factors.

The difficulty in the segmentation of macular layers was resolved with the higher resolution and denser sampling of SDOCT. Two segmentation algorithms were developed for the assessment of glaucoma in the macular region by SDOCT: Ganglion Cell Complex (GCC) and Ganglion Cell Inner Plexiform Layer (GCIPL). The segmentation of just the macular ganglion cell layer is not practical because of its low reflectivity. GCC refers to the segmentation of a combination of the three innermost layers of the retina: the RNFL, ganglion cell layer, and inner plexiform layer (IPL). These layers contain the axons, cell bodies, and dendrites of ganglion cells and are preferentially affected by glaucoma. Isolating these layers from the outer retina increases the diagnostic power of macular assessment and improves reproducibility compared to RNFL assessment [12]. Evaluating the macula is also helpful in advanced glaucoma and eyes with high myopia [35]. GCIPL refers to the segmentation of just the ganglion cell layer and IPL. The GCIPL thickness measurement performs as well as RNFL measurement in detection of early glaucoma [13].

GCC and GCIPL analysis can be limited by signal quality, image artifact, and errors in the software segmentation algorithm. In addition, any coexisting macular pathology like age-related macular degeneration (ARMD), macular edema, and epiretinal membrane can affect the macular analysis.

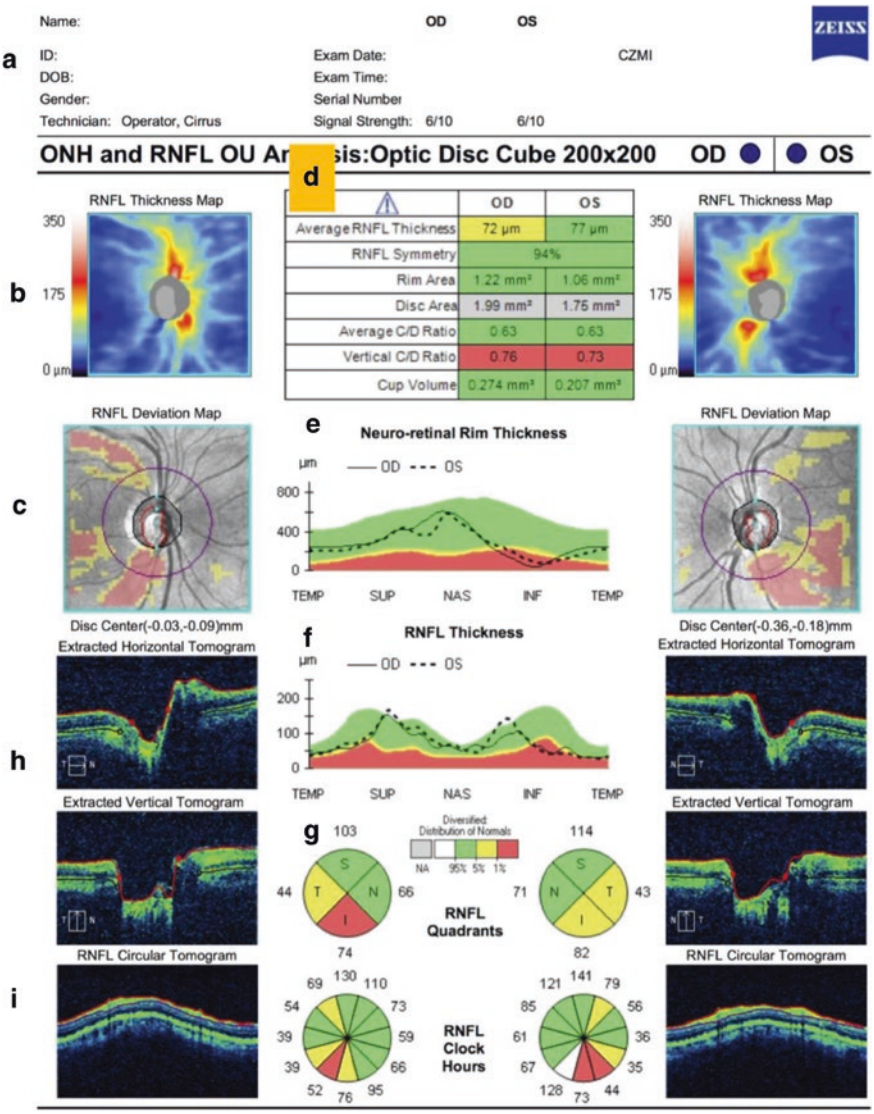

Fig. 2 Cirrus HD-OCT's ONH and RNFL OU Analysis printout of a glaucomatous patient. Sections of the printout are explained in the text. RNFL thinning can be seen in the supratemporal and inferotemporal region of both eyes in the Thickness map (**b**), Deviation map (**c**), RNFL TSNIT plot (**f**), and RNFL Quadrant and RNFL Clock-Hour Thickness (**g**), with the damage more severely affected the inferotemporal region. Note that the Neuro-Retinal Rim Thickness Profile is only affected in the inferior region

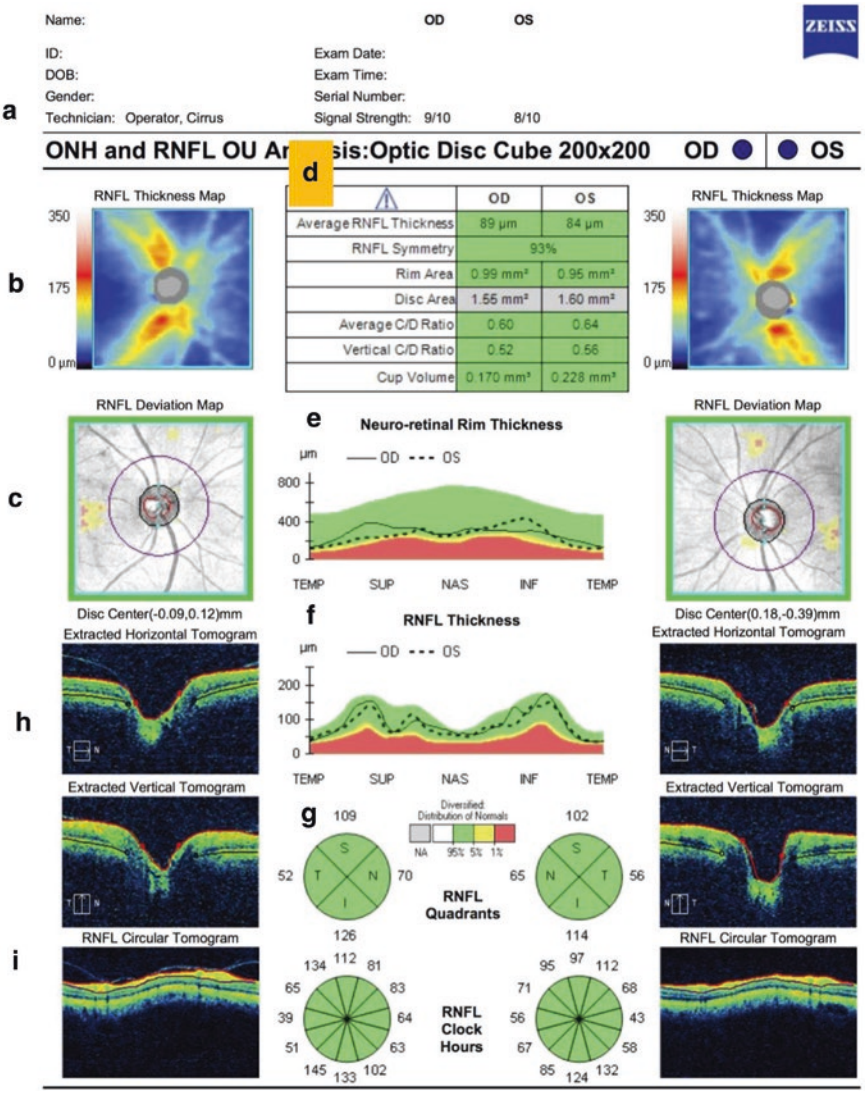

Fig. 3 Cirrus HD-OCT's ONH and RNFL OU Analysis printout of a normal patient. Sections of the printout are explained in the text. Note the hourglass shape or bow-tie shape of the normal RNFL in Thickness map (**b**) and normal double-hump shape of RNFL in TSNIT plot (**f**)

In this section the printouts from most popular OCT devices are explained. Clinicians should review the imaging printouts systematically as small details could be important for the final decision and artifacts or anatomical variations can lead to misdiagnosis. These artifacts will be discussed in detail in the chapter "Confocal Scanning Laser Ophthalmoscopy and Glaucoma".

Cirrus HD-OCT

The new generations of SDOCT have improved sensitivity in detecting structural changes in RNFL and ONH morphology achieving a resolution of 2 μm. Cirrus HD-OCT scans a 6 × 6 mm area comprised of 200 horizontal scans each consisting of 200 A-scans resulting in a three-dimensional RNFL thickness map with a resolution of 200 × 200 A-scans. It gives us both RNFL thickness map and circumpapillary RNFL circle measurements. Thickness map provides additional spatial and morphologic information and improved sensitivity of the circular measurements [14]. Cirrus OCT enable registration of the optic nerve through BMO, and thus reducing the test–retest variability. This is especially helpful when monitoring the patients using this device.

(a) Cirrus ONH and RNFL Printout

Figures 2 and 3 shows the most common printout of the Cirrus' HD-OCT machine for clinicians. Both ONH and peripapillary RNFL are provided in a single printout. Color codes are used for comparison of thickness values and the RNFL deviation map (except thickness map) to age-matched controls. Measurements in red are considered outside normal limits (<1 percentile). Measurements in yellow are considered borderline (1–5 percentile). 90% of measurements fall in the green area (5–95 percentile) and the thickest 5 percent of measurements fall in the white area (white > 95 percentile) (Fig. 4).

The following information must be checked when a printout is read: (Figs. 2 and 3).

1-Patient information and Signal Strength. Signal strength < 6 should be repeated. Hazy media, due to dense cataracts or dry eyes, or inability to fixate properly can decrease signal strength (Fig. 2a).

2-Topographic map of RNFL thickness (RNFL Thickness map). The thickness values measured throughout the ONH Cube are displayed using a color code. Cold colors (blue, green) represent thinner RNFL and warm colors (yellow, red) represent regions with thicker RNFL (Fig. 2b). This is in contrast to all other areas of color coding on the printout where yellow and red represent thinner measurements. Normally the topographic thickness resembles a vertical bow-tie as the superior and inferior RNFL is thicker than other regions (Fig. 3b). Cirrus OCT displays areas that cannot be scanned (due to blink artifact, posterior vitreous

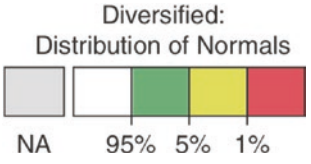

Fig. 4 Color codes used in the Cirrus HD-OCT for comparison to age-matched controls

detachment) in black. Black areas on the RNFL map can significantly affect the results of RNFL analysis data, especially when the areas fall within the measurement circle (see chapter "Confocal Scanning Laser Ophthalmoscopy and Glaucoma", Fig. 12).

3-RNFL Deviation Map. Compares the data from the ONH cube of the patient with age-matched controls and overlays the information on a black and white en face OCT image. No overlay color code is used for areas of normal thickness. Areas displaying an RNFL thickness thinner than 1 percentile and 5 percentile of the normative database are flagged in red or yellow, respectively (Fig. 2c).

4-Tabular data. RNFL and ONH parameter measurements including disc area, rim area, cup volume, cup/disc ratio, and others are presented with color codes indicating if the value is outside normal limits (Fig. 2d).

5-Neuro-Retinal Rim Thickness Profile (TSNIT plot). The Neuro-Retinal Rim Thickness is measured between the Bruch's membrane opening (BMO) (black circle on RNFL deviation map) and the border of the optic cup (red circle on RNFL deviation map) and compared with age- and disc-size-matched data from the normative database (Fig. 2e).

6-RNFL Thickness profile (TSNIT plot). The measurements from a 3.46 mm diameter calculation circle centered on the BMO are used for the TSNIT plot (Fig. 2f). A typical double hump configuration for the RNFL distribution is observed in normal eyes (Fig. 3f). The thickness values are compared with age- and disc-size-matched data of the normative database (color-coded area). This is one the best plots for detection of focal RNFL thinning and is more sensitive than RNFL quadrant and RNFL clock-hour thickness measurements for detection of early glaucoma. This region of interest (ROI) approach has been shown to be helpful for detecting and monitoring glaucoma [15].

7-RNFL Quadrant and RNFL Clock-Hour Thickness. Presents the average RNFL thickness in each quadrant or clock-hour (Fig. 2g).

8-Vertical and Horizontal Tomograms. Shows the vertical and horizontal scans and the segmentation used for ONH analysis (Fig. 2h).

9-RNFL Circular Tomogram. This includes an OCT image and segmentation of the calculation circle (Fig. 2i). The tomogram should be check by the reviewer for artifacts, segmentation errors, and retinal diseases or vitreo-retinal interface problems (as described in chapter "Confocal Scanning Laser Ophthalmoscopy and Glaucoma").

(b) Macula Ganglion Cell OU Analysis Printout

The macula region scan from Cirrus HD-OCT generates a 6×6 mm macular cube centered on the fovea and coded in colors similar to the ONH and RNFL analysis (Fig. 5). The following sections should be reviewed by the reader:

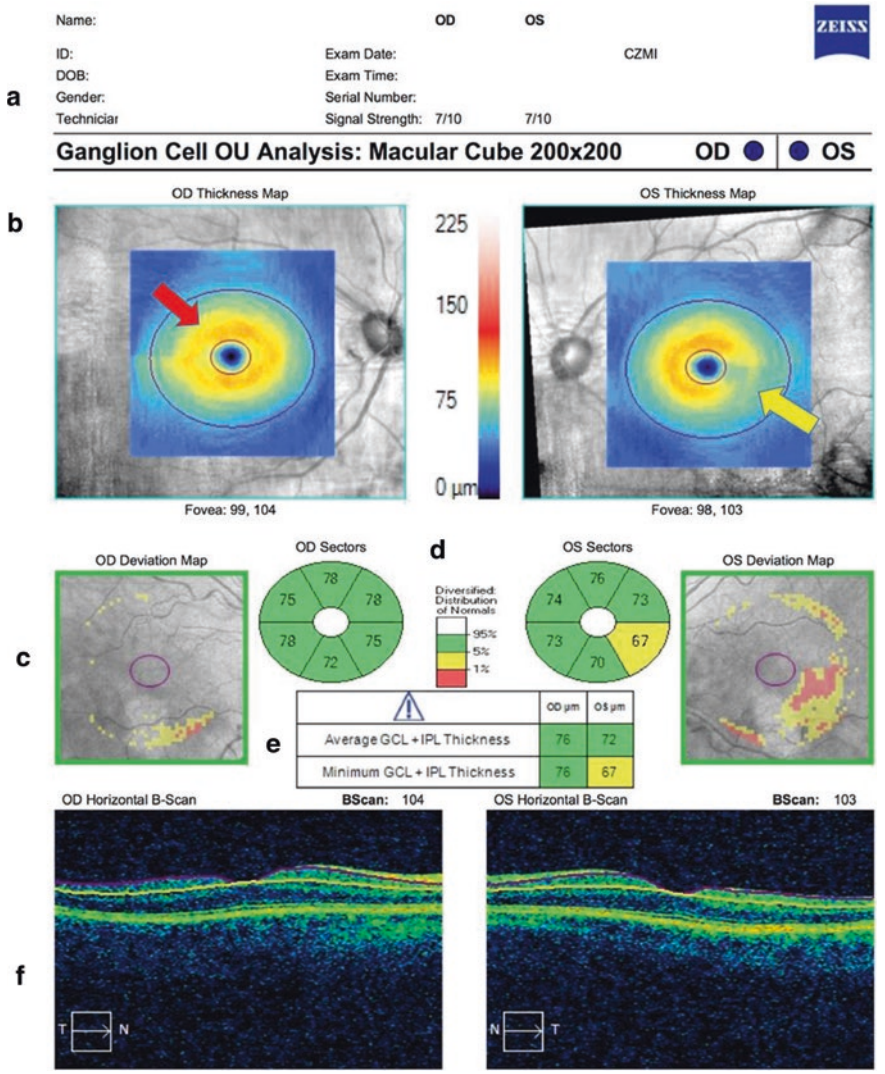

Fig. 5 Cirrus HD-OCT Ganglion Cell OU analysis of a patient with glaucoma in the left eye. Sections of the printout are explained in the text. Note the normal donut shape appearance of GCIPL thickness in the right eye (red arrow) and typical snail shape appearance due to abnormal GCIPL thickness in the left eye (yellow arrow). The GCIPL thinning can also be observed in the Deviation map (**c**) and Sector map (**d**) in the inferotemporal region in the left eye

1-Patient Data and Signal Strength. (Fig. 5a) Signal strength < 6 should be repeated.

2-Thickness Map. Raw GCL+IPL thickness are used for displaying thickness in the macula scan cube (Fig. 5b). The map has a doughnut shaped appearance in normal eyes.

3-Deviation Map. A 120×120 μm area is compared with normative database data and is displayed in a color-coded map similar to the RNFL deviation map (Fig. 5c).

4-Sector Map. The GCIPL thickness of an oval 4.8×4.0 mm region centered on the fovea is compared to age-matched controls and displayed in the same color code described previously (Fig. 5d).

5-Tabular data. Average GCIPL and minimum GCIPL are presented and color-coded (Fig. 5e).

6-Horizontal Tomogram of the Macula. This image includes a single B scan with segmentation of the GCIPL. The scan should be checked for macular pathologies and segmentation errors that can affect thickness measurements (Fig. 5f).

(c) The PanoMap Analysis

The PanoMap analysis combines a wide-field view of RNFL and ONH analysis with Ganglion Cell analysis of the right or left eye. This allows the reviewer to evaluate the peripapillary area, optic nerve head, and macula together on a single printout (Fig. 6).

Spectralis SDOCT

The Spectralis SDOCT (Heidelberg Engineering GmbH, Heidelberg, Germany) incorporates a real-time eye tracking system (TruTrack™) that couples cSLO and SDOCT scanners to adjust for eye movements. This ensures that the same precise location of the retina is scanned each time to reduce variability across longitudinal measurements. This method also allows B-Scans to be re-sampled in the same location to improve the signal-to-noise ratio (SNR), a technique called Automatic Real-time Tracking (ART). The Spectralis Glaucoma Module Premium Edition (GMPE) offers a proprietary feature called the "Anatomic Positioning System" (APS). All subsequent GMPE scans are aligned to the baseline landmarks and are

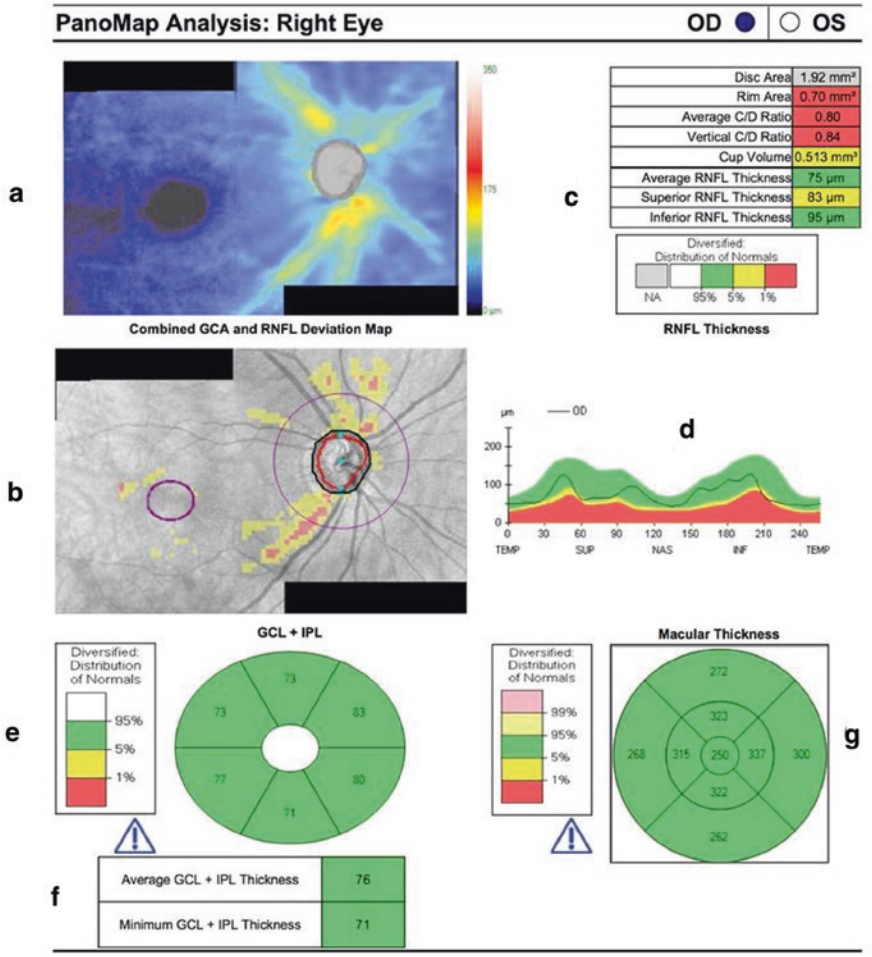

Fig. 6 The PanoMap analysis is a combination of a 200 × 200 Optic Disc Cube and a 512 × 128 Macular Cube scan. Sections of the printout are explained in the text. Note that in this glaucoma patient the RNFL defect can be observed in inferior and superior regions of optic nerve (**a**, **b**), while the macula GCIPL is within normal limits (**b**, **e**, **f**). The macular thickness map is also included (**g**) and is normal

automatically oriented according to the patient's fovea-BMO center (FoBMOC) axis. FoBMOC-aligned scans ensure all eyes are anatomically aligned correctly and compared with healthy control eyes regardless of anatomical differences, thereby improving accuracy of the sector analysis (Fig. 7a). In the BMO-MRW analysis, the minimum distance between BMO and internal limiting membrane (ILM) is measured from 48 equidistant data points. (Fig. 7b).

Different scan protocols and print-outs are available. The Standard RNFL Single Exam Report focuses on peripapillary RNFL thickness. The **Minimum**

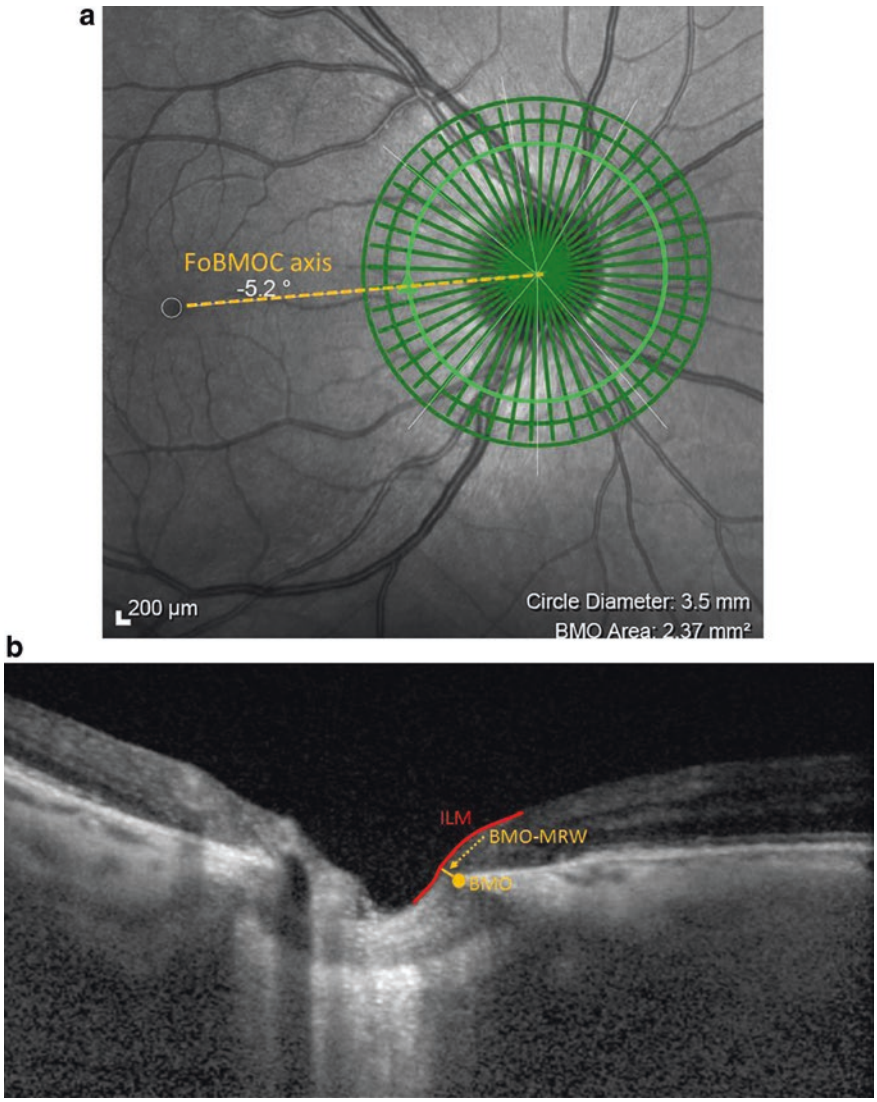

Fig. 7 **a** ONH-RC GMPE scan of Spectralis SDOCT demonstrating fovea to BMO center (FoB-MOC). Even if the angle of the fovea to the center of the ONH changes due to cyclotorsion or anatomical differences, the arcuate path of the RNFL bundles remains constant to this axis. This increase structure–function relationship and decreases variability of the measurements during follow-up. **b** Spectralis SDOCT image demonstrating the minimum rim width (BMO-MRW) parameter, which is the shortest distance from the ILM to BMO

Rim Width (MRW) Analysis focuses on ONH parameters. The **posterior pole (PPole) algorithm** focuses on the macula. The color codes in the Spectralis SDOCT reports are similar those that predominate in the Cirrus HD-OCT reports

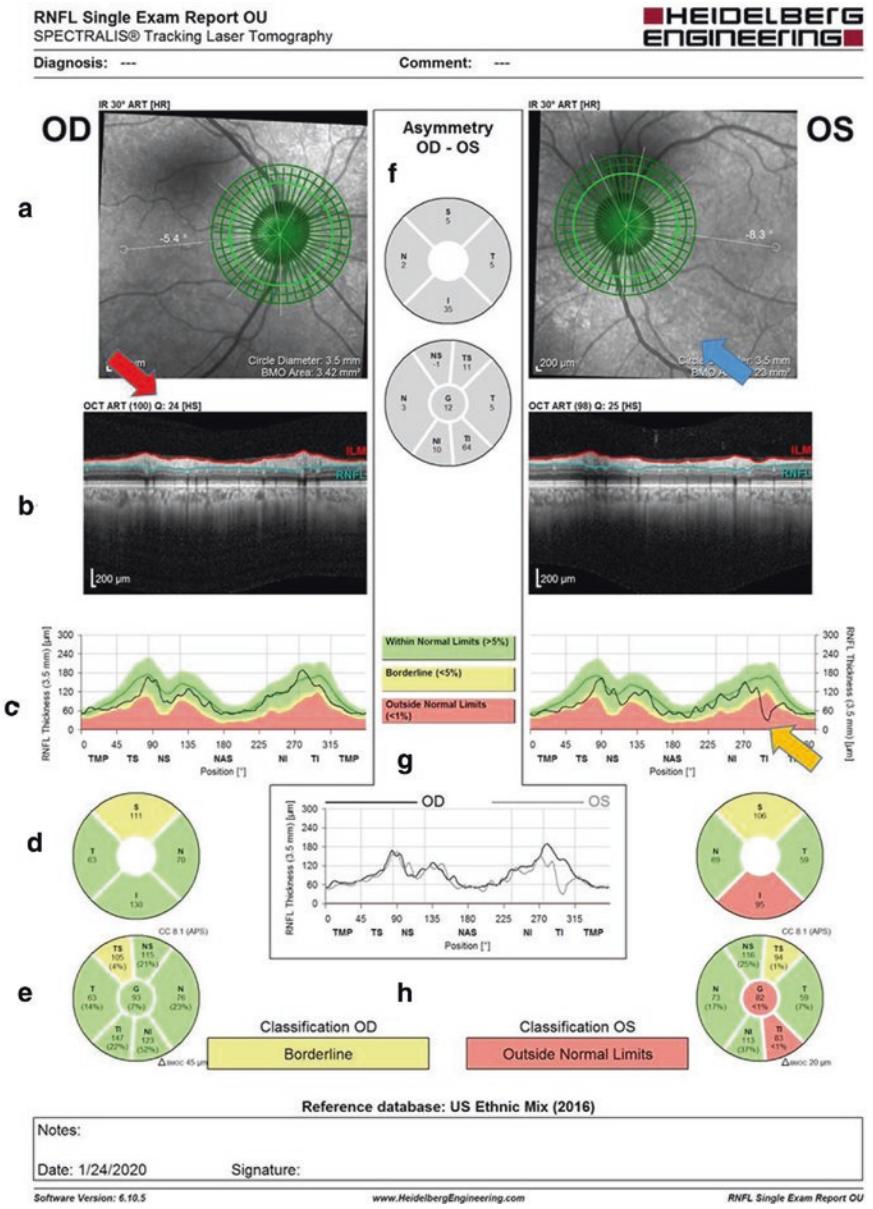

Fig. 8 Spectralis RNFL Single Exam Report of a patient with glaucoma in the left eye. Sections of the printout are explained in the text. Quality of the image is good (24, red arrow). Note the RNFL defect (blue arrow) in the IR image that can also be observed in the RNFL Thickness Profile (yellow arrow) and pie chart in the inferotemporal sectors

and indicate comparison against a normative database. Green represents values 'within normal limits' (measurements within the 95% prediction limits for normality), yellow represents 'borderline' values (measurements outside the 95% but within 99%), and red represents values 'outside normal limits' (measurements less than 99% of the normative database).

(A) **Standard RNFL Single Exam Report (Fig. 8)**

1-Patient and test information

2-Infrared reflectance (IR) image. Infrared image of the ONH with the location of the RNFL scan circle outlined in green. ART indicates that the image was captured using the automatic real-time function and "[HR]" indicates the resolution setting (High Speed vs. High Resolution) (Fig. 8a).

3-RNFL Circular Tomogram. This includes an OCT image and segmentation of the calculation circle. The image should be checked by the reviewer for artifacts, segmentation errors, and retinal disease or vitreo-retinal interface problems. The Q value associated with the image indicates the Quality Score (scale 1–40). Images with values < 15 are considered poor quality (Fig. 8b).

4-RNFL Thickness Profile. A TSNIT plot is created using measurements from a 3.4 mm diameter calculation circle centered on the BMO. Background colors indicate normative data ranges. The default setting of the circular scan in the GPME report (ONH-RC scan) is 3.5 mm, but it is possible to see the results of the other two circular scans diameters (Fig. 8c).

5-Pie chart. The RNFL thickness is averaged and compared to the normative database globally and in four quadrants and six sectors (temporal, temporal superior, nasal superior, nasal, nasal inferior, temporal inferior). Sector colors indicate classification compared to the normative database. The black values represent the average RNFL thickness in each sector. The numbers in parentheses (green) are the expected normal values, adjusted for age (Fig. 9). In the GPME report the green numbers are replaced by numbers in parentheses which represents the ranking of the RNFL thickness in percentile within the normative database (Fig. 8d, e).

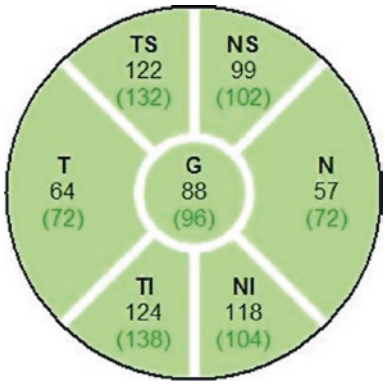

Fig. 9 Pie chart in circular scan of the RNFL Single Exam Report. The black values represent the average RNFL thickness in each sector. The numbers in parentheses (green) are the expected normal values, adjusted for age

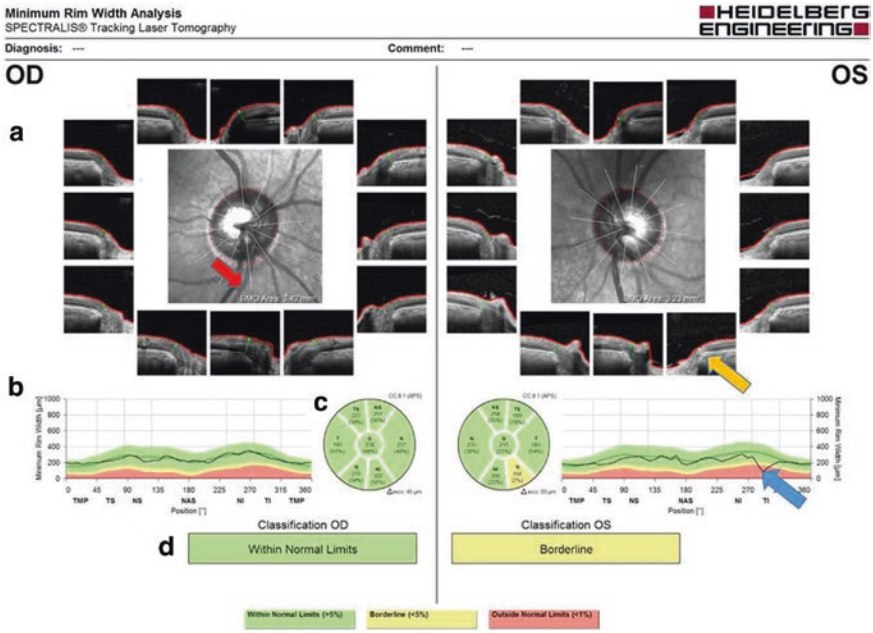

Fig. 10 Spectralis Minimum Rim Width Analysis Report of the same patient as Fig. 8. Sections of the printout are explained in the text. The BMO area is 2.42 mm^2 in the right eye (red arrow). Note the MRW thinning in the inferotemporal sectors in BMO-MRW Height Profile (blue arrow), pie chart, and BMO overview (yellow arrow)

6-Asymmetry Chart. Displays the difference (in microns) between the thickness of different regions of the right and left eye (Fig. 8f).

7-Combined RNFL Profile. Plots the TSNIT profiles of both eyes overlying one another (Fig. 8g).

8-Classification bar. Displays the classification of the worst sector in the pie chart with color coding as described above (Fig. 8h).

(B) **The Minimum Rim Width Analysis Report (Fig. 10)**

The information in the **Minimum Rim Width Analysis Report** includes:

1-Patient and test information.

2-BMO Overview. A central infrared image of the ONH is displayed with 12 surrounding B scans of radial cuts through the optic nerve head. The inner retina is segmented in red. A green arrow representing MRW starts at the BMO and terminates perpendicular to the inner retina. The infrared image includes a measurement of the total BMO area (Fig. 10a).

3-BMO-MRW Height Profile. The BMO-MRW is displayed in a TSNIT graph. In normal subjects, this profile demonstrates a slight double hump according to the ISNT rule (Fig. 10b).

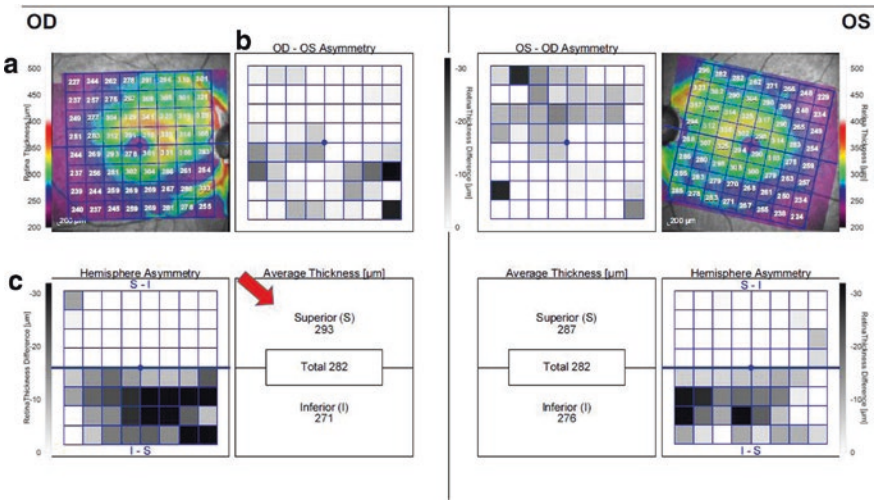

Fig. 11 Spectralis Posterior Pole Asymmetry analysis of a glaucoma patient. Sections of the printout are explained in the text. The prominent supratemporal nerve fiber bundles appear red. However, inferotemporal arcuate-shaped RNFL thinning can be seen in the inferior hemisphere of both eyes in the thickness map (**a**). Most of the superpixels in the inferior hemisphere are flagged various shades of gray in the hemisphere asymmetry chart (**c**) of both eyes. This represents thinning of the retina compared to the corresponding superpixels in the superior hemisphere. This can also be seen in the Average Thickness Chart with the values in the inferior hemisphere less than the superior hemisphere

4-Pie chart. The black numbers show the average MRW thickness values in each sector. The numbers in parentheses represents the percentile of the MRW thickness value of that sector (Fig. 10c).

5-Classification bar. Displays the classification of the worst sector in the pie chart with color coding compared to the normative database (Fig. 10d).

(C) The Posterior Pole Asymmetry Analysis Report

This report shows the color-coded thickness for each $3° \times 3°$ superpixel on an 8×8 grid (Fig. 11a), an **Inter-Ocular Asymmetry Map** (with intensity of the gray scale demonstrating the magnitude of differences between corresponding superpixels of both eyes) (Fig. 11b), a **Hemisphere Asymmetry Map** (with intensity of the gray scale reflecting the magnitude of differences between corresponding superpixels of the two hemispheres of one eye) (Fig. 11c)), and an **Average Thickness Chart (Fig. 11, red arrow)**. In the GMPE module the thickness of the whole macula, RNFL, GCL, or IPL layer can also be exported (Fig. 12).

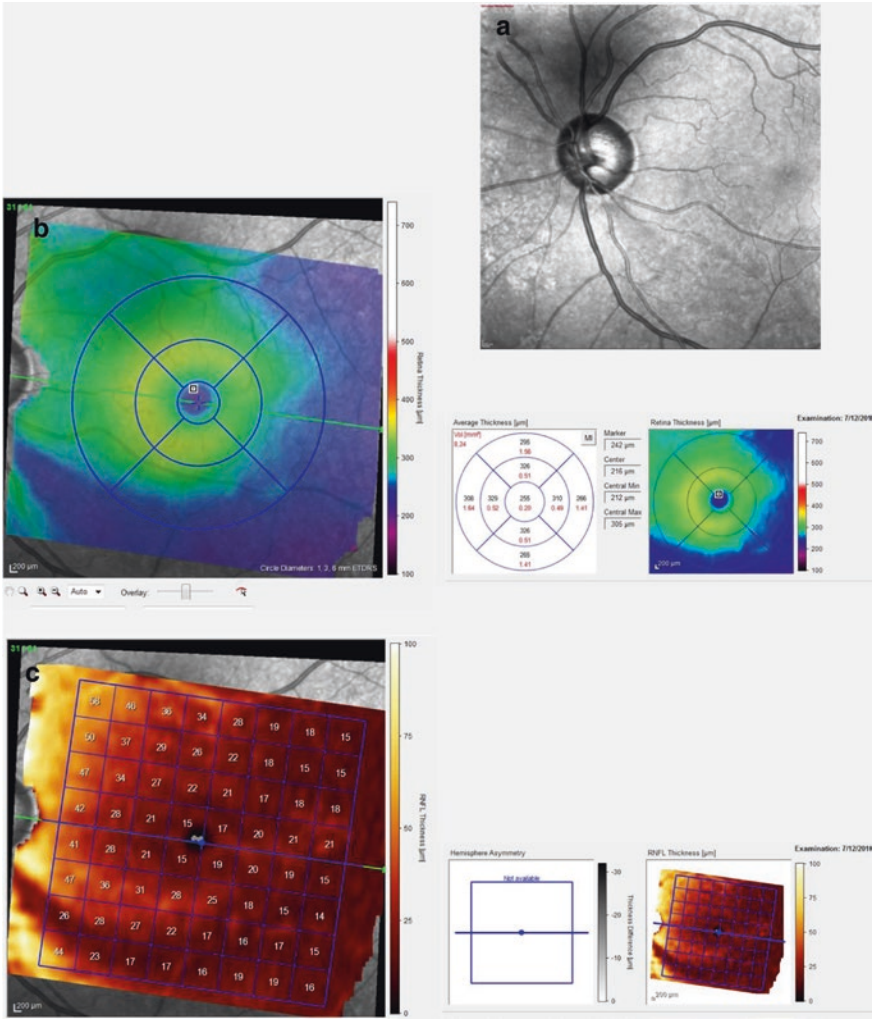

Fig. 12 Different thickness layers of macula can be exported with the GMPE module. In this glaucoma patient an RNFL defect can be seen in the inferotemporal region in the IR image (**a**), whole macula thickness map (**b**), and macula RNFL thickness map (**c**)

Optovue-Rtvue SDOCT

The RTVue (Optovue Inc., Fremont, CA) uses a superluminescent diode (SLD) with a center wavelength of 840 nm to provide high-resolution images. Optovue was the first SDOCT to include automatic measurements of macular GCC thickness. Also its first FDA-approved-OCT angiography has been used in many centers worldwide for evaluation of retinal disease and glaucoma.

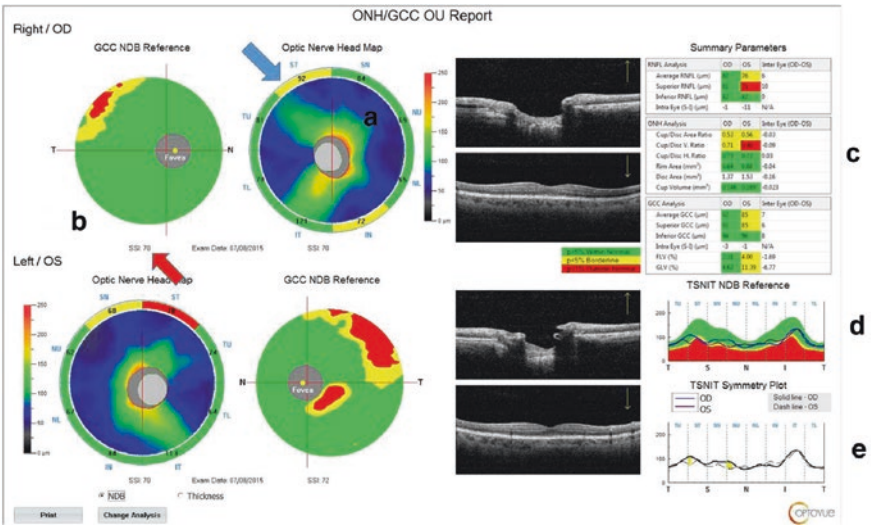

Fig. 13 Optovue ONH/GCC OU report of a glaucoma patient. Sections of the printout are explained in the text. Note that the quality of the image is good with an SSI of 70 in both eyes (red arrow). Supratemporal RNFL thinning can be seen in the optic nerve head map (**a**), significance band (blue arrow), GCC significance map (**b**), and TSNIT NDB reference plot (**d**). Asymmetry between the two eyes can be observed in the TSNIT symmetry plot (**e**)

ONH/GCC OU Report

This report is the most useful report from the RTvue and gives us information for ONH, RNFL and GCC thicknesses. They are compared to normative data and presented with similar color codes as previously described (green is within normal limits, yellow is borderline, and red is outside normal limits) (Fig. 13).

1-Patient and Test Information

2-Signal strength index (SSI) (scale 1–100). Values of<40 are considered poor quality image (Fig. 13, red arrow).

3-Optic nerve head map and significance band. The optic nerve head map provides a map of rim and RNFL thickness values with red and yellow colors indicating thicker measurements and green and blue colors indicating thinner measurements (Fig. 13a). A circular band frames the thickness map and includes RNFL thickness values as well as a color coded comparison to the normative database for 16 sectors of equal size (22.5°) (Fig. 13, blue arrow).

5-GCC significance map. The significance Map shows regions where the change from normal reaches statistical significance. The Significance Map is color-coded where green represents values within the normal range (5 to 95 percentile) yellow indicates borderline results (1 to 5 percentile), and red represents outside normal limits (<1 percentile) (Fig. 13b).

6-Tabular data. RNFL and ONH parameters measurements including disc area, rim area, cup volume, cup/disc ratio and others presented with color codes indicating comparison to the normative database. Parameters derived from the GCC analysis are also presented. Global loss volume (GLV) and focal loss volume (FLV) are parameters that reflect different aspects of GCC loss. GLV represents the total volume of significant GCC loss. The FLV parameter sums loss only in regions where the GCC is thin in both absolute (GCC < normal) and relative (pattern deviation less than fifth percentile) terms (Fig. 13c).

7-TSNIT NDB reference plot. Plots the RNFL thickness profile of both eyes with comparison to the normative database (Fig. 13d).

8-TSNIT symmetry plot. Compares the TSNIT plots for both eyes and represents significant differences with the color yellow. Differences in symmetry are often seen in glaucoma patients (Fig. 13e).

OCT and Progression

Glaucomatous optic neuropathy is characterized by progressive change over time. Ocular imaging has been used for earlier detection of change in glaucoma as structural progression frequently precedes functional progression [16]. It can also detect progression during the pre-perimetric stage of glaucoma [17]. The inter-visit reproducibility coefficient for average RNFL by different SDOCT devices is between 4.8 to 5 μm. Therefore, reduction of more than 5 μm in average RNFL thickness is considered a statistically significant change, with a false positive rate of 2.5% [18]. However, the repeatability of change and potential pathology or artifacts that could lead to thinner measurements should be fully evaluated to confirm progression. Aging is another confounding factor in detection of progression. The RNFL and GCL naturally thin over time by ~ 0.20 μm and ~ 0.30 μm per year, respectively [18]. Rates of thinning greater than this are more likely to represent glaucomatous progression.

Progressive changes of different parameters can be assessed either with an event analysis approach or with a trend analysis approach. Event analysis is based on the statistical comparison of a follow-up test with a baseline reference test; if the difference between the two exceeds the threshold of the test–retest variability the follow-up test is flagged as progression. Event analysis is limited by a lack of information about the rate of change over time. Trend analysis examines serial RNFL measurements across time and represents the rate of change in micrometers per year. Cirrus HD-OCT's Guided Progression Analysis (GPA) uses both event and trend analyses, while other OCT devices use trend analyses in their progression analysis software.

Cirrus HD-OCT GPA

GPA makes all the comparisons between the mean of the two baseline images and follow-up scans of the patient and thus is independent of the normative database. At least 4 observations are needed to run the algorithm. The clinician should review these items in the printout:

1-Patient Data (Fig. 14a).

2-Baseline and Follow-Up RNFL Thickness Maps. The two baseline scans and two most recent follow-up scans are displayed (Fig. 14b).

3-RNLF Thickness Change Maps (Event Analysis). A black and white en face image is displayed with overlying color codes indicating areas of thickness change. The super-pixels are flagged in orange ("possible loss") if the change is greater than the test–retest variability on the second most recent scan. The area is flagged in red ("likely loss") if the same region shows a similar or greater amount of thinning on the subsequent scan. Lavender color ("possible increase") flags an area with RNFL thickening beyond what is expected (Fig. 14c).

4-RNFL Thickness Change Plot (Trend Analysis). A linear regression line is drawn to calculate the rate of loss. The visits with "likely loss" or "possible loss" are presented with red and orange circles, respectively (Fig. 14d).

5-RNFL Thickness Profile Change Plot (Event Analysis). Three TSNIT profiles for the examined eye are plotted in overlapping style. C is the current scan and B1 and B2 are two baseline scans. Areas of "likely loss" are highlighted in red (Fig. 14e).

6-RNFL/ONH Summary: This is a summary of the four analyses used in GPA. Checkmarks using a similar color code are used to identify loss in any or all of the analyses (Fig. 14f).

7-Thickness and Change Maps Overview. Presents thickness change maps for all visits (rather than just baseline and most recent two visits) as described above (Fig. 14g).

8-RNFL and ONH Summary Parameters Table. Areas with thickness changes are denoted by boxes highlighted in the color scheme described above (Fig. 14h).

Spectralis OCT Progression Analysis

The new software utilizes APS technology to reduce test–retest variability. After the reference image is identified by the operator, the system automatically registers the reference image scanning area and scans the same region during follow-up examinations. Changes in the RNFL profile are displayed without measurements of significance. The summary of RNFL scans in each visit are displayed. The

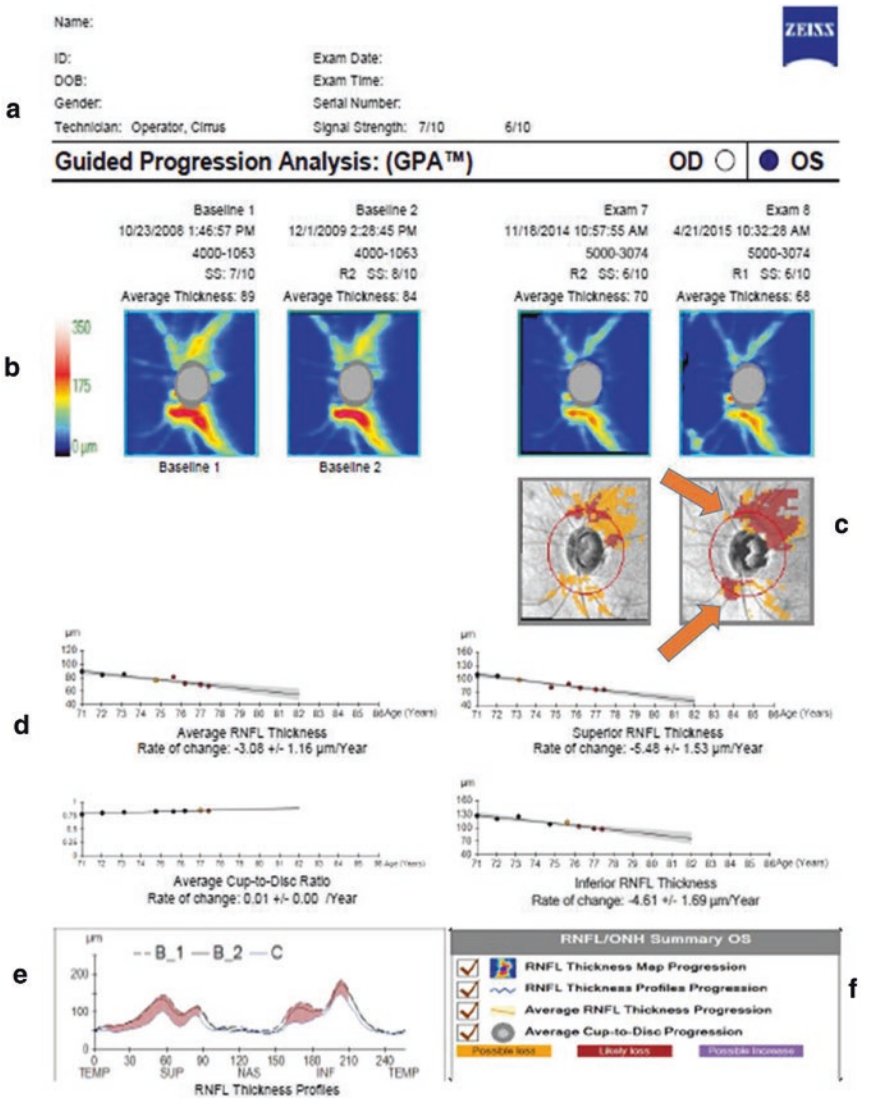

Fig. 14 Cirrus HD-OCT GPA, left eye (2008–2015). **a** RNFL thickness map progression analysis shows significant RNFL thinning in the inferior and superior quadrant. GPA marked these areas as "likely loss" and a red checkmark is present in the summary box because the thinning is present in consecutive scans. RNFL thickness profile progression plot also shows RNFL thinning in the superior and inferior quadrant and areas with significant progression are displayed in red (c, orange arrow). The trend analysis based RNFL thickness plots detected statistically significant progression as shown in the summary box. **f** The rate of progression is fastest in the superior quadrant. Average cup-to-disc ratio progression is also statistically significant. **d** The RNFL and ONH summary parameters table shows worsening of the average superior and inferior RNFL thickness measurement. Average RNFL thickness decreased from 89 µm in 2008 to 68 µm in 2015. **h** A trabeculectomy was performed in the left eye for this patient because of this fast progression rate despite IOP lowering medications

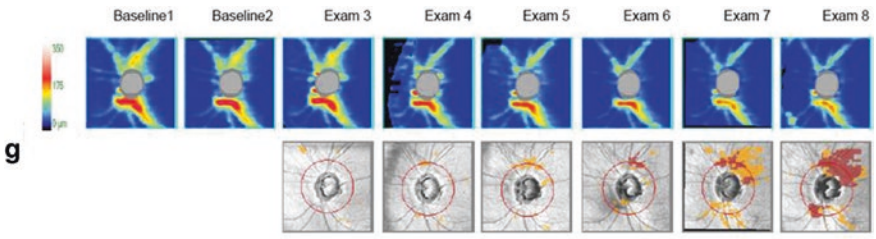

h

RNFL and ONH Summary Parameters

		Exam Date/Time	Serial Number	Registration Method	SS	Avg RNFL Thickness (µm)	Inf Quadrant RNFL (µm)	Sup Quadrant RNFL (µm)	Rim Area (mm²)	Average Cup-to-Disc Ratio	Vertical Cup-to-Disc Ratio	Cup Volume (mm³)
Baseline 1:	1	10/23/2008 1:46:57 PM	4000-1063		7/10	89	127	110	1.08	0.77	0.68	0.850
Baseline 2:	2	12/1/2009 2:28:45 PM	4000-1063	R2	8/10	84	120	106	0.95	0.80	0.73	0.963
	3	1/11/2011 10:04:58 AM	4000-1063	R1	8/10	85	125	99	0.82	0.82	0.77	0.960
	4	8/14/2012 10:05:55 AM	4000-1063	R1	9/10	75	107	81	0.83	0.83	0.75	1.078
	5	7/15/2013 10:15:09 AM	4000-1063	R1	7/10	81	113	89	0.86	0.82	0.75	1.170
	6	2/4/2014 11:31:09 AM	5000-3074	R1	6/10	71	103	80	0.75	0.83	0.77	1.099
	7	11/18/2014 10:57:55 AM	5000-3074	R2	6/10	70	99	77	0.72	0.85	0.78	1.205
Current:	8	4/21/2015 10:32:28 AM	5000-3074	R1	6/10	68	97	76	0.76	0.83	0.75	1.135

Fig. 14 (continued)

Follow-Up RNFL Thickness Plots (Fig. 15) compares the baseline TSNIT and follow up TSNIT profiles and highlights differences between individual exams with red indicating a decrease and green an increase in the thickness values.

In the **Spectralis RNFL Trend Report**, normalized global RNFL thickness and sectoral RNFL thickness are displayed as a line graph. The thickness measurements are normalized compared to the average global or sectoral measurements of the normative database. (Fig. 16a) Pie graphs and RNFL thickness values (Fig. 16b) and their change from the selected reference visit (Fig. 16c) are shown.

In RNFL Progression Trend Analysis Report, the trend analysis for RNFL/MRW is shown and is compared to the normal age-related slope. Color-coded normative database range will be used for the background of the graph (Fig. 17). The Glaucoma Module Premium Edition (GMPE) software also provides a progression trend analysis report for the MRW thickness similar to what was mentioned earlier for RNFL.

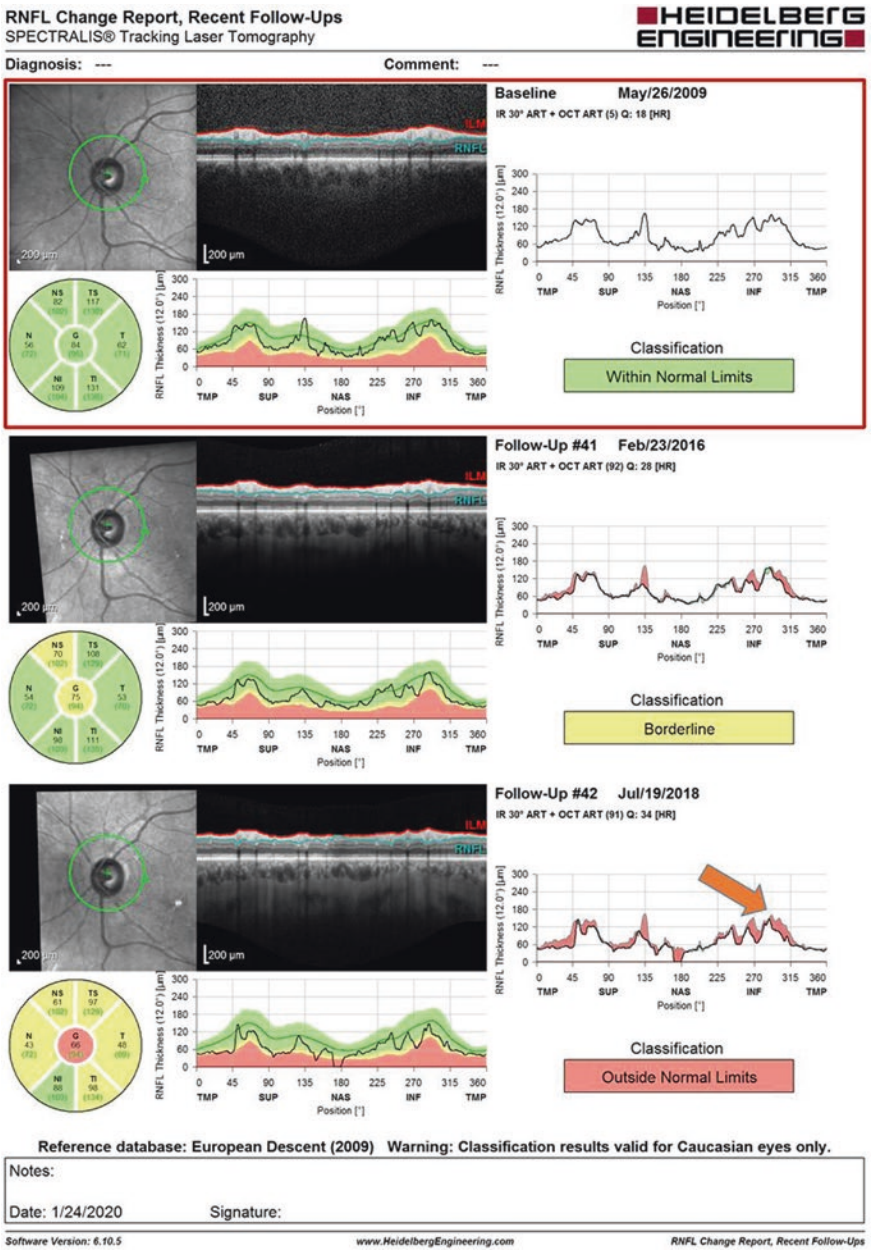

Fig. 15 Follow-up RNFL Thickness Plots of a patient that compares RNFL circle scan follow-up #41 (2016) and follow-up #42 (2018) with baseline exam (2009) using the Heidelberg Spectralis OCT. Apart from the usual classifications and overview of these exams, a difference graph is shown highlighting differences in TSNIT plots between individual exams (red indicating a decrease, green an increase) in the thickness values (orange arrow)

Fig. 16 The RNFL trend report of a glaucoma patient who developed choroidal neovascularization. The normalized RNFL thickness graph (**a**), global and sectoral RNFL thickness values of baseline and follow-up tests (**b**), and the differences between these values and the baseline measurements are shown (**c**)

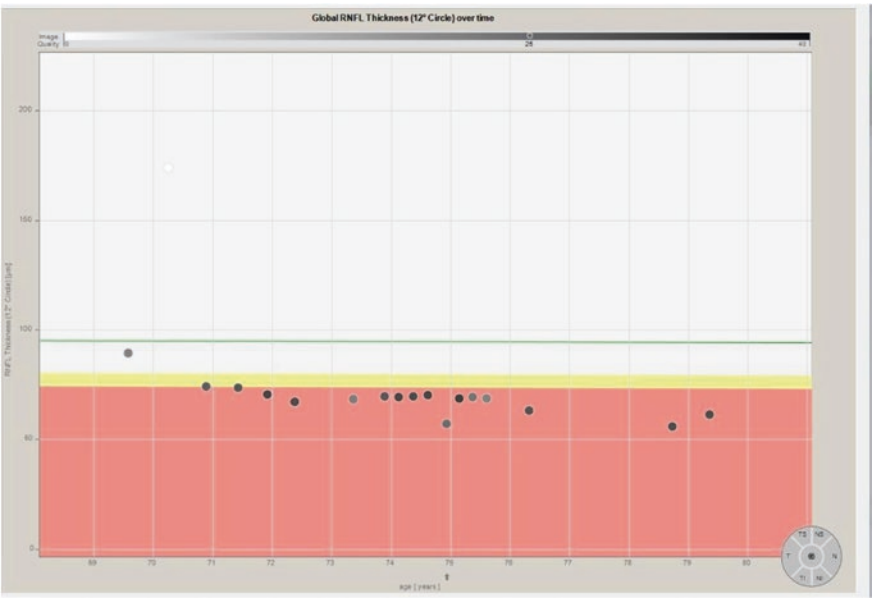

Fig. 17 Progression trend analysis report of a patient with slow progression over years. This patient had early glaucomatous damage on VFs at baseline and over time the RNFL thickness decline from 93 to 62 μm

Acknowledgements FUNDING/SUPPORT: Supported in part by National Institutes of Health/National Eye Institute grants R01 EY029058 (RNW), by core grant P30EY022589; by an unrestricted grant from Research to Prevent Blindness (New York, NY); by grants for participants' glaucoma medications from Alcon, Allergan, Pfizer, Merck, and Santen, and by the donors of the National Glaucoma Research Program, a program of the BrightFocus Foundation.

Financial Disclosure: S. Moghimi, None; M. Safizadeh, None; Andrew Camp, None; R.N. Weinreb, Heidelberg Engineering (F), Carl Zeiss Meditec (F, R), Konan (F), National Eye Institute (F), Optovue (F), Allergan (C), Bausch&Lomb (C,F), Eyenovia (C), Novartis (C).

References

1. Leitgeb R, Hitzenberger C, Fercher A, Performance of fourier domain vs. time domain optical coherence tomography. Opt Express. 2003; 11(8): 889–94.
2. Bowd C, et al. Estimating optical coherence tomography structural measurement floors to improve detection of progression in advanced glaucoma. Am J Ophthalmol. 2017;175:37–44.
3. Hood DC, et al. Structure versus function in glaucoma: an application of a linear model. Invest Ophthalmol Vis Sci. 2007;48(8):3662–8.
4. Leung CK et al. Retinal nerve fiber layer imaging with spectral-domain optical coherence tomography: a variability and diagnostic performance study. Ophthalmology. 2009; 116(7):1257–63, 1263 e1–2.

5. Blumenthal EZ, et al. Reproducibility of nerve fiber layer thickness measurements by use of optical coherence tomography. Ophthalmology. 2000;107(12):2278–82.
6. Chauhan BC, et al. Enhanced detection of open-angle glaucoma with an anatomically accurate optical coherence tomography–derived neuroretinal rim parameter. Ophthalmology. 2013;120(3):535–43.
7. Kuang TM, et al. Estimating lead time gained by optical coherence tomography in detecting glaucoma before development of visual field defects. Ophthalmology. 2015;122(10):2002–9.
8. Curcio C, Allen K. Topography of ganglion cells in human retina. J Comp Neurol. 1990;300:5–25.
9. Wu H, de Boer JF, Chen TC. Reproducibility of retinal nerve fiber layer thickness measurements using spectral domain optical coherence tomography. J Glaucoma. 2011;20(8):470–6.
10. Medeiros FA, et al. Evaluation of retinal nerve fiber layer, optic nerve head, and macular thickness measurements for glaucoma detection using optical coherence tomography. Am J Ophthalmol. 2005;139(1):44–55.
11. Huang D et al. Optical coherence tomography. Science (New York, NY). 1991; **254**(5035):1178–1181.
12. Tan O, et al. Detection of macular ganglion cell loss in glaucoma by Fourier-domain optical coherence tomography. Ophthalmology. 2009;116(12):2305-14.e142.
13. Mwanza J-C, et al. Glaucoma diagnostic accuracy of ganglion cell–inner plexiform layer thickness: comparison with nerve fiber layer and optic nerve head. Ophthalmology. 2012;119(6):1151–8.
14. Leung CK, et al. Retinal nerve fiber layer imaging with spectral-domain optical coherence tomography: analysis of the retinal nerve fiber layer map for glaucoma detection. Ophthalmology. 2010;117(9):1684–91.
15. Hood DC, et al. A region-of-interest approach for detecting progression of glaucomatous damage with optical coherence tomography. JAMA Ophthalmology. 2015;133(12):1438–44.
16. Hood DC, Kardon RH. A framework for comparing structural and functional measures of glaucomatous damage. Prog Retin Eye Res. 2007;26(6):688–710.
17. Na JH, et al. Detection of glaucoma progression by assessment of segmented macular thickness data obtained using spectral domain optical coherence tomography. Invest Ophthalmol Vis Sci. 2012;53(7):3817–26.
18. Leung CK-S et al. Retinal nerve fiber layer imaging with spectral-domain optical coherence tomography: a variability and diagnostic performance study. Ophthalmology. 2009; 116(7):1257–1263. e2.

OCT and Glaucoma: Case Review

Sasan Moghimi, Mona SafiZadeh, Andrew Camp and Robert N. Weinreb

Early diagnosis of glaucoma is essential to prevent significant visual impairment. Patients have already lost 25 to 40% of their retinal ganglion cells before they demonstrate visual field changes. However, structural changes usually precede functional visual field loss. Structural diagnostic modalities can detect glaucoma in earlier stages before irreversible functional damage has occurred. Optical coherence tomography (OCT) is the most promising technique for early detection of glaucomatous damage to the optic nerve head (ONH) and retinal nerve fiber layer (RNFL). In this chapter we present glaucoma cases in different stages of the disease and reviews role of OCT in diagnosis and monitoring of these cases.

Case 1- Glaucoma (Perimetric and Preperimetric)

RNFL OCT can detect glaucomatous change earlier than visual fields. This patient presented to clinic with an IOP of 24 mmHg OD and 22 mmHg OS. She has a superior visual defect in the right eye and normal visual field in left eye. Superior and inferior RNFL thinning in right eye and inferior RNFL thinning in the left eye can be seen in the Spectralis RNFL Report (Fig. 1a). The Minimum Rim Width Analysis Report also depicts areas of rim thinning in the superior and inferior regions bilaterally (Fig. 1b). The patient was diagnosed with perimetric glaucoma in the right eye and preperimetiric glaucoma in the left eye. Medication was started for both eyes.

S. Moghimi (✉) · A. Camp · R.N. Weinreb
Department of Ophthalmology, Hamilton Glaucoma Center, Shiley Eye Institute, University of California, San Diego, CA, USA
e-mail: sasanimii@yahoo.com

M. SafiZadeh
Tehran University of Medical Sciences, Tehran, Iran

M. Mohammadpour (ed.), *Diagnostics in Ocular Imaging*,
https://doi.org/10.1007/978-3-030-54863-6_26

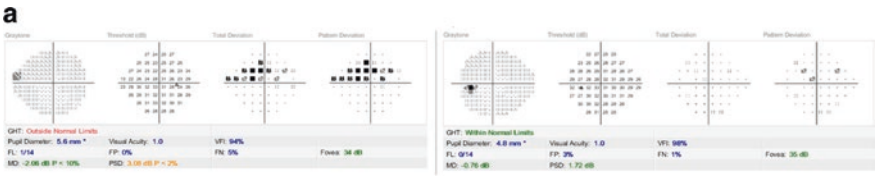

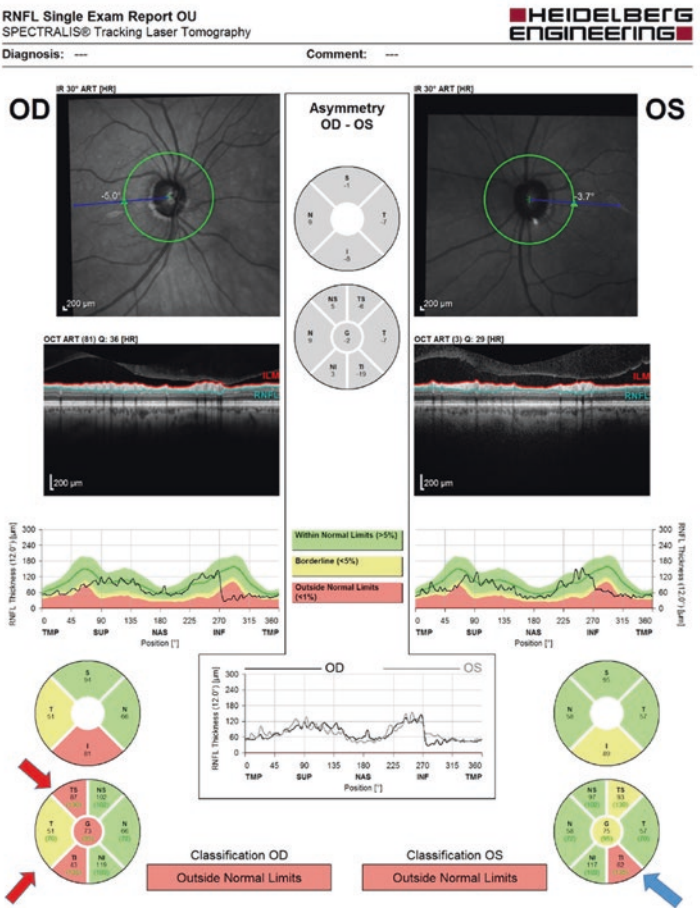

Fig. 1 **a** The Spectralis OCT single exam report demonstrates superior and inferior RNFL thinning in the right eye (red arrows) and inferior RNFL thinning in the left eye (blue arrow). The average RNFL is 75 µm and is flagged as 'borderline' in the left eye, which had a full visual field. **b** The Minimum Rim Width analysis demonstrates that the MRW parameter is borderline in the inferotemporal sector and supranasal sector of the left eye (blue arrows). However, the average MRW is still 'within normal limit'. In the right eye, the inferotemporal sectors are thinned and flagged as 'outside normal limit' (red arrow)

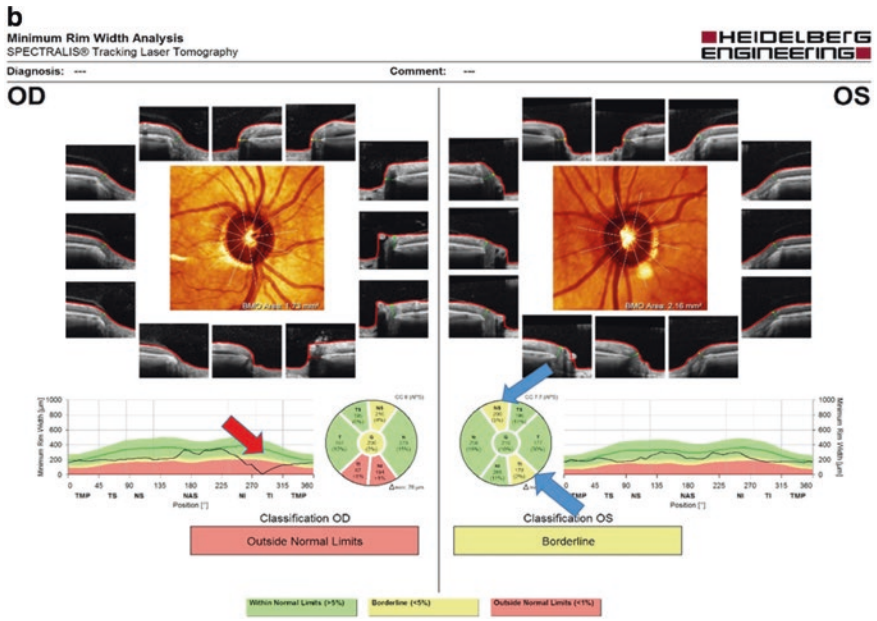

Fig. 1 (continued)

Case 2- Early Glaucoma with Central VF Damage

A 42-year-old woman was referred for glaucoma evaluation based on family history and elevated intraocular pressure. The IOP of her right eye was 23 mmHg and the left eye was 21 mmHg. She has a record of maximum IOP of 26 mmHg OU. Central corneal thickness is 525 μm OU. The optic nerve head showed a large cup-to-disc ratio but otherwise healthy-appearing disc (Fig. 2a). The 24–2 Visual fields are normal (Fig. 2a). The Cirrus ONH and RNFL OU Analysis report shows thinning in the supratemporal region of both eyes, left greater than right (Fig. 2b). The **Ganglion Cell OU Analysis Report** demonstrates ganglion cell Inner plexiform layer (GCIPL) thinning in the superior macula of the left eye (Fig. 2c). A 10–2 visual field was performed to better elucidate macular loss and an inferior arcuate was seen in the left eye (Fig. 2d). A prostaglandin analogue was started for the patient OU.

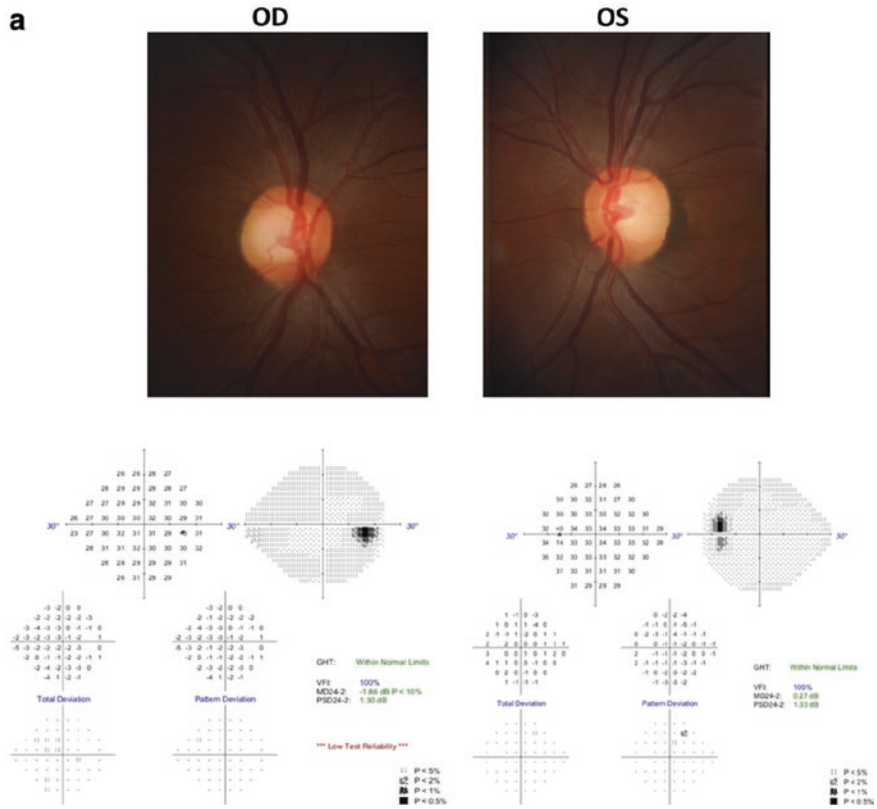

Fig. 2 **a** Optic nerve head shows a large cup-to-disc ratio but otherwise healthy-appearing disc. The 24–2 visual fields are normal in both eyes. **b** Cirrus HD-OCT shows an area of supratemporal RNFL thinning in both eyes (upper red arrows). Note that this thinning can be observed in both the Deviation map and RNFL Clock hours (red arrows).The RNFL profile is fairly symmetric and normal. Tabular data shows normal global RNFL OU. However, the ONH data (cup volume and average c/d ratio) is outside normal limit. **c** Cirrus Ganglion Cell OU report- an area of GCIPL thinning in the left eye can be seen in both the Thickness and Deviation map. The degree of thinning is abnormal in the superior sector and borderline in the supratemporal sectors. **d** An inferior arcuate defect is observed in the 10–2 visual field of the left eye (red arrow)

Raphe Sign

Various types of optic neuropathy, including compressive optic neuropathy and ischemic optic neuropathy, can affect the macula and GCIPL. However, in glaucoma, the inferotemporal region is frequently affected first. The temporal raphe sign is an important sign for distinguishing glaucoma from other neuropathies. The temporal raphe sign is positive if there is a horizontal straight line longer than one-half of the inner-to-outer-annulus length on the macular GCIPL thickness map (Fig. 3).

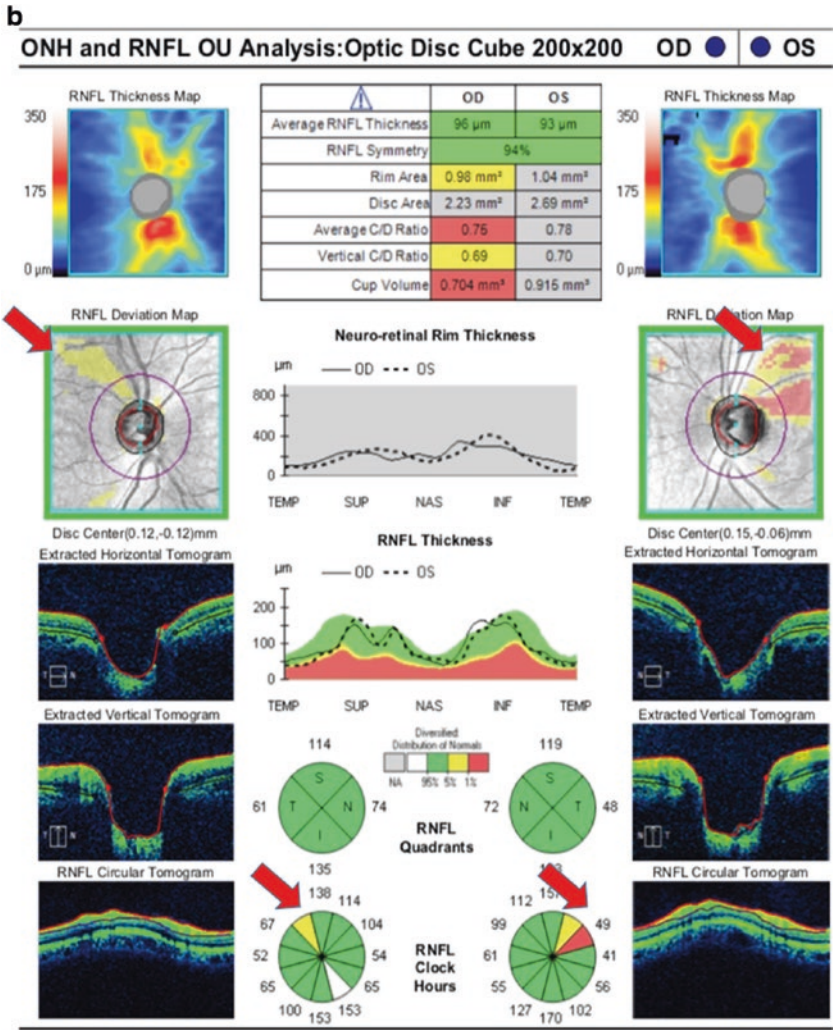

Fig. 2 (continued)

The temporal RNFL, the origins of which strictly respect the horizontal raphe, enters into the supratemporal and inferotemporal aspects of the optic disc. Glaucomatous structural damage and functional loss corresponding to the anatomic arrangement of the RNFL are often asymmetric across the horizontal meridian, especially in the early stages, leading to the temporal raphe sign on the GCIPL OCT thickness map [1].

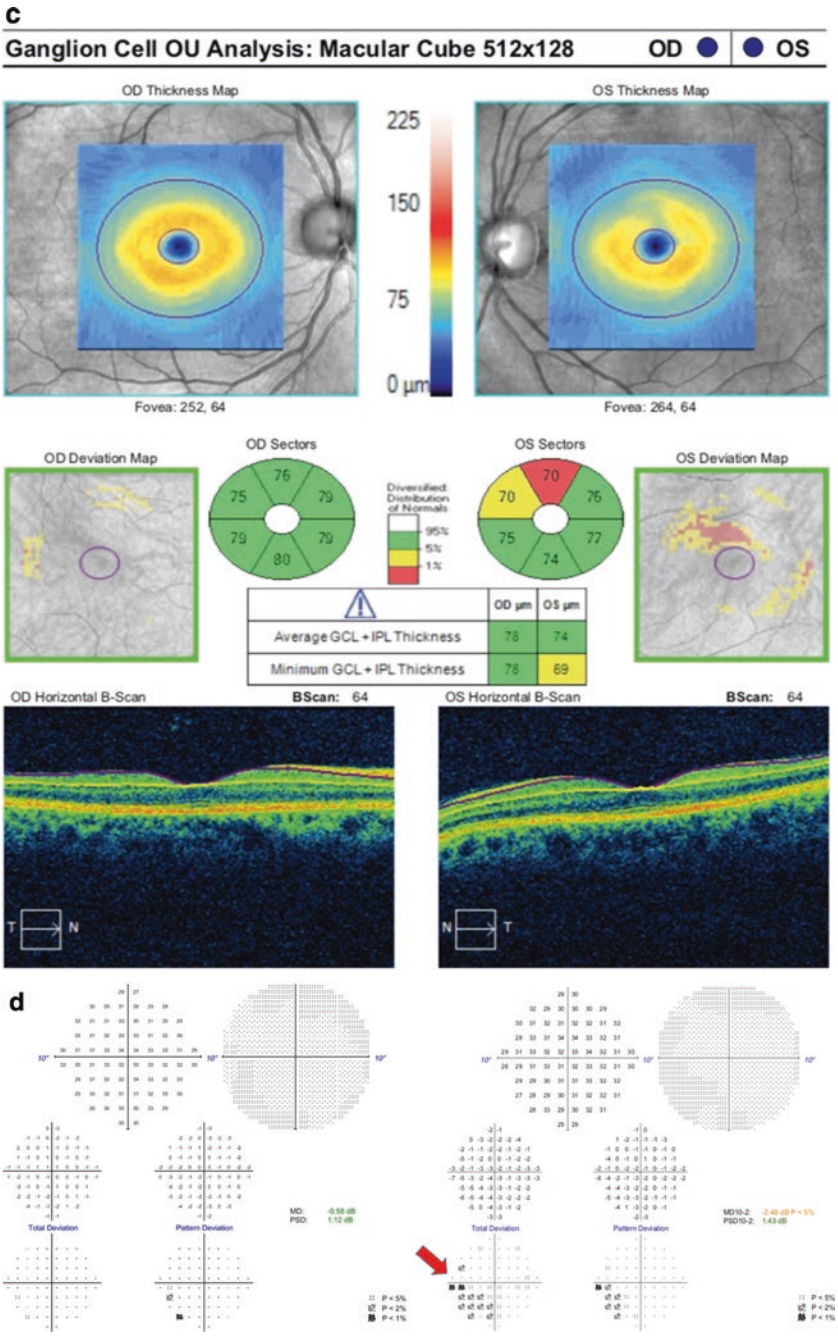

Fig. 2 (continued)

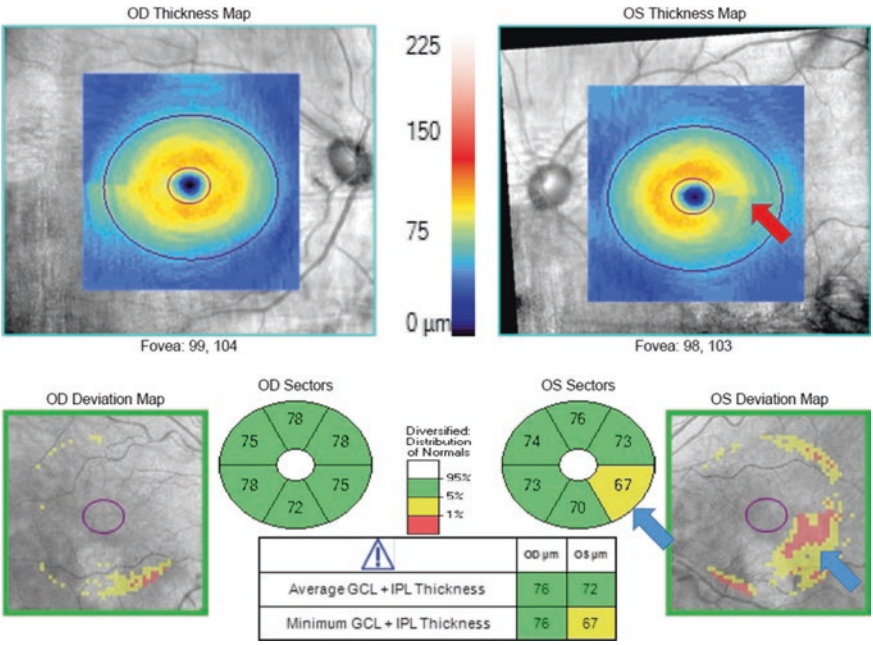

Fig. 3 Raphe sign. The GCIPL analysis demonstrates inferotemporal thinning in the left eye with a raphe sign on the thickness map (red arrow). The macula GCIPL thickness is shaped more like a snail, as opposed to the typical donut appearance. Inferotemporal thinning can also be seen in the deviation map and sectoral analysis (blue arrows). In the right eye the GCIPL looks normal

Case 3- Moderate Glaucoma with Raphe Sign

A 79-year old glaucoma patient was followed for 7 years in the clinic. The RNFL report showed superior wedge defects OU and an inferior wedge defect OS. The GCIPL analysis demonstrates inferotemporal thinning OU with a typical raphe sign. GCIPL thinning is suggestive of damage close to the fixation point, which can affect the quality of life more profoundly (Fig. 4a). A 10–2 visual field showed an arcuate scotoma close to fixation which was consistent with the GCIPL analysis (Fig. 4b).

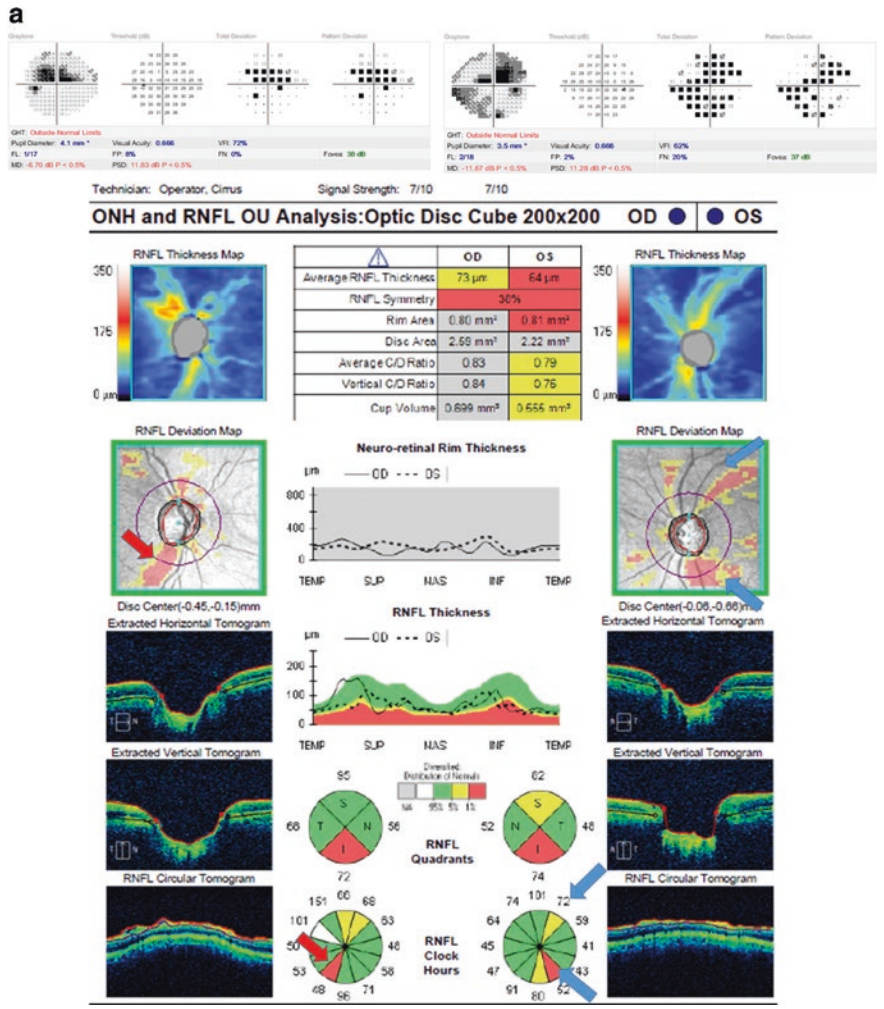

	OD	OS
Average RNFL Thickness	73 µm	64 µm
RNFL Symmetry	36%	
Rim Area	0.80 mm²	0.81 mm²
Disc Area	2.59 mm²	2.22 mm²
Average C/D Ratio	0.83	0.79
Vertical C/D Ratio	0.84	0.76
Cup Volume	0.699 mm³	0.655 mm³

Fig. 4 **a** Cirrus HD-OCT RNFL report demonstrating the inferior wedge defects in the right eye (red arrow) and superior and inferior wedge defects in the left eye (blue arrows). **b** The GCIPL analysis demonstrates inferotemporal thinning OU with a typical raphe sign on the thickness map of both eyes. The superior arcuate defect in both eyes is consistent with the loss demonstrated on GCIPL

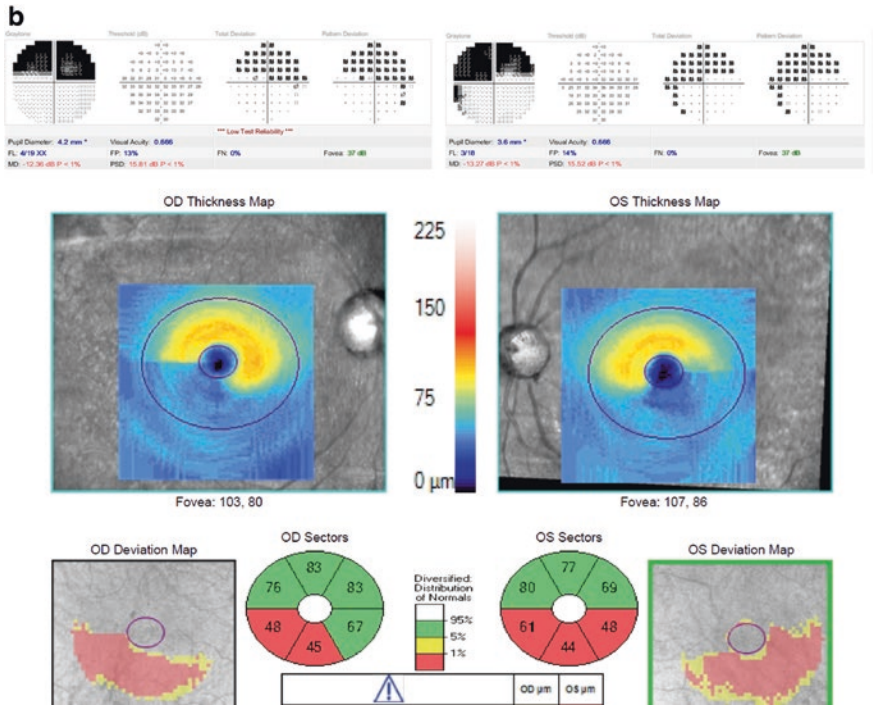

Fig. 4 (continued)

Case 4- Glaucoma Affecting the Central Field

A 79-year old female is followed in the glaucoma clinic with a diagnosis of normal tension glaucoma. Her visual field shows a paracentral scotomas in the right eye and is normal in the left eye. OCT shows inferior RNFL wedge defects in the inferotemporal region of both eyes (Fig. 5a). Significant asymmetrical inferior thinning in macula can be seen in both eyes, right eye more than left (Fig. 5b).

Case 5- Preperimetric Glaucoma with Abnormal OCT

OCT can detect glaucoma before any change in visual field. A 73-year woman with normal IOP is referred to glaucoma clinic for evaluation of a glaucomatous optic disc (Fig. 6a). Significant thinning is more prominent for ONH rim, and

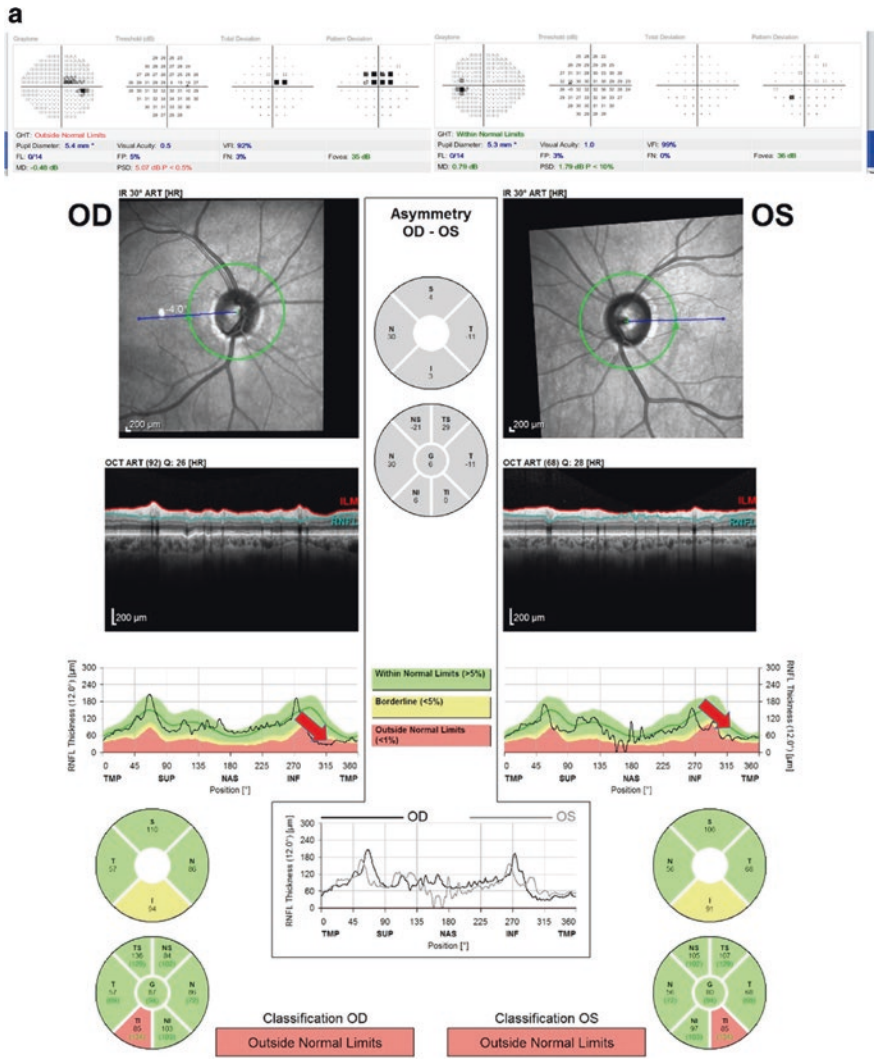

Fig. 5 **a** Spectralis RNFL report with good quality (Q = 26 and 28 in right eye and left eye, respectively) shows RNFL thinning in the inferotemporal region in both eyes. The RNFL thickness profile should be checked carefully as sometimes the narrow thinning of RNFL might not be flagged in the pie chart (red arrow). 24–2 visual field shows a superior paracentral scotoma in the right eye and is normal in the left eye. **b** Posterior pole Asymmetry Analysis Report shows arcuate thinning in the inferior macula in both eyes (red arrow). The Hemisphere Asymmetry map also demonstrates areas of significant thinning in the inferior hemisphere compare to superior hemisphere (blue arrow). This is also confirmed by the values shown in the Average Thickness Chart (orange arrow)

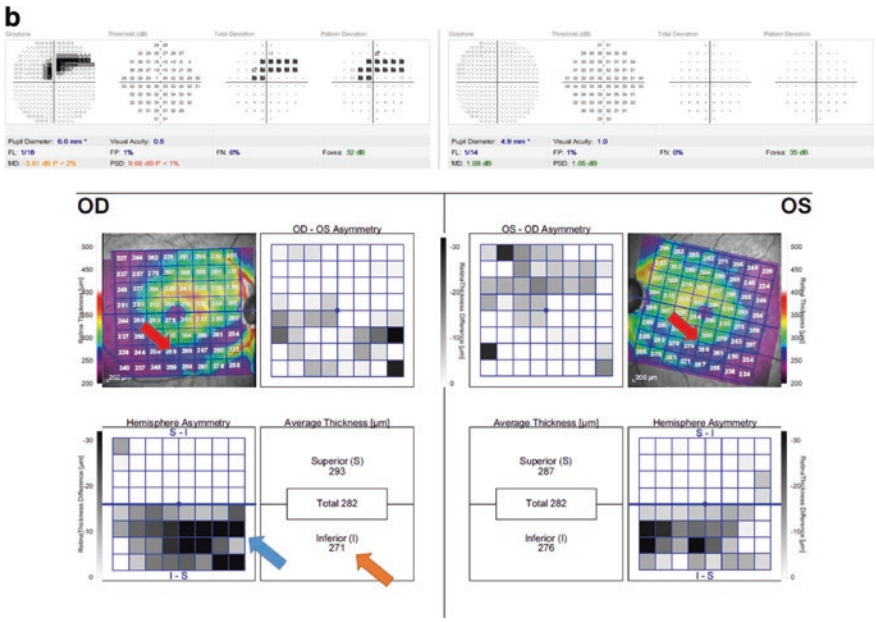

Fig. 5 (continued)

there is an inferotemporal wedge defect in RNFL. However, the 24–2 visual field is normal. Macular GCIPL does not showed significant thinning. The patient has preperimetric glaucoma and ocular hypotensive therapy has been started. Cirrus HD-OCT GPA analysis showed no progression in her eyes over 3 years (Fig. 6b and c).

Case 6- Moderate Glaucoma (Structure–Function Relationship)

GCIPL can detect changes in structure prior to RNFL. An 82-year male glaucoma patient is followed in glaucoma clinic. He has an inferior arcuate defect OD and biarcuate defects OS (Fig. 7a). He has significant RNFL thinning in the supratemporal region OU. The GCIPL report showed superior thinning in the right eye and

a

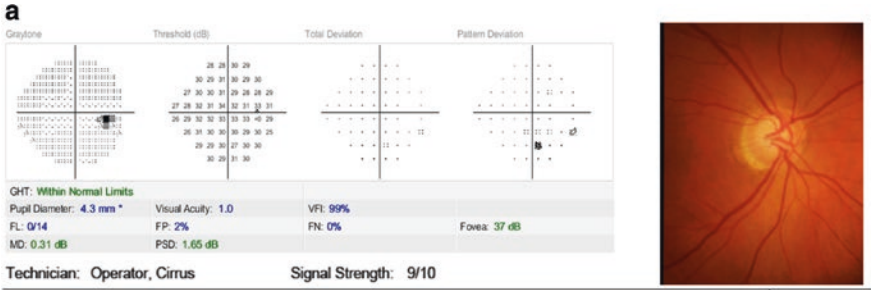

ONH and RNFL OU Analysis:Optic Disc Cube 200x200 OD ● ○ OS

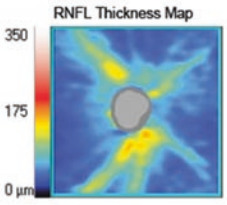

	OD	OS
Average RNFL Thickness	75 µm	X
RNFL Symmetry	X	
Rim Area	0.70 mm²	X
Disc Area	1.92 mm²	X
Average C/D Ratio	0.80	X
Vertical C/D Ratio	0.84	X
Cup Volume	0.513 mm³	X

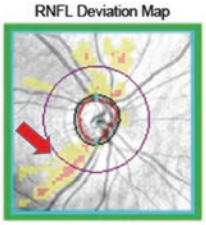

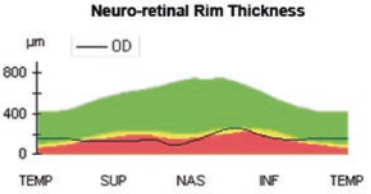

Disc Center(-0.24,0.12)mm

Extracted Horizontal Tomogram

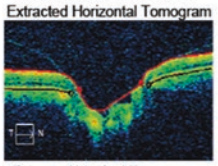

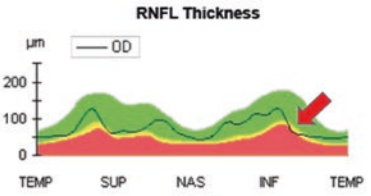

Extracted Vertical Tomogram

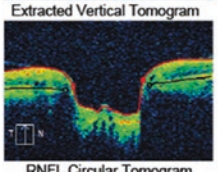

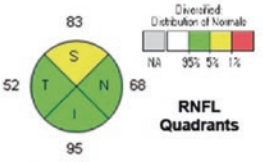

RNFL Circular Tomogram

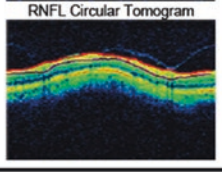

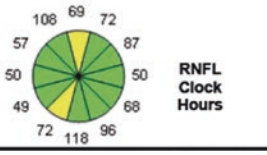

◀ **Fig. 6** **a** Cirrus HD-OCT ONH and RNFL OU report. The most useful parameters for differentiating normal and glaucomatous patients are: vertical thickness of neuroretinal rim, overall area of rim, vertical C/D ratio, average RNFL thickness, RNFL thickness in lower temporal zone and in the lower quadrant. Although average RNFL thickness is normal, deviation map shows significant thinning of the RNFL in inferotemporal region (red arrows). **b** PanoMap Analysis Report displays the information from ONH, and macula in one printout. ONH parameters are affected more than RNFL thickness parameters. GCIPL and macula thickness is pretty normal in this preperimetric case. **c** Cirrus HD-OCT GPA, right eye (2011–2014). No significant change has been shown in RNFL thickness map progression Analysis and trend analysis. In the summary analysis box, check boxes are not checked for RNFL thickness map progression, RNFL thickness profile progression, average RNFL thickness progression, and Average cup-to-disc ratio progression

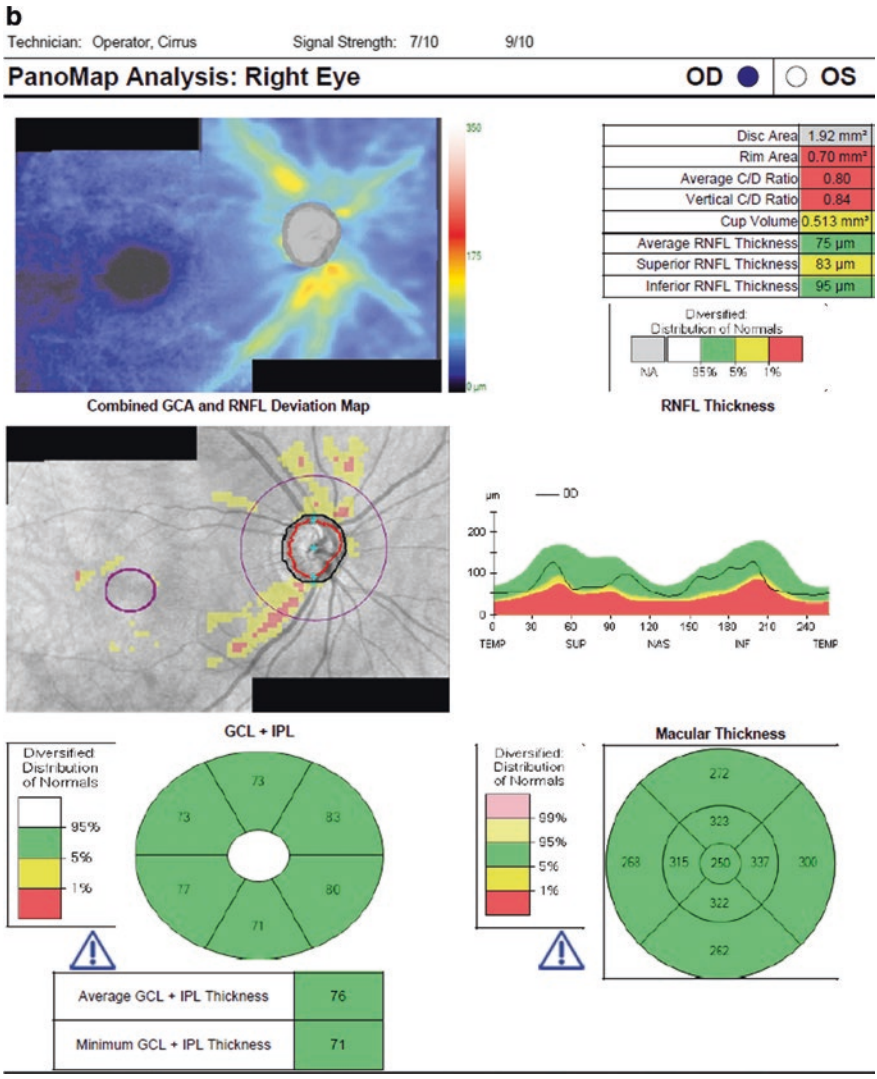

Fig. 6 (continued)

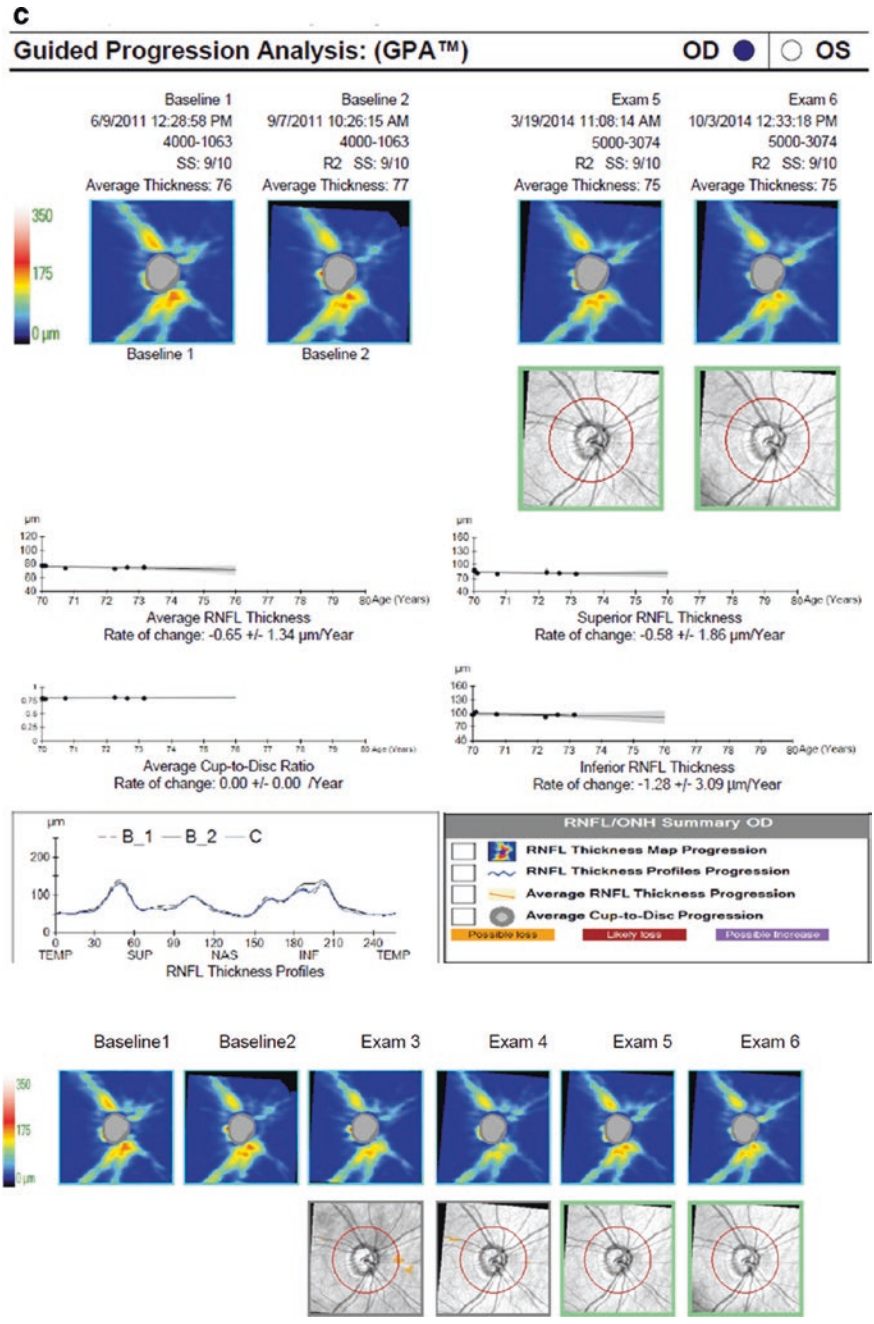

Fig. 6 (continued)

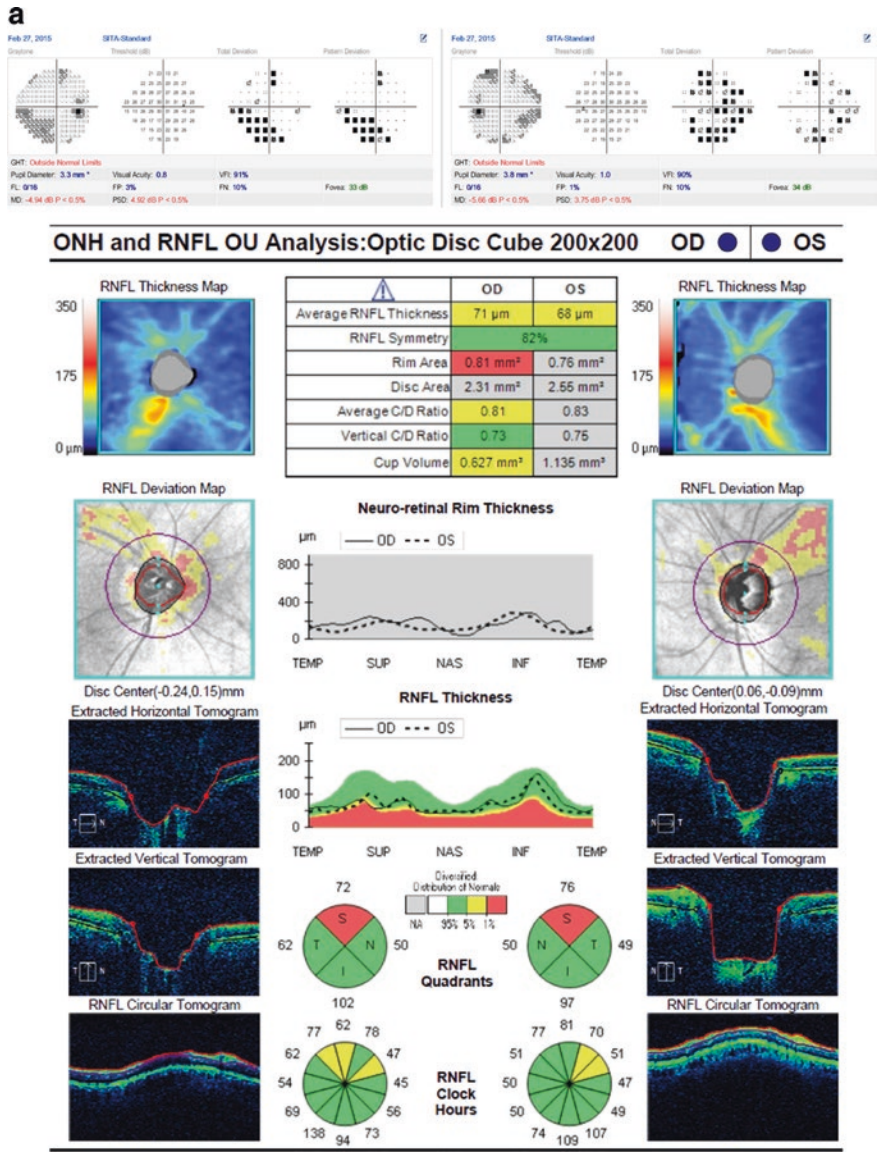

Fig. 7 **a** ONH and RNFL OU report shows a wedge-shaped RNFL defect in the superatemporal quadrant of the both eyes. The TSNIT profile, RNFL quadrant and clock hour graphs are abnormal in both eyes. The 24–2 visual field shows an inferior arcuate scotoma in the right eye and inferior and superior arcuate scotoma in the left eye. **b** Cirrus-HD OCT Ganglion Cell Analysis. A large area of GCIPL damage is evident in the inferotemporal and supratemporal regions of the left macula confirmed by abnormal sectors in average GCIPL thickness. In the right eye, although the GCIPL thinning can be detected in the superior sector, an area of increased thickness [focal hot area temporal to macula (red arrow), white sectors in pie chart (blue arrow)] can also be seen. The right eye has a parafoveal telangiectasia, and the macula scans are not reliable for glaucoma monitoring due to retinal edema in this eye

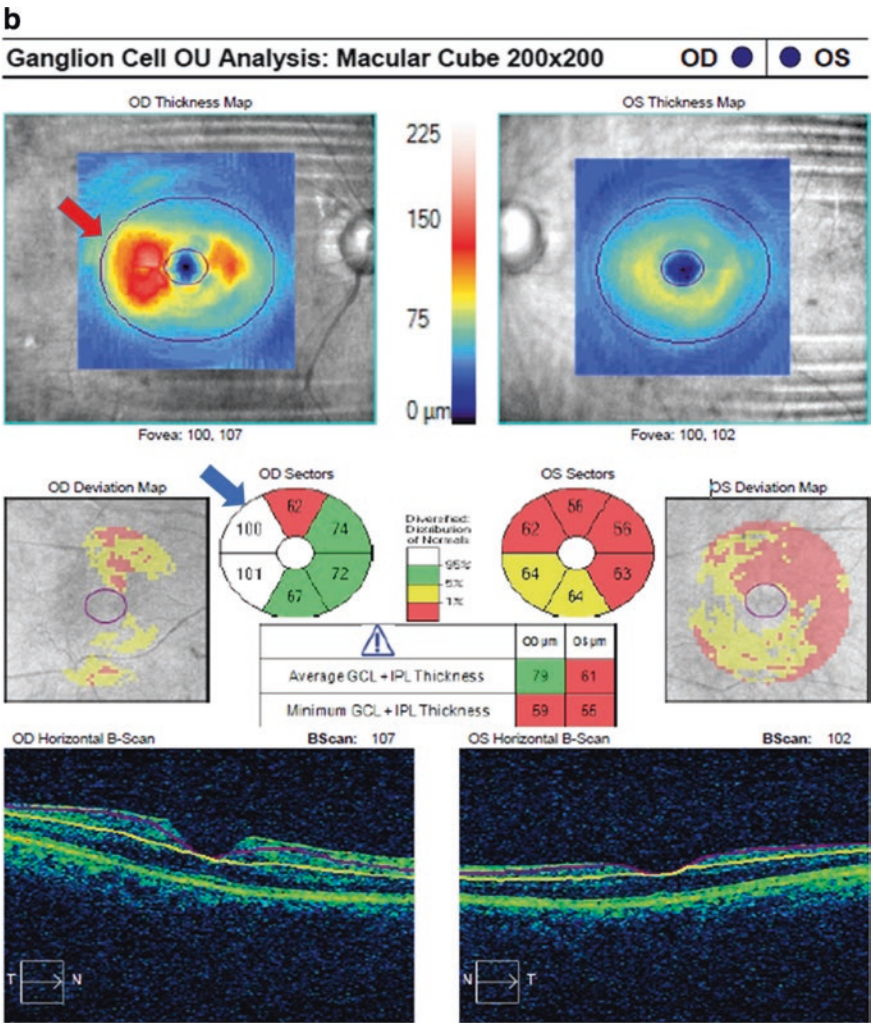

Fig. 7 (continued)

thinning in both hemispheres in the left eye. There is a good anatomical structure–function relationship between superior RNFL and GCIPL thinning and inferior visual defects in right eye. In the left eye the GCIPL detects inferior and superior macular thinning that is consistent with the biarcuate defect (Fig. 7b). However, the RNFL does not demonstrate inferior thinning expected with the biarcuate defect. In this case GCIPL showed earlier structural loss than RNFL.

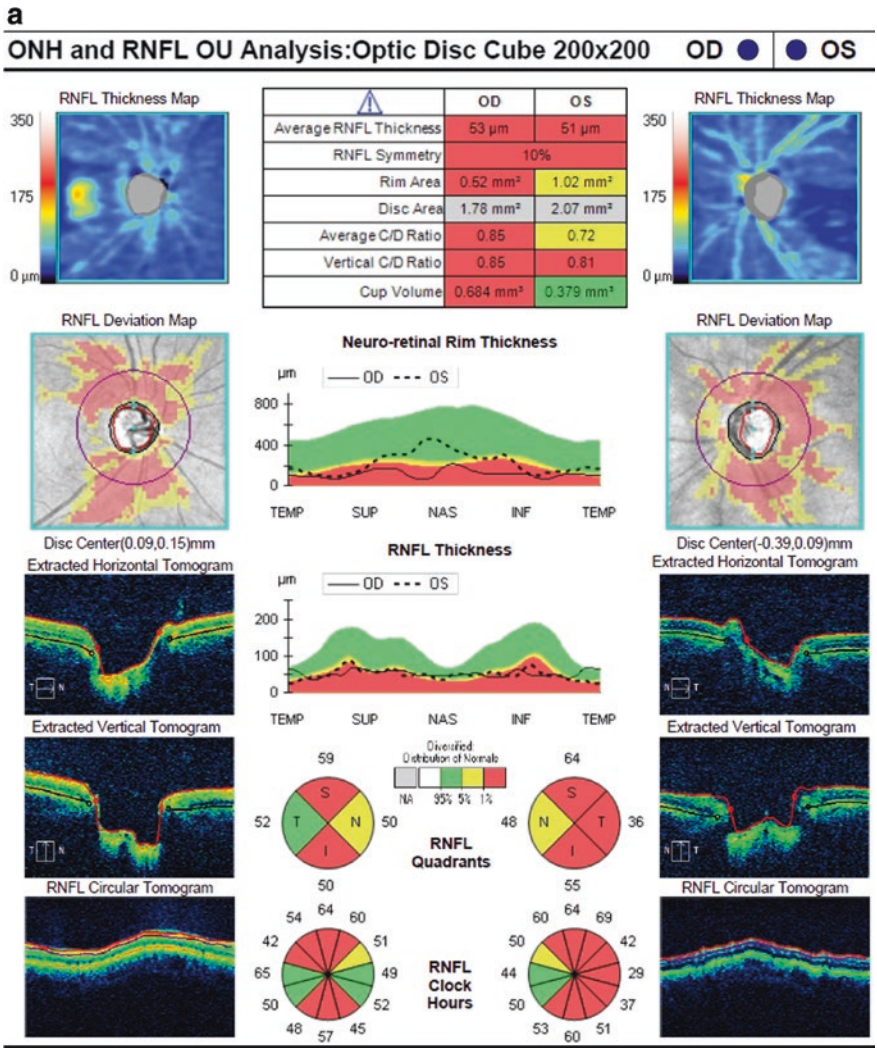

Fig. 8 **a** Cirrus HD-OCT report demonstrates that ONH and RNFL parameters are severely altered in both eyes. ONH morphological parameters are all pathological and average RNFL thickness of the right and left eye are 53 µm and 51 µm, respectively. However, certain areas (nasal and temporal sectors) show RNFL thickness within normal limits. The thickness maps are diffusely blue due to thinning. **b** Guided Progression Analysis of the right eye shows stable glaucoma without any significant change in the thickness map or RNFL thickness profile. The RNFL trends are also stable in the superior and inferior hemispheres. The visual field demonstrates functional damage, showing decrease of MD from –8.12 to –10.39 dB, and expansion of the inferior arcuate scotoma and development of a new scotoma superiorly. This is the end stage of the disease where functional damage outweighs OCT evidence of structural damage

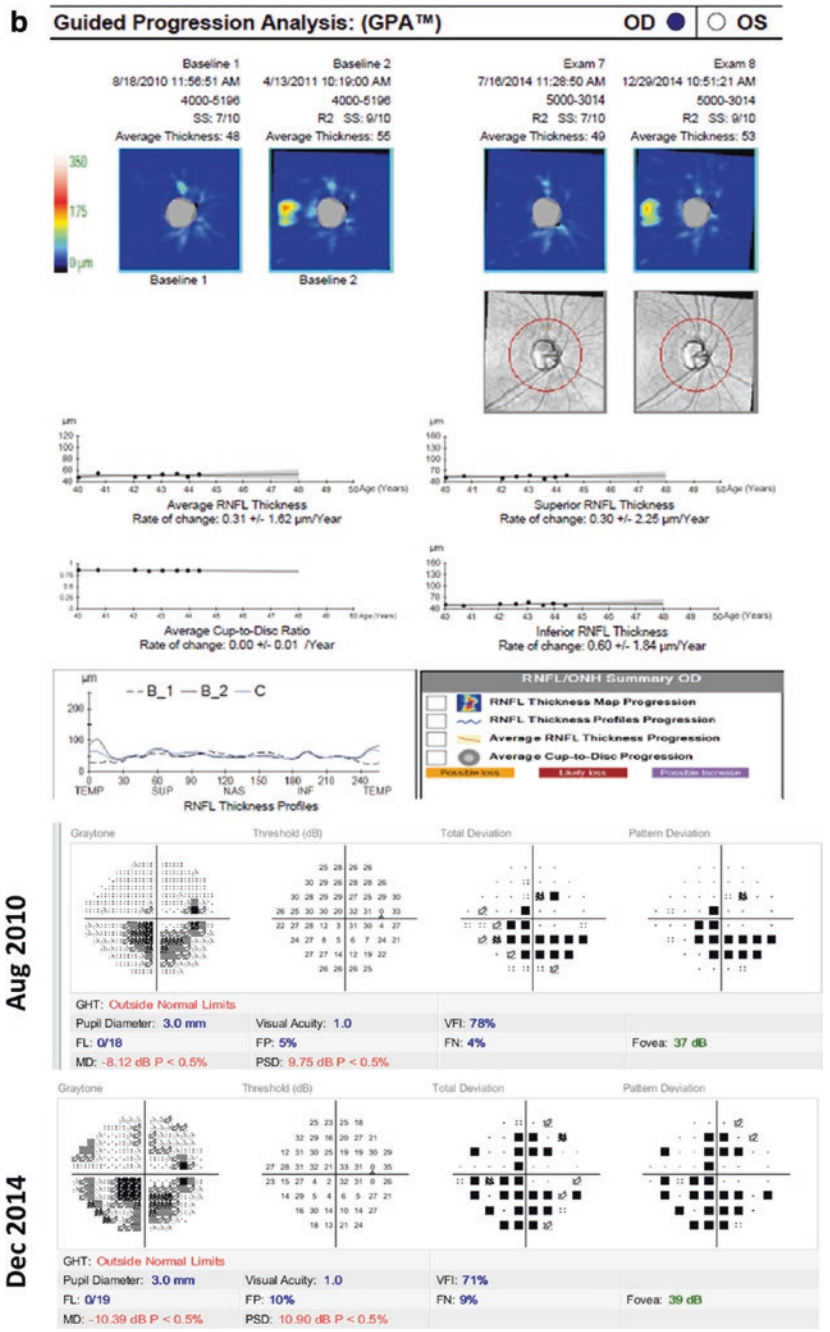

Fig. 8 (continued)

Floor Effect

Some evidence exists that in advanced disease SDOCT measurements are not useful for measuring tissue thickness because of the presence of a floor effect, after which no more thinning is observable. This floor effect, possibly owing to the presence of residual tissue (eg, glial cells, blood vessels or failure of tissue segmentation algorithms (ie, an artifactual floor)), is thought to be a serious problem for monitoring structural changes in eyes with advanced glaucoma [6]. It is often challenging to detect any observable change with optical imaging even though the patient with advanced disease may be progressing. The RNFL thickness values almost never decrease to less than 30 μm, and in most of the devices 50 μm is considered the floor of RNFL thickness.

Monitoring of disease in eyes with advanced glaucoma must rely on standard automated perimetry or other visual function tests. A longitudinal study [2] found that GCLIPL thickness was the least likely SDOCT parameter to reach the floor across most of the image area at baseline, suggesting that this parameter could be the most useful parameter for detecting change in advanced glaucoma. Recently, we demonstrated OCTA-measured vessel density parameters are promising tools for monitoring progression in late-stage glaucoma (particularly when VF MD is worse than -14 dB) because they do not have a detectable measurement floor [3].

Case 7- Advanced Glaucoma

A 44-year old female is monitored in clinic due to glaucoma. She has had trabeculectomy on both eyes, with IOP ranging from 15 to 18 mmHg OU. Although the OCT shows extensive thinning OU, there was no change in RNFL thickness over 4 years (Fig. 8a). Meanwhile, 24–2 demonstrates deterioration in both the superior hemifield and inferior hemifield of both eyes. The lack of RNFL progression is due to the floor effect (Fig. 8b).

RNFL Asymmetry

Inter-eye RNFL asymmetry is an early sign of glaucoma. 95% of normal eyes showed an asymmetry in mean inter-eye average RNFL thickness of 9 to 17 μm. The inter-eye difference of RNFL thickness for global average followed by superior and inferior were shown to be greatest among SDOCT machines in glaucomatous patients. The average inter-eye asymmetry of the mean RNFL thickness for global average is 6.60 times greater in open angle glaucoma than normal eyes by SDOCT (Spectralis; Heidelberg Engineering). Inter-eye average RNFL thickness

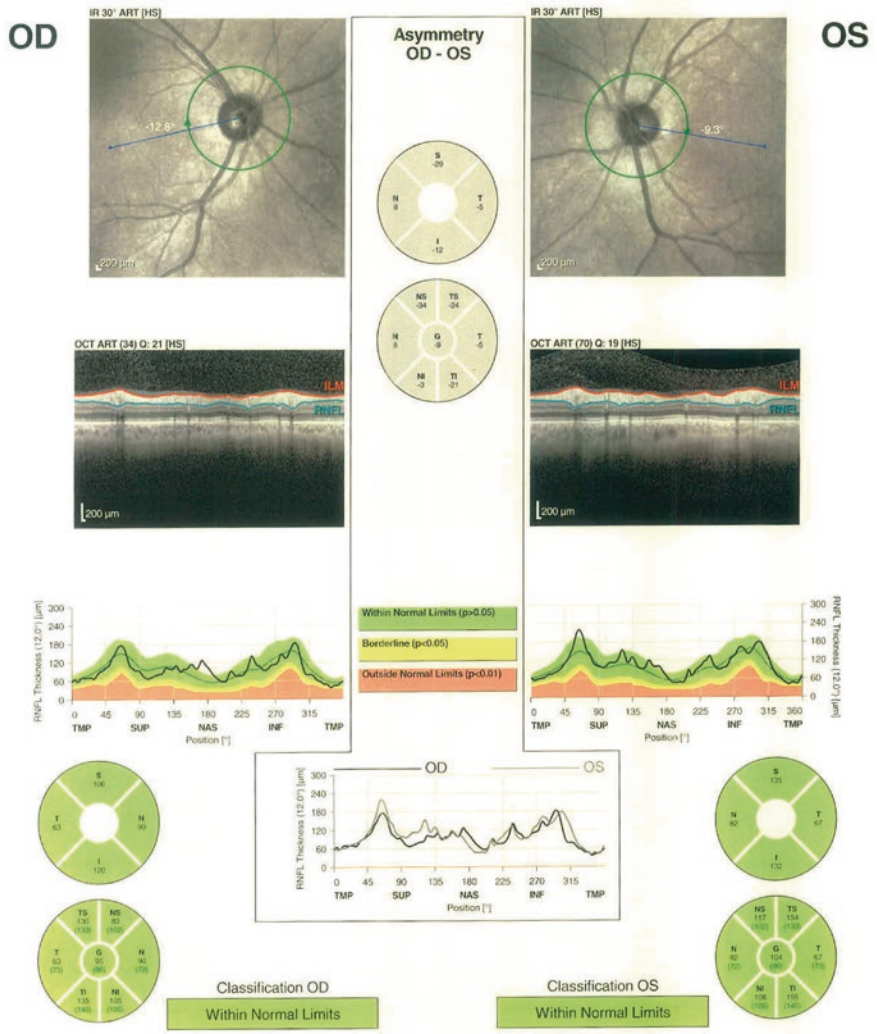

Fig. 9 Spectralis SDOCT retinal nerve fiber layer printout. The printout is for a 52-year-old woman with ocular hypertension. Average RNFL is 95 µm in the right eye and 104 µm in the left eye with an inter-eye global RNFL thickness difference of –9 µm. Although global average thickness is within normal limits (green), the asymmetry of 9 µm is an early sign of glaucomatous damage and early treatment is beneficial. This is an example of 'Green Disease'

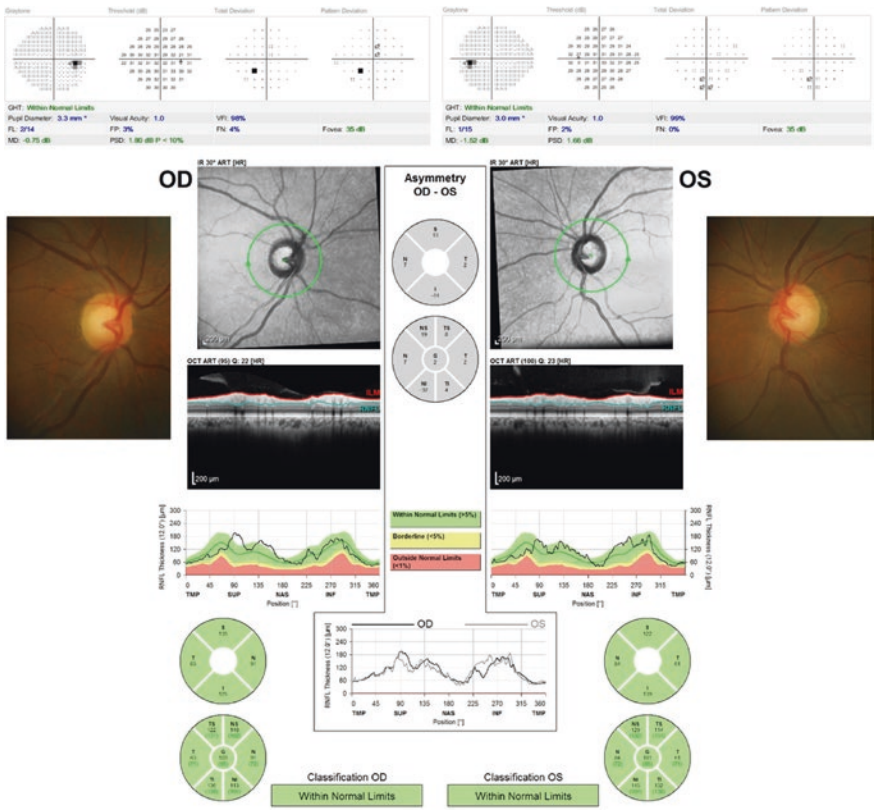

Fig. 10 Spectralis RNFL single report demonstrating normal RNFL profile and average thickness of 100 and 103 μm in right eye and left eye respectively. No obvious wedge defect is observed. Optic cup-to-disc ratio was 0.7 in right eye and 0.8 in the left eye. The visual field is full in both eyes

asymmetry is the best differentiator between normal and glaucoma subjects. Difference of inter-eye average RNFL thicknesses greater than 6 μm is suggestive of glaucoma.

Case 8- Preperimetric Glaucoma

A 52-year-old woman with a diagnosis of ocular hypertension was referred to our clinic. The IOP of her right eye was 26 and left eye was 25 mmHg. There was minimal disc excavation in either eye. Central corneal thickness was 524 and

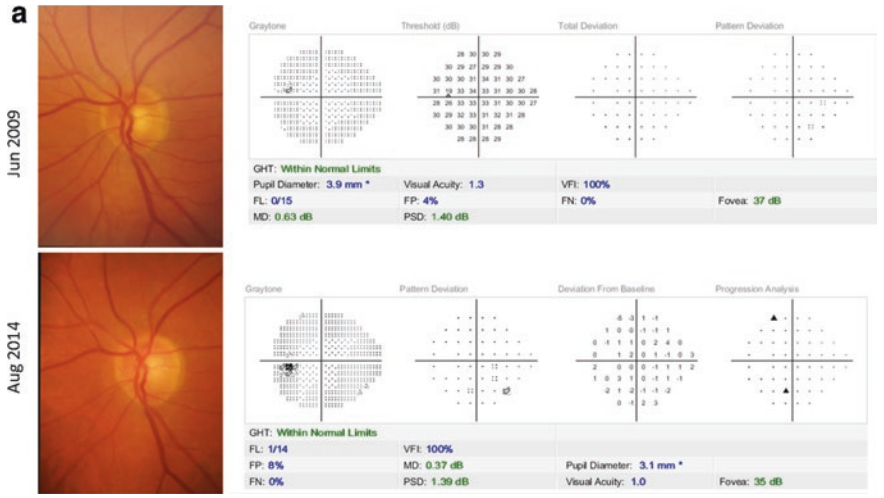

Fig. 11 **a** Optic disc photograph and visual field of the patient in 2009 and 2014. No significant change was found in disc and 24–2. **b** Cirrus HD-OCT GPA, Left eye (2009–2014). (a) RNFL thickness map progression analysis shows significant RNFL thinning in the inferior and superior quadrants (yellow arrow). The GPA marked these areas as "likely loss" and a red checkmark is present in the summary box because the thinning is present in consecutive scans. RNFL thickness profile progression plot also shows RNFL thinning in the superior quadrant and areas with significant progression are displayed in red. The trend analysis based RNFL thickness plots detected statistically significant progression as shown in the summary box. The rate of progression is fastest in the superior quadrant (red arrow). Average cup-to-disc ratio progression is also statistically significant. Repeatable changes in both the superior and inferior quadrants on the change maps can be observed after exam 5 which are flagged with red color (blue arrow)

526 μm in right eye and left eye, respectively. Visual fields were normal and the OCT printout sectors were all in the green zones. However, the average RNFL was 9 μm thinner in the right eye (Fig. 9). Due to RNFL asymmetry and thinned corneas an anti-glaucoma medication was started.

Case 9- Physiologic Cup

A 44-year old patient was referred to glaucoma clinic due to suspicious cupping. IOP is 16 mmHg OU. Optic cup-to-disc ratio was 0.7 in right eye and 0.8 in the left eye, with no obvious RNFL wedge defect. Visual field was normal in both eyes. RNFL thickness from Spectralis OCT report was also normal.(Fig. 10) A diagnosis of familial high cup-to-disc ratio was made and confirmed by examination of his brother and his son.

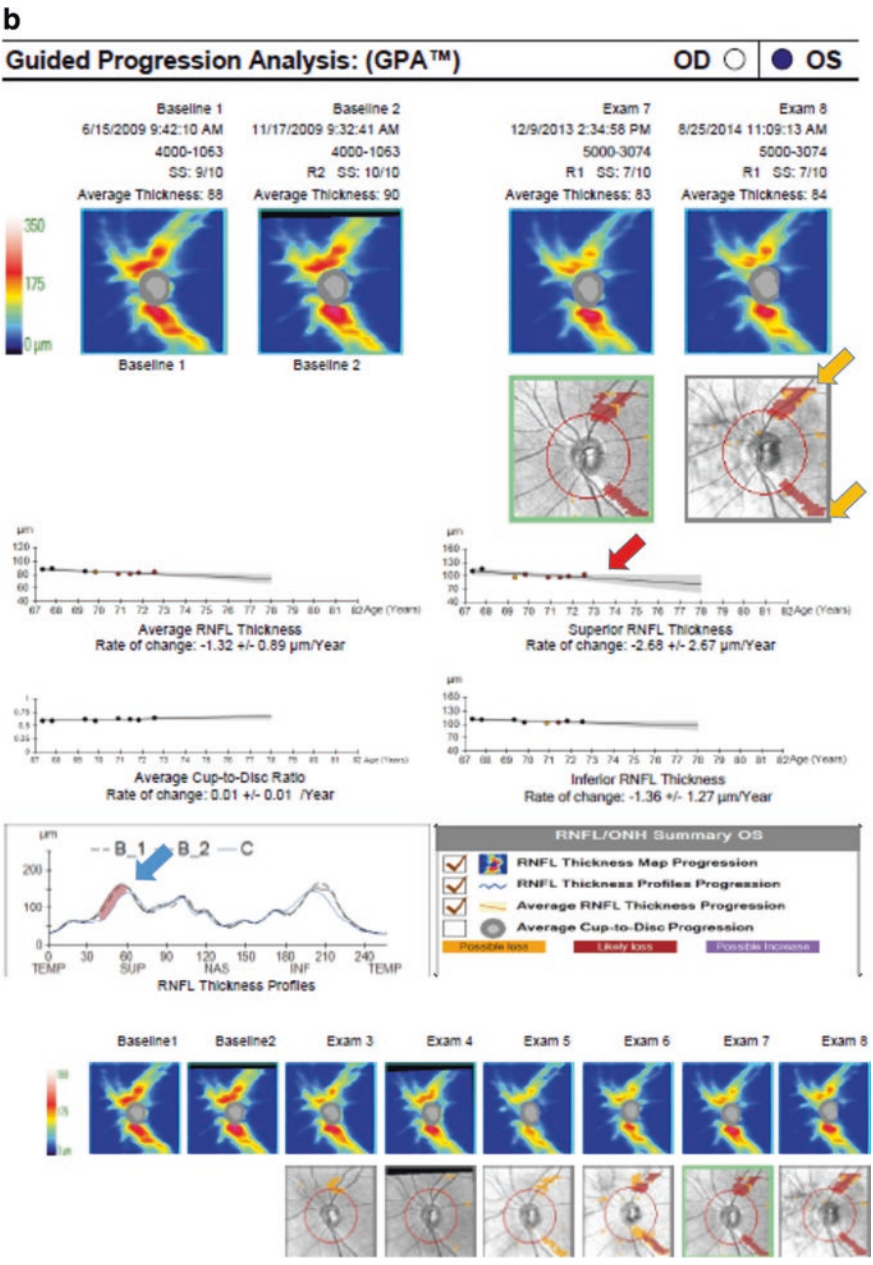

Fig. 11 (continued)

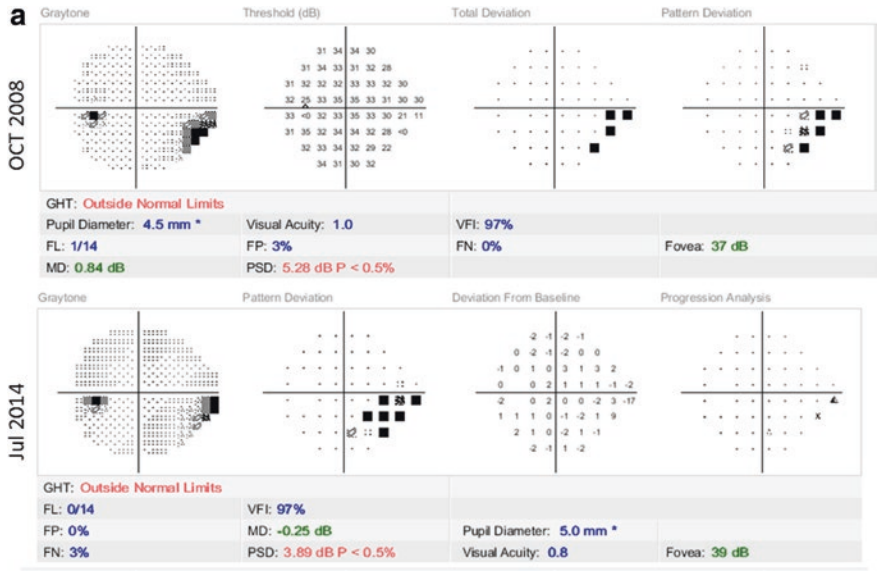

Fig. 12 **a** Visual field shows inferior nasal step in the left eye. No significant change was found in the VF GPA analysis on 2014. **b** Cirrus HD-OCT's GPA (2008–2014) shows stabilized thickness, and no likely loss in change map, RNFL thickness profile progression plot, trend analysis. The average RNFL thickness is stable around 70 μm. RNFL thickness map is flagged as probable progression but the change map does not shows a characteristic wedge shape defect (red arrow). This is probably artifactual due to an artifact of the image in the periphery of the image

Case 10- Glaucoma Progression in Early Glaucoma

A 67-year old was first seen in 2009. Her IOP in the right eye was 24 mmHg in 2009 and she was started on prostaglandin analogue drops. The IOP ranged between 18 and 21 mmHg during follow-up without any findings of optic nerve head progression on funduscopy. Multiple abnormal points on the visual field developed on the event tracker in 2014 but the GPA report did not show progression. Meanwhile, the **OCT GPA Report** showed significant progression in OCT (Fig. 11a). A fixed combination of a carbonic anhydrases inhibitor and beta blocker was added, which lowered the IOP to 14 mmHg (Fig. 11b).

Case 11- Early Glaucoma, no Progression

A 59-year old woman was referred to glaucoma clinic with an IOP of 23 mmHg in the left eye. Central corneal thickness was 535 μm. Optic disc was suspicious with an area of rim thinning inferiorly. The visual field showed inferior nasal step in the

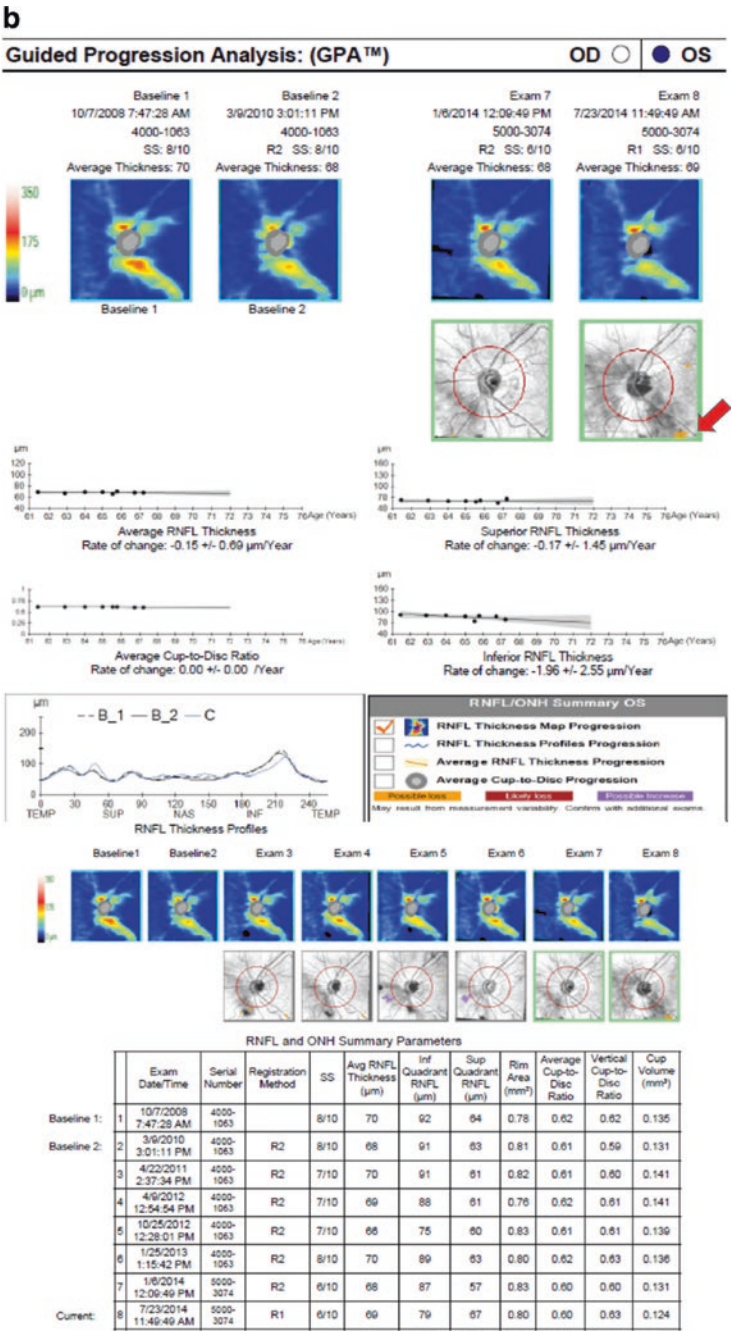

RNFL and ONH Summary Parameters

		Exam Date/Time	Serial Number	Registration Method	SS	Avg RNFL Thickness (µm)	Inf Quadrant RNFL (µm)	Sup Quadrant RNFL (µm)	Rim Area (mm²)	Average Cup-to-Disc Ratio	Vertical Cup-to-Disc Ratio	Cup Volume (mm³)
Baseline 1:	1	10/7/2008 7:47:28 AM	4000-1063		8/10	70	92	64	0.78	0.62	0.62	0.135
Baseline 2:	2	3/9/2010 3:01:11 PM	4000-1063	R2	8/10	68	91	63	0.81	0.61	0.59	0.131
	3	4/22/2011 2:37:34 PM	4000-1063	R2	7/10	70	91	61	0.82	0.61	0.60	0.141
	4	4/9/2012 12:54:54 PM	4000-1063	R2	7/10	69	88	61	0.76	0.62	0.61	0.141
	5	10/25/2012 12:28:01 PM	4000-1063	R2	7/10	66	75	60	0.83	0.61	0.61	0.139
	6	1/25/2013 1:15:42 PM	4000-1063	R2	8/10	70	89	63	0.80	0.62	0.63	0.136
	7	1/6/2014 12:09:49 PM	5000-3074	R2	6/10	68	87	57	0.83	0.60	0.60	0.131
Current:	8	7/23/2014 11:49:49 AM	5000-3074	R1	6/10	69	79	67	0.80	0.60	0.63	0.124

Fig. 12 (continued)

left eye. Anti-glaucoma medication was started. The patient was followed every 6 month with Cirrus HD-OCT and no significant change was found on VF or OCT during follow-up (Fig. 12a and b).

Acknowledgments FUNDING/SUPPORT: Supported in part by National Institutes of Health/National Eye Institute grants R01 EY029058 (RNW), by core grant P30EY022589; by an unrestricted grant from Research to Prevent Blindness (New York, NY); by grants for participants' glaucoma medications from Alcon, Allergan, Pfizer, Merck, and Santen, and by the donors of the National Glaucoma Research Program, a program of the BrightFocus Foundation.

Financial Disclosure: S. Moghimi, None; M. Safizadeh, None; Andrew Camp, None; R.N. Weinreb, Heidelberg Engineering (F), Carl Zeiss Meditec (F, R), Konan (F), National Eye Institute (F), Optovue (F), Allergan (C), Bausch&Lomb (C,F), Eyenovia (C), Novartis (C)

References

1. Lee J, et al. Temporal raphe sign for discrimination of glaucoma from optic neuropathy in eyes with macular ganglion cell–inner plexiform layer thinning. Ophthalmology. 2019;126(8):1131–9.
2. Bowd C, et al. Estimating optical coherence tomography structural measurement floors to improve detection of progression in advanced glaucoma. Am J Ophthalmol. 2017;175:37–44.
3. Moghimi S, et al. Measurement floors and dynamic ranges of OCT and OCT angiography in glaucoma. Ophthalmology. 2019;126(7):980–8.

OCT Artifacts in Glaucoma

Sasan Moghimi, Mona SafiZadeh, Andrew Camp and Robert N. Weinreb

Introduction

Recent evidence indicates that OCT imaging artifacts are a common finding in clinical practice. Poor scan quality can affect the ability of OCT to detect glaucoma and monitor its progression. In addition, these technological devices have biological, engineering, and biophysical limits so these devices cannot be 100% specific and 100% sensitive at all times. Therefore, it is important for clinicians to identify the various OCT imaging artifacts and critically evaluate test results to apply that knowledge to the interpretation of testing results. Otherwise, they will be managing false-positive 'Red Disease' and possibly over-treating patients. Errors in data acquisition due to media opacity, extreme myopia, difficulties comparing to normative databases, operator misalignment, individual blink, or software analysis difficulties can confound interpretation of OCT data and may falsely change the classification to abnormal. The factors that are correlated to the artifacts can be classified into patient-dependent, operator-dependent, and device-dependent factors.

On the other hand, recognition of false-negative 'green disease' is of importance in diagnosing and treating glaucoma. Understanding the limitations of imaging technologies coupled with the evaluation of serial OCT analyses, prompt clinical examination, and structure–function correlation is important to avoid missing real glaucoma requiring treatment. For example, progressively decreasing retinal nerve fiber layer (RNFL) thickness may reveal the presence of progressive glaucoma that, because of green labeling, can be missed by the clinicians. Ocular

S. Moghimi (✉) · A. Camp · R.N. Weinreb
Department of Ophthalmology, Hamilton Glaucoma Center, Shiley Eye Institute, University of California, San Diego, CA, USA
e-mail: sasanimii@yahoo.com

M. SafiZadeh
Tehran University of Medical Sciences, Tehran, Iran

M. Mohammadpour (ed.), *Diagnostics in Ocular Imaging*,
https://doi.org/10.1007/978-3-030-54863-6_27

conditions that can increase RNFL thickness (i.e. uveitis, diabetic macular edema, peripapillary choroidal neovascularization) can also lead to 'Green disease' and make the diagnosis of coexisting glaucoma difficult.

Blink Artifact

Blink artifact is usually recognized by a black horizontal band on the RNFL thickness map. It blocks the OCT signal and if it overlays the calculation circle can lead to 'Red Disease'. Interpretation of the OCT printout should be made carefully in these cases.

Case 1-Blink Artifact

OCT scan of a 55-year-old woman with ocular hypertension of her right eye and pseudoexfoliation glaucoma of her left eye (Fig. 1). IOP was 21 mmHg OD with latanoprost and 26 mmHg OS with topical latanoprost and dorzolamide-timolol fixed combination.

Case 2-'Red Disease' Due to Blink Artifact

Another case of blink artifact in a glaucomatous patient. The OCT image has low quality due to poor cooperation. The blink artifact affects the calculation circle and optic nerve head analysis of both eyes. The average RNFL is 22 μm OD and 0 μm OS; both these thicknesses are less than floor, indicating artifact (Fig. 2a). The scan was repeated multiple times. In an improved scan (Fig. 2b), the blink artifact does not affect the measurement circle, and a wedge defect in the superior quadrant is evident in the right eye. The average RNFL is 77 μm OD (Fig. 2b), which is similar to his RNFL thickness 4 years ago. The visual field reveals inferior arcuate defect in the right eye and normal in the left eye, which corresponds with the RNFL wedge defect in the right eye.

'Red Disease' Due to Contour Shift

Patients demonstrate RNFL bundle peaks superotemorally and inferotemporally. However, the OCT normative database does not factor in anatomic variation in RNFL bundle peak locations. If a patient has a contour shift, i.e. a shift in their RNFL bundle peak locations in comparison to the normative database, this can

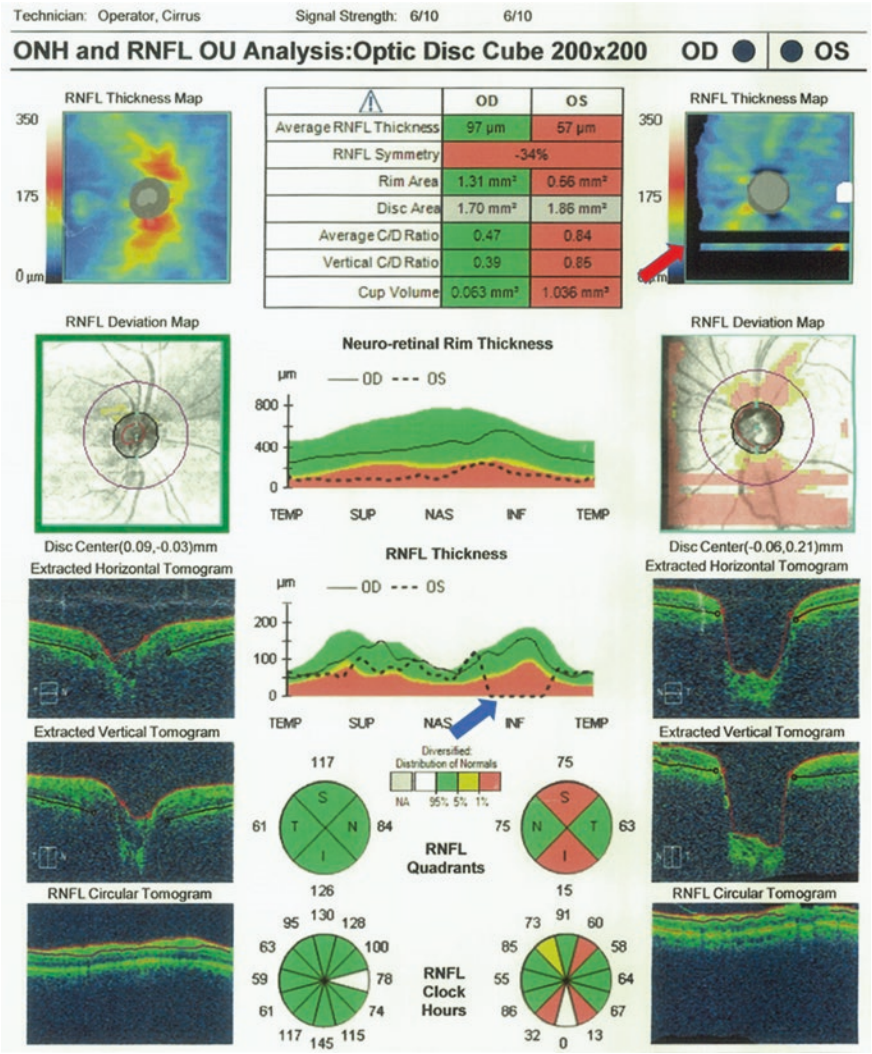

Fig. 1 Cirrus SD-OCT RNFL and ONH report. The quality of the scan is acceptable (Signal Strength = 6/10) in both eyes. The RNFL thickness map of the left eye shows blink artifact as an area of scanning blockage (red arrow). The segmentation of the inferior quadrant failed on the RNFL circular tomogram because the artifact coincides with the calculation circle in that area. The average RNFL thickness of the inferior quadrant is zero on the RNFL TSNIT (blue arrow) and pie graphs, which cannot occur due to floor effect

lead to an erroneous interpretation of RNFL thinning in healthy eyes. Contour shifts are most commonly seen in patients with high refractive errors. Contour shifts have been studied most extensively in myopic eyes. These studies have demonstrated that the superotemporal and inferotemporal bundles tend to converge temporally in myopic eyes [1].

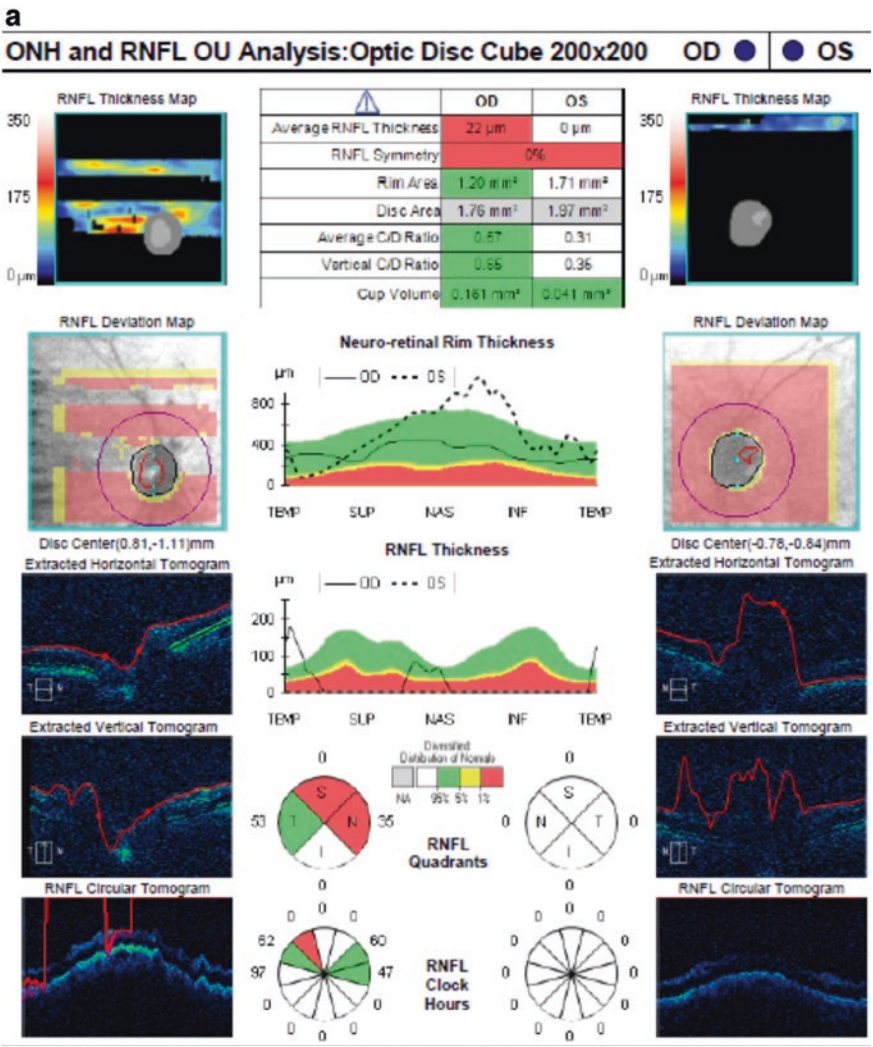

Fig. 2 **a** Cirrus SD-OCT RNFL and ONH report. The OCT image has low quality due to poor cooperation. The blink artifact affects the calculation circle and optic nerve head in the right eye. The average RNFL is 22 µm in the right eye. **b** The OCT is repeated. In this report, the blinking artifact does not affect the measurement circle, and the wedge defect in the superior quadrant is evident in the right eye. The average RNFL is 77 mm in right eye, which is similar to his RNFL thickness 4 years ago. **c** Visual Field indicating corresponding defects in the superior field in right eye. The visual field in left eye is full

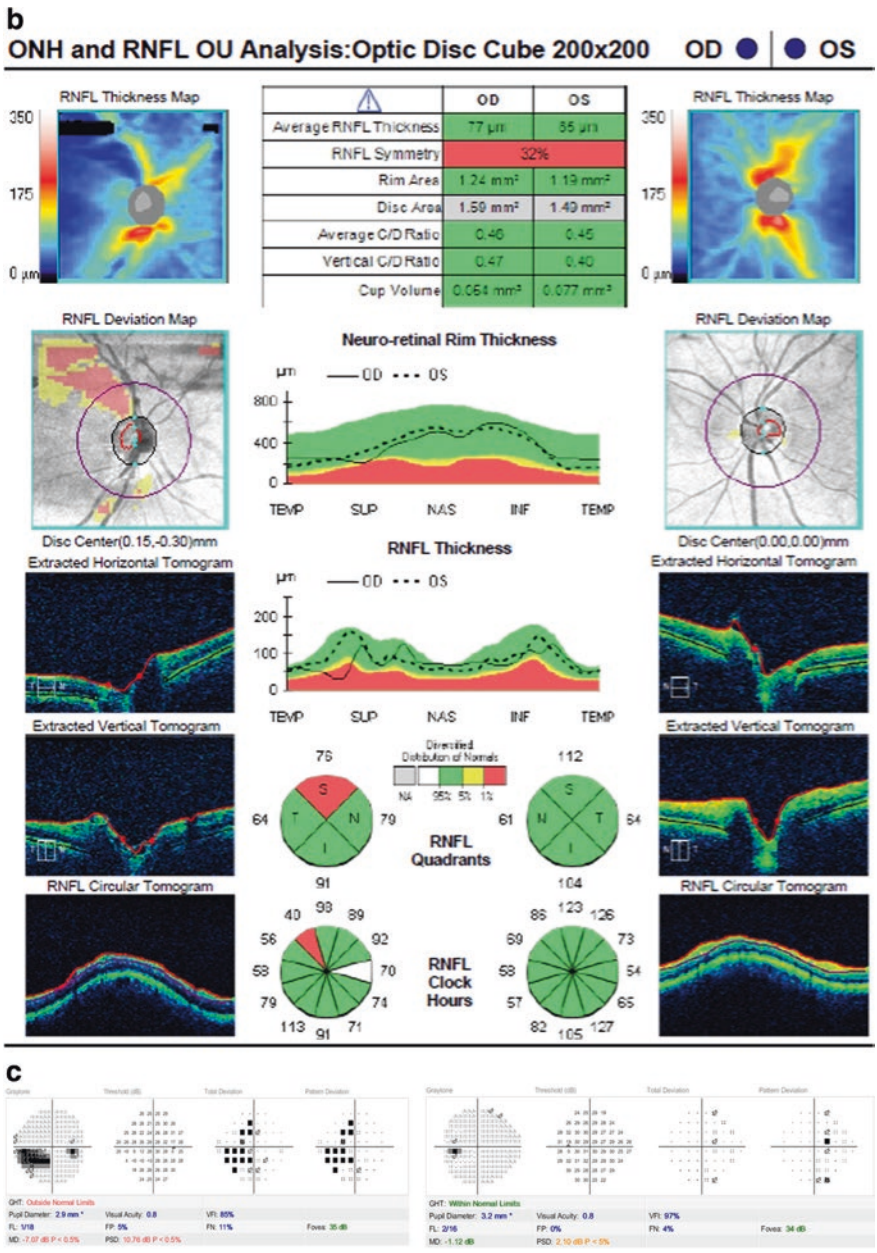

Fig. 2 (continued)

Case 3-'Red Disease' Due to Contour Shift

A 58-year old female with normal appearance of the optic nerve but a borderline IOP is referred for further work-up. Fundus examination and 24-2 visual field were normal. The patient had an OCT with reported abnormalities on the RNFL clock hours (Fig. 3). Contour shift is an anatomic variation from the average axis

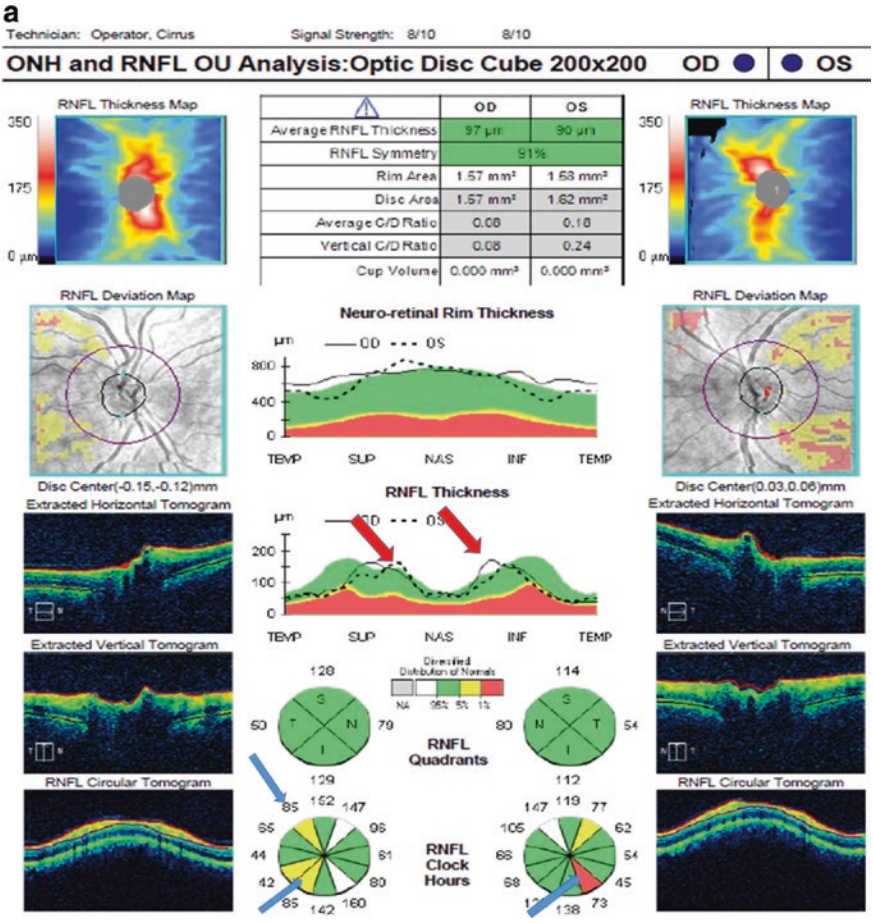

Fig. 3 **a** Cirrus SD-OCT RNFL and ONH report. The OCT image shows RNFL defects OU and the average RNFL thickness values were classified as normal by the normative database in both eyes. Inferotemporal and supratemporal RNFL thickness in both eyes and superior RNFL thickness in the left eye are outside of normal limits (blue arrows). The artifact is related to the nasal shift of the inferior and superior RNFL bundles (red arrows). If the RNFL thickness peaks were not shifted to the nasal area, the RNFL thickness lines would fit the normative database values. Note that ONH analysis (cup to disc ratio, rim area, and neuroretinal rim thickness) is within normal limit. **b** GCIPL OU analysis-Ganglion Cell Analysis of the patient shows the normal doughnut appearance in thickness map and green sectors

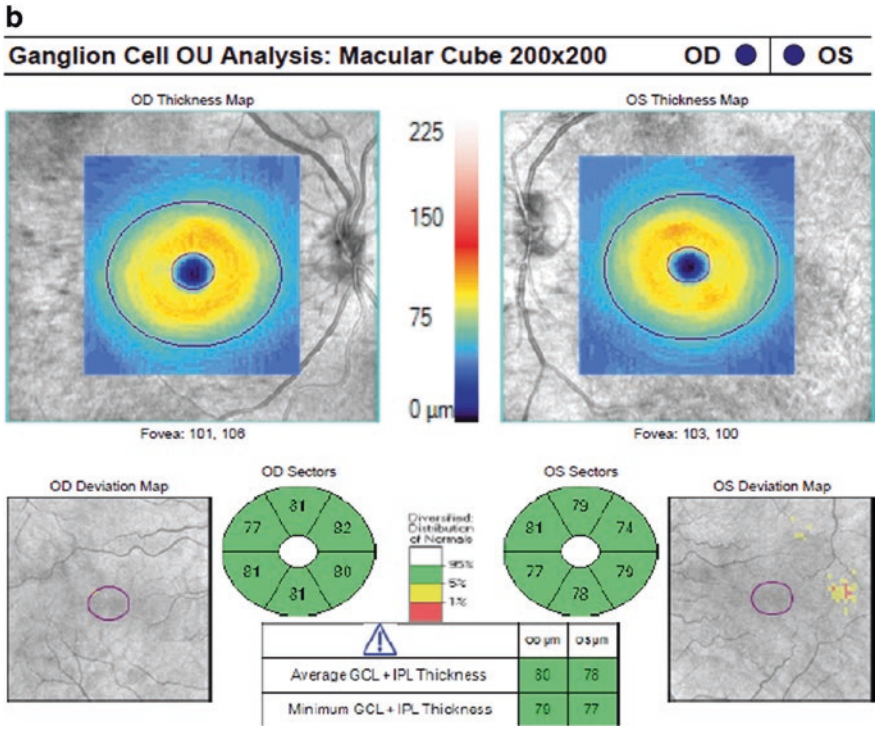

Fig. 3 (continued)

of a person's peak RNFL thickness. Note that the GCIPL OU report and ONH rim plot are normal. This is an example of red disease due to anatomic variation from the normative database and most commonly is seen in patients with high refractive errors. The locations of peak RNFL thicknesses in TSNIT profiles largely associated with the angles of major retinal vessels [2].

Case 4-'Red Disease' Due to Contour Shift

A 73-year old man is referred to clinic due to a reported abnormal RNFL OCT. His IOP was 21 mm Hg OD and 22 mmHg OS. CCT was 534 and 537 µm in right eye and left eye, respectively. The optic nerve head exam was normal, and no RNFL defect was found. RNFL OCT showed inferotemporal thinning in both eyes. However, a contour shift can be observed on the TSNIT plot with nasal shift of the inferotemporal RNFL bundle. This reassuring exam was confirmed by normal visual fields in both eyes. Glaucoma was excluded (Fig. 4). No further testing was performed and no treatment was started given the lack of glaucomatous optic neuropathy and artifactual thinning of the RNFL OCT.

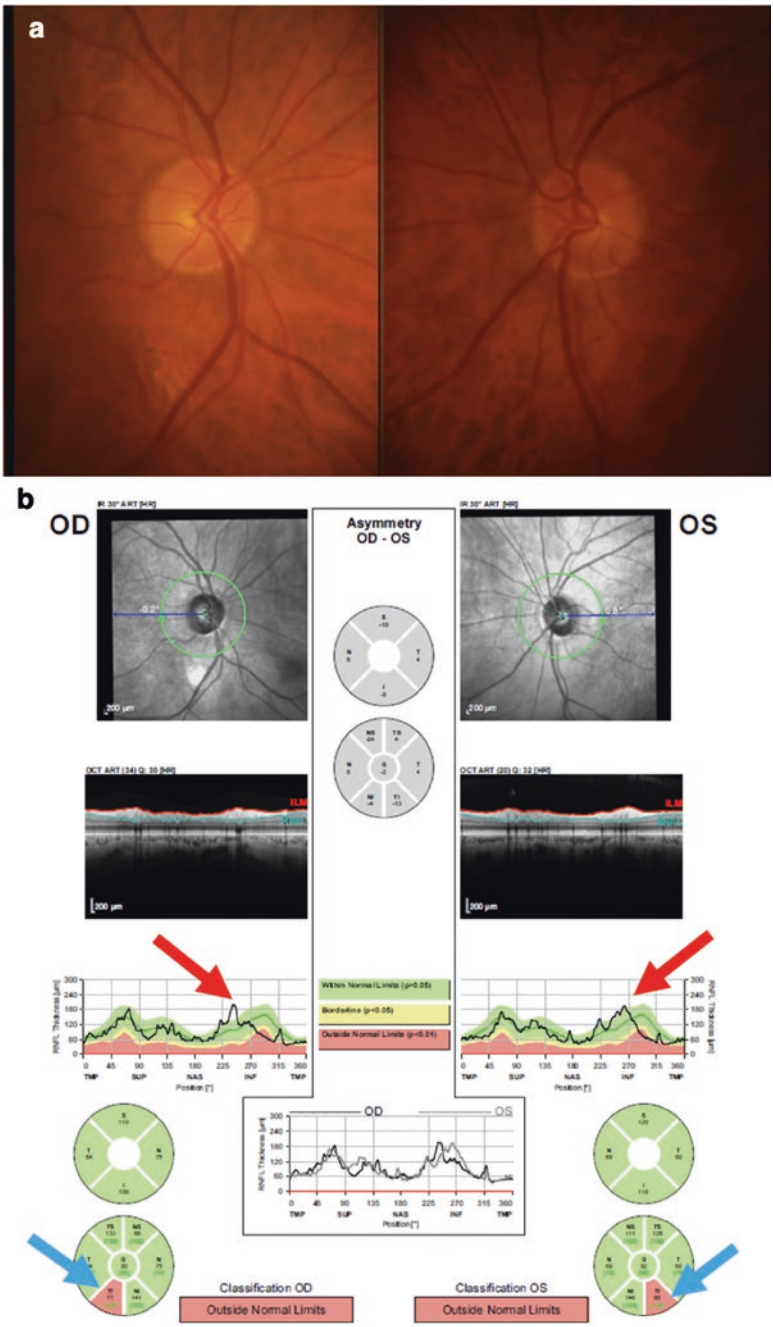

Fig. 4 **a** Optic nerve photos of right and left eyes demonstrating normal rim widths. **b** Contour shift of the RNFL OCT with nasal displacement of the inferotemporal RNFL bundles (red arrows) leading to artifactual inferotemporal thinning (blue arrows)

Case 5-Contour Shift: 'Red Disease' and 'Glaucoma'

A 67-year old female presented with suspicious optic nerve head excavation but a normal IOP of 18 mmHg right eye and 21 mmHg in the left eye. Gonioscopy showed open angles in both eyes. She is myopic −4.0 Diopter in both eyes. Central corneal thickness was 519 μm in the right eye and 521 μm in the left eye. On funduscopy, the right optic nerve was tilted. The vertical cup to disc ratio was borderline OU. RNFL OCT showed thinning of the inferior and superior quadrants. However, the peak of the RNFL was displaced temporally on TSNIT plot. Although the 'red disease' might be due to this displacement in the right eye, a decrease in the thickness of superior peak can be observed in left eye. This demonstrates that the wedge defect in the superior quadrant of the left eye is due to the glaucomatous process. This is confirmed by normal 24-2 visual field in right eye and inferior nasal step in the left eye (Fig. 4b). Prostaglandin analogue was prescribed for her left eye (Fig. 5a–c).

Case 6-High Myopia

A 66-year-old man is referred to the glaucoma clinic because of suspicious OCT printout. IOP is 17 mmHg OU. The optic nerve head is tilted without excavation OU. Previous visual field from 7 years prior shows a nonprogressive inferior arcuate defect in the right eye and a fairly normal visual in field left eye. RNFL OCT (Fig. 6a) demonstrates a different artifact like segmentation errors, and low signal strength. Nero-retinal TSNIT plots are normal as is the clinical rims. The patient is diagnosed as high myopic healthy subject. Stable scotoma has been reported in high myopic healthy eyes in Chinese population. Although macula scans are more helpful than RNFL thickness in high myopic patients, the patient shows diffuse GCIPL thinning in the GCIPL OU report (Fig. 6b). No raphe sign was observed. Diffuse GCIPL thinning can be seen in high myopic healthy eyes.

Case 7-Peripapillary Atrophy (PPA)

PPA is choroiretinal thinning and interruption of RPE in the peripapillary area and can interfere with proper segmentation of the RNFL. Below is an OCT scan of a 37-year-old woman with pathologic myopia: −21.00 diopter OD and −19.00 diopter OS. She had tilted discs, peripapillary atrophy, and staphylomas OU (Fig. 7).

FoDi Misalignment

On average, the fovea is located 7° below the level of the center of the ONH, but the angle can vary from 6° above to 29° below [3]. If these variations in fovea to disc (FoDI) axis are not taken into account, it may lead to artificially large

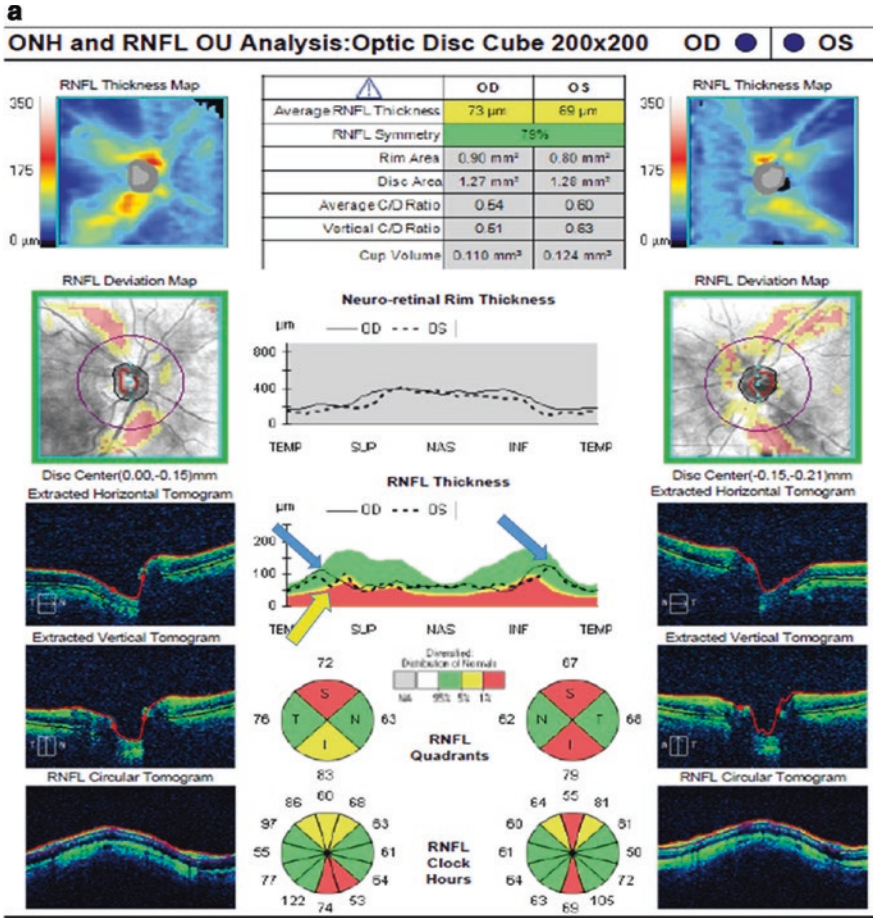

Fig. 5 **a** Cirrus SD-OCT RNFL and ONH report. The OCT image shows thinning of the inferior and superior quadrants. However, the peak of the RNFL is displaced to the temporal on TSNIT plot (blue arrows). Although the 'red disease' might be due to this displacement in the right eye, a decrease in thickness of superior peak can be observed in left eye (yellow arrow), suggesting glaucomatous damage in the left eye. **b** GCIPL OU analysis-Ganglion Cell Analysis of the patient Cirrus HD-OCT Macula GCL + IPL analysis shows the thinned area in the inferotemporal and inferior sectors in the left eye (blue arrow) with the typical Raphe sign in the thickness map (red arrow). **c** Visual field is normal in right eye and shows inferior nasal step in the left eye, corresponding to superior thinning of RNFL in right eye

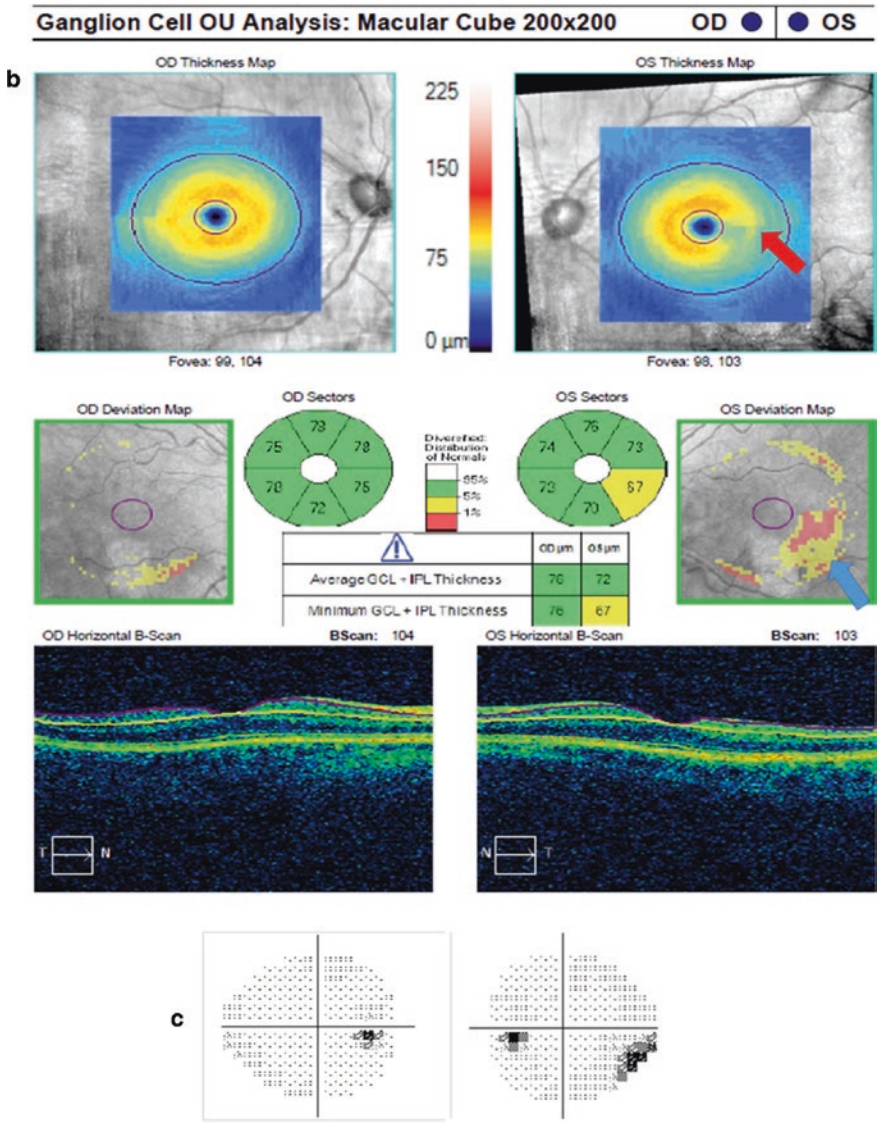

Fig. 5 (continued)

inter-individual differences in sectoral measurements, reducing the diagnostic precision of the device. Spectralis scan is automatically aligned with the FoDi axis. However, if FoDi is displaced from its true anatomical position, there would be a shift in the orientation of classification sectors relative to the normative database.

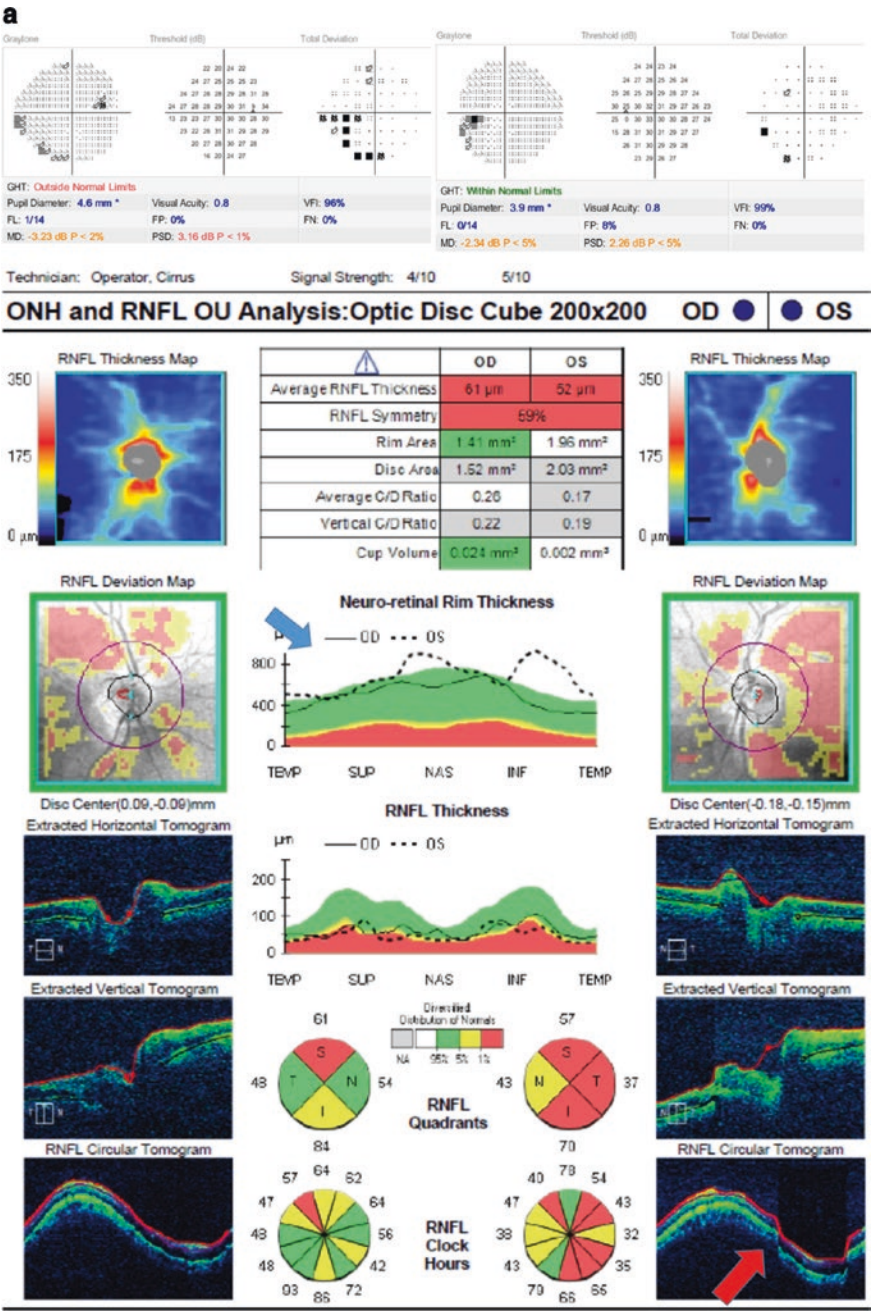

Fig. 6 **a** Cirrus SD-OCT RNFL and ONH report. Although this OCT report shows extensive RNFL defects OU on thickness map and pie charts, the signal strength is less than 6 OU, and segmentation errors can be seen on tomograms (red arrow). Rim thickness is normal throughout the plot (blue arrow). Note that, the validity of BMO in OCT images on high myopic eyes should be carefully investigated. **b** GCIPL OU analysis-The OCT image demonstrates diffuse GCIPL thinning in both eyes. No raphe sign was observed

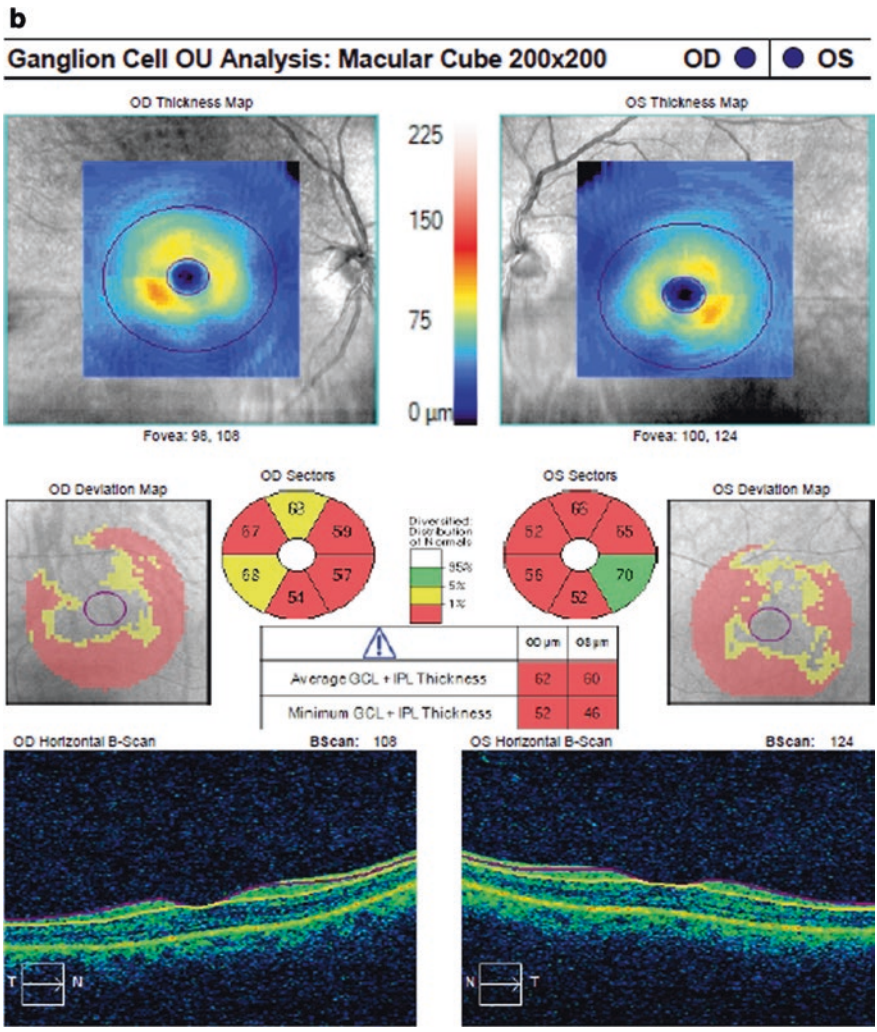

Fig. 6 (continued)

Case 8-'Red Disease' Due to FoDi Misalignment

OCT scan of a 52-year-old woman with diagnosis of primary angle closure glaucoma (Fig. 8a, b). Laser peripheral iridotomy was performed. IOP was 20 mmHg OD with latanoprost and 18 mmHg OS with latanoprost and dorzolamide-timolol. The C/D ratio was 0.4 OD and 0.85 OS. Spectralis OCT shows a displaced FoDi axis in the right eye. If FoDi is displaced from its true anatomical position there is a shift in orientation of the classification sectors relative to the normative database. After correction of FoDi alignment the sectoral thickness was classified as "within normal limits."

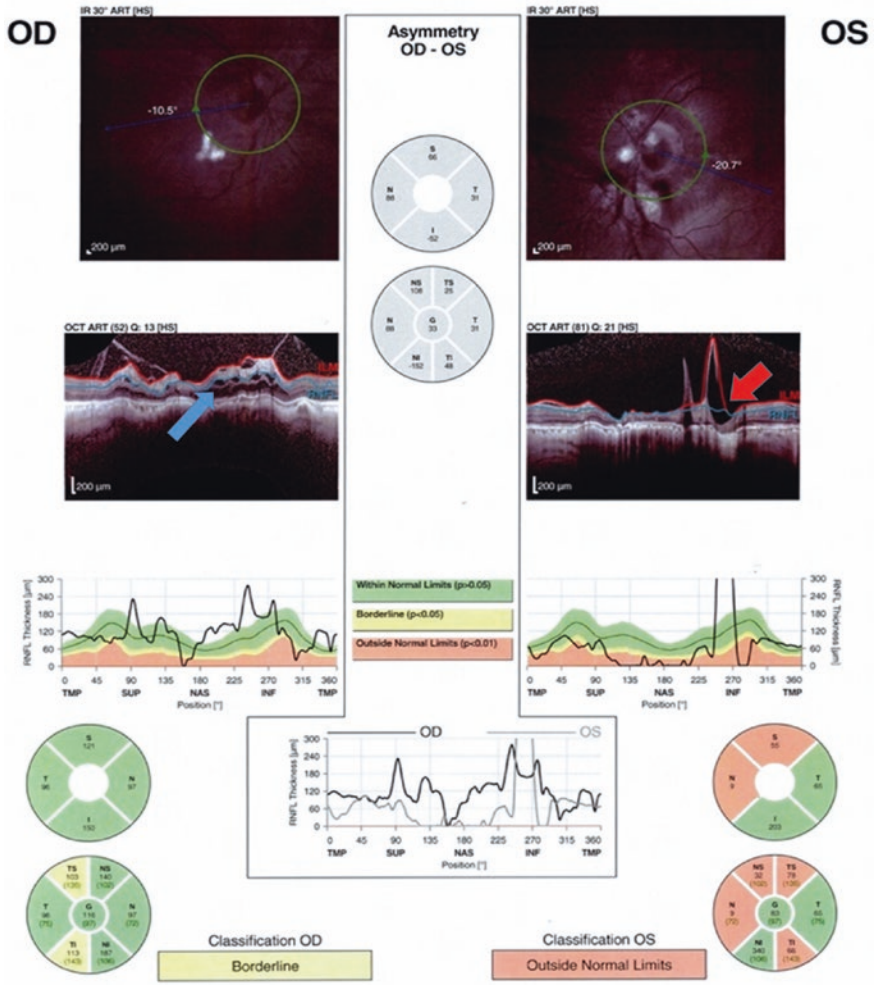

Fig. 7 SpectralisRNFL OU report. The scan quality of the right eye is low. Myopia and high axial length could be associated with low scan quality, as in the right eye of this patient. In her left eye, there are segmentation errors due to areas of peripapillary atrophy and vitreoretinal tractional band (red arrow). Multiple schisis cavities can also be found in the peripapillary area in RNFL Circular Tomogram of right eye (blue arrow)

Case 9-'Red Disease' Due to FoDi Misalignment

Another case of "Red Disease" due to the misalignment of the Fodi axis. The patient is healthy with an IOP of 16 mmHg and normal visual field. The average RNFL is 94 µm. Note that after the correction of the FoDi axis, the average thickness does not change. However, the RNFL profile shifts to the right, and the sectoral thickness are now green (Fig. 9).

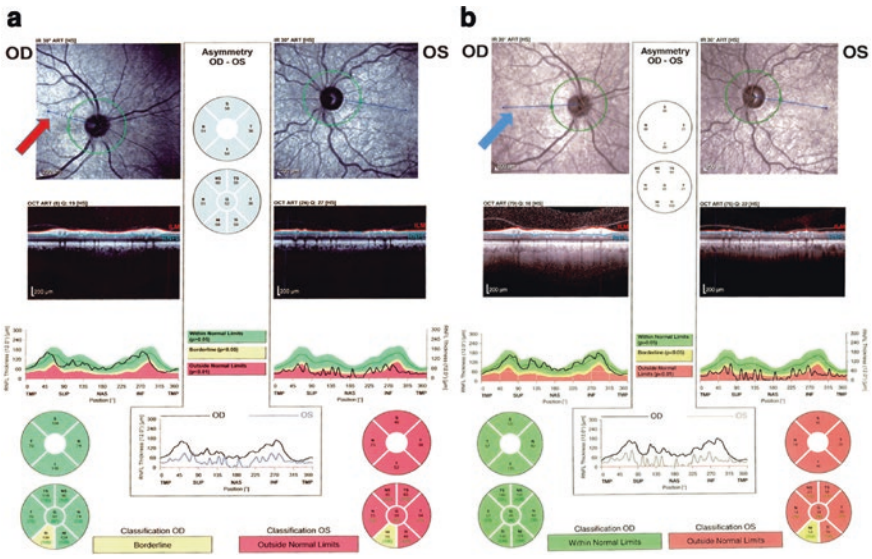

Fig. 8 **a** SpectralisRNFL OU report. As the left eye has advanced glaucoma, the RNFL became thin. But the reason of decreased RNFL thickness of nasal quadrant is posterior segmentation error. On the right eye, there is no segmentation error. But, the fovea is improperly positioned which result in alignment error. Spectralis scan is automatically aligned the FoDi axis (red arrow). If FoDi is displaced from its true anatomical position, there would be a shift in orientation of classification sectors relative to the normative database. The true anatomical position of the fovea of this patient is lower than selected location in the this OCT. Although the average global thickness is within normal limits and the temporal-inferior thickness appeared thinner than normative database. **b** The scan of the same patient. The alignment of FoDi is corrected (blue arrow) and the sectoral thickness is within normal limits

Case 10-'Red Disease' and Vitreous Floater

Vitreous opacities can cause red disease artifacts in the deviation map. However, when they are not overlying the calculation circle, the tabular data can be reliable and used cautiously (Fig. 10a, b).

Segmentation Artifacts

Anterior and Posterior RNFL Misidentification

Estimation of the RNFL thickness relies on the ability of OCT to distinguish the RNFL from the other retinal layers, a process known as segmentation. Several mechanisms may be responsible for inaccurate RNFL segmentation, such as OCT signal attenuation with decreased reflectance of the RNFL induced by ocular media opacities, shadowing of superficial retinal vessels, motion artifacts, or

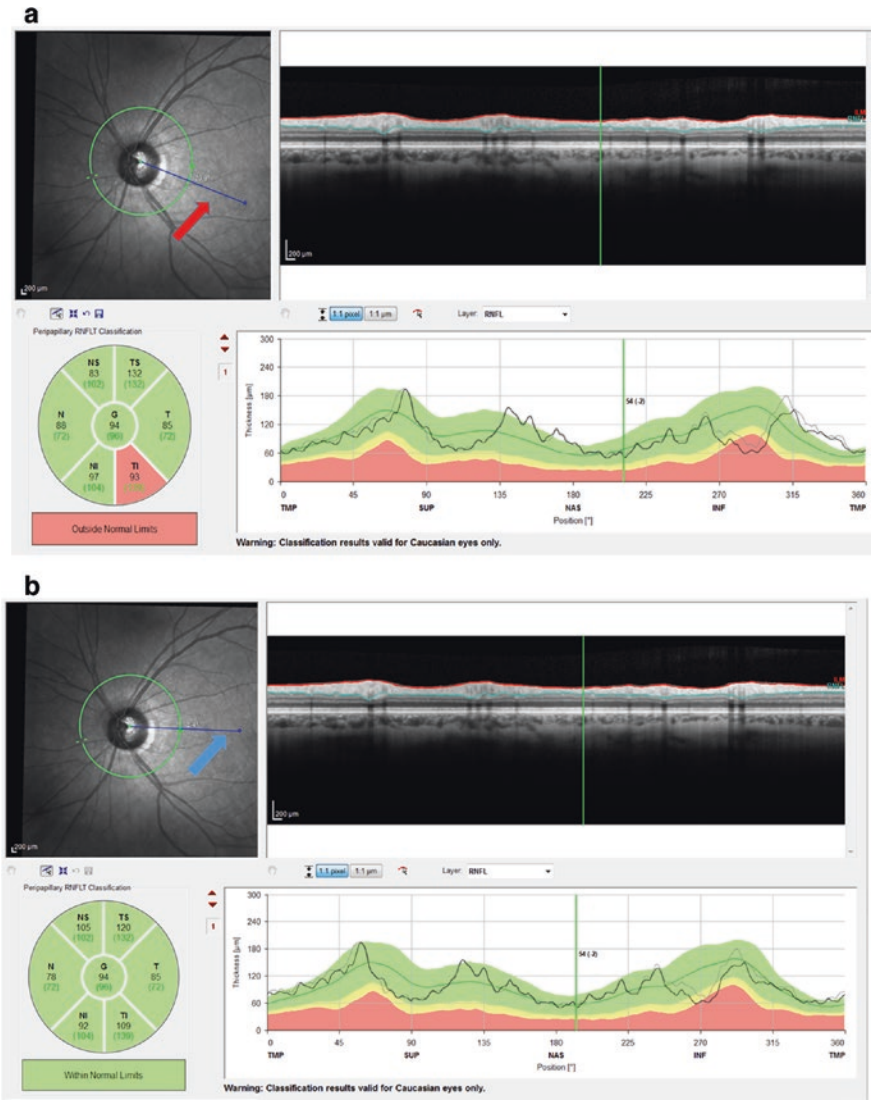

Fig. 9 SpectralisRNFL OU report with misalignment of FoDi (red arroew) and after correction of FoDi axis (blue arrow). The abnormal sector in the upper image is due to shift in the RNFL profile (**a**), which improves after the correction of FoDi axis (**b**)

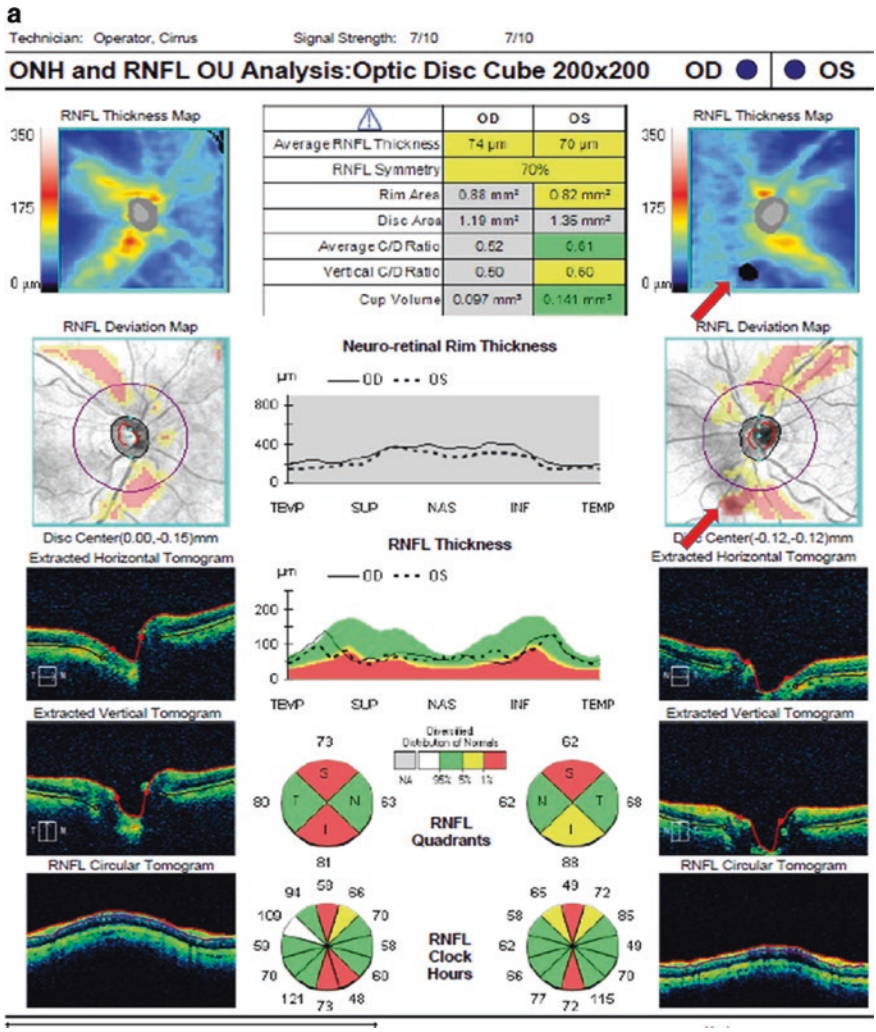

Fig. 10 **a** Cirrus SD-OCT RNFL and ONH report of a patient with glaucoma. The vitreous opacity is present in the scan in the left eye, and blocks an area close to the calculation circle (black area in the thickness map of the left eye). However, its position during the scan does not coincide with the calculation circle and does not affect the pie charts (red arrow). **b** Cirrus SD-OCT RNFL and ONH report of the same patient 3 years later. The vitreous opacity is in the periphery of the cube scan in the left eye (red arrow). The average RNFL thickness is approximately the same as the scan before

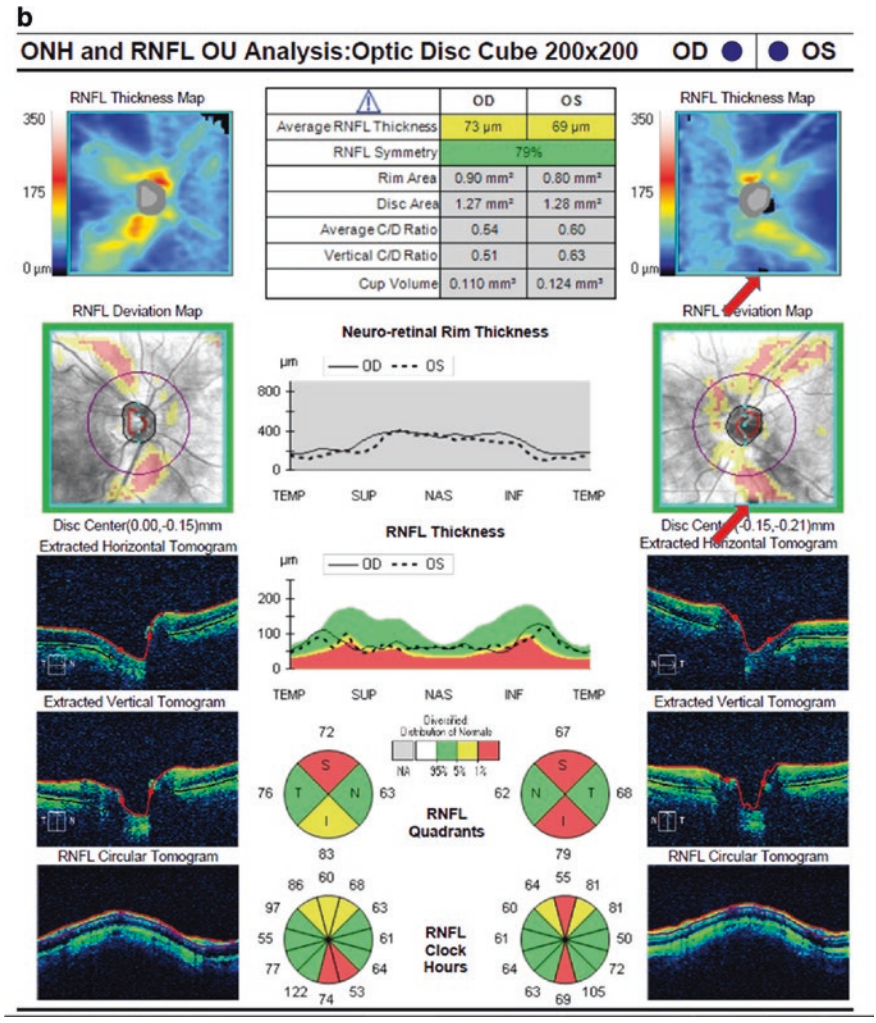

Fig. 10 (continued)

vitreoretinal interface problems. The posterior border of RNFL could not be segmented accurately in the areas of posterior shadowing. The segmentation error from poor scans or vitreoretinal interface problems may lead to an erroneous conclusion of RNFL thinning or thickening.

Case 11-'Green Disease' Due to Segmentation Artifact

OCT scan of a 62-year-old woman with diagnosis of ocular hypertension. The IOP was 28 mmHg OD and 26 mmHg OS, without any medication. Her BCVA was 20/20 OU (Fig. 11).

Case 12-'Green Disease' Due to Vitreoretinal Interface Problem

OCT scan of a 47-year-old woman who was referred to the clinic with primary open angle glaucoma. The measured IOP was 35 mmHg OD and 40 mmHg OS

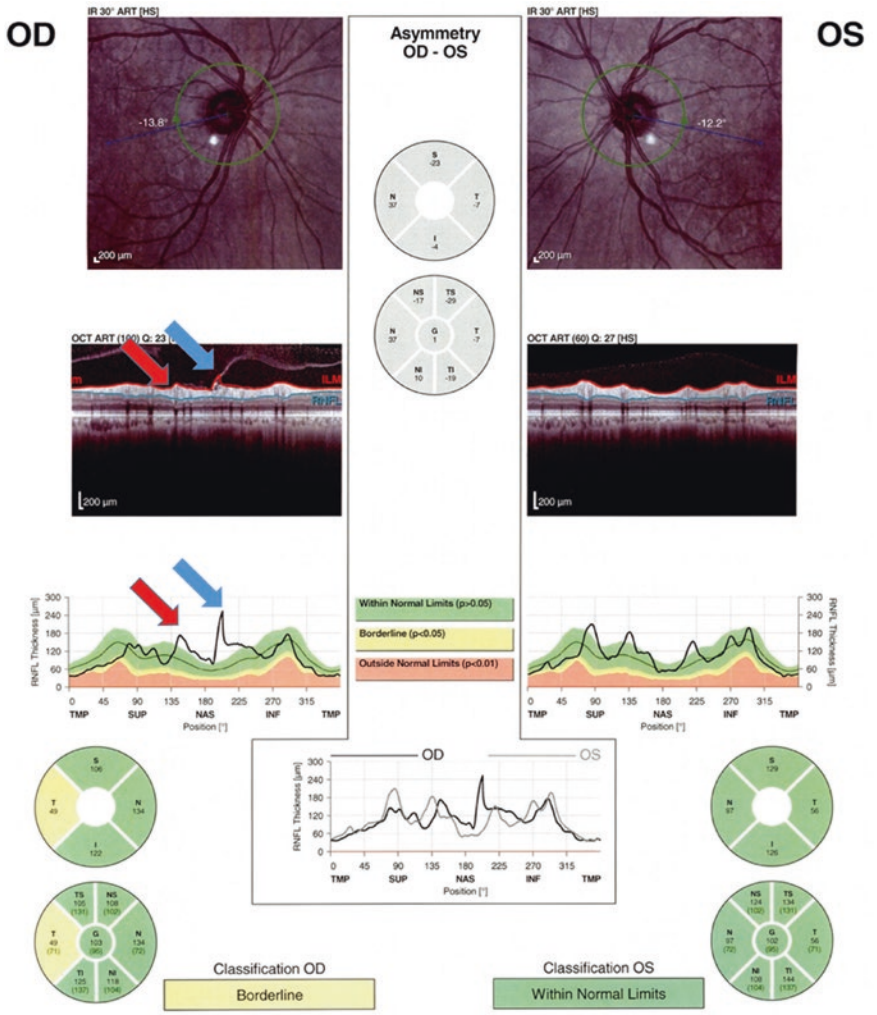

Fig. 11 Spectralis RNFL OU report. Global RNFL thickness is within normal in both eyes. Vitreoretinal traction is clearly visible on peripapillary raw image of the right eye. It causes RNFL thickness peaks in nasal quadrant (at 145°) (red arrow). It also causes misidentification of anterior RNFL in nearly 200° (blue arrow). The traction band is erroneously segmented as the anterior border of RNFL and causes an artifactual RNFL thickness peak in that zone

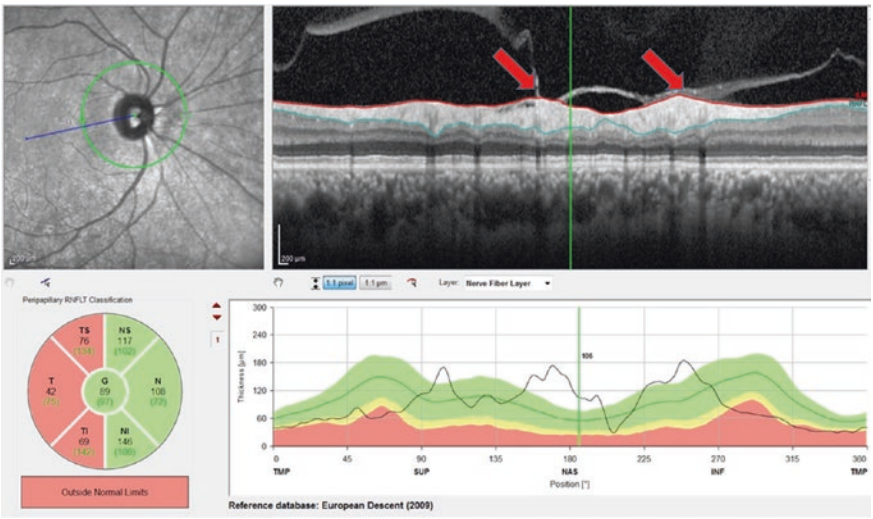

Fig. 12 Spectralis OCT scan. Vitreoretinal traction is visible on the peripapillary raw image of the right eye. The RNFL thickness peaks at the areas of the traction: supranasal, nasal and inferonasal segments

without any medication. On the Humphrey visual field test, MD was −8.20 DB and −17.34 DB for OD and OS, respectively (Fig. 12).

Case 13-'Green Disease' Due to Vitreoretinal Interface Problems

Another case of vitreoretinal interface problems in a 65-year glaucoma patient with a recent reduced vision in right eye. The patient has been on glaucoma medication because of presenting IOP of 25 mmHg and glaucomatous visual field defect since 5 years ago. An extensive epiretinal membrane can be seen in infrared image (Fig. ac). The RNFL Exam Report and The Posterior Pole Asymmetry Analysis Report shows area of thickness in peripapillary area and macula. The presence of an ERM can also cause the RNFL to falsely measure thicker than it actually is on OCT analysis. This is an example of 'Green Disease'.

Case 14-'Green Disease' Due to Narrow RNFL Defect

A very narrow RNFL defect might not be classified as 'outside normal limit' in pie charts and is an example of false negative for color-coded charts.

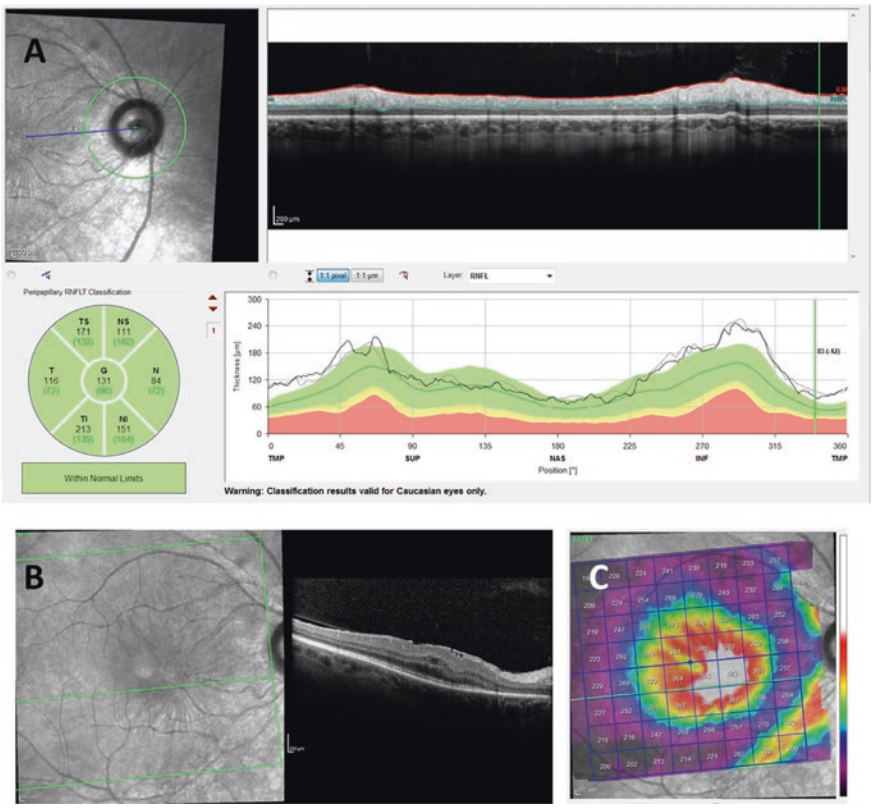

Fig. 13 **a** Spectralis RNFL circle scan demonstrates thickening of RNFL in RNFL Profile. Pie charts are all green with the thickness values higher than expected of healthy eyes. **b** An extensive epiretinal membrane can be seen in infrared image. **c** Posterior pole map shows that the epiretinal membrane in the macula of the right eye has caused macula thickening

A 63-year old monoocular female presented as a glaucoma suspect with IOP 20 mmHg in right eye. On fundus exam, there was rim thinning in both the superior pole and inferior pole. In addition, a narrow inferotemporal RNFL defect can be seen. Visual field is normal.

The Spectralis OCT images were misclassified as normal using the mean RNFL thickness values and in the Pie charts. Careful examination of RNFL Profile shows very narrow thinning corresponded to the location of the RNFL defect in optic disc photo. Interestingly, in The Minimum Rim Width Analysis Report abnormal inferotemporal thinning can be detected in the pie chart. The patient received antiglaucoma medication. In the follow-up of the patient the following year, although visual field was still normal, the RNFL defect is wider in OCT RNFL Profile and is reflected in pie chart as yellow color in the inferior quadrant (Fig. 14a–d).

Case 15-'Red Disease' Due to Retinal Disease

A 63-year-old man with suspicion for glaucomatous optic nerve damage was referred to the clinic. The measured IOP was 19 mmHg OD and 20 mmHg OS. The cup to disc ratio was 0.5 OD and 0.7 OS. Humphrey visual field testing showed a superior arcuate scotoma in both eyes. Careful examination of the retina shows diffuse chorioretinal atrophy along the inferior vascular arcade. Multifocal ERG revealed the diagnosis as sectoral retinitis pigmentosa. This is a red disease: decreased RNFL thickness is secondary to causes other than glaucoma (Fig. 15a–c).

Artifact in Progression Analysis

Scanning artifacts or development of new ocular pathology can cause errors in the glaucoma progression report. Before reaching a conclusion, the physician must carefully evaluate all parts of the report to identify artifacts that can influence the progression results. The RNFL Circular Tomogram, TSNIT plots, and other values must be checked for artifacts and pathologies that can influence the results.

Case 16-Development of Pathology

A glaucoma suspect patient who was following in the glaucoma clinic brings us his recent progression analysis. In 2017 he had a sudden increase in RNFL thickness which can be seen in the RNFL Trend report (Fig. 16a). Careful look at his scans showed development of pathology in the outer retinal layer thought to be peripapillary choroidal neovascularization (Fig. 16c).

Case 17-Alternating Devices and Progression

A 78-year-old male glaucoma patient was referred to the clinic due to the worsening of glaucoma. Although the visual field did not show any change since 2

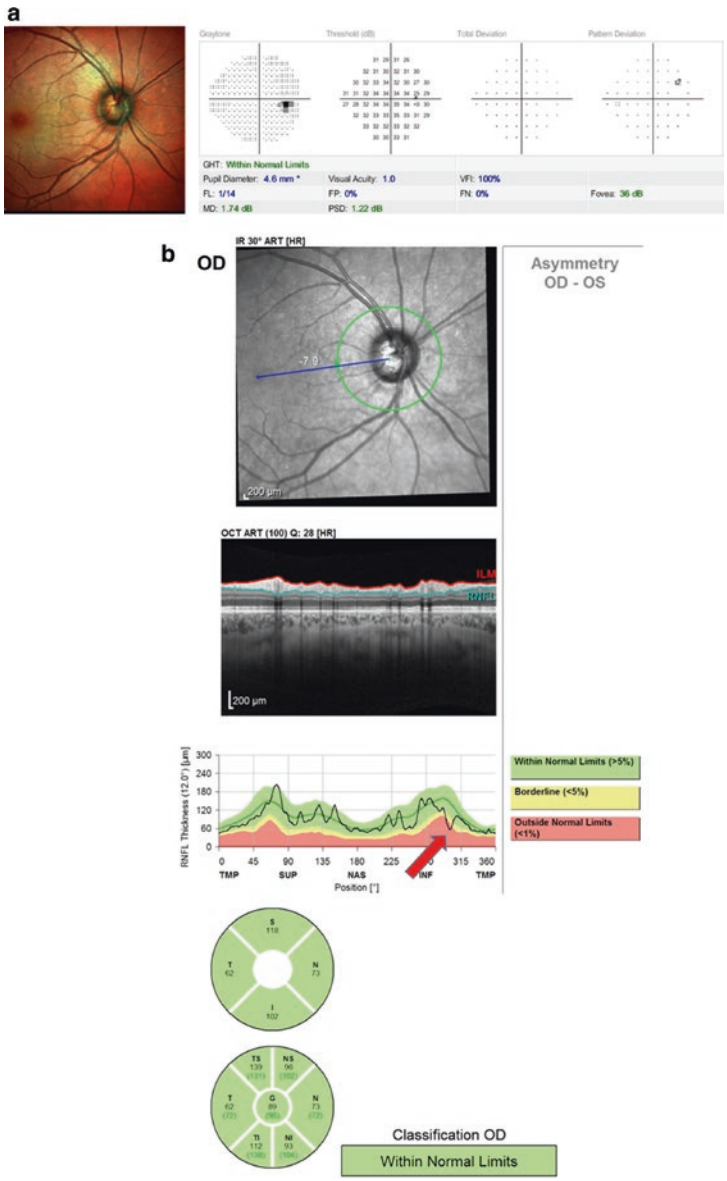

Fig. 14 **a** Narrow RNFL defect is obvious in the inferotemporal region. However the visual field is normal. **b** Spectralis RNFL Single report shows normal mean RNFL thickness values and normal sectoral value. Examination of the RNFL Profile shows very narrow thinning of RNFL corresponded to the location of RNFL defect in optic disc photo. **c** *The Minimum Rim Width Analysis Report shows* diffuse glaucomatous rim thinning in the right eye which is more pronounced in the inferotemporal sector. This eye is classified as outside normal limits. **d** Spectralis RNFL Single Report one year after the last visit. The RNFL defect is wider in OCT RNFL Profile and is reflected in the Pie chart as yellow color in inferior quadrant

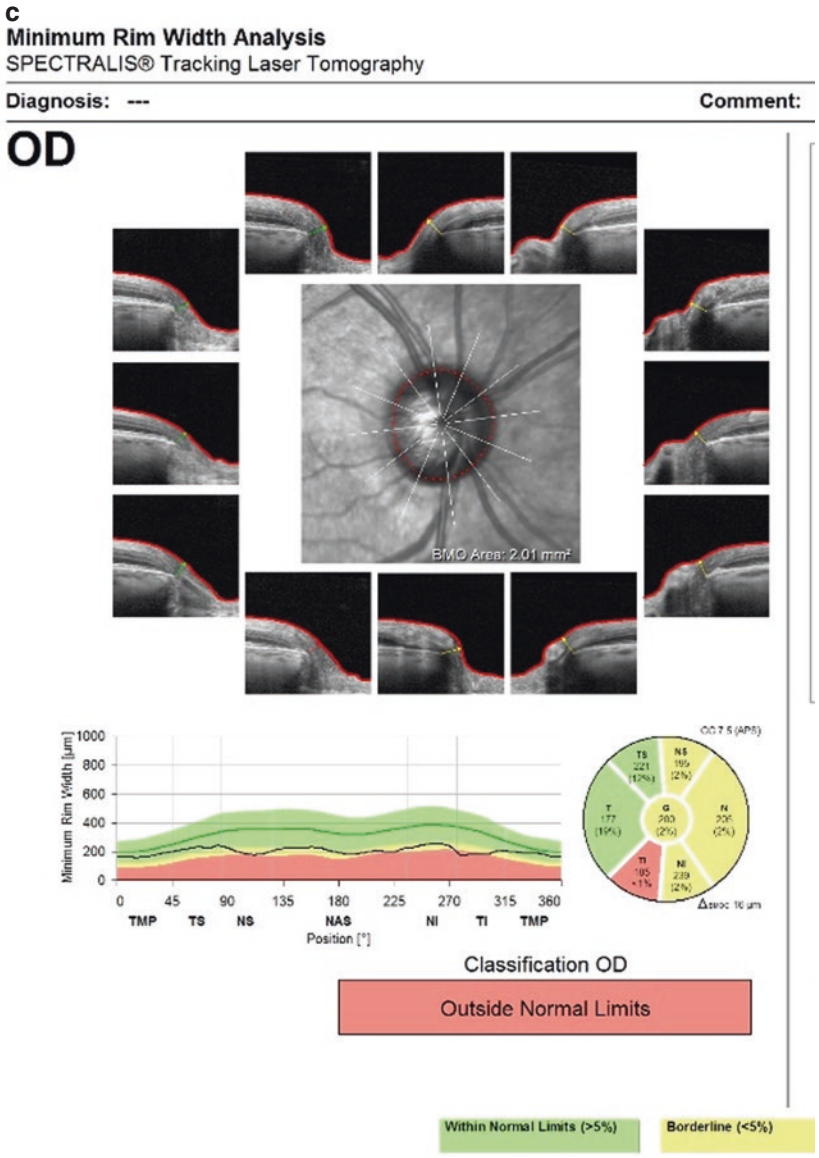

Fig. 14 (continued)

years ago, his Cirrus OCT demonstrates 9 µm thinning in right eye and 8 µm thinning in left eye compared to the OCT from 2 years ago (Fig. 17a, b). However, these OCTs were from different devices. A new OCT with Spectralis

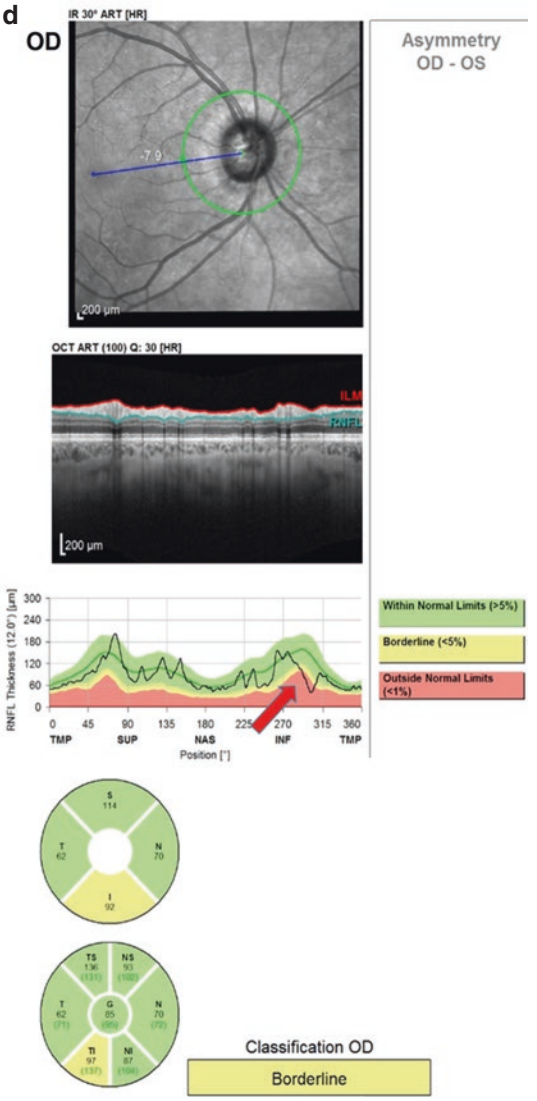

Fig. 14 (continued)

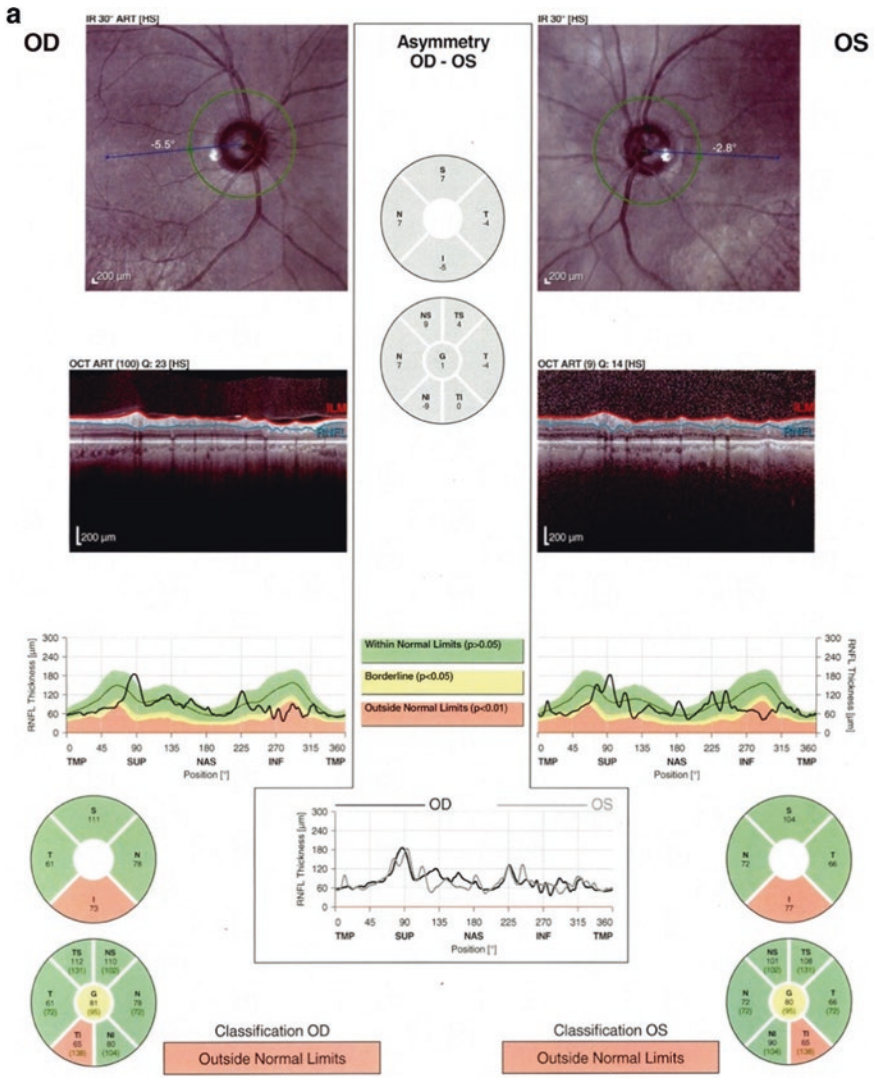

Fig. 15 **a** Spectralis OCT OU report. Global RNFL thickness is borderline. The RNFL thickness in inferior quadrant and inferotemporal segment are 'outside normal limits'. **b** The fundus photograph of the same patient. There is diffuse chorioretinal atrophy along the inferior vascular arcade which explains the RNFL loss on OCT imaging. Diagnosis of sectoral retinitis pigmentosa was made. This is an example of red disease: Decreased RNFL thickness is secondary to causes other than glaucoma. **c** Infrared and fundus *autofluorescence* image of the same patient. Inferotemporal chorioretinal atrophy is visible

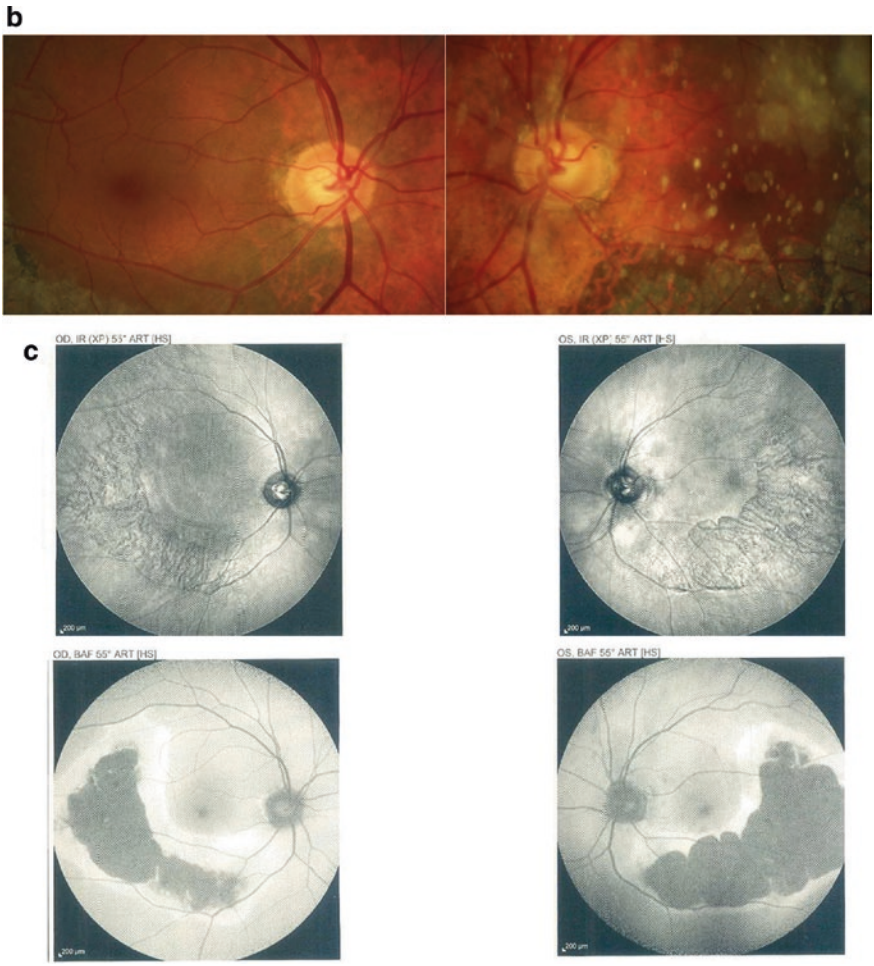

Fig. 15 (continued)

does not show any change from the values of Spectralis OCT 2 years ago. OCT values from different devices are not interchangeable. Cirrus HD-OCT gives lower values compared to Spectralis because the calculation circle in the former is larger than the latter.

a

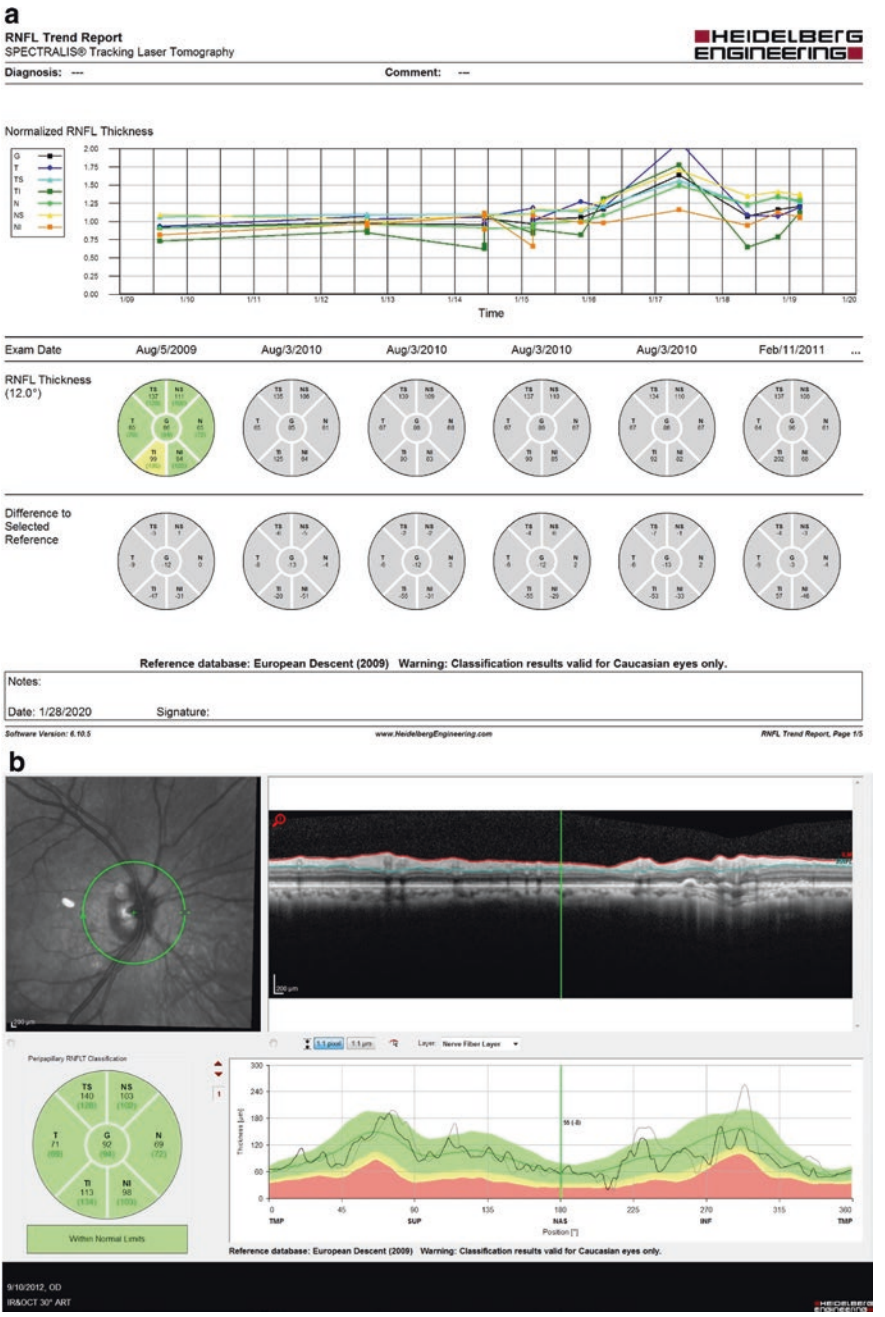
RNFL Trend Report
SPECTRALIS® Tracking Laser Tomography
HEIDELBERG ENGINEERING
Diagnosis: ---
Comment: ---
Normalized RNFL Thickness
G
T
TS
TI
N
NS
NI
Time
Exam Date
Aug/5/2009
Aug/3/2010
Aug/3/2010
Aug/3/2010
Aug/3/2010
Feb/11/2011
RNFL Thickness (12.0°)
Difference to Selected Reference
Reference database: European Descent (2009) Warning: Classification results valid for Caucasian eyes only.
Notes:
Date: 1/28/2020 Signature:
Software Version: 6.10.5
www.HeidelbergEngineering.com
RNFL Trend Report, Page 1/5

b

Peripapillary RNFLT Classification
TS 140
NS 103
T 71
G 92
N 69
TI 113
NI 98
Within Normal Limits
Thickness [µm]
Position [°]
TMP
SUP
NAS
INF
TMP
Reference database: European Descent (2009) Warning: Classification results valid for Caucasian eyes only.
9/10/2012, OD
IR&OCT 30° ART

◀ **Fig. 16** **a** Spectralis progression Trend Report of the patient followed since 2010 showing an increase in 2016 to 2017 in most sectors. **b** Spectralis Single RNFL report. OCT images in 2012 shows slight blunting of RNFL peak in inferior region. **c** Spectralis Single RNFL report one year later. Right eye shows destruction of RPE and outer retina with area of thickening and edema, most probably due to peripapillary CNV. Segmentation error in the RNFL is also a cause of increase in RNFL thickness in this patient. Average RNFL thickness increase from 92 µm in 2012 (**b**) to 109 µm in 2017 (**c**)

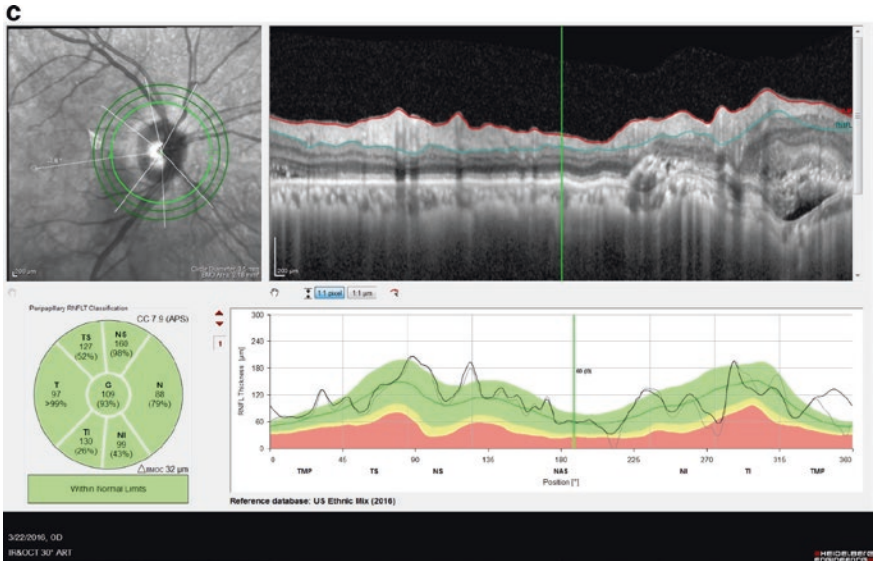

Fig. 16 (continued)

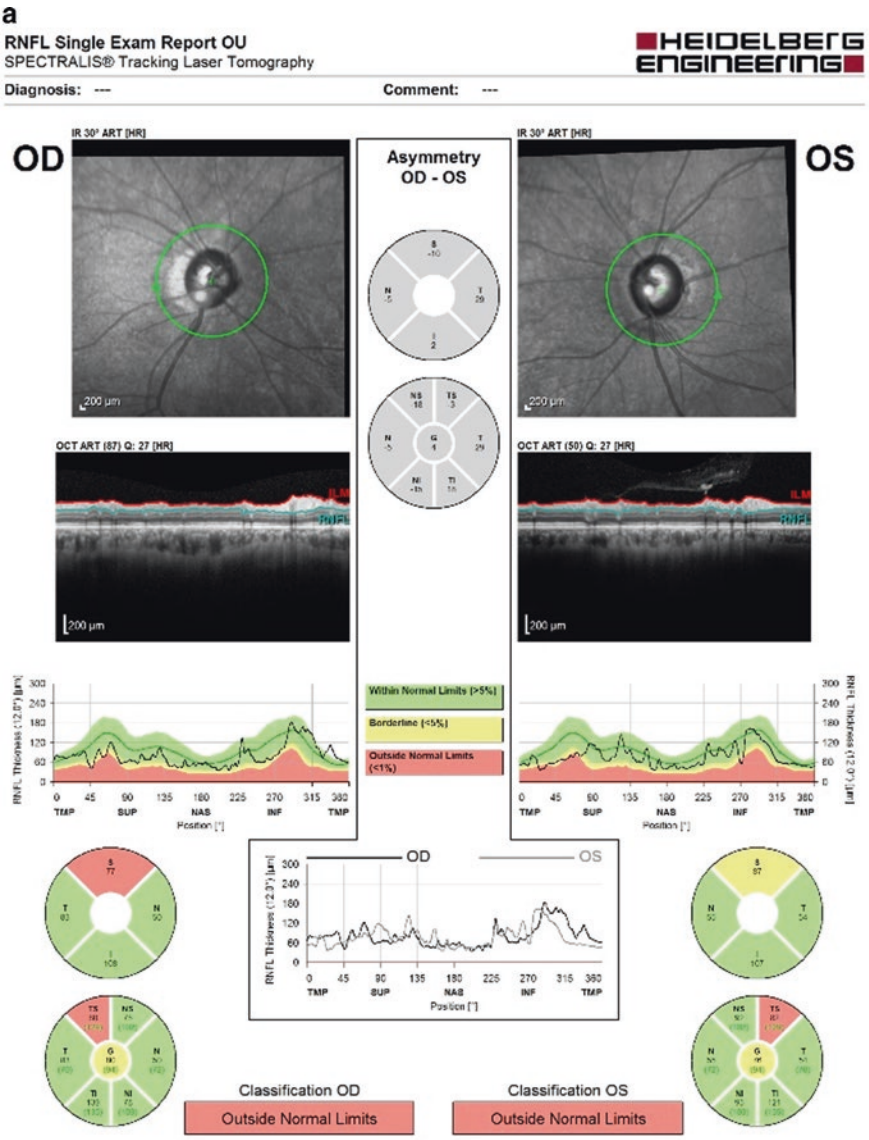

Fig. 17 **a** Previous Spectralis Single RNFL report in 2013 demonstrates supratemporal RNFL thinning and average RNFL thickness of 80 and 76 µm in right eye and left eye, respectively. **b** Cirrus HD-OCT OU report (current) showing superior quadrant wedge defect similar to Spectralis OCT 2 years ago (**a**). However, the average values are 9 µm thinner in right eye and 8 µm thinner in left eye than values. This is not necessarily mean progression as a new Spectralis OCT shows similar values to the Spectralis OCT 2 years ago (**c**). Measurements from different OCT devices are not interchangeable, and the determination of thinning should be assessed by the same device throughout follow-up. **c** Current Spectralis Single RNFL report in 2015 demonstrates supratemporal RNFL thinning and average RNFL thickness of 79 and 75 µm in right eye and left eye, respectively, which are comparable to the values of Spectralis Single RNFL report 2 years ago

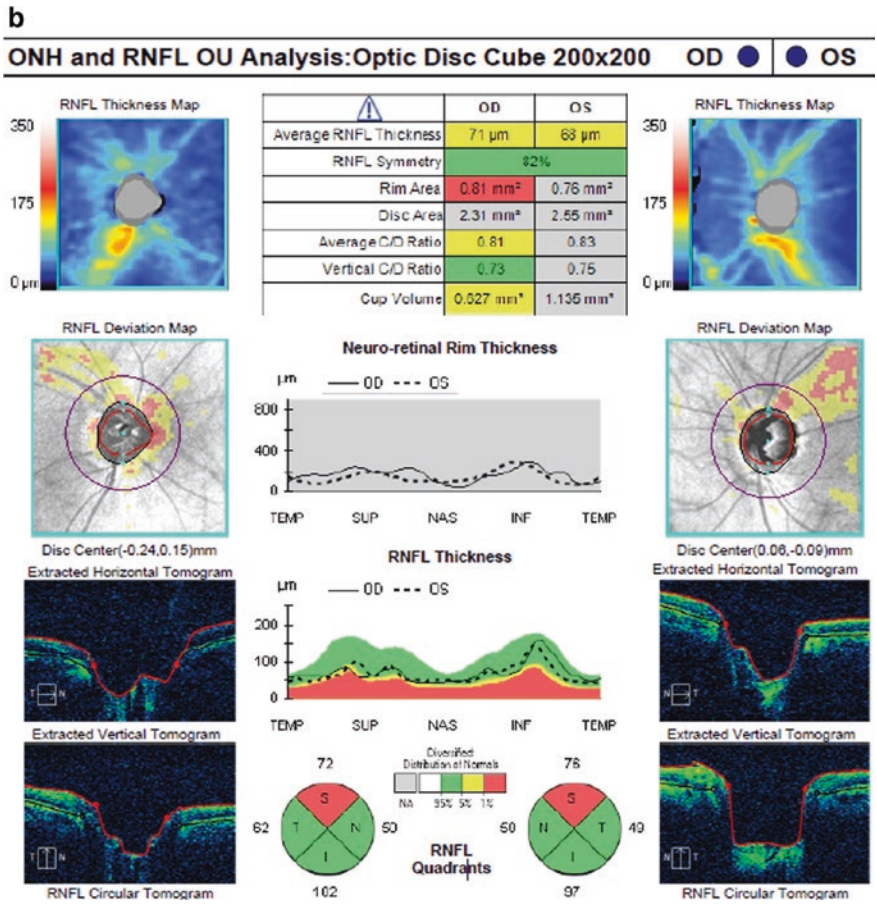

Fig. 17 (continued)

Financial Disclosure

S. Moghimi, None; M. Safizadeh, None, Andrew Camp, None; R.N. Weinreb, Heidelberg Engineering (F), Carl Zeiss Meditec (F, R), Konan (F), National Eye Institute (F), Optovue (F), Allergan (C), Bausch&Lomb (C,F), Eyenovia (C), Novartis (C)

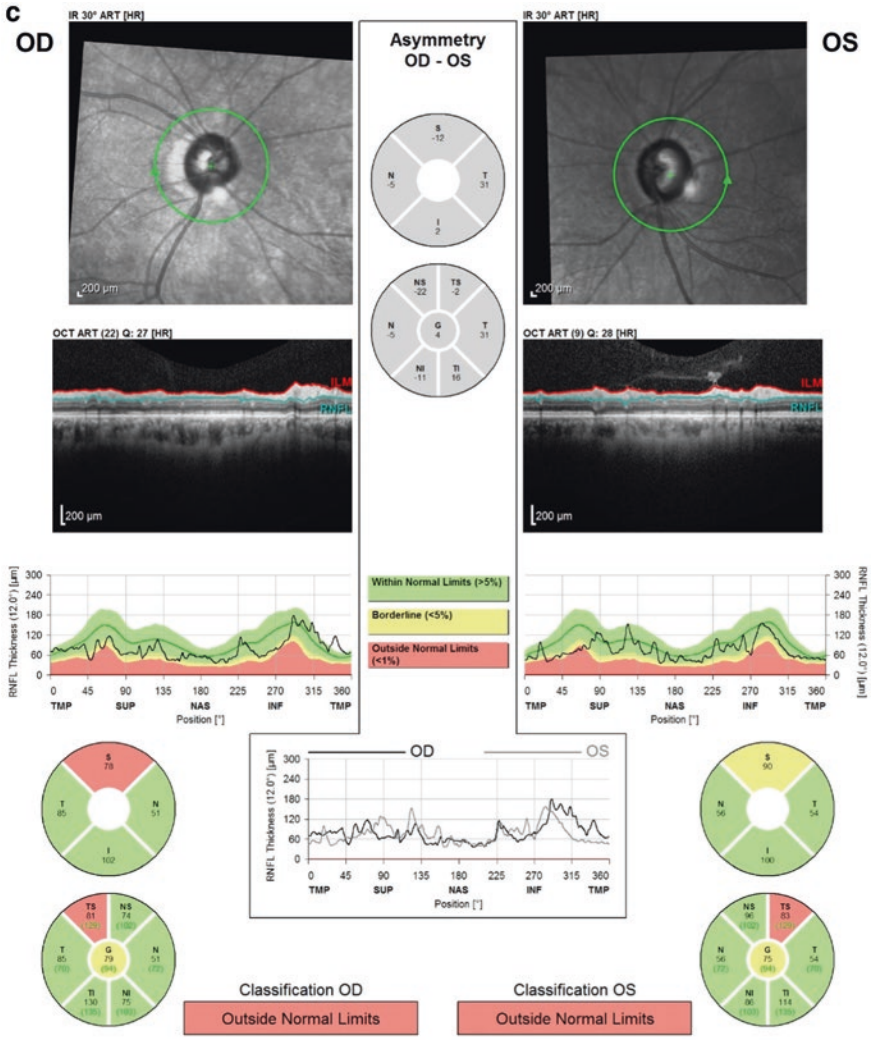

Fig. 17 (continued)

Acknowledgments Funding/Support: Supported in part by National Institutes of Health/National Eye Institute grants R01 EY029058 (RNW), by core grant P30EY022589; by an unrestricted grant from Research to Prevent Blindness (New York, NY); by grants for participants' glaucoma medications from Alcon, Allergan, Pfizer, Merck, and Santen, and by the donors of the National Glaucoma Research Program, a program of the BrightFocus Foundation.

References

1. Leung CK, et al. Retinal nerve fiber layer imaging with spectral-domain optical coherence tomography: interpreting the RNFL maps in healthy myopic eyes. Invest Ophthalmol Vis Sci. 2012;53(11):7194–200.
2. Hood DC, et al. The location of the inferior and superior temporal blood vessels and inter-individual variability of the retinal nerve fiber layer thickness. J Glaucoma. 2010;19(3):158.
3. Jonas, R.A., et al., *Optic disc-fovea angle: the Beijing Eye Study 2011.* PLoS One, 2015;**10**(11).

Confocal Scanning Laser Ophthalmoscopy and Glaucoma

Sasan Moghimi, Mona SafiZadeh, Jiun Do and Robert N. Weinreb

Introduction

Confocal scanning laser ophthalmoscopy (CSLO) to assess optic disc topography was first implemented in the late 1980s (Laser Tomographic Scanner, Heidelberg Instruments). With reductions in cost and the advent of improved hardware, the first practical commercial confocal scanning laser ophthalmoscope was the Heidelberg Retina Tomograph (HRT) introduced in 1991 (Heidelberg Engineering, Heidelberg, Germany).

The HRT is a scanning laser ophthalmoscope designed to acquire images of the optic nerve head, retinal nerve fiber layer, and posterior pole. A rapid scanning 670 nm diode laser is used to acquire images without mydriasis. Both the HRT II and HRT III obtain 16–64 high resolution, reflectance images with a 4 mm depth over an area of 15° by 15°. A three-dimensional topographic representation of the optic disc and peripapillary retina is constructed from multiple two-dimensional slices [1]. Three scans are aligned and analyzed to create the mean topography scan for each patient. Morphologic parameters (such as rim area and volume) are calculated from an arbitrary reference plane 50 μm below the surface of the temporal parapapillary retina along the disc margin included RNFL thickness [1] (Fig. 1). Other parameters such as the cup shape measure (CSM) are independent of the reference plane. The measurements of optic disc topography are highly reproducible and show very good agreement with clinical estimates of ONH structure and visual function [2]. The reproducibility of the local surface height

S. Moghimi (✉) · J. Do · R.N. Weinreb
Hamilton Glaucoma Center, Shiley Eye Institute, Department of Ophthalmology, University of California, San Diego, CA, USA
e-mail: sasanimii@yahoo.com

M. SafiZadeh
Tehran University of Medical Sciences, Tehran, Iran

M. Mohammadpour (ed.), *Diagnostics in Ocular Imaging*,
https://doi.org/10.1007/978-3-030-54863-6_28

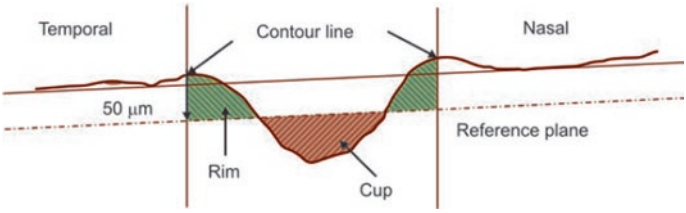

Fig. 1 The reference plane is located 50 µm posterior to the temporal disc margin between 350° and 356° (the papillomacular bundle). The volume enclosed by the contour line and above the reference plane is the rim and is shown in green. The cup is located below the reference plane and is shown in Red

Parameters	global	normal range	p-value	temporal	tmp/sup	tmp/inf	nasal	nsl/sup	nsl/inf
disc area [mm²]	2.03	1.63 - 2.43	-	0.47	0.26	0.28	0.48	0.28	0.25
cup area [mm²]	0.33	0.11 - 0.68	> 0.5	0.25	0.03	0.05	0.00	0.00	0.00
rim area [mm²]	1.70	1.31 - 1.96	> 0.5	0.23	0.23	0.24	0.48	0.28	0.25
cup/disc area ratio [ ]	0.16	0.07 - 0.30	> 0.5	0.52	0.12	0.17	0.00	0.00	0.00
rim/disc area ratio [ ]	0.84	0.70 - 0.93	> 0.5	0.48	0.88	0.83	1.00	1.00	1.00
cup volume [mm³]	0.02	-0.01 - 0.18	> 0.5	0.02	0.00	0.00	0.00	0.00	0.00
rim volume [mm³]	0.40	0.30 - 0.61	> 0.5	0.02	0.04	0.05	0.12	0.08	0.08
mean cup depth [mm]	0.13	0.10 - 0.27	> 0.5	0.16	0.13	0.16	0.06	0.06	0.06
maximum cup depth [mm]	0.32	0.32 - 0.76	> 0.5	0.33	0.29	0.33	0.16	0.18	0.17
height variation contour [mm]	0.31	0.31 - 0.49	0.34	0.13	0.18	0.17	0.13	0.03	0.08
cup shape measure [ ]	-0.13	-0.28 - -0.15	0.24	-0.02	-0.07	-0.02	-0.15	-0.18	-0.15
mean RNFL thickness [mm]	0.23	0.20 - 0.32	> 0.5	0.09	0.27	0.28	0.24	0.34	0.32
RNFL cross sectional area [mm²]	1.19	0.99 - 1.66	> 0.5	0.11	0.17	0.19	0.29	0.23	0.21
linear cup/disc ratio [ ]	0.40	0.27 - 0.55	> 0.5	-	-	-	-	-	-
maximum contour elevation [mm]	-0.06	-0.21 - -0.04	0.42	-	-	-	-	-	-
maximum contour depression [mm]	0.25	0.17 - 0.39	> 0.5	-	-	-	-	-	-
CLM temporal-superior [mm]	0.18	0.14 - 0.27	> 0.5	-	-	-	-	-	-
CLM temporal-inferior [mm]	0.19	0.13 - 0.29	> 0.5	-	-	-	-	-	-
average variability (SD) [µm]	11	-	-	-	-	-	-	-	-
reference height [µm]	299	-	-	-	-	-	-	-	-
FSM discriminant function value [ ]	1.48	-	-	-	-	-	-	-	-
RB discriminant function value [ ]	1.15	-	-	-	-	-	-	-	-
modified ISNT rule fulfilled	yes	-	-	-	-	-	-	-	-

Fig. 2 The morphometric parameters that are automatically calculated by HRT. These parameters are available for the entire optic disc (global) and for the different sectors

measurement at over the 384×384 pixel area is 20 µm for healthy and glaucomatous eyes with an acuity of 20/40 or better and cylindrical refractive error < 1 diopter.

Parameters

Once the optic disc contour is drawn, the software displays the stereometric parameters of the optic disc compared to a range of statistically "normal values." The parameters that are measured by HRT include optic disc area, cup area, cup-disc area ratio, rim area, cup volume, cup depth, retinal nerve fiber layer (RNFL) thickness, and cross-sectional retinal nerve fiber layer area. These parameters are available for the entire optic disc (global) and for segments of the optic disc (Fig. 2).

OU Printout

An informational printout of both eyes is now available and includes the quality of the image, topographic maps, topographic values for each eye, and the asymmetry. The color-coded optic disc image identifies the rim (green), rim slope (blue) and cup (red) (Fig. 3).

Comparison of topographic parameters to a normative database are represented with red crosses denoting 'outside normal limits', yellow exclamation marks denoting 'borderline', and green ticks denoting 'within normal limits'.

When a printout is read (Figs. 4 and 5), the following parameters should be evaluated:

1. Patient information
2. Quality (Fig. 4a): A standard deviation (SD) < 40 μm is acceptable quality while a SD < 30 μm is a good quality image
3. Disc size (Fig. 4b): Discs are classified as small (< 1.6 mm^2), average (1.6–2.6 mm^2), and large (> 2.6 mm^2) depending on cutoffs provided by the manufacturer
4. Cup Analysis (Fig. 4c): Shows the configuration of the cup shape measure (CSM) which represents the slope and the cup
5. Rim Analysis (Fig. 4d): Provides the rim area and Moorfields regression analysis based on the rim to disc area globally and for each sector
6. RNFL Analysis (Fig. 4e): Measures the thickness of the RNFL along the contour line and relative to the reference plane. Note that, unlike optical coherence tomography (OCT), it is not the actual measurement of RNFL thickness and suffers from variability as disease progresses.

Moorfields regression analysis (MRA) compares sectoral rim areas to a normative database adjusted for disc area, ethnicity, and age. The optic disc is divided into 6 sectors and each is classified as follows: within normal limits (0–95%),

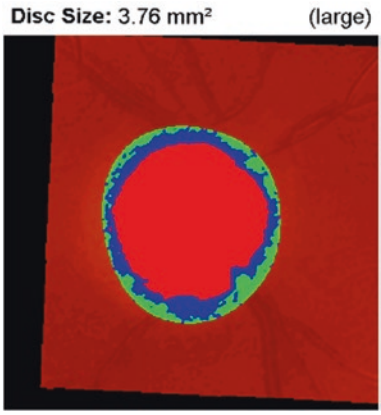

Fig. 3 Color coded optic disc with the rim shown in green, rim slope shown in blue, and cup shown in red

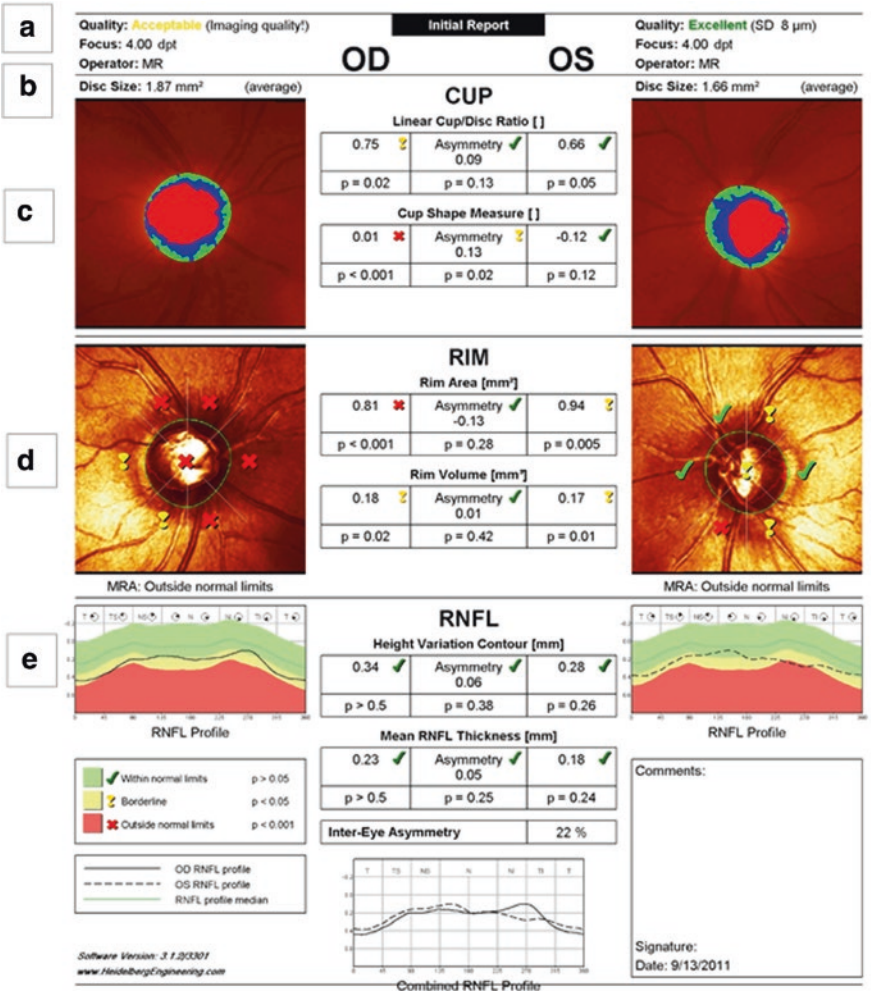

Fig. 4 A confocal scanning laser ophthalmoscopy image of a 68-year-old female with glaucoma. **a** The quality of the image is acceptable in the right eye and excellent in the left eye. **b** The disc size is average with a disc area of 1.87 mm^2 and 1.66 mm^2 in the right and left eye, respectively. The disc size is important because the normative values of the other parameters are relative to the disc size. **c** Cup analysis shows increased cupping in the right eye with an abnormal cup shape measure and normal cup shape measure in the left eye. **d** Rim analysis is one of the most important parts of the HRT printout. The Moorfields regression analysis (MRA) classifies most sectors in right eye as "outside normal limits." In the left eye, only significant inferonasal rim thinning is flagged by the MRA. The rim area is outside normal limits in the right eye and borderline in the left eye. **e** In the RNFL analysis, the right eye has a flattened plateau contour line with a loss of the double hump pattern. The left eye has a reduced height of the contour line from the reference plane in the inferior pole. However, the mean RNFL thickness is 'within normal limits' in both eyes. Of note, HRT is not a reliable device to measure RNFL thickness as the plot is the distance of the RNFL contour line to an arbitrary reference plane

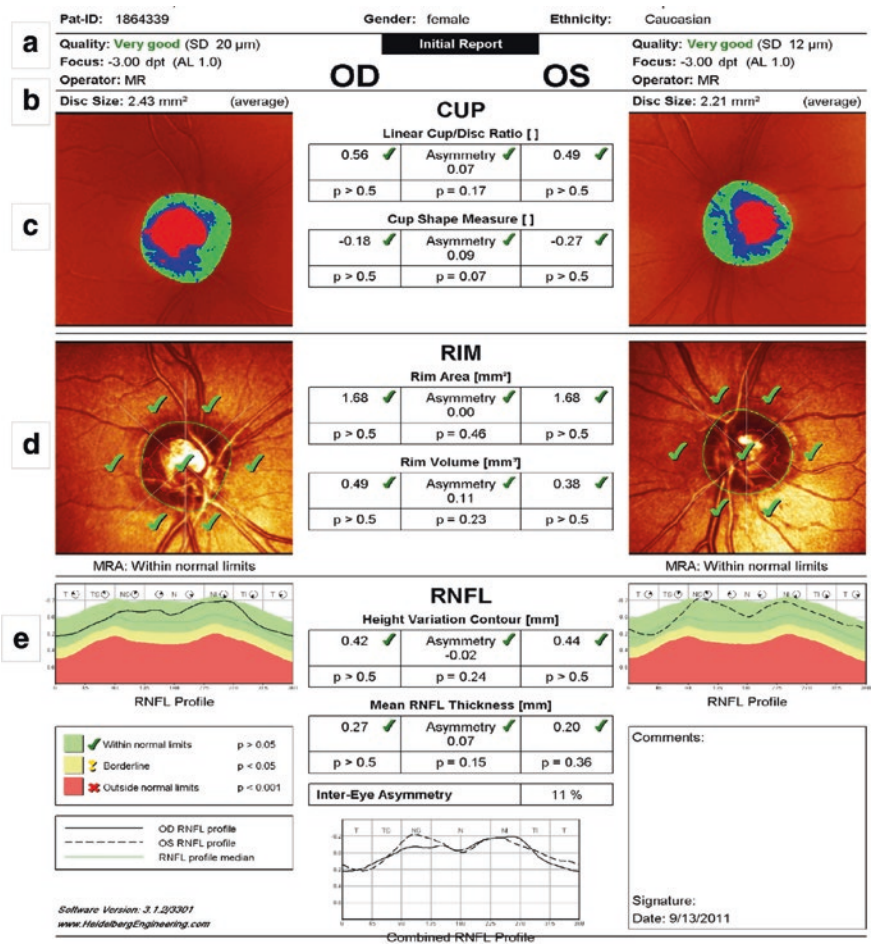

Fig. 5 A confocal laser scanning tomography image of a 55-year-old healthy female. **a** The quality of the image is very good in both the right and left eye. **b** The disc size is average with areas of 2.43 and 2.21 mm^2. **c** Cup analysis shows small cups in both eyes with a cup/disc ratio and cup shape measure 'within normal limits' in both eyes. **d** Rim analysis and the Moorfields regression is 'within normal limits' in all sectors.**e** In RNFL analysis, a double hump pattern can be seen in both eyes with normal values for mean RNFL thickness and height variation contour

borderline (95–99.9%), and outside normal limits (99.9–100%) [3] (Fig. 6). In a group of early glaucoma patients, the MRA showed a sensitivity of 84% and a specificity of 96% in detecting glaucoma [4].

Glaucoma Probability Score (GPS): The HRT III provides an additional means to analyze the optic nerve head without needing to manually delineate the optic disc margins. This method, the Glaucoma Probability Score, is based on fitting the optic nerve head to a predefined model to provide global and sectoral quantifications of the region [5] (Fig. 7).

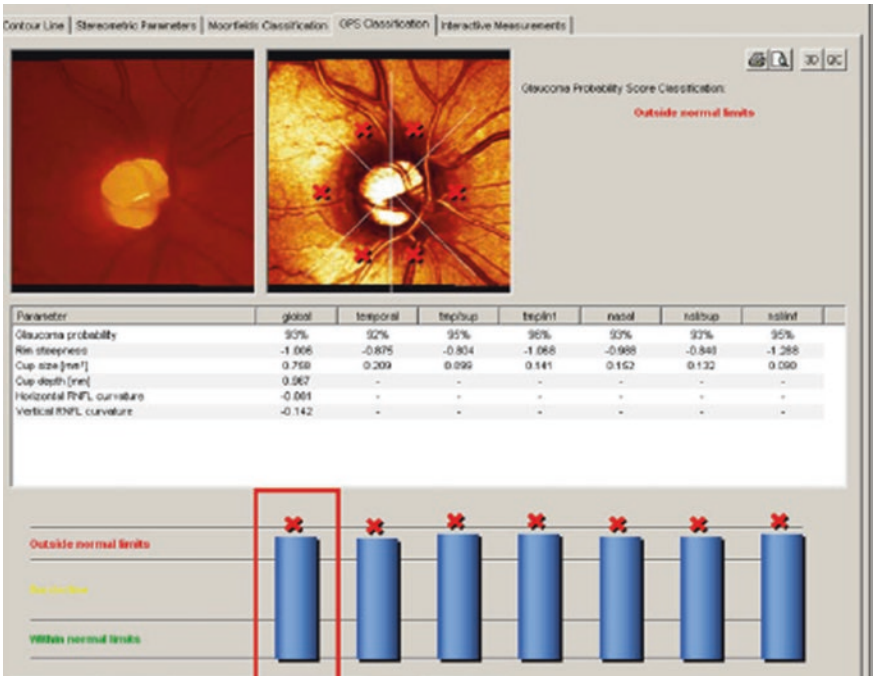

Fig. 6 Moorfields regression analysis of a glaucoma patient. All the sectors and the global rim area are flagged as 'outside normal limits' and depicted with a red "X"

Simply put, the GPS compares the shape of the optic disc excavation to a cone (normal) or cup (glaucoma) and classifies the ONH into three different groups based on the value obtained: normal (0–28), borderline or suspect (28–64), and 'outside normal limits' (64–100) group. The GPS has been shown to be more sensitive but less specific than minimum rim width (MRW) in detecting glaucoma. This suggests that an abnormal MRA classification is useful to confirm that a disc is glaucomatous, whereas a 'within normal limits' GPS classification is useful to confirm that a disc is normal [6].

Case 1–Early and Moderate Glaucoma

A 68-year-old woman presented with a visual acuity (VA) of 20/25 in the right eye and 20/50 in the left eye. IOP was 21 and 25 mmHg on latanopost in right and left eye, respectively. Examination of the optic disc showed sloping of the superior neuroretinal rim with decreased visibility of RNFL superiorly compared to inferiorly in the right eye and extensive cupping with loss of the neuroretinal rim and RNFL superiorly and inferiorly in the left eye. Automated perimetry was normal in right eye and revealed superior and inferior altitudinal defects in left

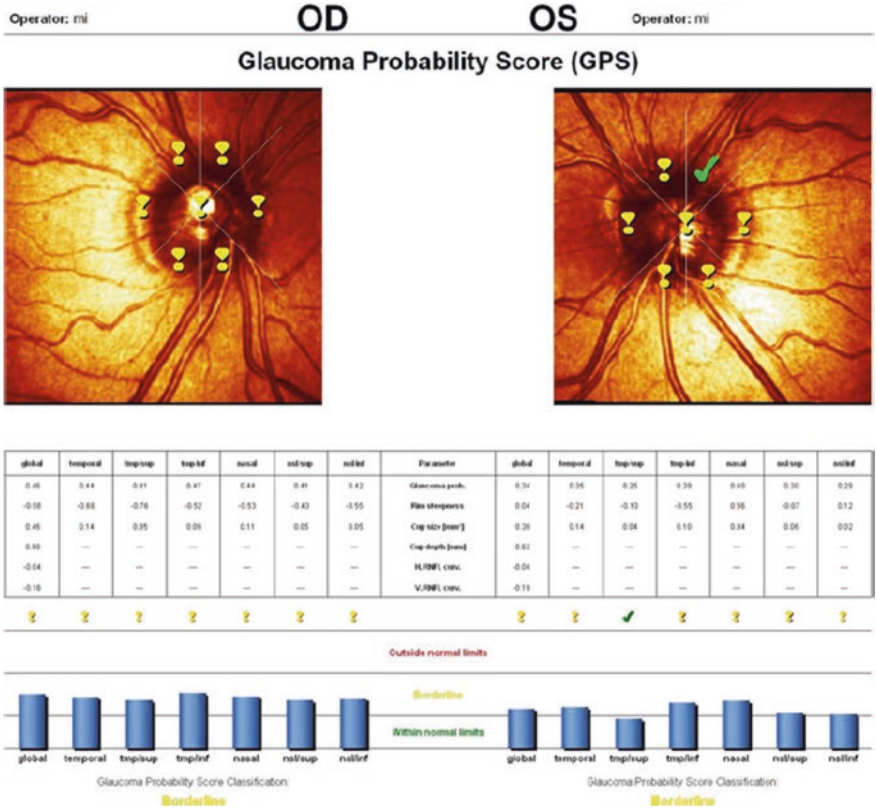

Fig. 7 Glaucoma Probability Score (GPS) of a patient with a normal intraocular pressure history. The disc is suspicious, and GPS shows the shape of the disc is 'borderline' in almost all sectors

eye. Confocal laser scanning tomography showed a Moorfields regression analysis of "borderline" globally in right eye and 'outside normal limits' in supratemporal sector. Cup, rim and RNFL parameters were within normal limit in right eye. Almost all the sectors in the left eye are flagged as "outside normal limits" in left eye (Figs. 8 and 9). Note that the GPS is 'outside normal limits' in both eyes. The GPS is more sensitive and less specific than MRA in diagnosing glaucoma.

Case 2–Advanced Glaucoma

A 75-year-old man presented with a visual acuity of 20/40 in the right eye and 20/200 in the left eye. IOP was 16 mm Hg in the right eye and 18 mmHg in the left eye. He was using latanopost and Cosopt. The visual field in both eyes revealed dense scotomas in both hemifields. The follow-up HRT scan showed an

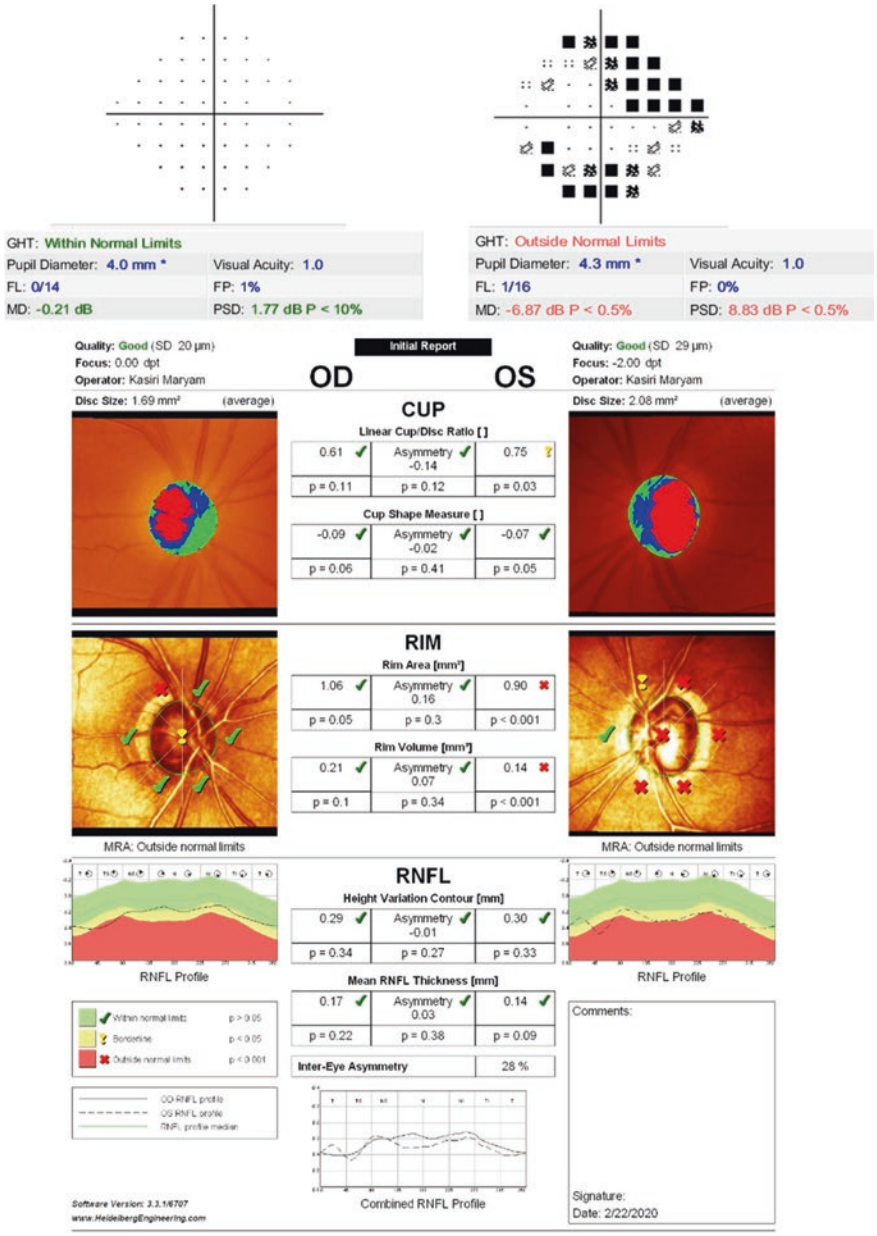

Fig. 8 Confocal laser scanning tomography image of a patient with early glaucoma (right eye) and moderate glaucoma (left eye). The quality of image is good in both eyes. The disc size is average. Cup analysis shows normal cup parameters in right eye and abnormal cup parameters in left eye. Rim analysis is 'within normal limits' in most sectors in right eye but "outside normal limit" in most sectors of the left eye. RNFL analysis shows blunting of RNFL profile. However, RNFL parameters are 'within normal limit' both eyes. Interestingly, the glaucoma probability score is 'outside normal limits' in all sectors in both eyes

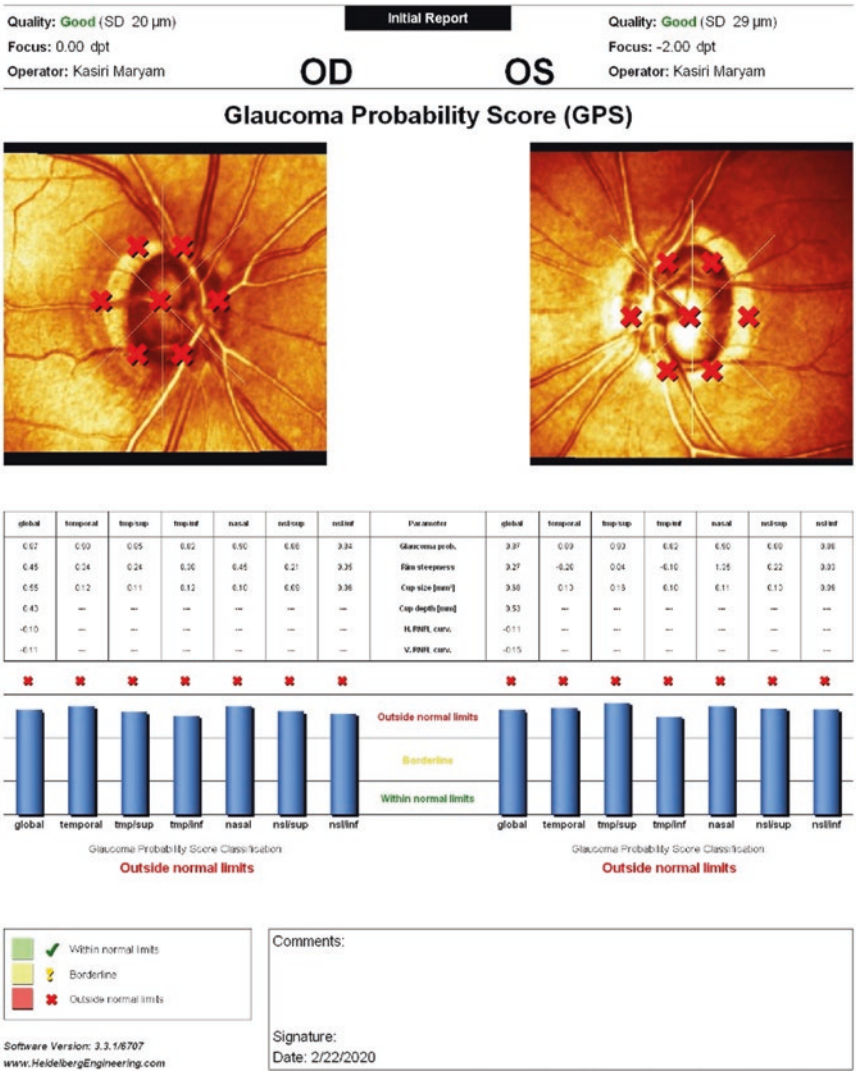

Fig. 9 The GPS is more sensitive and less specific than Moorfields regression analysis in diagnosing of glaucoma

acceptable image of the right eye but an unacceptable image for the left eye probably due to a cataract (Fig. 10). Although the MRA is abnormal in almost all sectors and the rim area is significantly reduced, RNFL analysis shows only blunting of RNFL profile and abnormal values in inferior region of left eye. As mentioned earlier, in contrast to OCT, RNFL analysis by the HRT is not a direct measure of the RNFL thickness and is not reliable for detecting or monitoring of glaucoma.

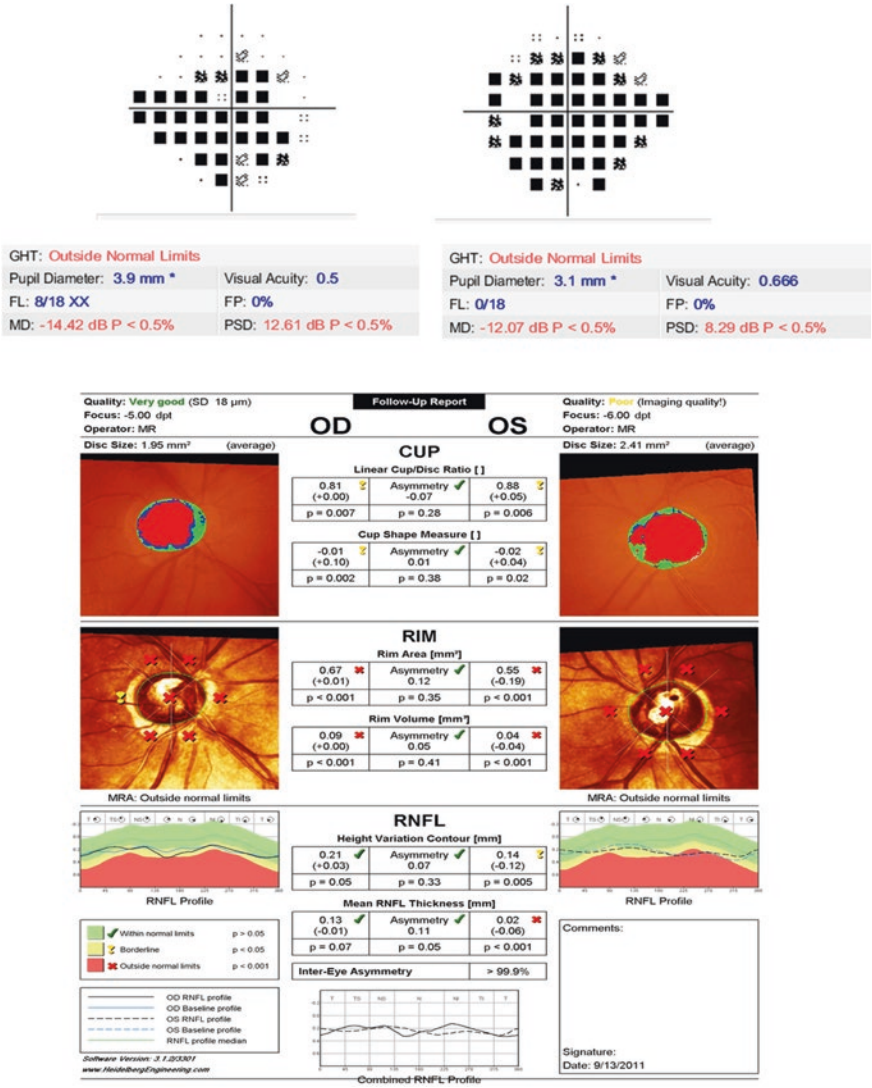

Fig. 10 Confocal laser scanning tomography image of a patient with advanced glaucoma. The quality of the image is very good in the right eye but poor in the left eye. The disc size is average. Cup analysis shows borderline cup parameters. Rim analysis is 'outside normal limits' in almost all sectors in both eyes. Although the patient has advanced glaucoma, RNFL analysis shows only blunting of the RNFL profile with values in inferior quadrant of left eye. Due to the poor image quality, the imaging should be repeated in the left eye

Case 3–Large Optic Disc

A 56-year-old woman was suspected of having glaucoma because of the appearance of the optic disc. Her cup-to-disc ratio was high and estimated to be 0.75 and 0.65 in her right and left eye, respectively. Her optic disc was also determined to be large. Visual fields were normal and the IOP was 19 mmHg in both eyes. She was evaluated with the Heidelberg Retina Tomograph (Fig. 11). The right eye had an average optic disc size (2.45 mm^2) and the left eye had a large optic disc size (2.96 mm^2). Moorfields Regression Analysis of both eyes were 'outside normal limits'. Large disc size (2.8 mm^2) can confuse the MRA. There would be increasing variability in rim area and also the specificity loss with larger disc size. The patient had a normal RNFL profile in both eyes using OCT (Fig. 12). The patient was diagnosed with large disc and physiologic cupping. This is a typical case of "Red Disease" for HRT in which false positive results increase with increasing disc size.

Glaucoma Progression

Progression is a hallmark of glaucomatous disease and plays an important role in determining the management of glaucoma. A major strength of the HRT is in monitoring glaucoma disease. HRT applies a robust statistical algorithm in order to differentiate real biological changes from test–retest variability. Another advantage is that each successive version of the analysis software is "backwards compatible" with previous iterations. The HRT II and HRT III software displays two methods for glaucoma progression analysis:

Topographic Change Analysis

With Topographic Change Analysis (TCA), retinal height measurements of super-pixels are used to compare changes between baseline and follow-up examinations. The criterion for significant change is the presence of a cluster of 20 super-pixels with a significant decrease within the ONH margin that is reproducible in follow-up exams. A high probability value indicates that the likelihood of a change is low. On the other hand, when the error probability of the height change is less than 5%, the likelihood that the difference was due to chance is low and the change is likely to be real. Areas in red are those that show a decrease and areas in

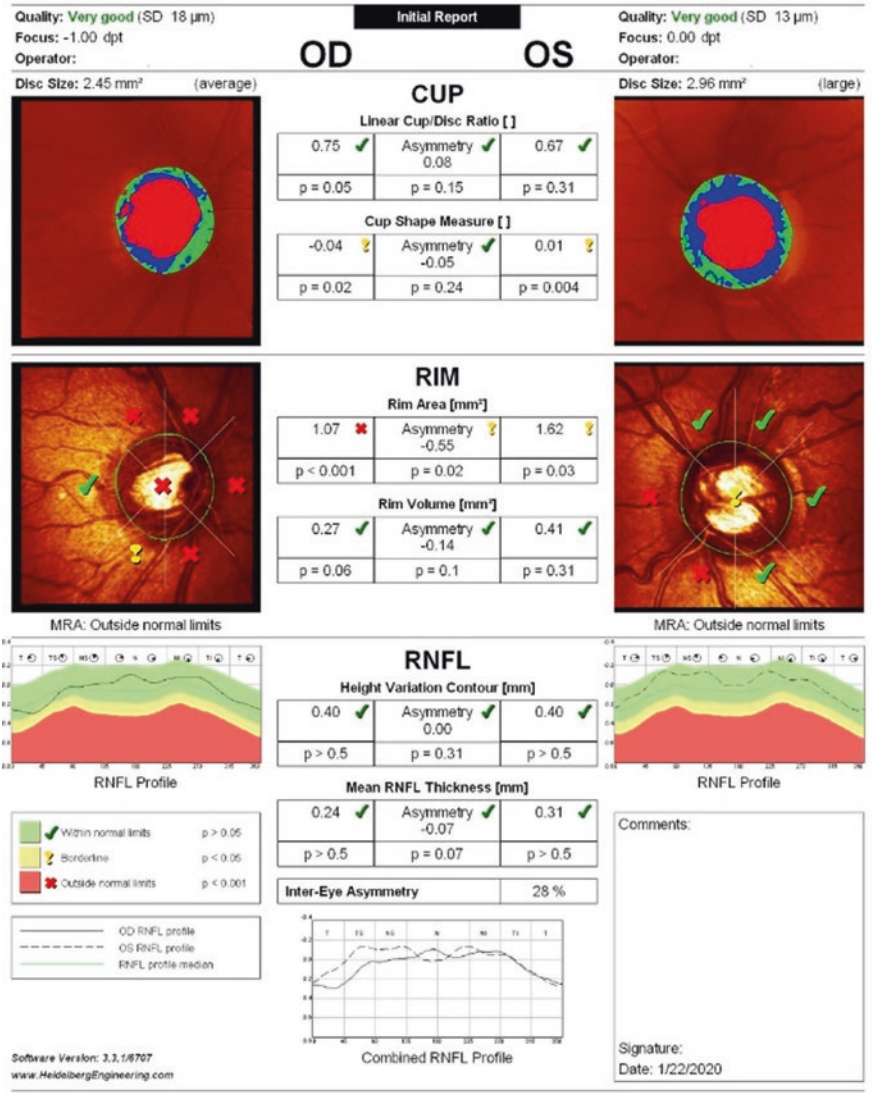

Fig. 11 Confocal laser scanning tomography image of a patient with large discs and physiologic cupping. The image quality is very good in both eyes. The right eye has an average optic disc size (2.45 mm^2) and the left eye has a large optic disc size (2.96 mm^2). Moorfields Regression Analysis (MRA) of both eyes was 'outside normal limits'. In HRT, false positive rates for the detection of glaucoma increase with increasing disc size

green are those that show an increase. The exact values for area, volume, and the change can be obtained each location of change (Fig. 13). Red areas located along the blood vessels or alternating clusters of red and green areas are typically artifacts and should not be considered progression [7].

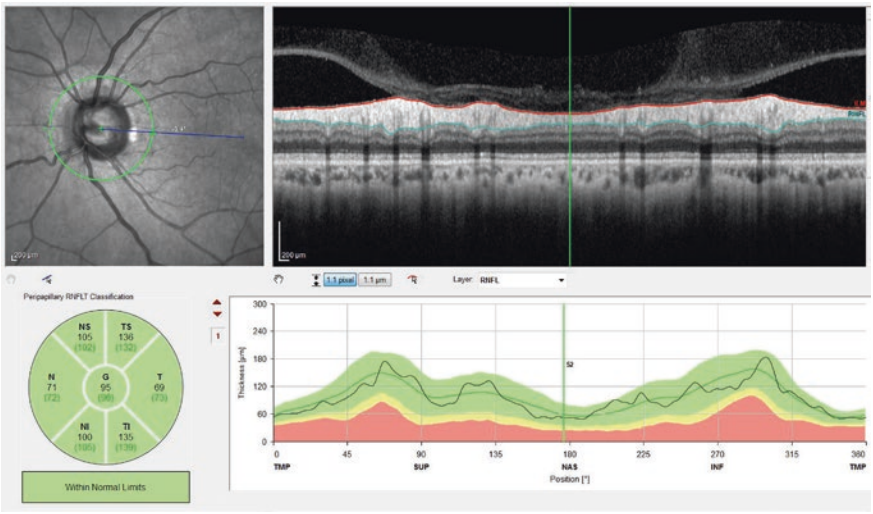

Fig. 12 SD-OCT (Spectralis) RNFL report of the left eye of the patient with large disc and physiological cupping. The patient has a normal RNFL profile in both eyes

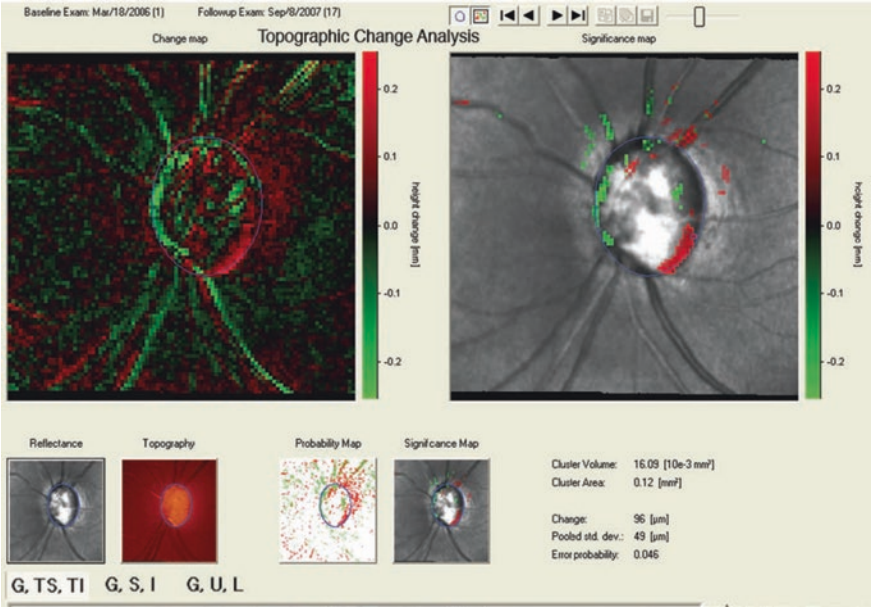

Fig. 13 Topographic Change Analysis of a glaucoma patient after 15 months of baseline HRT showing inferotemporal rim tinning in the left eye. Areas in red are those which show a depression and areas in green are those which show elevation. The red spots located along the superior blood vessels might be due to measurement variability and should not be considered progression

In a study comparing the detection of glaucomatous progression by expert examination of stereo photographs to HRT-2 TCA, there was agreement in only 65% of cases on progression status while 30% of patients showed progression by TCA alone and only 6% showed progression by stereo photographic assessment alone. One reason for the discrepancy is that stereo photographic examination assesses certain features of the optic disc, such as rim narrowing, blood vessel deviation and appearance of splinter hemorrhages, whereas TCA identifies areas of surface height change that are less easily appreciated on photographs [8].

Stereometric Parameter Analysis

Glaucoma progression can also be detected by trend analysis of stereometric parameters over time. Each value is normalized using the ratio of the difference between the measured value and baseline measurements and the difference between average values in a normal eye and an eye with advanced glaucoma. Thus, the change in different parameters of the optic disc over time can be easily displayed on the same scale (Fig. 14). Like many other algorithms, definite progression requires confirmation in at least two out of three consecutive tests. This strategy accounts for isolated events that misleadingly suggest progression but reverse with subsequent testing [9].

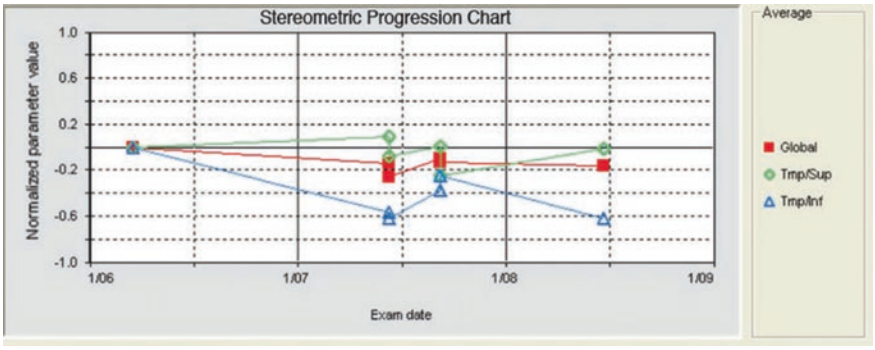

Fig. 14 Stereometric parameter analysis of the same patient after 2 years showing progressive inferotemporal rim thinning but stable supratemporal rim in the left eye

Acknowledgements Funding/Support: Supported in part by The National Institutes of Health/National Eye Institute grants R01 EY029058 (RNW), by core grant P30EY022589; by an unrestricted grant from Research to Prevent Blindness (New York, NY, USA); by grants for participants' glaucoma medications from Alcon, Allergan, Pfizer, Merck, and Santen, and by the donors of the National Glaucoma Research Program, a program of the BrightFocus Foundation.

Financial Disclosure: S. Moghimi, None; M. Safizadeh, None; J. do, None; R.N. Weinreb, Heidelberg Engineering (F), Carl Zeiss Meditec (F, R), Konan (F), National Eye Institute (F), Optovue (F), Allergan (C), Bausch & Lomb (C,F), Eyenovia (C), Novartis (C).

References

1. Weinreb RN, et al. Effect of repetitive imaging on topographic measurements of the optic nerve head. Arch Ophthalmol. 1993;111(5):636–8.
2. Bowd C, et al. Structure–function relationships using confocal scanning laser ophthalmoscopy, optical coherence tomography, and scanning laser polarimetry. Invest Ophthalmol Vis Sci. 2006;47(7):2889–95.
3. Wollstein G, Garway-Heath DF, Hitchings RA. Identification of early glaucoma cases with the scanning laser ophthalmoscope1. Ophthalmology. 1998;105(8):1557–63.
4. Harizman N, et al. Detection of glaucoma using operator-dependent versus operator-independent classification in the Heidelberg retinal tomograph-III. Br J Ophthalmol. 2006;90(11):1390–2.
5. Swindale NV, et al. Automated analysis of normal and glaucomatous optic nerve head topography images. Invest Ophthalmol Vis Sci. 2000;41(7):1730–42.
6. Zangwill LM, et al. The rate of structural change: the confocal scanning laser ophthalmoscopy ancillary study to the ocular hypertension treatment study. Am J Ophthalmol. 2013;155(6):971–82.
7. Chauhan BC, et al. Optic disc and visual field changes in a prospective longitudinal study of patients with glaucoma: comparison of scanning laser tomography with conventional perimetry and optic disc photography. Arch Ophthalmol. 2001;119(10):1492–9.
8. Kourkoutas D, et al. Comparison of glaucoma progression evaluated with Heidelberg retina tomograph II versus optic nerve head stereophotographs. Can J Ophthalmol. 2007;42(1):82–8.
9. Chauhan BC, et al. Technique for detecting serial topographic changes in the optic disc and peripapillary retina using scanning laser tomography. Invest Ophthalmol Vis Sci. 2000;41(3):775–82.

Anterior Segment Optical Coherence Tomography and Glaucoma

Sasan Moghimi, Mona SafiZadeh and Jiun Do

Introduction

Differentiating between primary open angle glaucoma (POAG) and primary angle closure glaucoma (PACG) is important. Treatments for PACG, such as laser peripheral iridotomy (LPI), laser iridoplasty, and cataract extraction (with or without goniosynechialysis), aim to open the iridocorneal angle and are not considered for treating POAG. In addition to management strategies, PACG and POAG also differ with regards to prognosis.

Gonioscopy is the gold standard for evaluating the angle but has disadvantages. The examination can be uncomfortable for patients and inconvenient to perform during clinic. Additionally, gonioscopy-based assessments are subjective with low reproducibility given high inter-observer and intra-observer variability, making it undependable for patient follow-up and clinical research. In recent years, imaging devices have been developed that enable the evaluation of the anterior segment and overcome the shortcomings of gonioscopy.

The first report of optical coherence tomography (OCT) imaging of the anterior segment was presented in 1994 [1]. It was a slit-lamp mounted, 830-nm, time-domain OCT system that acquired noncontact images of the anterior segment. Currently, commercial anterior segment OCT (ASOCT) devices are available that provide high resolution structural imaging for clinical use and the management of glaucoma. ASOCT systems can be classified according to the wavelength of the light source. Devices based on 1310 nm light sources include the Zeiss Visante (Carl Zeiss Meditec Inc., Dublin, CA), Heidelberg SL-OCT

S. Moghimi (✉) · J. Do
Department of Ophthalmology, Hamilton Glaucoma Center, Shiley Eye Institute, University of California, San Diego, CA, USA
e-mail: sasanimii@yahoo.com

M. SafiZadeh
Tehran University of Medical Sciences, Tehran, Iran

M. Mohammadpour (ed.), *Diagnostics in Ocular Imaging*,
https://doi.org/10.1007/978-3-030-54863-6_29

(Heidelberg Engineering Inc., Heidelberg, Germany), and Tomey CASIA (TOMEY Corp. Nagoya, Japan). A wavelength of 1310 nm allowed deeper penetration and cross-sectional imaging of the anterior chamber, including visualization of the angle. Systems converted from retinal scanners use an 830 nm light source and include the Spectralis OCT (Heidelberg Engineering Inc., Heidelberg, Germany), Cirrus HD-OCT (Carl Zeiss Meditec Inc., Dublin, CA), and Optovue RTVue (Optovue iVue; Optovue Inc., Fremont, CA).

The Visante was the first ASOCT to receive FDA approval and used time-domain technology to capture cross-sectional images of the entire anterior segment at a resolution of 10–18 μm [2]. This device provided quantitative measurements of corneal thickness, angle width, anterior chamber dimensions, iris thickness, and novel factors such as lens vault (LV) [3–14]. The advent of swept-source OCT (SSOCT) considerably improved the visualization of angle structures and facilitated more detailed assessments of the angle. The first generation of swept-source ASOCT was the CASIA SS-1000 OCT introduced by Tomey (Nagoya, Japan) in 2008. The CASIA SS-1000 OCT performs 30,000 A-scans per second and reaches an axial resolution of approximately 10 μm. Sixty-four evenly spaced radial scans, each with 512 A-scans spanning a distance of 16 mm, can visualize the entire anterior segment in less than 2 s. Parameters that could not be measured with time-domain and spectral-domain OCT instruments, such as the iris volume and the area of peripheral anterior synechiae, can be reliably measured with SSOCT [15, 16].

As a diagnostic and research tool for angle closure disease, ASOCT is revolutionary [17]. ASOCT can be performed easily in a noncontact fashion with relatively good repeatability and reproducibility [2]. In addition, ASOCT can acquire images under dim conditions and, thus, detect angle closure more efficiently [18]. The anterior segment images obtained using ASOCT can help in making decisions regarding performing laser treatments, choosing the appropriate surgical approach, and predicting success after procedures [9, 19–29]. Hence, ASOCT can be a useful adjunct tool in the diagnosis and management of glaucoma.

Anterior Segment Measurements

Numerous parameters and interactive measurements of various anatomical and pathological structures are made available with ASOCT. In addition to assessing images qualitatively, all commercial devices have built-in software to quantify angle parameters and make measurements of the anterior segment. Acquired ASOCT images can also be analyzed with third-party software such as the Zhongshan Angle Assessment Program (ZAAP, Guangzhou, China). Several anterior segment parameters can be measured [14, 25, 30–32] including:

(a) *Angle parameters*

The scleral spur is the most important landmark in evaluating the angle and making angle measurements. However, it can be difficult to identify the scleral spur in up to 20% of images acquired by the Visante. Fortunately, with newer high resolution SSOCT images, the scleral spur is identifiable in almost all cases [33].

The important angle parameters during anterior segment evaluations with ASOCT are the angle opening distance (AOD), angle recess area (ARA), and trabecular-iris space area (TISA) at 500 μm or 750 μm from the scleral spur (Figs. 1 and 2).

1. AOD is the distance from the cornea to iris at 500 μm or 750 μm from the scleral spur.
2. TISA at 500 μm or 750 μm from scleral spur is defined as the surface area of a trapezoid with the following boundaries: anteriorly, the angle opening distance at 500 μm or 750 μm from scleral spur; posteriorly, a line drawn from the

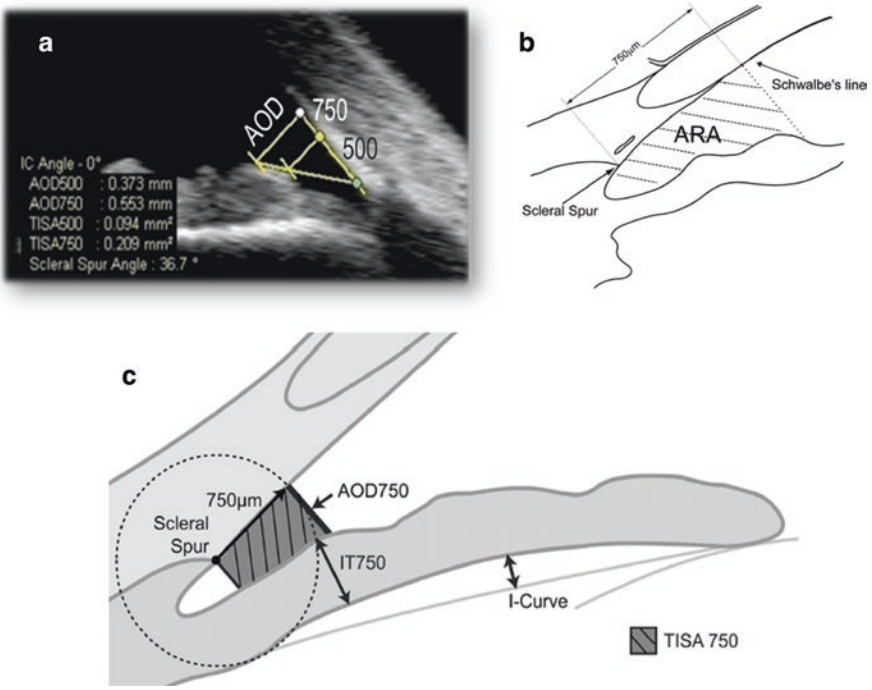

Fig. 1 **a** High magnification of ASOCT showing the angle parameters that provided by the device: angle opening distance (AOD), iris thickness at 750 μm, trabecular–iris space area (TISA) at 750 μm from the scleral spur, and the angle opening distance (AOD) at 750 μm. **b** Diagram of angle recess (ARA). **c** Iris curvature (I-Curve) and iris thickness at 750 μm (IT750)

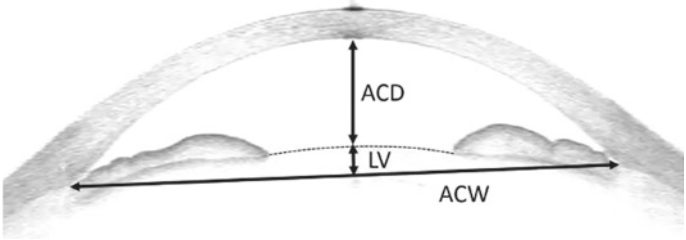

Fig. 2 Anterior segment optical coherence tomography image of anterior chamber demonstrating lens vault (LV), anterior chamber depth (ACD), and anterior chamber width (ACW)

scleral spur perpendicular to the plane of the inner scleral wall to the iris; superiorly, the inner corneoscleral wall; and inferiorly, the iris surface.
3. ARA is defined as triangular area bordered by the anterior iris surface, corneal endothelium, and a line perpendicular to the corneal endothelium drawn from a point 500 μm or 750 μm anterior to scleral spur to the iris surface

(b) *Anterior segment parameters*

In addition to anterior chamber depth (the axial distance from the corneal endothelium to the anterior lens surface), anterior chamber area (the cross-sectional area of the anterior chamber bordered by the posterior surface of the cornea, the anterior surface of the iris, and the anterior surface of the lens within the pupil), and volume, two novel anterior segment parameters have been introduced.

1. Anterior chamber width (ACW) is defined as the horizontal distance between the two scleral spurs.
2. Lens vault (LV) is the perpendicular distance from the anterior lens surface to the horizontal line connecting the two scleral spurs. When the anterior pole of the lens is located anterior to the scleral spur line, the LV is positive. When the anterior pole of the lens is posterior to the line connecting the scleral spurs, the LV is negative. The LV has been reported to be the most useful parameter associated with angle closure.

(c) *Iris parameters*

1. Iris thickness (IT) is defined as the shortest distance between designated locations at the anterior and posterior iris surface. The location is decided by the intersection point of a circle centered at the scleral spur with a radius of 750 μm (IT750, Fig. 1c) or 2000 μm (IT2000). This represents the thickness of the iris root and the iris pupil edge, respectively.
2. Iris area is calculated as the cumulative cross-sectional area of the full length of iris.
3. Iris curvature (I-Curve) is determined by creating a line from the most peripheral iris to the pupillary margin and measuring the perpendicular distance from this line to the point of greatest convexity along the posterior iris surface (Fig. 1c). It is considered a surrogate for the degree of pupillary block.

Table 1 lists the ASOCT parameters and their definitions used in the literature [14, 18–21].

Applications

Screening of Angle Closure Glaucoma

Primary angle closure glaucoma is a form of glaucoma with especially high prevalence in Asian countries. It is responsible for more cases of visual impairment than primary open angle glaucoma. Historically, anatomically narrow angles were

Table 1 Anterior segment parameters and their definitions for anterior segment optical coherence tomography images

Parameter	Definition
Anterior chamber depth (ACD)	The axial distance from the corneal endothelium to the anterior lens surface
Anterior chamber width (ACW)	The distance between the 2 scleral spurs
Anterior chamber area (ACA)	The cross-sectional area of the anterior chamber bordered by the posterior surface of the cornea, the anterior surface of the iris, and the anterior surface of the lens within the pupil
Anterior chamber volume (ACV)	The volume calculated by plotting a vertical axis through the center of the ACA and rotating ACA 360 degrees around this vertical axis
Angle opening distance at 250, 500, and 750 μm (AOD250, AOD500, AOD750)	The distance between the posterior corneal surface and the anterior iris surface along a line perpendicular to the posterior corneal surface 250, 500, and 750 μm from the scleral spur
Trabecular iris space area at 500 and 750 μm (TISA500, TISA750)	The surface area of a trapezoid with the following boundaries: anteriorly, the angle opening distance at 500 μm or 750 μm from the scleral spur; posteriorly, a line drawn from the scleral spur perpendicular to the plane of the inner scleral wall to the iris; superiorly, the inner corneoscleral wall; and inferiorly, the iris surface
Iris area (I-Area)	The cross-sectional area of the iris from the scleral spur to the pupil
Iris curvature (I-Curve)	The perpendicular distance between a line connecting the most central to the peripheral points of the iris pigment epithelium and the posterior iris surface at the point of greatest convexity
Iris thickness (IT)	Iris thickness at 750 μm or 2000 μm from the scleral spur (IT750 and IT2000)
Lens vault (LV)	The perpendicular distance from the anterior pole of the lens to the horizontal line between the scleral spurs
Anterior vault (AV)	The perpendicular distance from the corneal endothelium to the horizontal line between the scleral spurs
Posterior corneal arc depth	The arc distance of the posterior corneal border between scleral spurs [22]
Pupil diameter (PD)	The distance between the pupil edges of the iris

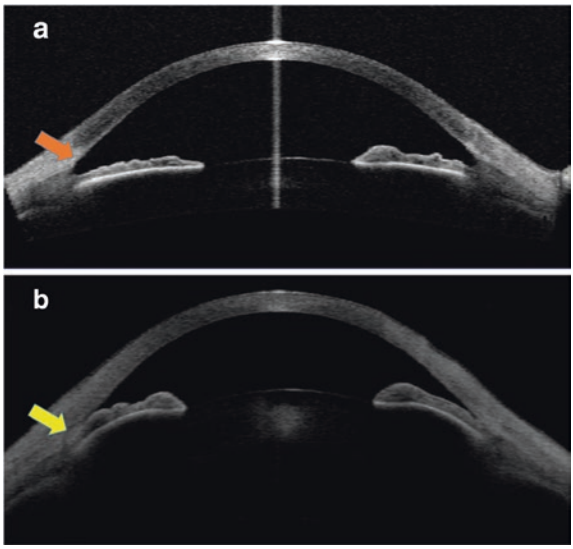

Fig. 3 **a** ASOCT of an eye with an open angle. Note the deep anterior chamber and flat iris profile. No evidence of iridotrabecular contact can be found in the ASOCT image (orange arrow). **b** ASOCT of an eye with a closed angle demonstrating a shallow anterior chamber, convex iris configuration, and iridotrabecular contact at the temporal and nasal angle (yellow arrow)

treated with a laser peripheral iridotomy to prevent the development of angle closure glaucoma. Therefore, early detection of the anatomically narrow angle was important.

Iridotrabecular contact (ITC), contact between the iris and the trabecular meshwork anterior to the scleral spur, is used to define angle closure in ASOCT images (Fig. 3) [18]. Synechiael angle closure can be differentiated from appositional angle closure by studying the differences in the angle configuration in the light and dark [15]. Both time-domain and swept source ASOCT can be used to identify eyes with narrow angles. The overall diagnostic performance of the CASIA SSOCT in detecting gonioscopically-defined angle closure was better than the Visante (area under the receiver operating curve (AUC): 0.84 and 0.73, respectively) [34, 35]. While several studies have shown moderate to good agreement between ASOCT and gonioscopy in classifying angle closure, ASOCT tends to diagnose angle closure in more subjects than gonioscopy [18]. Differences in lighting conditions and anterior chamber compression that widens the angle during gonioscopy are proposed as the main reasons for these discrepancies.

The Zhongshan Angle-Closure Prevention (ZAP) Trial in the Chinese population demonstrated a low incidence of vision threatening events. In this prospective trial involving 889 subjects in China aged 50–70 years with bilateral primary angle-closure suspects who received prophylactic LPI in 1 eye and observation in the fellow eye, the overall beneficial effect of prophylactic LPI was limited given the extremely rare development of angle closure glaucoma in both groups after 6 years of follow-up. Therefore widespread screening for angle closure is not recommended [22].

Pathophysiology of Angle Closure

Multiple anatomical and physiological factors contribute to the pathogenesis of angle closure glaucoma. Ocular biometric factors that increase the risk of angle closure include a short axial length, shallow anterior chamber, thick peripheral iris, and thick or anteriorly positioned lens. Recently, it is known that lens thickness and position has a key role in angle closure. However, its role is not similar in different subtype of the angle closure disease. Acute primary angle closure (APAC) eyes and their fellow eyes have greater lens vault and thickness compared to primary angle closure suspects (PACS) and PACG. Figure 4 depicts ASOCT image of eyes with APAC, Fellow eyes of APAC and PACG.

These characteristics can predispose the eye to pupillary block, one of the primary mechanisms of angle closure. In pupillary block, resistance to aqueous flow from the posterior to anterior chamber at the level of the pupil creates a pressure gradient that causes bombe´ of the peripheral iris and closure of the angle [28].

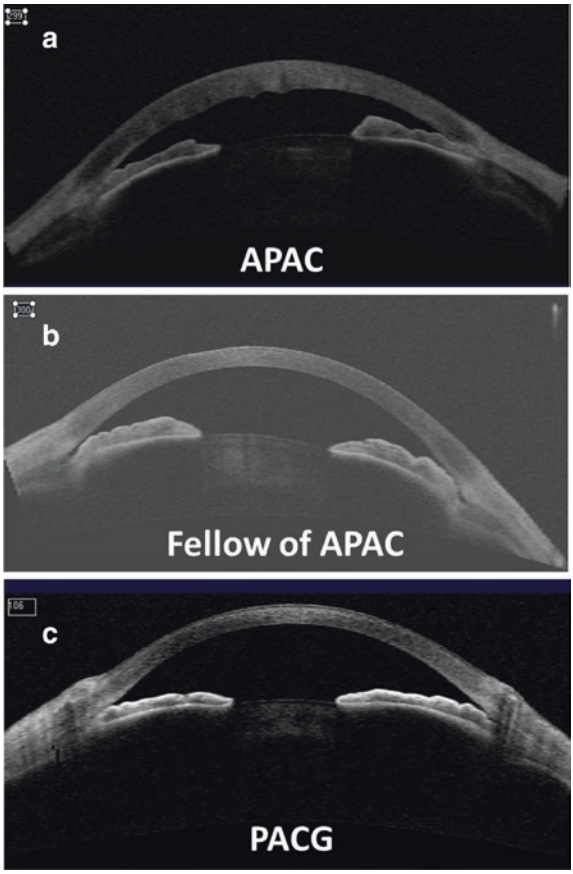

Fig. 4 ASOCT of an eye with **a** acute primary angle closure (APAC), **b** fellow eye of the APAC eye from (**a**), and **c** primary angle closure glaucoma (PACG). APAC eyes have a greater lens vault and very shallow anterior chambers. Corneal edema after the resolution of acute episode is evident. Note that fellow eye of the attack has more profound iris bowing compared to APAC eyes and PACG eyes

Fig. 5 Anterior segment-OCT images of a phacomorphic angle closure eye (**a**) and acute primary angle closure (APAC) (**b**) although the phacomorphic angle closure eye has a shallower anterior chamber and greater lens vault (LV), the angles are wider. The anterior chamber width (ACW) is comparable

In phacomorphic glaucoma, a type of secondary angle closure glaucoma in which a thick lens causes angle closure, ASOCT measurements demonstrate a greater lens vault, shallower ACD, and smaller anterior chamber area compared to APAC eyes (Fig. 5). In contrast, APAC eyes have a narrower angle and thicker iris, suggesting role for both iris and lens in the primary angle closure disease [36].

Angle closure can also occur in the absence of pupillary block such as in plateau iris syndrome. A plateau iris configuration is defined by a normal central anterior chamber depth (ACD), an extremely narrow or closed angle on gonioscopy, a flat iris plane, and a double hump configuration on indentation gonioscopy [37]. Plateau iris syndrome occurs in the setting of a plateau iris configuration in which angle closure occurs spontaneously or after dilation in the presence of a patent iridotomy. Ultrasound biomicroscopy is useful in detecting a plateau iris configuration by demonstrating anteriorly rotated ciliary processes, anterior displacement of the adjacent iris, and absence of the ciliary sulcus.

ASOCT allows for the quantitative evaluation of factors related to the iris, lens, and ciliary body that also play important roles in angle closure disease. Analyses of these parameters has improved the ability to differentiate between pupillary block and plateau iris and has broadened ophthalmologic understanding of the mechanisms that lead to angle closure [31].

Using ASOCT images, angle closure mechanisms can be categorized into four mechanisms: pupillary block, plateau iris configuration, thick peripheral iris roll (PIR), or exaggerated lens vault [8] (Fig. 6).

1. **Pupillary block** is defined as eyes with an anteriorly convex iris profile with a typical bombe' appearance, a small central zone of iridolenticular contact, and shallow peripheral AC.
2. **Plateau Iris** is defined as eyes in which the anterior chamber is deep, the central iris plane is flat, but the iris root rises steeply from its insertion and angles downward from the angle wall.
3. **Thick peripheral iris roll (Thick PIR)** is defined as eyes in which prominent circumferential folds of the peripheral iris occupy a large part of the angle.

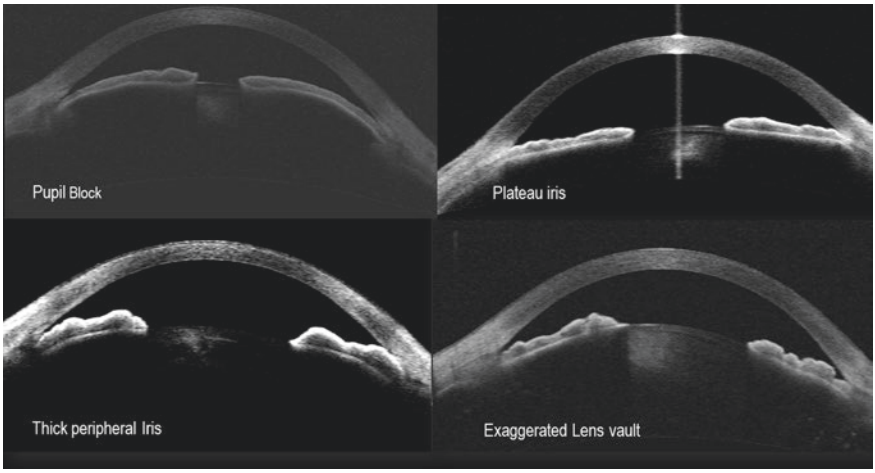

Fig. 6 ASOCT images of eyes with 4 different mechanisms of angle closure. Top left: Pupillary block mechanisms with a convex iris profile, a small central zone of iridolenticular contact, and shallow peripheral AC, and a typical bombe appearance. Top right: Plateau iris with a central flat iris plane and deep central anterior chamber. Bottom left: Thick peripheral iris roll with prominent folds of the peripheral iris occupying a large part of the angle. Bottom right: Exaggerated lens vault with a "volcano-like configuration" of the iris and small AC volume secondary to anterior displacement of the iris by the lens

4. **Exaggerated lens vault** is defined as eyes with a "volcano- like configuration" of the iris and small anterior chamber volume secondary to anterior displacement of the iris by the lens. The iris appears to drape over the anterior surface of the lens, and the space between iris surface and endothelium is markedly decreased. Acute primary angle closure eyes and their fellow eyes have greater lens vault and thickness compared to eyes that are PACS and PACG (Fig. 7).

Identifying the mechanism of angle closure is essential to determine the most effective treatment. For example, LPI can be used in pupillary block, laser peripheral iridoplasty for plateau iris or thick peripheral iris roll, or lens extraction in a patient with an exaggerated lens vault. Moghimi et al. developed an artificial intelligence algorithm to classify angle closure mechanisms from ASOCT images [5]. The algorithm aimed to identify the major mechanisms of angle closure: exaggerated lens vault, pupil block, thick peripheral iris roll, and plateau iris.

Efficacy of Procedures

Other applications of ASOCT include evaluating the efficacy of treatments such as LPI, laser iridoplasty, or cataract extraction.

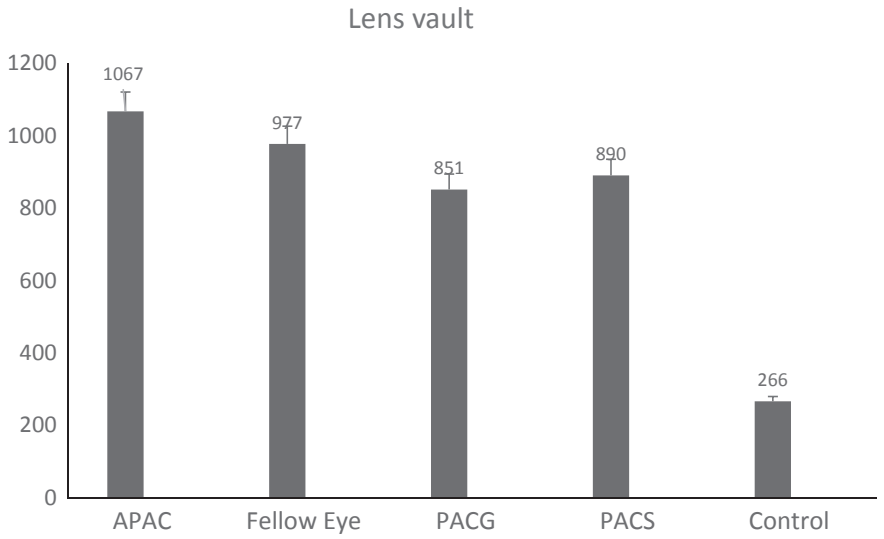

Fig. 7 Graph demonstrating lens vault in different subtypes of glaucoma. Note that lens vault is greater in acute primary angle closure (APAC) eyes and their fellow eyes compared to primary angle closure glaucoma (PACG), and primary angle closure suspects (PACS) eyes and the healthy controls

Laser Peripheral Iridotomy

ASOCT can be used to evaluate the responsiveness of an eye to an LPI. In PACS eyes, a thinner and steeper iris (greater iris bowing or bombe appearance) has been shown to be independent predictors of anterior chamber angle widening after LPI. In APAC eyes, the degree of angle opening following LPI is greater when the angle parameters (TISA and AOD) are smaller [38]. The patency of an iridotomy can also be determined on ASOCT by visualizing the anterior lens capsule behind the full-thickness iris defect created by the LPI. More importantly, following LPI treatment of pupillary block, ASOCT can show effectiveness of the LPI by demonstrating a lack of ITC and a decrease in iris bowing [24] (Fig. 8).

Cataract Extraction

The anterior segment changes dramatically after cataract removal. Cataract extraction deepens the anterior chamber and open the iridocorneal angle [10]. SSOCT has been used to assess the circumferential reduction of iridotrabecular area after

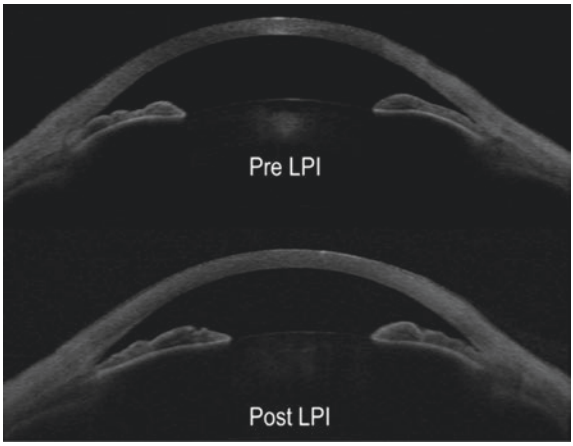

Fig. 8 ASOCT of a patient with primary angle closure suspect who had LPI. The iris profile is now flatter, angles are widened, and there is no iridotrabecular contact

phacoemulsification alone or in combination with goniosynechialysis. The investigators have found that phacoemulsification and goniosynechialysis surgery resulted in a greater reduction of iridotrabecular area (and the extent of PAS) than cataract surgery alone after adjusting for age, gender and baseline IOP, baseline PAS and preoperative pupil diameter. These biometric changes after cataract surgery are well documented in normal eyes as well as eyes with open angle and angle closure glaucoma [25, 27, 39] (Fig. 9). Furthermore, ASOCT can predict IOP responses after cataract surgery. The IOP reduction following cataract surgery is greater in eyes with a more anteriorly located lens (greater lens vault) and smaller anterior segment [29].

Bleb Morphology

ASOCT is a useful tool for evaluating filtering blebs in the postoperative period [40, 41] (Figs. 10 and 11). Clinically, blebs can be described as diffuse, cystic, encapsulated, or flat. However, these descriptions are subjective and there may be cases in which the clinical appearance does not correlate with bleb function. Visualizing bleb morphologies with anterior segment imaging provides objective measures and enhances our understanding of surgical outcomes and wound healing. Studies have shown that the information from bleb images is predictive of a successful filtering procedures [41]. Investigators have found that high blebs with thicker walls that showed multiple parallel hyporeflective layers within the bleb wall at 2 weeks posttrabeculectomy predicts good IOP control at 1 year post-trabeculectomy [41].

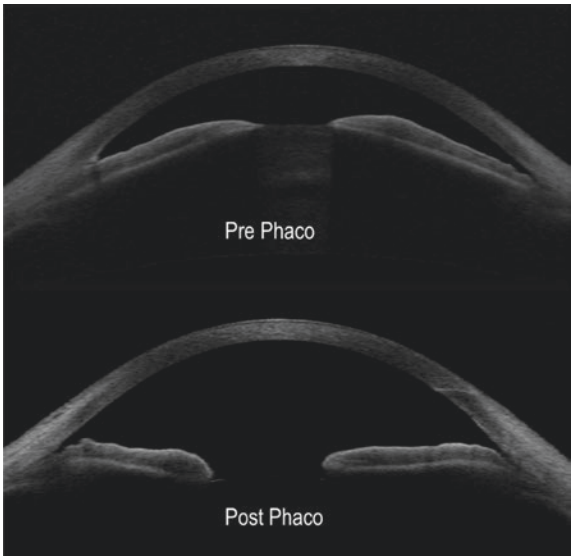

Fig. 9 ASOCT image of the dramatic changes in a patient with acute primary angle closure who has undergone phacoemulsification. Following surgery, the anterior chamber has deepened significantly, and the iridocorneal angles are wide open

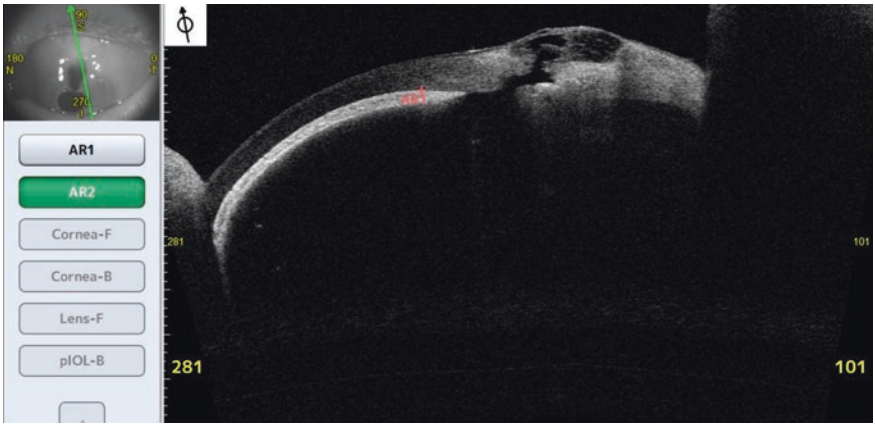

Fig. 10 ASOCT image of a functioning bleb. The sclerostomy is open. The low reflectivity of the conjunctiva and multiple microcystic spaces in the bleb space indicate imbibition of aqueous humor by the bleb. The patient has a flat anterior chamber due to overfiltration following laser suture lysis three days before

Other Applications

The noninvasive nature of ASOCT allows for its safe use in situations like early postoperative periods, penetrating trauma, or severe blunt trauma. ASOCT is also helpful in the assessment of anterior chamber when media or corneal opacities preclude evaluation (Fig. 12). In patients with keratoprosthetics and glaucoma

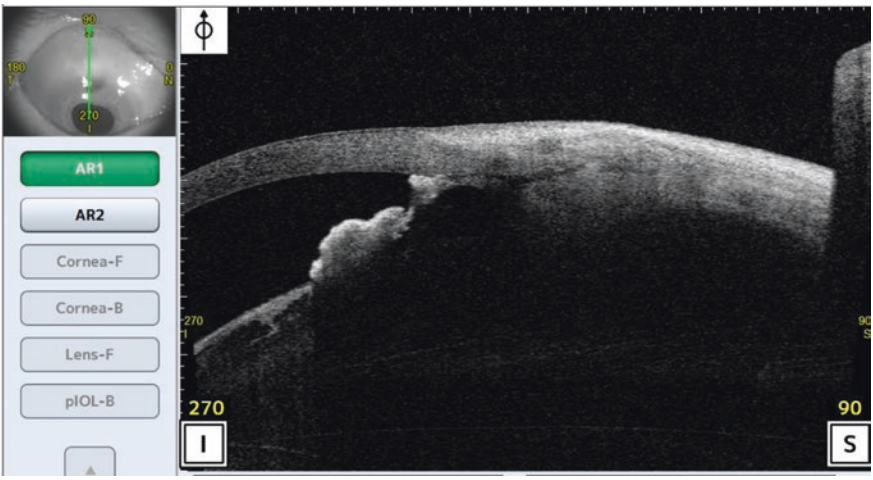

Fig. 11 ASOCT image showing a flat bleb. Although the sclerostomy is open, the conjunctiva is fused with a high reflectivity band in the underlying layer. No cystic space can be found in the conjunctiva. A bleb is absent and not functioning

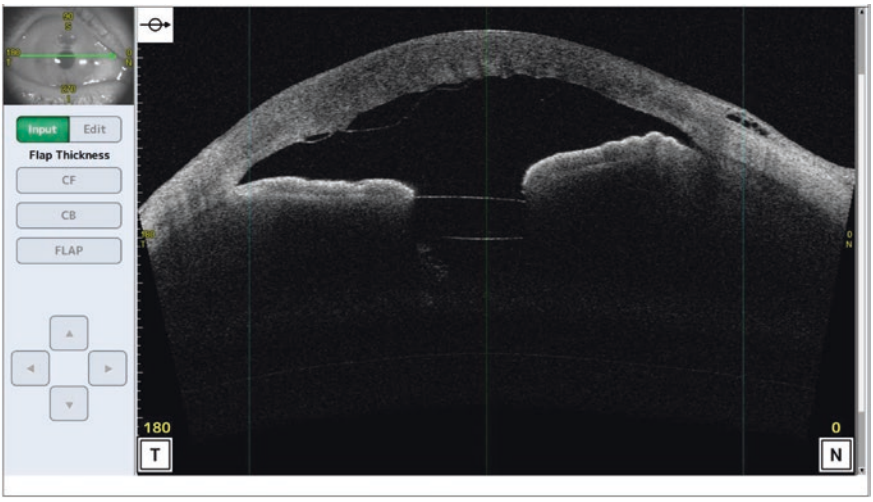

Fig. 12 A 56-year-old female with 4+ corneal edema after cataract surgery. ASOCT shows thickening of the cornea and an area of Descemet's membrane detachment

drainage devices in which visualization of the tube in the anterior chamber is not possible, we have shown that ASCOT can be used to assess tube patency and position [42] (Fig. 13).

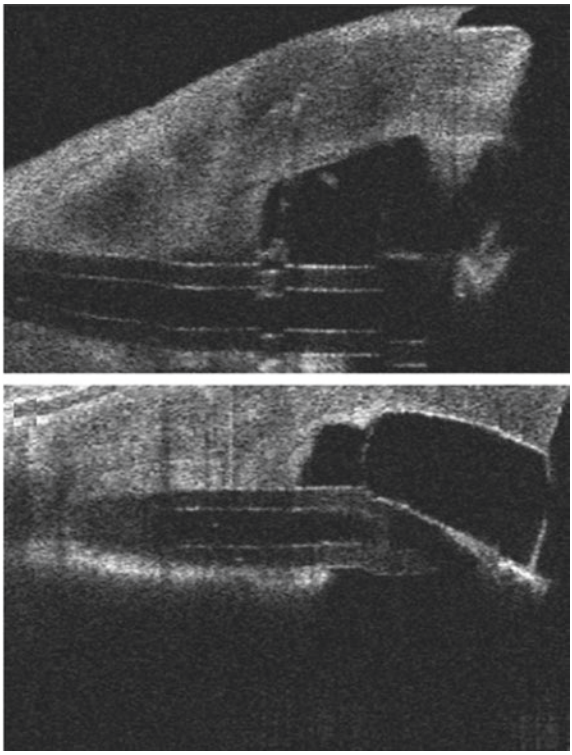

Fig. 13 ASOCT images has been used for evaluation of the position and patency of glaucoma drainage device tubes in a patient after combined glaucoma tube shunt and keratoprosthesis implantation. Top: drainage device tube positioned in the anterior chamber between the peripheral cornea and iris without blockage. Bottom: Glaucoma drainage device tube partially covered by a membrane. (Reprinted with permission from Lippincott Williams and Wilkins)

Limitations

Although ASOCT provides high resolution images of the anterior chamber angle, most devices acquire a single horizontal cross-section of the anterior chamber and do not readily assess the entire angle circumference. Furthermore, because of the properties of transmitted light, structures posterior to the iris are obscured in ASOCT images, and the ciliary body can only be partially revealed. Ultrasound biomicroscopy remains the only tool to visualize structures posterior to the iris. Lastly, even with new generations of ASOCT, the evaluation of synechiae is limited without the dynamic capabilities of indentation gonioscopy.

Acknowledgements Funding/support: None.

Financial Disclosure: S. Moghimi, None; M. Safizadeh, None; J. Do, None.

References

1. Izatt JA, et al. Micrometer-scale resolution imaging of the anterior eye in vivo with optical coherence tomography. Arch Ophthalmol. 1994;112(12):1584–9.
2. Li H, et al. Repeatability and reproducibility of anterior chamber angle measurement with anterior segment optical coherence tomography. Br J Ophthalmol. 2007;91(11):1490–2.
3. Gazzard G, et al. Light to dark physiological variation in irido-trabecular angle width. Br J Ophthalmol. 2004;88:1357–482.
4. Moghimi S, et al. Comparison of anterior segment-optical coherence tomography parameters in phacomorphic angle closure and acute angle closure eyes. Invest Ophthalmol Vis Sci. 2015;56(13):7611–7.
5. Moghimi S, et al. Classification of primary angle closure spectrum with hierarchical cluster analysis. PLoS ONE. 2018;13(7):e0199157.
6. Moghimi S, et al. Ocular biometry in the subtypes of angle closure: an anterior segment optical coherence tomography study. Am J Ophthalmol. 2013;155(4):664–73, 673 e1.
7. Moghimi S, et al. Role of lens vault in subtypes of angle closure in Iranian subjects. Eye. 2014.
8. Moghimi S, et al. Acute angle closure: qualitative and quantitative evaluation of the anterior segment using anterior segment optical coherence tomography. Clin Exp Ophthalmol. 2014;42(7):615–22.
9. Napier ML, Azuara-Blanco A. Changing patterns in treatment of angle closure glaucoma. Curr Opin Ophthalmol. 2018;29(2):130–4.
10. Nolan W. Anterior segment imaging: ultrasound biomicroscopy and anterior segment optical coherence tomography. Curr Opin Ophthalmol. 2008;19(2):115–21.
11. Nolan WP, et al. Changes in angle configuration after phacoemulsification measured by anterior segment optical coherence tomography. J Glaucoma. 2008;17(6):455–9.
12. Nongpiur M, et al. Anterior segment imaging-based subdivision of subjects with primary angle-closure glaucoma. Eye. 2016.
13. Nongpiur ME, et al. Subgrouping of primary angle-closure suspects based on anterior segment optical coherence tomography parameters. Ophthalmology. 2013;120(12):2525–31.
14. Nongpiur ME, et al. Lens vault, thickness, and position in Chinese subjects with angle closure. Ophthalmology. 2011;118(3):474–9.
15. Lai I, et al. Anterior chamber angle imaging with swept-source optical coherence tomography: measuring peripheral anterior synechia in glaucoma. Ophthalmology. 2013;120(6):1144–9.
16. Mak H, Xu G, Leung CK-S. Imaging the iris with swept-source optical coherence tomography: relationship between iris volume and primary angle closure. Ophthalmology. 2013;120(12):2517–24.
17. Dada T, et al. Comparison of anterior segment optical coherence tomography and ultrasound biomicroscopy for assessment of the anterior segment. J Cataract Refract Surg. 2007;33(5):837–40.
18. Nolan WP, et al. Detection of primary angle closure using anterior segment optical coherence tomography in Asian eyes. Ophthalmology. 2007;114(1):33–9.
19. Ang GS, Wells AP. Factors influencing laser peripheral iridotomy outcomes in white eyes: an anterior segment optical coherence tomography study. J Glaucoma. 2011;20(9):577–83.
20. Baskaran M, et al. Residual angle closure one year after laser peripheral iridotomy in primary angle closure suspects. Am J Ophthalmol. 2017;183:111–7.
21. Han S, et al. Outcomes of laser peripheral iridotomy in angle closure subgroups according to anterior segment optical coherence tomography parameters LPI. Invest Ophthalmol Vis Sci. 2014;55(10):6795–801.
22. He M, et al. Laser peripheral iridotomy for the prevention of angle closure: a single-centre, randomised controlled trial. The Lancet. 2019;393(10181):1609–18.

23. Lee RY, et al. Association between baseline iris thickness and prophylactic laser peripheral iridotomy outcomes in primary angle-closure suspects. Ophthalmology. 2014;121(6):1194–202.
24. Moghimi S, et al. Changes in anterior segment morphology after laser peripheral iridotomy in acute primary angle closure. Am J Ophthalmol. 2016;166:133–40.
25. Eslami Y, et al. Effect of adjunctive viscogonioplasty on drainage angle status in cataract surgery: a randomized clinical trial. Clin Exp Ophthalmol. 2013;41(4):368–78.
26. Hsia YC, et al. Anterior segment parameters as predictors of intraocular pressure reduction after phacoemulsification in eyes with open-angle glaucoma. J Cataract Refract Surg. 2017;43(7):879–85.
27. Huang G, et al. Association of biometric factors with anterior chamber angle widening and intraocular pressure reduction after uneventful phacoemulsification for cataract. J Cataract Refract Surg. 2012;38(1):108–16.
28. Kim M, et al. Anterior chamber configuration changes after cataract surgery in eyes with glaucoma. Korean J Ophthalmol. 2012;26(2):97–103.
29. Moghimi S, et al. Lens parameters as predictors of intraocular pressure changes after phacoemulsification. Eye. 2015;29(11):1469.
30. Kim YK, et al. Relative lens vault in subjects with angle closure. BMC Ophthalmol. 2014;14(1):93.
31. Wang D, et al. Ethnic difference of the anterior chamber area and volume and its association with angle width. Invest Ophthalmol Vis Sci. 2012;53(6):3139–44.
32. Wu RY, et al. Association of narrow angles with anterior chamber area and volume measured with anterior-segment optical coherence tomography. Arch Ophthalmol. 2011;129(5):569–74.
33. Rigi M, et al. Agreement between gonioscopic examination and swept source Fourier domain anterior segment optical coherence tomography imaging. J Ophthalmol. 2016;2016.
34. Lavanya R, et al. Screening for narrow angles in the Singapore population: evaluation of new noncontact screening methods. Ophthalmology. 2008;115(10):1720–7, 1727 e1–2.
35. Porporato N, et al. Assessment of circumferential angle closure with swept-source optical coherence tomography: a community based study. Am J Ophthalmol. 2019;199:133–9.
36. Mansouri M, et al. Anterior segment optical coherence tomography parameters in phacomorphic angle closure and mature cataracts. Invest Ophthalmol Vis Sci. 2014;55(11):7403–9.
37. Shabana N, et al. Quantitative evaluation of anterior chamber parameters using anterior segment optical coherence tomography in primary angle closure mechanisms. Clin Exp Ophthalmol. 2012;40(8):792–801.
38. Huang G, et al. Anatomic predictors for anterior chamber angle opening after laser peripheral iridotomy in narrow angle eyes. Curr Eye Res. 2012;37(7):575–82.
39. Tun TA, et al. Swept-source optical coherence tomography assessment of iris–trabecular contact after phacoemulsification with or without goniosynechialysis in eyes with primary angle closure glaucoma. Br J Ophthalmol. 2015;99(7):927–31.
40. Leung CK, et al. Analysis of bleb morphology after trabeculectomy with Visante anterior segment optical coherence tomography. Br J Ophthalmol. 2007;91(3):340–4.
41. Narita A, et al. Characteristics of early filtering blebs that predict successful trabeculectomy identified via three-dimensional anterior segment optical coherence tomography. Br J Ophthalmol. 2018;102(6):796–801.
42. Law SK, et al. Technique of combined glaucoma tube shunt and keratoprosthesis implantation. J Glaucoma. 2014;23(8):501–7.

Orbital Imaging

Imaging in Orbital Disorders

Mohammad Taher Rajabi

Introduction

Assessment of the orbit by imaging modalities is inseparable to clinical examination [1]. Most common orbital imaging techniques are Computed Tomography scan (CT scan) and Magnetic Resonance Imaging (MRI). The difference between ocular and orbital disorders is that ocular disorders usually have only visual symptoms; but orbital disorders have many signs and symptoms, such as proptosis, globe dystopia, diplopia, pain and many others. So, choosing between CT-Scan and MRI depends on many factors such as age of the patient, orbital signs and symptoms and the clinical suspicion that determines whether soft tissue matters or the bone is involved [1].

When we request an imaging, we have at least two purposes; first, to localize the disease and then to diagnose the nature of the orbital disease. Variety of orbital pathologic findings can be orbital mass lesions including tumors, orbital wall fractures, cellular infiltration, and infection and so on. In a systematic approach, we should evaluate all of the orbital and peri-orbital tissues in CT-scan and MRI, not to miss any pathology.

Since the CT-scan is based on X-ray and the X-ray is the best for the diagnosis of bone structure and pathology; axial CT scan with the thin sections is the top choice after trauma. Images are formatted to have multiplanar presentation [2]. In approaching a CT-scan, first, we focus on the orbital and paranasal bones and then consider the soft tissue, not to miss any component, we notice the orbital soft tissue in an ordered manner starting from globe, optic nerve, muscles, orbital apex, lacrimal gland, the sinuses and the brain as much as visible. When we find any mass lesion in the orbit, we should first, localize it to intraconal or extraconal, then we notice the border of the tumor that is well-defined or ill-defined; also density,

M. T. Rajabi (✉)
Tehran University of Medical Sciences, Tehran, Iran
e-mail: mt_rajabi@yahoo.com

M. Mohammadpour (ed.), *Diagnostics in Ocular Imaging*,
https://doi.org/10.1007/978-3-030-54863-6_30

homogeneity, and the mass effect on surrounding structures, should be noticed then. A mass lesion in the orbit can affect the surrounding tissues in different manners depending on its clinical behavior such as globe displacement or molding the globe, and also their effect on orbital bones would be remodeling of the bone, bone resorption or bone destruction.

Computed Tomography

CT-scan has three views each obtained parallel to one of the 3 dimensional spatial planes named axial, coronal and sagittal views. The main plane of imaging is the axial plane and the others are reformed. It has also two window settings that are soft tissue window setting and bone window setting. Usually we do not need the bone window setting in orbital disorders. So most of the time we request soft tissue window setting for evaluation of common orbital disorders. All views including coronal, sagittal and axial should be considered, to have a three dimensional evaluation to approach the orbit and its possible pathologies.

As mentioned before, choosing between CT-Scan and MRI depends on history and various clinical findings, such as age, lacrimal system enlargement or optic-nerve function disorders, the history of trauma, presence of proptosis or history of thyroid disease.

Axial View

An image of axial view CT-scan on the soft tissue window setting is shown in Fig. 1. Pay attention to bone, globe, optic nerve, muscles, sinuses, orbital apex, superior orbital fissure, optic canal, and fat [2]. Four distinct densities are noticed in the CT-scan. The first one is the bone density that is very high. The second one is the density of the muscles, sclera and optic nerve. The densities of these three components are considered fairly the same. The third density is of the vitreous and the brain which also can be considered of the same density. The forth one is the density of the fat and air. Any changes in the density of the fat tissue, helps us in diagnosis of any intra-conal or extra-conal disorders. So, we should check these four distinct densities in tissue window setting images to make sure that all the components are noted.

Coronal View

Coronal view of CT-scan on the tissue window setting is shown in Fig. 2. First, we should consider bone, muscles, optic-nerve, superior rectus, levator complex,

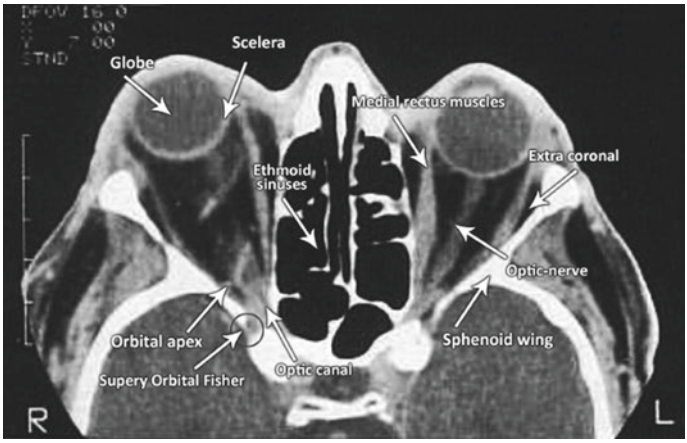

Fig. 1 CT-scan in axial view imaged at tissue window setting

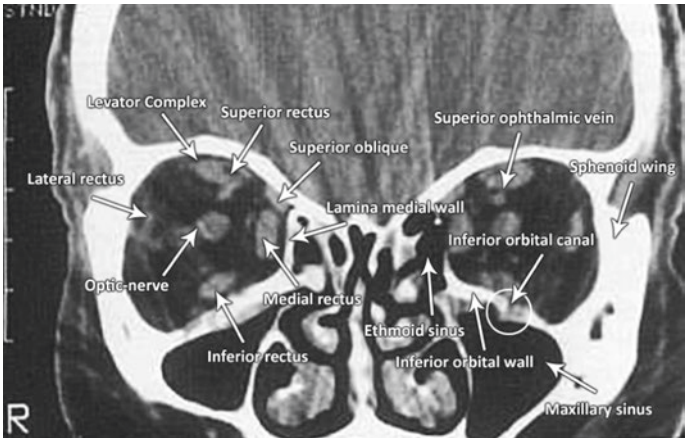

Fig. 2 CT scan in coronal view imaged at tissue window settings

lateral rectus, inferior rectus, medial rectus and superior oblique. Also superior ophthalmic vein is best visible in this view. Attention is needed to the superior ophthalmic vein in patient with proptosis, ocular vascular tortuosity and also red eye. In the next step, we should evaluate the orbital fat again. The fat density is like the air content of the sinuses. So, if there is any infiltration or mass in intra-conal space, the density of the fat will be changed. After evaluation of the orbit, the brain and the sinuses should be noticed. Figure 2 shows maxillary and ethmoidal sinuses. We should also evaluate the lamina papiracea, lamina cribrosa in medial wall and the inferior orbital canal that is within the inferior orbital wall.

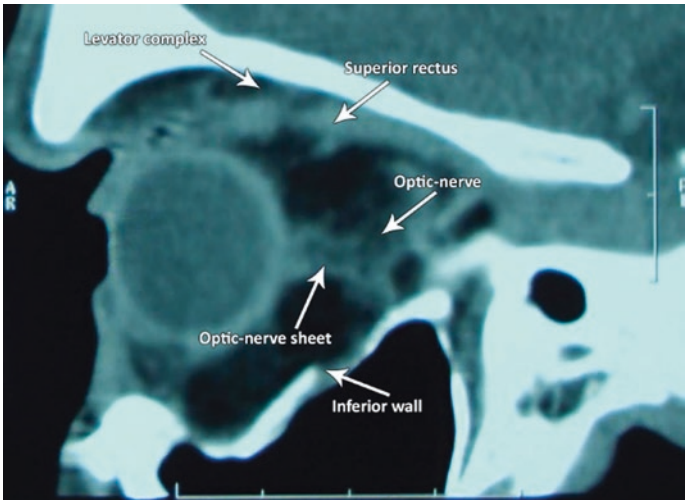

Fig. 3 CT-scan in sagittal view imaged at tissue window settings

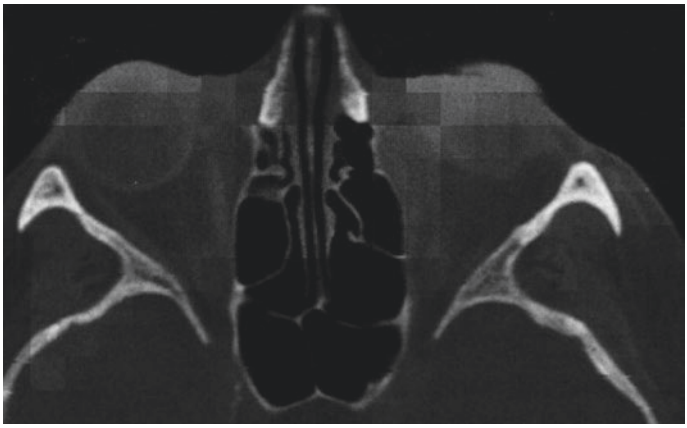

Fig. 4 Bone window of axial CT-scan

Sagittal View

The superior rectus-levator complex, inferior rectus, inferior wall, the bones, globe and the optic-nerve can be seen in sagittal orbital CT-scan in the Fig. 3. The high density around the optic-nerve is its sheath and the optic-nerve itself is within the sheath.

The bone window of axial CT-scan is shown in Fig. 4 that usually is not used. There is no need to request it in orbital disorders.

Magnetic Resonance Imaging

High resolution magnetic resonance imaging provides better lesion characterization [3]. MRI also has three views, which are axial, coronal, and sagittal. Furthermore, the basic types of sequences used in orbital MRI, create either T1-weighted or T2-weighted images. In T1W images, CSF, blood, and vitreous fluid appear dark. Fat has the highest intensity and seems bright. In T2W images, CSF and vitreous fluid have higher signal intensity than soft tissue. On both of T1W and T2W images, bones seem very dark [3]. So, for evaluating the bone, the MRI is not a good choice. And the best choice, as noted previously, for bone study is CT-scan which shows the bone as a white bright object.

In studying the MRI, similar to CT scan, it is suggested to study the images in an ordered manner. After evaluating the orbital fat specifically, other tissues are noticed. The best basis of comparison in tissue intensities is the brain, in orbital MRI, whereas the globe or muscles or optic-nerve also can be chosen as the reference point. In T1W images, the globe and water-filled masses such as cysts, can be seen as low intensity or named hypo-intense compared to the brain. So, if we notice T1W images, the globe is seen as darker area compared to the brain that is brighter. The same is true for globe compared to optic-nerve and muscles that are iso-intense with brain in T1W images.

In T2W images, the globe, vitreous fluid, and any abscess or cystic lesion looks bright. So, the globe can be seen white or bright compared to the brain. So the globe is considered hyper-intense in T2W images [3].

Again, the muscles and optic-nerve seem iso-intense compared to brain on T2W images. Fat may appear iso-intense, hyper-intense, or even hypo-intense. So, the study on fat tissue should not be performed on T2W images (Fig. 5).

Figure 6, shows T1W image with contrast and fat suppression. T1W images without any contrast reveal nearly all of the orbital tissues except fat which appears bright; if there is any abnormality within the orbit, when the contrast is administered, and the lesion is enhanced, it will seem bright and the brightness of the fat may mask it. For this reason, fat suppression technique, in T1W images taken after contrast administration, reveals more details of the orbital tissues such as muscles or optic-nerve and disorders will be distinguished more easily [3], this is very important in the study of intraconal region. In T1W images with contrast, all muscles around the globe and also lacrimal gland would be seen white due to the contrast enhancement. Optic-nerve would not enhance; so, any enhancement around or within the optic-nerve, should be considered for optic-nerve disorders.

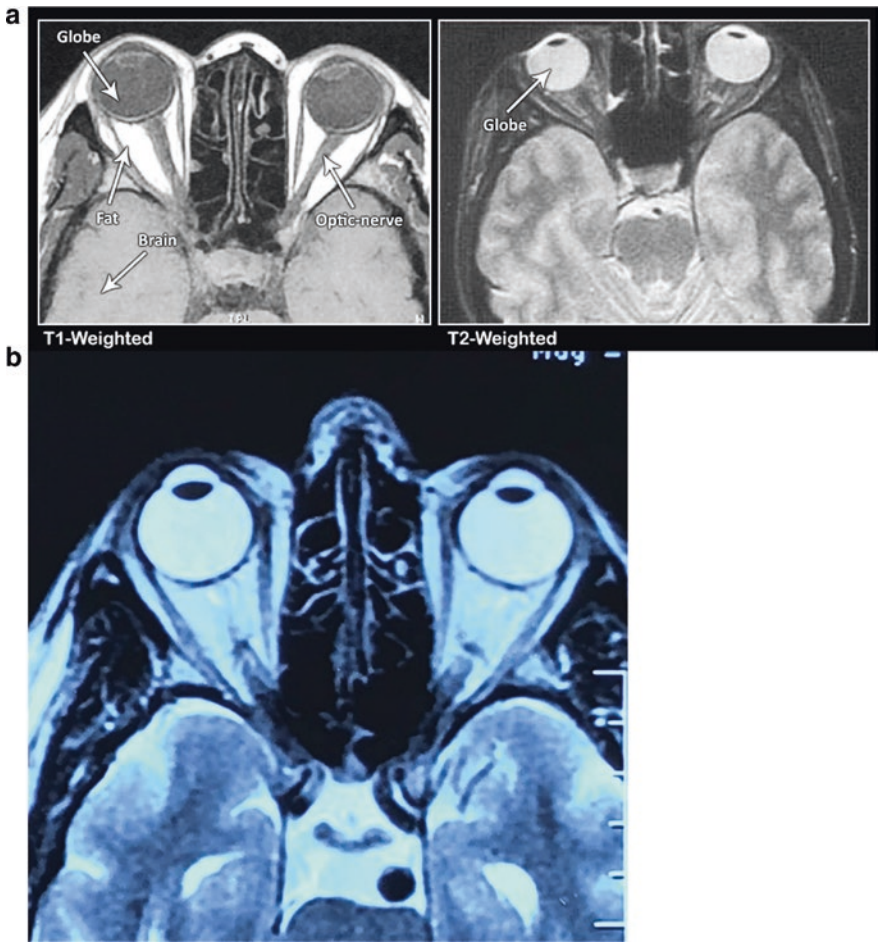

Fig. 5 **a** A T1W MRI in axial view. The vitreous fluid is typically dark, whereas the fat appears bright. **b** A T2W MRI in axial view. The vitreous appears bright, whereas the fat is intermediate. Another T2W image that fat appears in high signal intensity

MRI Patterns

MRI patterns in orbital lesions depend on the water content, vascularity and cellular density of the lesion. So, in masses with high water content, the tumor has very low intensity, similar to bone or air. Figure 7, the left side image, shows a mass posterior to the globe that is very dark compared to the globe. Due to its high water content, it seems to be a Hydatid cyst. But the right-side image in Fig. 7, demonstrates multiple masses posterior to the globe that indented the globe, but the signal intensity of the masses are higher in comparison to the globe, and are iso-intense with brain that can be orbital abscess.

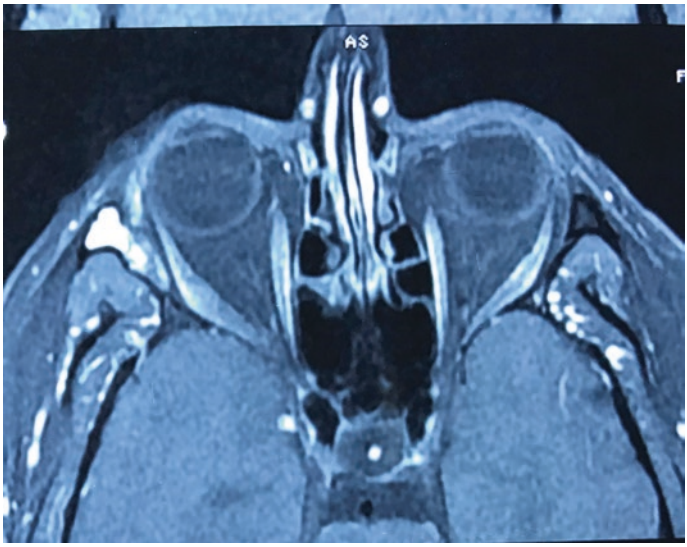

Fig. 6 T1W image with contrast administration and fat suppression

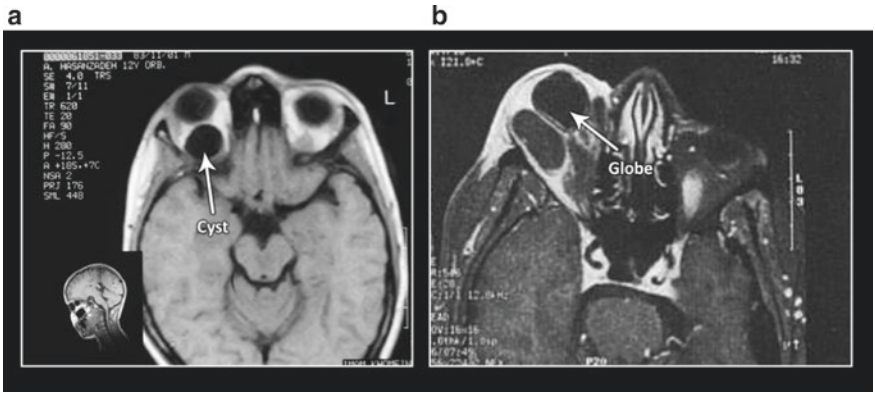

Fig. 7 **a** Left side image shows Hydatid cyst. **b** The right-side image shows multiple masses posterior to the globe which seem to be orbital abscess

If the patient has vascular disorder such as orbital cavernous hemangioma, it will appear iso-intense or hypo-intense with brain [4]. Due to the fibrous tissue that exists within the mass in the cavernous hemangioma tumors, these tumors seem to be iso-intense or hypo-intense compared to the brain in T1W images (Fig. 8a; but in tumors with low water content, they seem hyper-intense compared to the brain. For example, Fig. 8b demonstrates metastatic tumor that is hyper-intense compared to the brain similar to fat.

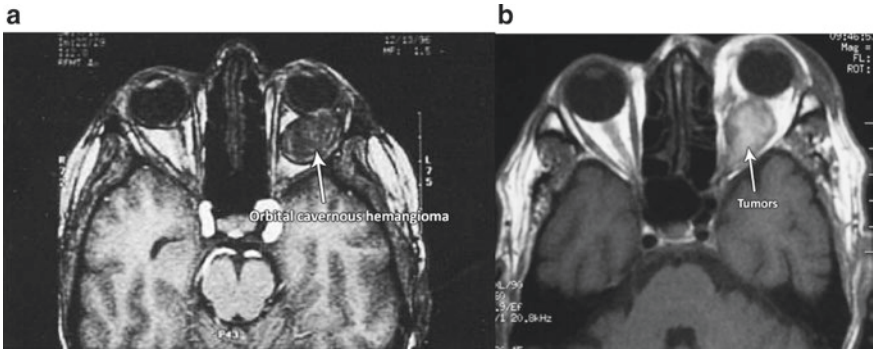

Fig. 8 **a** A mass lesion with medium water content in T1W image. **b** The mass with low water content in T1W image

Appearance of the lesion in the MRI, in addition to the water content, depends on vascularity of the lesion. In low to medium vascularity of lesions, such as optic-nerve glioma (Fig. 9a), lesion appears to be iso-intense compared to the brain in T1W image. In low vascular tissues, such as metastasis (Fig. 9b), tumors appear hyper-intense; and in highly vascular tissues, tumors seem to be hypo-intense similar to the globe. Cavernous hemangioma is hypo-intense (Fig. 9c) compared to the brain and it is similar to the globe in signal intensity. It can have lobular contour borders and bright signal in T2W image with dark fibrous septations between lobules [4].

According to MRI findings, 80–85% of orbital tumors are hypo-intense in T1W and hyper-intense in T2W images [5]. These lesions are classified into five subgroups (Table 1).

Cystic lesions such as abscesses, hematomas or mucocele have high water content and vascular lesions such as capillary or cavernous hemangioma have high blood content. Therefore, we expect that they will be hypo-intense in T1W images and hyper-intense in T2W images [5].

Some other tumors like lymphoid tumors, neural tumors such as schwannoma, even rhabdomyosarcoma and some metastatic tumors are characteristically hypo-intense in T1W and hyper-intense in T2W images [5, 6] (Table 1). In the Fig. 10, a mass exists within the medial rectus muscle that appears hypo-intense in T1W and hyper-intense in T2W images, that reveals an intramuscular cystic lesion.

The second category of lesions is iso-intense in T1W images and hyper-intense in T2W images. The most common type of these lesions is optic-nerve glioma [5, 6] (Fig. 11).

In the third type of lesions, tumors seem iso-intense or hypo-intense in T1W images and hypo-intense in T2W images. The most noticeable tumor in this category is the optic-nerve meningioma which is shown in Fig. 12.

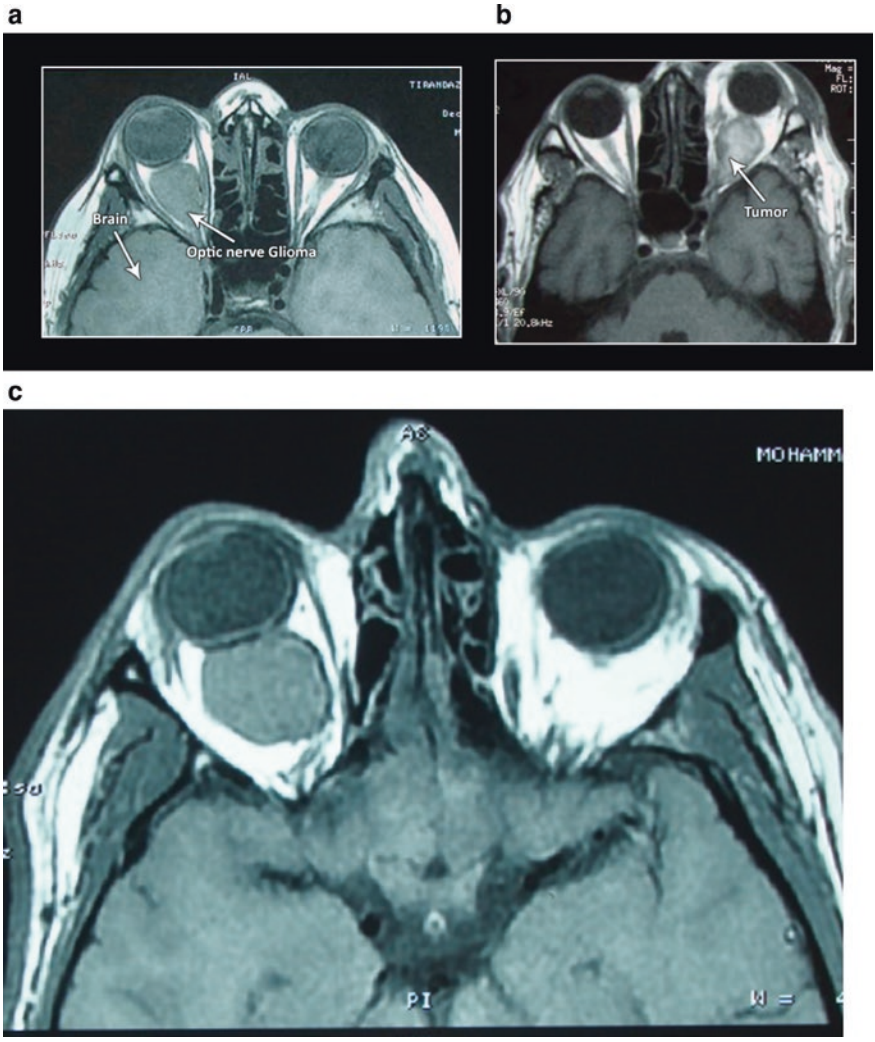

Fig. 9 **a** Optic-nerve glioma, iso-intense compared to the brain. **b** Orbital metastasis, hyper-intense compared to the brain. **c** Cavernous hemangioma, hypo- to iso-intense compared to the brain

The fourth category of orbital lesions is hypo-intense in both T1W and T2W images. These are tumors of bone origin such as osteoma. Osteoma or any other bone disorders such as greater wing meningioma or en-plaque meningioma can be seen hypo-intense in both T1W and T2W images [5, 6] (Fig. 13).

Table 1 Orbital lesions that are hypo-intense in T1W and hyper-intense in T2W images

1. Cystic; Abscess, Mucocele, Dermoid cyst (sometimes both iso-intense)
2. Vascular; Capillary hemangioma, Cavernous hemangioma, Varix, Hemangiopericytoma
3. Lymphoid: Lymphoma, Lymphangioma, Lymphoid neoplasm,
4. Neural; Schwannoma, Neurofibroma, Plexiform neurofibroma
5. Others. Rhabdomyosarcoma and some metastatic tumors

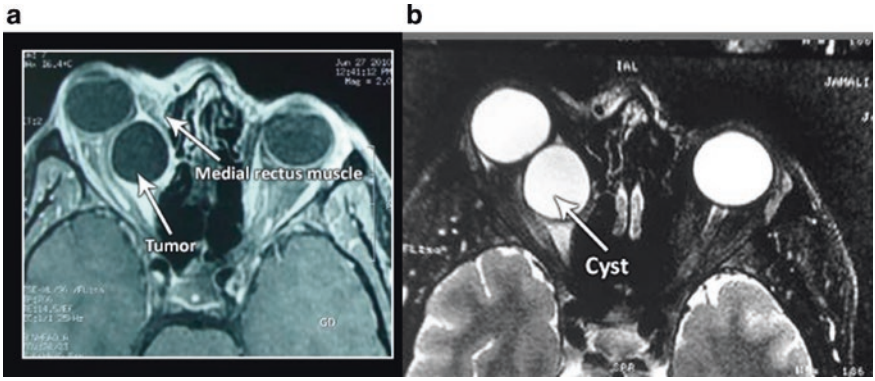

Fig. 10 **a** Cystic mass within medial rectus muscle, hypo-intense in T1W image and **b** hyper-intense in T2W image

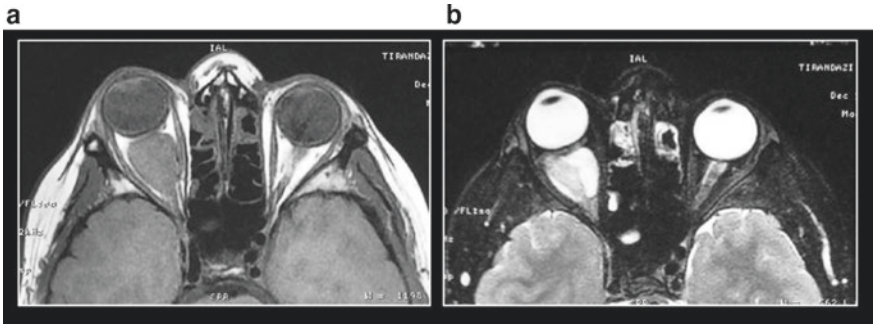

Fig. 11 **a** Optic-nerve glioma, iso-intense in T1W image and **b** hyper-intense in T2W image

Enhancement

Enhancement mostly depends on vascularity and cellular pattern of the mass lesion. In Fig. 14, the iso-intense mass is seen behind the globe in T1W image. After contrast injection, the tumor is enhanced partially. In Fig. 15, the patient has a vascular lesion, cavernous hemangioma, and after contrast injection, nearly

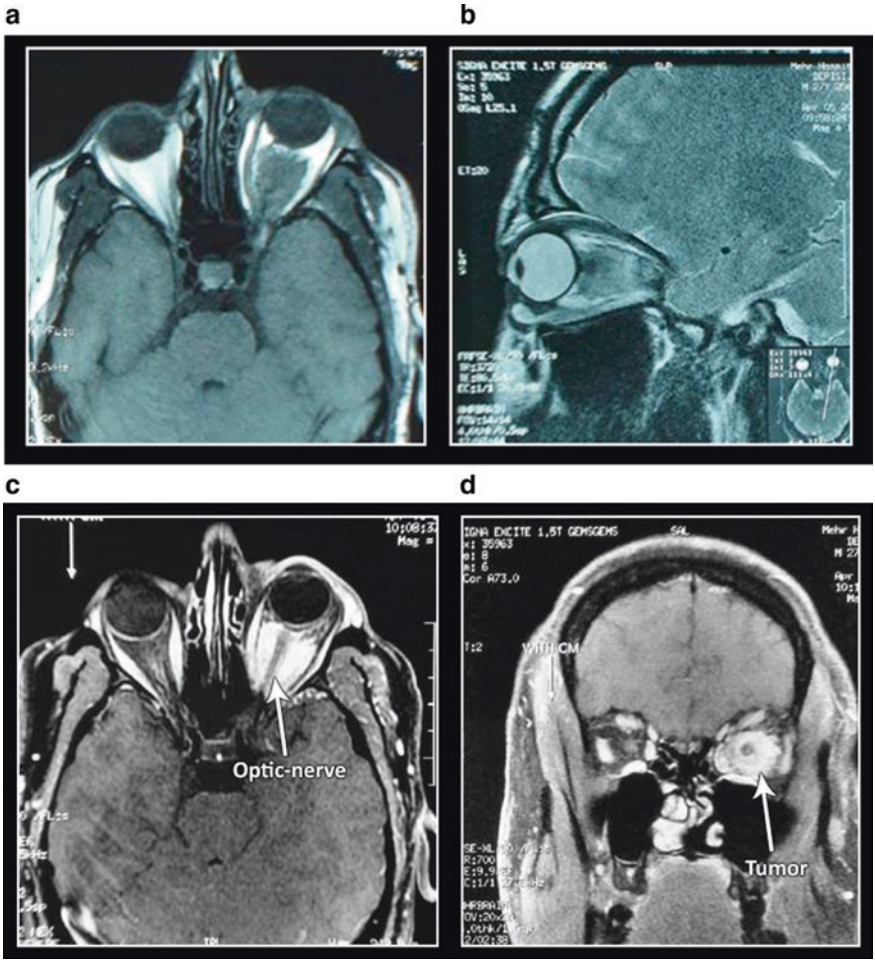

Fig. 12 **a**, **b** The tumor is iso-intense in T1W and hypo-intense in T2W image. **c** After contrast enhancement, optic-nerve is visible within the mass. **d** In the coronal view, optic-nerve is just visible within the tumor at the center

total enhancement of the tumor is revealed that starts from central or paracentral area and spreads peripherally. Some tumors and masses have rim-enhancement or ring-enhancement, such as abscess, long-standing hematomas, and some types of metastasis, simple cysts and some varieties of the dermoid cysts [5, 6]. The Fig. 16 demonstrates an orbital mass with ring enhancement.

On the basis of enhancement with contrast, there are three types of behavior; severe, moderate and no enhancement. Some lesions such as lymphoid tumors, optic-nerve meningioma, varix, and rhabdomyosarcoma reveal severe enhancement.

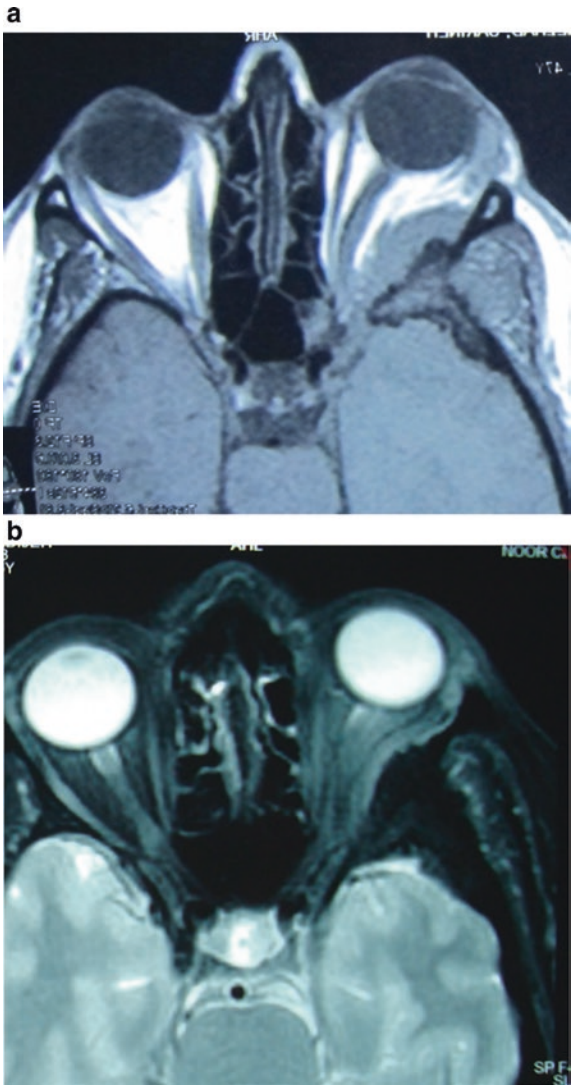

Fig. 13 Osteoma within the orbit and the ethmoidal sinus that appears hypo-intense in both of T1W (**a**) and T2W (**b**) images

Vascular tumors, adenoid cystic carcinoma (ACC), hemangiopericytoma and neurofibroma would enhance moderately. Figure 17 demonstrates a medial canthal mass lesion that seems hypo-intense or darker compared to the brain. After contrast enhancement, dimensions of the tumors can be seen completely (Table 2).

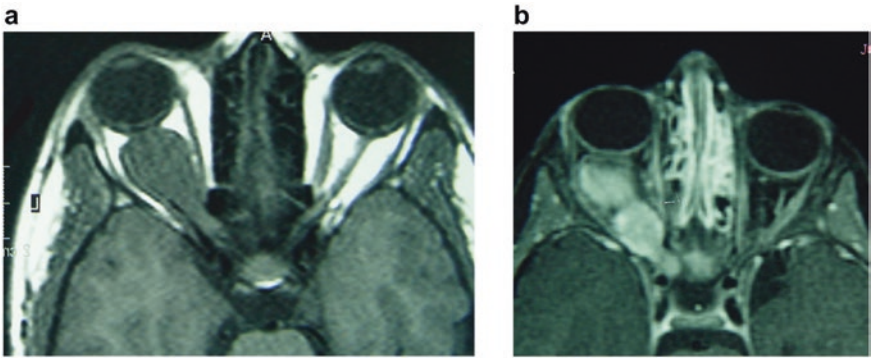

Fig. 14 **a** The iso-intense mass is seen behind the globe in T1W image **b** After contrast injection, the tumor is enhanced partially that can be seen in tumors like as optic nerve glioma. Double ring sign can be seen characteristically

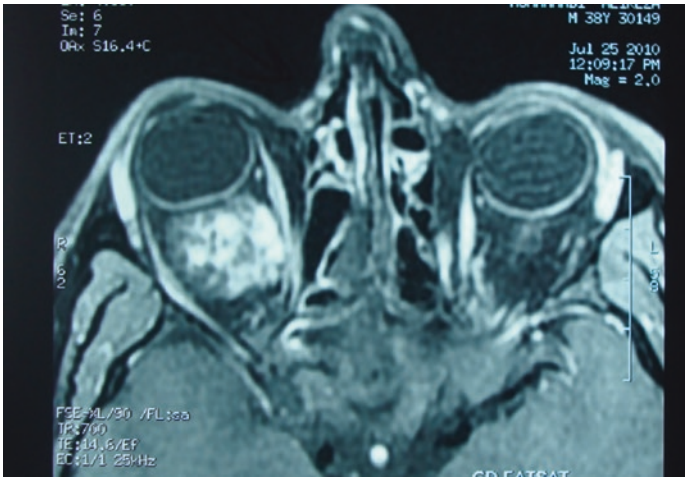

Fig. 15 In cavernous hemangioma, nearly total enhancement of the tumor is visible after contrast injection that start forms central or paracentral part

Figure 18 shows a patient with intra-conal mass. The tumor seems to be iso-intense compared to brain in T1W and hyper-intense in T2W images with para-central enhancement after contrast administration that spreads peripherally. This can be due to pattern of enhancement in cavernous hemangioma which is moderately enhanced [7].

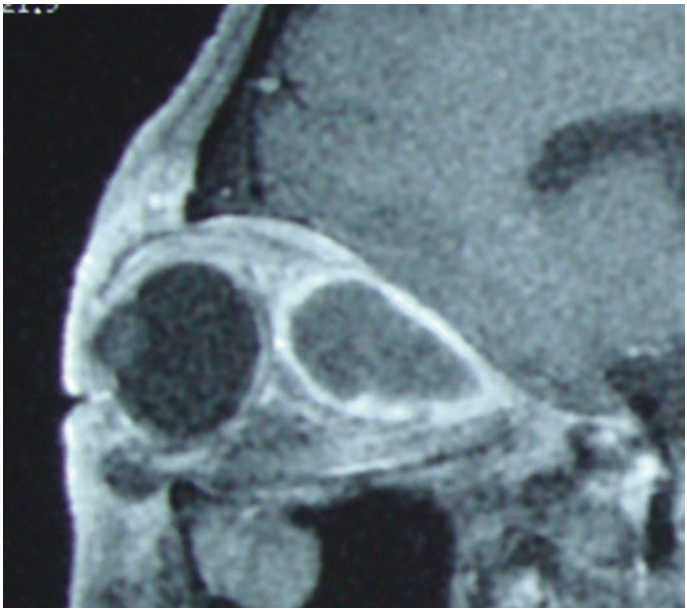

Fig. 16 Ring enhancement in a metastatic tumor

Some lesions would not enhance, such as hematic cyst, abscess, mucocele, and some dermoid cysts. Figure 19 shows a mass within the medial rectus without any contrast enhancement.

Ocular Prosthesis

The Fig. 20 reveals a patient that has been enucleated in the right side with prostheses implantation within the right orbital cavity. So, prostheses or hydroxyapatite can appear similar to bone intensity which is hypo-intense in both T1W and T2W images. He unfortunately, has a tumor within the medial rectus muscle that appears iso-intense in T1W and hyper-intense in T2W images that is compatible with neurofibroma.

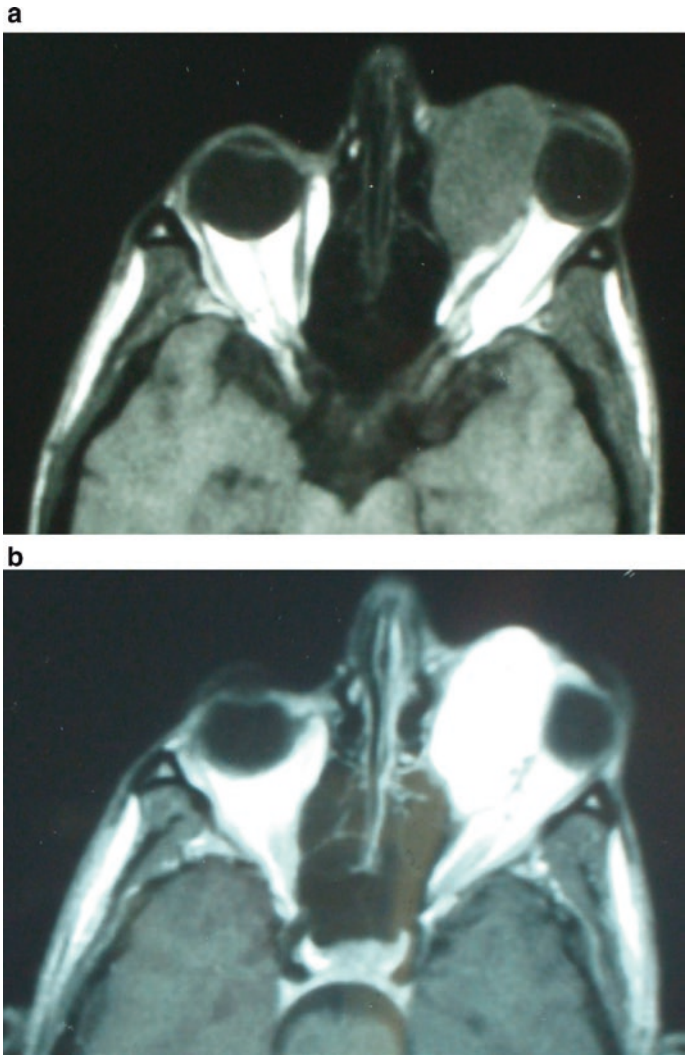

Fig. 17 **a** T1W without contrast shows a mass in medial canthal area. **b** After the contrast has been administered, when the fat signal has not been suppressed so the contrast-enhanced tumor has mixed up with the intraorbital fat

Table 2 Gadolinium enhancement severity pattern in MRI

• Severe enhancement; lymphoid neoplasm, optic sheath meningioma, Varix, rhabdomysarcoma, some sarcomas
• Moderate enhancement; capillary and cavernous hemangioma, adenoid cystic carcinoma, fibrous histiocytoma, hemangiopericytoma, lymphoma, glioma, pseudotumor, neurofibroma
• Lesions not enhanced with Gadolinium: Abscess, Hematic cyst, mucocele, Epithelial cyst, dermoid cyst, cellulitis

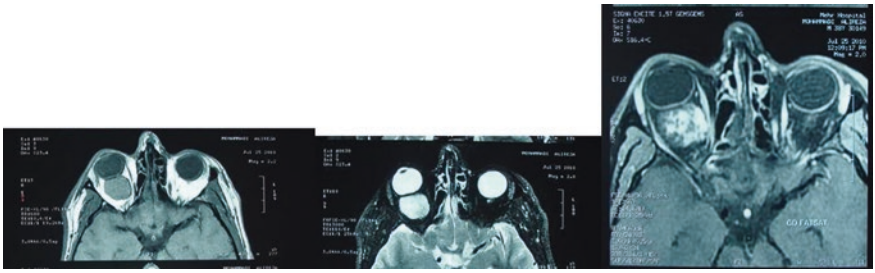

Fig. 18 Cavernous hemangioma iso-intense in T1W and hyper-intense in T2W images with para-central enhancement after contrast administration that spreads peripherally [7]

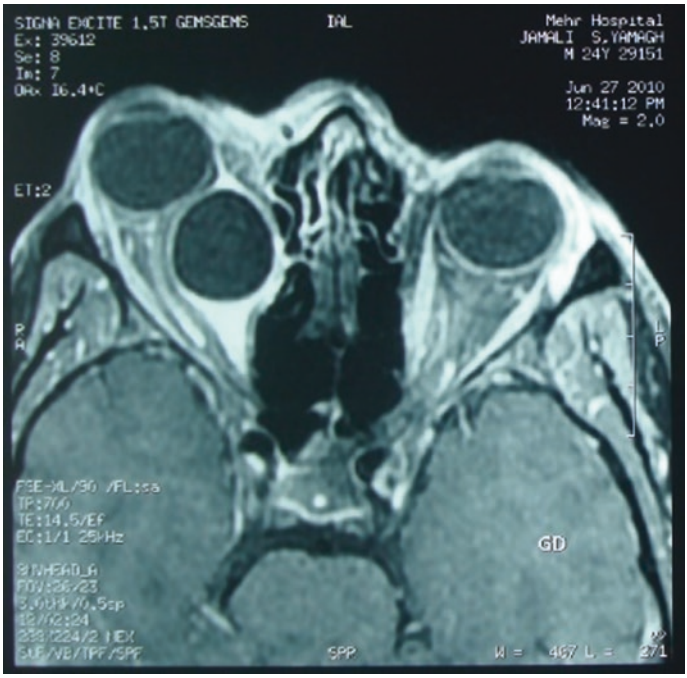

Fig. 19 A cystic mass within the medial rectus muscle without any contrast enhancement

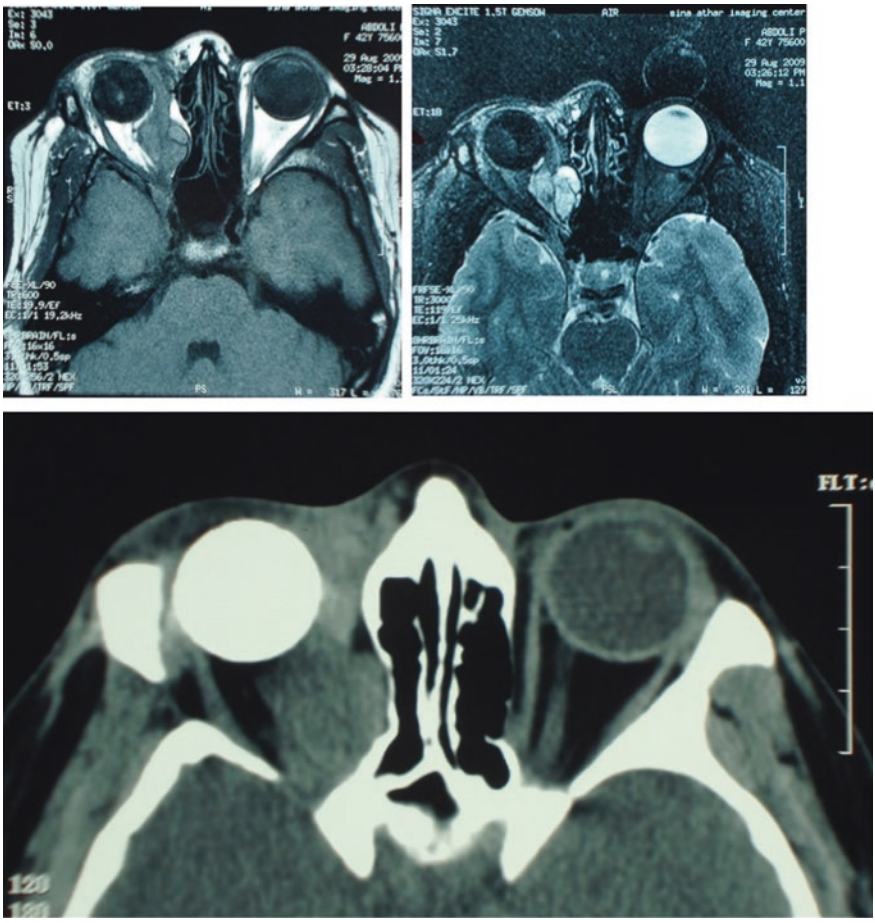

Fig. 20 A patient with prostheses or hydroxy apatite within the right orbital fossa with a neurofibroma tumor within the medial rectus muscle at the same side c. CT-scan of the same patient showing hydroxy apatite within the right orbit

Dermoid Cyst

Figure 21 shows a patient with a mass which is seen superior to the medial canthus that is seen dark or hypo-dense in CT-scan [3]. This tumor which seems to be similar to fat density, is a dermoid cyst. So, the best option to diagnose the dermoid cyst is CT-scan and not MRI [6].

Figure 22a shows a hyper-intense mass in T1W image that is hypo-intense in T2W (Fig. 22b) and after contrast administration not only does not enhance but seems to be disappeared (Fig. 22c).

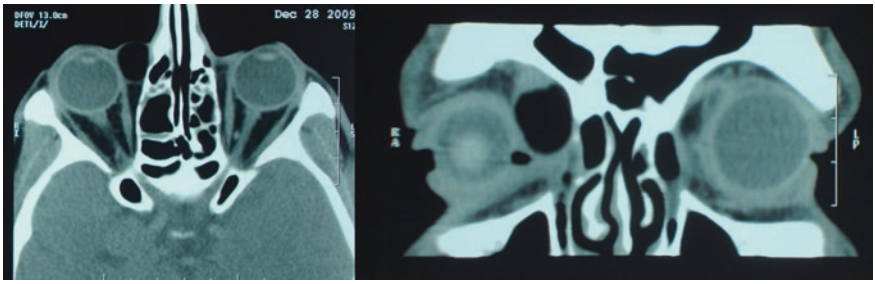

Fig. 21 CT-scan showing medial canthal mass that is hypo-dense and appears like fat; characteristic of dermoid cyst

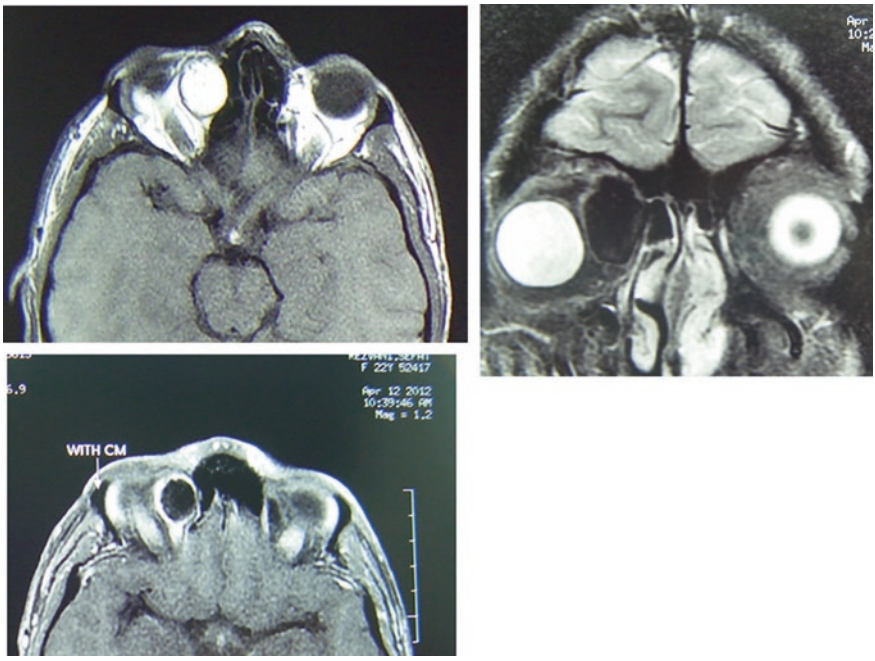

Fig. 22 Shows MRI findings of orbital dermoid cyst. **a** Shows a hyper-intense mass in T1W image that is hypo-intense in T2W (**b**) and after contrast administration not only does not enhance but seems to be smaller (**c**)

Imaging of Vascular Lesions of the Orbit

Density of the vascular lesion is more than brain and globe but less than bone in the CT-scan [5–7]. If there is a congenital capillary hemangioma, the mass may be a localized mass or may be an infiltrative lesion in all over the orbit as shown in Fig. 23.

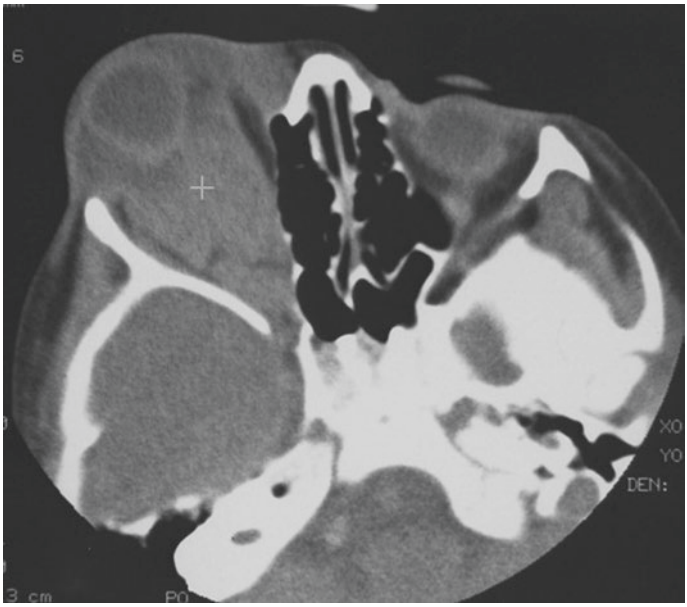

Fig. 23 Congenital capillary hemangioma is seen as an infiltrative intraorbital mass lesion

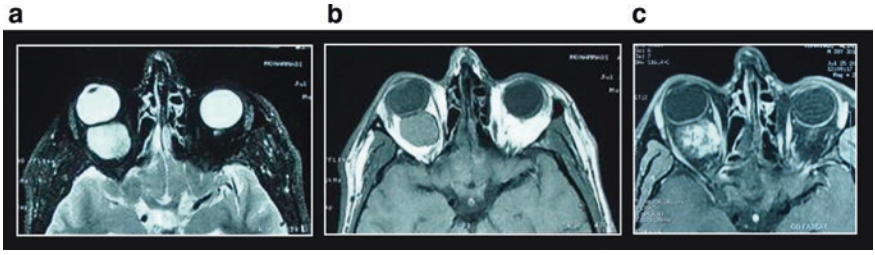

Fig. 24 In MRI images, the cavernous hemangioma can be seen hypo-intense or iso-intense in T1W (**a**) and hyper-intense in T2W images (**b**). After contrast enhancement, the tumor would have centrifugal pattern of enhancement (**c**)

For the diagnosis of the cavernous hemangioma [5], it is better to order MRI (Fig. 24). Also MRI may be helpful to distinguish either the tumor is separate from the optic-nerve or not. In MRI images, the cavernous hemangioma can be seen hypo-intense or iso-intense in T1W and hyper-intense in T2W images. After contrast enhancement, the tumor would have centrifugal pattern of enhancement [7] (Fig. 24).

There is a challenge in the diagnosis of schwannoma and cavernous hemangioma [6, 7]. Both of them can be hypo-intense in T1W and hyper-intense in T2W images. Also both will enhance with contrast. Pattern of gradual progression of

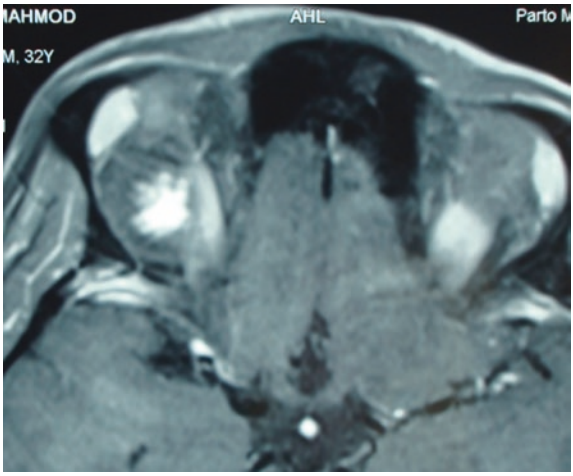

Fig. 25 Pattern of gradual progression of contrast enhancement, in the dynamic MRI, is used to differentiate between these two lesions. The enhancement starts from center toward peripheral region in cavernous hemangioma

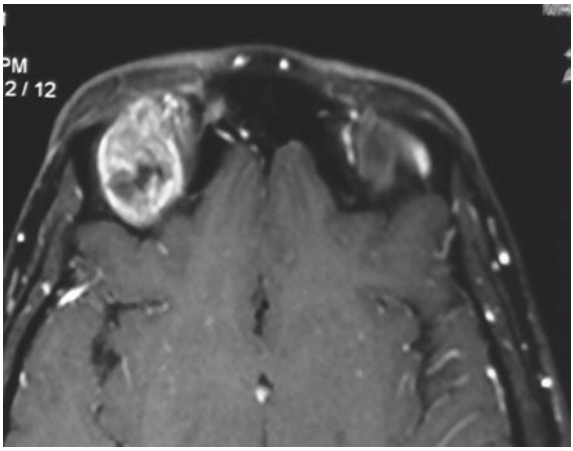

Fig. 26 Pattern of gradual progression of contrast enhancement, in the dynamic MRI, is used to differentiate between these two lesions. In schwannoma enhancement starts from peripheral region and progresses toward center

contrast enhancement, in the dynamic MRI, is used to differentiate between these two lesions (Fig. 25). So, if the patient has the cavernous hemangioma, the enhancement starts from center toward peripheral region (centrifugal pattern) as shown in Fig. 25 but in schwannoma it starts from peripheral region and progresses toward center (centripetal pattern) [7] (Fig. 26).

Ocular Melanoma

In ocular melanoma, the tumor would be seen hyper-intense in T1W (Fig. 27a) and hypo-intense in T2W images (Fig. 27b), due to para-magnetic effect of the melanin, and is enhanced moderately as shown in Fig. 27c. Signal intensity depends on the melanotic content of the tumor [8].

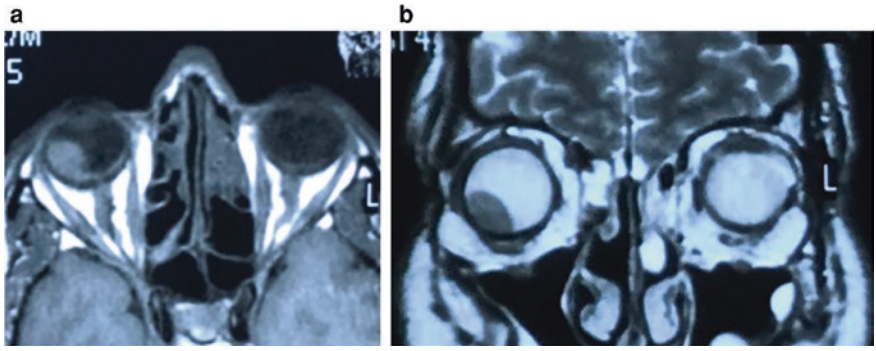

Fig. 27 Intraocular melanoma hyper-intense in T1W (**a**) hypo-intense in T2W images (**b**), and moderately enhanced with contrast (**c**)

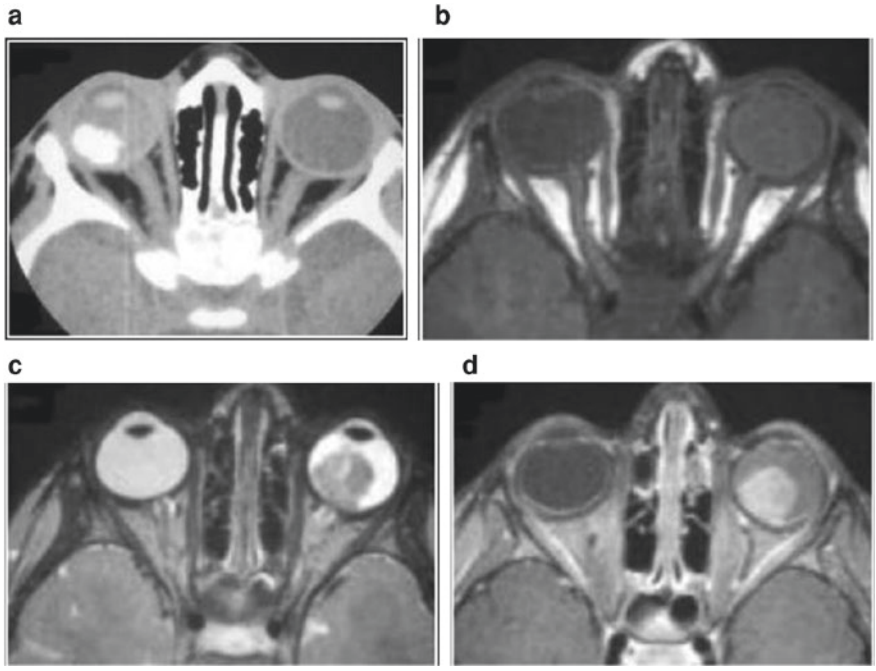

Fig. 28 Calcified retinoblastoma in the CT-scan (**a**, **b**). In MRI, the tumor and the vitreous in the right eye appears iso-intense compared to brain or hyper-intense compared to the fellow eye, which has smaller retinoblastoma with intact vitreous fluid (**c**, **d**, **e**). In figure **f**, the tumor in the left eye of another patient is demonstrated; that is hypo-intense compared to the brain in T2W image, iso-intense to brain in **g**, and has minimal enhancement with contrast (**h**)

Ocular Retinoblastoma

The best imaging technique in advanced retinoblastoma is CT-scan. In retinoblastoma the mass may have some calcification, as shown in Fig. 28a. The calcified foci in the tumor can appear dark in MRI. In MRI, in the T1W images, the

tumor and the vitreous in the right eye appears iso-intense compared to the brain or hyper-intense compared to the fellow eye, which has smaller retinoblastoma with uninvolved vitreous fluid [9] (Fig. 28c–e). The hyper-intensity of the vitreous in T1W images, can be due to vitreous seeding or increased globulin content that occurs with malignancy [9]. In Fig. 28f, it is hypo-intense compared to the brain in T2W image and has minimal enhancement with contrast in the Fig. 28h but moderate and marked enhancement can also occur in other cases. In the T2W images, the tumor is usually hypointense compared to a normal vitreous.

Orbital Trauma

Orbital wall fracture, vascular disorders, orbital hematoma and hemorrhage and also foreign bodies should be investigated in orbital trauma. First, patient should be examined for any abnormality in ocular motility, globe dystopia, diplopia, enophthalmos and any other disorder. Generally the primary imaging modality is CT scan in the case of orbital trauma because of its high sensitivity in detection of fracture line and also soft tissue entrapment [10]. As shown in Fig. 29a the coronal CT-scan is the best imaging technique for evaluating orbital walls, to rule out any orbital fracture. In Fig. 29a, a small fracture and small fat herniation is visible in the inferior orbital wall. Fat appears hypo-dense in CT-scan very close to air in the sinuses. But the fibrous tissue appears hyper-dense. So, inferior rectus muscle seems to be entrapped there beside the herniated fat. In Fig. 29b, c trap door fracture in the orbital floor is visible in the CT-scan with herniated interior rectus and orbital fat but fracture line is not visible [2, 10]. The best view for evaluating the anteroposterior extension of the inferior wall fracture is the sagittal view (Fig. 30).

In children, inferior wall fracture may have no displacement so called “trap door fracture” [4, 10]. So herniated material may be entrapped into the sinus and restrict ocular movement. The patient shown in Fig. 31 has limitation in upward gaze because of restriction of upward movement in the left eye, due to inferior rectus muscle herniation into the maxillary sinus through the orbital floor trap door fracture (Fig. 32a). Notice that, the fracture line is completely closed (Fig. 32b) best demonstrated in sagittal view CT-scan (Fig. 32c, d).

Carotid Cavernous Fistula

Carotid Cavernous Fistula (CCF) formation can occur after trauma or without any history of trauma. In ocular examination, tortuous conjunctival vessels and chemosis may be seen and the patient may not be able to move her or his eye in any direction. In CT-scan and MRI, the diameter of the superior ophthalmic vein (Figs. 33a and 34) is notably enlarged and dilated.

Some traumatic CCFs may have severe chemosis and blindness after trauma (Fig. 35). In the CT-scan of a CCF, all intra-orbital muscles such as all of the rectus muscles and inferior and superior oblique muscles (Fig. 36) are enlarged [11].

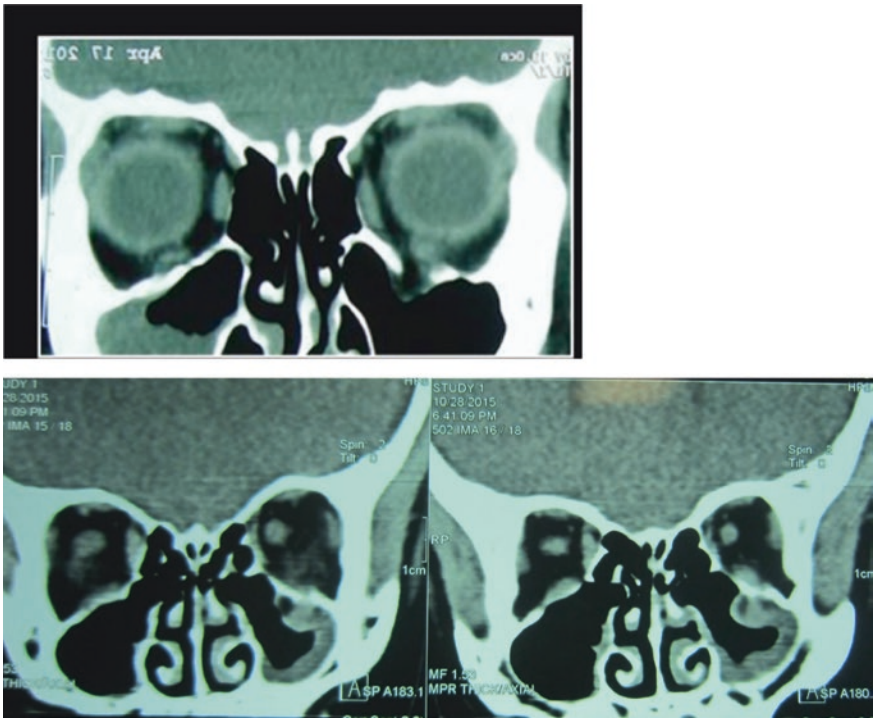

Fig. 29 In figure **a**, small fracture and small fat herniation is visible in the inferior orbital wall. Fat appears hypo-dense in CT-scan very close to air in the sinuses. But the fibrous tissue appears hyper-dense. So, inferior rectus muscle seems to be entrapped there, beside the herniated fat. In figure **c**, fracture in the orbital floor is visible in the CT-scan

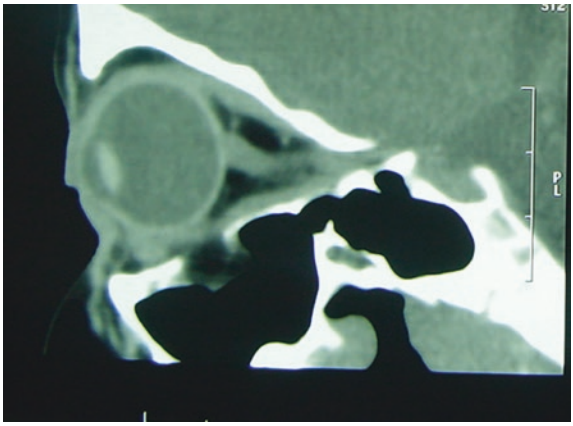

Fig. 30 Sagittal view better illustrates the extension of the inferior wall fracture from anterior to posterior

Fig. 31 This child has limitation in upward gaze because of restriction of upward movement in the left eye, due to inferior rectus muscle herniation into the maxillary sinus through the orbital floor trap door fracture

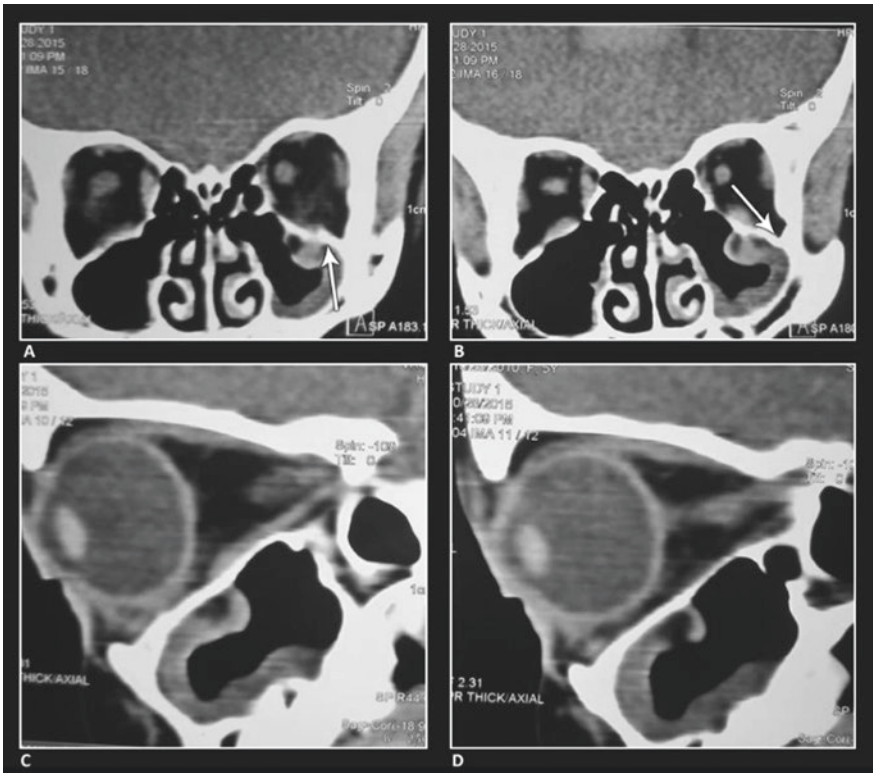

Fig. 32 Inferior rectus muscle herniation into the maxillary sinus through the orbital floor trap door fracture (**a**). Notice that, the fracture line is completely closed (**b**) best demonstrated in sagittal view CT-scan (**c**, **d**)

Orbital Foreign Body

If the patient has a history of trauma, after physical examination, first CT-scan should be taken, and if nothing abnormal was found in the CT scan, in next step, it is better to order MRI if there exists any clinical suspicion. Since MRI is

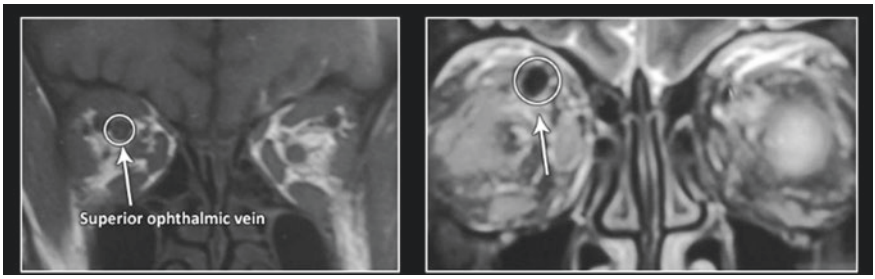

Fig. 33 In MRI, the diameter of the superior ophthalmic vein is notably enlarged and dilated

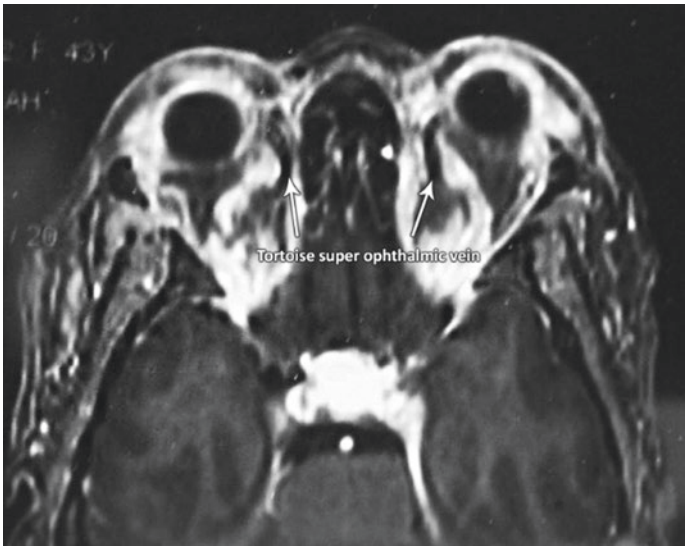

Fig. 34 The diameter of the superior ophthalmic vein is notably enlarged in this case with bilateral traumatic CCF

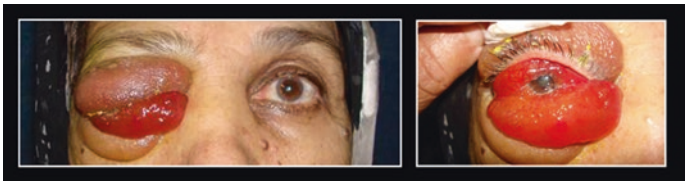

Fig. 35 Some traumatic CCFs may have severe chemosis and blindness after trauma

contraindicated in metallic foreign bodies, CT scan is the choice imaging [12]. In Fig. 37, patient has some air bubbles within the inferior rectus muscle, but it is not congruous. In MRI, the mass seems to be hypo-intense in both T1W and T2W images (Fig. 38). After contrast injection, it is not enhanced as shown in Fig. 38c.

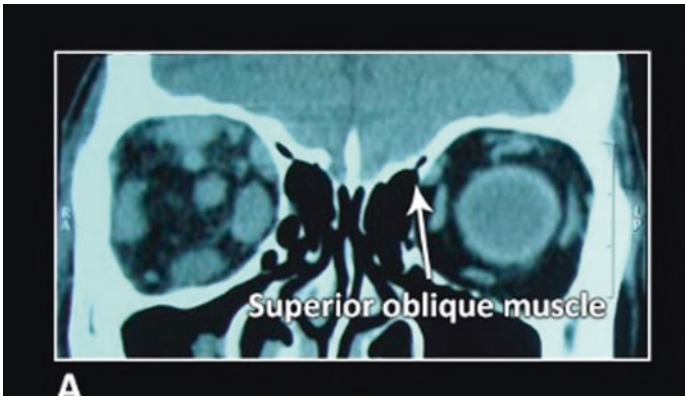

Fig. 36 In the CT-scan of a CCF, all intra-orbital muscles such as all of the rectus muscles and inferior and superior oblique muscles are enlarged

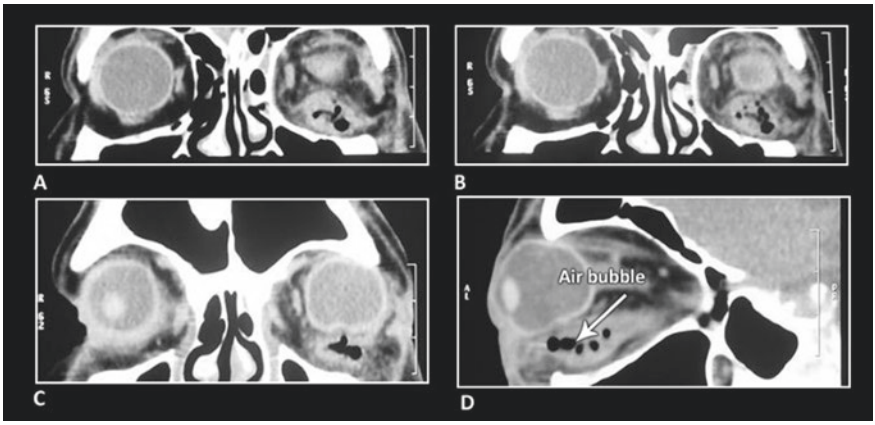

Fig. 37 Patient has some air bubbles within the inferior rectus muscle, but it is not congruous

In Fig. 38 there is the wooden foreign body within the inferior rectus muscle. So, the best imaging technique for diagnosis of this foreign body is MRI [13].

Sinus Disorders

The best imaging technique is CT-scan in disorders involving the sinuses [14]. Figure 39 reveals a patient presenting with inferior displacement of the left globe (globe dystopia). In the Fig. 40a, the mass is seen within the frontal and ethmoidal sinuses which is iso-intense in T1W (Fig. 40a) and hyper-intense in T2W images [15] (Fig. 40b). Extension of the tumor is visible in sagittal view (Fig. 40c). As

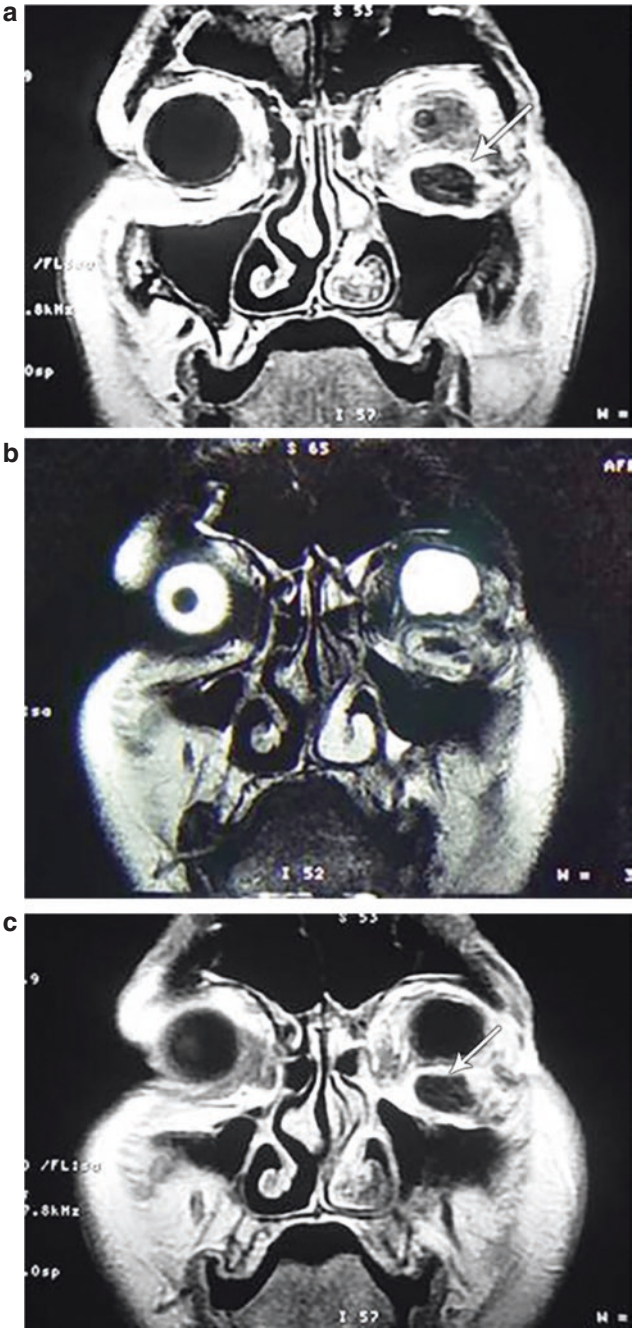

Fig. 38 **a** In MRI, the mass seems to be hypo-intense in T1W image. **b** The lesion is hypo-intense in T2W image. **c** After contrast injection, the mass in the inferior rectus muscle is not enhanced

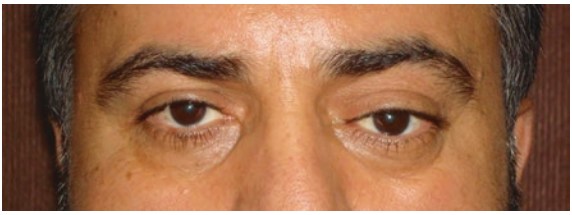

Fig. 39 A patient presenting with inferior displacement of the left globe

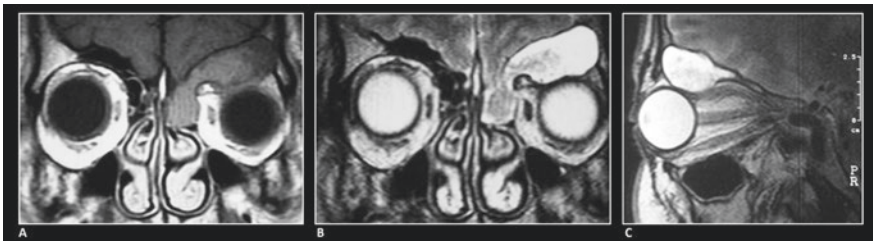

Fig. 40 A large mass is seen within the frontal and ethmoidal sinuses which is iso-intense in T1W image (**a**) and hyper-intense in T2W image (**b**). Extension of the tumor is visible in sagittal view (**c**)

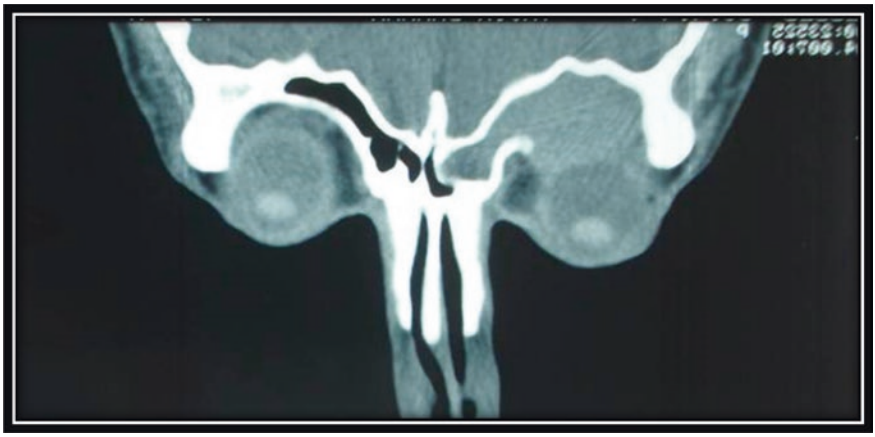

Fig. 41 CT-scan, shows mucocele within the frontal sinus leading to inferior displacement of the left globe

mentioned earlier, the best imaging for studying the sinuses and related disorders is CT-scan, which, in this case, shows mucocele within the frontal sinus leading to inferior displacement of the left globe (Fig. 39). Figure 41c shows the same patient with ethmoidal sinus mucocele. Figure 42 shows again a patient with globe displacement and telecanthus due to ethmoidal sinus mucocele (Fig. 43).

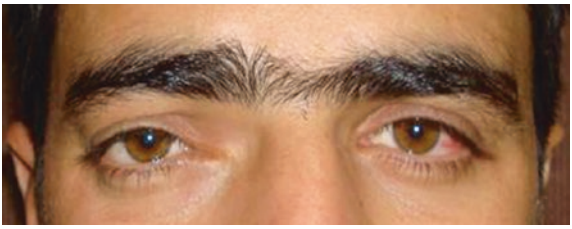

Fig. 42 A patient with lateral globe displacement and telecanthous due to ethmoidal sinus mucocele

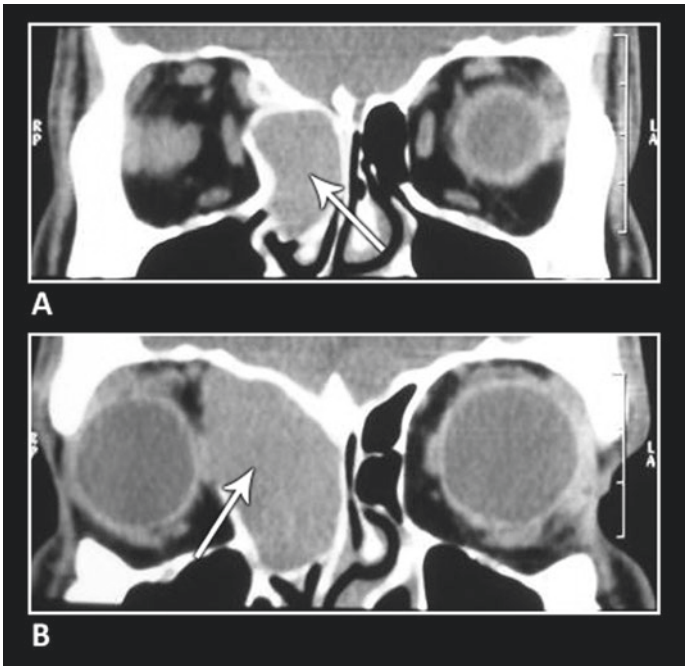

Fig. 43 Very large ethmoidal sinus mucocele

Thyroid and Inflammatory Orbital Disorders

In thyroid or orbital inflammatory disorders, the first choice of imaging is CT-scan. In Fig. 44 CT-scan of a case of monocular proptosis due to thyroid eye disease reveals enlargement of the inferior, medial, lateral and superior rectus muscles. It is noticeable that only the belly of the muscles are enlarged (Fig. 44b, c). In another patient with thyroid eye disease all of the muscles are severely enlarged, and it seems that optic-nerve is compressed [16] (Fig. 45).

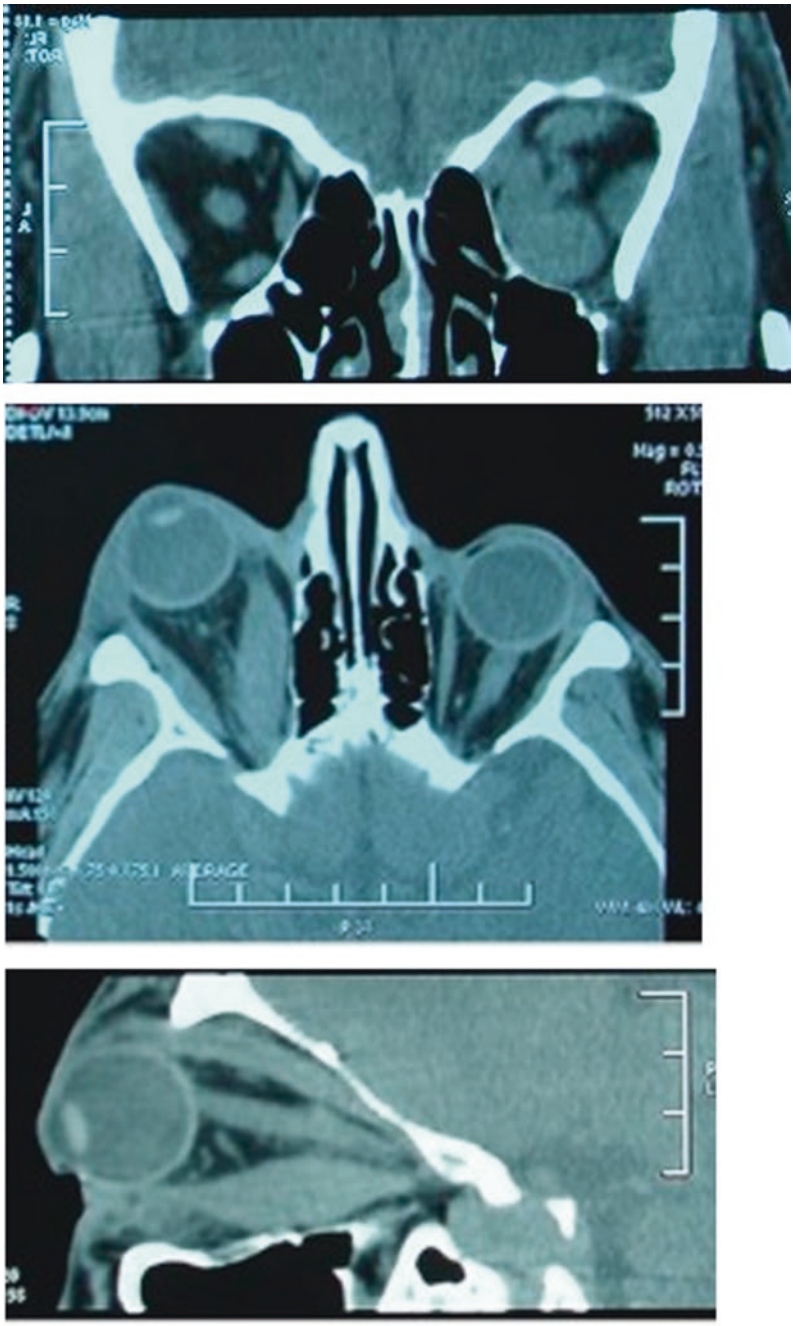

Fig. 44 **a** CT-scan in a patient with monocular proptosis due to thyroid eye disease, coronal view. **b**, **c**. CT-scan in a patient with monocular proptosis due to thyroid eye disease, axial and sagittal view reveals just hypertrophied muscle belly

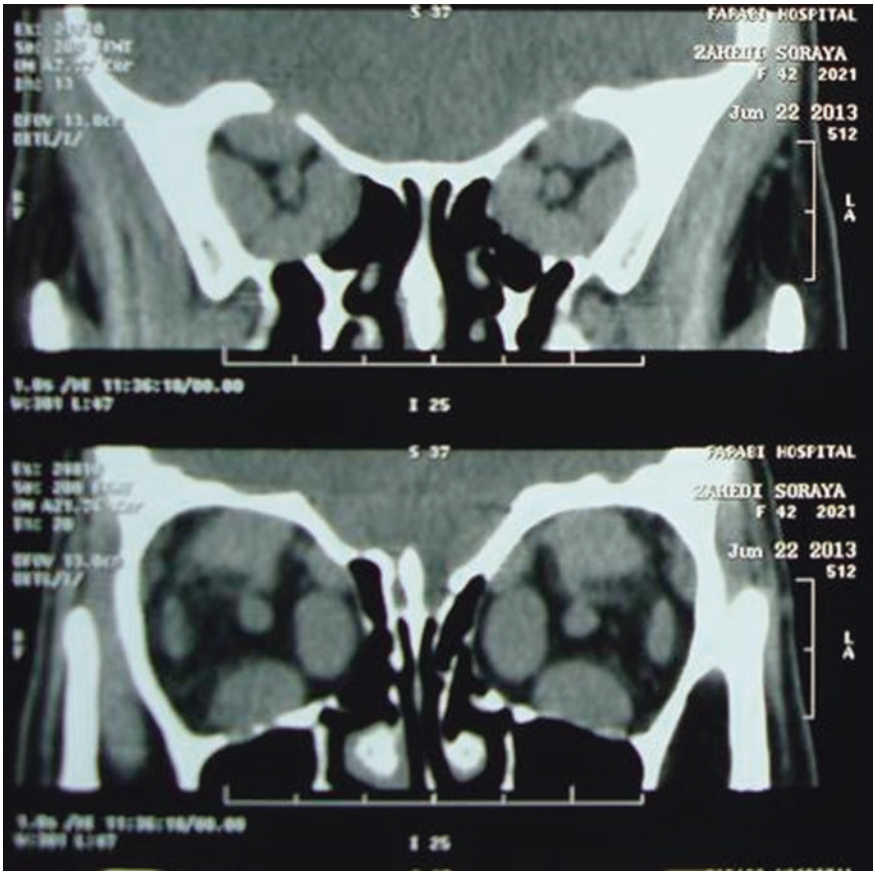

Fig. 45 All of the muscles is severely enlarged and it seems that optic-nerve is compressed by this massive enlargement of the muscles at orbital apex

Orbital Cellulitis

In cases with orbital cellulitis, patient may have gaze limitation and proptosis. The best option for imaging in orbital cellulitis is CT-scan [17]. In Fig. 46, ethmoidal sinus infiltration, and also mild infiltration within the orbit involving the medial wall are notable. There seems to be a subperiosteal abscess, which causes medial gaze limitation.

Orbital Mucormycosis

In mucormycosis, the patient may have frozen eye, and all gaze directions may be limited, but the patient does not have any proptosis or periorbital edema. The

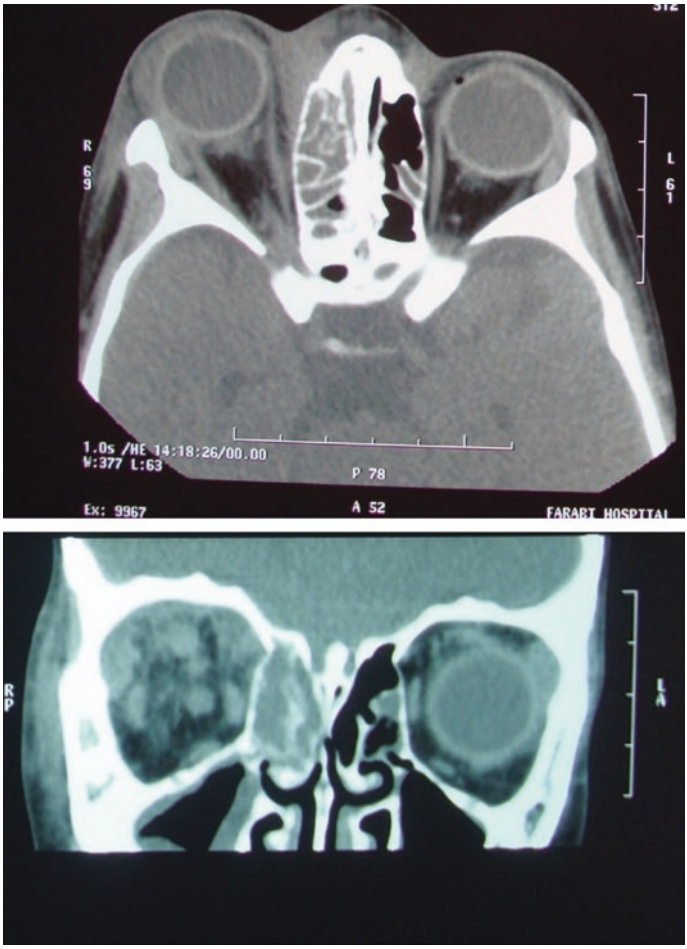

Fig. 46 CT-scan (Axial and coronal view) of a patient with orbital cellulitis due to ethmoidal sinusitis. Mild infiltration within the orbit involving the medial wall is notable. There seems to be a subperiosteal abscess

patient may be diabetic or immune compromised. In CT-scan, as shown in Fig. 47, proptosis is absent, and infiltration within the fat is very mild [18]. So called, neither the patient sees anything (or is blind) nor does the physician see anything!

Orbital Schwannoma

The most common site for orbital schwannoma is orbital roof in which the tumor arises from supraorbital nerve. In clinical examination, inferior displacement of the globe or globe dystopia is seen. In CT-scan, as shown in Fig. 48a, large

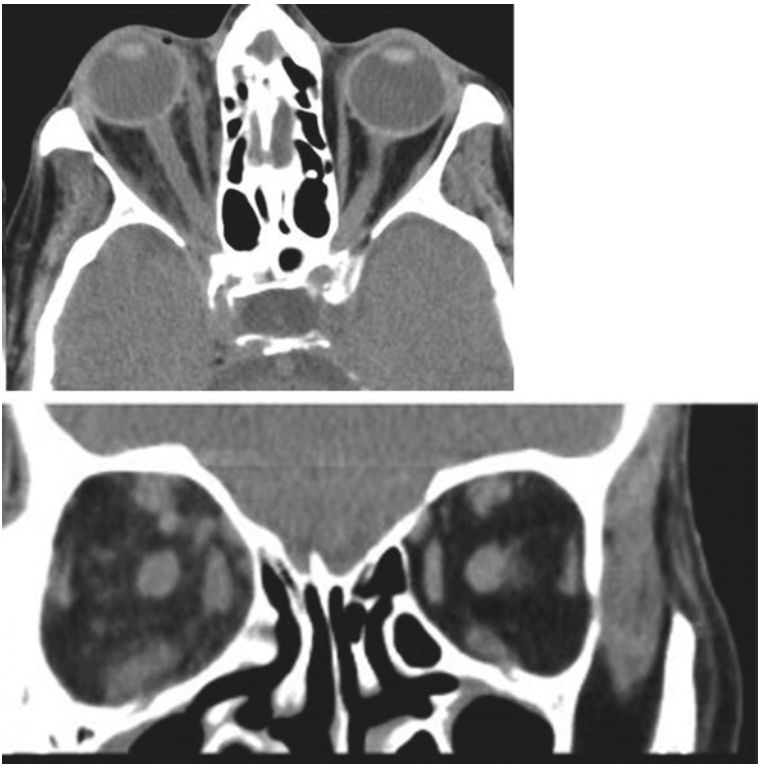

Fig. 47 Right orbital mucormycosis. In CT-scan, axial and coronal view, proptosis is absent, and infiltration within the fat is very mild compared to normal side

mass is found in superior of orbit that seems to be extraconal. Superior rectus muscle and levator muscle are visible and the tumor seems to be subperiosteal. It extends toward the superior orbital fissure. Figure 48b shows the coronal view CT-scan that reveals excavation in the orbital roof. In MRI, in Fig. 49, the tumor is hypo-intense in T1W and hyper-intense in T2W images. Images taken after contrast administration reveal ring enhancement or peripheral initiation of enhancement that may progress toward the center of the lesion [7].

Greater Sphenoid Wing Meningioma

The best option to diagnose thyroid eye disease and also osseous disorder is CT-scan, not MRI. In Fig. 50, the left side bone seems to be normal; dark lines represent the bone that is due to the bone marrow within the bones that is detectable in the MRI [19]. In comparison, this darkness seems to be enlarged in the right side but is hard to diagnose and needs more evaluation. Then, after performing

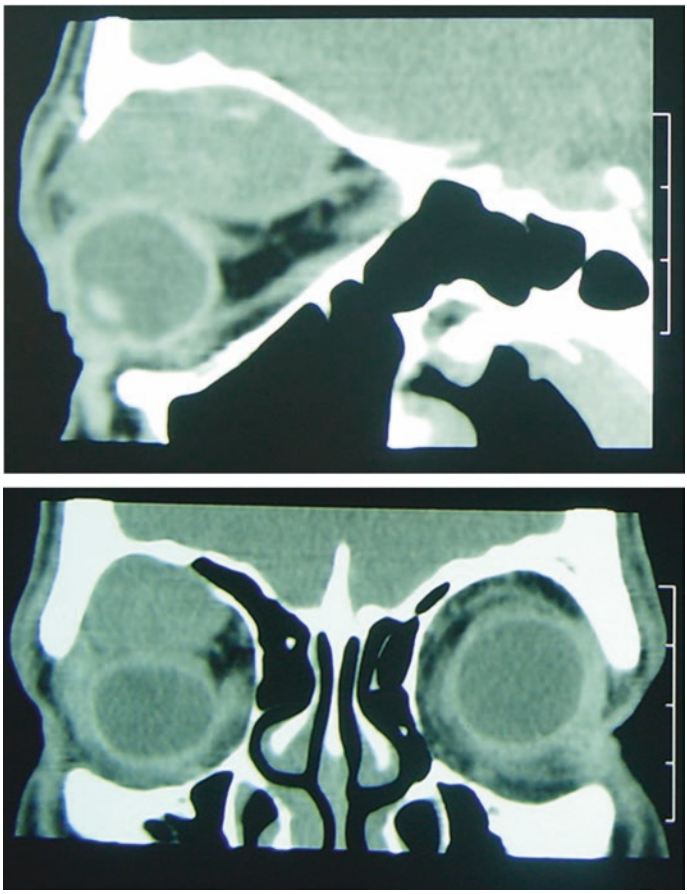

Fig. 48 **a** Large mass is found in superior of orbit that seems to be extraconal. Superior rectus muscle and levator muscle are visible and the tumor seems to be subperiosteal. **b** Coronal view of CT-scan that reveals excavation in the orbital roof

CT-scan, the greater wing of the sphenoid bone seems to be hypertrophied in the right side. This is due to the greater wing meningioma or en-plaque meningioma that is an osseous disorder within the greater wing of the sphenoid bone.

Orbital Rhabdomyosarcoma

Orbital rhabdomyosarcoma can originate from any tissue in the orbital cavity, fat, skin, lacrimal gland (Fig. 51), etc., and can present in any location in the orbit; it can be intra-conal or extra-conal [5, 6].

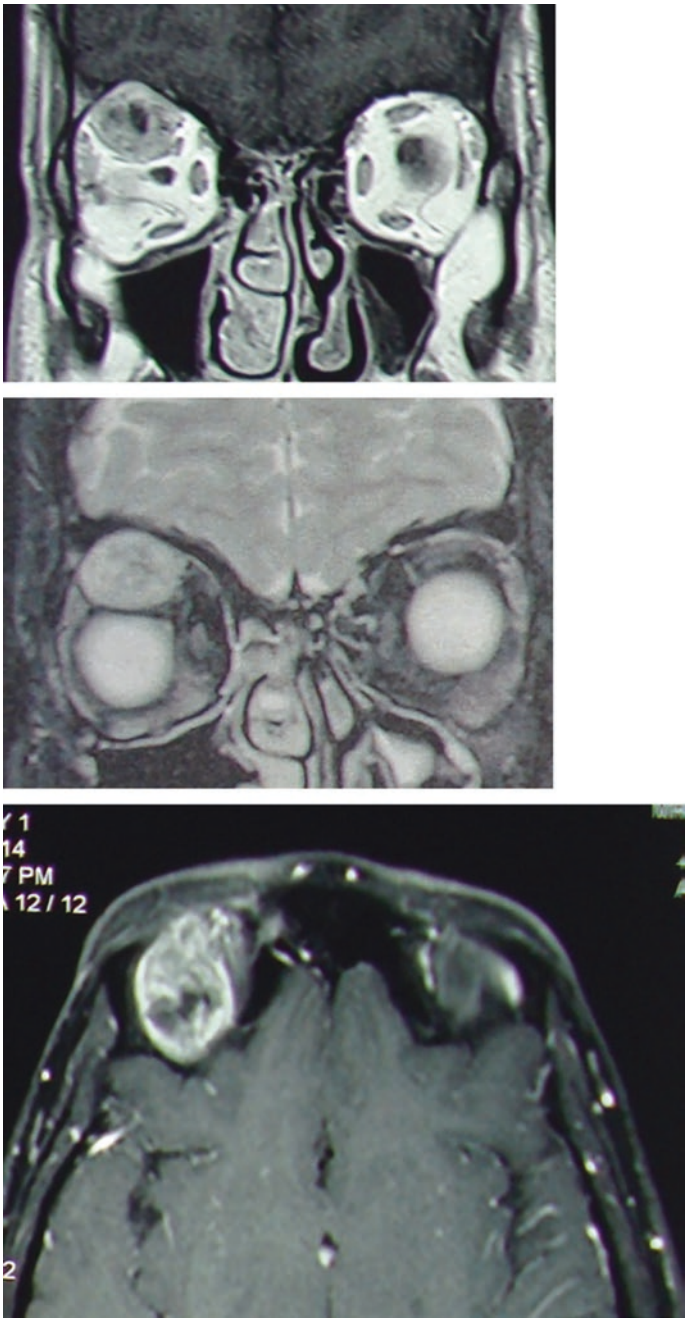

Fig. 49 MRI, reveals the tumor that is hypo-intense in T1W image (**a**) and hyper-intense in T2W image (**b**). After contrast administration enhancement starts from peripheral area (**c**)

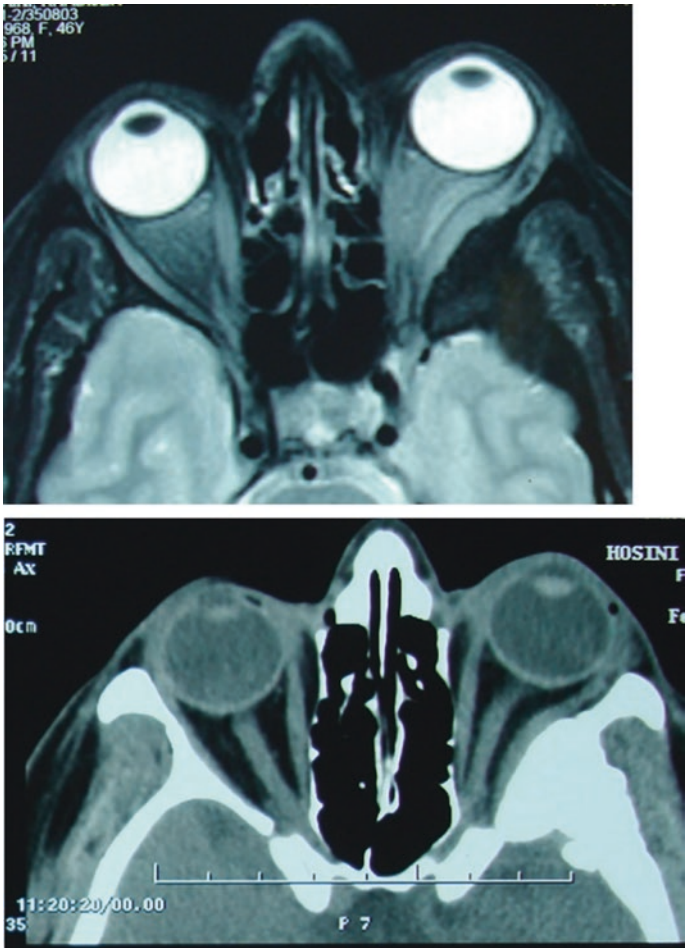

Fig. 50 Greater wing en-plaque meningioma. In MRI (**a**) dark mass is visible in the left side but it is absent in the right side. So, CT-scan is the best option which reveals precise borders of the en-plaque meningioma (**b**)

On MRI, presented in Fig. 52, a mass is seen at the site of lacrimal gland that is hypo-intense in T1W (Fig. 52a), and hyper-intense in T2W (Fig. 52b) images and with contrast administration, it reveals a heterogeneous pattern of enhancement and a none-enhanced area exists that is a typical finding in rhabdomyosarcoma. Figure 52c depicts coronal view MRI with a ring enhancement pattern due to necrosis within the rhabdomyosarcoma due to central ischemia that occurs after abrupt tumor enlargement [3–5].

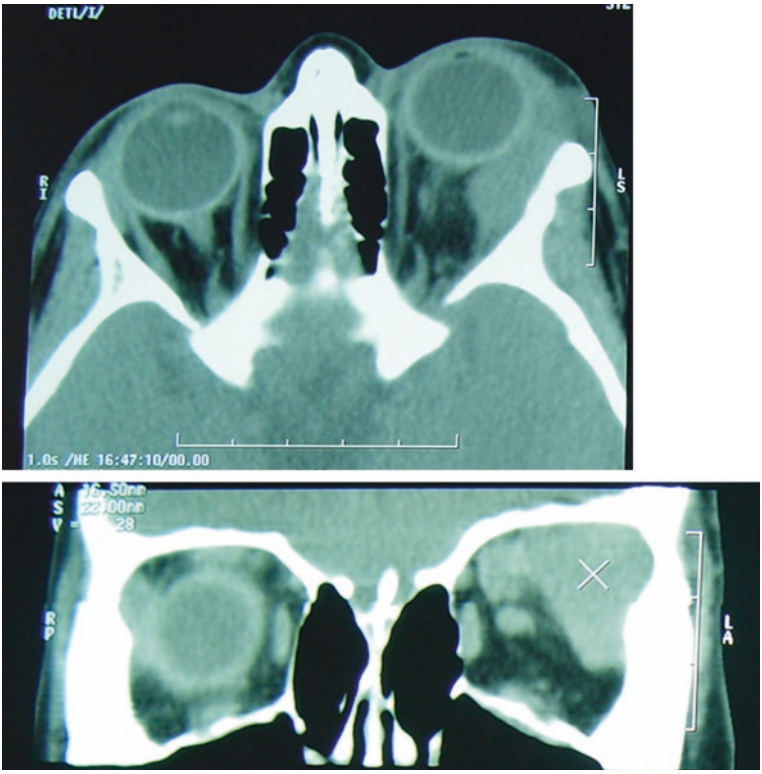

Fig. 51 **a** Demonstrates axial view CT-scan of a patient with tissue infiltration and mass lesion in the lateral of orbital cavity. **b** Coronal view reveals excavation of the lateral orbital wall due to the tumor

Lacrimal Gland Tumors

Clinical presentation of a patient with lacrimal gland tumor is globe dystopia or inferior displacement of the globe, proptosis, fullness in the temporal eyelid or even nothing.

Pleomorphic Adenoma

Figure 53a shows a well-defined mass that locates at the site of the lacrimal gland. Coronal plane (Fig. 53b) reveals a well-defined mass with excavation of the bone whereas the posterior border of the mass is completely well-defined [4, 5].

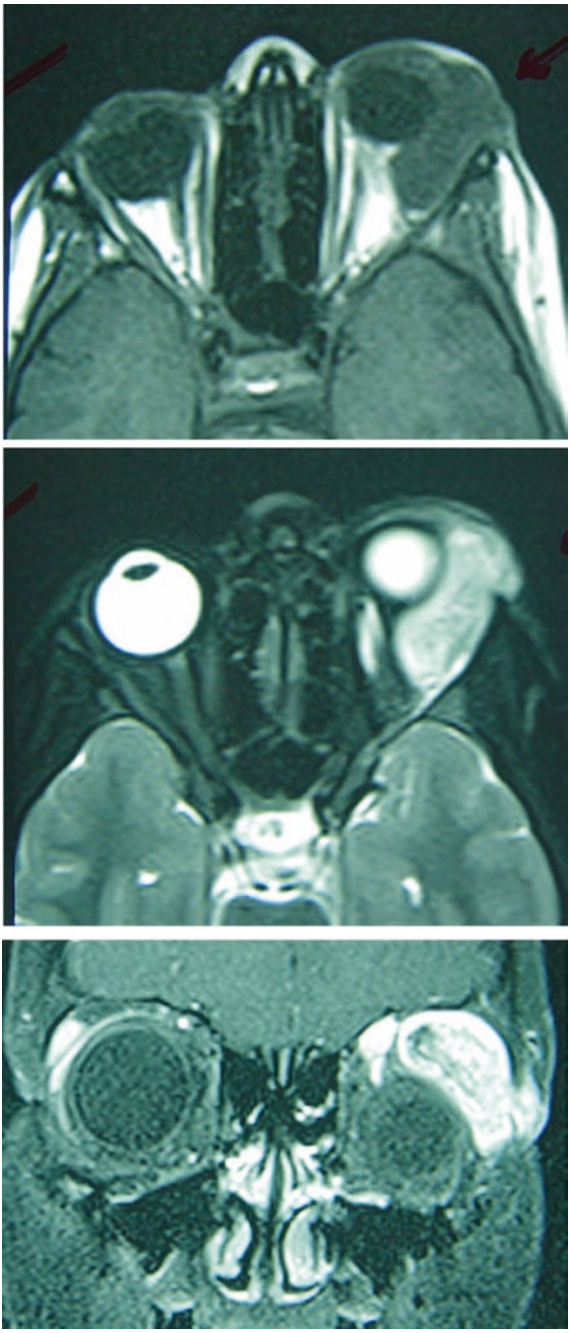

Fig. 52 MRI of the same case as shown in Fig. 51. **a** T1W MRI showing hypointense mass, T2W hyperintense that after contrast injection (**c**) shows some areas of enhancement with some ring pattern

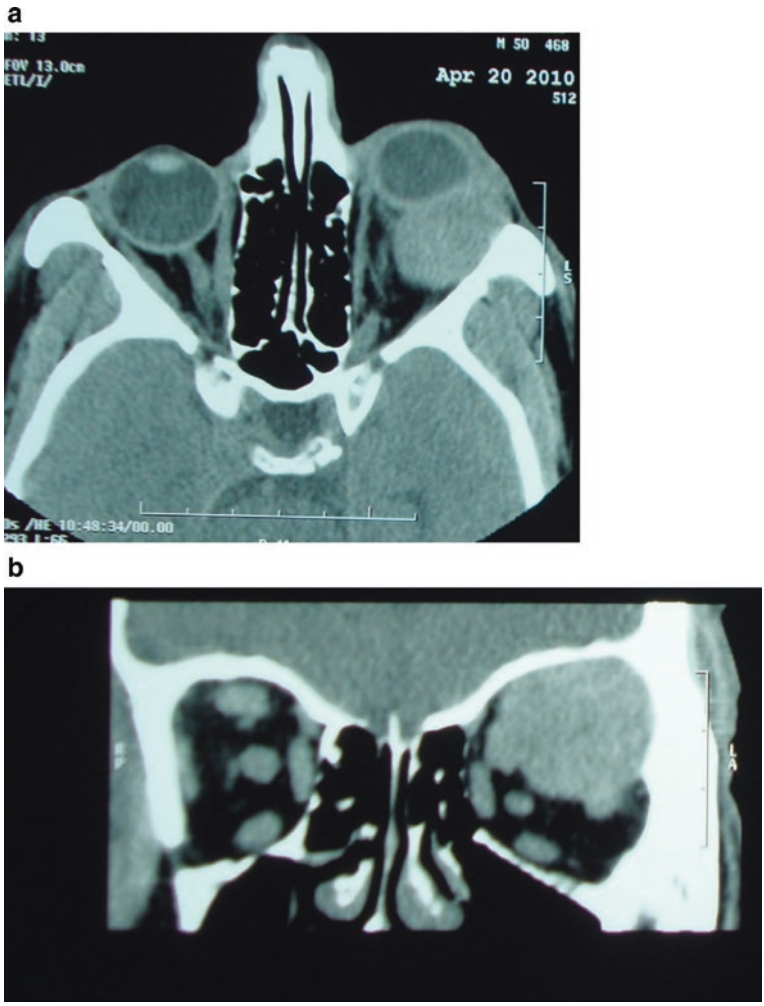

Fig. 53 **a** Well-defined mass at the site of lacrimal gland with heterogeneous contents. **b** Coronal view demonstrates supralateral orbit excavation that means longevity of the tumor

Adenoid Cystic Carcinoma

Compared to pleomorphic adenoma that is completely well-defined, Adenoid cystic carcinoma (ACC) is not well-defined and may not generally cause any bone destruction. The patient may have just less than 2 or 3 months' history of the symptoms, compared to a long-lasting history of symptoms in pleomorphic

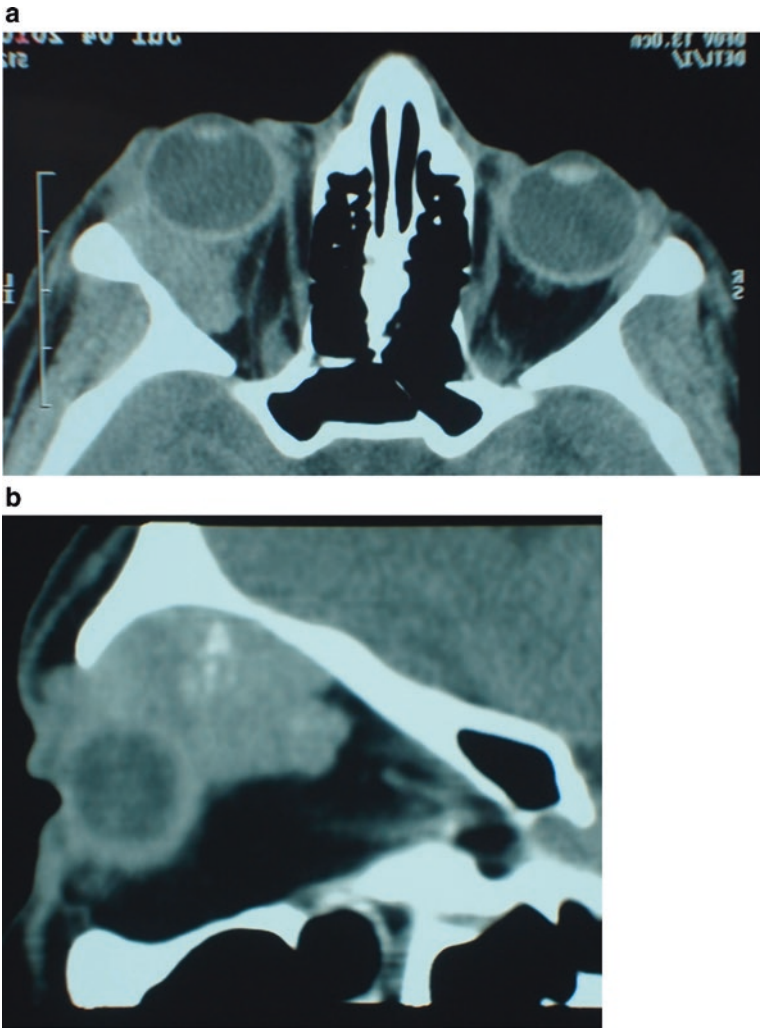

Fig. 54 CT scan of a patient with ACC. Posterior irregular border of the tumor (**a**), and foci of calcifications (**b**) are visible

adenoma. Therefore, ACC tumor may not have enough time to cause bone destruction; also it is unusual for ACC to be presented as a large mass. There are some irregularities at posterior border of the tumor in Fig. 54a, and calcification may be found within the ACC tumor (Fig. 54b). ACC may be found as a small mass lesion which is hypo-intense in T1W and hyper-intense in T2W images (Fig. 55). ACC has moderate-to-severe enhancement pattern and can extend toward the superior orbital fissure; it also has specific characteristics such as peri-neural invasion progressing toward the brain.

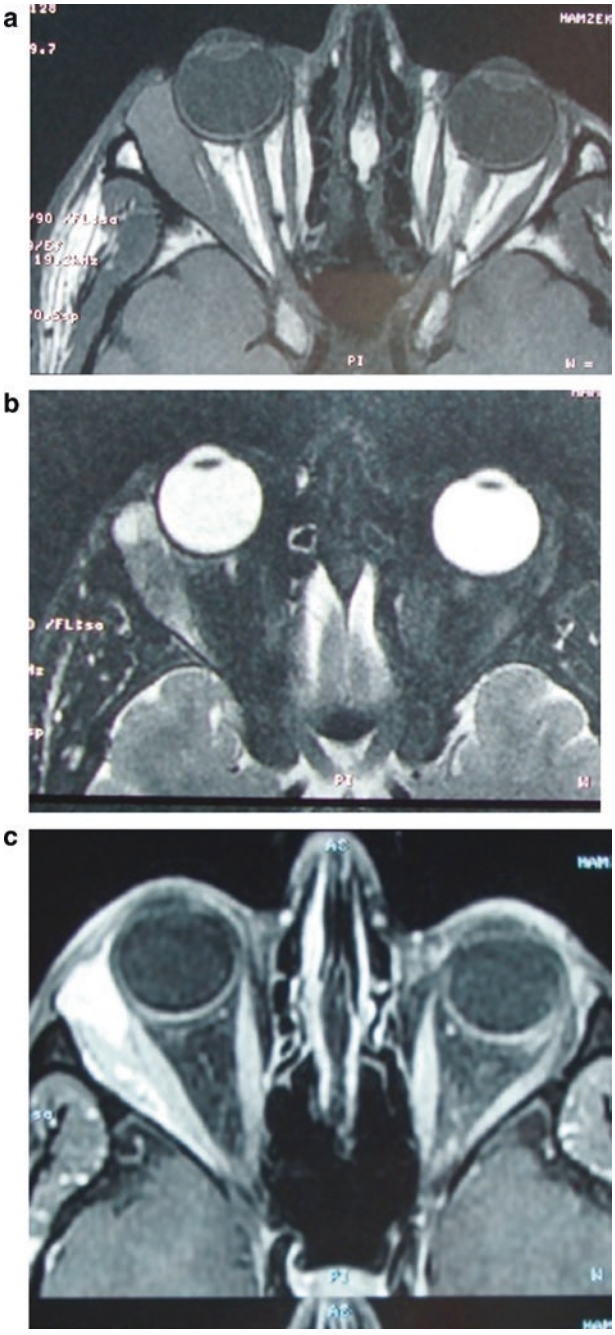

Fig. 55 **a** Patient with ACC, the tumor is hypo-intense in T1W and hyper-intense in T2W (**b**) and has posterior extension toward the brain. **c** Enhancement of the tumor shows posterior extension

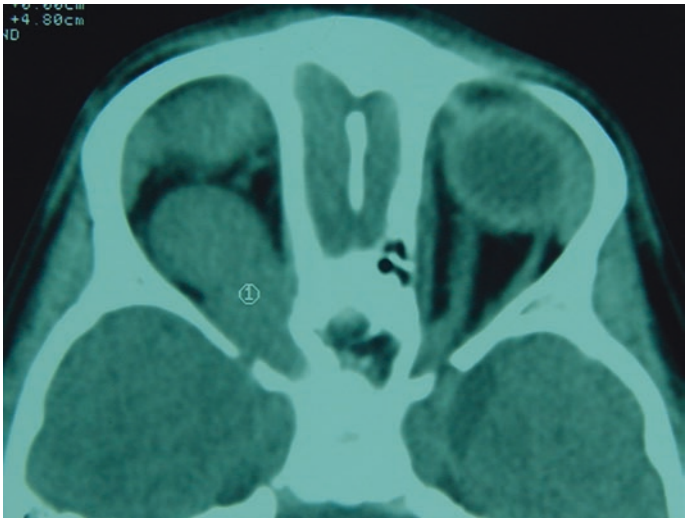

Fig. 56 CT-scan shows intraconal mass with extension to optic canal and enlargement of the canal

Optic-Nerve Glioma

Optic nerve glioma can be seen as an intra-conal mass in CT-scan [3]. Optic nerve seems to be enlarged (Fig. 56). On MRI, an iso-intense mass of the optic-nerve in T1W image and a double ring sign in T2W image with hyper-intense signal due to reaction of the optic-nerve sheath, in the form of leptomeningeal infiltration and proliferation rather than expansion of subarachnoid space [20]. A moderate enhancement is noticed in post-contrast images (Fig. 57).

Type 1 Neurofibromatosis

Figure 58 shows inferior displacement of the left globe and a mass lesion is notable in the lateral side of the eyelid that caused so-called S-shape ptosis. On CT-scan, the greater wing of the sphenoid bone is narrow in the left side, compared to the right (Fig. 59). Figure 59 also shows widening of superior ophthalmic fissure due to the hypoplasia of the greater wing [20] of the sphenoid bone (Mercedes-Benz sign) at neurofibromatosis. Also, a plexiform neurofibroma at the eyelid caused an infiltrative mass of the eyelid causing the S-shape ptosis.

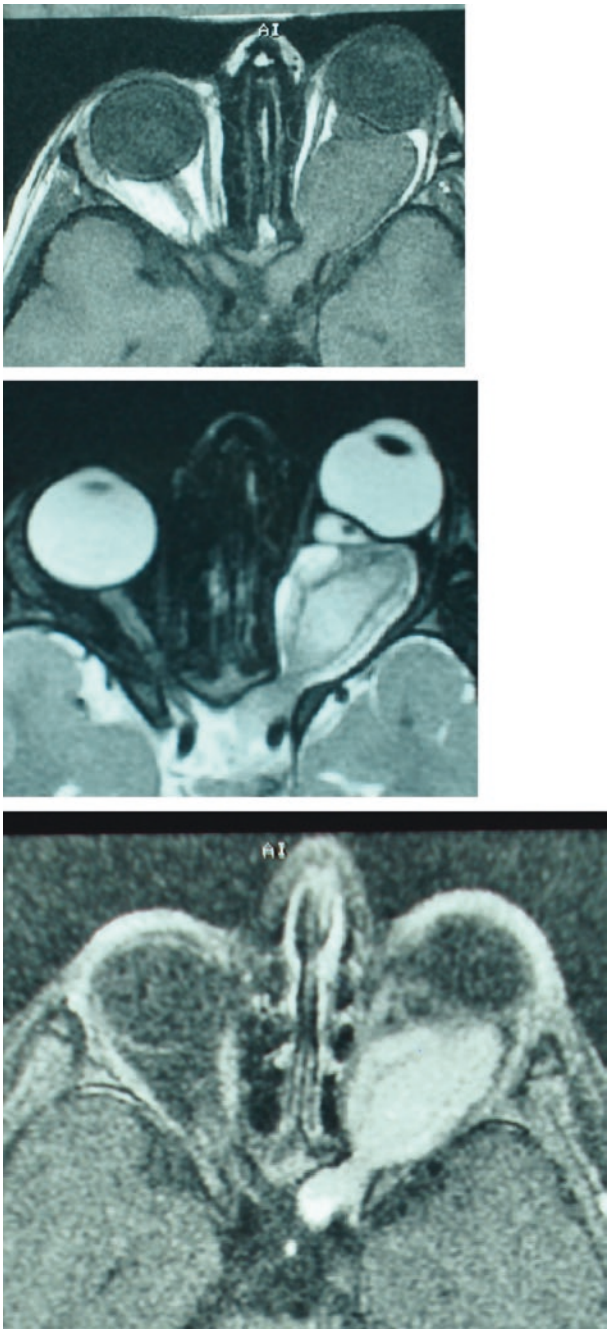

Fig. 57 Optic nerve glioma. Iso-intense on T1W image, hyper-intense on T2W image and high enhancement (**c**)

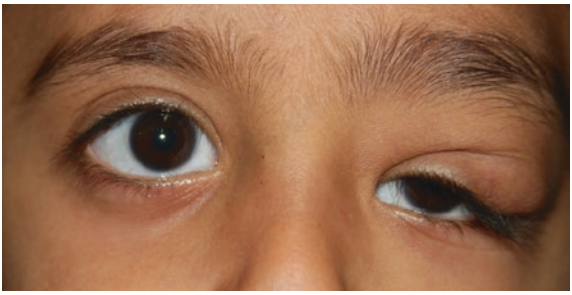

Fig. 58 Inferior displacement of globe and s-shape ptosis are visible at left site

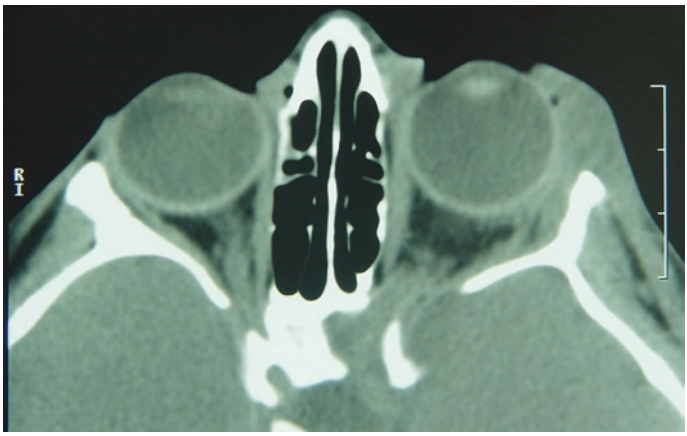

Fig. 59 Hypoplasia of the sphenoid wing and widening of superior ophthalmic fissure are characteristic of type 1 NF

References

1. Winegar BA, Gutierrez JE. Imaging of orbital trauma and emergent non-traumatic conditions. Neuroimaging Clin N Am. 2015;25(3):439–56.
2. Kubal WS. Imaging of orbital trauma. RadioGraphics. 2008;28:1729–39.
3. Gokharman D, Aydin S. Magnetic resonance imaging in orbital pathologies: a pictorial review. J Belg Soc Radiol. 2018;102(1):1–8.
4. Khan SN, Sepahdari AR. Orbital masses: CT and MRI of common vascular lesions, benign tumors, and malignancies. Saudi J Ophthalmol. 2012;26:373–83.
5. Purohit BS, Vargas ML, Ailianou A, Merlini L, Poletti PA, Platon A, et al. Orbital tumours and tumour-like lesions: exploring the armamentarium of multiparametric imaging. Insights Imaging. 2016;7:43–68.
6. Lope LA, Hutcheson KA, Khademian ZP. Magnetic resonance imaging in the analysis of pediatric orbital tumors: utility of diffusion-weighted imaging. J AAPOS. 2010;14(3):257–62.
7. Tanaka A, Mihara F, Yoshiura T, Togao O, Kuwabara Y, Natori Y, Sasaki T, Honda H. Differentiation of cavernous hemangioma from schwannoma of the orbit: a dynamic MRI study. AJR. 2004;183:1799–804.

8. Ferreira TA, Fonk LG, Jaarsma-Coes MG, et al. MRI of uveal melanoma. Cancers. 2019;11:337.
9. Razek AA, Elkhamary S. MRI of retinoblastoma. Br J Radiol. 2011;84(1005):775–84.
10. Lin KY, Ngai Ph, Echegoyen JC, Tao JP. Imaging in orbital trauma. Saudi J Ophthalmol. 2012;26:427–32.
11. Santos D, Monsignore LM, Nakiri GS, Cruz AAV, Colli BO, Abud DG. Imaging diagnosis of dural and direct cavernous carotid fistulae. Radiol Bras. 2014;47(4):251–5.
12. Pokhraj PS, Jigar JP, Mehta C, Narottam AP. Intraocular metallic foreign body: role of computed tomography. J Clin Diagn Res. 2014;8(12):RD01–3.
13. Li J, Zhou L-P, Jin J, Yuan H-F. Clinical diagnosis and treatment of intraorbital wooden foreign bodies. Chin J Traumatol. 2016;19:322–5.
14. Capra GG, Carbone PN, Mullin DP. Paranasal sinus mucocele. Head Neck Pathol. 2012;6:369–72.
15. Aggarwal SK, Bhavana K, Keshri A, Kumar R. Frontal sinus mucocele with orbital complications: management by varied surgical approaches. Asian J Neurosurg. 2012;7(3):135–40.
16. Goncalves ACP, Gebrim EMS, Monteiro MLR. Imaging studies for diagnosing Graves' orbitopathy and dysthyroid optic neuropathy. Clinics (Sao Paulo). 2012;67(11):1327–34.
17. Sepahdari AR, Aakalu VK, Kapur R, Michals EA, Saran N, French A, Mafee MF. MRI of orbital cellulitis and orbital abscess: the role of diffusion-weighted imaging. AJR. 2009;193:W244–50.
18. Karadeniz Uğurlu Ş, Selim S, Kopar A, Songu M. Rhino-orbital mucormycosis: clinical findings and treatment outcomes of four cases. Turk J Ophthalmol. 2015;45(4):169–74.
19. Saeed P, Furth WR, Tanck M, Kooremans F, Freling N, et al. Natural history of spheno-orbital meningiomas. Acta Neurochir. 2011;153:395–402.
20. Milburn JM, Gimenez CR, Dutweiler E. Imaging manifestations of orbital neurofibromatosis type 1. Ochsner J. 2016;16:431–4.

Index

M. Mohammadpour (ed.), *Diagnostics in Ocular Imaging*,
https://doi.org/10.1007/978-3-030-54863-6

I

K

L

M